Conference Proceedings of the Society for Experimental Mechanics Series

James De Clerck · David S. Epp *Editors*

Rotating Machinery, Hybrid Test Methods, Vibro-Acoustics & Laser Vibrometry, Volume 8

Proceedings of the 34th IMAC, A Conference and Exposition on Structural Dynamics 2016

SEM

Springer

Conference Proceedings of the Society for Experimental Mechanics Series

Series Editor
Kristin B. Zimmerman, Ph.D.
Society for Experimental Mechanics, Inc.,
Bethel, CT, USA

More information about this series at http://www.springer.com/series/8922

James De Clerck • David S. Epp
Editors

Rotating Machinery, Hybrid Test Methods, Vibro-Acoustics & Laser Vibrometry, Volume 8

Proceedings of the 34th IMAC, A Conference and Exposition on Structural Dynamics 2016

Springer

Editors
James De Clerck
Mechanical Engineering
Michigan Technological University
Houghton, MI, USA

David S. Epp
Sandia National Laboratory
Albuquerque, NM, USA

ISSN 2191-5644 ISSN 2191-5652 (electronic)
Conference Proceedings of the Society for Experimental Mechanics Series
ISBN 978-3-319-30083-2 ISBN 978-3-319-30084-9 (eBook)
DOI 10.1007/978-3-319-30084-9

Library of Congress Control Number: 2016941278

© The Society for Experimental Mechanics, Inc. 2016
This work is subject to copyright. All rights are reserved by the Publisher, whether the whole or part of the material is concerned, specifically the rights of translation, reprinting, reuse of illustrations, recitation, broadcasting, reproduction on microfilms or in any other physical way, and transmission or information storage and retrieval, electronic adaptation, computer software, or by similar or dissimilar methodology now known or hereafter developed.
The use of general descriptive names, registered names, trademarks, service marks, etc. in this publication does not imply, even in the absence of a specific statement, that such names are exempt from the relevant protective laws and regulations and therefore free for general use.
The publisher, the authors and the editors are safe to assume that the advice and information in this book are believed to be true and accurate at the date of publication. Neither the publisher nor the authors or the editors give a warranty, express or implied, with respect to the material contained herein or for any errors or omissions that may have been made.

Printed on acid-free paper

This Springer imprint is published by Springer Nature
The registered company is Springer International Publishing AG Switzerland

Preface

Rotating Machinery, Hybrid Test Methods, Vibro-Acoustics, and Laser Vibrometry represent one of ten volumes of technical papers presented at the 34th IMAC, A Conference and Exposition on Structural Dynamics, organized by the Society for Experimental Mechanics and held in Orlando, Florida, on January 25–28, 2016. The full proceedings also include volumes on Nonlinear Dynamics; Dynamics of Civil Structures; Model Validation and Uncertainty Quantification; Dynamics of Coupled Structures; Sensors and Instrumentation; Special Topics in Structural Dynamics; Structural Health Monitoring, Damage Detection, and Mechatronics; and Shock and Vibration, Aircraft/Aerospace, Energy Harvesting, Acoustics and Optics, and Topics in Modal Analysis and Testing.

Each collection presents early findings from experimental and computational investigations on an important area within Structural Dynamics. Topics represent papers on enabling technologies for Modal Analysis measurements and applications of Modal Analysis in specific application areas.

The organizers would like to thank the authors, presenters, session organizers, and session chairs for their participation in this track.

Houghton, MI, USA James De Clerck
Albuquerque, NM, USA David S. Epp

Contents

1 Practical Techniques for Scaling of Optically Measured Operating Deflection Shapes 1
Peyman Poozesh, Danilo Damasceno Sabino, Javad Baqersad, Peter Avitabile, and Christopher Niezrecki

2 Prediction of the Coupled Impedance from Frequency Response Data 19
Ramona Fagiani, Elisabetta Manconi, and Marcello Vanali

3 Real-Time State Detection in Highly Dynamic Systems 27
Ryan A. Kettle, Andrew J. Dick, Jacob C. Dodson, Jason R. Foley, and Steven R. Anton

4 Stereo-DIC Measurements of Thermal Gradient Effects on the Vibratory Response of Metals 35
Ryan Berke, Ravinder Chona, Arthur Ding, John Lambros, Eann Patterson, and Christopher Sebastian

5 Modal Testing of a Nose Cone Using Three-Dimensional Scanning Laser Doppler Vibrometry 43
Daniel P. Rohe

6 A Mathematical Model for Determining the Pose of a SLDV 57
Da-Ming Chen and W.D. Zhu

7 Operational Modal Analysis with a 3D Laser Vibrometer Without External Reference 75
Simon Marwitz and Volkmar Zabel

8 Scanning LDV Measurement Technology for Vibration Fatigue Testing 87
Fabrizio Magi, Dario Di Maio, and Ibrahim Sever

9 Optically Detecting Wavefronts and Wave Speeds in Water Using Refracto-Vibrometry 95
Matthew T. Huber, Brent K. Hoffmeister, and Thomas M. Huber

10 Stochastic Wavenumber Estimation: Damage Detection Through Simulated Guided Lamb Waves 105
Garrison N. Stevens, Kendra L. Van Buren, Eric B. Flynn, Sez Atamturktur, and Jung-Ryul Lee

11 Use of Continuous Scanning LDV for Diagnostics 127
Dario Di Maio

12 A Cost Effective DIC System for Measuring Structural Vibrations 139
Markus J. Hochrainer

13 Teaching DSP and Dynamic Measurements at the Graduate Level at Michigan Technological University... 147
Jason R. Blough

14 Flipping the Classroom for a Class on Experimental Vibration Analysis 155
Anders Brandt and Christopher Kjær

15 Lessons Learned from Operational Modal Analysis Courses at the University of Molise 161
Carlo Rainieri and Giovanni Fabbrocino

16 Authentic Engineering Assignments for an Undergraduate Vibration Laboratory Class 169
James P. De Clerck and Jean S. De Clerck

17 Vibration and Acoustic Analysis of Acoustic Guitar in Consideration of Transient Sound 177
Nobuyuki Okubo, Naoaki Iwanaga, and Takeshi Toi

18 Demarcation for the Coupling Strength in the MODENA Approach 187
Peng Zhang, Shaoqing Wu, Yanbin Li, and Qingguo Fei

19 Vibro-Acoustic Modal Model of a Traction Motor for Railway Applications 197
Fredrik Botling, Hanna Amlinger, Ines Lopez Arteaga, and Siv Leth

20 Operational Deflection Shapes of a PWM-Fed Traction Motor 209
Hanna Amlinger, Fredrik Botling, Ines Lopez Arteaga, and Siv Leth

21 Acoustic Fatigue and Dynamic Behavior of Composite Panels Under Acoustic Excitation 219
Canan Uz and Tamer T. Ata

22 Evaluation of Microphone Density for Finite Element Source Inversion Simulation of a Laboratory Acoustic Test 231
Ryan Schultz and Tim Walsh

23 Experimental Mapping of the Acoustic Field Generated by Ultrasonic Transducers 243
Songmao Chen, Christopher Niezrecki, and Peter Avitabile

24 Enhanced Spin-Down Diagnostics for Nondestructive Evaluation of High-Value Systems 255
David Sehloff, Clark Shurtleff, Josh Pribe, Colin Haynes, and John Heit

25 Performing Direct-Field Acoustic Test Environments on a Sandia Flight System to Provide Data for Finite Element Simulation 267
Eric C. Stasiunas, Ryan A. Schultz, and Mike R. Ross

26 Smooth Complex Orthogonal Decomposition Applied to Traveling Waves in Elastic Media 281
Rickey A. Caldwell Jr. and Brain F. Feeny

27 Subspace Algorithms in Modal Parameter Estimation for Operational Modal Analysis: Perspectives and Practices 295
S. Chauhan

28 An Application of Multivariate Empirical Mode Decomposition Towards Structural Modal Identification 303
Ayan Sadhu

29 Dynamic Characterization of Milling Plant Columns 311
Filippo Cangioli, Steven Chatterton, Paolo Pennacchi, and Edoardo Sabbioni

30 Mixed Force and Displacement Control for Base-Isolation Bearings in RTHS 323
Richard Erb, Matthew Stehman, and Narutoshi Nakata

31 Leveraging Hybrid Simulation for Vibration-Based Damage Detection Studies 333
Timothy P. Kernicky, Michael Tedeschi, and Matthew J. Whelan

32 Real Time Hybrid Simulation with Online Model Updating on Highly Nonlinear Device 343
Ge Ou and Shirley J. Dyke

33 Discrete-Time Compensation Technique for Real-Time Hybrid Simulation 351
Saeid Hayati and Wei Song

34 Evaluating the Effectiveness of a Lodengraf Damping Approach for String Trimmers 359
Nicholas Swanson and Jack Leifer

35 Using Operating Data to Locate and Quantify Unbalance in Rotating Machinery 375
Shawn Richardson, Mark Richardson, Jason Tyler, and Patrick McHargue

36 Gear Dynamics Characterization by Using Order-Based Modal Analysis 387
Emilio Di Lorenzo, Antonio Palermo, Simone Manzato, Andrea Dabizzi, Bart Peeters, Wim Desmet, and Francesco Marulo

37 A Design Framework to Improve the Dynamic Characteristics of Double Planet Planetary Gearsets 405
Dylan C. Fyler, Murat Inalpolat, Sang Hwa Lee, and Hyun Ku Lee

38 Dynamics and Pareto Optimization of a Generic Synchronizer Mechanism 417
Muhammad Irfan, Viktor Berbyuk, and Håkan Johansson

39 Modeling and Characterization of a Flexible Rotor Supported by AMB 427
Marcus Vinicius Fernandes de Oliveira, Adriano Borges Silva, Adailton Borges Silva, Edson Hideki Koroish, and Valder Steffen Jr.

40 Nonlinear Reduced Order Modeling of a Curved Axi-Symmetric Perforated Plate: Comparison with Experiments 437
David A. Ehrhardt and Matthew S. Allen

41 Reduced Order Models for Systems with Disparate Spatial and Temporal Scales 447
Shahab Ilbeigi and David Chelidze

42 Using NNMs to Evaluate Reduced Order Models of Curved Beam 457
Christopher I. VanDamme and Matthew S. Allen

43 Simulation of Rotor Damping Assembled by Disc Shrink Fits 471
Lothar Gaul and André Schmidt

44 Developments in the Prediction of Full Field Dynamics in the Nonlinear Forced Response of Reduced Order System Models 481
Sergio E. Obando and Peter Avitabile

45 On the Behaviour of Structures with Many Nonlinear Elements 509
T. Rogers, G. Manson, and K. Worden

46 Estimation of Instantaneous Speed for Rotating Systems: New Processing Techniques 521
Achyut Vemuri, Randall J. Allemang, and Allyn W. Phillips

47 Identification of Breathing Cracked Shaft Models from Measurements 537
Michael I. Friswell, Ralston Fernandes, Nidhal Jamia, and Sami El-Borgi

Chapter 1
Practical Techniques for Scaling of Optically Measured Operating Deflection Shapes

Peyman Poozesh, Danilo Damasceno Sabino, Javad Baqersad, Peter Avitabile, and Christopher Niezrecki

Abstract Operational Modal Analysis (OMA) is used to identify vibration patterns of large structures under unknown operating conditions. However, operating data extracted from output-only measurements is not scaled and cannot be used for Structural Dynamic Modification (SDM), frequency response function (FRF) synthesis, force estimation and structural response simulation. Therefore, developing an algorithm that is able to extract scaled mode shapes using measured operating data is desirable. In the current paper, two different scaling techniques including drive point scaling as well as mass sensitivity scaling are employed to scale optically measured operating deflection shapes (ODS). To evaluate the capability of each scaling technique, the scaled optically measured operating shapes are compared to mode shapes extracted using input–output measurements (reference mode shapes). Additionally, the scaled operating shapes are used in structural dynamic modification to demonstrate the benefits and drawbacks associated with the mass sensitivity technique. The results reveal that both mass sensitivity and drive point scaling techniques are capable of effectively scaling optically measured operating deflection shapes of the structure.

Keywords Operating deflection shapes • Scaling techniques • Operational modal analysis • Digital image correlation • Structural dynamics • Mass sensitivity

Nomenclature

$\{\Psi\}_{k1}$	ODS of the unmodified structure
$[M_1]$	Mass matrix of the unmodified structure
$\{\Psi\}_{k2}$	ODS of the modified structure
$[K_1]$	Stiffness matrix of the unmodified structure
$[E_1]$	Scaled ODS of the unmodified structure
$[M_2]$	Mass matrix of the modified structure
$[E_2]$	Scaled ODS of the modified structure
$[K_2]$	Stiffness matrix of the modified structure
$[E_{12}^{un}]$	Unscaled mode contribution matrix
$[A(s)]$	Residue matrix
$[\tilde{E}_2]$	Estimated mode shapes of the modified structure
α_k	Initial scaling factor for unmodified structure
$[E_{12}]$	Scaled mode contribution matrix
β_k	Initial scaling factor for modified structure
$[E_{ref}]$	Reference shapes extracted using input–output measurement
ω_{k1}	Natural frequencies of unmodified structure
p_k	Pole location
ω_{k2}	Natural frequencies of modified structure
$[\Delta M_{12}]$	Mass modification matrix

P. Poozesh (✉) • J. Baqersad • P. Avitabile • C. Niezrecki
Structural Dynamics and Acoustic Systems Laboratory, University of Massachusetts Lowell, One University Avenue, Lowell, MA 01854, USA
e-mail: Peyman_Poozeshstudent.uml.edu

D.D. Sabino
Unive Estadual Paulista, Ilha Solteira, SP, Brazil

© The Society for Experimental Mechanics, Inc. 2016

J. De Clerck, D.S. Epp (eds.), *Rotating Machinery, Hybrid Test Methods, Vibro-Acoustics & Laser Vibrometry, Volume 8*, Conference Proceedings of the Society for Experimental Mechanics Series, DOI 10.1007/978-3-319-30084-9_1

1.1 Introduction

Experimental Modal Analysis (EMA), based on input–output system identification technique, is extensively employed to identify dynamic characteristics of structures. In this approach, modal parameters of a structure can be identified using known applied forces and the measured responses [1]. However, there are some cases that measuring input forces is an arduous task and requires expensive tools [2, 3]. Unlike EMA, Operational Modal Analysis (OMA) is a technique that estimates modal parameters of the structure using the vibration response measurements [4, 5]. Because the input forces are not measured in OMA, the extracted shapes that are called unscaled operating mode shape are not mass normalized [6, 7]. These unscaled operating deflections shapes cannot be used for further structural dynamic studies such as damage detection, model updating, structural modification and force estimation. Several approaches based on updating finite element model and structural dynamic modification have been proposed to scale operating deflection shapes [8, 9]. Researchers have also used the single drive point measurement and mass sensitivity techniques to scale operating deflection shapes measured using conventional sensors [10, 11].

Using a single drive point measurement, the scale of each mode shape at the drive point location can be computed. The value of mode shapes at the drive point is then used to scale the operating deflection shapes. With this method, it is possible to only scale a single mode without the knowledge of any other modes. It is worth mentioning that this technique requires at least one force measurement [10]. After extracting the scaled mode shapes and poles (frequency and damping values), a FRF synthesis can be performed using operating data. The newly synthesized set of FRFs can accurately describe the system's dynamic behavior for the specified frequency range.

Mass sensitivity technique uses the structure's sensitivity to a change in mass to calculate the scaling factor. Adding a small mass to the structure will result in a shift in resonant frequencies. This frequency shift can be related to the derivative of the eigenvalue. Using this fact, the scaling factor can be extracted from operating data with no force measurement [12, 13]. The ideal mass modification in this technique depends on the mass and the flexibility of the structure. However, the mass modification must be small enough to prevent significant change in the mode shapes of the structure [14]. Aenlle et al. [11] proposed two mass sensitivity techniques based on structural dynamic modification and the accuracy of each method was evaluated by using simulated models. Furthermore, Parloo et al. [15] used mass sensitivity technique to scale the operating deflection shapes of a bridge. In another effort, Brincker et al. [14] utilized the mass change technique to estimate the scaling factors associated with operating deflections shapes of a four story building. In addition, the uncertainties on the estimated scaling factors using different mass sensitivity techniques were evaluated. In another work by Aenlle et al. [9], a technique was proposed to optimize the mass change strategy including the number, locations and the weight of the masses. Khatibi et al. [16] showed that mass-stiffness change can be effective in scaling operating deflection shapes. The numerical and experimental results revealed that the stiffness change method shows the same higher effect on the accuracy of the lower order modes than mass change method. Therefore, it was suggested that mass sensitivity technique in conjunction with the stiffness change technique is more effective than only the mass sensitivity technique in scaling operating deflection shapes extracted from output-only measurements.

Three-dimensional (3D) digital image correlation (DIC) and three-dimensional point tracking (3DPT) are non-contacting measurement approaches that provide alternatives to traditional measurement sensors and LDVs [17–19]. Both 3D DIC and 3DPT are based on stereophotogrammetry principles and rely on a pair of digital cameras to capture images of the structure over a period of time. For the DIC approach, speckled patterns are applied to a structure and can be used to obtain full-field displacement and strain over the entire area of interest. Likewise, 3DPT can be used to measure displacement at discrete points by mounting optical targets to the structure. DIC and 3DPT have matured over the last two decades and have been primarily applied to the field of experimental solid mechanics [20, 21]. However, more recently researchers have begun to exploit optically based approaches for measuring vibration and transient phenomena in turbine blades and rotors. There have been several published papers that use photogrammetry in conjunction with Operational Modal Analysis to measure vibration in non-rotating and rotating turbine blades [20, 22].

The current paper is built on a foundation of research to understand how to use a non-contact stereophotogrammetry technique with output-only system identification methods to accurately estimate modal parameters in a structure during operation. Within this paper, the single drive point measurement techniques as well as the mass sensitivity technique are employed to evaluate the effectiveness of each technique in scaling operating deflections shapes. Furthermore, the traditional mass sensitivity technique is improved by introducing SDM process and using the mode contribution matrix. The modal assurance criteria (MAC) [23], orthogonally check, and structural dynamic modification (SDM) [25] are the tools that will be used to evaluate the effectiveness of each of the scaling techniques.

1.2 Theoretical Background

Within the current paper, two significant techniques are utilized, drive point scaling and mass sensitivity scaling. Both techniques are described in the following sections.

1.2.1 Drive Point Scaling Technique

The operating deflections shapes tend to be highly correlated with the corresponding mode shape of the system. This correlation can be expressed as

$$\{\mathrm{u}\}_\mathrm{k} = \alpha_\mathrm{k}\{\Psi\}_\mathrm{k} \tag{1.1}$$

where $\alpha_{0\mathrm{k}}$ is the scale factor between the operating deflection shapes ($\{\Psi\}_\mathrm{k}$) and the scaled mode shapes ($\{\mathrm{u}\}_\mathrm{k}$) at the k^th^ mode of the structure. The scaled mode shapes and operating deflection shapes can be expressed as

$$\begin{Bmatrix} \mathrm{u}_{1\mathrm{k}} \\ \mathrm{u}_{2\mathrm{k}} \\ \mathrm{u}_{3\mathrm{k}} \\ \vdots \end{Bmatrix} = \{\mathrm{u}\}_\mathrm{k}, \begin{Bmatrix} \mathrm{o}ds_{1\mathrm{k}} \\ \mathrm{o}ds_{2\mathrm{k}} \\ \mathrm{o}ds_{3\mathrm{k}} \\ \vdots \end{Bmatrix} = \{\Psi\}_\mathrm{k} \tag{1.2}$$

The drive point scaling technique relies on the use of a single drive point measurement to properly scale operating deflection shapes. The FRF obtained from the single drive point measurement can be shown as

$$[\mathrm{H}(\mathrm{s})]_{\mathrm{s}=\mathrm{j}\omega} = [\mathrm{H}(\mathrm{j}\omega)] = \sum_{\mathrm{k}=1}^{\mathrm{m}} \frac{[\mathrm{A}_\mathrm{k}]}{(\mathrm{j}\omega - \mathrm{p}_\mathrm{k})} + \frac{[\mathrm{A}_\mathrm{k}^*]}{(\mathrm{j}\omega - \mathrm{p}_\mathrm{k}^*)} \tag{1.3}$$

For a particular mode k, Eq. (1.3) can be expressed as

$$[\mathrm{H}(\mathrm{s})]_{\mathrm{s}=\mathrm{p}_\mathrm{k}} = \{\mathrm{u}_\mathrm{k}\}\frac{\mathrm{q}_\mathrm{k}}{\mathrm{s}-\mathrm{p}_\mathrm{k}}\{\mathrm{u}_\mathrm{k}\}^\mathrm{T} \tag{1.4}$$

with the residue matrix calculated using

$$[\mathrm{A}(\mathrm{s})]_\mathrm{k} = \mathrm{q}_\mathrm{k}\{\mathrm{u}_\mathrm{k}\}\{\mathrm{u}_\mathrm{k}\}^\mathrm{T} \tag{1.5}$$

Equation (1.5) can be further simplified for a single reference point as

$$\begin{Bmatrix} \mathrm{a}_{1\mathrm{k}} \\ \mathrm{a}_{2\mathrm{k}} \\ \mathrm{a}_{3\mathrm{k}} \\ \vdots \end{Bmatrix} = \mathrm{q}_\mathrm{k}\mathrm{u}_{\mathrm{rk}} \begin{Bmatrix} \mathrm{u}_{1\mathrm{k}} \\ \mathrm{u}_{2\mathrm{k}} \\ \mathrm{u}_{3\mathrm{k}} \\ \vdots \end{Bmatrix} \to \mathrm{a}_{\mathrm{ijk}} = \mathrm{q}_\mathrm{k}\mathrm{u}_{\mathrm{ik}}\mathrm{u}_{\mathrm{jk}}, \ \mathrm{q}_\mathrm{k} = \frac{1}{2\mathrm{j}\omega_\mathrm{k}} \tag{1.6}$$

where u_{ik} and u_{jk} are the k^th^ mode of the structure at point i and j respectively. The residues are directly related to the system mode shapes and are scaled by q_k, the scaling constant for the k^th^ mode. From Eq. (1.6), it becomes evident that by taking a measurement at the drive point location, u_{rk}, a value for modal scaling can be determined. The drive point measurement provides a scaled mode shape for the drive point DOF as

$$\mathrm{a}_{\mathrm{rrk}} = \mathrm{q}_\mathrm{k}\mathrm{u}_{\mathrm{rk}}\mathrm{u}_{\mathrm{rk}} \tag{1.7}$$

With this drive point scaling, the scaled mode shapes, for the corresponding drive point measurement location, can be used to scale the operating mode shapes

$$\text{Scaled Operating Mode Shape} \rightarrow \begin{Bmatrix} \mathrm{ods}_{1k} \\ \mathrm{ods}_{2k} \\ \vdots \\ \mathrm{ods}_{ik} \\ \vdots \\ \mathrm{ods}_{nk} \end{Bmatrix} \frac{\mathrm{u}_{rk}}{\mathrm{ods}_{rk}} \tag{1.8}$$

It is important to note that the reference location selected for the operating deflection shape extraction does not need to be the same as the drive point selected for the scaling of the operating deflection shapes [10].

1.2.2 Mass Sensitivity Scaling Technique

Unlike the drive point scaling, the mass sensitivity scaling technique requires no FRF measurements. This technique relies on the sensitivity of the eigensolution of the system to an adequate change in the mass [15]. By adding masses to the structure, a shift in its natural frequency occurs. The frequency shift coupled with the value of the mass modification can be measured and used to determine the effective scaling constant. The eigensolution for a system without damping is

$$\left[[\mathrm{K}_1] - \omega_{k1}^2 [\mathrm{M}_1]\right] \alpha_k \{\Psi\}_{k1} = 0 \tag{1.9}$$

where $\{\Psi\}_{k1}$ is the unscaled mode shape of the original structure, ω_{k1} the natural frequency, $[M_1]$ mass matrix and $[K_1]$ the stiffness matrix. After mass modification ($[M + \Delta M]$), the new eigenvalues and eigenvectors can be found using

$$\left[[\mathrm{K}_1] - \omega_{k2}^2 [\mathrm{M}_1 + \Delta M_{12}]\right] \alpha_k \{\Psi\}_{k2} = 0 \tag{1.10}$$

where $\{\Psi\}_{k2}$ and ω_{k2} are the operating deflection shape and natural frequencies of the modified structures. Subtracting Eq. (1.10) from Eq. (1.9) gives a relation between these two equations. This relation will be used further in determining the scaling factors

$$[\mathrm{K}_1] \left(\alpha_k \{\Psi\}_{k1} - \alpha_k \{\Psi\}_{k2}\right) - [\mathrm{M}_1] \left(\alpha_k \{\Psi\}_{k1} \omega_{k1}^2 - \alpha_k \{\Psi\}_{k2} \omega_{k2}^2\right) - [\Delta \mathrm{M}_{12}] \alpha_k \{\Psi\}_{k2} \omega_{k2}^2 = 0 \tag{1.11}$$

Equation (1.11) can be greatly simplified by assuming that change in the mode shape due to the small mass modification is unnoticeable.

$$\{\Psi\}_{k1} = \begin{Bmatrix} ods_{11k} \\ ods_{12k} \\ \vdots \\ ods_{1ik} \\ \vdots \\ ods_{1nk} \end{Bmatrix}, \{\Psi\}_{k2} = \begin{Bmatrix} ods_{21k} \\ ods_{22k} \\ \vdots \\ ods_{2ik} \\ \vdots \\ ods_{2nk} \end{Bmatrix} \rightarrow \{\Psi\}_{k1} \cong \{\Psi\}_{k2} \cong \{\Psi\}_k \tag{1.12}$$

By assuming that mode shapes do not change after mass modification, Eq. (1.11) will be simplified as

$$\alpha_k \{\Psi\}_k^{\mathrm{T}} [\mathrm{M}_1] \alpha_k \{\Psi\}_k \left(\omega_{k1}^2 - \omega_{k2}^2\right) - \alpha_k \{\Psi\}_k^{\mathrm{T}} [\Delta \mathrm{M}_{12}] \alpha_k \{\Psi\}_k \omega_{k2}^2 = 0 \tag{1.13}$$

Scaled mode shapes ($[M_1]$) possesses the orthogonality properties given as

$$[\mathrm{E}_1]^{\mathrm{T}} [\mathrm{M}_1] [\mathrm{E}_1] = [\mathrm{I}] \rightarrow \alpha_k^2 \{\Psi\}_k^{\mathrm{T}} [\mathrm{M}_1] \{\Psi\}_k = 1 \tag{1.14}$$

Taking into account the orthogonality of mode shapes with respect to mass, Eq. (1.13) can be simplified as

$$\left(\omega_{k1}^2 - \omega_{k2}^2\right) - \alpha_k^2 \{\Psi\}_k^T \left[\Delta M_{12}\right] \{\Psi\}_k \omega_{k2}^2 = 0 \tag{1.15}$$

Equation (1.15) can now be solved for the scale factor, and the resultant equation is

$$\alpha_k = \sqrt{\frac{\left(\omega_{k1}^2 - \omega_{k2}^2\right)}{\omega_{k2}^2 \{\Psi\}_k^T \left[\Delta M_{12}\right] \{\Psi\}_k}} \tag{1.16}$$

Equation (1.16) is similar to the equation developed by Parloo et al. [24]. As can be seen from Eq. (1.16), only the operating deflection shapes and the resonant frequencies are needed to find the scaling factor associated to each mode. To determine scaling factors using Eq. (1.16), both modified and unmodified operating shapes can be used.

1.2.3 *Structural Dynamic Modification*

Because of several assumptions made to develop the mass sensitivity scaling technique, some sources of errors are present [10]. The structural dynamic modification concepts in conjunction with the mass sensitivity technique are used to evaluate the merits associated with the mass sensitivity technique. The basis for the theory of structural dynamic modification is directly related to the equation of motion [11]. The equation of motion for the modified structure in modal space is represented as

$$\left[\begin{bmatrix} \ddots & & \\ & I & \\ & & \ddots \end{bmatrix} + \left[\overline{\Delta M}_{12}\right]\right] \{P_2\} + \begin{bmatrix} \ddots & & \\ & \omega_2^2 & \\ & & \ddots \end{bmatrix} \{P_2\} = [0] \tag{1.17}$$

Modal mass modification matrix ($\overline{\Delta M}_{12}$), can be calculated using

$$\left[\overline{\Delta M}_{12}\right] = \left[E_1\right]^T \left[\Delta M_{12}\right] \left[E_1\right] \tag{1.18}$$

It is important to note that while part of Eq. (1.17) contains a diagonal representation of the modal mass of the original system, the modal mass modification part ($\left[\overline{\Delta M}_{12}\right]$) is not diagonal, and therefore Eq. (1.17) is coupled.

The eigenvector ($[E_{12}]$) is obtained from the eigensolution for Eq. (1.17) and can be used to transform from original modal space (unmodified system) to second modal space (modified structure).

$$\{P_1\} = \left[E_{12}\right] \{P_2\} \tag{1.19}$$

Equation (1.19) uncouples the set of equations that were coupled from modification from the original unmodified state to the second modified state. The original modal transformation is given by

$$\{X\} = \left[E_1\right] \{P\} \tag{1.20}$$

Substituting Eq. (1.19) into Eq. (1.20) will give

$$\{X\} = \left[E_1\right] \left[E_{12}\right] \{P_2\} \tag{1.21}$$

Estimated scaled mode shapes of the modified structure are obtained from linear combination of the unmodified scaled modes shapes with the normalizing matrix given as

$$\left[\tilde{E}_2\right] = \left[E_1\right] \left[E_{12}\right] \tag{1.22}$$

Equation (1.22), can be used to approximate the modified modal parameters due to structural changes using only the original modal parameters of the structure [25]. Figure 1.1 shows the mass modification process of a structure using SDM. The

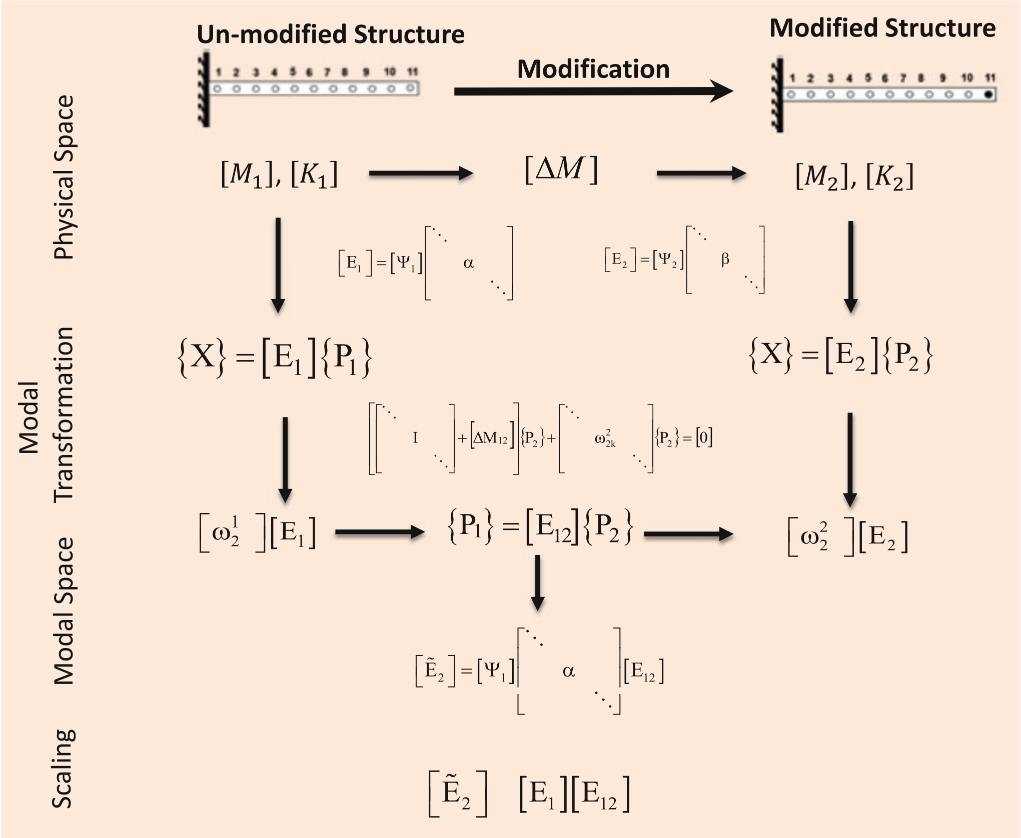
Un-modified Structure
Modification
Modified Structure
1 2 3 4 5 6 7 8 9 10 11
Physical Space
Modal Transformation
Modal Space
Scaling
$[M_1], [K_1]$
$[\Delta M]$
$[M_2], [K_2]$
$[E_1]=[\Psi_1]\begin{bmatrix}\ddots & & \\ & \alpha & \\ & & \ddots\end{bmatrix}$
$[E_2]=[\Psi_2]\begin{bmatrix}\ddots & & \\ & \beta & \\ & & \ddots\end{bmatrix}$
$\{X\}=[E_1]\{P_1\}$
$\{X\}=[E_2]\{P_2\}$
$\left[\begin{bmatrix}\ddots & & \\ & I & \\ & & \ddots\end{bmatrix}+[\Delta M_{12}]\right]\{P_2\}+\begin{bmatrix}\ddots & & \\ & \omega_{2k}^2 & \\ & & \ddots\end{bmatrix}\{P_2\}=[0]$
$[\omega_2^1][E_1]$
$\{P_1\}=[E_{12}]\{P_2\}$
$[\omega_2^2][E_2]$
$[\tilde{E}_2]=[\Psi_1]\begin{bmatrix}\ddots & & \\ & \alpha & \\ & & \ddots\end{bmatrix}[E_{12}]$
$[\tilde{E}_2]\ [E_1][E_{12}]$

Fig. 1.1 A schematic of the structural dynamic modification algorithm used to estimate the scaled mode shapes from operating deflection shapes of the modified and unmodified structure

scaling factors for modified and unmodified structures can be found using

$$\alpha_k = \sqrt{\frac{\left(\omega_{k1}^2 - \omega_{k2}^2\right)}{\omega_{k2}^2\{\Psi\}_{k1}^T\,[\Delta M_{12}]\,\{\Psi\}_{k1}}} \tag{1.23}$$

$$\beta_k = \sqrt{\frac{\left(\omega_{k1}^2 - \omega_{k2}^2\right)}{\omega_{k2}^2\{\Psi\}_{k2}^T\,[\Delta M_{12}]\,\{\Psi\}_{k2}}} \tag{1.24}$$

Because operating deflection shapes tend to be highly correlated with the corresponding scaled mode shapes of the system, the scaled mode shapes of the unmodified and modified structure can be expressed as

$$[E_1] = [\Psi_1]\begin{bmatrix}\ddots & & \\ & \alpha & \\ & & \ddots\end{bmatrix} \tag{1.25}$$

$$[E_2] = [\Psi_2]\begin{bmatrix}\ddots & & \\ & \beta & \\ & & \ddots\end{bmatrix} \tag{1.26}$$

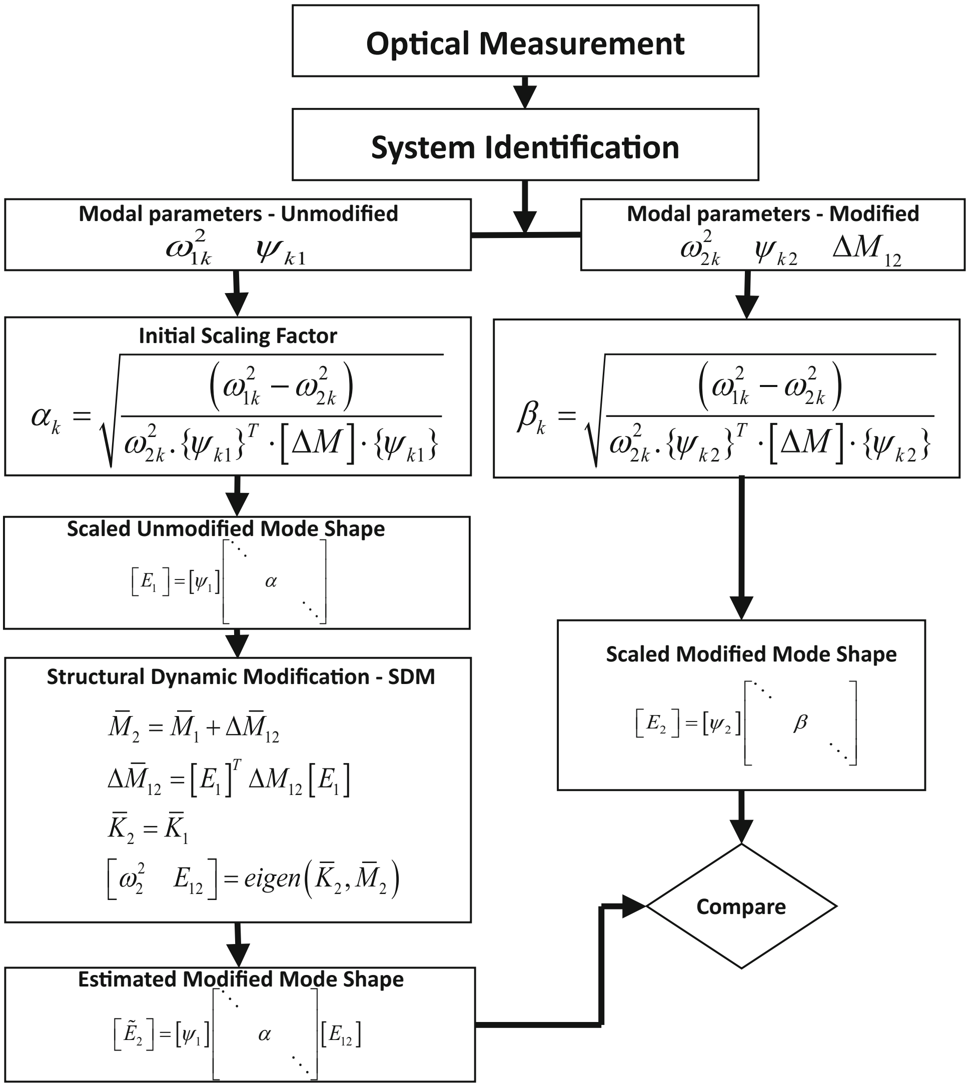
Optical Measurement
System Identification
Modal parameters - Unmodified
$\omega_{1k}^2 \quad \psi_{k1}$
Modal parameters - Modified
$\omega_{2k}^2 \quad \psi_{k2} \quad \Delta M_{12}$
Initial Scaling Factor
$\alpha_k = \sqrt{\frac{(\omega_{1k}^2 - \omega_{2k}^2)}{\omega_{2k}^2 \cdot \{\psi_{k1}\}^T \cdot [\Delta M] \cdot \{\psi_{k1}\}}}$
$\beta_k = \sqrt{\frac{(\omega_{1k}^2 - \omega_{2k}^2)}{\omega_{2k}^2 \cdot \{\psi_{k2}\}^T \cdot [\Delta M] \cdot \{\psi_{k2}\}}}$
Scaled Unmodified Mode Shape
$[E_1] = [\psi_1]\begin{bmatrix} \ddots & & \\ & \alpha & \\ & & \ddots \end{bmatrix}$
Scaled Modified Mode Shape
$[E_2] = [\psi_2]\begin{bmatrix} \ddots & & \\ & \beta & \\ & & \ddots \end{bmatrix}$
Structural Dynamic Modification - SDM
$\bar{M}_2 = \bar{M}_1 + \Delta\bar{M}_{12}$
$\Delta\bar{M}_{12} = [E_1]^T \Delta M_{12} [E_1]$
$\bar{K}_2 = \bar{K}_1$
$[\omega_2^2 \quad E_{12}] = eigen(\bar{K}_2, \bar{M}_2)$
Compare
Estimated Modified Mode Shape
$[\tilde{E}_2] = [\psi_1]\begin{bmatrix} \ddots & & \\ & \alpha & \\ & & \ddots \end{bmatrix}[E_{12}]$

Fig. 1.2 A flowchart showing the scaling of the modified and unmodified structure using mass sensitivity and comparison between estimated mode shapes and experimentally measured shapes

Using Eqs. 1.25 and 1.26, the estimated mode shape of the modified structure can be shown as

$$[\tilde{E}_2] = [\Psi_1]\begin{bmatrix} \ddots & & \\ & \alpha & \\ & & \ddots \end{bmatrix}[E_{12}] \tag{1.27}$$

The procedure shown in Fig. 1.2 is a general theory for the eigenvalue modification from SDM and scaling operating shapes using the mass sensitivity technique.

1.3 Experimental Test Setup

A measurement to experimentally validate the proposed approach for scaling operating deflections shapes was performed on a 5-ft cantilevered aluminum beam (see Fig. 1.3). The cross section of the beam was a rectangular tube with dimensions of 1-in by 2-in and a thickness of 1/8-in. One stereovision system composed of two synchronized complementary metal-oxide

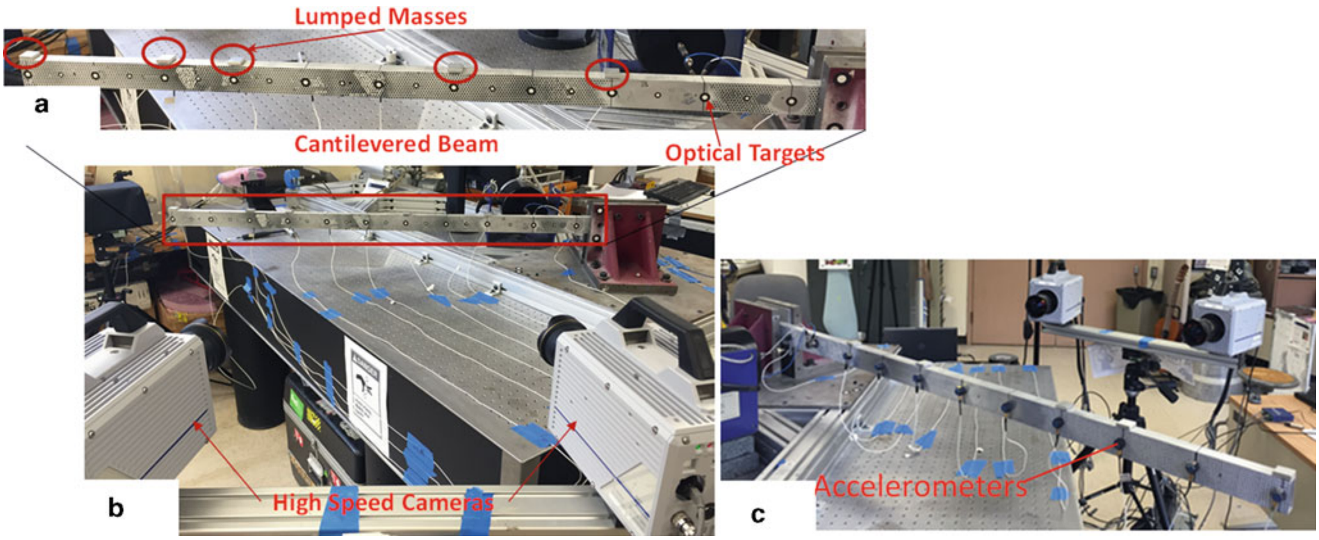

Fig. 1.3 A photo of the test setup showing the measurement system and test structure; (**a**) optical measurement system including two CMOS cameras and position of optical targets mounted on the cantilevered beam, (**b**) lumped masses distributed on the beam to quantify the sensitivity of the structure to the mass changes. (**c**) Locations of accelerometer mounted to the beam

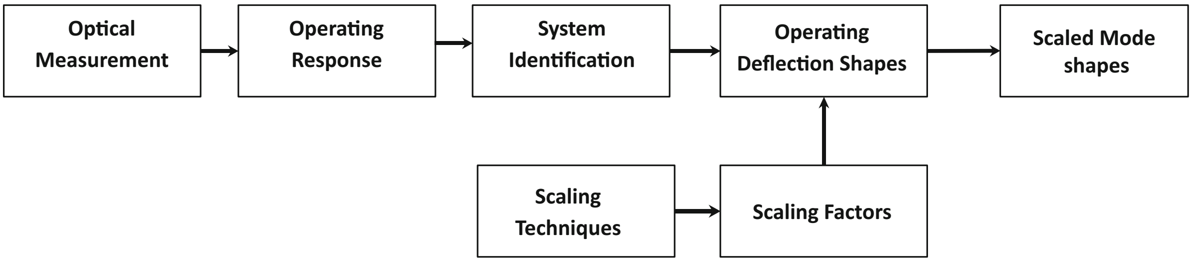

Fig. 1.4 A flowchart showing the scaling of optically measured operating deflection shapes using output only system identification

semiconductor (CMOS) high speed cameras were used to capture the operating response of the beam to the impulse excitation. Figure 1.4a shows a pair of four megapixel (2048 × 2048 pixels) PHOTRON high-speed cameras equipped with 14-mm lenses used for the measurement. The procedure to identify lens distortions was performed by calibrating individual cameras and capturing a series of images from a 1-m calibration cross in different positions/orientations for each camera. The final image was taken when the cameras were installed in their final positions relative to the beam allowing for the identification of the camera positions with respect to each other. The calibration deviation (average intersection error) for the test was calculated as 0.0225 pixels (0.007 mm for the measured field of view). According to the PONTOS™ user manual [26] for a good calibration, the calibration deviation needs to be less than or equal to 0.04 pixels. The stereo-vision system was placed approximately 1.3-m away from the beam such that the entire beam was fitted in the field of view of each camera (see Fig. 1.3). The system was configured to record at a rate of 1500 frame per second. Furthermore, proper illumination was provided using several lights.

To conduct a good operational modal test, general testing rules similar to a traditional modal test must be followed. To capture the mode shapes of the system, 3DPT technique in conjunction with stochastic subspace system identification (SSI) [27, 28] were employed to estimate dynamic characteristics of the beam. A set of eleven optical targets were mounted along the length of the beam (see Fig. 1.3). This arrangement of optical targets results in a proper spatial resolution of the identified operating deflection shapes. The measurement locations and position of cameras are shown in Fig. 1.3.

To perform the drive point measurement, a 100 mv/g accelerometer was mounted to the tip of the beam and an impulse signal generated by an impact hammer was used to excite the beam at the location of the accelerometer (tip of the beam). The acquired data was processed in LMS Test. Lab [29] to compute the FRF used to scale in the drive point scaling technique. The optical measurement system and 3DPT were used to capture the operating vibration response of the beam subjected to the single impact test. The measured response of the beam was processed using SSI to extract the operational deflection shapes and natural frequencies of the structure. Furthermore, eleven 100 mv/g PCB accelerometers were mounted to the opposite side of the beam in longitudinal locations similar to the optical targets to conduct a modal survey using input–output system identification as the reference data (Fig. 1.3c)

1.4 Test Cases Studied

Two different scaling techniques were employed to scale deflection shapes extracted using the operating response of the cantilevered beam subjected to the single impact. The location of the reference point and drive point were chosen to be at the tip of the beam. The operating data was collected using the 3DPT technique and then modal parameters of the structure were extracted using SSI. Figure 1.4 represents the workflow that was used to scale the operating deflection shapes. The first operational modal analysis was carried out on the unmodified structure, and then operating shapes were scaled using the drive point scaling technique. Furthermore, the mass sensitivity technique was used to estimate appropriate scaling factors to scale operating deflection shapes. The effectiveness of each technique was evaluated using different correlation tools such as the modal assurance criteria (MAC) and orthogonality check.

1.4.1 Case A: Drive Point Measurement

The first scaling approach uses a drive point measurement to scale the optically measured operating deflection shapes of the cantilevered beam. This technique is a linear transformation that scale the deflection shapes by a scaling factor. The scaling factor is calculated by dividing the value of mode shapes (extracted using experimental modal analysis) by the value of the ODS at the drive point degree of freedom, (see Eq. 1.8). These scaling factors can be represented by a diagonal matrix. To scale a deflection shape by a computed scaling vector, each point at different modes would need to be multiplied with this scaling vector.

Orthogonality between the reference shapes (input–output measurement) and scaled operating shapes can be computed using

$$\left[[\Psi_{\mathrm{k}}] \begin{bmatrix} \ddots & & \\ & \alpha & \\ & & \ddots \end{bmatrix} \right]^{T} [M]\,[\mathrm{E}_{\mathrm{ref}}] \Rightarrow \mathit{Orthogonality} \tag{1.28}$$

Mass matrix in Eq. (1.28) is experimental mass given as

$$[M] = [\mathrm{E}_{\mathrm{ref}}]^{g^{T}} [\mathrm{E}_{\mathrm{ref}}]^{g} \tag{1.29}$$

Figure 1.5 compares the optically measured operating deflection shapes to reference mode shapes (EMA). The differences between unscaled operating shapes and scaled mode shapes (see Fig. 1.5) indicates the importance of finding an appropriate scaling factor. As can be seen in Fig. 1.6, the scaled ODS shows an excellent agreement with the reference mode shapes. The correlation of the scaled operating shapes and reference mode shapes are depicted in Fig. 1.7. All four scaled operating shapes show strong correlations to the reference mode shapes. As can be seen in Fig. 1.7, high orthogonality between impact test (input–output measurement) and scaled operating shaped indicates that operating shapes are well correlated with reference modes in both shapes and scale.

1.4.2 Case B: Mass Sensitivity Scaling Technique

As the second approach in this paper, the operating data was scaled using the conventional mass sensitivity approach. The mass sensitivity technique relies on the amount of mass added to the structure as well as the size of the added masses. With small mass changes, the frequency shift will be minimal and it may be impossible to appropriately scale the data using mass sensitivity. On the other hand, large mass changes will result in mode distortion and consequently in-accurate scaling factors.

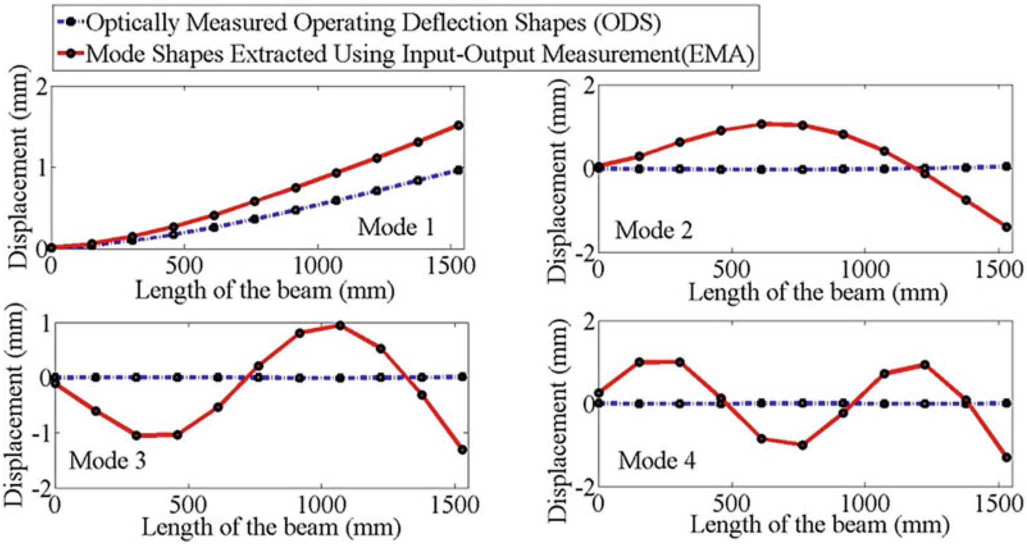

Fig. 1.5 Comparison of the operating deflection shapes (OMA test) and reference mode shapes (input–output measurement) for the first four bending modes

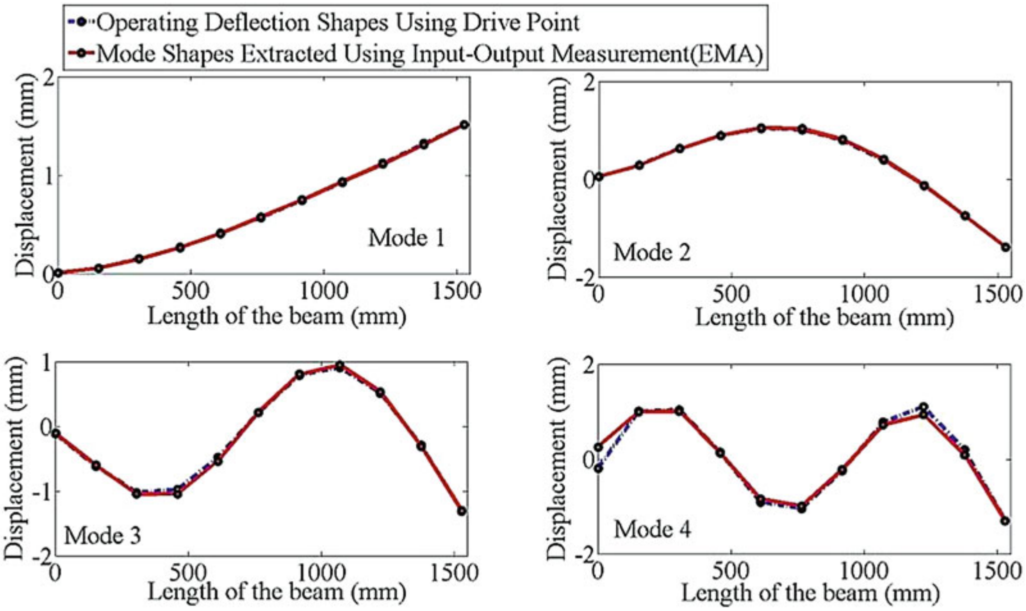

Fig. 1.6 Comparison of the scaled operating deflection shapes (OMA test) using the drive point technique and reference mode shapes (input–output measurement) for the first four bending modes

Therefore, selecting appropriate mass to evaluate the sensitivity of the structure to mass changes is critical. Within this work, five lumped mass modifications (6 % of the beam's weight) are used to examine the sensitivity of the beam to the mass changes. The estimated natural frequencies of the unmodified and modified structure using SSI for the first four bending modes are shown in Fig. 1.8.

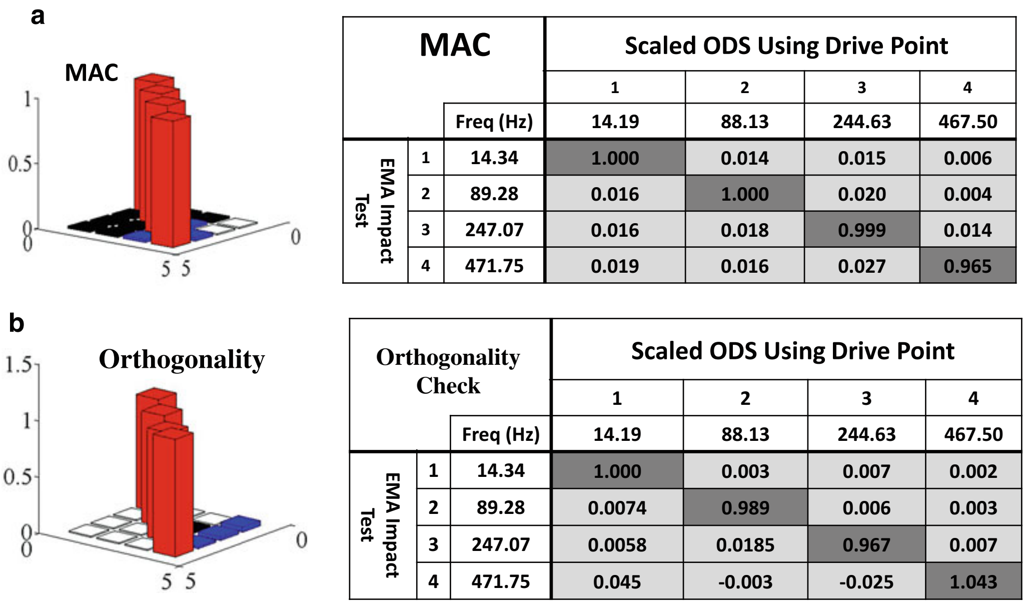

MAC		Scaled ODS Using Drive Point			
		1	2	3	4
	Freq (Hz)	14.19	88.13	244.63	467.50
EMA Impact Test 1	14.34	1.000	0.014	0.015	0.006
2	89.28	0.016	1.000	0.020	0.004
3	247.07	0.016	0.018	0.999	0.014
4	471.75	0.019	0.016	0.027	0.965

Orthogonality Check		Scaled ODS Using Drive Point			
		1	2	3	4
	Freq (Hz)	14.19	88.13	244.63	467.50
EMA Impact Test 1	14.34	1.000	0.003	0.007	0.002
2	89.28	0.0074	0.989	0.006	0.003
3	247.07	0.0058	0.0185	0.967	0.007
4	471.75	0.045	-0.003	-0.025	1.043

Fig. 1.7 Correlation between operating deflections shapes, scaled using drive point measurement, and reference mode shapes. (**a**) MAC values indicating degree of consistency between scaled operating shapes and reference mode shapes (input–output measurement). (**b**) Experimental mass weighted orthogonality check between the scaled operating shapes and reference modal vectors

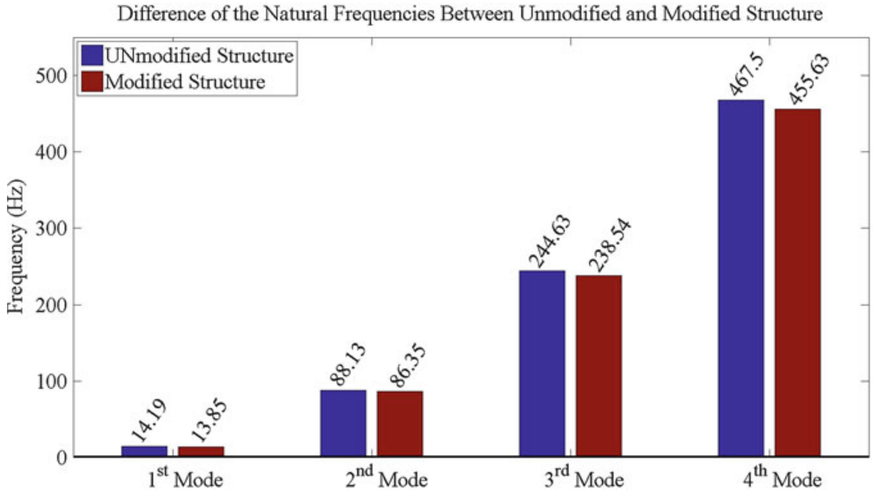

Fig. 1.8 Comparison of the natural frequencies of the modified (*red bar*) and unmodified (*blue bar*) cantilevered beam estimated using stochastic subspace identification (SSI)

1.4.3 Case B.1: Estimating Mode Shapes of the Modified Structure Using Unscaled Deflection Shapes

Structural dynamic modification can be used to find the mode shapes of a modified structure using the modes of the original structure and the mode contribution matrix ($[E_{12}]$). In order to demonstrate the necessity of scaling ODS, the operating shapes of the unmodified structure in conjunction with unscaled mode contribution matrix ($[E^{un}_{12}]$) were used in the SDM process to estimate the modified ODS (blue lines in Fig. 1.9). The mode contribution matrix extracted using ODS does not represent the real contribution of each original mode shapes in the response of modified structure. Figure 1.9 shows that the unscaled ODS used in the SDM process does not yield the appropriate modes shapes of the modified structure, and the estimated mode shapes do not correlate well to the final mode shapes of the modified structure. The inconsistency between the estimated and experimentally measured modes is more evident when third and fourth modes are compared (see Fig. 1.9). Orthogonality values, shown in Fig. 1.10, indicate the importance of scaling operating shapes before executing structural

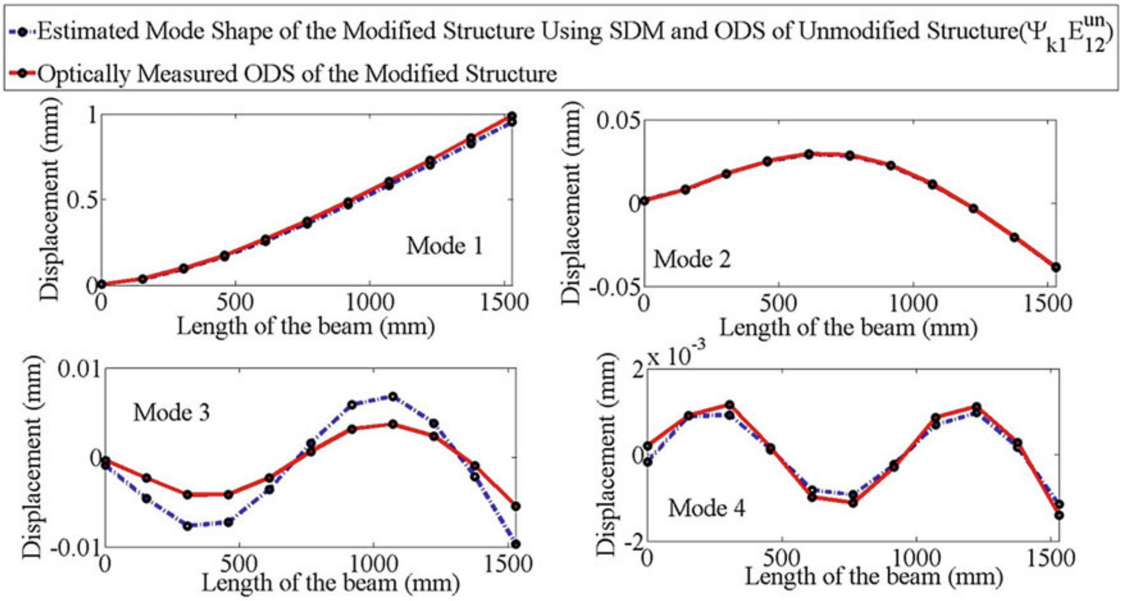

Fig. 1.9 Comparison of the first operating deflection shapes (OMA test) and estimated mode shape of modified structure using SDM and unscaled mode shapes (ODS) of modified structure

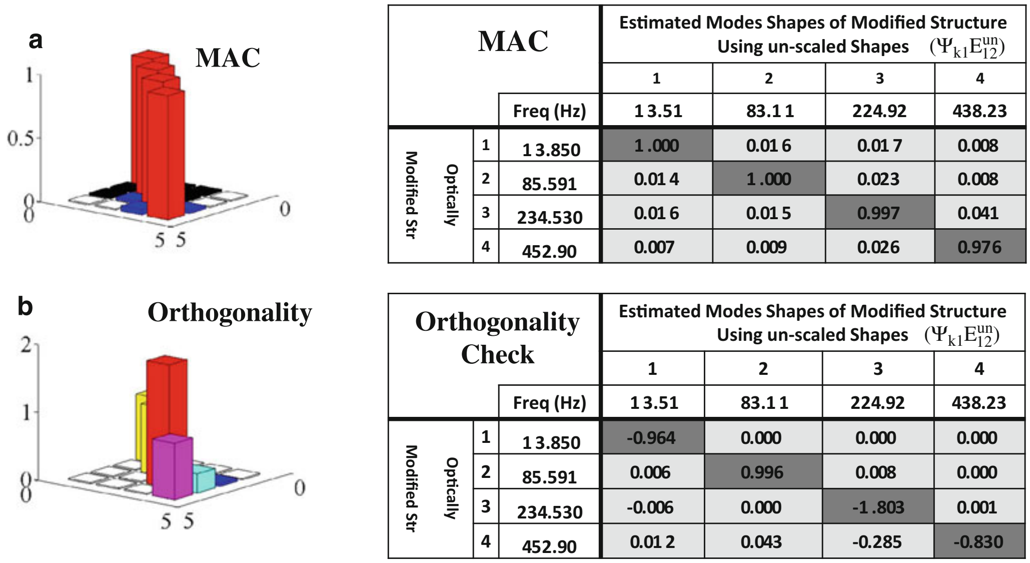

MAC			Estimated Modes Shapes of Modified Structure Using un-scaled Shapes ($\Psi_{k1}E_{12}^{un}$)			
			1	2	3	4
		Freq (Hz)	13.51	83.11	224.92	438.23
Optically Modified Str	1	13.850	1.000	0.016	0.017	0.008
	2	85.591	0.014	1.000	0.023	0.008
	3	234.530	0.016	0.015	0.997	0.041
	4	452.90	0.007	0.009	0.026	0.976

Orthogonality Check			Estimated Modes Shapes of Modified Structure Using un-scaled Shapes ($\Psi_{k1}E_{12}^{un}$)			
			1	2	3	4
		Freq (Hz)	13.51	83.11	224.92	438.23
Optically Modified Str	1	13.850	-0.964	0.000	0.000	0.000
	2	85.591	0.006	0.996	0.008	0.000
	3	234.530	-0.006	0.000	-1.803	0.001
	4	452.90	0.012	0.043	-0.285	-0.830

Fig. 1.10 Correlation between experimentally measured operating deflection shapes and estimated shapes using SDM. (**a**) MAC values indicating degree of consistency between operating shapes and estimated mode shapes. (**b**) Experimental mass weighted orthogonality check between the measured operating shapes and estimated mode shapes

dynamic modification. The unscaled mode contribution matrix can be calculated using

$$\left[\begin{bmatrix} \ddots & & \\ & I & \\ & & \ddots \end{bmatrix} + \{\Psi\}_k^T [\Delta M] \{\Psi\}_k\right] \{P_2\} + \begin{bmatrix} \ddots & & \\ & \omega_2^2 & \\ & & \ddots \end{bmatrix} \{P_2\} = [0] \tag{1.30}$$

Mode shape of the modified structure is estimated using

$$\left[\tilde{E}_2\right] = [\Psi_1] \left[E_{12}^{un}\right] \tag{1.31}$$

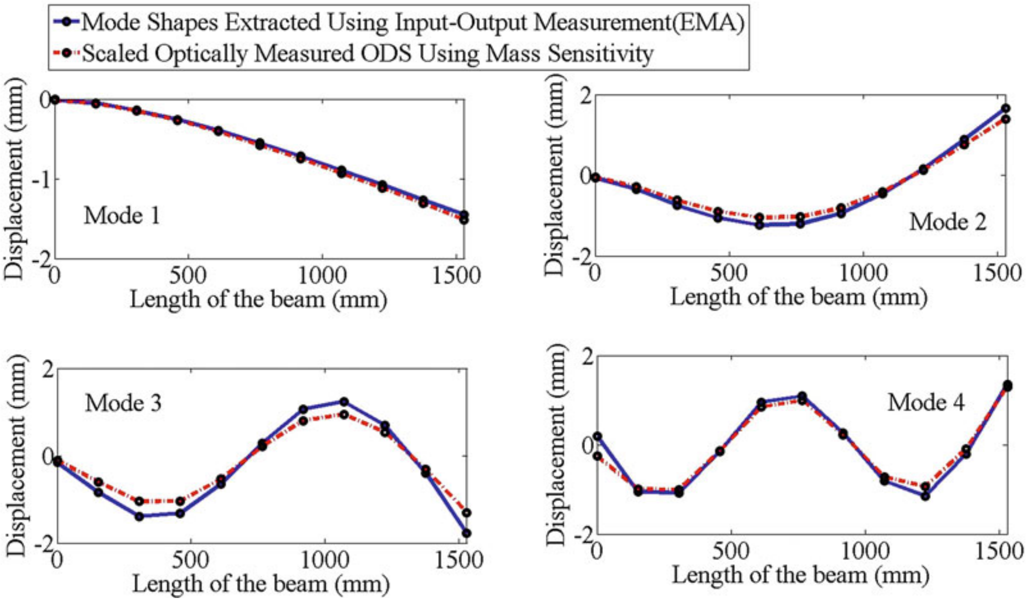

Fig. 1.11 Comparison between the first four reference mode shapes (EMA) and the scaled operating deflection shapes (OMA test) using mass sensitivity

1.4.4 *Case B.2: Mass Sensitivity Scaling Technique*

Figure 1.11 shows the shape comparison of scaled operating deflection shapes and reference mode shapes (impact test). The operating shapes scaled using mass sensitivity is well correlated with the reference mode shapes. The MAC values between the reference mode shapes and the scaled shapes are shown in Fig. 1.12a. The MAC is only a comparison of shape and has no regard for scale. The orthogonality, however, takes into account both scale as well as shape. While the diagonal values of MAC matrix are close to one, the orthogonality values are far from one, especially for mode three (see Fig. 1.12b). The orthogonality values for the second and third mode shapes indicate that the scale values for these modes are not very accurate. Therefore, some error is still present in the scaling factor.

1.4.5 *Case B.3: SDM Using Scaled Operating Deflection Shapes*

To evaluate the accuracy of the scaling factors (Eq. 1.23) and the mode contribution matrix (Eq. 1.17), the estimated mode shapes of the modified structure are compared with to the scaled operating shapes and reference mode shapes (EMA) of the modified structure. Figure 1.13 shows the shape comparison between the estimated and measured mode shapes of the modified structure after being scaled. Figure 1.14 shows the correlation and orthogonality between the estimated mode shapes and optically measured shapes of the modified structure. Orthogonality and MAC values shown in Fig. 1.14 demonstrate that scaling obtained using mass sensitivity has appropriately scaled both modified and unmodified operating shapes.

Figure 1.15 demonstrates the comparison between estimated mode shapes and reference mode shapes of the modified structure (EMA). The MAC results shown in Fig. 1.16a demonstrate that the estimated shapes of the modified structure are in strong correlation with the reference mode shapes. Furthermore, orthogonality values (see Fig. 1.16b) reveal that by using the mass sensitivity technique all the four modes have been scaled to reference mode shapes (EMA).

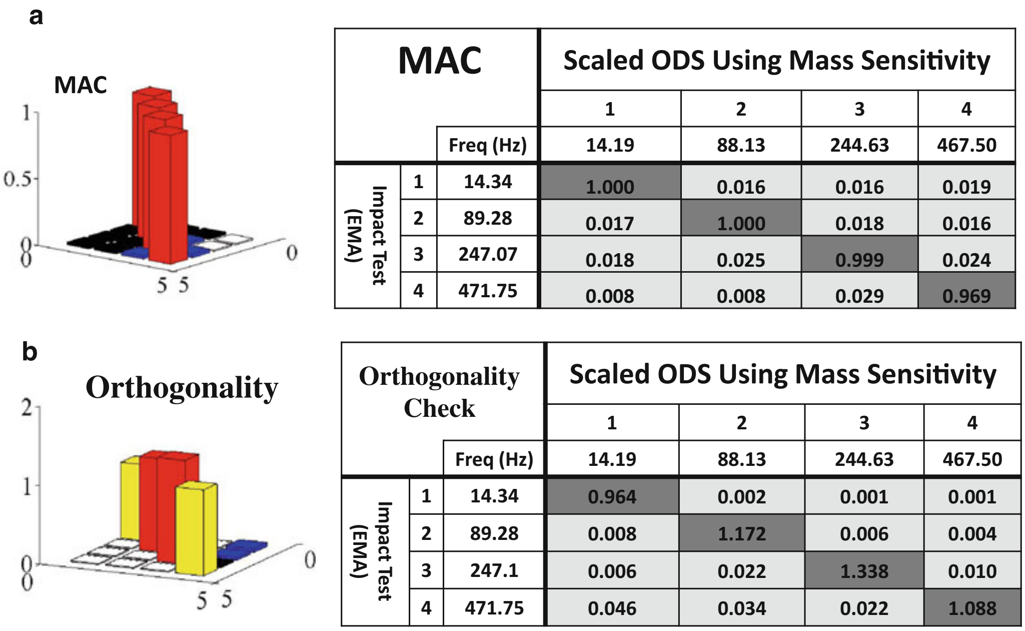

MAC			Scaled ODS Using Mass Sensitivity			
			1	2	3	4
		Freq (Hz)	14.19	88.13	244.63	467.50
Impact Test (EMA)	1	14.34	1.000	0.016	0.016	0.019
	2	89.28	0.017	1.000	0.018	0.016
	3	247.07	0.018	0.025	0.999	0.024
	4	471.75	0.008	0.008	0.029	0.969

Orthogonality Check			Scaled ODS Using Mass Sensitivity			
			1	2	3	4
		Freq (Hz)	14.19	88.13	244.63	467.50
Impact Test (EMA)	1	14.34	0.964	0.002	0.001	0.001
	2	89.28	0.008	1.172	0.006	0.004
	3	247.1	0.006	0.022	1.338	0.010
	4	471.75	0.046	0.034	0.022	1.088

Fig. 1.12 Correlation between operating deflections shapes, scaled using mass sensitivity, and the reference mode shapes (EMA). (**a**) MAC values indicating the degree of consistency between scaled operating shapes and reference mode shapes (MAC). (**b**) Orthogonality check between the scaled operating shapes and reference modal vectors with the experimental mass matrix

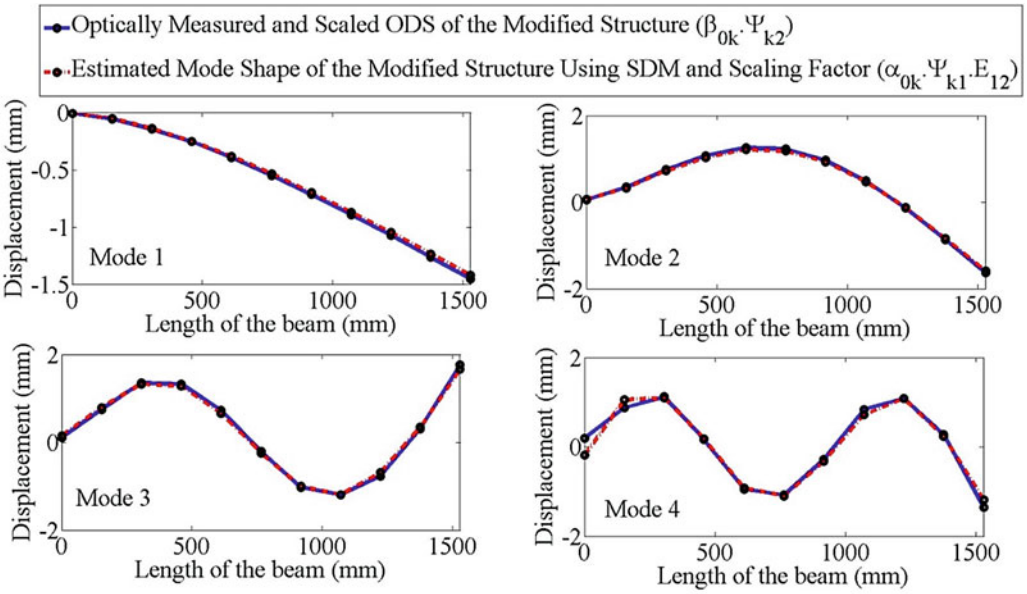

Fig. 1.13 Comparison between the first four scaled operating scaled deflection shapes of modified structure and estimated mode shapes of the modified structure using SDM

1.5 Conclusion

The results of the study revealed that both drive point and mass sensitivity scaling techniques offer a great prospect to be used as a scaling technique. The choice for one of these techniques generally relies on the feasibility of measuring input force. Drive point scaling proves to be more accurate than mass sensitivity technique. However, mass sensitivity is more practical to be used for scaling operating shapes. Using a searching algorithm, scaling factors minimizing the error between

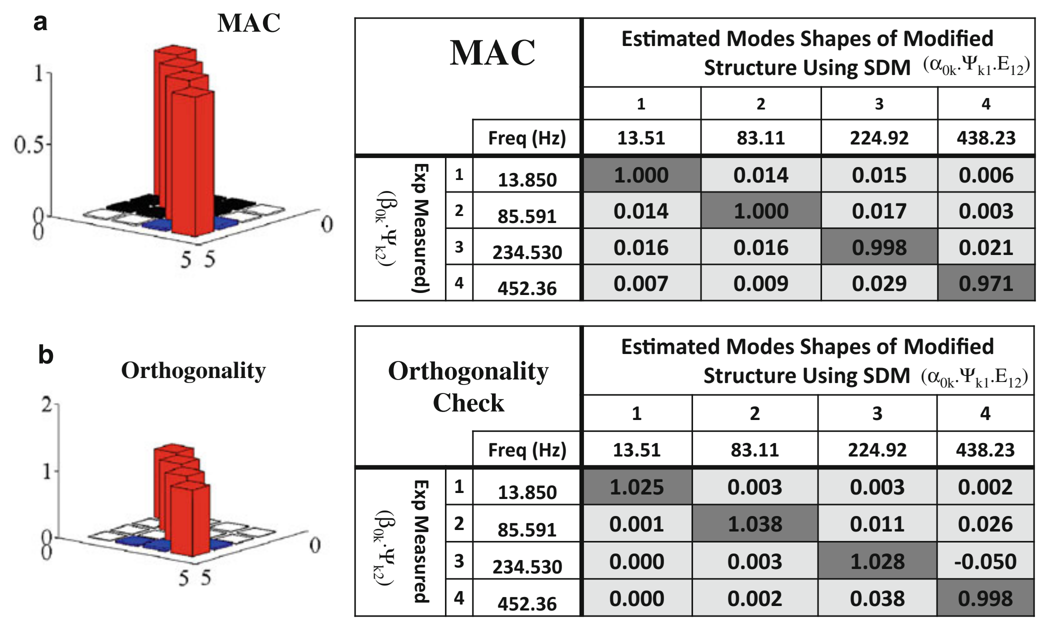

MAC			Estimated Modes Shapes of Modified Structure Using SDM ($\alpha_{0k}.\Psi_{k1}.E_{12}$)			
			1	2	3	4
		Freq (Hz)	13.51	83.11	224.92	438.23
Exp Measured) ($\beta_{0k}.\Psi_{k2}$)	1	13.850	1.000	0.014	0.015	0.006
	2	85.591	0.014	1.000	0.017	0.003
	3	234.530	0.016	0.016	0.998	0.021
	4	452.36	0.007	0.009	0.029	0.971

Orthogonality Check			Estimated Modes Shapes of Modified Structure Using SDM ($\alpha_{0k}.\Psi_{k1}.E_{12}$)			
			1	2	3	4
		Freq (Hz)	13.51	83.11	224.92	438.23
Exp Measured ($\beta_{0k}.\Psi_{k2}$)	1	13.850	1.025	0.003	0.003	0.002
	2	85.591	0.001	1.038	0.011	0.026
	3	234.530	0.000	0.003	1.028	-0.050
	4	452.36	0.000	0.002	0.038	0.998

Fig. 1.14 Correlation and orthogonality between scaled operating deflection shapes, and estimated mode shapes using SDM. (**a**) MAC values indicating the degree of consistency between scaled operating shapes and estimated mode shapes using SDM. (**b**) Experimental mass weighted orthogonality check between the scaled operating shapes and estimated mode shapes using SDM

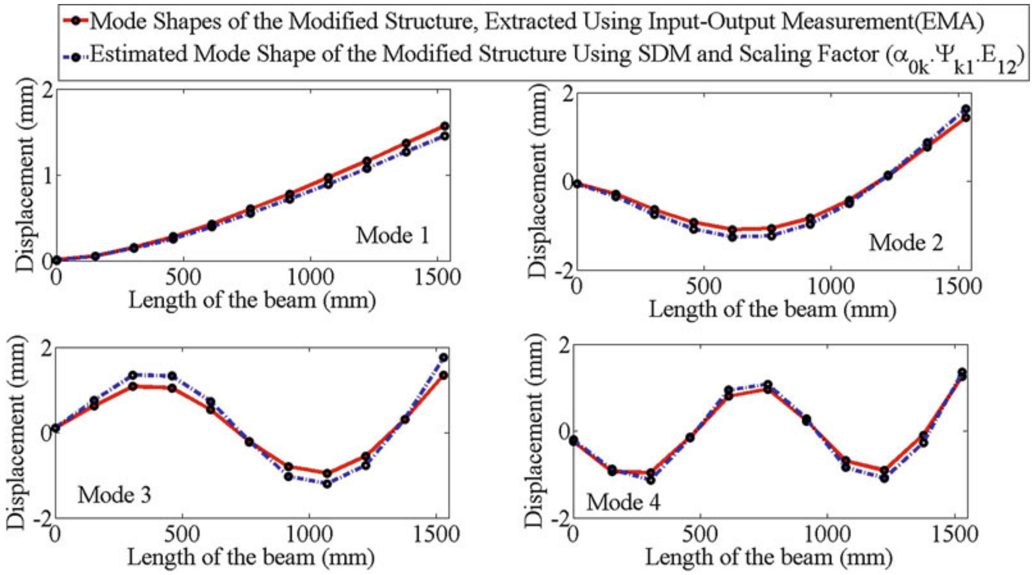

Fig. 1.15 Comparison between the first four reference mode shapes (EMA) and estimated mode shapes of the modified structure using SDM

estimated and experimental mode shapes were determined. The selection of mass sensitivity scaling factor as a starting value is important to ensure that the algorithm converges to an optimal value for the scaling factor. The MAC and orthogonality values indicate that the proposed method was capable of obtaining optimal scaling factors and all resulting operating modes show strong correlations to their corresponding mode shapes.

Acknowledgements The authors gratefully appreciate the financial support for this work provided by the Massachusetts Clean Energy Center (CEC), Task Order 13-2. Any opinions, findings, and conclusions or recommendations expressed in this material are those of the authors and do not necessarily reflect the views of Mass CEC.

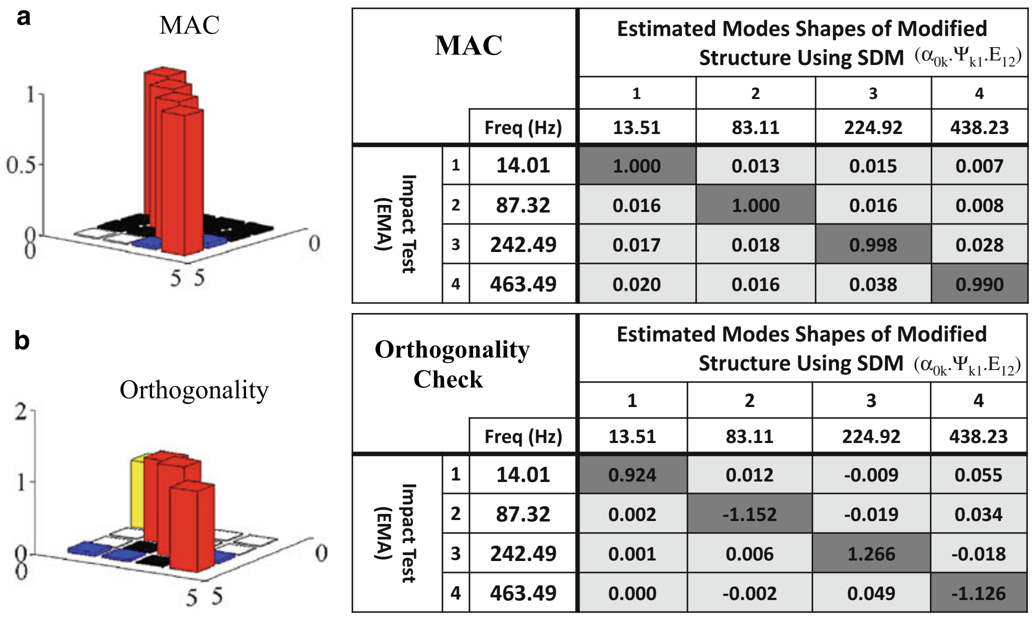

MAC			Estimated Modes Shapes of Modified Structure Using SDM $(\alpha_{0k}.\Psi_{k1}.E_{12})$			
			1	2	3	4
		Freq (Hz)	13.51	83.11	224.92	438.23
Impact Test (EMA)	1	14.01	1.000	0.013	0.015	0.007
	2	87.32	0.016	1.000	0.016	0.008
	3	242.49	0.017	0.018	0.998	0.028
	4	463.49	0.020	0.016	0.038	0.990

Orthogonality Check			Estimated Modes Shapes of Modified Structure Using SDM $(\alpha_{0k}.\Psi_{k1}.E_{12})$			
			1	2	3	4
		Freq (Hz)	13.51	83.11	224.92	438.23
Impact Test (EMA)	1	14.01	0.924	0.012	-0.009	0.055
	2	87.32	0.002	-1.152	-0.019	0.034
	3	242.49	0.001	0.006	1.266	-0.018
	4	463.49	0.000	-0.002	0.049	-1.126

Fig. 1.16 Correlation and orthogonality between estimated scaled operating deflections shapes, and the reference mode shapes (EMA). (**a**) MAC values indicating degree of consistency between estimated scaled operating deflections shapes, and the reference mode shapes. (**b**) Experimental mass weighted orthogonality check between estimated scaled operating deflections shapes, and the reference mode shapes

References

1. Baqersad, J., Poozesh, P., Niezrecki, C., Avitabile, P.: Comparison of modal parameters extracted using MIMO, SIMO, and impact hammer tests on a three-bladed wind turbine. In: Proceeding of the 32nd IMAC, A Conference and Exposition on Structural Dynamics, Orlando, FL, pp. 185–197, February 3–6, 2014
2. Devriendt, C., Guillaume, P., Brussel, V.U., Reynders, E., Roeck, G.D.: Operational modal analysis of a bridge using transmissibility measurements. In: Proceeding of the 25th IMAC, Conference & Exposition on Structural Dynamics, Orlando, Florida, February 19–22, 2007
3. Rainieri, C., Fabbrocino, G.: Operational Modal Analysis of Civil Engineering Structures. Springer, New York (2014)
4. Peeters, B., Van der Auweraer, H., Vanhollebeke, F., Guillaume, P.: Operational modal analysis for estimating the dynamic properties of a stadium structure during a football game. Shock Vib. **14**(4), 283–303 (2007)
5. Poozesh, P., Baqersad, J., Niezrecki, C., Avitabile, P.: A multi-camera stereo DIC system for extracting operating mode shapes of large scale structures. In: Proceeding of the SEM Annual Conference on Experimental and Applied Mechanics, Costa Mesa, CA, June 8–11, 2015
6. Tcherniak, D., Chauhan, S., Hansen, M.H.: Applicability limits of operational modal analysis to operational wind turbines. In: Proceeding of the 28th IMAC, A Conference and Exposition on Structural Dynamics, Springer New York, pp. 317–327, February 1–4, 2010
7. López-Aenlle, M., Brincker, R., Pelayo, F., Canteli, A.F.: On exact and approximated formulations for scaling-mode shapes in operational modal analysis by mass and stiffness change. J. Sound Vib. **331**(3), 622–637 (2012)
8. Ventura, C.E., Lord, J.F., Turk, M., Brincker, R., Andersen, P., Dascotte, E.: FEM updating of tall buildings using ambient vibration data. In: Proceeding of the Sixth International Conference on Structural Dynamics (EURODYN), Paris, France, 2005
9. López-Aenlle, M., Fernández, P., Brincker, R., Fernández-Canteli, A.: Scaling-factor estimation using an optimized mass-change strategy. Mech. Syst. Signal Process. **24**(5), 1260–1273 (2010)
10. Hout, B., Avitabile, P.: Application of operating data scaling techniques. In: Proceeding of the 22nd IMAC, A Conference on Structural Dynamics, Dearborn, MI, pp. 52–58, January 26–29, 2004
11. López-Aenlle, M., Brincker, R., Fernández-Canteli, A.: Some methods to determine scaled mode shapes in natural input modal analysis. In: Proceeding of the 23rd IMAC, Conference & Exposition on Structural Dynamics, Orlando, Florida, pp. 165–176, January 31–February 3 2005
12. Aenlle, M.L., Fernández, P.F., Brincker, R., Canteli, A.F.: Scaling factor estimation using an optimized mass change strategy, part 1: theory. In: Proceeding of the, International Operational Modal Analysis Conference (IOMAC), pp. 421–428, 2007
13. Fernández, P., Reynolds, P., López-Aenlle, M.: Scaling mode shapes in output-only systems by a consecutive mass change method. Exp. Mech. **51**(6), 995–1005 (2011)
14. Brincker, R., Rodrigues, P., Andersen, P.: Scaling the mode shapes of a building model by mass changes. In: Proceeding of the 22nd IMAC, International Modal Analysis Conference, Dearborn, MI, pp. 119–126, January 26–29, 2004
15. Parloo, E., Verboven, P., Guillaume, P., Van Overmeire, M.: Sensitivity-based operational mode shape normalisation. Mech. Syst. Signal Process. **16**(5), 757–767 (2002)
16. Khatibi, M.M., Ashory, M.R., Malekjafarian, A., Brincker, R.: Mass-stiffness change method for scaling of operational mode shapes. Mech. Syst. Signal Process. **26**, 34–59 (2012)

17. Baqersad, J., Carr, J., Lundstrom, T., Niezrecki, C., Avitabile, P., Slattery, M.: Dynamic characteristics of a wind turbine blade using 3D digital image correlation. In: Proceeding of the SPIE Symposium on Smart Structures & Materials/NDE and Health Monitoring, pp. 21–29, April 20, 2012
18. Helfrick, M.N., Niezrecki, C., Avitabile, P., Schmidt, T.: 3D digital image correlation methods for full-field vibration measurement. Mech. Syst. Signal Process. **25**(3), 917–927 (2011)
19. Poozesh, P., Baqersad, J., Niezrecki, C., Harvey, E., Yarala, R.: Full field inspection of a utility scale wind turbine blade using digital image correlation. In: Proceeding of the Composites and Advanced Materials, CAMX, Orlando, FL, October, 2014
20. Baqersad, J., Poozesh, P., Niezrecki, C., Avitabile, P.: Predicting full-field strain on a wind turbine for arbitrary excitation using displacements of optical targets measured with photogrammetry. In: Proceeding of the 33rd IMAC, A Conference on Structural Dynamics, pp. 99–114, 2015
21. Carr, J., Baqersad, J., Niezrecki, C., Avitabile, P., Slattery, M.: Dynamic stress–strain on turbine blade using digital image correlation techniques Part 1: static load and calibration. In: Proceeding of the 30th IMAC, Jacksonville, FL, pp. 215–220, February 2–5, 2012
22. Lundstrom, T., Baqersad, J., Niezrecki, C., Avitabile, P.: Using high-speed stereophotogrammetry techniques to extract shape information from wind turbine/rotor operating data. In: Proceeding of the 30th IMAC, Conference & Exposition on Structural Dynamics, Jacksonville, FL, pp. 269–275, February 2–5, 2012
23. Allemang, R.J., Brown, D.L.: Correlation coefficient for modal vector analysis. In: Proceeding of the 1st IMAC, International Modal Analysis Conference & Exhibit, Orlando, FL, USA, pp. 110–116, 1982
24. Parloo, E., Cauberghe, B., Benedettini, F., Alaggio, R., Guillaume, P.: Sensitivity-based operational mode shape normalisation: application to a bridge. Mech. Syst. Signal Process. **19**(1), 43–55 (2005)
25. Avitabile, P.: Twenty years of structural dynamic modification-a review. Sound Vib. **37**(1), 14–27 (2003)
26. PONTOS v6.3, GOM mbH, Braunschweig, Germany
27. Peeters, B., De Roeck, G.: Reference-based stochastic subspace identification for output-only modal analysis. Mech. Syst. Signal Process. **13**(6), 855–878 (1999)
28. Ljung, L.: System Identification, Signal Analysis and Prediction. Birkhäuser, Boston, ISBN 978-1-4612-7273-1, pp. 163–173, 1998
29. LMS Test.Lab 14A, LMS International, Leuven, Belgium

Chapter 2
Prediction of the Coupled Impedance from Frequency Response Data

Ramona Fagiani, Elisabetta Manconi, and Marcello Vanali

Abstract This work deals with the common case of large mechanical systems which can be modelled considering two main sub-structures: a source structure, corresponding for example to the engine, and a receiving structure, as the accommodation area/cabin in these machines. Numerical models are highly desired for predicting the vibroacoustic behaviour of the receiver at a design stage and for design optimisation. In many cases the mechanical systems must be studied using sub-structuring techniques

Here a standard frequency response coupling technique (or impedance coupling technique) is applied for the prediction of the complex power transmitted between a source structure and a receiving structure in a multi-point-connection case. The data required in this case are the frequency response functions (FRFs) of both the source and the receiver and the velocity at the connecting points under operating conditions. Experimental aspects and issues associated with this technique are investigated considering a simplified mechanical model. This consists of a driven beam connected in two or more points to a source. Results are discussed and compared with those obtained from a numerical model.

Keywords Coupled impedance • Coupled structures • Modal analysis

2.1 Introduction

Determining the vibro-acoustic behaviour of complex mechanical structures can be very challenging, since several components be simultaneously involved [1, 2]. In order to quantify the force transmitted through substructures for structure-born noise estimation, the knowledge of mechanical mobility and impedance at the connecting points is necessary [3]. In this regard, Dynamic Substructuring (DS) [4] plays a significant role for investigating a structural system by the analysis of the single sub-structure dynamic features and the way in which they combine. The substructuring approach has some significant advantages over the consideration of the full structure, in particular it allows evaluation of the dynamic behaviour of large and complex structures when the analysis of the all structure is unrealistic. Moreover, combining analytically, numerically or experimentally single modelled parts of the whole structure, local dynamic behaviour can be recognized more easily and neglected when it has no significant impact on the assembled system. In many cases this results in a simplified and clearer representation of the structure overall dynamics and in a significant reduction of the analysis time.

Despite all the attention received in the last years, DS still requires additional research, especially concerning a number of challenges associated with the coupling of experimentally obtained substructures. Just to cite a few works, a review of the difficulties encountered in experimental DS are summarised in [4], errors related to truncation of modal degrees of freedom in [5] and the estimation of rotational degrees of freedom in [6], inclusion of rigid body modes in [7], non-linear mechanical coupling in [8], random measurement noise which may result in low signal-to-noise ratio, especially in the case of lightly damped structures in [9], inexact determination of the antiresonance modes in [10].

In this paper a frequency response coupling technique (or impedance coupling technique) is revised for the prediction of the complex impedance. Data required are the frequency response functions (FRFs) of the source and the receiver and the velocity/accelerations at the connecting points under operating conditions. These can be either experimental data or numerical data obtained from finite element analysis or modal analysis. The FRF coupling technique is first applied to a simple case study concerning two beams for validating the method numerically and experimentally and for investigating its accuracy according to the frequency range of interest.

R. Fagiani • E. Manconi • M. Vanali (✉)
Industrial Engineering Department, Università degli Studi di Parma, Parco Area delle Scienze 181/A, 43124 Parma, Italy
e-mail: marcello.vanali@unipr.it

© The Society for Experimental Mechanics, Inc. 2016

J. De Clerck, D.S. Epp (eds.), *Rotating Machinery, Hybrid Test Methods, Vibro-Acoustics & Laser Vibrometry, Volume 8*,
Conference Proceedings of the Society for Experimental Mechanics Series, DOI 10.1007/978-3-319-30084-9_2

2.2 FRF Coupling

This section is dedicated to revise a methodology for coupling a flexible structure to another structure (e.g. a source machine) using the FRF matrices, e.g. [4]. The objective is to describe an approach for evaluating the power input from a large machine to a flexible structure when forces and responses data of the separated structures can be measured and only acceleration/velocity responses data of the whole coupled structure in operation are available.

Figure 2.1 shows structure 1 (source) connected to structure 2 (receiver) through multiple points together with the model the free body diagram for each substructure. Each connection is modelled using a connector system C_i. These can be a rigid connections or flexible-damped connections. Dynamics of structures 1 and 2 is often studied using a discretised model, e.g. as in standard FE or modal analysis, and generally the DOFs at which the internal forces act, $\mathbf{u}_1 = [u_{11}, u_{12}, \ldots, u_{1n}]^T; \mathbf{u}_2 = [u_{21}, u_{22}, \ldots, u_{2n}]^T$, are a subset of the DOFs used to discretise the structure, $\mathbf{y}_1 = [y_{11}, y_{12}, \ldots, y_{1m}]^T$ and $\mathbf{y}_2 = [y_{21}, y_{22}, \ldots, y_{2q}]^T$. The same situation arises in experimental modal analysis when the responses evaluated at the connection points are a subset of the responses used for characterizing the dynamic structure behaviour. This situation is pictured in Fig. 2.1.

In this case, the DOFs of structure j corresponding to the connected ones can be expressed in terms of the DOFs of the structure using an influence matrix $\mathbf{W}_j = [\mathbf{W}_{j1} \ldots \mathbf{W}_{jn}]$. Here $[\mathbf{W}_{j1} \ldots \mathbf{W}_{jn}]$ are column vectors of zeros and ones, e.g. $\mathbf{W}_{j1} = [0, 0, 1, 0 \ldots 0]^T$, where the ones identifies the position of the DOFs corresponding to the DOFs of structure on which the internal forces $\mathbf{F}_{Cj}$ act. Thus the influence matrix relates displacements and internal forces of structure 2, structure 1, and connectors C_j as

$$\begin{aligned} \mathbf{F}_{C1}(\omega) = -\mathbf{W}_1\mathbf{F}_{1C},\ \mathbf{u}_1 = \mathbf{W}_1^T\mathbf{y}_1 \\ \mathbf{F}_{C2}(\omega) = -\mathbf{W}_2\mathbf{F}_{2C},\ \mathbf{u}_2 = \mathbf{W}_2^T\mathbf{y}_2 \end{aligned} \tag{2.1}$$

Dynamic equilibrium of each free body diagram in Fig. 2.1 can be written as

$$\begin{cases} \mathbf{F} + \mathbf{F}_{C1} = \mathbf{H}_1(\omega)\mathbf{y}_1 \\ \mathbf{F}_{1C} = \mathbf{H}_c(\omega)\,(\mathbf{u}_1 - \mathbf{u}_2) \\ \mathbf{F}_{C2} = \mathbf{H}_2(\omega)\mathbf{y}_2 \end{cases} \Rightarrow \begin{cases} \mathbf{F} - \mathbf{W}_1\mathbf{F}_{1C} = \mathbf{H}_1(\omega)\mathbf{W}_1\mathbf{u}_1 \\ \mathbf{F}_{1C} = \mathbf{H}_C(\omega)\,(\mathbf{u}_1 - \mathbf{u}_2) \\ \mathbf{F}_{C2} = \mathbf{H}_2(\omega)\mathbf{y}_2 \end{cases} \tag{2.2}$$

Since $\mathbf{F}_{C1} = -\mathbf{W}_1\mathbf{F}_{1C}$, combining the first and the second of Eq. (2.6) the relative displacement becomes $(\mathbf{u}_1 - \mathbf{u}_2) = [\mathbf{H}_1(\omega)\mathbf{W}_1 + \mathbf{W}_1\mathbf{H}_C(\omega)]^{-1}\mathbf{F} - [\mathbf{H}_1(\omega)\mathbf{W}_1 + \mathbf{W}_1\mathbf{H}_C(\omega)]^{-1}\mathbf{H}_1(\omega)\mathbf{W}_1\mathbf{u}_2$. The internal force transmitted to structure 2 is thus

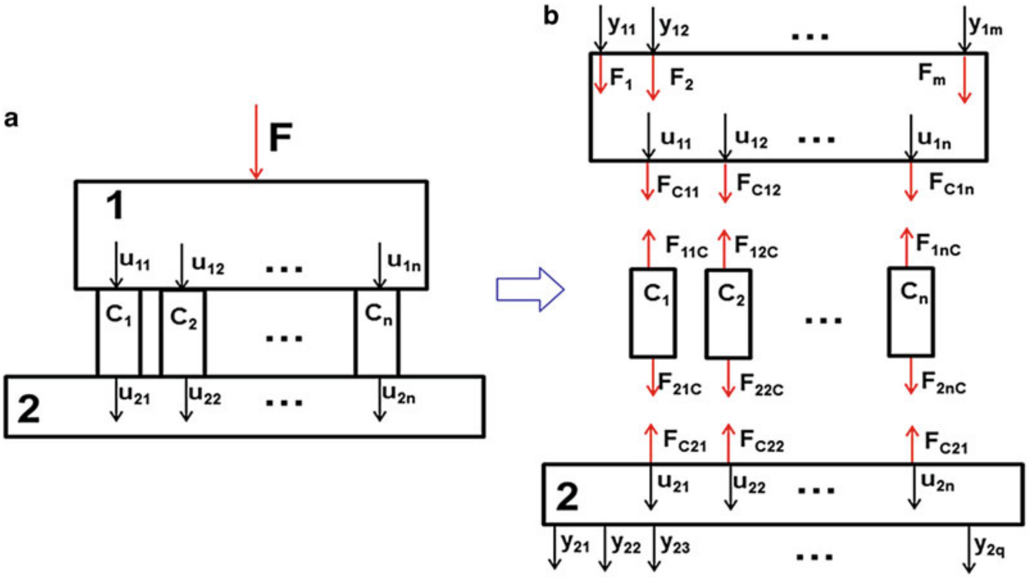

Fig. 2.1 Schematic representation of a machine-source (structure 1) connected to a receiving structure (structure 2) through multiple points: (**a**) coupled system, (**b**) uncoupled system

$$\mathbf{F}_{2C} = -\mathbf{F}_{1C} = -\mathbf{H}_C(\omega)\mathbf{U}_1(\omega)^{-1}\mathbf{F} + \mathbf{H}_C(\omega)\mathbf{U}_1(\omega)^{-1}\mathbf{H}_1(\omega)\mathbf{W}_1\mathbf{u}_2 \tag{2.3}$$

where $\mathbf{U}_1(\omega) = \mathbf{H}_1(\omega)\mathbf{W}_1 + \mathbf{W}_1\mathbf{H}_C(\omega)$. Using Eq. (2.5)

$$\mathbf{F}_{C2} = \mathbf{W}_2\mathbf{H}_C(\omega)\mathbf{U}_1(\omega)^{-1}\mathbf{F} - \mathbf{W}_2\mathbf{H}_C(\omega)\mathbf{U}_1(\omega)^{-1}\mathbf{H}_1(\omega)\mathbf{W}_1\mathbf{W}_2^T\mathbf{y}_2 \tag{2.4}$$

Given $\mathbf{F}_{C2} = \mathbf{H}_2(\omega)\mathbf{y}_2$, Eq. (2.8) becomes

$$\mathbf{F} = \left[\mathbf{U}_1(\omega)\mathbf{H}_C(\omega)^{-1}\mathbf{W}_2^T\mathbf{H}_2 + \mathbf{H}_1(\omega)\mathbf{W}_1\mathbf{W}_2^T\right]\mathbf{y}_2 \tag{2.5}$$

Hence the frequency response matrix of the coupled structure evaluated at the receiver is

$$\mathbf{H}(\omega) = \mathbf{U}_1(\omega)\mathbf{H}_C(\omega)^{-1}\mathbf{W}_2^T\mathbf{H}_2 + \mathbf{H}_1(\omega)\mathbf{W}_1\mathbf{W}_2^T \tag{2.6}$$

If structure 2 is excited by the external force F while structure 1 is free to vibrate, the transfer matrix modifies as

$$\mathbf{H}(\omega) = \mathbf{H}_2 + \mathbf{W}_2\mathbf{H}_C(\omega)\mathbf{U}_1(\omega)^{-1}\mathbf{H}_1(\omega)\mathbf{W}_1\mathbf{W}_2^T \tag{2.7}$$

Once the transfer matrix of the coupled structure is known, the impedance and inertance matrices are $\mathbf{Z}(\omega) = \mathbf{H}(\omega)/i\omega$ and $\mathbf{I}(\omega) = -\mathbf{H}(\omega)/\omega^2$.

The above formulation has been applied to a simple experimental case and results are discussed in the next section.

2.3 Experimental Setup

The example shown in this section consists of a simplified model. The model is used for validating the coupling technique. Two steel beams are considered as depicted in Fig. 2.2. The first beam, named ‘source’, is linked to the other one, called ‘receiver’, at two points (points 1 and 2 in the figure). In the real case these are welded, thus the connection in the numerical case is modelled as rigid. Material properties are: Young modulus 210 GPa, density 7860 kg/m^3, Poisson’s coefficient 0.33. The receiver is 3240 mm long and has a square cross section of 25 mm. The source is 400 mm long and has a cross section of 25 × 50 mm. Both the coupled and uncoupled source and receiver are suspended by two rubber bands in order to simulate free-free boundary conditions.

Source and receiver accelerance matrices, $\mathbf{G}_S$ and $\mathbf{G}_R$ respectively are evaluated experimentally or numerically. These are obtained exciting the structure and evaluating the acceleration at the connection points $\ddot{\mathbf{y}}_1 = \mathbf{G}_S\mathbf{F}_1$ and $\ddot{\mathbf{y}}_2 = \mathbf{G}_R\mathbf{F}_2$. Thus, according to the scheme in Fig. 2.1, the impedance matrices are $\mathbf{H}_S = -\omega^2\mathbf{G}_S^{-1}$ $\mathbf{H}_R = -\omega^2\mathbf{G}_R^{-1}$. Equation (2.7) is then

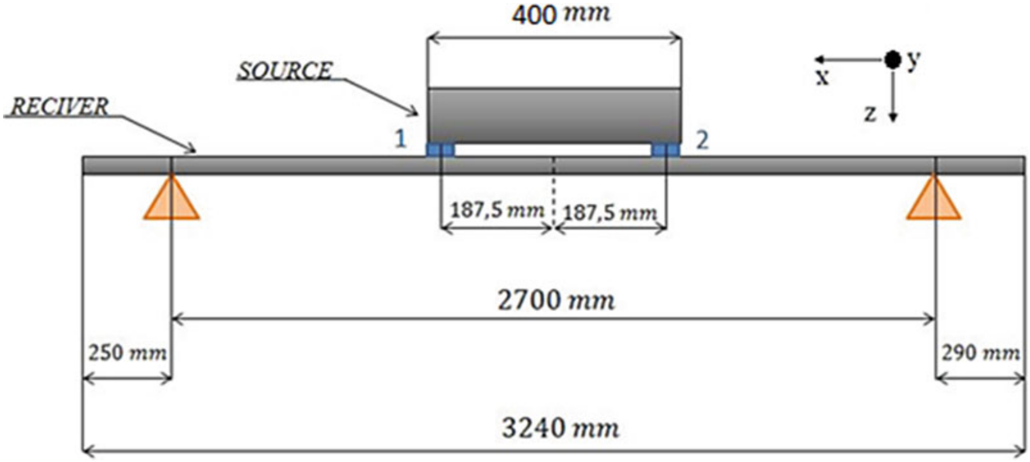

Fig. 2.2 Schematic representation of the case study

applied to obtain the FRFs matrix of the coupled structure $\mathbf{H}_{RS}$. Since only the degrees of freedom corresponding to points 1 and 2 are coupled and the connections are modelled as rigid, becomes Eq. (2.7) $\mathbf{H}_{RS} = \mathbf{H}_R + \mathbf{H}_S$. The accelerance matrix $\mathbf{G}_{RS}$ of the coupled structure can be also rewritten explicitly in terms of $\mathbf{G}_S$ and $\mathbf{G}_R$ using the Woodbury matrix identity as shown in [11, 13, 14]

$$\mathbf{G}_{RS} = \mathbf{G}_R - \mathbf{G}_R(\mathbf{G}_R + \mathbf{G}_S)^{-1}\mathbf{G}_R \tag{2.8}$$

Due the symmetry of the structure, the matrices are expected to be symmetric and the elements on the diagonal corresponding to point 1 and 2 are expected to be the same.

2.3.1 Experimental Case Study

The accelerance matrices of the single beams and of the coupled structure have been measured by impact testing (impact hammer PCB 086C03) in the nearby area of the triaxial accelerometers (PCB M352C66) placed at points 1 and 2. The points correspond to the connection points of the coupled structure (Figs. 2.2, 2.3, and 2.4). All data were sampled at 6400 Hz.

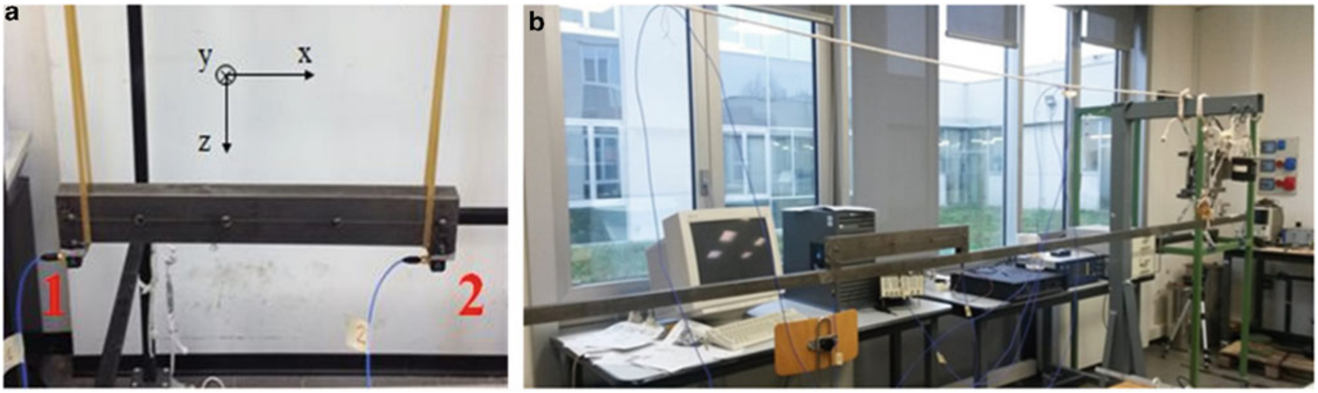

Fig. 2.3 Experimental case study: (**a**) source, (**b**) coupled structure

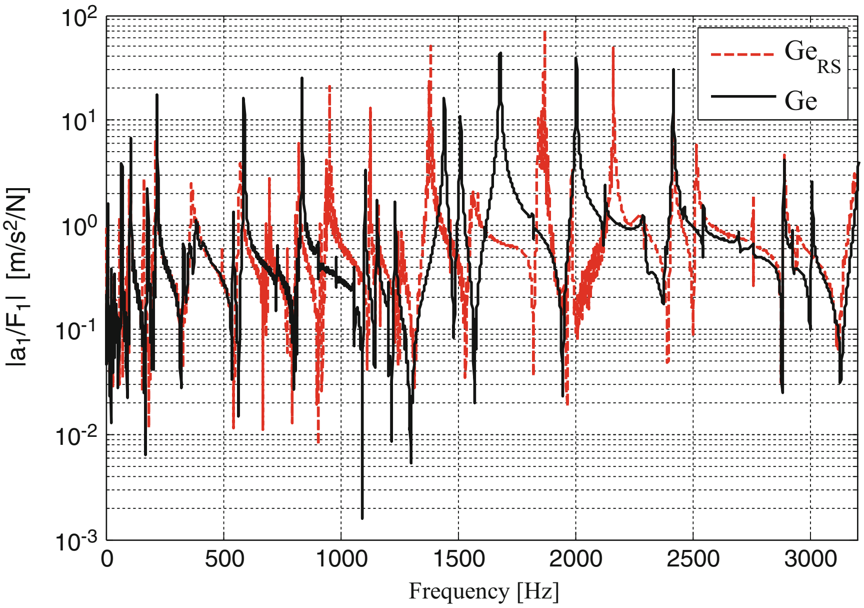

Fig. 2.4 Experimental case study. Comparison between measured FRF for the coupled structure $\mathbf{G}_e$ and those obtained coupling the FRF matrices of the source and the receiver $\mathbf{G}_{eRS}$ using Eq. (2.12)

The structures were excited in the all x, y, z and accelerations were measured in the same directions at point 1 and point 2. The measure of rotations for a simple structure like this is very difficult and becomes impossible for more realistic structures, thus moments and rotational responses were disregarded. All the cross combination of input force and output acceleration were measured. Therefore the size of the FRF matrices is 6×6. The experimental data were processed and H1 method was used as the FRF estimator [12].

Figure 2.4 shows the comparison between the modulus of the measured accelerance FRF function $\mathbf{G}_e$ of the coupled structure at point and those obtained applying Eq. (2.10) $\mathbf{G}_{eRS}$, viz. coupling the measured FRF matrices of the source $\mathbf{G}_{eS}$ and the receiver $\mathbf{G}_{eR}$. Only the component along the z-axis is showed as an example but the same results apply to all other directions. As expected, this first sets of experimental results shows that the coupling model gives good prediction at low frequency. At higher frequency results become less and less reliable. Differences can be due to several factors such as a lack in modelling the connections between the source and the receiver, uncertainties in measuring, e.g. force applied in z direction is not perfectly aligned along the z axis and so on. However, it is expected that the main errors have been introduced neglecting moments and rotational responses. This is investigated in the next section.

2.4 Numerical Model

The aim of this section is validating numerically the coupling technique and investigating the influence of the moments and rotational displacements in the FRF coupling model. The structure depicted in Fig. 2.2 is discretised using BEAM elements with 6DOFs per node, three translations and three rotations. The receiver is discretised using 324 elements while the source using 40 elements. Source and receiver are solved separately to obtain their FRF matrices, $\mathbf{G}_{nS}$ and $\mathbf{G}_{nR}$. These are coupled using Eq. (2.8) to obtain $\mathbf{G}_{nRS}$. The FRF matrix, $\mathbf{G}_n$, obtained from an FE model of the coupled structure, is also evaluated to model the real coupled structured and compare the results. Figure 2.5 shows the comparison between the direct frequency responses function G_{nRS} and G_n at point 1. It can be seen that the curves are in perfect agreement and thus coupling approach theoretically predicts the dynamics accurately when all the forcing and moments and displacements and rotations are considered. The experimental measure of the rotational displacements can be so difficult that in many practical cases only translation forces and responses are considered.

In order to simulate numerically this realistic situation, the FRF matrices of the source and the receiver are evaluated only for the translational degrees of freedom. Figure 2.6 shows the comparison between FRF for the coupled structure $\mathbf{G}_n$ and those obtained coupling the FRF matrices of the source and the receiver $\mathbf{G}_{nRS}$ when only the translational degrees of

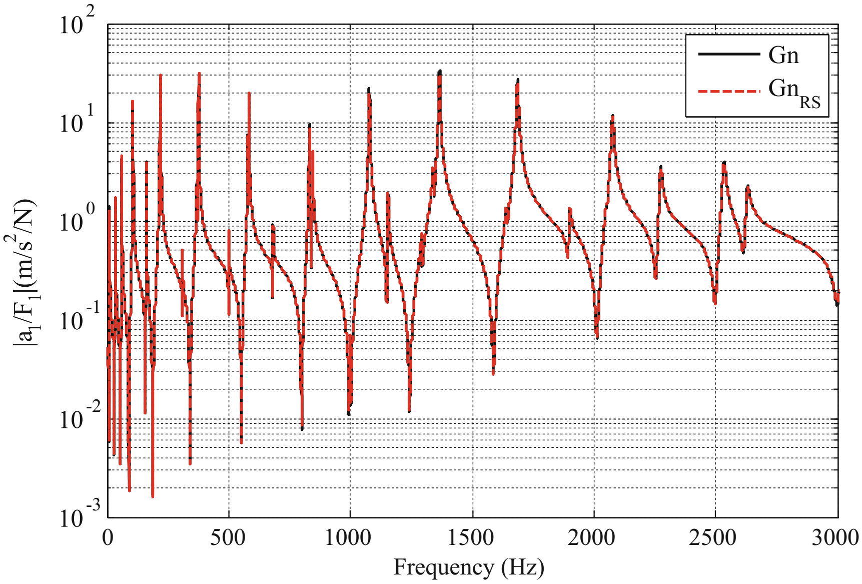

Fig. 2.5 Numerical case study. Comparison between numerical FRF for the coupled structure $\mathbf{G}_n$ and those obtained coupling the FRF matrices of the source and the receiver $\mathbf{G}_{nRS}$ using Eq. (2.12)

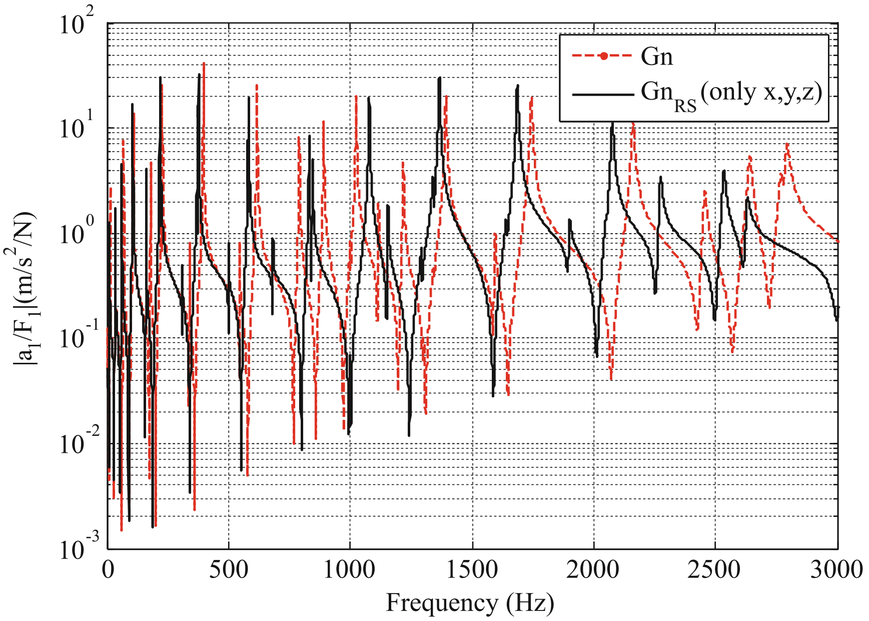

Fig. 2.6 Numerical case study. Comparison between numerical FRF for the coupled structure $\mathbf{G}_n$ and those obtained coupling the FRF matrices of the source and the receiver $\mathbf{G}_{nRS}$ using Eq. (2.12) when rotational responses were neglected

freedom were considered. This implies that the matrices used in Eq. (2.7) $\mathbf{G}_{nR}$ and $\mathbf{G}_{nS}$ are now 6×6 matrices, as measured in the experimental case, instead of 12×12. As expected the curves are now different showing that neglecting moments and rotational degrees of freedom lead to inaccurate results.

2.5 Conclusions

In this paper a frequency response coupling technique (or impedance coupling technique) was revised for the prediction of the overall impedance matrix of a coupled structure. The data required are the frequency response functions (FRFs) of the source and the receiver and the velocity/accelerations at the connecting points under operating conditions. These can be either experimental data, or numerical data obtained from finite element analysis or modal analysis, or both experimental and numerical results for different substructures. A simplified model was considered for investigating the validity of the procedure numerically and experimentally. Numerical results showed very good agreement between the FRF functions of the coupled structure and those obtained coupling the impedance matrices of the source and the receiver, while experimental results showed significant differences between at higher frequencies. These were investigated using the numerical model. Although some experimental errors were introduced due to lack in modelling the connections between the source and the receiver and uncertainties in measuring (e.g. force applied in z direction is not perfectly aligned along the z axis and so on) it was found that the main errors is introduced in neglecting moments and rotational responses.

References

1. Di Sante, R., Revel, G.M., Rossi, G.L.: Measurement techniques for the acoustic analysis of synchronous belts. Meas. Sci. Technol. **11**, 1463–1472 (2000)
2. Di Sante, R., Rossi, G.L.: A new approach to the measurement of transverse vibration and acoustic radiation of automotive belts using laser Doppler vibrometry and acoustic intensity techniques. Meas. Sci. Technol. **12**, 525–533 (2001)
3. Petersson, B.A.T., Plunt, J.: On effective mobilities in the prediction of structure-borne sound transmission between a source structure and a receiving structure, part I: theoretical background and basic experimental studies. J. Sound Vib. **82**, 517–529 (1982)
4. De Klerk, D., Rixen, D.J., Voormeeren, S.N.: General framework for dynamic substructuring: history, review, and classification of techniques. AIAA J. **46**, 1169–1181 (2008)

5. Hermands, L., et al.: Estimation and use of residual modes in modal coupling calculations: a case study. In: Proceedings of the Eighteenth International Modal Analysis Conference, Society for Experimental Mechanics, Bethel, CT, pp. 930–936 (2000)
6. Montalvao, D., et al.: Estimation of the Rotational Terms of the Dynamic Response Matrix. Shock. Vib. **11**, 333–350 (2004)
7. O'Callahan, J., et al.: Consistent scaling of rigid body and experimental fluxural modes. In: Proceedings of the Fifth International Modal Analysis Conference, Society for Experimental Mechanics, Bethel, CT, pp. 1538–1544 (1987)
8. Hunter, T.P.N.: Nonlinear behavior of a 45 degree bolted lap joint. In: Proceedings of the Twenty-Fourth International Modal Analysis Conference, Society for Experimental Mechanics, Paper 204 (2006)
9. Mayes, R., Stasiunas, E.: Combining lightly damped experimental substructures with analytical substructures. In: Proceedings of the Twenty-Fifth International Modal Analysis Conference, Society for Experimental Mechanics, Paper 207 (2007)
10. Rixen, D.J., Godeby, E.P.: Dual assembly of substructures and the FBS method: application to the dynamic testing of a guitar. In: Proceedings of the Twenty-Eighth International Conference on Noise & Vibration Engineering (ISMA), Paper 195 (2006)
11. Woodbury, M.A.: Inverting modified matrices. Statistical Research Group, Memo. Rep. No. 42, Princeton University, Princeton (1950)
12. Brandt, A.: Noise and Vibration Analysis: Signal Analysis and Experimental Procedures. Wiley, Chichester (2010)
13. Cappellini, A., Manzoni, S., Vanali, M.: Quantification of damping effect of humans on lightly damped staircases. In: Proceedings of XXXI International Modal Analysis Conference, Garden Grove (California, USA), February 11–14 (2013)
14. Busca, G., Cappellini, A., Manzoni, S., Tarabini, M., Vanali, M.: Quantification of changes in modal parameters due to the presence of passive people on a slender structure. J. Sound Vib. **333**(21), 5641–5652 (2014). Original Research Article

Chapter 3
Real-Time State Detection in Highly Dynamic Systems

Ryan A. Kettle, Andrew J. Dick, Jacob C. Dodson, Jason R. Foley, and Steven R. Anton

Abstract This article investigates the feasibility of real-time state detection on a microsecond timescale for use in highly dynamic systems and presents an experimental setup of a high-rate dynamic system coupled with real-time measurement architecture with the goal of detecting changes in the interfacial state of the system. The feasibility of microsecond state detection is assessed through a preliminary timing study. The experimental setup consists of two colliding aluminum bars and includes the option of changing the bar's boundary conditions and the interface material between the bars. A piezoelectric transducer will be used for detecting changes in dynamic interfacial state by employing electromechanical impedance monitoring and the measurement data from this will be acquired and processed at high speeds using deterministic real-time tools and methodology. Damage detection algorithms from the structural health monitoring community will be used for rapid detection of changes in state. The eventual goal of this work is to adapt currently used methods or to develop entirely new high speed state detection algorithms to be implemented on the real-time system for state detection. This technology has the potential to be used in many applications, including the aerospace, civil, and energy industries among others.

Keywords Real-time • Structural health monitoring (SHM) • Electromechanical impedance (EMI) method • State detection • Dynamic systems

3.1 Introduction

The overall goal of this research is to create a system that enables rapid, microsecond detection in changes of state in highly dynamic environments. In this case state change is defined as any change to the physical properties of a material and can include changes in stiffness, boundary conditions, and mass. Detection of changes in state will be accomplished through high-speed sensing of a system's mechanical impedance, which is made possible by adapting the structural health monitoring (SHM) community's electromechanical impedance (EMI) method for damage detection. A potential benefit of this technology is the possibility to pair it with a control system that could work on the same microsecond time scale as the monitoring. This pairing would enable systems to react nearly instantaneously to changes in state as they occur in real-time. Possible applications for this technology are far reaching because it could be implemented in any situation where microsecond monitoring, decision making based on such monitoring, or rapid automated reaction via a control system is required or advantageous. One potential use of this technology is on the drill strings used in the mining industry. As a drill bit digs down deeper into the ground they will often dig into different layers of rock with different material properties, thus causing a change in the boundary conditions. With this technology immediate adjustments in torque, speed, etc. can be made. Additionally, a multitude of problems can occur due to different parts of the drill string making contact with the side of the wellbore and this could potentially be properly identified in real-time. Another potential use is to enable real-time monitoring of fluid flow around a hypersonic aircraft. This information could then be used to make rapid adjustments in the aircraft's control surfaces allowing for enhanced flight handling characteristics. A final application of this technology to be considered is deployment in buildings. Building conditions could be monitored in real-time during an earthquake. If the system detects

---

R.A. Kettle (✉) • S.R. Anton
Department of Mechanical Engineering, Tennessee Technological University, Cookeville, TN 38505, USA
e-mail: rakettle42@students.tntech.edu

A.J. Dick
Department of Mechanical Engineering, Rice University, Houston, TX 77005, USA

J.C. Dodson • J.R. Foley
Air Force Research Laboratory (AFRL/RWMF), Eglin AFB, FL 32542-5430, USA

© The Society for Experimental Mechanics, Inc. 2016

J. De Clerck, D.S. Epp (eds.), *Rotating Machinery, Hybrid Test Methods, Vibro-Acoustics & Laser Vibrometry, Volume 8*,
Conference Proceedings of the Society for Experimental Mechanics Series, DOI 10.1007/978-3-319-30084-9_3

that the building's structural integrity has become compromised it could alert the occupants of the building to evacuate, or conversely it could assure the occupants that the building is still stable and they should remain under cover inside the building.

3.2 EMI Method and Current State of Real-Time SHM

The electromechanical coupling properties of piezoelectric materials (PZTs) are the key to the SHM impedance method. The direct and converse coupling allows the piezoelectric materials to act as both a sensor and an actuator. By attaching a PZT patch to a structure, the electrical impedance of the PZT becomes a function of the mechanical impedance of the host structure in the area where the PZT is located [1]. Assuming that the properties of the PZT remain constant, any changes in the electrical impedance of the PZT can be ascribed to changes in the mechanical impedance of the structure. These changes in mechanical impedance are typically classified as "damage" to the structure.

To measure the electrical impedance of a PZT the SHM community has commonly used a HP4194A or other commercially available impedance analyzers [1]. Unfortunately these impedance analyzers have several drawbacks such as being large, heavy, expensive, and slow to make measurements and because of this there has been significant effort in the SHM community to develop better alternatives. There have been several suggested replacements including using a spectrum analyzer [2], a digital signal processor (DSP) [3], and a standard data acquisition device [4, 5]. It has been shown though that both the spectrum analyzer and digital signal processor hold a few disadvantages compared to the conventional data acquisition device. The spectrum analyzer method is essentially just an approximation based off of a resistor value which tends to make it inaccurate at high frequencies and the DSP method is restricted by the small memory space available on the chip, which restricts the range and frequency resolution [5]. The data acquisition device method is advantageous because it allows for a large range of hardware options, including the use of data acquisition devices with exceptionally high sampling rates.

Several recent papers have investigated real-time SHM being performed on, or developed for, buildings [6–8]. Data sampling rates range from 1 to 200 Hz in these works with one stating that the real-time data was only available once every 10 min [8]. These data sampling rates and data availability times are inadequate for real-time microsecond state detection. There was also the development of a real-time system with multiple sensors and temperature compensation with a sampling rate of 1.25 MS/s with a stated a completion time of 3 s [9]. This is certainly an improvement, but it is still several magnitudes away from microsecond monitoring. There have, however, been previous efforts made to push real-time SHM into the microsecond timescale. One technique that was explored was the use of an output only modal shape method which was used to detect simulated damage on a finite element model of an aluminum plate [10]. This method did successfully detect damage in the finite element model, but lacked any sort of time study for either the simulation or a real world application. Another technique investigated was wave-propagation, which is a method similar to EMI but measures mechanical waves that have propagated through the structure. Pairs of PZT transducers were used to detect damage by monitoring for changes in impact-induced waves as they travel through the structure [11]. An "instantaneous baseline" is created by the first PZT affected by the excitation and damage is detected by comparing this baseline measurement to the measurement of the next PZT in the path of the wave. This technique showed some promising results and was able to detect damage in the form of small cuts on a plate. While this work does make mention of techniques that can be used to reduce data collection time, it also unfortunately lacked any sort of time study and so it is unclear precisely how long the method takes to complete.

3.3 Adaptation of SHM Impedance Method and Equipment

A key difference in this work compared to conventional SHM is the use of higher frequencies in the excitation signal. Conventionally, most SHM uses excitation signals in the realm of tens or hundreds of kilohertz [1]. In an effort to reduce measurement time, the real-time approach investigated in this work will utilize excitation signals up to 50 megahertz. Higher excitation signals have also been shown to have a more local influence on a structure [12], which can be advantageous if there are only particular locations on a structure that are of interest.

Another key differentiating factors between this research and what is typically done in the SHM community is this work is concerned with the evaluation of system state, such as changes in boundary conditions and interfaces, rather than looking exclusively for structural damage. It should be noted that the detection in changes of boundary conditions is not something new to the SHM community [13] and has also been defined as damage before [14]. What is different is the idea that changes in boundary conditions, or any other changes detected in the system, are not necessarily indications of structural damage, but can provide critical information about the system.

The stepped sine wave measurement method utilized by impedance analyzers is simply not capable of measuring fast enough to be of use for real-time state detection. A faster excitation signal is necessary, therefore a chirp signal will be utilized. A chirp signal allows for the excitation of a very large frequency band in a relatively short amount of time which is exactly what is needed in order to make fast measurements. Chirp signals have been used successfully in SHM measurements and have been shown to give results similar to impedance analyzers [4, 5, 15].

In place of the impedance analyzer a field-programmable gate array (FPGA) will be used for both data acquisition and signal processing. An FPGA is a reprogrammable integrated circuit that offers two advantages over conventional data acquisition methods. First, an FPGA allows for high sample rates, in the realm of 100 MS/s or higher, which are necessary for microsecond data acquisition. Second, FPGAs are inherently well suited for use in real-time computing systems. Here it becomes necessary to define what "real-time" means in terms of a computer systems because it has a separate and distinct meaning compared to how the term real-time was used previously in this paper. When discussing computer systems, real-time refers to both hardware and software that runs with very precise timing and high reliability. Two additional terms are used when discussing real-time computer systems. The first is jitter, which is a measure in the amount of variation in completion time that occurs through multiple iterations of a process. The second is determinism, which refers to the guarantee that a process will be completed within a certain time frame. Standard personal computers use x86 processor architectures and are paired with conventional operating systems (OS) such as Windows and because of this have a relatively high amount of jitter and are not deterministic. This can be minimized by using a real-time OS, which helps reduce jitter and increase determinism by not allowing system interrupts such as user input, not running background programs, etc. Furthermore, the use of FPGAs and other integrated circuits allow for significantly lower jitter and higher determinism. Real-time computer systems help to ensure consistent and accurate data, which make them ideal for use in a real-time data acquisition and processing system.

3.4 Preliminary Timing Study

The following section is a "back-of-the-napkin" style analysis which gives an estimated completion time for the entire process of real-time state detection using impedance analysis. The process begins with the generation of the chirp excitation signal at the output pins of the FPGA DAQ card via digital-to-analog convertors (DAC). Then the signal travels across the PZT and is changed due to the PZT impedance. This response signal is then sampled at the input pins of the DAQ with analog-to-digital convertors (ADCs) simultaneously to the signal generation. The generation of the chirp signal [5] is given by

$$x\left[n\right] = A * \sin\left(\frac{2\pi}{F_S}n\left(\frac{f_2 - f_1}{2N}n + f_1\right)\right) \tag{3.1}$$

where N is the number of samples, $n = 0, 1, \ldots, N-1$, f_1 is the initial frequency, f_2 is the final frequency, F_S is the sampling rate, and A is the amplitude. The next step is the processing of the acquired data in order to calculate the electrical impedance of the PZT. The first, and by far most time consuming, stage is the calculation of the fast Fourier transform (FFT). The FFT is then used to calculate the frequency response function (FRF) which can then be used to solve for the impedance of the PZT [4, 5]. This step is unique to the method of impedance analysis that utilizes data acquisition devices because the impedance analyzers normally used by the SHM community step through and record the impedance at each frequency one at a time and therefore don't require the use of an FFT. In order to improve the statistical certainty of the measurement averages can be taken, which would result in repeating the previous two steps. Once the impedance of the measurement is calculated to the desired statistical certainty the root-mean-squared deviation is calculated by comparing the measurement to a known stored state and if this value exceeds a certain predefined value it is concluded that a change in state has occurred.

The time calculations are made by using just three input variables. The desired spectral resolution d_f which is given by F_s/N, the highest frequency to be generated in the excitation signal f_2, and the number of averages desired. These input values dictate the essential characteristics of the measurement system, F_s and N, which determine the timing of the various processes. F_s is calculated by using the relationship $F_s = 4f_2$ which was chosen because it limits F_s from becoming unnecessarily high, which can have a negative impact on timing, while ensuring that the sampling frequency is well above the Nyquist frequency. N is given by manipulating the previously mentioned relationship for the desired spectral resolution giving $N = F_s/d_f$. An important note is that most FFT architectures require the number of samples taken to be a power of 2 [16] because they are based off of the radix-2 implementation of the Cooley-Tuckey FFT algorithm [17]. This works by

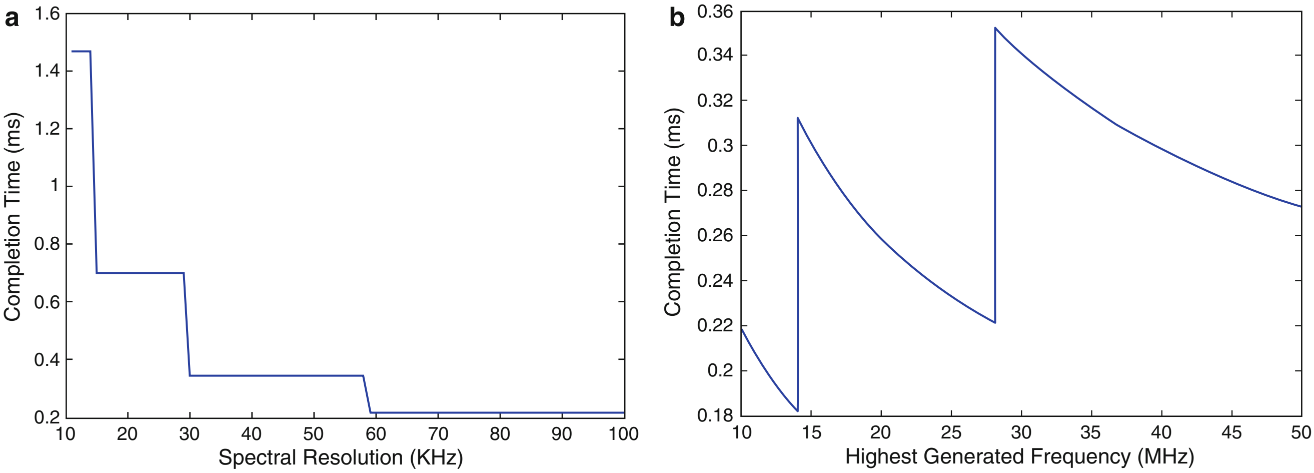

Fig. 3.1 Completion time with 5 averages being taken for (**a**) varying spectral resolution with the highest generated frequency being 30 MHz and (**b**) varying the highest generated frequency with the spectral resolution at 55 kHz

taking N and separating it into two interleaved $N/2$ discrete Fourier transforms and makes simplifying assumptions to reduce calculation times based on N being a power of two. With this in mind, the previously calculated value of N is increased to the next power of two, which can be called N_{P2}.

The time to generate the excitation signal is given by N/F_s [5]. The completion time of an FFT is dependent on several factors, including the FFT processor architecture chosen and the transformation length N_{P2}. Several different FFT architectures are available, all of which offer some compromise between the amount of space used on the FPGA and the time taken to perform the transformation [16, 18]. The FFT architecture used in this analysis was the pipelined streaming method, which favors speed at the expense of using more space on the FPGA [16]. The time required to perform the various calculations is completely dependent on FPGA clock speed, which will normally be on the order of several hundred MHz. However, the FPGA clock speed is dependent on the transform length of the FFT [16, 19], therefore the clock rate used in calculations needs to be adjusted as N_{P2} varies.

Recalling the steps necessary to complete the entire state detection process from earlier, averaging requires all of the steps to be repeated with the exception of the last two calculations, which have a negligible impact on total completion time. This means that the amount of averages taken has a nearly linear effect on the results. Figure 3.1 shows the effects that the spectral resolution and the highest generated frequency have on process completion time, both have 5 averages being taken. The stepped nature of the graphs is due to N_{P2} varying by powers of two. It can be seen from these graphs that through careful selection of variables it is possible to complete the entire measurement, calculation, and decision making process on the order of microsecond time scales, even with averages being taken. These predictions prove feasibility of real-time state detection using impedance analysis at the microsecond scale.

3.5 Design of Experimental Setup

The experimental setup chosen in this work is designed to create a highly dynamic event in the form of a collision, which will cause a change in state via a brief change in the boundary condition and internal stress state of the system. With this in mind the experimental setup was built around a piece of track in order to constrain the motion to one dimension in which one aluminum bar collides end-to-end with another. One bar is completely constrained and is instrumented with a single piezoelectric ceramic wafer for active measurement using the impedance method outlined earlier. The other aluminum bar that is used to strike the instrumented bar is not directly fastened to any part of the rest of the experimental setup. Instead, the striker bar rests on two raised portions of low friction material which is itself fastened to a cart the order to uncouple the striker bar from the cart. The cart that the striker bar rests on is hand launched down the track to impact the instrumented bar. Although hand launching is an inherently inconsistent method to give the impactor bar motion, it was chosen for its simplicity. To offset this inconsistency, a laser extensometer is used to measure the velocity immediately prior to impact. Figure 3.2 shows a CAD model of the experimental setup and Fig. 3.3 shows the experimental setup itself.

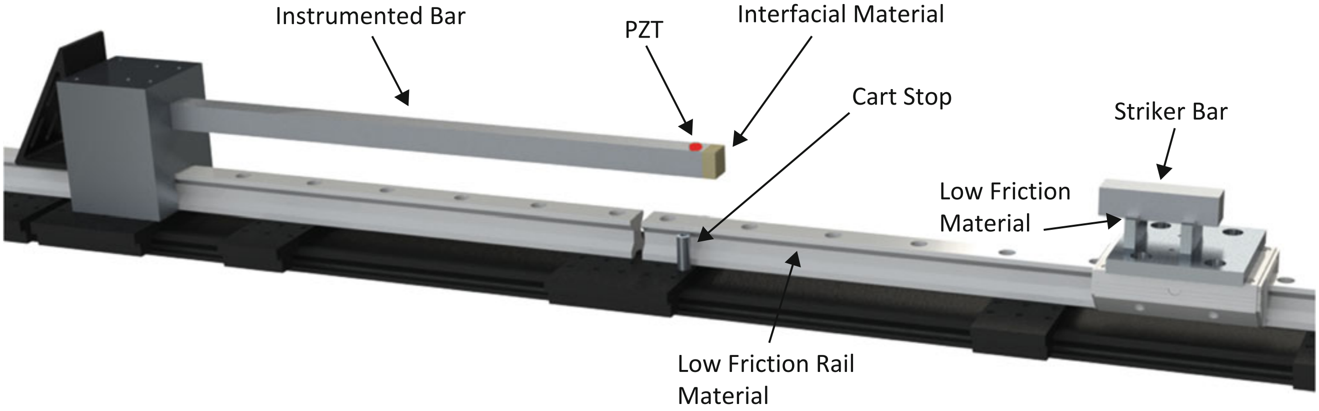

Fig. 3.2 CAD model of the experimental setup

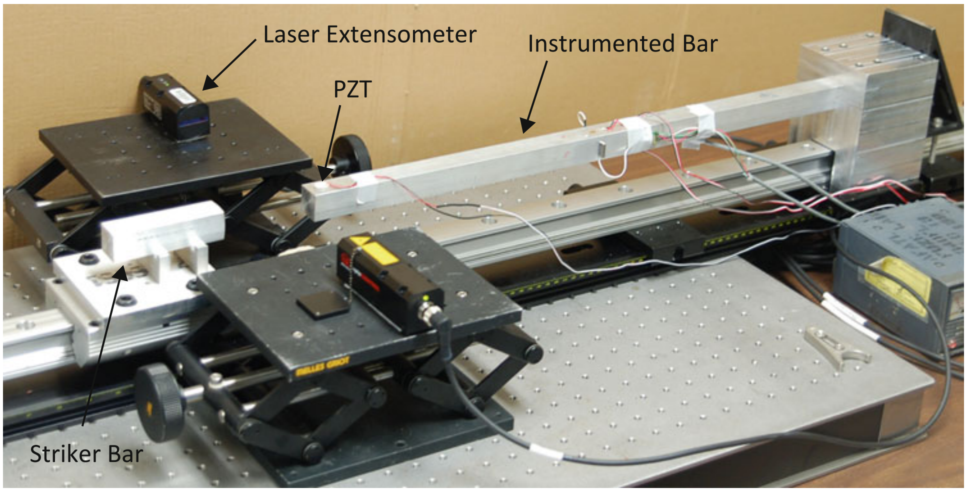

Fig. 3.3 Overall view of the experimental setup

An important consideration in the design of the test setup was to make the components modular. This includes the options of changing aspects of the experiment such as the bar lengths and materials. Of particular importance to this research is the configuration of the boundary conditions of the instrumented bar. The non-contact side of which can be configured as a cantilever or with springs of varying stiffness. The impacted side of the instrumented bar can have an elastic material bonded to it, thus adding an interface between the two bars during impact. This is of significant interest because it could be possible to detect the varying levels of compression the elastic interfacial material would undergo during impact. Most importantly though, the modular design allows others to investigate state detection in highly dynamic environments as well by allowing them to make non-permanent changes to the experimental setup to suit the needs of their own research.

Another design consideration was the choice of materials to use for the various parts of the structure. Aluminum was chosen for the bars because it was inexpensive, lightweight, and readily available. The geometry of both the instrumented bar and impactor bar were chosen to meet certain criteria. For example, the end of the impactor bar that strikes the instrumented bar is slightly rounded, sometimes called “bull nosed,” in order to ensure a good impact even if there are small misalignment issues. Another consideration was the bonding of the PZT onto the instrumented bar. PZTs are very brittle ceramics that are commercially available primarily as flat discs or wafers. It is possible to buy PZTs with custom geometry, but it is, in this case, a needlessly expensive option. So, a square cross section was chosen for the bars so a relatively inexpensive PZT would be easy to mount.

Another important aspect of the experimental setup is the equipment used for data acquisition. The FPGA DAQ used for this test setup is an NI PXIe-7965R with a NI 5781 adapter module which is capable of measuring at 100 MS/s. These are housed in an NI PXIe-1082 chassis that also holds an NI PXIe-8133 controller running a real-time OS. This controller is connected via an ethernet cord to a normal laptop running the programming software LabVIEW on a Windows OS. The controller running the real-time OS adds more real-time computing resources that can be leveraged. The most important of

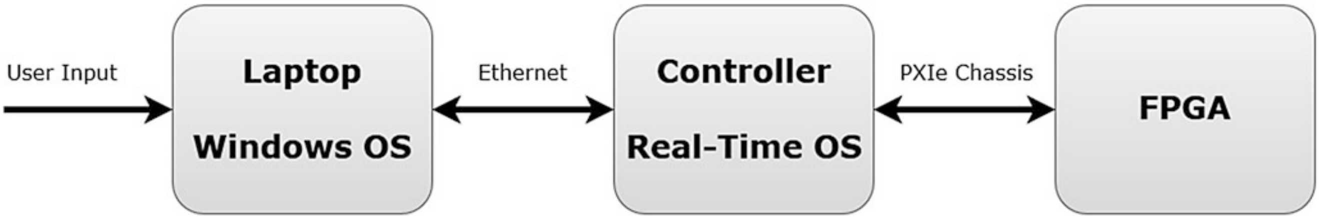

Fig. 3.4 Information flow of the real-time data acquisition system

which is data storage which will have relatively low jitter and so is better suited to interact with the FPGA. Since real-time OSs don't allow for typical user inputs, such as using a mouse or keyboard, user input can instead be entered into the laptop. This information can then be sent to the real-time OS on the controller via the ethernet and from there through the PXIe chassis to the FPGA. This information flow can be seen in Fig. 3.4. Although balancing the relationship between the three systems can be a bit of a challenge at times, this setup offers a tremendous amount of flexibility and options.

3.6 Non-Real-Time Data Acquisition

Initial results have been collected from the experimental setup using a simplified non-real-time data acquisition system and using a single frequency in the kilohertz range to excite the PZT. This set of data, although limited in scope, is meant to serve as a proof of concept for detecting collisions at high speed using the EMI method. An NI PXI-6133 S Series multifunction DAQ card was used to generate the excitation signal and acquire the response using a sampling frequency of 2.5 MS/s. Figure 3.5 shows a zoomed in section of data from the extensometer and the voltage response signal from the PZT, spanning from immediately before to immediately after the impact. The measurement circuit used was taken from the literature [8] and is shown in Fig. 3.6 where $x(t)$ is the excitation signal, R_s is a precision resistor used to limit the current, $y(t)$ is the response signal, Z_{PZT} is the impedance of the PZT, and Z_{in} is the input impedance of the data acquisition device. Because everything else in the measurement circuit is constant, the change in the voltage response of the measurement circuit is due to the change in impedance of the PZT caused by the impact. This proves that state detection through EMI in highly dynamic environments is possible.

3.7 Conclusions

This paper presented a plan to adapt currently used methods and technologies employed by the SHM community for use in real-time state detection on the microsecond time scale for use in highly dynamic systems. A timing feasibility study was then conducted which outlined the steps required to make a measurement using the electromechanical impedance method. It was shown that real-time state detection could be done on the microsecond time scale. Then a modular experimental setup was presented that is intended to replicate a highly dynamic system through the creation of a collision and was designed for the express purpose of being highly customizable and having potential use even outside the goals of this research. Finally, a set of non-real-time data was presented which proves that state detection through EMI in highly dynamic environments is possible.

3.8 Future Work

In order to obtain experimental results, a program for real-time data acquisition needs to be created. Of primary concern is the volume of data that has to be handled when monitoring on the microsecond scale for even just a few seconds. Once the data acquisition program is completed and the results can start being collected and evaluated, further strides in the research can be made. This includes the possibility to develop better state detection algorithms, investigating the use of different FFT architectures that may be more efficient, and discovering empirically how many averages are necessary for a reliable impedance measurement.

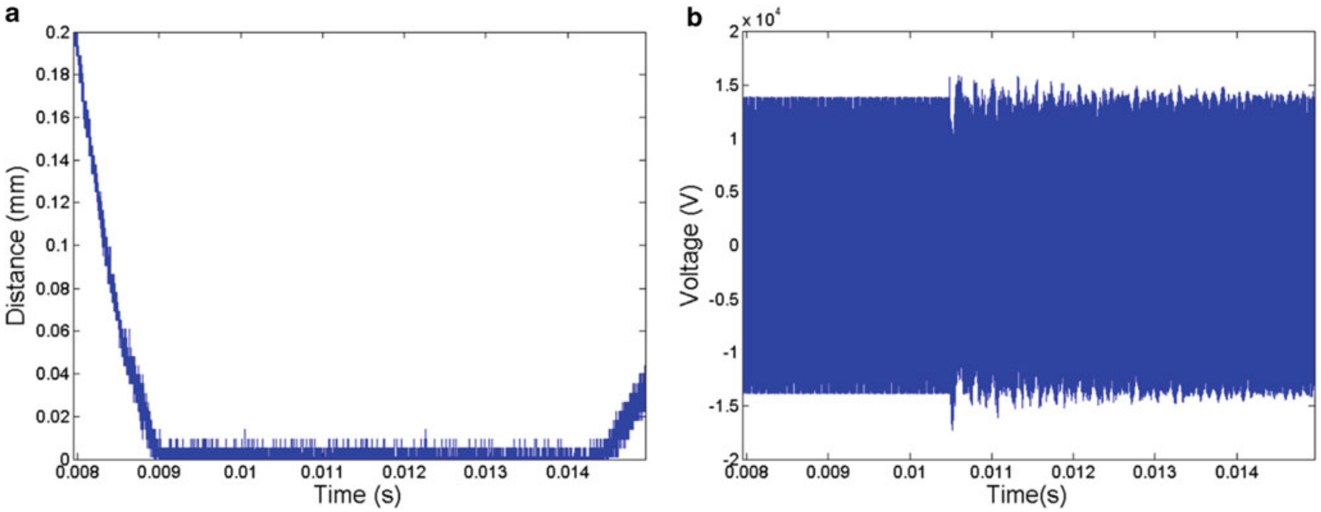

Fig. 3.5 Part (**a**) shows the extensometer readings during an impact of 6.20 m/s. The corresponding voltage response measurement using an excitation frequency of 79.580 kHz is shown in part (**b**)

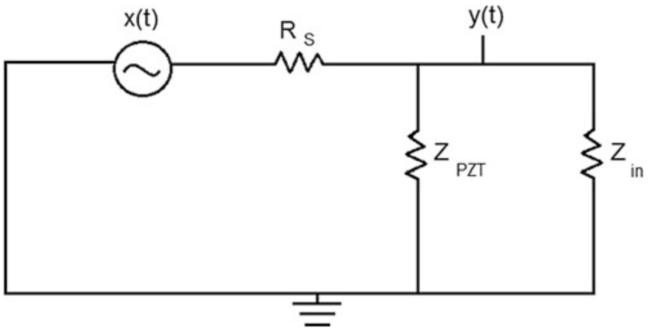

Fig. 3.6 Measurement circuit used for data collection

References

1. Park, G., Sohn, H., Farrar, C.R., Inman, D.J.: Overview of piezoelectric impedance-based health monitoring and path forward. Shock Vib. Digest **35**(6), 451–463 (2003)
2. Peairs, D.M., Park, G., Inman, D.J.: Improving accessibility of the impedance-based structural health monitoring method. J. Intell. Mater. Syst. Struct. **15**(2), 129–139 (2004)
3. Kim, J., Grisso, B.L., Ha, D.S., Inman, D.J.: A system-on-board approach for impedance-based structural health monitoring. Proc. SPIE **6529**(1), (2007)
4. Xu, B., Giurgiutiu, V.: A low-cost and field portable electromechanical (E/M) impedance analyzer for active structural health monitoring. In: 5th International Workshop on Structural Health Monitoring (2005)
5. Baptista, F.B., Filho, J.V.: A new impedance measurement system for PZT-based structural health monitoring. IEEE Trans. Instrum. Measure. **58**(10), (2009)
6. Kaya, Y., Safak, E.: Real-time structural health monitoring and damage detection. In: Topics in Dynamics of Civil Structures: Proceedings of the 31st IMAC, A Conference on Structural Dynamics, pp. 11–19 (2013)
7. Linderman, L.E., Mechitov, K.A., Spencer Jr., B.F.: TinyOS-based real-time wireless data acquisition framework for structural health monitoring. Struct. Control Health Monit. **20**(6), 1007–1020 (2013)
8. Kijewski-Correa, T., Kwon, D.K., Kareem, A., Bentz, A., Guo, Y., Bobby, S., Abdelrazaq, A.: SmartSync: an integrated real-time structural health monitoring and structural identification system for tall buildings. J. Struct. Eng. **139**, 1675–1687 (2013)
9. Baptista, F.B., Filho, J.V., Inman, D.J.: Real-time multi-sensors measurement system with temperature effects compensation for impedance-based structural health monitoring. Struct. Health Monit. **22**(2), 173–186 (2012)
10. Dodson, J.C., Inman, D.J., Foley, J.R.: Microsecond structural health monitoring in impact loaded structures. Proc. SPIE **7259**(1), (2009)
11. Dodson, J.C., Foley, J.R., Inman, D.J.: Structural health monitoring of an impulsively loaded structure using wave-propagation based instantaneous baseline. Proc. SPIE **7650**(1), (2010)
12. Worden, K., Farrar, C.R., Manson, G., Park, G.: The fundamental axioms of structural health monitoring. Proc. R. Soc. Lond. A: Math. Phys. Eng. Sci. **463**(2082), 1639–1664 (2007)

13. Sun, F.P., Chaudhry, Z.A., Rogers, C.A., Majmundar, M., Liang, C.: Automated real-time structure health monitoring via signature pattern recognition. Proc. SPIE **2443**(1), (1995)
14. Farrar, C.R., Worden, K.: An introduction to structural health monitoring. In: New Trends in Vibration Based Structural Health Monitoring, pp. 1–17 (2010)
15. Saar, T.: Robust piezo impedance magnitude measurement method. Elektronika Ir Elektrotechnik **113**(7), (2011)
16. Xilinx LogiCORE IP Fast Fourier Transform v7.1
17. Cooley, J.W., Tukey, J.W.: An algorithm for the machine calculation of complex Fourier series. Math. Comput. **19**(90), 297–301 (1966)
18. Saeed, A., Elbably, M., Abdelfadeel, G., Eladawy, M.I.: Efficient FPGA implementation of FFT/IFFT processor. Int. J. Circuits Syst. Signal Process. **3**(3), 103–110 (2009)
19. Uzun, I.S., Amira, A., Bouridane, A.: FPGA implementations of fast Fourier transforms for real-time signal and image processing. Vis. Image Signal Process. IEE Proc. **152**(3), 283–296 (2005)

Chapter 4
Stereo-DIC Measurements of Thermal Gradient Effects on the Vibratory Response of Metals

Ryan Berke, Ravinder Chona, Arthur Ding, John Lambros, Eann Patterson, and Christopher Sebastian

Abstract Thermomechanical problems have been much less studied than their room temperature counterparts as challenges arise both with metrology and with interpretation of results. This effort aims to shrink this knowledge gap by investigating the influence of thermal effects on the high frequency vibratory response of metals. The present study concentrates on how an inhomogeneous temperature field (max. 600 °C) affects the vibratory response, and specifically mode shapes and resonant frequencies, of a vibrating plate. A plate made of a nickel-based superalloy, Hastelloy X, was heated by induction heating and the temperature distribution was estimated by measuring the out-of-plane curvature resulting form heating. Harmonic vibratory loading at frequencies exceeding 1 kHz was applied using a programmable shaker. Stereo-vision digital image correlation (stereo-DIC) was used to obtain a full-field representation of the vibrating plate. An image decomposition analysis technique based on Tchebichef polynomials was used to compare room and high temperature mode shapes. Results indicate that there is a small influence of temperature on resonant frequencies, even though mode shapes remain similar between room and high temperature vibration.

Keywords Stereo digital image correlation • High temperature measurement • Thermo-acoustic loading • Induction heating • Image decomposition analysis

4.1 Introduction

Motivated by the increasing interest in applications involving significant thermal effects, such as aero-engines, spacecraft re-entry, aircraft hypersonic flight, and nuclear power applications, recent efforts have extended the upper temperature limit of the Digital Image Correlation (DIC) technique by the use of optical bandpass filters and narrow band lighting, which reduces the influence of light radiated by the specimen at high temperatures [1–6]. However, in many of the high temperature applications mentioned above high temperatures are accompanied by significant vibratory loading, both transient and steady-state. Such combined extreme thermomechanical environments have not been studied as much as room temperature vibrations. In the few studies that do exist high speed imaging has been used to study the transient response over small time intervals limiting the time window of recording [7, 8]. Consequently, thermomechanically coupled phenomena are not well understood and predictive models in these extreme environments are sometimes inaccurate. The present study seeks to address the lack of such experimental data and aims to (1) obtain high quality experimental data suitable for validation of numerical results in a combined thermal and mechanical/vibratory environment, (2) study the influence of elevated temperature on the vibratory response of a metallic plate, and specifically investigate the change of resonant modes at elevated temperatures.

R. Berke
Mechanical and Aerospace Engineering, Utah State University, 4130 Old Main Hill, Room 419P, Logan, UT 84322-4130, USA

R. Chona
Aerospace Systems Directorate, Air Force Research Laboratory, 2130 Eighth Street, Bldg 45, Rm 190,
Wright-Patterson AFB, OH 45433-7542, USA

A. Ding • J. Lambros (✉)
Aerospace Engineering, University of Illinois Urbana-Champaign, 104 S., Wright St., Urbana, IL 61801, USA
e-mail: lambros@illinois.edu

E. Patterson • C. Sebastian
Centre for Materials and Structures, University of Liverpool, The Quadrangle, Brownlow Hill L69 3GH, UK

© The Society for Experimental Mechanics, Inc. 2016

J. De Clerck, D.S. Epp (eds.), *Rotating Machinery, Hybrid Test Methods, Vibro-Acoustics & Laser Vibrometry, Volume 8*,
Conference Proceedings of the Society for Experimental Mechanics Series, DOI 10.1007/978-3-319-30084-9_4

4.2 Experimental Method

Experiments were conducted on 120 × 80 × 1 mm plates of Hastelloy-X, a nickel-based superalloy. A 5 mm diameter hole was drilled through the center and a threaded stinger rod was attached to the plate. A mechanical shaker was then used to excite the plate via the stinger rod. The front surface of the plate was speckled using high temperature refractory paints with a white paint serving as the background and a black paint used to speckle the white background with random speckles. The plate was heated by magnetic induction using a pancake-type coil [9]. The coil was positioned behind the plate so as not to obstruct image capture of the front surface of the plate. An opening was included in the center of the coil for the stinger rod to connect to the specimen without either the rod or the specimen coming into contact with the coil. The temperature was monitored using a single K-type thermocouple bonded to the back of the plate at the position where the threaded rod was attached. A schematic of the experimental apparatus which includes the plate/rod/shaker assembly is given in Fig. 4.1.

Heating of the initially nominally flat plate by the induction coil was heterogeneous both in-plane and through-thickness, resulting in significant out-of-plane deformation. The shape of the plate was measured from stereo image pairs collected before and after heating using Vic-3D, a commercially available stereo-DIC algorithm from Correlated Solutions Inc. [Columbia, SC, USA]. A typical set of measurements for the front surface of the plate after heating are plotted in Fig. 4.2a. This measurement determined the starting geometry prior to the application of vibratory loading. This measured deformed shape was also used to estimate the in-plane temperature distribution across the front surface of the plate. This was accomplished by (1) taking the static images of the speckled surface before and after heating, (2) calculating the thermal strains from these images, and (3) dividing the thermal strains by the temperature-dependent coefficient of thermal expansion (CTE) of Hastelloy-X provided by the manufacturer and which was assumed to be isotropic and constant through the thickness of the plate. The resultant estimated temperature distribution, which is shown in Fig. 4.2b, is non-uniform due to the irregular shape and spacing of the induction coil. It has a maximum estimated temperature of around 600 °C occurring at the bottom edge of the plate, in this case.

The out-of-plane displacement of the plate was monitored from the front using a laser vibrometer connected to an oscilloscope (Fig. 4.1, components 11 and 12). Resonant frequencies were then found by adjusting the sine wave over a range of frequencies until a local maximum in the amplitude of the displacement was observed. A total of 9 resonant frequencies were observed at room temperature, and another 9 were observed at high temperature. For each of the resonant

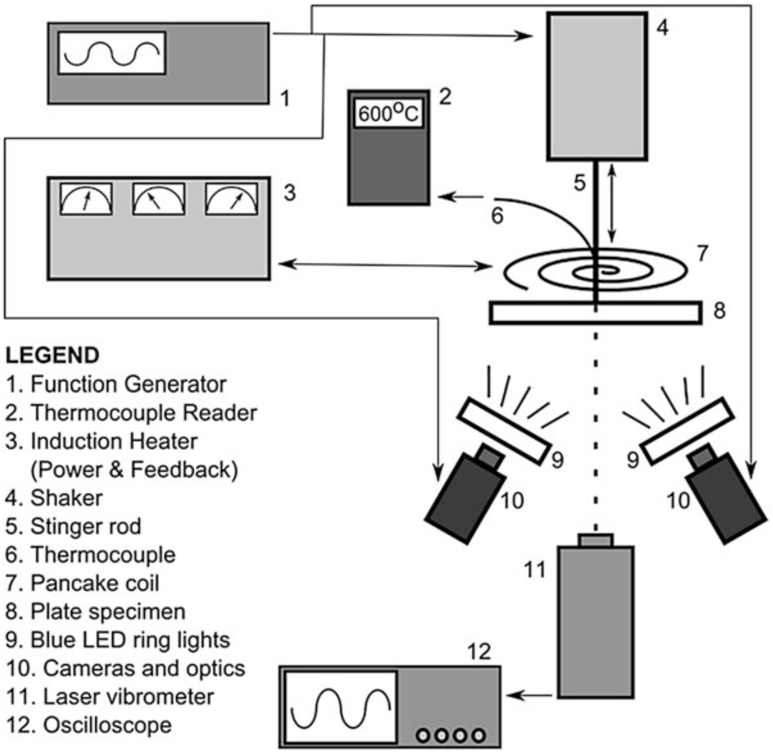

Fig. 4.1 Schematic of experimental setup

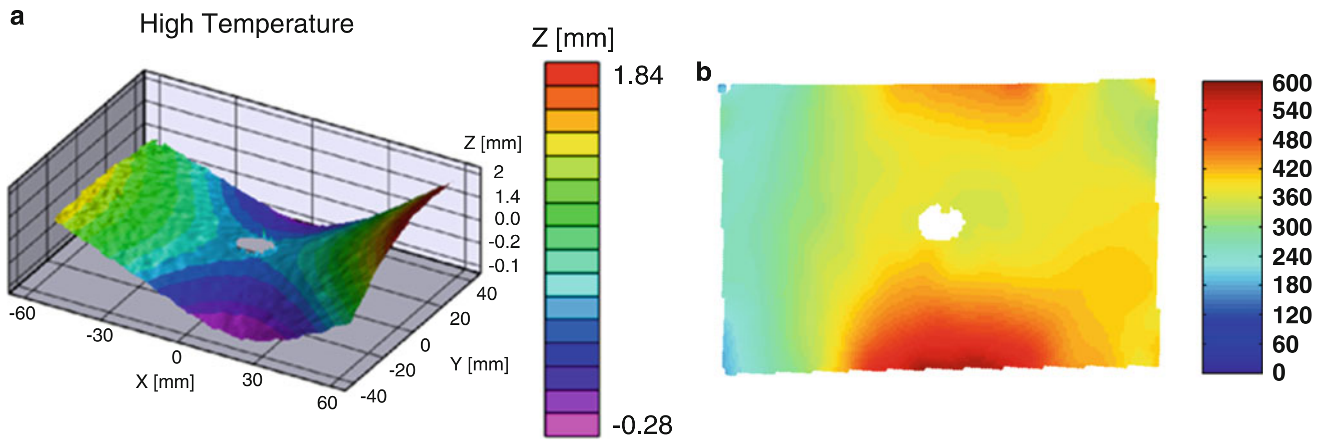

Fig. 4.2 (**a**) Out-of-plane deformation (in mm) measured for the entire front surface of the plate using stereo DIC for the stationary plate at elevated temperature. (**b**) Estimated temperature distribution (in °C) on the front surface of the plate computed from the stereo DIC data on *left*

frequencies, a series of stereo images were taken using a pair of 1024 × 1024 pixel CCD cameras and 50 mm lenses with blue-range bandpass optical filters resulting in an average magnification of 0.13 mm/pixel. The cameras were triggered using the Fulcrum module of the Vic-Snap image acquisition software provided by Correlated Solutions. The maximum frame rate of the cameras was 112 fps, which was much slower than the oscillation of the plate. To correct for the slower frame rate, the Fulcrum software uses phase-locking to time image acquisition such that images taken from successive periods of oscillation can later be reconstructed into one representative period. Image pairs were acquired every 5° in the period of the oscillation, resulting in a total of 71 image pairs for each resonant mode. Displacements and strains were computed using Vic-3D. The analysis was performed with a 29 × 29 pixel subset at an interval of 7 pixels, which were found to work satisfactorily based on rigid-body motion experiments of the specific patterns in each case. Pixel subsets which overlapped with the attachment nut were excluded from all DIC computations. These experimental parameters were chosen based on prior work in which detailed assessment of uncertainties of 3-dimensional dynamic measurements were made [10].

4.3 Results and Discussion

The modal shapes were measured by DIC at room temperature and at elevated temperature. An example for the third mode (first deformation mode-bending) is shown in Fig. 4.3a, c for room and elevated temperature, respectively. Furthermore a finite element simulation was also conducted to numerically obtain the corresponding mode shape, shown in Fig. 4.3b, c for the room and high temperature cases respectively. The FEA analysis used the temperature field in Fig. 4.2b to assign thermally softened properties to each corresponding region of the material.

The simulated mode shapes are compared quantitatively to the experimentally measured mode shapes using a recently developed image decomposition technique [11, 12]. In brief, the technique works by using a set of polynomials to describe the modal shapes such that a knowledge of the polynomials used and their coefficients provides a complete description of the modal shape. In this work, two-dimensional Tchebichef polynomials were used with 55 terms to ensure a high-fidelity representation of the modal shapes; however, in most cases the contribution from the higher order terms was small or negligible with the first 15 terms dominating. The kernels for these 15 terms are shown in the left hand side of Fig. 4.4. The value of the coefficient corresponding to each kernel can be considered to represent the contribution of that kernel to representing the modal shape. A summation of the contribution from the kernels allows the modal shape to be reconstructed. The error in the decomposition process can be assessed by comparing the original and reconstructed data and calculating the average squared residual for the images, u^2. The Tchebichef decomposition and reconstruction process is illustrated in the top right part of Fig. 4.4, using DIC data for Mode 6 at high temperature as an example. In step 1, the DIC data is rotated and mapped onto a square domain. In step 2, a decomposition algorithm computes the Tchebichef coefficients which are shown in the bar chart [11–13]. In step 3, the shape is reconstructed by taking the summation of each kernel multiplied the coefficients computed in step 2. The reconstructed data, which contain no hole for the attachment nut, are then compared to the initial data to assess the error produced by the decomposition, in terms of the average squared residual, u^2

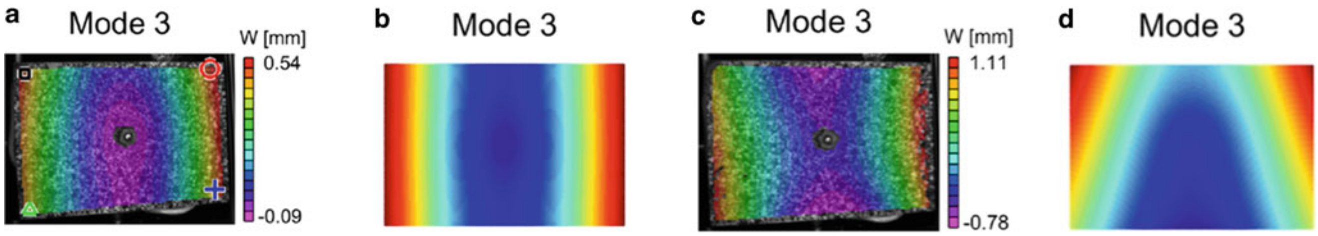

Fig. 4.3 Modal shapes for mode 3 (bending) obtained at (**a**) DIC room temperature, (**b**) finite elements, room temperature, (**c**) DIC high temperature, (**d**) finite elements, high temperature

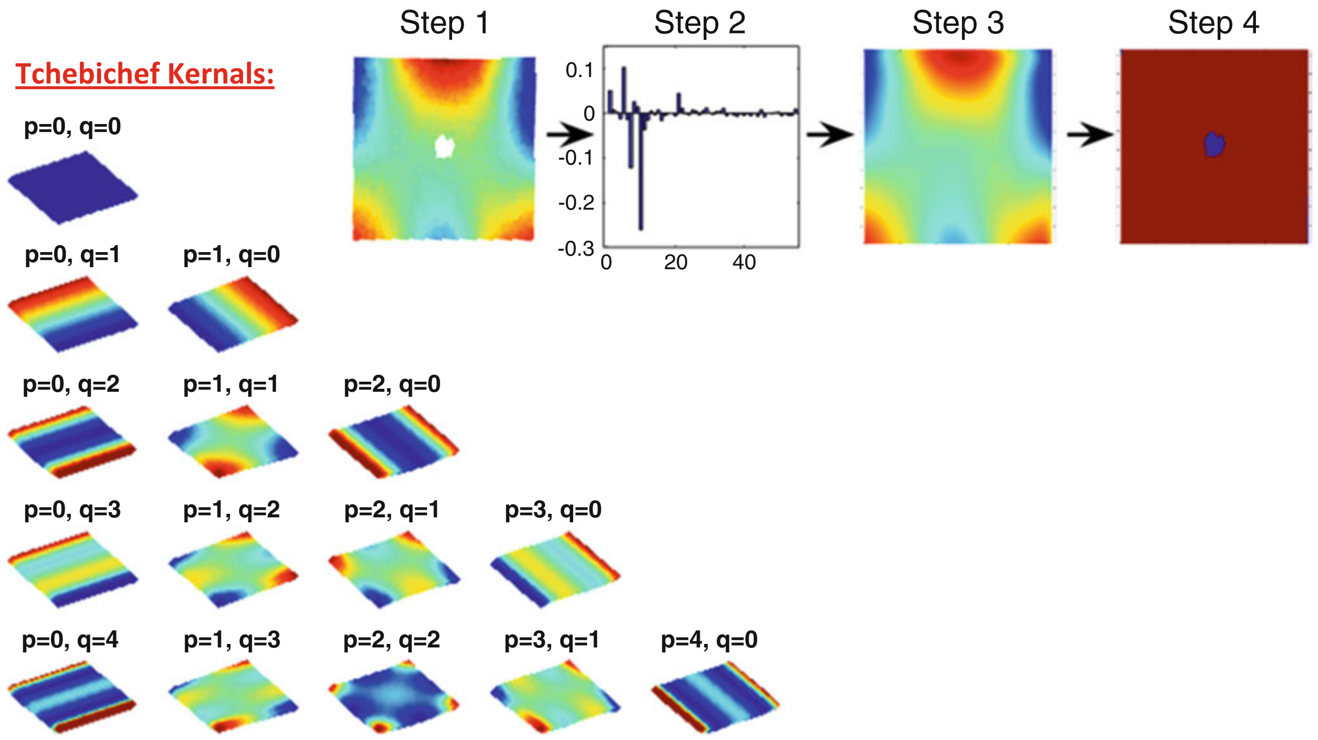

Fig. 4.4 First 15 Tchebichef kernels (*lower left*) and schematic of image decomposition process (*upper right*)

$$u^2 = \frac{1}{N}\Sigma_{i,j}^{N}\left(\widehat{I}\,(i,j) - I\,(i,j)\right)^2$$

where $\hat{I}(i,j)$ is the reconstructed value of the original image, $I(i,j)$. In step 4, it is ensured that no location shows a clustering of residuals greater than $3u$ where a cluster is defined as a group of adjacent pixels comprising 0.4 % or more of N, the total number of pixels in the region of interest [13]. Consequently, the error in the reconstruction is expected to be less than $3u$, except for the pixels corresponding to the hole in the data. In Fig. 4.4, the pixels with residuals less than $3u$ are plotted in red and the pixels greater than $3u$, corresponding only to the hole in the data, are plotted in blue.

In this study, the average residual, u_{resid} varied from 0.034 to 0.138 for the room temperature experimental results and from 0.027 to 0.071 for the high temperature results. The total uncertainty in the Tchebichef feature vector, $u(S_E)$, is defined by combining the average residual from the reconstruction process with the uncertainty in the experimental setup, u_{meas} as follows:

$$u\,(S_E) = \sqrt{u_{meas}^2 + u_{resid}^2}$$

For this study, the results from a previous dynamic assessment of a high-speed DIC system [13] were used as typical values for u_{meas}. Relative uncertainty of 1.8 % of the total measurement range was used, which resulted in a value of $u_{meas} = 0.018$.

The Tchebichef coefficients representing each experimentally measured mode shape are plotted against those for each corresponding simulated mode shape for room temperature in Fig. 4.5a and for high temperature in Fig. 4.5b. The coefficient

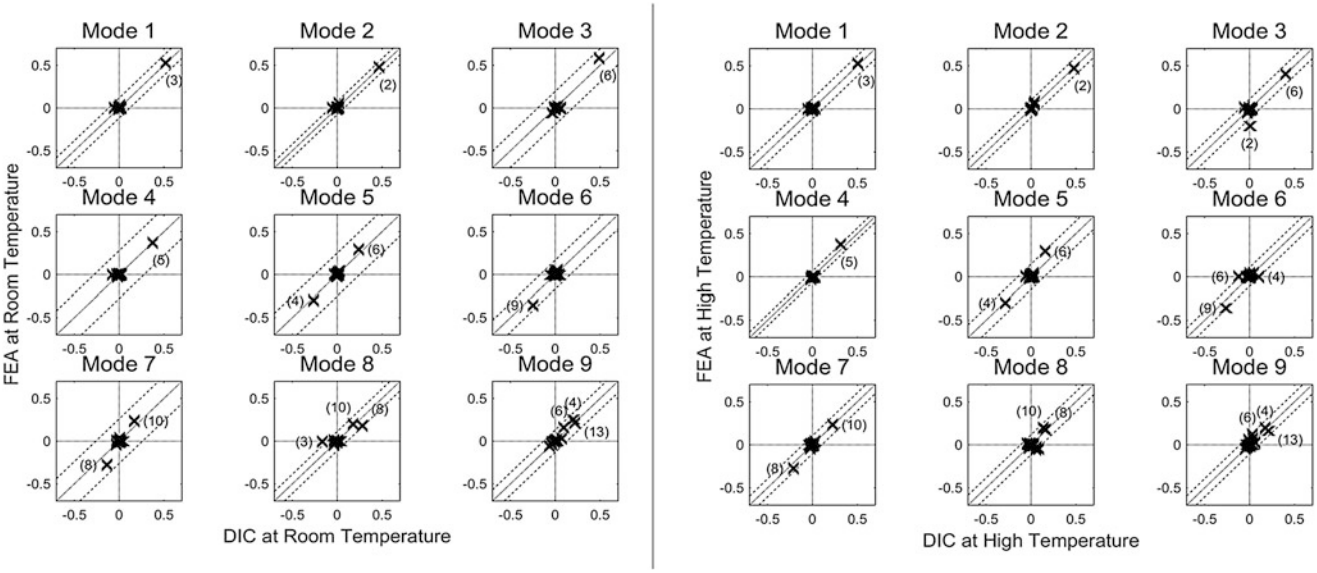

Fig. 4.5 Comparison of Tchebichef coefficients representing the data obtained from experiment (*horizontal axis*) and simulation (*vertical axis*) at (**a**) room temperature, and (**b**) elevated temperature. Kernels which have significantly large coefficients are indicated by their kernel number in parentheses

of the first kernel, which corresponds to a rigid out-of-plane translation, as shown in Fig. 4.4, and is unrelated to the deformation of the plate, is excluded from the figures. The remaining 54 coefficients are all included, although in reality most of the mode shapes can be reconstructed using relatively few coefficients or kernels. The coefficients with larger magnitudes are farther away from the plot origin and hence represent those kernels that contribute most strongly to the modal shape. The largest coefficients are labeled with the numbers in parentheses corresponding to the kernels in Fig. 4.4.

Each plot in Fig. 4.5 also includes a line of gradient one, which is indicative of perfect agreement between the simulation and the experimental results. The closer a data point lies to this line, the better the agreement is for that coefficient between simulation and experiment [11, 13]. In the comparison, it is likely that there will be noise in the experimental data and errors in the simulation which will cause the points to deviate from this line. Therefore an acceptable area can be defined around the ideal line as $+/-2u(S_E)$, defined by the dashed line pairs in the figures. If all of the data points from the comparison of the Tchebichef feature vectors fall within this area then the simulation can be deemed an acceptable representation of the experiment [13].

In general, the uncertainty bands are smaller for the high temperature results (Fig. 4.5b) than for the room temperature results (Fig. 4.5a). This is a result of a lower average residual in the reconstruction of the high temperature experimental results because the larger displacements have less noise. For the majority of the plots, all of the data points fall within the acceptable area, and many of the data points fall on the ideal line, indicating agreement between the simulation and the experiment. For example for Mode 3 in Fig. 4.5, only one Tchebichef kernel is dominant—specifically #6 in Fig. 4.4—which corresponds to a shape produced by bending about the vertical axis. Most other kernels have coefficients clustered at the origin of the plot in Fig. 4.5, i.e., they are near zero. Overall Fig. 4.5a and b show that there is a very good comparison of the spatial distribution of out-of-plane displacements between the predicted and measured resonant modes. One notable exception to this is mode 3 at high temperature (Fig. 4.5b). In this mode there is a kernel, #2, which falls outside the acceptable area defined by $+/-2u(S_E)$. This kernel has a significant non-zero value for the simulation data but is zero-valued for the DIC data. Kernel #2 corresponds to a rigid body out-of-plane rotation about a horizontal axis, and is the dominant kernel in mode 2.

The data presented in Fig. 4.5a and b can be summarized as in Fig. 4.6. Each mode is represented by a row in the figure in which those Tchebichef coefficients that were more than 20 % of the value for the largest coefficient for each mode shape have been plotted as bars under the corresponding column for the Tchebichef kernel. Data from both experiment (red) and simulation (blue) have been included as well as at room (dark colors) and high (bright colors) temperature. The exclusion of low value coefficients following the approach of [14] simplifies the figure without excluding any significant information. The shape represented by the kernels is shown along the top of the figure. A comparison of the height of the bars in each chart provides information both about the changes in behavior from room to high temperature (left pair for experiment or right pair for simulation) and about the degree to which the simulation represents the experiment (right pair relative to left pair).

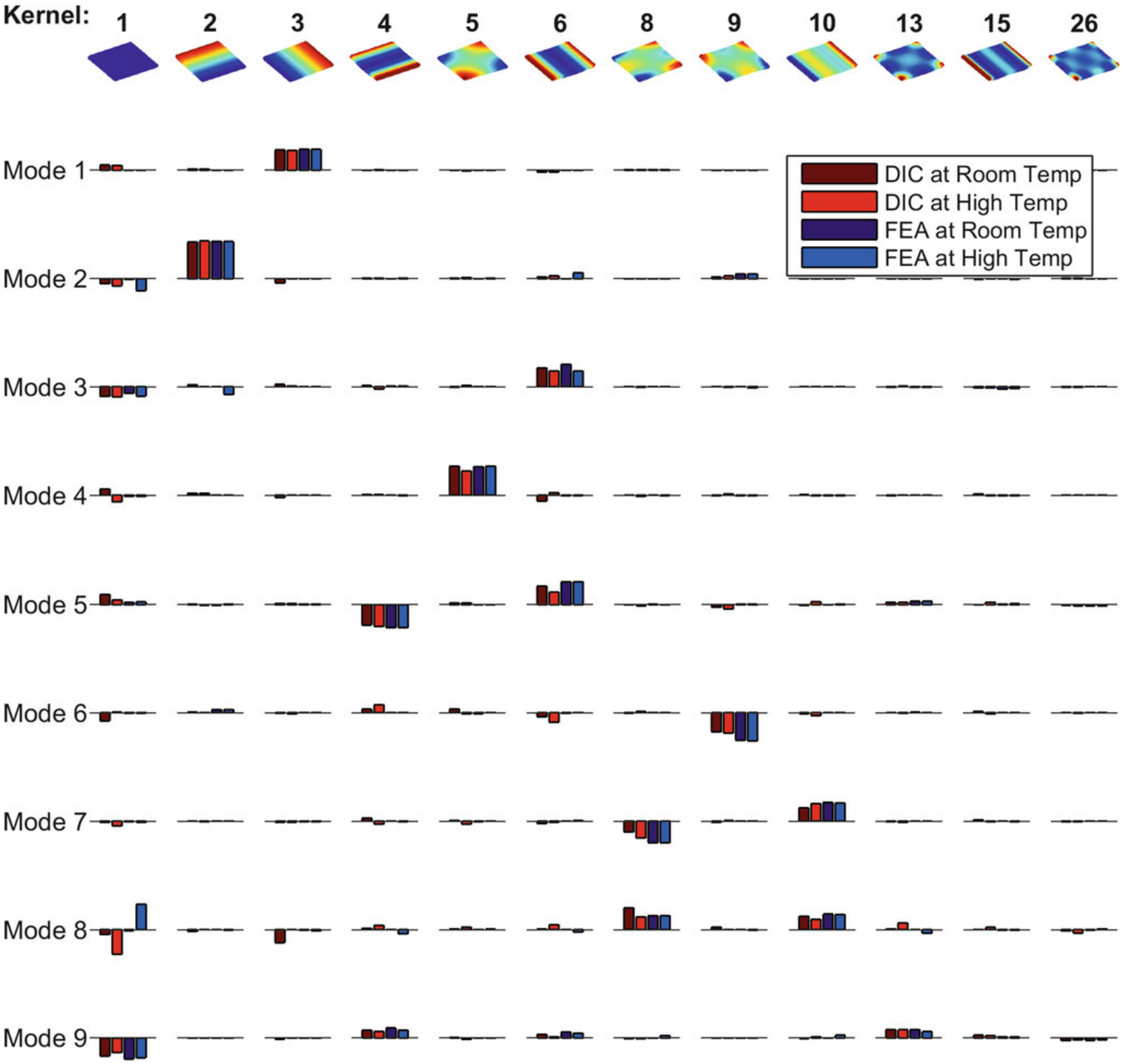

Fig. 4.6 A schematic diagram summarizing the results with the Tchebichef kernels shown along the top row with the corresponding coefficients from both room (*darker color*) and high (*bright color*) temperature tests shown in the bar charts from both the experiment (*red*) and simulation (*blue*)

The column in which the larger bars appear for a particular mode provide an indication of the dominant components of the deformation. Note that negative values simply indicate that the out-of-plane deformation was in the opposite orientation to the Tchebichef kernels. So, for instance examining mode 3 again, it can be seen that the simulation reproduces the decrease in the sixth coefficient with increasing temperature observed in the experiment but predicts a significant value for the second coefficient which is not present in the experiment. The dominant role of the second coefficient in mode 2 can also be observed. When the first coefficient is ignored, which represents the ‘piston term’ or average magnitude, the figure shows a trend in which the higher magnitude bars are found along the diagonal from top left to bottom right, i.e., the higher order, more complex kernels are used to represent the higher order modes, which is entirely expected. The higher order modes also tend to require more kernels to represent them, which is again expected due to their more complex shape. Overall, the figure supports the conclusion that the simulation is a good representation of the experiment and permits the more complex modal shapes to be visualized in terms of the simpler kernel shapes.

4.4 Conclusions

The work described here has combined, for the first time, high frequency vibratory loading (up to about 1300 Hz) at elevated temperature (up to 600 °C) with the full-field optical diagnostics of stereo-DIC. This combination has provided high quality experimental data suitable for the validation of numerical results. Using this combined loading experimental set-up with induction heating and shaker-induced vibration, the thermo-acoustic behavior of a rectangular plate of Hastelloy-X was explored. By investigating the first 9 resonant modes at both room temperature and high temperature, and measuring mode shapes for each of the resonant frequencies using stereo-DIC, the influence of temperature on the thermomechanical vibratory response of the plate was assessed. A decrease in resonant frequencies was seen with increasing temperature, although the first 9 mode shapes themselves were similar. Companion finite element numerical simulations that accounted for the temperature dependence of elastic modulus also produced very similar mode shapes, although the influence of temperature on modal frequencies was not as significant as observed experimentally. As a model process for validating simulation results based on this type of experimental data collection an image decomposition technique based on 2D Tchebichef polynomials [13] was used. The image decomposition, which allows comparison between numerics and experiments using the fitted Tchebichef coefficients rather than the entire images, confirmed quantitatively the qualitative observation that as temperature increased the resonant mode shapes remained very similar. Overall, the results of this combined thermal-mechanical study point to the conclusion that the simulation is a good representation of the experiment both at room temperature and at high temperature (in fact a little better at high temperature as the signal to noise ratio in that experiments is larger).

Acknowledgements This effort was sponsored by the Air Force Office of Scientific Research, Air Force Material Command, USAF under grant numbers FA8655-11-3083 and FA9550-12-1-0386. The U.S. Government is authorized to reproduce and distribute reprints of Governmental purpose notwithstanding any copyright notation thereon. Major Matt Synder (EOARD) and Dr. David Stargel (AFOSR) respectively are the program officers for these grants. EAP is the recipient of a Royal Society Wolfson Research Merit Award. The collaboration that was central to this study was supported by a Royal Academy of Engineering Distinguished Visiting Fellowship awarded to JL.

References

1. Grant, B.M.B., Stone, H.J., Withers, P.J., Preuss, M.: High-temperature strain field measurement using digital image correlation. J. Strain Anal. Eng. Des. **44**(4), 263–271 (2009)
2. Novak, M.D., Zok, F.W.: High-temperature materials testing with full-field strain measurement: experimental design and practice. Rev. Sci. Instrum. **82**(11), 115101 (2011)
3. Chen, X., Xu, N., Yang, L., Xiang, D.: High temperature displacement and strain measurement using a monochromatic light illuminated stereo digital image correlation system. Meas. Sci. Technol. **23**(12), 125603 (2012)
4. Pan, B., Wu, D., Wang, Z., Xia, Y.: High-temperature digital image correlation method for full-field deformation measurement at 1200 °C. Meas. Sci. Technol. **22**(1), 015701 (2011)
5. Hammer, J.T., Seidt, J.D., Gilat, A.: Strain measurement at temperatures up to 800 °C utilizing digital image correlation. In: Jin, H., Sciammarella, C., Yoshida, S., Lamberti, L. (eds.) Advancement of Optical Methods in Experimental Mechanics, vol. 3, pp. 167–170. Springer International Publishing (2014)
6. Berke, R.B., Lambros, J.: Ultraviolet digital image correlation (UV-DIC) for high temperature applications. Rev. Sci. Instrum. **85**(4), 045121 (2014)
7. Abotula, S., Heeder, N., Chona, R., Shukla, A.: Dynamic thermo-mechanical response of Hastelloy X to shock wave loading. Exp. Mech. **54**(2), 279–291 (2014)
8. Vautrot, M., Balland, P., Hopperstad, O.S., Tabourot, L., Raujol-Veillé, J., Toussaint, F.: Experimental technique to characterize the plastic behaviour of metallic materials in a wide range of temperatures and strain rates: application to a high-carbon steel. Exp. Mech. **54**(7), 1163–1175 (2014)
9. Zinn, S., Semiatin, S.L.: Induction Coil Design and Fabrication Tech Note - Part 1. Heat Treating Magazine, Jun-1988
10. Hack, E., Lin, X., Patterson, E.A., Sebastian, C.M.: A reference material for establishing uncertainties in full-field displacement measurements. Meas. Sci. Technol. **26**, 075004 (2015)
11. Wang, W., Mottershead, J.E., Ihle, A., Siebert, T., Reinhard Schubach, H.: Finite element model updating from full-field vibration measurement using digital image correlation. J. Sound Vib. **330**(8), 1599–1620 (2011)
12. Sebastian, C., Hack, E., Patterson, E.: An approach to the validation of computational solid mechanics models for strain analysis. J. Strain Anal. Eng. Des. **48**(1), 36–47 (2013)
13. CWA16799: Validation of Computational Solid Mechanics Models. Comite Europeen de Normalisation, Brussels (2014)
14. Lampeas, G., Pasialis, V.P., Lin, X., Patterson, E.A.: On the validation of solid mechanics models using optical measurements and data decomposition. Simul. Model. Pract. Theory **52**, 92–107 (2015)

Chapter 5
Modal Testing of a Nose Cone Using Three-Dimensional Scanning Laser Doppler Vibrometry

Daniel P. Rohe

Abstract The Structural Dynamics department at Sandia National Laboratories has acquired a 3D Scanning Laser Doppler Vibrometer system for making vibration and modal test measurements. This paper presents the results of testing performed to examine the capabilities and limitations of that system. The test article under consideration was a conical part with two different surface materials which allowed the examination of the effect of angle of incidence and surface reflectivity on the measurement. The system was operated in both 1D and 3D modes, and the results from the 1D scan were compared to a scan performed with a previous generation system to evaluate the improvements between the generations. Data from the laser systems were exported to standard curve fitting software, and modes were fit to the data.

Keywords 3D • SLDV • Alignment • Incidence • Modal

5.1 Introduction

Scanning Laser Doppler Vibrometry (SLDV) has been shown to have advantages over traditional mounted sensors [1]. For example, it allows for non-contact measurements which do not mass-load the test article. Additionally, a finer measurement point resolution can often be achieved through the use of scanning mirrors in the laser heads which are much more precise than a roving hammer or roving accelerometer test. The Structural Dynamics department at Sandia National Laboratories has owned and operated a Polytec PSV-400 1D SLDV system for several years, and during that time identified a number of limitations with the 1D SLDV system. The 1D system always measures in the direction of the beam, which limits the measurement of in-plane motions. It was also subject to unfamiliar (at least from the point of view of a modal engineer) optical issues such as signal dropouts, visibility minima, and speckle noise. These issues limited the use of the system for general-purpose or production testing.

To improve the SLDV capability at Sandia National Laboratories, a Polytec PSV-500 3D SLDV system was recently purchased. The 3D system has the obvious advantage of being able to produce three-dimensional measurements at each measurement point. These full-field measurements can then be used to perform more complex operations such as computing strain. Additionally, the SLDV hardware improved significantly between the purchase of the two systems, which can limit some of the unfamiliar optical issues. The goal of this effort was to gain experience using the 3D SLDV system and compare it to the previous 1D SLDV system for general modal testing.

5.2 Test Descriptions

To examine the capabilities and limitations of the 3D SLDV system, a series of modal test were performed on a conical test article, shown in Fig. 5.1. The test article was chosen because it had both dark and light surfaces which would allow comparison of signal return, and its conical shape would allow investigation of the angle of incidence (AoI) of the laser beam on the quality of the data.

Sandia National Laboratories is a multi-program laboratory managed and operated by Sandia Corporation, a wholly owned subsidiary of Lockheed Martin Corporation, for the U.S. Department of Energy's National Nuclear Security Administration under contract DE-AC04-94AL85000.

D.P. Rohe (✉)
Structural Dynamics and X-ray/NDE Department, Sandia National Laboratories, P.O. Box 5800 - MS0557, Albuquerque, NM 87185, USA
e-mail: dprohe@sandia.gov

© The Society for Experimental Mechanics, Inc. 2016

J. De Clerck, D.S. Epp (eds.), *Rotating Machinery, Hybrid Test Methods, Vibro-Acoustics & Laser Vibrometry, Volume 8*,
Conference Proceedings of the Society for Experimental Mechanics Series, DOI 10.1007/978-3-319-30084-9_5

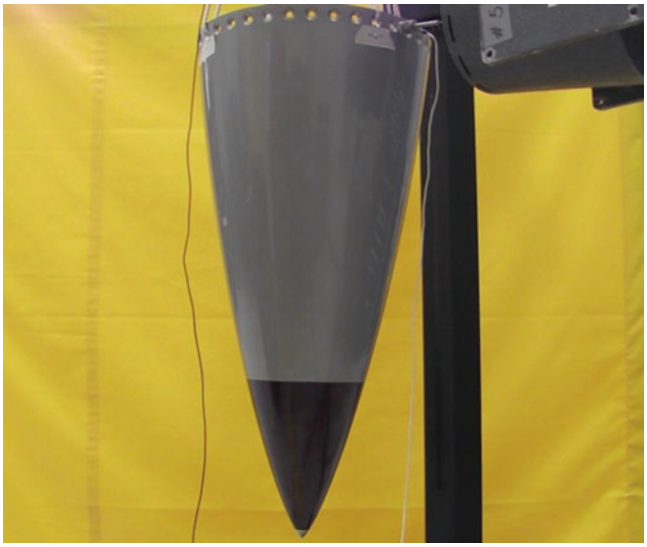

Fig. 5.1 Conical test article

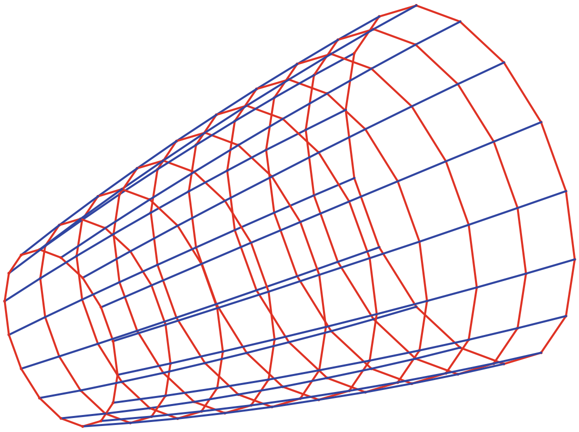

Fig. 5.2 Test geometry created to ensure consistent scan points between tests

The part was tested using three different measurement configurations. The first test used the previous generation 1D SLDV system; this will be referred to throughout this work as the baseline test. The second test used the newer system in a 1D configuration (only utilizing one of the three scanning heads), and the third test used the newer system in 3D configuration (utilizing all three scanning heads). By performing 1D tests with both SLDV systems, a more accurate estimate of the hardware improvements could be obtained. To ensure consistent points were scanned for meaningful comparisons between tests, a test grid was created with 10 axial stations and 16 circumferential stations. The coordinates for each scan point were derived from drawings of the part, with the global x axis along the axis of revolution of the test article. This geometry is shown in Fig. 5.2.

In order to point at measurement locations on the part defined by geometry, the lasers first needed to be aligned with the part coordinate system. The alignment procedure was complicated by the lack of sharp features on the part where coordinates were known: the only features available for alignment were the tip of the test article and the ring of holes near the base. The coordinates of these features were extracted from drawings, but there was a significant amount of uncertainty in positioning the lasers at these features: the lasers cannot point at a hole, so some point around the hole needed to be selected. For this test, the point was placed at the boundary of the countersink closest to the tip of the test article. Figure 5.3 shows example laser alignments at features on the test article.

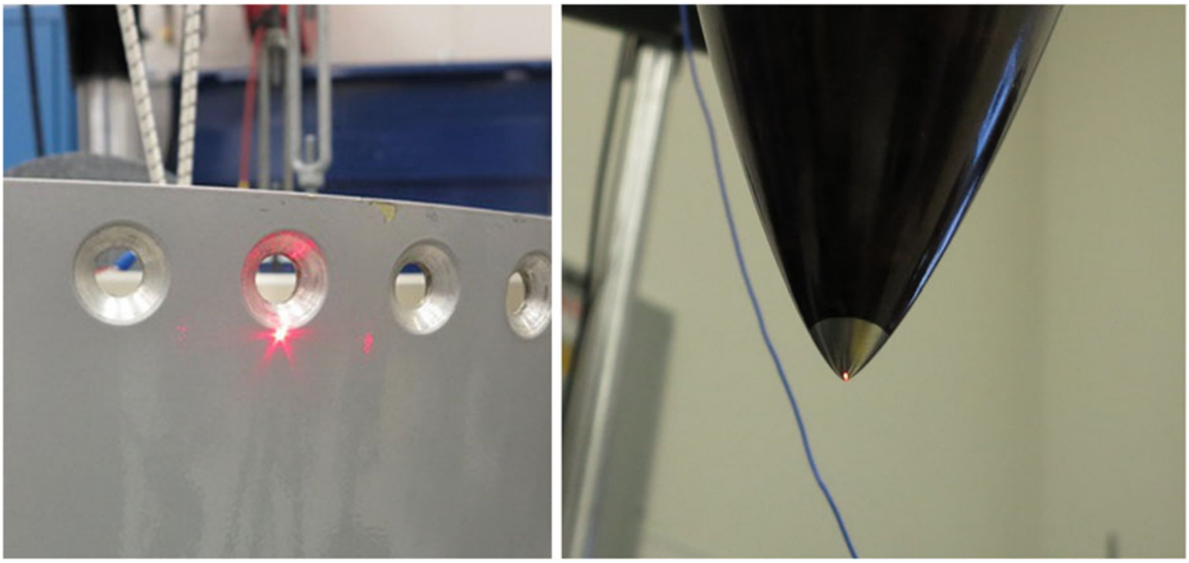

Fig. 5.3 Positioning the laser spots at features on the test article for alignment

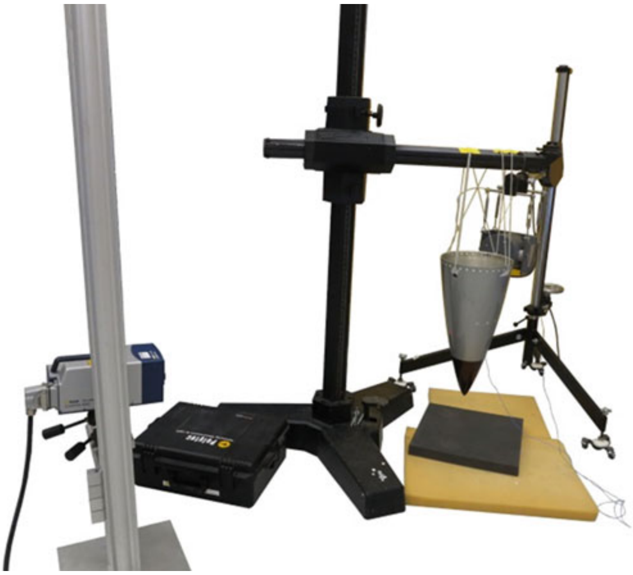

Fig. 5.4 Baseline test setup

5.2.1 Baseline Test

The baseline test was set up using the 1D laser system as shown in Fig. 5.4. The laser head was positioned approximately 1.35 m (53.1 in) from the test article, which was suspended on soft bungee cords. A modal shaker and force transducer were attached to the exterior of the part at the same axial position as the ring of holes, and a drive point accelerometer was mounted on the interior of the test article directly aligned with the force transducer.

Since the laser requires line-of-sight to a point to make a measurement, multiple scans were needed to measure all sides of the test article. For each scan, the laser head was aligned with the test article's coordinate system using the features described in Sect. 5.2, generally using four or five holes and the tip of the test article for alignment. Figure 5.5 shows an example of the alignment points used for one scan. The error in the alignment calculated by the laser system was on average 1.3 mm; compared to the grid spacing of 50–60 mm, it was thought that this error was acceptable. With the lasers aligned, the geometry could be imported and reduced to the points visible from that scan direction. Figure 5.6 shows an example of the measurement points. The baseline system struggled to measure more than four circumferential stations in one scan due to

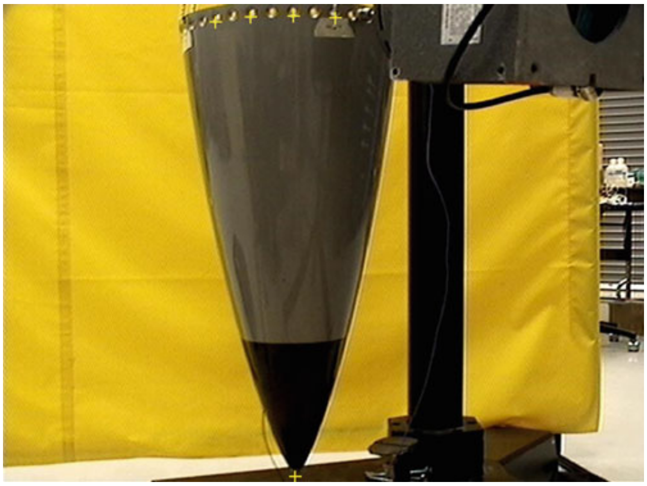

Fig. 5.5 Laser camera view showing points used for alignment (marked with *plus*)

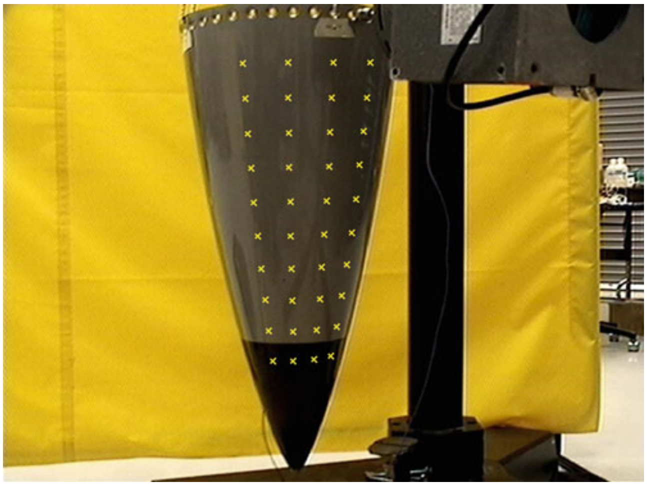

Fig. 5.6 Laser camera view showing measurement points for a given baseline scan

poor signal return from the high AoI. The maximum AoI for a measured point in this test was 55°. With 16 circumferential stations, this required four separate scans to measure the entire part with each scan measuring 40 points.

Frequency response functions (FRFs) were measured up to 2000 Hz with a frequency resolution of 1.25 Hz. Random excitation was applied to the shaker and 20 averages were measured at each scan point. Hann windows were applied to the measured responses. For this test, all signal enhancement parameters were set to their highest levels. This allowed the laser system to detect when poor quality data were measured and add up to 100 total averages to improve the data.

It became obvious during the test that the baseline system was struggling to get good measurements from the darker surface due to poor signal return. Signal dropouts and their resulting over-ranges were prevalent. The system was not able to measure FRFs for 10 of the 16 points on the darker surface, and the FRFs of the points that were measured were very noisy (see, for example, Fig. 5.7).

5.2.2 1D Test with New System

The same test article was scanned with the new system in 1D mode to compare the results to the previous test. Due to lab space constraints, the original test setup had to be dismantled between tests, but the shaker hardware was left attached to the test article to ensure consistent drive point excitation locations. When the test was set back up, the same bungee cords were used to suspend the test article, and the stinger was simply re-attached to the force gauge that was left attached to the test article.

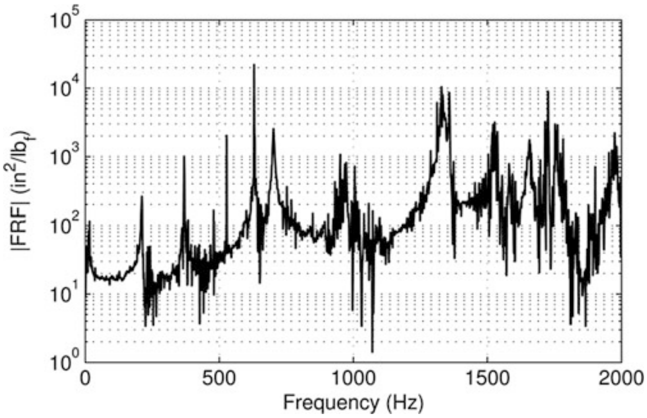

Fig. 5.7 Example FRF from darker surface with an AoI of 41°

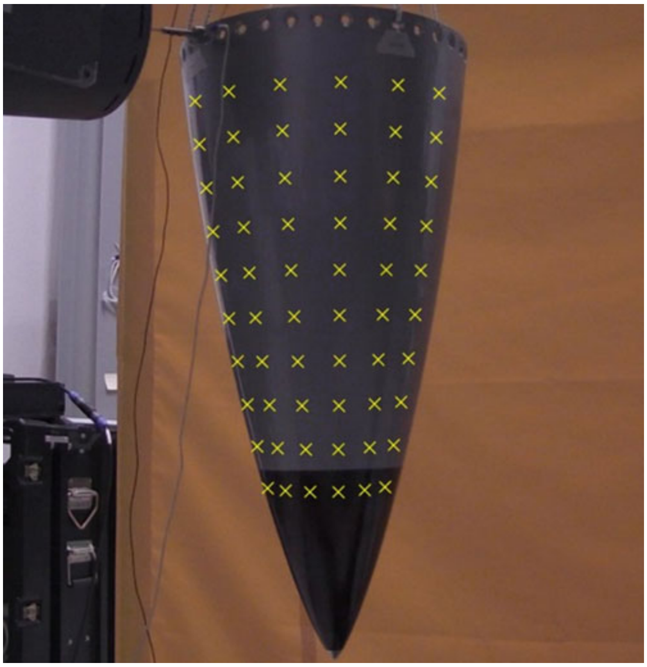

Fig. 5.8 Laser camera view showing measurement points for one scan

The laser head was positioned approximately 1.26 m (49.9 in) from the test article. Four scans were used for this test to measure all sides of the test article. A similar alignment scheme was used for this test, utilizing the ring of holes and tip of the test article as alignment points. The error in the alignment for this test was on average 2.6 mm, which is twice the value of the previous test. Note that this should not imply that the newer system is somehow less accurate than the baseline system: the alignment process depends greatly on operator interaction and test setup. Given the uncertainty in placing the alignment points on the test article and the spacing of the test grid, both of these alignments were considered 'good enough' and no further improvement in the alignment was sought.

For this test, the frequency resolution was increased to try to better separate the repeated modes. The bandwidth was set to 2500 Hz with a frequency resolution of 0.78 Hz. Pseudorandom excitation was used for this test, so only five averages were used and no windows were applied. All signal enhancement parameters were set to their highest levels.

During testing it was immediately obvious that significant improvements had been made between the newer SLDV system and the previous generation system. The laser was able to measure clean frequency response functions at up to six circumferential stations at a time (see Fig. 5.8), at angles of incidence up to 66° from the surface normal. The new system also had much less difficulty measuring on the darker surface, and was able to measure relatively clean FRFs at high AoI as shown in Fig. 5.9.

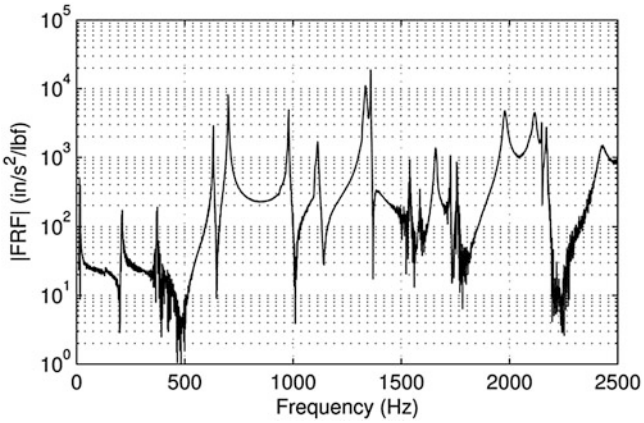

Fig. 5.9 FRF measured with the new SLDV system in 1D mode on the darker surface at an AoI of 66°

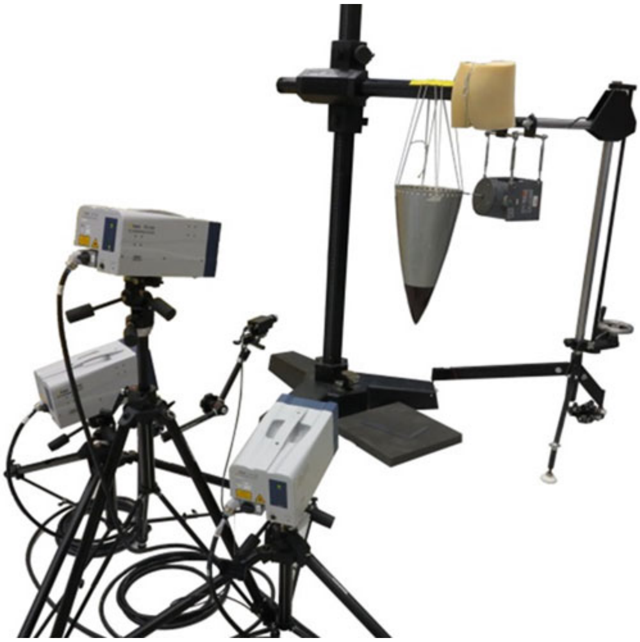

Fig. 5.10 3D test setup

5.2.3 3D Test with New System

After the 1D test with the new system, a 3D test was performed. The laser heads were placed an average of 1.42 m (56.1 in) from the test article. The average separation between two laser heads was 0.649 m (25.5 in). Figure 5.10 shows an example setup. Each laser head was individually aligned with features on the part as described in Sect. 5.2. The average error in the alignment was 2.0 mm. Four measurements were required to scan all sides of the test article.

Because there were no markings on the part to designate measurement points, it was difficult to determine the alignment error during the 1D scans at points other than those used to set the alignment (e.g. Fig. 5.5). There was no reference point to measure the laser positioning against at any given measurement point; unless the laser spot was so far from the correct measurement point that it was obviously misplaced, it was impossible to draw any kind of conclusions about measurement point uncertainty. With the 3D measurement, one can get an idea of the position error due to the error in the alignment of the laser spots.

When the lasers are perfectly aligned, the laser spots should be exactly on top of one another on any point on the test article's surface. However, if the lasers have some alignment error, the laser spots will generally appear as three distinct points. This effect will become more pronounced at a higher AoI to the test article, as the same angular misalignment will

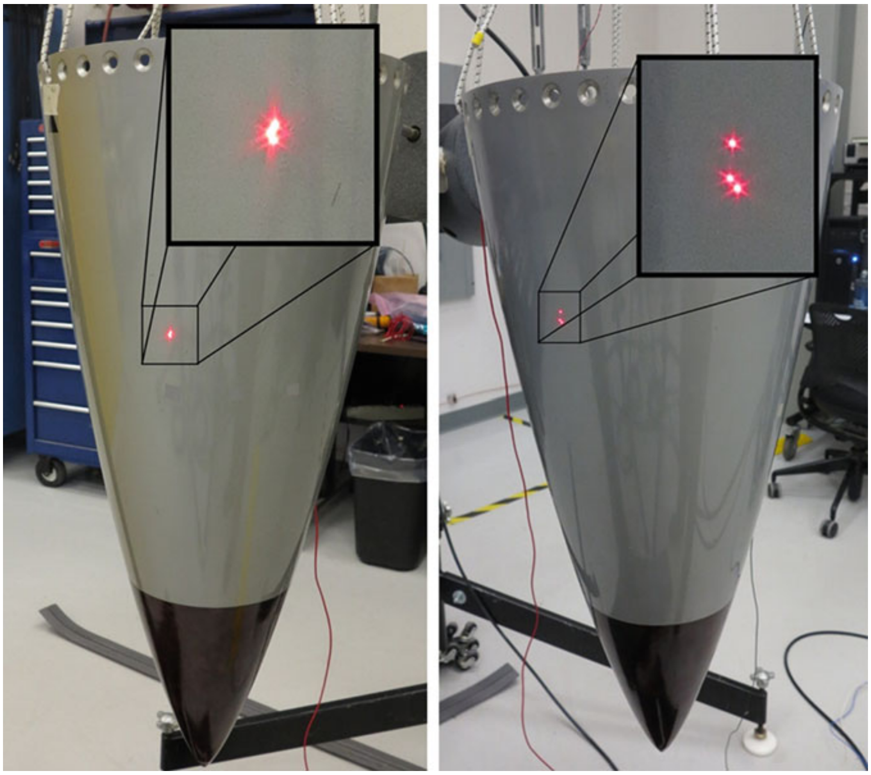

Fig. 5.11 Misalignment of laser spots at small AoI (*left*) and at large AoI (*right*)

result in a greater displacement of the spot along the surface. One can use the spread of these points as an estimate for the error in the measurement point locations. Figure 5.11 shows two examples of spot misalignment during the laser scan.

To correct this misalignment, a technique known as video triangulation was used. This technique detects each laser spot on the laser camera image and moves the lasers so the spots are collocated. This technique was very helpful to get the laser spots to converge on one point, as the alignment could not be easily improved.

This test used the same data acquisition parameters as the 1D test in Sect. 5.2.2. The bandwidth was set to 2500 Hz with a frequency resolution of 0.78 Hz. Pseudorandom excitation was used for this test, so only five averages were used and no windows were applied. All signal enhancement parameters were set to their highest levels.

5.3 Analysis and Comparisons

Often times with plate-like structures with the laser system sufficiently far away, it is an adequate assumption to assume that all of the measurements are perpendicular to the surface; however, for this test the laser beams formed angles over 50° with the test article's surface normal direction, so that assumption would not be valid. For each of the 1D tests, the test geometry needed to be updated so the measurement coordinate systems matched the actual direction of measurement.

A coordinate system was assigned to each measurement point based on that point's position in space and the laser head's origin. The local z axis, denoted by the unit vector $\hat{\mathbf{z}}$, was defined as the vector from the measurement point (located at $\mathbf{p}_n$) to the laser's origin (located at $\mathbf{p}_o$). The local x and y axes were then placed orthogonal to one another and the local z axis, with the x axis pointing away from the tip of the test article towards the global x direction. This was achieved by defining the local y axis, denoted by the unit vector $\hat{\mathbf{y}}$, as the cross product between the local z axis and the global x axis, denoted by the unit vector $\widehat{\mathbf{X}}$. Finally, the local x direction, denoted by $\widehat{\mathbf{x}}$, was defined as the cross product between the local y and z directions. A transformation matrix $\mathbf{T}$ could then be formed from the local axes. These computations are shown in (5.1)–(5.6). Figure 5.12 shows the measurement directions for the baseline test.

$$\mathbf{z} = \mathbf{p}_o - \mathbf{p}_n \tag{5.1}$$

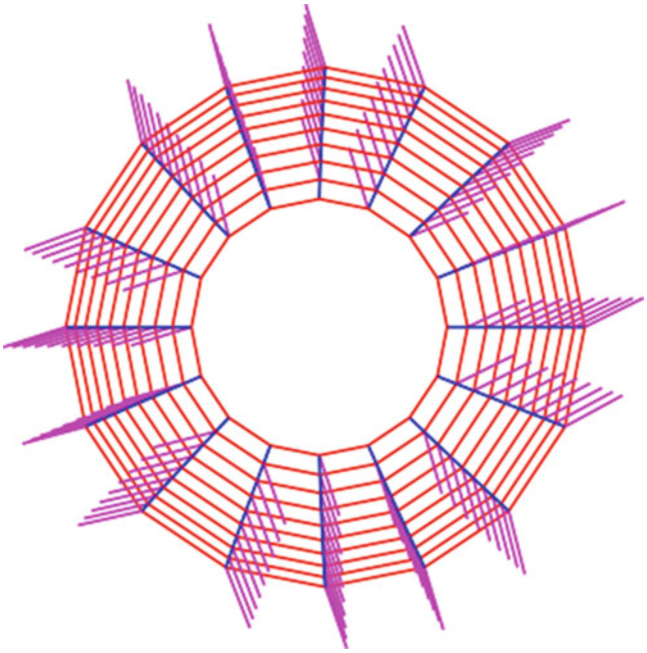

Fig. 5.12 Example measurement vectors for the baseline test

$$\widehat{\mathbf{z}} = \frac{\mathbf{z}}{\|\mathbf{z}\|} \tag{5.2}$$

$$\mathbf{y} = \widehat{\mathbf{z}} \times \widehat{\mathbf{X}} \tag{5.3}$$

$$\widehat{\mathbf{y}} = \frac{\mathbf{y}}{\|\mathbf{y}\|} \tag{5.4}$$

$$\widehat{\mathbf{x}} = \widehat{\mathbf{y}} \times \widehat{\mathbf{z}} \tag{5.5}$$

$$\mathbf{T} = \begin{bmatrix} \mathbf{x}^T \\ \mathbf{y}^T \\ \mathbf{z}^T \end{bmatrix} \tag{5.6}$$

5.3.1 Frequency Response Function Comparisons

Data were then compared between the baseline test using the previous generation laser hardware and 1D test using the current generation laser hardware. Because the test setup had to be dismantled between the baseline and 1D tests, there were differences in the positioning of the laser head with respect to the test article between the two tests. FRF comparisons between the two tests were only made at points where the measurement vectors were within 10° of one another. Except for cases of modes shifting between the tests (which will be discussed in Sect. 5.3.2), the frequency response functions show good agreement on the lighter grey surface; however, the baseline data is significantly noisier for the darker surface. These comparisons are shown in Fig. 5.13. Many points on the darker surface were not able to be measured with the baseline system due to the high rate of signal dropouts which would cause over-ranges of the data acquisition system.

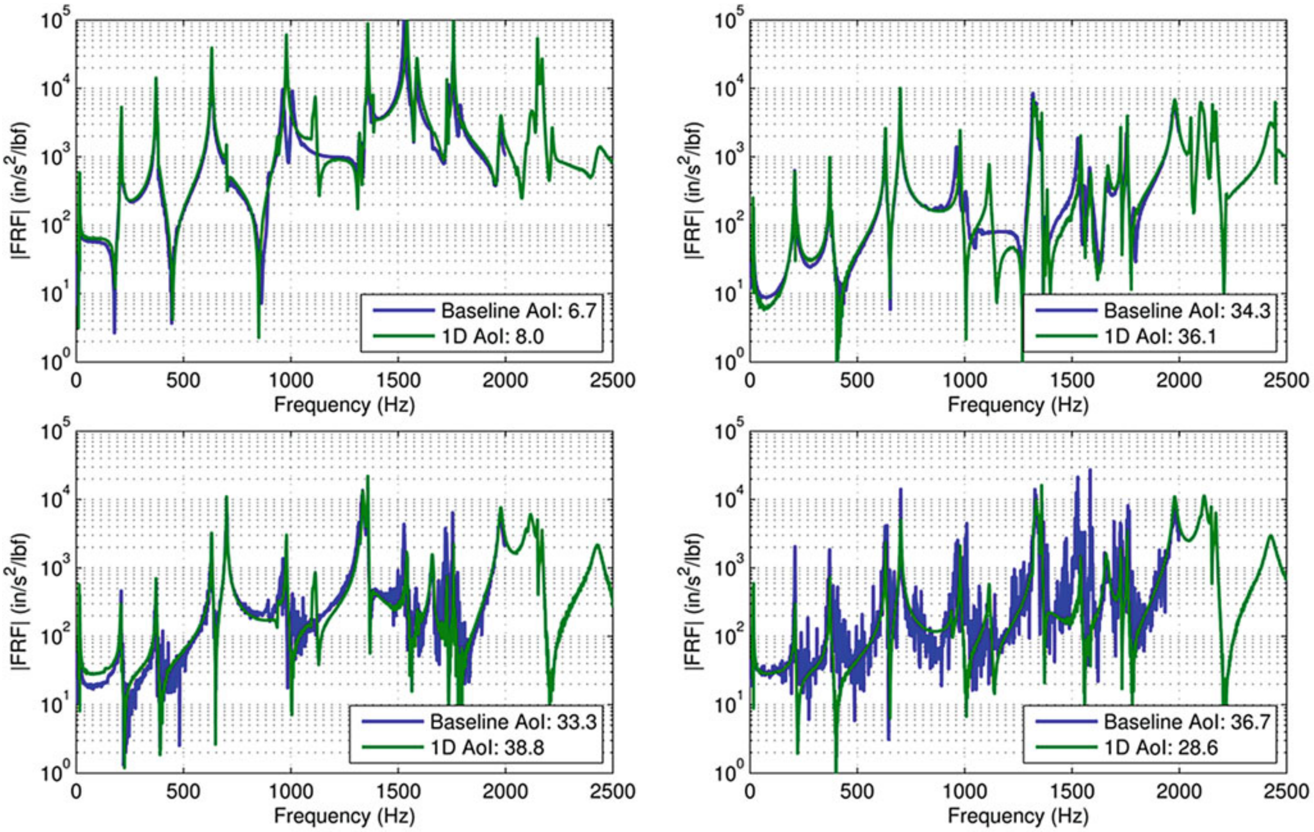

Fig. 5.13 Frequency response function comparison for two points on the lighter surface (*top*) and two points on the darker surface (*bottom*)

5.3.2 *Mode Shape Comparisons*

Modes were fit to each data set using the SMAC algorithm [2]. Due to the symmetry of the structure, a number of mode pairs were present, but it was often difficult to extract both modes because only one input location was used. Often SMAC would converge on both modes, but one would have a negative drive point coefficient, so it would be discarded. Generally good fits to the experimental data were achieved. A complex mode indicator function (CMIF) is shown for each test in Fig. 5.14, and the extracted modal parameters are listed in Table 5.1.

To compare the shapes between the different tests, common degrees of freedom needed be used, but all three tests used different local coordinate systems at the measurement points. Since the 3D test had data for all three directions, it could be transformed into coordinate systems consistent with the baseline and 1D tests using the **T** matrix from (5.6) at each measurement location. After the data were transformed, they were reduced to the one-dimensional measurements from the baseline and 1D tests. The modal assurance criterion (MAC) matrix could then be computed between the three data sets, as shown in Fig. 5.15. High off-diagonal values were found between the modes from 940 to 1127 Hz.

The CMIF in Fig. 5.14 and fits in Table 5.1 show good agreement between the three tests for the majority of natural frequencies. Due to the increased frequency resolution and bandwidth, the 1D and 3D tests found modes that were not found in the baseline test; however other interesting differences were noted as well, particularly in the 5-lobed ovaling modes from 900 to 1150 Hz. While the mode shapes matched very well between the three tests, these modes showed a large change in frequency between baseline test and the other two tests. Some small change in the modal parameters may be expected between the two tests because the test setup was dismantled between the baseline test and the subsequent tests, an approximately 100 Hz shift indicates issues other than minor differences in boundary conditions.

Another observation which raised suspicion regarding these modes was that a significant shift in natural frequency occurred between laser scans for the three modes near 1100 Hz. This was discovered while fitting modes to the 3D test: the SMAC algorithm fit three modes for the 5-lobed ovaling modes near 1100 Hz, but generally these types of modes should appear in pairs. The second and third mode of this group each looked like half a mode shape, as shown in Fig. 5.16, and the CMIF computed from the FRFs from each of the four scans in the 3D test showed a distinct shift between the four scans, shown in Fig. 5.17.

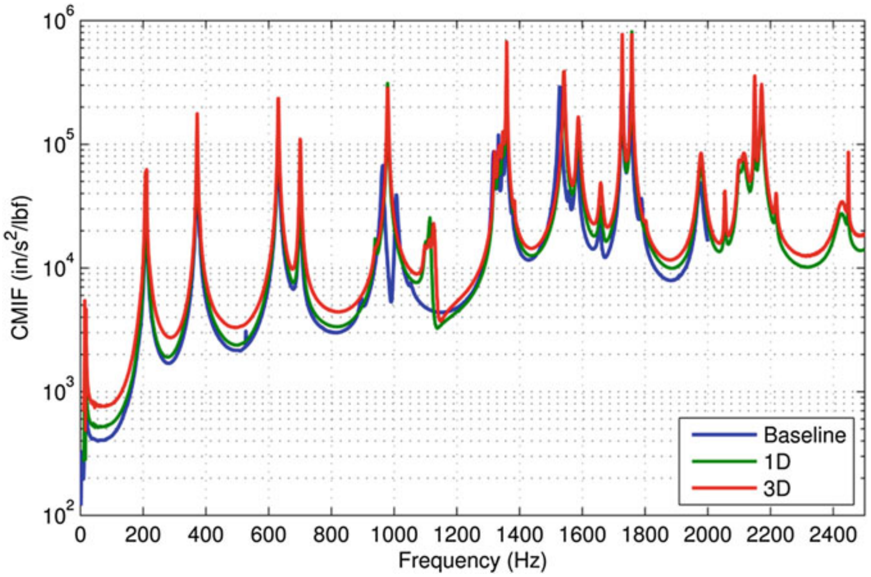

Fig. 5.14 CMIFs for the three tests

The shift in the natural frequencies between two scans taken 2 h apart raised a great deal of suspicion about the validity of this set of modes. The suspension of the test article did not change during this time, so significant changes in natural frequency were not expected. The stinger and shaker hardware was therefore investigated as the culprit. The shaker and force gauge were removed from the test article and a drive point measurement was performed using a modal hammer, and the measured drive point FRF is shown in Fig. 5.18. The hammer data suggests that the group of modes near 1100 Hz extracted from the 1D and 3D scans are indeed false modes. Additionally, the mode near 980 Hz was split into two peaks in the baseline test, similar to a tuned vibration absorber like what was seen in [3]. The hammer impact data also showed somewhat higher natural frequencies, likely due to the removal of the relatively massive force gauge from the relatively thin shell structure. This suggests that mass-loading may also be an issue during these tests.

5.4 Lessons Learned

The tests described in this report were helpful in understanding the capabilities and improvements of the new 3D SLDV system. The new system was able to get better signal return off of both surfaces tested, and was able to make adequate measurements even on the dark surfaces and at high angles of incidence with the structure. Adding to that the capability to make 3D measurements at a large number of points, the new system was seen as a substantial improvement over the previous generation system owned by Sandia National Laboratories.

This test also identified areas of improvement for testing with the 3D SLDV system. The lasers were aligned with what few features were available on the part; however, these features were not sharp points but were instead broad features that introduced uncertainty into the alignment. For a number of points, the laser spots were not collocated and appeared as three distinct spots on the test article. Video triangulation of the laser spots was successful for this test article, but future test articles may not be as successful due to sharp edges or reflective surface finishes. In tests performed since this investigation, a reference object with features at known coordinates has been used to align the laser heads accurately. Subsequently, then a coordinate transformation is applied to transform from the reference object's coordinate system to the test article's coordinate system. This way, even if there is uncertainty in the locations of the points used to transform between coordinate systems, the relative positions of the laser heads within that coordinate system will still be accurate, which lets the laser beams converge at any point in space.

Another area of improvement was reducing mass loading and shaker effects. SLDV has the advantage over traditional sensors in that it is non-contact and does not mass load the part. However, it would seem that this test suffered from both contact issues (coupling with the shaker stinger to produce false modes) and mass loading issues (significant shifts in natural frequency between hammer and shaker input). Accordingly, more effort and investment have been put into excitation methods

Table 5.1 Extracted modes from the three tests. Modes 11 through 13 are thought to be due to false stinger modes

	Baseline test		1D test		3D test		
Mode	Frequency (Hz)	Damping ratio	Frequency (Hz)	Damping ratio	Frequency (Hz)	Damping ratio	Description
1	209.1	0.69 %	208.8	0.90 %	208.2	0.88 %	First 2-lobed Ovaling
2	–	–	–	–	211.4	0.24 %	Pair with Mode 1
3	371.9	0.40 %	372.4	0.30 %	372.5	0.25 %	First 3-lobed Ovaling
4	381.3	0.34 %	381.1	0.28 %	381.3	0.23 %	Pair with Mode 3
5	630.5	0.19 %	631.3	0.18 %	631.1	0.17 %	First 4-lobed Ovaling
6	640.2	0.29 %	–	–	–	–	Pair with Mode 5
7	700.9	0.25 %	701.0	0.18 %	701.1	0.18 %	Second 2-lobed Ovaling
8	–	–	–	–	703.2	0.16 %	Pair with Mode 7
9	–	–	940.0	0.29 %	940.8	0.86 %	First 5-lobed Ovaling
10	963.0	0.32 %	979.4	0.15 %	980.0	0.17 %	Pair with Mode 9
11	1007	0.35 %	1099	0.30 %	1098	0.57 %	5-lobed Ovaling*
12	–	–	1115	0.25 %	1114	0.35 %	Pair with Mode 11*
13	–	–	–	–	1127	0.47 %	Pair with Mode 11*
14	1317	0.20 %	1320	0.19 %	1320	0.19 %	Second 3-lobed Ovaling
15	1331	0.26 %	1332	0.29 %	1333	0.29 %	Third 2-lobed Ovaling
16	1334	0.32 %	1335	0.32 %	1336	0.33 %	Pair with Mode 15
17	1345	0.21 %	1347	0.18 %	1347	0.19 %	Pair with mode 14
18	1358	0.09 %	1359	0.04 %	1359	0.05 %	First 6-lobed Ovaling
19	1528	0.15 %	1541	0.15 %	1542	0.16 %	Second 5-lobed Ovaling
20	1558	0.13 %	–	–	–	–	Pair with mode 19
21	1583	0.23 %	1587	0.23 %	1587	0.24 %	Second 4-lobed Ovaling
22	1593	0.16 %	–	–	–	–	Pair with mode 21
23	1657	0.27 %	1659	0.26 %	1659	0.26 %	First Bending
24	–	–	1667	0.25 %	1667	0.26 %	Pair with mode 23
25	1727	0.09 %	1727	0.05 %	1727	0.04 %	7-lobed Ovaling
26	1755	0.10 %	1758	0.04 %	1758	0.06 %	6-lobed Ovaling
27	1788	0.20 %	1802	0.16 %	1802	0.16 %	6-lobed Ovaling
28	1975	0.37 %	1978	0.34 %	1979	0.39 %	Third 3-lobed Ovaling
29	–	–	2054	0.08 %	2054	0.08 %	5-lobed Ovaling of Tip
30	–	–	2055	0.09 %	2056	0.07 %	Pair with mode 29
31	–	–	2099	0.24 %	2099	0.25 %	4-lobed Ovaling of Tip
32	–	–	2116	0.39 %	2116	0.40 %	Fourth 3-lobed Ovaling
33	–	–	2149	0.04 %	2124	0.49 %	Pair with Mode 32
34	–	–	2172	0.13 %	2150	0.04 %	8-lobed Ovaling
35	–	–	2218	0.12 %	2172	0.13 %	Higher-order Ovaling
36	–	–	2428	0.74 %	2218	0.12 %	Higher-order Ovaling
37	–	–	–	–	2427	0.66 %	Fifth 3-lobed Ovaling

that have a less significant impact on the structure, especially as smaller articles are tested. Smaller force transducers have since been purchased, and impact testing has been successfully used on a number of test articles since this test was performed.

Impact testing with the 3D SLDV system has its own challenges that need to be addressed. Some type of automatic hammer is desirable for SLDV testing due to the large number of impacts that are sometimes required. These hammers can be inconsistent, and often times they are not designed for frequent impacts over long durations. This can increase testing time as the automatic hammer may require time to cool down between impacts. Additionally hammers often impart large rigid body deflections on the test article, and this can reduce the accuracy of SLDV tests as the part moves with respect to the fixed laser spot. Hammer testing has been successful by using a smaller hammer that is swung by the automatic hammer, as shown in Fig. 5.19. The smaller hammer is then partially decoupled from the inertia of the automatic hammer, and this imparts less rigid body motion and leads to shorter ring-down times.

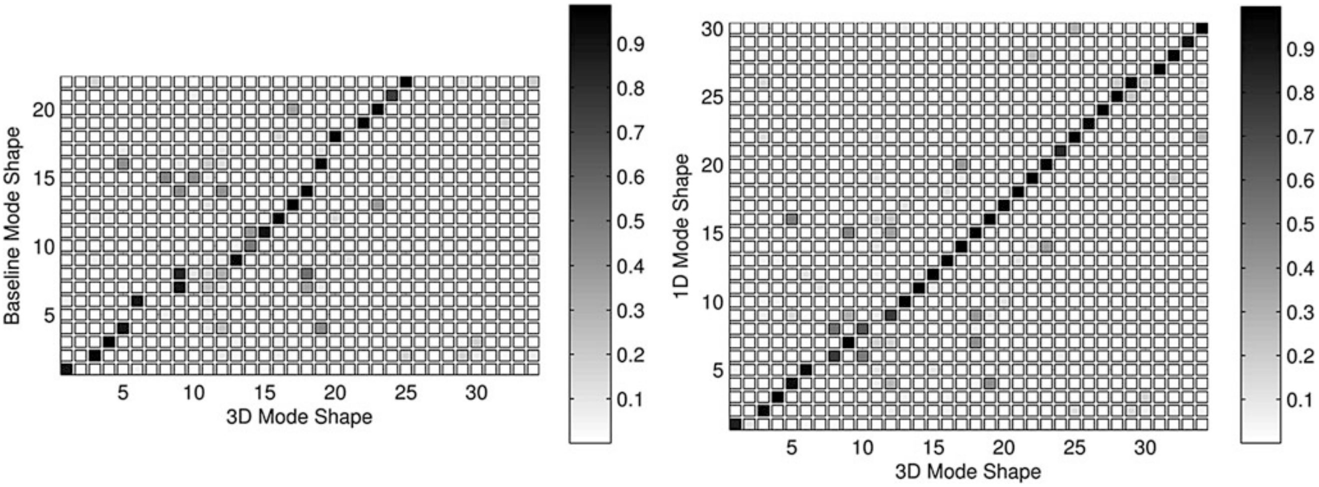

Fig. 5.15 MAC matrices showing mapping between extracted modes

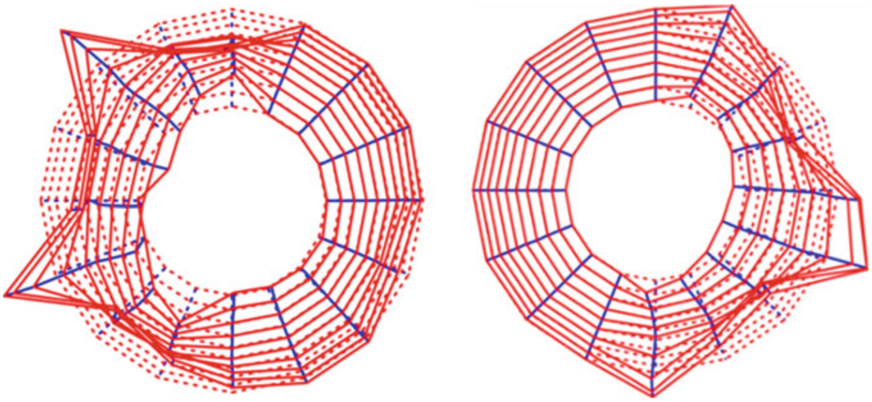

Fig. 5.16 Two extracted mode shapes each having motion on one half of the shape

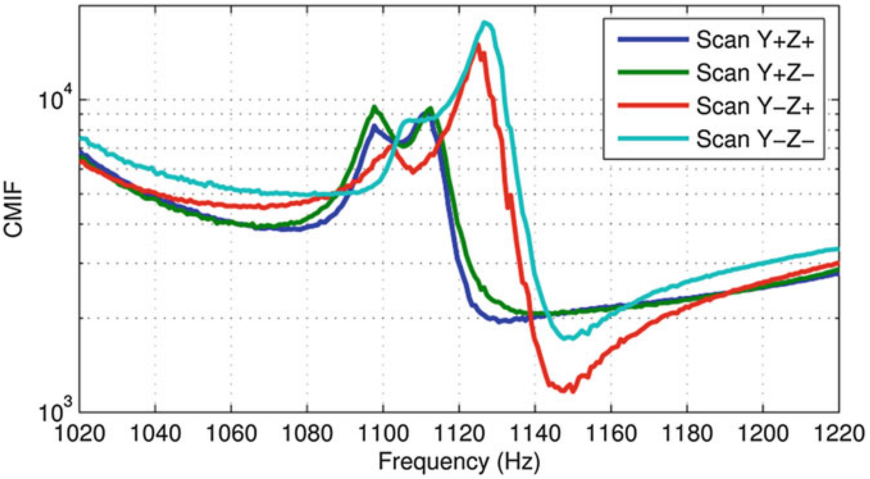

Fig. 5.17 Complex mode indicator function showing a shift in frequency between scans taken approximately 2 h apart

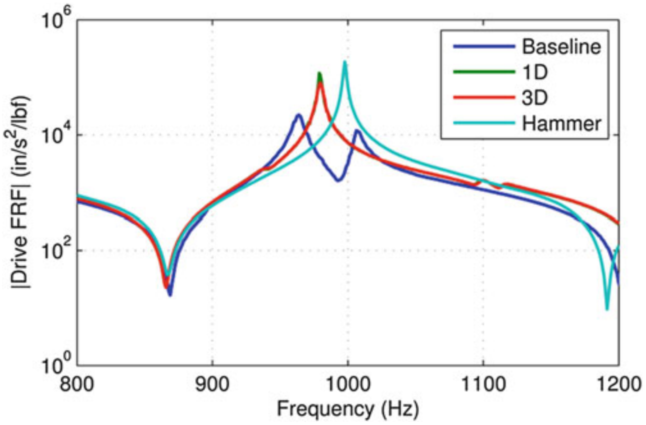

Fig. 5.18 Drive point FRF showing the three tests compared to a hammer impact near the suspicious modes

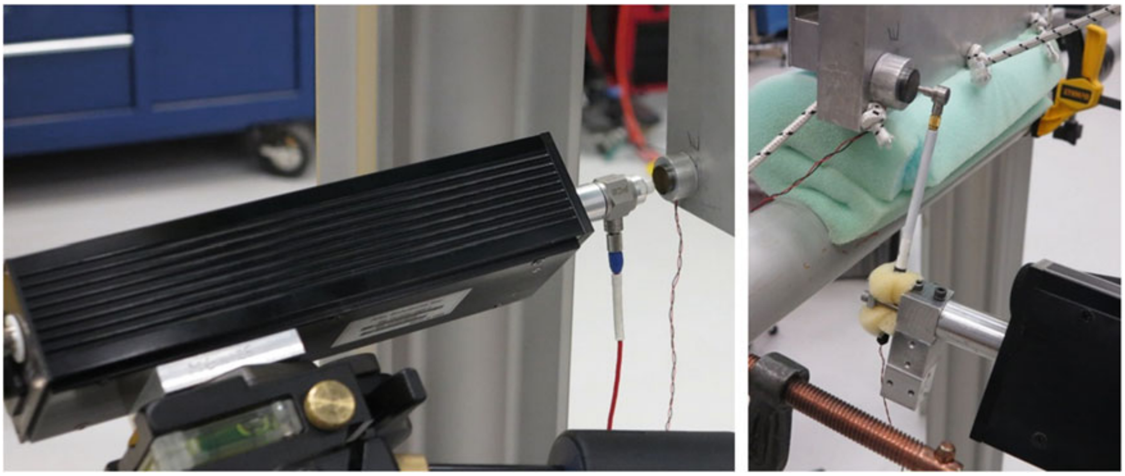

Fig. 5.19 Automatic hammers for impact testing with SLDV

5.5 Conclusions

A series of modal tests were performed on a conical test article with two surface finishes to identify the capabilities of a newly purchased 3D SLDV system. The new SLDV system performed significantly better than the previous generation system and was able to produce clean FRFs at high angle of incidences and on dark surfaces. During modal analysis, it was found that the shaker hardware that was used to excite the test article produced false modes and imparted mass loading effects. These were identified by performing a quick hammer tap test and comparing drive point frequency response functions.

This investigation allowed test personnel to gain experience with using the new 3D SLDV system and identify gaps in the capability that could be improved for production tests. Alignment procedures and excitation methods have since been improved, and a number of production articles have been tested successfully.

References

1. Castellini, P., Martarelli, M., Tomasini, E.P.: Laser Doppler Vibrometry: development of advanced solutions answering to technology's needs. Mech. Syst. Signal Process. **20**(6), 1265–1285 (2006)
2. Hensley, D.P., Mayes, R.L.: Extending SMAC to multiple references. In: Proceedings of the 24th International Modal Analysis Conference, pp. 220–230, February 2006
3. Avitabile, P.: Back to basics. Exp. Tech. **29**(6), 23–24 (2006)

Chapter 6
A Mathematical Model for Determining the Pose of a SLDV

Da-Ming Chen and W.D. Zhu

Abstract A laser Doppler vibrometer (LDV) combined with a pair of orthogonal scan mirrors is a scanning LDV (SLDV). A mathematical model based on the scan mirrors configuration for determining the orientation and position of a SLDV in a structure coordinate system (SCS) is presented in this work. Coordinates of a scan point in a scan mirrors coordinate system (SMCS) are derived from the mathematical model and the relation of coordinates of the same scan point in the SMCS and SCS is derived using the rigid transformation theory. A rotation matrix and a translation vector from the SMCS to SCS are obtained by applying the least squares method and singular value decomposition. An experiment to scan a 3D structure was performed with three SLDVs placed at three different locations. Rotation matrices obtained from two different sets of reference points are almost the same at the three locations, which validates that the proposed methodology is reliable. Another experiment to scan a 2D clamped plate was performed and the rotation matrices were calculated from the proposed methodology as a special case, which shows universal applicability of the proposed methodology and extends its application scope from 3D structures to 2D structures.

Keywords Scanning laser Doppler vibrometer • Rigid transformation theory • Least squares method • Singular value decomposition • 3D and 2D structures

6.1 Introduction

A laser Doppler vibrometer (LDV) is a non-contact measurement device that can measure the surface velocity of a vibrating structure along the laser line-of-sight direction. The LDV combined with a pair of orthogonal scan mirrors is defined as a scanning LDV (SLDV). A laser beam emitted from the LDV can be directed to any position on the structure surface by rotating the scan mirrors in a SLDV. This technology has greatly expanded application areas of the LDV, including making full-field measurement of the surface velocity of a vibrating structure.

There are two different kinds of scanning modes that depend on types of input signals to two scan mirrors. One is stepped scanning, in which the laser beam is stepped from point to point, pausing at each point for long enough time to acquire sufficient vibration data of that point before moving to the next point. Another is continuous scanning where the laser beam is continuously swept over a vibrating structure surface [1]. Both scanning modes have been widely applied in vibration measurement and modal testing to analyze structure dynamic responses under different excitations. An operating deflection shape (ODS) of a clamped plate was obtained from a continuous SLDV (CSLDV) using a uniform-rate rectangular scan in [1]. Area vibration mode shapes were also obtained using the CSLDV by giving two different scan frequencies to two scan mirrors in [2]. Details on how to perform a measurement test and calculate ODSs of different structures using the CSLDV were summarized in [3, 4].

Up to date, a single SLDV is mainly applied to measure the out-of-plane vibration of a structure surface. The laser line-of-sight direction, which is the velocity measurement direction, is assumed to be aligned with the out-of-plane direction, whereas there is actually a small angle between them during scanning. This angle can be neglected when the area of the scanned structure surface is small. However, with a large scanning area and a short distance between the SLDV and measured structure this assumption can amplify the measurement error and an out-of-plane ODS of the structure may not completely agree with the corresponding measured ODS. Further, three-dimensional (3D) measurements of vibrating structures by SLDVs have been of interest, where there are three laser beams coming from three different directions, simultaneously directing to a measured point [5–7]. The orientations of three laser beams with respect to a structure coordinate system (SCS) must be

---

D.-M. Chen • W.D. Zhu (✉)
Department of Mechanical Engineering, University of Maryland, Baltimore County, 1000 Hilltop Circle, Baltimore, MD 21250, USA
e-mail: wzhu@umbc.edu

© The Society for Experimental Mechanics, Inc. 2016

J. De Clerck, D.S. Epp (eds.), *Rotating Machinery, Hybrid Test Methods, Vibro-Acoustics & Laser Vibrometry, Volume 8*,
Conference Proceedings of the Society for Experimental Mechanics Series, DOI 10.1007/978-3-319-30084-9_6

known to transform measured velocities to the SCS as one out-of-plane motion and two in-plane motions. The orientation of a SLDV is often expressed using a rotation matrix. Zeng et al. [8] presented an algorithm to calculate the rotation matrix of a SLDV. This algorithm has an iterative process and uncertainty of the rotation matrix needs to be identified in the calculation. Hence, it may not be convenient to implement it. Later, Xu and Miles [9] summarized an identification technique to obtain the rotation matrix by calculating the inverse of a coordinate matrix. However, the rotation matrix is not guaranteed to be an orthogonal matrix with this technique and the inverse of the coordinate matrix does not exist when the structure is two-dimensional (2D) because two rows of the matrix are much close to linear dependent.

In this work, a mathematical model based on the scan mirrors configuration is presented and coordinates of a scan point in a scan mirrors coordinate system (SMCS) are derived from it. The relation of coordinates of the same scan point in the SMCS and SCS is obtained using the rigid transformation theory. A rotation matrix and a translation vector from the SMCS to SCS are obtained using the least squares method and singular value decomposition (SVD). Experiments to scan a 3D structure and a 2D clamped plate with three SLDVs placed at three different locations were performed to validate the mathematical model. The experimental results show that the proposed methodology is reliable in calculating the rotation matrix. Rotation angles of two scan mirrors calculated using the rotation matrix and translation vector are in excellent agreement with corresponding measured angles.

6.2 Mathematical Model of a SLDV

A galvanometer scanner has two orthogonal scan mirrors called X mirror and Y mirror, as shown in Fig. 6.1. In a SLDV, X mirror and Y mirror control the horizontal movement and vertical movement of a laser beam, respectively. Hence, the laser beam can be directed to any visible position on a structure surface by rotating the mirrors; the rotations of the mirrors are driven by input voltages. The rotation angle range of either mirror in Fig. 6.1 is ±10°, which corresponds to an input voltage of ±10 V; the sensitivity of the scanner is 1°/V. Initial positions of the two mirrors are 45° with respect to the horizontal plane when the input voltages are zero.

A mathematical model of the SLDV that describes the geometric relation for a scan point between its coordinates and rotation angles of two mirrors is shown in Fig. 6.2. There are two coordinate systems that need to be defined. The SCS o-xyz is usually fixed on the structure to be scanned so that coordinates of all scan points on it can be easily determined. The SMCS o'-$x'y'z'$ is specified as follows: the x'' axis and y' axis are along the rotation axes of X mirror and Y mirror, respectively. The positive directions of the x'' axis and y' axis are directed to motors of X mirror and Y mirror, respectively (Fig. 6.1). The x' axis is parallel to the x'' axis and has the intersection point o' with the y' axis. The z' axis is perpendicular to the plane formed by the x' axis and y' axis; it goes through o' and has the intersection point o'' with the x'' axis. Both the SCS and SMCS are right-handed coordinate systems.

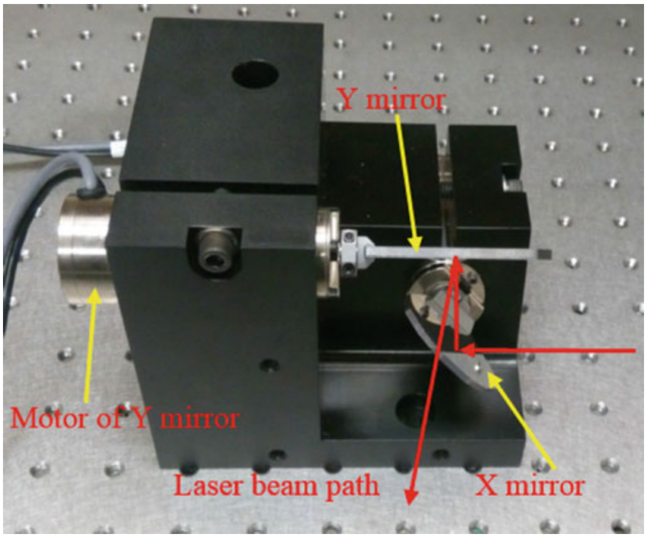

Fig. 6.1 A galvanometer; the motor of X mirror is on the opposite of X mirror, which cannot be seen in the picture

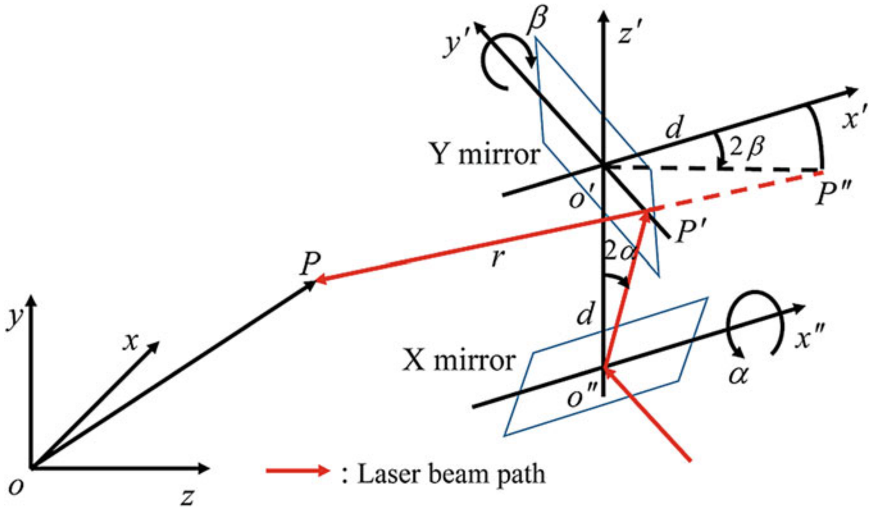

Fig. 6.2 Mathematical model of the SLDV, and the two coordinate systems o-xyz and o'-$x'y'z'$

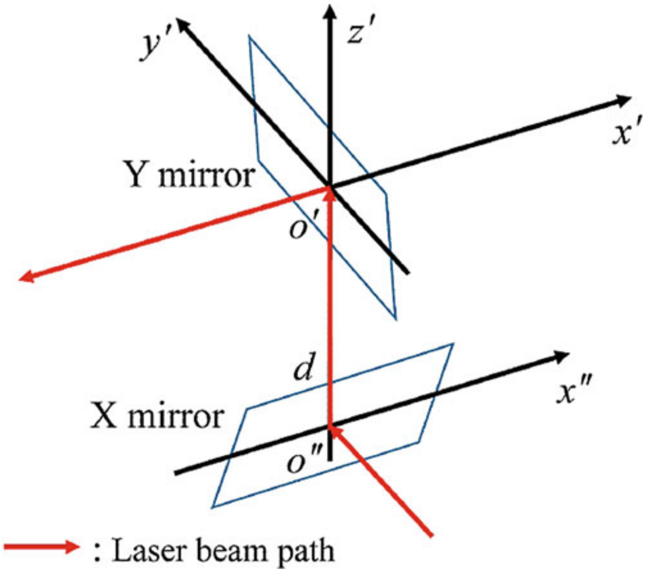

Fig. 6.3 Direction of the laser beam when both mirrors are at their initial positions

The constant distance of $o'o''$, denoted by d, is defined as the separation distance between two mirrors (Fig. 6.2). Variables α and β are rotation angles of X mirror and Y mirror measured from their initial positions, respectively. The positive directions of α and β are shown in Fig. 6.2. Each scan point P corresponds to a unique set of rotation angles α and β. Hence, a scan point P with coordinates in the SCS can also be expressed in the SMCS in terms of parameters α, β, d and r, where r is the distance from point P', which is the incident laser point of Y mirror, to point P (Fig. 6.2). Details on how to derive coordinates of the scan point P in the SMCS in terms of parameters α, β, d and r are described in what follows.

6.2.1 Case When Only X Mirror Rotates

A laser beam directing to X mirror is perpendicular to the x'' axis, as shown in Fig. 6.3, which indicates that the laser beam comes out from o' in the negative direction of the x' axis when both mirrors are at their initial positions. When $\beta = 0$ and X mirror rotates with an angle α, the relation between the reflected laser beam and incident laser beam with respect to X mirror is shown in Fig. 6.4a based on the principle of light reflection, which indicates that the reflected laser beam rotates

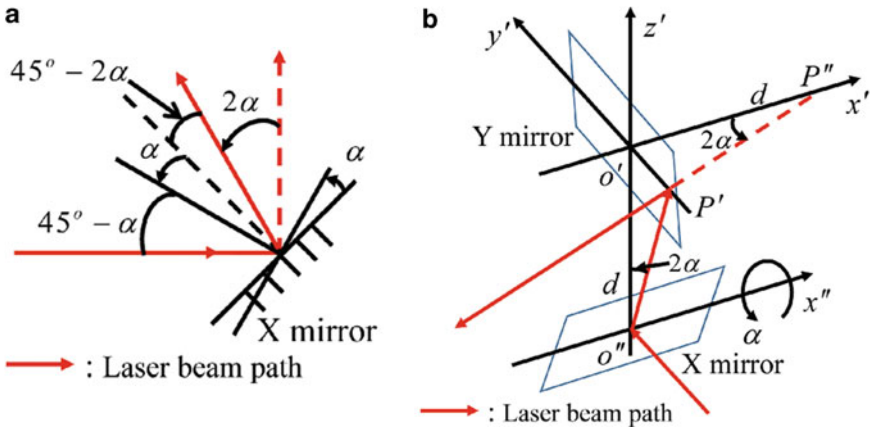

Fig. 6.4 (**a**) Relation between the reflected laser beam and incident laser beam when X mirror rotates with an angle α, and (**b**) the direction of the laser beam when only X mirror rotates with an angle α

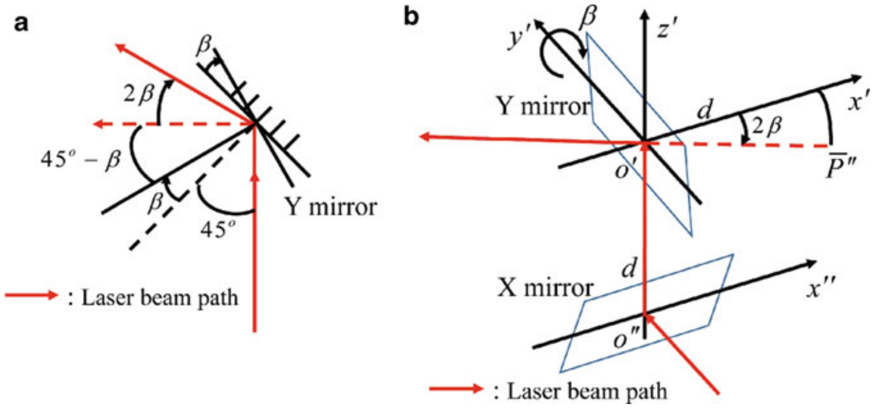

Fig. 6.5 (**a**) Relation between the reflected laser beam and incident laser beam when Y mirror rotates with an angle β, and (**b**) the direction of the laser beam when only Y mirror rotates with an angle β

with an angle 2α from its initial position when X mirror rotates with an angle α from its initial position. Figure 6.4b shows the direction of the laser beam that comes out from Y mirror when only X mirror rotates with an angle α. Point P' is the incident point of Y mirror and point P'' is the image point of o''. Hence, triangle $o'o''P'$ and triangle $o'P''P'$ are congruent. Coordinates of point P' in the SMCS are expressed as

$$P' = [0, -d\tan(2\alpha),\ 0]^T \tag{6.1}$$

where the superscript T denotes transpose of a vector or a matrix.

6.2.2 Case When Only Y Mirror Rotates

The relation between the reflected laser beam and incident laser beam when only Y mirror rotates with an angle β is shown in Fig. 6.5a, which indicates that the reflected laser beam rotates with an angle 2β from its initial position when Y mirror rotates with an angle β from its initial position; this is also the case for X mirror. Figure 6.5b shows the direction of the laser beam that comes out from Y mirror when only Y mirror rotates with an angle β. Point P'' rotates with an angle 2β along the y' axis with a radius d, and the direction of the reflected laser beam is $P''o'$. Hence, coordinates of point P'' in the SMCS are

$$P'' = [d\cos(2\beta),\ 0,\quad -d\sin(2\beta)]^T \tag{6.2}$$

6.2.3 General Case

With the aid in Sects. 6.2.1 and 6.2.2, one can conclude that when X mirror and Y mirror rotate with angles α and β, respectively, the direction of the laser beam that comes out from Y mirror is the line from point P'' to point P' (Fig. 6.2). The vector $P''P'$ in the SMCS is expressed as

$$P''P' = P' - P'' = [-d\cos(2\beta), -d\tan(2\alpha),\ d\sin(2\beta)]^T \tag{6.3}$$

The unit direction vector of $P''P'$ is

$$e_{P''P'} = \frac{P''P'}{|P''P'|} = [-\cos(2\beta)\cos(2\alpha), -\sin(2\alpha),\ \sin(2\beta)\cos(2\alpha)]^T \tag{6.4}$$

It is seen from Eq. (6.4) that the direction of the laser beam in the SMCS is only determined by the rotation angles α and β. Coordinates of the scan point P in the SMCS are

$$\begin{aligned} P &= P' + re_{P''P'} \\ &= [0, -d\tan(2\alpha),\ 0]^T + [-r\cos(2\beta)\cos(2\alpha), -r\sin(2\alpha),\ r\sin(2\beta)\cos(2\alpha)]^T \\ &= [-r\cos(2\beta)\cos(2\alpha), -r\sin(2\alpha) - d\tan(2\alpha),\ r\sin(2\beta)\cos(2\alpha)]^T \end{aligned} \tag{6.5}$$

which can be determined by the rotation angles α and β, and the distance r; note that d is a constant that is specified with the scanner.

6.3 Rigid Transformation from the SMCS to SCS

Section 6.2 shows that the position of a scan point P_i ($i = 1, 2, \ldots, N$) can be expressed in both the SCS and SMCS. Hence, there exists a rigid transformation, including a 3 by 3 rotation matrix **R** and a 3 by 1 translation vector **t**, which satisfies

$$\mathbf{p}_i = \mathbf{t} + \mathbf{R}\mathbf{p}_i' \tag{6.6}$$

where $\mathbf{p}_i = [x_i, y_i, z_i]^T$ and $\mathbf{p}_i' = [x_i', y_i', z_i']^T$ are coordinates of the same scan point P_i in the SCS and SMCS, respectively. One can find the optimal solution of **R** and **t** by N ($N \geq 3$) scan points based on the least squares method [10]. The optimization problem is

$$F(\mathbf{t}, \mathbf{R}) = \delta^2 = \min \sum_{i=1}^{N} \left\| \mathbf{p}_i - \left(\mathbf{t} + \mathbf{R}\mathbf{p}_i'\right) \right\|^2 \tag{6.7}$$

Differentiating F with respect to **t** and setting it to zero yield

$$\frac{\partial F}{\partial \mathbf{t}} = \sum_{i=1}^{N} -2\left[\mathbf{p}_i - \left(\mathbf{t} + \mathbf{R}\mathbf{p}_i'\right)\right] = \mathbf{0} \tag{6.8}$$

Let

$$\overline{\mathbf{p}} = \frac{\sum_{i=1}^{N} \mathbf{p}_i}{N},\ \overline{\mathbf{p}}' = \frac{\sum_{i=1}^{N} \mathbf{p}_i'}{N} \tag{6.9}$$

Then **t** is obtained by

$$\mathbf{t} = \overline{\mathbf{p}} - \mathbf{R}\overline{\mathbf{p}}' \tag{6.10}$$

Substituting Eq. (6.10) into Eq. (6.7) yields

$$\delta^2 = \min \sum_{i=1}^{N} \left\| (\mathbf{p}_i - \overline{\mathbf{p}}) - \mathbf{R}\left(\mathbf{p}'_i - \overline{\mathbf{p}}'\right) \right\|^2 \tag{6.11}$$

Let

$$\mathbf{x}_i = \mathbf{p}_i - \overline{\mathbf{p}},\ \mathbf{y}_i = \mathbf{p}'_i - \overline{\mathbf{p}}' \tag{6.12}$$

Substituting Eq. (6.12) into Eq. (6.11) yields

$$\begin{aligned} \delta^2 &= \min \sum_{i=1}^{N} \|\mathbf{x}_i - \mathbf{R}\mathbf{y}_i\|^2 \\ &= \min\ tr\left[(\mathbf{X} - \mathbf{RY})^T (\mathbf{X} - \mathbf{RY})\right] \\ &= \min\ tr\left[\mathbf{X}^T\mathbf{X} + \mathbf{Y}^T\mathbf{R}^T\mathbf{RY} - \mathbf{Y}^T\mathbf{R}^T\mathbf{X} - \mathbf{X}^T\mathbf{RY}\right] \end{aligned} \tag{6.13}$$

where $\mathbf{X} = [\mathbf{x}_1, \mathbf{x}_2, \ldots, \mathbf{x}_N]$ is a 3 by N matrix that consists of coordinates of N scan points with respect to the SCS, $\mathbf{Y} = [\mathbf{y}_1, \mathbf{y}_2, \ldots, \mathbf{y}_N]$ is a 3 by N matrix that consists of coordinates of N scan points with respect to the SMCS, and *tr* denotes the trace of a matrix.

The rotation matrix $\mathbf{R}$ is an orthogonal matrix with $\mathbf{R}^T\mathbf{R} = \mathbf{I}$, where $\mathbf{I}$ is an identity matrix. The first two terms in Eq. (6.13) do not depend on $\mathbf{R}$; excluding them would not affect the optimization problem. Hence, Eq. (6.13) becomes

$$\min\ tr\left[-\mathbf{Y}^T\mathbf{R}^T\mathbf{X} - \mathbf{X}^T\mathbf{RY}\right] = \min\ tr\left[-\mathbf{X}^T\mathbf{RY} - \mathbf{X}^T\mathbf{RY}\right] = \min\ tr\left[-2\mathbf{RYX}^T\right] \tag{6.14}$$

The minimization problem in Eq. (6.14) is equivalent to a maximization problem:

$$\min\ tr\left[-2\mathbf{RYX}^T\right] = \max\ tr\left[2\mathbf{RYX}^T\right] = \max\ tr\left[\mathbf{RYX}^T\right] \tag{6.15}$$

Let $\mathbf{A} = \mathbf{YX}^T$, which is called a covariance matrix. By SVD, the covariance matrix $\mathbf{A}$ is decomposed as

$$\mathbf{A} = \mathbf{UDV}^T \tag{6.16}$$

where $\mathbf{U}$ is a 3 by 3 orthogonal matrix, $\mathbf{D}$ is a 3 by 3 diagonal matrix with non-negative real values in the descending order on the diagonal, and $\mathbf{V}$ is a 3 by 3 orthogonal matrix. Substituting Eq. (6.16) into Eq. (6.15) yields

$$\max\ tr\left[\mathbf{RYX}^T\right] = \max\ tr\left[\mathbf{RUDV}^T\right] = \max\ tr\left[\mathbf{DV}^T\mathbf{RU}\right] \tag{6.17}$$

Note that $\mathbf{V}$, $\mathbf{R}$ and $\mathbf{U}$ are all orthogonal matrices; $\mathbf{M} = \mathbf{V}^T\mathbf{RU}$ is also an orthogonal matrix. This means that columns of $\mathbf{M}$ are orthonormal vectors and the magnitude of each column is 1. Hence, the domain of entry M_{ij} in $\mathbf{M}$ satisfies $-1 \le M_{ij} \le 1$. Equation (6.17) is expressed as

$$\max\ tr\left[\mathbf{DV}^T\mathbf{RU}\right] = \max\ tr\left[\mathbf{DM}\right] = \max \sum_{i=1}^{3} \lambda_i M_{ii} \le \sum_{i=1}^{3} \lambda_i \tag{6.18}$$

where λ_i is the ith non-negative singular value of $\mathbf{A}$.

The optimization problem in Eq. (6.18) attains a maximum when $M_{ii} = 1$. Because $\mathbf{M}$ is an orthogonal matrix, this means that $\mathbf{M}$ has to be an identity matrix. The rotation matrix $\mathbf{R}$ is obtained by

$$\mathbf{R} = \mathbf{VIU}^T = \mathbf{VU}^T \tag{6.19}$$

Since $\mathbf{R}$ is a rotation matrix, the determinant of $\mathbf{R}$ is 1. If the determinant of $\mathbf{R}$ derived from Eq. (6.19) is -1, $\mathbf{R}$ is a reflection matrix rather than a rotation matrix [10]. If $\mathbf{R}$ is a reflection matrix when $M_{ii} = 1$, one needs to find the next maximization solution to get a rotation matrix. Equation (6.18) can be expanded as

$$\max \sum_{i=1}^{3} \lambda_i M_{ii} = \max\ (\lambda_1 M_{11} + \lambda_2 M_{22} + \lambda_3 M_{33}) \tag{6.20}$$

The objective function in Eq. (6.20) is a linear function of variables M_{11}, M_{22} and M_{33}. Since the domain of each variable is $[-1, 1]$, the objective function attains its extremum on boundaries of the domains. If $\mathbf{R}$ is a reflection matrix when $M_{ii} = 1$, the next maximization solution is $M_{11} = 1$, $M_{22} = 1$, and $M_{33} = -1$ since $\lambda_1 > \lambda_2 > \lambda_3 \geq 0$. $\mathbf{R}$ is given by

$$\mathbf{R} = \mathbf{V}\begin{bmatrix} 1 & 0 & 0 \\ 0 & 1 & 0 \\ 0 & 0 & -1 \end{bmatrix}\mathbf{U}^T \tag{6.21}$$

A general formula is derived to calculate the rotation matrix $\mathbf{R}$ that includes both cases in which the determinant of $\mathbf{VU}^T$ is 1 or -1:

$$\mathbf{R} = \mathbf{V}\begin{bmatrix} 1 & 0 & 0 \\ 0 & 1 & 0 \\ 0 & 0 & \det\left(\mathbf{VU}^T\right) \end{bmatrix}\mathbf{U}^T \tag{6.22}$$

After $\mathbf{R}$ is calculated, $\mathbf{t}$ is obtained by Eq. (6.10). Coordinates of an arbitrary scan point Q in the SMCS are obtained by

$$\left[x'_Q, y'_Q, z'_Q\right]^T = \mathbf{R}^T\left(\left[x_Q, y_Q, z_Q\right]^T - \mathbf{t}\right) \tag{6.23}$$

where coordinates of point Q in the SCS are known. Further, coordinates of point Q in the SMCS can be transformed to corresponding rotation angles of two mirrors and the distance r_Q:

$$\beta_Q = \frac{1}{2}\tan^{-1}\left(-\frac{z'_Q}{x'_Q}\right),\ \alpha_Q = \frac{1}{2}\tan^{-1}\left(\frac{y'_Q}{\frac{x'_Q}{\cos(2\beta_Q)} - d}\right),\ r_Q = -\frac{x'_Q}{\cos\left(2\alpha_Q\right)\cos\left(2\beta_Q\right)} \tag{6.24}$$

A laser beam can be automatically directed to point Q with corresponding input voltages to the two mirrors.

6.4 Procedure to Determine the Orientation and Position of a SLDV

From Sect. 6.3, $\mathbf{R}$ and $\mathbf{t}$ can be obtained with known coordinates of at least three scan points in both the SCS and SMCS. These scan points are defined as reference points, whose coordinates in the SCS can be easily obtained and corresponding rotation angles of two mirrors can be accurately measured from experiment. The parameter r in Eq. (6.5) needs to be calculated by a geometric method shown in Fig. 6.6. The distance between reference point P_i and reference point P_j remains the same when their coordinates are expressed in the SCS and SMCS:

$$\sqrt{(x_i - x_j)^2 + (y_i - y_j)^2 + (z_i - z_j)^2} = \sqrt{\left(x'_i - x'_j\right)^2 + \left(y'_i - y'_j\right)^2 + \left(z'_i - z'_j\right)^2} \tag{6.25}$$

where i is from 1 to $N - 1$ and j is from $i + 1$ to N.

It is seen from Eq. (6.6) that coordinates of scan points in the SMCS can be transformed to those in the SCS using the rotation matrix and translation vector. For a 3D structure, the reference points should be selected to cover all the different heights of the structure in order to map the whole structure from the SMCS to SCS. The frame made up by the reference points should roughly outline the geometry of the structure. The N reference points have N unknown distances r (Fig. 6.6) and can form $N \times (N - 1)$ equations like Eq. (6.25). This is an over-determined nonlinear problem if N is larger than 3, which can be solved by nonlinear least squares method. The initial value of the distance r_i can be estimated using a ruler to measure the distance from Y mirror to reference point P_i. This is a good approach to obtain good estimates of the initial values to solve the equations.

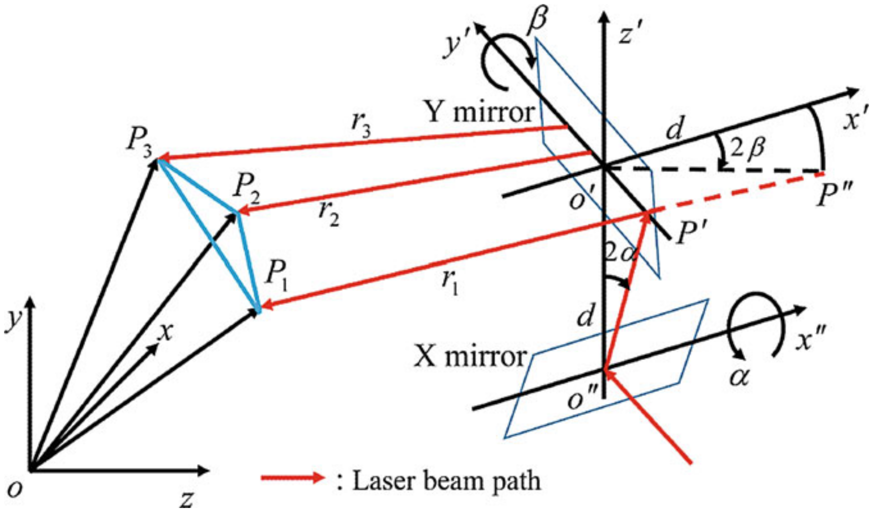

Fig. 6.6 Geometric method to determine the distance *r*

The procedure to determine the orientation and position of a SLDV with respect to the SCS can be summarized as follows:

Step 1: Select at least four reference points that can roughly outline the geometry of the structure and whose coordinates in the SCS are known. Control two scan mirrors to direct the laser beam to the reference points and record corresponding rotation angles of the two mirrors. Measure the initial distances from Y mirror to the reference points.
Step 2: Use Eq. (6.5) to calculate initial coordinates of each reference point in the SMCS. Obtain the exact distance *r* of each reference point by solving the equations formed by Eq. (6.25), and then calculate exact coordinates of all the reference points in the SMCS.
Step 3: Calculate **R** and **t** using Eqs. (6.22) and (6.10), respectively.

It is seen from the procedure that the proposed methodology does not need to solve the inverse problem as in [9] and the rotation matrix **R** is guaranteed to be orthogonal by using SVD. The methodology can be applied to a 2D structure as a special case, as shown in Sect. 6.5.2.

6.5 Experimental Validation

Two experiments were performed using the Polytec PSV-500 system to validate the methodology presented in this work. The internal mirrors configuration of the PSV-500 system and its mathematical model are shown in Fig. 6.7a and b, respectively. It can be seen that the layout of two mirrors in the PSV-500 system is different from that in Fig. 6.1. However, the mathematical model in Fig. 6.7b is similar to that in Fig. 6.2, and coordinates of a scan point *P* in the SMCS under this layout is expressed as

$$\begin{aligned} P &= P' + r e_{P''P'} \\ &= [-d\tan(2\beta),\ 0,\ 0]^T + [-r\sin(2\beta), -r\cos(2\alpha)\cos(2\beta), -r\sin(2\alpha)\cos(2\beta)]^T \\ &= [-d\tan(2\beta) - r\sin(2\beta), -r\cos(2\alpha)\cos(2\beta), -r\sin(2\alpha)\cos(2\beta)]^T \end{aligned} \tag{6.26}$$

where the separation distance *d* of the two mirrors is 36 mm.

6.5.1 3D Structure Scanning

Figure 6.8a shows the first experiment where a 3D structure was scanned by three SLDVs placed at three different locations. The structure is precisely machined and has marked reference points with known coordinates. There are a main flat surface and two different heights of raised blocks on it. Four reference points are selected to outline four corners of the main surface

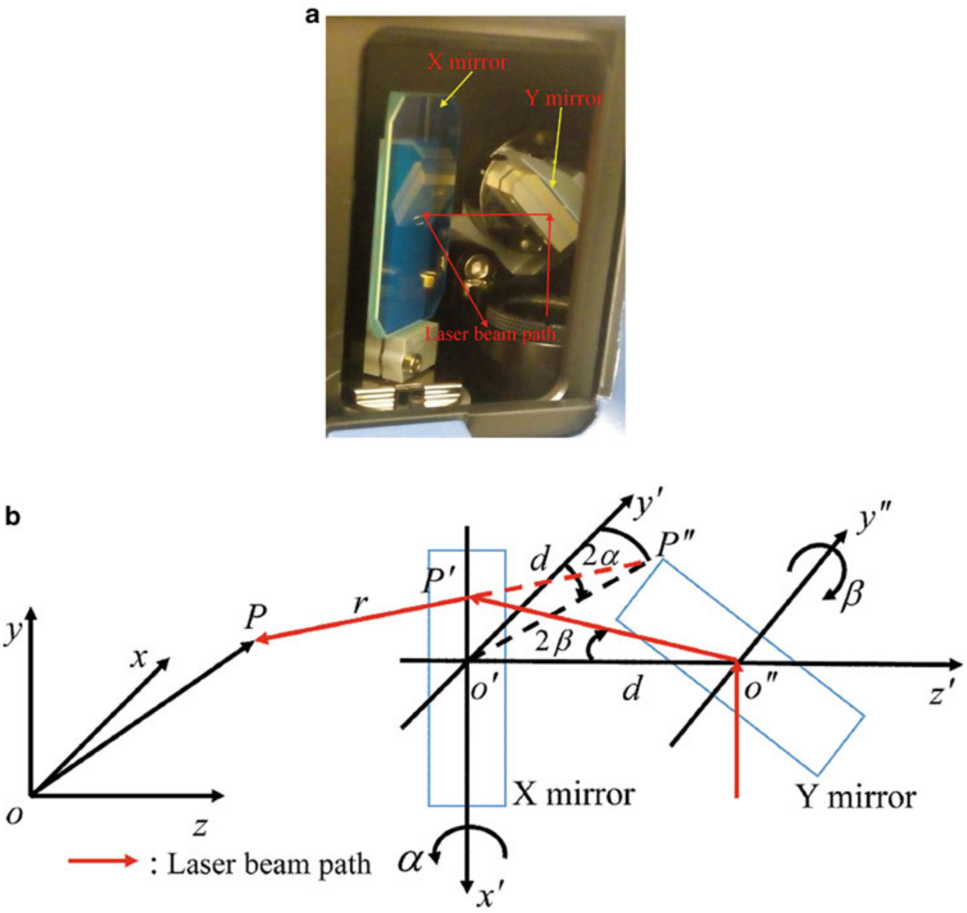

Fig. 6.7 (**a**) Internal mirrors configuration of the Polytec PSV-500 system, and (**b**) the corresponding mathematical model

of the structure, and one additional reference point is selected on each raised block. A frame can be formed by the six reference points (Fig. 6.8b). In order to evaluate the reliability of the proposed methodology, two different sets of reference points are selected to calculate rotation matrices at the three locations. The reference points on the main surface are the same in the two sets and different reference points on the raised blocks are selected (Fig. 6.8b). Rotation angles of two mirrors (obtained by the corresponding input voltages and sensitivity of the scanner) and initial distances corresponding to different reference points are listed in Table 6.1.

With the procedure in Sect. 6.4, **R** and **t** are obtained at the three locations, as listed in Tables 6.2 and 6.3, respectively. Table 6.2 shows that the rotation matrices calculated from two different sets of reference points are almost the same at the three locations, which indicates that the proposed methodology is reliable. Note that the SLDVs at location 2 and location 3 have large angles with the normal direction of the scanned structure, which indicates that the methodology can be used to calculate any orientation of a SLDV. Translation vectors calculated from Set 1 and Set 2 in Table 6.3 slightly differ since **t** is calculated from mean values of coordinates, as shown in Eq. (6.10). Different sets of reference points have different mean values, which causes slight differences of **t**.

In order to evaluate the accuracy of the rotation matrices and translation vectors, twenty scan points with known coordinates in the SCS are selected and their corresponding input voltages are measured. One also can calculate the rotation angles by the following equations based on the mathematical model in Fig. 6.7b:

$$\mathbf{p}' = \mathbf{R}^T (\mathbf{p} - \mathbf{t}) \tag{6.27}$$

$$\alpha = \frac{1}{2}\tan^{-1}\left(\frac{z'}{x'}\right),\ \beta = \frac{1}{2}\tan^{-1}\left(\frac{y'}{\frac{x'}{\cos(2\alpha)} - d}\right),\ r = -\frac{x'}{\cos(2\alpha)\cos(2\beta)} \tag{6.28}$$

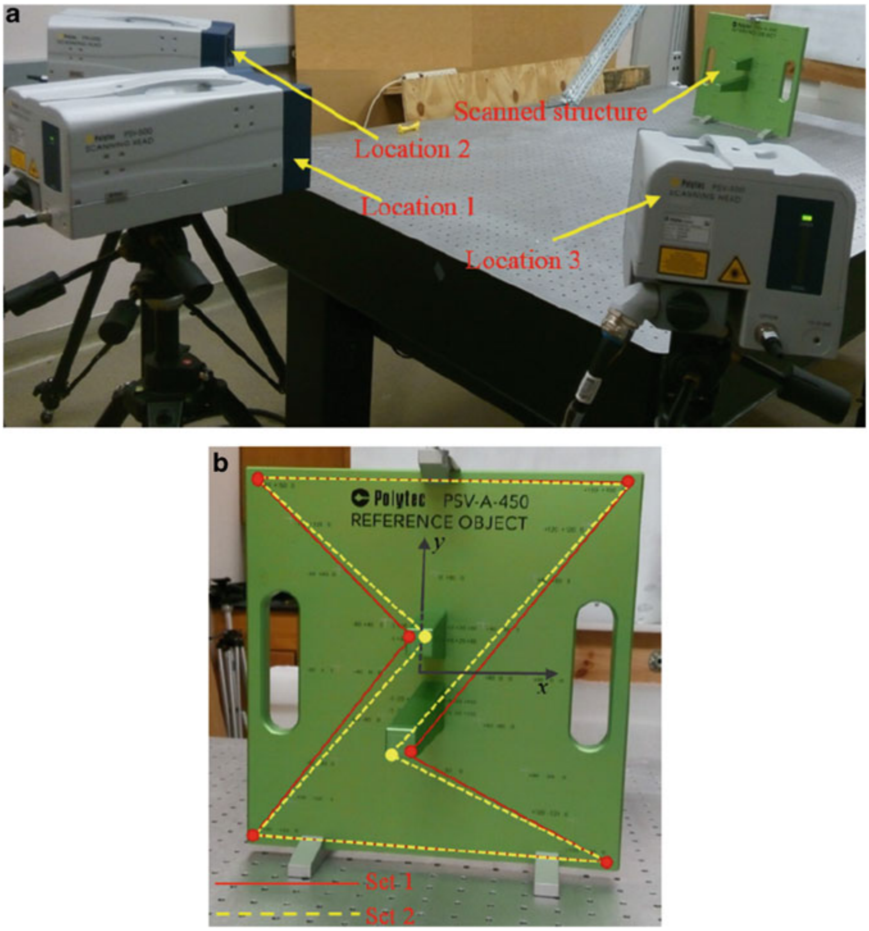

Fig. 6.8 (**a**) A 3D structure scanned by three SLDVs placed at three different locations, and (**b**) frames made up by two different sets of reference points

Table 6.1 Rotation angles and initial distances corresponding to different reference points

Coordinate (mm)			Location 1			Location 2			Location 3		
x	y	z	α (°)	β (°)	r_0 (mm)	α (°)	β (°)	r_0 (mm)	α (°)	β (°)	r_0 (mm)
−150	150	0	−1.121	1.381	1600	−6.669	3.107	1370	2.844	5.132	1600
150	150	0	4.168	1.443	1590	−1.463	3.012	1520	7.786	5.059	1470
150	−150	0	4.215	−3.712	1620	−1.381	−2.403	1540	7.551	−0.502	1500
−150	−150	0	−1.072	−3.755	1630	−6.538	−2.806	1410	2.765	0.019	1630
−5	35	80	1.409	−0.610	1520	−3.257	0.892	1370	4.355	3.015	1460
5	−35	150	1.578	−1.967	1450	−2.349	−0.546	1320	3.825	1.587	1410
5	35	80	1.590	−0.610	1520	−3.082	0.902	1370	4.523	3.000	1460
−5	−35	150	1.384	−1.967	1450	−2.530	−0.556	1320	3.825	1.587	1410

Once the coordinates of the scan points in the SMCS are obtained by Eq. (6.27), they can further be transformed to rotation angles of two mirrors and distances r by Eq. (6.28). Comparison of measured and calculated rotation angles is shown in Tables 6.4, 6.5 and 6.6. At location 1 the maximum relative errors of rotation angles are 2.5 % in Set 1 and 3.5 % in Set 2. For most scan points, the relative errors are less than 1 %. The rotation matrix and translation vector provide good estimates of the orientation and position of the SLDV at location 1. The same conclusion can be obtained from Tables 6.5 and 6.6, where the relative errors for most scan points are less than 0.5 %. In Table 6.6 there are two large relative errors of over 30 % in both sets because the rotation angles of Y mirror are very small and close to zero.

It is seen from Tables 6.4, 6.5 and 6.6 that relative errors between measured and calculated rotation angles are less than 2 % for most scan points at the three locations. One can find that the distance r in Eq. (6.26) also plays an important role in

Table 6.2 Rotation matrices **R** at the three locations

		Set 1			Set 2		
Unit: °		x	y	z	x	y	z
Location 1	x'	90.609	179.387	89.933	90.627	179.373	90.009
	y'	84.764	89.989	5.236	84.431	90.070	5.570
	z'	174.729	89.387	84.765	174.395	89.377	84.430
Location 2	x'	91.807	177.753	88.663	91.747	177.918	88.867
	y'	124.768	87.871	34.852	124.986	88.070	35.055
	z'	145.171	89.280	124.819	144.957	89.220	125.031
Location 3	x'	84.635	171.322	83.198	84.584	171.150	83.022
	y'	52.582	81.322	38.762	52.736	81.150	38.663
	z'	142.064	90.054	52.064	142.207	90.008	52.207

Table 6.3 Translation vectors **t** at the three locations

	Set 1			Set 2		
Unit: mm	x	y	z	x	y	z
Location 1	61.159	69.357	1618.285	70.443	67.089	1617.261
Location 2	−670.036	39.961	1314.570	−675.003	34.724	1312.340
Location 3	724.280	97.372	1380.617	723.445	102.490	1387.096

Table 6.4 Comparison of measured and calculated rotation angles at location 1

Coordinate (mm)			Measurement		Calculation from Set 1				Calculation from Set 2			
x	y	z	α (°)	β (°)	α_1 (°)	β_1 (°)	$\delta_{\alpha 1}$[a] (%)	$\delta_{\beta 1}$ (%)	α_2 (°)	β_2 (°)	$\delta_{\alpha 2}$ (%)	$\delta_{\beta 2}$ (%)
−150	150	0	−1.121	1.381	−1.114	1.378	0.554	0.218	−1.112	1.377	0.784	0.307
150	150	0	4.168	1.443	4.174	1.443	0.149	0.003	4.177	1.444	0.222	0.132
150	−150	0	4.215	−3.712	4.230	−3.722	0.360	0.261	4.235	−3.725	0.483	0.352
−150	−150	0	−1.072	−3.755	−1.058	−3.752	1.265	0.090	−1.055	−3.753	1.568	0.059
−5	35	80	1.409	−0.610	1.393	−0.604	1.082	0.833	1.387	−0.603	1.556	1.080
5	35	80	1.590	−0.610	1.579	−0.603	0.649	1.125	1.573	−0.601	1.066	1.378
5	25	80	1.590	−0.781	1.581	−0.784	0.524	0.432	1.575	−0.783	0.938	0.246
−5	25	80	1.412	−0.791	1.395	−0.786	1.151	0.556	1.389	−0.785	1.621	0.736
−5	−25	150	1.381	−1.786	1.347	−1.773	2.429	0.713	1.333	−1.771	3.492	0.868
5	−25	150	1.578	−1.780	1.542	−1.772	2.268	0.436	1.528	−1.769	3.195	0.591
5	−35	150	1.578	−1.967	1.544	−1.961	2.136	0.295	1.530	−1.959	3.060	0.429
−5	−35	150	1.384	−1.967	1.350	−1.963	2.490	0.219	1.335	−1.960	3.547	0.354
−120	120	0	−0.592	0.873	−0.585	0.871	1.041	0.236	−0.583	0.870	1.414	0.334
120	120	0	3.643	0.921	3.649	0.920	0.188	0.068	3.652	0.921	0.262	0.062
120	−120	0	3.684	−3.219	3.694	−3.219	0.293	0.013	3.699	−3.221	0.409	0.093
−120	−120	0	−0.547	−3.247	−0.540	−3.246	1.251	0.045	−0.537	−3.247	1.774	0.008
−80	80	0	0.124	0.194	0.123	0.191	0.594	1.786	0.125	0.190	0.957	2.076
80	80	0	2.946	0.223	2.949	0.221	0.109	0.809	2.952	0.221	0.189	0.618
80	−80	0	2.970	−2.540	2.979	−2.543	0.330	0.128	2.983	−2.544	0.441	0.195
−80	−80	0	0.153	−2.561	0.153	−2.563	0.295	0.075	0.156	−2.564	1.904	0.121

[a] $\delta_{\alpha 1} = |\alpha_1 - \alpha|/\alpha \times 100\,\%$, similar calculation for $\delta_{\beta 1}$, $\delta_{\alpha 2}$, and $\delta_{\beta 2}$

calculating coordinates of a scan point in the SMCS. Slight changes of rotation angles can cause large movement of the laser beam when the standoff distance between a SLDV and a structure is far. This is the reason why the SLDV can scan a large structure with limited rotation angles. To further evaluate the rotation matrix and translation vector, measured rotation angles with the calculated distance r are substituted into Eq. (6.26) and one can then use Eq. (6.6) to obtain corresponding estimated coordinates of the scan point in the SCS. These estimated coordinates are compared with exact coordinates in the xy plane at the three locations, as shown in Fig. 6.9, to give a better visualization of the differences between measured and calculated rotation angles. Table 6.7 shows the corresponding Euclidean-norm differences between the exact and estimated coordinates in the xy plane. Table 6.7 indicates that the maximum Euclidean-norm differences at location 1 are 1.880 mm in Set 1 and

Table 6.5 Comparison of measured and calculated rotation angles at location 2

Coordinate (mm)			Measurement		Calculation from Set 1				Calculation from Set 2			
x	y	z	α (°)	β (°)	α_1 (°)	β_1 (°)	$\delta_{\alpha 1}$ (%)	$\delta_{\beta 1}$ (%)	α_2 (°)	β_2 (°)	$\delta_{\alpha 2}$ (%)	$\delta_{\beta 2}$ (%)
−150	150	0	−6.669	3.107	−6.669	3.100	0.008	0.220	−6.667	3.102	0.021	0.149
150	150	0	−1.463	3.012	−1.463	3.007	0.022	0.178	−1.473	3.001	0.693	0.358
150	−150	0	−1.381	−2.403	−1.383	−2.394	0.216	0.345	−1.388	−2.398	0.573	0.191
−150	−150	0	−6.538	−2.806	−6.543	−2.801	0.077	0.148	−6.540	−2.801	0.026	0.154
−5	35	80	−3.257	0.892	−3.256	0.893	0.014	0.066	−3.253	0.897	0.110	0.602
5	35	80	−3.082	0.902	−3.077	0.896	0.171	0.621	−3.074	0.900	0.258	0.118
5	25	80	−3.082	0.702	−3.073	0.697	0.279	0.583	−3.071	0.702	0.371	0.072
−5	25	80	−3.257	0.702	−3.253	0.693	0.119	1.148	−3.249	0.698	0.218	0.459
−5	−25	150	−2.530	−0.349	−2.526	−0.349	0.129	0.083	−2.517	−0.338	0.476	3.051
5	−25	150	−2.349	−0.345	−2.342	−0.341	0.289	1.037	−2.333	−0.331	0.643	3.973
5	−35	150	−2.349	−0.546	−2.338	−0.548	0.429	0.300	−2.330	−0.538	0.790	1.554
−5	−35	150	−2.530	−0.556	−2.523	−0.556	0.262	0.120	−2.514	−0.546	0.616	1.746
−120	120	0	−6.091	2.514	−6.094	2.509	0.057	0.175	−6.093	2.511	0.038	0.112
120	120	0	−1.933	2.479	−1.932	2.474	0.045	0.210	−1.940	2.470	0.370	0.382
120	−120	0	−1.867	−1.898	−1.865	−1.894	0.085	0.190	−1.869	−1.898	0.147	0.025
−120	−120	0	−5.999	−2.181	−5.997	−2.182	0.022	0.060	−5.995	−2.181	0.066	0.045
−80	80	0	−5.345	1.733	−5.343	1.732	0.040	0.051	−5.343	1.733	0.043	0.005
80	80	0	−2.571	1.743	−2.571	1.744	0.000	0.106	−2.577	1.741	0.224	0.061
80	−80	0	−2.520	−1.209	−2.523	−1.209	0.124	0.017	−2.527	−1.211	0.263	0.179
−80	−80	0	−5.282	−1.375	−5.282	−1.365	0.006	0.658	−5.280	−1.365	0.021	0.676

Table 6.6 Comparison of measured and calculated rotation angles at location 3

Coordinate (mm)			Measurement		Calculation from Set 1				Calculation from Set 2			
x	y	z	α (°)	β (°)	α_1 (°)	β_1 (°)	$\delta_{\alpha 1}$ (%)	$\delta_{\beta 1}$ (%)	α_2 (°)	β_2 (°)	$\delta_{\alpha 2}$ (%)	$\delta_{\beta 2}$ (%)
−150	150	0	2.844	5.132	2.843	5.126	0.040	0.125	2.844	5.121	0.014	0.209
150	150	0	7.786	5.059	7.802	5.062	0.211	0.058	7.792	5.050	0.081	0.172
150	−150	0	7.551	−0.502	7.567	−0.505	0.214	0.656	7.558	−0.494	0.095	1.549
−150	−150	0	2.765	0.019	2.760	0.012	0.153	36.667	2.764	0.025	0.023	30.408
−5	35	80	4.355	3.015	4.348	3.015	0.140	0.013	4.352	3.010	0.066	0.159
5	35	80	4.523	3.000	4.517	3.007	0.128	0.263	4.520	3.002	0.065	0.083
5	25	80	4.520	2.822	4.512	2.820	0.156	0.067	4.515	2.815	0.091	0.232
−5	25	80	4.355	2.828	4.344	2.828	0.245	0.008	4.347	2.824	0.169	0.150
−5	−25	150	3.653	1.793	3.634	1.811	0.513	0.991	3.644	1.806	0.254	0.731
5	−25	150	3.825	1.784	3.807	1.799	0.466	0.854	3.816	1.794	0.229	0.582
5	−35	150	3.825	1.587	3.802	1.604	0.576	1.089	3.812	1.600	0.336	0.835
−5	−35	150	3.650	1.609	3.630	1.617	0.541	0.497	3.640	1.613	0.279	0.256
−120	120	0	3.292	4.618	3.289	4.607	0.070	0.249	3.290	4.603	0.061	0.324
120	120	0	7.230	4.523	7.245	4.519	0.203	0.080	7.236	4.510	0.086	0.278
120	−120	0	7.059	0.095	7.070	0.094	0.164	0.891	7.063	0.103	0.059	8.369
−120	−120	0	3.219	0.479	3.212	0.473	0.188	1.222	3.215	0.484	0.111	0.996
−80	80	0	3.891	3.901	3.894	3.897	0.072	0.089	3.893	3.895	0.061	0.144
80	80	0	6.510	3.812	6.520	3.806	0.164	0.148	6.514	3.801	0.066	0.291
80	−80	0	6.408	0.883	6.416	0.883	0.120	0.111	6.410	0.890	0.033	0.794
−80	−80	0	3.841	1.108	3.833	1.105	0.200	0.253	3.834	1.112	0.177	0.440

2.642 mm in Set 2, which appear on the highest raised block. At location 2 the maximum Euclidean-norm differences are less than 1 mm in both sets. At location 3, the maximum Euclidean-norm differences are 1.323 mm in Set 1 and 0.897 mm in Set 2, which also appear on the highest raised block. For an engineering application of a SLDV, errors of measured velocities caused by these Euclidean-norm differences between exact and estimated coordinates can be neglected because the vibration of such small zones can be considered as purely translational. By scanning the 3D structure, the methodology for determining the orientation and position of a SLDV is validated. The rotation matrix and translation vector can map coordinates of a scan point from the SMCS to SCS with high accuracy.

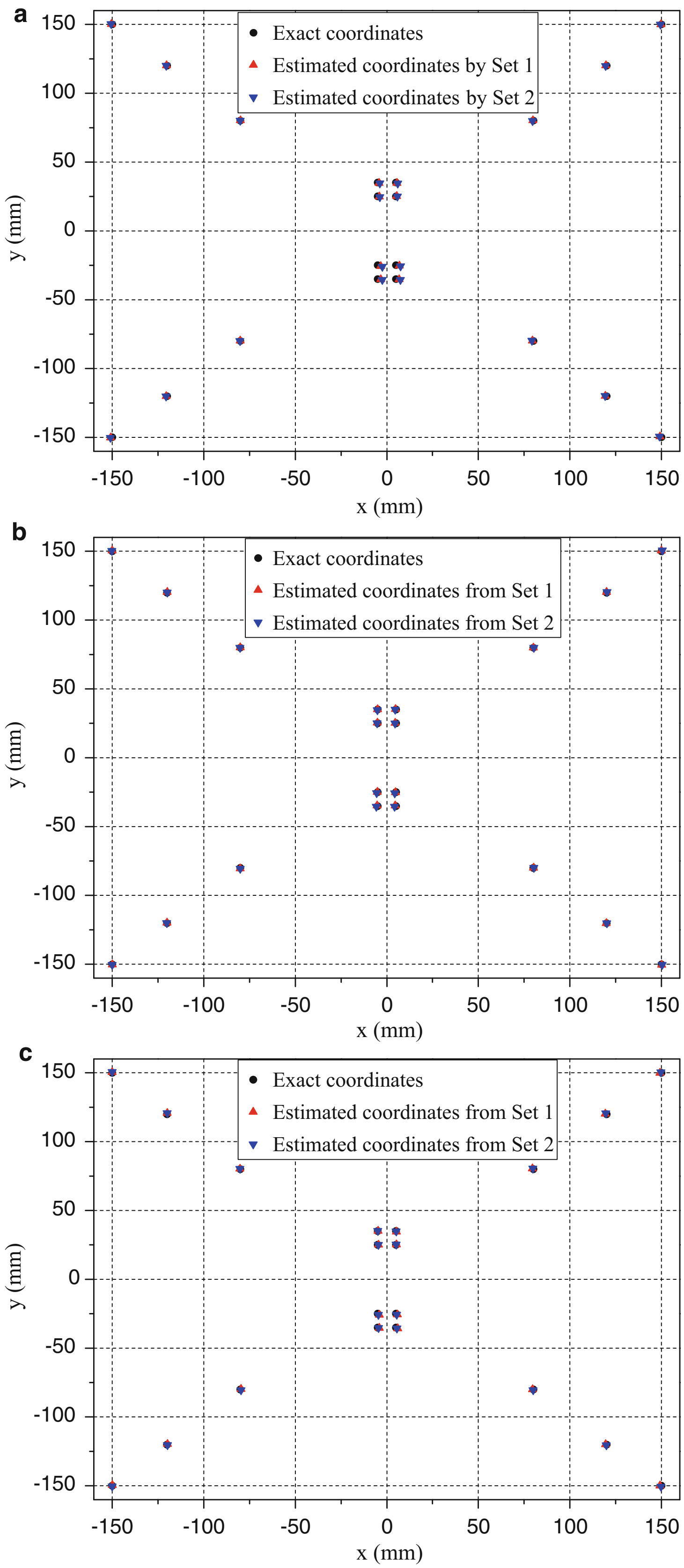

Fig. 6.9 Comparison between exact and estimated coordinates in the *xy* plane: (**a**) location 1, (**b**) location 2, and (**c**) location 3

Table 6.7 Euclidean-norm differences (unit: mm) between exact and estimated coordinates for the 3D structure

Exact coordinate (mm)			Location 1		Location 2		Location 3	
x	y	z	Set 1	Set 2	Set 1	Set 2	Set 1	Set 2
−150	150	0	0.391	0.553	0.347	0.245	0.378	0.626
150	150	0	0.351	0.535	0.296	0.740	0.799	0.552
150	−150	0	1.022	1.371	0.472	0.432	0.816	0.530
−150	−150	0	0.787	0.955	0.307	0.229	0.443	0.343
−5	35	80	0.865	1.231	0.035	0.310	0.277	0.285
5	35	80	0.670	1.020	0.362	0.346	0.497	0.190
5	25	80	0.484	0.807	0.424	0.493	0.332	0.393
−5	25	80	0.906	1.269	0.437	0.346	0.483	0.401
−5	−25	150	1.847	2.603	0.134	0.715	1.240	0.798
5	−25	150	1.880	2.642	0.328	0.909	1.113	0.665
5	−35	150	1.755	2.514	0.416	0.865	1.323	0.897
−5	−35	150	1.782	2.542	0.271	0.794	0.959	0.497
−120	120	0	0.368	0.501	0.272	0.175	0.673	0.873
120	120	0	0.388	0.540	0.289	0.605	0.723	0.739
120	−120	0	0.610	0.867	0.214	0.128	0.568	0.467
−120	−120	0	0.395	0.548	0.089	0.187	0.434	0.337
−80	80	0	0.205	0.243	0.108	0.105	0.239	0.342
80	80	0	0.209	0.324	0.100	0.269	0.596	0.641
80	−80	0	0.584	0.792	0.144	0.329	0.372	0.392
−80	−80	0	0.114	0.244	0.466	0.484	0.397	0.443

Table 6.8 Coordinates and measured rotation angles of nine scan points on the clamped plate

	Coordinates (mm)			Location 1			Location 2			Location 3		
Index	x	y	z	α (°)	β (°)	r_0 (mm)	α (°)	β (°)	r_0 (mm)	α (°)	β (°)	r_0 (mm)
1	−78.5	62	0	2.778	2.159	1400	−0.864	3.907	1320	4.707	5.808	1340
2	65.5	57.5	0	5.635	2.099	1410	1.600	3.698	1400	7.487	5.701	1260
3	67.8	−55.4	0	5.685	−0.095	1410	1.654	1.486	1400	7.408	3.269	1260
4	−82.8	−63	0	2.673	−0.251	1410	−0.943	1.349	1320	4.514	3.288	1340
5	−44.5	31.2	0	3.444	1.568	1400	−0.257	3.253	1320	5.301	5.174	1340
6	23.5	39.2	0	4.813	1.748	1410	0.921	3.384	1400	6.637	5.339	1260
7	40.9	−22.8	0	5.154	0.529	1410	1.206	2.127	1400	6.907	3.987	1260
8	−40.8	−36.5	0	3.546	0.246	1410	−0.159	1.863	1320	5.336	3.764	1340
9	0	0	0	4.338	0.961	1410	0.530	2.593	1320	6.129	4.501	1300

6.5.2 2D Clamped Plate Scanning

Figure 6.10a shows the second experiment where a clamped plate was scanned by three SLDVs. The locations and orientations of the three SLDVs are the same as those in the first experiment. Since there would be no marked reference points in a practical structure as in Fig. 6.8b, nine scan points are selected here and a SCS is built to determine coordinates of these points, as shown in Fig. 6.10b. The coordinates of the nine scan points measured by a ruler and their corresponding rotation angles of two mirrors are listed in Table 6.8. Based on the rectangular shape of the plate, four scan points with indices 2, 4, 5 and 7 are selected as the reference points to calculate rotation matrices and translation vectors. The rotation matrices with respect to three different locations are listed in Table 6.9. Since the orientations of the three SLDVs are the same as those in the first experiment, there are little differences between the rotation matrices in Tables 6.2 and 6.9. Figure 6.11 shows comparison between exact and estimated coordinates that are calculated using the same method as described in Sect. 6.5.1. Table 6.10 lists the corresponding Euclidean-norm differences between the exact and estimated coordinates. All the Euclidean-norm differences are less than 1.7 mm and are acceptable for an engineering application. This experiment indicates that the methodology can also be used to obtain the rotation matrix of a SLDV with high accuracy when a structure with less precise coordinates of reference points in the SCS is scanned.

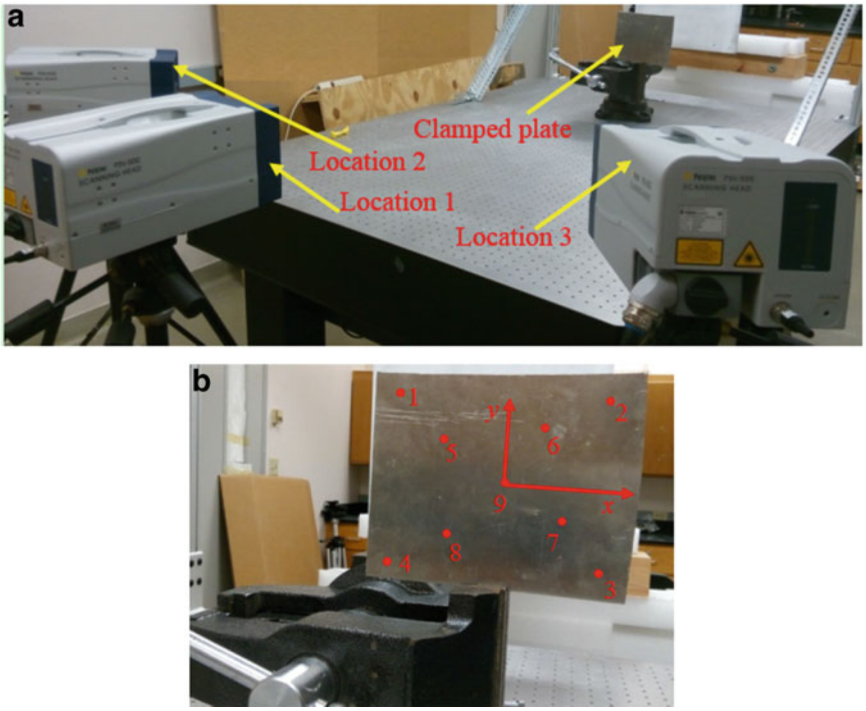

Fig. 6.10 (**a**) A 2D clamped plate scanned by three SLDVs placed at three different locations, and (**b**) the SCS of the clamped plate with nine scan points on it

Table 6.9 Rotation matrices with respect to three different locations for the clamped plate

Unit: °		x	y	z
Location 1	x'	90.436	171.829	81.840
	y'	85.120	81.907	9.467
	z'	175.101	88.878	85.231
Location 2	x'	91.374	177.873	88.376
	y'	123.447	87.887	33.531
	z'	146.518	89.750	123.481
Location 3	x'	83.791	171.370	84.030
	y'	50.520	81.419	40.774
	z'	139.839	90.904	49.853

6.6 Conclusion

A mathematical model based on the scan mirrors configuration is developed in this work to determine the orientation and position of a SLDV. Coordinates of a scan point in the SMCS is derived from the mathematical model and the relation of coordinates of the same scan point in the SMCS and SCS is derived using the rigid transformation theory. The least squares method and SVD are used to calculate the rotation matrix and translation vector from the SMCS to SCS. A procedure to determine the orientation and position of a SLDV with respect to the SCS is presented. Experiments to scan a 3D structure and a 2D clamped plate are performed to validate the methodology. The 3D structure is scanned by three SLDVs placed at three different locations and two different sets of reference points are selected to obtain the rotation matrices and translation vectors. Results indicate that the proposed methodology is reliable and has high accuracy in estimating the orientation and position of a SLDV. The 2D clamped plate is a special case of a 3D structure and the rotation matrix and translation vector can also be obtained with high accuracy; this shows universal applicability of the proposed methodology and extends its application scope from 3D structures to 2D structures, which is a major improvement over previous techniques. Based on the methodology presented in this work, measured velocities by a SLDV can be transformed to the SCS in which one can better describe the ODS of a structure and analyze its dynamic response.

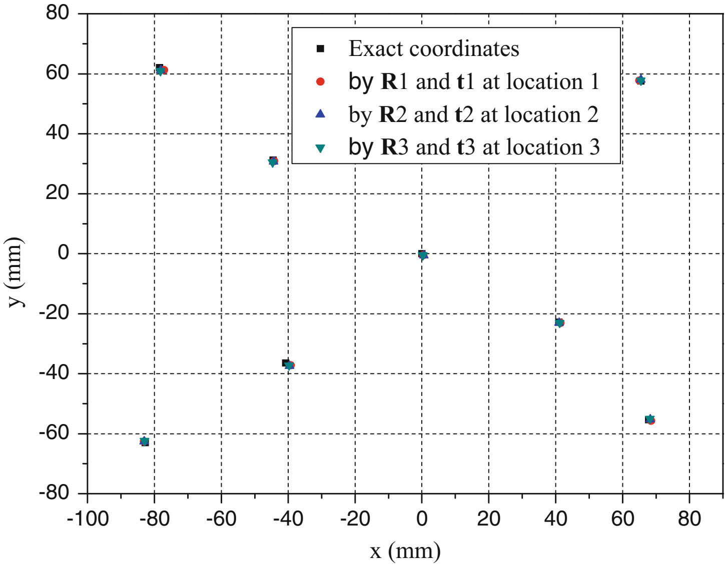

Fig. 6.11 Comparison between exact and estimated coordinates for the clamped plate

Table 6.10 Euclidean-norm differences (unit: mm) between exact and estimated coordinates for the clamped plate

Exact coordinates (mm)					
x	*y*	*z*	Location 1	Location 2	Location 3
−78.5	62	0	1.592	0.932	1.123
65.5	57.5	0	0.568	0.491	0.309
67.8	−55.4	0	0.737	0.455	0.485
−82.8	−63	0	0.480	0.415	0.648
−44.5	31.2	0	0.456	0.586	0.727
23.5	39.2	0	0.753	0.819	0.814
40.9	−22.8	0	0.574	0.298	0.371
−40.8	−36.5	0	1.664	1.521	1.287
0	0	0	0.661	0.830	0.558

Acknowledgement The authors are grateful for the financial support from the National Science Foundation under grant numbers CMMI-1229532 and CMMI-1335024.

References

1. Stanbridge, A.B., Ewins, D.J.: Modal testing using a scanning laser Doppler vibrometer. Mech. Syst. Signal Process. **13**(2), 255–270 (1999)
2. Stanbridge, A.B., Martarelli, M., Ewins, D.J.: Measuring area vibration mode shapes with a continuous-scan LDV. Measurement **35**(2), 181–189 (2004)
3. Di Maio, D., Ewins, D.J.: Continuous Scan, a method for performing modal testing using meaningful measurement parameters; Part I. Mech. Syst. Signal Process. **25**(8), 3027–3042 (2011)
4. Allen, M.S., Sracic, M.W.: A new method for processing impact excited continuous-scan laser Doppler vibrometer measurements. Mech. Syst. Signal Process. **24**(3), 721–735 (2010)
5. Castellini, P., Martarelli, M., Tomasini, E.P.: Laser Doppler Vibrometry: development of advanced solutions answering to technology's needs. Mech. Syst. Signal Process. **20**(6), 1265–1285 (2006)
6. Vuye, C., Vanlanduit, S., Presezniak, F., Steenackers, G., Guillaume, P.: Optical measurement of the dynamic strain field of a fan blade using a 3D scanning vibrometer. Opt. Lasers Eng. **49**(7), 988–997 (2011)

7. Weekes, B., Ewins, D.J.: Multi-frequency, 3D ODS measurement by continuous scan laser Doppler vibrometry. Mech. Syst. Signal Process. **58**, 325–339 (2015)
8. Zeng, X., Wicks, A.L., Mitchell, L.D.: Geometrical method for the determination of the position and orientation of a scanning laser Doppler vibrometer. Opt. Lasers Eng. **25**(4), 247–264 (1996)
9. Xu, Y., Miles, R.N.: An identification algorithm for directing the measurement point of scanning laser vibrometers. Opt. Lasers Eng. **22**(2), 105–120 (1995)
10. Arun, K.S., Huang, T.S., Blostein, S.D.: Least-squares fitting of two 3-D point sets. IEEE Trans. Pattern Anal. Mach. Intell. (5), 698–700 (1987)

Chapter 7
Operational Modal Analysis with a 3D Laser Vibrometer Without External Reference

Simon Marwitz and Volkmar Zabel

Abstract The use of Scanning Laser Doppler Vibrometers (SLDV) is a common practice in the context with modal analysis. 3D SLDV have been used with classical experimental modal analysis for several years. In this case, three laser heads, which simultaneously point to the same location, are used and an additional input reference signal is required to combine the results of consecutive records. In operational modal analysis the input reference signal is replaced by an output reference signal, which may be obtained, for example, from an additional vibrometer or accelerometer.

Alternatively, if a 3 dimensional laser vibrometer is used, one of the three laser heads can be used to provide a reference signal for the other two heads, which can then position their laserbeams independently. However, this requires an appropriate post-estimation method for the transformation of 3D local skew coordinates since the common, built-in routines of commercially available 3D SLDV perform the respective coordinate transformation directly on the simultaneously acquired time series.

In the presented study a respective algorithm has been developed and applied to measured vibration data. For the modal identification the SSI cov/ref algorithm and three different merging strategies have been employed.

Keywords 3D scanning laser vibrometer • 3D SLDV • Coordinate transformation • Operational modal analysis • OMA • Reference signals

7.1 Introduction

Laser Doppler Vibrometers (LDV) are widely used for noncontact measurement of vibrations, mainly under laboratory conditions. They provide several advantages over accelerometers that are typically used for vibration measurements. The most prominent is probably the elimination of additional mass loading effects on the dynamic behavior of the structure under test. Scanning LDV can position the laser beam onto different points of a structure automatically and thus speed up the process of multi-point measurements significantly. However, an LDV is limited to measuring vibrations along the direction of the laser beam. 3D SLDV combine three laser scan heads, that are placed in different locations and direct their laser beams simultaneously to the same point on a test structure. Vibrations in the Cartesian spatial directions can then be computed for each point of measurement. To combine the multiple single-point measurements, an input or an output reference signal is needed.

In operational modal analysis (OMA) one or more output reference signals are used. Thus, the input or excitation of the structure needs not to be known, which eliminates the demand for any loading device connected to the structure, that might influence the dynamic behavior. Over the years, several methods for the analysis of output-only measurements have been developed. Most of them are adapted from traditional input-output modal analysis. Among the most established methods are the stochastic subspace identification (SSI) modal estimation algorithms with the covariance-driven and the data-driven versions. They originate from system realization theory [5] and are used for the identification of a stochastic state-space model, from which the modal parameters can be extracted.

The combination of multiple measurements based on reference signals can be performed in different ways, depending on the modal estimation algorithm that is employed. The three steps usually involved are: modal analysis, rescaling and merging the data. For the reference-based covariance-driven stochastic subspace identification there exist three such algorithms, described in [1] and [3]. They differ in the order in which the aforementioned steps are performed.

S. Marwitz (✉) • V. Zabel
Institute of Structural Mechanics, Faculty of Civil Engineering, Bauhaus-University Weimar,
Marienstraße 15, 99421 Weimar, Germany
e-mail: simon.jakob.marwitz@uni-weimar.de

© The Society for Experimental Mechanics, Inc. 2016

J. De Clerck, D.S. Epp (eds.), *Rotating Machinery, Hybrid Test Methods, Vibro-Acoustics & Laser Vibrometry, Volume 8*,
Conference Proceedings of the Society for Experimental Mechanics Series, DOI 10.1007/978-3-319-30084-9_7

As mentioned before, merging of modal components identified from different setups by means of OMA requires at least one output reference signal. If all three laser beams of a 3D SLDV always point at the same time at a single measuring point, this requirement can only be fulfilled by using an additional sensor, which can also be an SLDV. In this study an approach is presented which allows to circumvent the application of additional sensors.

7.2 Theory

7.2.1 3D SLDV: Mode Shape Coordinate Transformation

In the course of a series of 3D SLDV measurements, the velocities at each measuring point are recorded successively. A single laser vibrometer only measures vector components of any vibration along the direction of its laser beams. Therefore, the quantities at each DOF are available in local skew coordinate systems, too. These quantities may be measured vibration time histories or the components of the estimated mode shapes, also known as modal coordinates. For the visual representation of the mode shapes, an appropriate coordinate transformation at each measuring point is necessary. This cannot be done by simple vector addition of the respective quantities.

As the determined quantity $\mathbf{v_i}$ is only a vector component of the actual quantity $\mathbf{v_r}$ in the direction of measurement, any component perpendicular to this direction is unknown. Thus, the effective quantity has to lie on a line or plane perpendicular to $\mathbf{v_i}$, $\mathbf{v}_{\perp,\mathbf{i}}$. This can be represented by the Hesse normal form of a line in $\mathbb{R}^2$ or a plane in $\mathbb{R}^3$

$$\mathbf{v}_{\perp,\mathbf{i}}: \qquad \mathbf{n_i}\cdot\mathbf{r} = d_i \qquad \text{with} \quad \|\mathbf{n_i}\| = 1, \quad d_i \geq 0\,. \tag{7.1}$$

In this case the normal vector is the normalized quantity and the distance from the origin d_i is simply it's length

$$\begin{aligned} \mathbf{n_i} = \frac{\mathbf{v_i}}{\|\mathbf{v_i}\|}\,, \quad d_i &= \mathbf{v_i}\cdot\mathbf{n_i} \\ &= \|\mathbf{v_i}\|\,. \end{aligned} \tag{7.2}$$

This holds at any DOF for quantity $\mathbf{v_i}$ with $i = 1, 2, 3$ (number of measurement directions or scan heads). The intersection point of the lines or planes $\mathbf{v_r}$ can be found by solving the linear system of equations with respect to the components of $\mathbf{r}$.

The principle of such a transformation can be shown clearly in the planar case (see Fig. 7.1a), where $\mathbf{v_i} : [a_i, b_i]^\mathsf{T}$ with $i = 1, 2$ and $\mathbf{v_r} : [x_r, y_r]^\mathsf{T}$. The solution is found e.g. by applying Cramer's rule

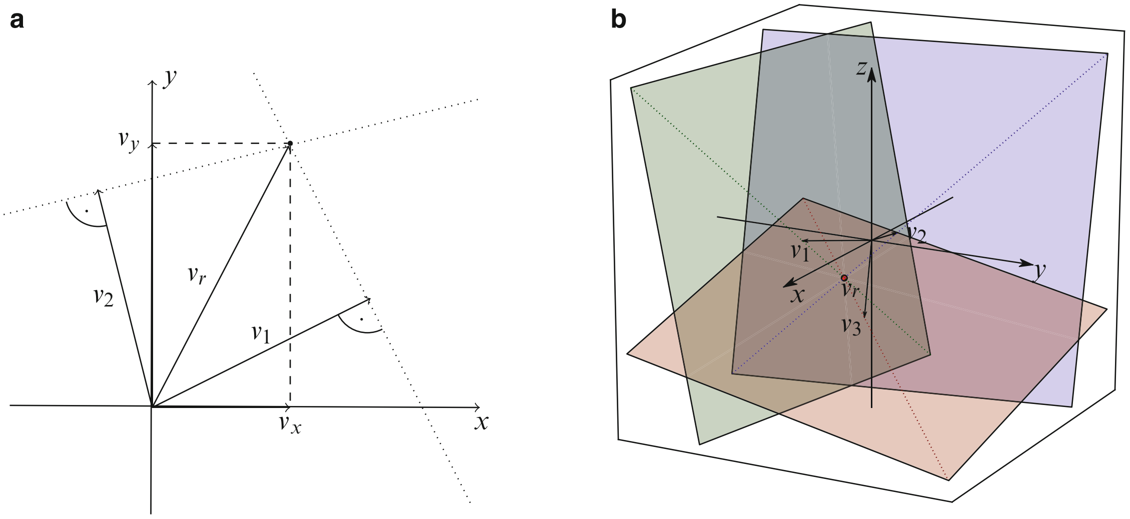

Fig. 7.1 3D transformation of modal coordinates. (**a**) ... in the x-y-plane. (**b**) ... in 3D Space

$$x_r = \frac{-\Delta_x}{\Delta}, \quad y_r = \frac{-\Delta_y}{\Delta}, \quad \text{with} \quad \Delta = \begin{vmatrix} a_1 & b_1 \\ a_2 & b_2 \end{vmatrix}, \quad \Delta_x = \begin{vmatrix} -d_1^2 & b_1 \\ -d_2^2 & b_2 \end{vmatrix} \text{ and } \Delta_y = \begin{vmatrix} a_1 & -d_1^2 \\ a_2 & -d_2^2 \end{vmatrix}. \tag{7.3}$$

It has to be mentioned, though, that if the amplitude of either of the quantities $\mathbf{v_i}$ vanishes (e.g. the direction of vibration is perpendicular to the laser beam), the solution fails.

In the 3-dimensional case the DOFs are extended by another dimension $\mathbf{v_i} : [a_i, b_i, c_i]^\mathsf{T}$ and the system of linear equations by a third variable, $\mathbf{v_r} : [x_r, y_r, z_r]^\mathsf{T}$. The actual derivation of the procedure holds for any dimension ≥ 2. An intuitive representation of the procedure would be to find the intersection point v_r of three planes $\mathbf{v}_{\perp,\mathbf{i}}$ in $\mathbb{R}^3$ (see Fig. 7.1b). Again, the application of Cramer's rule (under the condition of non-zero amplitudes of the respective quantities) leads to the following solution

$$x_r = \frac{-\Delta_x}{\Delta}, \quad y_r = \frac{-\Delta_y}{\Delta}, \quad z_r = \frac{-\Delta_z}{\Delta} \tag{7.4}$$

with

$$\Delta = \begin{vmatrix} a_1 & b_1 & c_1 \\ a_2 & b_2 & c_2 \\ a_3 & b_3 & c_3 \end{vmatrix}, \quad \Delta_x = \begin{vmatrix} -d_1^2 & b_1 & c_1 \\ -d_2^2 & b_2 & c_2 \\ -d_3^2 & b_3 & c_3 \end{vmatrix}, \quad \Delta_y = \begin{vmatrix} a_1 & -d_1^2 & c_1 \\ a_2 & -d_2^2 & c_2 \\ a_3 & -d_3^2 & c_3 \end{vmatrix}, \quad \Delta_z = \begin{vmatrix} a_1 & b_1 & -d_1^2 \\ a_2 & b_2 & -d_2^2 \\ a_3 & b_3 & -d_3^2 \end{vmatrix}. \tag{7.5}$$

Finally, it should be noted that at each point of measurement, the laser beams intersect at different angles. Hence the local skew coordinate system is different at each point. Regarding the solution of the linear systems of equations, due to the nature of 3D SLDV measurements parallel lines or planes should not occur, but there may be cases where either of the quantities vanishes. A three-dimensional transformation is then reduced to a planar case in the plane of the remaining DOFs.

In this study only the quantities at each DOF obtained as parts of estimated mode shapes were used. These are mostly real valued, but there are cases where mode shapes exhibit significant relative phase angles, i.e. the amplitudes are complex valued. It has been verified by a parametric study that the proposed algorithm can be successively applied to complex valued quantities and that the phase angles are transformed appropriately. Nevertheless a mathematical proof is yet to be provided.

7.2.2 *Operational Modal Analysis: Stochastic Subspace Identification*

The use of stochastic subspace identification techniques is a well known method in operational modal analysis. The main algorithm and equations of the reference-based, covariance-driven stochastic subspace identification that has been used in this study, will be briefly recalled as given in [4].

By introducing the state vector

$$\mathbf{x}(t) = \left[\mathbf{y}(t)\ \dot{\mathbf{y}}(t)\right]^\mathsf{T} \tag{7.6}$$

into the general equation of motion of a multi degree of freedom, linear, time-invariant system, a state-space model can be derived. Following the discretization and replacing the unknown input terms by stochastic white noise terms $\mathbf{w_k}$ and $\mathbf{v_k}$ a discrete time stochastic state-space model is obtained

$$\begin{aligned} \mathbf{x}_{k+1} &= \mathbf{A}_d\mathbf{x}_k + \mathbf{w}_k \\ \mathbf{y}_k &= \mathbf{C}\mathbf{x}_k + \mathbf{v}_k\,, \end{aligned} \tag{7.7}$$

where $\mathbf{A}_d$ denotes the state matrix and $\mathbf{C}$ the output matrix, respectively. In the covariance-driven stochastic subspace identification such a state-space model is estimated from measured time series. The following expected values can be obtained from the state-space model

$$\begin{aligned} \mathbf{G}^{ref} = \mathrm{E}\left[\mathbf{x}_{k+1} \quad \mathbf{y}_k^{ref\,\mathsf{T}}\right], \qquad \mathbf{R}_i^{ref} &= \mathrm{E}\left[\mathbf{y}_{k+i} \quad \mathbf{y}_k^{ref\,\mathsf{T}}\right] \\ &= \mathbf{C}\mathbf{A}^{i-1}\mathbf{G}^{ref}\,. \end{aligned} \tag{7.8}$$

Here $\mathbf{G}^{ref}$ denotes the next-state output covariance matrix and $\mathbf{R}_i^{ref}$ the output-covariance matrix at time-lag i. In the case of reference-based stochastic subspace identification these matrices are computed only between the output-channels and selected reference channels. Equation 7.8 is especially important, as the covariances can be estimated directly from the recorded timeseries. Several covariance matrices at ascending time lags i are arranged into a block-Toeplitz-Matrix

$$\hat{\mathbf{T}}_{1|i}^{ref} = \begin{bmatrix} \hat{\mathbf{R}}_i^{ref} & \hat{\mathbf{R}}_{i-1}^{ref} & \dots & \hat{\mathbf{R}}_1^{ref} \\ \hat{\mathbf{R}}_{i+1}^{ref} & \hat{\mathbf{R}}_i^{ref} & \dots & \hat{\mathbf{R}}_2^{ref} \\ \vdots & \vdots & \ddots & \vdots \\ \hat{\mathbf{R}}_{2i-1}^{ref} & \hat{\mathbf{R}}_{2i-2}^{ref} & \dots & \hat{\mathbf{R}}_i^{ref} \end{bmatrix} \tag{7.9}$$

where $\hat{\circ}$ denotes "estimate". The matrix $\mathbf{T}_{1|i}^{ref}$ can also be written in terms of the state variables

$$\begin{aligned} \mathbf{T}_{1|i}^{ref} &= \begin{bmatrix} \mathbf{C} \\ \mathbf{CA} \\ \vdots \\ \mathbf{CA}^{i-1} \end{bmatrix} \begin{bmatrix} \mathbf{A}^{i-1}\mathbf{G}^{ref} & \dots & \mathbf{AG}^{ref} & \mathbf{G}^{ref} \end{bmatrix} \\ &= \mathbf{O}_i \boldsymbol{\Gamma}_i , \end{aligned} \tag{7.10}$$

$\mathbf{O}_i$ and $\boldsymbol{\Gamma}_i$ denote the observability matrix and controllability matrix, respectively. A singular value decomposition

$$\hat{\mathbf{T}}_{1|i}^{ref} = \begin{bmatrix} \mathbf{U}_1 & \mathbf{U}_2 \end{bmatrix} \begin{bmatrix} \mathbf{S}_1 & \mathbf{0} \\ \mathbf{0} & \mathbf{S}_2 \end{bmatrix} \begin{bmatrix} \mathbf{V}_1^{\mathsf{T}} \\ \mathbf{V}_2^{\mathsf{T}} \end{bmatrix} \tag{7.11}$$

and the truncation of singular values at the desired model order is employed to obtain the matrices

$$\mathbf{O}_i = \mathbf{U}_1 \mathbf{S}_1^{0.5} , \quad \text{and} \quad \boldsymbol{\Gamma}_i = \mathbf{S}_1^{0.5} \mathbf{V}_1^{\mathsf{T}} . \tag{7.12}$$

The output matrix $\mathbf{C}$ can be extracted from the first l rows of $\mathbf{O}_i$, with l being the number of analyzed channels. There exist several alternatives for the computation of the state matrix $\mathbf{A}$. One common method is given by

$$\mathbf{A} = \mathbf{O}_i^{\uparrow\dagger} \mathbf{O}_i^{\downarrow} \tag{7.13}$$

where $\circ^{\dagger}$ denotes a pseudoinverse. $\mathbf{O}_i^{\uparrow}$ and $\mathbf{O}_i^{\downarrow}$ are obtained by removing the last and the first block rows of $\mathbf{O}_i$, respectively. An eigendecomposition of the state matrix $\mathbf{A}$ leads to the eigenvalues $\boldsymbol{\Lambda} = \operatorname{diag}(\lambda_r)$ and eigenvectors $\boldsymbol{\Psi}$, which occur in complex conjugate pairs. The natural frequencies f_r and damping values ζ_r can be computed from the eigenvalues

$$\mu_r = \frac{\ln(\lambda_r)}{\Delta t}, \quad f_r = \frac{|\mu_r|}{2\pi}, \quad \zeta_r = \frac{\operatorname{Re}(\mu_r)}{|\mu_r|} . \tag{7.14}$$

Multiplying the matrix of eigenvectors with the output matrix yields the mode shape matrix

$$\boldsymbol{\Phi} = \mathbf{C}\boldsymbol{\Psi} . \tag{7.15}$$

7.2.3 Multi-setup Merging Strategies

In operational modal analysis it is frequently required to carry out measurements on multiple points of a structure in order to obtain an adequate representation of the mode shapes of a structure. Limitations regarding the number of available sensors may apply and consequently, consecutive measurements using different sensor location setups are performed. In order to recombine these afterwards, one or more common output reference sensors, which remain at the same position throughout

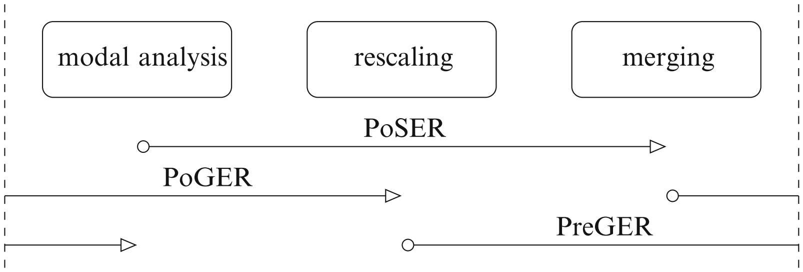

Fig. 7.2 Order of steps for the three merging strategies for SSI cov/ref

all measurements, are used. Mevel et al. [3] and Döhler et al. [1] introduce three different strategies for data merging of multi-setup measurements using reference sensor data. These approaches mainly differ in the order of the steps: modal analysis, data merging and data re-scaling (see Fig. 7.2).

The classic approach, termed PoSER (Post Separate Estimation Re-scaling), is the common practice in operational modal analysis. Each setup $j = 1 \dots n_s$ is processed individually to obtain the modal parameters f_r^j, ζ_r^j and mode shapes $\boldsymbol{\phi}_r^j$ for the one mode r. The separate, incomplete mode shapes are then combined and rescaled relative to measurement j^*

$$\boldsymbol{\phi}_s = \begin{bmatrix} \boldsymbol{\phi}_r^{ref,j*} \\ \boldsymbol{\phi}_r^{m,j*} \\ \alpha_r^{j*,1}\boldsymbol{\phi}_r^{m,1} \\ \vdots \\ \alpha_r^{j*,n_s}\boldsymbol{\phi}_r^{m,n_s} i \end{bmatrix} \quad \text{with} \quad \alpha_r^{j*,j} = \left(\boldsymbol{\phi}_r^{ref,j*\mathrm{H}}\boldsymbol{\phi}_r^{ref,j*}\right)^{-1} \boldsymbol{\phi}_r^{ref,j*\mathrm{H}}\boldsymbol{\phi}_r^{ref,j}\,, \tag{7.16}$$

where $\circ^r$ and $\circ^m$ denote reference channels and moving channels, respectively and $\circ^{\mathrm{H}}$ denotes a conjugate transpose. Especially if a large number of DOFs need to be included, this approach requires many measurements to be processed individually.

The second merging approach, termed PoGER (Post Global Estimation Re-scaling), aims at reducing the manual workload by processing all setups together. However this can only be done if the tested structure exhibits linear behavior (e.g. no frequency shifts due to temperature, loading amplitudes, etc.). The reference sensors, whose signals are used to compute the covariances are required to stay on the same location in all setups. The reference-based covariance matrices are stacked block-row-wise

$$\hat{\mathbf{R}}_i^{all} = \begin{bmatrix} \hat{\mathbf{R}}_i^1 \\ \hat{\mathbf{R}}_i^2 \\ \vdots \\ \hat{\mathbf{R}}_i^{n_s} \end{bmatrix}. \tag{7.17}$$

These total covariance matrices for different time lags i are then assembled into a block-Toeplitz-matrix, that is used for system identification and modal analysis, as described in the previous section. The resulting mode shapes $\boldsymbol{\phi}_r^j$ come out stacked in the same manner. Each setup's part has to be rescaled separately similarly to the PoSER approach, Eq. (7.16), and the reference channels are removed afterwards.

To overcome the limitations regarding the linear behavior of the tested structures, a third approach, termed PreGER (Pre Global Estimation Re-scaling), was introduced. A detailed derivation of the procedure is given in [3], here it is briefly described. In contrast to the other approaches, rescaling is now applied to the covariance matrices, before merging the setups. The scaling matrices are obtained in state-space by means of a common controllability matrix, which reflects the differences in excitation between all setups. In order to compute this matrix, the covariance-matrices of only the reference channels $\hat{\mathbf{R}}_i^{j,ref}$ are built for all setups j and stacked block-column-wise

$$\hat{\mathbf{R}}_i^{all,ref} = \left[\hat{\mathbf{R}}_i^{1,ref} \dots \hat{\mathbf{R}}_i^{n_s,ref}\right]. \tag{7.18}$$

Thus the next-state covariance matrices turn out to be stacked in the same manner and can be obtained from the factorization property

$$\mathbf{R}_i^{all,ref} = \mathbf{C}^{ref}\mathbf{A}^{i-1}\mathbf{G}^{all} \quad \text{with} \quad \mathbf{G}^{all} = \left[\mathbf{G}^1 \ldots \mathbf{G}^{n_s}\right] . \tag{7.19}$$

A common controllability matrix $\boldsymbol{\Gamma}_i^{all}$ can then be computed by means of a singular value decomposition of a block-Toeplitz matrix assembled from the stacked covariance matrices equation (7.12). Recalling the definition from Eq. (7.10) and considering Eq. (7.19), the single-setup controllability matrices $\boldsymbol{\Gamma}^j$ can be extracted from the common controllability matrix by selecting the appropriate row-columns. Fitting the single matrices with respect to the controllability matrix of a selected setup $j*$, yields the rescaling matrices $\overline{\boldsymbol{\alpha}}^{j,j*}$

$$\boldsymbol{\Gamma}^j = \boldsymbol{\Gamma}^{j*}\overline{\boldsymbol{\alpha}}^{j,j*} . \tag{7.20}$$

A Moore-Penrose pseudoinverse † can be used to provide a least-squares solution to this overdetermined linear system of equations

$$\overline{\boldsymbol{\alpha}}^{j,j*} = \boldsymbol{\Gamma}^{j^\dagger}\boldsymbol{\Gamma}^{j*} . \tag{7.21}$$

The block-Toeplitz matrices of covariance matrices built from the moving sensor data can be rescaled with the obtained scaling factors

$$\overline{\mathbf{T}}^{j,m} = \mathbf{T}^{j,m}\overline{\boldsymbol{\alpha}}^{j,j*} . \tag{7.22}$$

Block-row-wise interleaving of the rescaled block-Toeplitz matrices yields a global block-Toeplitz matrix that can be used to apply the system identification and modal analysis, as described in the previous section.

7.3 Proposed Approach

With commercially available 3D SLDV, single-point measurements with pre-estimation coordinate transformations are compulsory. That means, vibration time histories or power spectral densities are transformed at the time of recording to be available in the tested structure's Cartesian coordinates. In order to combine consecutive single-point measurements, an additional input or output reference signal is needed. In both cases this requires connecting sensors or excitation devices to the structure. These may influence the dynamic behavior, especially of lightweight structures. To circumvent this interaction an additional LDV may be used to provide a reference signal, which is costly and requires additional effort in terms of synchronized data acquisition.

The derivation of a post-estimation coordinate transformation approach in the presented study opens the possibility for multi-point measurement schemes. Hence, single-point measurements are not required anymore and the time histories can be used as measured by the single scan heads. In a multi-point measurement scheme, each laser beam is directed toward a different measuring point. In a series of consecutive measurements each measuring point is scanned by each scan head, once. Merging the modal results of all measurements yields complete mode shapes. Nevertheless, these are available in local skew coordinates where the axes are pointing toward the locations of the three scan heads. These local coordinate systems are different for each measuring point and have to be transformed into global Cartesian coordinates for visualization and comparison purposes.

Taking it one step further, this opens the possibility to use each scan head to provide a reference signal for the remaining scan heads, respectively. Figure 7.3 shows the general procedure. A multi-point measurement scheme, consisting of multiple setups is partitioned into three sets of setups. In each set, a different scan head provides the reference signals. An additional "all-reference" measurement is required, where all scan heads direct their laser beams to the respective reference positions at the same time. Subsequently, the modal data of all setups is merged in a two-step approach. In the first step the setups of each set are merged, using one of the three presented merging strategies. In the second step, the three sets are merged using the PoSER approach with aid of the "all-reference" measurement. Finally, the transformation of the mode shapes from local skew coordinates into global Cartesian coordinates is performed.

As with every other type of multi-setup measurement, the key for good results lies in the selection of appropriate reference sensor positions. The typical requirements for reference sensor positions arise from the need for a sufficient

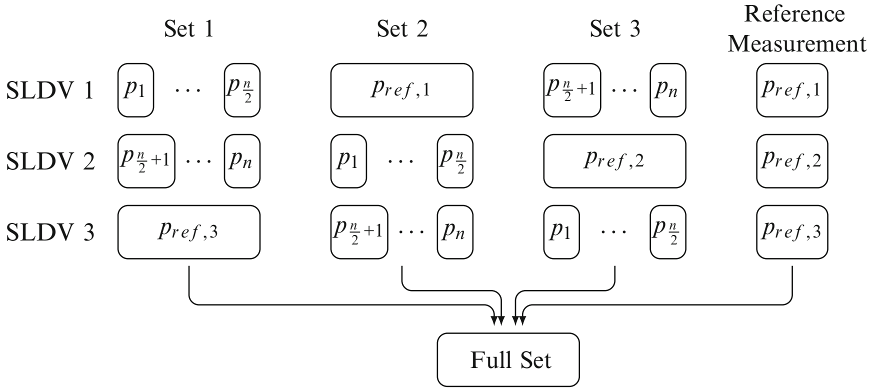
Set 1
Set 2
Set 3
Reference Measurement
SLDV 1
SLDV 2
SLDV 3
p_1 ⋯ $p_{\frac{n}{2}}$
$p_{ref,1}$
$p_{\frac{n}{2}+1}$ ⋯ p_n
$p_{ref,1}$
$p_{\frac{n}{2}+1}$ ⋯ p_n
p_1 ⋯ $p_{\frac{n}{2}}$
$p_{ref,2}$
$p_{ref,2}$
$p_{ref,3}$
$p_{\frac{n}{2}+1}$ ⋯ p_n
p_1 ⋯ $p_{\frac{n}{2}}$
$p_{ref,3}$
Full Set

Fig. 7.3 Procedure of measurement according to the proposed approach, with p_i: measuring point i; n: total number of measuring points and $p_{ref,j}$: reference point for scan head j

representation of each mode of interest in the recorded signal. Therefore, the nodal points of any mode of vibration should be avoided. Furthermore, under consideration of the expected excitation, each mode of vibration should create acceptably high amplitudes at the selected locations. A sufficient number of reference locations should be chosen to account for all spatial directions of vibrations. In the proposed approach another requirement stems from the inability of the LDV to measure vibrations perpendicular to the direction of the laser beam. Therefore the measurement directions cannot be arbitrarily chosen, as e.g. in the case of accelerometers, but are predetermined by the positions of the scan heads relative to the tested structure. In summary, each scan head needs a reference point that shows sufficient amplitudes in each mode of vibration and in the respective measurement direction. Typically a numerical model is created for a preliminary modal analysis that can be used to determine adequate reference positions for each scan head. Alternatively, a preliminary measurement can be used for this purpose.

7.4 Application

The proposed approach was applied using a commercial 3D SLDV (Polytec PSV 400-3D) that is available at the Bauhaus University in Weimar, Germany. A small-scale, tower-like, skeletal structure was chosen for the tests, as it vibrates in at least two directions and can be tested in the laboratory. Figure 7.4 shows a 3D view of the structure. The columns are made of steel threaded rods and the single platforms consist of flat steel bars that are connected to form a relatively stiff slab. Additional bracing can be attached between all levels. In this case the lowest storey was braced in y-direction to avoid the coupling of modes in the horizontal directions.

In general, when conducting SLDV measurements there has to exist a line of sight between the SLDV and the measuring point. In the case of a 3D SLDV, only the points that satisfy this requirement for all scan heads can be used for measurements. Thus it is clear, that only a part of a 3D structure can be included without changing the positions of the scan heads (or using special mirrors). To maximize the number of available measuring points the structure was positioned diagonally towards the plane of the three scan heads, such that one corner faces the SLDV at the top. Two additional accelerometers were mounted to the structure, which were used for conducting a preliminary measurement but left in place unused afterwards to avoid mass change effects. The exact positioning of the structure and the three scan heads are also illustrated in Fig. 7.4.

7.4.1 Experimental Setup

A first insight into the dynamic behavior of the structure was gained from a numerical FEM analysis. Based on these results, the positions of the three scan heads were chosen and reference accelerometers were placed on measuring point d_5 in both horizontal directions. The accelerometers were used for a preliminary reference measurement that was conducted using single-point measurements with pre-estimation coordinate transformation, in the way that is intended by the manufacturer of the 3D SLDV.

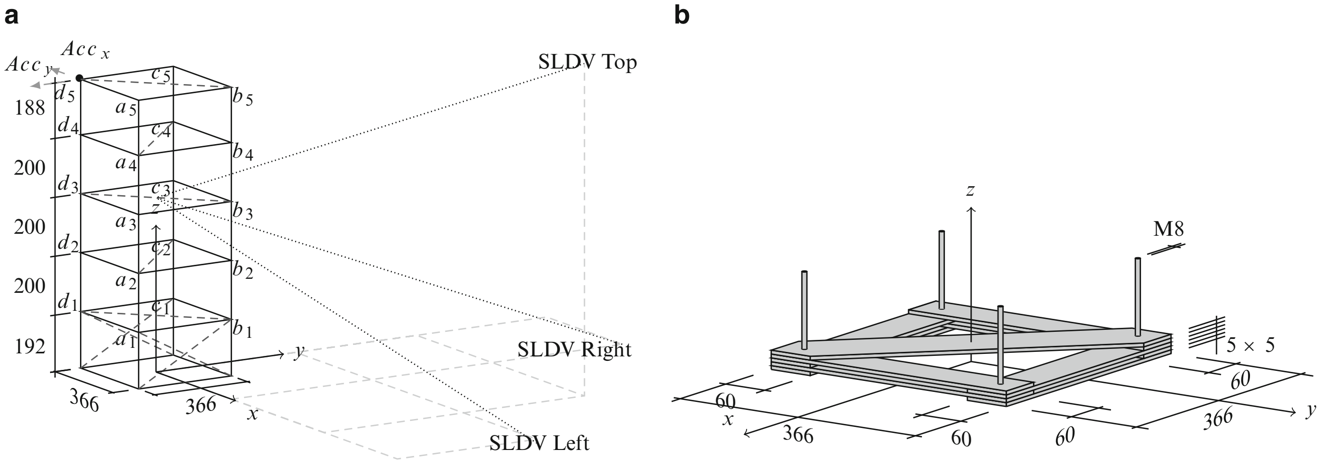

Fig. 7.4 3D view of the test structure with dimensions in mm. (**a**) Overview, labeling of points. (**b**) Detailed view of one platform of the tower

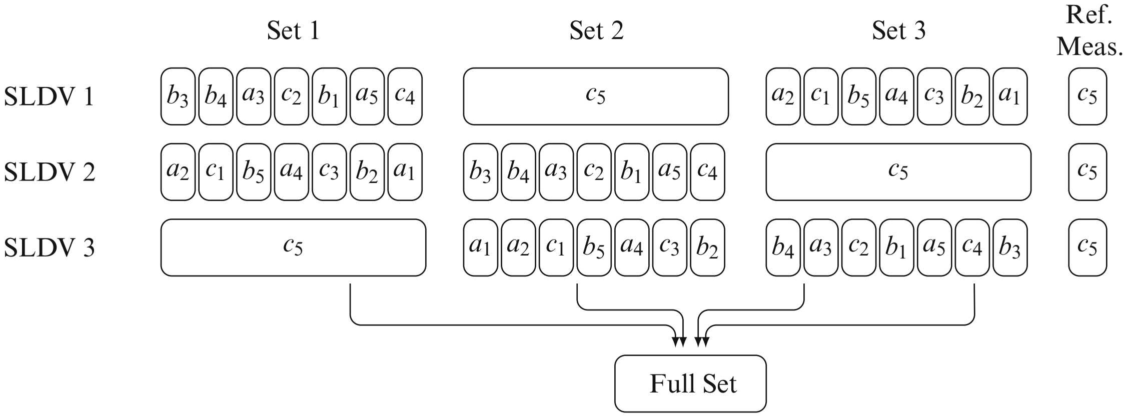

	Set 1	Set 2	Set 3	Ref. Meas.
SLDV 1	b_3 b_4 a_3 c_2 b_1 a_5 c_4	c_5	a_2 c_1 b_5 a_4 c_3 b_2 a_1	c_5
SLDV 2	a_2 c_1 b_5 a_4 c_3 b_2 a_1	b_3 b_4 a_3 c_2 b_1 a_5 c_4	c_5	c_5
SLDV 3	c_5	a_1 a_2 c_1 b_5 a_4 c_3 b_2	b_4 a_3 c_2 b_1 a_5 c_4 b_3	c_5

Fig. 7.5 All setups used in the experimental study, refer to Fig. 7.4 for labels of the measuring points

The final experimental setup for the application of the proposed approach was created based on the results of the preliminary measurement. The reference locations were chosen to be at the same point, namely point c_5, for all scan heads in order to reduce influencing factors on the final results. A sufficient representation of all modes of interest in each single setup was the objective for combining moving points into setups. The resulting 22 setups are shown in Fig. 7.5. An independent positioning of the laser beams was achieved by utilizing the macro programming capabilities of the software provided by the manufacturer.

Another aim of the experimental application was the comparison and evaluation of the performance of the three multi-setup merging strategies presented in Sect. 7.2.3. Therefore ambient excitation (i.e. non-stationary power spectrum) was required and achieved through the use of two moving ventilators, exciting the structure aerodynamically.

The vibration velocities were recorded at a sampling frequency of 512 Hz for a duration of 256 s. However prior to the analysis the data was decimated by a factor of 2. The analysis was performed with an own implementation of the SSI cov/ref algorithm, with parameters $i = 200$ (number of block rows) and $n_{max} = 200$ (maximum model order). After the manual selection of stable poles for each mode of interest, the setups were merged following the PoSER strategy. In the case of 22 setups this is a time consuming process. To evaluate the performance and accuracy of the other two merging strategies, those were applied as well. In that case all setups belonging to one set were merged following the PoGER and PreGER approach, respectively, and subsequently the three sets were merged using the PoSER algorithm. Finally, the coordinates of the mode shapes were transformed to Cartesian coordinates. That allowed not only for the visualization, but also for the comparison with the mode shapes obtained from the preliminary measurement.

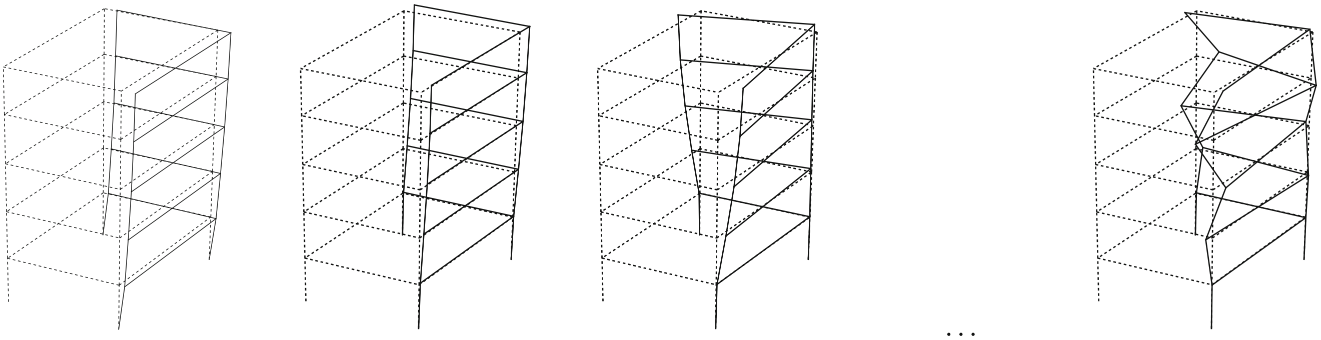

bending x_1; $f = 2.20\,\text{Hz}$

bending y_1; $f = 2.95\,\text{Hz}$

torsion t_1; $f = 4.28\,\text{Hz}$

. . .

Torsion t_4; $f = 25.53\,\text{Hz}$

Fig. 7.6 Examples of experimentally identified mode shapes of the test structure

Table 7.1 All 14 experimentally identified natural frequencies and damping coefficients of the test structure

1: bending x_1	2: bending y_1	3: torsion t_1	4: bending x_2[a]	5: bending x_2	6: bending y_2	7: torsion t_2
$f = 2.20\,\text{Hz}$	$f = 2.95\,\text{Hz}$	$f = 4.28\,\text{Hz}$	$f = 6.95\,\text{Hz}$	$f = 9.00\,\text{Hz}$	$f = 11.62\,\text{Hz}$	$f = 13.78\,\text{Hz}$
$\zeta = 1.3\,\%$	$\zeta = 1.8\,\%$	$\zeta = 0.4\,\%$	$\zeta = 6.6\,\%$	$\zeta = 1.7\,\%$	$\zeta = 1.3\,\%$	$\zeta = 1.5\,\%$

8: bending x_3	9: bending y_3	10: bending x_4	11: torsion t_3	12: longitud. z_1[b]	13: diagonal d_1[c]	14: torsion t_4
$f = 14.15\,\text{Hz}$	$f = 17.59\,\text{Hz}$	$f = 18.79\,\text{Hz}$	$f = 20.94\,\text{Hz}$	$f = 22.09\,\text{Hz}$	$f = 22.23\,\text{Hz}$	$f = 25.53\,\text{Hz}$
$\zeta = 0.4\,\%$	$\zeta = 0.7\,\%$	$\zeta = 0.3\,\%$	$\zeta = 0.2\,\%$	$\zeta = 0.7\,\%$	$\zeta = 0.5\,\%$	$\zeta = 0.1\,\%$

[a] Mode 4 could only be completely identified using the PoGER merging approach
[b] Mode 12 could not be identified in all setups and is therefore incomplete
[c] Mode 13 could only be completely identified using the PoGER merging approach

7.4.2 Discussion of Results

As a result of the modal analysis, 14 modes of vibration were identified with varying quality. Figure 7.6 shows examples of the mode shapes, as identified in the reference measurement. The modal parameters resulting from the measurements following the proposed approach are summarized in Table 7.1.

However, not every merging strategy led to the identification of all modes of interest. Additionally, the modal parameters showed varying deviations with respect to the reference measurement. Figure 7.7a shows the frequency deviations for each mode of interest and separately for all merging strategies. In a similar manner the absolute damping values are shown in Fig. 7.7b. Here the results obtained from the reference measurement are marked by a dashed horizontal line for comparison. Finally, the modal assurance criterion (MAC) [2, p. 424] of the identified mode shapes was calculated with respect to the mode shapes obtained from the reference measurement, which is shown in Fig. 7.7c.

Especially the modes 4, 12 and 13 could not be identified or show high deviations in the respective parameters. A good agreement was reached for most of the bending modes in x-direction (1, 5, 8,10) as well as the torsional modes (3, 7, 11, 14). But a general pattern regarding the identifiability could not be found. Nevertheless, the mode shapes show significant differences, especially if the PreGER merging approach was used. Here the separate identification and subsequent merging (PoSER) leads to the best results, while the PoGER approach is still feasible.

There are several reasons, explaining those differences. First of all, it has to be mentioned that the reference measurement and the measurement following the proposed approach were performed under marginally different boundary conditions. There was an error in the data acquisition during the first run of the second measurement which was not noted until the structure was already moved from its original location and changed structurally. Thus, after restoration, it became apparent that the dynamic behavior of the structure had slightly changed.

Secondly, the merging of several setups is highly dependent on the quality of the reference signals. As a result any inaccuracies in the combined mode shapes lead to major errors during the following 3D transformation. In this case the reference points were chosen to be at the same location for all scan heads. This choice was based upon engineering judgment, but choosing different reference points for each scan head might have resulted in better quality reference signals.

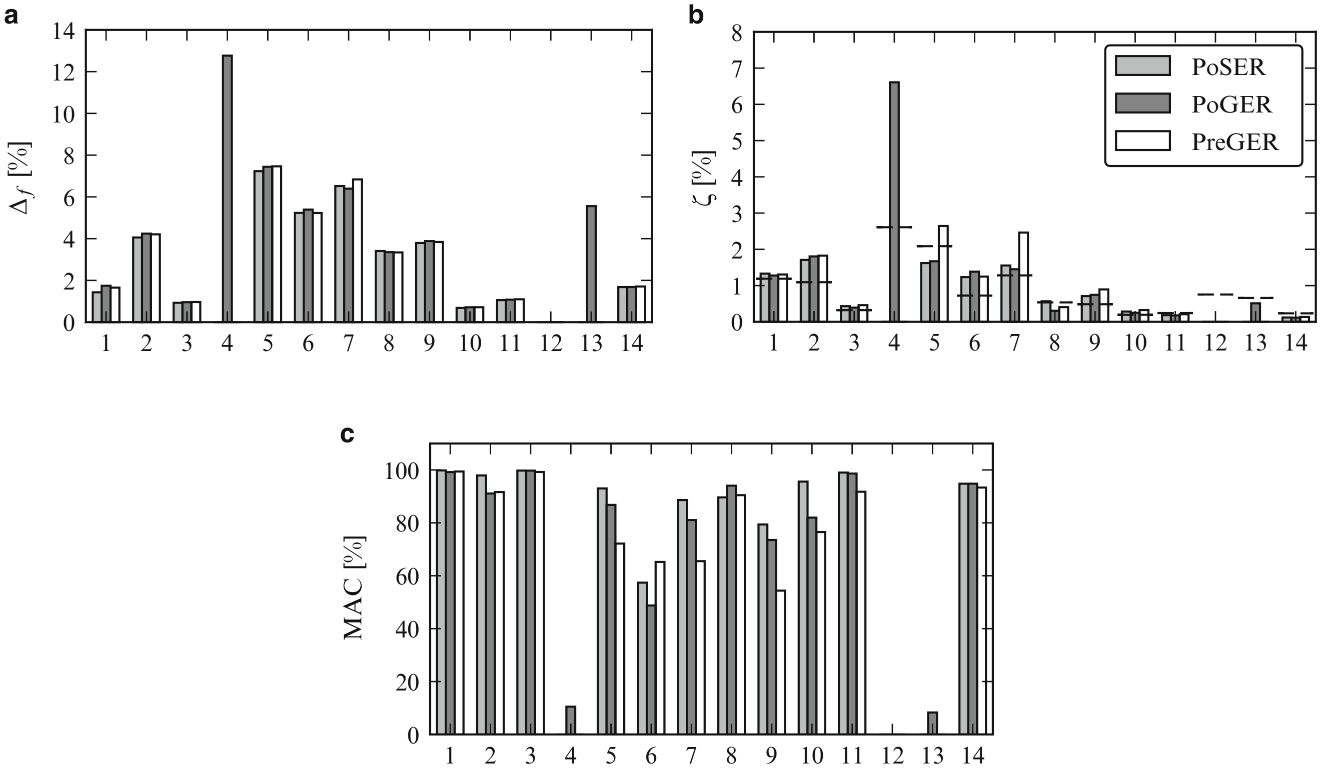

Fig. 7.7 Manually selected modal parameters for 14 modes of vibration that were chosen. No bar indicates that the respective mode could not be identified. The comparison of the three merging strategies is based on the same experimental data. (**a**) Frequency differences in percent relative to the reference measurement. (**b**) Absolute damping values. Reference measurement is marked by a *dashed horizontal line*. (**c**) Modal Assurance Criterion of identified modeshapes with respect to the reference measurement

In order to improve the results, several measures are conceivable. The placement of the scan heads relative to the structure could be optimized based on a preliminary experimental and/or numerical modal analysis. Additionally the aerodynamic excitation might not be the best choice to obtain a proper modal analysis. Therefore, different types of excitation could be chosen. As mentioned already the selection of suitable reference points for each scan head could also be based on preliminary and/or numerical studies to further improve the quality of the reference signals. And finally, there was no evaluation of adequacy of the chosen parameters for the data acquisition, the data processing, the stochastic subspace identification algorithm and the selection of stable poles.

7.5 Conclusion

In the presented study, it was shown, that it is possible to conduct 3D SLDV measurements without any additional input or output reference signal. A post-estimation 3D coordinate transformation algorithm was developed and applied to experimental data. Three different merging strategies were evaluated in terms of their applicability and accuracy in the context of the reference-based, covariance-driven stochastic subspace identification method.

In this study, the classical PoSER approach led to the best results, while the PreGER approach was not satisfying. The PoGER merging approach was found to be a good compromise between accuracy of results and time expenditure. The proposed 3D coordinate transformation algorithm was shown to be applicable, but prone to errors. In particular any inaccuracy that occurred during merging led to large errors after the 3D coordinate transformation. However, these deficiencies seem to be mainly related to the selection of suitable reference points.

For further research it is recommended to evaluate the proposed approach using a different test structure and/or different modal analysis methods. Additionally, it should be generally possible to use two and more single SLDV to imitate commercial 3D SLDV. However, synchronized demodulation of the doppler signal and data acquisition must be tackled.

References

1. Döhler, M., Reynders, E., Magalhaes, F., Mevel, L., Roeck, G.D., Cunha, A.: Pre-and post-identification merging for multi-setup OMA with covariance-driven ssi. In: 28th International Modal Analysis Conference. Springer, New York (2010)
2. Ewins, D.J.: Modal Testing: Theory, Practice, and Application. Mechanical Engineering Research Studies. Research Studies Press, Philadelphia (2000)
3. Mevel, L., Basseville, M., Benveniste, A., Goursat, M.: Merging sensor data from multiple measurement set-ups for non-stationary subspace-based modal analysis. J. Sound Vib. **249**(4), 719–741 (2002)
4. Peeters, B., de Roeck, G.: Reference-based stochastic-subspace identification for output-only modal analysis. Mech. Syst. Signal Process. **13**, 855–878 (1999)
5. Rainieri, C., Fabbrocino, G.: Operational Modal Analysis of Civil Engineering Structures - An Introduction and Guide for Applications. Springer, Berlin/Heidelberg (2014)

Chapter 8
Scanning LDV Measurement Technology for Vibration Fatigue Testing

Fabrizio Magi, Dario Di Maio, and Ibrahim Sever

Abstract Vibration fatigue testing is a verification method for structural components. It is rapid and cost efficient, and it is often performed for aero-engine components because it replicates closely stresses under normal operation conditions. This testing methodology is well known for metallic components but it can also be applied to composites for studying failure caused by high cycle fatigue. Resonant frequency decay is usually the main parameter used to assess fatigue behaviour of metallic components at a given excitation level. However for composites this alone is not very useful and several measurement parameters need to be monitored in order to understand the behaviour and develop a set of failure criteria. Scanning LDV is an excellent measurement system which enables a variety of options thanks to its non-contact nature. This manuscript will show how this system can be used for monitoring several parameters during vibration fatigue testing. A custom made control panel called MONTEVERDI and the independent use of the scanning mirrors allow the SLDV to perform several tasks: (1) Phase Lock Loop (PLL) to excite the component always at resonance, (2) measuring of Operational Deflection Shape (ODS) using either step or continuous scanning method, (3) custom calibrated strain measurement and (4) phase portrait for nonlinear vibration analysis. This paper will present the great potential of using SLDV for performing time consuming vibration fatigue testing via an automated control panel.

Keywords Scanning laser Doppler velocimeter • Automated testing • Vibration fatigue • Operative deflection shape

8.1 Introduction

Vibration fatigue is a testing technique that allows a rapid and cost-efficient evaluation of the fatigue life of a component. It consists of exciting a structure by an excitation force at any resonance frequency, causing the structure to respond according to its dynamic characteristics. This method closely replicates the operational conditions of components undergoing vibratory stresses, allowing high excitation levels with relatively low input power.

Vibration fatigue testing is well standardized for metals. It was developed during the 1950s [1–3] by Lazan et al. and it consisted in exciting a specimen around its resonant frequency by rotating an eccentric mass. The vibration amplitude was fed back to the controller thanks to an accelerometer mounted on the top of the specimen grip. In spite the reliability of accelerometers, sometimes there is a need of non-contact sensor for measuring vibration amplitude without interfering with the system response. Non-contact control systems rely on either video extensometer sensors or laser triangulation sensors [4], with the drawback of being dedicated to measure the vibration of a single point.

This manuscript shows how to carry out an automated fatigue test to characterise the fatigue behaviour of composite components using a Scanning Laser Doppler Velocimeter (SLDV) system. The SLDV system is used (1) for performing both an amplitude and a phase lock loop control, (2) for calibrating the displacement with the relative strain and (3) for measuring important dynamic parameters such as nonlinearities in the vibration and ODS.

F. Magi
Advanced Composite Centre for Innovation and Science (ACCIS), University of Bristol, University Walk, BS8 1TR Bristol, UK
e-mail: fabrizio.magi@bristol.ac.uk

D. Di Maio (✉)
Department of Mechanical Engineering, University of Bristol, University Walk, BS8 1TR Bristol, UK
e-mail: dario.dimaio@bristol.ac.uk

I. Sever
Rolls-Royce plc, Derby DE24 8BJ, UK

© The Society for Experimental Mechanics, Inc. 2016

J. De Clerck, D.S. Epp (eds.), *Rotating Machinery, Hybrid Test Methods, Vibro-Acoustics & Laser Vibrometry, Volume 8*,
Conference Proceedings of the Society for Experimental Mechanics Series, DOI 10.1007/978-3-319-30084-9_8

8.2 Material and Methods

The test setup used here consists of a component which is excited at its first bending mode, clamped within the two rods of a steel fixture, and attached to the head of a shaker (see Fig. 8.1). As shown in Fig. 8.2, the component is a rectangular specimen, 100 mm wide and 260 mm long, with an added weight at 50 mm away from one edge, clamped at 110 mm and with ply drops in the centreline, at 130 mm. By adding the ply-drop, the component is forced to break in a desired location, along a line, away from the clamp.

MONTEVERDI software, coded in LabVIEW, was specifically designed to automate the fatigue tests and used for this research work. The flowchart in Fig. 8.3 shows the entire test procedure, from the modal test to the endurance test. The software is made to perform a series of operations including Frequency Response Function (FRF), Stepped Sine Test (SST), calibration of strain-amplitude relationship, thermal imagining and endurance test. One accelerometer, attached at the fixture, was chosen for referencing the FRF and for the Phase Lock Loop (PLL) control during the fatigue test.

The steps reported in Fig. 8.3 are required to study the dynamic behaviour of the system before, during and after the fatigue test. First of all the response of the structure is measured so as to identify the response target mode. After the first bending mode is identified, the stepped sine test is carried out at different vibration levels. In addition the strain–displacement calibration is made. This practice is adopted because the extreme dynamic environment, which either (1) forces the strain gauges to peel off from the specimen and/or (2) fatigues the cable after few thousands cycles. To overcome such an issue, the strain and the LDV output signal are synchronously measured, as shown in Fig. 8.4a. The measured data are then correlated

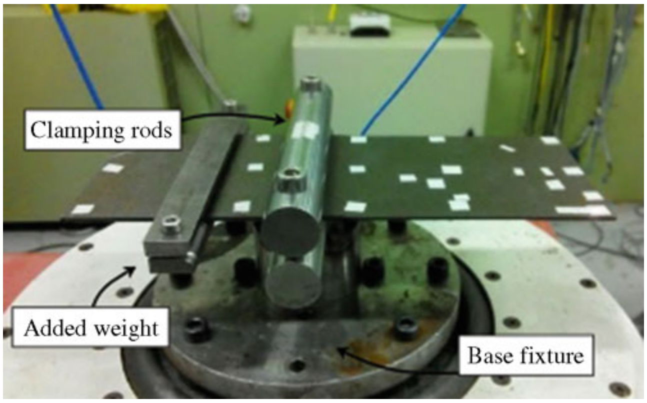

Fig. 8.1 Fixture set-up

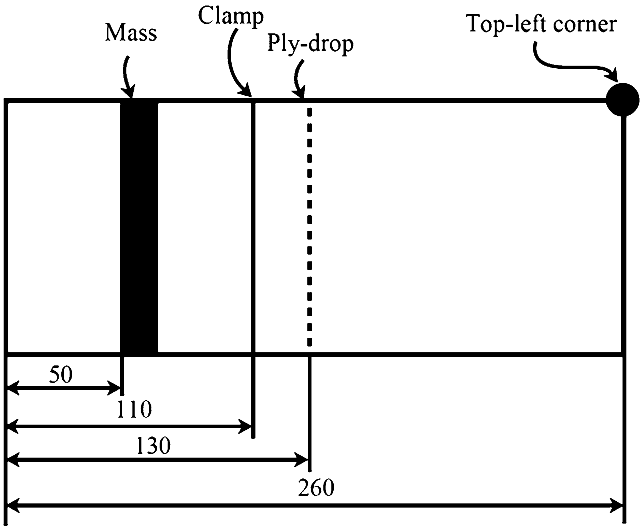

Fig. 8.2 Specimen dimensions

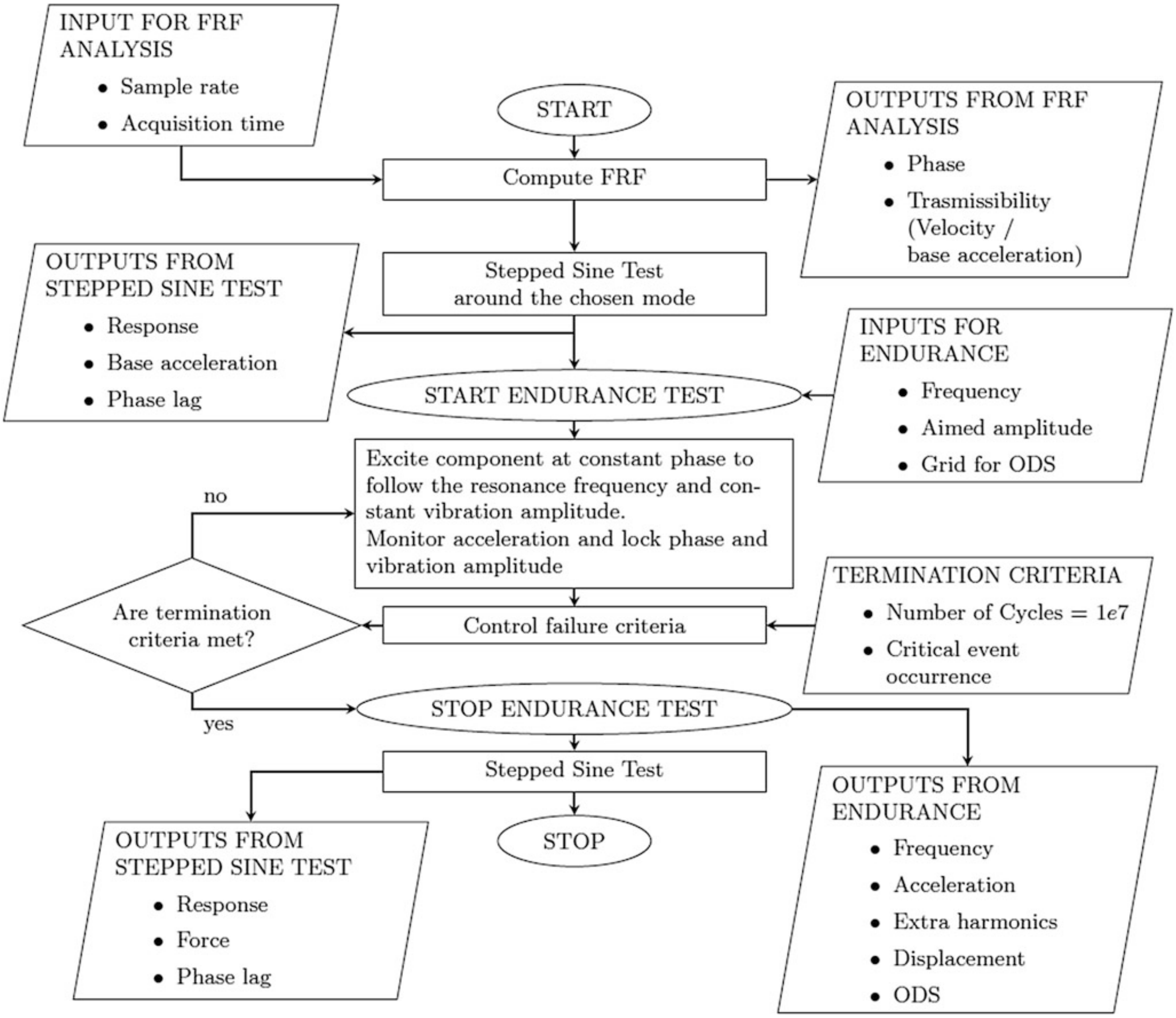
INPUT FOR FRF ANALYSIS
Sample rate
Acquisition time
START
Compute FRF
OUTPUTS FROM FRF ANALYSIS
Phase
Trasmissibility (Velocity / base acceleration)
OUTPUTS FROM STEPPED SINE TEST
Response
Base acceleration
Phase lag
Stepped Sine Test around the chosen mode
INPUTS FOR ENDURANCE
Frequency
Aimed amplitude
Grid for ODS
START ENDURANCE TEST
Excite component at constant phase to follow the resonance frequency and constant vibration amplitude. Monitor acceleration and lock phase and vibration amplitude
no
Are termination criteria met?
Control failure criteria
TERMINATION CRITERIA
Number of Cycles = 1e7
Critical event occurrence
yes
STOP ENDURANCE TEST
Stepped Sine Test
STOP
OUTPUTS FROM STEPPED SINE TEST
Response
Force
Phase lag
OUTPUTS FROM ENDURANCE
Frequency
Acceleration
Extra harmonics
Displacement
ODS

Fig. 8.3 Process flowchart

and a linear calibration curve is obtained as in Fig. 8.4b. As long as the mode shape does not change and the resonance frequency does not change, it is fair to consider the strain amplitude relationship constant throughout the test.

After the stepped sine test, the software saves the strain–displacement relationship to use during the fatigue test. The measured point of the laser is stored and the software requires a grid of points for a discrete scanning and/or the measurement parameters for executing CLSDV measurement technique; this latter requires both the scan rates and amplitudes of the sinusoidal voltages for the X-Y scanning mirrors. The measured area is controlled to be within the measurable range of the LDV.

Referring to Fig. 8.5, when the fatigue test starts, the vibration phase and amplitude are constantly fed back to the software control. The PLL control locks the phase between the input and the output by changing the excitation frequency. As soon as the output phase exceeds an upper and lower threshold spaced apart the target phase, the controller is activated. The amplitude control is based on the same principle. In addition, while the test is running, nonlinear vibrations are monitored. Controls stop working at regular interval in order to allow the ODS measurement, which would capture any changes in ODSs by delamination propagation. When failure criterion is met or 10 million cycles are reached, the fatigue test stops and modal analysis is carried out.

Several specimens were tested with this procedure but only few test data are reported in here. Thanks to the LDV system it was possible to study the evolution of four recordings:

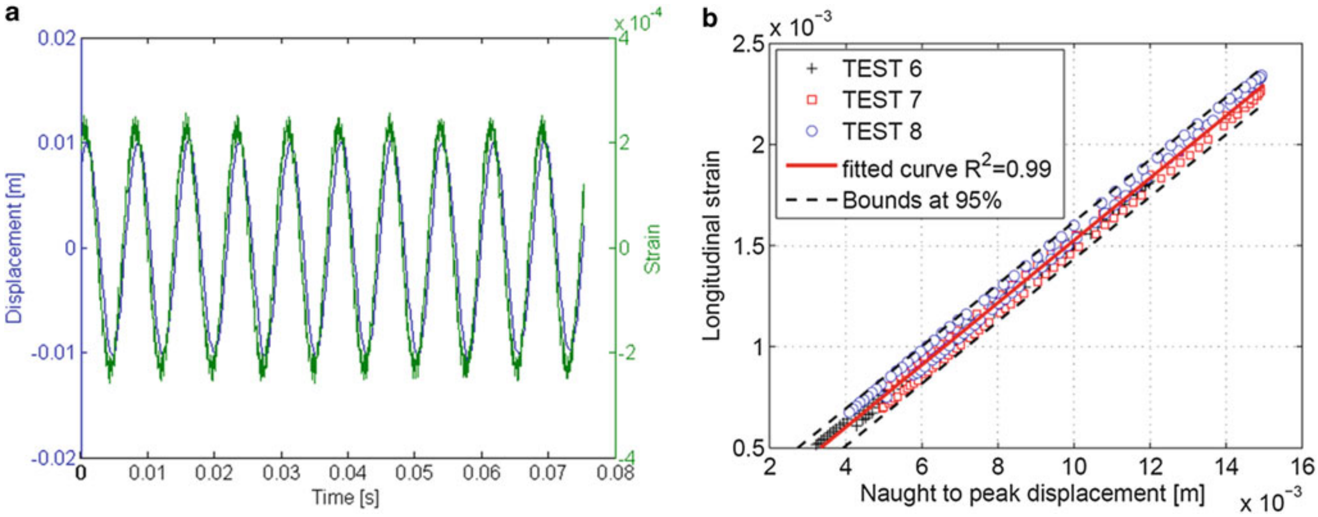

Fig. 8.4 (**a**) Displacement (*blue*) and strain (*green*) time signals at one vibration amplitude used for the strain–displacement calibration. (**b**) The linear strain–displacement relationship at different vibration levels

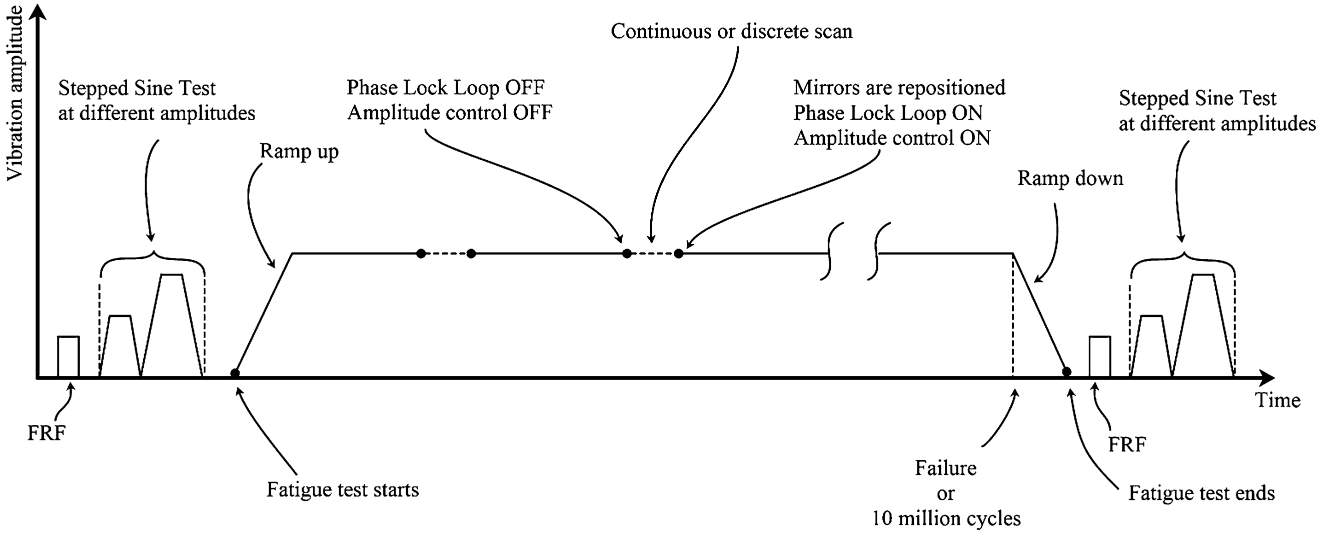
Vibration amplitude
Stepped Sine Test
at different amplitudes
Ramp up
Phase Lock Loop OFF
Amplitude control OFF
Continuous or discrete scan
Mirrors are repositioned
Phase Lock Loop ON
Amplitude control ON
Ramp down
Stepped Sine Test
at different amplitudes
Time
FRF
Fatigue test starts
Failure
or
10 million cycles
FRF
Fatigue test ends

Fig. 8.5 Time sequence of the software operations

- Resonant frequency decay
- Changes in ODS during the endurance
- Presence of extra harmonics in the response vibration
- Changes in vibration amplitude response before and after the endurance.

8.3 Results

The damage evolution in fatigue tests can be monitored by measuring the residual stiffness of the component. In a dynamic environment that means to monitor the resonant frequency decay (Fig. 8.6). Further, by capturing the surface temperature of the component, one can correlate the drops in frequency with the delamination initiation and propagation. From Fig. 8.7 one can observe how the temperature could help to identify the damage onset temporally (maximum temperature evolution over number of cycles) and spatially (thermal images).

Test 2 was carried out at low vibration amplitude, its natural frequency never changed. It ran for 10 million cycles without developing damage. This test is considered as benchmark reference for comparisons with failed specimens. The outcomes

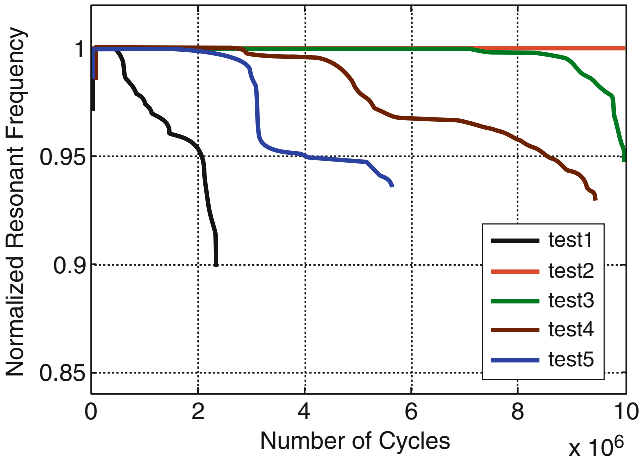

Fig. 8.6 Compared frequency decays

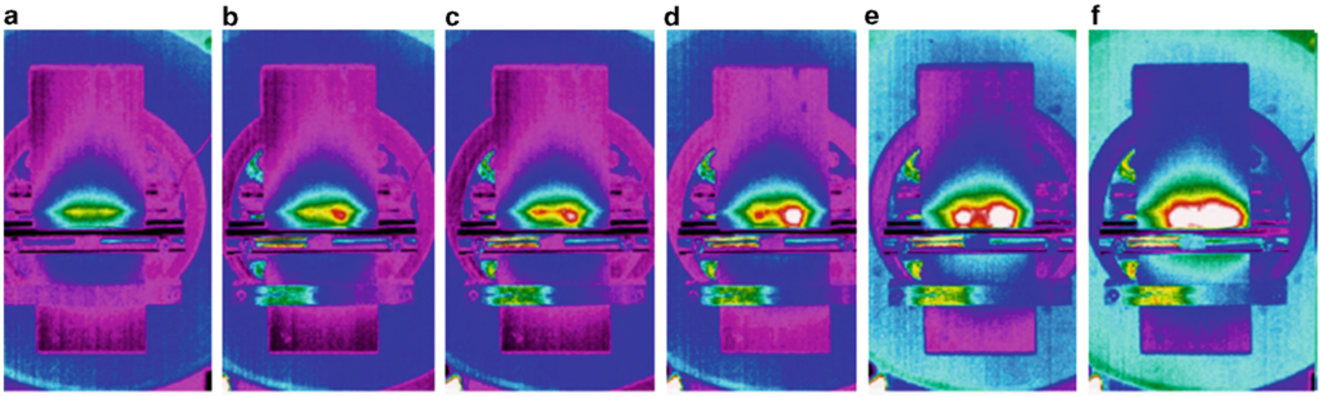

Fig. 8.7 Compared temperature profiles for Test 3. (**a**) 4, (**b**) 7.6, (**c**) 8, (**d**) 9, (**e**) 9.5, (**f**) 10 million of cycles

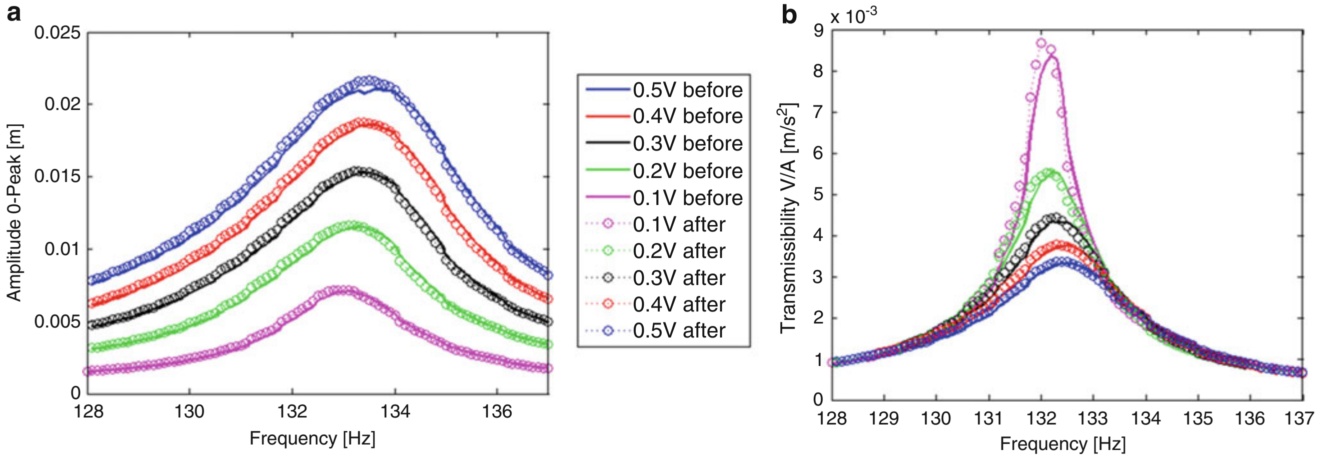

Fig. 8.8 Response (**a**) and transmissibility (**b**) of Test 2 before and after fatigue

from the stepped sine test performed before and after fatigue match, since no damage was occurred. The response and the magnitude of the transmissibility are reported in Fig. 8.8. Instead, the other test data present much clearer signs of structural degradation. Referring to Test 3, the resonance frequency dropped by 6 % as shown in Fig. 8.9. In addition the nonlinearity got enhanced due to buckling delamination and fretting between delaminated plies.

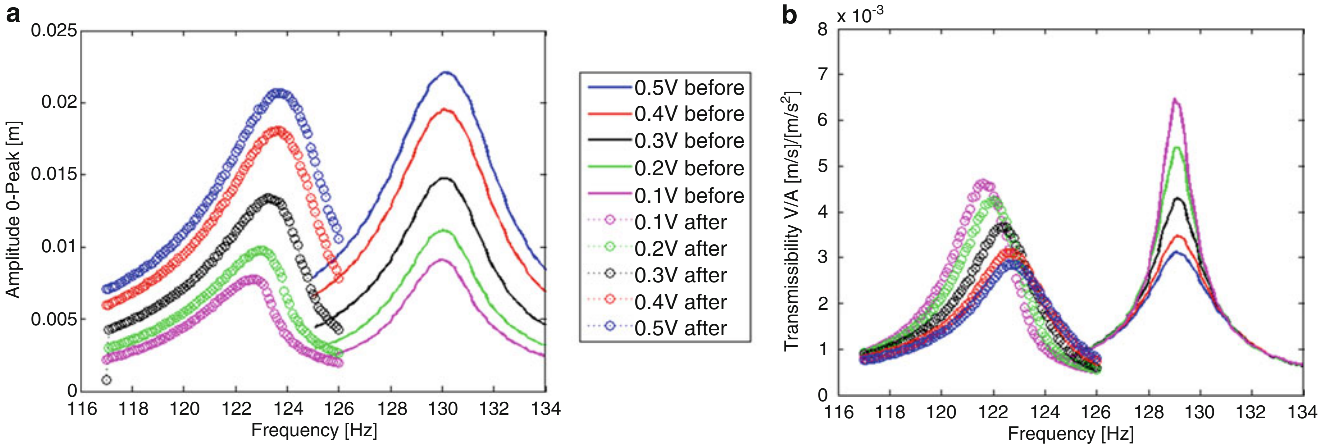

Fig. 8.9 Response (**a**) and transmissibility (**b**) of Test 3 before and after fatigue

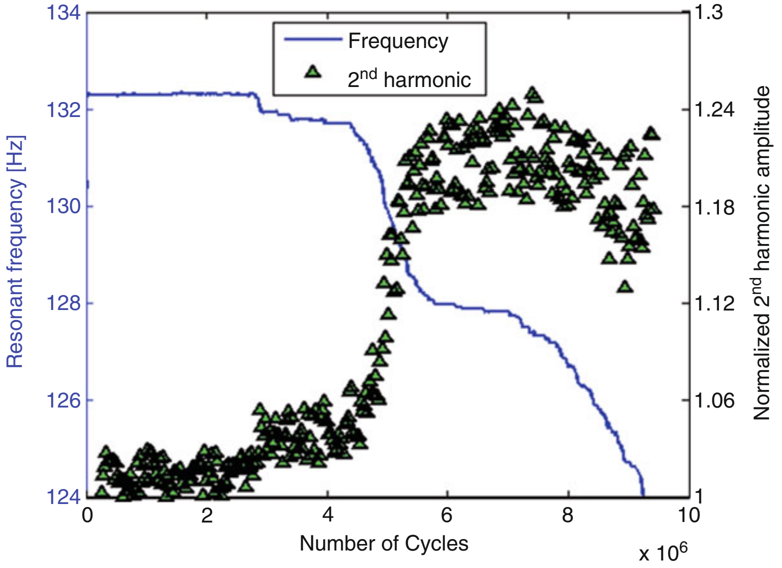

Fig. 8.10 Increase of the second harmonic of the vibration velocity

The modal analysis carried out before and after the endurance proved to be useful for understanding the structural modification that the specimen has undergone. Nevertheless, it does not provide any information about the temporal evolution of the damage and the appearance of nonlinearities.

Measuring the ODSs and controlling the presence of higher harmonics in the response vibration while fatigue testing helps to identify in time the damage evolution. By using the LDV while the PLL and the amplitude control are active, it is possible to gather rapid information about the level of nonlinearity. For the reference test, the presence of higher harmonics was not captured during the 10 million cycles. However, referring to Fig. 8.10 as soon as the first damage occurs, the vibration becomes highly nonlinear, with a second harmonic that increases by 4 % after the first drop in frequency at 3 million cycles. After that, as a consequence of delamination propagation, the second harmonic reaches a value 20 % higher than its initial value.

In addition to the nonlinear behaviour, delaminations cause changes in the ODSs. The SLDV scanning performed at regular intervals captured changes of the deflection shape due to developing damages. Referring to Fig. 8.11, it is possible to see how the onset of the delamination in the right side of the specimen causes a torsional movement, changing the target strain field. Thanks to this observation, it was possible to understand that referring the fatigue test to a constant strain after the delamination initiation is misleading.

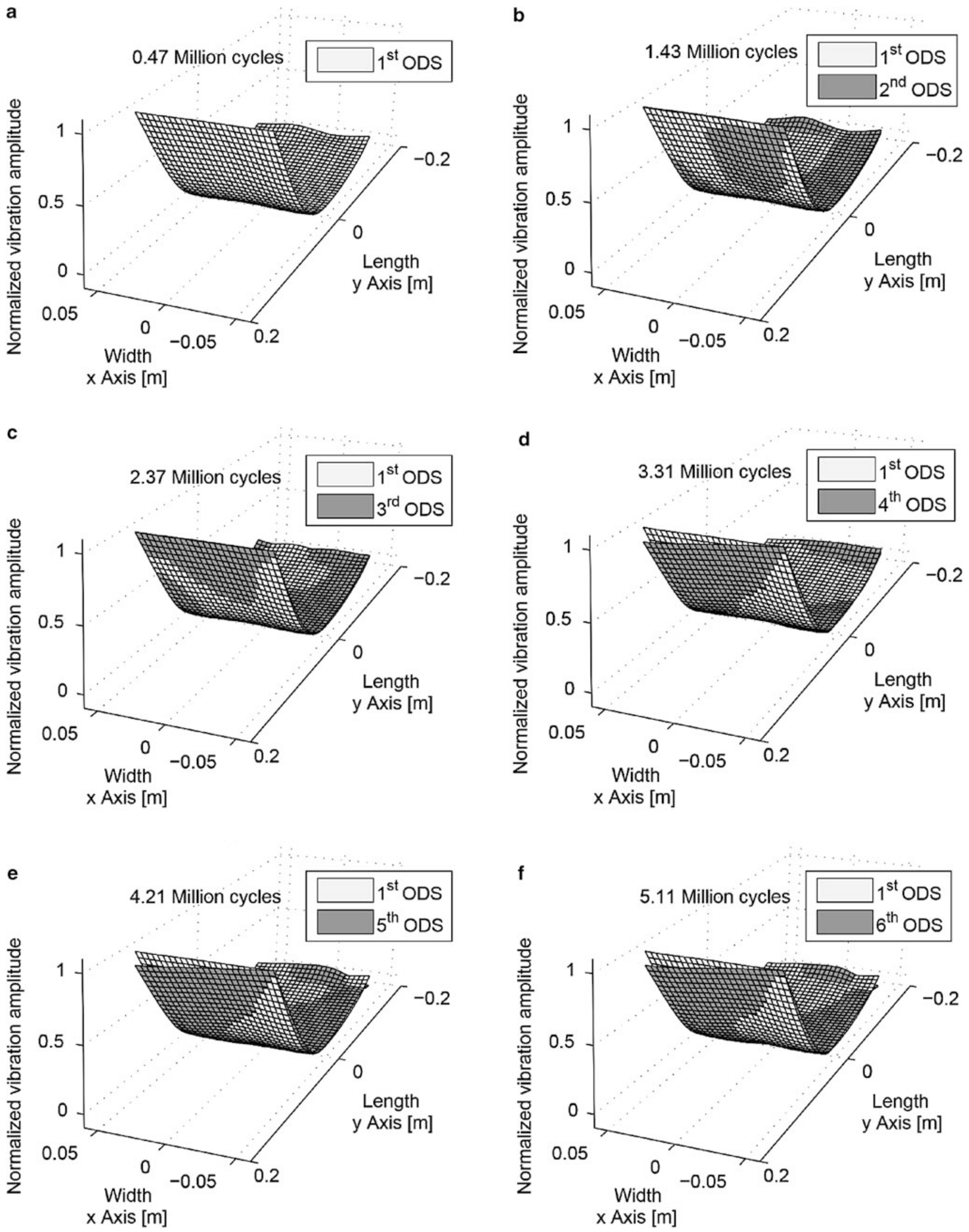

Fig. 8.11 Time sequence of ODSs for Test 3

8.4 Conclusions

This paper has presented a testing strategy based on SLDV technology for monitoring the fatigue behaviour of composites components under vibratory tests. It is important to say that these tests are executed at large vibration amplitudes, sometimes in the order of 80 mm peak to peak. Due to such amplitudes, the SLDV seemed the only measurement technology capable of tackling these levels and, thanks to its contactless feature; SLDV has enabled several different measurement techniques. MONTEVERDI software was designed around such a technology with the intent of fully automating lengthy vibration fatigue tests.

Some of the tests results obtained during an ongoing research programme are presented and discussed in the paper. The composite fatigue behaviour is complex and several parameters are required for understanding the evolution of damage. In this paper, the temperature was shown to be a useful indicator for identifying the damage initiation. Tracing of resonant frequency alongside the acquisition of deflection shapes helps to understand how the damage tends to propagate. Similar signs are given by the mapping of additional nonlinear spectral harmonics, which are caused by the increasing level of damage, from the LDV output signal. Additional information regarding the failure criteria for composites from vibratory conditions are discussed in more details in dedicated composites journals.

Acknowledgements The authors would like to acknowledge the support of Rolls-Royce plc for the support of this research through the Composites University Technology Centre (UTC) at the University of Bristol, UK.

References

1. Lazan, B., Gannett, A., Kirmser, P., Klumpp, J., Brown, J.: Dynamic testing of materials and structures with a new resonance-vibration exciter and controller. Ohio (1952)
2. Lazan, B.: Fatigue Failure Under Resonant Vibration Conditions (1954)
3. Wozney, G.: Resonant-vibration fatigue testing. Exp. Mech. **2**(1), 1–8 (1962)
4. Bertini, L., Santus, C., Boulet, J., Leclerc, P., Desmazures, C.: Resonant bench for fatigue testing of steel drill pipe connections. In: AIAS 41° CONVEGNO NAZIONALE, pp. 5–8 (2012)

Chapter 9
Optically Detecting Wavefronts and Wave Speeds in Water Using Refracto-Vibrometry

Matthew T. Huber, Brent K. Hoffmeister, and Thomas M. Huber

Abstract Refracto-vibrometry is a technique that uses a laser Doppler vibrometer to measure acoustic pressure fields. The vibrometer laser is directed through a medium towards a stationary retroreflective surface. Acoustic waves (density variations) for which the wavefronts pass through the laser, as the beam travels from the vibrometer to the retroreflector and back, cause variations in the integrated optical path length. This results in a time-varying modulation of the laser signal returning to the vibrometer, enabling optical detection of the acoustic wavefronts. In the current experiment, a Polytec PSV-400 scanning laser Doppler vibrometer, sampled at 100 MHz, monitored the waves emitted by a 1 MHz Panametrics V303 ultrasound transducer immersed in a water tank. The time-varying signal detected by the vibrometer at numerous scan points was used to generate videos of the time evolution of acoustic wavefronts; these videos will be presented. Refracto-vibrometry was also used for optical measurements of the time of flight of ultrasonic waves through different materials, including samples of lead and fabricated bone. This enabled determination of wave propagation speeds. The wave speeds obtained with optical detection using refracto-vibrometry were in agreement with measurements using a conventional ultrasonic transducer to detect the wavefronts.

Keywords Acoustics • Vibrometry • Ultrasound • Refracto-vibrometry • Wave propagation

9.1 Introduction

Ultrasound is used in a wide variety of applications ranging from the medical field to structural testing and dynamics. However, one of the challenges associated with the use of ultrasound is that there are limited non-invasive options available for observing traveling wavefronts and visualizing how they react to their surroundings. This means that systems often must be physically altered in order for one to have an understanding of what is going on in them. Refracto-vibrometry, [1–5] which involves using a laser Doppler vibrometer to optically sample the acoustic field, provides an alternative to the conventional ultrasound measurement methods traditionally performed by transducers.

Much of the research performed with ultrasound takes place underwater because water functions as a coupling medium between the transducer and the object being analyzed. This means the amount of signal attenuated by the water is usually not significant. Ultrasonic transducers, for emission and detection of ultrasonic waves in water, are generally constructed using piezo-electric detectors. When acoustic waves strike the detector, an electrical signal is generated. Alternately, for measurements of acoustic regions with a resolution on the order of 1 mm, needle hydrophones are often used. To characterize sound fields with hydrophones, it is necessary to raster the position of the hydrophone to multiple locations and observe the acoustic field at each point.

Refracto-vibrometry provides an alternative to the conventional methods of characterizing sound fields and analyzing ultrasound signals. The instrument utilized for this technique is a laser Doppler vibrometer [6]. A vibrometer is designed to measure the Doppler shift of a laser after it is reflected from a vibrating surface. However, in the Refracto-vibrometry method used for the current study, the vibrometer is directed at a motionless retroreflective surface and is used to detect the wavefront of the ultrasound pulse [2]. The acoustic waves are fluctuations of the density of the medium, in the current case, water. Because the index of refraction of water is related to its density, acoustical wave density variations also result in a variation of index of refraction. If an acoustic wave passes through the laser from the vibrometer, the index of refraction

M.T. Huber • B.K. Hoffmeister
Department of Physics, Rhodes College, 2000 North Parkway, Memphis, TN 38112, USA

T.M. Huber (✉)
Department of Physics, Gustavus Adolphus College, 800 College Avenue, Saint Peter, MN 56082, USA
e-mail: huber@gac.edu

© The Society for Experimental Mechanics, Inc. 2016

J. De Clerck, D.S. Epp (eds.), *Rotating Machinery, Hybrid Test Methods, Vibro-Acoustics & Laser Vibrometry, Volume 8*,
Conference Proceedings of the Society for Experimental Mechanics Series, DOI 10.1007/978-3-319-30084-9_9

variations cause a change in optical path length along the laser's path [5]. The time varying modulation of the laser is detected by the vibrometer, just as it would Doppler shift on the light reflected from a vibrating surface. The vibrometer is thus able to interpret the modulating laser to detect passage of acoustic waves. By repeatedly emitting pulses from a transducer and measuring the time of arrival at acoustic waves at a large number of laser scan points, the vibrometer software can reconstruct an image of a traveling wavefront.

Schlieren photography is a comparable non-invasive technique that can be used for sound field characterization [7]. Schlieren systems, like refracto-vibrometry setups, observe density variations in fluids. In Schlieren systems the density variations create enough of a disturbance in the fluid that sound can be directly imaged using a camera if the fluid is properly illuminated. To produce images of traveling wavefronts, a Schlieren system will sequentially record video frames with successively longer delays between the emission of an ultrasound pulse and a short-duration, very high intensity light flash [8]. While a finely tuned Schlieren system can produce images similar to those produced by a vibrometer, there are several distinct advantages to using a vibrometer. First, vibrometer systems produce easily quantifiable results. The output at each scan point for a vibrometer is a voltage reading that can directly be interpreted in the context of the system being analyzed. With a Schlieren system, quantifying the image produced requires some secondary analysis of variations in intensity recorded in the video pixels. In addition, for refracto-vibrometry the cross-sectional area of the laser beam is the size of the area being observed. This means minute sections can be studied individually, and the beam can be placed wherever a measurement needs to be taken. In Schlieren systems pixels from the video must be picked and chosen for analysis, and this analysis is limited by the resolution of the camera used. Refracto-vibrometry also enables very high time resolution; for example, the system used for the current experiment had a sampling rate of 100 MegaSamples/s.It is clear that refracto-vibrometry is a fundamentally different type of imaging modality compared to conventional techniques. The current study demonstrates two applications of this unique technique: the capability to image traveling wavefronts as they pass through and are reflected from different samples, and the ability to use these detected wavefronts to measure the speed of the sound waves.

9.2 Theory

9.2.1 Refracto-Vibrometry

A vibrometer measures Doppler shift through interferometric techniques. A modulated laser in a Mach-Zehnder interferometer is split into a reference beam that is recombined with a beam that has been reflected from the target [9]. The time variations of the interference pattern are normally due to a Doppler shift of the reflected beam; however, in the case of refracto-vibrometry, the retroreflected target is motionless so the time variations are due to changes in the optical path length between the vibrometer and target. The optical path length, $\varnothing$, is defined as the integral of the index of refraction $n(s)$ along the path the light travels [10]

$$\varnothing = \int_{path} n(s)\, ds. \tag{9.1}$$

When a portion of a wavefront with higher density, thus larger index of refraction, passes through the vibrometer laser, it will increase slightly the optical path length and thus the time the laser takes to travel from the vibrometer to the surface and back. Similarly, a lower density region with lower index of refraction will result in a shorter optical path length and thus shorter light travel time. These alterations in optical path length show up as time variations in the interference between the reference and measurement beam. A noteworthy feature of refracto-vibrometry is that it samples the line integral of density variations along the laser's path. This is different than most conventional ultrasound transducers and needle hydrophones that measure the surface integral of the waves that strike the surface of the detector.

9.2.2 Speed of Sound Measurement

The standard approach to speed of ultrasound measurements involves sending an ultrasound pulse from one transducer to another with no blocking materials. Then, by placing an intervening sample of known thickness, L, in between the transducers, the time-of-flight difference can be used to find the speed of the sound wave through the sample, c_s, given the speed of sound in water, c_w [11]

$$TOF = L\left(\frac{1}{c_s} - \frac{1}{c_w}\right). \tag{9.2}$$

The accuracy of this measurement can be increased by measuring the time-of-arrival for multiple thicknesses and using the slope, *m*, of the linear plot of time of wave arrival versus thickness to calculate the speed of sound in the sample, c_s, using

$$c_s = \frac{1}{m + \frac{1}{c_w}}. \tag{9.3}$$

In the current experiment, this technique was used to determine the speed of sound through a homogenous solid, lead, and a heterogeneous solid, a fabricated bone-like material. The speed of sound was determined using time of ultrasound pulse arrival optically measured with the vibrometer. This was compared to the speed of sound determined using the established technique for time-of-arrival at the receiving ultrasound transducer. This enables direct comparison between the relatively new measurement technique and a conventional method used for speed of sound determination.

9.3 Experimental Setup

The setup for detection of incident, reflected, and transmitted wavefronts and speed of sound through different samples involved pointing the vibrometer laser into a glass water enclosure housing two ultrasound transducers, the sample, and all of the supporting fixtures. A schematic of this setup can be seen in Fig. 9.1. A 1 MHz Panametrics V303 ultrasound transducer was used to generate acoustic waves. This transducer emitted waves with a near field length of 26.9 mm. The transducer was held in place by a clamp. Cylindrical support rods running alongside the transducer held a tray 23.9 mm above the transducer that had a 37 mm diameter hole. This enabled the sample to be supported by its edges and ensonified by the transducer below. When no sample was present, no reflections of the emitted pulse were observed to reflect from the support structure. In addition, the entire support system was rigid, and was not subject to vibrational modes due to the transducer releasing a pulse.

A second 1 MHz Panametrics V303 ultrasound transducer was used as a receiver of the ultrasound signals. The receiving transducer was oriented facing downward 62.3 mm above the transmitting transducer. This spacing was used to ensure all

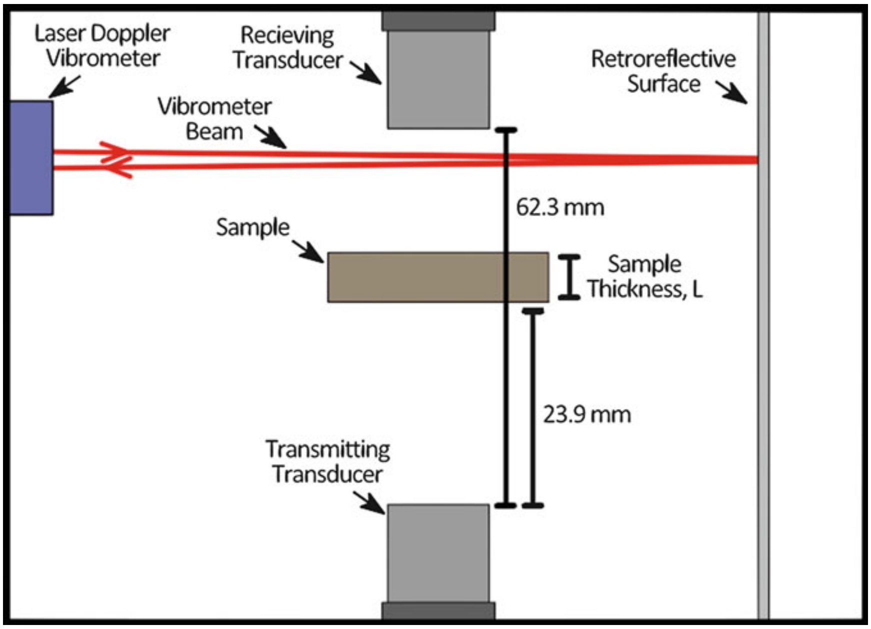

Fig. 9.1 Experimental setup for refracto-vibrometry and transducer wave readings. For wave detection experiments, the vibrometer beam scanned through points around the whole system. For speed of sound measurements, the vibrometer recorded time-of-flight from wave emission at the transducer to wave arrival at a point past the sample

the samples could fit between the transducers without needing to vary the distances. Behind this vertical transducer/sample arrangement a piece of 3 mm thickness aluminum covered in retroreflective tape was placed to reflect the vibrometer laser. To avoid reflections of the laser from the water tank glass, the enclosure was placed at an angle of approximately 15° from being normal to the laser.

Signals for the ultrasound transducers were produced and processed using a Panametrics 5055P pulser [12]. The signal for the emitting transducer was a single, narrow negative voltage pulse. Ultrasound signals that arrived at the receiving transducer were amplified by the pulser to produce an analog output signal. Coincident with the emission of the ultrasound pulse, the pulser output a TTL trigger pulse.

A Polytec PSV-400 scanning laser vibrometer [6] was used for optical detection of the ultrasound wavefronts. The laser was emitted from the vibrometer, passed through the glass face of the tank into the water filled region of the tank, was reflected off a retro-reflective surface, and then returned to the vibrometer along the same path. The mirrors in the vibrometer allowed the laser to be positioned to measure the optical path length variation at many different scan points. The vibrometer velocity decoder was set to a scale that allowed detection of the modulation of the laser signal at frequencies up to 1.5 MHz. For each ultrasound pulse, the TTL trigger from the pulser was used as a trigger for the PSV-400 data acquisition system. The acquisition system digitized, sampling at a rate of 102.4 MSamples/s, a brief pre-trigger interval along with time-domain output of the vibrometer typically for a total of about 80 μs. The vibrometer acquisition system simultaneously can digitize a reference signal; in the current experiment, the reference signal used was the analog output of the pulser that was proportional to the signal measured by the receiving ultrasound transducer. To suppress random noise, the acquisition system averaged between 50 and 1000 individual ultrasound pulses at each laser scan point. By performing these measurements for many separate laser vibrometer scan points, this refracto-vibrometry technique allowed determination of the time-varying acoustic wavefronts.

9.3.1 Optical Detection of 1 MHz Acoustic Wave and Its Reflections

A 1 MHz wave was emitted by the transducer with a 5.9 mm thick lead block placed on the sample tray. The vibrometer scanned through the ultrasound field and measured the signal intensity in the time domain. By compiling all the data points in a two-dimensional grid, the sound field, composed of an emitted wave and all the reflections and transmissions occurring at the sample, could be characterized.

This was repeated without a sample in the tray. By observing the wave traveling from the transmitting transducer to the receiver without interruption, a measurement of the speed of an unattenuated ultrasound wave through water was performed. This was done by finding the distance of wave travel and dividing it by the time of flight from wave emission to reception. By relating the distance of wave travel in an image of the setup to the size of a known object, the actual distance was found. Combining this with the time of flight as measured by the two transducers, the velocity of the wave was determined.

9.3.2 Speed of Sound Measurement Through Lead and Bone

In order to calculate speed of sound through both lead and fabricated bone, different thicknesses of each were used. For speed of sound measurements through lead, four different lead thicknesses were used. For the fabricated bone, five different thicknesses of Sawbones 15 PCF Open Cell bone [13] were cut. The samples were placed underwater in a vacuum chamber for 10 min to remove air pockets from their pores.

Time-of-flight measurements were taken for each of the different thicknesses and for the setup with no sample. Time of flight was determined as being from the time the ultrasound pulse was emitted, to the first major zero-cross time on the received signal; a representative time trace is shown in Fig. 9.2. Frame a of this figure displays the entire signal reading for the vibrometer and transducer. The output signal is seen in the red trace from the transducer several microseconds into the graph. There was a 2.38 μs pre-trigger time period before the pulse emission. The time of flight was measured from the beginning of the sampling period until the zero-cross as marked in frame b of the exploded view of the wave reception portion of the graph. The zero-cross time was chosen as the measurement feature because it is easy to identify and there is a low margin of error in choosing the proper spot.

By combining the previously calculated speed of sound in water with the time-of-flight time for the various thicknesses through Eq. 9.3, it was possible to determine the speed of sound through the different media.

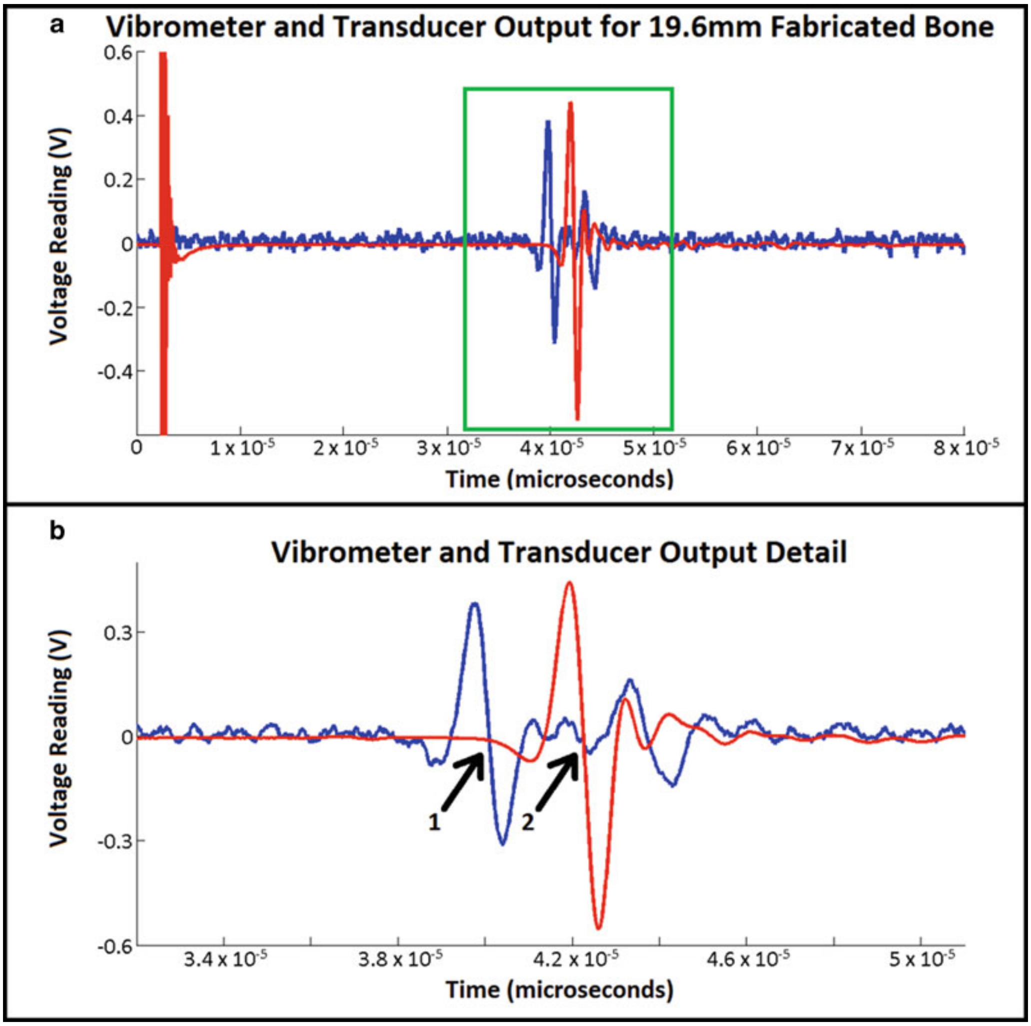

Fig. 9.2 Instrument readings from vibrometer and transducer. The vibrometer beam was placed just below the receiving transducer face in this measurement, and the 19.6 mm fabricated bone was used as the sample. (**a**) The complete time-domain signals from the vibrometer and transducer. The *blue trace* shows the vibrometer output. The vibrometer receives the wave signal before the transducer, seen as the *red trace*, registers the signal. This is expected since the vibrometer beam is positioned slightly in front of the transducer. The large transducer return 2.6 μs into the signal is generated from the electrical noise associated with the transducer emitting an ultrasound pulse. (**b**) Expanded view of boxed section from frame **a**. The zero-cross time-of-flight measurement points are marked. Point 1 is the measured zero-cross time for the vibrometer, and point 2 is the measured zero-cross time for the transducer

9.4 Results

9.4.1 Wavefront Transmission and Reflection

Using the 1 MHz transducer as an ultrasound transmitter and the laser Doppler vibrometer as a refracto-vibrometry wave detector, wavefronts were seen as they were emitted, as they traveled, and after they were transmitted and reflected.

In Fig. 9.3, a wavefront produced by the transducer can be seen at different intervals from when it was emitted. Figure 9.3a shows the wavefront at 12.6 μs after it was emitted. The wavefront is approximately planar, and maintains its shape as it travels vertically up towards the specimen. The speed of the traveling wave was calculated by comparing the distance it moves over a time interval to a known object dimensions. In this case, the transducer was used as the reference object since it had a measured shaft diameter of 15.9 mm. The sound speed in water, as measured this way, was 1460 ± 10 m/s. The accepted value for the speed of sound in water near room temperature [14] is 1483 ± 6 m/s with the uncertainty due to an uncertainty in the temperature of the water in the tank.

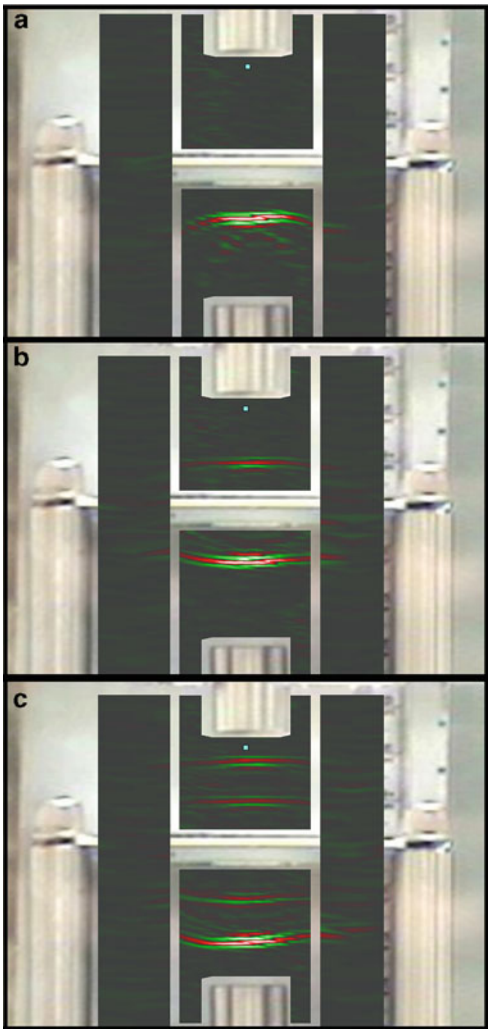

Fig. 9.3 Traveling wavefronts at various points after wave emission. (**a**) Initial wave 12.6 microseconds after release. (**b**) The wave reflected off the sample and the wave transmitted through the sample 24.6 microseconds after transducer ultrasound pulse. (**c**) First reflected and transmitted wave, along with secondary reflections from inside lead 30.6 microseconds after wave emission

When the wavefront came in contact with the 6.35 mm lead plate there was both a transmission and reflection. This transmission and reflection can be seen in Fig. 9.3b, taken 24.6 μs after the emission of the wave. While the transmitted wavefront's speed and shape remains largely unchanged compared to the wavefront incident of the lead plate, the amplitude is somewhat diminished. This is because much of the original wave was deflected downwards by the lead plate. This deflected wave maintains a similar structure to the incoming wave, despite now traveling in the opposite direction back towards its source.

As time progresses further after the wave emission, more reflections can be seen from the lead plate. Figure 9.3c shows the positions of the wavefronts after 30.6 μs. In the time since the last image, the upper and lower waves have continued their progressions in their respective directions. Their amplitudes, speed, and shape remain constant. In addition to these two waves, two new wavefronts are visible at this time. These waves originate from the waves reverberating inside the lead plate.

9.4.2 *Speed of Sound Measurement in Lead*

Four different thicknesses of lead disks were used, in addition to a measurement with an empty target. This data set is depicted in graphs of Fig. 9.4. The times given are the first zero-crosses of the received signals for either the vibrometer or the ultrasound transducer

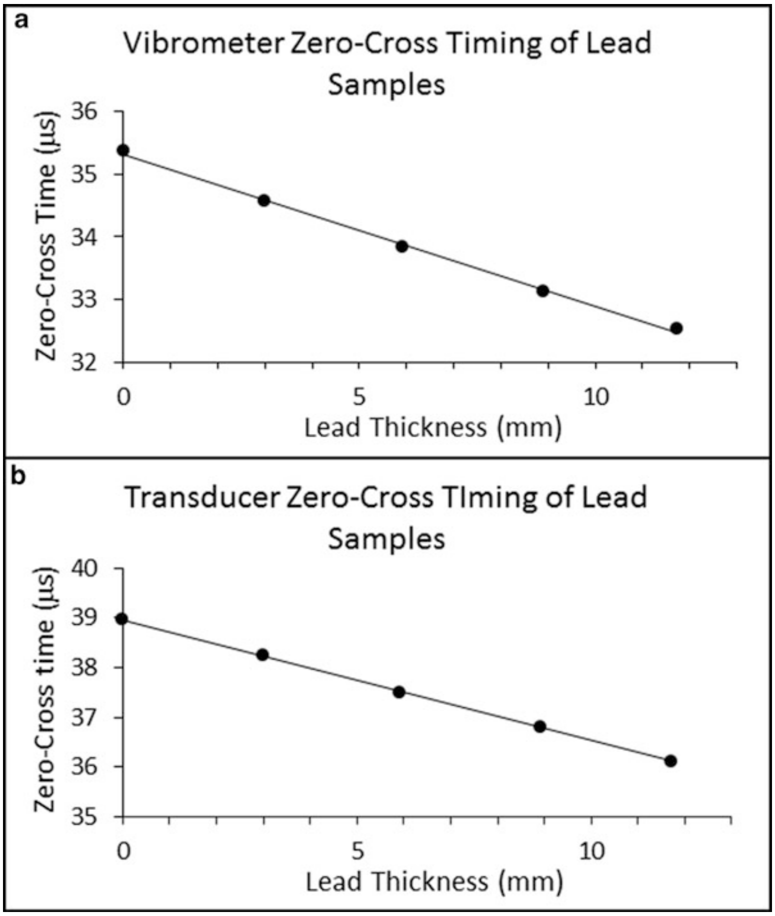

Fig. 9.4 Time of flight versus sample thickness for lead. Note that error bars are present in this data set, but they are small enough that they don't show up relative to the data points. (**a**) Vibrometer measured data. (**b**) Transducer measured data

Using the slope m of the data, and the speed of sound in water previously measured to be $c_W = 1460 \pm 10$ m/s, the speed of longitudinal waves in lead, c_{Pb}, was found using Eq. 9.3. The speed of longitudinal waves c_{Pb} through lead as measured by the vibrometer was 2260 ± 20 m/s. The speed of sound through lead as measured by the ultrasound transducer was 2270 ± 30 m/s. These values are in agreement with each other within the bounds of their uncertainties. These values are slightly larger than accepted values for lead [15] which are 2160 m/s when annealed and 1960 m/s when rolled. It was not known what physical form the lead disks used for this experiment were.

9.4.3 *Speed of Sound Measurement in Synthetic Bone*

A similar method was used to determine the speed of sound in a synthetic bone material immersed in water. Five different thicknesses of synthetic bone were cut. These thicknesses were used as samples in a speed of sound calculation, along with a trial containing no intervening sample. Both the vibrometer and transducer were placed above the sample so the ultrasound pulse would pass through the sample before being recorded. On the transmitted pulse, the time for the first main zero-cross was recorded for each instrument. Figure 9.5 graphs the resulting time values for each of the fabricated bone thicknesses.

From the slope of the linear fit to this data, the speed of sound was found. For the data taken with the vibrometer the speed of sound through the bone sample is 1507 ± 11 m/s. From the transducer data the speed of sound through the bone samples comes out to be 1497 ± 13 m/s. There have been no published studies discussing the speed of sound in this synthetic bone media. However, the measured speed is roughly consistent with the 1500 m/s speed of waves in cancellous bone material [11].

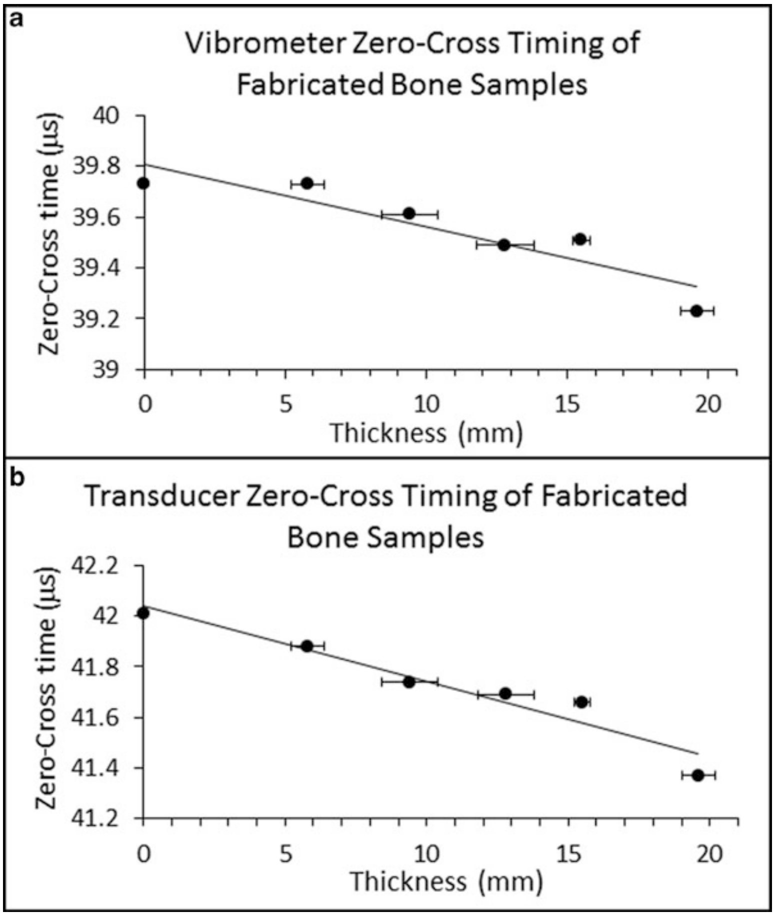

Fig. 9.5 Time of flight versus sample thickness for fabricated bone. (**a**) Vibrometer measured data. (**b**) Transducer measured data

9.5 Conclusions

This study compared a vibrometer used with refracto-vibrometry techniques to conventional transducers. By scanning the vibrometer beam, it was possible to create videos of the transducer transmitting ultrasonic pulses through water. This is valuable because it allows for examination of the ways sound is reflected off and transmitted through various materials. Looking at how ultrasound scatters off a diffuse scattering media like bone is of particular interest as Osteoporosis diagnosis is commonly done by making inferences on bone structure from the signals that pass through the bone.

The refracto-vibrometry technique was shown to be comparable to transducers when it comes to make quantitative measurements of ultrasound waves. Speed of sound calculations through both homogeneous and heterogeneous solids produced results that believable given the sample size and potential for error. These experiments demonstrate that refracto-vibrometry is a viable non-invasive method for characterizing sound fields and obtaining speed of sound measurements through a diverse array of materials.

Acknowledgements This material is based upon work supported by the National Science Foundation under Grant Number 1300591. Any opinions, findings and conclusions or recommendations expressed in this material are those of the author(s) and do not necessarily reflect the views of the National Science Foundation (NSF).

Research reported in this paper was supported by the National Institute of Arthritis and Musculoskeletal and Skin Diseases of the National Institutes of Health under Award Number R15AR066900. The content is solely the responsibility of the authors and does not necessarily represent the official views of the National Institutes of Health.

References

1. Buick, J.M., Cosgrove, J.A., Douissard, P.A., Greated, C.A., Gilabert, B.: Application of the acousto-optic effect to pressure measurements in ultrasound fields in water using a laser vibrometer. Rev. Sci. Instrum. **75**(10), 3203–3207 (2004)
2. Harland, A.R., Petzing, J.N., Tyrer, J.R.: Non-invasive measurements of underwater pressure fields using laser Doppler velocimetry. J. Sound Vib. **252**(1), 169–177 (2002)
3. Harland, A.R., Petzing, J.N., Tyrer, J.R.: Nonperturbing measurements of spatially distributed underwater acoustic fields using a scanning laser Doppler vibrometer. J. Acoust. Soc. Am. **115**(1), 187–195 (2004)
4. Olsson, E., Tatar, K.: Sound field determination and projection effects using laser vibrometry. Meas. Sci. Technol. **17**, 2843–2851 (2006)
5. Malkin, R., Todd, T., Robert, D.: A simple method for quantitative imaging of 2D acoustic fields using refracto-vibrometry. J. Sound Vib. **333**(19), 4473–4482 (2014)
6. Polytec GmbH, Waldbronn Germany, PSV-400 Scanning Laser Doppler Vibrometer Data Sheet (2011)
7. Settles, G.S.: Schlieren and Shadowgraph Techniques. Springer, Berlin, Heidelberg (2001)
8. Azuma, T., Tomozawa, A., Umemura, S.: Observation of ultrasonic wavefronts by synchronous Schlieren imaging. Jpn. J. Appl. Phys. Part 1-Regul. Pap. Short Notes Rev. Pap. **41**(5B), 3308–3312 (2002)
9. Polytec: Basic Principles of Vibrometry. [Online]. Available: http://www.polytec.com/us/solutions/vibration-measurement/basic-principles-of-vibrometry/. Accessed 5 Aug 2015
10. Hecht, E.: Optics, 4th edn. Addison-Wesley, Reading, MA (2001)
11. Laugier, P., Haïat, G. (eds.): Bone Quantitative Ultrasound, 2011 edition. Springer, New York (2014)
12. Pulser Receivers. [Online]. Available: http://www.olympus-ims.com/vi/products/pulser-receivers/. Accessed 05 Aug 2015
13. Sawbones|Open Cell Block 15 PCF. [Online]. Available: http://www.sawbones.com/Catalog/Biomechanical/Biomechanical%20Test%20Materials/1522-524. Accessed 05 Aug 2015
14. Greenspan, M., Tschiegg, C.E.: Speed of sound in water by a direct method. J. Res. Natl. Bur. Stand. **59**(4), Research Paper 2795 (1957)
15. Lide, D.R. (ed.): Section 14, geophysics, astronomy and acoustics. In: CRC Handbook of Chemistry and Physics, 84th ed. CRC/Taylor & Francis, Boca Raton, FL (2003)

Chapter 10
Stochastic Wavenumber Estimation: Damage Detection Through Simulated Guided Lamb Waves

Garrison N. Stevens, Kendra L. Van Buren, Eric B. Flynn, Sez Atamturktur, and Jung-Ryul Lee

Abstract Acoustic Wavenumber Spectroscopy (AWS) is a technique for nondestructive testing and evaluation capable of identifying local damage in thin plates through the estimation of the characteristic wavenumber of propagating elastic waves. Current state of the art in AWS estimates wavenumber based on the maximum data fit of the wavenumber dispersion curve and derives thickness deterministically through the Lamb wave equations. Successful determination of thickness from the measurements through inverse analysis is dependent upon two aspects: uncertainties regarding material properties of the system (parametric uncertainty) and uncertainties regarding data collected in the field under less than ideal conditions (experimental uncertainty). Thus, the deterministic approach may lead to large false positives in the presence of parametric and experimental uncertainties. The focus of this paper is to develop a stochastic approach for inferring thickness from the measurements in which both parametric and experimental uncertainties are accounted for. Herein, parametric uncertainty is managed by calibrating material-dependent properties using wavenumber measurements. Experimental uncertainty is controlled through incorporation of expert judgment by means of an elicited prior uncertainty of thickness. The technological advancement produced in this study is demonstrated on a case study application of an aluminum plate with imposed thinning.

Keywords Bayesian inference • Inverse analysis • Model calibration • Non-destructive testing • Ultrasonic guided waves

10.1 Introduction and Background

Internal damages such as corrosion and delamination are local defects that may compromise the integrity of thin-walled structures such as pipes, airplane hulls and wings, and wind turbine blades. These structures are often critical components of infrastructure systems exposed to harsh operating environments and are highly susceptible to damage. Internal damages are not identifiable by visual inspection, making them difficult to detect through non-invasive means. Identifying these defects as early as possible is necessary to avoid further damage, which may ultimately result in failure of the overall system. Structural health monitoring (SHM) and non-destructive testing and evaluation (NDE) are methods to avoid such. Effective SHM and NDE campaigns are those which do not require high costs or significant downtime of vital infrastructure systems. These fields of research strive to detect and quantify the severity of damage in structures through non-destructive methods. More specifically, they seek to (1) detect the presence of damage, (2) locate where damage has occurred and (3) quantify the degree of damage [1, 2]. Techniques that are useful in practice must not only locate, but most importantly, quantify the degree of damage in a structure [3].

For many years, research in SHM has focused on changes in natural frequencies and mode shapes as indicators of damage. These response features are global metrics measured using a finite number of sensors located at discrete positions on the structure. As a result, a number of different damage scenarios may result in similar changes in the natural frequencies and mode shapes obtained from these limited number of sensors (a phenomenon commonly known as non-uniqueness) [4–6]. Furthermore, the limited number of sensors may result in spatial aliasing and limit experimentally obtained modal parameters to lower order modes [4, 7–9]. Additionally, modal parameters tend to have a low sensitivity to local damage [10, 11] as local

---

G.N. Stevens • S. Atamturktur
Glenn Department of Civil Engineering, Clemson University, Clemson, SC 29634, USA

K.L. Van Buren (✉) • E.B. Flynn
Engineering Institute, Los Alamos National Laboratory, Los Alamos, NM 87545, USA
e-mail: klvan@lanl.gov

J.-R. Lee
Department of Aerospace Engineering, KAIST University, Daejeon, South Korea

© The Society for Experimental Mechanics, Inc. 2016

J. De Clerck, D.S. Epp (eds.), *Rotating Machinery, Hybrid Test Methods, Vibro-Acoustics & Laser Vibrometry, Volume 8*,
Conference Proceedings of the Society for Experimental Mechanics Series, DOI 10.1007/978-3-319-30084-9_10

damage tends to only cause shifts in high-order modal frequencies [4]. However, obtaining such high order modes is typically infeasible due to experimental limitations. Detecting a shift in natural frequency also becomes challenging due to the high experimental variability that is often present in modal tests [12, 13].

NDE techniques, such as scanning ultrasound, tend to provide higher densities of measurement points over SHM, at the expense of generally requiring that the inspected system be taken offline. These higher density measurements enable a more direct inference of the mechanical properties of a structure, resulting in an improved ability to detect and characterize defects [14, 15]. Acoustic Wavenumber Spectroscopy (AWS), which will be implemented in this study, is an emerging inspection technique that relies on full-field, non-contact, guided wave measurements for assessing damage using local estimates of wavenumber [16].

Methods for detecting damage can be separated into two distinct categories: model-based and non-model-based. Model-based methods compare experimental measurements to analytical, physics-based model predictions to localize and quantify the severity of damage in a structure. Non-model-based methods correlate data from undamaged and damaged scenarios to detect the presence of damage and are typically only capable of damage detection and sometimes localization [5], meaning that they cannot quantify the severity of damage. Model-based methods result in an inverse analysis, where observed measurements are used to infer model parameters related to the damage feature [17]. While model-based methods tend to be more computationally expensive, they carry the distinct advantage of quantifying the severity of damage. The focus herein is a model-based method for NDE.

While AWS measurements alone may successfully locate damage in a structure, the severity of damage cannot be quantified without the assistance of a guided Lamb wave propagation (LWP) model. Given material properties of the structure (elastic modulus, density, and Poisson's ratio), the LWP model uses Lamb wave equations to relate the local wavenumber to the effective thickness. Hence, AWS based damage detection becomes an inverse procedure, where the thickness of the material is back-calculated given known material properties and measured local wavenumber. The identified change in effective thickness of a material indicates, for instance, corrosion in metals and delamination of interior layers in composites.

In the AWS based damage detection procedure, a prominent issue is the need to know the healthy condition of the structure, referred to as "baseline" model. Model-based inverse analysis relies on comparison of this baseline model (i.e. healthy state) to experimental measurements collected from the structure in its current condition (i.e. unhealthy state). Obtaining the baseline model requires the knowledge of the *true* material property values. In practical applications, these material property values are typically uncertain, and their experimental determination is hindered by the fact that obtaining experimental measurements from the healthy system is often infeasible [4, 7, 12, 18]. Furthermore, the reliance of inverse analysis on a comparison of model predictions to experimental measurements results in a dependence on the quality of measurements, meaning that uncertainty in experimental measurements propagates to uncertainty in the quantification of damage severity.

The current AWS based damage detection procedure estimates wavenumber and calculates thickness in a deterministic manner without taking the uncertainties in material properties (parametric uncertainty) or uncertainties in the experiments (experimental uncertainty) into account. The lack of consideration for uncertainties can lead the deterministic AWS procedure to significantly overestimate damage, resulting in an unduly number of false positives. Such false positives would reduce the confidence infrastructure managers place on the SHM system and hence, degrade the effectiveness and practical feasibility of the AWS procedure.

In this paper, we propose damage detection through back-calculation of thickness utilizing the LWP model and Bayesian inference to explicitly consider two critical sources of uncertainty: parametric and experimental uncertainties. *Parametric uncertainty* due to the lack of knowledge regarding *true* material properties needed in the LWP model is the first type of uncertainty addressed. Herein, the inverse analysis is treated as a stochastic calibration process; one which takes advantage of experimentally obtained wavenumber measurements to infer not only thickness (e.g. damage) but also the poorly-known material properties (e.g. unknown baseline model). Therefore, a significant advantage of the approach implemented herein is the ability to detect and quantify the severity of damage simultaneously in a single step without requiring data from the healthy state of the structure.

Experimental uncertainty refers to the presence of spurious peaks in the experimental data due to noise present in measurements taken on site under less than ideal conditions. Specifically, laboratory testing of the current AWS method is often completed using dangerous and costly scanning Q-switched laser equipment. Safer, less invasive equipment, such as a scanning Laser Doppler Vibrometer (LDV), is often necessary for practical field applications, but results in a decrease in measurement quality due to the poor signal to noise ratio (SNR) inherit to LDV systems at high frequencies [19]. The noise in these lower quality field measurements, which often manifest as non-physical high wavenumber components, run the risk of producing false positives for damage detection. A distinct benefit of the proposed approach is the ability to implement prior probabilities to incorporate engineering judgment regarding the expected severity of damage [5]. Incorporating expert judgment by defining prior knowledge of material thickness helps significantly reduce the degrading effects of spurious peaks in low quality data that may otherwise lead to false damage detection.

The remainder of the paper is organized as follows. First, Sect. 10.2 provides an overview of the theoretical background of the Rayleigh-Lamb wave equations and Bayesian inference. We include a discussion of our mathematical reasoning for why we believe inverse modeling has the potential to apply to AWS. Section 10.3 provides a discussion of the sources of uncertainty in AWS measurements. Section 10.4 provides a case study of our implementation as applied to an aluminum plate with imposed thinning. Section 10.5 presents our main conclusions and avenues for future work.

10.2 Inverse Modeling of Lamb-Wave Propagation

10.2.1 Rayleigh-Lamb Wave Equations

AWS is based on the physics of Rayleigh-Lamb equations for propagation of Rayleigh-Lamb waves (also referred to as guided Lamb waves) in thin-walled structures, which was first discussed by Horace Lamb [20]. In the frequency ranges of interest in this study, the primary wave modes of thin-walled structures are the zero order antisymmetric, A_0, mode (particle motion perpendicular to direction of wave propagation as shown in Fig. 10.1a) and zero order symmetric, S_0, mode (particle motion parallel to the wave propagation direction as shown in Fig. 10.1b). Given specific material properties, structure thickness, and excitation frequency, each of these modes travels through a plate with a particular period, or wavelength, λ. Wavenumber, k, is the spatial frequency of the wave mode and is the inverse of wavelength.

Following the Rayleigh-Lamb wave governing equations, the wavenumber of the A_0 and S_0 wave modes may be determined by finding the roots of Eq. (10.1). The parameters α and β are the Rayleigh-Lamb frequency equations and are dependent upon longitudinal wave velocity, c_l, and transverse wave velocity, c_t, as well as the temporal frequency, ω, as shown in Eq. (10.2) [21].

$$\frac{\tan(\beta t/2)}{\tan(\alpha t/2)} = -\frac{\left(k_A{}^2 - \beta^2\right)^2}{4\alpha\beta k_A{}^2} \quad \text{and} \quad \frac{\tan(\beta t/2)}{\tan(\alpha t/2)} = -\frac{4\alpha\beta k_S{}^2}{\left(k_S{}^2 - \beta^2\right)^2} \tag{10.1}$$

$$\alpha^2 = \frac{\omega^2}{c_l{}^2} - k^2 \quad \text{and} \quad \beta^2 = \frac{\omega^2}{c_t{}^2} - k^2 \tag{10.2}$$

Material properties are introduced to the problem through the longitudinal and transverse shear wave velocities, which are dependent upon elastic modulus, E, density, ρ, and Poisson's ratio, υ.

$$c_l = \sqrt{\frac{E(1-\upsilon)}{\rho(1+\upsilon)(1-2\upsilon)}} \quad \text{and} \quad c_t = \sqrt{\frac{E}{2\rho(1+\upsilon)}} \tag{10.3}$$

Propagation of the guided Lamb waves becomes a model-based inverse analysis by implementing Eqs. 10.2 and 10.3 for the quantification of thickness, t, when the wavenumber, k, is collected by experimental measurements.

As discussed further in Sect. 10.5, the experimental data is collected using broadband excitation. As such, we are able to evaluate the wavenumber of the A_0 and S_0 modes, k_A and k_S, for multiple frequencies. The excitation frequency, ω, and the obtained wavenumber, k_A and k_S, can be plotted against one another to provide what is known as the dispersion curve.

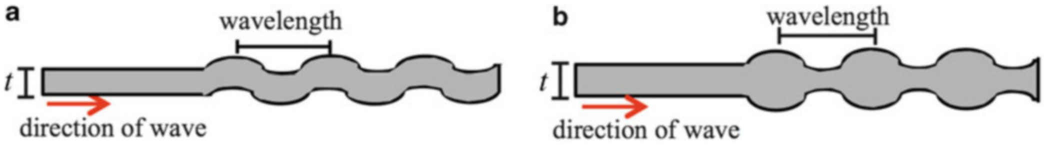

Fig. 10.1 Wavelength measurement of a guided Lamb wave (**a**) antisymmetric, A_0 and (**b**) symmetric, S_0 modes

10.2.2 Feasibility for Inverse Modeling

Inspection of Eq. (10.3) reveals that the formulation of the longitudinal and transverse shear wave velocities provides potential complications for integrating AWS into the inverse-modeling paradigm. This is due to the fact that the Young's modulus, E, and density, ρ, are proportional to each other. Clearly, there is no unique solution for c_l and c_t due to the fact that there are two equations with three unknowns: Young's modulus, E, density, ρ, and Poisson's ratio, υ. Further, the two equations are not dependent on Young's modulus and density, but rather on the ratio of Young's modulus to density. This can be described by the fact that the ratio of c_l to c_t is dependent on neither Young's modulus nor density, as detailed in Eq. (10.4).

$$c_l = c_t\sqrt{\frac{2\,(1-\upsilon)}{(1-2\upsilon)}} \tag{10.4}$$

Thus, the first take-away is that, for successful implementation of inverse modeling of LWP, either the Young's modulus or the density needs to be known a priori. If both are unknown a priori, then the best that we can do is calibrate the longitudinal and transverse shear waves directly. Hence, if both parameters (E and ρ) are considered unknown in the inverse-modeling paradigm, the results will be non-unique. This is because increasing the value of Young's modulus will have the same effect on damage predictions as decreasing the density. The "best" that we can do is consider the ratio of Young's modulus to density as uncertain.

The second point of discussion is to determine the minimum amount of information necessary in order to return unique solutions for damage detection. Clearly for damage detection, the thickness will be considered unknown. When material properties of the structure are also unknown, non-uniqueness becomes a concern. This problem may be mitigated if a suitable number of unique measurement control settings are available for calibration. In the case of AWS we will use varying excitation frequencies in order to fit the LWP model to the dispersion curve, rather than a single measurement point.

10.3 Sources of Uncertainty in AWS

AWS is a recently developed laser-based technique that collects full field measurements of an ultrasonic induced wave up to 30 times faster than existing methods, considerably increasing the speed of nondestructive evaluation for detection of hidden damage. Full-field measurement refers to the collection of data across an entire area by dividing the area into pixels, each of which is a specific x and y coordinate location on the surface. Spatial sampling using a fine grid of pixels constructs the wave field for the entire scan area. The local nature of these measurements makes the method highly sensitive to damage. Specifically, a change in thickness or delamination directly results in a local change of wavenumber (i.e. spatial frequency), as shown in Fig. 10.2.

There are two methods available for collecting wavefield measurements: (1) excitation of an ultrasonic wave at each pixel while a sensor at a single location collects measurements and (2) excitation of the ultrasonic wave at a single location while measurements are collected at every pixel. The method selected is often determined by the equipment available for testing. The first method requires a powerful scanning Q-switched laser to excite a Lamb wave at each pixel through local thermoelastic expansion [22], while measurements are collected by a stationary sensor, such as a piezoelectric transducer or a LDV. Through reciprocity, these measurements can create a full-field image of the Lamb wave traveling across the plate through time (Fig. 10.3a). The second method relies on a single excitation point for the wave, which may be excited by a Q-switched laser or an ultrasonic transducer, and utilizes a scanning LDV to collect measurements at every pixel. A full-field image of Lamb wave propagation collected using this setup is shown in Fig. 10.3b.

Comparison of the Lamb wave snapshots obtained in Fig. 10.3a and b clearly illustrates the decrease in measurement quality when the second method is used. This is primarily due to the reduction in the amount of backscattered light that is

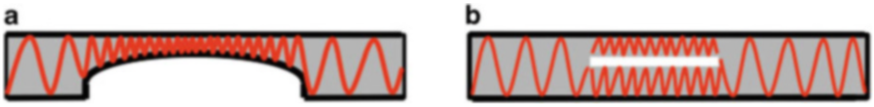

Fig. 10.2 Change in wavenumber due to (**a**) thinning and (**b**) delamination

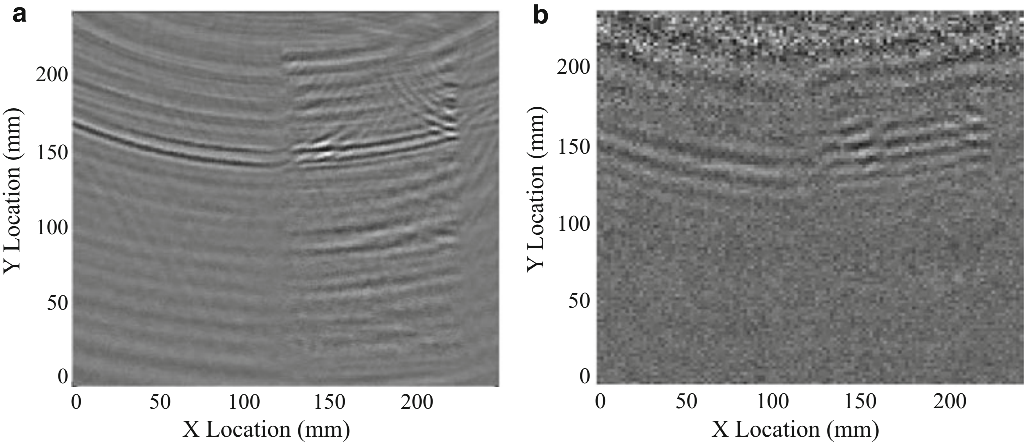

Fig. 10.3 Propagation of guided Lamb wave captured experimentally. (**a**) SLGU measurements. (**b**) LDV measurements

collected by the LDV when, during scanning, the angle of incidence on the specimen significantly deviates from normal. Since scanning excitation does not rely on backscattered light, it does not suffer the same problem during scanning. While the first method involving scanning excitation is clearly more desirable for collecting what will be referred to as "laboratory data", implementation of this method in industry is often not practical due to the cost and safety issues associated with high-power, scanning lasers [23].

A detailed description of the signal processing for wavenumber estimation is provided in [16]. Herein, a summary of the process as necessary for background understanding is provided. At each pixel, samples are measured for a given interval of time. The resulting data is a three-dimensional measurement matrix of x coordinates, y coordinates, and time samples, $v[x,y,t]$ in the space-time domain. The discrete Fourier transform can be applied along all directions of the measurement matrix to produce a frequency-wavenumber matrix, $V[k_x,k_y,f]$, where k_x and k_y are the x-direction wavenumber and y-direction wavenumber, respectively, and f is the time sample frequency. Wave modes (i.e. A_0 and S_0) are first isolated through windowing in the Fourier domain.

Next, each wave mode is passed through a narrowband-frequency filter in order to isolate a single frequency. The measurement is then passed through a bank of narrowband-wavenumber filters, each with a different central wavenumber, k_c. Each filter bank result is spatially enveloped, and finally summed along the time dimension. Once assembled together, this set of narrowband wavenumber, enveloped responses forms a space-wavenumber magnitude matrix, $z[x,y,k_c]$. Through this process, wavenumber-intensity curves are obtained at every pixel in the scan area. Nominally, the location of the maximum in the curve corresponds to the true wavenumber of the propagating wave for the given wave mode and frequency. As represented in Fig. 10.4a, SLGU measurements tend to produce smooth curves where the peak is close to the true wavenumber. Figure 10.4b, however, highlights a case where a spurious peak occurs in the data, potentially leading to an incorrect wavenumber estimate, and in turn, a false positive for damage.

While AWS measurements alone may successfully locate damage, the thickness at the damage location cannot be quantified without the assistance of an accurate wave model. Eqs. 10.2–10.4 may be implemented to develop the LWP model. However, this model is dependent upon knowledge of elastic modulus, density, and Poisson's ratio. These parameters may be known or measured accurately in some cases, but may remain highly uncertain in other applications or cases where the original design specifications are considered proprietary information that is not made available by the manufacturer. Therefore, AWS based damage detection is limited by its dependency on potentially poorly known material properties. Without reducing the uncertainty in these parameters, the severity of damage cannot be meaningfully quantified.

The second shortcoming of AWS based damage detection is related to the experimental uncertainty, which has practical importance due to the cost of equipment and settings needed to obtain high quality data. Achieving testing conditions for laboratory data, which produces measurements that a deterministic approach can successfully function with, is not practical for onsite applications. Realistically, AWS must be applied in situations where logistics limit what data acquisition equipment is practical, resulting in lower quality on site data, and in turn, higher experimental uncertainty.

The local nature of AWS measurements, as well as the sensitivity of wavenumber to change in thickness, makes the method ideal for thin-walled structures susceptible to damage related to thickness change. A decrease in thickness results in a shorter wavelength and thus, a higher wavenumber. Structures prone to thinning, such as pipes exposed to conditions

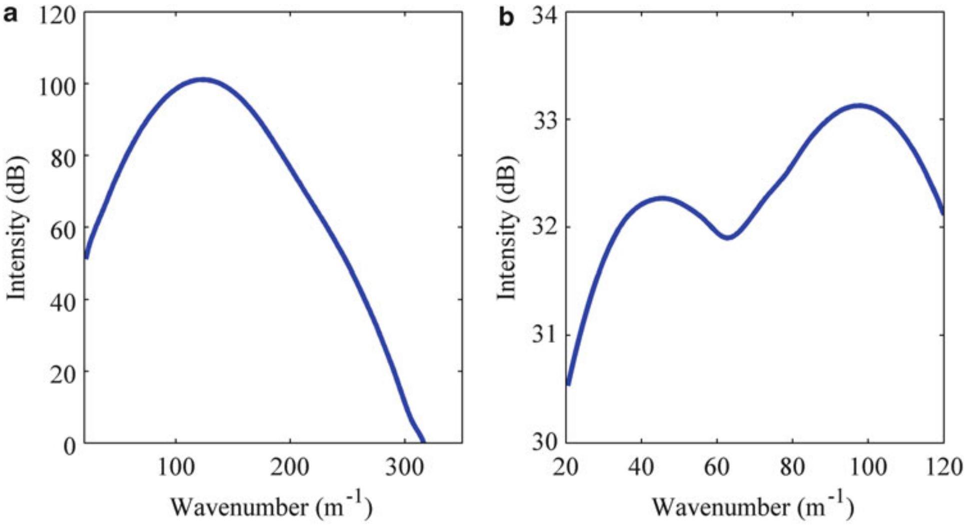

Fig. 10.4 Experimental variability in wavenumber where spurious peaks are observed in the LDV measurements. (**a**) SLGU measurements. (**b**) LDV measurements

causing corrosion, would exhibit an increase in wavenumber (recall Fig. 10.2a) in the presence of damage. A change in the effective thickness may also result from cases where materials in a structure separate, such as delamination in composites and debonding in pipes with protective coating, resulting in an increased wavenumber (recall Fig. 10.2b).

10.4 Methodology

10.4.1 Damage Detection Through Inverse Analysis

Damage detection methods can be separated into two distinct categories: model-based and nonmodel-based. Model-based methods compare experimental measurements to analytical, physics-based model predictions to localize and quantify the severity of damage in a structure. Nonmodel-based methods correlate data from undamaged and damaged scenarios to detect the presence of damage and are typically only capable of damage localization [5], meaning that they cannot quantify the severity of damage. Model-based methods result in an inverse analysis, where observed measurements are used to infer model parameters related to the damage feature [17]. While model-based methods tend to be more computationally expensive, they carry the distinct advantage of quantifying the severity of damage. The focus herein is a model-based method for NDE.

For model-based damage detection, a numerical model that mathematically describes the phenomenon of interest is used to predict the behavior of a physical process at a specified control setting. Numerical models seek to represent engineering principles defining the underlying physics of the problem, $\eta(x,t)$, where t is the true value of physical parameters (material properties in this application) and x is the control settings that define the domain of the application (excitation frequency in this application). True parameter values are often unknown and as such, best estimates of these parameter values, θ, are used in the model. Incomplete representation of these engineering principles results in model form error (or model bias), $\psi(x)$. Model form error is only known at settings where experiments have been conducted. Thus, an estimate of model form error is necessary for untested settings of the domain. Model form error can be estimated at untested settings using an empirically trained function, referred to as discrepancy, $\delta(x)$. Similarly, experimental measurements, $y(x)$, contain experimental error, ε, as they are noisy representations of reality. Thus, experimental measurements are related to the numerical model accordingly:

$$y\left(x_i\right) = \eta\left(x_i, \theta_i\right) + \delta\left(x_i\right) + \varepsilon_i \text{ where } i = 1, 2, \ldots, n \tag{10.5}$$

Said differently, experiments, $y(x)$, can be described as the sum of the best estimate numerical model predictions, $\eta(x,\theta)$, discrepancy, $\delta(x)$, and experimental error, ε for n unique experimental settings within this framework.

Table 10.1 details the parameters of the guided Lamb wave propagation (LWP) model for the application of the model within this framework.

Table 10.1 Parameters of LWP model

Experimental measurements ($y(x)$)		Wavenumber (k_A)
Control parameter (x)		Excitation frequency (ω)
Calibration parameters (θ)	Damage indicator	Thickness (t)
	Material properties	Elastic modulus (E)
		Density (ρ)
		Poisson's ratio (υ)

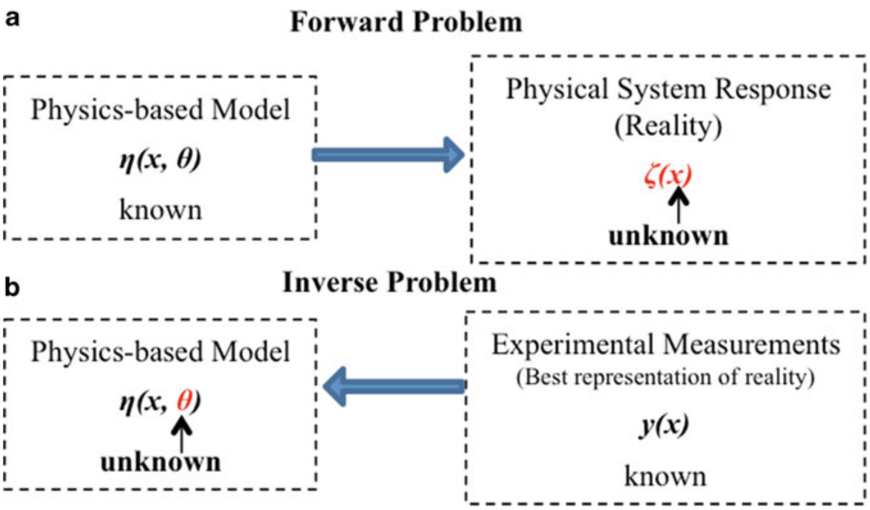

Fig. 10.5 Numerical model formulation for (**a**) forward problem where system response is unknown compared to (**b**) inverse problem where model parameters are unknown

Model-based damage detection results in an inverse problem when at least one of the input parameters, θ, of a model are considered to be indicative of damage incurred by the structure and is updated based on information gained from collected data [3, 8] (Fig. 10.5).

An important note in this formulation is that if model form error is present, evaluation of this model form error and parameter uncertainty must be completed simultaneously. Failure to consider model form error during parameter calibration may result in parameters compensating for incorrect physics formulation, causing parameters to converge to incorrect values [24–26].

10.4.2 *Bayesian Inference for Inverse Problems*

Herein, a fully Bayesian context, as described in [27] and implemented in [28], is used here to infer uncertain parameter values in the LWP model. The Bayesian approach is particularly useful for approaching problems with multiple sources of uncertainty [29]. This approach is based on Bayes theorem, by which the prior distribution of a parameter is updated based on knowledge gained from new data, which can be used to infer the posterior distribution:

$$P\left(\theta \middle| y(x)\right) \propto P\left(y(x) \middle| \theta\right) \times P(\theta) \tag{10.6}$$

where $P(\theta)$ is the prior distribution of the uncertain parameters, $P\left(y(x)\middle|\theta\right)$ is the likelihood (also written as $L(\theta)$), which is the probability of observing the data, and $P\left(\theta\middle|y(x)\right)$ is the posterior distribution of parameters. Essentially, Bayes theorem allows us to make an inference of uncertain parameters conditioned upon prior knowledge and experimental measurements.

The posterior distribution, $P\left(\theta\middle|y(x)\right)$ may be developed once the likelihood function and prior distributions are defined. The likelihood function is determined by sampling the numerical model with a number of different parameter sets [30]. Markov chain Monte Carlo (MCMC) sampling is used to explore the full parameter domain. This approach requires a large number of model runs (nearly always on the order of thousands), which is computationally infeasible to implement with the LWP model. Therefore, a Gaussian Process Model (GPM) is used as an emulator to replace the LWP model, defined by a mean function $\mu(x,\theta)$ and covariance:

$$\mathrm{Cov}\left(\left(\mathbf{x},\boldsymbol{\theta}\right),\left(\mathbf{x}',\boldsymbol{\theta}'\right)\right)=\frac{1}{\lambda_\eta}\prod_{k=1}^{p_x}\rho_{\eta k}^{4\left(x_k-x_k'\right)^2}\times\prod_{k=1}^{p_\theta}\left(\rho_{\eta k+p_x+k}\right)^{4\left(x_k-x_k'\right)^2} \tag{10.7}$$

where λ_η and ρ_η are hyperparameters of the GPM to be calibrated.

Herein, a Gaussian Process Model (GPM) is implemented for representation of the discrepancy function. For discrepancy, a GPM is defined by a mean function, μ, that is identically zero and a covariance:

$$\mathrm{Cov}\left(\mathbf{x},\mathbf{x}'\right)=\frac{1}{\lambda_\delta}\prod_{k=1}^{p_x}\rho_{\delta k}^{4\left(x_k-x_k'\right)^2} \tag{10.8}$$

where λ_δ and ρ_δ are hyperparameters of the GPM to be calibrated.

GPM is a desirable form of emulator in this case as it does not restrict the model to a specific functional form [25, 31] and has been shown to work well for applications in structural dynamics [32, 33]. A training set of data is generated from the physics-based numerical model. In the application presented herein, a multi-level full-factorial design of experiments is used to develop the training data. Multi-level full-factorial was selected due to the small number of calibration parameters making the development of a set of training data with many levels feasible. A full-factorial design is also desired so that the edges of the domain are fully explored. Details of the design for training data specific to the case study application will be presented in Sect. 10.5. The data is standardized to have a mean of zero and a standard deviation of one so that the units of all parameters may be consistent. Posterior distributions are represented as:

$$P\left(\theta,\mu,\lambda_n,\rho_n,\lambda_\delta,\rho_\delta\middle|\boldsymbol{D}\right)\propto L\left(\boldsymbol{D}\middle|\theta,\mu,\lambda_n,\rho_n,\lambda_\delta,\rho_\delta\right)\times P\left(\theta\right)\times P\left(\mu\right)\times P\left(\lambda_n\right)\times P\left(\rho_n\right)\times P\left(\lambda_\delta\right)\times P\left(\rho_\delta\right) \tag{10.9}$$

where $\boldsymbol{D}$ represents a vector of model outputs and experimental data.

Gibbs sampling, a specific case of the Metropolis-Hastings algorithm [34], is implemented for sampling the model. Each step of the sampling is a full conditional distribution of one parameter, cycling through each parameter individually while exploring the domain [35]. Acceptance criteria for the model samples is defined by Eq. (10.5). If a model sample meets the acceptance criteria it is kept in the likelihood function, otherwise the step returns to the previous parameter value and continues from there.

For determining the need for discrepancy in this application, the capability of the LWP model to predict wavenumber matching to the true physical process is evaluated through test analysis correlation. Model predictions for a 4 mm aluminum plate were found to match experimental measurements collected at various excitation frequencies, as shown in Fig. 10.6. The accuracy of model predictions demonstrated in the test analysis correlation led to the conclusion that the importance given to discrepancy should be limited. Such a limitation was placed on discrepancy by limiting the GPM hyperparameter, λ_δ, with a Gamma prior having distribution parameters $\alpha = 1$ and $\beta = 10^{-5}$. It should be noted that this is an application to an isotropic homogenous metal structure. Other applications, such as composite plates where different materials are layered together, may have increased error in the model form, requiring consideration of the discrepancy function.

10.4.3 Application to AWS: Stochastic Wavenumber Estimation

There is a desire to be able to use AWS measurements to quantify the severity of damage present in a structure. Thus far, the severity of damage is quantified deterministically by relating a change in wavenumber to a decrease in thickness. However, the deterministic estimation is complicated due to uncertainty in material properties and noise causing spurious peaks in experimental data. Bayesian inference presents a framework with distinct capabilities to resolve both of these issues, as shown in Fig. 10.7. This section provides details on the use of Bayesian inference to infer damage considering the presence of *parametric uncertainty* in the LWP model as well as *experimental uncertainty* in wavenumber measurements. The framework is implemented with the LWP model representing the physics and wavenumber measurements, described in Sect. 10.2.

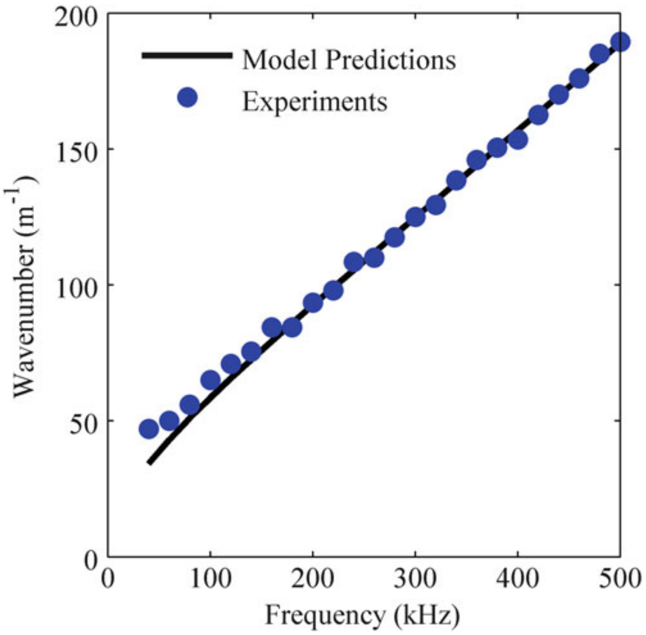

Fig. 10.6 Test-analysis correlation of LWP model

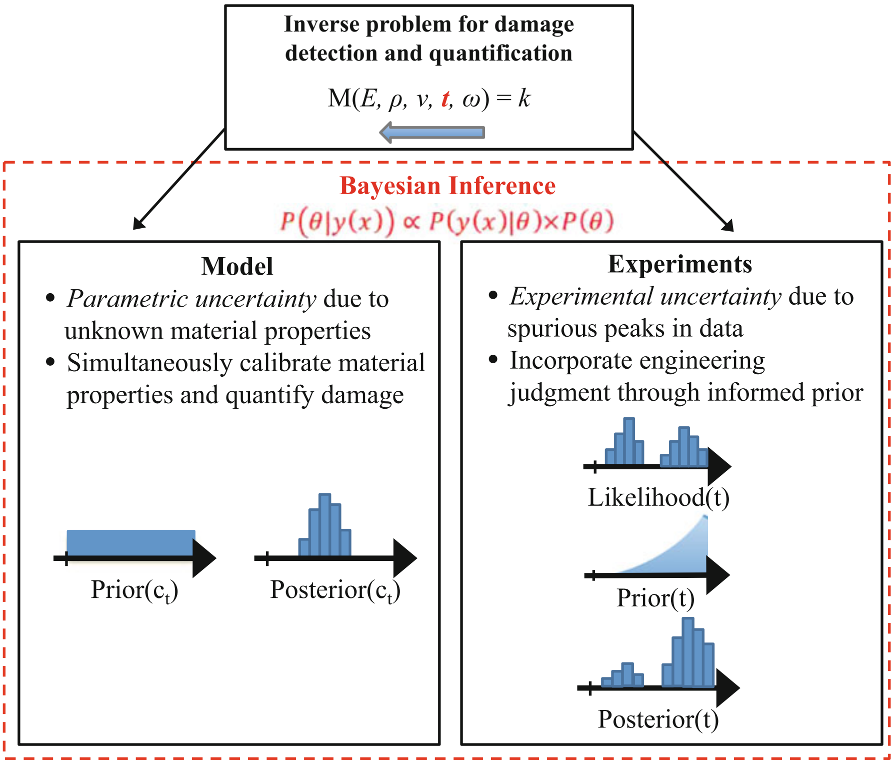
Inverse problem for damage detection and quantification
M(E, ρ, ν, t, ω) = k
Bayesian Inference
P(θ|y(x)) ∝ P(y(x)|θ)×P(θ)
Model
• Parametric uncertainty due to unknown material properties
• Simultaneously calibrate material properties and quantify damage
Prior(c_t)
Posterior(c_t)
Experiments
• Experimental uncertainty due to spurious peaks in data
• Incorporate engineering judgment through informed prior
Likelihood(t)
Prior(t)
Posterior(t)

Fig. 10.7 Framework for Stochastic Wavenumber Estimation to mitigate uncertainties in AWS procedure

10.4.3.1 Parametric Uncertainty

As discussed previously, the ability to apply a model for inverse calculation of a damage indicator depends on the predictive capability of the model. Without confidence in the numerical model parameters, severity of damage may not be accurately quantified. While calibrating uncertain parameters to a baseline model of a "healthy" state remedies the issue, there is a desire to remove the need for baseline measurements altogether. Therefore, we seek to overcome the challenges associated with lack of a baseline model (due to the presence of parametric uncertainties) by simultaneously calibrating the material properties and thickness of the experimental specimen. Evaluating the damage indicating parameters and material properties simultaneously helps eliminate the need for baseline measurements of the structure.

Recall that AWS measurements produce a full-field time history, meaning that a wavenumber is determined at every pixel of the structure's surface. Assuming the material is uniform throughout the entire area of interest on the structure, calibration may be carried out in a two-step process. The first step is calibration of material properties and thickness simultaneously at a single pixel. For the pixel selected, calibration is completed using wavenumber measurements at multiple excitation frequencies. Carrying out the calibration as a functional fit, rather than an individual measurement, helps avoid the possibility of non-unique solution sets (i.e. multimodal posterior distributions).

The second step is to apply the material properties calibrated in step one as "known" parameters in the LWP model and calibrate thickness for all other pixels. Breaking the procedure into a two-step process significantly reduces computational cost by reducing the number of calibration parameters to one (thickness) at the majority of pixels, since there are typically tens of thousands of pixels in a scan area. In the case of a structure with non-uniform section or material properties (such as a wind turbine blade), this step would need to be completed for each individual pixel or in groups of pixels known to have the same section and material properties.

10.4.3.2 Experimental Uncertainty

AWS measures the intensity of a wavenumber sensed by the LDV over a range of excitation frequencies, resulting in a dispersion curve intensity map (recall the discussion provided in Sect. 10.3 and Fig. 10.4). The wavenumber-intensity relationship may then be determined at a particular excitation frequency for each pixel in the scan area. Measurements completed with a Q-switch laser in controlled conditions are capable of producing a dispersion curve with low levels of noise and thus, result in wavenumber-intensity data with a single, well-defined peak (Fig. 10.8). However, measurements carried out in more realistic, on site applications often have higher levels of noise in the dispersion curve, causing spurious peaks in the wavenumber-intensity data (Fig. 10.9). Spurious peaks in AWS measurements most often relate to a false positive for detection of damage. Though Fig. 10.9 illustrates an example with two peaks, it is possible for multiple peaks to appear in the data. In the deterministic approach, the high frequency peak, which is due to noise in the data, corresponds to a decreased thickness and results in a false positive.

The approach presented herein takes advantage of the ability to define probability density functions to incorporate prior knowledge of plate thickness for Stochastic Wavenumber Estimation. Doing so allows for the consideration of expert knowledge regarding the expected degree of damage in the structure. For example, if one knows a range of reasonable corrosions rates, as well as how long it has been since the last inspection, one can produce a meaningful prior on the depth

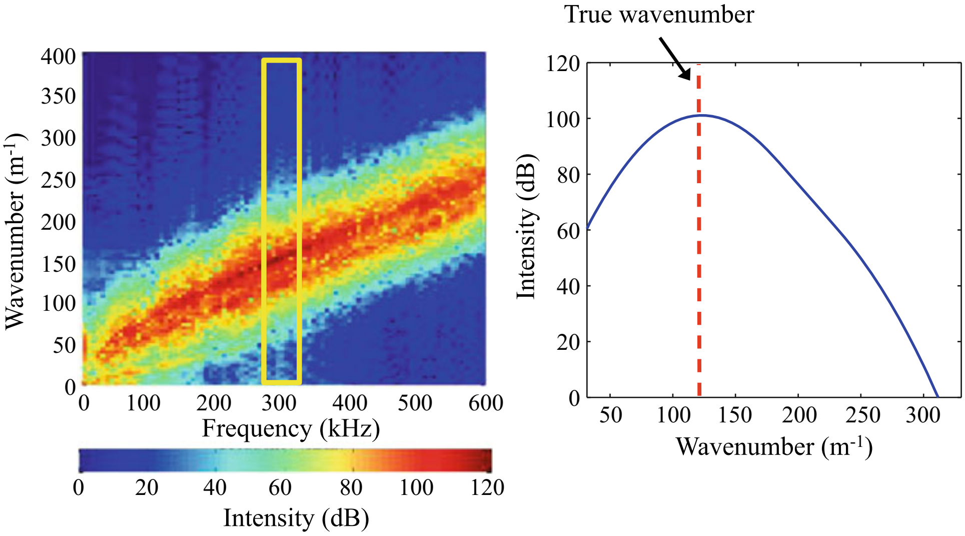

Fig. 10.8 Experimental variability in laboratory dataset (*left*) frequency-wavenumber map and (*right*) wavenumber-intensity at 300 kHz

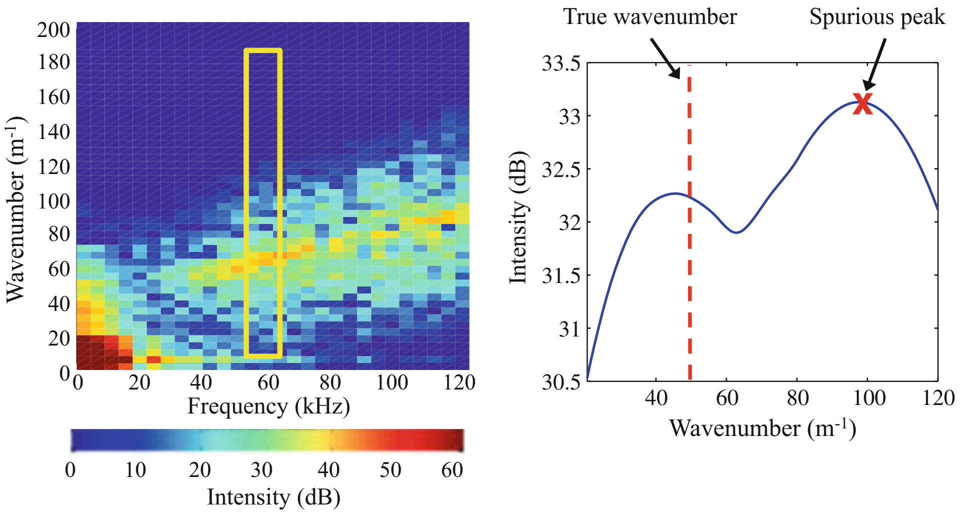

Fig. 10.9 Experimental variability in on site dataset (*left*) frequency-wavenumber map and (*right*) wavenumber-intensity at 80 kHz

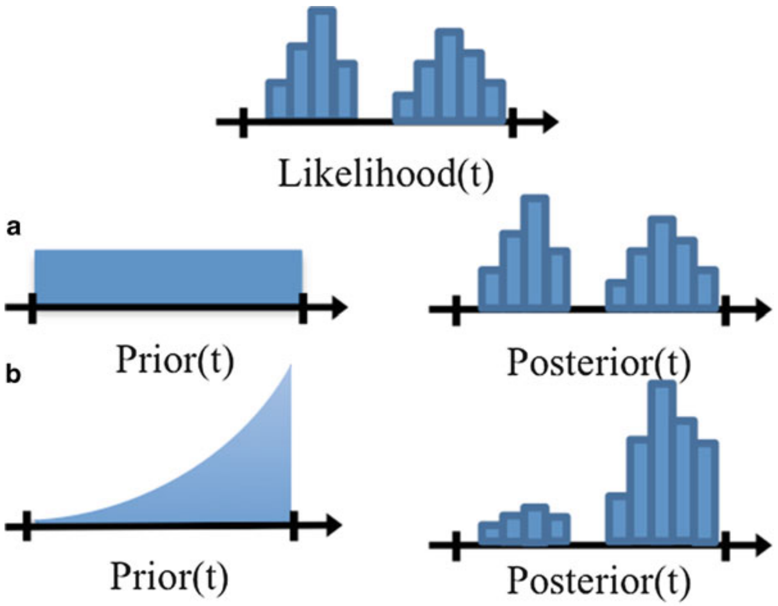

Fig. 10.10 Hypothetical posterior for a noisy likelihood with (**a**) uniform prior and (**b**) informative prior applied to the thickness parameter

potential corrosion. The noise manifests itself in the data almost always as spurious peaks at high wavenumbers. Therefore, if there are multiple peaks, those at lower wavenumbers are expected to be representative of the true damage and thus, should be weighted more by the prior. This knowledge is incorporated by implementing a prior distribution to the thickness parameter of the LWP model, effectively providing more weight to low wavenumber peaks and less weight to high wavenumber peaks (which are likely to be related to noise), resulting in a more realistic posterior distribution.

One example of the effect of defining such prior knowledge is shown in Fig. 10.10. In this example, the likelihood function, as determined by the MCMC is shown at the top of the figure. The likelihood is shown to have two peaks, representative of the case where multiple peaks occur in the wavenumber-intensity measurements. Two prior distributions of the thickness are shown: one in which a uniform prior is assumed (Fig. 10.10a), representing prior knowledge only of the upper and lower bound on the parameter but no expected behavior in between, and another where expert knowledge regarding the low wavenumber peaks being associated with noise is incorporated (Fig. 10.10b).

It is emphasized that for damage to be detected with the prior distribution of Fig. 10.10b, the majority of experimental evidence must be related to severe damage in the structure in order for the posterior to infer severe damage. Thus, in the case where experimental evidence indicates little to no damage with one peak and spurious peaks relate to severe damage, the informative prior aids in selection of the correct solution. It is important to note that spurious peaks almost always occur at higher wavenumbers, relating to damage. Therefore, if severe damage truly exists, there would be no low wavenumber peaks in the data, resulting in a wavenumber-intensity curve with only a single peak, which would not be affected by the prior distribution.

10.5 Case Study Application: Quantifying Severity of Damage in an Aluminum Plate Under Uncertainty

10.5.1 Model Development

Wavenumber for a particular mode of a thin-walled structure may be empirically determined by finding the root of the Rayleigh-Lamb equations (recall Eqs. 10.2 and 10.3). In the LWP model, formulation of the Rayleigh-Lamb equations necessitates the use of an optimization algorithm to solve for the wavenumber. In this study, a genetic algorithm, which is found effective in identifying local minima despite the highly nonlinear nature of the objective function with several local minima, is used.

The genetic algorithm is an optimization method based on the theory of natural selection where populations, containing a set of individuals representing possible designs, are refined through multiple generations until converging to a population of solutions that best solve an objective [36]. First, an initial population is developed by randomly selecting individuals. Individual designs are evaluated to determine which best optimizes the objective function. A select number of individual designs that provide the best solution are kept for the next generation as elite individuals. The next generation is developed using elite individuals, crossovers, and mutations. Crossovers and mutations are formed from individuals in the previous (or parent) generation. Crossovers combine features from two parents to produce an individual that is expected to outperform the parents individually. Mutations randomly change parameters of a parent, which helps to avoid convergence to local minima.

The model presented herein implements a genetic algorithm for the optimization of Eq. (10.10). The genetic algorithm is set to evaluate a maximum of 200 generations, with 500 individuals in each population and 50 elite individuals kept for every generation. To ensure that the genetic algorithm explores the entire input space, the first generation is populated using a latin-hypercube design. In this application, only the A_0 mode is considered, as it is the first mode of the system and the out of plane vibrations of this mode are most readily picked up by LDV measurements [37]. Wavenumber, k_A, is determined using genetic algorithm optimization to minimize the objective function:

$$k_A = \min_{k_A} \left| \frac{\tan(\beta t/2)}{\tan(\alpha t/2)} + \frac{\left({k_A}^2 - \beta^2\right)^2}{4\alpha\beta {k_A}^2} \right| \tag{10.10}$$

Subject to: $0 \le \mathrm{k_A} \le 500\ \mathrm{m}^{-1}$

10.5.2 Parametric Uncertainty

10.5.2.1 Experimental Campaign

The specimen used in this case study is a 600 mm by 600 mm aluminum plate with a thickness of 4 mm. AWS measurements are collected over a laser scan area located in a 240 mm by 240 mm square whose center is co-located with the center of the entire plate. Towards the center of the plate, a 100 mm by 200 mm area has been milled to a thickness of 2 mm to represent damage as a result of thinning, as shown in Fig. 10.11. The smooth side of the plate, where no damage is visually detectable, is used as the scan surface for wavenumber measurements. While no damage is visible from the testing side (Fig. 10.12b), the milled area is clearly noticeable on the reverse side (Fig. 10.12a). Material properties for the aluminum plate are provided in Table 10.2.

Analysis of parametric uncertainty is completed independent of experimental uncertainty by conducting experiments in a well-controlled laboratory setting where a SLGU laser is used to excite the structure at each pixel. The 240 mm by 240 mm scan area is sampled spatially by a pixel spacing of 1 mm in both the x and y directions. For each pixel location,

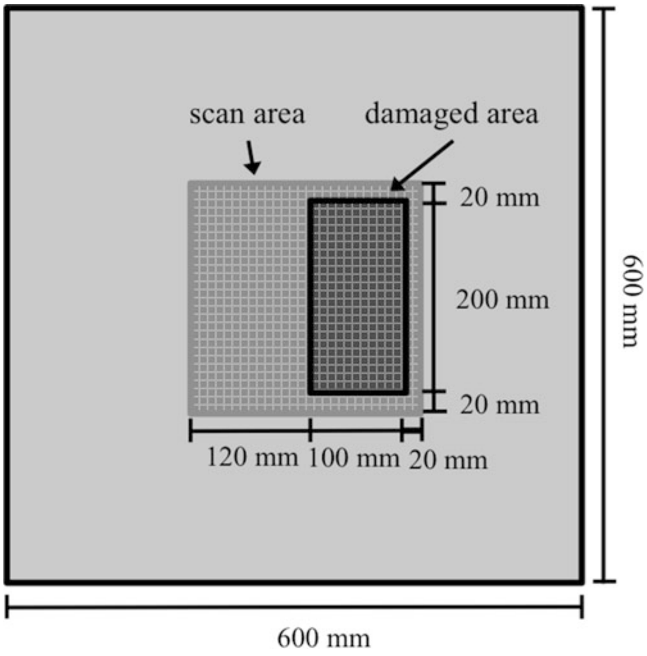

Fig. 10.11 Dimensions of damaged aluminum plate specimen

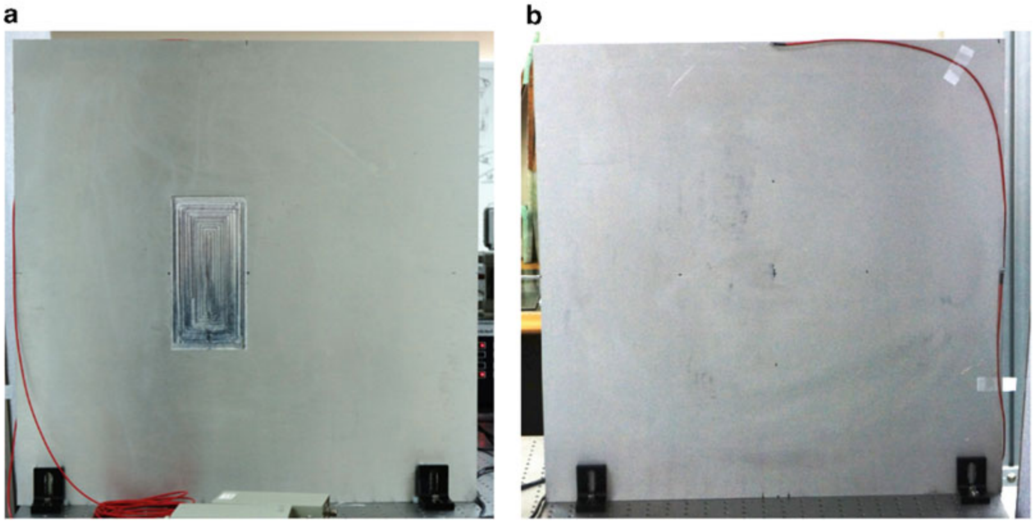

Fig. 10.12 Scan area of plate specimen with damaged area milled to 2 mm thickness. (**a**) Reverse side where damage is visible. (**b**) Scan side where damage is not visible

Table 10.2 Material properties of test specimen

Property	Nominal value
Elastic modulus (E)	69 GPa
Density (ρ)	2700 kg/m^3
Poisson's ratio (υ)	0.33

500 time samples are recorded by a LDV at a stationary location 180 mm above the center of the scan area. This sampling results in a 240 × 240 × 500 matrix of data. For the case where the sensor is a fixed point, the full-field time history of a wave propagating through the structure from a virtual excitation point at the sensor is obtained through reciprocity [16]. A diagram of the scan setup is shown in Fig. 10.13. Data collected in this experimental setup results in the well-defined dispersion curve and wavenumber-intensity diagram, shown previously in Fig. 10.4a.

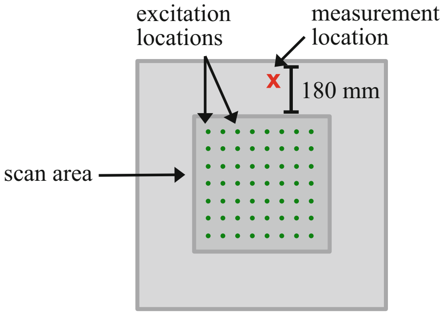

Fig. 10.13 Experimental measurement setup for high quality, laboratory data used to study parametric uncertainty

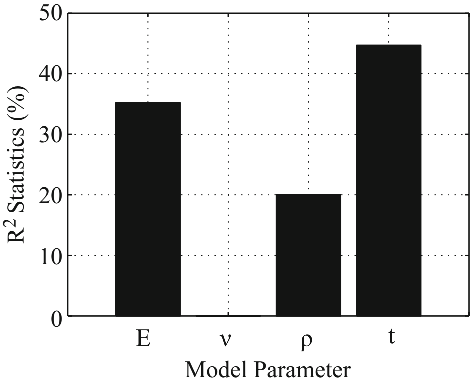

Fig. 10.14 Model sensitivity to material properties

Table 10.3 Results of elastic modulus calibration without preexisting knowledge of severity of damage

Plate properties		Prior uncertainty		Posterior uncertainty		
Condition	Aluminum (truth)	Magnesium (min)	Steel (max)	Mean	Standard deviation	Error
Undamaged	69 GPa	45 GPa	200 GPa	66.1 GPa	7.5 GPa	4.2 %
Damaged	69 GPa	45 GPa	200 GPa	67.2 GPa	5.6 GPa	2.6 %

10.5.2.2 Results and Discussion

In the case of parametric uncertainty, material properties of the structure are assumed to be unknown. This is representative of many real-life scenarios where the original design of a structure is unavailable or unknown. Of course, the degree of damage present in the structure is considered to be unknown, meaning that the thickness parameter is also uncertain.

Parametric uncertainty stems from lack of knowledge of the best values defining influential model parameters, in this case, material properties (elastic modulus, E, density, ρ, and Poisson's ratio, υ) as well as the severity of damage in the plate (thickness, t). A sensitivity analysis is performed using analysis of variance to test the effect each parameter has on the model predictions. As shown in Fig. 10.14, material properties E and ρ are the two parameters related to material properties that are influential to the model response (wavenumber, k). Additionally, thickness, which is the indicator of damage, is found to be most influential, thus confirming that the damage metric is highly sensitive. Poisson's ratio, υ, is found to have little to no influence on the wavenumber model and thus, is considered as a constant parameter for the remainder of the analysis.

First, a simplified case where only the elastic modulus of the material is unknown is considered as a proof-of-concept. Elastic modulus is a parameter that is often highly uncertain in existing structures. For this reason, a large range of potential elastic modulus values is assumed, bounded by the Magnesium and Steel metals as shown in Table 10.3. The elastic modulus is given a normal prior distribution about the mean of the bounded range. Excitation frequency, ω, is used as a control parameter. Five excitation frequencies were selected for measurements at a single pixel with the goal of fitting the model to the shape of the dispersion curve, rather than a single point. Therefore, local wavenumber estimates at 150 kHz, 200 kHz, 250 kHz, 300 kHz, and 350 kHz are all used as experimental data for calibration. Five thousand MCMC samples are completed. For the purpose of decreasing computational time, a Gaussian Process Model (GPM) is used as a surrogate for the LWP model. The GPM is trained using a seven level full-factorial design of experiments in the LWP model.

Emphasis is placed on the fact that no prior knowledge of the thickness is required to calibrate the elastic modulus, since these two parameters are calibrated simultaneously. To emphasize this point, the elastic modulus and thickness were calibrated simultaneously for two different points on the plate, one undamaged (thickness of 4 mm) and one damaged

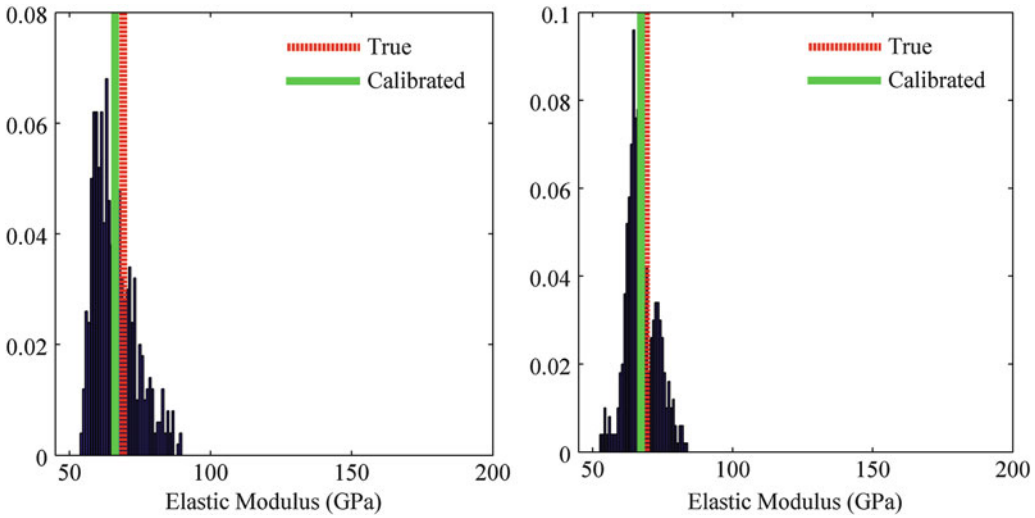

Fig. 10.15 Posterior distributions of elastic modulus inferred from wavenumber data using (*left*) measurements at an undamaged location and (*right*) measurements at a damaged location

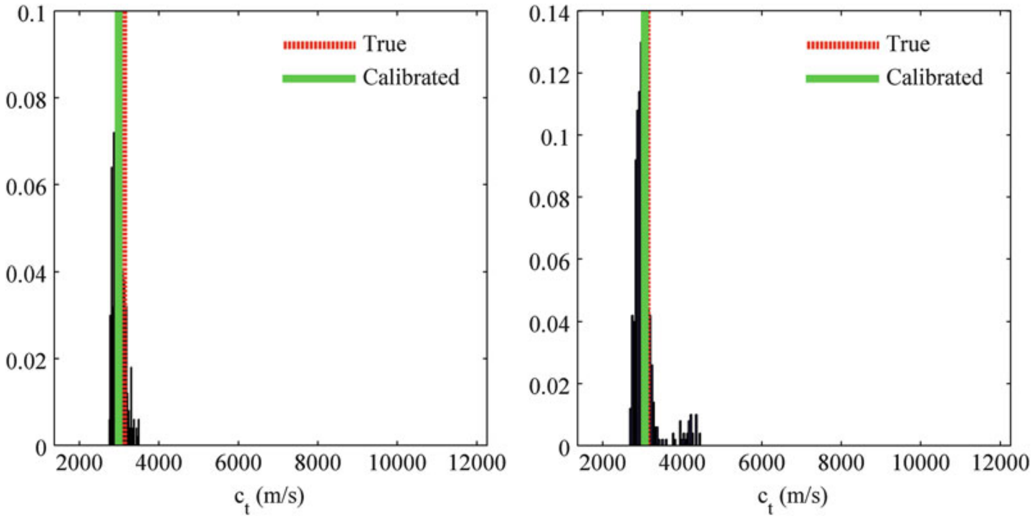

Fig. 10.16 Posterior distributions of transverse wave velocity inferred from wavenumber data using (*left*) measurements at undamaged locations and (*right*) measurements at damaged location

(thickness of 2 mm). Calibrated values of the elastic modulus are determined to be the mean value of the posterior distribution. Results show that through Stochastic Wavenumber Estimation, elastic modulus is estimated within 5 % of the true value without any knowledge of the severity of damage (i.e. thickness) or any data from the undamaged structure for establishing a baseline. Resulting posteriors are shown in Fig. 10.15 and the corresponding calibrated values are detailed in Table 10.3. Calibration using data at a damaged location of the plate resulted in 4.2 % error and calibration using data collected at an undamaged location resulted in 2.6 % error.

After successfully quantifying elastic modulus and thickness under uncertainty, the method is extended to consider all influential model parameters (elastic modulus, E, density, ρ, and thickness, t) as uncertain. Referring back to Eqs. 10.6 and 10.7, it is clear that E and ρ are parameters that will compensate for one another, therefore making accurate identification of either parameter difficult. Said differently, the mathematical result of increasing the values defined for E will have a similar effect on model output as decreasing the values of ρ. In this application, the wave velocities, which are a function of material parameters, may be taken advantage of to circumvent this compensation issue. Since wave velocity is the only portion of the LWP model dependent upon E and ρ, material properties do not need to be directly determined. In fact, the longitudinal and transverse wave velocities are related by a factor, which becomes constant as long as Poisson's ratio is not varied (recall Eq. 10.4).

Table 10.4 Results of transverse wave velocity calibration without preexisting knowledge of severity of damage

Plate properties		Prior uncertainty		Posterior uncertainty		
Condition	Aluminum (truth)	MDF (minimum)	Carbon fiber (maximum)	Mean	Std. Dev.	Error
Undamaged	3100 m/s	1370 m/s	12,263 m/s	3061 m/s	319 m/s	1.3 %
Damaged	3100 m/s	1370 m/s	12,263 m/s	3049 m/s	317 m/s	1.6 %

Table 10.5 Average error of deterministic and stochastic approaches for parametric uncertainty

	Undamaged area		Damaged area	
	Average error	Percent error	Average error	Percent error
Stochastic	−0.07 mm	−1.75 %	−0.06 mm	−3.00 %
Deterministic	−0.43 mm	−10.75 %	−0.34 mm	−17.00 %

Using this mathematical representation, only transverse wave velocity, c_t, is considered as a calibration parameter related to material properties. Longitudinal wave velocity, c_l, is determined by scaling c_t according to Eq. (10.4). Calculating the wave velocities in this manner ensures that the physical relationship between the two is preserved. Following the same process as before, transverse wave velocity and thickness are inferred simultaneously such that the degree of damage in the structure does not need to be known a priori.

Resulting posteriors for transverse wave velocity are shown in Fig. 10.16 and the corresponding calibrated values are detailed in Table 10.4. Calibration using data at a damaged location of the plate resulted in 1.3 % error and calibration using data collected at an undamaged location resulted in 1.6 % error.

For a homogeneous structure, once material properties have been determined for a single pixel, they may be applied as a "known" parameter for all other pixels, such that only thickness needs to be calibrated. The ability to determine uncertain material properties is the most distinct advantage of Stochastic Wavenumber Estimation over the currently implemented deterministic approach.

To demonstrate this advantage, let's assume that an inspector is lacking knowledge regarding the exact material properties of a system. The inspector assumes an elastic modulus of 75.9 GPa, (10 % overestimation from the true value of 69 GPa). In the stochastic approach, elastic modulus is calibrated from the range shown in Table 10.3, rather than assuming a constant, preset value. For calibration of modulus and thickness in this case, a 10 level full factorial design is used to train the GPM and 2000 MCMC samples were required to converge to a calibrated elastic modulus of 70 GPa.

Results shown in Table 10.5 demonstrate the danger of assuming material properties in the deterministic approach. The ability to recognize uncertainty in the problem and address it accordingly results in the stochastic approach estimating thickness significantly closer to the true value than the deterministic. In this case the result is an underestimation of thickness (therefore overestimation of damage), however, it could easily be the case where elastic modulus was underestimated by the inspector, leading to an overestimation of thickness (underestimation of damage).

10.5.3 Experimental Uncertainty

10.5.3.1 Experimental Campaign

The second aspect of the case study focuses on experimental uncertainty. Experimental uncertainty is introduced in this problem through the creation of an experimental setup replicating conditions that are often encountered in one-site testing. Specifically, a reduced cost setup is utilized where the structure is excited at a single location 50 mm above the center of the scan area and 200 time samples are collected by the LDV at each pixel. In this case, the scan area is discretized into pixels with a 2 mm spacing in the x and y directions. A diagram of the scan setup is shown in Fig. 10.17. Data collected in this experimental setup results in the noisy dispersion curve and wavenumber-intensity diagram with spurious peaks, shown previously in Fig. 10.9.

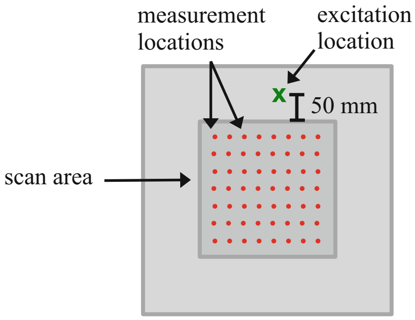

Fig. 10.17 Experimental measurement setup for low quality, noisy data used to study experimental uncertainty

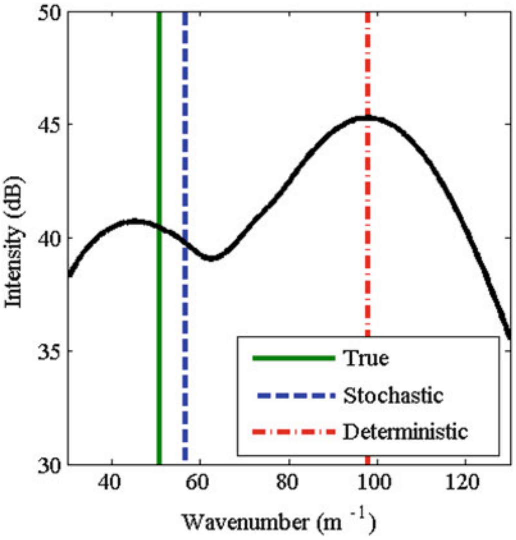

Fig. 10.18 Wavenumber-intensity snapshot at one pixel, where deterministic estimation fits to spurious peak causing false positive for damage

10.5.3.2 Results and Discussion

In wavenumber analysis, the most common form of noise is revealed as lower wavelength, therefore higher wavenumber. When using the deterministic approach, noise which may have a higher intensity than the true wavenumber will be selected, resulting in a false positive for damage. Figure 10.18 illustrates the improvement in wavenumber estimation for one specific pixel, where the deterministic approach selects a wavenumber related to noise (which would result in a false positive for damage) while the Bayesian inference is able to better estimate the true wavenumber.

Stochastic Wavenumber Estimation improves upon the deterministic approach by incorporating engineering judgment into the problem in the form of prior knowledge, as detailed in Sect. 10.4.3. For this application, in the case of corrosion, it is considered more likely that only slight thinning has occurred, as opposed to severe damage, given the environmental conditions. For these reasons, a beta prior (Eq. 10.11) with parameters α equal to 5 and β equal to 1 is implemented for this case study.

$$\mathrm{f}\left(\theta\middle|\alpha,\beta\right)=\frac{\Gamma\left(\alpha+\beta\right)}{\Gamma\left(\alpha\right)\Gamma\left(\beta\right)}\theta^{\alpha-1}(1-\theta)^{\beta-1},\ 0<\theta<1 \tag{10.11}$$

Using the experimental setup described in Sect. 10.5.3.1, wavenumber-intensity curves similar to that in Fig. 10.4b are obtained for every pixel to define the experimental variability at each x–y grid point location. Assuming all model parameters are known, or determined through the procedure previously described in Sect. 10.5.2, the wavenumber estimate obtained for the pixel may used to quantify the thickness of the plate at each pixel. In this case study, the milled plate specimen was tested with a grid spacing of 120 × 120 pixels. Figures 10.19 and 10.20 demonstrate the improvement in both damage localization and quantification with the application of Bayesian inference with an informed prior.

As shown in Fig. 10.21, the stochastic approach tends to perform better in the undamaged region of the plate while the deterministic approach performs slightly better in the damaged region. More specifically, the deterministic approach tends to underestimate the plate thickness in the undamaged region and the stochastic approach tends to overestimate the thickness in the damaged region. Underestimation of thickness with the deterministic approach is likely due to the method fitting to noise

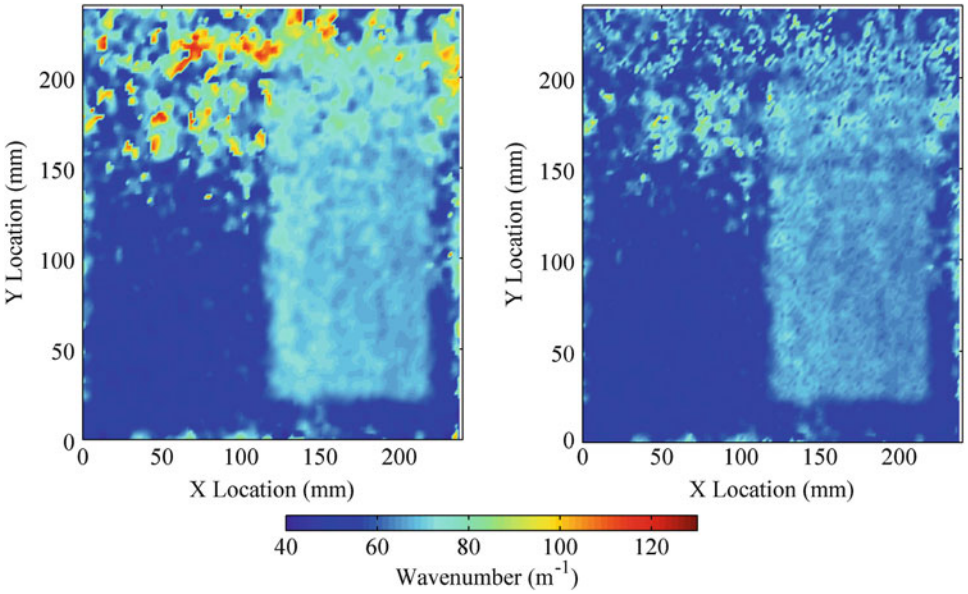

Fig. 10.19 Wavenumber estimation (*left*) deterministic approach (*right*) stochastic approach with informed prior

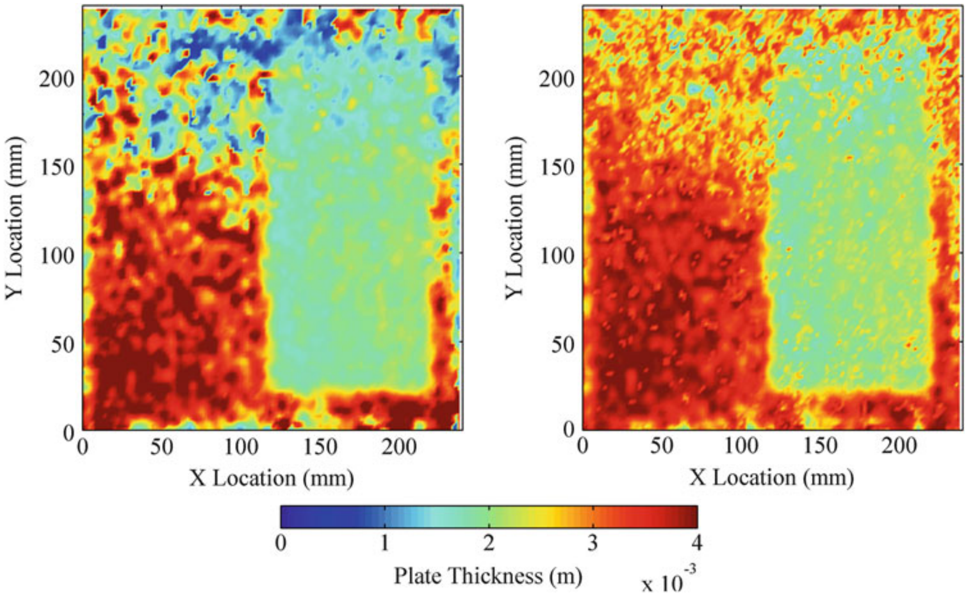

Fig. 10.20 Thickness estimation (*left*) deterministic approach (*right*) stochastic approach with informed prior

and thus, generating false signs of damage. Overestimation of thickness in the damage region using the stochastic approach is likely an effect of the strong prior implemented. It should be noted, however, that the degree to which the stochastic approach incorrectly overestimates is less than half that of which the deterministic approach underestimates. This finding is further illustrated in Fig. 10.22, where the deterministic approach produces an average percent error of 23.3 % and the stochastic approach performs better overall with an average percent error of 16.9 %.

In addition to improving nominal thickness predictions, stochastic wavenumber estimation also bears the benefit of quantifying uncertainty in the posterior estimates. This uncertainty quantification, illustrated in Fig. 10.23, provides a sense of confidence in the predictions. Most important to note is that pixels having high standard deviation in the posterior distribution are those resulting in false, and missed, damage detection in the nominal predictions. Incorporating this knowledge of uncertainty into the damage assessment may help a decision-maker differentiate between damaged locations and false positives. Finally, considering the uncertainty in the posterior distributions we may evaluate an upper and lower bound on the predicted thickness in addition to the nominal predictions. Figure 10.24 demonstrates these bounds, set at one standard

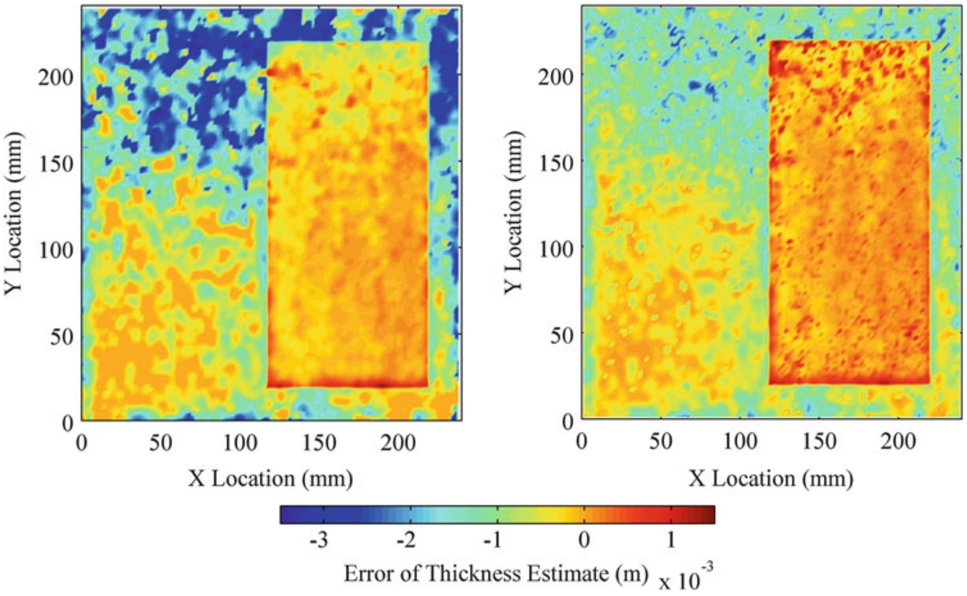

Fig. 10.21 Error of thickness quantification for (*left*) deterministic approach (*right*) stochastic approach with informed prior

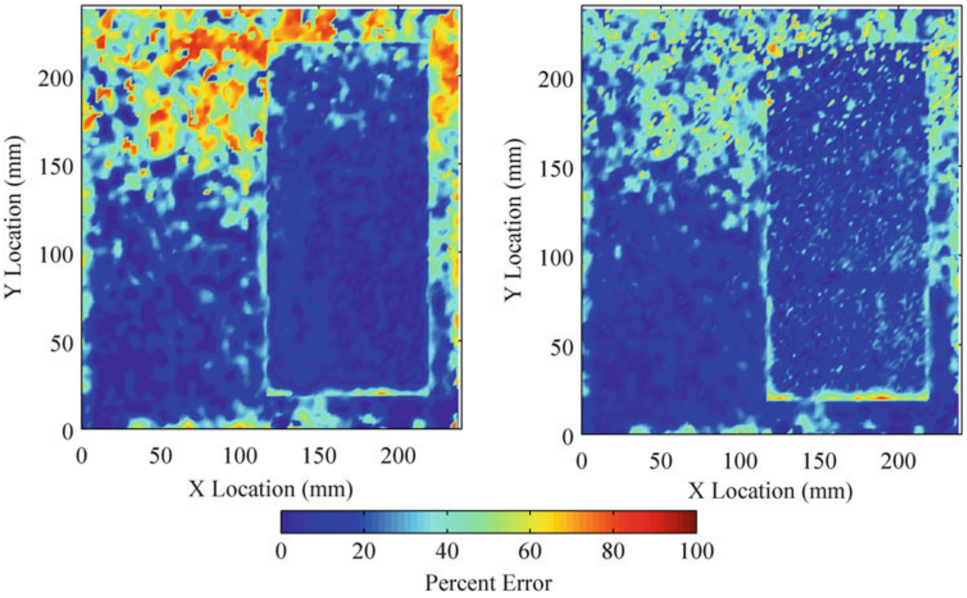

Fig. 10.22 Percent error of thickness quantification for (*left*) deterministic approach (*right*) stochastic approach with informed prior

deviation from the posterior mean. Similar to evaluating the standard deviation at each pixel, this figure provides the decision-maker with a differentiation between measurements detecting true damage and those being interfered with by noise in the measurements.

10.6 Conclusion

Internal defects, often unobservable during visual inspections, threaten the performance of structural systems and may result in catastrophic failure if left untreated. Corrosion and delamination are examples of local damages that affect the performance of pipe systems, wind turbine blades, aircraft, and many other infrastructure systems impacting society. Existing structural health monitoring techniques attempt to mitigate hazards due to internal damage by detecting and quantifying the damage

Fig. 10.23 Standard deviation of stochastic thickness estimates

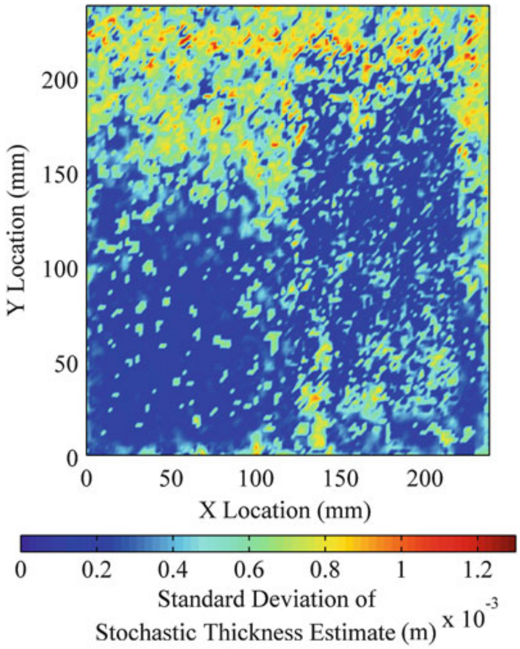

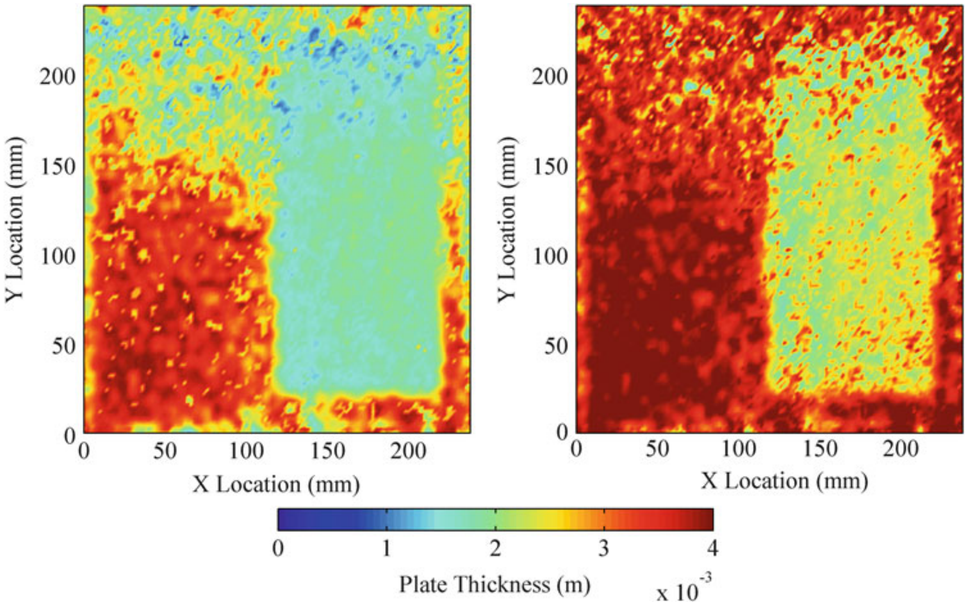

Fig. 10.24 Lower (*left*) and upper (*right*) level bounds of stochastic thickness estimate when considering predictions within one standard deviation of the posterior mean

through non-destructive techniques. Many existing methods, however, are unable to adequately capture the damage due to insensitivity of global response metrics to small, localized damage. Acoustic Wavenumber Spectroscopy (AWS) has been shown to be able to detect these local damages because of the local nature of measurements and high sensitivity of wavenumber to damage. As such, AWS offers a real potential to prevent failure of a system due to continued undetected damage. The main drawback is that AWS currently is unable to *quantify* the level of damage in a structure.

This paper introduced a method for incorporating parametric and experimental uncertainty in AWS inverse problems through the use of Stochastic Wavenumber Estimation. Inverse analysis applied to AWS measurements can not only detect, but also quantify the severity of local damage in thin walled structures. Uncertainties, however, pose a problem for the method when there exists uncertainties in material properties or spurious peaks in experimental data. The methodology has been demonstrated herein through a case study in which thinning of an aluminum plate was detected and its severity quantified. The proposed approach successfully mitigates the degrading effects of parametric uncertainty, demonstrating the ability to quantify material properties without requiring a baseline "healthy" structure for calibration. Furthermore, calibration of the transverse wave velocity rather than specific material properties eliminates the possibility of compensating effects that occur when considering elastic modulus and density. Due to its deterministic nature, current AWS methodology is also poorly suited to operate in conditions containing experimental uncertainty resulting from measurement tools commonly used in practice. The approach presented herein is shown to improve thickness estimates from wavenumber data exhibiting spurious peaks by considering expert judgment in prior distributions. Most importantly, the new method is shown to result in less false positives of damage than the existing deterministic approach and provides a means of quantifying uncertainty remaining in the predictions.

While the calibration framework presented herein is shown to improve the damage detection and quantification of current state of the art methods, assumptions and limitations remain which should be addressed in future studies, as summarized below.

- *Consideration of uncertainties simultaneously.* This paper assumes that parametric and experimental uncertainties can be analyzed independently. In realistic field applications, both types of uncertainties will likely be present simultaneously. Considering multiple uncertainties simultaneously within the framework presented is possible, but further work should be done to verify this approach.
- *Additional sources of uncertainty should also be considered*. Particularly, experimental uncertainty has been presented herein as spurious peaks in data due to the quality of equipment available for testing. Another problem commonly occurring in practice is the inability to set up experiments such that scans are conducted perfectly perpendicular to the structure, especially for curved surfaces. The nature of experimental noise introduced by this operational condition may vary from that which we have presented and thus, requires further investigation.
- *Applications with increased complexity in the structure.* Structures composed of composite materials, which are produced by bonding different materials, may have differences in the manner that guided Lamb waves propagate. If the layering of materials were to alter the wave propagation, the numerical model used to develop training data would likely exhibit some form of model form error. Thus, future studies including composite structures may potentially require more influence from the discrepancy function to account for this model form error.
- *Structures having less severe damage than that presented herein.* For example, corrosion of pipes will likely occur as gradual damage where there is not a dramatic change from one thickness to another. While AWS has been proven capable of detecting gradual damage [38], the new method implementing Bayesian inference should also be evaluated for this application.

References

1. Farrar, C.R., Worden, K.: An introduction to structural health monitoring. Philos. Trans. R. Soc. Math. Phys. Eng. Sci. **365**(1851), 303–315 (2007)
2. Rytter, A.: Vibration based inspection of civil engineering structures. Ph.D., Aalborg University, Denmark (1993)
3. Atamturktur, H.S., Gilligan, C.R., Salyards, K.A.: Detection of internal defects in concrete members using global vibration characteristics. ACI Mater. J. **110**(5), (2013)
4. Doebling, S.W., Farrar, C.R., Prime, M.B., Shevitz, D.W.: Damage Identification and Health Monitoring of Structural and Mechanical Systems from Changes in Their Vibration Characteristics: A Literature Review. Los Alamos National Lab., NM (United States) (1996)
5. Sohn, H.: A Bayesian probabilistic approach for structure damage detection (1997)
6. Alampalli, S.: Effects of testing, analysis, damage, and environment on modal parameters. Mech. Syst. Signal Process. **14**(1), 63–74 (2000)
7. Stubbs, N., Kim, J.T.: Damage localization in structures without baseline modal parameters. AIAA J. **34**(8), 1644–1649
8. Friswell, M.I.: Damage identification using inverse methods. Philos. Trans. R. Soc. Math. Phys. Eng. Sci. **365**(1851), 393–410 (2007)
9. Prabhu, S., Atamturktur, S.: Selection of optimal sensor locations based on modified effective independence method: case study on a gothic revival cathedral. J. Archit. Eng. **19**(4), 288–301 (2013)
10. Nataraja, R.: Structural integrity monitoring in real seas. In: Proceedings of the 15th Annual Offshore Technology Conference, pp. 221–228 (1983)
11. Atamturktur, S., Bornn, L., Hemez, F.: Vibration characteristics of vaulted masonry monuments undergoing differential support settlement. Eng. Struct. **33**(9), 2472–2484 (2011)
12. Beck, J.L., Au, S.K., Vanik, M.W.: A Bayesian probabilistic approach to structural health monitoring. In: American Control Conference, 1999. Proceedings of the 1999, vol. 2, pp. 1119–1123 (1999)
13. Atamturktur, S., Pavic, A., Reynolds, P., Boothby, T.: Full-scale modal testing of vaulted gothic churches: lessons learned. Exp. Tech. **33**(4), 65–74 (2009)
14. Kino, G.S.: Acoustic imaging for nondestructive evaluation. Proc. IEEE **67**(4), 510–525 (1979)
15. Croxford, A.J., Wilcox, P.D., Drinkwater, B.W., Konstantinidis, G.: Strategies for guided-wave structural health monitoring. Proc. R. Soc. Math. Phys. Eng. Sci. **463**(2087), 2961–2981 (2007)

16. Flynn, E.B., Chong, S.Y., Jarmer, G.J., Lee, J.-R.: Structural imaging through local wavenumber estimation of guided waves. NDT E Int. **59**, 1–10 (2013)
17. Tarantola, A.: Inverse Problem Theory and Methods for Model Parameter Estimation. Siam (2005)
18. Huang, Q., Gardoni, P., Hurlebaus, S.: A probabilistic damage detection approach using vibration-based nondestructive testing. Struct. Saf. **38**, 11–21 (2012)
19. Lee, J.-R., Jeong, H., Ciang, C.C., Yoon, D.-J., Lee, S.-S.: Application of ultrasonic wave propagation imaging method to automatic damage visualization of nuclear power plant pipeline. Nucl. Eng. Des. **240**(10), 3513–3520 (2010)
20. Lamb, H.: On waves in an elastic plate. Proc. R. Soc. Lond., 114–128 (1917)
21. Achenback, J.: Wave Propagation in Elastic Solids. Elsevier (1984)
22. Lee, J.-R., Yenn Chong, S., Jeong, H., Kong, C.-W.: A time-of-flight mapping method for laser ultrasound guided in a pipe and its application to wall thinning visualization. NDT E Int. **44**(8), 680–691 (2011)
23. Monchalin, J.P.: Non contact generation and detection of ultrasound with lasers. In: Proceedings of the 16th World Conference on Nondestructive Testing, pp. 1–9 (2004)
24. Draper, D.: Assessment and propagation of model uncertainty. J. R. Stat. Soc. Ser. B Methodol. **57**(1), 45–97 (1995)
25. Kennedy, M.C., O'Hagan, A.: Bayesian calibration of computer models. J. R. Stat. Soc. Ser. B Stat. Methodol. **63**(3), 425–464 (2001)
26. Farajpour, I., Atamturktur, S.: Error and uncertainty analysis of inexact and imprecise computer models. J. Comput. Civ. Eng. **27**(4), 407–418 (2013)
27. Higdon, D., Gattiker, J., Williams, B., Rightley, M.: Computer model calibration using high-dimensional output. Am. Stat. Assoc. **103**(482), 570–583 (2007)
28. Unal, C., Williams, B., Hemez, F., Atamturktur, S.H., McClure, P.: Improved best estimate plus uncertainty methodology, including advanced validation concepts, to license evolving nuclear reactors. Nucl. Eng. Des. **241**(5), 1813–1833 (2011)
29. Bayarri, M.J., Berger, J.O., Paulo, R., Sacks, J., Cafeo, J.A., Cavendish, J., Lin, C.-H., Tu, J.: A framework for validation of computer models. Technometrics **49**(2), 138–154 (2007)
30. Higdon, D., Kennedy, M., Cavendish, J.C., Cafeo, J.A., Ryne, R.D.: Combining field data and computer simulations for calibration and prediction. SIAM J. Sci. Comput. **26**(2), 448–466 (2004)
31. Bastos, L.S., O'Hagan, A.: Diagnostics for Gaussian process emulators. Technometrics **51**(4), 425–438 (2009)
32. DiazDelaO, F.A., Adhikari, S.: Structural dynamic analysis using Gaussian process emulators. Eng. Comput. **27**(5), 580–605 (2010)
33. Van Buren, K.L., Atamturktur, S., Hemez, F.M.: Model selection through robustness and fidelity criteria: modeling the dynamics of the CX-100 wind turbine blade. Mech. Syst. Signal Process. **43**(1–2), 246–259 (2014)
34. Metropolis, N., Rosenbluth, A.W., Rosenbluth, M.N., Teller, A.H., Teller, E.: Equation of state calculations by fast computing machines. J. Chem. Phys. **21**(6), 1087 (1953)
35. Gelfand, A.E., Smith, A.E.: Sampling-based approaches to calculating marginal densities. J. Am. Stat. Assoc. **85**(412), 398–409
36. Mitchell, M.: An Introduction to Genetic Algorithms, 3rd edn. MIT, Cambridge, MA (1998)
37. Gannon, A., Wheeler, E., Brown, K., Flynn, E.B., Warren, W.: A high-speed dual-stage ultrasonic guided wave system for localization and characterization of defects. In: Structural Health Monitoring and Damage Detection, vol. 7, pp. 123–136 (2015)
38. Flynn, E.B., Lee, J.R., Jarmer, G.J., Park, G.: Frequency-wavenumber processing of laser-excited guided waves for imaging structural features and defects. In: 6th European Workshop on Structural Health Monitoring (2012)

Chapter 11
Use of Continuous Scanning LDV for Diagnostics

Dario Di Maio

Abstract Nowadays, diagnostic is an important assessment of integrity of structural components. Amongst the technologies capable of monitoring structural integrity the continuous scanning (CS) measurement method can be a valid alternative in *quasi* real-time acquisition methods. Its major feature is the capacity of continuously recording vibration response by sweeping a laser beam over a surface. The LDV output signal will be amplitude modulated because of the periodicity of the scanning for a given vibration oscillation. The spectral content of the LDV output signal is made of sidebands, which can be used for representing an Operational Deflection Shape of the structure. This paper proposes a numerical study focused on the changes of the spectral signature of the sidebands when a damage occurs in a structure. The major objective is to map these changes against an undamaged spectral signature and evaluate if this approach can be used for diagnostic purposes.

Keywords Continuous scanning • ODS • Diagnostics • Damage • Real-time

11.1 Introduction

Diagnostic is important for assessing the structural integrity either at component or at system level. There are many technologies researched and available in literature some of which generated useful outcomes and, eventually, used for monitoring structural performances. It is not the scope of this paper to discuss such a broad topic but the final objective is to show how a novel measurement technology, the continuous scanning LDV measurement methods, can be used for performing diagnostics. Researchers have been using ODS technology for damage assessment as presented in [1, 2] and some of those used the continuous scanning technology as presented in [3, 4]. The continuous scanning measurement method is based on a contactless sensor, like a laser beam, which can be scanned continuously over a vibrating path. The laser beam will measure an amplitude modulated time signal, the modulation of which depends on the scanning rate. The set of spectral sidebands generated by such a modulation can be used for recovering Operational Deflection Shape (ODS) information. This approach was used by some authors for different applications one of which is damage detection [5]. In fact, the process of recovering ODS by CSLDV technique is rather fast and accurate thus allowing rapid implementation of diagnostics based on ODSs. The process of recovering the ODS is based on a transformation matrix which allows to transform the amplitudes of the spectral sidebands in polynomial coefficients thus a polynomial function describing the ODS.

The novelty in this paper regards the sidebands as indicator of structural integrity. The sidebands can be considered as good as measured without any further signal processing. In fact, one can say that for an undamaged, or pristine, structure the spectral sidebands for a given excitation frequency and force level would stay unchanged as long as the structure would not be subjected to any structural deterioration. These spectral sidebands can be assumed as the pristine signature of a healthy structure. In the presence of structural deterioration the original signature will change and the new sidebands will not correlate any longer with the pristine case. This can be repeated for any excitation frequency and any forcing level. The most immediate outbreak of using spectral sidebands is to enable a *quasi* real-time assessment of structural changes. The CSLDV measurement technique allows fast scanning of the laser beam which can continuously measure modulation LDV time signal. This work on diagnostic was exploited for assessing damage during vibration testing of structures under fatigue. An example of experimental data will show what is expected to observe when a structure changes its response shape while fatiguing. This observation led the investigation of this matter by virtual testing where measurement parameters can be more easily controlled.

D. Di Maio (✉)
University of Bristol, University walk, BS8 1TR Bristol, UK
e-mail: dario.dimaio@bristol.ac.uk

© The Society for Experimental Mechanics, Inc. 2016

J. De Clerck, D.S. Epp (eds.), *Rotating Machinery, Hybrid Test Methods, Vibro-Acoustics & Laser Vibrometry, Volume 8*,
Conference Proceedings of the Society for Experimental Mechanics Series, DOI 10.1007/978-3-319-30084-9_11

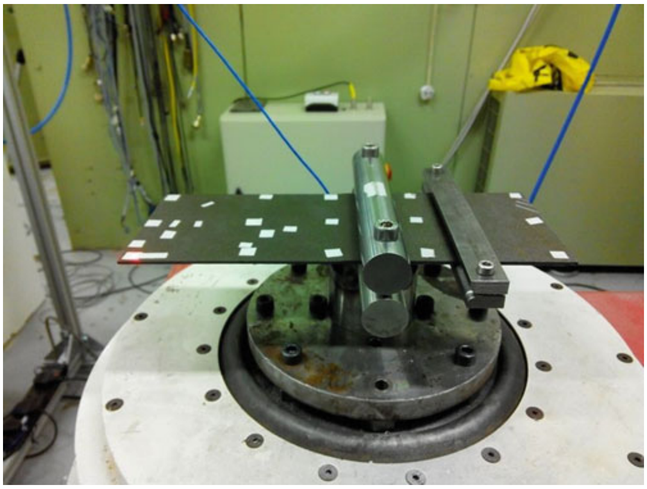

Fig. 11.1 Fixture and sample

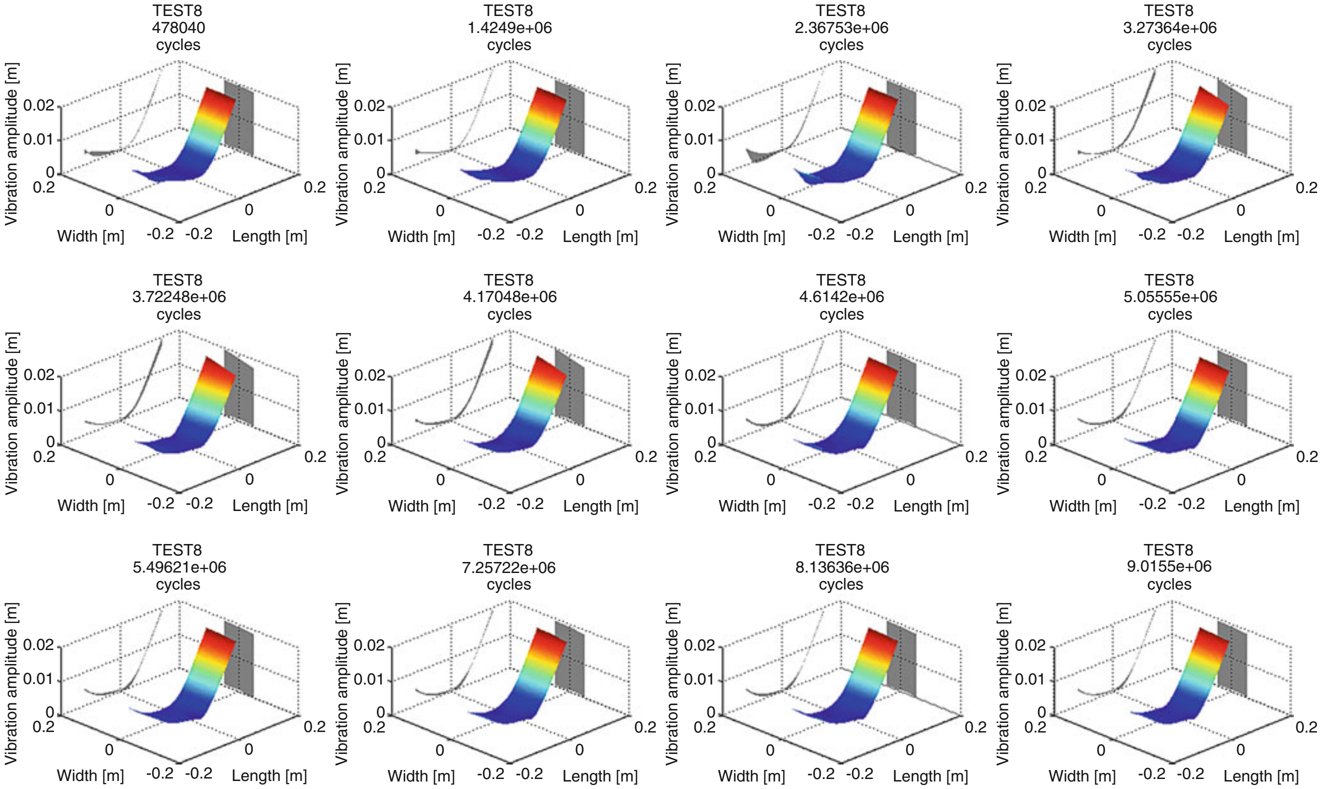

Fig. 11.2 ODS change

11.1.1 Background

As introduced earlier, the observation which led to the investigation of CSLDV measurement technology as real-time diagnostic tool is the endurance test of composites structures, as seen in Fig. 11.1 [6]. One of the measurement parameters monitored during such tests is the ODS, which is measured by step scanning method. The downside of that type of technology is the off-line post processing, which is required to visualize the test data. An example of ODS data which shows such a change during an endurance test is shown in Fig. 11.2.

By performing an area scan, by mean of CSLDV, of the longest side visible in Fig. 11.1, it was possible to acquire spectral sidebands (see Fig. 11.3) and track their possible change while testing. Despite the scatter due to noise, the third component

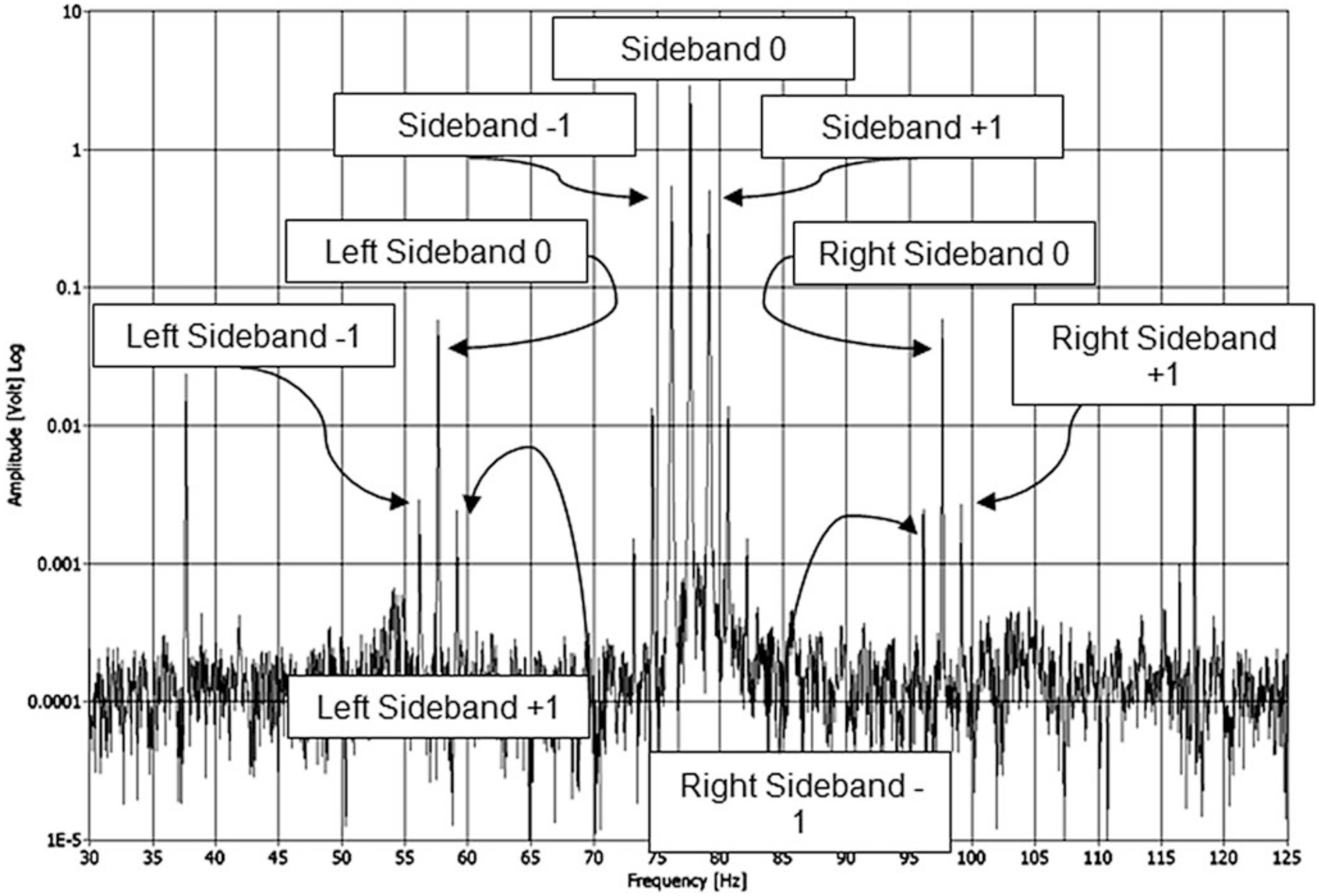

Fig. 11.3 Spectral sidebands and notation

of the central cluster of sidebands presented a clear systematic change, see Fig. 11.4. Trends of spectral harmonics changes were observed also for other tests. The endurance is a destructive type of test aimed at characterizing certain properties of materials, so this did not provide controllable experimental conditions for assessing a possible exploitation of CSLDV as diagnostic. It was decided to create a synthetic environment where to explore the capacity of CSLDV in the presence of an occurring damage condition. This will be presented in the next sections.

11.2 Design of Experiment

The experimental evidences were used to start a numerical work on damage detection based on the change of the sidebands. In an earlier work [6], simulations were calculated by modelling the response mode as similar as the one in the experiment showed in Fig. 11.2. However, in here, unconstrained specimen is considered adequate for performing a pilot study on the use of ODS sidebands for diagnostic purposes.

11.2.1 Design of Damage by Finite Element

The test coupon was designed with the following dimensions that are 300 × 100 × 5 mm. At this stage the material properties were considered isotropic, despite the real component was made of carbon fibre. The Young’s modulus was chosen from the list of metallic materials and was set 200 GPa, whereas the material density was set at 7800 kg/m^3 with a Poisson’s ratio of 0.3. The damage is an artefact and not intended to represent any failure observed during HCF conditions. So, the damage

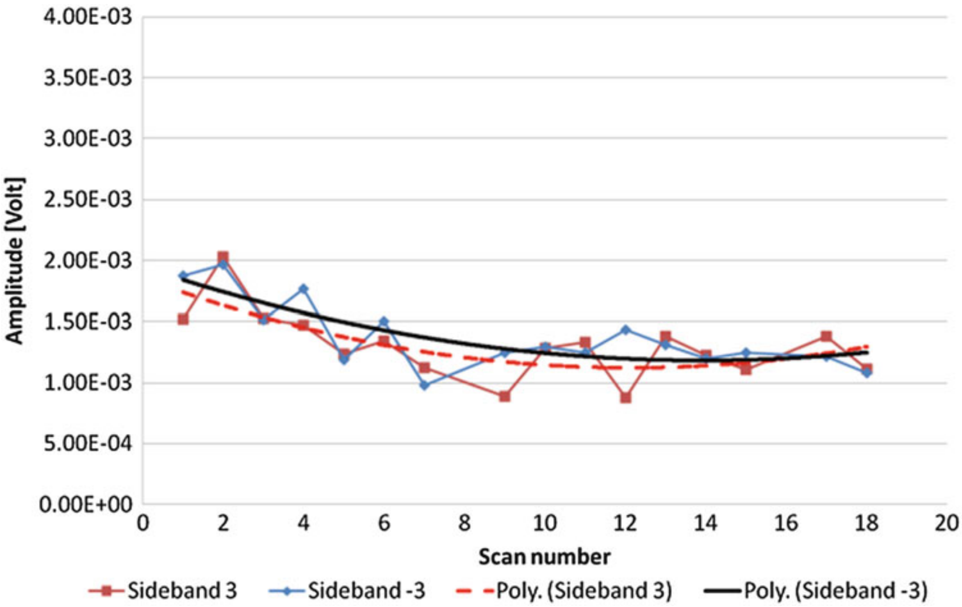

Fig. 11.4 Monitoring of third component

Table 11.1 Natural frequencies of the selected modes

Mode shape	Mode-0	Mode-1	Mode-2	Mode-3	Mode-4	Mode-5	Mode-6
Natural frequency (Hz)	29.64	53.78	82.24	113.54	161.69	184.94	263.90

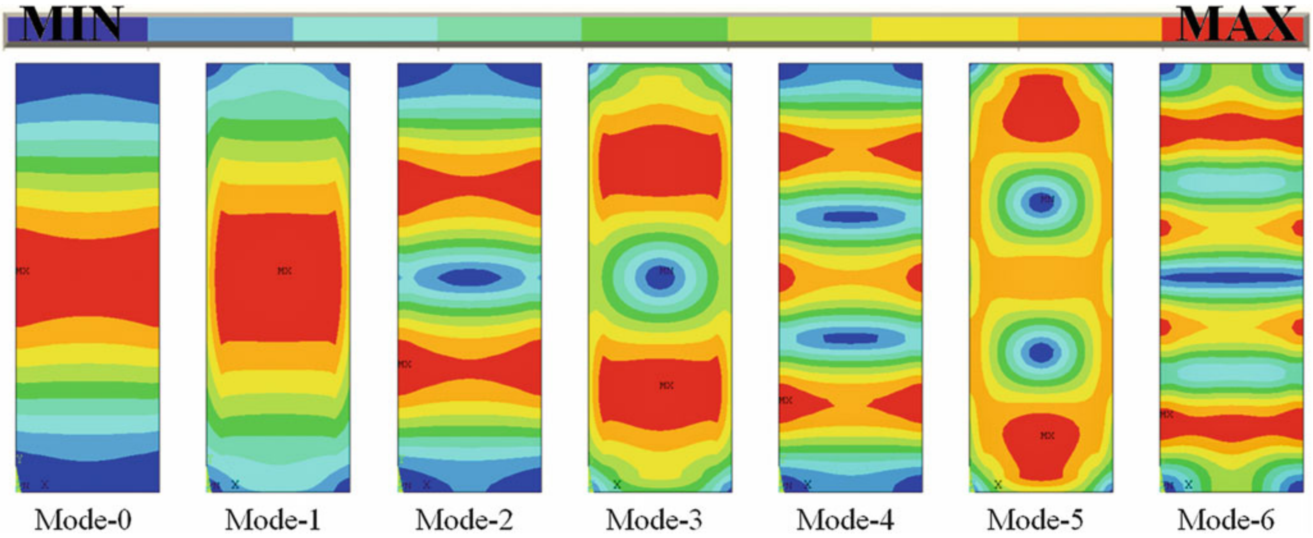

Fig. 11.5 Modal strain (Von Misses)

was created by changing the thickness of a number of elements. Two types of damages were created such as (1) damage-*n* and (2) damage-A*n*. The first one has got the "damaged" element thickness of 4.5 mm instead of 5 mm for a pristine one, whereas the second type the "damage" element thickness was set at 4 mm. Seven mode shapes were used for this work and their natural frequencies are reported in the Table 11.1.

Instead plotting the mode shapes, the modal strains (Von Misses) are plotted for the pristine condition. The damage location was chosen based on the modal strain amplitude. So, it is possible to see from Fig. 11.5 that by placing the damage at the centre of the specimen four out of seven modes would be experience some changes due to the damage location. That is verifiable by looking at Fig. 11.6 where the frequency change caused by the damage severity is plotted. Figure 11.7 shows the sizes of the damages used for the simulations, where the smallest one is represented by change of geometrical properties

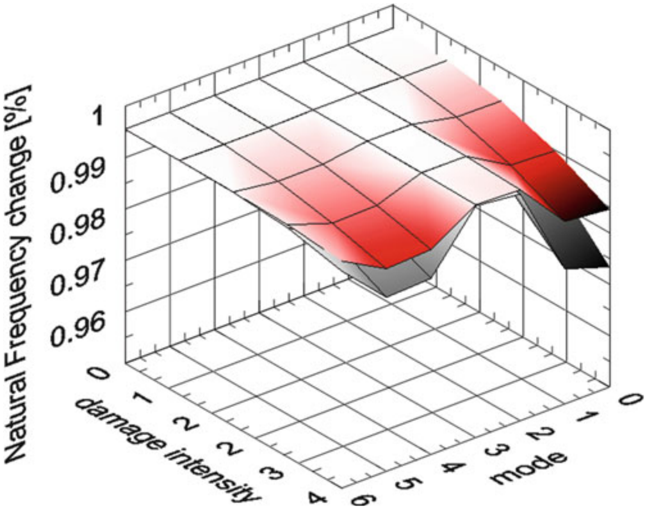

Fig. 11.6 Change of natural frequency for different modes and damage severity

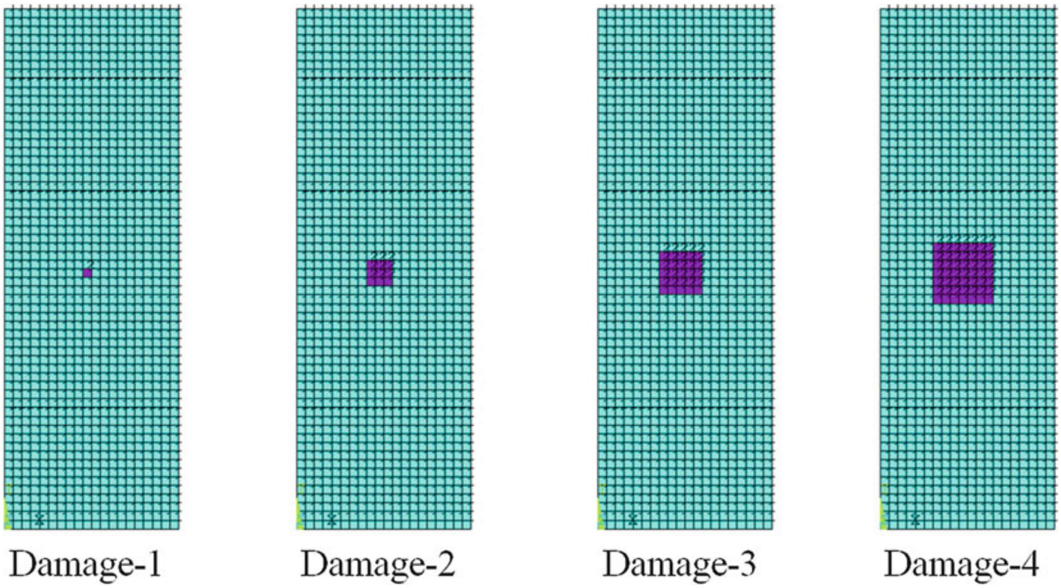
Damage-1 Damage-2 Damage-3 Damage-4

Fig. 11.7 Damage severity

of a single element (magenta) in the FE model. The modal displacements, $\{\phi\}_r$, of the seven simulated modes, were used for calculating the ODSs as showed by Eq. (11.1).

$$\{X\} = \sum_{r=1}^{N} \frac{\{\varphi\}_r^T \{F\} \{\varphi\}_r}{\omega_r^2 - \omega^2 + i\eta_r\omega_r^2} \tag{11.1}$$

where η_r is damping loss factor, which was set 0.001 for all modes. The output of Eq. (11.1) was used for simulating the LDV output signal for an excitation position always set at node number 1, which is the top left hand corner of the specimen. The next section will summarize the mathematics developed for the LDV time signal simulations.

11.2.2 Virtual Test Simulation

The virtual test simulation was developed to study the evolution of the spectral sidebands with respect of the damage growth. The type of test simulated in here is an area scan. The laser beam can be continuously scanned over a structure which is vibrating sinusoidally at any frequency. The measured LDV output signal can be quickly post-processed to obtain the spectral sidebands. All continuous scanning techniques employed in ODS recovering involve sinusoidal excitation of the structure so the response at any point, measured at any direction, is also sinusoidal at the same excitation frequency, assuming the linearity of the structure. The vibration response measured by the SLDV system, which can be expressed as velocity in the z-direction, perpendicular to the structure surface nominally in the X-Y plane and measured at any point (x, y) along the scan path $s(x, y)$ will be:

$$v_z(s,t) = V_R(s)\cos(\omega t) + V_I(s)\sin(\omega t) \tag{11.2}$$

V_R and V_I being the real and imaginary components of the vibration and expressed by:

$$\begin{aligned} V_R(s) &= \sum_{m,n=0}^{p,q} V_{Rn,m} f(m,n,s) \\ V_I(s) &= \sum_{m,n=0}^{p,q} V_{In,m} f(m,n,s) \end{aligned} \tag{11.3}$$

By substituting Eq. (11.6) into Eq. (11.5), the vibration velocity can be expressed as a function of time only:

$$v_z(t) = \sum_{m,n=0}^{p,q} V_{Rn,m} f(m,n,s)\cos(\omega t) + \sum_{m,n=0}^{p,q} V_{In,m} f(m,n,s)\sin(\omega t) \tag{11.4}$$

When the X-Y mirrors of the scanning device are driven sinusoidally by two functions at two non-fractional frequencies, Ω_x and Ω_y, the laser beam will perform an area scan which describes an open Lissajou figure. Hence, in order to sweep a normalized area of dimension 2 × 2, with zero position the centre of the square, the mirror drivers should be fed by two sinewaves of equations:

$$\begin{aligned} x(t) &= \cos(\Omega_x t) \\ y(t) &= \cos\left(\Omega_y t\right) \end{aligned} \tag{11.5}$$

The complex amplitude of the ODS appearing in the general Eq. (11.6) can be written as a two-dimensional polynomial series:

$$\begin{aligned} V_R(x,y) &= \sum_{n,m=0}^{p,q} V_{Rn,m} x^n y^m \\ V_I(x,y) &= \sum_{n,m=0}^{p,q} V_{In,m} x^n y^m \end{aligned} \tag{11.6}$$

p and *q* being the polynomial order in x- and y-direction respectively. The vibration velocity, following the principle of the general Eq. (11.5), translated to a two-dimensional structure, becomes:

$$v_z(x,y;t) = V_R(x,y)\cos(\omega t) + V_I(x,y)\sin(\omega t) \tag{11.7}$$

Substituting Eq. (11.5) into Eq. (11.6) and again into Eq. (11.7), this can be rewritten as:

$$v_z(t) = \sum_{n,m=0}^{p,q} V_{Rn.m}\cos^n(\Omega_x t)\cos^m\left(\Omega_y t\right)\cos(\omega t) + \sum_{n,m=0}^{p,q} V_{In.m}\cos^n(\Omega_x t)\cos^m\left(\Omega_y t\right)\sin(\omega t) \tag{11.8}$$

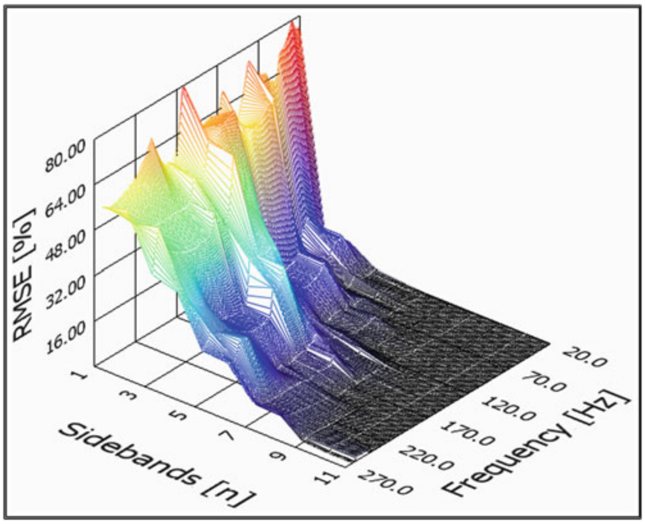

Fig. 11.8 RMSE between ODS and polynomial fitting (the polynomial order is expressed as sidebands number)

Expanding out trigonometrically, the following representation of the vibration signal is derived:

$$v_z(t) = \sum_{m,n=0}^{p,q} V_{Rn,m} \cos\left[\left(\omega \pm n\Omega_x \pm m\Omega_y\right) t\right] + \sum_{m,n=0}^{p,q} V_{In,m} \sin\left[\left(\omega \pm n\Omega_x \pm m\Omega_y\right) t\right] \tag{11.9}$$

For simplicity, we assume that the ODS is entirely Real so that the Imaginary part is negligible. In order to deal with the ODS as displacement we have to integrate the equation:

$$\{x_z\} = \sum_{m,n=0}^{p,q} X_{Rn,m} \int \cos\left[Kt\right] dt = \sum_{m,n=0}^{p,q} X_{Rn,m} K \sin\left[Kt\right] + \cos t \tag{11.10}$$

where $K = \omega \pm n\Omega_x \pm m\Omega_y$. The ODSs calculated in Eq. (11.1) were used for generating the polynomial functions as presented in Eq. (11.6). The polynomial order was identified by minimizing the error, less than 1 %, between the ODS and its polynomial form. The polynomial order was calculated for every simulated ODS and the Root Mean Square Error (RMSE) plot is presented in Fig. 11.8. The higher the ODS complexity the higher the polynomial order.

The polynomial function obtained from the calculated ODS was used for simulating the LDV output signals, one from the undamaged and one from the damaged component. The RMSE was calculated between the two sets of sidebands and plotted as shown in Fig. 11.9. It is interesting to notice that even for the smallest damage severity, which is the alteration of one single element in the FE model, the change of spectral sidebands is very clear. This is visible in Fig. 11.9 from the plots labelled Damage 1 and Damage A1, respectively. As the damage severity increases as the change of the spectral sidebands shows more clearly. However, a noise free test data is rather impossible. The next set of simulations regards the same ODS data sets but noise is added for creating a more realistic measurement environment.

The LDV output signal was added with broadband white noise. The assessment of the noise on the sidebands is presented in Fig. 11.10 which shows how the sidebands with and without noise were correlated. The calculation was carried out as follows. Every pair of sideband set, with and without noise, were correlated and averaged by the number of sidebands. So a single averaged number was calculated for every excitation frequency. Clearly, the sidebands near the resonances were less sensitive to the noise and the degree of correlation was rather high for the given level of noise.

Despite the addition of noise, signs of sidebands changes are still present in the error plots as shown in Fig. 11.11. Clearly, if Damage 1 in Fig. 11.9 presented sings of changes for frequencies between 20 and 70 Hz this is not visible any longer in the plot of Damage 1 in Fig. 11.11.

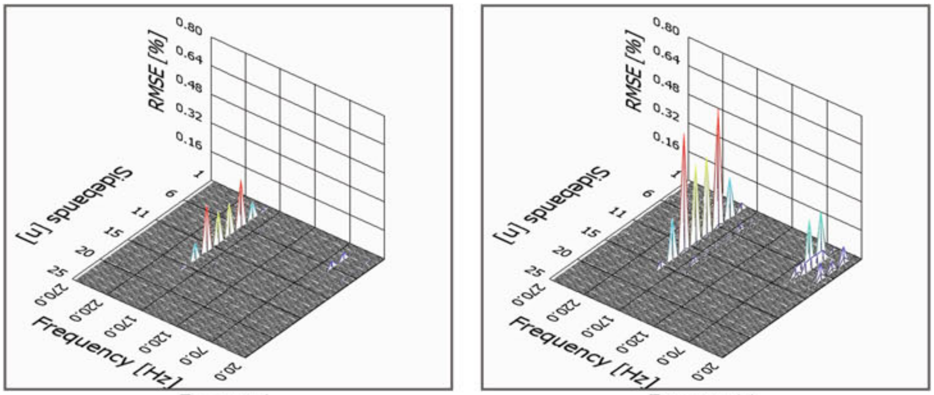

Damage 1 Damage A1

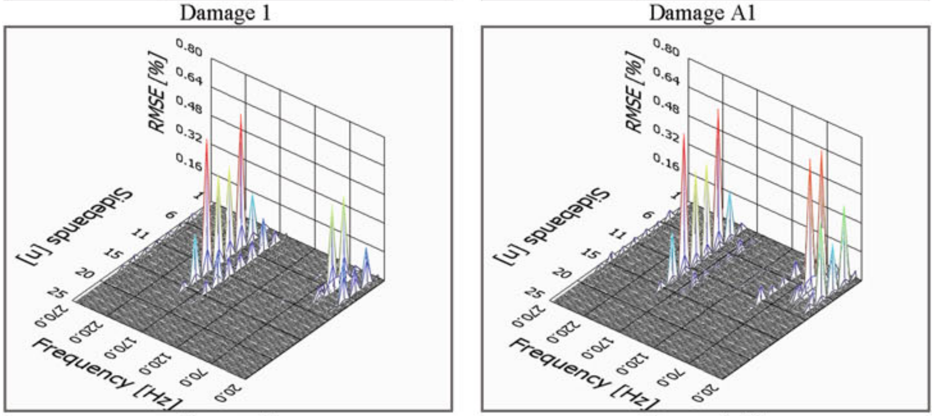

Damage 2 Damaged A2

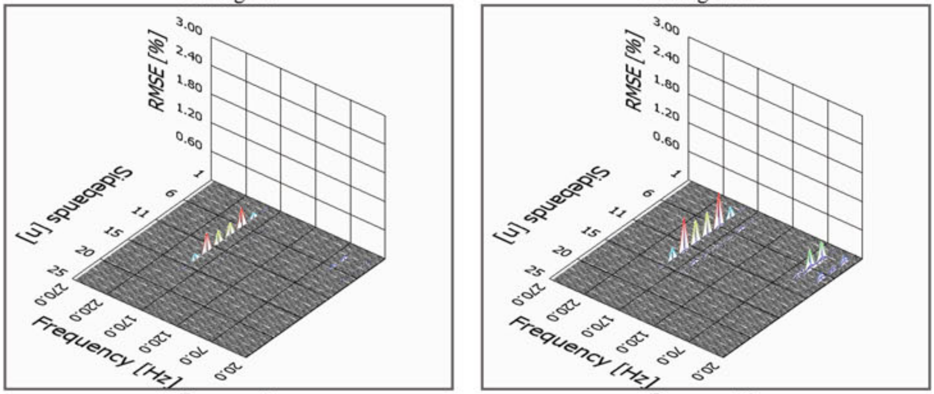

Damage 3 Damage A3

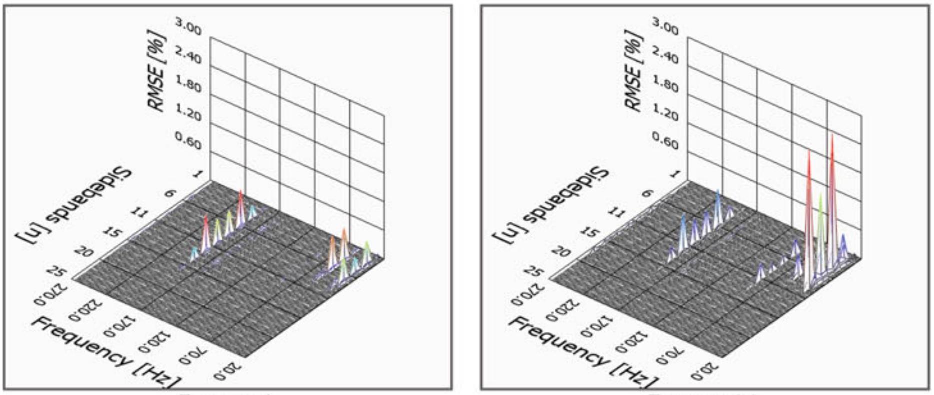

Damage 4 Damage A4

Fig. 11.9 RMSE between undamaged and damaged sidebands

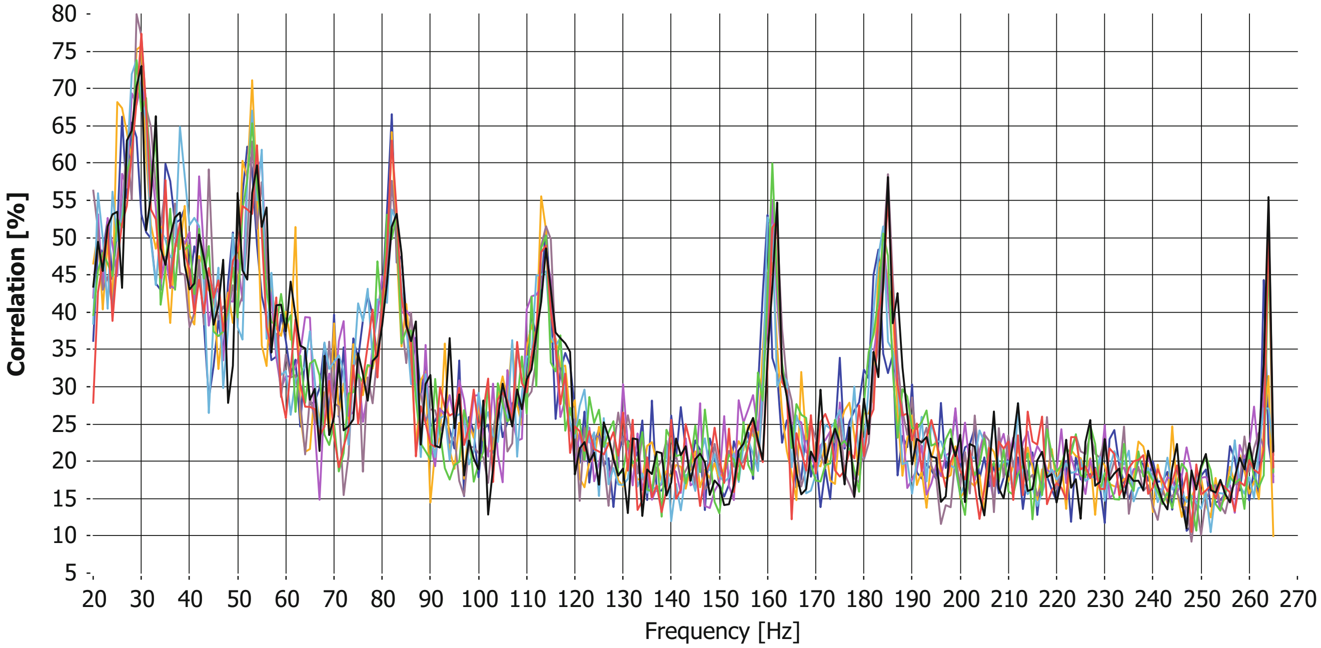

Fig. 11.10 Degree of correlation between averaged sum of the sidebands with and without noise

The proposed simulations suggest that the spectral sidebands of the calculated ODS show changes from its undamaged configuration. So, mapping the evolution of such changes could provide useful insight on the health state of structures under diagnosis. However, the number of cases studied in here is still too small for generalizing conclusions. Nevertheless, the correlation of the sidebands can offer an advantage in terms of *quasi* real-time diagnostic. This is possible thanks to the continuous scanning which can provide both spatial and temporal information. Finally, this technology could be implemented in several applications but more vigorously, for example, in the assessment of bolted structures. Future works will need to consider additional damage cases, different boundary conditions and also experimental validation for one of the test cases simulated.

11.3 Conclusions

This short paper wished to demonstrate the capacity of continuous scanning as diagnostic tool. The CSLDV is often used in modal analysis thanks to its high resolution ODS. However, that requires data processing which for cases of *quasi* real-time assessment would not be suitable. The same applies to the standard stepped scanning method where the ODS recovery can be even lengthier. This paper showed that the sole use of ODS spectral sidebands is sufficient for monitoring the health state of a structure, whose surface can be continuously scanned and monitored by the laser beam. The work was based on numerical simulation of the LDV output signal from structures which were artificially modified by reducing the thickness of some elements. Levels of damage severity were considered and those showed clear alteration of the sidebands. Similar output was achieved by adding noise to the simulated time signals. Future works will try to address more complicated test cases and experimental validation.

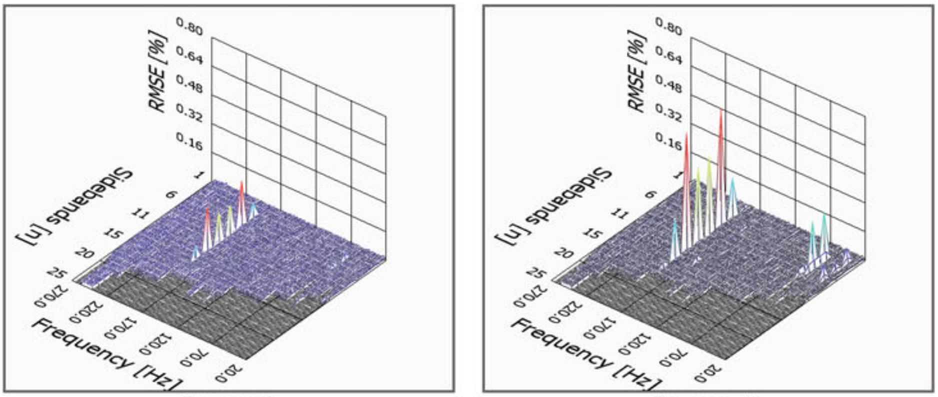

Damage 1 Damage A1

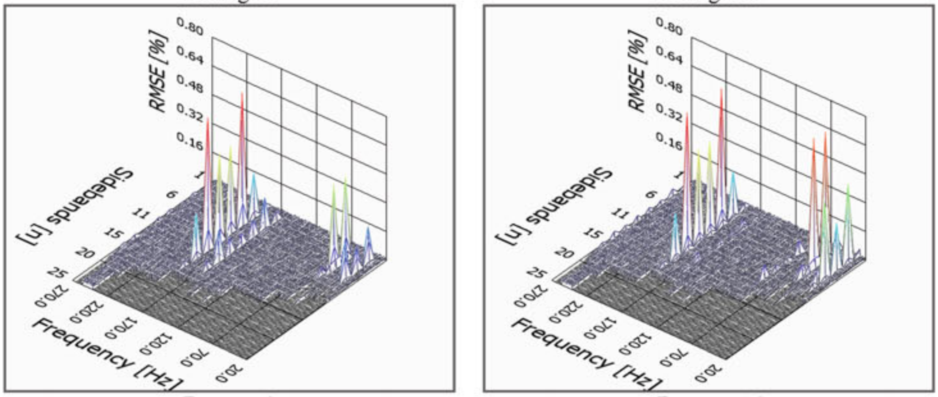

Damage 2 Damage A2

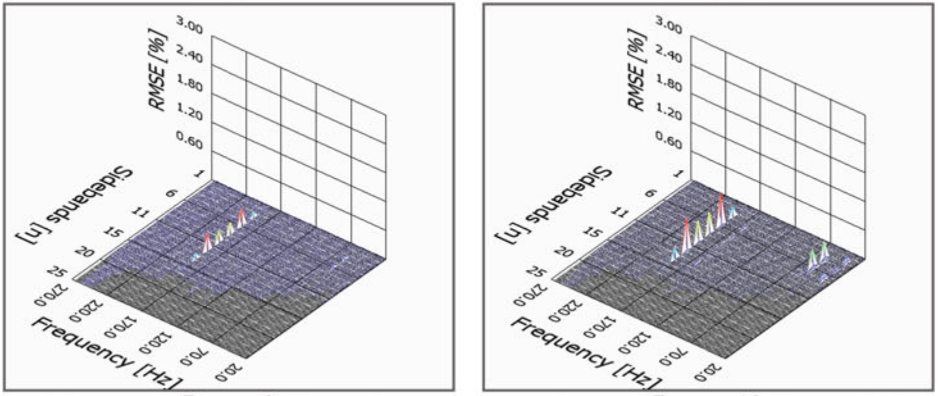

Damage 3 Damage A3

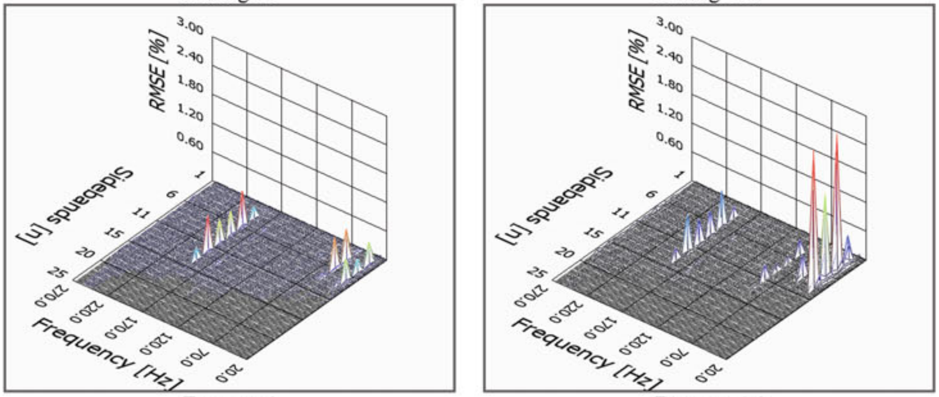

Damage 4 Damage A4

Fig. 11.11 RMSE between undamaged and damaged sidebands with added noise

References

1. Abdul Rahman, A.G., Noroozi, S., Dupac, M., Al-Attas, S.M.S.M., Vinney, J.E.: A hybrid approach for nondestructive assessment and design optimisation and testing of in-service machinery. Nondestruct. Test. Eval. **28**(1), 44–57 (2013)
2. Zhong, S., Oyadiji, S.O.: Crack detection in simply supported beams using stationary wavelet transform of modal data. Struct. Control. Health Monit. **18**(2), 169–190 (2011)
3. Chiariotti, P., Revel, G.M., Martarelli, M.: Exploiting continuous scanning laser Doppler vibrometry and wavelet processing for damage detection. In: De Clerk, J. (ed.) Experimental Techniques, Rotating Machinery, and Acoustics, vol. 8, pp. 189–196. Springer, New York (2015)
4. Yang, S., Allen, M.S.: Transfer functions to measure translational and rotational velocities with continuous-scan laser Doppler vibrometry. In: Topics in Modal Analysis, vol. 7, pp. 597–615. Springer, New York (2014)
5. Di Maio, D., Zampognaro, N., Zang, C., Ewins, D.J.: Effect of vibration excitation locations on structural damage detection using the CSLDV technique: simulation and testing. In: Proceedings of the SPIE, vol. 6345, pp. 63450O–63450O–10 (2006)
6. Di Maio, D.: Damage monitoring using continuous scanning LDV methods: numerical approach. Optical Measurement Techniques for Systems and Structures III. Editor Joris Dirckx, (2016). ISBN 978-90-423-0439-0

Chapter 12
A Cost Effective DIC System for Measuring Structural Vibrations

Markus J. Hochrainer

Abstract In modern data acquisition a constantly growing number of applications using technically advanced image processing systems has been observed in recent years. The work presented proves, that it is possible to use standard webcams combined with an innovative lighting concept to precisely measure displacements of high frequency structural oscillations. By means of stroboscopic light, the actual frequency of a periodic high frequency oscillation is shifted to the low detection rate of the cameras applied. Object or surface deformations are measured and visualized by well-established 3D digital image correlation procedures. The excellent performance of the proposed system is confirmed by a wide range of experimental studies. All results indicate that this innovative system is a perfect supplement to traditional modal analysis measurement systems, particularly in the context of teaching vibrations.

Keywords Digital image correlation • Stereo-vision • Stroboscope • Optical vibration measurement • Stereo imaging

12.1 Introduction

The measurement of structural vibrations has a long tradition in engineering sciences, and is performed with accelerometers in the vast majority of applications. They are attached to the structure at exactly defined positions, and since the number of sensors as well as the number measurement channels is limited, the measurements are generally performed sequentially by moving the sensors across the structure to create spatial information. Experimental modal analysis (EMA) techniques are often used to determine characteristic structural system parameter like natural frequencies, damping and mode shapes. In EMA, the stimulating forces must be known and therefore impact hammer or shaker excitation are widely used during dynamic testing. If this type of excitation is not feasible, it is still possible to measure the operation deflection shapes (ODS) or even perform operational modal analysis, if statistical properties of the excitation are known.

The inevitable sensor-structure interaction has led to the application of contactless optical measurement methods when testing light structures. Due to their outstanding amplitude and frequency dynamics laser doppler vibrometer (LDV) are commonly used if traditional vibration transducers are not applicable and high precision measurements are required. LDV can be configured to measure vibrations of large structures like bridges or towers and, on the other side, there a many applications in micro-engineering. Depending on the measurement equipment and its configuration linear, planar or even spatial deflections can be captured. Similar to traditional sensors a field of structural displacements is scanned sequentially by moving the laser beam to de desired location. For simultaneous recording of all structural displacements different optical measurement techniques have been developed, e.g. the electronic speckle pattern interferometry (ESPI) for periodically vibrating surfaces or fringe projection methods which originally have been developed for static measurements. In recent years, however, digital image correlation (DIC) methods have become very popular and widely available. Originally developed for plane, static deflection measurements in the field of material testing, modern 3D DIC methods use a set of calibrated stereo-cameras, allowing determining both, the structure's geometry and the dynamic deflections [1]. Similar to traditional vibration measurements, the sampling rate of the measurement system has to match the structural dynamics. Thus, high speed stereo camera systems with suitable image resolutions have to be applied to analyze medium to high frequency vibrations. Similar to LDV, high speed camera systems are excellent with respect to accuracy but still very expensive. This work proves that it is possible to measure high frequency periodic vibrations with webcams or standard industrial cameras using an innovative light concept. This is particularly interesting for the determination of operation deflection shapes or experimental modal analysis with periodic forcing.

M.J. Hochrainer (✉)
University of Applied Sciences, 2700 Wiener Neustadt, Austria
e-mail: markus.hochrainer@fhwn.ac.at

© The Society for Experimental Mechanics, Inc. 2016

J. De Clerck, D.S. Epp (eds.), *Rotating Machinery, Hybrid Test Methods, Vibro-Acoustics & Laser Vibrometry, Volume 8*,
Conference Proceedings of the Society for Experimental Mechanics Series, DOI 10.1007/978-3-319-30084-9_12

12.2 Theoretical Background

The automated extraction of 3D-spatial information out of two images representing the same scene is commonly referred to as computer stereo vision, which is comparable to human binocular vision. The horizontally spaced human eyes observe the surroundings from slightly altered perspectives. During small child development the brain learns to extract spatial information from left and right eye's view. The technical process is almost identical: two separated cameras are capturing the site of interest, and the spatial information of the scene can be reconstructed from analyzing the image differences. Unlike human vision, a computer stereo vision system requires several steps of pre-processing. Firstly, each camera has to be calibrated to remove all kinds of optical lens and image distortions to ensure the image is truly projective, which is commonly referred to as intrinsic parameter identification. Secondly, the extrinsic parameter defining the position (displacement vector) and orientation (rotation matrix) of the right camera coordinate systems with respect to the left (reference) is determined. Both, intrinsic and extrinsic parameters are generally obtained from analyzing several sets of calibration images in a least squares procedure. The quality of the calibration process is crucial, because it largely influences the absolute accuracy of the 3D information. The same is true for the relative position and orientation of the camera with respect to each other, which fundamentally influences the sensitivity and accuracy of the relative and absolute deflection measurements. With increasing camera separation $\mathbf{t}$ the depth information (out of plane) will become more accurate at the price of reduced in plane resolution. The basic principle of stereo-imaging is given in Fig. 12.1, the subscript l and r indicate the respective quantities of the left and right camera.

Assuming that a point $\mathbf{P}$ in space is projected onto the coordinates (x_l, y_l) and (x_r, y_r) on the left and right stereo image, the lines of sight s_l and s_r can be constructed from the camera origins (focal point) and they ideally intersect at point $\mathbf{P}$. Since lines generally do not intersect in space, the center point $\mathbf{P}$' of the shortest distance d between the lines is taken as reconstructed point which also represents the intersection point in a least squares sense. Having extracted $\mathbf{P}$' from stereo images, an entire object geometry can be found by repeating this procedure for all points describing the object. Once the initial geometry is determined, a single point movement can be captured by analyzing a sequence of stereo images. Accordingly, the object's movement and deformation is obtained by analyzing a set of points describing the surface of an object. Since every selected measurement point renders a spatial displacement, it can be regarded as a "virtual sensing position". If a deformation field has to be determined with reasonable resolution, generally thousands of virtual measurement points must be analyzed. This requires fast, robust and highly automated methods to unambiguously identify corresponding points on every pair of stereo images. For this reason random speckle pattern are used in digital image correlation to obtain both, high density of measurement points as well as a unique correspondence on both stereo images. The random speckle pattern can be applied to the surface by spraying, printing, sticking or by projection. Once a point of interest has been located exactly in both stereo images its spatial reconstruction according to Fig. 12.1 is straightforward. A useful measure for the quality of the 3D-point estimate is the length of the normal distance d between s_l and s_r. DIC methods have proven to work precise and highly reliable because they do not consider a single point projection only, but always include the neighboring information collected from a subset S. The subset typically consists of several hundred additional points which are processed by the image correlation algorithm, thereby improving the measurements by the intended averaging effect. Assuming the

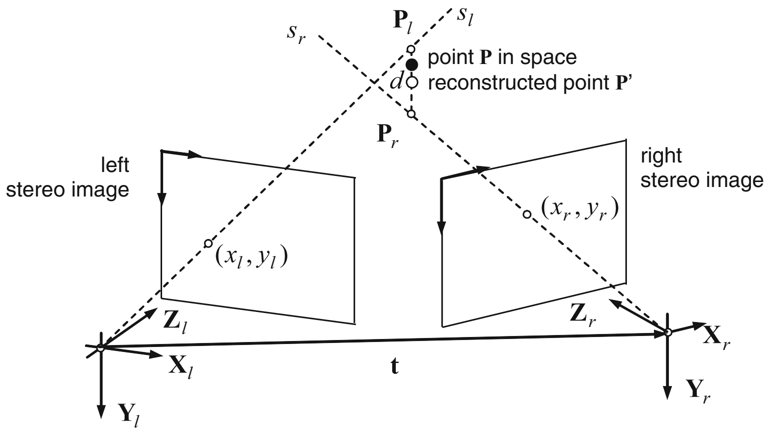

Fig. 12.1 Principle of stereo triangulation, the *left* camera is taken as reference

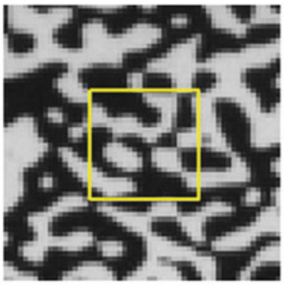

(a) reference image

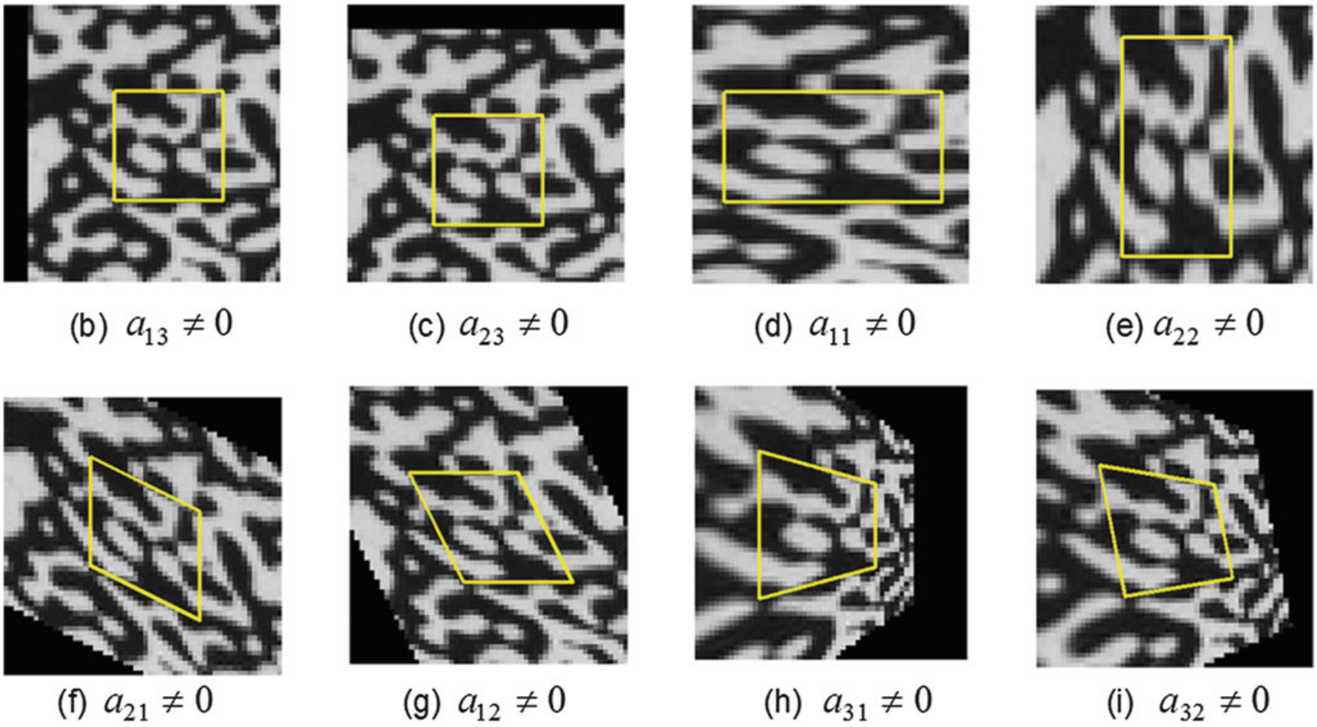

(b) $a_{13} \neq 0$ (c) $a_{23} \neq 0$ (d) $a_{11} \neq 0$ (e) $a_{22} \neq 0$

(f) $a_{21} \neq 0$ (g) $a_{12} \neq 0$ (h) $a_{31} \neq 0$ (i) $a_{32} \neq 0$

Fig. 12.2 Distortion of a rectangular reference image for different transform parameter

subset points to be located on a plane element, the transform between the left (reference) and right stereo image can be given by the perspective projection [2]

$$\begin{pmatrix} \alpha\, x_r \\ \alpha\, y_r \\ \alpha \end{pmatrix} = \mathbf{A}\,(\mathbf{p}) \begin{pmatrix} x_l \\ y_l \\ 1 \end{pmatrix}, \quad \mathbf{A}\,(\mathbf{p}) = \begin{pmatrix} 1 + a_{11} & a_{12} & a_{13} \\ a_{21} & 1 + a_{22} & a_{23} \\ a_{31} & a_{32} & 1 \end{pmatrix}. \tag{12.1}$$

The unknown coefficients a_{ij} of the transform matrix $\mathbf{A}(\mathbf{p})$ are collected in the parameter vector $\mathbf{p} = (a_{11},\ a_{12},\ a_{13},\ a_{21},\ a_{22},\ a_{23},\ a_{31},\ a_{32})^T$. The unknown elements a_{13}, a_{23} and $a_{11}, a_{12}, a_{21}, a_{22}$ denote the relative displacements as well as the strain and the shearing of the reference element in horizontal and vertical direction, respectively, see Fig. 12.2b–g. The perspective distortion is represented by a_{31}, a_{32}, see Fig. 12.2h–i. Equation (12.1) directly renders the pixel coordinates (x_r, y_r)

$$x_r = \frac{(1 + a_{11})\, x_l + a_{12} y_l + a_{13}}{1 + a_{31} x_l + a_{32} y_l}, \quad y_r = \frac{a_{21} x_l + (1 + a_{22})\, y_l + a_{23}}{1 + a_{31} x_l + a_{32} y_l}. \tag{12.2}$$

Although the reference pixel coordinates (x_l, y_l) are integer valued, the projected coordinates (x_r, y_r) are floating numbers, leading to the challenge of evaluating the right image at subpixel coordinates. This requires a two dimensional subpixel interpolation which can, e.g. be implemented using well accepted and thoroughly studied b-splines [3, 4]. In the work presented the required interpolation was performed using bi-quintic splines, which guarantee a very smooth interpolation based on a quadratic set of 5×5 pixels. An exact and powerful subpixel interpolation is fundamental for DIC because the method requires accurate pixel measurements in the range of several 1/100 pixel.

Because the transform matrix $\mathbf{A}(\mathbf{p})$, see Eq. (12.1), has eight unknown parameters, the plane mapping between the left and the right image is described completely by four points. Similar to finite element formulations, it is possible, to extend the transform, Eq. (12.2), by nonlinear terms which is advantageous when working with strongly curved surfaces. This will, however, increase the number of unknown parameter. All DIC methods share the basic idea of transforming the right image subset until the difference to the reference subset becomes minimal. An intuitive measure for the similarity between subsets is the discrete correlation coefficient C_{CC}. However, instead of maximizing C_{CC}, it is, from an optimization point of view, advantageous to minimize the subset least squares correlation error C_{LS}, see e.g. [1]

$$C_{CC} = \sum_{i \in S} \frac{\left(f\left(x_{l,i}, y_{l,i}\right) - f_m\right)\left(g\left(x_{r,i}, y_{r,i}\right) - g_m\right)}{\sqrt{f_n g_n}}, \quad C_{LS} = \sum_{i \in S} \left(\frac{f\left(x_{l,i}, y_{l,i}\right) - f_m}{\sqrt{f_n}} - \frac{g\left(x_{r,i}, y_{r,i}\right) - g_m}{\sqrt{g_n}}\right)^2 \tag{12.3}$$

where $f(x_{l,i}, y_{l,i})$ and $g(x_{r,i}, y_{r,i})$ denote the grayscale information of the *i-th* point (element) of the corresponding left and right subset S. To compensate for brightness variations across the image, the subset data is corrected by the average subset brightness $f_m = 1/n\sum_{i \in S} f\left(x_{l,i}, y_{l,i}\right)$ and $g_m = 1/n\sum_{i \in S} g\left(x_{r,i}, y_{r,i}\right)$, respectively, with n denoting the number of subset elements. Furthermore the grayscale variations $f_n = \sum_{i \in S}\left(f\left(x_{l,i}, y_{l,i}\right) - f_m\right)^2$ and $g_n = \sum_{i \in S}\left(g\left(x_{r,i}, y_{r,i}\right) - g_m\right)^2$, respectively, are applied for further normalization. When working with colored images, e.g. a red, green and blue color channel, a conversion to grayscale pixel information is necessary before processing. The parameter vector $\mathbf{p}$ to be determined, effects the performance measure C_{LS} via the transformed pixel coordinates (x_r, y_r), cf. Eq. (12.2). Although only the displacement parameter a_{13}, a_{23} are required for calculating the 3D coordinates of the subset center point, all other transform parameter are needed for the least squares image correlation. Without accounting for normal strain, shearing and perspective distortion there will be little correlation for medium sized subsets. The optimization criterion $C_{LS}(\mathbf{p}) = \min$ renders a nonlinear optimization problem which can be solved for suitable initial values $\mathbf{p}_{k=0}$ applying several iterations of the Gauss-Newton algorithm

$$\mathbf{p}_{k+1} = \mathbf{p}_k + \Delta\mathbf{p}_k, \quad \Delta\mathbf{p}_k = -\nabla\nabla C_{LS}(\mathbf{p}_k)^{-1} \nabla C_{LS}(\mathbf{p}_k). \tag{12.4}$$

Apparently, the calculation of the gradient vector $\nabla C_{LS}(\mathbf{p}_k)$ and the Hesse matrix $\nabla\nabla C_{LS}(\mathbf{p}_k)$ must be repeated in each iteration step. In the direct formulation every update of $\mathbf{p}_k$ renders new floating point coordinates for the subset elements $g(x_{r,i}, y_{r,i})$ thereby raising the need for permanently calculating the least squares correlation an its derivatives at subpixel coordinates. To circumvent this is computationally costly direct calculation, the "inverse calculation" was developed, with the basic idea of evaluating the parameter vector $\Delta\mathbf{p}_k$ with respect to the reference subset. In this case, the coordinates of the subset elements are given by integer values preventing time consuming subpixel interpolations when calculating $\nabla C_{LS}(\mathbf{p}_k)$ and $\nabla\nabla C_{LS}(\mathbf{p}_k)$, respectively. If the reference subset is kept at its initial position both, gradient and Hesse matrix, remain constant during all iterations, thereby saving a lot of computational time. This can be accomplished by a modified (inverse) update of the parameter vector to account for the effect that the subset position update is applied to the right image subset, and not to the left reference image where $\Delta\mathbf{p}_k$ has been calculated for. The updated parameter vector $\mathbf{p}_{k+1}$ can be given by the respective elements of the updated transform matrix [2], cf. Eq. (12.1),

$$\mathbf{A}(\mathbf{p}_{k+1}) = \mathbf{A}(\mathbf{p}_k)\,\mathbf{A}(\boldsymbol{\Delta}\mathbf{p}_k)^{-1} \tag{12.5}$$

The calculation of gradient and Hesse matrix can be further simplified as the least squares correlation criterion C_{LS} is based on a quadratic optimization function which can be approximated by [2]

$$\nabla C_{LS}(\mathbf{p}_k) \approx \frac{2}{\sqrt{f_n}} \sum_{i \in S} \left(\frac{f\left(x_{l,i}, y_{l,i}\right) - f_m}{\sqrt{f_n}} - \frac{g\left(x_{r,i}, y_{r,i}\right) - g_m}{\sqrt{g_n}}\right) \mathbf{g}_i \tag{12.6}$$

$$\nabla\nabla C_{LS}(\mathbf{p}_k) \approx \frac{2}{f_n} \sum_{i \in S} \mathbf{g}_i \mathbf{g}_i^T, \quad \mathbf{g}_i = \frac{d}{d\mathbf{p}} f\left(x_{l,i}, y_{l,i}\right) \tag{12.7}$$

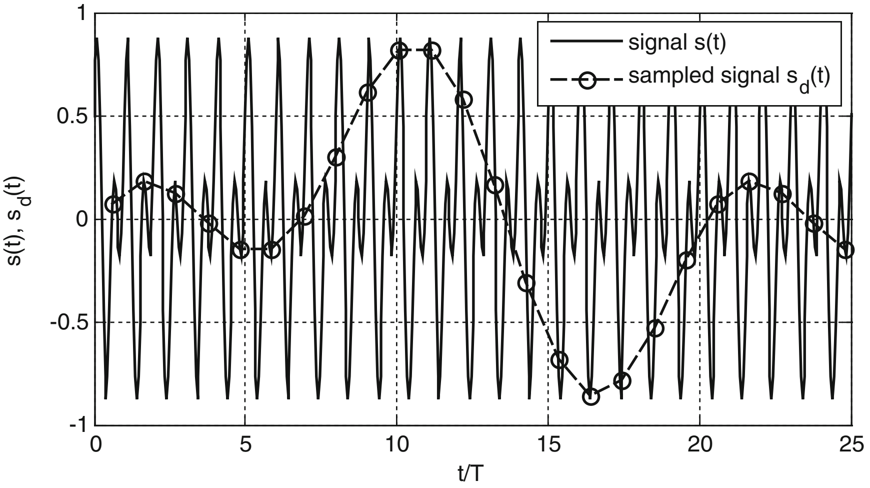

Fig. 12.3 Frequency shift of a periodic function as a result of undersamping, $f = 1/T, f_S = 0.95f, f_a = 0.05f$

assuming that the mean subset brightness f_m is independent of **p**. This optimization has proven to converge within three to four iterations if the initial displacements (a_{13}, a_{23}) are, certainly depending on the random speckle pattern, correct within several pixels. During digital image correlation the parameter optimization has to be performed independently for all virtual sensor positions. Therefore it can be parallelized e.g. using GPU processing. To obtain usable estimates of the initial displacements, a scale invariant feature transform (SIFT) algorithm is used, because it can handle highly distorted images, and is available as Matlab library [5]. Applying the inverse calculation to a sequence of corresponding stereo images, it is possible to reconstruct the 3D motion of the observed object.

From Shannon's theorem it is well known, that, whenever a continuous process is discretized by taking equally spaced samples, the sampling rate must match the dynamics of the continuous process to avoid corruption of the measured data by changing the signal or system information. This is certainly true for image acquisition systems raising the need for high speed camera systems when analyzing medium to high frequency dynamic processes. Although generally undesired, it is exactly the effect of changing the frequency content of the observed motion by controlled undersamping (aliasing) which the current application is based on. A central component of the presented DIC setup is the homogenous illumination of the vibrating object by several arrays of high power light emitting diodes in a stroboscopic configuration. Assuming a periodic structural motion of base frequency f, an arbitrary frequency shift can be achieved by violating Shannon's sampling theorem, and selecting the sampling frequency $f_S < 2f$. Consequently, the original high frequency motion is mirrored about $f_S/2$ rendering the visible alias frequency f_a, which can be found by the simple relation $f_a = f - nf_S$ where n is the closest integer multiple of the sampling rate f_S to the signal f, see Fig. 12.3.

Conversely, the actual mode shapes remain unaffected and the real structure seems to vibrate in slow motion. This strategy works for any structure as long as the vibration amplitudes are within the resolution of the applied DIC setup. If performed correctly, undersampling can be applied to periodic or band-pass signals without loosing signal information, because the correct reconstruction of the original signal is still possible. Since the webcams are not suitable for real time high speed image acquisition, the periodic light of the stroboscope undersamples the movement of the structure and the resulting slow motion is captured by the low cost cameras.

12.3 Proposed Setup

The experimental setup applied essentially consists of a set of calibrated standard webcams rigidly mounted on tripod forming a stereo vision system directed at the vibrating object, see Fig. 12.4a. The object under test is periodically excited by an electrodynamic shaker, and homogenously illuminated by a custom made stroboscopic light, see e.g. [6]. Before first measurements are taken, the stereo-vision system is calibrated using a checkerboard plate of known dimensions. Having finished the calibration process [7], several lens aberrations and sensor distortions can be corrected (intrinsic calibration), and the camera positions as well as their directions are determined with respect to each other in an automated registration process (extrinsic calibration). The extrinsic calibration process must be repeated if camera positions or directions change

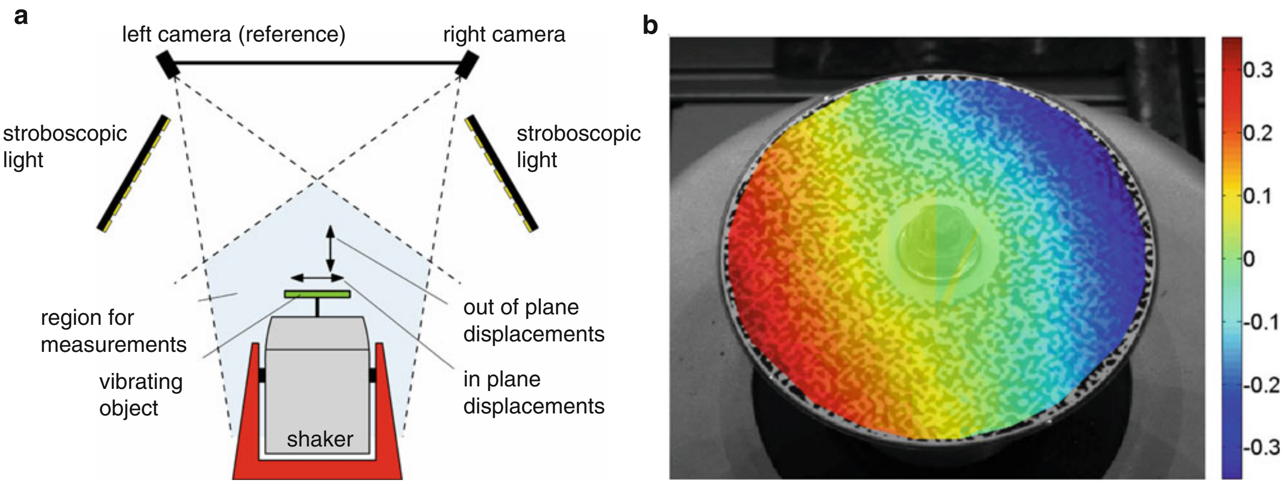

Fig. 12.4 (**a**) Schematics of the stereo-vision setup (**b**) Deformation field of the polycarbonate plate at 112 Hz

with respect to each other. An intrinsic calibration is only necessary, if e.g. the camera lens system is modified. This, however, is not possible for the Logitech HD C270 webcams used in the project. The webcams have a resolution of 1280 × 720 pixels at a frame rate of up to 30 Hz. They are USB 2.0 based and thus do not contain an external trigger line. As a result it is not possible to record a sequence of simultaneous images. Therefore the deformation measurement is only possible for statics or very low frequency vibrations. Due to the stroboscopic effect, the recorded aliasing frequency f_a can be set arbitrarily, even far below 1 Hz. The stroboscopic light is controlled by digital inputs coming from the same signal generator used to create the periodic excitation signal. This is important for a linear phase increase of the alias-motion if the measurement period $T_a = 1/f_a$ is stretched to several seconds.

Experiments have revealed, that best optical effects are obtained if ambient and especially artificial light is reduced to a minimum. The higher the stroboscope's duty cycle, the better the illumination level, however, at the price of slightly blurring the captured motion. If the structure has shiny or painted surfaces, the moving light reflections might interfere with the speckle pattern, and a temporal dull finish might be applied using e.g. chalk spray. Consequently, it is, from a technical point of view beneficial to use cameras with high light sensitivity, good contrast and short exposure times, as this will increase the image quality and thus contribute to excellent DIC results. For an improved setup it is thus recommended, to apply low cost industrial cameras with exchangeable lens systems and an external trigger line. If the camera allows for triggered image acquisition with very short exposure times, the stroboscopic effect can be achieved by only using the camera shutter at the price of a fairly low image contrast.

12.4 Experimental Results

To prove the efficiency of the proposed system a circular polycarbonate plate with a diameter of approximately 120 mm is attached to an electrodynamic shaker at its centre. A correlation pattern has been printed on the plate for dynamic DIC measurements. If it is possible to print the random pattern on a self adhesive film, it can be easily adapted to the size of the object as well as the density of the "virtual sensors". As a consequence the correlation pattern will also determine the minimal wavelength of the detected deformation and certainly influence the accuracy of the measurement. However, the experiments conducted show that the generation of the speckle pattern is not critical for most applications. To reduce image noise a long expose time was selected and consequently the frame rate was chosen between 2 and 5 Hz for aliased vibration periods of several seconds. The measurement results (ODS) are given in Fig. 12.4b for an excitation frequency of 112 Hz. For comparison, the deflection was also monitored using a LDV, showing an accuracy of less than 30μm for vertical deflections. The same measurement was repeated using low cost industrial cameras of type DMK23F618 (The Imaging Source) with matching lenses of type T0812FICS (computar) and a resolution of only 640 × 480 pixels. To obtain comparable results, the external trigger was not activated. Even with this very low pixel resolution, the vertical displacement error of the entire system has been below 20μm.

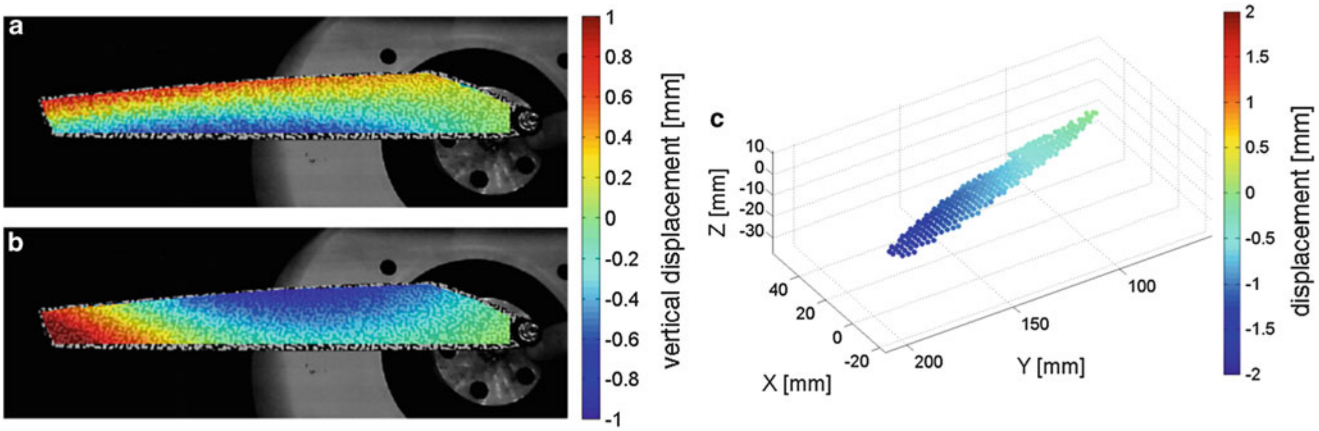

Fig. 12.5 Operation deflection shapes (ODS) of a vertically excited elastic rotor at (**a**) 103 Hz and (**b**) 139 Hz (**c**) Deformation of a quadcopter rotor due to aerodynamic forces a 3900 rpm

Next, the deformation of an elastic rotor of 250 mm length and a maximal width of 40 mm due to vertical shaker excitation is studied. Again, this is a very light structure and the use of contactless measurement techniques is obligatory. This time, the random pattern is printed on a self adhesive film and transferred to the moderately curved rotor. Although the rotor represents a kind of slender, beam type structure, the DIC displacement analysis works satisfactorily, see Fig. 12.5a, b, where the measured operation deflection shapes at frequencies of $f = 103$Hz and $f = 139$Hz are illustrated. As before, the stereo image acquisition was performed using standard webcams with $f_a = 0.1$Hz. The results indicate excellent full field measurements which can be easily interpreted, and furthermore, interesting deflection properties like, e.g. nodal lines can be extracted directly.

In the last example the deflections of an elastic quadcopter rotor due to aerodynamic forces were analyzed during normal operation. The quadcopter was fixed to a test rig while performing an engine run-up between 1900 and 4000 rpm. Because the rotor was in permanent rotation, the triggering of the stroboscopic light had to be synchronized to the rotation angle using a simple laser light barrier. Due to the high velocity of the rotor tip, the duration of the stroboscopic light flash was reduced to less than 2μs and thus the illumination level was low. Consequently, relatively long expose times were necessary for good quality imaging. Again, all measurements were taken with the calibrated webcams in stereo configuration. In Fig. 12.5c the rotor deformation is given for 3900 rpm. Apparently, the rotor tip is raised to approximately 2 mm. Of course, the vertical lift of the rotor as a function of the rpm can be visualized in a computer animation. Additionally, the curvature of the rotor is clearly visible because the dynamic DIC renders both, the static geometry and the dynamic deflections.

Looking at these results, it is possible to conclude, that the low cost stereo-DIC system has performed well during experimental testing. All calculations have been performed using standard Matlab code, partly optimized for matrix calculations and thus possible parallel processing. When limiting the analysis to several hundred virtual measurement points, and working with image frame rates in the range of 2–5 Hz, the analysis was performed in real-time. With respect to measurement accuracy, the system is also performing well. Commercial DIC systems define the displacement resolution by the ratio $e = s/l$ of measurement accuracy s over the length of the visible image section l. Depending on the image acquisition system, usual values are in the range of $e_h = 1/50000$ up to $e_h = 1/100000$ for horizontal (inplane) measurements. Depending on the distance and orientation of stereo vision system this value is reduced for vertical (out of plane) measurements by a factor between 2 and 3. Experiments with the proposed system indicate a vertical accuracy measure of $e_v = 1/10000$. In the setup used, the webcams lenses have turned out to be the limiting factor since there are no variable settings and depth of field, focus and measurement range cannot be changed.

12.5 Conclusions

The work presented proves that standard webcams combined with an innovative lighting concept can be used to precisely measure dynamic structural displacements. Using stroboscopic light, the actual frequency of a periodic high frequency oscillation is shifted to the low image acquisition rate of the cameras applied. All vibration measurements indicate that the proposed system has exceeded the expectation with respect to flexibility and accuracy. When compared to high end commercial systems, the webcam-setup performs well, however the lenses of the webcams have been identified as the limiting element. Therefore, a set of industrial cameras has turned out to be useful complement to the setup. When applying standard industrial cameras it possible to achieve accuracy similar to commercial DIC systems.

References

1. Sutton, M.A., Orteu, J.-J., Schreier, H.W.: Image Correlation for Shape, Motion and Deformation Measurements. Springer Science, New York (2009)
2. Schauer, F.: Spatial vibration measurements based on stereo digital image correlation. Master thesis (in German), Fachhochschule Wiener Neustadt, Austria (2015)
3. Schreier, H.W., Braasch, J.R., Sutton, M.A.: Systematic errors in digital image correlation caused by intensity interpolation. Opt. Eng. **39**, 2915–2921 (2000)
4. Kutluay, S., Yagmurlu, N.M.: Derivation of the modified Bi-quintic B-spline base functions: an application to poisson equation. Am. J. Comp. Appl. Math. **3**, 26–32 (2013)
5. Naveen, C.: SIFT (Scale invariant Feature Transform) algorithm, mathworks central file exchange. http://www.mathworks.com/matlabcentral/fileexchange (2015)
6. Hochrainer, M.J.: Visualizing structural vibrations using a novel strobe light setup. Sound Vib. Mag. **48**, 14–18 (2014)
7. Bouguet, J.-Y.: Camera calibration toolbox for Matlab. http://www.vision.caltechedu/bouguetj/calib_doc (2013)

Chapter 13
Teaching DSP and Dynamic Measurements at the Graduate Level at Michigan Technological University

Jason R. Blough

Abstract This paper will present the topics and methods which are used in the graduate level digital signal processing and dynamic measurements course (ME5700) at Michigan Technological University. How topics such as the FFT, order tracking, leakage, . . . etc. are taught will be discussed. Differences in how the course is taught relative to the number of students in the course will also be discussed, large numbers of students require a different teaching approach than just a few students! The author has been teaching this course for over 10 years and will share various other insights as to the most effective way to present these topics to a variety of students with a diverse background.

Keywords Laboratory assignments • Digital signal processing • Dynamic measurements • Education • Teaching

13.1 Introduction

Any graduate student which is doing experimental research must have the ability to acquire and analyze data. This includes students doing fluids experiments, exploring engine or powertrain calibration methods, exploring the combustion process using a combustion vessel, noise and vibration related research, prosthesis limb development, robotics, and controls, as well as many other fields of research. The ME5700, Dynamic Measurements and Signal Processing course at Michigan Technological University is the one course that is beneficial to all of the students in these fields when it comes to acquiring and processing data.

Up until 2004 this course, or its previously offered equivalent, had been taught from an experimental dynamics perspective where nearly all of the examples and talking points were noise and vibration related. This course has evolved over time to accommodate the interests of a broad range of students. This has led to many of the examples and talking points in the course spanning a wide variety of fields to keep the students interested in the topics and to provide them context where they might use the various methods.

This goal of this course is to provide the students a very strong working knowledge of various digital signal processing and dynamic measurement methods. None of the topics in the course are taught from a purely theoretical perspective, all topics are discussed in the context of how they would be used in the laboratory or to process actual data. In many instances, test questions are developed such that the student is asked for an explanation on how to make a particular measurement, how to process some data, or to give an example of where it would be appropriate to use a given technique as opposed to questions relative to the math or theory of a topic. My ultimate objective is to get the students enough knowledge about taking and processing data that they can be productive in a laboratory and not so that they can write all of their own software from scratch, though they do a fair amount of Matlab programming throughout the semester.

13.2 Teaching Approach

The teaching philosophy used in this course is to emphasize the practical application of every topic taught and not the math behind the topic. The mathematics are presented only when necessary and are done so to make a point as to why an algorithm or topic behaves the way it does when used in the "real world" never just to make the students memorize the math itself. Realizing that in this era of "Google" and the vast information available on the World Wide Web, if the students need to see

---

J.R. Blough (✉)
MEEM Department, Michigan Technological University, 1400 Townsend Drive, Houghton, MI 49931, USA
e-mail: jrblough@mtu.edu

© The Society for Experimental Mechanics, Inc. 2016

J. De Clerck, D.S. Epp (eds.), *Rotating Machinery, Hybrid Test Methods, Vibro-Acoustics & Laser Vibrometry, Volume 8*,
Conference Proceedings of the Society for Experimental Mechanics Series, DOI 10.1007/978-3-319-30084-9_13

Table 13.1 DSP topics presented in course

Quantization	Digital filters (FIR/IIR)
Sampling	Interpolation/Decimation
Fast Fourier transform	Adaptive resampling
Leakage/Windows	Order tracking
Auto/Cross powers	Averaging
Auto/Cross spectral density	Kalman/Vold Kalman filters
Frequency response function	Wavelet/WignerVille transform
Coherence	Time domain statistics

or fully understand the math, there is a vast resource available for them to explore on their own along with their textbook. The textbook chosen for this course is meant to be a reference that the students can open and proceed directly to the topic they wish to understand, without having to start at the beginning of the book to become completely versed in the prior material. For this reason, of the many digital signal processing textbooks available many of them are not appropriate as the math is too intensive for a practicing engineer to use the book as a quick reference.

The lectures in this course are presented from pre-prepared Powerpoint slides that contain only the basic talking points, plots and figures, and the rare equation. Many of the slides contain only pictures/plots and a few words and no equations.

13.3 Topics Presented

The topics presented in this course start with the basic data acquisition topics and run through to advanced order tracking methods. Different types of transducers are discussed along with test setup issues as well. Table 13.1 below shows a comprehensive list of DSP topics which are presented.

13.4 Assignments

Given the broad list of topics presented in this course, it is not possible to have students do an assignment on each topic. The students are assigned six different assignments that are a combination of data acquisition and Matlab programming.

The list below shows a typical list of assignments which the students are assigned. It is noted for each assignment whether the work is to be done in the laboratory or just in Matlab.

List of Assignments

Basic Data Acquisition (Experimental and Matlab)
Sampling and Quantization (Experimental and Matlab)
Leakage, Windows, and FFT (Experimental and Matlab)
FRF and Coherence (Experimental and Matlab)
Digital Filtering (Matlab)
Order Tracking (Experimental and Matlab)

If an assignment is listed as “Experimental” this indicates that time histories are acquired using *National Instruments Sound and Vibration Assistant with a CompactDAC system with a 9234 module* and/or a digital oscilloscope. In both cases the data would be imported into Matlab for plotting and report purposes.

If an assignment is listed as “Matlab” there is simulation and/or programming which is done in Matlab as a part of the assignment.

13.4.1 Basic Data Acquisition

This assignment includes the acquisition of data using both a digital oscilloscope and the NI software. This assignment is given in the first week of the semester with the sole purpose of exposing the students to the process of acquiring data using both instruments, importing the data into Matlab, and plotting the data in Matlab.

13.4.2 Sampling and Quantization

This assignment involves acquiring data using both the oscilloscope and the NI system as well as simulating both systems in Matlab. The students are given signal characteristics, frequency and amplitude as well as waveform type, which they use a signal generator to generate for acquisition and which they must generate themselves in Matlab. If the data is generated in Matlab, the students use "uencode" and "udecode" to simulate the effects of quantization. The students then plot the functions, sine waves and square waves of varying amplitudes, and see the effects of both sampling and quantization as the NI 9234 module has a 24 bit ADC while the oscilloscope has an 8 bit ADC.

13.4.3 Leakage, Windows, and FFT

The students first acquire data which are sine waves with different frequencies. The students set the sample frequency of the NI system based on a combination of a few digits of their student ID numbers, this forces the students to have different sample rates and hence differences in their assignments as a way to reduce collaboration and at least require them to each acquire their own data. In this assignment the students must generate frequencies with minimum leakage, maximum leakage, and then apply the Rectangular, Hanning, and Flattop windows to their effects on these frequencies. This assignment also has the students using the "FFT" command in Matlab to compute linear spectra. The "FFT" command in Matlab requires that the students apply several scaling factors to their results and discard the negative frequency information. The scaling which the students must do includes applying the Amplitude Correction Factor based on the window used, dividing by the blocksize, multiplying all frequencies above DC by 2 to account for energy discarded with the negative frequencies. No averaging is done as a part of this assignment. The students struggle to get the scaling correct, the most common error being the wrong scaling to the DC component of the spectra, the students want to multiply this value by 2 but since there is no DC component discarded with the negative frequencies this frequency is not multiplied by 2.

In the lectures to support this assignment, the Fourier Transform is derived using both the mathematics of the transform and a series of pictures/plots which show that the reason the that transform works so well, and that any transform works, is that the kernel of the transform "looks like" the aspects of the data that is desired to be understood. Having the students realize that we are performing this "coordinate transformation" so that the data is easier to understand helps them gain much more confidence as to why the transform works. I have them visualize trying to describe a pop can using a Cartesian coordinate system, a Spherical coordinate system, and a Cylindrical coordinate system and ask them which is easier to do . . . obviously the cylindrical coordinate system because the can looks like a cylinder. It would be very difficult to look at the coordinates of a can in spherical coordinates and realize what you were looking at!

13.4.4 FRF and Coherence

This assignment includes the students making FRF measurements with broadband random noise and estimating the gain of the system using individual sine waves. Students also acquire the time domain signals of the broadband input and the response. In this assignment, the system used in the experiments is shown in Fig. 13.1.

In this assignment the students program in Matlab both the H1 and H2 FRF estimators as well as coherence. Linear averaging is implemented as part of the processing. The FRFs and the individual frequency based gain measurements are overlaid in plots so that the students can see that it does not matter whether an FRF is measured using broadband or individual frequencies for a linear system. The most common mistake the students make in this assignment is averaging the linear

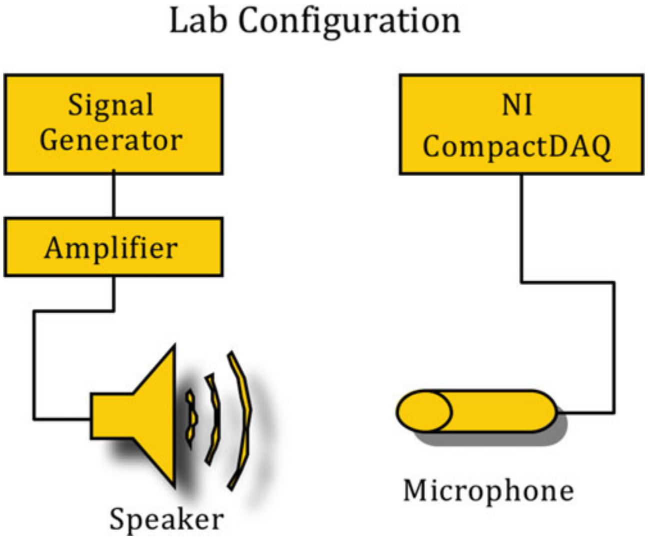

Fig. 13.1 System used for FRF measurements

spectra before computing the auto and cross powers needed to estimate the FRFs and coherence. Averaging the linear spectra results in a reduction in energy as they can and most likely will average destructively given that there is no phase reference to ensure only constructive averaging.

13.4.5 Digital Filtering

The digital filtering assignment is the only assignment done entirely in Matlab. For this assignment the students are given 4 or 5 different time histories which are made up of various combinations of signals. The students are required to separate a signal of two sine waves for instance into two different time histories or to filter out simulated line noise of 60 Hz, 120 Hz, 180 Hz, . . . etc. from a square wave signal. The students have the choice of using zero phase bandpass filtering and subtracting filtered time histories from the original signal or using bandstop filters. The students can use IIR or FIR filters and can either use the various filtering commands in Matlab or use the "fdatool" or "sptool" GUI tools. When presenting the digital filtering topics to the students numerical efficiency is stressed as one of the major tradeoffs that must be considered when choosing an ideal filter. The student which completes the whole filtering assignment with the fewest total number of filter coefficients is given 5 bonus points on their midterm score, this is done to encourage the students to use the most computationally efficient filtering approach possible.

13.4.6 Order Tracking

The order tracking assignment involves students taking accelerometer data from a benchtop rotating rig along with a pulse train to indicate rpm of the rotating shaft. The students operate the rig at both steady state speeds and through a series of speed sweeps where the sweep rate is varied from very slow to very fast. The time domain data is again acquired using the NI 9234 modules. The pulse train, measured with an ICP LaserTach, is processed to obtain estimates of the rpm at each delta_t of the response data. The response data from the speed sweeps is processed using FFT based order tracking and the Time Variant Discrete Fourier Transform (TVDFT) to obtain order cuts. FFT's are also used to generate waterfall and colormap plots of the speed sweeps. The steady state data is processed using Autopowers and used to identify the dominant orders to track. The fast and slow sweep rates are used to illustrate the different behaviors of the order tracking methods when the rpm and hence the acceleration amplitude change quickly vs. slowly. The students struggle to understand the details of this assignment because most of them are not accomplished programmers and find tasks such as identifying zero crossings when processing the tachometer signals difficult. The students also struggle to understand the frequency modulation which is the basis of the TVDFT.

The discussions which support this assignment go into depth as to the importance of the tachometer signal and its processing as well as why different order tracking methods work or don't work on various datasets. The order tracking methods are again presented graphically like the FFT and the coordinate system examples. Additionally, many of the differences in the answers generated by the various order tracking methods have to do with how they estimate an "average" amplitude over their respective transform times. The different methods average over different amounts of time based on their implementations, this leads to different amplitude estimates.

13.5 Instrumentation

In addition to the DSP topics which are covered in this course, there are also lectures on accelerometers, microphones, strain gages, and calibration. The accelerometer lecture is a lecture presented by Patrick Walter [1] and the acoustics and microphone lecture is a presentation put together by Mark Valentino [2]. Both of these lectures were presented at previous IMAC conferences in instrumentation related sessions. While these lectures go into a fair amount of detail about how different types of accelerometers and microphones are designed and built it is stressed to students that they should use the application engineers at transducer companies to help them select the appropriate transducer for their testing. It is explained that application engineers know their products very well and also have significant experience and exposure as to how their customers use their products and can therefore provide more assistance in many cases than just which transducer to use. Additionally, there is some discussion about foil based strain gages, ICP strain gages, thermocouples, and pressure transducers.

Test setup is also discussed in some lectures with many pictures of both good and bad test setups. It is stressed to the students that test logs are imperative to use and keep accurate as they may have to re-visit a dataset months or even years after acquiring it and that an accurate and complete test log is the only way they will be successful in doing this.

13.6 Distance Learning and Class Size

This course has been taught with varying class sizes over the years and with various combinations of on campus and distance learning students. Whether there is a small number (<15) of students or a large number of students has a large impact on the types of things which can be accomplished in a graduate course.

In the early years of the author teaching this course the students were all on campus and the class sizes were less than 15 students. With these relatively small groups of students the course had a midterm exam and a final project. The final projects were completed by groups of 2 or 3 students over the course of 4–5 weeks. The students were not assigned the order tracking assignment as there was not enough time to complete it. Each project culminated in a written report, typically 8–12 pages, and a presentation to the rest of the class. It was stressed that the presentations and report had to include what the students tried that did not work as well as what the students tried and did work. The thought behind including failed methods was that all of the students could learn from what worked as well as what did not work. It was also acknowledged that not all projects would be successful given the limited time that was available to complete them, and that just because the project wasn't a success from the perspective of getting the "right" answers there was significant learning that was done. A partial list of projects that students had done in the course is given below.

Partial List of Projects

- Development of DSP methods for IC engine knock detection
- Prediction of diesel engine misfire based on a engine block mounted accelerometer
- Use of a heat flux to surface temperature FRF to estimate type of material
- Transient Response of a Fuel Injection Rate Meter
- Using the ion signal to investigate the in cylinder combustion turbulence level
- Estimation of unwanted noise in a torque converter dynamometer test cell
- Characterization of a single cylinder engine dynamometer controller to reduce speed fluctuation
- Calibration of Real Time Film Thickness Sensor
- FFT Based Convolution on Graphics Processing Units
- Acoustical Absorption Characterization of Smart Panels using Piezoelectrics

In recent years the enrollment in this course has grown to a large enough size that it is no longer possible to ask the students to perform a final project. The ME-EM department at MTU does not have the resources available to support the large number of students doing real world projects. As can be seen from the project list above, many of these projects required that students have access to engine dynamometers or significant research laboratories. When there was a fewer students in the course, nearly all of the students were doing research as part of their graduate degree and hence already had access to a research laboratory to do the project. One of the reasons the enrollment in the course has grown so much is that the ME-EM department at MTU has significantly increased the number of graduate students enrolled, both PhD and MS. The bulk of the increase in the number of MS students has been coursework only students who do not have access to laboratory facilities to do projects. Given that it is not possible to do the final projects the course now requires the students to do the Order Tracking assignment and take a final exam.

There have also been a number of students over the years who have requested to take the course even though they are off campus working at a company. These students are either on co-op assignments or working full time. To offer the course to these students the on-campus lectures have been recorded and streamed to the the DL students on demand. To ensure that the students have the resources to complete the assignments each student has been interviewed prior to allowing them to register for the course. Through the discussion and email with the potential students it is determined what equipment they have available to them which can be used in the assignments. Given that not all DL students have the same equipment as is available on campus, the assignments are adapted to the equipment available. This approach for the DL students has worked very well though it only allows a small number of students to take the course as most students don’t have the necessary equipment available.

13.7 Grading

The grading for the course is based off of a combination of the students grades from the assignments (45 %), Quizzes (15 %), Midterm Exam (20 %), and Final Exam (20 %).

One unusual aspect about the grade for the assignments is that the students are given two chances to complete each assignment except the Order Tracking assignment which is due late enough in the semester that a second chance is not possible. The goal is that the students learn the material, if their first submission does not result in a grade above 85 %, it is marked “Fix and Return” and the students get another chance to improve their grade with no penalty for requiring the second submission.

The midterm exam is a combination of an in-class exam, 70 % of grade, and a take-home exam, 30 % of grade. The in-class exam is required to eliminate the possibility of cheating as that was becoming a problem when only a take home exam was given. The take-home exam is still given as it contains Matlab processing, a question where the students have to describe how they would make a measurement in a real world scenario and a problem where the students have to identify and get a price quote for a data acquisition system which meets a given criteria. The real world problem is given to force the students to put the presented material in context of how to use it. The data acquisition system problem is given to force the students to understand what choices and prices are available when they have to procure a system on their own, it also forces them to learn how to determine the capabilities of a system by reading specification sheets, manuals, advertisements, …etc.

Both the in-class midterm exam and the final exam are 1.5 h long and require the students to write significant Matlab code based on their assignments to keep them honest in doing their own assignments.

13.8 Conclusions

This course with its combination of experimental data acquisition and digital signal processing in Matlab has proven to be very successful in teaching the students a broad background in many different DSP and measurement methods. The value of the course is shown by the size of the enrollment in the course and the fact that most faculty in the ME-EM department at MTU which do experimental work require their students to take the course. Over the years the course continues to evolve to handle different groups of students and to keep topics relevant to the research which is being performed by faculty in the ME-EM department. Occasionally, a EE student has taken the course and provided feedback that “They finally understood the DSP which they had seen in their undergraduate signal processing course!”, this was due to the practical discussions and lectures vs. the theoretical lectures in their previous course.

The feedback from students who have taken the course over the years has always been that it was a very difficult class to get through but that it was one of the best courses they have taken at MTU! Again, their appreciation for the course has always been rooted in the practical nature of the course and the realization that they didn't have to learn a bunch of math they would never use again!

References

1. Walter, P.: The accelerometer bible. In: IMAC –XXIV Conference, Saint Louis, February 2006
2. Valentino, M.: Acoustics. In: IMAC-XXIV Conference, Saint Louis, February 2006

Chapter 14
Flipping the Classroom for a Class on Experimental Vibration Analysis

Anders Brandt and Christopher Kjær

Abstract Flipped classroom is a relatively new teaching form in higher education which is aimed at improving the learning process by engaging students in pre-class video activities fostering more active discussions between lecturer and student in-class. The concept is that the students watch recorded lectures (lower-order thinking skills) at home prior to class. During the class the students work on assignments and discuss the course content which can make better use of the teacher as a facilitator, so the focus can be on the more difficult things (higher-order cognitive skills) in the course content. In the present paper, the design and implementation using the flipped classroom technique for a course on experimental vibration analysis is presented. Some important experiences are discussed and an evaluation of student experiences is presented. The outcome is that the teaching technique is relatively time consuming to implement, but that the students appreciate being able to watch the lectures at their own pace and having more time working with the difficult things together with the teacher. Also, it turned out that the way the videos were used was very different among different students.

Keywords Flipped classroom • Experimental vibration analysis • Video lectures • Multiple-choice questions • Evaluation

14.1 Introduction

According to [1] the pedagogical approach of flipping the classroom has emerged from an evolution of existing pedagogical practice. In [2] it is pointed out that the concept is not new but has been given a renaissance caused by a changed focus in the classroom from a teacher-to a student centered approach and because of present and future technologies. Technologies which now make it easy for the teachers to create and distribute online resources like videos. Actually they trace the concept back to the year 1817 where the introduction of the Thayer-model pointed out that students should prepare at home for active participation in class [2].

Our understanding of the flipped classroom is "... that students gain first exposure to new material outside of class, usually via reading or lecture videos, and then use class time to do the harder work of assimilating that knowledge, perhaps through problem-solving, discussion or debates" [3]. The starting point is of course always the learning outcome of the course and by using Bloom's revised taxonomy [4] it becomes important to identify what learning goals can be characterized as lower levels of cognitive work which students can work with outside of class and which learning goals can be characterized as the higher forms of cognitive work where the students' needs to have support in class by the more experienced teacher.

The present paper describes how the flipped classroom concept was implemented for a course in experimental vibration analysis, based on the course book [5] by the first author of the present paper.

A. Brandt (✉)
Department of Technology and Innovation, University of Southern Denmark, Campusvej 55, 5230 Odense M, Denmark
e-mail: abra@iti.sdu.dk

C. Kjær
Center for Teaching and Learning, University of Southern Denmark, Campusvej 55, 5230 Odense M, Denmark
e-mail: ckjaer@sdu.dk

© The Society for Experimental Mechanics, Inc. 2016

J. De Clerck, D.S. Epp (eds.), *Rotating Machinery, Hybrid Test Methods, Vibro-Acoustics & Laser Vibrometry, Volume 8*,
Conference Proceedings of the Society for Experimental Mechanics Series, DOI 10.1007/978-3-319-30084-9_14

14.2 Motivation

Traditional teaching often results in lectures that are spent by the lecturer giving an overview of the subject, perhaps highlighting some of the points that, based on experience, are known to be difficult for the students. Exercises are usually left for the students' to work on by their own, or passed on to some special classes—many times conducted by less experienced teachers or PhD students. This means that the time for the professor to use his/her special competences in explaining unclear things to the students is limited. In addition, for many students, the efficiency of learning by listening alone is poor. Thus, the effective learning can many times be rather low. Alternative teaching techniques, which incorporate more of the students' senses and which are activating the students more, are desirable.

The flipped classroom concept is addressing these very issues with teaching. By letting the students prepare before the class, by watching one or more videos with the lecture, and reading the corresponding text in the text book, the class time can be used for discussions, problem solving, and in-depth explanations of concepts perceived as difficult by the students. This is also using the professor's competences more efficiently, since the professor can focus on discussing the more difficult and advanced parts of the topic, rather than spending time on the lighter content.

There are several challenges in implementing the flipped classroom. It is well-known that many students are not very motivated to work during the entire semester, but rather focus their work load to the end of the semester up to the exams. This behavior or learning culture needs to be changed for the flipped classroom concept to work properly. In addition, students have to be motivated to actually watch the videos and read the textbook before the lecture, to show up well prepared for the class discussions. Next, the lectures have to be planned and exercises suitable to be used for the purpose of focusing on the highlights of the topic are to be designed.

14.3 Organization

The present class on experimental vibration analysis consists of twelve lectures of four hours each, and eight home assignments. The course is running over a full semester in a two-semesters-per-year system. In the pilot class that was taught using the new concept, there were eight students on master's level.

Since the flipped classroom concept is new, at least to the students that were exposed to the class described here, in the first class, the principles were pointed out and the students were given an overview of the new study technique that they were supposed to use.

Several methods for motivating students to prepare well before class has been tried in conjunction with flipped classroom teaching [3]. To address this issue for the present course, each class (except the first one for obvious reasons) starts by asking multiple-choice questions (MCQs), where the students use clickers to respond. The teacher and students thus get feedback on how many of the students are giving the different alternatives as the correct answer. This is motivating the students to work pre class, because they typically feel embarrassed if they do not successfully answer the questions. Five to seven multiple choice questions with four alternative answers to each question were used for each class.

There are many clicker systems available on the market. For the present class, the web based system by Poll Everywhere (See www.polleverywhere.com), was used because it has the advantage that the students can use their cell phones, laptops, or tablets to respond, and thus there is no need for any additional hardware clickers. An account can be created where the questions can be entered and organized for each class. If the lecturer so wishes, the questions can be incorporated into PowerPoint presentations, although this was not done for the present class.

After the MCQs were answered, a short summary of the topic of the lecture was presented by a few PowerPoint slides, to trigger a discussion of details of the lecture topic. The idea with this is that by addressing the same issue several times (through the video, the textbook, and again in class) with slightly different angles, the students are more likely to come to a thorough understanding, and at least some of the angles will make more sense to each student, but not the same angles for each student.

The next part of the class consisted of the lecturer presenting several smaller problems, for the students to solve within 15–30 min for each problem. After giving the students the time to try to solve each question, a discussion of the answers was instigated, and the student's presented and discussed their different solutions.

The last 30–60 min of each class were used to go through the home assignment for the coming week, and for the students to start working on it. This was partly done because the assignments used were designed before turning the class into a flipped classroom class, and therefore the assignments required more time than the students had available, now that they also had to watch videos etc. prior to each class. Therefore the home assignments were made easier for the students by giving some hints on how to best solve them, and highlighting the difficulties and their principle solution.

14.4 Lecturer's Experience

The first experience is that videos take a very long time to record; at least it did for the first author. Videos were designed as talk-over to PPT slides. This format was chosen over having more authentic lectures where the lecturer is teaching, because it is believed to be more focused for the students watching. This format does, however, probably need a narrator capable of keeping the voice interesting otherwise the student may lose concentration through boredom. It should also be mentioned that the slides from each video were given to students prior to each class by putting PDF files on the class web site, so students could view the slides together with watching the videos.

In the present case, the videos were recorded and put on YouTube [6], by adding a channel with a playlist. By making the videos public, copyright issues become a matter, so the slide presentations have to be rid of any copyrighted material not owned by the author, or permission has to be sought. In the present case this was not an issue, and it was considered an advantage to have the videos publicly available to all readers of the textbook [5].

It turned out that students came prepared to class, however it also turned out that the pre-class learning could have been better, which was discovered by the MCQs often resulting in incorrect responses. This could indicate that the course content is difficult to understand (as is well known that signal and vibration analysis is for many students) and is not necessarily meaning that the result of the flipped classroom was not working. The result has to be evaluated at the end of the course. To increase the outcome of the students' self-learning during preparing for the class, next time the course is taught, the home assignments will be modified to allow them to be solved before class, as an example of just-in-time teaching [Mazur]. These assignments will then be used as the base for the discussions in class.

Class exercises also took a long time to prepare and will be modified for the second time this class is taught, but this is probably normal to do for any lecturer. The exercises have to be well designed in order to cover as much of the course content as possible, and they have to be possible to solve in the short time available. By changing the concept used in the present class as explained in the previous paragraph, this will likely be positively addressed.

The overall experience is that the flipped classroom technique was very hard to develop, but that it worked satisfactorily. Also, the second time, there will be more time for the lecturer to prepare the in-class discussions and home assignments, now that the videos are recorded.

14.5 Students' Experience

At the end of the course, the second author of the present paper conducted interviews with the eight students of the class. Overall, the students' experiences of the flipper learning design were surprisingly positive. The most important experiences reported by the students, who all experienced a flipped classroom class for the first time, will be presented in this Section.

We tried to investigate the following points in the interviews.

- How did the students experience using the videos to prepare before the class?
- How did the students use, or work with, the videos?
- How did the students experience the classes in this new teaching style?

14.5.1 The Students' Experience with the Videos

The question "How did you like using videos to prepare for class?" was answered very positively. Among the comments from students was "It gave me a different freedom . . . which means you can get answers to some questions before you go to class. I felt much better prepared for the classes we had than I normally do. It also meant that the lectures we had were used more for deeper discussions about some examples and stuff." [Student]

In this quote the student reflects both the experience of being better prepared, and that there are more time to work (in class) on some examples. Another student expressed it differently:

> "I really liked it; I thought it was a good way to prepare for class, and then the fact that you can go back into the video again and again, if there is one or another thing you did not really grasp. And you could also decide when you wanted to watch them, and you can pause them whenever." [Student]

Here, it especially the flexibility that the videos give to the student that is positively experienced. Yet another student emphasizes the possibility to rewind the videos and watch over again. He also thought the videos were a good complement to the book:

> "Generally I was very satisfied with it because you could always go back to a video from an earlier lecture and here Anders explains the principles again. I used that a lot. It is super good and you cannot do that in normal classroom where you only have 'one chance' to get it – whereas here you can always go back. To read things in the book is always good but when you have a teacher that explains the book content verbally, it is a really good complement to the book. He uses the same examples as in the book, but from a slightly different angle and a little more pedagogically, let me say, and also a little more compactly, perhaps." [Student]

14.5.2 How Did the Students Work with the Videos?

The students used the videos in different ways when they prepared the class. One student described his way to work with the videos such:

> "First I read the relevant chapter, or sections, in the book, and then I watched the corresponding videos. For me it worked best that way, in that I got something more out of the videos. I sat down with a notepad in front of me and watched the videos while taking notes." [Student]

The special point here is that the student took notes while watching the videos, and only watched the videos once. Another student had a different approach:

> "The way I prepared was, that first I skimmed the textbook briefly. Then I watched the videos, and then I went back and reread the parts of the book that I was not sure about, in detail. Most of the understanding I got from the videos, and then extra depth from the book. I wouldn't take notes while watching a video; then I rather watch it again." [Student]

The point here is that the students used the videos in very different ways. The flipped classroom thus opens up, perhaps, for different students to use a study technique by which they feel most comfortable.

14.5.3 How Did the Students Experience the Classes in This New Teaching Style?

Also in this respect the students were very positive. Among the comments is that

> "The great thing is definitely that you obtain a better understanding of the topic of the class, and that means that in class there is less time spent on the factual stuff and more time is spent on actually using it for practical problem solving. We got more time to work on examples. It is more like we can have great discussions in class." [Student]

Another student had the complementing answer to the question "Did you experience it as a strength that you had the videos to help prepare, so that you got more time in class for discussions?", to which he responded

> "Yes, I really think so. You see, you can use the videos to get some of the fundamental things in place, and then you can extend it with more difficult things in class. I thought that worked really well." [Student]

Here, the student himself touches on the key point that the home work can address the lower levels of cognitive skills, and then the tougher things can be dealt with in class, which higher cognitive skills being practices.

14.6 Conclusions

To conclude, the class on experimental vibration analysis we have been reporting on in the present paper was turned into a flipped classroom class by:

- Recording videos of the most important issues, as voice-over slide presentations
- Letting the lectures consist of multiple choice questions, followed by a summary of the topic content, and then a discussion around some examples of the use of the topic of the lecture.

The lecturer experienced that especially recording the videos, but also designing the multiple choice questions and discussion examples, took much longer than first anticipated. This is, however, a one-time task, and the following years more time can be spent on making better questions and examples.

The students expressed very high satisfaction with the new teaching technique. Although they used the videos in very different ways, they were all very happy about the flipped classroom concept, and thought it had many good points compared to traditional teaching.

References

1. Estes. M.D., Ingram, R., Liu, J.C.: A review of flipped classroom research, practice, and technologies. Int. HETL Rev. **4**(7), 55–64 (2014)
2. Hachmann, R., Holmboe, P.: Flipped learning – mere end bare video (2. udgave ed., Danish). Copenhagen: Nyt Teknisk Forlag (2014)
3. Brame, J.C.: [online], Flipping the Classroom. https://cft.vanderbilt.edu/guides-sub-pages/flipping-the-classroom/. (2015) Accessed 21 Oct 2015]
4. Anderson, L.W., Krathwohl, D.R., et al. (eds.): A Taxonomy for Learning, Teaching, and Assessing: A Revision of Bloom's Taxonomy of Educational Objectives. Allyn & Bacon, Boston (2001). Pearson Education Group
5. Brandt, A.: Noise and Vibration Analysis – Signal Analysis and Experimental Procedures. Wiley, Chichester (2011)
6. www.youtube.com, channel "Anders Brandt, ABRAVIBE", https://youtu.be/9BfH-GGgEw8?list=PLwxKUpykKU4gBEUj9htiQH_jZoZMOnO2E, last accessed Jan (2016)

Chapter 15
Lessons Learned from Operational Modal Analysis Courses at the University of Molise

Carlo Rainieri and Giovanni Fabbrocino

Abstract Operation Modal Analysis (OMA) is the testing procedure yielding experimental estimates of the modal parameters from measurements of the structural response only. Over the years OMA has evolved as an autonomous discipline and courses about this topic have been recently issued in some Italian universities.

The increasing interest for OMA is motivated by the possibility to carry out cheap and fast tests, which do not interfere with the normal use of the structure. In fact, the idea is to take advantage of naturally induced vibrations in the structure to avoid artificial input. As a consequence, the identified modal parameters are representative of the actual behavior of the structure in its operational conditions, since they refer to levels of vibration actually present in the structure.

The present review paper reports the experience gained by the Authors in giving classes about OMA for the M.Sc. Program in Civil Engineering at the University of Molise. The relevant role of practical applications is remarked. In fact, the main difficulties in approaching the study of OMA are usually related to the proper understanding of the mathematical background. Thus, a more practical approach to teaching and learning has been adopted with little penalty for theoretical derivations.

Keywords Vibration • Teaching • Operational modal analysis • Course • M.Sc. undergraduate

15.1 Introduction

The experimental identification of the modal parameters can be dated back to the middle of the Twentieth Century [1]. Since the origin, testing equipment and data processing algorithms have significantly evolved. Operational Modal Analysis (OMA) is the modal testing procedure that allows the experimental estimation of the modal parameters of the structure from measurements of the vibration response only. The idea behind OMA is to take advantage of the natural and freely available excitation due to ambient forces and operational loads (wind, traffic, micro-tremors, etc.) to replace the artificial excitation.

In the field of civil and earthquake engineering, OMA is very attractive. In fact, tests are cheap and fast, and they do not interfere with the ordinary use of the building or infrastructure. Moreover, modal parameters representative of the actual behavior of the structure in its operational conditions are identified. On the other hand, the low amplitude of vibrations in operational conditions requires very sensitive, low-noise measurement equipment [2].

Several successful applications of OMA in different fields are well documented in the literature. Unfortunately, the documentation about the different OMA methods was traditionally disseminated in a huge number of publications. This limitation has prevented the organization of specific courses for undergraduate students in civil engineering. The first book entirely devoted to OMA and its applications has been only very recently published [2], thus allowing a big step towards the dissemination of the discipline.

The present paper reports the experience of the Authors in organizing courses on OMA for undergraduate students in civil engineering at the University of Molise. Such courses are not frequently issued in Italian universities, so sharing the teaching experience within the scientific community committed with modal analysis and its applications can effectively support the enhancement of the general quality of courses about OMA. After general statements about our teaching activities, their methods and objectives, the organization of a course about OMA that covers all the fundamental aspects to understand its theoretical background and properly apply it is illustrated. The availability of a book entirely dedicated to OMA of civil engineering structures [2] definitely simplified the work.

C. Rainieri (✉) • G. Fabbrocino
DiBT Department, Structural and Geotechnical Dynamics Laboratory StreGa, University of Molise, Viale Manzoni, 86100 Campobasso, Italy
e-mail: carlo.rainieri@unimol.it; giovanni.fabbrocino@unimol.it

© The Society for Experimental Mechanics, Inc. 2016

J. De Clerck, D.S. Epp (eds.), *Rotating Machinery, Hybrid Test Methods, Vibro-Acoustics & Laser Vibrometry, Volume 8*,
Conference Proceedings of the Society for Experimental Mechanics Series, DOI 10.1007/978-3-319-30084-9_15

15.2 Teaching Methodology and Objectives

The basic background statement, supported by the experience, is that effective teaching and learning can come only from a genuine passion. Lectures, discussions, experiments are fundamental means to convey ideas and concepts but they can be ineffective if they do not reach the hearth and mind of students. For this reason, the main objective of the teaching activity is to raise passion for the subject in students, so creating an inspirational environment. However, raising passion towards certain topics, such as structural dynamics and OMA, can be difficult in the absence of a careful reflection about the teaching method and, above all, of a genuine passion of the teacher. In the Authors' opinion this circumstance can occur whenever a strong connection between research and teaching activities in a given domain exists. The possibility to carry out research as well as teaching activities in the field of structural dynamics makes possible the presentation of structural dynamics from different perspectives (direct/numerical and inverse/experimental). This, together with the presentation of a number of applications that connect the classroom to the real world outside, is the most appreciated aspect of the proposed course.

The main difficulties in approaching the study of OMA are usually related to the heavy mathematical formulations and derivation of mathematical models and equations. Thus, a more practical approach to teaching and learning is advisable with no penalty for theoretical derivations. For this reason, first the students receive the basic notions of LabView programming. Then, class applications and homework are assigned throughout the course to stimulate the students, who are motivated to develop their own software. The presentation of the results of applications compels them to review and analyze also the basic mathematical derivations.

This approach fosters the development of problem solving skills and encourages the students to work collaboratively, reducing at the same time the math anxiety. Illustrating the fundamentals of LabView programming gives the students the opportunity to develop simple data acquisition and processing systems and do practical modal identification experiments. The development of collaborative projects like this promotes the interaction among classmates with different background. The definition of different roles when cooperating in a project enhances the teamwork abilities. Public presentations of the completed exercises at the middle and the end of the course support the review of the main concepts of the course and an open discussion among the students, who can share ideas, make proposals to improve the work of the colleagues and focus on less investigated aspects.

However, a course cannot be effective and reach the hearth and mind of students if it is based only on technicalities and theoretical derivations. Thus, a continuous effort is made to give the students the big picture and not only the individual notions. Real applications coming from our research experience are often illustrated and discussed, pointing out the advantages of OMA for practical applications and eventual weaknesses related to specific case studies.

Lectures usually follow a path based on three key points. In fact, memorization is simplified if no more than three messages/concepts are presented. A recursive approach is also used, repeating the three key points and providing more and more details and illustrative examples during the lecture. The Authors finally try to be mentors for students, in the sense that an open door policy is operated whenever possible, encouraging students to ask for clarifications about specific aspects of the class even outside the scheduled office hours.

15.3 Organization of the Course

The course is organized in five parts:

1. Basic principles of OMA and fundamental tools for signal analysis;
2. Test planning;
3. Data acquisition and pre-treatment;
4. Modal parameter estimation;
5. Validation and post-processing of modal identification results.

In each moment, applications are proposed to foster the understanding of the theoretical notions and gain sufficient experience to carry out OMA tests independently.

In the first part of the course, after having presented the LabView environment [3] and having become familiar with it, the basic principles of OMA and the fundamental mathematical tools for signal analysis are presented. The first critical aspect to explain is how the modal properties can be identified without controlling the input. In this perspective, the roles of sensor layout and unmeasured sources of excitation are critically analyzed.

Even if the input is immeasurable, it is important to remark that some assumptions about it are needed. For instance, the assumption of broadband excitation ensures that all the structural modes in the frequency range of interest are excited. Assuming that the combined system is excited by a random input, the second order statistics of the response carry all the physical information about the system and play a fundamental role in output-only modal identification. The focus on second order statistics has to be justified by referring to the central limit theorem, pointing out that the structural response is approximately Gaussian in most cases, no matter of the distributions of the (independent) input loads, which are often not Gaussian. The spatial distribution of the input also affects the performance of OMA methods, in particular in the presence of closely spaced modes. A distribution of random in time and space inputs provides better modal identification results [4].

In order to illustrate this concepts and the role of sensor layout, it is possible to present the problem of modal identification as one of matrix rank computation. In fact, taking into account that the output power spectral density (PSD) matrix $[S_{YY}(\omega)]$ can be expressed in terms of the Frequency Response Function (FRF) matrix $[H(\omega)]$ of the structure and the input PSD matrix $[S_{FF}(\omega)]$ as follows:

$$[S_{YY}(\omega)] = [H(\omega)]^* [S_{FF}(\omega)] [H(\omega)]^T \tag{15.1}$$

its rank cannot be larger than the rank of the individual matrices appearing in the product. This implies that closely spaced modes cannot be estimated if the rank of the input PSD matrix is equal to one. Based on this simple mathematical concept, it becomes easy to show that closely spaced modes cannot be identified if only one input is present, or the inputs are fully correlated. Rank deficiency over a limited frequency band in the proximity of the considered closely spaced modes can partially hide the actual physical properties of the structure (for instance, by revealing only one of the modes, or a combination of the two modes). Thus, a proper design of sensor layout and a preliminary evaluation of the sources of excitation acting on the structure in its operational conditions play a primary role in ensuring the possibility to obtain high quality information from modal testing.

The following general rule is mentioned: a large number of sensors allow maximizing the rank of the FRF matrix, while several uncorrelated inputs ensure the maximization of the rank of the input PSD matrix. On the contrary, correlated inputs or input applied in a single point limit the rank of the input PSD matrix; sensors placed in nodes of the mode shapes or multiple sensors measuring the same DOF (thus, adding no new independent information) limit the rank of the FRF matrix. This rule gives valuable suggestions for proper test execution.

Having shown that all the physical information can be found in second order statistics, correlation functions and power spectral density functions are introduced. The basic ideas behind Fourier analysis and relevant theory behind correlation functions and power spectral densities are reviewed. Then, their practical estimation based on measured data is illustrated. The proper computation of correlation functions and power spectral densities is critical in view of the application of OMA methods. Thus, specific applications have been designed for the students to learn how to compute these functions from measured random vibrations with the support of their laptop (Fig. 15.1).

High quality measurements represent another fundamental step for a successful modal identification. Any OMA method is ineffective if measurements are totally corrupted by noise. Poor measurements can be the result of an incorrect choice of sensors or measurement hardware, but they can be due also to incorrect wiring. In fact, for a given choice of the measurement hardware and sensors, different measurement schemes can often be adopted. The choice of the most appropriate cabling scheme and the adoption of the related specifications for the entire analog signal path play a primary role in the collection of high quality data.

The sensing technologies available on the market are presented, pointing out advantages and limitations of different measurement solutions. In particular, the difference between grounded and floating sensors, and between single ended and differential measurement systems are illustrated in detail. In order to encourage the participation of the students and simplify the presentation of concepts that are usually far from the typical background of civil engineers, datasheets of different accelerometers and measurement devices are delivered to the students in order to set up an appropriate measurement chain for output-only modal identification. To this aim it is also important to summarize the main characteristics of different sensing solutions. In this perspective, a comparative analysis of the sensors usually used for modal testing of civil structures (piezoelectric and force balance accelerometers) is proposed. The presentation of the measurement principle of the sensors is fundamental to understand why different sensors show different advantages and limitations. For instance, the comparative analysis makes easy to understand why force balance accelerometers can measure up to the DC component while piezoelectric accelerometers cannot, or why different accelerometers, even of the same type (i.e. piezoelectric accelerometers), are characterized by a different bandwidth.

Fig. 15.1 Students developing their classwork with the support of their laptop

Starting from the analysis of sensor specifications, the question of appropriate attachment of the sensors is introduced, showing how it can affects the bandwidth and even alter the measurements. Applicative examples are proposed, showing that accelerometers can be mounted by a variety of methods, including magnet, adhesive, and stud or screwed bolt. Each of these methods has advantages and limitations. The importance of stiff connection and adequate preparation of the surface is remarked.

As previously mentioned, sensor location is responsible for the observability of structural modes. The fundamental reasons, which may require moving the sensors from one location to another, are presented. In particular, the problems related to the installation of sensors in correspondence or very close to nodes of the structural mode shapes, to poor spatial resolution of measurements and unfortunate choice of sensor layout are presented by means of applicative examples.

Typical sensor layouts for different structural schemes are also presented (Fig. 15.2). Even if they represent only crude guidelines for the design of appropriate sensor layouts, they are useful to simplify test planning in the presence of regular structures. In order to apply the previously mentioned notions, at least one field application on a real structure (Figs. 15.3 and 15.4) or a scaled model (Fig. 15.5) is proposed. All relevant details are provided in order to allow the student to autonomously set up their first experimental test.

After having collected their first dataset, taking into account the importance of the appropriate setting of sampling frequency and total record duration [2], they are committed with data validation and pre-treatment. In particular, a specific application is proposed, where the students visually inspect the individual time histories and estimate the corresponding probability density functions and power spectral density functions in order to detect anomalies, such as excessive noise, noise spikes, clipping, and so on. Then, they apply basic linear algebra tools (least squares) or filters to remove eventual spurious trends in the data.

Once validated and pre-treated data are available, the students have to develop their own modal parameter estimation software. Among the OMA methods available in the literature, the peak picking method [5] and the Frequency Domain Decomposition (FDD) method [6] are proposed because they are characterized by a simple theoretical background and ensure a fast implementation once auto- and cross-power spectra are estimated. When these methods are implemented and applied, the main difficulty is related to the need of dealing with complex numbers and complex-valued vectors. In our experience, it is important to recall the basics and the different representations of complex numbers before illustrating the OMA algorithms.

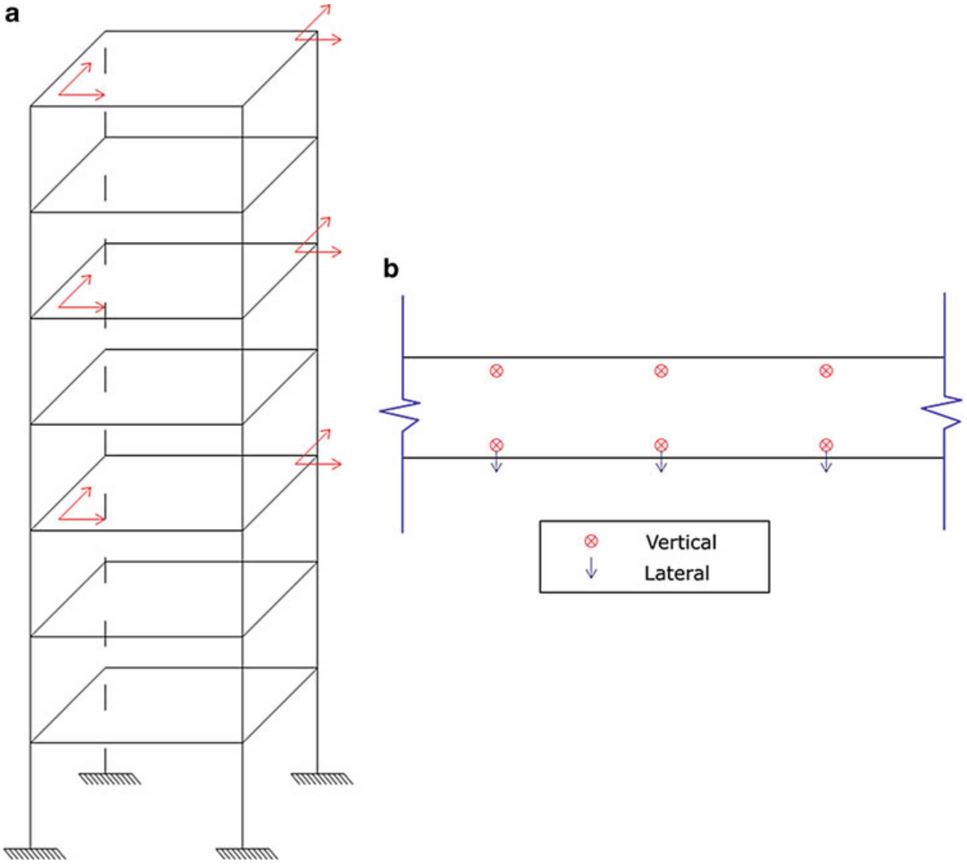

Fig. 15.2 Recurrent sensor layout for building-like structures (**a**) and bridge spans (**b**)

Fig. 15.3 Students involved in the application of OMA to a real bridge [7]

The course ends with an overview of the different OMA methods, their classification and comparative analysis. The theoretical basis of the most popular methods is briefly presented, inviting the students interested in more details to refer to the textbook and the scientific literature. An extensive analysis of the theoretical background of all OMA methods is, in fact, impossible due to the limited amount of hours of lesson. Nevertheless, popular OMA methods, such as the Stochastic Subspace Identification method and the (polyreference) Least Squares Complex Frequency method [2], are presented from an applicative point of view, based on the software included in the textbook [2].

Tools for validation and post-processing of modal identification results are finally presented, together with a number of case studies derived from our research experience. Most of them are also reported in the fifth chapter of the textbook [2].

Fig. 15.4 Application of OMA to the historical bell tower of the Trisulti Charterhouse [8, 9]

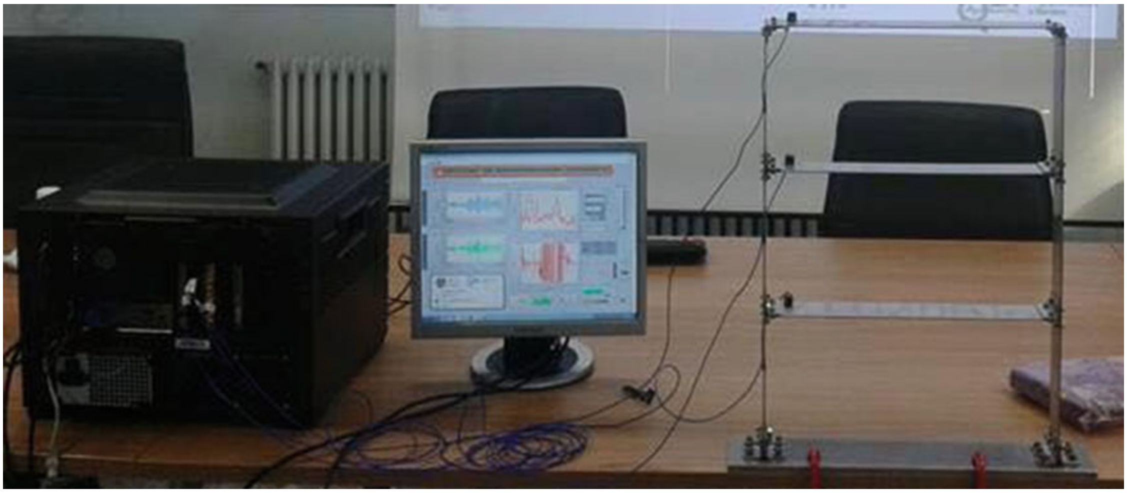

Fig. 15.5 Application of OMA to a scaled model of frame in the laboratory

15.4 Conclusions

The lessons learned from OMA courses for undergraduate students in civil engineering at the University of Molise (Italy) have been presented. In particular, it has been remarked how an effective teaching of OMA at the undergraduate level requires a perfect combination and balance of theory and application. Moreover, it is important to present not only the notions but also the big picture, that is to say, the potential applicative perspectives of the discipline in the real life. Availability of a dedicated textbook about OMA and its applications in the civil engineering field is definitely an advantage.

Acknowledgments The Authors would like to thank their students for their valuable feedback in the organization of one of the first courses about Operational Modal Analysis for undergraduate students in civil engineering in Italy. The present work was partially supported by the ReLuis-DPC Executive Project 2014–2016, RS4 Special Project "Monitoring" coordinated by Prof. G. Fabbrocino and Prof. F. Ponzo, whose contribution is also gratefully acknowledged. Opportunities provided by research carried out in the context of the Agreement Arcus—DG PaBAAC Rep. n. 113/2011 del 30/09/2011 issued by MiBac for the seismic assessment of the Carthusian monastery of Trisulti in Collepardo, and Project PON-FESR 2007–2013 (PON01_02366, STRIT) "Tools and Technologies for the Management of the Transportation Infrastructures", coordinated by STRESS S.c.ar.l., are gratefully acknowledged. Authors are also really grateful to Prof. S. Gerbino, Chair of the M.Sc. Course in Civil Engineering at the University of Molise for his support and motivation in the development of innovative forms of education based even on the experience, out of the class, in the context of real applications. Support of administrative staff for all the issues related to the management of activities is also acknowledged.

References

1. Ewins, D.J.: Modal Testing: Theory, Practice and Application, 2nd edn. Research Studies Press Ltd., Baldock (2000)
2. Rainieri, C., Fabbrocino, G.: Operational Modal Analysis of Civil Engineering Structures-An Introduction and Guide for Applications, p. 322. Springer, New York (2014)
3. National Instruments: LabView Fundamentals. LabView Manual. National Instruments Corporation, Austin (2005)
4. Herlufsen, H., Andersen, P., Gade, S., Møller, N.: Identification techniques for operational modal analysis – an overview and practical experiences. In: Proceedings of the 1st International Operational Modal Analysis Conference, Copenhagen (2005)
5. Bendat, J.S., Piersol, A.G.: Random Data: Analysis and Measurement Procedures, 3rd edn. Wiley, New York (2000)
6. Brincker, R., Zhang, L., Andersen, P.: Modal identification of output-only systems using frequency domain decomposition. Smart Mater. Struct. **10**, 441–445 (2001)
7. Pecce, M.R., Ielardi, A., Rainieri, C., Fabbrocino, G.: Dynamic modeling and operational modal analysis of a steel-concrete composite bridge. In: Proceedings of the XXV CTA Congress, Salerno (2015)
8. Rainieri, C., Marra, A., Fabbrocino, G.: On the estimation of the fundamental modal properties of Italian Historical Masonry Towers. Ingegneria Sismica: Int. J. Earthq. **31**(3) (2014)
9. Rainieri, C., Marra, A., Rainieri, G.M., Gargaro, D., Pepe, M., Fabbrocino, G.: Integrated non-destructive assessment of relevant structural elements of an Italian heritage site: the Carthusian monastery of Trisulti. Journal of Physics: Conference Series. In: Proceedings of the 11th International Conference on Damage Assessment of Structures DAMAS 2015, vol. 628 (2015)

Chapter 16
Authentic Engineering Assignments for an Undergraduate Vibration Laboratory Class

James P. De Clerck and Jean S. De Clerck

Abstract Authentic problem-solving experiences were used for a three-lab sequence on vibrations, offered as part of a required course for all mechanical engineering students at Michigan Tech, in order to guide undergraduates in building problem solving abilities. The sequence covers free-vibration, forced vibrations and tuned absorbers. In previous delivery of this course, a generic single degree of freedom test structure with no physical connection to a real-world application was used for all three activities. These initial lab activities guided the students through a process of gathering and interpreting measurements with little application of these engineering skills for solving realistic engineering problems.

The authors added context to assignments by simulating an engineering problem to be solved and requiring that the students frame their report as a recommendation to an engineering decision-maker (i.e. Chief Engineer). Students are held accountable for making specific recommendations and supporting their recommendations with simulation and test results. Most students claim that they enjoy this experience more than traditional lab activities and that the use of context motivates them to understand the material.

Keywords Laboratory assignments • Vibration course • Scenario-based assignments • Problem solving • Surrogate structures

16.1 Introduction

The mechanical engineering curriculum at Michigan Tech has a laboratory class with a three-lab sequence covering free vibration, forced vibration, and multiple degree of freedom systems. Student teams measure the vibration of standard single degree of freedom (SDOF) system (Fig. 16.1) that is specifically designed to easily accommodate changes to mass stiffness and damping. Another spring mass system can easily be attached to the main mass to represent a tuned absorber or generic two-DOF system.

The initial laboratory instructions guided students through academic exercises of making acceleration measurements to verify mass, damping, and stiffness (MCK) models. Students followed the instructions and wrote lab reports with little understanding of how these activities might apply to real world systems. Students struggled with the lab activities because: (1) the test structure did not resemble a realistic vibrating system and (2) students could not envision how test results contribute to real world engineering problem solving and decision making.

16.2 Redesign of Laboratory Experiments as Authentic Assignments

The authors reframed the three-lab sequence with authentic problem-posing scenarios to support students in ongoing efforts to build a rhetorical technê for mechanical engineering problem solving. Rhetorical technê, originally explored by Aristotle, is a set of flexible, theoretical approaches or principles for understanding and investigating situations where persuasive action is possible for problem solving [1].

J.P. De Clerck (✉)
MEEM Department, Michigan Technological University, 1400 Townsend Drive, Houghton, MI 49931, USA
e-mail: jdeclerck@mtu.edu

J.S. De Clerck
Instructional Design and Assessment Specialist, Michigan Technological University, Jackson Center for Teaching and Learning,
1400 Townsend Drive, Houghton, MI 49931, USA

© The Society for Experimental Mechanics, Inc. 2016

J. De Clerck, D.S. Epp (eds.), *Rotating Machinery, Hybrid Test Methods, Vibro-Acoustics & Laser Vibrometry, Volume 8*,
Conference Proceedings of the Society for Experimental Mechanics Series, DOI 10.1007/978-3-319-30084-9_16

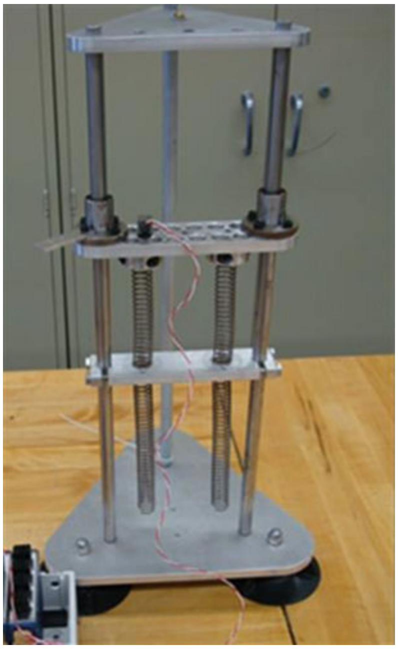

Fig. 16.1 Single degree-of-freedom test structure

Authentic problem-posing scenarios are well-suited for undergraduates who typically have minimal understanding of industry practice. This pedagogical approach builds on traditional teaching that is focused on the dissemination of knowledge on a specific topic [2, 3] and includes two key aspects linking topical knowledge to engineering practice: (1) a problem scenario with a physical system that is familiar to the students and (2) an audience willing to implement their solution. The problem scenario frames the activity so students develop their abilities to situate problem-solving processes and apply disciplinary knowledge within the context of engineering problems. The scenario includes a specific decision making audience which reinforces the value of engineers because someone is waiting to review the work and implement their solution. Students build confidence writing test reports that are intended to contribute to engineering decision-making.

The authors drew from their industry experience and their understanding of required curriculum, in particular the first-year composition course, when redesigning the three-lab sequence on vibrations. The authors brainstormed scenarios to link laboratory topics to real-world scenarios that emphasized requirement verification. The Chief Engineer was selected as the authentic audience for the test reports. Also, the report title was changed from "lab report" to "test report".

Due to budget and space constraints, the authors could not replace the test structures with the actual physical test articles. The existing test structure was used as a surrogate structure for all lab activities. Surrogate systems are also used in industry to break down complex systems in order to emphasize and study aspects that are important to the function of the design.

For each of the three topical modules, students meet for a 1-hour recitation and a 3-hour lab. During the recitation, the instructor presents the scenario and reviews the applicable engineering knowledge and skills. Students also do a pre-lab activity using a computer simulation to practice concepts and calculations prior to acquiring and processing actual data. During the lab meeting, three to four member student groups follow the lab instructions using the surrogate system, and then each student communicates findings and recommendations in individual test reports to the scenario's decision-making audience, the Chief Engineer.

16.3 Lab Activity 1: Free Response of an Aircraft Wing

The scenario for the free-vibration lab activity is a fixed-wing aircraft. A customer is concerned that one wing of their small aircraft vibrates too much. The student engineers are asked to measure the free vibration of a prototype aircraft to determine the equivalent mass, stiffness and damping. They also verify the design requirement values for natural frequency and damping. The student engineers then use free vibration measurements to determine the equivalent mass, stiffness and damping of the customer's wing. Deliverables of the test report are (1) the quantitative discrepancy of the equivalent mass, stiffness, and damping of the prototype wing and the customer's wing and (2) validation of natural frequency and damping of customer's wing relative to the design requirements.

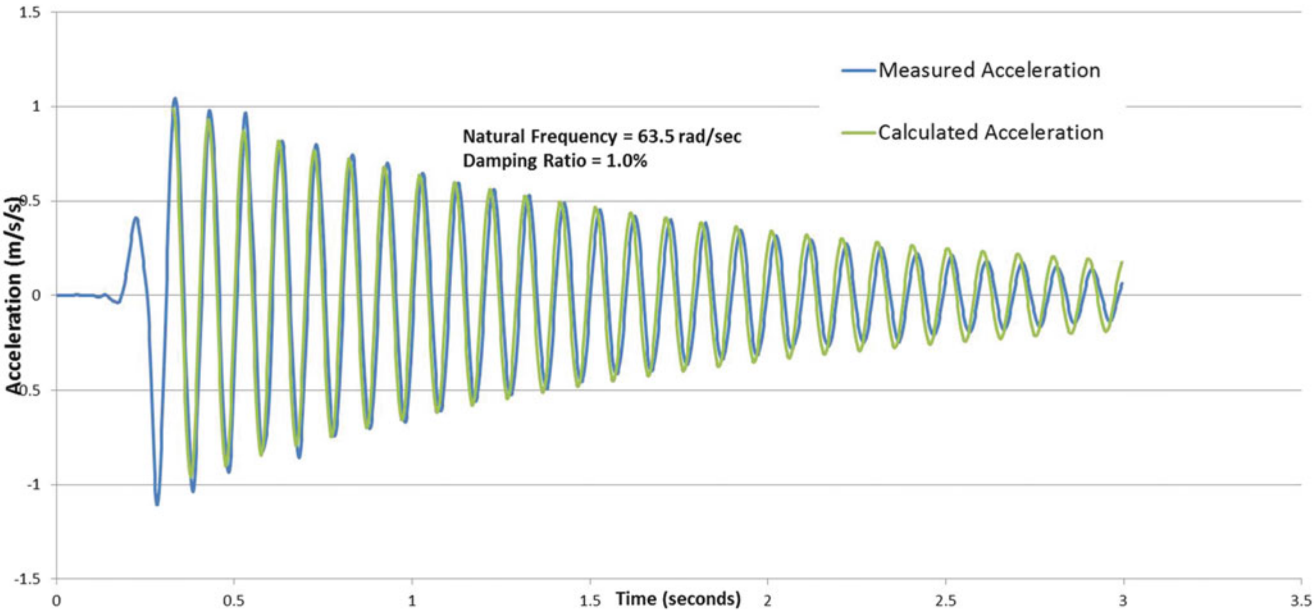

Fig. 16.2 Sample verification of natural frequency and damping ratio estimates using an overlay of free-response model and the original data

The pre-lab activity begins with a brief lecture on the basics of free vibration analysis. Students are instructed how to estimate damped natural frequency by (1) counting the number of cycles in unit of time and (2) computing the average period over several cycles. Students are also instructed to use the log-dec method to estimate damping ratio.

The PhET *Masses and Springs* [4] is used to demonstrate basic analysis of SDOF free vibration. Students use the PhET during a pre-lab activity to practice measuring static stiffness and the period of a vibrating system. A worksheet guides student engineers through a series of steps similar to the subsequent lab activity.

In the lab, students are instructed to pretend that the standard test structure is a surrogate prototype aircraft wing. Teams measure static stiffness by applying weights and use a machinist dial to measure deflection of the surrogate wing tip. Students use a pluck test to acquire free response acceleration and estimate natural frequency and damping ratio. An overlay of the recreated decaying sinusoid and the original data is used to verify the estimated parameters, as shown in Fig. 16.2. Now, the students use the static stiffness and natural frequency to estimate the equivalent mass. The next step is to add a known mass and make another free response measurement. They can now estimate mass, stiffness, and damping using the results of two free vibration measurements. These results are presented as validation that the design requirements are achievable.

Teams continue practicing their skills by making an unknown stiffness change by shortening or lengthening the springs. This change is estimated and verified/updated using another free response measurement. A dashpot is added as an unknown damping change, which is also estimated and verified. These results are included in the appendix of the report to demonstrate credibility of the student engineers.

At this point, the surrogate structure (Fig. 16.3) looks and performs different than when the students entered the lab (Fig. 16.1) and every team has made slightly different changes. Teams exchange test structures as the customer's aircraft. They proceed to make free response measurements to estimate the mass, stiffness, and damping of the customer's wing. The deliverable for the test report is the quantitative difference between the surrogate prototype wing and the customer's wing.

16.4 Lab Activity 2: Spin Speed for Washing Machine

The scenario for the forced-response activity requires a recommendation for the range of acceptable speeds for the spin cycle of a washing machine. The requirement is that the washing machine must not have more than 5 mm peak displacement for the standard imbalance. In addition to recommending a speed band that will meet the requirement, students are asked to recommend system changes (mass, stiffness, damping) that will increase the range of acceptable spin speeds. Again, the decision-making audience for the report is the Chief Engineer.

Fig. 16.3 Standard structure configured to simulate the customer's aircraft wing

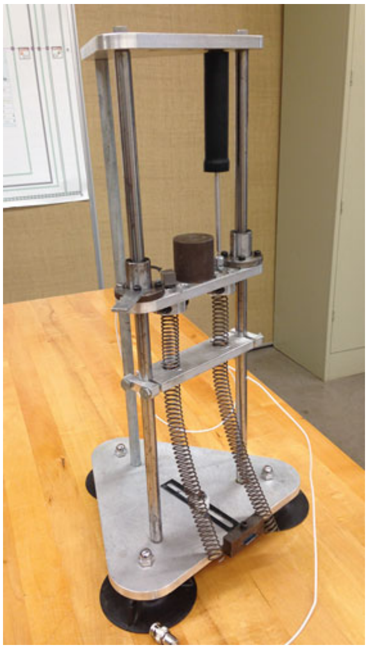

Fig. 16.4 Standard structure configured to simulate a washing machine with an imbalance

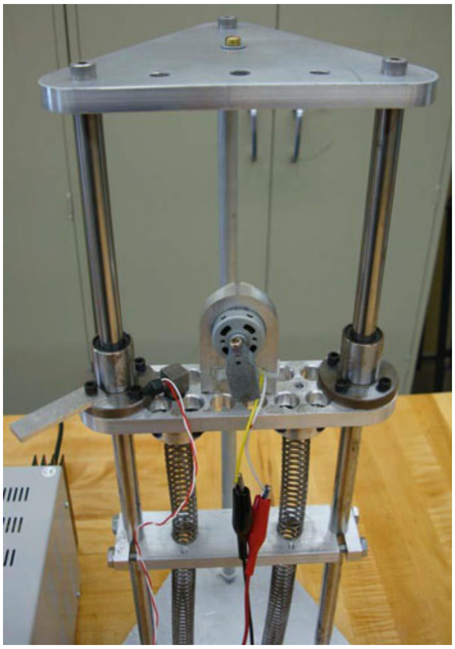

The pre-lab activity begins with a brief lecture on the basics of forced vibration analysis. Students are instructed how to estimate compliance and accelerance frequency response functions and use them to determine peak amplitude of steady state forced vibration. Determining the force due to a rotating imbalance is also reviewed.

The PhET *Resonance* [5] is used to demonstrate basic analysis of SDOF forced vibration. Students use the PhET during a pre-lab activity to practice measuring peak steady-state displacement and external force at discrete excitation frequencies. The ratio of these quantities is compared to the compliance frequency response function determined using the mass, stiffness, and damping values. Students then differentiate their measured displacement and compare their results to the accelerance frequency response function. The lab activity requires the inverse of this process, beginning with measured acceleration and integrating to estimate compliance.

In the lab, an electric motor with imbalance mass is added to the surrogate test structure, shown in Fig. 16.4. Students are instructed to pretend that the surrogate test structure is a washing machine that they can control the voltage to the spin motor. The standard imbalance has a known eccentricity and the students measure the mass of their particular part.

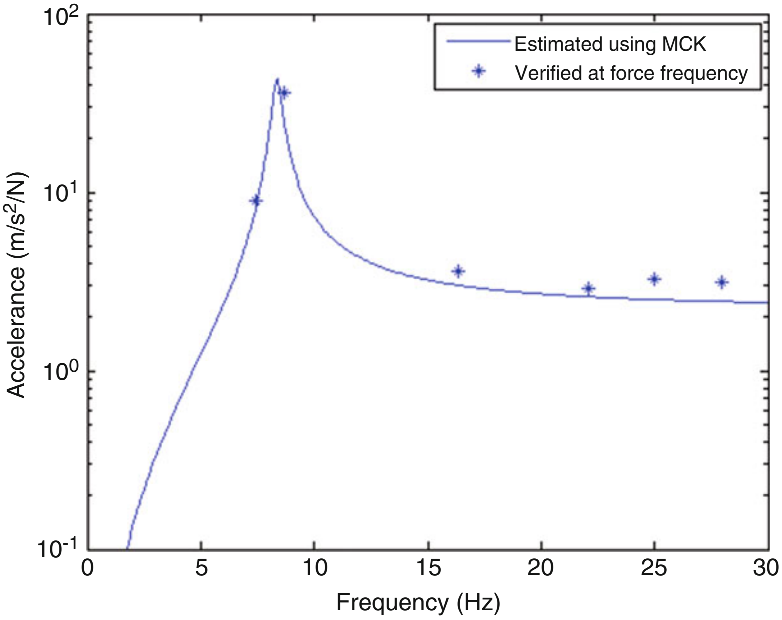

Fig. 16.5 Sample accelerance plot with single frequency verification

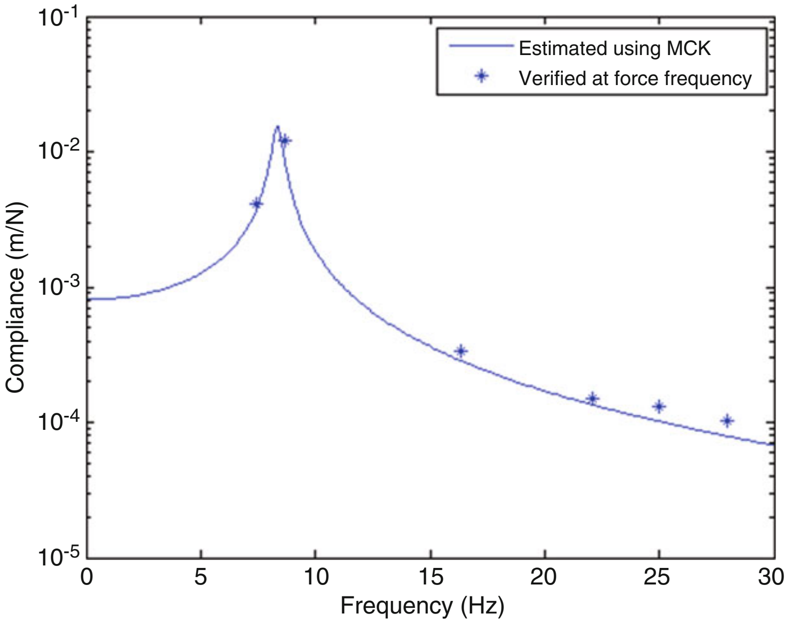

Fig. 16.6 Sample compliance plot with single frequency verification

The first step is to use their skills from the previous lab to estimate the mass, stiffness, and damping of the baseline system. They use these estimates to compute compliance (displacement/force) and accelerance (acceleration/force) frequency response functions.

To establish credibility with the decision maker, the student engineers verify the accelerance curve by measuring acceleration response at specific motor speeds and dividing the peak acceleration by the corresponding peak imbalance force, shown in Fig. 16.5. These data points are integrated to verify the compliance plot, shown in Fig. 16.6.

The final step is to multiply the imbalance force spectrum and the compliance to identify the frequency band(s) that yield displacement less than the requirement value. In their test report to the Chief Engineer, students make recommendations for changes to move the resonance and how to pass through resonance to the isolation band.

16.5 Lab Activity 3: Tuned Absorber to Reduce Steering Wheel Vibration

The scenario for the multiple degree of freedom (MDOF) experiment is to design a tuned absorber for the steering wheel of a luxury automobile. The problem is that engine firing frequency at idle is the same as the natural frequency of the steering column causing excessive vibration. The Chief Engineer asks the students to investigate using a tuned absorber to reduce the steering column vibration. The student engineers are asked to recommend a design (mass and stiffness) for a tuned absorber and provide quantitative evidence of the reduction in vibration.

The pre-lab activity begins with a brief lecture on the basics of two degree of freedom free vibration analysis. Frequency response functions for one and two degrees of freedom are compared. The key concept is that anti-resonance is a special case where the specific degree of freedom will not move even when a high amplitude force is applied at that frequency.

The PhET *Resonance* [5] is used to demonstrate how system can have multiple natural frequencies. This tool is also used to demonstrate how a reed tach works. The PhET *Normal Modes* [6] is used to demonstrate mode shapes and natural frequencies.

In the lab, the first step is to identify the natural frequency of the simulated steering column. The surrogate engine is a Modal Shop Model 2002E Miniature Electrodynamic Inertial Shaker [7] attached to a piezo-electric load cell which is attached to the surrogate test structure, as shown in Fig. 16.7.

Because the shaker is part of the system, the pluck test cannot be used to estimate the natural frequency. Student engineers must use skills from the previous activity to estimate the accelerance and compliance using a series of measurements at discrete frequencies.

Once the natural frequency is identified, the excitation frequency is set at resonance. The students then attach the tuned absorber (mass and spring steel) and adjust the stiffness by moving the mass in and out until the simulated steering column stops moving. Students also notice that the added mass has high amplitude of vibration.

The student engineers use two methods to validate their solution. The first requires inserting a stiff block between ground and the surrogate steering column and measuring the free response of just the tuned absorber. The natural frequency of the tuned absorber should match the frequency that they wanted to cancel. The second method is to repeat measuring accelerance to demonstrate that the proposed solution results in a system has two natural frequencies and anti-resonance at the frequency they wanted to cancel. A sample plot is shown in Fig. 16.8.

In their test report to the Chief Engineer, students recommend adding a tuned absorber to the steering column and specify values for the mass and stiffness to guide the design of the tuned absorber.

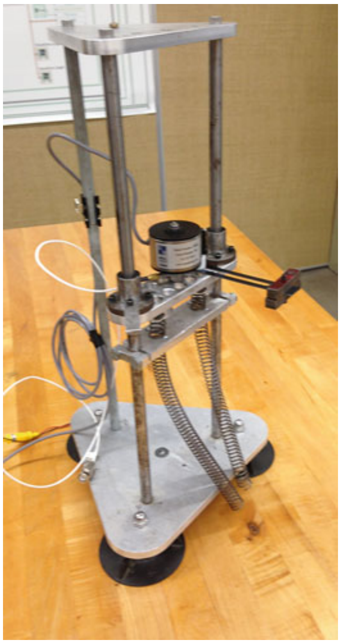

Fig. 16.7 Surrogate steering column with tuned absorber shown as a mass attached to slotted spring steel

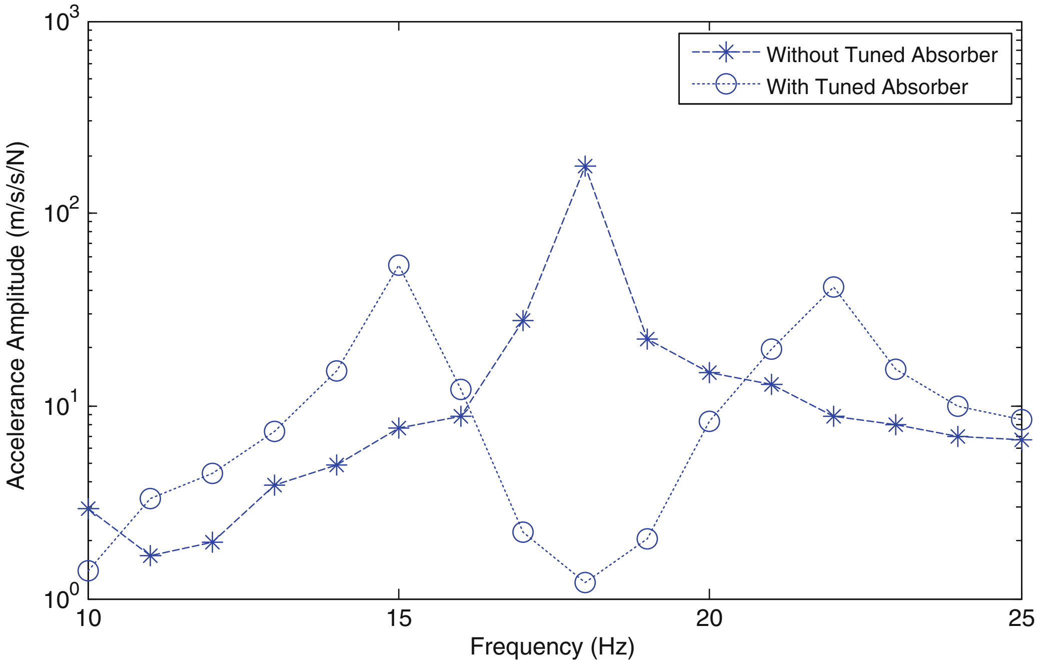

Fig. 16.8 Sample frequency response functions to validate proper tuning of the tuned absorber

16.6 Conclusions

Authentic problem framing was successful in providing students with opportunities to contextualize use of testing protocols and to practice crafting written communication to influence decision making. From course evaluation and informal feedback, students appreciated the contextual framing. While data are not available, general impressions from the instructor and teaching assistants reviewing student lab report submissions suggests that asking students to craft lab reports for a decision-making audience produced better quality reports.

Authors' time required for redesigning the assignment and surrogate system was reasonable, students preferred the laboratory experiences with scenarios, and student learning performance continues to be encouraging. An additional and unintended transferable skill was also realized; students gained experience using surrogate test systems to understand and study complicated engineered systems (such as airplanes). This experience will be useful when students encounter or need to design surrogates in subsequent courses and when they become practicing engineers. The authors plan to continue using authentic problem scenarios in other classes to help students build their problem-solving abilities.

References

1. De Clerck, J.S.: Exigencies for engaging undergraduates in rhetorical problem solving: insights from engineering managers and A3 report analyses. Master's Thesis, Michigan Technological University (2012)
2. Pierrakos, O., Zilberberg, A., Anderson, R.: Understanding undergraduate research experiences through the lens of problem-based learning: implications for curriculum translation. Interdiscip. J. Problem-Based Learn. **4**(2):35–62 (2010). Available from: Education Abstracts (H.W. Wilson), Ipswich, MA. Accessed 18 October 2015
3. Filipe, N.; Pritchett, A.: Applying problem-based learning to instruction of system dynamics and controls. In: American Control Conference (ACC), 2014, pp.2530–2535, 4–6 June 2014. doi:10.1109/ACC.2014.6859216
4. University of Colorado Boulder, PhET Interactive Simulations, Masses & Springs [Online]. https://phet.colorado.edu/en/simulation/mass-spring-lab
5. University of Colorado Boulder, PhET Interactive Simulations, Resonance [Online]. https://phet.colorado.edu/en/simulation/resonance
6. University of Colorado Boulder, PhET Interactive Simulations, Normal Modes [Online]. https://phet.colorado.edu/en/simulation/normal-modes
7. Modal Shop [Online]. http://www.modalshop.com/filelibrary/Miniature-Electrodynamic-Inertial-Shaker-Model-2002E.pdf

Chapter 17
Vibration and Acoustic Analysis of Acoustic Guitar in Consideration of Transient Sound

Nobuyuki Okubo, Naoaki Iwanaga, and Takeshi Toi

Abstract The sound characteristic of an acoustic guitar is empirically designed for long time. The up to date vibration and acoustic analysis are applied to investigate the difference between typical guitars especially focused on transient vibration and sound just after picking a string at keynote and higher harmonic frequencies. By using a simplified front plate model of a guitar with bracings, structural modification method is utilized to realize the Operational Deflection Shape in order to meet the target sound characteristic.

Keywords Guitar • Transient sound • Bracing modification • Keynote sound • ODS

17.1 Introduction

Musical instruments have a long history in accordance with cultural development and been improved based on designer experience. The main function of instrument is to make a sound generated by the vibration of string, body and/or air. Good or bad sound is depend on human sensation and difficult to judge quantitatively or qualitatively. Also the amplitude and frequency contents of generated sound is changed in function of time with respect to playing style such as stringed, percussion instrument and therefore influence significantly on human liking. In order to meet the diversity of human liking, the structural design of instrument is aimed to be able to control the sound.

In this study the acoustic guitar (hereafter guitar) is focused and the vibration and acoustic analysis are applied to investigate the relation between the structure and sound quality. Finally the structural modification is utilized to realize the target sound.

17.2 Vibration and Acoustic Characteristic of Guitar

The comparison of fundamental vibration and acoustic characteristic of two typical guitars, guitar A and B is made. The strings are tuned as 1st = 330 Hz, 2nd = 247 Hz, 3rd = 196 Hz, 4th = 147 Hz, 5th = 110 Hz and 6th = 82.4 Hz.

17.2.1 Structure of Guitar

By picking the string, the vibration is transmitted through the bridge and front plate to side and back plate and the vibration induced sound is radiated from the body and sound hall [1]. Especially the front plate plays an important role to generate the sound. Therefore in this study only the front plate is dealt with. The back side of front plate (body inside) is reinforced by ribs so called bracing as shown in Fig. 17.1 and by modifying the placement or shape of bracing, it is experienced that the sound can be controlled. Guitar A and B have the same bracing pattern as X crossing (d) but the generated sound has different characteristic.

N. Okubo (✉) • N. Iwanaga • T. Toi
CAMAL Chuo University, 1-13-27 Kasuga, Bunkyo-ku, 112-8551 Tokyo, Japan
e-mail: okubo@mech.chuo-u.ac.jp

© The Society for Experimental Mechanics, Inc. 2016

J. De Clerck, D.S. Epp (eds.), *Rotating Machinery, Hybrid Test Methods, Vibro-Acoustics & Laser Vibrometry, Volume 8*,
Conference Proceedings of the Society for Experimental Mechanics Series, DOI 10.1007/978-3-319-30084-9_17

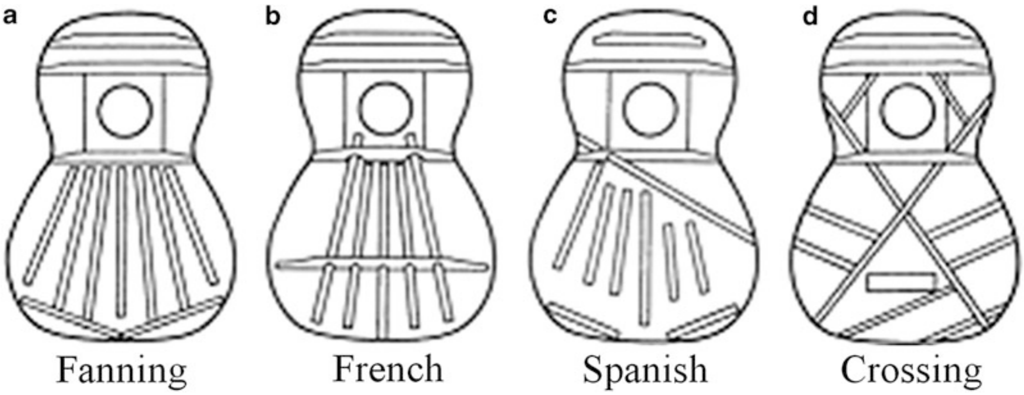

Fig. 17.1 Examples of bracing pattern [1]

Fig. 17.2 Experiment setup

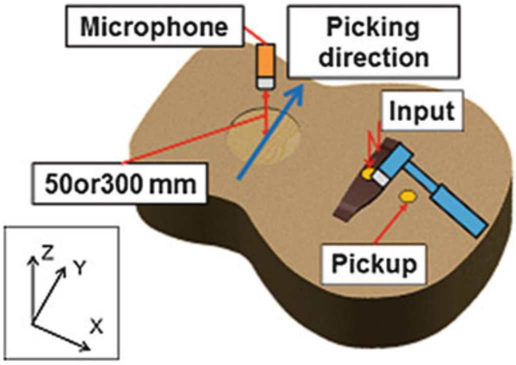

17.2.2 Measurement of Vibration and Sound

The experiment set up is shown in Fig. 17.2 where the guitar is placed on rubber cords connected to a fixture as free-free condition and in vibration measurement acceleration pickups are used to detect the response in z direction while in sound measurement 1/2 inch microphones are used to measure the sound pressure in anechoic room. Impact by hummer with load cell at bridge or picking a string with a pick by hand in y direction is applied as excitation. The picking position is on the center line above the sound hall. Only one string is picked and other strings are suppressed by gum tape not to vibrate.

17.2.3 Steady State Characteristic

The acoustic Frequency Response Functions, FRFs are measured between the impact force and the sound as shown in Fig. 17.3. Three fundamental resonance frequencies are observed; f1 (guitar A: 98 Hz, B: 91 Hz), f2 (guitar A: 185 Hz, B: 170 Hz) and f3 (guitar A: 366 Hz, B: 328 Hz). Guitar B has lower resonance frequencies, f1, f2 and f3 and higher level for 0–1024 Hz range than that of guitar A which reveals that guitar B radiates more sound against the same input.

Also the vibration FRFs based on the acceleration response against the impact force are measured on the front plate and three mode shapes at f1, f2 and f3 are obtained as shown in Fig. 17.4 which are similar each for guitar A and B.

17.2.4 Transient Characteristic

Figures 17.5 and 17.6 show the sound spectrogram in function of time and frequency after picking 6th string for guitar A and B respectively. Guitar A has just after picking, lower sound level at keynote frequency (=82.4 Hz) than the second and third harmonic sound and the second harmonic decays slower, namely sustains longer. On the one hand in guitar B the keynote sound level is higher than the third harmonic opposite of guitar A and the keynote decays slower while the second and higher harmonics die out quickly.

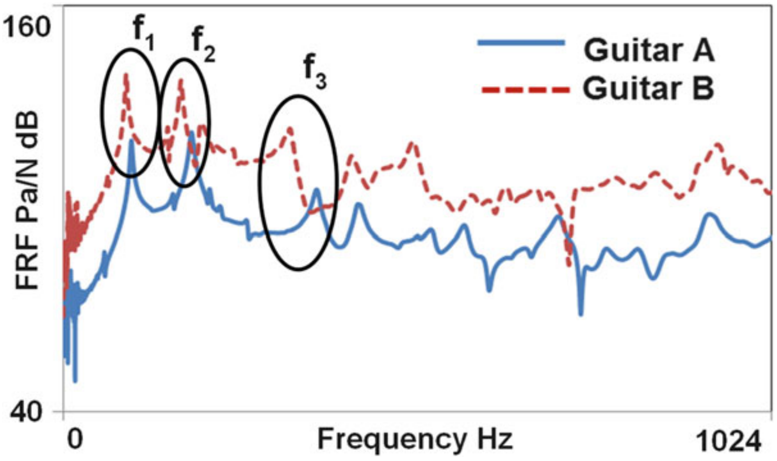

Fig. 17.3 Acoustic FRF

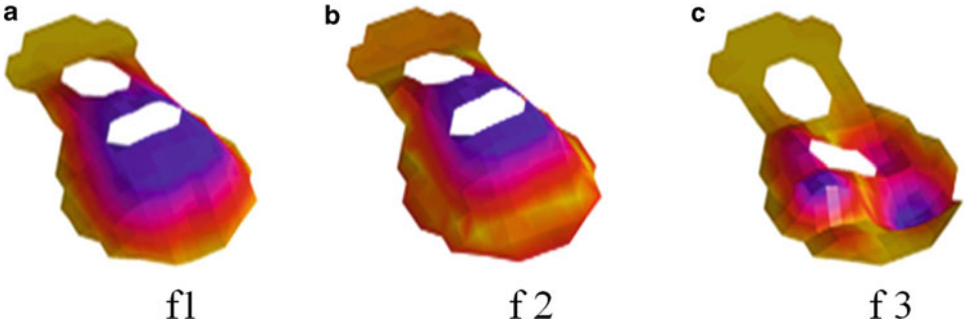

Fig. 17.4 Mode shapes of front plate

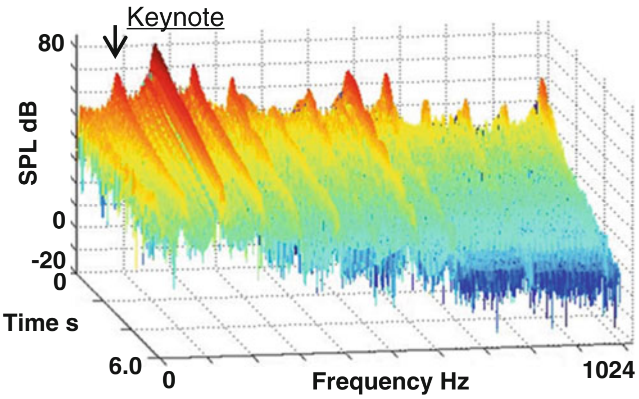

Fig. 17.5 Guitar A 6th string sound spectrogram

17.3 Sound Quality Change

As an example of sound quality change, "high harmonic sound more sustains", "low frequency sound starts up quickly" are commonly discussed. But the relation between those changes felt by player and listener and the sound modification is not clear. Therefore the original sound of guitar A 6th string picking is modified and evaluated as follows.

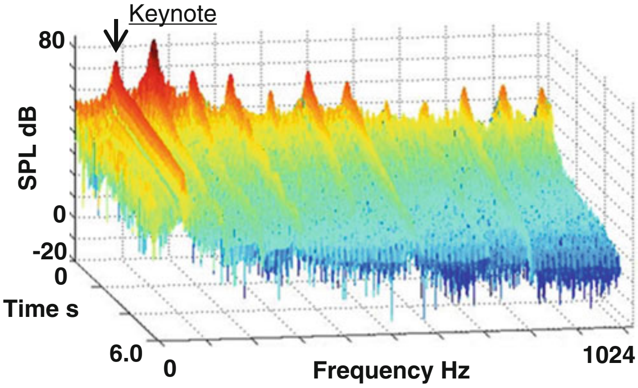

Fig. 17.6 Guitar B 6th string sound spectrogram

17.3.1 Evaluation on Modified Sound

Two types of sound modification are carried out for evaluation; addition of specific frequency sound on the original and application of frequency filter to damp out the specific frequency sound. That is,

(1) addition of sine wave at keynote frequency tailored by exponential window,
(2) heavily damped sine wave at the first resonance frequency, f1 of front plate,
(3) damping filter at keynote frequency.

17.3.2 Evaluation Result

Twenty subjects in the 20s with headphone in anechoic room listen the original sound and modified one in turn to answer the question "feel the difference?". Seventeen of them recognize the difference between the original sound and (1) and 12 does (3) filtered. On the contrary (2) increases slightly the volume just after the picking but only 1 recognizes the difference.

As a result, it is found that the sound quality can be controlled by modification of harmonics in time history. Therefore in order to meet the demand for sound quality target, the strength at harmonics in time history should be taken into consideration.

17.4 Operational Deflection Shape, ODS

Since the vibration of the front plate influences significantly on the sound quality, the structural modification should be investigated to control. Therefore the ODS of front plate in time history after picking is discussed.

17.4.1 ODS Measurement

ODS expresses how the structure behaves after excitation [2]. Ideally the simultaneous measurement at all response points is conducted but due to the limitation of number of acceleration pickups etc., repeated measurement is carried out in practice. Thus one reference point is selected throughout and used to compensate the amplitude and phase of other responses among the repeated measurements.

There are two types of ODS expression; frequency domain ODS at specific frequency and time domain ODS in time history which can be converted by Fourier or inverse transformation.

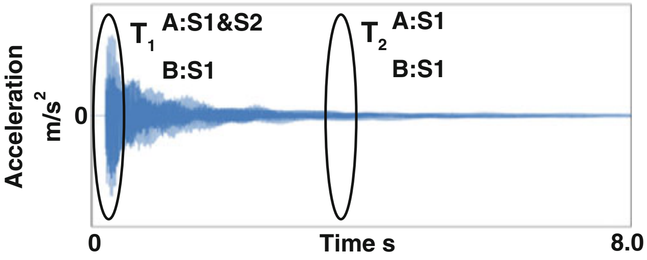

Fig. 17.7 Acceleration response on front plate

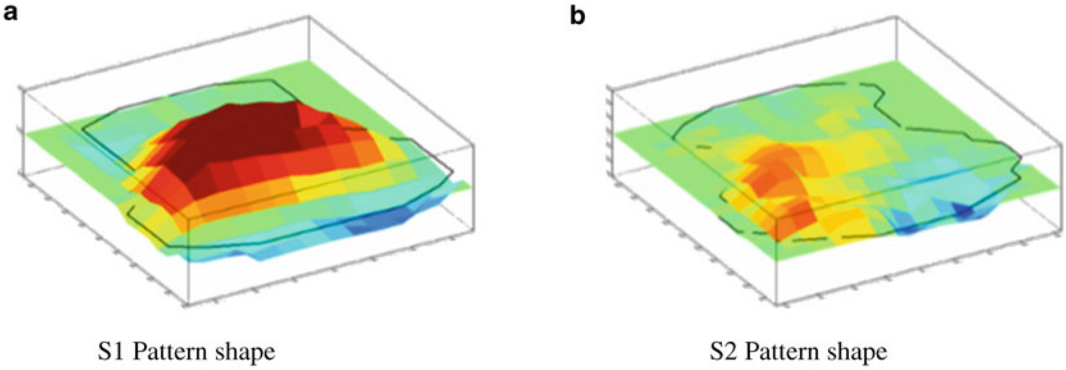

S1 Pattern shape

S2 Pattern shape

Fig. 17.8 Typical time domain ODS patterns

17.4.2 Front Plate ODS

The ODS of front plate of guitar A and B after picking is measured under the same condition as shown in Fig. 17.2. The acceleration responses at 30 mm distance interval are captured among repeated measurements remaining the reference point. Figure 17.7 shows a typical time history of acceleration response after picking 6th string, where T1 stands for the period just after picking and T2 does after damped out. Typical ODS at T1 and T2, S1 and S2 pattern are shown in Fig. 17.8a, b respectively, where the deformation in right and left plate is divided.

17.4.3 Relation Between ODS and Sound Quality

According to the observation of ODS in time domain for guitar A, S1 and S2 pattern shown in Fig. 17.8 together with other patterns are mixed at period T1 then, decayed later, only S1 pattern is appeared at period T2. On the contrary in case of guitar B, even at T1, S1 pattern is dominantly observed and maintained continuously until decay out.

Also ODS in frequency domain reveals that S1 pattern is observed at not only tuned keynote frequency, 82.4 Hz but also the second harmonic, 165 Hz both for guitar A and B. The mode shapes at resonance frequency at f1 and f2 in Fig. 17.4a, b influence much on this S1 pattern while S2 pattern resembles the mode shape at f3 in Fig. 17.4c which is close to the ODS in frequency domain of guitar A at 4th harmonic of keynote, 330 Hz. This draws the conclusion that the front plate successively generates various ODS at specific frequencies just after picking.

Under consideration of string motion due to picking, an impact force is applied which includes high frequency contents to excite the mode shapes at form low to high resonances. After decay only the lower resonance mode shapes are remained due to damping. Therefore at T1, ODS becomes complex in combination with various mode shapes but at T2 after decay lower resonance mode shapes in the vicinity of keynote frequency are dominant.

On the assumption that the same impact force by picking is applied to guitar A and B, guitar B damps out quickly the higher resonance mode shapes because S1 pattern is dominant at T1, which indicates only lower harmonic frequency ODS should be taken into account. This trend is also confirmed in Fig. 17.6, guitar B 6th string sound spectrogram and thus the transient sound quality is depend on the transient vibration behavior of front plate.

17.5 ODS Design

These observation lead that the sound quality can be properly controlled by ODS design, namely structural modification on front plate. Therefore a simple FE plate model is introduced to discuss how ODS can be designed to meet the sound quality target and then a simple experiment is carried out for verification.

17.5.1 *Front Plate FE Model*

Figure 17.9a shows the original front plate FE model consisted of 3 mm thickness plate, a 100 mm diameter hall like sound hall and a few bracings. The material is acrylic and the four ridges are fixed. The excitation input point is marked in the figure, which is deviated from the center line as picking position.

17.5.2 *Frequency ODS Formulation*

Since the response at one point of front plate is expressed by superimpose of one degree of freedom vibration against the input, response X at frequency ω can be written as,

$$\{x(\omega)\} = \sum_{r=1}^{N} \gamma_r \{\phi_r\} \tag{17.1}$$

where N is the number of mode, γ_r r th modal weighting coefficient and ϕ_r r th mode shape [3]. The eigen value λ and the mode shape can be derived from the mass matrix M and stiffness matrix K as eigen problem,

$$(M - \lambda K)\{\phi\} = \{0\} \tag{17.2}$$

By solving Eqs. (17.1) and (17.2), the frequency ODS, X(ω) at frequency ω can be calculated.

17.5.3 *Mode Shape Sensitivity*

In order to control ODS, the r th mode shapeϕ_r sensitivity with respect to design variable P is utilized as,

$$\frac{\partial \phi_r}{\partial P} = \sum_{k=1}^{N} c_{rk}\phi_k \tag{17.3}$$

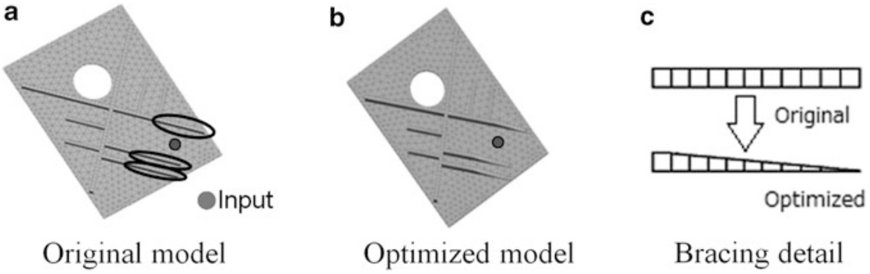

Original model Optimized model Bracing detail

Fig. 17.9 Plate FE model

where the coefficient c_{rk} can be obtained by mode orthogonality as,

$$\begin{cases} c_{rk} = \frac{\{\phi_k\}^T\left(\lambda_r \frac{\partial[M]}{\partial P} - \frac{\partial[K]}{\partial P}\right)\{\phi_r\}}{\lambda_k - \lambda_r} \ (k \neq r) \\ c_{rr} = \frac{-\{\phi_r\}^T\left(\lambda_r \frac{\partial[M]}{\partial P}\right)\{\phi_r\}}{2} \end{cases} \tag{17.4}$$

17.5.4 ODS Design by Non-Linear Programing

By substituting Eq. (17.3) into (17.1), the target response x′ at point n can be described on the assumption that γ remains the same as,

$$x'_n(\omega) = \sum_{r=1}^{N} \gamma_r \phi'_{nr} = \sum_{r=1}^{N} \gamma_r \left(\phi_{nr} + \frac{\partial \phi_{nr}}{\partial P} \partial P\right) \tag{17.5}$$

Then the difference *dx* between the target response and original one can be formulated as,

$$\{dx\} = \begin{bmatrix} \sum_{r=1}^{N} \gamma_r \frac{\partial \phi_{1r}}{\partial P_1} & \sum_{r=1}^{N} \gamma_r \frac{\partial \phi_{1r}}{\partial P_2} & \cdots & \sum_{r=1}^{N} \gamma_r \frac{\partial \phi_{1r}}{\partial P_e} \\ \sum_{r=1}^{N} \gamma_r \frac{\partial \phi_{2r}}{\partial P_1} & \ddots & \ddots & \vdots \\ \vdots & \ddots & \ddots & \vdots \\ \sum_{r=1}^{N} \gamma_r \frac{\partial \phi_{nr}}{\partial P_1} & \cdots & \cdots & \sum_{r=1}^{N} \gamma_r \frac{\partial \phi_{nr}}{\partial P_e} \end{bmatrix} \begin{Bmatrix} \partial P_1 \\ \partial P_2 \\ \vdots \\ \partial P_e \end{Bmatrix} \tag{17.6}$$

where e is the number of design variable P. In practice, ∂ P should be constrained. In this example, the mass density ρ of 30 hexahedron elements at the bracing marked in Fig. 17.9 is chosen which corresponds to cut the height of the bracing. Then the constraint equation becomes as,

$$-\rho_0 < \partial \rho_e \leq 0 \tag{17.7}$$

where ρ_o is the original value.

The optimum design variable to minimize dx in Eq. (17.6) is difficult to determine due to a large number of response point under consideration even by iterative manner. Therefore the norm of *dx* and ∂ P between the current and next iteration step are taken into account as the objective function to minimize in non-linear programing [4, 5]. As convergence criterion, Displacement Assurance Criterion, DAC which indicates the correlation between the target response and the current one is introduced as,

$$DAC = \frac{\left|\{x'\}^t \{x\}\right|^2}{\left|\{x'\}^t \{x'\}\right| \left|\{x\}^t \{x\}\right|} \tag{17.8}$$

where 0 means no correlation and 1 does the perfect correlation. This improves the convergence in non-linear programing.

17.5.5 Optimized Design

Figure 17.10 shows the driving FRF of front plate FE model and Fig. 17.11 does the mode shapes at 1st, 2nd and 3rd resonance frequency. The target ODS in this study is chosen at 120 Hz which does not coincide with any resonance frequencies as shown in Fig. 17.10 similar to guitar. Besides the target ODS at 120 Hz is given as shown in Fig. 17.12b compared with the original Fig. 17.12a, which intends larger deformation at the bottom part of front plate.

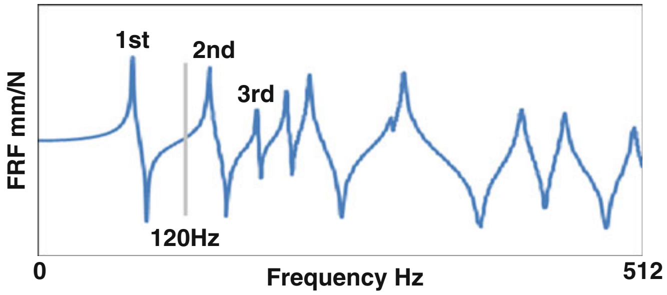

Fig. 17.10 Driving point FRF of plate FE model

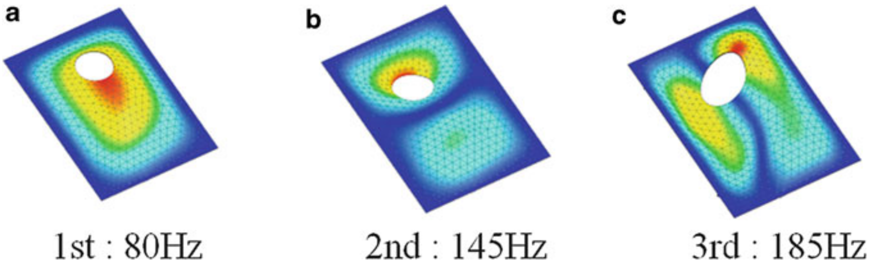

1st : 80Hz   2nd : 145Hz   3rd : 185Hz

Fig. 17.11 Mode shapes of plate FE model

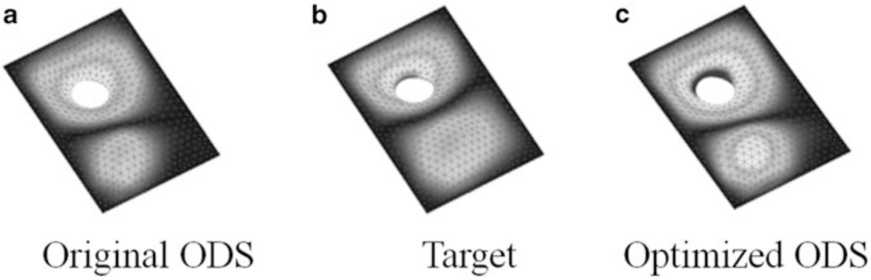

Original ODS   Target   Optimized ODS

Fig. 17.12 120 Hz ODS of FE model

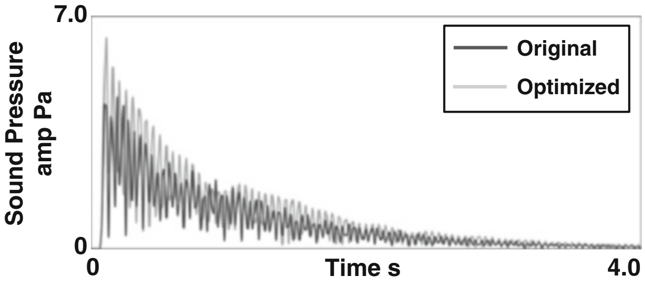

Fig. 17.13 120 Hz acoustic response

By applying the proposed ODS design procedure, the bracings are cut as shown in Fig. 17.9c and as a result 120 Hz ODS is optimized as shown in Fig. 17.12c, which realizes larger deformation. Also against the impact input force, the radiated sound is calculated in time domain as shown in Fig. 17.13 compared with the original and optimized, which confirms the improvement of 120 Hz sound.

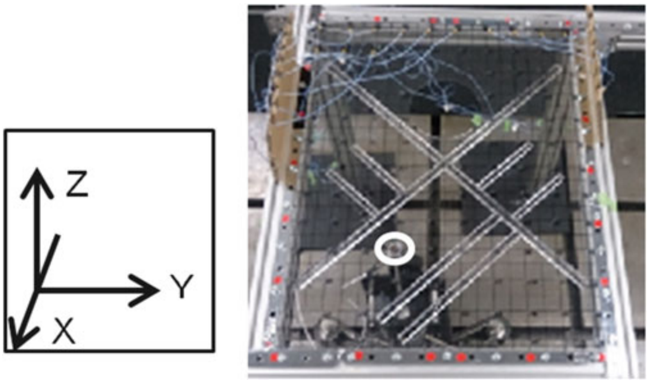

Fig. 17.14 Experiment setup (*circle*: input point)

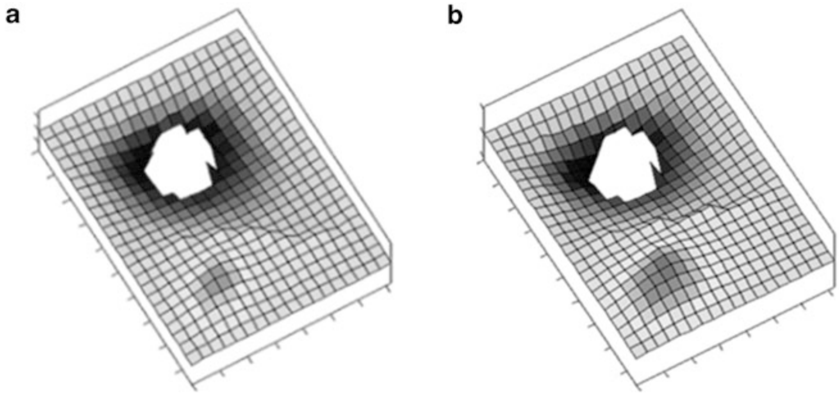

Original

Optimized

Fig. 17.15 Experimental 120 Hz ODS

17.5.6 *Experimental Verification*

The experimental set up is shown in Fig. 17.14 where the acrylic plate with the same dimension as FE model is excited by an electromagnetic exciter at o marked position under four ridges fixed condition. 120 Hz ODS is measured for the original and optimized in which bracings are cut according to the result of ODS design as mentioned above. Figure 17.15 shows the comparison of 120 Hz ODS which verify the ODS design to realize larger deformation.

17.6 Conclusion

(1) The strength of harmonic frequency sound of guitar influences significantly on human sensation.
(2) Based on the comparison of two typical guitars, the Operational Deflection Shape, ODS of front plate in time and frequency domain is found to characterize the transient sound quality.
(3) ODS design can be conducted by good use of mode shape sensitivity with non-linear programing how to modify the structure such as bracing cut.

References

1. Fletcher, N.H, et al.: Physics of Musical Instruments. Maruzen press (1997)
2. McHargue, P.L., et al.: Operating deflection shapes from time versus frequency domain measurement. In: IMAC, 1993
3. Nagamatsu, A.: Introduction of Modal Analysis. Korona, Tokyo (1993)
4. Yamakawa, H.: Design Optimization, p. 83. Baifukan, Tokyo (1993)
5. Ichimori, T.: Programing. Kyoritsu press, Tokyo (1994)

Chapter 18
Demarcation for the Coupling Strength in the MODENA Approach

Peng Zhang, Shaoqing Wu, Yanbin Li, and Qingguo Fei

Abstract MODal ENergy Analysis (MODENA) is an energy-based approach which is proposed recently to provide a pure tone analysis of power flow. The net exchanged power between two coupled oscillators is proportional to the weighted difference of total energies of oscillators. Contrary to Statistical Energy Analysis (SEA) or Statistical modal Energy distribution Analysis (SmEdA), the MODENA approach can deal with strong coupling case where the power can flow from the oscillator with lower energy to the one with higher energy. The level of coupling strength between oscillators may affect the accuracy of the MODENA approach. This research work aims to propose a criterion to determine the level of coupling in the MODENA approach. A non-dimensional parameter named coupling strength factor is defined to clearly demonstrate the level of coupling strength. Two numerical examples: (a) a two-oscillators coupling case and (b) a multi-modal coupling case are conducted to show the effectiveness of the proposed criterion.

Keywords Coupling strength • MODal ENergy analysis • Statistical energy analysis • Statistical modal energy distribution analysis • Dual modal formulation

18.1 Introduction

MODal ENergy Analysis (MODENA) approach proposed by Totaro and Guyader [1] is an energy-based method which provides a pure tone analysis of power flow. It is suitable for analyzing the dynamic response of vibro-acoustic systems. There are other two energy-based methods for the dynamic analysis of a vibro-acoustic system, named Statistical Energy Analysis (SEA) [2–5] and Statistical modal Energy distribution Analysis (SmEdA) [6–8].

SEA is developed in the early 1960s, which is based on the study of the power flow between two lightly coupled, linear oscillators excited by independent white noise sources [2]. It is noted that the power flow is proportional to the difference in the average modal energy of the two oscillators while the coupling is conservative, and the power always flowed from the oscillator with higher energy to the lower one [3]. With the assumptions such as large population of modes, 'rain-on-the-roof' excitation, large modal overlap, diffuse field, equipartition of energy, light and conservative coupling [9], etc. on the framework of the SEA theory, the power flow was extended to multi-modal coupling systems in which each mode was considered as an oscillator. Since only statistical parameters are required (such as damping loss factors, coupling loss factors, modal density and input power of external excitations [10–14]), SEA is particularly good at the responses analysis of complex vibro-acoustic systems when numerous modes exist within the analysis frequency band [15]. In addition, SEA is well suited for a population of nearly identical structures and can thus give useful information on mean and variance of responses [16, 17]. At present, SEA is still widely used and the theory has been improved to deal with new cases [18–21].

SmEdA is proposed based on the dual modal formulation (DMF) described in [22] and the basic SEA relations in [5] describing the power flow exchanged between two oscillators. DMF can be used for calculating the response of coupled subsystems from prior knowledge of the modes of each uncoupled subsystem [23]. It is suitable for describing the dynamic behavior of a flexible panel coupled with acoustic cavities. DMF has also been extended to the general case of the coupling of two elastic continuous mechanic systems [22, 24]. Compared with SEA, SmEdA improves the applications of energy prediction in three aspects: (a) subsystems with low modal overlap, (b) heterogeneous subsystems and (c) localized excitations, etc [6]. Recently, an extension of SmEdA [25] was presented to takes into account the contributions of the

---

P. Zhang • S. Wu • Y. Li • Q. Fei (✉)
Jiangsu Key Laboratory of Engineering Mechanics, Southeast University, Nanjing 210096, China

Department of Engineering Mechanics, School of Civil Engineering, Southeast University, Nanjing 210096, China
e-mail: QGFei@seu.edu.cn

© The Society for Experimental Mechanics, Inc. 2016

J. De Clerck, D.S. Epp (eds.), *Rotating Machinery, Hybrid Test Methods, Vibro-Acoustics & Laser Vibrometry, Volume 8*,
Conference Proceedings of the Society for Experimental Mechanics Series, DOI 10.1007/978-3-319-30084-9_18

non-resonant modes, which plays a significant role in the case of sound transmission through a thin structure, and the presented approach can take into account the non-resonant contribution of the structure in evaluating the transmission loss.

MODENA is developed within the framework of SmEdA [1], it solves the system of equations of two coupled oscillators at a pure tone, which can take the non-resonant contributions of oscillators into account intrinsically. In MODENA, the net exchanged power between two coupled oscillators is proportional to the weighted difference of total energies of oscillators, which is similar to SEA or SmEdA. The coupling between two oscillators was extended to the coupling between two continuous subsystems using dual modal formulation, as done in SmEdA. The MODENA approach hold similar advantages and extensions as SmEdA, which are: (1) the calculation of modal coupling loss factor at pure tone only based on quantities which can be easily obtained with FEM, (2) finite element computations are only necessary on uncoupled subsystems, (3) subsystems with low modal overlap and local excitations can be considered and (4) it is possible to estimate the energy distribution into subsystems by using modal energy of subsystems.

In MODENA, when dealing with the weak coupling case, approximations can be made to simplify the calculation on the injected power of external excitation. A question has to be answered in order to properly use the MODENA approach, i.e. what kind of circumstance can be treated as week coupling or vice versa? To solve this problem, a non-dimensional parameter named coupling strength factor is defined to clearly demonstrate the level of coupling strength. Two numerical examples: (a) a two-oscillator coupling case, and (b) a multi-modal coupling case are conducted to show the effectiveness of the proposed criterion.

This paper is organized as follows:

- The theory of the MODENA approach is introduced in Sect. 18.2;
- A numerical example for a two-oscillator coupling case is investigated in Sect. 18.3. A non-dimensional parameter, named "coupling strength factor", is proposed to straight forwardly demonstrates the coupling strength. Based on the numerical results, a criterion for determining the level of coupling strength in the MODENA approach is proposed;
- Another numerical examples with a multi-modal coupling case are given in Sect. 18.4 to validate the applicability of the criterion, which was proposed in Sect. 18.3.

18.2 Theoretical Basis of MODENA

18.2.1 Dual modal formulation (DMF)

From prior knowledge of the modes of each subsystem, DMF can be used to calculate the response of coupled subsystems [23]. Modes of the uncoupled subsystems are expressed either in terms of displacement (free at the coupling interface) or in terms of stress (blocked at the coupling interface). In that case, no coupling exists between two modes in the same subsystem, and the coupling between modes of different subsystems is gyroscopic, the modes of subsystems can be considered as sets of oscillators. DMF has been well-known for decades, and it is suitable for describing the dynamic behavior of a flexible panel coupled with acoustic cavities. DMF has also been extended to the general case of the coupling of two elastic continuous mechanic systems [22].

Two coupled continuous subsystems P and Q as presented in Fig. 18.1 were considered, DMF was used to describe the system [1, 23], as done in the SmEdA approach.

$$\begin{cases} M_p\ddot{y}_p + \left(1 + \mathrm{j}\eta_p\right) k_p y_p - \sum_j^Q G_{pj}\dot{y}_j = f_p, & p \in P \\ M_q\ddot{y}_q + \left(1 + \mathrm{j}\eta_q\right) k_q y_q + \sum_i^P G_{iq}\dot{y}_i = f_q, & q \in Q \end{cases} \tag{18.1}$$

Where M_p, η_p and k_p are the modal mass, damping and stiffness of mode p, and f_p is the force applied on mode p, $G_{pq} = \sqrt{M_pM_q}\,\gamma_{pq}$, γ_{pq} is the gyroscopic coefficient of mode p and mode q, y_p and y_q are modal amplitudes.

18.2.2 Power Balance Between Two Coupled Oscillators at Pure Tone

For the two-oscillator coupling case, which corresponds to that each system in Fig. 18.1 contains only one oscillator, the DMF writes

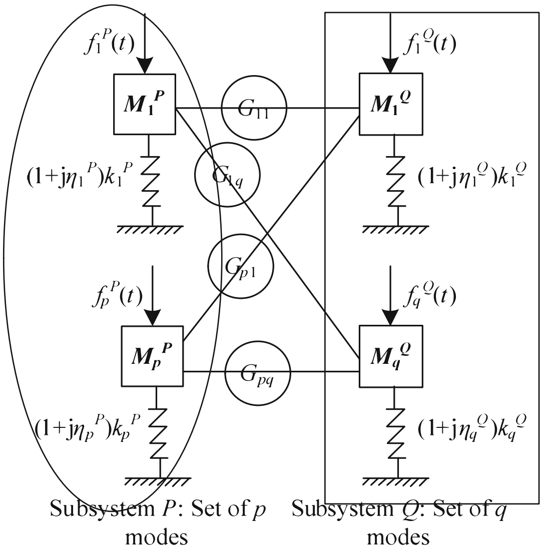

Fig. 18.1 Coupling between two sets of modes

$$\begin{cases} M_1\ddot{y}_1(t) + (1 + j\eta_1)\,k_1 y_1(t) - G\dot{y}_2(t) = f_1(t), \\ M_2\ddot{y}_2(t) + (1 + j\eta_2)\,k_2 y_2(t) + G\dot{y}_1(t) = f_2(t). \end{cases} \tag{18.2}$$

where the subscripts denote the number of the two oscillators.

Assuming the forces applied on the two oscillators are uncorrelated with each other, the net exchanged power transmitted from oscillator 1 to oscillator 2 at pure tone writes [1]

$$\Pi_{12}(\omega) = \alpha_{12}(\omega)\,E_t^1(\omega) - \alpha_{21}(\omega)\,E_t^2(\omega)\,, \tag{18.3}$$

where E_t^i is the total energy of oscillator i, $\alpha_{ij}(\omega)$ is a coupling factor whose expression writes

$$\alpha_{ij}(\omega) = \frac{2\gamma^2}{1+\omega_i^2/\omega^2}\,\frac{\omega\omega_j\Delta_j\left(\left(\omega_i^2-\omega^2\right)^2+\omega_i^2\Delta_i^2\right)+\omega^3\omega_i\gamma^2\Delta_i}{\left(\left(\omega_i^2-\omega^2\right)^2+\omega_i^2\Delta_i^2\right)\left(\left(\omega_j^2-\omega^2\right)^2+\omega_j^2\Delta_j^2\right)-\omega^4\gamma^4}. \tag{18.4}$$

where ω_i is the eigen-frequency and $\Delta_i = \eta_i\omega_i$ is the damping bandwidth of oscillator i.

At each angular frequency, a critical coefficient γ^{crit} exists when the denominator of the right part of Eq. (18.4) equals to zero and the coefficient $\alpha_{ij}(\omega)$ and $\alpha_{ji}(\omega)$ tend to infinity at the same time. However, even at this condition, the net power exchange defined in Eq. (18.3) tends to a finite value as have been demonstrated in [1]. The expression of γ^{crit} is

$$\gamma^{\text{crit}}(\omega) = \frac{\sqrt[4]{\left(\left(\omega_i^2-\omega^2\right)^2+\omega_i^2\Delta_i^2\right)\left(\left(\omega_j^2-\omega^2\right)^2+\omega_j^2\Delta_j^2\right)}}{\omega}. \tag{18.5}$$

The power injected into oscillator i is equals to the sum of the power dissipated by oscillator i and the power transmitted from i to j

$$\Pi_i^{\text{inj}}(\omega) = \Pi_i^{\text{diss}}(\omega) + \Pi_{ij}(\omega)\,. \tag{18.6}$$

In case of structure damping,

$$\Pi_i^{\text{diss}}(\omega) = 2\eta_i\omega E_p^i(\omega) = 2\eta_i\omega\frac{E_t^i(\omega)}{1+\omega^2/\omega_i^2} = \tilde{\Delta}_i(\omega)\,E_t^i(\omega)\,, \tag{18.7}$$

where $\tilde{\Delta}_i(\omega) = 2\eta_i\omega/\left(1+\omega^2/\omega_i^2\right)$.

The power injected into oscillator i due to F_i is given by

$$\Pi_i^{\text{inj}}(\omega) = \frac{1}{2}\text{Re}\left(F_i^*(\omega)\,\dot{Y}_i(\omega)\right) = \frac{1}{2}S_i(\omega)\,\text{Re}\,(\text{j}\omega H_{ii}(\omega))\,. \tag{18.8}$$

where F_i and Y_i are the Fourier transformation of f_i and y_i, respectively. $S_i(\omega) = F_i(\omega)F_i^{\,*}(\omega)$ is the auto-spectra of F_i, H_{ii} is a transfer function, Re(•) denotes the real part of a complex number.

18.2.3 Power Balance of Multi-Modal Coupling System

To extend the power balance of the two-oscillator coupling case as shown in Eq. (18.6) to the multi-modal coupling case, some assumptions had been proposed [1]:

1. The coupling between two modes has to be conservative.
2. External forces applied on subsystems have to be uncorrelated.
3. Isolating two modes, the ensemble of coupling forces due to other modes of the subsystems is considered as uncorrelated to external excitations.

Under these assumptions, the power injected into mode p in subsystem P, $\Pi_p^{\text{inj}}(\omega)$, is either dissipated by the modal damping loss factor or transmitted to mode q in subsystem Q

$$\Pi_p^{\text{inj}}(\omega) = \Pi_p^{\text{diss}}(\omega) + \sum_q \alpha_{pq}(\omega)\,E_t^p(\omega) - \sum_q \alpha_{qp}(\omega)\,E_t^q(\omega). \tag{18.9}$$

The energy responses of the system can be calculated by Eq. (18.9) as the modal base of each subsystems and external excitations are given.

18.3 Numerical Example 1: A Two-Oscillator Coupling Case

In this section, the influence of gyroscopic coupling strength on the two oscillators coupling case is studied, and a non-dimensional parameter, named coupling strength factor, is proposed to straight forwardly reflect the coupling strength. Then, error analysis on the MODENA approach is conducted due to the approximation made on the calculation of injected power. Finally, a criterion for determining the level of coupling strength in the MODENA approach is proposed.

A numerical example is given to investigate the influence of gyroscopic coupling strength on the power balance between two oscillators at a pure tone which has been shown in Eq. (18.6). In this case, the parameters of the two oscillators in Eq. (18.2) are $M_1 = M_2 = 1, f_1 = 410$ Hz, $f_2 = 620$ Hz, $\eta_1 = \eta_2 = 0.02$.

To examine the influence of gyroscopic coupling strength on the coupled system, attention is paid on the power injected into oscillator 1 when $\gamma = 1000$ which is shown in Fig. 18.2, where f_i^{c} represents the ith eigen-frequency of the coupled system and V_i^{P1} represents the value of P_1 at frequency f_i^{c} (similarly hereinafter). It is noted from Fig. 18.2 that the values of γ^{crit} at frequency f_i^{c} equal to γ, as if the min and max frequencies where γ^{crit} equals to γ were the eigen-frequencies of the coupled system when γ is larger than the minimum value of γ^{crit}. Here the minimum value of γ^{crit} is represented by γ_0. In this case $\gamma_0 = 413.26$. It is noted that γ_0 may be used as a boundary to distinguish between the weak coupling case and the strong coupling case.

18.3.1 Definition of the Coupling Strength Factor

The value of γ_0 is only determined by the eigen-frequencies of the two oscillators (f_1 and f_2) when the damping parameters are given. The value of γ_0 is shown as a function of f_1 and f_2 in Fig. 18.3 when the structural damping $\eta_1 = \eta_2 = 0.02$. It is found that the more difference between f_1 and f_2 is, the bigger the value of γ_0 will be, i.e. the harder interaction between oscillator 1 and oscillator 2.

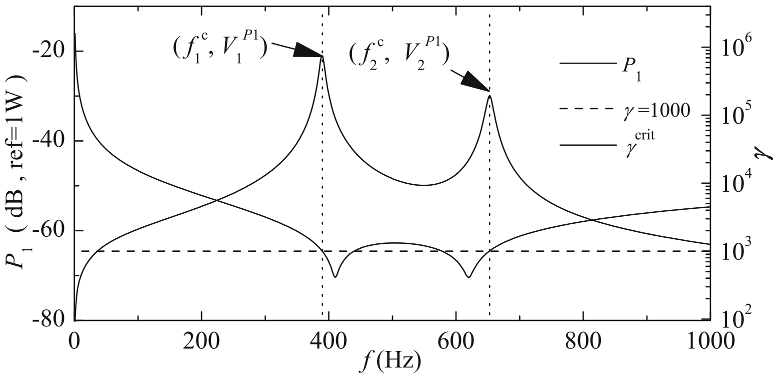

Fig. 18.2 Power injected into oscillator 1 when $\gamma = 1000$

Fig. 18.3 The value of γ_0 as a function of f_1 and f_2

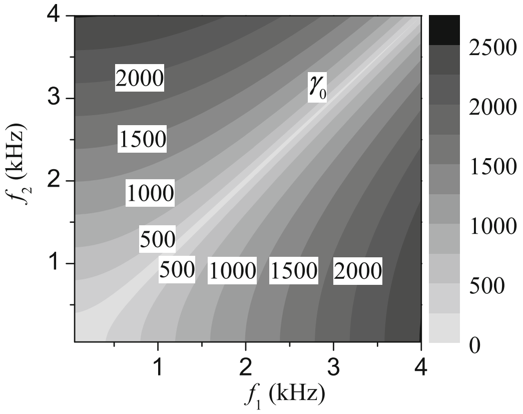

It is noted that the gyroscopic coupling coefficient γ cannot straight forwardly reflect the system coupling strength. For example, in case 1 when $f_1 = f_2 = 500$ Hz, it is found from Fig. 18.3 that $\gamma_0 < 500$; in case 2 when $f_1 = 500$ Hz, $f_2 = 2000$ Hz, $\gamma_0 > 500$. While $\gamma = 500$, in case 1, $\gamma > \gamma_0$; and in case 2, $\gamma < \gamma_0$. Which means that case 1 may be a strong coupling case with $\gamma = 500$ while case 2 may be a weak coupling case with the same gyroscopic coupling coefficient.

Therefore, a coupling strength factor θ is proposed to characterize the coupling strength,

$$\theta = \gamma / \gamma_0, \tag{18.10}$$

Then, a critical coupling strength factor θ^{crit} exist at each frequency,

$$\theta^{\text{crit}}(\omega) = \gamma^{\text{crit}}(\omega) / \gamma_0. \tag{18.11}$$

Here θ is non-dimensional parameter. With different values of f_1 and f_2, the coupling strength factor θ can straight forwardly reflects the coupling strength rather than γ, e.g. when $\theta < 1$, $\gamma < \gamma_0$, the coupling of the system is defined as weak and when $\theta > 1$, $\gamma > \gamma_0$, the coupling of the system may be defined as strong.

18.3.2 Error Analysis

When the coupling is weak, $H_{ii}(\omega)$ in Eq. (18.8) can be approximated by $H_i(\omega)$, the transfer function of oscillator i when it is uncoupled, to simplify the calculation of the injected power. Before the approximation is made, the question "when the coupling of the system would be weak?" should be answered. In the following study, error analysis will be conducted under different coupling strength when the injected power is approximated.

With numerical simulation, the two eigen-frequencies of the coupled system (f_1 and f_2) can be obtained as a function of the coupling strength factor θ as shown in Fig. 18.4, as well as the value of E_1 and E_2 at each eigen-frequency as shown

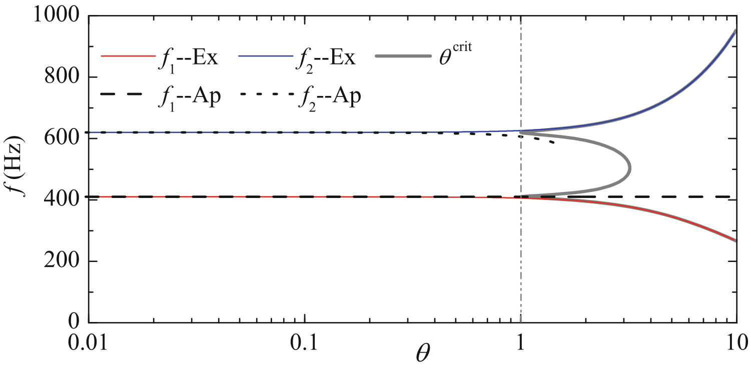

Fig. 18.4 Eigen-frequencies of the coupled system as a function of the coupling strength factor θ. "Ex" denotes "Exact results", "Ap" denotes "Approximated results"

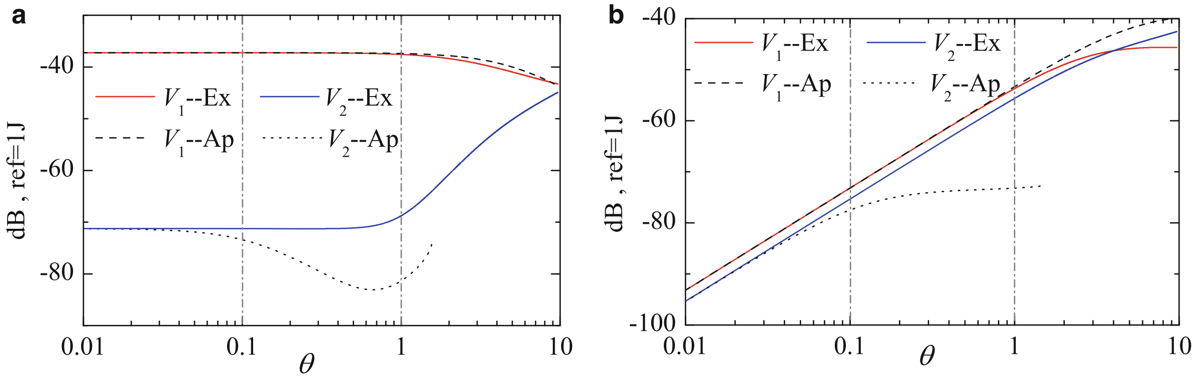

Fig. 18.5 The value of the energy responses of the two oscillators at the eigen-frequencies of the system as a function of the coupling strength factor θ: (**a**) oscillator 1; (**b**) Oscillator 2. "Ex" denotes "Exact results", "Ap" denotes "Approximated results"

in Fig. 18.5. The "exact results" are obtained by solving Eq. (18.6) when no approximation is made. The "approximated results" are calculated by solving Eq. (18.6) when the injected power is calculated approximately. Errors can be evaluated by comparing the "exact results" with the "approximated results".

The "exact results" show: both eigen-frequencies of the coupled system are close to those of uncoupled oscillators when $\theta < 1$ as shown in Fig. 18.4, and the curves of f_1 and f_2 are overlapped with parts of the curve of θ^{crit} when $\theta > 1$.

The "approximated results" show: In this two-oscillator coupling case, the approximation of the injected power may introduce errors in analysis results. When $\theta < 0.1$, the "exact results" and the "approximated results" agree with each other very well; however, when $\theta > 0.1$, significant errors exist in E_1 and E_2 near the one of the eigen-frequencies of the coupling system; and when $\theta > 1$, the analysis errors of the eigen-frequencies of the system emerge and become larger when the coupling getting stronger, as well, the calculation errors of E_1 and E_2 near both the two eigen-frequencies of the coupling system are not neglectable.

18.3.3 Criterion for Determining the Level of Coupling Strength

In the two-oscillator coupling case, $\theta = 1$ and $\theta = 0.1$ can be used as two boundaries which divide the level of coupling strength. When $\theta < 0.1$, the coupling is weak and exact results can be acquired even when the injected power is approximately calculated; When $\theta > 1$, the coupling is strong and the approximation on calculation of the injected power will result in large errors in the predicted system energy responses. When $0.1 < \theta < 1$, due to the approximation of the injected power, the analysis errors exist in the system energy responses near the eigen-frequency of the indirectly excited oscillator. This will slightly affect the global frequency energy response of the directly excited oscillator because of its large difference near the two eigen-frequencies; however, it will strongly affect the global frequency energy response of the indirectly excited oscillator since its values near the two eigen-frequencies are more close to each other. Therefore, when $0.1 < \theta < 1$, it may be regarded as weak coupling for the directly excited oscillator and strong coupling for the indirectly excited oscillator. When the coupling is strong, the injected power cannot be approximated in order to get accurate results.

18.4 Numerical Example 2: A Multi-Modal Coupling Case

In this section, a multi-modal coupling case is studied to investigate whether the criterion proposed in Sect. 18.3.3 is still valid, and an error analysis is conducted due to the approximation made on the calculation of injected power in the MODENA approach.

18.4.1 System Definition and External Excitation

A numerical example including two sets of modes as shown in Fig. 18.1 is conducted. In this case, 10 modes and 6 modes are included in subsystem P and subsystem Q, respectively. The parameters of the system are

$$M_i^P = M_j^Q = 1, \quad \eta_i^P = \eta_j^Q = 0.02, \quad f_i^P = 150i, \quad f_j^Q = 300j - 200, \quad i \in [1, 10], \quad j \in [1, 6]. \tag{18.12}$$

The gyroscopic coupling coefficient matrix $\boldsymbol{\gamma}^{PQ}$ is given by

$$\boldsymbol{\gamma}^{PQ} = \theta \cdot \boldsymbol{\gamma}_0^{PQ}, \tag{18.13}$$

where matrix $\boldsymbol{\gamma}_0^{PQ}$ can be obtained by numerical method based on the parameters of the modes in the system. Matrix element $\boldsymbol{\gamma}^{PQ}(i,j)$ is the gyroscopic coupling coefficient between the ith and the jth mode from different subsystem.

In this case, only modes in subsystem Q are excited by a rain-on-the-roof excitation, i.e. all modes in subsystem Q are equally excited by uncorrelated excitations.

18.4.2 Energy Response of the Multi-Modal Coupling System

The total energy response of subsystem P and subsystem Q (E_P and E_Q) are calculated under different coupling strength as shown in Figs. 18.6 and 18.7, respectively. The "approximated results" are obtained when approximation is made on the calculation of inject power, while the "exact results" are obtained when the approximation is not made.

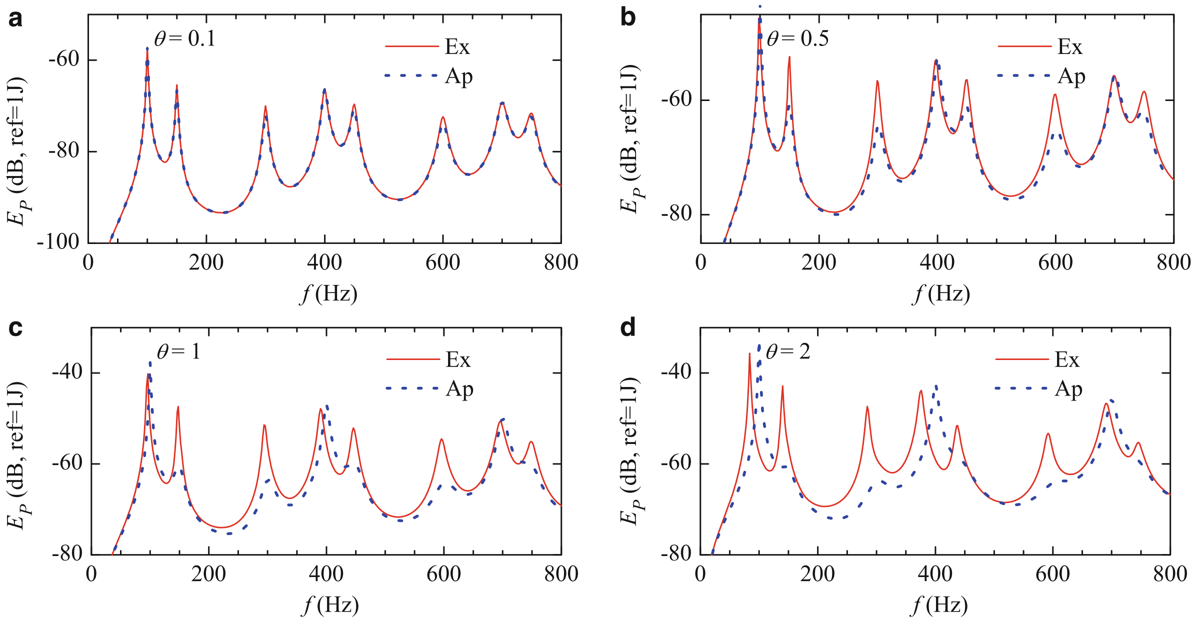

Fig. 18.6 The total energy responses of subsystem P. "Ex" denotes "Exact results", "Ap" denotes "Approximated results"

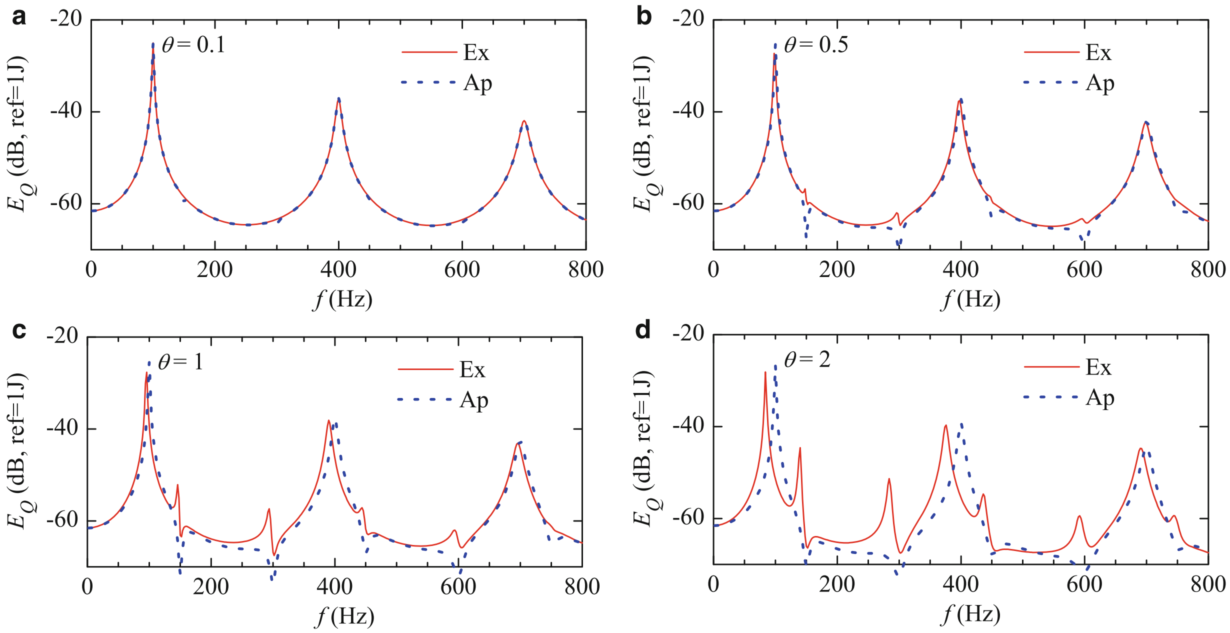

Fig. 18.7 The total energy responses of subsystem Q. "Ex" denotes "Exact results", "Ap" denotes "Approximated results"

It is noted from Fig. 18.6 that when $\theta = 0.1$, the "exact results" and the "approximated results" of E_P agree with each other very well as shown in Fig. 18.6a; however, when $\theta > 0.1$, significant errors exist in E_P near the eigen-frequencies of the subsystem P, and the errors increase with the coupling strength as shown in Fig. 18.6b–d. When $\theta = 2$, the peaks corresponding to the eigen-frequencies of the subsystem P in E_P almost disappear, and shifting on the system eigen-frequencies occurs.

It is noted from Fig. 18.7 that when $\theta = 0.1$, the "exact results" and the "approximated results" of E_Q agree with each other very well;, in the cases when $\theta = 0.5$ and $\theta = 1$, the analysis errors, due to the approximation of the calculation on injected power, exist in E_Q near the eigen-frequencies of subsystem P, and they become larger with the growth of the coupling strength; however, the approximation can slightly affect the analysis accuracy of E_Q. The results in Fig. 18.7d indicate that the error exist in E_Q near the eigen-frequencies of subsystem P is not neglectable when $\theta = 2$, and shifting on the system eigen-frequencies occurs.

The results investigated in the multi-modal coupling and two-oscillator coupling cases agree with each other very well, which proves the "criterion for determining the level of coupling strength" proposed in Sect. 18.3.3 is valid to the multi-modal coupling case. In the multi-modal coupling case, $\theta = 1$ and $\theta = 0.1$ can also be used as two boundaries which divide the level of coupling strength. When $\theta < 0.1$, the coupling is weak; when $\theta > 1$, the coupling is strong; when $0.1 < \theta < 1$, the coupling is weak for the directly excited subsystem and strong for the indirectly excited subsystem. When the coupling is weak, exact results can be acquired even when the injected power is calculated approximately; when the coupling is strong, the approximation on calculation of the injected power will result in large errors in the predicted system energy responses, which cannot be made in order to get accurate results.

18.5 Conclusions

Since the gyroscopic coupling coefficient γ involved in the MODENA approach cannot directly reflect the system coupling strength. A non-dimensional parameter named coupling strength factor is defined to clearly demonstrate the level of coupling strength. Two numerical examples are conducted to show the effectiveness of the proposed criterion for determining the level of coupling strength in the MODENA approach. Results show that:

1. The coupling strength factor θ can straight forwardly reflects the coupling strength rather than the gyroscopic coupling coefficient γ, e.g. when $\theta < 1$, $\gamma < \gamma_0$, the coupling of the system may be defined as weak and when $\theta > 1$, $\gamma > \gamma_0$, the coupling of the system may be defined as strong.

2. When $\theta < 0.1$, the coupling is weak and exact results can be acquired even when the injected power is calculated approximately; when $\theta > 1$, the coupling is strong and the approximation on calculation of the injected power will result in large errors in the predicted system energy responses; when $0.1 < \theta < 1$, it may be regarded as weak coupling for the directly excited oscillator and strong coupling for the indirectly excited oscillator.
3. If the coupling strength is weak, i.e. $\theta < 0.1$, the injected power can be calculated approximately to improve computational efficiency; otherwise, it should be calculated exactly to decrease analysis error.

Acknowledgments The work described in this paper was supported by a Program for New Century Excellent Talents in University (NCET-11-0086), a Research Grant from National Natural Science Foundation of China (No. 10902024) and also funded by Jiangsu Natural Science Foundation (No. BK2010397).

References

1. Totaro, N., Guyader, J.L.: Modal energy analysis. J. Sound Vib. **332**(16), 3735–3749 (2013)
2. Lyon, R.H., Dejong, R.G.: Theory and Application of Statistical Energy Analysis. Butterworth-Heinemann, London (1995)
3. Lyon, R.H., Maidanik, G.: Power flow between linearly coupled oscillators. J. Acoust. Soc. Am. **34**(5), 623–639 (1962)
4. Newland, D.E.: Calculation of power flow between coupled oscillators. J. Sound Vib. **3**(3), 262–276 (1966)
5. Scharton, T.D., Lyon, R.H.: Power flow and energy sharing in random vibration. J. Acoust. Soc. Am. **43**, 1332–1343 (1968)
6. Maxit, L., Guyader, J.L.: Extension of the SEA model to subsystems with non-uniform modal energy distribution. J. Sound Vib. **265**(2), 337–358 (2003)
7. Totaro, N., Dodard, C., Guyader, J.L.: SEA coupling loss factors of complex vibro-acoustic systems. J. Vib. Acoust. **131**(2), 041009 (2009)
8. Totaro, N., Guyader, J.L.: Extension of the statistical modal energy distribution analysis for estimating energy density in coupled subsystems. J. Sound Vib. **331**, 3114–3129 (2012)
9. Le Bot, A., Vincent, C.: Validity diagrams of statistical energy analysis. J. Sound Vib. **329**(2), 221–235 (2010)
10. Pankaj, A.C., Sastry, S., Murigendrappa, S.M.: A comparison of different methods for determination of coupling factor and velocity response of coupled plates. J. Vibroeng. **15**(4), 1885–1897 (2013)
11. Souf, B., Bareille, O., Ichchou, M.N., et al.: Variability of coupling loss factors through a wave finite element technique. J. Sound Vib. **332**(9), 2179–2190 (2013)
12. Secgin, A.: Numerical determination of statistical energy analysis parameters of directly coupled composite plates using a modal-based approach. J. Sound Vib. **332**(2), 361–377 (2013)
13. Ji, L., Huang, Z.: A simple statistical energy analysis technique on modeling continuous coupling interfaces. J. Vib. Acoust. **136**(1), 014501 (2014)
14. Maxit, L., Berton, M., Audoly, C., et al: Discussion about different methods for introducing the turbulent boundary layer excitation in vibroacoustic models. In: Flinovia-Flow Induced Noise and Vibration Issues and Aspects, pp. 249–278. Springer, Switzerland (2015)
15. Fahy, F.J.: Statistical energy analysis: a critical overview. Philos. Trans. R. Soc. Lond. Ser. A Phy. Eng. Sci. **346**(1681), 431–447 (1994)
16. Ji, L., Mace, B.R.: Statistical energy analysis modelling complex structures as coupled sets of oscillators: ensemble mean and variance of energy. J. Sound Vib. **317**, 760–780 (2008)
17. Cotoni, V., Langley, R.S., Kidner, M.R.F.: Numerical and experimental validation of variance prediction in the statistical energy analysis of built-up systems. J. Sound Vib. **288**, 701–728 (2005)
18. Xie, S.L., Zhang, Y.H., Xie, Q., et al.: Identification of high frequency loads using statistical energy analysis method. Mech. Syst. Signal Process. **35**(1), 291–306 (2013)
19. Legault, J., Woodhouse, J., Langley, R.S.: Statistical energy analysis of inhomogeneous systems with slowly varying properties. J. Sound Vib. **333**(26), 7216–7232 (2014)
20. Díaz-Cereceda, C., Poblet-Puig, J., Rodríguez-Ferran, A.: Automatic subsystem identification in statistical energy analysis. Mech. Syst. Signal Process. **54**, 182–194 (2015)
21. Aragonès, À., Guasch, O.: Ranking paths in statistical energy analysis models with non-deterministic loss factors. Mech. Syst. Signal Process. **52**, 741–753 (2015)
22. Maxit, L., Guyader, J.L.: Estimation of SEA coupling loss factors using a dual formulation and FEM modal information, Part I: theory. J. Sound Vib. **239**(5), 907–930 (2001)
23. Karnopp, D.: Coupled vibratory-system analysis, using the dual formulation. J. Acoust. Soc. Am. **40**(2), 380–384 (1966)
24. Maxit, L., Guyader, J.L.: Estimation of SEA coupling loss factors using a dual formulation and FEM modal information, Part II: numerical applications. J. Sound Vib. **239**(5), 931–948 (2001)
25. Maxit, L., Ege, K., Totaro, N., et al.: Non resonant transmission modelling with statistical modal energy distribution analysis. J. Sound Vib. **333**(2), 499–519 (2014)

Chapter 19
Vibro-Acoustic Modal Model of a Traction Motor for Railway Applications

Fredrik Botling, Hanna Amlinger, Ines Lopez Arteaga, and Siv Leth

Abstract A vibro-acoustic modal model of a traction motor for railway applications is presented based on an experimental modal analysis of the system. Noise requirements for railway traction motors are getting more and more demanding as part of the overall levels of new rolling stock. It is therefore of great interest to understand and predict the vibro-acoustic behaviour of electromagnetic noise generated by traction motors. The modal parameters are derived from an experimental modal analysis. The primary source for the radiated sound of the tested traction motor is the radial deflections of the stator shield. The modal parameters for the radial deflections are implemented in a reduced order modal model in a state space format using Matlab/Simulink. Only the structural modes that have a match in both the frequency and the spatial domain with the excited electromagnetic force will cause important vibro-acoustic response. This makes it possible to create an accurate and efficient reduced order modal model with only a fraction of the total number of structural modes. The simulation results from the modal model are compared to measurements of operational deflection shapes and acoustic measurements of the motor.

Keywords Modal analysis • Vibro-acoustics • Rotating machines • Electro-magnetic forces

19.1 Introduction

Electrically driven trains are today often characterized by an annoying tonal noise which is generated during acceleration and deceleration from platforms [1, 2]. This noise is audible both for people on the platforms and passengers on the train. The focus on this issue has increased the last years, both regarding legalisation and contractual requirements but also because of expectations from citizens and travellers.

The dominating acoustic noise at low train speeds (below 50 km/h) is in many cases coming from the traction motors. Three different type of noise sources can be found for electrical motors namely; aerodynamic, mechanical and electromagnetic noise. At low speed the electromagnetic noise from the electrical components on the train, especially the traction motor, can be clearly dominating since other sources on the train as the rolling noise is low at low speeds.

The electromagnetic noise from traction motors are mainly generated by radial air-gap Maxwell forces that excite stator vibrations causing audible noise.

To be able to design electrical and mechanical components that reduces the acoustic radiation without compromising other requirements as i.e. weight, size and efficiency requires full understanding of the process of electromagnetic noise generation.

The cause of the electromagnetically generated audible noise is influenced by several different physical domains. See Fig. 19.1.

- Acoustic domain
- Structural domain
- Electromagnetic domain

F. Botling (✉) • H. Amlinger • S. Leth
KTH Royal Institute of Technology, The Marcus Wallenberg Laboratory for Sound and Vibration Research (MWL), KTH Railway Group, 100 44 Stockholm, Sweden

Bombardier Transportation Sweden AB, Centre of Competence Acoustics and Vibration, 722 14 Västerås, Sweden
e-mail: botling@kth.se

I.L. Arteaga
KTH Royal Institute of Technology, The Marcus Wallenberg Laboratory for Sound and Vibration Research (MWL), KTH Railway Group, 100 44 Stockholm, Sweden

© The Society for Experimental Mechanics, Inc. 2016

J. De Clerck, D.S. Epp (eds.), *Rotating Machinery, Hybrid Test Methods, Vibro-Acoustics & Laser Vibrometry, Volume 8*,
Conference Proceedings of the Society for Experimental Mechanics Series, DOI 10.1007/978-3-319-30084-9_19

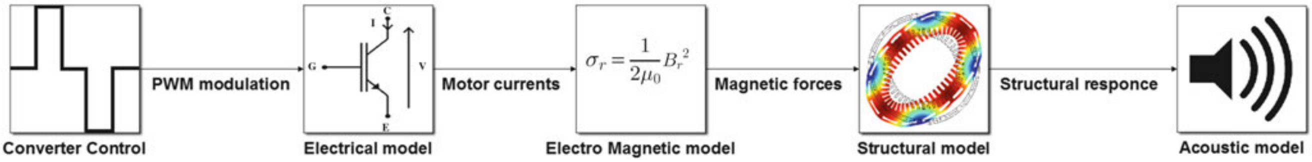

Fig. 19.1 Physical domains related to magnetic noise

- Electrical domain
- Software domain

The acoustic sound received by passengers or people near the rail is caused by sound pressure variations caused by surface velocities of the vibrating stator shield of the traction motor. The stator shield vibrations are caused by radial Maxwell forces acting on the structure. The electromagnetic Maxwell forces are introduced by the motor stator currents. The motor currents are controlled by the converter electronics via high power switching devices (IGBT's). These switching devices are controlled by software based Pulse Width Modulated (PWM) control to generate the demanded torque of the traction motors.

It is important to understand and predict the influence of all the five domains to fully understand the causes of the magnetic noise.

This paper focuses on the modelling and prediction of the behaviour of the structural domain with excitation forces caused by radial Maxwell forces. The sound generation caused by structural vibrations are dominated by radial deflections of the stator shield of the traction motor.

A model of the structural behaviour can be derived by analysing the structural response in both time and spatial domain for a known input excitation force. The method used in this work is the experimental modal analysis.

The results from the experimental modal analysis is used to create a modal model of the structural dynamics that can be used to simulate the response from estimated Maxwell forces caused by PWM converter fed operation.

19.2 Experimental Modal Analysis

One experimental technique to investigate vibrations of built-up structures is the experimental modal analysis method, as described in [3]. The method uses measured frequency response functions as input data describing the properties of the structure. The modal analysis technique numerically fits a mathematical model to the measured data. The fitted mathematical model is based on a physical description of the vibrating structure, not merely a mathematical expression fitted to some measured data.

The experimentally obtained modal model, can be used in various ways for systematic analysis and diagnosis of sound and vibration related problems. Today experimental modal analysis has become a popular analysis tool often used as a complement to Finite Element analysis. Software and hardware for experimental modal analysis are used at almost all larger industries producing machines and vehicles.

One other well-known method for structural analysis is the Finite Element method. Unfortunately, Finite Element methods and other numerical methods are cumbersome to use on complex built-up structures. Reliable modelling of realistic structures requires tuning of the model using data measured on the real structure. The main difficulties are to model realistic boundary conditions and to model the losses of a real structure. In many cases the results from FEM analysis does not have enough accuracy, but is still valuable for prototyping guidelines.

19.2.1 Mode Shape

A vibration mode is defined by its eigenfrequensies and the eigenmodes, or mode shapes. The mode shape for a cylindrical structure is described both in the circumferential direction **m**, and in the axial direction **n**. This can be written as, **mode** (**m**, **n**), where **m** = number of maxima over the circumference, and **n** = number of nodal circles in axial direction. As described later in this paper not only the eigenfrequency of a structure is needed for analysing the structural behaviour related to radiated audible noise, but also the mode shape is very important.

19.2.2 Modal Parameter Extraction

How many observation points N is needed to find the vibration modes of interest? To be able to answer this question we need to know or guess which mode shapes that are relevant. Circumferential modes with orders of up to 4 are shown to be of importance for the radiated noise from the literature [1]. The number of observation points on the circumference are recommended to be five times the mode order. It is also wise to choose the number of observation points as an order of 4 (4, 8, 12 etc.).

The decision for this test was Nc = 24 observation points on the circumferential, and Na = 3 in the axial direction.

Each mode with N degrees of freedom requires at least input data from N independent measurements, one column or one row in the FRF or impulse response function matrix. In cases with closely coupled modes or if the modal density is high, the number of measured FRFs must be increased. As explained in Sect. 19.2.3 four different excitation points were chosen.

19.2.3 Test Setup

The traction motor was tested in Bombardier Power Laboratory in Västerås, an environment representative of the physical conditions during real train operation. The traction motor is mounted with rubber bushings and is vibration insulated for higher frequencies but cannot fully be treated as a free-free condition for low frequencies. The interesting frequency region for the audible sound is however high enough for giving a reasonably good vibration isolation from the mounting positions.

The traction motor tested is not symmetrical in neither axial direction nor circumferential direction, see Fig. 19.2, making it difficult to apply a symmetrical measurement grid. The only possibility to apply a symmetrical measurement grid was to place the measurement points in the middle of the stator shield.

Seventy-two accelerometers were mounted in a symmetrical grid on the stator shield in tree circular positions with 24 accelerometers per circle. The acquisition equipment used could only measure eight accelerometers each time but by repeat the same excitation with nine different setups of eight accelerometers all measurement points could be covered. This was then repeated for the other three excitation points resulting in 8*9*4 = 288 measurements. Each impact test where repeated 10–15 times to be able to calculate the average of the force and accelerometer measurements resulting in over 3000 measurements files.

The measurement grid makes it possible to resolve mode shapes of up to mode (x, 2) in the axial direction and up to mode (12, x) in the circumferential direction, but due to unsymmetrical circumferential responses modes higher than mode (x, 4) were hard to extract from the measurements. The high number of circumferential measurement points (24) was very useful for redundant information beneficial for deriving mode shapes up to mode (4, x).

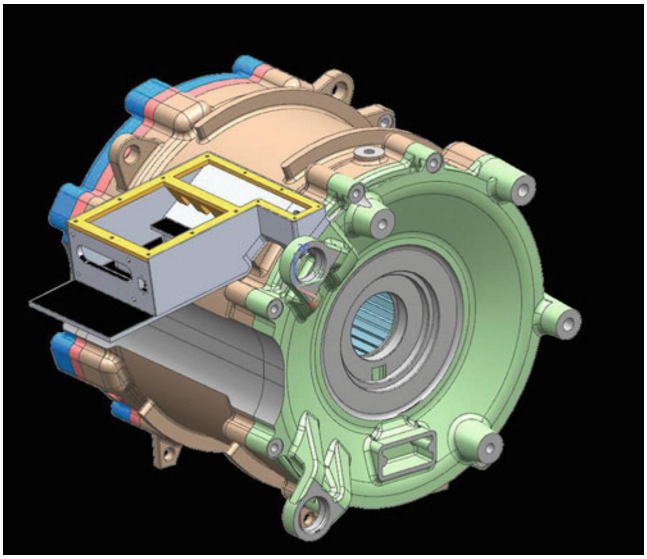

Fig. 19.2 Tested traction motor

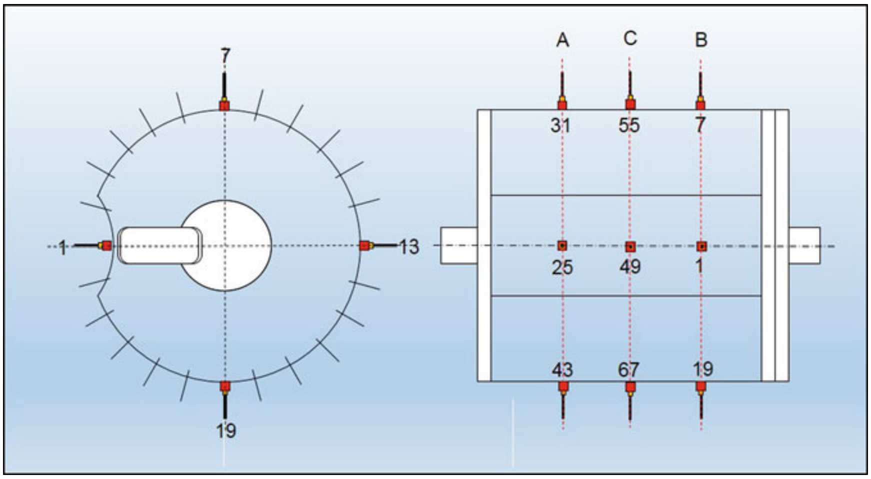

Fig. 19.3 Measurement grid

Four excitation points were used for the multi reference force excitation, all placed on the circumferential A, see Fig. 19.3, in points close to four of the accelerometer positions 30, 32, 33 and 36. It is important that the excitation points are as close as possible to one of the accelerometer positions. The dimension of the impact hammer head sets the minimum distance possible to achieve without moving the accelerometer in/close to the excitation point.

Measurement Equipment

- Data acquisition system NetdB (12 channels) with SW 01 dB.
- Single axis accelerometers: Bruel & Kjaer 4507B004, 0.3–6 kHz (±10 %), 50 g range.
- Impact hammer, with steel tip

Measurement of

- Impact hammer force
- Accelerations

19.2.4 Result

A Finite Element (FE) model can be used to predict the modal behaviour of the stator core. It is of great help to use numerical methods to study higher order modes that is hard to determine from experimental tests. Even if a FE model is difficult to use to acquire accurate modal parameters it is a simple and good method to understand the general behaviour of a circular thick walled cylinder [4] that is a good approximation of the stator shield in a traction motor. The simple thick walled FE analysis actually gives similar results as detailed FE models of real traction motors.

Tables 19.1 shows the results from a Finite Element model of some of the structural mode shapes with their eigenfrequencies, and Tables 19.2 the results from the experimental modal analysis.

19.2.5 Discussion

The high number of structural modes and the high modal densities at higher frequencies makes it hard to resolve mode shapes higher than mode (4,1).

Table 19.1 Mode shapes from finite element analysis

	m = 0	m = 2	m = 3	m = 4
n = 0	Not found	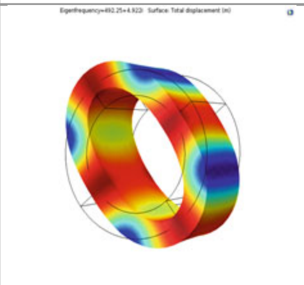 Eigenfrequency=492.25+4.922i Surface: Total displacement (m) 492 Hz	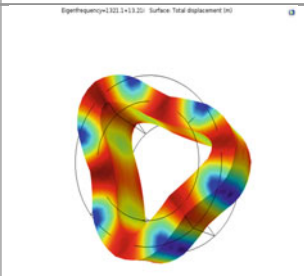 Eigenfrequency=1321.1+13.21i Surface: Total displacement (m) 1321 Hz	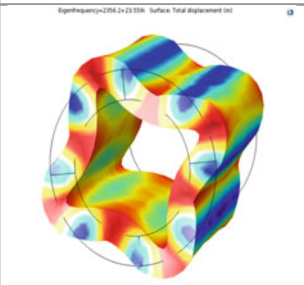 Eigenfrequency=2356.2+23.559i Surface: Total displacement (m) 2356 Hz
n = 1		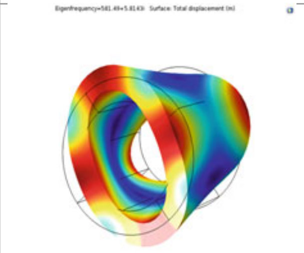 Eigenfrequency=581.49+5.8143i Surface: Total displacement (m) 581 Hz	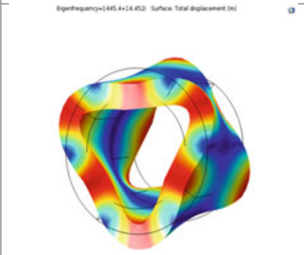 Eigenfrequency=1445.4+14.452i Surface: Total displacement (m) 1445 Hz	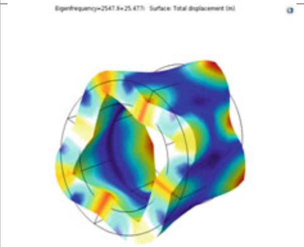 Eigenfrequency=2547.9+25.477i Surface: Total displacement (m) 2548 Hz

Table 19.2 Mode shapes from experimental modal analysis

	m = 0	m = 2	m = 3	m = 4
n = 0	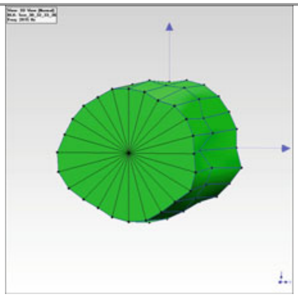 2915 Hz	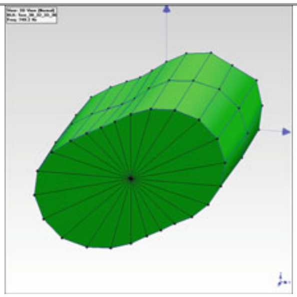 749 Hz	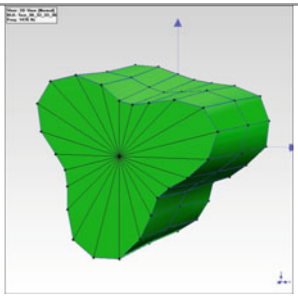 1476 Hz	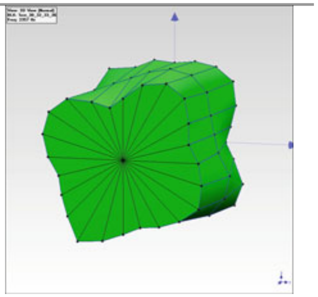 2357 Hz
n = 1			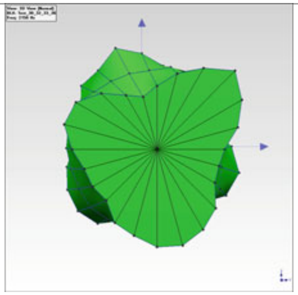 2156 Hz	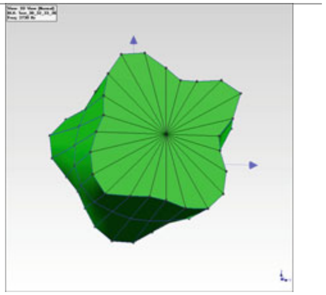 2730 Hz

19.3 Reduced Order Modal Model

The experimental modal analysis results in several hundred modal modes within the frequency region of interest. Only a fraction of these modes are relevant for the generation of electromagnetic noise during converter fed operation. Therefore the knowledge of the characteristics of the input forces is very important when deciding which modes that are relevant.

By analysing the Maxwell forces generated by the electro magnetics a model can be made for the excitation forces acting on the structure during converter operation.

19.3.1 *Maxwell Forces*

Air gap field harmonics discussed in [5, 6], are caused by Maxwell forces. The Maxwell stress tensor is defined as:

$$\sigma_{ij} = \epsilon_0 \left(E_i E_j - \frac{1}{2}\delta_{ij} E^2 \right) + \frac{1}{\mu_0} \left(B_i B_j - \frac{1}{2}\delta_{ij} B^2 \right) \tag{19.1}$$

Electric field $E_{i,j}$ can be disregarded for motors.

$$\sigma_{ij} = \frac{1}{\mu_0} \left(B_i B_j - \frac{1}{2}\delta_{ij} B^2 \right) \tag{19.2}$$

For cylindrical objects as the rotor/stator

$$\sigma_{rt} = \frac{1}{\mu_0} B_r B_t - \frac{1}{2\mu_0} \delta_{ij} \left({B_r}^2 - {B_t}^2 \right) \tag{19.3}$$

The tangential component σ_t corresponds to the wanted motor torque, and the radial component σ_r gives unwanted stator deflections.

$$\sigma_t = \frac{1}{\mu_0} B_r B_t \tag{19.4}$$

$$\sigma_r = \frac{1}{2\mu_0} \left({B_r}^2 - {B_t}^2 \right) \tag{19.5}$$

The magnetic field in the radial direction B_r is much larger than in the tangential direction B_t.

$${B_r}^2 \gg {B_t}^2 \tag{19.6}$$

By using the relation (19.6) in Eq. (19.5) gives:

$$\sigma_r = \frac{1}{2\mu_0} {B_r}^2 \tag{19.7}$$

This gives that the radial forces are proportional to the squared magnetization current of the motor.

$$f \sim {B_r}^2 \sim {I_S}^2$$

19.3.2 *Spatial Force Distribution*

Figure 19.4 shows the result from a detailed electromagnetic FE analysis of the spatial Maxwell pressure distribution for the tested motor.

From Fig. 19.4 it is hard to tell which spatial orders this force pattern corresponds to. A spatial FFT can be done to visualise the orders much clearer. Figure 19.5 shows the spatial FFT for the same set of data.

It is clear from the spatial FFT analysis that the Maxwell forces for this specific application only have spatial orders of 0,4,8 etc. This is a very important finding for the knowledge of generated electromagnetic noise. The structural modes 1,2,3,5,6,7,9 and so on does not get excited by the electromagnetic forces. Only the axis symmetric modes (0,0) and (4,0) are interesting to investigate which makes it possible to significantly reduce the number of structural modes that has to be studied.

19.3.3 Structural Model

As described in [3], any vibration field in a structure can be written as a sum of contributions from the structure's vibration modes. A vibration mode is defined by its characteristic shape, the mode shape $\varnothing_{pn}$, and its eigen-value or eigen-frequency ω_n. These parameters were derived from the experimental modal analysis.

$$h_{pq}(\omega) = \sum_{n=1}^{N} \frac{\varnothing_{pn}\varnothing_{qn}}{\omega_n^2 - \omega^2} \tag{19.8}$$

The structural behaviour can be expressed as a transfer function H (or FRF), excited by the point force vector **f** with length Q, resulting in vibrations with displacement vector **x** with length P.

$$\hat{\boldsymbol{x}} = \boldsymbol{H} \times \hat{\boldsymbol{f}} \tag{19.9}$$

The transfer matrix **H** contains all of the modal elements h_{pq},

$$\boldsymbol{H} = \begin{bmatrix} h_{11} & \cdots & h_{1Q} \\ \vdots & \ddots & \vdots \\ h_{P1} & \cdots & h_{PQ} \end{bmatrix} \tag{19.10}$$

where each element is a sum of all modes N

$$h_{pq} = h_{pq}^1 + \cdots + h_{pq}^N \tag{19.11}$$

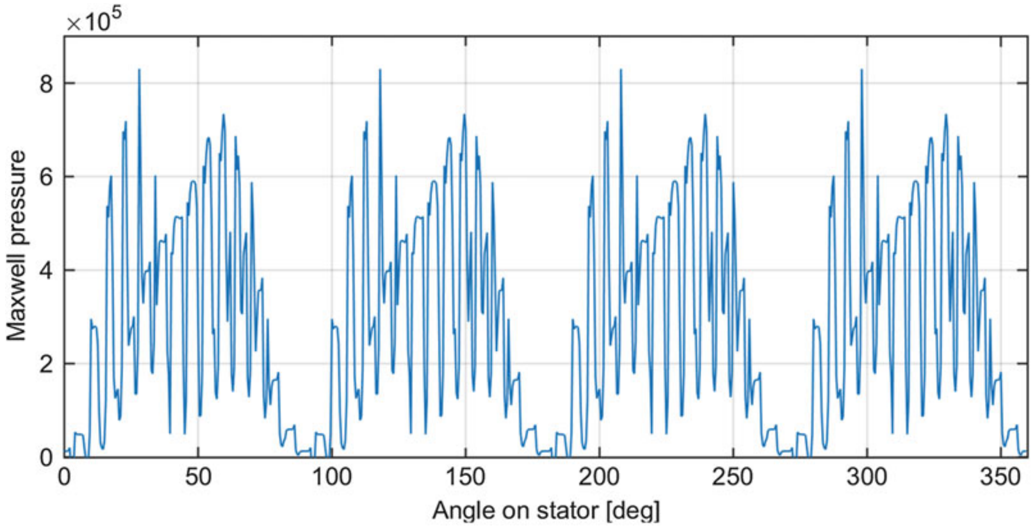

Fig. 19.4 Maxwell force spatial distribution

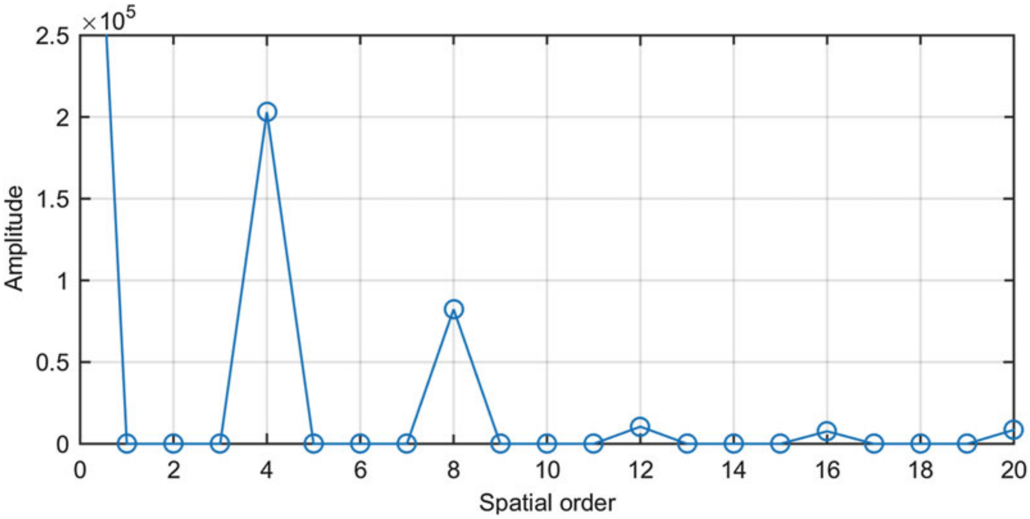

Fig. 19.5 Maxwell force spatial FFT

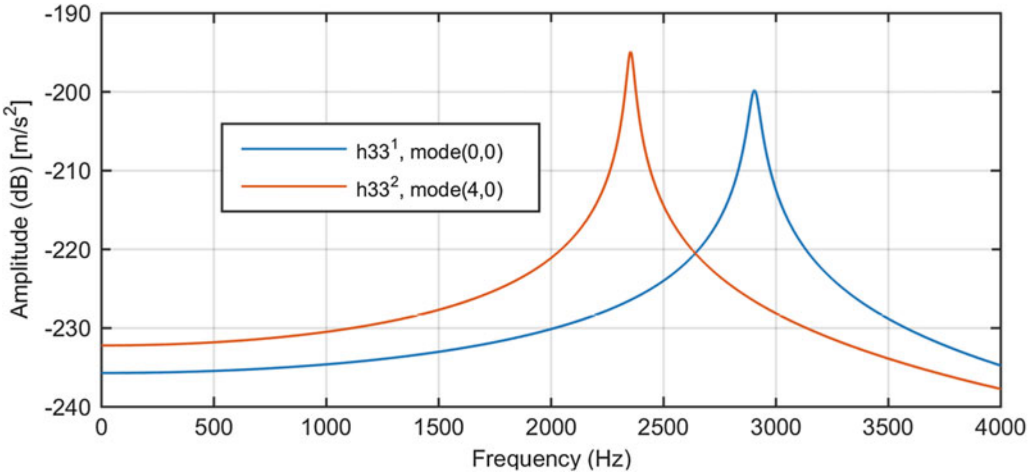

Fig. 19.6 Receptance elements h_{33}^1 and h_{33}^2

In the experimental modal analysis we measure the FRFs and numerically determine mode parameter values $\varnothing_{pn}$ and ω_n so that the measured FRFs are approximated as closely as possible. The mode parameters determined in this manner can be used as a modal model to analyse the vibrations of the structure.

As explained in Sect. 19.3.2 the only relevant modes for estimating the structural response related to operational conditions are the two modes (0,0) and (4,0). The reduced modal model only uses these two modes (N = 2), from a selection of several hundred modes derived from the experimental modal analysis.

The number of observation points discussed in Sect. 19.2.3 corresponds to the number of accelerometers, P = 72. The number of force excitation points used in the experiments were 4, but this does not correspond to a value of Q = 4, because of the reciprocity principle the transfer matrix is symmetric giving the possibility to simulate force excitation points in all of the positions corresponding to Q = 72.

One example of two receptance elements h_{33}^1 and h_{33}^2 corresponding to the two modes (4,0) and (0,0), are plotted in Fig. 19.6.

19.4 Simulation Results

19.4.1 Simulation Setup

The input magnetic forces used for the structural response simulations are based on the estimated Maxwell forces explained in Sect. 19.3.1. The magnetisation currents used for the estimated forces were measured from real PWM converter fed motor operation.

The simulated structural response was compared with real structural vibration measurements with the same number of observation points N as used for the modal analysis and the reduced order model.

The validation criteria for the model was chosen as the six frequency components corresponding to the highest vibrational responses.

Simulations were performed with a switching frequency of $f_{sw} = 670$ Hz, and a train speed of 20 km/h corresponding to a motor frequency of $f_m = 32$ Hz. The six frequency components with largest structural responses were chosen as evaluation frequencies for the comparison of the simulation model vs. real measurements. These frequencies can be calculated analytically as:

$$f_1 = 2f_{sw} = 1340\ Hz$$
$$f_2 = 2f_{sw} - 2f_m = 1276\ Hz$$
$$f_3 = 2f_{sw} + 2f_m = 1404\ Hz$$
$$f_4 = 4f_{sw} = 2680\ Hz$$
$$f_5 = 4f_{sw} - 2f_m = 2616\ Hz$$
$$f_6 = 4f_{sw} + 2f_m = 2744\ Hz$$

It is shown in [7] that the operational deflection shapes of the centre frequencies f1 and f4 corresponds to a structural mode (0,0), and the first side lobes are mode (4,0).

As a comparison, the relevant resonance frequencies from the experimental modal analysis are for mode (0,0) = 2915 Hz and mode (4,0) = 2357 Hz.

19.4.2 Results

Figures 19.7 and 19.8 shows the measured and simulated frequency spectra for the six dominating vibration frequencies.

19.4.3 Discussion

The two spectra in Figs. 19.7 and 19.8 above shows the interesting effect that the response is primarily governed by the excitation in the narrow banded magnetic force rather than the structural resonances. The amplitudes of the narrow banded magnetic force components are very high (50 dB) compared to the variations in the structural amplitude in the frequency region of interest (35 dB). Picture 19.9 shows the principal behaviour of the structural response during electromagnetic excitation from operational conditions (Fig. 19.9).

The structural responses at $2f_{sw}$ and $4f_{sw}$ differs only 7 dB even though the structural modal model shows a difference in amplification of 28 dB. The reason for this is that the electromagnetic force is 21 dB lower at $4f_{sw}$ compared to $2f_{sw}$. This is an important finding for the selection of a switching frequency for low noise radiation.

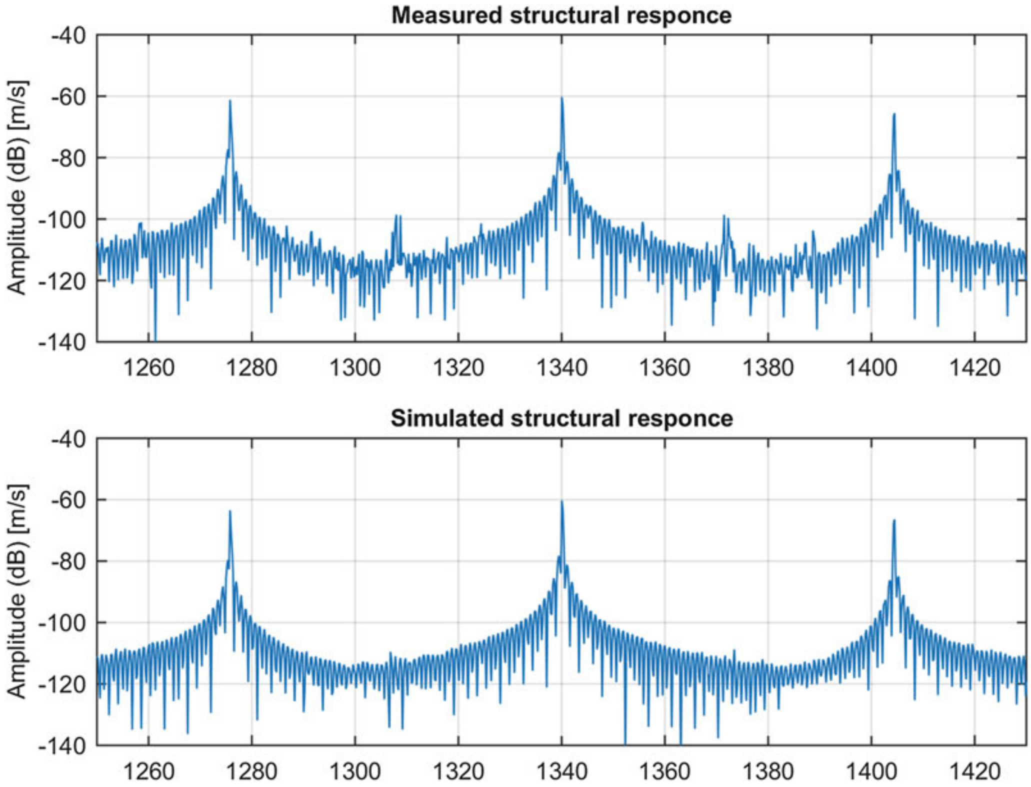

Fig. 19.7 Comparison of measured and simulated response for frequencies f_1 to f_3

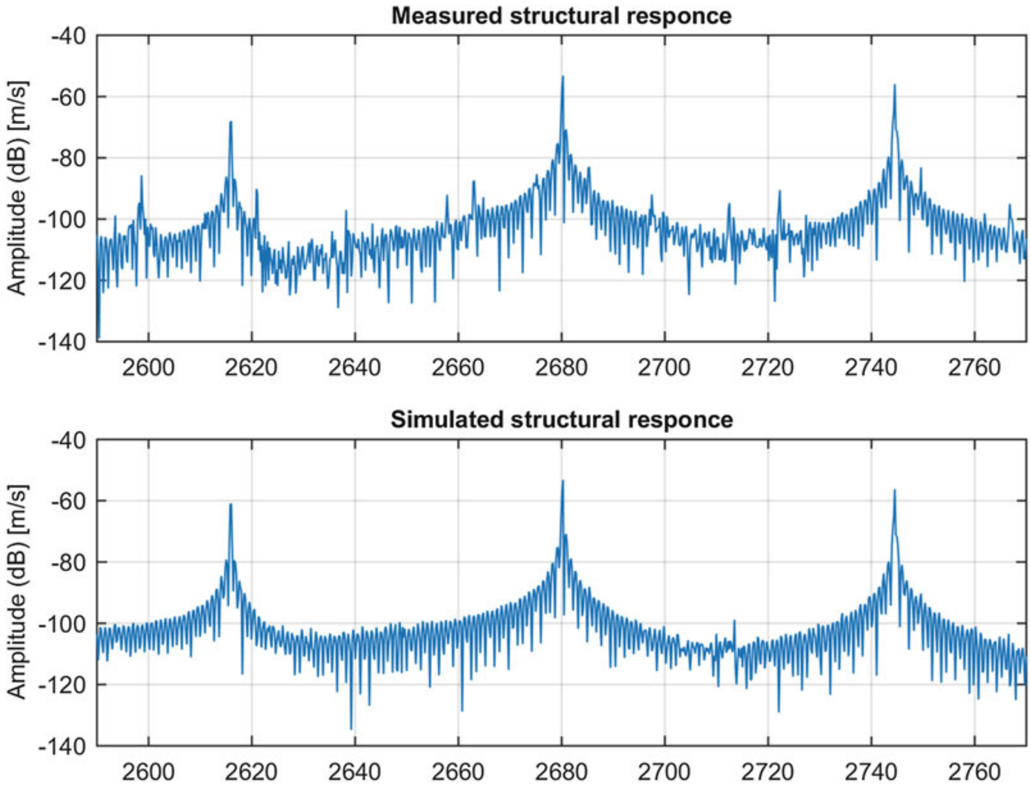

Fig. 19.8 Comparison of measured and simulated response for frequencies f_4 to f_6

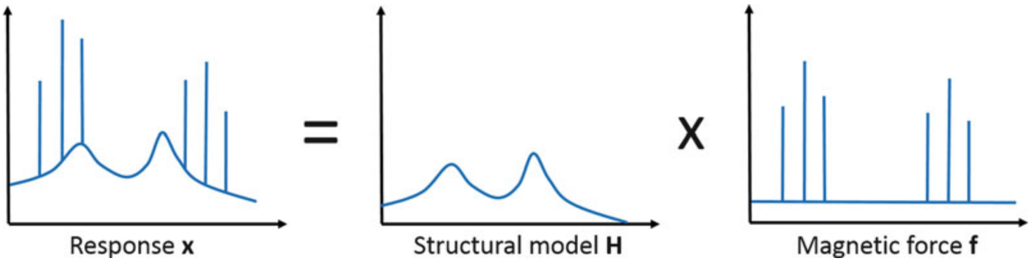

Fig. 19.9 Operational structural response

19.5 Conclusion

A reduced order modal model of a traction motor for railway applications has been presented in this paper. The modal parameters were derived from an experimental modal analysis. It could be concluded that only a fraction of all of the measured structural modes in the frequency region of interest is needed to accurately model the vibro-acoustic behaviour during converter fed operation. This is achieved by analysing the spatial order of the excitation from the electromagnetic Maxwell forces caused by the converter fed PWM operation of the motor.

The reduced order modal modes were implemented in a simulation model in Matlab/Simulink. The estimated Maxwell forces were used as input to the model and the resulting structural vibrations were compared to measured vibrations during a real converter fed operation. The simulation results fits the measured values very well.

Acknowledgment The authors would like to thank the KTH Railway group at the Royal Institute of Technology in Stockholm, Sweden, and to Propulsion and Controls, at Bombardier Transportation AB in Västerås, Sweden.

References

1. Besnerais, J.L., Lanfranchi, V., Hecquet, M., Brochet, P.: Characterization and reduction of audible magnetic noise due to PWM supply in induction machines. IEEE Trans. Ind. Elec. **57**(4), 1288–1295 (2010)
2. Tsoumas, I.P., Tischmacher, H.: Influence of the inverter's modulation technique on the audible noise of electric motors. IEEE Trans. Ind. Appl. **50**(1), 269–278 (2014)
3. Carlsson U.: Experimental structure dynamics. KTH Aeronautical and Vehicle Engineering (2009)
4. Farshidianfar, A., Oliazadeh, P.: Free vibration analysis of circular cylindrical shells: comparison of different shell theories. Int. J. Mech. Appl. **2**, 74–80 (2012)
5. Franck, D., Giet, M.V.D., Hameyer, K.: Active reduction of audible noise exciting radial force-density waves in induction motors. In: IEEE Int. Elec. Mach. & Drives Conference, pp. 1213–1218, May 2011
6. Giet, M.V.D.: Asymptotic Fourier decomposition of tooth forces in terms of convolved air gap field harmonics for noise diagnosis of electrical machines. Int. J. Comp. Math. **28**, 804–818 (2009)
7. Amlinger, H., Botling, F., Arteaga, I.L., Leth, S.: Operational deflection shapes of a PWM-fed traction motor. In: IMAC XXXIV, Orlando, 2016

Chapter 20
Operational Deflection Shapes of a PWM-Fed Traction Motor

Hanna Amlinger, Fredrik Botling, Ines Lopez Arteaga, and Siv Leth

Abstract Operational deflection shapes of an asynchronous traction motor for railway applications are investigated. The radiated noise from the traction motor on a train is, especially at low speeds, dominated by noise generated by electromagnetic forces. The tested motor is fed by a pulse-width-modulated (PWM) frequency converter for which the voltage is modulated as a series of pulses that are switched with a certain frequency. In this case, PWM force lines can be expected to influence the radiated noise. Therefore, detailed knowledge about the frequencies and deflection shapes of vibrations generated by PWM forces is of great importance for understanding and controlling the radiated noise and its spectral content. Vibration levels are measured on the stator shield and the operational deflection shapes are studied for several PWM switching frequencies and motor speeds. The deflection shapes with the largest vibration levels are determined. These are then compared to the expected excitation resulting from the pure PWM force lines. Changing the switching frequency, will shift the frequencies of the exciting forces. An appropriate selection of the PWM switching frequency is therefore important for the resulting acoustic radiation from the motor.

Keywords Traction motor • Pulse-width-modulation (PWM) • Operational deflection shapes (ODS) • Vibrations • Electromagnetic noise

20.1 Introduction

As the attention for acoustic comfort increases for rolling stock, a deep knowledge of the emitted acoustic noise is important. Already on the design stage, the acoustic noise needs to be evaluated and accounted for.

There are many types of acoustic noise on a train, e.g. rolling noise, aerodynamic noise from fans, mechanical noise from bearings, and electromagnetic noise from the drive system caused by magnetic forces acting on structures. Especially at low speeds, when rolling noise is very low, the noise of electromagnetic origin is dominating and it is often annoying because of high tonalities in the spectrum.

An important contributor to the electromagnetic noise on trains is the traction motor that also passengers are exposed to. Since this noise is dominating at low speeds, passengers on platforms as well as in the compartments are exposed to this noise.

The generation of acoustic noise of electromagnetic origin in a traction motor is a process involving several different physical domains. The motor current induces a magnetic field that generates magnetic forces in the air-gap of the motor. These forces act radially on the stator and cause vibrations, i.e. structural deflections of the stator, that will result in noise radiated from the motor. The frequency spectra of the radiated noise, the vibrations, and the exciting forces are identical.

The electromagnetic noise from induction motors increases when they are operated from pulse-width modulated (PWM) converters (in comparison to sinusoidal operation). PWM has a large impact on the force spectrum since the modulation strategy adds many harmonics to the air-gap Maxwell forces. Therefore, the influence of PWM force lines is important to understand in order to describe the electromagnetic generated acoustic noise.

H. Amlinger (✉)• F. Botling • S. Leth
KTH Royal Institute of Technology, The Marcus Wallenberg Laboratory for Sound and Vibration Research (MWL),
KTH Railway Group, SE 100 44 Stockholm, Sweden

Center of Competence Acoustics and Vibration, Bombardier Transportation Sweden AB, SE 722 14 Västerås, Sweden
e-mail: amlinger@kth.se

I.L. Arteaga
KTH Royal Institute of Technology, The Marcus Wallenberg Laboratory for Sound and Vibration Research (MWL),
KTH Railway Group, SE 100 44 Stockholm, Sweden

© The Society for Experimental Mechanics, Inc. 2016

J. De Clerck, D.S. Epp (eds.), *Rotating Machinery, Hybrid Test Methods, Vibro-Acoustics & Laser Vibrometry, Volume 8*,
Conference Proceedings of the Society for Experimental Mechanics Series, DOI 10.1007/978-3-319-30084-9_20

The acoustic generated noise from traction motors at PWM operation depends on various electromagnetic, mechanical, acoustic, and control parameters, e.g. pole number, stator slot number, rotor slot number, motor operating frequency, PWM switching frequency, and mechanical natural frequencies and vibration modes of the system. That is, many different aspects and properties are involved in the noise generation.

Electromagnetic noise from induction motors has been subject to research for a very long time, starting with the characterization of acoustic noise generated by Maxwell forces [1]. Also the influence of PWM supply has been addressed extensively [2–4], and the interaction between PWM harmonics and the mechanical structure (slotting) has been studied [5, 6]. Later, this work has continued, considering different force lines at PWM operation and modeling, simulations, and experimental validation of the same [7–10].

In this paper the operational deflection shapes of a three-phase asynchronous motor at PWM operation are investigated. The results of experimental tests are presented, discussed and compared to what is expected based on literature research.

In an accompanying paper [11] a reduced order modal model of the same motor, based on experimental modal analysis, is presented and evaluated.

20.2 Magnetic Noise Characterization at PWM Operation

The electromagnetically generated acoustic spectrum can be determined from the radial component of the air-gap Maxwell forces. The electromagnetic force spectrum results from the interaction between two flux density waves, i.e. a combination of two permeance harmonics and two magnetomotive (mmf) harmonics. These harmonics can be expressed using Fourier series. The vibration forces for a motor at PWM operation can be divided into three main types: slotting vibrations, PWM vibrations and slotting PWM vibrations [5, 7].

The number of force harmonics is infinite, but the amplitude of the corresponding harmonics in the vibration response is inversely proportional to m^4 where m is the spatial order. Therefore, only the lowest spatial order forces result in vibration levels (and thereby noise) of significance. For traction motors, the spatial orders of interest are those of order zero to four [9].

Resonances with large vibration levels occur when there is a match in both frequency, between exciting force and structural mode natural frequency, as well as spatial order, between exciting force and structural mode shape.

The propagation direction of the vibration waves can be indicated with positive/negative frequencies, or positive/negative spatial orders. The latter is used in this paper.

20.2.1 Slotting Vibrations

The interaction between some slotting permeance harmonics and the fundamental stator mmf causes so called slotting vibrations. Slotting vibrations are independent of the type of supply, which means they are equally strong for both sinusoidal and PWM supplies. Therefore, a motor that is noisy at sinusoidal supply will remain noisy also at PWM operation. The main slotting forces can be divided into three groups, characterized by frequency and spatial order, see Table 20.1. Variables k_r and k_s are positive integers from the Fourier series of the permeance distribution, Z_r and Z_s are the number of rotor and stator slots respectively, s is the slip, and p the number of pole pairs. The higher k_r and k_s are, the lower are the permeance harmonics, and the lower is the corresponding force harmonic. Therefore, the force harmonics with highest magnitude are given by $k_r = k_s = 1$ [8].

Table 20.1 Frequency and spatial order of the main slotting vibrations

Name	Frequency f	Spatial order m
F^{-}_{slot}	$f_s(k_rZ_r(1-s)/p-2)$	$k_rZ_r - k_sZ_s - 2p$
F^{0}_{slot}	$f_s(k_rZ_r(1-s)/p)$	$k_rZ_r - k_sZ_s$
F^{+}_{slot}	$f_s(k_rZ_r(1-s)/p+2)$	$k_rZ_r - k_sZ_s + 2p$

20.2.2 PWM Vibrations

The interaction between a fundamental stator mmf and a harmonic mmf caused by a PWM time harmonic of the stator current, will result in so called PWM vibrations. Each harmonic of the stator current causes two groups of force harmonics, F_{pwm}^{-} and F_{pwm}^{+}, with the properties listed in Table 20.2. f_s is the fundamental stator frequency, f_n^s is the frequency of the PWM harmonic and η_s is ± 1 that indicates the propagation direction of the harmonic mmf. Since both the stator mmf wave and the PWM harmonic has spatial order p, the resulting force line will have spatial order 0 or $2p$, depending on the propagation directions of the interacting waves. That is, as indicated in Table 20.2, all pure PWM vibrations have a spatial order of 0 or $2p$ [9].

For PWM with triangular carrier, the harmonics f_n^s can be written as [4]

$$f_n^s = n_1 f_s \pm n_2 f_c, \text{ where } \mathrm{n}_1 \text{ and } \mathrm{n}_2 \text{have an opposite parity.} \tag{20.1}$$

The amplitude of the harmonics of the stator current depends on both the carrier type of the PWM as well as the modulation index. For a triangular carrier, the amplitude of $2f_c \pm f_s$ is largest during the starting phase but at maximum speed the amplitude of $f_c \pm 2f_s$ is dominating, see Fig. 20.1 [4].

Substituting these frequencies in Table 20.2 gives the frequencies corresponding to the main peaks in the PWM related vibration response for a triangular carrier signal and their spatial orders as listed in Table 20.3 [9].

20.2.3 Slotting PWM Vibrations

The combination of a harmonic mmf caused by a PWM time harmonic of the stator current, a fundamental stator mmf, and slotting permeance harmonics will result in so called slotting PWM vibrations. Their characteristics are listed in Table 20.4 [10]. As can be seen, these vibrations have the same spatial order as the slotting vibrations but they occur at a higher frequency.

Table 20.2 Frequency and spatial order of pure PWM force lines

Name	Frequency f	Spatial order m
F_{pwm}^{-}	$f_s - \eta_s f_n^s$	$p - p = 0$
F_{pwm}^{+}	$f_s + \eta_s f_n^s$	$p + p = 2p$

Fig. 20.1 Relationship between amplitude of harmonics and modulation index, f_l is the fundamental stator frequency [4]

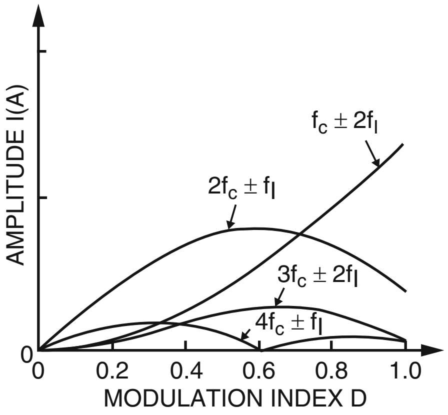

Table 20.3 Frequencies and spatial orders of main PWM-related vibration peaks for a triangular carrier

	($f_n^s = 2f_c \pm f_s$) Frequency f	($f_n^s = 4f_c \pm f_s$) Frequency f	($f_n^s = f_c \pm 2f_s$) Frequency f	($f_n^s = 3f_c \pm 2f_s$) Frequency f	Spatial order m
F_{pwm}^{+}	$2f_c - 2f_s$	$4f_c - 2f_s$	$f_c + f_s$	$3f_c + f_s$	$-2p$
F_{pwm}^{-}	$2f_c$	$4f_c$	$f_c + 3f_s$	$3f_c + 3f_s$	0
F_{pwm}^{-}	$2f_c$	$4f_c$	$f_c - 3f_s$	$3f_c - 3f_s$	0
F_{pwm}^{+}	$2f_c + 2f_s$	$4f_c + 2f_s$	$f_c - f_s$	$3f_c - f_s$	$2p$

Table 20.4 Frequency and spatial order of slotting PWM vibrations

	Frequency f	Spatial order m
$F^{-}_{slotpwm}$	$f_s(k_rZ_r(1-s)/p-1)-\eta_s f_n^s$	$k_rZ_r-k_sZ_s-2p$
$F_{slotpwm}$	$f_s(k_rZ_r(1-s)/p-1)-\eta_s f_n^s$	$k_rZ_r-k_sZ_s$
$F_{slotpwm}$	$f_s(k_rZ_r(1-s)/p+1)+\eta_s f_n^s$	$k_rZ_r-k_sZ_s$
$F^{+}_{slotpwm}$	$f_s(k_rZ_r(1-s)/p+1)+\eta_s f_n^s$	$k_rZ_r-k_sZ_s+2p$

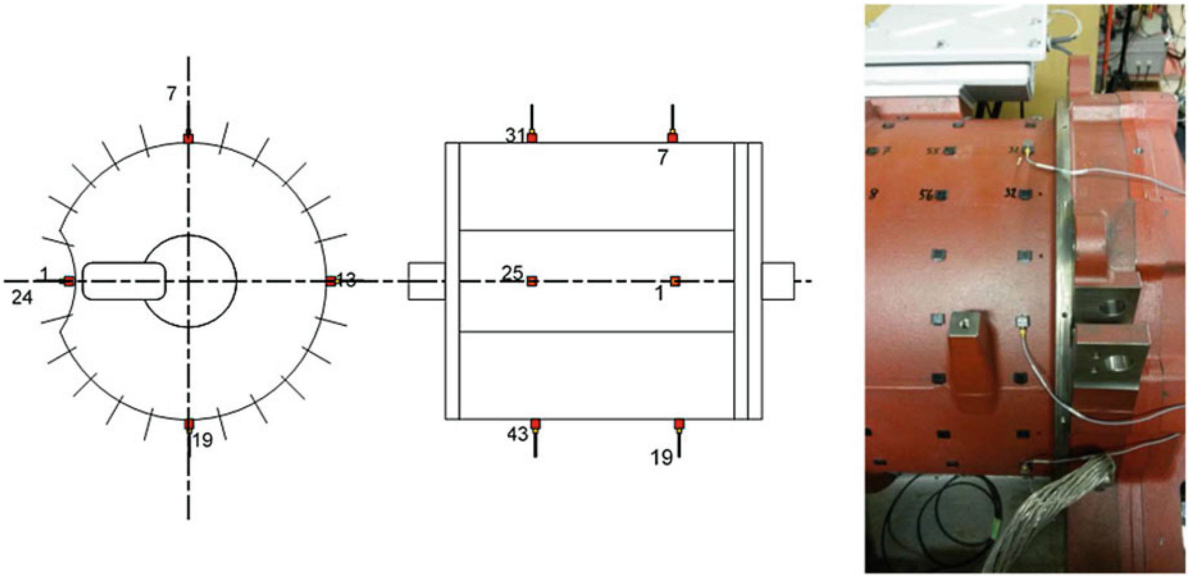

Fig. 20.2 A schematic figure of the measured points and a picture from the measurement set-up

20.3 Experimental Set-Up

In order to study the operational deflection shapes (ODS), a three-phase asynchronous motor is tested in the power lab at Bombardier Transportation. The running conditions for the motor in the lab is identical to the physical conditions during real train operation. The tested motor has two polepairs (p), 56 rotor slots (Z_r) and 48 stator slots (Z_s). During the tests, the motor is run at full load and fed by a PWM frequency converter where the PWM has a triangular carrier.

For the acquisition, a 01dB Metravib NetdB front-end with 12 channels and a sample rate of 51.2 kHz is used. Accelerometers (Brüel and Kjær 4507B-005) are placed in two circles around the circumference to measure the radial acceleration of the stator shield. For each circle, 24 different points are measured.

The measurements are performed in six measurement sets, where eight positions and one fix reference position are measured in each set. In addition, the rotational speed of the motor, the motor current, and one microphone are also recorded within each measurement set.

A schematic figure of the measured points as well as a picture from the measurement set-up are shown in Fig. 20.2.

The measurement data is analyzed using Vibrant Technologys ME'Scope ODS software. Since the excitation forces cannot be measured, frequency response functions (FRFs) with respect to the reference accelerometer are created using calculated cross and auto spectra. Since the measurement is executed in several measurement sets, the FRFs are scaled with respect to the reference point [12]. The ODS are analyzed by plotting the deflections at different frequencies using ME'Scope.

The maximum frequency range for the used accelerometers is 6000 Hz, therefore the analysis is focused on frequencies below this limit. The natural modes of interest of the stator are well below this limit [11] and the damping is higher for high frequencies. Therefore, the vibrations of interest are also expected to be found within the studied frequency range.

20.4 Results

ODS are studied for two different switching frequencies (f_c) and two different rotational speeds (f_s) of the motor, see Table 20.5. For the train this motor is designed for, these motor speeds correspond to a velocity of the train of 20 kph and 40 kph respectively.

To obtain a first overall view of the vibrations, the power spectral density of one accelerometer measurement during an acceleration is plotted, see Fig. 20.3. The acceleration is constant, hence time is corresponding to motor speed. In the obtained spectrum, all three main types of vibrations earlier described can be observed. The slotting vibrations are depending on motor speed with the corresponding force lines starting in the origin. Both PWM vibrations and slotting PWM vibrations are located around multiples of the switching frequency (1050 Hz in this case) but with different dependence on the motor speed.

The two selected rotational speeds are investigated closer and for each test case, the FRFs are calculated. The ODS with largest deformation amplitude are determined from the root mean square (RMS) of the real part of the FRFs for all 24 measurement points, see Fig. 20.4. In general, the deformation amplitudes are significantly lower for switching frequency 670 Hz compared to switching frequency 1050 Hz.

The spatial orders are resolved by plotting the deflections at the frequencies of interest in ME'Scope. The frequencies and spatial orders for the four ODS with largest deformation amplitude for each test case are presented in Tables 20.6 and 20.7.

As an example, Fig. 20.5 shows the plotted deflection shapes for the first case with switching frequency 1050 Hz and motor speed 940 rpm.

Evaluating the frequencies of the dominant ODS, it is noticed that all can be related to the pure PWM lines. For the first test case, 940 rpm correspond to an electrical stator frequency of 31.3 Hz. Thus, 2100 Hz $= 2f_c$ and 2166 Hz $\approx 2f_c + 2f_s$ etc. In the same way, all frequencies can be expressed in terms of PWM lines as shown in Tables 20.8 and 20.9.

Table 20.5 Switching frequencies and rotational speeds used in the experiments

Switching frequency f_c	Speed f_s
1050 Hz	940 rpm
1050 Hz	1880 rpm
670 Hz	940 rpm
670 Hz	1880 rpm

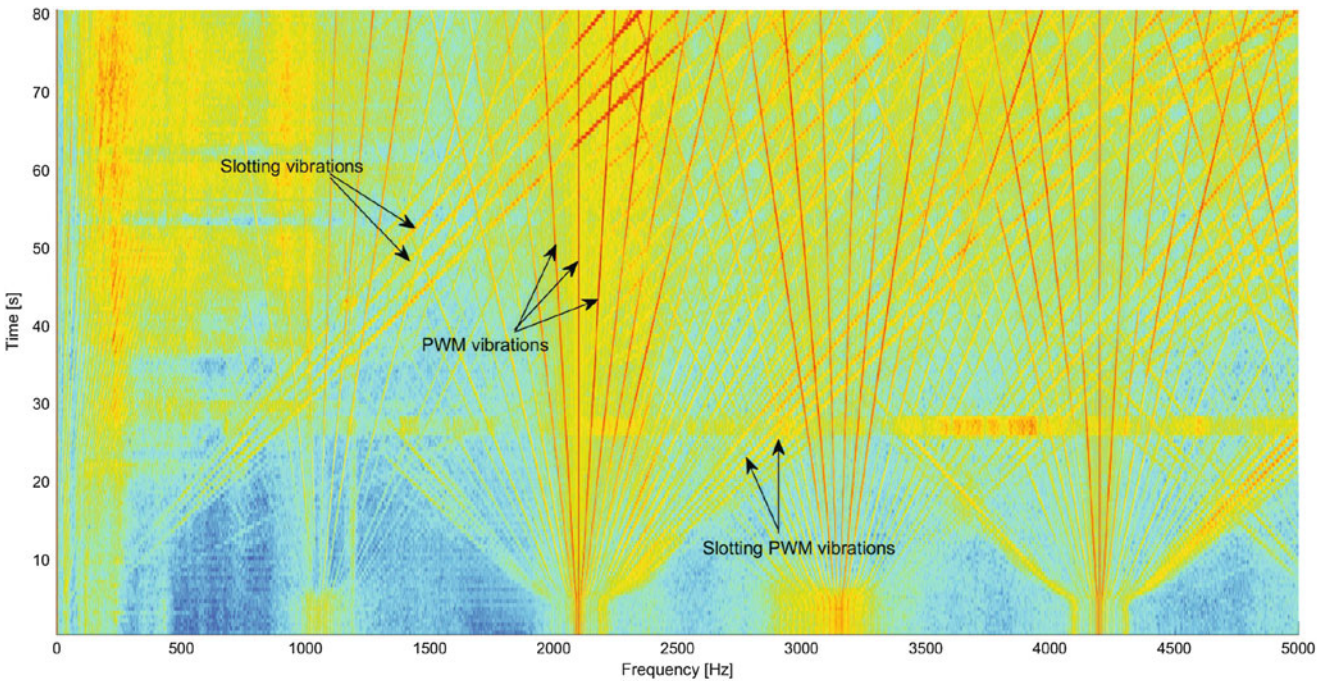

Fig. 20.3 Spectrogram of one of the accelerometers during constant acceleration, switching frequency 1050 Hz

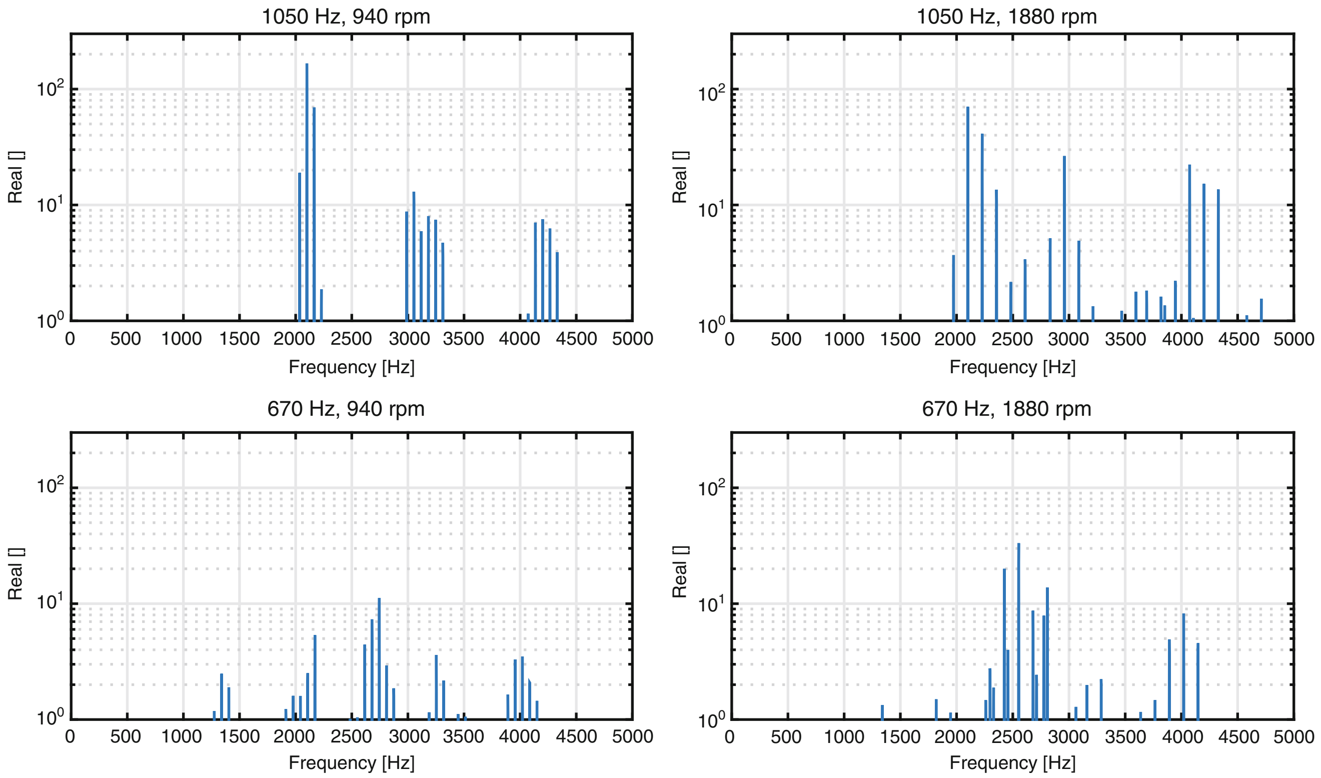

Fig. 20.4 RMS of the real part of the FRFs for all measurement points for the different test cases

Table 20.6 Spatial order and frequencies of the dominant ODS for switching frequency 1050 Hz

f_c=1050 Hz, f_s=940 rpm	f_c=1050 Hz, f_s=1880 rpm
Order 4, 2100 Hz	Order 4, 2100 Hz
Order 4, 2166 Hz	Order 4, 2228 Hz
Order 4, 2036 Hz	Order 0, 2959 Hz
Order 0, 3053 Hz	Order 4, 4073 Hz

Table 20.7 Spatial order and frequencies of the dominant ODS for switching frequency 670 Hz

f_c=670 Hz, f_s=940 rpm	f_c=670 Hz, f_s=1880 rpm
Order 4, 2745 Hz	Order 4, 2553 Hz
Order 0, 2680 Hz	Order 4, 2425 Hz
Order 4, 2172 Hz	Order 4, 2808 Hz
Order 4, 2616 Hz	Order 0, 2680 Hz

20.5 Discussion

As shown in Tables 20.8 and 20.9, the frequencies of the dominating ODS can all be related to the pure PWM force lines.

The tested motor has $Z_r = 56$ rotor slots and $Z_s = 48$ stator slots. This means that the largest slotting vibrations ($k_r = k_s = 1$), as well as the largest PWM slotting vibrations, will have spatial order 4, 8 and 12. Since only low spatial orders will result in significant vibrations, the force line that could be of interest is the one that has a spatial order 4.

The largest slotting vibration ($k_r = 1$) will occur at frequency $f_s(56(1-s)/2-2)$ that is far away in frequency from the natural mode 4 of the stator. Therefore, no large slotting vibration is expected to be measured in the studied test cases.

Compared to the slotting vibrations, the slotting PWM vibrations occur at higher frequencies but no dominating slotting PWM vibrations are observed when analyzing the measured vibrations.

The rotor and stator slot combination for this motor therefore result in that no main influence from slotting harmonics are expected. Instead, it is expected that the electromagnetic acoustic noise is dominated by the excitation of the PWM force lines. This is verified by the ODS measurements.

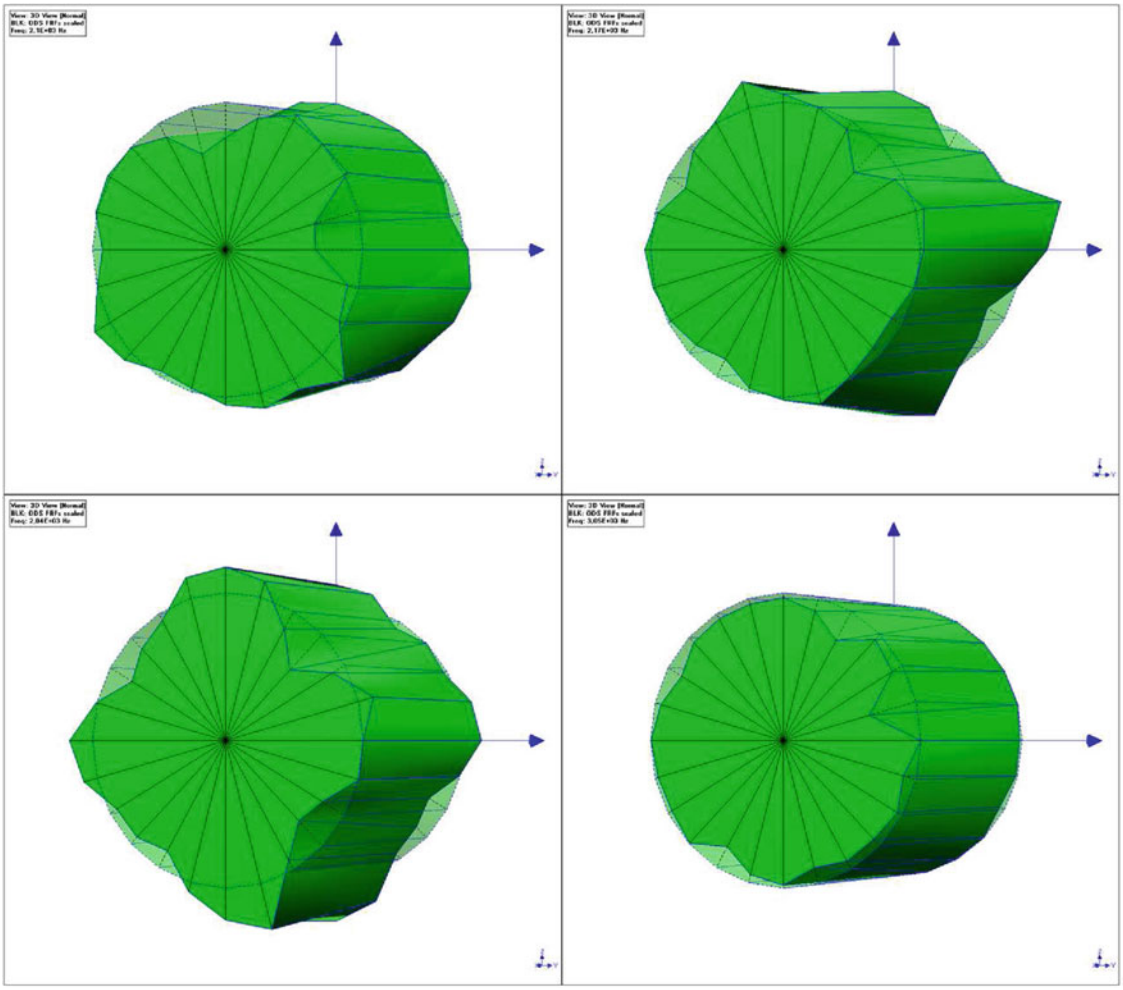
View: 3D View [Normal]
BLK: ODS FRFs scaled
Freq: 2.1E+03 Hz
View: 3D View [Normal]
BLK: ODS FRFs scaled
Freq: 2.17E+03 Hz
View: 3D View [Normal]
BLK: ODS FRFs scaled
Freq: 2.04E+03 Hz
View: 3D View [Normal]
BLK: ODS FRFs scaled
Freq: 3.05E+03 Hz

Fig. 20.5 From *upper left* to *lower right*, the deflection shapes at 2100 Hz, 2166 Hz, 2036 Hz, and 3053 Hz

Table 20.8 Relation to pure PWM lines of the dominant ODS for switching frequency 1050 Hz

f_c=1050 Hz, f_s=940 rpm	f_c=1050 Hz, f_s=1880 rpm
Order 4, $2f_c$	Order 4, $2f_c$
Order 4, $2f_c$+$2f_s$	Order 4, $2f_c$+$2f_s$
Order 4, $2f_c$-$2f_s$	Order 0, $3f_c$-$3f_s$
Order 0, $3f_c$-$3f_s$	Order 4, $4f_c$-$2f_s$

Table 20.9 Relation to pure PWM lines of the dominant ODS for switching frequency 670 Hz

f_c=670 Hz, f_s=940 rpm	f_c=670 Hz, f_s=1880 rpm
Order 4, $4f_c$+$2f_s$	Order 4, $4f_c$-$2f_s$
Order 0, $4f_c$	Order 4, $4f_c$-$4f_s$
Order 4, $3f_c$+$5f_s$	Order 4, $4f_c$+$2f_s$
Order 4, $4f_c$-$2f_s$	Order 0, $4f_c$

The spatial mode shapes of the studied ODS can all be identified as mode 0 or mode 4. Since the ODS are related to the PWM force lines, this is as expected since the PWM lines are of order 0 or $2p$, i.e. 0 or 4 for the tested motor. However, for switching frequency 1050 Hz and the ODS at $2f_c$, the spatial mode is not as clear as for the other modes. The PWM line should be of order 0, since it is the result of the interaction between the fundamental stator mmf at f_s of spatial mode p and the PWM harmonic at $2f_c - f_s$ with spatial mode $-p$. Surprisingly, the response looks more similar to a mode 4. This is not as expected and the reason for this could not yet be fully explained. For $f_c = 1050$ Hz, the spatial mode looks similar for both the tested motor speeds at frequency $2f_c$. On the other hand, the ODS at $2f_c$ for switching frequency 670 Hz has spatial mode 0 which would indicate that there are also some difference between the studied test cases and it could not be considered to be a general deviation for $2f_c$.

One reason for the not expected spatial mode at $2f_c$ for 1050 Hz could be that the excitation is not a pure mode 0. Another point that could be studied closer is the impact of the fact that in this case $2f_c$ is much closer in frequency to the natural mode 4 than the natural mode 0 [11]. Especially if there are some disturbances to the excitation force that result in an excitation that is not a pure mode 0, this could have an influence. Furthermore, the measurement set-up itself, e.g. the attachment of the motor, could effect the measured deflection shapes.

The dominating vibrations are mainly located in the frequency range 2000–3000 Hz which is as expected since this is the range where the experimental modal analysis of the motor shows that the natural spatial mode 0 and 4 are located [11]. Force lines around $2f_c$ are expected to be largest and for $f_c = 1050$ Hz this is also were the largest vibrations were measured. For $f_c = 670$ Hz, $2f_c$ is far away in frequency from the natural modes 0 and 4 of the motor which would explain why the largest vibrations for these cases are instead measured around $4f_c$. The resulting vibration level is dependent on match in both frequency and spatial mode. This also explains the difference in the amplitude of the largest deformations between the two studied switching frequencies. A different switching frequency results in a shift in frequency of the excitation forces. For the lower switching frequency, the current harmonics with highest magnitude around $2f_c$ are shifted away from the natural modes and thereby the resulting vibration levels decrease.

For some shapes, the deflections of the driving end dominate and for others, the deflections of the non-driving end dominate. However, the influence of the installation of the motor in the test setup is not further investigated in this study.

It is observed that there are some deviations for the reference channel between the measurement sets. There are indications that these deviations could be related to temperature differences of the motor between the measurement sets but this is not fully validated. It is assumed that all accelerometers are affected in a similar way for a specific measurement and that scaling with the reference accelerometer is still valid.

20.6 Conclusions

In this paper, the operational deflection shapes of a three-phase induction motor fed by a pulse-width-modulated frequency converter are studied. At operation, the radial deflections of the stator are measured with a mesh of accelerometers. From the measurements, the frequency response functions with respect to a reference accelerometer are calculated. The frequency and spatial modes of the deflections with largest amplitude are determined.

The dominating deflections have spatial mode 0 or 4. They can all be related to pure PWM force lines that are of spatial mode 0 and 4. The frequencies of the deflections with the largest amplitude are mainly located in the range 2000–3000 Hz. The structural modes of order 0 and 4 are from an experimental modal analysis [11] shown to be in this same frequency range. This emphasizes that the resulting high levels of vibration are associated with the match in both domains, frequency and space, between excitation and structural modes. Thus, knowledge about both the structural modes, as well as the magnetic excitation forces resulting from the PWM operation, is necessary to achieve a low noise design of the motor.

The pure PWM force lines are a result of the combination of the fundamental flux density and its time harmonics. The fundamental flux density is given by the stator frequency, and its harmonics by the stator frequency and the switching frequency of the PWM. The frequency of the PWM force lines can therefore be determined from the stator frequency and the switching frequency. There is a significant difference in amplitude of the largest deflections, and radiated noise, for the two different tested switching frequencies. Changing the switching frequency, will shift the frequencies of the excitation forces and thereby influence the match between the structural mode natural frequency of the stator and the PWM excitation. An appropriate selection of the PWM switching frequency is therefore a powerful tool to influence the acoustic radiation of the motor originating from the electromagnetic excitation.

Acknowledgements The authors are grateful to the KTH Railway Group and Bombardier Transportation Sweden AB for the support in this research.

References

1. Alger, P.: The magnetic noise of polyphase induction motors. Trans. Am. Inst. Electr. Eng. Part III Power Appartus Syst. **73**(1), 118–125 (1954)
2. Belmans, R.J.M., D'Hondt, L., Vandenput, A.J., Geysen, W.: Analysis of the audible noise of three-phase squirrel-cage induction motors supplied by inverters. IEEE Trans. Ind. Appl. **IA-23**(5), 842–847 (1987)
3. Iida, S., Okuma, Y., Masukawa, S., Miyairi, S., Bose, B.K.: Study on magnetic noise caused by harmonics in output voltages of PWM inverter. IEEE Trans. Ind. Electron. **38**(3), 180–186 (1991)

4. Ueda, S., Honda, K., Ikimi, T., Hombu, M.: Magnetic noise reduction technique for an AC motor driven by a PWM inverter. IEEE Trans. Power Electron. **6**(3), 470–475 (1991)
5. Lo, W.C., Chan, C.C., Zhu, Z.Q., Xu, L., Howe, D., Chau, K.T.: Acoustic noise radiated by PWM-controlled induction machine drives. IEEE Trans. Ind. Electron. **47**(4), 880–889 (2000)
6. Hubert, A., Friedrich, G.: Influence of power converter on induction motor acoustic noise: interaction between control strategy and mechanical structure. IEE Proc. Electr. Power Appl. **149**(2), 93–100 (2002)
7. Le Besnerais, J., Lanfranchi, V., Hecquet, M., Brochet, P., Friedrich, G.: Acoustic noise of electromagnetic origin in a fractional-slot induction machine. COMPEL Int. J. Comput. Math. Electr. Electron. Eng. **27**(5), 1033–1052 (2008)
8. Le Besnerais, J., Lanfranchi, V., Hecquet, M., Romary, R., Brochet, P.: Optimal slot opening width for magnetic noise reduction in induction motors. IEEE Trans. Energy Convers. **24**(4), 869–874 (2009)
9. Le Besnerais, J., Lanfranchi, V., Hecquet, M., Brochet, P.: Characterization and reduction of audible magnetic noise due to PWM supply in induction machines. IEEE Trans. Ind. Electron. **57**(4), 1288–1295 (2010)
10. Le Besnerais, J.: Reduction of magnetic noise in PWM-supplied induction machines - low-noise design rules and multi-objective optimisation. PhD dissertation, Ecole Centrale de Lille (2008)
11. Botling, F., Amlinger, H., Aretaga, I.L., Leth, S.: Vibro-acoustic modal model of a traction motor for railway applications. In: Presented at the 24th International Modal Analysis Conference, Orlando (2016)
12. Schwarz, J.B., Richardson, H.M.: Introduction to operating deflection shapes. In: CSI Reliability Week, Orlando (1999)

Chapter 21
Acoustic Fatigue and Dynamic Behavior of Composite Panels Under Acoustic Excitation

Canan Uz and Tamer T. Ata

Abstract Composite panels in aircraft structures are exposed to fluctuating sound pressure originating mostly from engine noise and air flow. In this paper, acoustic fatigue and dynamic response of composite panels under acoustic excitation are investigated numerically. Composite panel is simulated with finite element analysis. The panel is considered clamped at one edge, whereas the opposite edge is assumed to be free. The panel is subjected to random repeated loading generated by sound waves. The analysis estimates probabilistic amplitude frequency response to acoustic loading and natural frequencies of the panel. Maximum random vibration amplitude and the corresponding natural frequency are used for the fatigue life calculation. Critical element identification of the model regarding response is a major approach as part of this work performed to predict the element with maximum probabilistic response, i.e. root mean square strain. This allows fast and accurate result for the models with high number of elements by identifying root mean square strain at the most critical element on the panel without requiring the post-analysis for each element. At the end of this study, the results of finite element analysis and the effect of acoustic loading and critical element selection on fatigue life of the composite panels are presented.

Keywords Acoustic fatigue • Composite panel • Random vibration • Sound pressure level • Root mean square strain

21.1 Introduction

Usage of composite materials due to their high specific stiffness and strength has been increasing steadily in aerospace, automotive and other engineering applications where high stiffness, high strength, and low weight are required. Weight reduction is the greatest advantage of composite material especially in aerospace industry and is one of the key factors in decision regarding its selection. Other advantages include its high corrosion resistance and its resistance to damage from fatigue. These factors play a role in reducing operating costs of the aircraft in the long run, further improving its efficiency. Considering all these advantages, major and minor structural elements of recent commercial aircraft are made of composite materials rather than aluminum alloys such as in the ailerons [1]. Therefore, it is very important to analyze static and dynamic failure modes of the composite components in aircraft through numerical, analytical and statistical methods. Acoustic fatigue analysis that can be employed to composite parts is one of the considerations in order to prevent unexpected vibration failures and noise problems. Inspections and practices on aircrafts have shown that high frequency low amplitude pressure fluctuations combined with random acoustic excitation may lead to structural fatigue or severe damage which requires high maintenance costs of the composite components. Acoustic fatigue damages on aircrafts so far have been seen mainly in regions of jet flow, near jet fan blade tips, rear end of airbrakes, inside of pipes of fan engines. Wing skin panels are also in the path of jet air flux and can be treated as the most acoustically loaded parts due to their location close to the jet noise source [2].

In this paper, a wing box model is analyzed through finite element analysis in order to obtain the dynamic characteristics and response of the skin panels subjected to acoustic excitation. Box structure is a conventional design of an imaginary composite aileron consisting upper and lower skins, spars and ribs in aircrafts [3]. Engineering Sciences Data Unit (ESDU) Acoustic Fatigue Series documents are used as a reference guide explaining the main concepts and formulas for fatigue analysis of skin panels and box structures in aerospace industry [2]. Acoustic dynamic loading sources can be jet engine noise, aerodynamic flow, boundary layer fluctuating pressure where the skins outside surfaces are exposed. The dynamic

---

C. Uz (✉)
Department of Mechanical Engineering, Middle East Technical University, Ankara 06800, Turkey
e-mail: uzcanan@yahoo.com

T.T. Ata
Department of Aerospace Engineering, Middle East Technical University, Ankara 06800, Turkey

© The Society for Experimental Mechanics, Inc. 2016

J. De Clerck, D.S. Epp (eds.), *Rotating Machinery, Hybrid Test Methods, Vibro-Acoustics & Laser Vibrometry, Volume 8*,
Conference Proceedings of the Society for Experimental Mechanics Series, DOI 10.1007/978-3-319-30084-9_21

behavior of the skin panels excited by jet noise is investigated in the concept of this paper [4]. The excitation force in acoustic loading is randomly varying in time that leads to use of statistical methods while defining input and requesting output. Power spectral density function (PSDF) is used to define these random excitations. Static loading is distributed as unit pressure at lower surface of the panel and dynamic loading is applied as a function of frequency to introduce sound pressure for the interested frequency range. Statistical magnitude of the sound pressure loading is defined in the analysis to determine probabilistic system response in terms of strain [5]. The aim is to estimate natural frequencies and mode shapes by modal analysis, while root mean square (rms) and PSDF of micro strain of the model by random response analysis. However, for the fine meshed model (with high number of elements) the output file size can be too big to extract and select the highest rms micro strain. Hence, critical element selection is performed based on maximum strain which can be considered as pre-analysis. The highest rms micro strain on the selected critical element is then obtained as post-process. In order to verify the application of critical element identification random frequency response analysis for each element of the finite element model is performed. Results have shown that the highest rms micro strain is matched with the value at the selected critical element. This allows the acoustic analysis post-run for a set of selected elements instead of using all elements in the model that shortens run time and decrease the output text file size significantly. The outputs of the random analysis which are rms micro strain and PSDF of the response (strain) at the most sensitive element achieved rapidly can be used as input for the fatigue life calculation. The corresponding frequency used in life calculation is selected at which the PSDF of the strain has its maximum value.

21.2 Model

A simplified wing box structure with plate model for panels is constituted instead of complex finite element model. The model is tapered in chordwise direction to represent airfoil profile, while there is no incline angle in spanwise direction. This type of structure of more complex geometry can be seen in the control components of an aircraft i.e. aileron, wing, elevator, flap and rudder. The model which is shown in Fig. 21.1 with 2D elements can be represented as imaginary aileron of the wing which provides a flight control of rolling, rotation of the aircraft along X axis. The rolling mechanism of the aircraft is obtained by rotation of the aileron along Y axis. The simplified aileron model (Fig. 21.1) is used for the analysis of the dynamic behavior of the aerodynamic structure subjected to randomly varying noise.

Components of our imaginary aileron are upper and lower panels, ribs, front and rear spars, actuator fittings (AFs) and hinge fittings (HFs) as shown in Fig. 21.2 which is the exploded view. There are 1050 linear quadratic CQUAD4 shell elements, 909 Nodes, and 7 MPCs in the simplified aileron finite element model having a total mass of 70.5 kg. Mass properties of the components are defined to MSC NASTRAN in terms of mass density (mass/unit volume). In the background process of MSC NASTRAN solver, the mass density is multiplied by the element volume to determine the total mass of the element [6].

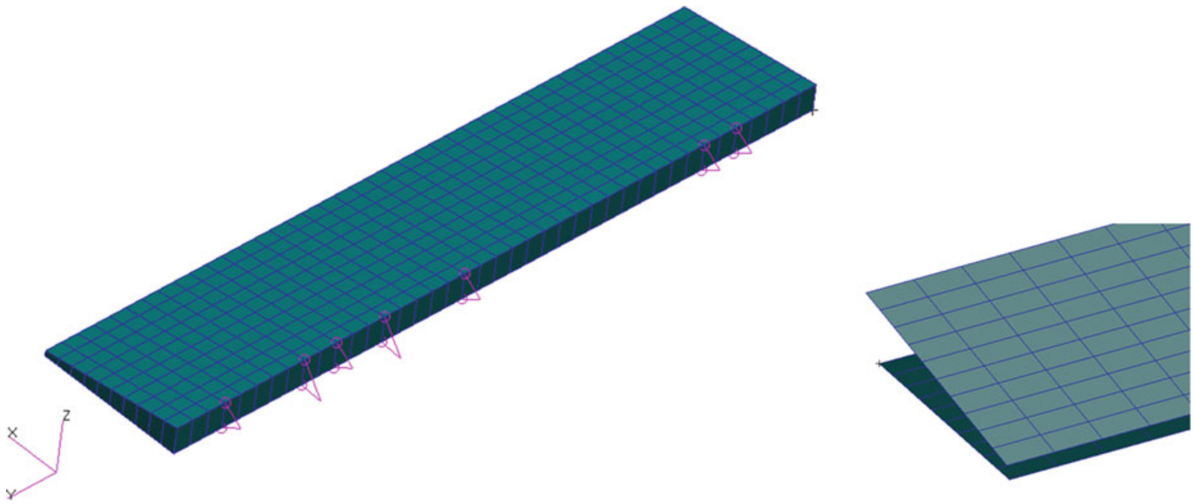

Fig. 21.1 General model of the tapered wing box

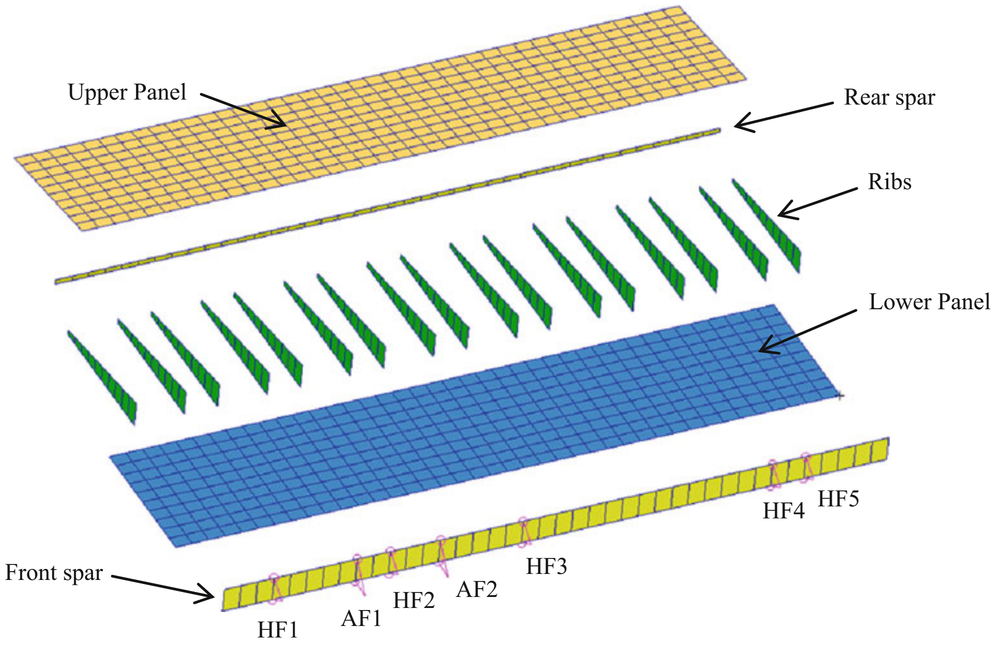

Fig. 21.2 Components of the imaginary aileron

Table 21.1 Material properties of T300/5208 carbon/epoxy unidirectional plies [7]

E_{11} (GPa)	E_{22} (GPa)	ν_{12}	G_{12} (GPa)	Density (kg/m^3)
180.0	10.0	0.28	7.0	1600

Table 21.2 Material properties of AS4/8552 fabric [8]

E_{11} (GPa)	E_{22} (GPa)	ν_{12}	G_{12} (GPa)	Density (kg/m^3)
62.0	62.0	0.05	4.2	1570

Table 21.3 Ply sequences of aileron components

Component	Ply sequence
Upper panel	(−45/45/0/90/45/−45/90/0/45/90/−45/45/−45/−45/90/45)s
Lower panel	(−45/45/0/90/45/−45/90/0/45/90/−45/45/−45/−45/90/45)s
Front spar	(±45/0/±45/0/±45)s
Rear spar	(±45/0/±45/0/±45)s
Ribs	(±45/0/±45/0/±45)s

The composite materials that have been used in the design of the imaginary aileron are T300/5208 carbon/epoxy unidirectional tape (UD) and AS4/8552 2×2 twill woven fabric. T300/5208 carbon/epoxy UD of which mechanical properties are given in Table 21.1 [7] are defined as the material for upper and lower skin panels since composite skins subjected to aerodynamic and acoustic loads directly. On the other hand, AS4/8552 2×2 twill woven fabric (see Table 21.2 [8]) is defined as the material for regions such as spars and ribs since they are not subjected to aerodynamic loads directly. Specifically, the upper and lower panels are 32 symmetric and balance ply laminate of T300/5208 carbon/epoxy UD which are laid up in stacking sequences as defined in Table 21.3, front and rear spars and ribs are 10-ply laminate of AS4/8552 2×2 twill woven fabric as also defined in Table 21.3.

The model is connected to the wing via hinge fittings which allow rotational degrees of freedom. The translational and/or rotational degrees of freedoms are constrained via the fitting locations and assigned in the model as MPCs (multipoint constraint set) which can be seen in Fig. 21.3. Clamped boundary condition is assumed at two locations where the aileron is deployed at two actuator fitting locations. On the other hand, FEM model is assumed hinged-hinged supported at five hinge fitting locations. Figure 21.3 illustrates the boundary conditions and simply-supported and fixed locations in the model.

- HF1, HF2, HF3, HF4, HF5 are constrained in translational degrees of freedom: UX, UY, UZ
- AF1 and AF2 are constrained in both translational and rotational degrees of freedom: UX, UY, UZ, RX, RY, RZ

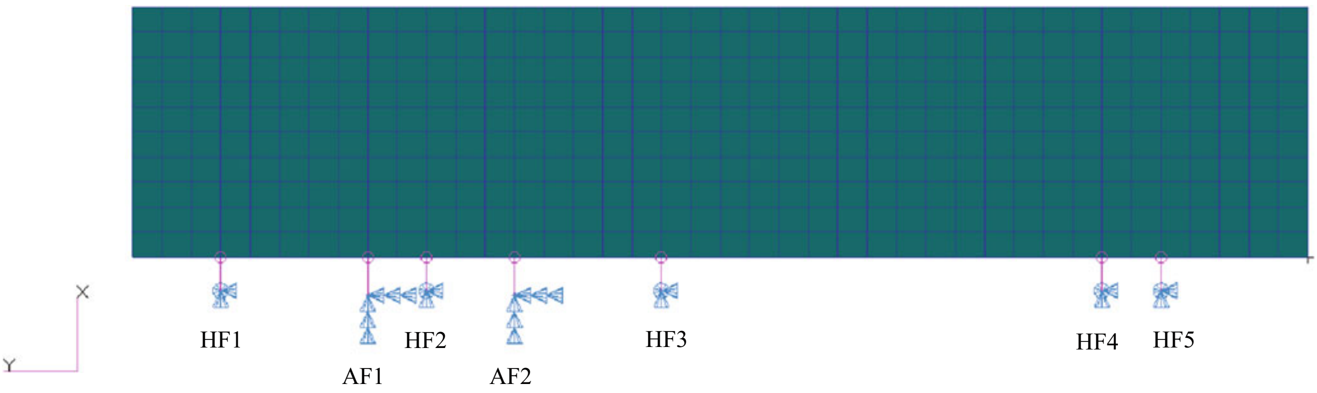

Fig. 21.3 Hinged and clamped boundary conditions at fitting locations

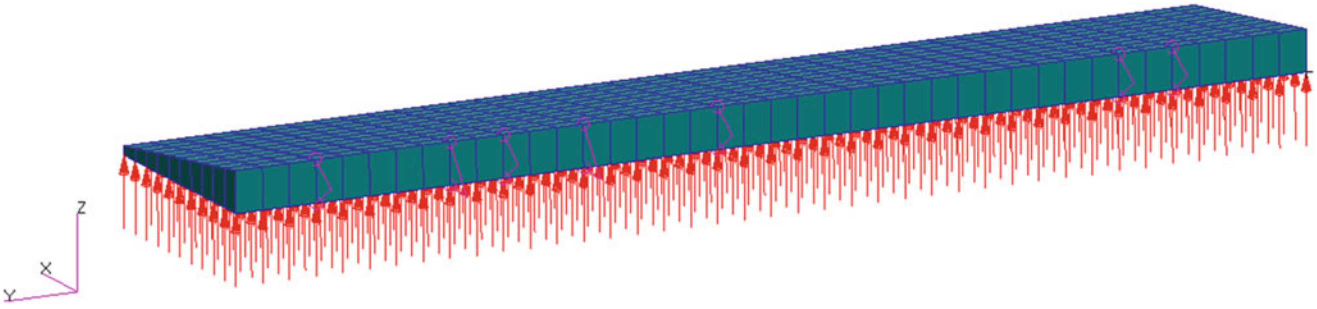

Fig. 21.4 Unit pressure loading on the lower panel surface

Acoustic fatigue analysis of a structure necessitates to determine all vibration modes, and of their natural frequencies for the interested frequency range and the dynamic random response of the structure. As a result, the fatigue life of the structure can be estimated in terms of rms strain or stress subjected to random acoustic excitation. Damping definition and the noise (pressure) field characteristics are the main input parameters for the finite element analysis [2]. Modal and random frequency response analyses have been performed using MSC NASTRAN and MSC PATRAN as pre/post processor.

As stated earlier ailerons provide a flight control of rolling during flight and therefore exposed to various loading types. Aerodynamic load is one of these loading types which strongly depends on angle of attack, flight altitude, ambient air temperature, and speed. These affiliated values actually correspond to operating conditions of the aircraft [3]. There are different flight missions of the subsonic jet aircraft such as take-off, landing, climb, and cruise. The pressure fluctuations are affected from different flight missions, the engine characteristics whether it is in full thrust or reverse thrust, engine position relative to the surface investigated under acoustic pressure. It has been stated in reference [2] that during take-off mission, when the engine is at full throttle and the forward speed is very low, the acoustic loading is generally at the most severe phase for the conventional design subsonic jets. While in the event of cruising, due to high forward speed and lower throttle adjustments the relative velocity of the jet exhaust is lower than the value during take-off condition. Because of this difference, the structure is exposed to less acoustic loading levels which results in reduced rms stress or strain [2]. Static loading is distributed is applied on the lower panel surface of the wing box as unit pressure shown in Fig. 21.4. Acoustic dynamic loading spectrum is assumed for take-off phase which can be expressed as sound pressure level over a frequency range. It is then defined in terms of power spectral density function to represent its statistical nature.

Random vibration fatigue test results under acoustic loading are available to obtain material properties, K_{rms} and b_{rms}, of T300/5208 composite specimen in reference [9] for acoustic fatigue which is high cycle fatigue life calculations. The curve fit is constructed in Fig. 21.5 which shows relationship between root mean square micro strain, ε_{rms}, and number of cycles to failure, N_f, where K_{rms} and b_{rms} can be calculated from expression for data points of straight line in Fig. 21.5 (X axis is logarithmic, while Y axis is linear) [10]:

$$N_f \times (\varepsilon_{rms})^{b_{rms}} = K_{rms}{}^{b_{rms}} \tag{21.1}$$

Therefore, material constants $K_{rms} = 8746$ and $b_{rms} = 8.47$ are obtained using curve fit in Fig. 21.5.

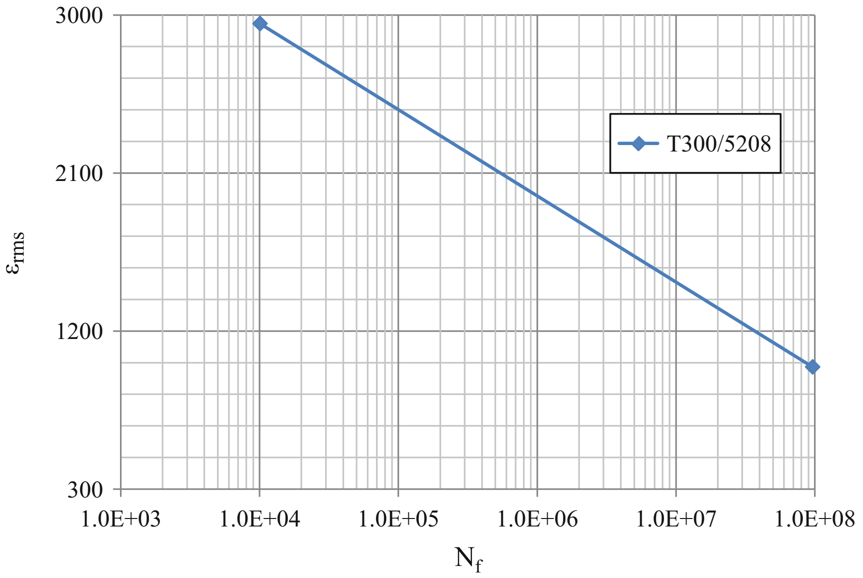

Fig. 21.5 Curve fitting of rms of micro-strain (*linear scale*) vs. number of cycles to failure (*log-scale*) for T300/5208 carbon/epoxy fiber-reinforced laminated plain specimen

Table 21.4 SPL spectrum for acoustic analysis

1/3 Octave band center frequency (Hz)	50	63	80	100	125	160	200	250	315	400	500	630	800	1000
SPL (dB)	135	136	137	137	136	135	135	134	133	131	130	129	127	126

Phase difference exists in terms of pressure at different locations on the panel surface subjected to random acoustic loading since the excitation force varies randomly. The sound pressure distribution is a description of averaging the phase difference over a period of time which makes pressure level a function of frequency. According to measurements of aircraft panels, surface pressure distribution coming from the jet noise generally shows gradual change with variable frequency. The panel exhibits in-phase relationship with sub-structures and pressures are presumed to be in-phase in the response estimation. This provides relatively small amplitude deflection of the ribs and/or spars [2]. Estimated sound pressure fluctuations due to jet noise are defined as sound pressure level (SPL) spectrum in one-third octave bands on the lower panel surface and the center frequencies of the bands as given in Table 21.4 [9, 11].

Sound pressure level can be defined as pressure spectrum level (PSL) in dB/Hz through a frequency range. The bandwidth correction is performed according to reference [12, 13]. PSL definition from SPL can be given as

$$PSL_{sub-total} = SPL_{sub-total} - 10 \times \log_{10}(\Delta f) \tag{21.2}$$

where the bandwidth is

$$\Delta f = 0.23156 \times f_c \tag{21.3}$$

with f_c is center frequency of 1/3 octave band interval.

Total PSL is the sum of any two levels 1 and 2 can be given as [14]

$$PSL_{total} = PSL_1 + 10 \times \log_{10}\left(1 + 10^{\left(\frac{PSL_2 - PSL_1}{10}\right)}\right) \tag{21.4}$$

Pressure in terms of rms can now be found as [13]

$$P_{rms} = 10^{\frac{PSL_{total}}{20} - 4.69897}\ \mathrm{Pa} \tag{21.5}$$

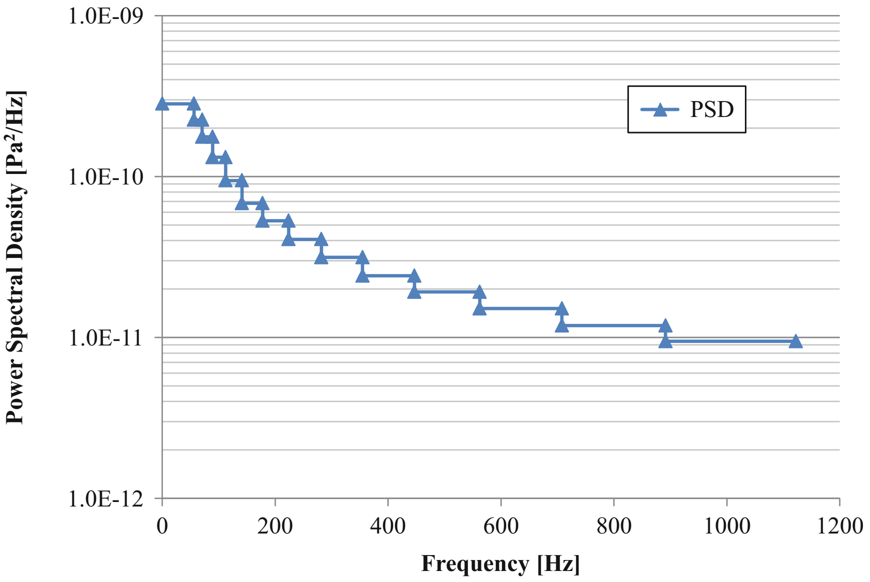

Fig. 21.6 Power spectral density [Pa^2/Hz] vs. frequency [Hz] of the imaginary aileron for the SPL spectrum (Table 21.4)

Power spectral density can be calculated using pressure in terms of rms and bandwidth as [13]

$$G_p(f) = \frac{{P_{rms}}^2}{\Delta f} \mathrm{Pa}^2/\mathrm{Hz} \tag{21.6}$$

Power spectral density which is a function of frequency can be found in Fig. 21.6.

Damping is the dissipation of energy that has the effect of reducing oscillations in a vibratory system. In defining the response of a structure to high intensity acoustic loading, damping is a considerable parameter. The amplitude of vibration response (related stresses and strains, etc.) can be reduced by increasing damping in the structure. Reference [15] presents some guidance on the range of values likely to be found on different types of aircraft structure. There are different theoretical damping models such as viscous, hysteretic and friction, differing in energy dissipation mechanism. In acoustic analysis, critical damping is set considering global damping in the structure. It is defined as 2 % modal damping based on the measurements of damping ratio for typical aircraft skin panels vibrating in their fundamental mode. The damping ratio range is given as 0.005 to 0.03 for skin panels [15].

It has been shown that the rms stress and strain response to broadband noise pressures is inversely proportional to the square root of the modal damping. Hence an increase in damping reduces the response to acoustic loading [2]. If increasing damping is needed according to analyses, damping treatments can be applied. Using viscoelastic damping materials is effective way of improving damping. Nevertheless, it is necessary to select a suitable material since its properties are highly dependent on frequency and temperature.

21.3 Modal Analysis

Natural frequencies and the related mode shapes and effective modal mass fractions are obtained by performing modal analysis using SOL 103 solver in MSC NASTRAN. The interested frequency range is 0–1000 Hz. Dominant modes are the first three modes according to the modal effective mass fraction list given in Table 21.5. It can be stated that the fundamental mode is the most effective mode of the imaginary aileron under acoustic loading. Since T3 is the excitation axis for the aileron the modal mass fraction is selected along T3. The cumulative modal effective mass throughout 0–1000 Hz frequency range is also extracted which represents 95 % of total mass for the imaginary aileron along T3 (see Table 21.5). Bold emphasized values represent % effective modal mass fraction greater than 5 %, whereas italic emphasized values represent cumulative % effective modal mass greater than 90 % in Table 21.5. (Figs. 21.7, 21.8, and 21.9)

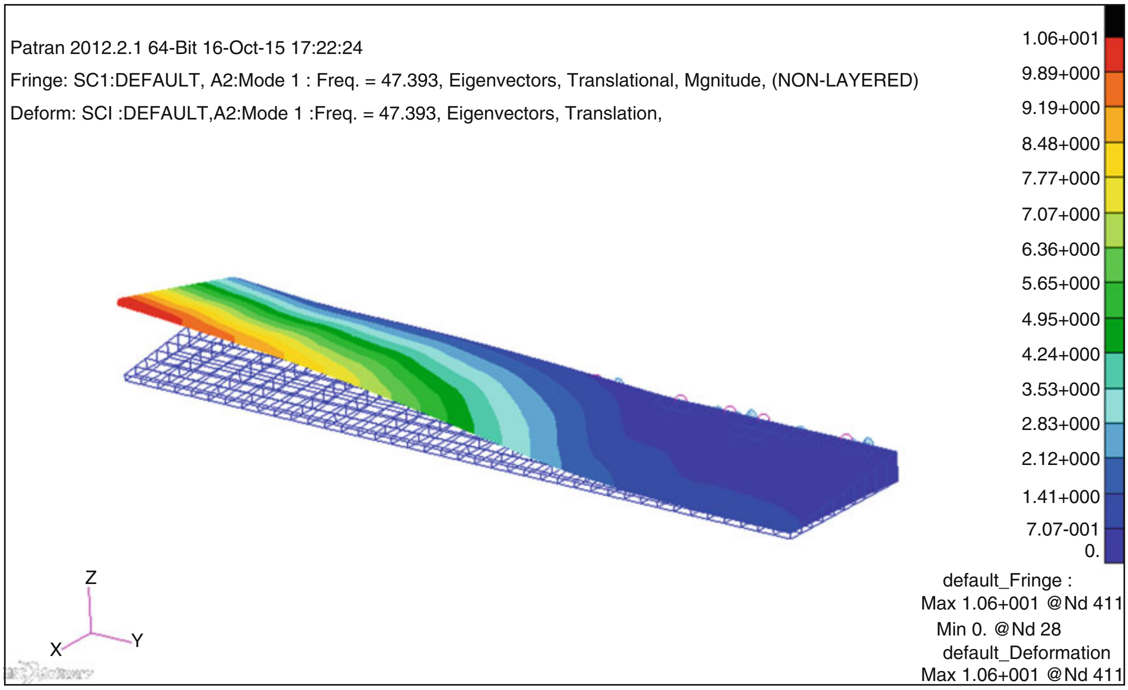
Patran 2012.2.1 64-Bit 16-Oct-15 17:22:24
Fringe: SC1:DEFAULT, A2:Mode 1 : Freq. = 47.393, Eigenvectors, Translational, Mgnitude, (NON-LAYERED)
Deform: SCI :DEFAULT,A2:Mode 1 :Freq. = 47.393, Eigenvectors, Translation,
1.06+001
9.89+000
9.19+000
8.48+000
7.77+000
7.07+000
6.36+000
5.65+000
4.95+000
4.24+000
3.53+000
2.83+000
2.12+000
1.41+000
7.07-001
0.
default_Fringe :
Max 1.06+001 @Nd 411
Min 0. @Nd 28
default_Deformation
Max 1.06+001 @Nd 411
Z
Y
X

Fig. 21.7 First mode of the imaginary aileron

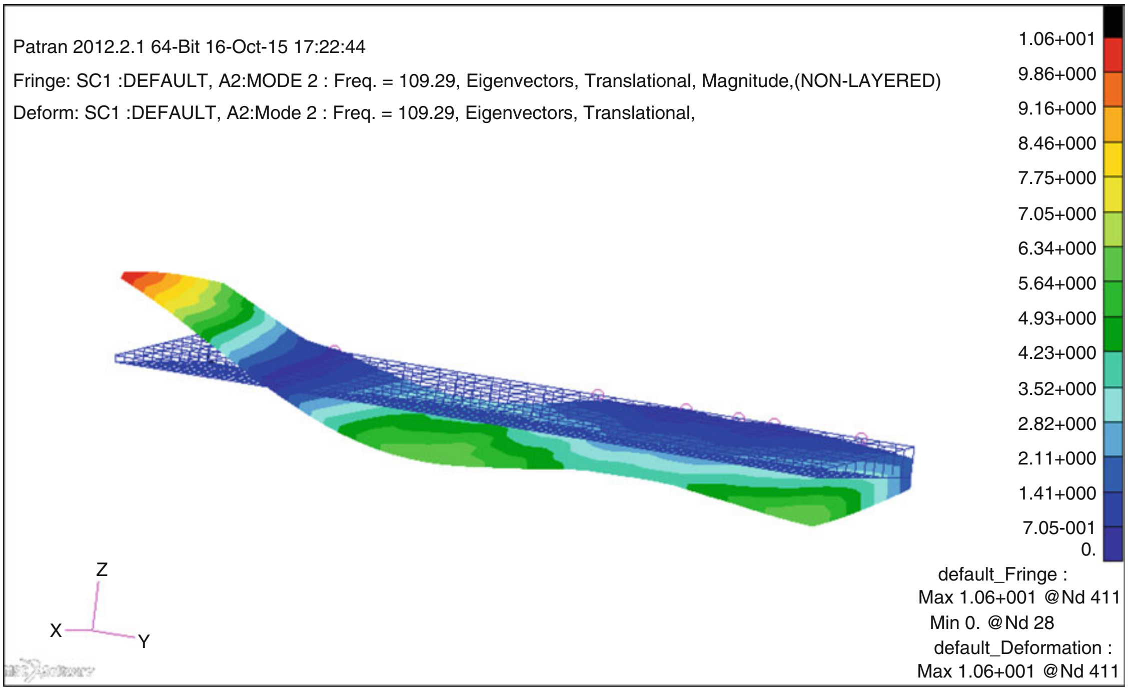
Patran 2012.2.1 64-Bit 16-Oct-15 17:22:44
Fringe: SC1 :DEFAULT, A2:MODE 2 : Freq. = 109.29, Eigenvectors, Translational, Magnitude,(NON-LAYERED)
Deform: SC1 :DEFAULT, A2:Mode 2 : Freq. = 109.29, Eigenvectors, Translational,
1.06+001
9.86+000
9.16+000
8.46+000
7.75+000
7.05+000
6.34+000
5.64+000
4.93+000
4.23+000
3.52+000
2.82+000
2.11+000
1.41+000
7.05-001
0.
default_Fringe :
Max 1.06+001 @Nd 411
Min 0. @Nd 28
default_Deformation :
Max 1.06+001 @Nd 411
Z
X
Y

Fig. 21.8 Second mode of the imaginary aileron

21.4 Random Response Analysis

Outputs of random response analysis are mainly cumulative rms and PSDF of the response. Random analysis tool in MSC Nastran is associated with frequency response analysis solver. The frequency response analysis serves a function of generating transfer function between PSDF of the response and PSDF of input loading [16]. Acoustic response is obtained

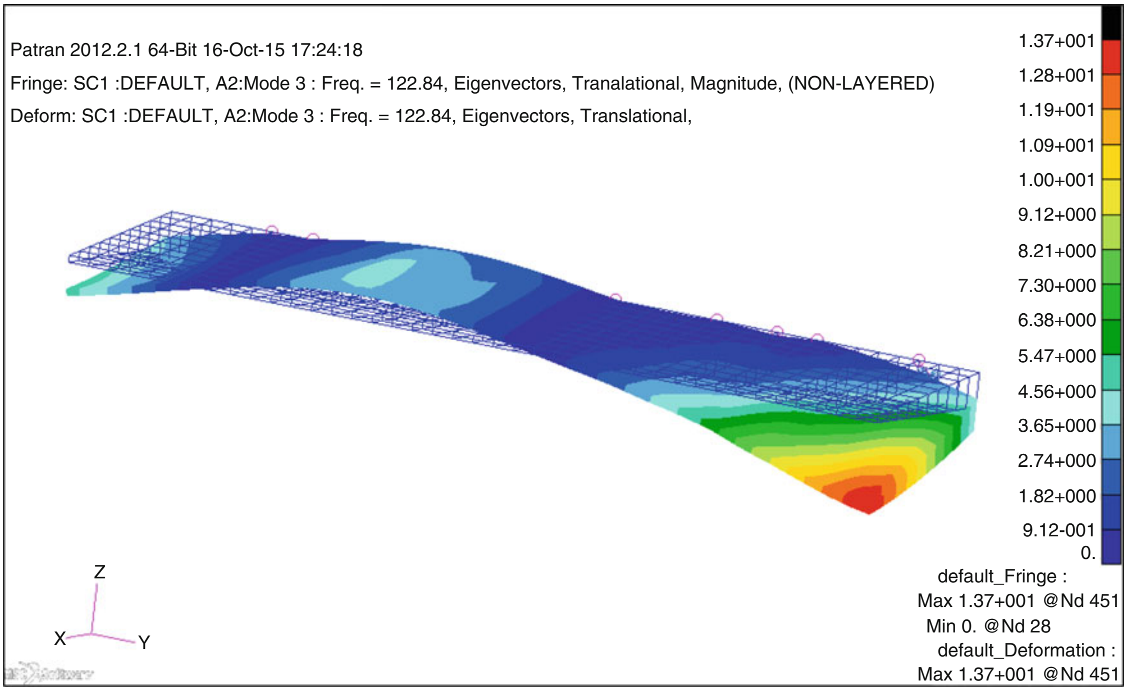
Patran 2012.2.1 64-Bit 16-Oct-15 17:24:18
Fringe: SC1 :DEFAULT, A2:Mode 3 : Freq. = 122.84, Eigenvectors, Tranalational, Magnitude, (NON-LAYERED)
Deform: SC1 :DEFAULT, A2:Mode 3 : Freq. = 122.84, Eigenvectors, Translational,
1.37+001
1.28+001
1.19+001
1.09+001
1.00+001
9.12+000
8.21+000
7.30+000
6.38+000
5.47+000
4.56+000
3.65+000
2.74+000
1.82+000
9.12-001
0.
Z
X
Y
default_Fringe :
Max 1.37+001 @Nd 451
Min 0. @Nd 28
default_Deformation :
Max 1.37+001 @Nd 451

Fig. 21.9 Third mode of the imaginary aileron

Table 21.5 Modal effective mass fraction for translational degrees of freedom for the associated mode

Mode	Natural Frequency	T1		T2		T3	
		FRACTION	SUM	FRACTION	SUM	FRACTION	SUM
1	47.4	0.2%	0.2%	0.0%	0.0%	**53.5%**	53.5%
2	109.3	0.1%	0.2%	0.0%	0.0%	**13.9%**	67.4%
3	122.8	0.0%	0.3%	0.0%	0.0%	**8.1%**	75.5%
4	181.8	0.0%	0.3%	0.0%	0.0%	1.4%	76.9%
5	219.6	0.0%	0.3%	0.0%	0.0%	0.0%	76.9%
…	…	…	…	…	…	…	…
29	341.7	0.0%	0.4%	0.0%	0.5%	0.0%	83.4%
…	…	…	…	…	…	…	…
150	796.6	0.0%	52.3%	0.0%	90.7%	0.0%	*93.6%*
…	…	…	…	…	…	…	…
180	887.5	0.0%	54.0%	0.0%	90.9%	0.0%	*94.3%*
…	…	…	…	…	…	…	…
221	998.0	0.0%	54.1%	0.0%	91.0%	0.0%	*94.9%*

in terms of strain for composite materials (along axis X, Y and shear XY), rather than stress which is used for fatigue life estimation of metallic components. The rms value of the strain response to random acoustic loading is then used for acoustic fatigue input to estimate number of cycles to failure [10]. Rms term is used to define energy level of the signal in vibration and acoustic systems under random excitation. Rms is calculated by averaging the squared magnitude of the signal, then taking the square root of the mean value. Rms value determination is applicable for the typical vibrational response levels i.e. accelerations, velocities, displacements, strains, or stresses. Specifically in this paper, for composite panels rms strain calculation is investigated as vibration response. Moreover, PSDF of the response is obtained since the statistical approach is applied while defining the load by means of spectral density. The relation can be constructed between PSDF and rms of the strain where the rms value is square root of the area under the PSDF of the strain vs. frequency plot.

The dominant mode of vibration of the imaginary aileron is obtained in its fundamental mode as mentioned in modal analysis section. Frequency response analysis is performed for all modes using SOL 111 solver of MSC NASTRAN and focused on the response at fundamental frequency (the frequency of the 1st mode) since the frequency at which the maximum value of power spectral density function response is reached at the lowest natural frequency of the imaginary aileron which is consistent with the results of the modal analysis. Principal rms strain which is not rms value of principal strain is computed for the whole frequency range. Principal direction flow of the strain depends on frequency and is different at each frequency. Thus, it is not convenient to determine rms of the maximum or minimum principal strain extracted from analysis. For each element at each frequency, principal rms strain is calculated using cumulative rms strain matrix given in Eq. (21.7).

$$\begin{bmatrix} \varepsilon_{x_{rms}} & \varepsilon_{xy_{rms}} \\ \varepsilon_{xy_{rms}} & \varepsilon_{y_{rms}} \end{bmatrix} \tag{21.7}$$

Principal rms strain formulation based on principal stress/strain calculation can be given as follows

$$\varepsilon_{principal\ rms\ strain} = \frac{\varepsilon_{x_{rms}} + \varepsilon_{y_{rms}}}{2} + \sqrt{\left(\frac{\varepsilon_{x_{rms}} - \varepsilon_{y_{rms}}}{2}\right)^2 + \left(\varepsilon_{xy_{rms}}\right)^2} \tag{21.8}$$

The aircraft is assumed to encounter turbulent gusts during take-off phase. Especially wings and control surfaces are exposed to these random gust loads. Hence, while plotting the results Von Mises strain tensor has been used considering random loading condition. Strain tensor as a result of pre-process solution using SOL 111 analysis is determined for each element in the model to pick up the possible high rms micro strain elements for both upper and lower panels. Exceed font database (.xdb) file is attached to MSC PATRAN and fringe results are plotted. For the large models MSC NASTRAN output (.f06) text file size will be too large to examine. Fringe range for strain tensor can be seen in Fig. 21.10 for lower panel and in Fig. 21.11 for upper panel. Critical elements identification is pick up according to the fringe label for each panel separately. These elements can be used for rms micro strain determination.

Critical element identification is performed based on maximum strain. A set of possible critical element IDs are imported to MSC NASTRAN runner (.dat) file and post analysis is employed only for those elements. Rms and PSDF strain values are requested for the selected elements. The highest rms micro strain is then determined among the selected elements as post-process and this is verified by analyzing rms of the micro strain for each element of the finite element model. This allows managing the small size output (.f06) file easily for random response investigation. It can be clearly seen from Table 21.6 that the maximum micro strain is obtained for element #27 which is consistent with the selection in Fig. 21.10. Therefore, critical element ID corresponds to lower panel element #27. It is expected to obtain in lower panel since the pressure is distributed on lower panel surface.

The micro strain, ε_{rms}, obtained for element #27 can be substituted into Eq. (21.1) to obtain number of cycles to failure of the imaginary aileron as follows

$$N_f = 8746^{8.47} \times (102.53)^{-8.47} = 2.27 \times 10^{16} \tag{21.9}$$

21.5 Conclusion

Aerodynamic flow, fluctuating pressure and engine noise are the main sources of acoustic dynamic loading. This type of loading may cause structural fatigue and noise problems. Acoustic fatigue analysis of aerospace structures is carried out with the aid of finite element method in order to verify that structural integrity of the component is not disrupted under cyclic acoustic loads. The number of the elements of the model is proportional to the size of the structure. Hence the model of the

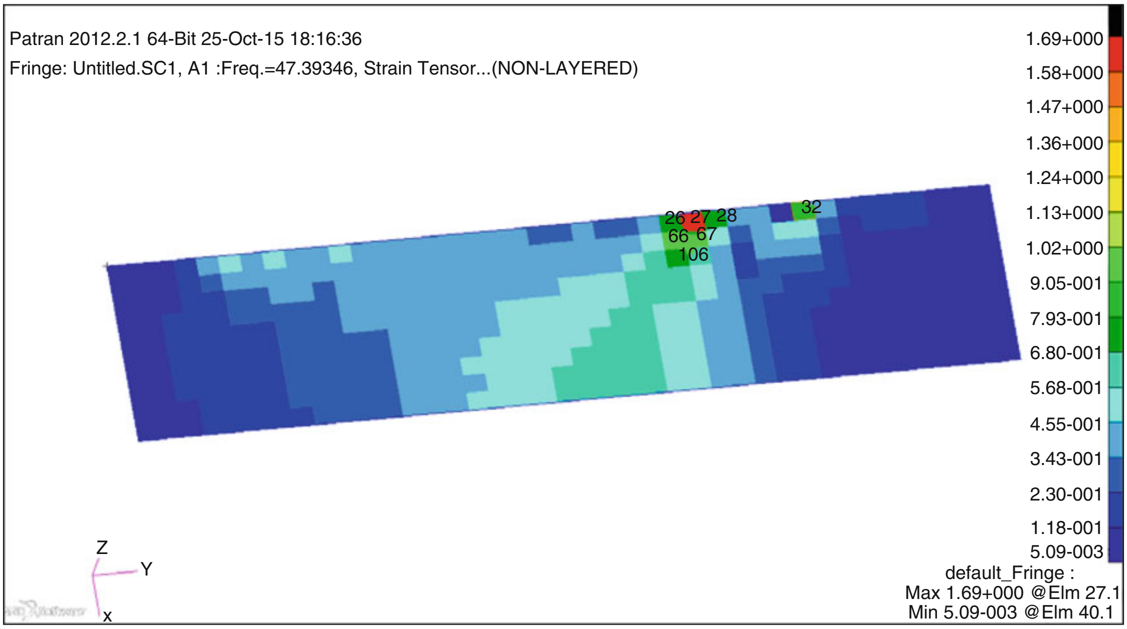

Fig. 21.10 Strain tensor and possible critical element marker for *lower panel*

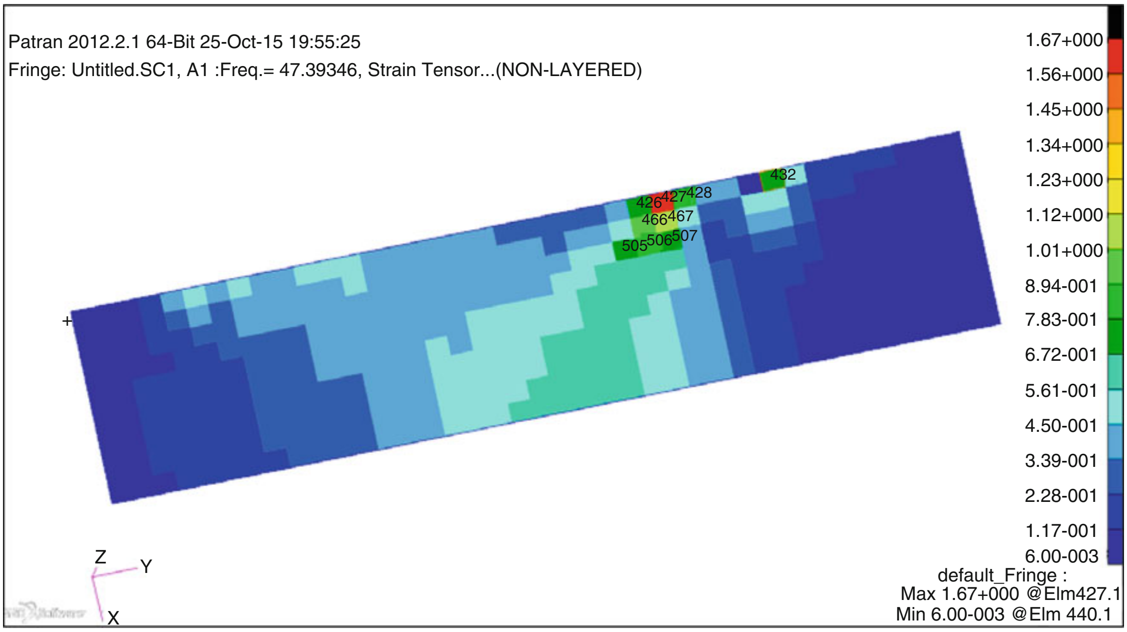

Fig. 21.11 Strain tensor and possible critical element marker for *upper panel*

structure such as wing or aileron consists of so many finite elements that take so much time to analyze all the structure under different type of loadings. Specially, aerostructures are exposed to so many different type of loadings considering operating conditions. The main purpose of the acoustic fatigue analysis is to determine critical part of the structure under defined various loads. In means of finite element model, the critical region of the structure corresponds to critical elements. In this paper, critical element identification of the model regarding response can be considered as pre-analysis performed to predict the element with maximum probabilistic response, i.e. root mean square strain. The highest rms micro strain on the selected critical element is then obtained as post-process. In order to verify the application of critical element identification, frequency response analysis for each element of the finite element model is performed. Results have shown that the highest rms micro

Table 21.6 Principal rms strain for the potential critical elements

Element ID	Cumulative rms strain/element coordinate system			Principal rms strain	Micro strain
	X	Y	XY		
27	3.2E-05	2.4E-05	7.4E-05	1.025E-04	102.53
427	2.6E-05	2.8E-05	7.4E-05	1.012E-04	101.24
467	2.5E-05	8.7E-06	3.8E-05	5.606E-05	56.06
466	4.3E-06	1.8E-05	4.3E-05	5.540E-05	55.40
66	2.0E-05	4.4E-06	4.2E-05	5.464E-05	54.64
67	3.4E-06	2.3E-05	3.8E-05	5.281E-05	52.81
32	1.4E-05	1.4E-05	3.6E-05	5.061E-05	50.61
432	1.5E-05	1.2E-05	3.5E-05	4.849E-05	48.49
106	6.6E-06	8.8E-06	3.5E-05	4.282E-05	42.82
506	9.6E-06	2.7E-06	3.6E-05	4.260E-05	42.60
428	2.9E-05	2.3E-06	1.9E-05	3.884E-05	38.84
505	3.9E-07	1.1E-05	3.0E-05	3.644E-05	36.44
26	2.2E-05	8.3E-06	1.6E-05	3.286E-05	32.86
28	5.0E-06	2.7E-05	1.1E-05	3.125E-05	31.25
426	9.6E-06	2.2E-05	1.4E-05	3.061E-05	30.61
507	1.8E-05	5.8E-06	2.3E-05	2.350E-05	23.50

strain is matched with the value at the selected critical element. This allows fast and accurate result for the models with high number of elements by identifying root mean square strain at the most critical element on the panel without requiring the post-analysis for each element. At the end of this study, the results of finite element analysis and the effect of acoustic loading and critical element selection on fatigue life of the composite panels are also presented.

References

1. Akbulut, M., Sonmez, F.O.: Design optimization of laminated composites using a new variant of simulated annealing. Comput. Struct. **89**, 1712–1713 (2011)
2. ESDU 74037: Introduction and Guide to ESDU Data on Acoustic Fatigue. IHS Global, ESDU International Plc, 27 Corsham Street, London, 1–3 (1989)
3. Niu, M.C.Y.: Airframe Stress Analysis and Sizing, vol. 36–38, 2nd edn, pp. 221–226. Hong Kong Conmilit Press, Hong Kong (1999)
4. ESDU 74025: Natural Frequencies of Box Structures, 2 (2011)
5. ESDU 06011: Spectral Methods for the Estimation of Fatigue Life, 4 (2013)
6. MSC NASTRAN Version 68: Basic Dynamic Analysis User's Guide
7. Bauchau, O.A., Craig, J.I.: Structural Analysis with Applications to Aerospace Structures, pp. 85–87, Science and Business Media, New York (2009)
8. Marlett, K.: Hexcel 8552S AS4 Plain Weave Fabric Prepreg 193 gsm & 38% RC Qualification Material Property Data report, National Institute for Aviation Research, Wichita State University, Report No: CAM-RP-20110-006 Revision N/C (2011)
9. ESDU 84027: Endurance of Fiber-Reinforced Composite, Laminated Structural Elements Subjected to Simulated Random Acoustic Loading, 16 (2014)
10. ESDU 06009: Fatigue Damage and Life Under Random Loading, pp. 8–10. IHS Engineering Products Inc, London (2012)
11. ESDU 99009: An Introduction to Statistical Energy Analysis, 16 (1999)
12. ESDU 66016: Bandwidth Correction, 1 (1966)
13. Harris, C.M.: Handbook of Noise Control. McGraw-Hill, New York (1957)
14. ESDU 66017: Combination of Levels in dB, 1 (1978)
15. ESDU 73011: Damping in Acoustically Excited Structures, 1 (1974)
16. MSC NASTRAN Dynamic Analysis User's Guide, Random Analysis with Coupled Excitations

Chapter 22
Evaluation of Microphone Density for Finite Element Source Inversion Simulation of a Laboratory Acoustic Test

Ryan Schultz and Tim Walsh

Abstract Simulation of the response of a system to an acoustic environment is desirable in the assessment of aerospace structures in flight-like environments. In simulating a laboratory acoustic test a large challenge is modeling the as-tested acoustic field. Acoustic source inversion capabilities in Sandia's Sierra/SD structural dynamics code have allowed for the determination of an acoustic field based on measured microphone responses—given measured pressures, source inversion optimization algorithms determine the input parameters of a set of acoustic sources defined in an acoustic finite element model. Inherently, the resulting acoustic field is dependent on the target microphone data. If there are insufficient target points, then the as-tested field may not be recreated properly. Here, the question of number of microphones is studied using synthetic data, that is, target data taken from a previous simulation which allows for comparison of the full pressure field—an important benefit not available with test data. By exploring a range of target points distributed throughout the domain, a rate of convergence to the true field can be observed. Results will be compared with the goal of developing guidelines for the number of sensors required to aid in the design of future laboratory acoustic tests to be used for model assessment.

Keywords Acoustics • Direct field acoustic test • Source inversion • Acoustic finite element • Modal assurance criterion

Nomenclature

DFAT	Direct Field Acoustic Test
FE	Finite Element
MAC	Modal Assurance Criterion
PSD	Power Spectral Density
ROL	Rapid Optimization Library
SPL	Sound Pressure Level, ref. 20 μPa

22.1 Introduction

System structural response in acoustic environments is important to understand for a variety of aerospace structures because these can be significant environments. Therefore, modeling system response to acoustic environments is required, as well as an assessment of model performance to capture the response to that distributed pressure-type loading. When performing model calibration, validation or assessment simulations against some laboratory test data, understanding the loading is critical. Traditionally, a structural dynamics finite element (FE) model will be calibrated using modal test data. In that

---

Sandia National Laboratories is a multi-program laboratory managed and operated by Sandia Corporation, a wholly owned subsidiary of Lockheed Martin Corporation, for the U.S. Department of Energy National Nuclear Security Administration under Contract DE-AC04-94AL85000.

R. Schultz (✉)
Analytical Structural Dynamics Department, Sandia National Laboratories, Albuquerque, NM 87185, USA
e-mail: rschult@sandia.gov

T. Walsh
Computational Solid Mechanics and Structural Dynamics Department, Sandia National Laboratories, P.O. Box 5800 – MS0840, Albuquerque, NM 87185, USA

© The Society for Experimental Mechanics, Inc. 2016

J. De Clerck, D.S. Epp (eds.), *Rotating Machinery, Hybrid Test Methods, Vibro-Acoustics & Laser Vibrometry, Volume 8*,
Conference Proceedings of the Society for Experimental Mechanics Series, DOI 10.1007/978-3-319-30084-9_22

case, system response is due to well-measured force inputs at a few discrete points. Similarly for validation, the structural dynamics FE model response predictions will be compared to some measured response from a test, for example a single-axis shaker test. Here again the loading can be well characterized using accelerometers or force gages. Now, when making model assessments for responses to acoustic loading, the issue of defining loads to the finite element model becomes much more difficult. In contrast to a shaker input, an acoustic input is distributed all over the wetted surface of the system, has non-uniform magnitude and phase, and the pressure loading can be coupled to the response of the system. Additionally, measuring the acoustic loads over the entire wetted surface is likely not possible. Therefore, some method for determining the wetted surface acoustic pressure using microphones away from the test item is needed.

Recently, a methodology has been developed to use an acoustic finite element model to determine wetted surface pressures using test-measured microphone data. This method leverages the source inversion optimization solution capability in the finite element code Sierra/SD. This source inversion capability leverages optimization routines from the Rapid Optimization Library (ROL) [1] to determine a set of acoustic sources on the acoustic finite element model that match a user-provided set of target pressure data—for example, microphone data from a test. This target pressure data is assigned at nodes in the FE model called target nodes. When modeling a test, the analyst would locate target nodes at test microphone locations. As the acoustic sources determined by this optimization routine rely on the provided pressure target data, the resulting acoustic field and therefore the wetted surface pressure loading on the structure, is heavily reliant on the provided target pressure data. Understanding the effect of the number of microphones, or more generally, number of nodal pressure points distributed throughout the acoustic domain, required to constrain the wetted surface pressure for this source inversion methodology is the focus of this paper. To study the effects of the number of target nodes on the resulting field, the source inversion simulations will be run for a wide range of target node counts over a wide frequency range for an acoustic FE model of a direct field acoustic test (DFAT). By using synthetic data, rather than test data, for the target pressures, this study can explore the effects on the full acoustic field. Understanding the number of target nodes required has impacts in terms of performing acoustic source inversion simulations using Sierra/SD as well as for defining the instrumentation of future acoustic tests to be used for structural dynamics model assessment.

22.2 Description of the Direct Field Acoustic Test

The FE model studied here represents the acoustic portion of a direct field acoustic test performed at Sandia. In this test, an aerospace structure was connected to a rack and hung from a crane inside a stack of loudspeakers. Several microphones were located around the test article to measure the acoustic field and also serve as control points for the MIMO control system. Figure 22.1 shows the test setup.

22.3 Model of a Flight System DFAT Test

The acoustic finite element model used here was created to model the laboratory DFAT of a flight system surrounded by a stack of loudspeakers as shown in Fig. 22.1. The model includes an acoustic domain with a void in the center to represent the flight system and a void for the rack that connects the flight system to the crane.

For this study, a purely acoustic model was used as coupling with the intended structure was assumed to be small. Rather than try to model an acoustic domain representative of a physical acoustic domain from a test—including all the various materials, and range of boundary conditions, a subdomain approach was employed instead. This subdomain is an ellipsoidal volume surrounding the flight system with the exterior surface discretized using a large number of patches, Fig. 22.2. This subdomain is approximately 2.5 times less volume than the volume of the test's volume—a large computational cost savings. Covering the outer surface in candidate sources allows for great flexibility in the type of field that can be generated by this model. However, the number of patches is user-specified and inherently impacts the type of field that can be created by the model and also the sources have a fixed direction, governed by the surface normal. Quantifying the effects of these model limitations is the focus of separate work. Boundary conditions for this model are straightforward: on the exterior surface there is an absorptive condition and on the wetted surface a reflective condition. Figure 22.3 below shows the results of a transient simulation to demonstrate the boundary conditions behave as expected. The pressure increases as the wave front hits the reflective surface at the structure's void in Fig. 22.3a. Then, in Fig. 22.3b, the absorbing boundary condition on the outer surface appears to be working properly as the wave front is undistorted as it propagates along the outer boundary.

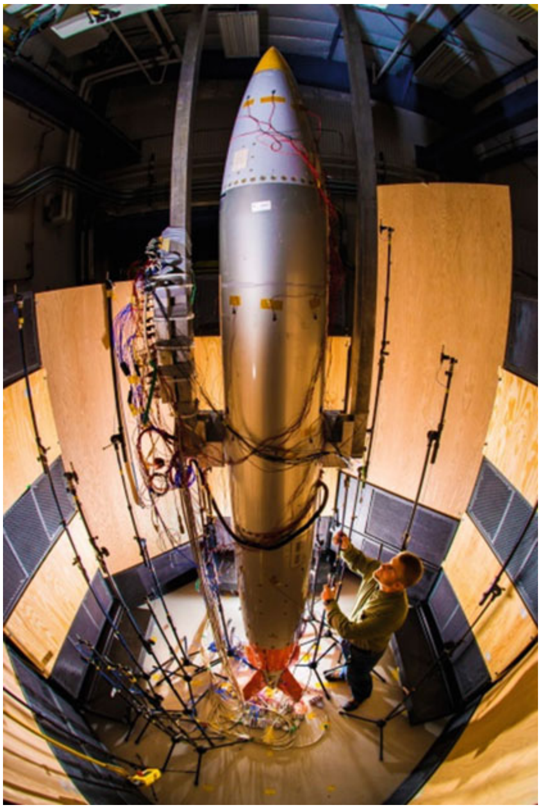

Fig. 22.1 Photo of the DFAT test setup being modeled

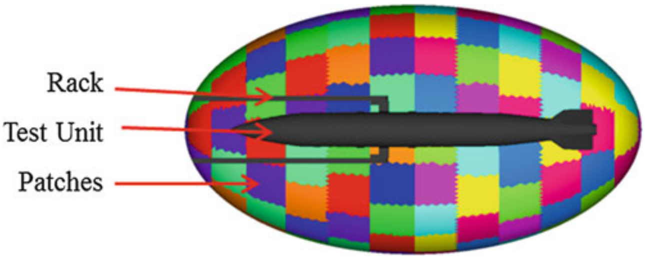

Fig. 22.2 Ellipsoidal acoustic FE model, including a void to represent the aerospace structure of interest attached to a rack and suspension system as used in a DFAT test, and multiple source patches on the outer surface of the domain

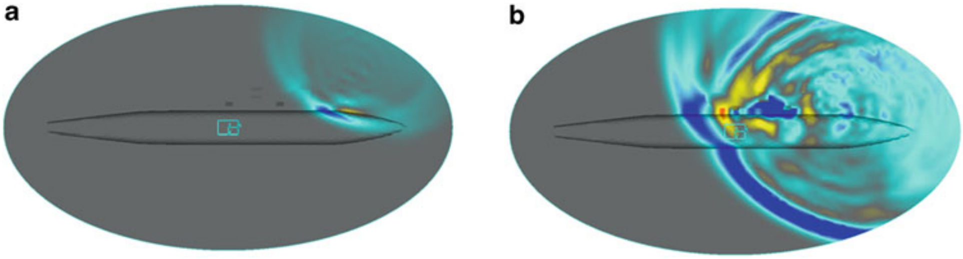

Fig. 22.3 Visualization an acoustic pressure wave propagating across the ellipsoidal acoustic domain in a transient simulation to demonstrate boundary conditions. (**a**) Reflective condition at the structure's void. (**b**) Absorbing condition working properly, indicated by no wave front distortion at the boundary

This ellipsoidal model is meshed with linear tetrahedral elements with a nominal size of 0.02032 m. With a maximum frequency of 2000 Hz, the minimum wavelength is 0.172 m and so the mesh has at a minimum 8.4 elements per wavelength. There are 14.8 million elements and 2.5 million nodes (and therefore degrees of freedom) in this model. It is run using the parallel capability of Sierra/SD on 128 processors.

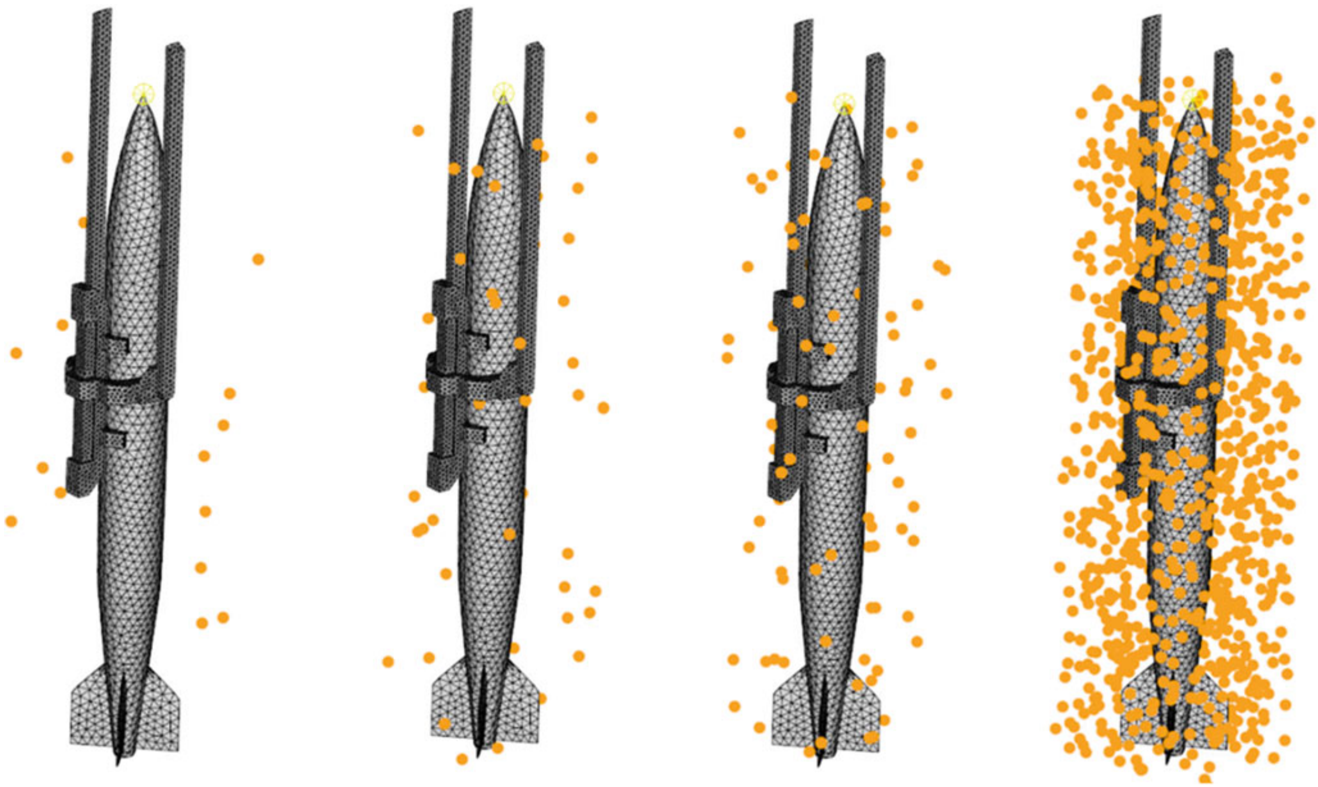

Fig. 22.4 Location of target nodes in set with 18, 50, 100, and 1000 nodes (from *left* to *right*)

For making comparisons of the effects of number of target points on the acoustic field, the wetted surface (the acoustic-structural interface) is of primary interest as these are the pressures that would load the structure. Several node sets were located both on the wetted surface and throughout the acoustic domain to provide data for comparison of the fields resulting from the various simulations.

In this study, the number of nodes in the target set is varied from 18 to 1000. This range includes target node (microphone) counts that are realizable in a DFAT test, as well as very large counts to allow for convergence to be observed. It may be possible to achieve a large microphone count in a real test by employing a roving microphone technique wherein microphones are repositioned between nominally similar runs. Nodes in the target set are chosen by first subdividing a candidate volume (approximately a cylinder of radius 24 inches in the center of the domain) into N bins by cutting axially, radially and circumferentially. Then, a single node within each bin is chosen at random and added to the target set. Nodes on the wetted surface are not allowed as it is generally assumed that surface microphones will be more challenging to employ in a test. Each target set has nodes chosen at random so nodes are not necessarily common among sets. This method allows for some control over the spatial distribution of target nodes as compared to randomly choosing N nodes within the candidate volume. Figure 22.4 shows the target points for several cases.

To generate the target data used for the inverse portion of this study, an initial forward simulation was performed. For this direct frequency response simulation, loading for the patches on the exterior of the ellipsoid were taken from a prior simulation and applied for frequencies ranging from 40 to 2000 Hz in 40 Hz steps. Nodal pressure data, in the form of acoustic pressure linear spectra, was then saved from the output files not only at the target node points, but also at several other points on the wetted surface and throughout the field to serve as comparison data with results of the various inverse simulations.

22.4 Acoustic Source Inversion in Sierra/SD

The objective of this simulation process is to generate an acoustic field that matches the pressure at the target nodes. For example, if this simulation were run to replicate a real direct field acoustic test, the target data would be the microphone pressures measured in the test, and the acoustic source inversion optimization would be used to determine the finite element

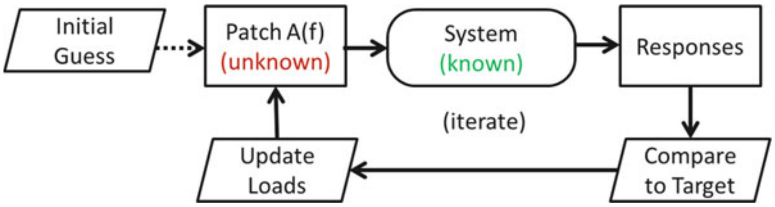

Fig. 22.5 Graphical depiction of the acoustic source inversion optimization process

loading that generates a field that matches the as-tested acoustic field at the microphone locations. An obvious question is: why not just use the loudspeaker cone velocities as inputs to the finite element model? First, this would be challenging to measure in-test, and second, this would require modeling the entire acoustic domain of the actual test setup—including not only geometry but also surface impedance boundary conditions, etc.

The Sierra/SD finite element code has options to run this acoustic source inversion in either the time or frequency domain [2]. For most problems, quantities of interest are power spectral densities (PSDs), and therefore this problem was run in the frequency domain with a direct frequency response solution. The loads are acoustic acceleration linear spectra and the outputs are acoustic pressure linear spectra, each with real and imaginary parts at discrete frequency lines.

This acoustic source inversion optimization process changes the model's acoustic loads to minimize an objective function. In this case, the objective function is a difference between the pressure linear spectra at the target nodes [3]. The optimization process is shown graphically below in Fig. 22.5. This process provides solutions that satisfy the wave equation.

This optimization problem begins with a user-specified initial guess for the acoustic acceleration linear spectra for each of the available sources. In this case, as the sources are not physically representative of the loudspeakers and also because the simulation is performed in the frequency domain and therefore the loads have both real and imaginary components, supplying an informed initial guess is very difficult. Instead, an initial guess of zero is supplied for all sources. A pair of forward solves are performed using these zero loads and the resulting response at the target nodes and the gradient are obtained. Next, the Newton-based optimization routine from ROL, connected to Sierra/SD, perturbs the sources based on the objective function value and the gradient. Then, another solve is performed, and the new nodal pressures are compared with the target data. For the specific problem described in this work, the target data are the pressure spectra extracted from an initial simulation run (synthetic data). This process continues until the objective function and change in the gradient is sufficient to be considered converged by the user.

22.5 Target Node Study Description

The objective of this study is to demonstrate how the acoustic field resulting from a source inversion simulation is affected by the number of target nodes used as target data. One would suppose that for a simple acoustic field; say a small number of plane waves at a single frequency, that a smaller number of target nodes would be required for the source inversion simulation to completely replicate the original acoustic field. Similarly, one would suppose that more target nodes would be required for the inverse simulation to replicate a more complicated field—say one created with a large number or sources or boundaries. This study aims to address both the total count and the target node density in the context of a realistic setup of an aerospace structure in an acoustic field from a DFAT field.

For each set of target nodes, direct frequency response inverse simulations were performed from 40 to 2000 Hz in 40 Hz steps. Each simulation was run for several iterations to achieve sufficient change in the norm of the gradient and objective function value. That said, the optimization for some Target sets did not work as well as others—the change in gradient value was not as large for similar iteration counts. For these sets, further optimization iterations were used, however the change in gradient was still not as large as perhaps desirable. After the source inversion optimization simulations were completed for each Target set, the determined loads for each were applied and then comparisons of the resulting fields were made.

22.6 Results

In this case, the wetted surface pressure was important as was the field surrounding the wetted surface. Resulting pressure data at sensing node sets located on the wetted surface were compared several ways with the goal of identifying and quantifying differences in the field shape, amplitude and the dependency of those differences on frequency and density of target points. One might expect the solutions to converge with increasing number of target points and that convergence point should be dependent on the volume density (number of target points per domain size) or perhaps on normalized frequency which we refer to as wavelength density (number of target points per cubic wavelength). Additionally, it was of interest to assess the similarity of the pressure shapes on the wetted surface as this is important in loading the structure. As such, a modal assurance criteria (MAC) calculation was performed on the truth field at all nodes on the wetted surface compared with each generated field [4]. This provides a scalar valued measure for the similarity of the wetted surface pressure field shape for each case with respect to frequency. In modal analysis, decades of experience have provided some guidelines for acceptable MAC values when comparing structural mode shapes. In this case, however, while the calculation is the same, those rules of thumb may not translate and the MAC applied to this type of problem has not been studied sufficiently to develop similar guidelines. Instead, the MAC results should serve only to observe convergence of the spatial distribution of pressure.

22.6.1 Comparison of Target Node Pressure

To assess how well the source inversion optimization achieved the goal of determining acoustic accelerations that generate a field which matches the pressures at the target node locations, the target node pressure spectra from the inverse simulations are compared with the provided target pressure data from the initial truth run. Figure 22.6 shows the pressure magnitude and phase as a function of frequency for the 18 target node case. Figure 22.7 shows the same pressures for the 250 target node case. Just a single node in the target set is shown, but the results are similar for the other nodes in the set. Other target node runs exhibit similar behavior—the fields generated by the inverse simulations match the target data nearly exactly, even for the low-target count cases.

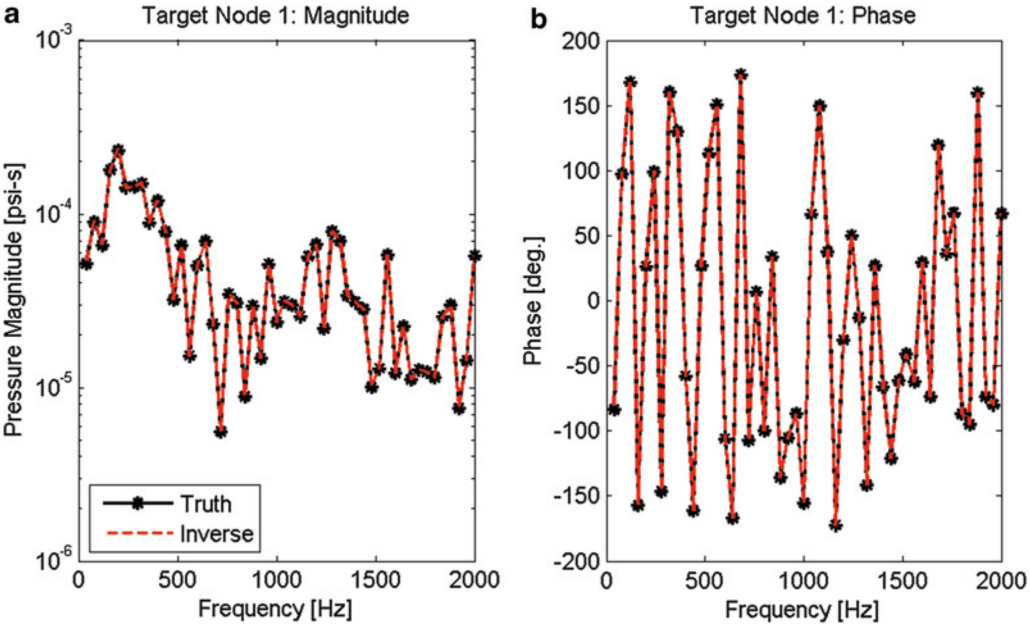

Fig. 22.6 Comparison of the truth (target) pressure data with the pressures at two target nodes from the inverse simulation for the 18 target node case. (**a**) Magnitude comparison for Node 1 in the target set. (**b**) Phase

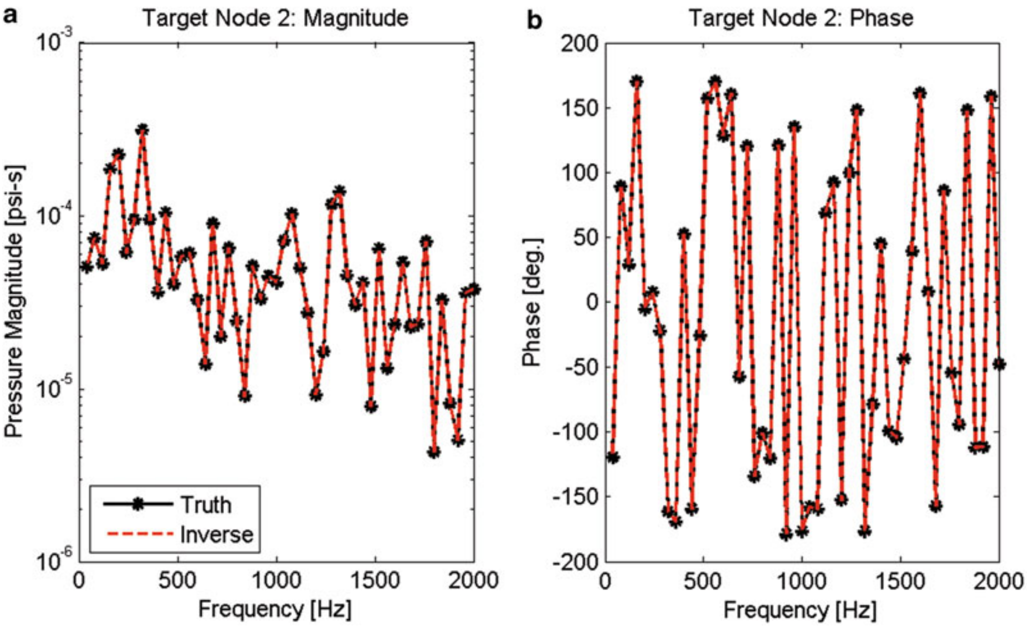

Fig. 22.7 Comparison of the truth (target) pressure data with the pressures at two target nodes from the inverse simulation for the 250 target node case. (**a**) Magnitude comparison for Node 2 in the target set. (**b**) Phase

22.6.2 Comparing Mean Sound Pressure Level

To assess the overall level of the pressure loading on the structure for the various target sets, two metrics are used. To assess the differences on a node-by-node basis, the sound pressure level (SPL) at single nodes on the wetted surface are averaged over frequency and then compared over all the target sets. The second metric uses a mean over all nodes in the wetted surface of the calculated sound pressure level. This provides an estimate of the change in level with respect to frequency. Sound pressure level is calculated from the pressure linear spectra by [5]:

$$SPL = 10\log_{10}\left(d_f^2 \left|X_p\right|^2 / p_{ref}^2\right), \tag{22.1}$$

where d_f is the frequency resolution, $|X_p|$ is the magnitude of the pressure linear spectrum, and p_{ref} is the reference pressure, 20 μPa.

Taking the mean over the nodes or frequencies yields the same takeaway: the low target node count cases provide a lower level acoustic field over all frequencies at all non-target points. As more nodes are added to the target set the levels increase toward the truth field levels, as indicated in Fig. 22.8.

22.6.3 Comparing Mean Percent Difference in the Real and Imaginary Parts of Pressure

To assess how well the pressure field is replicated at the wetted surface the percent difference in the real and imaginary parts of the acoustic pressure linear spectra are calculated. Because there are both real and imaginary parts for each node at each frequency, this percent difference data is averaged. First, the real and imaginary parts' percent differences are averaged. Then, the data is averaged over nodes in the wetted surface, or averaged over the frequency range.

The percent difference averaged over frequency results indicate that the 250 and 1000 target node cases have significantly lower error than the lower target node cases, as indicated by Fig. 22.9. In fact, the 1000 target node case could be considered an exact replica of the original truth field. The percent difference results averaged over all the nodes on the wetted surface indicate some frequency dependency for the lower target node cases—an expected trend. Interestingly, the 250 and 1000 target node cases do not exhibit much change in the percent difference with frequency.

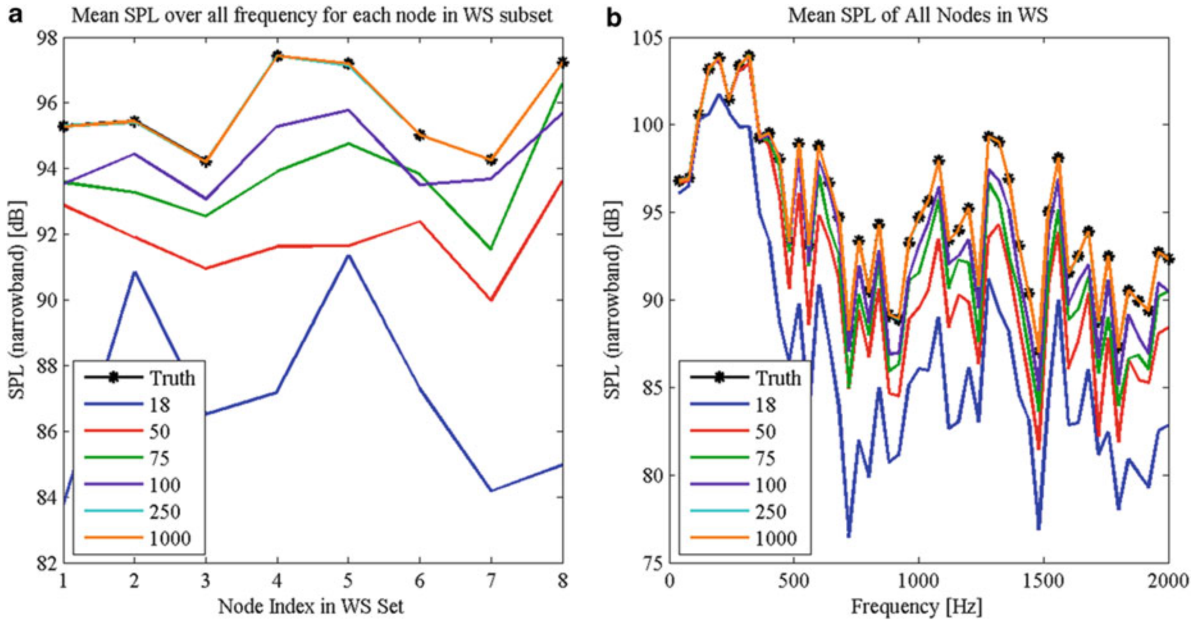

Fig. 22.8 (**a**) Mean SPL, averaged over frequency, for nodes on the wetted surface for simulations using target node sets of 18 to 1000. (**b**) Mean SPL of a subset of nodes on the wetted surface for simulations using target node sets of 18 to 1000

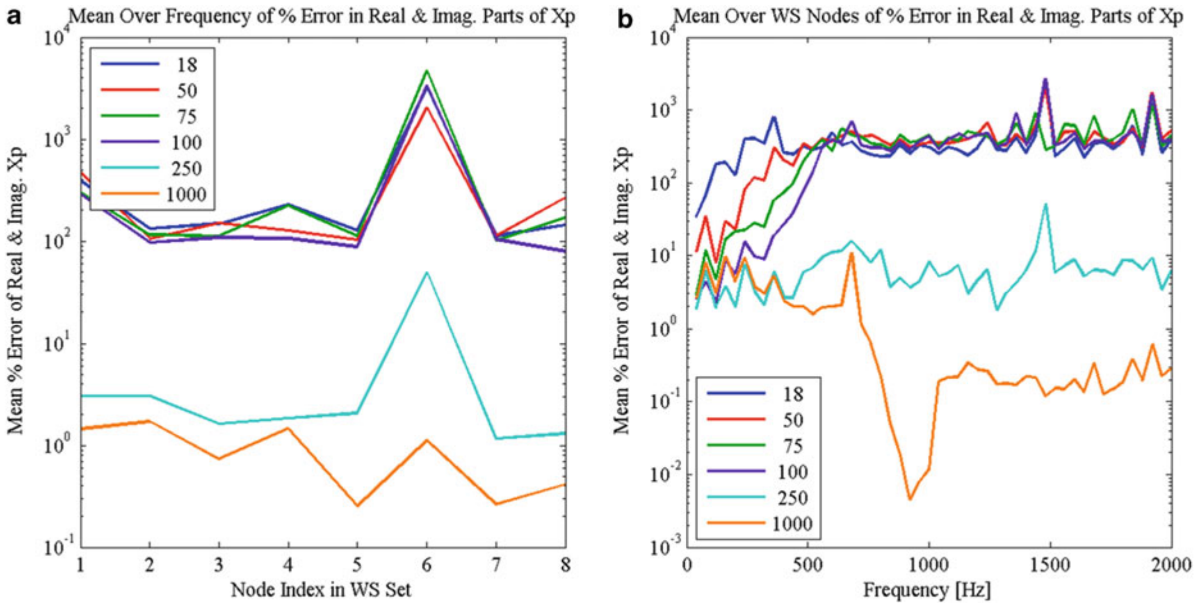

Fig. 22.9 (**a**) Mean percent difference from the truth simulation of frequency-averaged real and imaginary parts of pressure. (**b**) Mean percent difference from the truth simulation of node-averaged real and imaginary parts of pressure

22.6.4 *Comparing MAC of the Pressure Shape on the Wetted Surface*

A MAC allows comparison of the shapes represented by two vectors. Here, the shape of interest is the pressure spectrum on the wetted surface. The baseline shape vector is the pressure field from the original forward run, here called the truth data. The comparison vectors are the pressure fields from the various target set runs. MACs are computed using pressure shapes based on the magnitude, the phase, real and imaginary parts to see if the results depend on the chosen representation. In each case, the pressure MAC diagonal values are plotted against frequency.

It can be seen in Fig. 22.10 that there is frequency dependence to the various comparison metrics presented. Generally, at lower frequencies the agreement to the truth field is good even for low target node counts. As frequency increases, however,

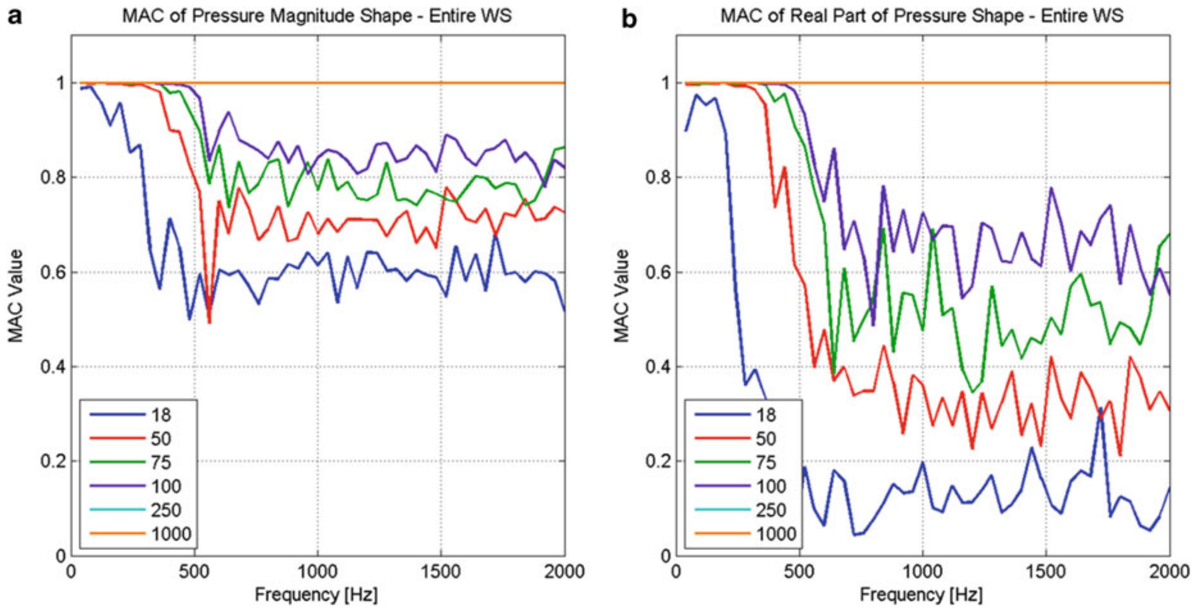

Fig. 22.10 (**a**) MAC of the pressure magnitude shape for the various target node sets, as a function of frequency. (**b**) MAC of the real part of pressure shape

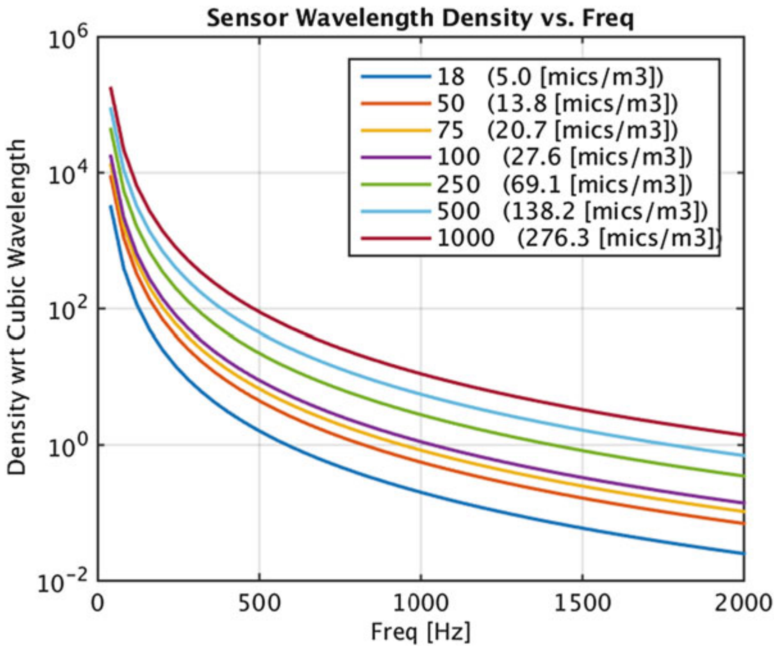

Fig. 22.11 Sensor wavelength density as a function of frequency for the various target node counts

more target nodes are required for the source inversion routine to provide an acoustic field similar to the truth field at non-target locations. To explore this apparent frequency dependence in a slightly different way, the pressure MAC was plotted not against frequency, but instead against what here is called sensor wavelength density. Sensor wavelength density is the number of target nodes in the inverse simulation, per cubic wavelength. Equation 22.2 shows the sensor wavelength density calculation. Figure 22.11 demonstrates the expression. At low frequency when wavelengths are large, the number of target nodes per cubic wavelength is high. As frequency increases, the wavelengths become shorter and the density decreases.

$$Sensor\ Wavelength\ Density = \frac{\#\ target\ nodes}{Volume}\,\lambda^3\,. \tag{22.2}$$

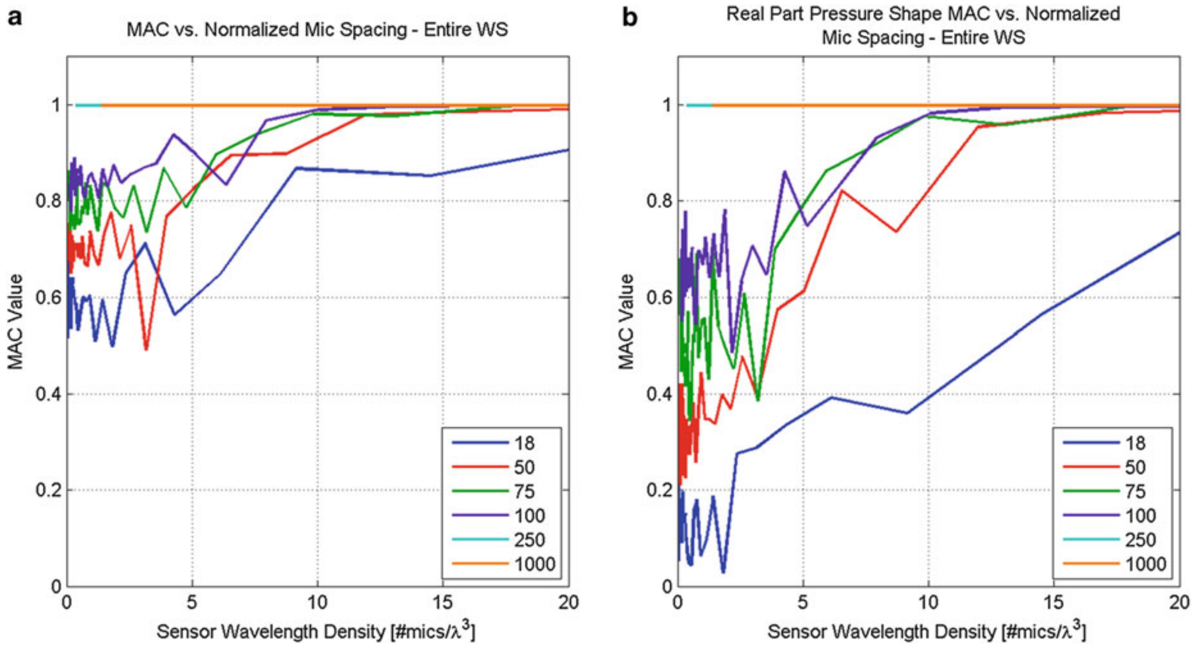

Fig. 22.12 (**a**) MAC of the pressure magnitude shape for the various target node sets, as a function of target node wavelength density. (**b**) MAC of the real part of pressure shape

The idea is there should be some number of target nodes required to constrain the acoustic field on a per-wavelength basis. Low frequencies, longer wavelengths, should need much larger target node spacing as compared with higher frequencies with shorter wavelengths. By normalizing the number of target nodes in the given volume by the cube of the wavelength, convergence to the truth field might be observed. Figure 22.12a shows how the MAC computed using the pressure magnitude shape trends with the sensor wavelength density for each target node set. Figure 22.12b shows the MAC computed using the real part of pressure shape. In either case two interesting things can be observed. First, the MAC value is nearly 1.0 for the 250 and 1000 target node cases, irrespective of wavelength density. Second, the 50, 75, and 100 target node cases follow approximately the same trend in that the MAC value is low when sensor wavelength density is low, but approaches 1.0 when the density increases to around 10 target nodes per cubic wavelength. It should be noted that this study and these metrics are constrained by a constant domain size and constant source to target distances, which may explain why these curves do not all exhibit similar trends as was initially expected by normalizing the data with respect to wavelength. It appears that if there are a large number of target nodes, above some threshold count—in this case between 100 and 250—then the field can be perfectly replicated even for high frequencies where the sensor wavelength density is low. Below that threshold, the sensor wavelength density does appear to influence the quality of the replicated field. The trend of improved field replication with increase in sensor density matches intuition.

22.6.5 Visualizing the SPL

A qualitative comparison of the acoustic pressure fields can also provide insight. By converting the pressure spectra to SPL, the acoustic field magnitude can be visualized at each frequency. Figures 22.13 and 22.14 below shows the acoustic field for a low frequency (520 Hz) and higher frequency (1520 Hz) for three different target node sets as well as the truth field. It can be seen that for both high and low frequencies the general pressure shape is approximately similar to the truth field for the 75 and 250 target node cases but not for the 18 target node case.

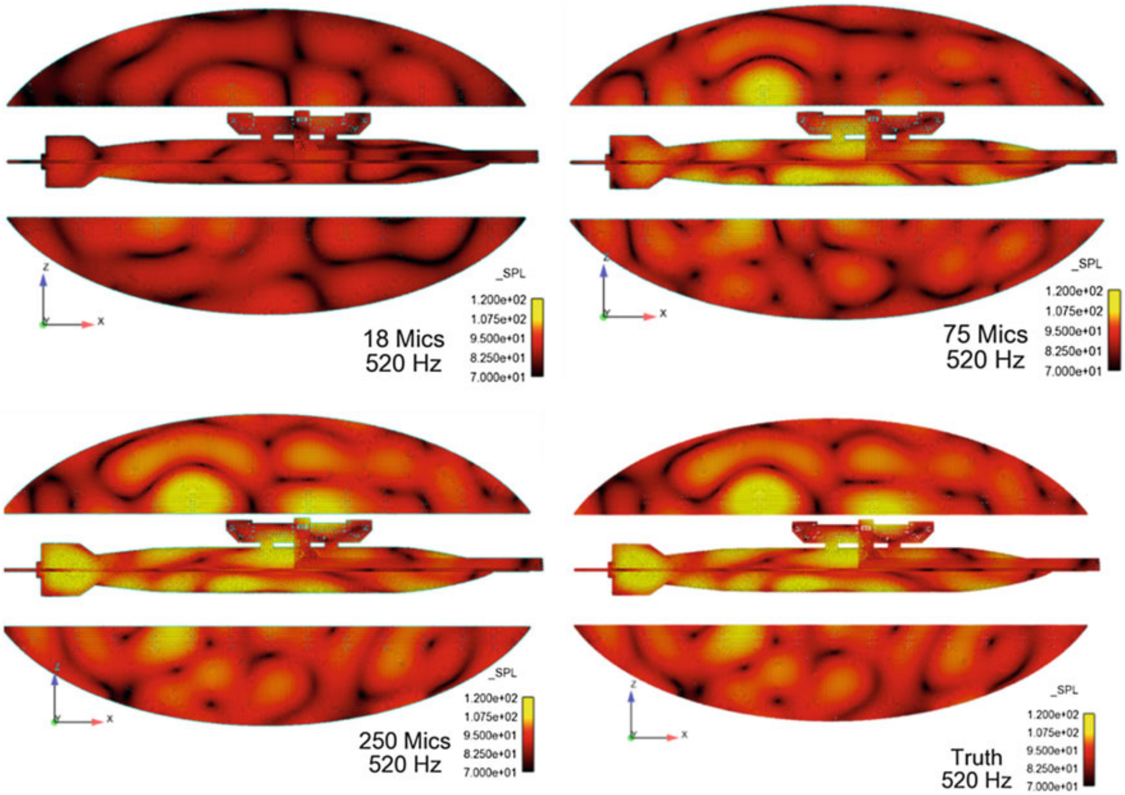

Fig. 22.13 Visualization of the sound pressure level throughout the acoustic field for 18, 75, 250 target nodes, compared with the truth field at 520 Hz

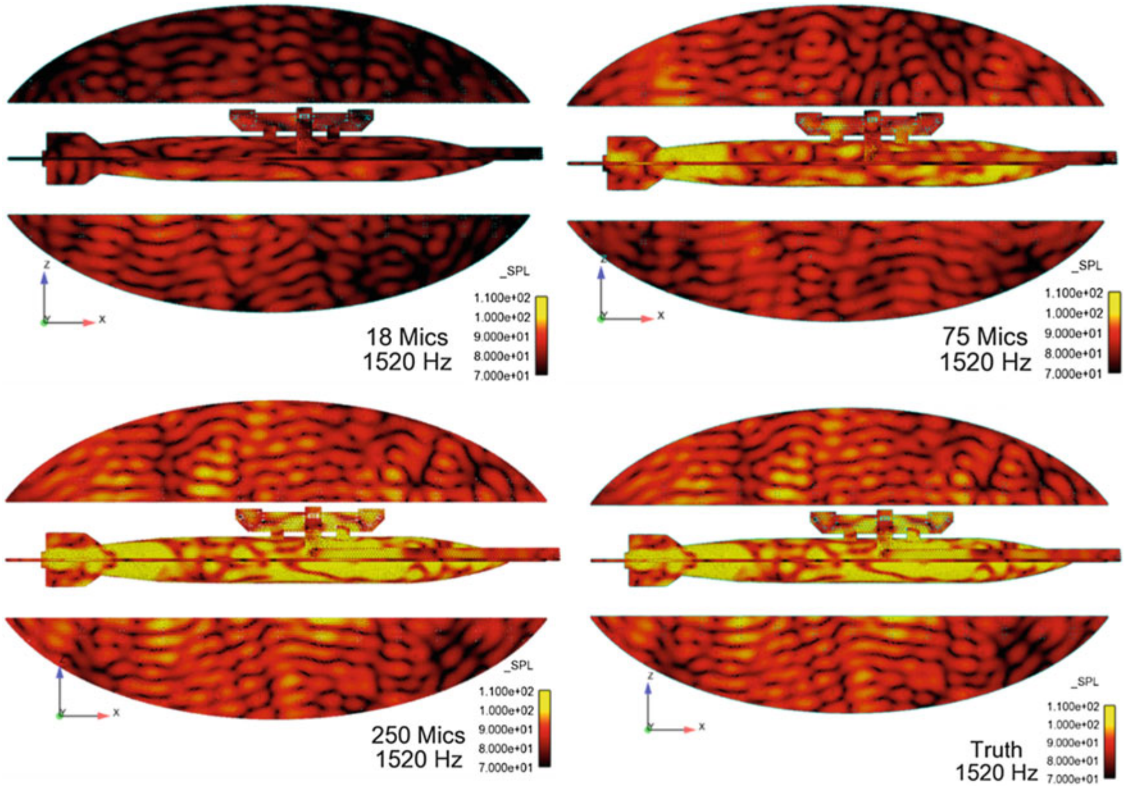

Fig. 22.14 Visualization of the sound pressure level throughout the acoustic field for 18, 75, 250 target nodes, compared with the truth field at 1520 Hz

22.7 Conclusions and Future Work

Direct field acoustic testing appears promising for exploring acoustic environments for aerospace structures, and validating structural dynamics models in these test environments is of interest. Providing accurate finite element model loading to replicate the as-tested acoustic field is critical in this validation process, and the relatively new code capabilities in Sierra/SD for acoustic source inversion methodology seem promising for providing these hard to define acoustic loads. First, however, the analysts must understand how modeling choices and target data affect the ability of the source inversion optimization algorithm to accurately replicate the as tested field at non-target points in the domain. This work addresses the impact of the number of target points in the field for an acoustic model used to simulate an acoustic test of a flight system, though with synthetic rather than test target pressure data, allowing thorough assessment of the acoustic field.

Multiple metrics were explored as each provides unique information in terms of the field level, pressure distribution, and relationship between target node count or density with respect to frequency or wavelength. The general takeaway from this study is that more target nodes provide a more accurate replication of the acoustic field. Using 1000 target node points produced an acoustic field nearly identical to the truth field by all the metrics explored here. Lower target node sets provide more accurate replication at lower frequencies, where there are more target nodes per unit volume or per unit cubic wavelength.

Future work will focus on extending this type of study to different models to explore the domain dependence of these results. Additionally, establishment of a threshold minimum target node count is of interest in the design of future simulations and future laboratory acoustic tests used for simulation. Also, there could be some improvement to the replicated field accuracy by locating the target points intelligently to maximize their usefulness to the inverse optimization algorithm in an attempt to reduce the required count and still achieve field replication. For example, it would be pertinent to study the effect on field replication of locating some nodes near key sources, or near regions of interest for more accurate replication—near the wetted surface.

References

1. Kouri, D.P., Ridzal, D., van Bloemen Waanders, B.G., von Winckel, G.: Rapid Optimization Library. Sandia National Laboratories, https://trilinos.org/packages/rol, SAND2014-19572 (2014)
2. Sierra Structural Dynamics Development Team: Sierra Structural Dynamics – User's Notes. Sandia National Laboratories SAND Report (2015)
3. Walsh, T., Aquino, W., Ross, M.: Source Identification in Acoustics and Structural Mechanics using SIERRA/SD. Sandia National Laboratories SAND Report (2013)
4. Allemang, R.: The modal assurance criterion – twenty years of use and abuse. Sound Vib. 8–21 (2003)
5. Gabrielson, T.: Penn State ACS516: Acoustic Data Measurement and Analysis Course Notes (2013)

Chapter 23
Experimental Mapping of the Acoustic Field Generated by Ultrasonic Transducers

Songmao Chen, Christopher Niezrecki, and Peter Avitabile

Abstract In recent years, a laboratory noncontact excitation method based on the focused ultrasound radiation force, generated by an ultrasonic transducer has been exploited to excite vibrations within structures with size ranging from the micro to macro scale. The excitation frequency has a range from a few kHz to 1 MHz and can potentially be used for modal testing. However, the inability to monitor the real time acoustic radiation force prevents this approach from being used as a practical technique for measuring the frequency response functions in modal testing. This work deals with understanding the acoustic field generated from ultrasonic transducers in order to monitor and control the acoustic radiation pressure and force imparted to a structure.

In this paper, the acoustic field generated by circular ultrasonic transducers was calculated based on the Rayleigh Integral and a boundary element method. The vibration velocity distribution of the vibration surface of an ultrasonic transducer at certain frequencies was measured, linearly interpolated, and mapped to the radially discretized elements of transducer surface, which was then used to map the acoustic pressure generated. A microphone array was built to measure the frequency response functions (FRFs) of acoustic pressure with respect to the drive voltage at several spatial locations within three vertical and one horizontal planes in front of the transducer. The comparison between the simulation results and experimental results is presented and shows good agreement.

Keywords Ultrasound radiation force • Modal testing • Mapping • Boundary element method • Rayleigh integral

23.1 Introduction

In modern modal testing practices, excitations imparted using an impact hammer or shakers [1] are commonly used. These conventional excitation techniques require that the excitation sources be physically in contact with the structures to be tested, resulting in mass loading, stiffness loading effects [2] and other physical issues that may distort the structure's true dynamic characteristics. In some cases, this type of contact excitation may even be physically impossible due to space or bandwidth excitation limitations, like excitation of arteries [3] and micro structures [4]. Providing physical excitation of a structure in the ultrasonic range (>20 kHz) can be a challenge.

In recent years, a laboratory noncontact excitation method based on the focused ultrasound radiation force has been exploited to excite vibrations within structures with size ranging from the micro to macro scale. The ultrasound radiation force is generated by the superposition of two modulated ultrasound signals applied to an ultrasound transducer that can be used to drive structures at the difference frequency [5]. The excitation frequency has a range from a few kHz to 1 MHz and can potentially be used for modal testing. Huber et al., used this ultrasound radiation force for non-contact modal excitation in air and measured the frequencies and corresponding operating deflection shapes [6] for a brass reed used in air [7]. The technique was also used for objects such as microcantilevers with resonance frequencies over 1 MHz [4], hard drive suspensions [8], and a classical guitar with resonance frequencies below 100 Hz [9]. Roozen et al., illustrated the application of acoustic radiation force to excite a sphere on rod and tried to quantify the force by using an inverse method from the induced structural deformation [10]. Some theoretical works have been published to simulate the dynamic acoustic radiation force acting on spheres [11] and cylindrical shells [12]. However, only a limited amount of work has been done to fully understand the acoustic radiation of an operating ultrasound transducer in air. The inability to monitor the real time acoustic radiation force prevents this approach from being used as a practical technique for measuring the frequency response functions in modal testing.

S. Chen (✉) • C. Niezrecki • P. Avitabile
Structural Dynamics and Acoustic Systems Laboratory, University of Massachusetts Lowell, One University Avenue, Lowell, MA 01854, USA
e-mail: Songmao_Chen@student.uml.edu

© The Society for Experimental Mechanics, Inc. 2016

J. De Clerck, D.S. Epp (eds.), *Rotating Machinery, Hybrid Test Methods, Vibro-Acoustics & Laser Vibrometry, Volume 8*,
Conference Proceedings of the Society for Experimental Mechanics Series, DOI 10.1007/978-3-319-30084-9_23

As one of the first steps, this work aims to gain a comprehensive understanding of acoustic field generated from ultrasonic transducers numerically and experimentally in order to monitor and control the acoustic radiation pressure and force imparted to a structure. In this paper, a numerical boundary element model based on the Rayleigh Integral and boundary element method was first established. In this model, the transducer surface was radially discretized into 5401 source elements. Then, test setups and experimental methods for measuring vibrations and acoustic FRFs were described. After that, the vibration FRFs were examined and velocity profile of the surface of an ultrasonic transducer at certain frequencies were measured, the velocity profiles were linearly interpolated, and mapped to the source elements representing the transducer surface and was then used to calculate acoustic beam profiles by using the previous built boundary element model. The acoustic FRFs in four plane slices before the transducer were also tested and acoustic pressure profiles were then derived for these four planes. Comparison between the simulation and experimental results was made and a good agreement was found in terms of both beam profile and pressure amplitude.

23.2 Theoretical Background

To simulate the acoustic field generated by ultrasonic transducers, a boundary element model based on the Rayleigh Integral and boundary element method was built. As shown in Fig. 23.1, the surface of the test transducer used in this work was discretized into a circular element at the center and 30 annular sections each with 180 source elements. In total, there are 5401 source elements and to obtain a better approximation, each source element was set in a way that its dimensions were smaller than the wavelength of the sound wave. For example, wavelength $\lambda = c/f$, where c is the speed of sound in a particular medium at certain temperature and f is the wave frequency. If $f = 50$ kHz, $\lambda = \sim 6.8$ mm.

The sound pressure of a field point p(x,y,z) produced by one source element can be represented by [13]

$$p(x, y, z) = \frac{j\omega\rho U(x', y')\, e^{j(\omega t - kr)}}{2\pi r} ds \tag{23.1}$$

where, r is the distance between the field point and the center of the source element, ds is the area of that element source, and

$$r = \sqrt{(x - x')^2 + (y - y')^2 + z^2} \tag{23.2}$$

$$ds = rs * drs * dphi \tag{23.3}$$

The overall pressure at a field point is a superposition of from all of the source elements and can be formulated by

$$P(x, y, z) = \sum_{l} \sum_{m} p(x, y, z) \tag{23.4}$$

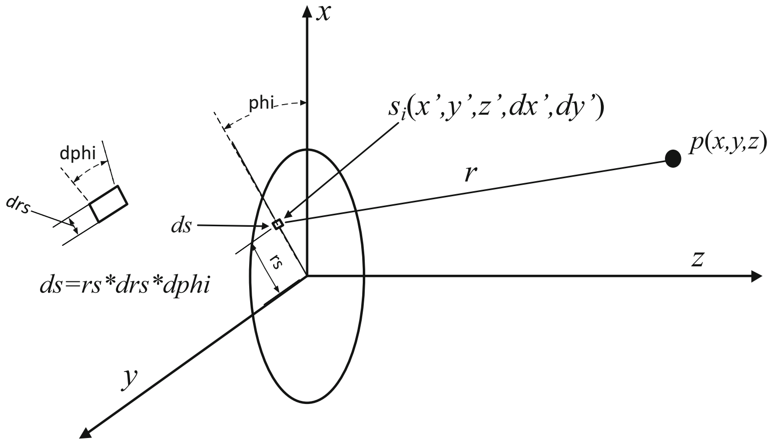

Fig. 23.1 Schematic of the boundary element model used to simulate the acoustic field generated by ultrasonic transducer

23.3 Testing Performed

In this work, a non-contact plane type circular ultrasonic transducer Ultran NCG50-D50 [14] was tested, as shown in Fig. 23.2. The transducer is air-coupled and designed to generate plane traveling wave in both air and solids. It has an effective diameter of 50 mm and a nominal operating frequency of 50 kHz. To characterize the ultrasonic transducer, a laser scanning vibrometer, Polytec PSV-400 [15], was used to measure the vibration characteristics for the transducer's surface. In Fig. 23.2, a circular pattern of 217 numbered grid points (for instance, point #7 on the inner most ring) including the one at the center (Point #1) was defined to represent the transducer surface. Initially, a test was performed to determine the FRFs of the transducer surface velocity with respective to the drive voltage. In the test, a periodic chirp signal generated by the Polytec laser vibrometer's function generator was used as the excitation signal, which went through a power amplifier PZD700 [16] and finally was applied to the test transducer; surface vibration was recorded by the Polytec system. The testing frequency used was from 0 to 80 kHz with a sampling frequency of 204.8 kHz and frequency resolution of 6.25 Hz. Then, the vibration velocity profile of the transducer surface was measured by using the Polytec scanning laser vibrometer at different frequencies within the effective operating frequency range determined by the above test.

Experiments were also performed to measure the acoustic FRFs for the ultrasonic transducer over the same frequency range identified by vibration test. In these experiments, an array of ten 10-mm spaced precision microphones (Model 378C01) [17] was located in the acoustic field before the ultrasonic transducer, as shown in Fig. 23.3a.

Three finite vertical measurement planes (in XY plane), P1, P2 and P3, and one finite horizontal plane (in XZ plane) P4 were tested, as illustrated in Fig. 23.3b. The distances between planes P1, P2, and P3 and the transducer surface were 160, 140 and 180 mm, respectively. Plane P4 was located at the center of the transducer with the near and far end limits of the plane located 110 and 210 mm from the transducer, respectively. Note that distance was measured from the front of the microphone protection grid to the surface of the ultrasonic transducer plane. In each plane, a rectangular measurement pattern of 441 grid points evenly distributed within a range of 100 mm × 100 mm was employed, as seen in Fig. 23.3c, a local coordinate system x′ (represents a column) and y′ (represents a row) was set to define the measurement points in a plane. The distance between two adjacent points along either x′ or y′ direction was 5 mm.

In performing the acoustic FRF measurement, the Polytec laser system was used to provide the periodic chirp excitation signal. A multi-Channel LMS Test.Lab Spectral Analyzer [18] was used to measure the data and process the FRFs. The frequency resolution for both Polytec and LMS system was 6.25 Hz.

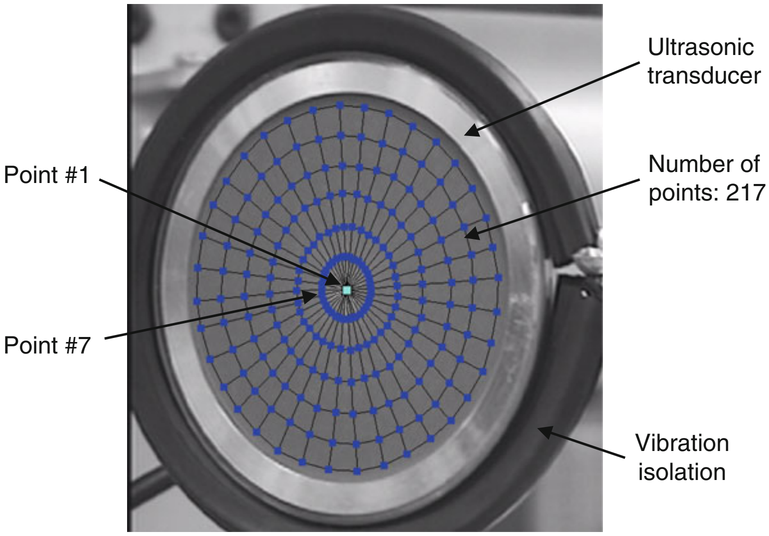

Fig. 23.2 Ultrasonic transducer and pattern of grid points for measuring the ultrasonic transducer surface vibration

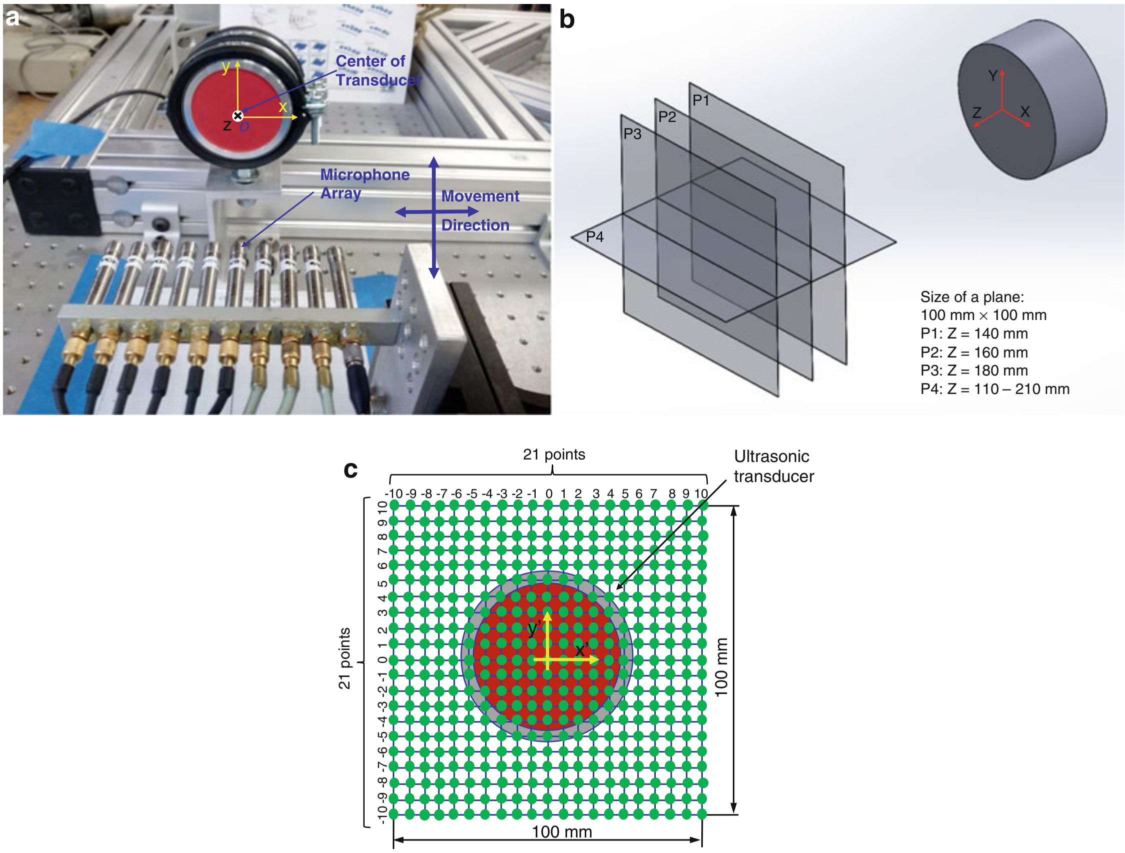

Fig. 23.3 Experimental setup for measuring the acoustic FRFs generated by the ultrasonic transducer. (**a**) The ultrasonic transducer and Microphone array; (**b**) measurement planes; (**c**) points pattern in each plane

23.4 Results and Discussion

A typical FRF of vibration for a point on the surface of the test transducer is shown in Fig. 23.4. It was observed that even though there might be minor differences among FRF curves for all of the 217 points, they generally exhibited similar behavior as the response shown in Fig. 23.4. The FRFs indicate that the effective operating frequency range for the ultrasonic transducer is between approximately 40 and 70 kHz. The frequencies in the range below 40 kHz and above 70 kHz generated a lower transducer response for a given excitation voltage. Since the pressure generated by ultrasonic transducers is proportional to the vibration velocity of transducer surface, it is reasonable to assume that acoustic radiation is also higher in this operating frequency range. Therefore, the acoustic characterization was focused on this frequency range.

The velocity profile can be acquired by conducting a pure sinusoidal excitation test at a single frequency. In such a test, a sinusoidal excitation at a specific frequency is applied to the ultrasonic transducer, the velocities for the entire previously defined grid points representing the transducer surface are then measured by the Polytec system, resulting in the experimental velocity profile.

As shown in Fig. 23.5, the velocity profiles were acquired for 40, 45, 50, 55, 56, 57, 58, 59, 60, 65 and 70 (all in kHz), respectively, when the transducer was operating with an applied sinusoidal voltage of 30 Vrms. It can be seen that, the overall velocity distribution on the transducer surface has a relatively higher amplitude and better uniformity within the frequency range from 55 to 60 kHz than for other frequencies; a closer interrogation found that, in this case, the velocity profile at 56, 57 and 58 kHz are among the best.

Using the boundary element model in Fig. 23.1, a MATLAB [19] script was written to linearly interpolate the experimental velocity profile to the model and simulate the acoustic beam profile. For comparison purposes, only beam profiles at 56, 57 and 58 kHz were calculated, as shown in Fig. 23.6. It can be seen that these three beam profiles appears to be similar to each other. This is due to the close proximity of operating frequencies. The pressure level is of the same magnitude with the one at 57 kHz of the highest. Also can be observed that the transitional point between the near and far field is the same for all of

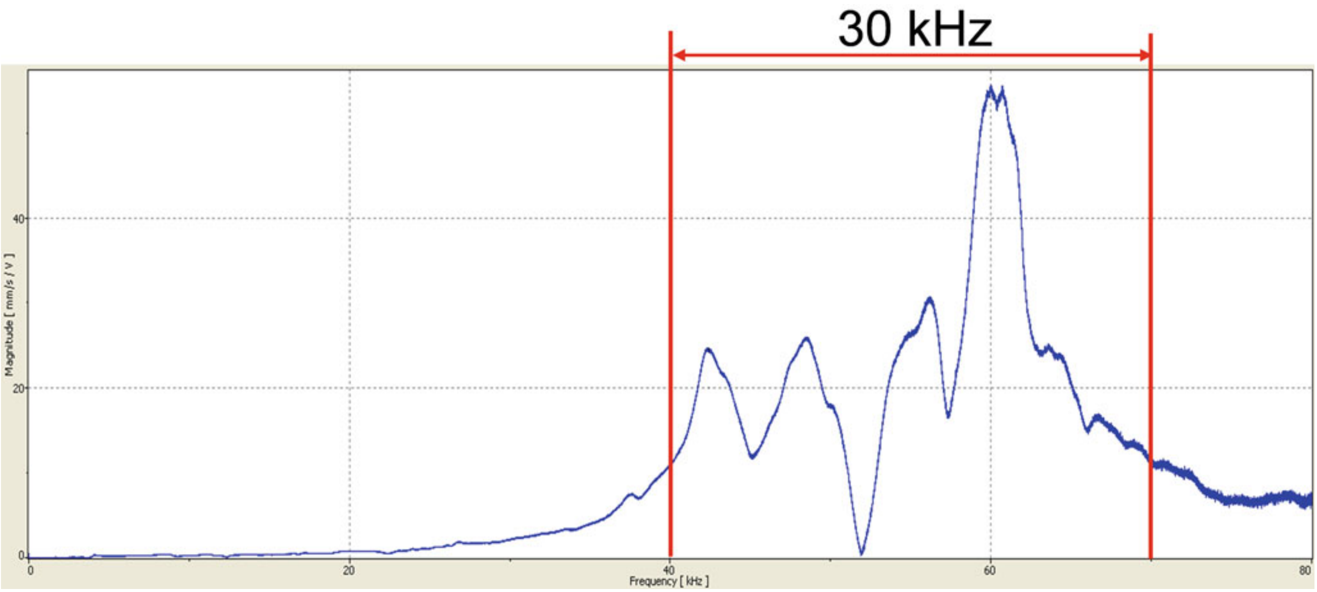

Fig. 23.4 Vibration FRF of point #7 on the transducer surface (velocity with respect to applied voltage) over the 80 kHz bandwidth

the three frequencies and 9 mm away from the ultrasonic transducer surface. In the near field, the sound pressure has a large fluctuation; in the far field, the sound pressure decreases monotonically as a field point gets further away from the ultrasonic transducer surface.

The measured acoustic FRFs and coherence functions in the frequency range between 40 and 70 kHz were obtained. Figure 23.7 shows the measurement results for the measurement points of the middle row ($y' = 0$).

Figure 23.7 illustrates that, for all of the four planes, the operating frequency range that generated the most pressure ranges from 55 to 60 kHz. This is in accordance with the measured velocity profile and different from its nominal frequency. It is also found that the maximum pressure does not occur at the center point. This is probably due to the non-uniformity and asymmetry of the vibration of the transducer surface. The coherence over the measured frequency range, except for a few discrete frequencies, is equal to unity indicating a direct relation between output (sound pressure) and input (excitation voltage). The measurement results for all of the other points on these planes show a similar phenomenon.

With the acoustic FRFs available, the sound pressure for a point in the acoustic field can be readily obtained by the following equation,

$$p_f = FRF_f \times V_{drv} \tag{23.5}$$

where p_f is the acoustic pressure at the frequency f, and V_{drv} is the root-mean-square drive voltage applied on the transducer.

The simulation and experimental pressure in planes P1, P2, P3 and P4 when the transducer operated with a 30 Vrms sinusoidal at frequencies of 56, 57 and 58 kHz are shown in Fig. 23.8a, b and c, respectively.

These figures illustrate that the simulation results and experimental results are in good agreement. Even though an appreciable interference effect exists in the experimental results, the sound pressure can still be observed to possess similar beam profile and the acoustic spot size can be clearly identified for all of the four acoustic fields. The simulated and experimentally measured maximum pressure amplitudes were compared in all of the four measurement planes, as shown in Table 23.1. It can be seen that the biggest percent difference is 16 % and most are within less than 10 %.

The difference in acoustic pressure lies in a variety of factors. First, the interference caused by the microphone array is most significant and would affect the measurement precision of each microphone in the array. Second, the simulation calculates literally a point pressure, whereas, microphones in the array is only able to measure the average pressure over the area of its piezoelectric measurement diaphragm. Third, the fact that the distances between the piezoelectric measurement diaphragm, which is not accessible, and the transducer surface were actually a little larger than that shown in Fig. 23.2b also contribute to the pressure difference.

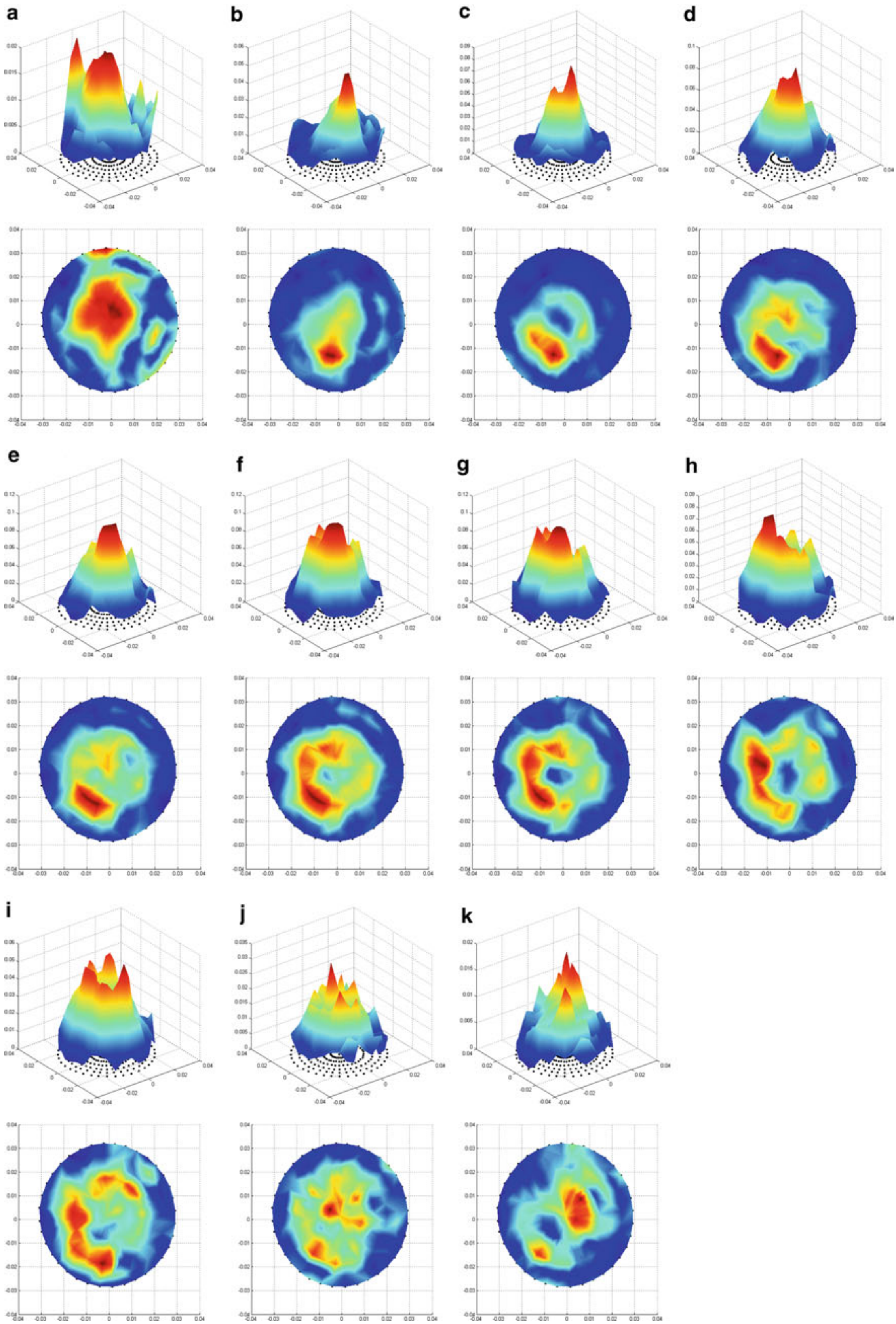

Fig. 23.5 Experimentally measured velocity profiles (Unit: m/s) when the ultrasonic transducer operated under sine excitations at various frequencies and a constant voltage of 30 Vrms. (**a**) 40; (**b**) 45; (**c**) 50; (**d**) 55; (**e**) 56; (**f**) 57; (**g**) 58; (**h**) 59; (**i**) 60; (**j**) 65; (**k**) 70 (all in kHz). Both isometric and top views are shown

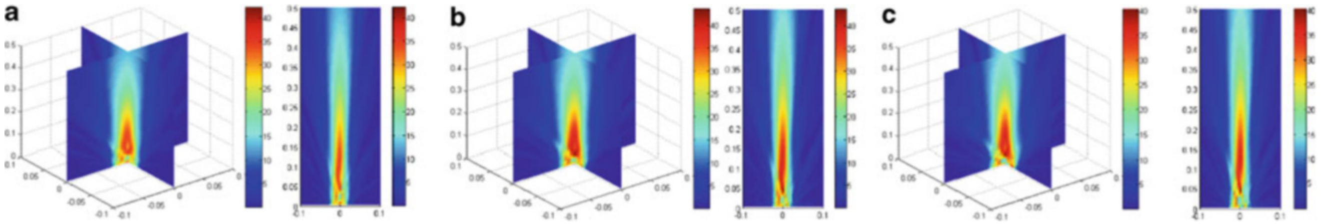

Fig. 23.6 Simulated acoustic beam profile generated by the ultrasonic transducer at individual frequencies. (**a**) 56 kHz, (**b**) 57 kHz, (**c**) 58 kHz (Unit: Pa)

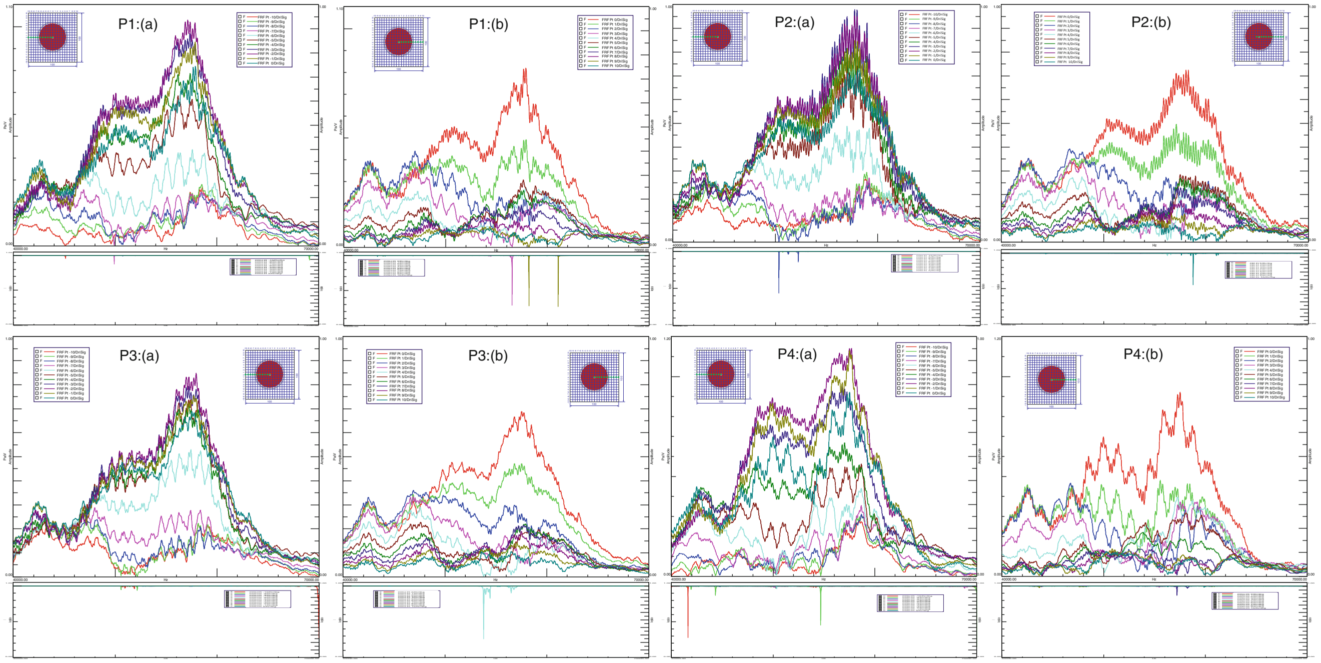

Fig. 23.7 The measured acoustic FRFs and coherence functions in planes P1, P2, P3 and P4 over the frequency range from 40 to 70 kHz. (**a**) Points: x′: −10 to 0, y′: 0. (**b**) Points: x′: 0 to 10, y′: 0. *Top*: FRFs; *Bottom*: Coherence (Unit: Pa/V)

23.5 Conclusion

A boundary element model based on the Rayleigh Integral and boundary element method was created to simulate the sound field generated by an ultrasound transducer. The vibration characteristics of the transducer surface were tested and velocity profiles were acquired by driving the test transducer with 30 Vrms sinusoidal signals at frequencies of 56, 57 and 58 kHz, respectively. A microphone array was constructed to measure the actual sound pressure in four planes in the acoustic field in front of the transducer. Simulation results and experimentally measured acoustic pressure profiles were compared at several frequencies and good agreement was found. Some of the differences stem from the ¼″ diameter microphones not being completely suitable to measure the detailed resolution required for ultrasonic waves. Future studies will involve using a fiber-optic acoustic microphone to better quantify the acoustic radiation and limit the interference between microphones caused by wave reflections.

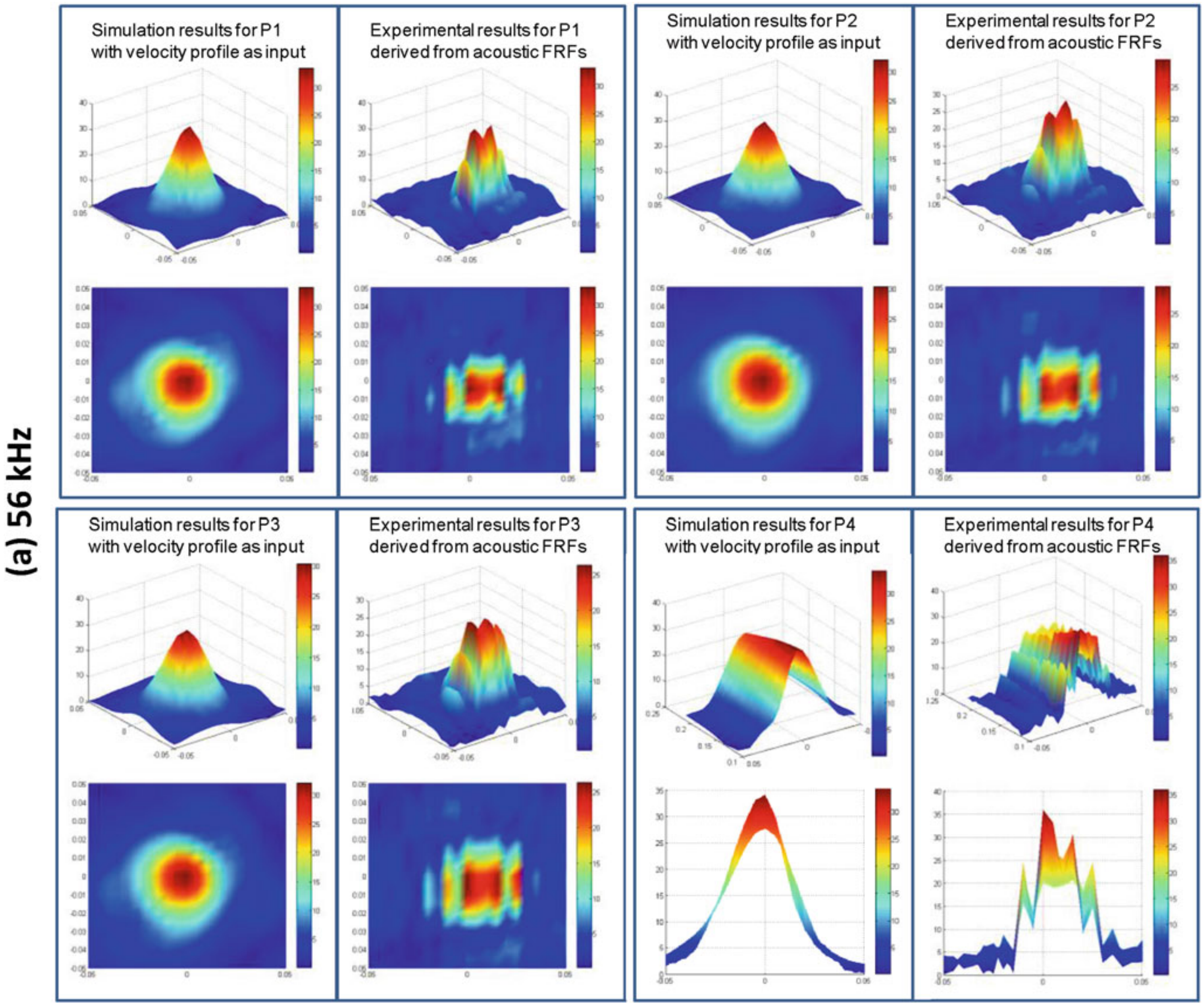

Fig. 23.8 (**a**) Comparison of simulation and experimentally measured acoustic pressure in planes P1, P2, P3 and P4 when the transducer operated under a 30 Vrms sinusoidal excitation at 56 kHz. (**b**) Comparison of simulation and experimentally measured acoustic pressure in planes P1, P2, P3 and P4 when the transducer operated under a 30 Vrms sinusoidal excitation at 57 kHz. (**c**) Comparison of simulation and experimentally measured acoustic pressure in planes P1, P2, P3 and P4 when the transducer operated under a 30 Vrms sinusoidal excitation at 58 kHz

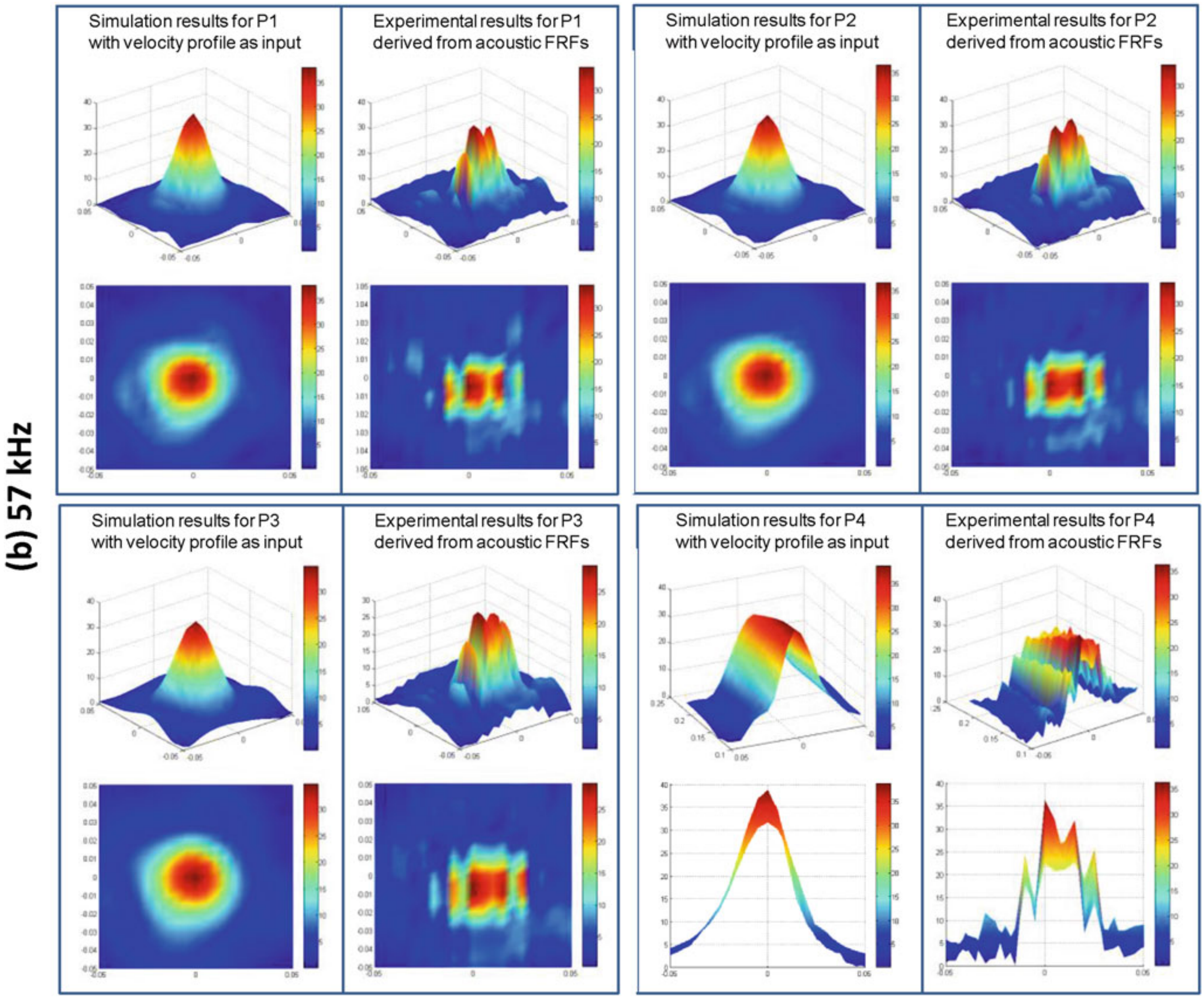

Fig. 23.8 (Continued)

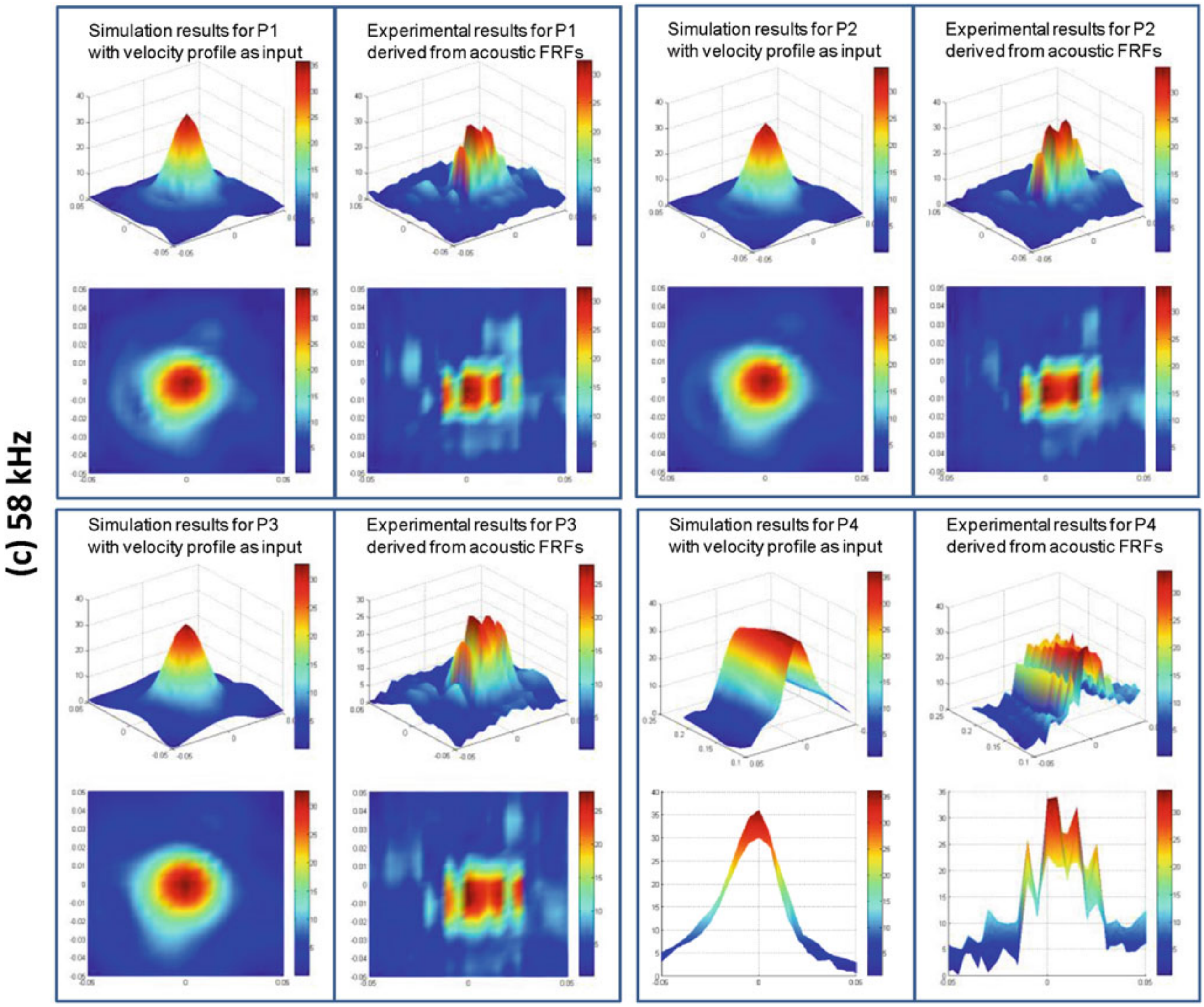

Fig. 23.8 (Continued)

Table 23.1 Comparison of maximum pressure in all of the four measurement planes when the transducer operated with a 30 Vrms sinusoidal excitation at 56, 57 and 58 kHz

	Maximum pressure in a measurement plane											
	P1			P2			P3			P4		
Frequency (kHz)	Simulation	Experimental	Diff(%)	Simulation	Experimental	Diff(%)	Simulation	Experimental	Diff(%)	Simulation	Experimental	Diff(%)
56	33.4	33.2	0.6	32	29.3	8.4	30.3	26.3	13.2	34	35.8	−5.3
57	38.1	34.2	10.2	36.5	33.8	7.4	34.6	29	16.2	38.7	36.2	6.5
58	35.7	32.2	9.8	34.4	34.6	−0.6	32.7	27.8	15.0	36	33.9	5.8

Acknowledgements The work presented herein was funded by the NSF Civil, Mechanical and Manufacturing Innovation (CMMI) Grant No. 1266019 entitled “Collaborative Research: Enabling Non-contact Structural Dynamic Identification with Focused Ultrasound Radiation Force”. Any opinions, findings, and conclusions or recommendations expressed in this material are those of the authors and do not necessarily reflect the views of the particular funding agency. The authors are grateful for the support obtained. We are also indebted to some of the Ph.D. Students at the Structural Dynamics and Acoustic Systems Lab, in particular, Tina Dardeno and Patrick Logan for helpful discussion throughout the work and Peyman Poozesh for helping setting up part of the testing equipments.

References

1. Avitablie, P.: Experimental modal analysis - a simple non-mathematical presentation. Sound Vib., Jan. 1–11 (2001)
2. Avitabile, P.: Back to basics – why is mass loading and data consistency important for modal parameter estimation? Exp. Tech. **24**(6), 19–20 (2000)
3. Zhang, X., Fatemi, M., Greenleaf, J.F.: Vibro-acoustography for modal analysis of arterial vessels. In: Proceedings of 2002 IEEE International Symposium on Biomedical Imaging (2002)
4. Huber, T., Abell, B., Mellema, D., Spletzer, M., Raman, A.: Mode-selective noncontact excitation of microcantilevers and microcantilever 159 arrays in air using the ultrasound radiation force. Appl. Phys. Lett. **97**, 214101 (2010)
5. Fatemi, M., Greenleaf, J.: Ultrasound-simulated vibro-acoustic spectrography. Science **280**, 83–85 (1998)
6. Richardson, M.: Is it a mode shape, or an operating deflection shape? Sound Vib. **31**, 1–11 (1997)
7. Huber, T., Fatemi, M., Kinnick, R., Greenleaf, J.: Noncontact modal analysis of a pipe organ reed using airborne ultrasound stimulated 163 vibrometry. J. Acoust. Soc. Am **119**(4), 2476–2482 (2006)
8. Huber, T., Calhoun, D., Fatemi, M., Kinnick, R., Greenleaf, J.: Noncontact modal testing of hard-drive suspensions using ultrasound radiation force. In: Proceedings of IMAC XXIV, Louis, Missouri, USA, Jan. 30–Feb. 2, 2005
9. Huber, T., Beaver, N., Helps, J.: Noncontact modal excitation of a classical guitar using ultrasound radiation force. Exp. Tech. **37**, 38–46 (2013)
10. Roozen, N., Nuij, P., Nijmeijer, H.: Sonic excitation by means of ultrasound: an experimental illustration of acoustic radiation force. In: Proceedings of Forum Acusticum 2011, Aalborg, Denmark, June 2011
11. Silva, G., Chen, S., Greenleaf, J., Fatemi, M.: Dynamic ultrasound radiation force in fluids. Phys. Rev. E **71**, 056617 (2005)
12. Mitri, F., Fatemi, M.: Dynamic acoustic radiation force acting on cylindrical shells: theory and simulations. Ultrasonics **43**, 435–445 (2005)
13. Blackstock, D.: Fundamentals of Physical Acoustics, John Wiley & Sons, New York, pp. 441–442 (2000)
14. Non-contact Ultrasound, Ultran Group, State College, PA
15. Polytec Scanning Laser Doppler Vibrometer, Polytec Optical Measurement Systems, Waldbronn, Germany
16. TREK Model PZD700, High Voltage Power Amplifier/Piezo Driver, TREK Inc., Lockport, New York
17. PCB Model 378C01, PCB Piezotronics Inc., Depew, NY
18. LMS Test.Lab – Leuven Measurement Systems, Leuven, Belgium
19. MATLAB - Matrix Analysis Software, The MathWorks, Inc., Natick, MA

Chapter 24
Enhanced Spin-Down Diagnostics for Nondestructive Evaluation of High-Value Systems

David Sehloff, Clark Shurtleff, Josh Pribe, Colin Haynes, and John Heit

Abstract The nature of some high-value systems requires that damage be detected without disassembly of the test article. Spin-down testing, one such nondestructive evaluation method, involves spinning a test article and observing its angular deceleration. An increase in angular deceleration compared to an identical test of a healthy system indicates damage has occurred. However, current testing is limited, providing only a binary result of “damaged” or “undamaged”. More sophisticated techniques are required to identify the location, extent, and type of damage. To achieve this, non-contact and surface-mounted sensors were used to monitor the test article in this experiment. A spin-down unit was used to test both a healthy specimen and a specimen with simulated damage. The signals from each sensor were compared across tests. Correlation of anomalous signals with rotational position and multi-sensor triangulation techniques were used to localize damage. Analysis of the frequency content and amplitude of output signals allowed for a degree of characterization of the damage. Through these techniques, spin-down testing was enhanced from a binary detector to a more thorough testing method giving detailed information about the type and location of damage.

Keywords Spin-down testing • Rotating system • Nondestructive evaluation • Acoustic emissions sensing • Linear predictive coding

24.1 Introduction

Non-destructive evaluation is an essential tool for monitoring the status of high-value systems. In many cases, the cost (in both time and effort) of disassembling a system to evaluate its structural health is prohibitive. Such situations call for alternate means of evaluation. In this study, a novel strategy for assessing the health of a system is employed.

Spin-down testing is based on monitoring the angular deceleration of a test article. After the test article is accelerated to some speed and released, angular velocity is monitored by an encoder. It is expected that damage in the form of a loose or broken component, or in cracking or other mechanical degradation, acts as a dissipative mechanism. The energy dissipated by damage results in a loss of angular momentum, meaning that the test article will come to rest more quickly than a pristine system. Thus, by comparing the deceleration characteristics of an unknown article to those of healthy specimens, an unknown article can be classified as damaged or undamaged.

The test as described requires a specialized setup. To maximize the signal to noise ratio of damage indicators, it is important that the article is spun on bearings with extremely low friction. One way this is achieved is with an air bearing, in which the shaft is supported by compressed air. Data is output by an angular position encoder and is used as described above to detect damage. This indicator has sufficient precision, for example, to detect damage when a small impact occurs, or when masses shift slightly over the course of the spin-down. It should be noted that the test article is spun about a horizontal axis.

D. Sehloff
Department of Electrical and Systems Engineering, Washington University in St. Louis, St. Louis, MO, USA

C. Shurtleff
Department of Materials Science and Engineering, University of Pennsylvania, Philadelphia, PA, USA

J. Pribe
Department of Mechanical and Aerospace Engineering, Missouri University of Science and Technology, Rolla, MO, USA

C. Haynes (✉) • J. Heit
Weapons Engineering, Los Alamos National Laboratory, Los Alamos, NM, USA
e-mail: cmhaynes@lanl.gov

© The Society for Experimental Mechanics, Inc. 2016

J. De Clerck, D.S. Epp (eds.), *Rotating Machinery, Hybrid Test Methods, Vibro-Acoustics & Laser Vibrometry, Volume 8*,
Conference Proceedings of the Society for Experimental Mechanics Series, DOI 10.1007/978-3-319-30084-9_24

In the frame of reference of the test article, acceleration due to gravity changes as the article changes orientation. This allows for analysis techniques that have not previously been applied to spin-down testing.

This method is intended for multi-component systems, such as small satellites, where it would be advantageous to detect damage from a single full-system test. As noted earlier, spin-down testing allows this test to be done without disassembling the test article. It also does not require extensive instrumentation or preparation of the test article. However, the method currently has major drawbacks. Most important is that it serves as a binary detector. Spin-down testing gives no information beyond the classification of damaged or undamaged. As a result, a satellite, for example, must be disassembled in order to locate and evaluate detected damage. This study aims to improve this by the implementation of novel techniques in spin-down testing.

Three major goals are considered: damage detection, localization, and characterization. As previously discussed, the problem of damage detection can already be addressed by monitoring the angular deceleration profile of a specimen. Localization and classification of damage present significantly more difficult challenges. Time-of-flight or time-delay methods for impact localization struggle to perform in complex, multi-component systems [1]. Machine learning methods that localize an unknown impact based on previously recorded impacts rely on extensive pre-testing of the test article, which can be impractical and expensive for complex systems [2]. The methods presented in this study provide some degree of localization without requiring knowledge of material properties or extensive pre-testing of the test article.

Our method takes advantage of the fact that the system is spinning about an axis perpendicular to gravity. Any loose or broken components in a test article, due to the changing orientation of centripetal force and the gravity vector, result in predictable, periodic signals. By associating the time history of sensors with the angular position of the test article, a periodic signal can be associated with a particular orientation of the test article. By combining knowledge of the orientation of the system with knowledge of the geometry of the test object, it is possible to estimate the location of the damage to within some radial section of the system.

24.2 Experimental Procedures

24.2.1 Experimental Setup

Data acquisition relied on several separate units. An incremental optical encoder (Encoder Products Company Model 711) was used in conjunction with a National Instruments Data Acquisition Board and LabVIEW to collect data on the angular position of the test article. A laser proximity sensor was mounted alongside the outer edge of the test article to measure the rotating disk's deviation from its axis, or out-of-plane displacement. The aim of this measurement was to provide insight into the orientation of mass in the disc, specifically eccentricity. This is discussed further in Sect. 2.2. The laser data was also routed through the NI DAQ system. The rotation of the system prevented the use of an external DAQ system for ride-along sensors. Thus, data from several acoustic emission sensors (Wsα broadband AE sensor, Physical Acoustics) was collected on a DTS Slice Micro data logger that was also mounted to the rotating system. Acquisition was initiated simultaneously on both systems using a manual trigger.

Testing was completed on two different systems. The first was a small-scale article, which will be referred to as the "surrogate" testing rig from this point forward. The surrogate system consisted of two aluminum flywheels on a steel shaft, mounted on a lab table (see Fig. 24.1 below). The two flywheels served distinct purposes. The first flywheel will be referred to as the "damaged" flywheel. Damage was simulated by placing marbles inside of coupling nuts that were mounted on the damaged flywheel, indicated by the lettered rectangles in Fig. 24.2. Bolts were inserted on top of the marbles to restrict their movement. Four acoustic emission (AE) sensors were mounted on the damaged flywheel, indicated by the numbered circles in Fig. 24.2. The data logger and the battery powering the sensors were mounted on the second flywheel. The laser proximity sensor was mounted alongside the shaft to measure out of plane displacement. The encoder, with 1200 counts per revolution, was connected to the shaft. After initiation of the data acquisition systems, the system was spun by hand, then allowed to decelerate to a stop.

The second system involved a larger test article mounted on an air bearing. The test article, referred to as the "top hat," was based on an aluminum cylinder. A series of concentric phenolic resin half-rings were placed within the cylinder as shown in Fig. 24.3 below. A circular top plate, not pictured, was used to secure the rings within the cylinder. Each concentric half-ring was held in place by set screws in the top plate, modeling an undamaged state. Loosening the screws that secured individual rings allowed these rings to shift and impact other rings or the aluminum cylinder, resulting in several different simulated damage configurations. The aluminum cylinder also included a base which connected to a shaft supported by two air bearings. The air bearing was connected to an optical encoder (8 counts per revolution) to measure angular displacement. Similar to

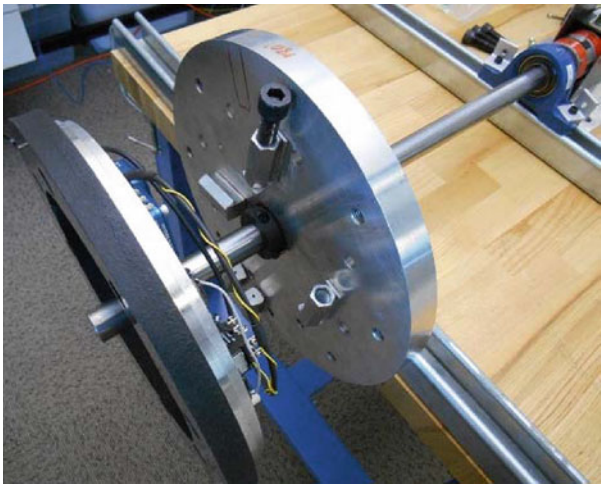

Fig. 24.1 Surrogate test setup; the damaged flywheel is shown at *right*

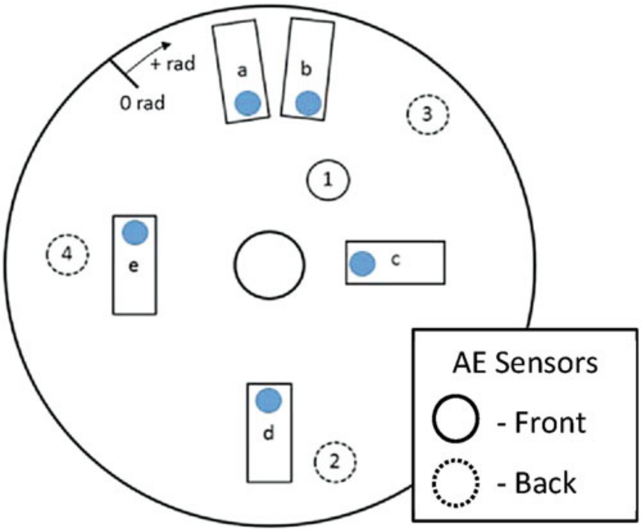

Fig. 24.2 Schematic of the damaged flywheel

the surrogate setup, additional sensors were placed on the test article. Three acoustic emission sensors were mounted to the top plate. A laser displacement sensor was mounted alongside the aluminum cylinder to measure out of plane displacement. These sensors and the encoder were connected to the same data acquisition systems as those used in the surrogate system. Once these were triggered, the system was spun to one revolution per second and allowed to spin down.

The top hat setup had several improvements over the surrogate setup. First, the low friction due to the air bearings resulted in a very low noise floor for the acoustic emission sensors and much longer tests (on the order of about 15 min; the surrogate setup was limited to about 30 s). Additionally, clay was used to balance the top hat before testing, minimizing the eccentricity during nominally undamaged tests. Difficulties with this setup that became evident during data processing are discussed in the following section.

24.2.2 Analysis Methods

The first step in data analysis was finding the angular position and angular velocity of the test article with respect to time. The raw encoder signal in both the surrogate and top hat test setups was approximately a square wave with each rise corresponding to an incremental position increase. To convert this signal to angular position and velocity, the angular position relative to

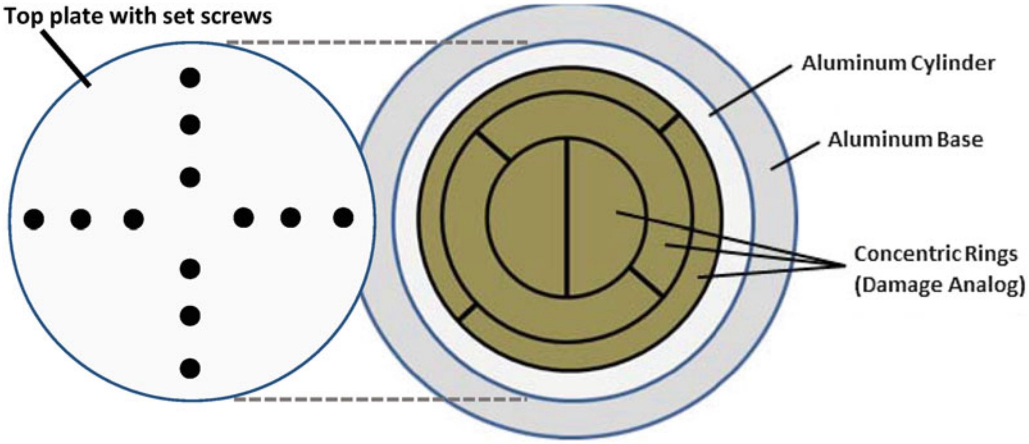

Fig. 24.3 Schematic of the top hat test article

a chosen orientation was found at the beginning of the test. The signal was accumulated into a count of the successive increments, which resulted in a signal that was not a uniform time series, but interpolation with a piecewise polynomial or spline fit gave the position with the same sample frequency as the measurements. This was multiplied by an appropriate factor depending on which encoder was used to obtain angular position. The resulting signal and its first derivative (angular velocity) were used in the analysis that follows.

24.2.3 Linear Predictive Coding for Detection and Localization

Linear predictive coding (LPC) was one of the methods used to detect damage. LPC, as its name suggests, is a linearly predictive algorithm. An Nth-order LPC model predicts each point in a time series by linearly combining the N preceding points according to a vector of predictive coefficients (α) [3]. Let A be a given dataset. Each point in B, a modeled signal, is calculated as follows:

$$B(n) = \sum_{i=0}^{N} \alpha_i * A\,(n - i) \tag{24.1}$$

In our study, LPC was used only on the AE sensors. First, a baseline dataset was used to produce a matrix of predictive coefficients. This matrix was applied to a new dataset (A) to produce a modeled signal (B). The modeled signal was then directly compared to the actual signal at each data point, and the residual errors were summed as follows. Let N be the length of the signal. A "damage parameter" was defined as:

$$\left[\sum_{i=0}^{N} (A_i - B_i)^2\right]^{1/2} \tag{24.2}$$

Time and facility constraints limited the number of tests that were completed. The small number of tests restricted our ability to use formal statistical analysis techniques to define a damage classifier. Consequently, the results presented here, while encouraging, are primarily qualitative.

24.2.4 "Binning Method" for Localization

A second technique, which will be referred to as the binning method, used the AE sensors to determine the angular location of the damage. This was done by first designating a single undamaged test as a baseline and assuming that the sensor responses showed Gaussian noise. All of the sensor responses were then demeaned and a threshold was set at four standard deviations.

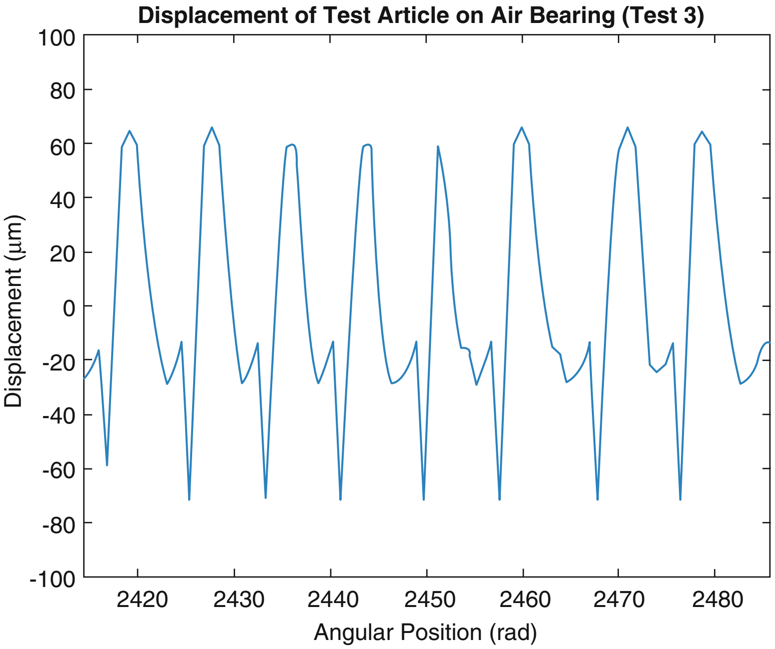

Fig. 24.4 Displacement of top hat during undamaged test

Any data point from an AE sensor that exceeded this threshold was designated as a count [4]. These counts were then lined up with the angular position at which they occurred. Finally, the angular position points were divided into sixteen bins (each one being π/8 rad wide). In this way, the orientation of the test article when counts were recorded was used to help determine the location of the damage.

24.2.5 Cross-Correlation of Laser Displacement Sensors

Another method which was used with the goal of characterizing damage relied on analysis of the data from the laser displacement sensors. The signal from these sensors, which shows the out-of-plane displacement of the rotating article, followed a periodic pattern. These oscillations, which were on the order of several hundred µm in the surrogate setup and about 100 µm in the air bearing setup, repeated approximately every revolution. This can be seen in Fig. 24.4.

Though the shaft of the surrogate setup was hardened steel and the test article on the air bearing was rigidly fastened, these displacements were seen due to imbalances in the rotation. Such imbalances can be described by the eccentricity vector, which is the location of the center of mass of the object with respect to the axis of rotation. This eccentricity causes the rotating article to deviate away from the axis of rotation [5]. A shift in the center of mass of the article results in a change in the eccentricity vector and thus, in the displacement profile seen by a displacement sensor.

Cross-correlation calculations were employed to characterize how this profile changed when damage was introduced. Tests with the same mass orientations and damage analogs were expected to correlate well, while the damaged tests were expected to deviate from the undamaged tests. This method requires a high signal-to-noise ratio so that these deviations can be picked out from noise, which arises from sources such as surface irregularities, external vibrations, and movements of the displacement sensor.

24.2.6 General Notes

The low noise floor of the air bearing system was ideal for testing the LPC and laser proximity detection schemes. However, the delocalized nature of the damage rendered it unsuitable for testing the binning method of damage localization. The highly localized, uncoupled damage of the surrogate rig made it very helpful for testing our damage localization techniques. As such, the surrogate rig was primarily used for verification of the binning method of localization.

24.3 Results

24.3.1 Linear Predictive Coding

The LPC method described earlier was first applied to the time histories from the acoustic emission sensors. Then, speed information (angular speed vs. time) was added to the AE data. During data collection, the two datasets were synchronized by a trigger. This allowed them to be summed—at each timestep, the angular speed was added to the output from the AE sensor. The LPC process was then repeated on this combined signal. The results of these applications are show below. The damage parameter referred to here is defined in Sect 2.2 (Eq. 24.2) (Table 24.1). The dataset A in that equation is the AE signal (for the results in Table 24.2, the AE signal with the added speed data).

The acoustic emission output was also plotted as a function of the test article's angular position, resulting in data in the position domain. The same process was then repeated (before being added to the acoustic emission data, the speed data was also plotted as a function of position). The results are shown below (Tables 24.3 and 24.4).

Unfortunately, too few tests were completed to thoroughly assess the different detection methods. Any conclusions, then, must be qualitative.

Table 24.1 Damage parameter in time domain, speed data not added

	Sensor 1	Sensor 2	Sensor 3
Outer damage	571	755	1322
Inner damage	666	772	1148
Outer + center	498	567	461
All damage	262	329	348
Undamaged	331	470	453
Undamaged	213	418	373

Table 24.2 Damage parameter in time domain, speed data added

	Sensor 1	Sensor 2	Sensor 3
Outer damage	2053	2091	2404
Inner damage	860	932	1301
Outer + center	646	691	618
All damage	1355	1370	1375
Undamaged	331	445	459
Undamaged	602	679	678

Table 24.3 Damage parameter in position domain, speed data not added

	Sensor 1	Sensor 2	Sensor 3
Outer damage	582	770	1348
Inner damage	669	775	1153
Outer + center	522	595	483
All damage	559	703	743
Undamaged	331	470	453
Undamaged	231	453	405

Table 24.4 Damage parameter in position domain, speed data added

	Sensor 1	Sensor 2	Sensor 3
Outer damage	600	723	1410
Inner damage	694	783	1202
Outer + center	548	605	510
All damage	2866	2899	2911
Undamaged	331	445	459
Undamaged	235	415	412

The addition of the speed data, for both the time and position domains, seemed to improve the separation between the damaged and undamaged cases. This follows from the nature of the speed data. The undamaged test article has characteristic deceleration behavior—the LPC model reflects this. The introduction of simulated damage changes the deceleration trend, resulting in a worse-fitting model that gives larger residual errors and a higher damage parameter. In the "Speed Added" methods, the time and position domains seemed to detect damage comparably. While several of the damaged cases had a higher damage parameter in the time domain, the undamaged cases were more tightly spaced in the position domain. Taken as a whole, the position domain signals with speed added were most useful for detection using LPC. More extensive testing is required to validate these results in a statistically significant sense.

24.3.2 Damage Location Binning

The binning method was applied to AE sensor data in the position domain for both the surrogate and air bearing rigs. On the surrogate, this method indicated differences between two types of damage located π radians apart (i.e. located on opposite sides of the front side of the damage flywheel). Shown below in Figs. 24.5 and 24.6 are histograms of the AE sensor counts

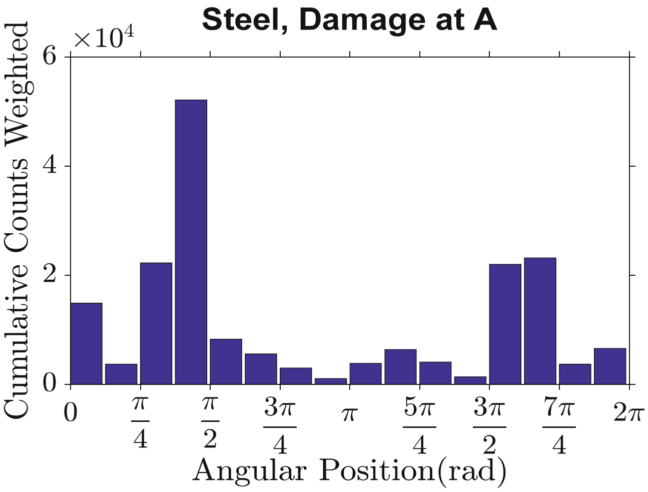

Fig. 24.5 Histogram of counts for loose steel ball in location a

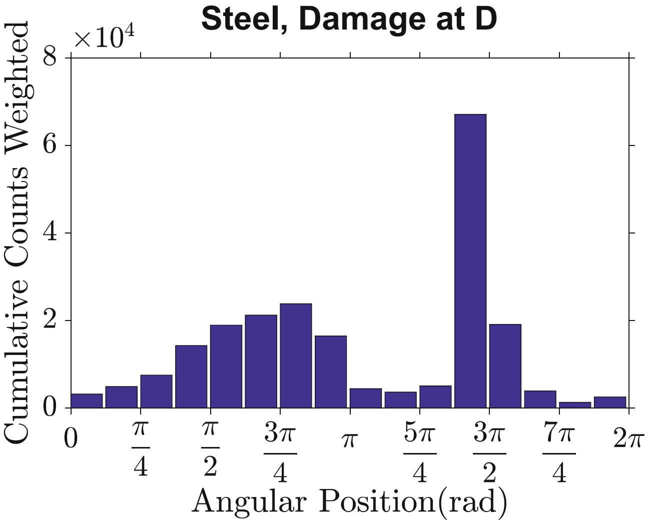

Fig. 24.6 Histogram of counts for loose steel ball in location d

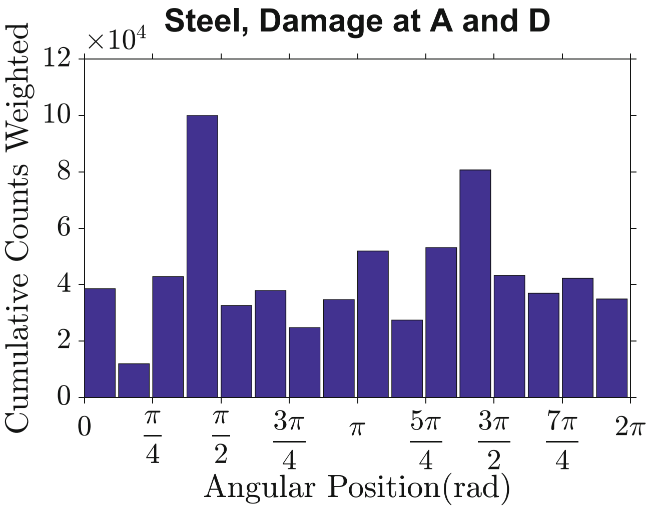

Fig. 24.7 Histogram of counts for loose steel balls in locations a and d

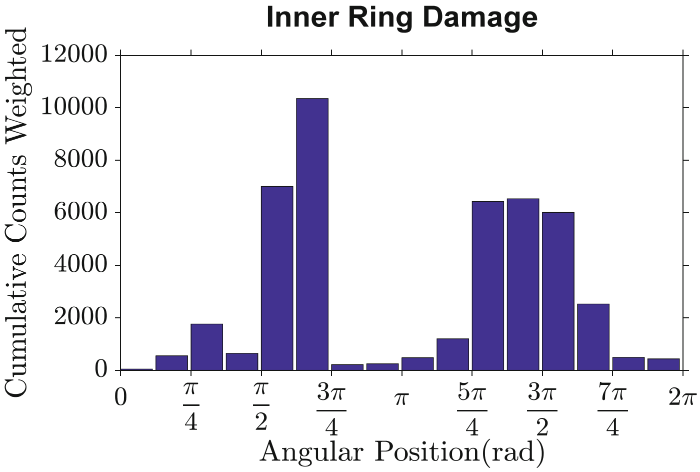

Fig. 24.8 Histogram of counts for loosened inner ring on top hat setup

in tests of damage at location "a" and at location "d" on the surrogate, as described in Fig. 24.2 in the Introduction. On the y axis, "Cumulative Counts Weighted" is the sum of the amplitudes of the counts in each angular position bin.

Based on the locations of a and d relative to the designated 0 position, AE sensor counts would be expected to occur between approximately 3π/8 and 5π/8 rad (i.e. when damage location a is at the bottom of the flywheel and damage location d is at the top) and between approximately 11π/8 and 13π/8 rad (i.e. when damage location a is at the top of the flywheel and damage location d is at the bottom). This is because gravity would cause the steel ball—the simulated damage—to impact the top or bottom of the coupling nut at these two locations. According to Fig. 24.5, the sensor response was greatest when the simulated damage was near the bottom of the flywheel—near π/2 rad. Similarly, the sensor response in Fig. 24.6 was also greatest when the simulated damage was near the bottom of the flywheel—near 3π/2 rad. Thus, the binning method demonstrated the difference between damage approximately π radians apart on the flywheel. Additionally, Fig. 24.7 below shows the results of a test done with damage at both location "a" and location "d."

This histogram is essentially a superposition of Figs. 24.5 and 24.6, with the two largest peaks occurring π radians apart. On the top hat setup, Fig. 24.8 below was obtained when the inner ring of the top hat was damaged.

After the test data was divided into four segments, further analysis revealed that the first two spikes on the right-hand side of Fig. 24.8 were in fact due to set screws falling out of the top hat, striking the setup, and causing large sensor responses. Thus, as expected, the spikes due to the simulated damage (between π/2 and 3π/4 rad and between 3π/2 and 7π/4 rad) are approximately π radians apart, indicating that the loose segments of the top hat impacted each other approximately twice

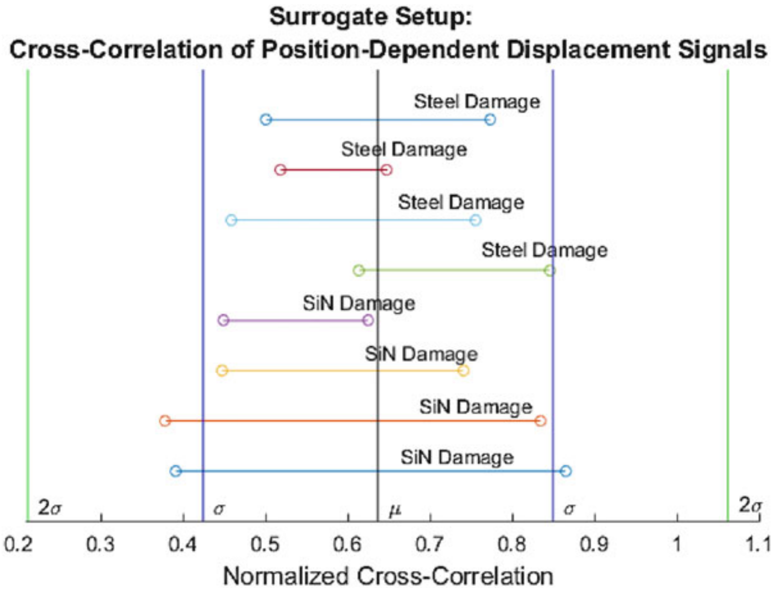

Fig. 24.9 Cross correlation of laser displacement signals on surrogate setup

per revolution. As with the LPC method, more data would be required to quantitatively assess the accuracy of the binning method. However, these tests on the surrogate setup showed potential for absolute damage localization and some knowledge of the extent of the damage when the technique was applied to the air bearing rig.

24.3.3 Out-of-Plane Displacement

The final analysis technique involved the data from the displacement sensors. When analyzing this data from the surrogate setup, the necessity of a high signal-to-noise ratio became clear. Factors such as the performance of the bearings contributed significantly to variability in displacement signals. In addition, the setup had several loose wires and other parts other than the controlled damage analogs that were allowed to shift slightly during and between tests. These uncontrolled variations also contributed to variability in the orientation of mass. The maxima of the cross-correlations of a baseline test with several other undamaged tests had high variance, as shown by the vertical lines in Fig. 24.9. This figure also shows the range of maxima of cross-correlation of the damage case signals with the undamaged signals, labeled by test number. This showed that the damage analog of a loose ball in a cylinder could not be detected with this technique on this setup.

The top hat setup had less uncontrolled variability in each test, along with a larger shifting mass in the damage case, which we expected to contribute to detection using this method. Cross-correlations were done on both the displacement vs. time and displacement vs. position signals.

The displacement vs. time data gave low correlations overall for all tests. This effect is due to the relative lengths of the different tests and corresponding compression or stretching of the signals in time. For example, the baseline tests spun the longest, while the tests with damage dissipated energy and decelerated more quickly. Since the displacement signature was periodic with angular position and not time, the correlation between the damage tests and baselines with respect to time was quite low. See Fig. 24.10 below for these results. This obvious deviation from the baseline is based heavily on the rate of deceleration during the test, which is the metric that has been used previously to detect damage. As seen in the figure, it is difficult to perform any characterization of the damage from these correlation results.

Displacement vs. angular position data, which showed periodic patterns, had greater correlations, but, similar to the surrogate setup, encountered difficulties from the signal-to-noise ratio. The undamaged signals did not have high correlation with the signals from the baseline test, and the range was large. Similarly, the cross-correlation of the damage tests with the baseline showed a large range which was not greatly separated from that of the undamaged tests. The laser displacement data therefore was unable to relate shifts in the center of mass to damage state for the articles tested.

The low correlation of the signals across undamaged tests shows that the laser displacement sensor did not obtain consistent displacement signatures from cases which we expected to exhibit similar eccentricities. Little can be said from

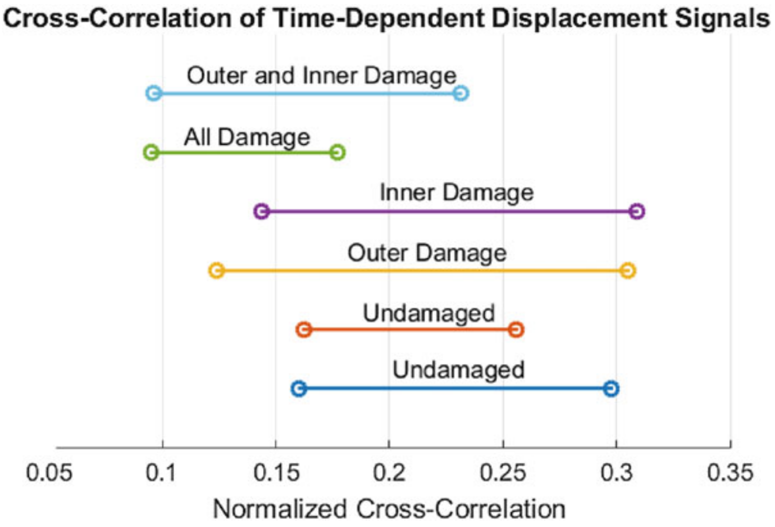

Fig. 24.10 Cross correlation of laser displacement signals on top hat setup

our results about whether this expectation was correct or not, as the variability of the signals could be attributed to factors including external movement or vibrations or nonuniformities in the test article surface. To determine whether out of plane displacement due to shifts in mass can be observed at the speeds of the tests, more tests are needed, with the laser thoroughly secured so that movement between tests and vibration during tests are minimized. The surface of the article should also be prepared with a uniform, nonreflective surface around the entire circumference of the article to be used as the displacement reference surface. Finally, a more precise displacement measurement device, such as a laser doppler vibrometer, may be required. With these tests, similar cross-correlation analyses could show the effectivess of measurement of the displacement signature, revealing a change in eccentricity.

If a change in eccentricity can be observed by the displacement sensor, for localization of damage, the next step would be to place another displacement sensor 90° from the first to obtain two-dimensional displacement information. If the article can be modeled, the differential equations describing this two-dimensional motion can be solved to obtain an eccentricity vector, which can give the location of the center of mass to help localize damage. This modeling approach was presented and implemented in a simulation by Gyekenyesi et al. [5].

24.4 Conclusions

Each technique used in this study—linear predictive coding, the binning method, and cross correlation of the laser displacement data—applied new techniques to spin-down testing. LPC validated the use of spin-down testing for damage detection, as including rotational information improved the detection result. A denser array of AE sensors might allow this technique to be used for localization as well by comparing the damage parameter across sensors at different locations. The binning method provided basic angular localization and distinguished between different types of damage. Again, however, more data is needed to determine the absolute location of the damage. Finally, while the laser proximity cross-correlations were inconclusive, the method could be improved by refining the sensor setup, and useful information could be gained by implementing a second sensor above the test article. This method could then be used in conjunction with the binning method for improved localization. The methods presented here do not represent a fully-developed nondestructive evaluation method, but provide strong starting points for further research into spin-down testing.

Acknowledgments This work is approved for public release and distribution is unlimited under LA-UR-15-28240. The authors would like to acknowledge the support of John Bernardin, Jack Gioia, and Matthew Fagan for their help with the air bearing testing. This project was funded through the Los Alamos Dynamics Summer School program of the Los Alamos National Laboratory under the direction of Charles Farrar.

References

1. Kundu, T., Source, A.: Localization. Ultrasonics **54**(1), 25–38 (2012)
2. Coverley, P.T., Staszewski, W.J.: Impact damage location in composite structures using optimized sensor triangulation procedure. Smart Mater. Struct. **12**(5), 795–803 (2003)
3. Farrar, C.R., Doebling, S.W., Nix, D.A.: Vibration-based structural damage identification. Philos. Trans. A **359**(1778), 131–149 (2001)
4. Masmoudi, S., El Mahi, A., Turki, S.: Use of piezoelectric as acoustic emission sensor for in-situ monitoring of composite structures. Compos. Part B **80**, 307–320 (2015)
5. Gyekenyesi, A., Sawicki, J.T., Haase W.C.: Modeling disk cracks in rotors by utilizing speed dependent eccentricity. J. Mater. Eng. Perform. (Springer, New York) **19**(2), 207–212 (2010)

Chapter 25
Performing Direct-Field Acoustic Test Environments on a Sandia Flight System to Provide Data for Finite Element Simulation

Eric C. Stasiunas, Ryan A. Schultz, and Mike R. Ross

Abstract Aero-acoustic loading has been established as the primary source of excitation for a Flight System at Sandia National Laboratories. However, flight data of this system does not exist, limiting estimations of system or component response in this environment. Therefore, an experimental acoustic simulation was performed on a heavily-instrumented Flight System, using the direct-field acoustic test (DFAT) method with a multi-input multi-output (MIMO) control system. The combination of DFAT and MIMO resulted in attaining uniform and gradient acoustic fields as high as 127 dB OASPL. This paper will discuss the design of the test, the speaker and controller configurations, and the test results of this unique test method. Additionally, an overview of the method used to apply the measured test data to the pressure-loading finite element simulations of the Flight System will be discussed as well.

Keywords Direct-field acoustic testing (DFAT) • Multi-input multi-output (MIMO) control • Model validation • Uniform /gradient field • Acoustic finite element modeling

25.1 Introduction

At Sandia National Laboratories, response predictions are required of a Flight System under yet-to-be-flown aero-acoustic loading environments. These predictions are required to inform component designers of environment specifications in advance of future flight tests. Additionally, flight tests suffer from a lack of instrumentation and often do not explore the entire design envelope of the Flight System. As such, making response predictions with a high-fidelity finite element model is desirable.

The response predictions of the Flight System are performed using a structural dynamics (SD) model in a pressure-loading scenario. Typically, the SD models are calibrated/validated in single-axis, point force input cases. However, flight loads are a combination of vibration inputs from the aircraft/system interface *and* aeroacoustic loading from aircraft noise and flow-generated pressure fluctuations. An acoustic ground test was desired because it better replicates this loading scenario, more so than an experimental modal or random vibration test. Acoustic test results would provide both model assessment data as well as an experimentally derived model that could be used to estimate component responses based on acoustic pressures in the surrounding field.

The details of the acoustic ground tests are the primary focus of this paper, which includes the design of test, the acoustic excitation method, the closed-loop controller configurations, and the resulting acoustic fields achieved. The test technique used is fairly unique and justified an in-depth discussion. The structural responses of the Flight System are only briefly discussed, as is the method used to apply the test data to the acoustic and structural dynamics models.

Sandia National Laboratories is a multi-program laboratory managed and operated by Sandia Corporation, a wholly owned subsidiary of Lockheed Martin Corporation, for the U.S. Department of Energy's National Nuclear Security Administration under contract DE-AC04-94AL85000.

E.C. Stasiunas (✉) • R.A. Schultz • M.R. Ross
Sandia National Laboratories, Albuquerque, NM, USA
e-mail: ecstasi@sandia.gov

© The Society for Experimental Mechanics, Inc. 2016

J. De Clerck, D.S. Epp (eds.), *Rotating Machinery, Hybrid Test Methods, Vibro-Acoustics & Laser Vibrometry, Volume 8*,
Conference Proceedings of the Society for Experimental Mechanics Series, DOI 10.1007/978-3-319-30084-9_25

25.2 DFAT with MIMO Control

Direct-field acoustic testing (DFAT) is an acoustic test method that consists of exciting a test item the direct acoustic field—the portion of the field in which sound waves have not undergone any reflection—of a sound source. In practice, the direct field is created by surrounding a test article with a wall of specially modified concert-style loudspeakers, and placing multiple control microphones in-between the test article and speakers. A closed-loop control system uses the control microphone measurements to adjust the speaker outputs in order to obtain the desired test specification. Multiple response microphones are placed around the test item to better characterize the acoustic field [1].

When applying multi-input multi-output (MIMO) control to DFAT, the multiple independent controls and corresponding drives of the control system allow for detailed tailoring of the resulting acoustic field. Since each control microphone has an independent test specification as well as a defined phase and coherence between them, it is possible to create both uniform acoustic fields and shaped acoustic fields, depending on the control parameters. The uncorrelated outputs used in MIMO control have also been shown, in analytical models and in experiments conducted in the industry, to reduce both standing waves and spatial variability in the resulting acoustic field, which is highly desirable for hardware safety and realistic acoustic environment simulation [2, 3].

25.3 Test Design

Sandia's current acoustic test system consists of twelve MSI VT-99 speaker cabinets and six MSI VS-Q speaker cabinets. The VT-99 cabinets contain low, mid, and high frequency speakers and are driven by six acoustic amplifiers circuits; the VS-Q cabinets contain low frequency speakers and are driven by 3 acoustic amplifier circuits. In the large-scale Sandia reverberation chamber, this acoustic system is capable of achieving an overall sound pressure level (OASPL) of approximately 146 dB. Outside of the reverberation chamber in a DFAT configuration, levels of 136 dB OASPL have been achieved. While this DFAT level is much lower than the realistic acoustic loading environment, it was still a desirable test method due to the ability to obtain shaped acoustic fields, which is difficult to achieve in a reverberation chamber (due to acoustic reflections).

With the given number of speakers and independent drives available, analytical simulations were performed to determine the optimal test configuration. Vertical and horizontal test item orientations were examined as well as various speaker stack configurations. Simulation output data in the form of acoustic sound pressures levels (SPL) throughout the stack volume, as shown in Fig. 25.1a, was analyzed to assess any spatial dependence of sound pressure level. The final design, a vertical test article surrounded by an octagon of speaker stacks with reflective panels between speakers as illustrated in Fig. 25.1b, was chosen because this allowed for a fairly even field in the angular direction while allowing for a length-wise gradient by

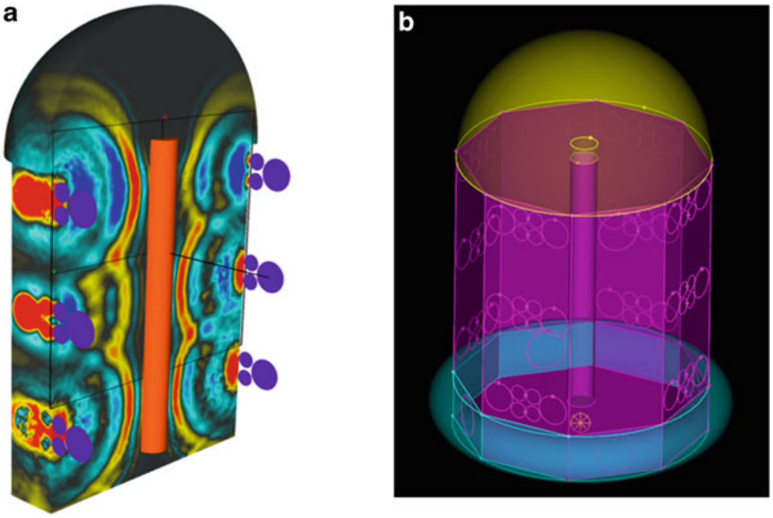

Fig. 25.1 (**a**) Pre-test analysis SPL and (**b**) final test design

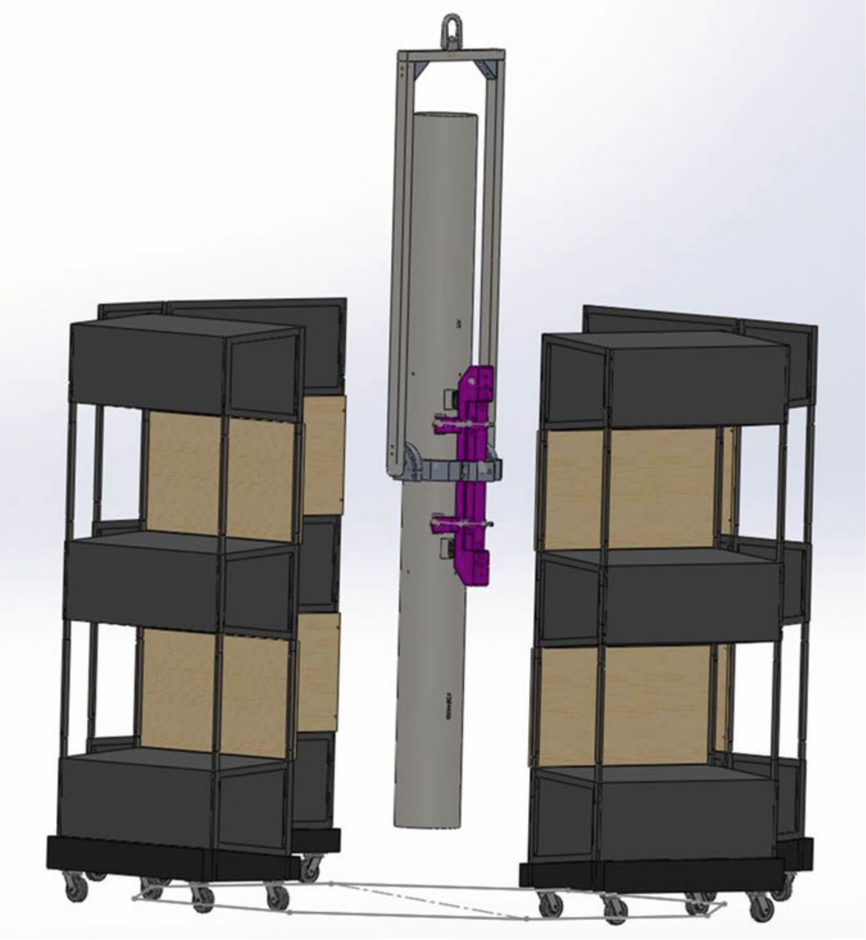

Fig. 25.2 Sandia Flight System and speaker configuration

controlling the top speaker row to a different test specification than the bottom two speaker rows. Reflective panels on the sides of the octagonal stack increased the overall level inside the stack and provided some additional smoothing of the field in contrast to a design with open walls.

25.4 Test Setup

As discussed in the test design analysis results, the DFAT configuration consisted of suspending the Flight System vertically in the center of a 10-foot diameter octagon of speakers, 1 foot above the floor. Four towers of the VT-99 cabinets (low-mid-high frequencies) were stacked three high and placed 90-degrees apart, as shown in the simplified diagram of Fig. 25.2. In order to provide more speaker coverage along the length of the Flight System, 2-foot long extension bars were installed in-between the short VT-99 cabinets, resulting in an 11-foot high stack. The six VS-Q subs (low frequency speakers) were stacked alternating one and two high, and were placed on the floor at the 45-degree locations (not shown in diagram). Analysis determined that the low frequency VS-Qs were not as location-dependent as the VT-99s. The reflective panels required by the test design were provided by ¾-inch thick plywood, installed in the open spaces of the speaker configuration, such as on the extension bars between the VT-99s, and the space above the VT-Qs. Adding panels between loudspeaker cabinets was predicted to increase the overall sound pressure, though the increase in reflection may affect the ability of the control system to achieve high spatial pressure gradients.

The Flight System was suspended using a specially-designed test fixture that incorporated a pivot joint near the center of gravity of the test item, when suspended by a strongback (shown in as purple in Fig. 25.2). With this fixture, instrumentation could be attached to the Flight System in a horizontal configuration at a comfortable working height. Once ready for testing,

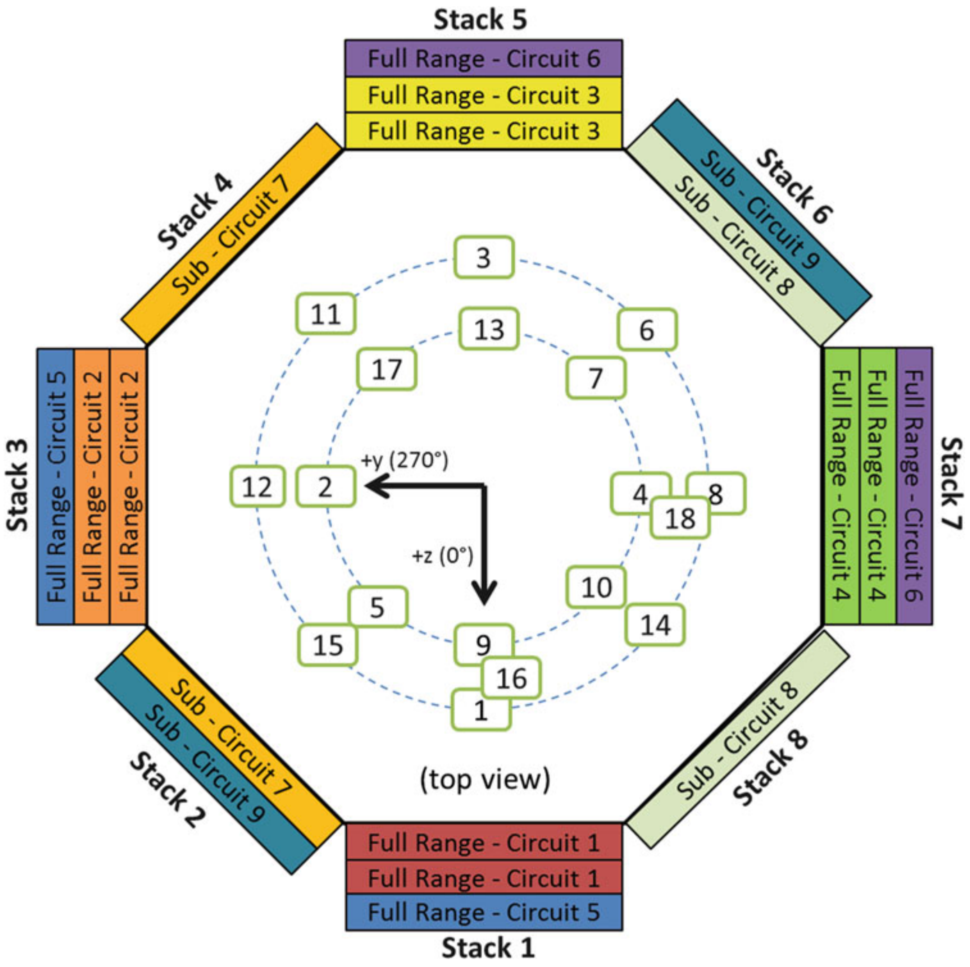
Stack 5
Full Range - Circuit 6
Full Range - Circuit 3
Full Range - Circuit 3
Stack 6
Sub - Circuit 9
Sub - Circuit 8
Stack 7
Full Range - Circuit 6
Full Range - Circuit 4
Full Range - Circuit 4
Stack 8
Sub - Circuit 8
Full Range - Circuit 1
Full Range - Circuit 1
Full Range - Circuit 5
Stack 1
Stack 2
Sub - Circuit 7
Sub - Circuit 9
Stack 3
Full Range - Circuit 5
Full Range - Circuit 2
Full Range - Circuit 2
Stack 4
Sub - Circuit 7
3
11
13
6
17
7
12
2
+y (270°)
4
8
18
+z (0°)
10
5
14
15
9
16
1
(top view)

Fig. 25.3 Microphone and speaker circuit placement

an overhead crane was used to lift the entire assembly high enough to rotate the test unit into a vertical configuration, and place it at the center of the speaker stacks, 1 foot above the floor. Casters installed on the VT-99 speaker stacks allowed for easy opening and closing of the speaker enclosure.

Acoustic instrumentation for the Flight System DFAT consisted of a total of 18 microphones, located no closer than 3-ft to the speakers in order to measure a more uniform sound field, and no closer than 1-ft to the test article to reduce microphone distortion due to reflections and surface effects (per standard DFAT practices [1]). Microphone heights varied from 2-ft to 11-ft above the floor. The exact locations of the individual microphones, represented by the green squares, are shown in the top-view diagram of Fig. 25.3 and listed in Table 25.1. Pre-polarized ¼-inch diameter pressure-field microphones were used for this test, with sensitivities ranging from 0.7 mV/Pa to 1.2 mV/Pa.

The diagram of Fig. 25.3 also displays the individual speaker cabinets that make up each speaker stack along with their corresponding amplifier circuits. In this diagram, Full Range cabinets represent the VT-99s which contain low-mid-high speakers, and the Sub cabinets represent the VS-Q low frequency speakers. The speakers are stacked as the radius increases out from the center—for example, Stack 1 consists of a Full Range—Circuit 1 cabinet on the bottom, a Full Range—Circuit 1 cabinet in the middle, and a Full Range—Circuit 5 cabinet on the top.

Each of these amplifier circuits was driven by an independent output from the MIMO control system which was determined by a corresponding control microphone placed nearby. If placed too far away, there was a potential of speaker damage due to the control system outputting more voltage than speaker could withstand in order to reach the desired specification. Therefore, as seen in the diagram, control microphones (Microphones #1–6) were placed near their associated speaker circuits and at various heights to aid in achieving the acoustic field gradient. The remaining response microphones (Microphones #7–18) were placed randomly in the field.

As mentioned previously, the test was designed with six independent speaker circuits/control system drives, which accounts for the twelve Full Range cabinets (two cabinets per circuit). In order to supplement the low frequency portion

Table 25.1 Microphone coordinate locations

Mic. (Ch #)	Radius (in)	Angle (deg.)	Height (feet)
1	24	0	3
2	18	270	5
3	24	180	4
4	18	90	7
5	18	315	10
6	24	135	11
7	18	135	6
8	24	90	9
9	18	0	8
10	18	45	6
11	24	225	7
12	24	270	10
13	18	180	8
14	24	45	11
15	24	315	4
16	21	0	5
17	18	225	7
18	21	90	2

of the test specification, the six Sub cabinets driven by 3 additional independent speaker circuits, were integrated with the six main drive circuits using an acoustic mixer (Circuit 7 added to Circuit 1 and 3, Circuit 8 added to Circuit 2 and 4, and Circuit 9 added to Circuit 5 and 6).

Accelerometers were used to measure the structural response of the Flight System due to the simulated acoustic environment. A total of 84 internal and 75 external locations were instrumented with both uni-axial and tri-axial accelerometers, ranging in sensitivity from 100 mV/g to 100 mV/g. Twelve channel gather boxes were used to collect both the microphone and accelerometer data from the center of the speaker circle and transmit them to external signal conditioners. The completed test setup is shown in Fig. 25.4; the external accelerometers (red cables), the microphones, the speaker stacks, the plywood panels, and the 12-channel gather boxes can all be seen in the photo.

25.5 Test Environment

The test specification used in the laboratory ground tests to simulate the aero acoustic loads is shown as 1/6-octave bands in Fig. 25.5. While the desired test environment was much larger in magnitude, acoustic test equipment limitations (speaker/amplifier output, number of speakers) resulted in scaling down this test specification to approximately 127 dB OASPL. In addition to the test specification, the coherence and phase values were defined in the MIMO control system as well. The defined coherence values determined how close the resulting phase was to the defined phase values. With a 0-degree phase for example, a high coherence test should result in phases very close to 0-degrees; alternately, a low coherence test should result in a random phase (not 0-degrees). With the test specification and various MIMO control parameter settings, four different acoustic fields were applied to the Flight System, defined as Truth Tests #1–4.

The first two tests consisted of a uniform field, where the same test specification was used at each control location. The coherence between control locations was set with a high coherence (0.9) for Truth Test #1, and a low coherence (0.1) for Truth Test #2; the phase for both tests was set to 0-degrees. The goal of this test was to determine if the uncorrelated random phase, provided by the low coherence, would reduce spatial variability in the acoustic field. Past acoustic tests, performed with a single correlated (high coherence) drive exhibited strong positive and negative interference, resulting in very large spatial variability [4].

The next two tests attempted a gradient field, where the aft end of the Flight System would experience the test specification and the forward end would experience the test specification scaled down 6 dB. This gradient was desirable, as it simulates a realistic acoustic loading scenario. To achieve this gradient with the MIMO control system, the nominal test specification was applied at the control locations/speaker circuits at the bottom of the speaker stack (Microphones #1–4); the nominal test specification scaled by −6 dB was applied to the control locations/speaker circuits at the top of the speaker stack (Microphones #5–6). As with the first set of tests, both a high coherence (0.9) was used for Truth Test #3, and a low coherence (0.1) was used for Truth Test #4.

Fig. 25.4 Sandia Flight System DFAT setup

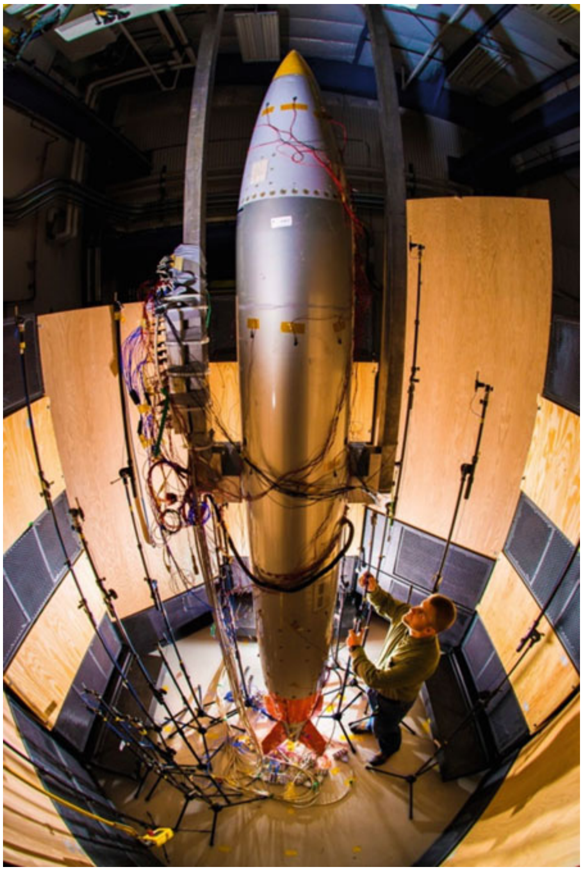

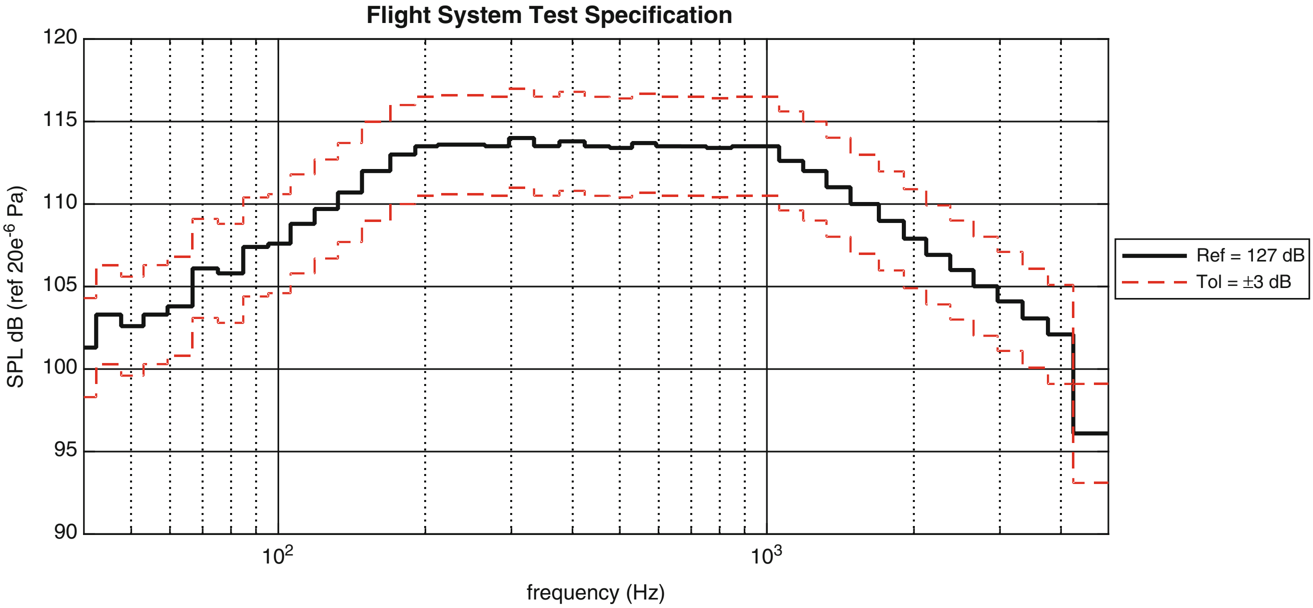

Fig. 25.5 Sandia Flight System acoustic test specification (127 dB OASPL)

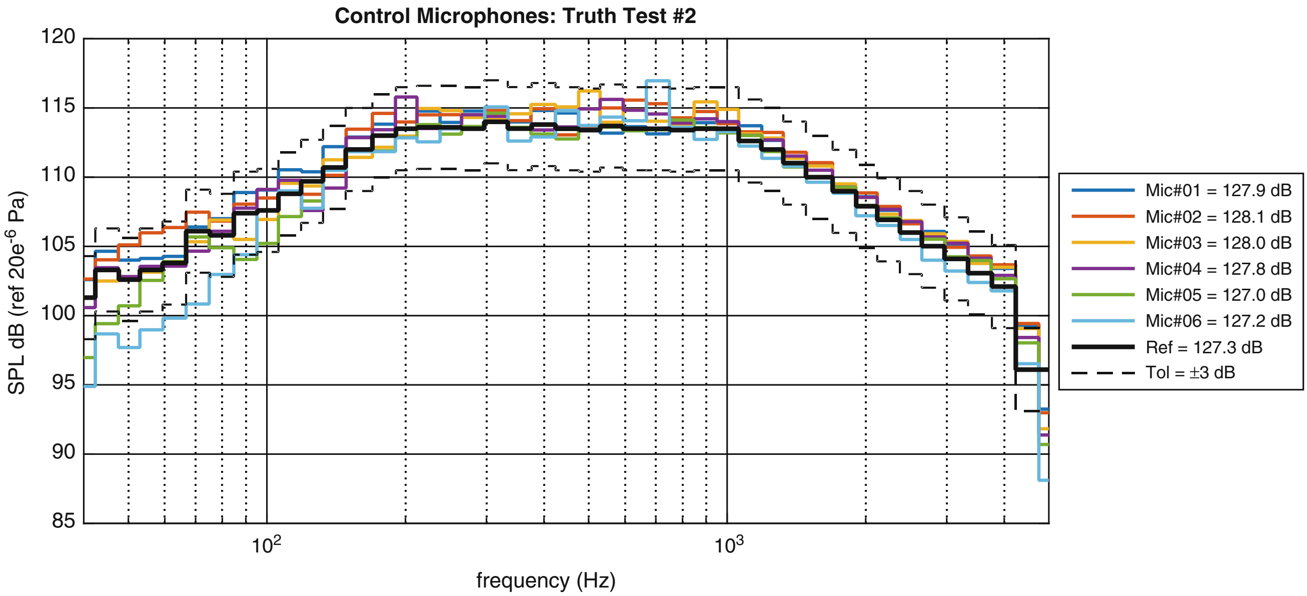

Fig. 25.6 Truth Test #2 control microphone sound pressure levels

25.6 Test Results: Truth Test #2

For the sake of brevity, this paper will plot only the acoustic field test results for Truth Test #2 (uniform field, low coherence) and Truth Test #4 (gradient field, low coherence), although comparisons to Truth Test #1 (uniform field, high coherence) and Truth Test #3 (gradient field, high coherence) will be discussed. Additionally, the structural response data will not be shown, as this paper is primarily focused on the unique DFAT MIMO test technique applied to the Flight System and the resulting acoustic fields.

Truth Test #2 consisted of a uniform field by applying the test specification at all the control microphone with a low coherence value (0.1) and phase of 0-degrees between control locations. The resulting 1/6th octave sound pressure levels for the six control microphones, along with the test specification (reference) and recommended ±3 dB tolerance, are shown in Fig. 25.6; the OASPL values are listed in the legend for each microphone. The control microphones were all within the frequency band tolerance except for Microphone #6, which was below tolerance up to 100 Hz (and above at 700 Hz). Microphone #5 was also low relative to the test specification at low frequencies. Also seen in Truth Test #1, the low SPL of these two microphones was thought to be due to their location (10–11 feet above the floor) relative to the VS-Q sub speaker cabinets placed on the floor. The OASPL levels for all control microphones are similar as well, with the two control microphones located at the top of the stack (Microphone #5 and #6) being slightly lower in magnitude.

The 1/6th octave SPL for the 12 response microphones are shown in Fig. 25.7, along with the test specification (reference), the ±3 dB tolerance, and the OASPL values. The response microphones are larger in magnitude and vary much more than the control, especially for frequency bands 180 Hz and above. While some difference from the control specification was expected for these non-control locations, the general increase in level for all response microphones was interesting and will be discussed in a subsequent section. When compared to the response microphones of Truth Test #1 (high coherence), which were also larger in magnitude than the control, the low coherence control MIMO parameter setting did not seem to reduce the spatial variability as expected. This may be due to the physical speaker stack configuration or the lack of full speaker coverage in the stack; it may not be physically realizable to reduce the spatial variation in this configuration. Finally, when comparing the individual response microphone OASPL values, they are almost equal to the Truth Test #1 values, and ranged from 131.7 dB to 136.4 dB, about +4 dB to +9 dB higher than the test reference.

The mean, maximum, and minimum of the SPL for the control and response microphones were calculated for each 1/6th octave band and plotted in Fig. 25.8. The plot clearly shows the accuracy of the control microphones, as well as the amplification and spread of the response microphones that occurs at 180 Hz and above. Comparing the spatial variabilities of Truth Test #1 and Truth Test #2, the low coherence MIMO parameter reduced the variability at some frequency bands, but not others.

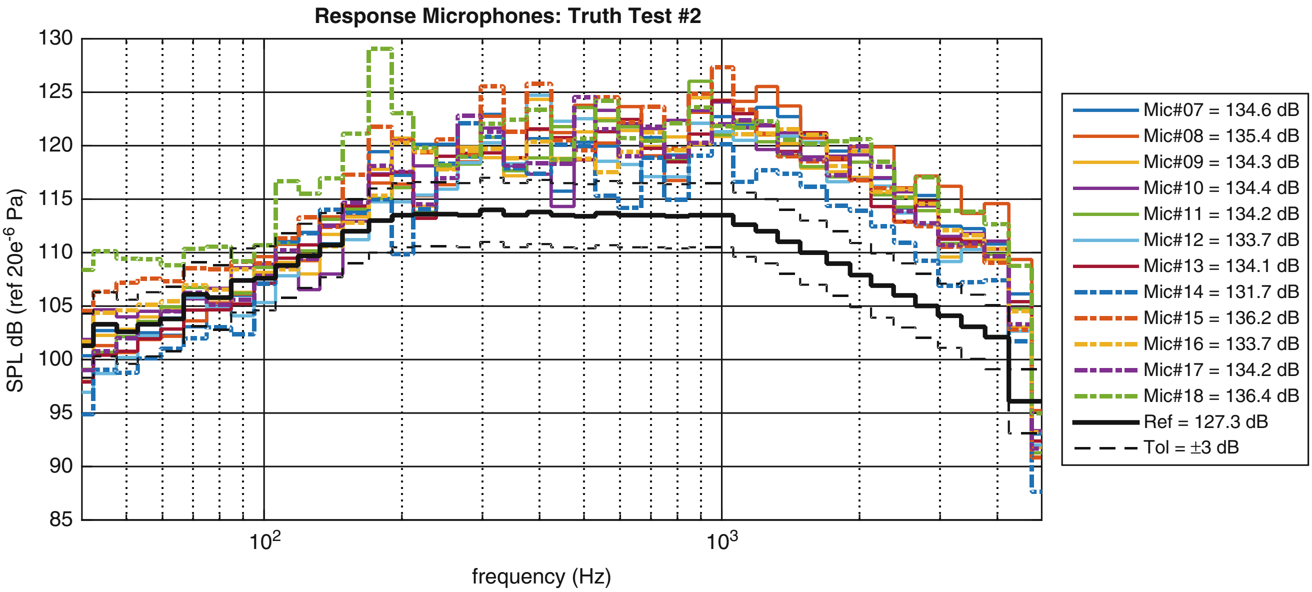

Fig. 25.7 Truth Test #2 response microphone sound pressure level

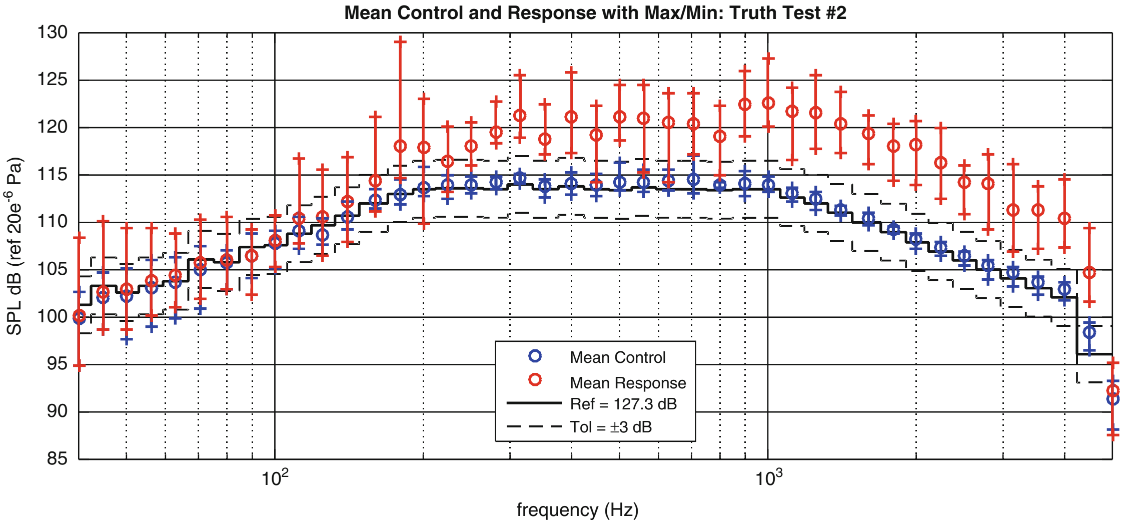

Fig. 25.8 Truth Test #2 mean, maximum, and minimum SPL (control and response)

In order to better visualize the overall shape of the resulting acoustic field, the calculated OASPLs for each microphone are plotted versus microphone height in Fig. 25.9. It must be mentioned that the OASPL is one number that describes the total energy contained in the SPL spectrum; therefore this plot should only be used for a general, simplified view of the acoustic field. The shape of the control microphones is somewhat uniform as expected, while the response microphone levels seem to decrease from the bottom of the setup to the top.

25.7 Test Results: Truth Test #4

The Truth Test #4 consisted of a shaped, gradient acoustic field by applying the test specification to the lower control microphones located near the aft end of the Flight System (Microphones #1–4), and applying the test specification scaled −6 dB to the upper control microphones located near the forward end of the Flight system (Microphones #5–6). A low coherence value (0.1), and a phase value of 0-deg was used between all control microphone locations.

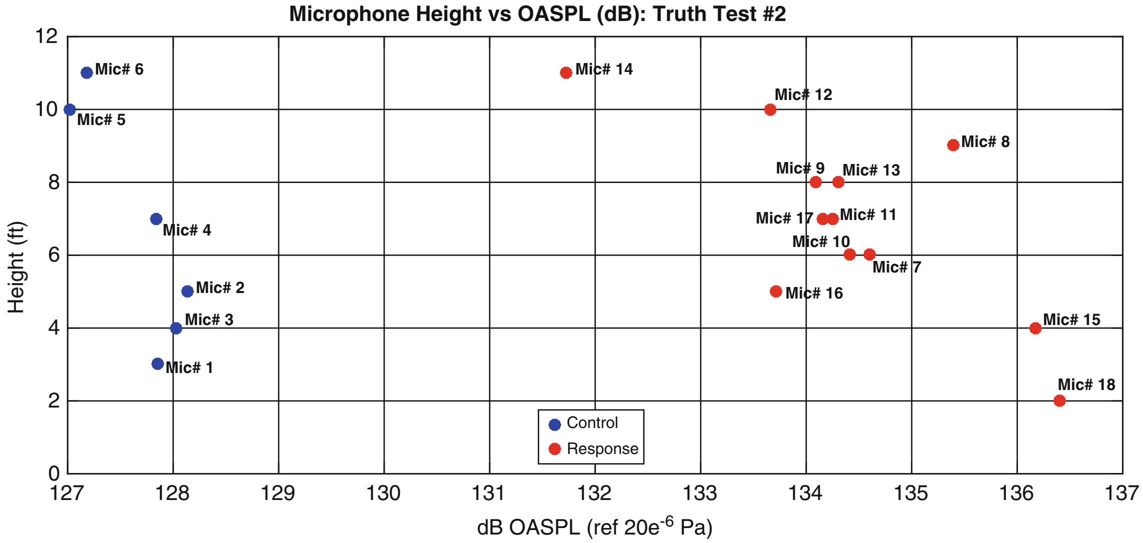

Fig. 25.9 Truth Test #2 OASPL versus microphone height

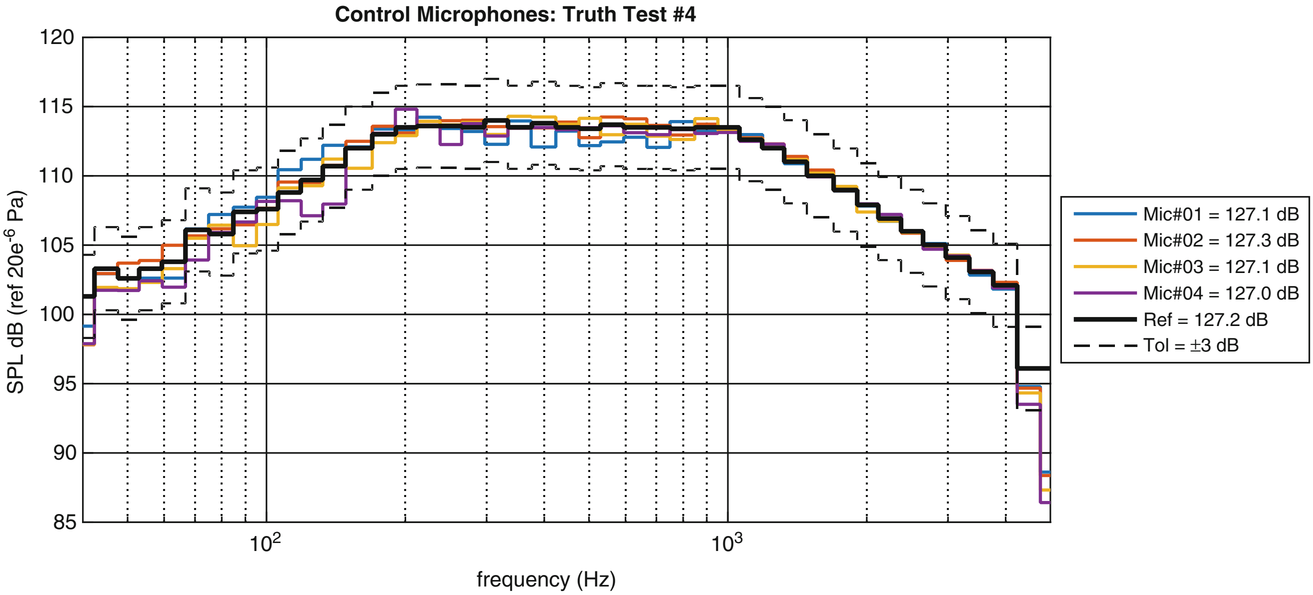

Fig. 25.10 Truth Test #4 control microphone aft end (mic #1–4) SPL

Since there were two test specifications used for this testing depending on control microphone location, two separate 1/6th-octave SPL control microphone plots are shown. The results for the lower control microphones located near the aft end of test unit are shown in Fig. 25.10; the results for the upper control microphones located near the forward end of the test unit are shown in Fig. 25.11. The test specifications, the recommended ±3 dB tolerance lines, and OASPL are shown as well.

The aft end control microphone data shown in Fig. 25.10 indicates the control SPL was within tolerance over the entire test spectrum. The forward-end control microphones data shown in Fig. 25.11 indicate that the SPL was consistently higher than the reference and exceeded tolerances at a few frequency bands. When comparing this data to the Truth Test #3 data (high coherence), the spread in control microphone data was much less, which may be due to the low coherence value used for Truth Test #4 control.

The higher-than-desired levels of the forward-end microphones indicate that controlling a shaped field with a 6 dB gradient may have been too ambitious for this particular test setup; the reflective panels, control microphone locations, and speaker stack configuration may have contributed to the inability to reduce acoustic levels on the forward end. If the OASPL levels are examined, they indicate a 4 dB gradient present in the acoustic field. Therefore, for this test setup, if the control system

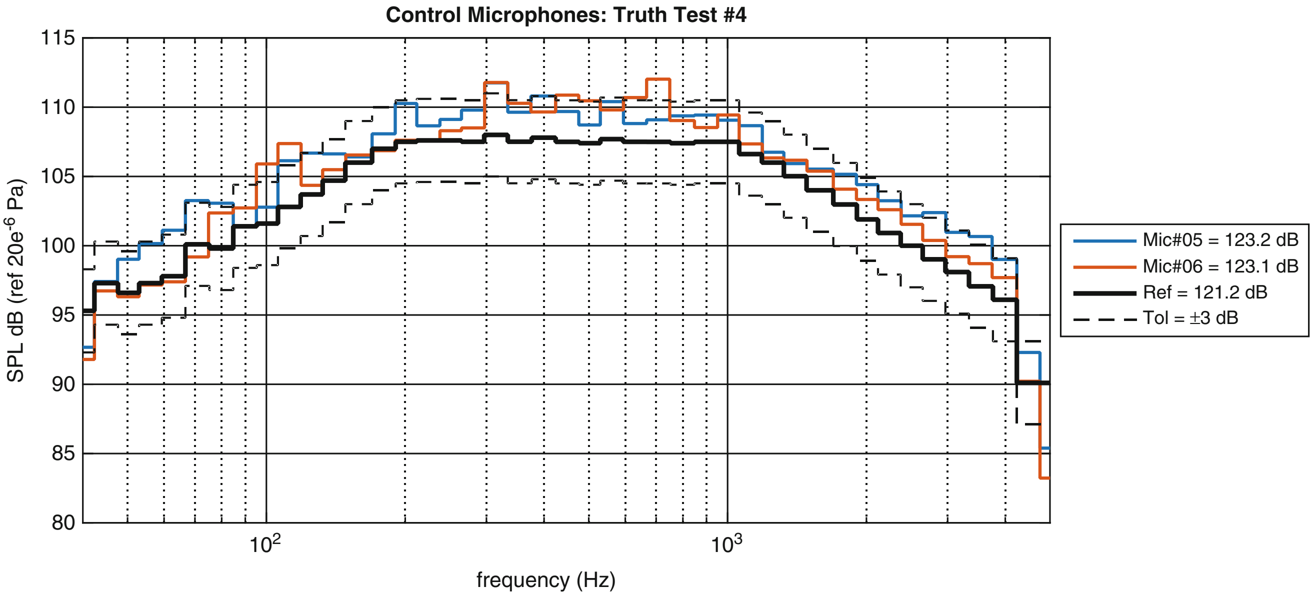

Fig. 25.11 Truth Test #4 control microphone forward end (mic #5–6) SPL

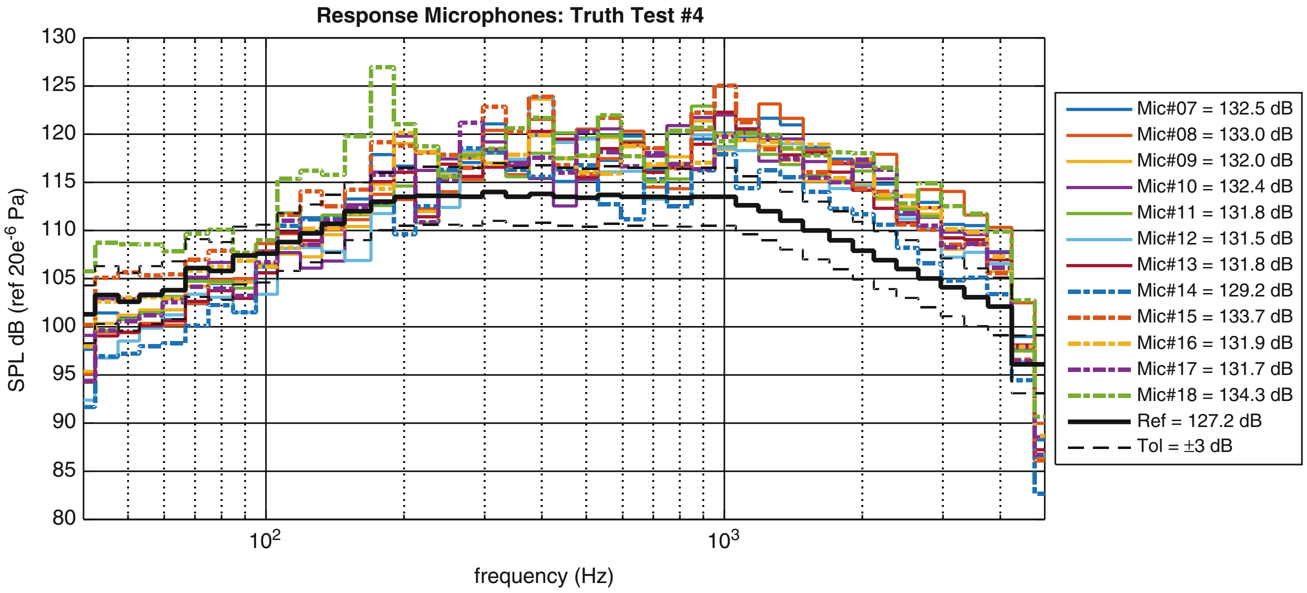

Fig. 25.12 Truth Test #4 response microphone sound pressure level

specification gradient had been 4 dB or lower, then the control microphones at the forward end may have been closer to the desired values.

The 1/6th-octave SPL for the 12 response microphones are shown in Fig. 25.12, along with the test specification, the ±3 dB tolerance lines, and the OASPL values. Because of the gradient control specification used for this test, this response data should be expected to have more spatial variability than the Truth Test #1 and #2 results. While not directly comparable to the Truth #2 response data due to the gradient control, it should be noted that the Truth Test #4 response data illustrates a similar offset of +5 dB to +7 dB relative to the control.

The shape of the acoustic field due to the gradient test specifications can clearly be seen in the OASPL versus microphone height data shown in Fig. 25.13. The control microphones are well-grouped by location (maximum difference of 0.4 dB), better than the Truth Test #1 and #2 (maximum difference of 1.5 dB), although that may be primarily due to control

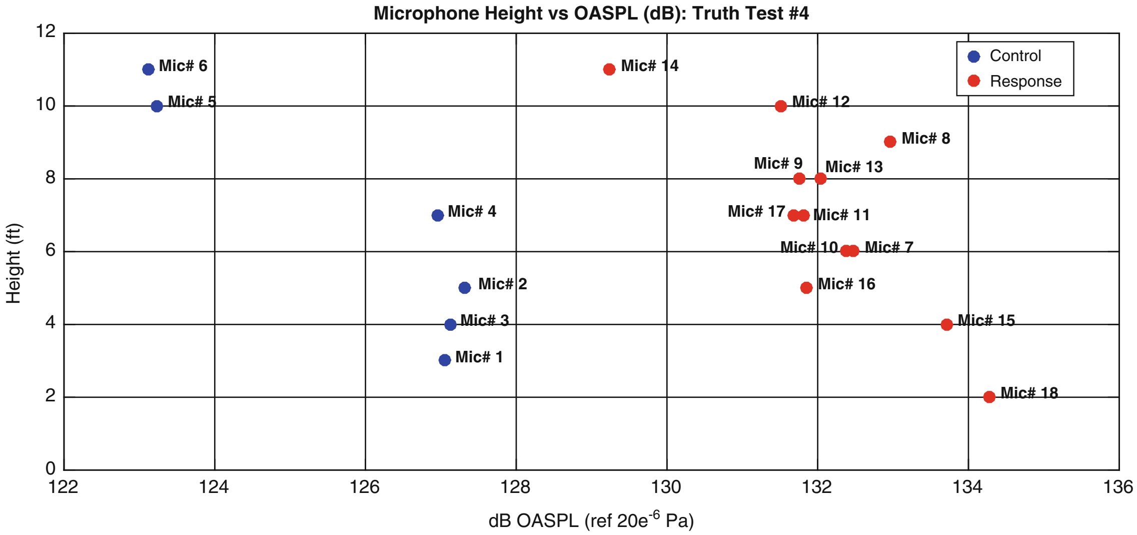

Fig. 25.13 Truth Test #4 OASPL versus microphone height

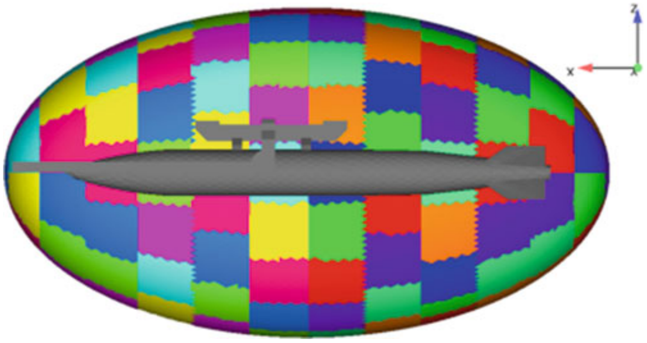

Fig. 25.14 Acoustic finite element subdomain

microphone location relative to the speakers. The response microphones have a larger range as expected, but only by approximately 1 dB, resulting in a gradual shaped acoustic field.

25.8 Test Data Applied to Acoustic Finite Element Simulation

A motivation for performing the laboratory acoustic tests was to provide data for the Sandia structural dynamics finite element model for acoustic loading. The loads on the structural dynamics model in this case are pressures on the external surface. As measuring on-surface pressures during the DFAT test was not possible, an acoustic source inversion methodology was employed wherein experimentally measured pressures (microphone pressures) are used to determine the loads on an acoustic finite element model—an ellipsoidal subdomain of the acoustic test environment from the test, as seen in Fig. 25.14. A benefit of this subdomain approach is a large savings in computational cost; the volume of the subdomain is about 2.5 times smaller than the as-tested acoustic volume (10-foot diameter speaker stack octagon). However, this method eliminates the true sources and boundary conditions from the experiment and instead relies on a large number of representative sources on the outer surface of the subdomain, indicated as multi-colored patches in the figure. Ultimately, the acoustic source inversion simulation determines acoustic acceleration loads for each of these patches, which generate a field at microphone locations that match the target data, in this case the as-tested microphone pressures [5, 6].

Results of the source inversion simulations provided excellent agreement with the test pressures at the test microphone locations. As the acoustic finite element model includes a void for the Flight System, wetted surface pressures on the Flight System can be extracted from the acoustic simulation. These wetted surface pressures are then applied to the structural dynamics model of the flight system to obtain predictions for system and component acceleration response to this acoustic

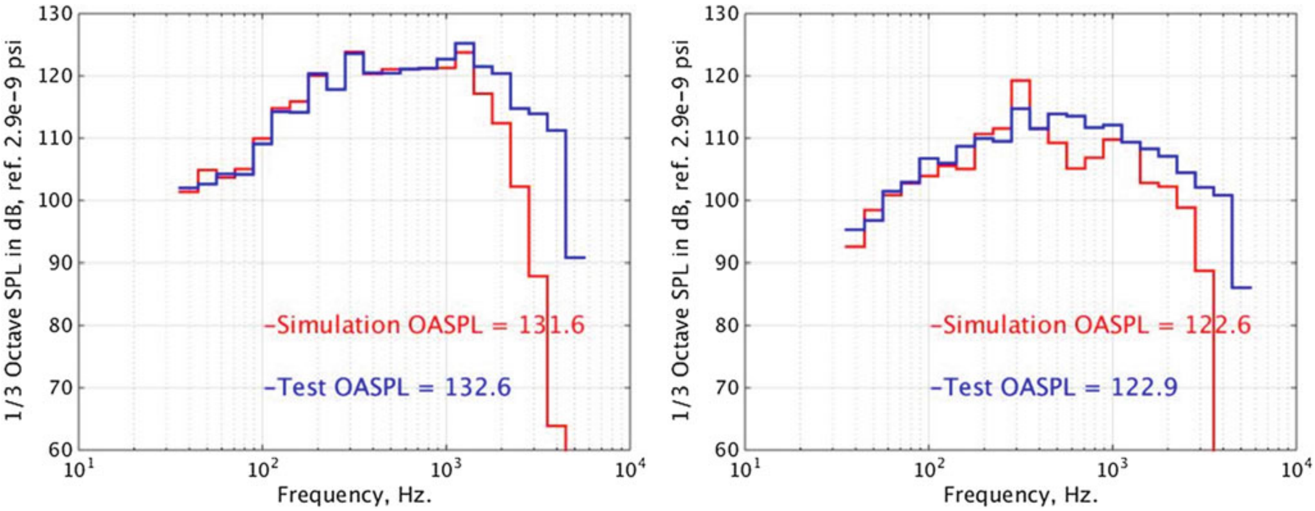

Fig. 25.15 Response microphone #7 (*left*) and control microphone #6 (*right*)

field. Simulated accelerations were then compared with the accelerations measured in the DFAT test to assess the model in this acoustic environment.

25.9 Response Microphone Examination

As noted in the test results, the response microphone for all Truth Tests measured anywhere from 4 dB to 9 dB larger in magnitude than the control microphones. Analysis of noise floor measurements verified that there was no bias error due to erroneous test setup; the noise floors were nominally the same for the control and response channels. Therefore, it was hypothesized that the amplification of the acoustic field at the response locations must have been a real occurrence in the experimental acoustic field. To validate this statement, the acoustic source inversion simulation method, (as described in the previous section) was performed to predict the pressures at the six control microphone locations (Microphone #1–6) using *only* the measured pressures from the twelve response microphones (Microphone #7–18) as input.

Overall, the resulting predictions agreed well with the test data up to 1 kHz; the simulation data dropped off at frequencies greater than 1 kHz due to the coarse mesh used in the model, which is not useful at predicting higher frequencies. A comparison of the predicted (red) versus the test data (blue) can be seen in Fig. 25.15 for response microphone #7 and control microphone #6 on the left and right, respectively. Based on the results of the noise floor and simulation analysis, it can be stated that the response microphone data was correct and the magnification of the acoustic environment at these locations did occur in the acoustic field. Further study into the control algorithm, influence of coherence and mixing parameters, and acoustic modes of the speaker stack may provide useful insight into this phenomenon.

25.10 Conclusions

Direct-field acoustic tests were performed on a heavily instrumented Sandia Flight System in order to obtain test data for yet-to-be-flown acoustic loading environments. A realistic test specification was applied to the Flight System using a closed-loop multi-input multi-output control system; the six independent controls allowed for testing with both uniform and shaped acoustic fields with varying (high and low) coherence values. Maximum overall sound pressure levels of approximately 127 dB were successfully obtained with this setup.

The resulting control microphone pressures were within the ±3 dB test specification tolerances for the uniform acoustic field test. For the shaped acoustic field test, which consisted of a −6 dB gradient from aft to nose, the resulting control microphones pressures were within the ±3 dB tolerance for the aft end of the Flight System. However, the control microphone pressures at the nose of the Flight System were above the desired −6 dB test specification, but grouped closely together. It was surmised that the 6 dB gradient was too large for the system to achieve, and a smaller gradient of 4 dB would have more than likely controlled better.

While the controls were within tolerance, the response microphones for all acoustic fields consistently measured acoustic pressures ranging +4 dB to +9 dB above the various test specifications. This was unexpected, but not unreasonable, as these microphones had no effect on the acoustic control and were only measuring the resulting field. Analysis of measured instrumentation noise floor data, as well as analytical predictions of the pressures at the control microphone locations based off of response microphone data, proved that the larger magnitude data was valid and this response did occur in the acoustic field during the various tests.

There was no discernable difference in the spatial variation of the response microphones with the different MIMO coherence values (0.1 and 0.9) used to perform the acoustic tests. Based on theory and various references, it was expected that the lower coherence would result in a less variable acoustic field. The reduction of spatial variation may have not been realizable with this test configuration due to the boundary conditions and the physical test configuration used (placement of the speaker stacks and plywood panels).

An acoustic source inversion methodology was used with the measured acoustic pressures (microphones) to determine multiple acoustic sources of an acoustic finite element subdomain, used to model the acoustic test. The acoustic sources were then used to predict the acoustic pressures at the microphone locations as well as predict the wetted surface acoustic pressures of a high fidelity structural dynamics model of the Flight System to provide structural response predictions. The microphone predictions and simulated accelerations were compared to the measured test data to assess the model in the acoustic environment.

References

1. Direct Field Acoustic Testing: IEST-RP-DTE400.1, submitted to IEST for review (2012)
2. Larkin, P.: Direct Field Acoustic Testing update 2012. In: Spacecraft and Launch Vehicle Dynamic Environments Workshop. The Aerospace Corporation, El Segundo, CA (2012)
3. Rouse, J.W., Mesh, M., Stasiunas, E.C.: Analytical modeling of the acoustic field during a direct field acoustic test. In: 26th Aerospace Testing Seminar. The Aerospace Corporation, Los Angeles, CA (2011)
4. Stasiunas, E.C., Babuska, V., Skousen, T.J., Gurule, D.J.: Experiences in performing a high-intensity, direct-field acoustic test on a contamination sensitive system. In: 27th Aerospace Testing Seminar. The Aerospace Corporation, Los Angeles, CA (2012)
5. Sierra Structural Dynamics Development Team: Sierra Structural Dynamics – User's Notes. Sandia National Laboratories SAND Report (2015)
6. Walsh, T., Aquino, W., Ross, M.: Source Identification in Acoustics and Structural Mechanics using SIERRA/SD. Sandia National Laboratories SAND Report (2013)

Chapter 26
Smooth Complex Orthogonal Decomposition Applied to Traveling Waves in Elastic Media

Rickey A. Caldwell Jr. and Brain F. Feeny

Abstract A novel method called smooth complex orthogonal decomposition (SCOD) was applied to a simulated infinite beam and an experimental beam that emulated a semi-infinite beam. The beam was instrumented with accelerometers, and the accelerations were numerically integrated to compute displacements and velocities. These measurements were converted into complex analytic displacements and velocities ensembles, which were used to compute two correlation matrices. These correlation matrices formed a complex generalized eigenvalue problem whose eigenvalues and eigenvectors led to the extractions of the frequencies and wavenumbers of the constituent waves of the traveling pulse. SCOD directly extracts the frequencies of the traveling waves from the eigenvalues. SCOD was able to extract the geometric relationship, phase velocity, and group velocity, and agrees with analytical predictions.

Keywords SCOD • COD • Dispersion relationship • Wavenumber • Frequency

26.1 Introduction

During the middle of the twentieth century various researchers independently developed proper orthogonal decomposition (POD) [1, 14–16] which was applied to statistics and turbulent fluid flows. POD later caught the interest of structural engineers and was used to extract mode shapes from vibrating structures [2, 11–13]. Other generalizations of POD were developed, such as the smooth orthogonal decomposition (SOD) for finding the natural frequencies and linear normal modes [4, 6], and the state variable modal decomposition (SVMD) [7] for finding natural frequencies, normal modes, and (in theory) modal damping.

Soon after POD, was expanded to measuring traveling waves modes using complex orthogonal decomposition [8]. Complex orthogonal decomposition (COD) [9] can extract nonsynchronous and standing waves of vibrating structures. When waves are traveling through and elastic media COD can be used to extract the wavenumbers, frequencies, and the dispersion relationship of the waves. In the application of COD the wavenumber is extracted from the eigenvector, and the frequency is extracted from the modal coordinate.

A new generalization of COD is outlined here called the smooth complex orthogonal decomposition (SCOD). It will be shown that with SCOD the wavenumber and frequency can be extracted from the eigenvector and eigenvalue of the SCOD eigenvalue problem (EVP). A mathematical development for SCOD will be covered in Sect. 26.2. SCOD will be applied to a simulated infinite beam in Sect. 26.3, and experimentally to a rectangular beam in Sect. 26.4. A primer for SOD is reviewed in the Appendix.

The application of SCOD involves gathering state measurements. Accelerometers were used in this body of work. After the accelerations are measured the data is post-processed to derive velocity and displacement. The velocities are collected in a velocity ensemble, $\mathbf{V}$, and displacements are organized in a ensemble matrix, $\mathbf{X}$. The ensembles are organized so each sensor is allocated to a row such that all the data from the ith sensor is in the ith row. Measurement samples are then in each column. For example, $\mathbf{X}_{ij}$ contains the ith sensor's jth sample, for $i = 1, \cdots, M$ and $j = 1, \cdots, N$, where M is the number of sensors and n is the number of time samples.

Typically, the mean of each row is subtracted from each element of that row. The two ensembles are converted to analytic matrices, $\mathbf{Z}$ and $\mathbf{Z_v}$. Next, two correlation matrices are computed, one from the analytic displacements $\mathbf{R} = \mathbf{Z}\mathbf{Z}^T/N$ and

---

R.A. Caldwell Jr. (✉) • B.F. Feeny
Department of Mechanical Engineering, Michigan State University, 428 South Shaw Lane,
RM East Lansing, RM 2328C East Lansing, MI 48824, USA
e-mail: caldwe20@msu.edu; feeny@egr.msu.edu

© The Society for Experimental Mechanics, Inc. 2016

J. De Clerck, D.S. Epp (eds.), *Rotating Machinery, Hybrid Test Methods, Vibro-Acoustics & Laser Vibrometry, Volume 8*,
Conference Proceedings of the Society for Experimental Mechanics Series, DOI 10.1007/978-3-319-30084-9_26

the other from analytic velocities $\mathbf{S} = \mathbf{Z_v}\mathbf{Z_v}^T/N$. Finally the SCOD eigenvalue problem in the time domain is posed as $\boldsymbol{R\Phi\Lambda} = \boldsymbol{S\Phi}$. Then $\boldsymbol{\Psi} = \boldsymbol{\Phi}^{-H}$ provides an estimate of the modal matrix. The frequencies are the square root of the diagonals in $\boldsymbol{\Lambda}$. The wavenumbers are computed from the $\boldsymbol{\Psi}$. Each column of $\boldsymbol{\Psi}$ is used to extract a wavenumber where the wavenumber is the gradient of the angle.

26.2 Mathematical Development for Smooth Complex Orthogonal Decomposition

In this section we will develop the framework for SCOD in the time domain for distributed mass systems. Starting with the partial differential equation (PDE) for a beam, an eigenvalue problem will be derived, and relationships for eigenfunctions, eigenvalues, wavenumbers and frequencies will be uncovered.

Chelidze and Zhou [4] had approximated $\mathbf{V} \cong \mathbf{X}\mathbf{D}^T$, where $\mathbf{D}$ is a simple finite difference operator matrix, and had shown that

$$\mathbf{V}\mathbf{V}^T \cong \mathbf{X}\mathbf{D}\mathbf{D}^T\mathbf{X}^T \cong -\mathbf{X}\mathbf{A}^T.$$

Expanding $\mathbf{S} = \mathbf{V}\mathbf{V}^T/N$ to create the integral form of the correlation matrix starts with

$$\mathbf{S} = \frac{1}{N}\begin{bmatrix} v_1(t_1) & \cdots & v_1(t_N) \\ \vdots & & \vdots \\ v_M(t_1) & \cdots & v_M(t_N) \end{bmatrix}\begin{bmatrix} v_1(t_1) & \cdots & v_M(t_1) \\ \vdots & & \vdots \\ v_1(t_N) & \cdots & v_M(t_N) \end{bmatrix}$$

such that each element is

$$\mathbf{S}_{ij} = \frac{1}{N}\sum_{k=1}^{N} v_i(t_k)v_j(t_k) = \frac{1}{N\Delta t}\sum_{k=1}^{N} v_i(t_k)v_j(t_k)\Delta t.$$

Converting this into an integral form

$$\mathbf{S}_{ij} = \frac{1}{T}\int_0^T v_i(t)v_j(t)\,dt \tag{26.1}$$

and integrating by parts yields

$$S_{ij} = \frac{1}{T}\dot{x}_i x_j|_0^T - \frac{1}{T}\int_0^T \ddot{x}_i(t)x_j(t)\,dt, \tag{26.2}$$

where $T = N\Delta t$. Since the first term diminishes as T gets large, in the limit we have

$$S_{ij} = -\frac{1}{T}\int_0^T \ddot{x}_i(t)x_j(t)\,dt. \tag{26.3}$$

The associated discrete form is

$$S_{ij} = -\frac{1}{N}\sum_{k=1}^{N} a_i(t_k)x_j(t_k)\,dt = -\frac{1}{N}\mathbf{A}\mathbf{X}^T = -\frac{1}{N}\mathbf{X}\mathbf{A}^T, \tag{26.4}$$

the latter of which comes from symmetry in Eq. (26.1) and the steps that follow.

This shows that the form of $\mathbf{D}$ does not matter, and $\mathbf{V}\mathbf{V}^T = -\mathbf{X}\mathbf{A}^T$ also applies for the continuous problem.

Starting with the PDE for the beam equation in the linear operator form

$$m(x)\ddot{u} + Lu = 0 \tag{26.5}$$

where $m(x)$ is the mass per unit length and $u = u(x, t)$ is a function of space and time and is complex and analytic with the form

$$u(x, t) = e^{i\omega t}(c(x) + id(x)) = e^{i\omega t}\phi(x).$$

Taking the partial derivative of $u(x, t)$ with respect to t twice,

$$\frac{\partial^2}{\partial t^2}\{u(x, t)\} = -\omega^2 e^{i\omega t}\phi(x)$$

and substituting it into Eq. (26.5) leads to the continuous eigenvalue problem

$$L\phi(x) = \omega^2 m(x)\phi(x), \tag{26.6}$$

where the eigenfunction $\phi(x)$ is a complex modal function.

Let $u(x, t)$, $u(y, t)$, $v(x, t)$, $v(y, t)$ be complex analytic displacement and velocity time signals from points on the beam. We define

$$R(x, y) = \frac{1}{N}\sum_{k=1}^{N} u(x, t_k)\bar{u}(y, t_k)$$

$$S(x, y) = \frac{1}{N}\sum_{k=1}^{N} v(x, t_k)\bar{v}(y, t_k)$$

where $\bar{u}(y, t_k)$ and $\bar{v}(y, t_k)$ are the complex conjugates. Multiplying inside the summation and dividing outside the summation by Δt gives

$$R(x, y) = \frac{1}{N\Delta t}\sum_{k} u(x, t_k)\bar{u}(y, t_k)\, \Delta t$$

$$S(x, y) = \frac{1}{N\Delta t}\sum_{k} v(x, t_k)\bar{v}(y, t_k)\, \Delta t$$

Letting the Δt become infinitesimal results in

$$r(x, y) = \frac{1}{T}\int_0^T u(x, t)\bar{u}(y, t)\, dt$$

$$s(x, y) = \frac{1}{T}\int_0^T v(x, t)\bar{v}(y, t)\, dt. \tag{26.7}$$

Discretizing spatially, $R_{ij} = r(x_i, y_j)$ and $S_{ij} = s(x_i, y_j)$, and then temporally leads back to $\mathbf{R}$ and $\mathbf{S}$, as

$$\mathbf{R} = \frac{1}{T}\int_0^T u(x_i, t)\bar{u}(y_i, t)\, dt \cong \frac{1}{N}\mathbf{U}\bar{\mathbf{U}}^T$$

$$\mathbf{S} = \frac{1}{T}\int_0^T v(x_i, t)\bar{v}(y_i, t)\, dt \cong \frac{1}{N}\mathbf{V}\bar{\mathbf{V}}^T$$

where here $\mathbf{U}$ is the displacement ensemble matrix. The SCOD EVP is $\lambda\mathbf{R}\underline{\boldsymbol{\phi}} = \mathbf{S}\underline{\boldsymbol{\phi}}$ where $\underline{\boldsymbol{\phi}}$ is a discrete eigenvector. We will show that $\underline{\boldsymbol{\phi}}$ approximates a discretization of the system modal functions. For very high spatial resolution and infinitesimal time we approach the continuum limit and the EVP can be approximated as

$$\lambda\sum_{k=1}^{M} R_{ik}\,\underline{\phi}_k\,\Delta y = \sum_{k=1}^{M} S_{ik}\,\underline{\phi}_k\,\Delta y, \tag{26.8}$$

where M is the number of measurement points. Then following the development from above leads to

$$\lambda \sum_{k=1}^{M} r(x_i, y_k)\, \boldsymbol{\phi}(y_k)\, \Delta y = \sum_{k=1}^{M} s(x_i, y_k)\, \boldsymbol{\phi}(y_k)\, \Delta y$$

and finally,

$$\lambda \int r(x,y)\phi(y)\, dy = \int s(x,y)\phi(y)\, dy \tag{26.9}$$

which is the continuous SCOD in the time domain. Substituting (26.7) into (26.9) gives,

$$\frac{\lambda}{T} \int_y \left(\int_0^T u(x,t)\bar{u}(y,t)\, dt \right) \phi(y)\, dy = \frac{1}{T} \int_y \left(\int_0^T v(x,t)\bar{v}(y,t)\, dt \right) \phi(y)\, dy.$$

Plugging (26.2) into the above equation yields

$$\frac{\lambda}{T} \int_y \left(\int_0^T u(x,t)\bar{u}(y,t)\, dt \right) \phi(y)\, dy = -\frac{1}{T} \int_y \left(\int_0^T \ddot{u}(x,t)\, \bar{u}(y,t)\, dt \right) \phi(y)\, dy. \tag{26.10}$$

Using the symmetry mentioned after Eq. (26.2), the content of the parenthesis on the right hand side of equation is Hermitian in the continuous sense, such that

$$-\frac{1}{T} \int_0^T \ddot{u}(x,t)\, \bar{u}(y,t)\, dt = -\frac{1}{T} \int_0^T u(x,t)\, \ddot{\bar{u}}(y,t)\, dt.$$

Solving (26.5) for $\ddot{u}$ and substituting into (26.10) brings us to

$$\lambda \int_y \left(\int_0^T u(x,t)\bar{u}(y,t)\, dt \right) \phi(y)\, dy = \int_y \left(\int_0^T u(x,t)\, \frac{L\bar{u}(y,t)}{m(y)}\, dt \right) \phi(y)\, dy.$$

Next move everything onto one side of the equation, make $\int_y$ the inner integral move all the terms into the inner integral yielding

$$\int_0^T \int_y \left(\lambda\, u(x,t)\, \bar{u}(y,t)\phi(y) - u(x,t) \frac{1}{m(y)} L\bar{u}(y,t)\, \phi(y) \right) dy\, dt = 0$$
$$\int_0^T u(x,t) \left(\int_y \left[\lambda\, \bar{u}(y,t)\phi(y) - \frac{1}{m(y)} L\bar{u}(y,t)\, \phi(y) \right] dy \right) dt = 0.$$

Applying the adjoint $< Lq, p > = < q, L^* p >$ to move the linear operator and factoring out $\bar{u}(y,t)$ and moving all the terms back into the inner integral produces

$$\int_0^T \int_y u(x,t)\, \bar{u}(y,t) \left(\lambda\, \phi(y) - L^* \left[\frac{\phi(y)}{m(y)} \right] \right) dy\, dt = 0. \tag{26.11}$$

For this equation to have a non-trivial solution the expression inside of the parenthesis must be equal to zero producing the following relationship

$$\lambda \phi(y) = L^* \left[\frac{\phi(y)}{m(y)} \right]. \tag{26.12}$$

Multiplying both sides of (26.12) by $\psi(y)$ and integrating with respect to y creates

$$\int_y \lambda \phi(y)\psi(y)\, dy = \int_y L^* \left[\frac{\phi(y)}{m(y)} \right] \psi(y)\, dy.$$

Using the adjoint once more leads to

$$\int_y \lambda\phi(y)\psi(y)\,dy = \int_y \frac{\phi(y)}{m(y)} L\left[\psi(y)\right]\,dy.$$

Then

$$\int_y \left(\lambda\psi(y) - \frac{L\left[\psi(y)\right]}{m(y)}\right)\phi(y)\,dy,$$

which implies

$$\lambda\psi(y)m(y) = L\left[\psi(y)\right]. \tag{26.13}$$

Comparing Eqs. (26.13) and (26.6) shows that the SCOD eigenvalues and eigenvectors approximate the system eigenvalues and eigenfunctions. Let $\phi(y) = m(x)\psi(y)$ analogously as was done in the Appendix. Then substituting into (26.13) yields

$$\lambda m(y)\psi(y) = L^*\psi(y) = L\psi(y) \tag{26.14}$$

if the linear operator is self adjoint where $L^* = L$. This matches the relationship in Eq. (26.6). This shows that ϕ and ψ are related by the mass distribution.

26.3 Simulated Infinite Euler-Bernoulli Beam

The response of an infinite Euler-Bernoulli beam was simulated in the works of Graff [10], Feeny [8]. The initial conditions for the beam are

$$y(x,0) = f_0 e^{\left(\frac{-x^2}{4b_0^2}\right)}$$
$$\dot{y}(x,0) = 0$$

which is a Gaussian distribution on the initial displacement, where $f_0 = 1$ mm and $b_0 = 0.01$ m. The analytical solution to the Euler-Bernoulli beam with the initial condition given above is [10] (Table 26.1)

$$y(x,t) = \frac{f_0}{(1 + a^2t^2/b_0^4)^{1/4}} e^{\left(-\frac{x^2 b_0^2}{4(b_0^4 + a^2t^2)}\right)} \cos\left(\frac{atx^2}{4(b_0^4 + a^2t^2)} - \frac{1}{2}\arctan\left(\frac{at}{b_0^2}\right)\right). \tag{26.15}$$

The sensor network on the simulated beam was designed to be the same as the beam experiment (described later), with identical sensor spacing of $\Delta x = 0.0461$ m over a length of $L = 1.42875$ m, where sensor 1 is located at the origin. However, the sample rate in the simulation was 100,000 Hz, whereas in the beam experiment the sampling rate was 25,000 Hz.

Table 26.1 Simulated beam dimensions

Simulated beam dimensions	
Length	∞
Cross section	0.069 m × 0.0045 m
Density	7870 kg/m^3
Modulus of elasticity	200 GPa

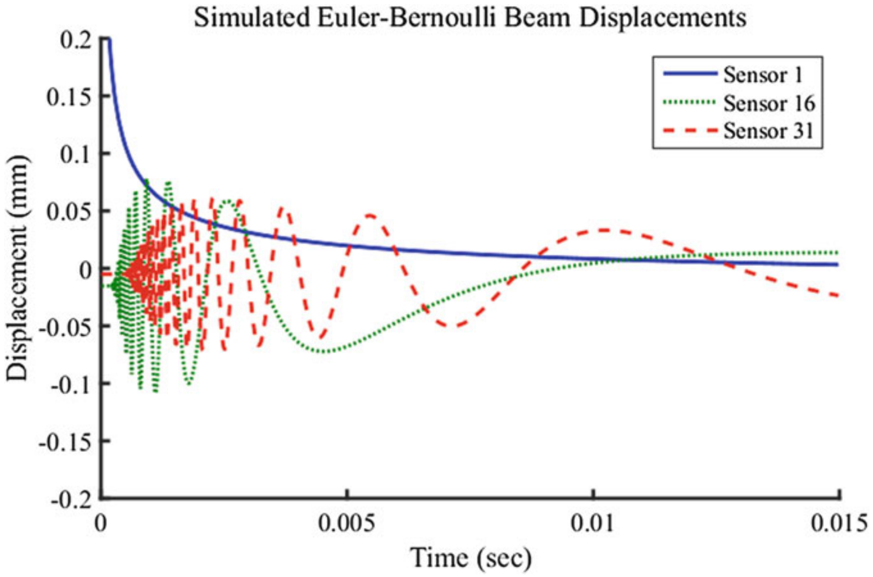

Fig. 26.1 Displacements vs. time from the analytical solution for sensor 1, sensor 16, and sensor 31

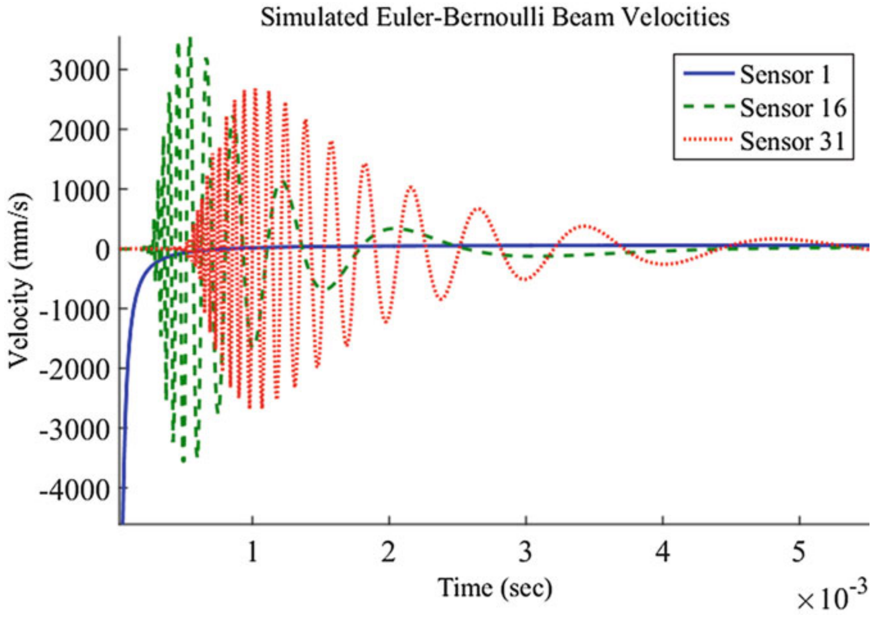

Fig. 26.2 Velocities vs. time from finite difference numerical derivatives of the displacements for sensor 1, sensor 16, and sensor 31

26.3.1 Data Processing

First displacements were computed from the analytical solution from Eq. (26.15), and the means were subtracted from each "sensor's" time history. Next, using central difference, the velocity ensemble, **V**, was computed and the means were removed. Central differencing reduces the ensemble matrix dimensions by $2h$, where h is the index interval used in the central difference. So, in order to make each ensemble dimensionally compatible, the first and last h rows of the time samples of displacement were removed from the ensemble. We used $h = 1$. The resulting displacements for sensors 1, 16, and 31 are shown in Fig. 26.1. The same plots are also shown for velocities in Fig. 26.2. Next, the signals were converted into complex analytic signals by taking the FFT of each row, zeroing out the negative frequencies and multiplying the remaining spectra by two. Finally, the IFFT was applied to obtain the analytic form of **X** and **V** as **Z** and $\mathbf{Z}_v$ respectively.

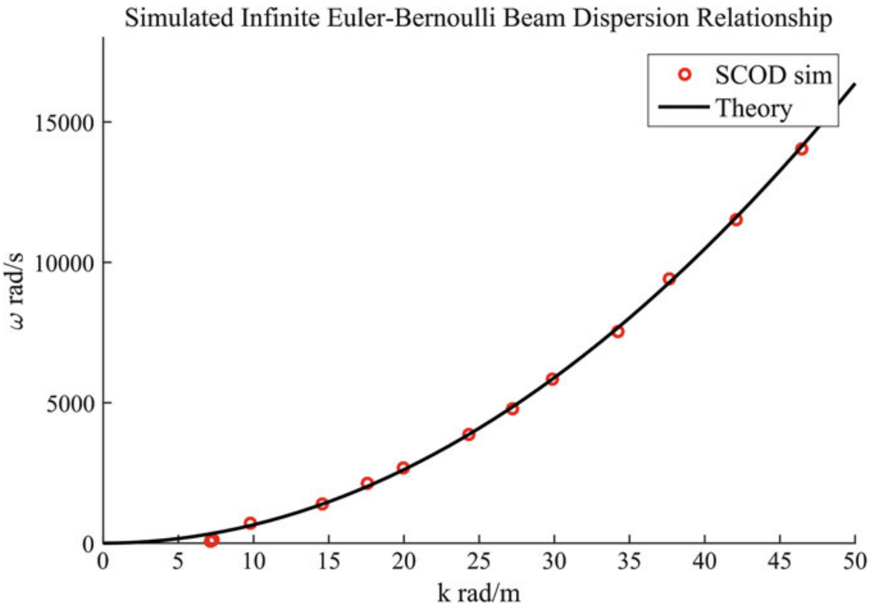

Fig. 26.3 Geometric dispersion relation obtained using SCOD for a simulated infinite Euler-Bernoulli beam

26.3.2 Results

The analytic measurement ensembles were used to create correlation matrices for the SCOD EVP. The natural frequencies were extracted directly from SCOD's eigenvalues, λ, instead of modal coordinate histories as done in the application of COD [3, 9]. The complex modal matrix was computed from the inverse Hermitian transpose of the eigenvector matrix as $\boldsymbol{\Psi} = \boldsymbol{\Phi}^{-H}$. The wavenumbers were than computed with a numerical derivative as $k_i = d\angle\boldsymbol{\psi}_i/dx$, where $\boldsymbol{\psi}_i$ is a column of the matrix $\boldsymbol{\Psi}$. A forward difference was used along the spatial index of the discretized modal vector in place of the derivative d/dx. The value of k_i was chosen from a spatial interval of uniform values.

The computed modal frequencies versus modal wavenumbers are plotted in Fig. 26.3. The least squares fit of the data in Fig. 26.3 to the equation $\omega = ak^2$ has an $a_{sim} = 6.52\,\mathrm{m}^2/\mathrm{s}$ compared to $a_{theory} = 6.56\,\mathrm{m}^2/\mathrm{s}$, which is 0.41 % error.

26.4 Experimental Beam

26.4.1 Setup

The test specimen was a rectangular steel beam with a constant cross section. In effort to emulate a semi-infinite free beam, the beam was suspended with elastic cords, such that one end was free, and the other was embedded in a sand pit, as done by Önsay and Haddow [3, 17]. A schematic of the experiment is shown in Fig. 26.4. In this case, the sandbox was filled with unpacked coarse sand. The beam had a 0.0045 m × 0.0698 m cross section. The length of the beam was 2.04 m. The unburied part of the beam measured 1.43 m, such that approximately 0.609 m was buried in the sand. This arrangement emulates a semi-infinite beam as the sand absorbs the wave and prevents reflections off the buried end of the beam. The density and modulus of elasticity of the beam were 7870 kg/m^3 and 200 GPa, respectively, based on published values for steel. From the geometry and material properties the theoretical value for $a = \sqrt{\frac{EI}{\rho A}}$ is $a = 6.548\,\mathrm{m}^2/\mathrm{s}$. This relationship is derived by using $y(x,t) = \sin(kx - \omega t)$ as the solution and substituting into the Euler-Bernoulli beam equation [10].

The beam was sensed with 31 accelerometers placed at a distance $\Delta x = 0.0458\,\mathrm{m}$ apart over a distance of $L = 1.4198\,\mathrm{m}$ and was sampled at $f = 25{,}000\,\mathrm{Hz}$ using a National Instruments PXI data acquisition system. The beam was struck with a PCB model 086C80 mini impact hammer, lightly such that bending deflections were not visible.

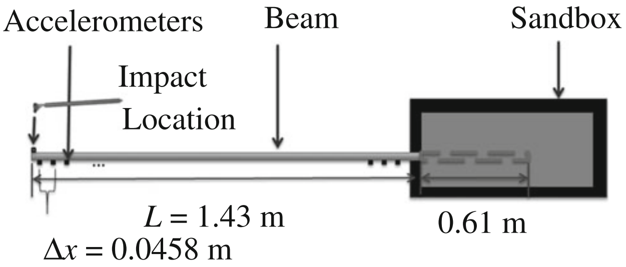

Fig. 26.4 Schematic of experimental setup

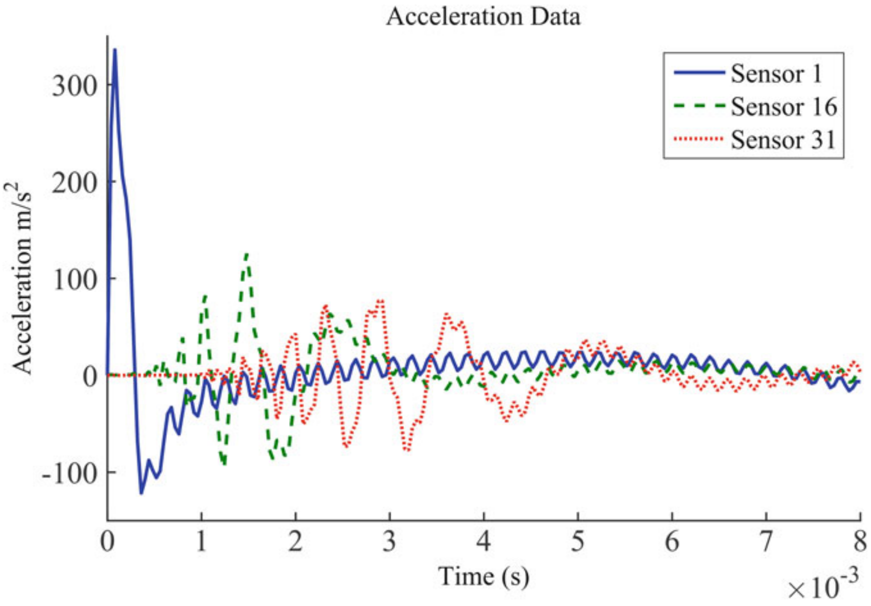

Fig. 26.5 Accelerations from sensors 1,16, and 31

26.4.2 Data Processing

The data included 100 samples before the hammer impact and 300 samples after the impact for a total of 400 samples. We integrated the acceleration data to obtain velocity and displacement. Numerical integration can be problematic because an integration constant is introduced, and low-frequency noise is amplified and can cause the integrated signal to drift. To reduce these effects the following steps were taken. First the data was filtered forward and backward with a high-pass filter with a cutoff frequency of 100 Hz. Second, the mean of each sensor's time history was subtracted from its samples using Matlab's `"detrend"` with a `"constant"` modifier. Third, any linear trends were removed using the same command as above with a `"linear"` modifier. Fourth, the signals were translated on the time axis such that the sample before the hammer impact had a time and force value of zero. The first and last 100 samples were truncated leaving the start of the impact plus 200 samples. Figure 26.4 shows a sample of the acceleration signals. The figure shows the delayed arrival of the wave to the more distant sensors, and also the dispersion of the pulse. The residual high frequency is due to the waves propagating (and reflecting) vertically along the height of the beam.

Next, to get velocities, the signals were numerically integrated using the `"cumtrapz"` command. The means were subtracted from the velocities, which were then high pass filtered, and integrated once more to get displacements. The means were subtracted from displacements and the displacements were filtered for a final time. These $N = 200$ samples of displacements were then used for SCOD. A sample of displacement is shown in Fig. 26.5.

The minimum detectable wavenumber defined by the span of sensors, L, is $k_{min_s} = \dfrac{2\pi}{L} = 4.4$ rad/m. The maximum detectable wavenumber is defined by a spatial Nyquist criterion as $k_{max_s} = \dfrac{\pi}{\Delta x} = 68.6$ rad/m. Based on the sampling rate $f = 25{,}000$ Hz and time record of $N/f = 0.008$ s, the maximum detectable frequency is $f_{max_t} = 12{,}500$ Hz and the minimum detectable frequency is $f_{min_t} = 125$ Hz.

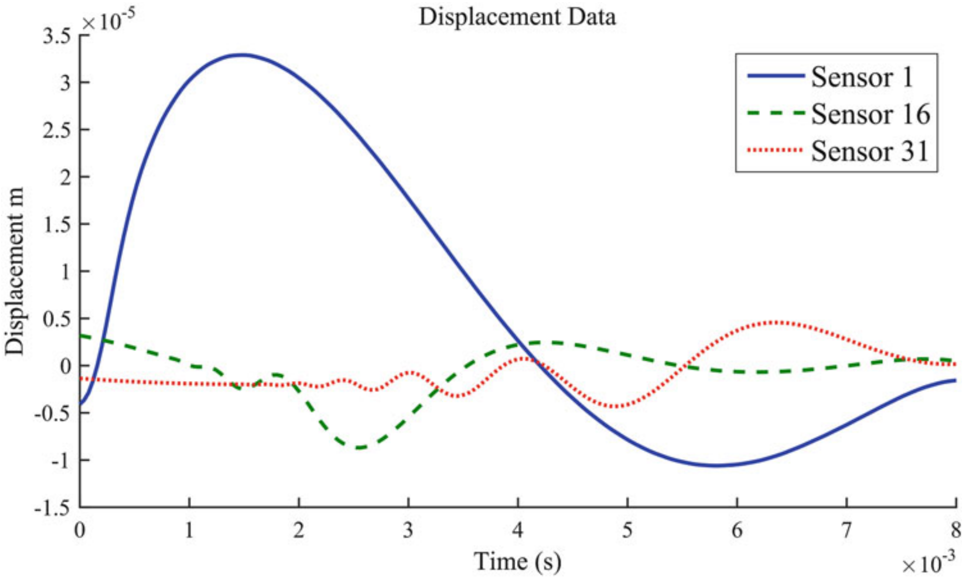

Fig. 26.6 Displacements from sensors 1, 16, and 31

Making use of the theoretical dispersion relation $\omega = ak^2$, or $k = \sqrt{2\pi f/a}$, we find that the temporal sampling parameters correspond to theoretical wavenumber limits of $k_{max_t} = 109\,\text{rad/m}$ and $k_{min_t} = 10.9\,\text{rad/m}$. The approximate total wavenumber limits are thus $k_{max} = min(k_{max_s}, k_{max_t}) = 68.6\,\text{rad/m}$, and $k_{min} = max(k_{min_s}, k_{min_t}) = 10.9\,\text{rad/m}$. Thus, the upper limit on extractable wavenumbers, (and hence frequencies) is determined by the spatial sampling interval Nyquist criterion, and the lower limit on extractable wavenumbers is determined by the length of the time record.

26.4.3 Results

SCOD was applied to the beam experiment, and frequencies were directly computed from the eigenvalues which saves some computational effort when compared to COD for obtaining frequency information. Samples of SCOMs are shown in Fig. 26.6. SCOMs were not as whirling as COMs for higher modes (see [3]). The modal wave numbers were estimated from the whirl rates of the SCOMs, and paired with the associated smooth complex orthogonal values, λ, to obtain the dispersion relationship. SCOD extracts data over a smaller wavenumber range for the same data with similar accuracy. Figures 26.7 and 26.8 show the results obtained when SCOD was applied to the experimental beam data. The COD results in Fig. 10 were taken from the work of Caldwell Jr and Feeny [3]. The least squares approximation of a using the SCOD estimated ω and k gives $a_{SCOD} = 6.72\,\text{m}^2/\text{s}$, which is a error of 2.6 % when compared to $a_{theory} = 6.56\,\text{m}^2/\text{s}$. SCOD deviated from theory only 2.6 %.

26.5 Conclusions

This paper outlined the mathematical development and application of smooth complex orthogonal decomposition to estimate complex modal characteristics. In using SCOD in the time domain one can directly compute frequencies from the eigenvalues. The complex structural modes are computed from the inverse conjugate transpose of the SCOD eigenvector matrix. For a nearly harmonic traveling complex mode, the wavenumber can be obtained from the gradient of the phase of the mode shape. SCOD was shown to accurately extract waves traveling through a simulated infinite beam, and an experimental beam.

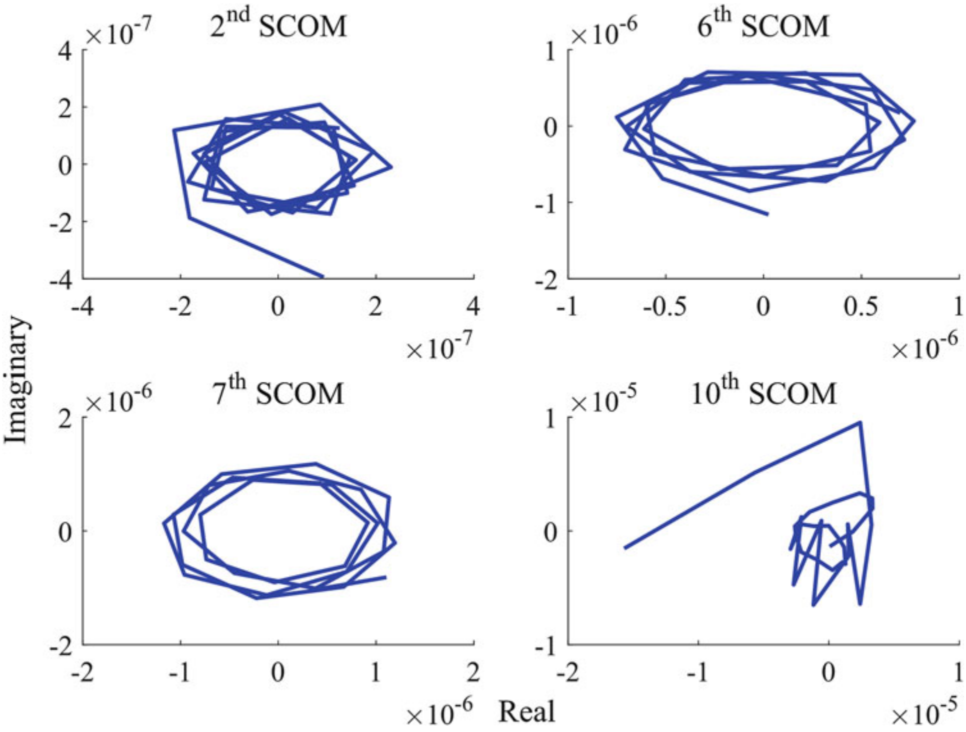

Fig. 26.7 Selected SCOMs. *Top left*: 2nd modal SCOM. *Top right*: 6th SCOM which is less circular than second. This trends continues and is illustrated in the *Lower left*: 7th SCOM. *Lower right*: 10th SCOM

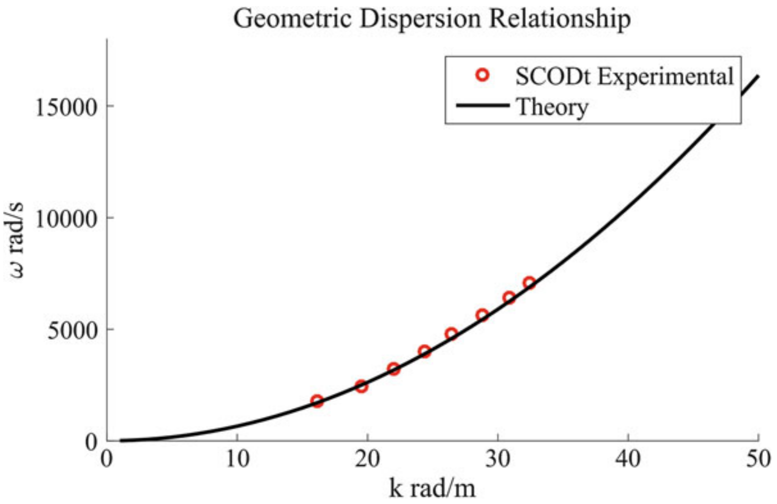

Fig. 26.8 Geometric dispersion relationship for an experimental beam using SCOD

Currently, efforts are being applied in which SCOD is applied spatially, where displacements and slope or curvature is used, depending on the model's PDE, to extract the parameters of waves propagating in an elastic medium. Applied spatially, in some systems wavenumbers are extracted directly from the eigenvalues and the frequencies are extracted from the whirling rates of the eigenvectors.

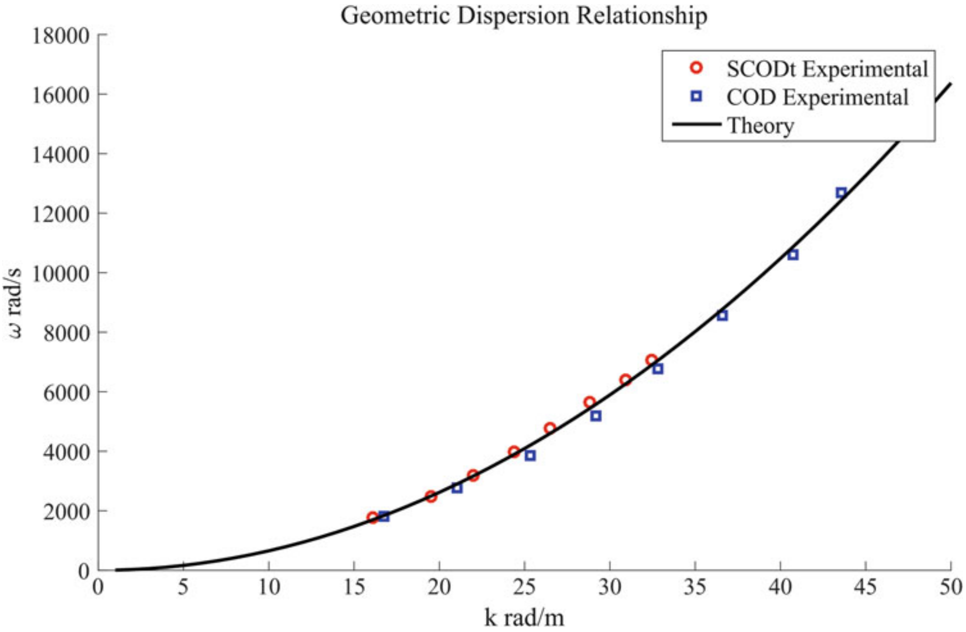

Fig. 26.9 Geometric dispersion relationship for SCOD (*open circle*) and COD (*open square*)

Appendix: Primer of Smooth Orthogonal Decomposition

We will start by relating SOD [4] to the mass-spring system, following [5]. Given the general undamped freely vibrating mass-spring equation

$$\mathbf{M}\ddot{\mathbf{x}} + \mathbf{K}\mathbf{x} = 0 \tag{26.16}$$

and substituting in the assumed solution of $\mathbf{x} = \boldsymbol{\phi} e^{i\omega t}$ leads to the generalize eigenvalue problem in the form of

$$\lambda \mathbf{M}\underline{\boldsymbol{\phi}} = \mathbf{K}\underline{\boldsymbol{\phi}}, \tag{26.17}$$

where the eigenvalues $\lambda = \omega^2$ are modal frequencies squared, and the eigenvectors $\underline{\boldsymbol{\phi}}$ are the mode shapes. In matrix form, we can write

$$\mathbf{M}\boldsymbol{\Phi}\boldsymbol{\Lambda} = \mathbf{K}\boldsymbol{\Phi}, \tag{26.18}$$

where $\boldsymbol{\Phi}$ is a matrix consisting of columns $\underline{\boldsymbol{\phi}}_i$ and $\boldsymbol{\Lambda}$ is a diagonal matrix whose elements are ω_i^2. We will show the relationship between the mass-spring system and the smooth orthogonal decomposition. SOD is defined by

$$\lambda \mathbf{R}\underline{\boldsymbol{\psi}} = \mathbf{S}\underline{\boldsymbol{\psi}}, \tag{26.19}$$

or in matrix form,

$$\mathbf{R}\boldsymbol{\Psi}\boldsymbol{\Lambda} = \mathbf{S}\boldsymbol{\Psi}, . \tag{26.20}$$

where λ is a smooth orthogonal value (SOV) and is equal to the modal frequency squared, Λ is a diagonal matrix whose elements are the λ_i, ψ is the smooth orthogonal mode, and $\boldsymbol{\Psi}$ is a matrix consisting of columns $\boldsymbol{\psi}_i$. SOD involves two correlation matrices, $\overline{\mathbf{R}}$ and $\mathbf{S}$, where

$$\mathbf{R} = \frac{\mathbf{X}\mathbf{X}^T}{N}$$

$$\mathbf{S} = \frac{\mathbf{V}\mathbf{V}^T}{N},$$

$\mathbf{X}$ is a measurement ensemble of displacements, and $\mathbf{V}$ is a measurement ensemble of velocities. Typically the mean of the time history of each sensor is subtracted from each of the data samples of that sensor. The general form of all ensembles used in this body work is

$$\mathbf{X} = \begin{bmatrix} x_1(0) & x_1(\Delta t) & \cdots & x_1((N-1)\Delta t) \\ x_2(0) & x_2(\Delta t) & \cdots & x_2((N-1)\Delta t) \\ \vdots & \vdots & \ddots & \vdots \\ x_M(0) & x_M(\Delta t) & \cdots & x_M((N-1)\Delta t) \end{bmatrix} \tag{26.21}$$

where M is the number of sensors and N is the number of samples. The time history for each sensor is organized in rows, such that each column is a set of samples at each sampling interval.

Starting with the SOD eigenvalue problem, as

$$\mathbf{R\Psi\Lambda} = \mathbf{S\Psi}$$

and substituting in the expressions for $\mathbf{R}$ and $\mathbf{S}$, leads to

$$\mathbf{XX}^T\mathbf{\Psi\Lambda} = \mathbf{VV}^T\mathbf{\Psi}.$$

Chedize and Zhou [4] used the approximation $\mathbf{V} \cong \mathbf{XD}^T$, and showed that $\mathbf{XDD}^T\mathbf{X}^T \cong -\mathbf{XA}^T$, where $\mathbf{D}$ is a matrix that performs a simple finite difference numerical derivative. Plugging this into $\mathbf{S}$, the EVP becomes

$$\mathbf{XX}^T\mathbf{\Psi\Lambda} = -\mathbf{XA}^T\mathbf{\Psi}.$$

Now noting that $\mathbf{A}$ is an ensemble of accelerations, then from $\mathbf{MA} + \mathbf{KX} = 0$, we have $\mathbf{A} = -\mathbf{M}^{-1}\mathbf{KX}$. Then

$$\mathbf{XX}^T\mathbf{\Psi\Lambda} = \mathbf{X}[\mathbf{M}^{-1}\mathbf{KX}]^T\mathbf{\Psi}$$

or

$$\mathbf{XX}^T\mathbf{\Psi\Lambda} = \mathbf{XX}^T\mathbf{KM}^{-T}\mathbf{\Psi}$$

since $\mathbf{K}$ and $\mathbf{M}$ are symmetric. Assuming $\mathbf{XX}^T$ has full rank, and is invertible, we have

$$\mathbf{\Psi\Lambda} = \mathbf{KM}^{-T}\mathbf{\Psi}.$$

The assumption that $\mathbf{XX}^T$ is full rank corresponds to a fully multimodal motion with $N \geqq M$ (or a sufficient noise level). Taking the inverse transpose of the above equation yields,

$$\left[\mathbf{\Psi\Lambda} = \mathbf{KM}^{-T}\mathbf{\Psi}\right]^{-T}.$$

Again from symmetry we have

$$\mathbf{K\Psi}^{-T} = \mathbf{M\Psi}^{-T}\mathbf{\Lambda}. \tag{26.22}$$

Comparing Eq. (26.22) with Eq. (26.18) we see that the SCOD eigenvalues represent the structural eigenvalues, i.e. the modal frequencies squared, and that the SOD eigenvectors and the linear normal modes (LNMs) of the mass spring system are related as $\mathbf{\Phi} = \mathbf{\Psi}^{-T}$. These conclusions were reached in [4, 5].

Another relationship worth noting can be shown if we step back to equation (26.22) and let $\mathbf{\Phi} = \mathbf{M\Psi}$, which yields,

$$\mathbf{K}(\mathbf{M\Phi})^{-T} = \mathbf{M}(\mathbf{M\Phi})^{-T}\mathbf{\Lambda}$$
$$\mathbf{KM}^{-T}\mathbf{\Phi}^{-T} = \mathbf{MM}^{-T}\mathbf{\Phi}^{-T}\mathbf{\Lambda}$$

using symmetry

$$\begin{aligned}\mathbf{K}\mathbf{M}^{-1}\boldsymbol{\Phi}^{-T} &= \quad \boldsymbol{\Phi}^{-T}\boldsymbol{\Lambda}\\ \mathbf{M}^{-1}\boldsymbol{\Phi}^{-T} &= \mathbf{K}^{-1}\boldsymbol{\Phi}^{-T}\boldsymbol{\Lambda}\end{aligned}$$

take the inverse transpose of both sides of the equation and using symmetry

$$\begin{aligned}\mathbf{M}\boldsymbol{\Phi} &= \mathbf{K}\boldsymbol{\Phi}\boldsymbol{\Lambda}^{-1}\\ \mathbf{M}\boldsymbol{\Phi}\boldsymbol{\Lambda} &= \quad \mathbf{K}\boldsymbol{\Phi}.\end{aligned}$$

Therefore, $\boldsymbol{\Psi}$ and $\boldsymbol{\Phi}$ are related through $\mathbf{M}$ as

$$\boldsymbol{\Phi} = \mathbf{M}\boldsymbol{\Psi}. \tag{26.23}$$

This relationship will be important in mathematical development of SCOD.

In summary, for linear undamped, symmetric, multimodal free vibration systems, the two relationships for the eigenvectors of the mass spring system and smooth orthogonal decomposition were just established to be $\boldsymbol{\Psi} = \boldsymbol{\Phi}^{-T}$ and $\boldsymbol{\Psi} = \mathbf{M}\boldsymbol{\Phi}$. Furthermore, the SOD eigenvalues approximate the squares of the modal frequencies. These relationship will be approximated in experiments, since agreement with the model is an idealization.

References

1. Berkooz, G., Holmes, P., Lumley J.L.: The proper orthogonal decomposition in analysis of turbulent flows. Annu. Rev. Fluid Mech. **25**(539–575), 137–146 (1967)
2. Brincker, R., Zhang, L., Andersen, P.: Modal identification of output-only systems using frequency domain decomposition. Smart Mater. Struct. **10**, 441 (2001). doi:10.1088/0964-1726/10/3/303
3. Caldwell Jr., R.A., Feeny, B.F.: Characterizing wave behavior in a beam experiment by using complex orthogonal decomposition. ASME J Vib Acoust (2016). doi:10.1115/1.4633268
4. Chelidze, D., Zhou, W.: Smooth orthogonal decomposition-based vibration mode identification. J. Sound Vib. **292**, 461–473 (2006)
5. Farooq, U., Feeny, B.F.: Smooth orthogonal decomposition for modal analysis of randomly excited systems. J. Sound Vib. **316**(1–5), 137–146 (2008)
6. Farooq, U., Feeny, B.F.: Smooth orthogonal decomposition for randomly excited systems. J. Sound Vib. **316**(3–5), 137–146 (2008)
7. Farooq, U., Feeny, B.F: An experimental investigation of a state-variable modal decomposition method for modal analysis. J. Vib. Acoust. **132**(2), 021017 (8 pages) (2012)
8. Feeny, B.F.: A complex orthogonal decomposition for wave motion analysis. J. Sound Vib. **310**(1–2), 77–90 (2008)
9. Feeny, B.F.: Complex modal decomposition for estimating wave properties in one-dimensional media. J. Vib. Acoust. **135**(3), 031010 (2013)
10. Graff, K.F.: Wave Motion in Elastic Solids. Courier Dover Publications, New York (1975)
11. Han, S., Feeny, B.F.: Application of proper orthogonal decomposition to structural vibration analysis. Mech. Syst. Signal Process. **17**(5), 989–1001 (2003)
12. Ibrahim, S.R., Mikulcik, E.C.: A time domain modal vibration test technique. Shock Vib. Bull. **34**(4), 21–37 (1973)
13. Ibrahim, S.R., Mikulcik, E.C.: A method for the direct identification of vibration parameters from the free response. Shock Vib. Bull. **47**(4), 183–198 (1977)
14. Karhunen, K.: Zur Spektral theorie Stochastischer Prozesse. Ann. Acad. Sci. Fenn. A. **37**, 1–34 (1946)
15. Kosambi, D.: Statistics in function space. J. Indian Math. Soc. **7**, 76–88 (1943)
16. Lumley, J.: Stochastic Tools in Turbulence. Academic, New York (1970)
17. Önsay, T., Haddow, A.G.: Wavelet transform analysis of transient wave-propagation in a dispersive medium. J. Acoust. Soc. Am. **95**(3), 1441–1449 (1994)

Chapter 27
Subspace Algorithms in Modal Parameter Estimation for Operational Modal Analysis: Perspectives and Practices

S. Chauhan

Abstract Subspace based algorithms for estimating modal parameter have now become common within modal analysis domain. This is especially true for Operational Modal Analysis, where Stochastic Subspace Identification (SSI) algorithm is a well-known and commonly used algorithm. Despite their increasing use and popularity, one often encounters basic questions such as (and not limited to)

1. How are these algorithms related to (or different from) traditional matrix polynomial coefficient based algorithms like Polyreference Time Domain (PTD) etc.?
2. What is the link between covariance and data driven approaches to SSI?
3. What is the need for having different variants of SSI (Covariance-driven and Data-driven)?

In fact, even before addressing the questions listed above, there is a fundamental need to look at these algorithms from the perspective of modal parameter estimation, whose requirements and demands differ from those of system identification within Control Systems Engineering, where these algorithms originated.

This paper aims at addressing these issues and examine subspace algorithms from a purely modal parameter estimation perspective. The author expects that this paper will provide readers with a simple and clear understanding of these algorithms towards their utilization for modal parameter estimation.

Keywords Stochastic subspace identification • Data-driven • Covariance-driven • State space modelling • Modal parameter estimation

Abbreviations

ERA	Eigensystem realization algorithm
ITD	Ibrahim time domain
OMA	Operational modal analysis
SSI	Stochastic subspace identification
SSI-Cov	Covariance-driven SSI
SSI-Data	Data-driven SSI
SVD	Singular value decomposition

Nomenclature

$\mathbf{x}$	State vector
$\mathbf{y}$	Response vector
$\mathbf{A}$	State transition matrix
$\mathbf{C}$	Output matrix
$\mathbf{w}$ and $\mathbf{v}$	Process and measurement noise vectors
$\mathbf{Y}$	Hankel data matrix

S. Chauhan (✉)
Bruel and Kjær Sound and Vibration Measurement A/S, Skodsborgvej 307, 2850 Naerum, Denmark
e-mail: schauhan@bksv.com

© The Society for Experimental Mechanics, Inc. 2016

J. De Clerck, D.S. Epp (eds.), *Rotating Machinery, Hybrid Test Methods, Vibro-Acoustics & Laser Vibrometry, Volume 8*,
Conference Proceedings of the Society for Experimental Mechanics Series, DOI 10.1007/978-3-319-30084-9_27

$\mathbf{H}$	Hankel matrix of covariance matrices
$\mathbf{\Lambda}$	Covariance matrix
$\overline{\mathbf{O}}$	Extended observability matrix
$\overline{\mathbf{C}}$	Extended controllability matrix
$\mathbf{\Sigma}$	State covariance matrix
$\overline{\alpha}$	Matrix polynomial coefficients
$\mathbf{P}_{fp}$	Projection of future output responses on past output responses
$\widehat{\mathbf{X}}_i$	Kalman filter state estimate

27.1 Introduction

There are several applications, including modal parameter estimation where parametric models are sought. These include signal processing, defect detection, design of control systems and many others. Subspace algorithms belong to the class of system identification algorithms that utilize state-space models of time series for estimating parametric models. The use of these algorithms for parameter estimation in modal analysis is not new. Several popular algorithms, such as *Ibrahim Time Domain* (ITD) [1, 2] and *Eigensystem Realization Algorithm* (ERA) [3, 4], use state space formulations for estimating modal parameters.

The aim of this paper is to understand state space modelling in context of modal parameter estimation, with a focus on one of the most commonly used Operational Modal Analysis (OMA) algorithm, Stochastic Subspace Identification (SSI) [5–7], along with its two variants: Covariance-driven SSI (SSI-Cov) and Data-driven SSI (SSI-Data).

In order to understand state-space models in the context of modal analysis, it is vital to state the objective of modal analysis, which is ***to estimate modal parameters, i.e. natural frequency, damping and mode shape, of a structure***. Thus, unlike system identification problem in control system design or forecasting problem in econometrics, the goal of a parameter estimation algorithm is not estimation of matrices **A**, **C** (defined in Sect. 27.2) or associated quantities such as state vectors, observability or controllability matrix, etc. but modal parameters.

The paper starts with a general discussion on SSI algorithm and describes sequentially its two variants, Covariance-driven SSI (SSI-Cov) and Data-driven SSI (SSI-Data). In Sect. 27.2.1, two separate approaches are provided for the development of SSI-Cov. First, traditional formulation of SSI-Cov is provided along with a modified formulation. Then an alternate formulation is provided that takes inspiration from, and explores, the relationship between the polynomial model and state-space model representation of a dynamic system. Additionally, this section explains how estimation of extended observability matrix in the conventional formulation is not a requirement from modal analysis point of view and desired results can be achieved in comparatively simple steps. The section concludes by noting how various formulations of SSI-Cov simply differ in how the covariance matrices are stacked.

Same approach is taken while discussing SSI-Data (Sect. 27.2.2). Given the framework of modal parameter estimation, the aim is to connect the two variants of SSI. In this context, it is explained how the need to estimate state vectors necessitates the availability of raw output data for SSI-Data algorithm and it is emphasized that these requirements do not form a part of modal parameter estimation. The formulation of SSI-Data is then explained in light of this knowledge and it is shown how SSI-Data is not much different from SSI-Cov in the absence of the need to estimate state vectors.

27.2 Stochastic Subspace Identification Algorithm

Stochastic Subspace Identification (SSI) is a well-known operational modal analysis (OMA) algorithm [5–7]. It is based on state-space representation of a discrete linear time invariant (LTI) system described as

$$\begin{aligned} \mathbf{x_{k+1}} &= \mathbf{A}\mathbf{x_k} + \mathbf{w_k} \\ \mathbf{y_k} &= \mathbf{C}\mathbf{x_k} + \mathbf{v_k} \end{aligned} \tag{27.1}$$

where **y** is the vector of measured responses, **x** is the vector of state variables matrix, **A** is the state transition matrix, **C** is the output matrix and **w** and **v** are process and measurement noise vectors. As is clear from Eq. (27.1), SSI algorithm operates on measured output response data only (input excitation is not measured in OMA). From the point of view of modal parameter estimation, it is the estimation of state transition matrix **A** that is most important as eigenvalue decomposition of this matrix reveals modal parameters.

There are two variants of this algorithm that are popular in practice: data-driven (SSI-Data) and covariance-driven (SSI-Cov) [6]. These variants differ in terms of the data on which they operate. SSI-Data operates directly on measured output response data without processing it. On the other hand, SSI-Cov requires that covariance functions are first estimated from raw output time histories and it is these covariance functions that SSI-Cov utilizes for the purpose of modal parameter estimation. The discussion in this section centers on understanding the finer aspects of these two variants. In this context, traditional development of these algorithms is studied to understand the reasons that led to the development of these two variants.

Typically, the output response data is assembled in a Hankel data matrix, which is further divided into a partition of past ($\mathbf{Y}_p$) and future responses ($\mathbf{Y}_f$) (see [6, 7] for more details). This arrangement aids in theoretical formulation of SSI and is given as

$$\mathbf{Y} = \begin{bmatrix} \mathbf{Y}_p \\ \mathbf{Y}_f \end{bmatrix} \tag{27.2}$$

The two variants of SSI are now discussed in Sects. 27.2.1 and 27.2.2.

27.2.1 *Covariance Driven Stochastic Subspace Identification Algorithm*

SSI-Cov algorithm, as the name suggests, operates on covariance functions. Typically, the raw response data is processed into covariance functions, which are then utilized in SSI-Cov algorithm. This processing of raw response data to covariance (or correlation) functions can be done in several ways, including obtaining covariance functions directly from response data without involving any intermediary signal processing steps. This is in contrast to, for e.g. Welch Peridogram method [8], where data is processed to estimate power spectra, which is then inverse Fourier transformed to obtain covariance functions, and involves signal-processing techniques like averaging, windowing etc.

In literature, SSI-Cov is generally developed using the Hankel (or Toeplitz) matrix of covariance functions. The algorithm then utilizes the fact that the Hankel matrix equals the covariance between future responses and past responses, i.e. $\mathbf{H} = \mathbf{Y}_f \mathbf{Y}_p^T$. In case of SSI-Cov, it is typically assumed that covariance functions are calculated a priori and access to raw output responses is not available.

This section is arranged in the following manner. First, the traditional formulation of SSI-Cov, based on estimation of extended observability and controllability matrices, is presented. It is then shown that estimation of extended observability and controllability matrices is redundant from the perspective of modal parameter estimation and how state transition matrix **A** can be directly obtained from Hankel matrix of covariance functions. Finally, a new formulation of SSI-Cov is suggested in Sect. 27.2.1.2 underlining the fact that SSI-Cov can be formulated in multiple ways; each differing in the manner the covariance functions are arranged.

27.2.1.1 SSI-Cov Based on Traditional Formulation

Traditional formulation of SSI-Cov begins with formulation of a Hankel (or Toeplitz) matrix of covariance matrices, which equals $\mathbf{H} = \mathbf{Y}_f \mathbf{Y}_p^T$ ($\mathbf{Y}_f, \mathbf{Y}_p$ are defined in Eq. 27.2).

$$\mathbf{H} = \mathbf{Y}_f {\mathbf{Y}_p}^T = \begin{bmatrix} \mathbf{\Lambda}_1 & \mathbf{\Lambda}_2 & \cdots & \mathbf{\Lambda}_m \\ \mathbf{\Lambda}_2 & \mathbf{\Lambda}_3 & \cdots & \mathbf{\Lambda}_{m+1} \\ \vdots & \vdots & \ddots & \vdots \\ \mathbf{\Lambda}_m & \mathbf{\Lambda}_{m+1} & \cdots & \mathbf{\Lambda}_{2m} \end{bmatrix}_{mN_o \times mN_o} \tag{27.3}$$

As explained previously, for modal parameter estimation purposes, one is interested in estimation of state transition matrix **A**. Typically, estimation of state transition matrix **A** is done on the basis of extended Observability matrix $\overline{\mathbf{O}}$, which is obtained using singular value decomposition (SVD) of **H**.

$$\mathbf{H} = \mathbf{U}\,\mathbf{S}\,\mathbf{V}^T = \overline{\mathbf{O}}\,\overline{\mathbf{C}} \tag{27.4}$$

Note that $\overline{\mathbf{C}}$ in the Eq. (27.4) represents extended Controllability matrix. The extended observability matrix is obtained in following manner,

$$\overline{\mathbf{O}} = \mathbf{U}\,\mathbf{S}^{\frac{1}{2}} \tag{27.5}$$

and state transition matrix $\mathbf{A}$ is estimated as

$$\mathbf{A} = \overrightarrow{\mathbf{O}}\,\overline{\mathbf{O}}^{+}_{\mathrm{m}-1} \tag{27.6}$$

where $\overrightarrow{\mathbf{O}}$ is the block shifted version of extended observability matrix (obtained after removing the first block of $\overline{\mathbf{O}}$) and $\overline{\mathbf{O}}^{+}_{\mathrm{m}\text{-}1}$ represent pseudo-inverse of first $(m-1)$ rows of $\overline{\mathbf{O}}$.

The reason for taking this approach in conventional system identification framework is that identification of observability and controllability matrices is often part of the overall identification problem. This however, is not the case with modal parameter estimation, where the aim is to obtain modal parameters. Shown below is another approach of estimating state transition matrix $\mathbf{A}$, using the Hankel matrix expressed in Eq. (27.3). This formulation is based on the work presented in [9], where it is shown that state transition matrix $\mathbf{A}$, can be directly obtained from Hankel matrix $\mathbf{H}$ in following manner.

$$\mathbf{A} = \overrightarrow{\mathbf{H}}\,\mathbf{H}^{+}_{\mathrm{m}\text{-}1} \tag{27.7}$$

where $\overrightarrow{\mathbf{H}}$ is the block shifted version of Hankel matrix and $\mathbf{H}^{+}_{\mathrm{m}\text{-}1}$ represent pseudo-inverse of first $(m-1)$ rows of $\mathbf{H}$.

It should be noted that state transition matrix estimated using Eq. (27.7) is related to that obtained using the traditional approach (described by Eqs. 27.4, 27.5, and 27.6) by means of a similarity transformation (see [9] for details) and hence possesses the same Eigen structure. In other words, modal parameters estimated on the basis of either state transition matrix will still be the same.

27.2.1.2 Alternate Formulation

By defining state vectors $\mathbf{x}_{\mathbf{k}}$, in Eq. (27.1), in following manner, it is easy to understand the relationship between state-space representation and the polynomial model representation of a dynamic system. The state transition matrix in this case becomes a companion matrix.

$$\mathbf{x}_k = \begin{bmatrix} \mathbf{y}_{k+1} \\ \mathbf{y}_{k+2} \\ \vdots \\ \mathbf{y}_{k+m} \end{bmatrix}, \quad \mathbf{A} = \begin{bmatrix} 0 & 1 & 0 & \cdots & 0 \\ 0 & 0 & 1 & \cdots & 0 \\ \vdots & \vdots & \vdots & \ddots & \vdots \\ 0 & 0 & 0 & \cdots & 1 \\ -\overline{\alpha}_0 & -\overline{\alpha}_1 & -\overline{\alpha}_2 & \cdots & -\overline{\alpha}_{m-1} \end{bmatrix} \tag{27.8}$$

Defining covariance matrix between output responses as $\mathbf{\Lambda}_i = E\left[\mathbf{y}_{k+i}\mathbf{y}_k^T\right]$ and state covariance matrix as $\mathbf{\Sigma} = E\left[\mathbf{x}_k\mathbf{x}_k^T\right]$, it is easy to show, using Eq. (27.1), that

$$\mathbf{\Lambda}_i = \mathbf{C}\mathbf{A}^{i-1}\mathbf{\Sigma}\mathbf{C}^T \tag{27.9}$$

Expanding state equation in Eq. (27.1) and using Eq. (27.8),

$$\begin{bmatrix} \mathbf{0} & \mathbf{I} & \mathbf{0} & \cdots & \mathbf{0} \\ \mathbf{0} & \mathbf{0} & \mathbf{I} & \cdots & \mathbf{0} \\ \vdots & \vdots & \vdots & \ddots & \vdots \\ \mathbf{0} & \mathbf{0} & \mathbf{0} & \cdots & \mathbf{I} \\ -\boldsymbol{\alpha}_{\mathbf{0}} & -\boldsymbol{\alpha}_{\mathbf{1}} & -\boldsymbol{\alpha}_{\mathbf{2}} & \cdots & -\boldsymbol{\alpha}_{\mathbf{m-1}} \end{bmatrix} \begin{bmatrix} \mathbf{y}_{i+0} \\ \mathbf{y}_{i+1} \\ \vdots \\ \mathbf{y}_{i+m-2} \\ \mathbf{y}_{i+m-1} \end{bmatrix} = \begin{bmatrix} \mathbf{y}_{i+1} \\ \mathbf{y}_{i+2} \\ \vdots \\ \mathbf{y}_{i+m-1} \\ \mathbf{y}_{i+m} \end{bmatrix} \tag{27.10}$$

Since the state transition matrix **A** is constant (the system is time invariant), a number of equations similar to Eq. (27.10) can be formed as shown below.

$$\begin{bmatrix} \mathbf{0} & \mathbf{I} & \cdots & \mathbf{0} \\ \mathbf{0} & \mathbf{0} & \cdots & \mathbf{0} \\ \vdots & \vdots & \ddots & \vdots \\ -\boldsymbol{\alpha}_{\mathbf{0}} & -\boldsymbol{\alpha}_{\mathbf{1}} & \cdots & -\boldsymbol{\alpha}_{\mathbf{m-1}} \end{bmatrix} \begin{bmatrix} \mathbf{y}_{i+0} & \mathbf{y}_{i+1} & \cdots & \mathbf{y}_{i+m-1} \\ \mathbf{y}_{i+1} & \mathbf{y}_{i+2} & \cdots & \mathbf{y}_{i+m} \\ \vdots & \vdots & \ddots & \vdots \\ \mathbf{y}_{i+m-1} & \mathbf{y}_{i+m} & \cdots & \mathbf{y}_{i+2(m-1)} \end{bmatrix}$$
$$= \begin{bmatrix} \mathbf{y}_{i+1} & \mathbf{y}_{i+2} & \cdots & \mathbf{y}_{i+m} \\ \mathbf{y}_{i+2} & \mathbf{y}_{i+3} & \cdots & \mathbf{y}_{i+m+1} \\ \vdots & \vdots & \ddots & \vdots \\ \mathbf{y}_{i+m} & \mathbf{y}_{i+m+1} & \cdots & \mathbf{y}_{i+2m-1} \end{bmatrix} \tag{27.11}$$

For the sake of simplicity, Eq. (27.11) can be written in a compact form as

$$\mathbf{AP} = \mathbf{F} \tag{27.12}$$

which can be solved for **A** in a least squares manner as,

$$\mathbf{A} = \mathbf{FP}^T\left[\,\mathbf{PP}^T\right]^{-1} \tag{27.13}$$

The two products in the above equation, $\mathbf{FP}^T$, $\mathbf{PP}^T$ are two Toeplitz matrices comprising covariance functions

$$\mathbf{PP}^T = \begin{bmatrix} \Lambda_0 & \Lambda_1 & \cdots & \Lambda_{m-1} \\ \Lambda_{-1} & \Lambda_0 & \cdots & \Lambda_{m-2} \\ \vdots & \vdots & \ddots & \vdots \\ \Lambda_{-(m-1)} & \Lambda_{-(m-2)} & \cdots & \Lambda_0 \end{bmatrix}, \qquad \mathbf{FP}^T = \begin{bmatrix} \Lambda_1 & \Lambda_2 & \cdots & \Lambda_m \\ \Lambda_0 & \Lambda_1 & \cdots & \Lambda_{m-1} \\ \vdots & \vdots & \ddots & \vdots \\ \Lambda_{-m} & \Lambda_{-(m-1)} & \cdots & \Lambda_1 \end{bmatrix}$$

It is recognizable that the two matrices $\mathbf{FP}^T$, $\mathbf{PP}^T$ have similar structure as $\overrightarrow{\mathbf{H}}$, $\mathbf{H}_{m-1}$, described in Eq. (27.7). This explains the connection between the traditional approach (based on $\mathbf{H} = \mathbf{Y}_f\mathbf{Y}_p^T$) and the approach suggested in this paper.

Based on above observations, it can be argued that there is no fundamental difference between various formulations of SSI-Cov. The biggest difference is perhaps how the covariance matrices are formed and stacked, and as shown in this paper, this can be done in several ways without having any impact on the final outcome in terms of estimation of modal parameters.

27.2.2 Data Driven Stochastic Subspace Identification Algorithm

Formulation of SSI-Cov algorithm assumes that covariance functions are available and raw output data does not play any role irrespective of whether it is available or not. Various formulations shown in previous section assume that raw data is available, but it is easily noticeable that this is not a requirement and, starting with Eq. (27.3) (or Eq. 27.13) the formulations can be arrived at without much difficulty by simply using the covariance functions in case they are available a priori. SSI-Data, on the contrary, makes it mandatory to have the raw data available. This is the oft-quoted difference between the two popular variants of SSI. However, it can be argued that this requirement is driven more by the need to estimate state vectors **x** within controls engineering domain than by requirements associated with modal parameter estimation. Estimation of state vectors is typically done by means of Kalman filter [5–7], which provides optimal prediction of state vector. It is this requirement that necessitates the availability of raw output time data.

SSI-Data is based on the concept of projection [5, 10], where future outputs are projected on the past outputs. This projection is defined as

$$\mathbf{P}_{fp} = \left[\mathbf{Y}_f\mathbf{Y}_p^T\right]\,\left[\mathbf{Y}_p\mathbf{Y}_p^T\right]^{+}\mathbf{Y}_p \tag{27.14}$$

The Kalman filter state estimates are given as

$$\widehat{\mathbf{X}}_k = \overline{\mathbf{C}} \left[\mathbf{Y}_p \mathbf{Y}_p^T\right]^+ \mathbf{Y}_p \tag{27.15}$$

Using Eqs. (27.3) and (27.4), it is easy to follow that projection defined in Eq. (27.14) can be written as

$$\begin{aligned} \mathbf{P}_{fp} &= \overline{\mathbf{O}}\,\overline{\mathbf{C}} \left[\mathbf{Y}_p \mathbf{Y}_p^T\right]^+ \mathbf{Y}_p \\ &= \overline{\mathbf{O}}\,\widehat{\mathbf{X}}_i \end{aligned} \tag{27.16}$$

This paves the way for decomposing projection $\mathbf{P}_{fp}$ such that extended observability matrix $\overline{\mathbf{O}}$ and Kalman filter states $\widehat{\mathbf{X}}_i$ can be estimated. This is done by means of singular value decomposition of $\mathbf{P}_{fp}$. It is noticeable that estimation of extended observability matrix remains same.

$$\begin{aligned} \overline{\mathbf{O}} &= \mathbf{U}\,\mathbf{S}^{\frac{1}{2}} \\ \widehat{\mathbf{X}}_i &= \mathbf{S}^{\frac{1}{2}} \mathbf{V}^T \end{aligned} \tag{27.17}$$

The state transition matrix can now be easily obtained using the expression provided in Eq. (27.6). However, it is common to provide an alternate expression based on the estimated Kalman filter state and its shifted version $\widehat{\mathbf{X}}_{k+1}$. Using Eq. (27.1) it is easy to obtain $\mathbf{A}$, in terms of estimated state vectors, as

$$\widehat{\mathbf{X}}_{k+1}\,\mathbf{A} = \widehat{\mathbf{X}}_k \tag{27.18}$$

It is clear from above discussion that the reason for using SSI-Data is estimation of state vectors. However, as has been mentioned, this is not a requirement from modal parameter estimation perspective. More importantly, even after estimation of Kalman filter states, one can still utilize the extended observability matrix for estimating state transition matrix [7]. Thus, if estimating the state vectors is not the goal, it is easy to follow that SSI-Data can be formulated simply on the basis of extended observability matrix. In that case, there is no difference between this approach and the one expressed in previous section that described SSI-Cov. Note that basic formulation of SSI-Cov is based on covariance functions and one cannot estimate state vectors only on the basis of covariance functions.

The major distinction between the two variants of SSI is in terms of implementation; unlike SSI-Cov, SSI-Data can be implemented such that calculation of covariance matrices is not required [6]. Otherwise, the only distinction between the two approaches is that in case of SSI-Cov, covariance functions are supposed to be pre-calculated, which is not the case with SSI-Data. SSI-Cov starts directly from the formation of Hankel matrix $\mathbf{H}$ (Eq. 27.3) where as in SSI-Data the raw output data is arranged in terms of past and future responses (Eq. 27.2) so that the covariance functions are calculated as a part of the algorithm.

27.3 Conclusions

This paper reviews the Stochastic Subspace Identification (SSI) algorithm and its two variants (SSI-Cov and SSI-Data) within the framework of modal parameter estimation. One underlining aspect of SSI pointed out in this paper is the fact that the goals of modal parameter estimation stage of operational modal analysis, i.e. estimation of natural frequency, damping and unscaled mode shape, can be achieved through several formulations of SSI. This fact is highlighted by means of an alternate formulation of SSI-Cov presented in this paper. This is done by exploring the relationship between state-space model and high order polynomial model representation of a dynamic system.

The paper further emphasizes that, when viewed within the framework of modal parameter estimation, there is not much difference between SSI-Cov and SSI-Data. This is due to the fact that the aim of these variants differ from when they are applied in Controls Engineering domain (where these algorithms were originally developed) to their application in modal analysis domain. It is understandable from the formulation of SSI-Data that one of its primary goal is state estimation, a goal that is not shared by modal parameter estimation. That state transition matrix can be obtained using the estimated states is an auxiliary step, as estimation of state transition matrix does not rely solely on state vector. State transition matrix can be obtained simply on the basis of extended observability matrix, in which case, there is not much distinction between SSI-Data and SSI-Cov.

References

1. Ibrahim, S.R., Mikulcik, E.C.: A method for direct identification of vibration parameters from the free response. Shock Vib. Bull. **47**(Part 4), 183–198 (1977)
2. Pappa, R.S.: Some statistical performance characteristics of the ITD modal identification algorithm. AIAA Paper Number 82-0768, p. 19 (1982)
3. Juang, J.N., Pappa, R.S.: An eigensystem realization algorithm for modal parameter identification and model reduction. AIAA J. Guid. Control Dyn. **8**(4), 620–627 (1985)
4. Longman, R.W., Juang, J.N.: Recursive form of the eigensystem realization algorithm for system identification. AIAA J. Guid. Control Dyn. **12**(5), 647–652 (1989)
5. Van Overschee, P., De Moor, B.: Subspace identification for linear systems: theory-implementations-applications. Kluwer Academic, Dordrecht, Netherlands (1996)
6. Peeters, B., De Roeck, G.: Stochastic system identification for operational modal analysis: A review. ASME J. Dyn. Syst. Meas. Control **123**, 659–667 (2001)
7. Brincker, R., Andersen, P.: Understanding stochastic subspace identification. In: Proceedings of the 24th International Modal Analysis Conference (IMAC), St. Louis (MO), USA, 2006
8. Kay, S.M.: Modern Spectral Estimation. Prentice Hall, Englewood Cliffs, NJ (1988)
9. Chauhan, S.: Using the unified matrix polynomial approach (UMPA) for the development of the stochastic subspace identification (SSI) algorithm. J. Vib. Control **19**(13), 1950–1961 (2013)
10. Strang, G.: Introduction to Linear Algebra. Wellesley Cambridge Press, Wellesley, MA (2009)

Chapter 28
An Application of Multivariate Empirical Mode Decomposition Towards Structural Modal Identification

Ayan Sadhu

Abstract In this paper, multivariate empirical mode decomposition (MEMD) method is explored to perform structural modal identification. The MEMD is undertaken to estimate the joint information of modal functions utilizing multiple channels of vibration measurements of structures. The mixing of modal responses is alleviated using ensemble EMD (EEMD). The proposed method is validated using numerical studies containing low energy modes and measurement noise. The results show a significant potential of the MEMD method as a modal identification tool.

Keywords MEMD • EMD • EEMD • Ambient modal identification • Multichannel measurements

28.1 Introduction

Output-only modal identification has shown excellent capabilities in real-time monitoring, retrofitting and rehabilitation of large civil infrastructure. Several time and frequency domain algorithms have been studied extensively, and the wealth of literature on this topic is vast [1, 2]. More recently, powerful signal processing methods including short-time Fourier transform [3, 4], blind source separation (BSS) [5–7], empirical mode decomposition (EMD) [8, 9] and Hilbert-Huang transform [10, 11] have been investigated in numerous applications of structural health monitoring.

As compared to any other time-frequency decomposition methods, the EMD method [10] is capable of analyzing nonlinear and nonstationary signals using an *adaptive* transformation. In fact, the EMD method utilizes just a single sensor vibration measurement to extract a subset of modal information [8]. Recently multivariate EMD (MEMD), a variant of EMD, is proposed to utilize multichannel signals under the framework of a data-driven time-frequency analysis [12]. In this paper, the MEMD method is explored as a possible tool for modal identification technique employing multiple vibration measurements.

Due to its self-adaptive nature, EMD method has gained a significant attention in the field of time-frequency decomposition. Huang et. al. [10] developed the EMD method which is able to decompose a signal into several oscillatory waveforms named as intrinsic mode functions (IMF). Using the classical modal superposition theorem, the IMFs can be treated as the modal responses of the structures [8]. IMFs are primarily obtained from multiple averaging and interpolation of the raw signal, known as *sifting* operation. However, the sifting operations involving several interpolations introduce significant mode mixing in the resulting IMFs [10].

Recently, EMD is used for structural modal identification in conjunction with Hilbert transform (e.g., Hilbert-Huang transform) [8, 9, 11], where the mode mixing is alleviated using band-pass filtering. EMD is also integrated with BSS [13, 14] and random decrement technique [15] to perform modal identification using *fewer* sensor measurements. In [16], closely-spaced modes are extracted using the EMD method. However, significant user-intervention in form of *intermittency criteria* based on band-pass filtering is a prerequisite in these methods. Recently, a noise assisted data analysis, ensemble EMD (EEMD) method [17] is developed to circumvent the mode mixing issue in EMD. In EEMD, an artificial noise is introduced repeatedly and then an ensemble of EMD operations are carried out to cancel the effect of mode mixing.

The traditional EMD method uses only a single real-valued signal. While dealing with the multiple measurements, the EMD method faces two fundamental problems [12], (a) there is no guarantee that the decomposition of IMFs from multiple channels of measurements will match in terms of number or their frequency contents, and (b) The joint information between multiple sensors is not exploited because the signals from multiple sensors are treated individually. The traditional EMD method is recently extended to its multivariate version suitable for multichannel signals [12]. In multivariate EMD (MEMD),

---

A. Sadhu (✉)
Department of Civil Engineering, Lakehead University, Thunder Bay, ON, Canada P7B 5E1
e-mail: asadhu@lakeheadu.ca

© The Society for Experimental Mechanics, Inc. 2016

J. De Clerck, D.S. Epp (eds.), *Rotating Machinery, Hybrid Test Methods, Vibro-Acoustics & Laser Vibrometry, Volume 8*,
Conference Proceedings of the Society for Experimental Mechanics Series, DOI 10.1007/978-3-319-30084-9_28

multidimensional envelopes are first developed by utilizing the projections of the raw signal along different directions, and then the average of these envelopes is denoted as the local mean. In this paper, MEMD is attempted to explore for modal identification of structures while dealing with multichannel vibration measurements.

28.2 Multivariate EMD

The traditional EMD method is recently extended to its multivariate version that is amenable to multichannel signals [12]. In multivariate EMD (MEMD), multidimensional envelopes are first developed by utilizing the projections of the raw signal along different directions, and then the average of these envelopes is denoted as the local mean. For a general case of n-dimensional signal, quasi-Monte Carlo-based low-discrepancy sequences are exploited to generate a set of uniformly distributed points on a unit $(n-1)$-sphere [12, 18]. Let us consider a sequence of n-dimensional vectors $\mathbf{z(t)} = \{z_1(t), z_2(t), \ldots, z_n(t)\}$ that represents a multivariate signal with n components, and $D^k = \{u_1^k, u_2^k, \ldots, u_n^k\}$ denotes a set of direction vectors along the k-th directions on a $(n-1)$ sphere. Then MEMD is performed using the following steps [18]:

- Select a suitable set of direction vectors, D.
- Compute the k-th projection, $p^k(t)$ of the input signal $\mathbf{z(t)}$ along the k-th direction vector, X^k, for all k (i.e. $k = 1, 2, \ldots, L$, where L is the total number of direction vectors in D).
- Find the time instants, t_i^k corresponding to the maxima of the projected signal, $p^k(t)$ for all k.
- Interpolate $[t_i^k, \mathbf{z(t_i^k)}]$ to obtain multivariate envelopes, $e^k(t)$, for all k.
- For a set of L direction vectors, the mean $E(t)$ of the envelope curves is obtained as:

$$E(t) = \frac{1}{L}\sum_{k=1}^{L} e^k(t) \tag{28.1}$$

- Extract the residual $r(t)$ using $r(t) = z(t) - E(t)$. If $r(t)$ satisfies the stopping criterion for a multivariate IMF, apply the above steps to $(z(t) - r(t))$ to extract the IMF $(\tilde{i}(t))$, otherwise apply it to $r(t)$.

In order to illustrate the working principles of MEMD, a simple example involving a mixture of sine waves [as shown in Eq. (28.2)] is utilized where $\omega = \{1.0, 2.2, 4.0\}$ Hz.

$$A = \begin{bmatrix} 5 & -1 & 1 \\ -1 & 3 & -2 \\ 1 & -2 & 5 \end{bmatrix} \begin{bmatrix} \sin(\omega_1 t) \\ \sin(\omega_2 t) \\ \sin(\omega_3 t) \end{bmatrix} \tag{28.2}$$

The measurement noise with SNR=10 is further added in the resulting mixtures. Three mixtures are then analyzed using the MEMD and the resulting IMFs of each mixture $x_i(t)$ for $i = 1, 2, 3$ are shown in Fig. 28.1. In order to check the accuracy of the estimated IMFs, each $x_i(t)$ is reconstructed back using the IMFs and compared with the true mixtures. It can be seen the estimated signals match significantly well with the exact signals.

Equation (28.2) is analogous to the modal superposition of the structural systems where the sine waves represent the modal responses and A is the corresponding mode shape matrix. In real situations, there are several low energy modes in the vibration responses of a flexible civil structure. In order to such conditions, the amplitude of the sine signal with frequency 2.2 Hz [in Eq. (28.2)] is reduced by multiplying with a factor of 0.1 and MEMD is employed to separate the sources. Figure 28.2 shows the typical results of identified sources and it can be seen that IMF-2 contains substantial amount of mode mixing due to its low energy contents in the vibration measurements. This is a one of the key results and reveals the basic motivation for a generalized MEMD method to perform structural modal identification using the vibration measurements with practical challenges.

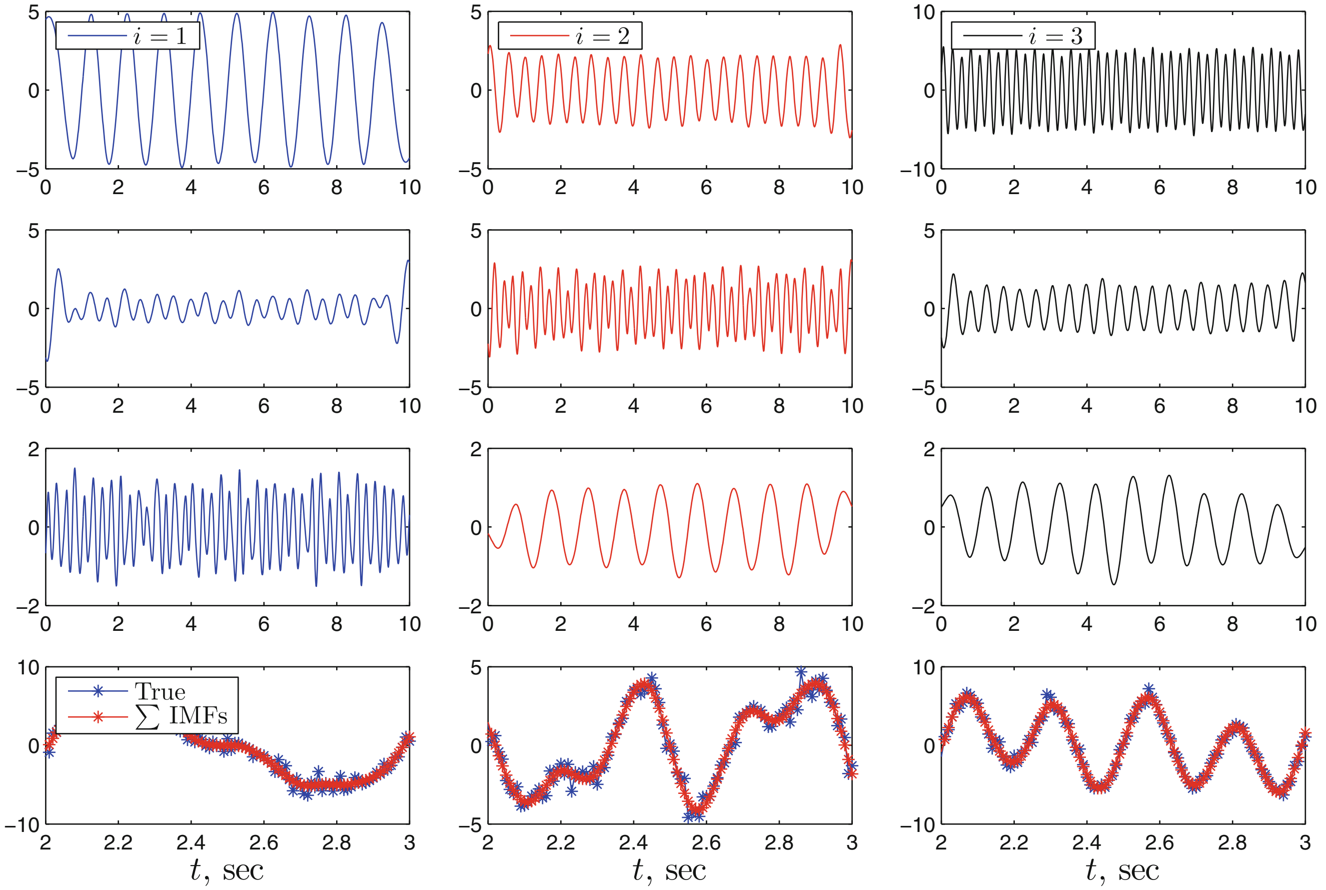

Fig. 28.1 Illustration of the MEMD method under a mixture of sine signals

28.3 A Hybrid MEMD Method

Consider a linear, proportionally damped, and lumped-mass n degrees-of-freedom (DOF) structural system, subjected to a wide-band random input force. The physical response of the structure can be expressed as an expansion of vibration modes:

$$\mathbf{x} = \boldsymbol{\Theta}\mathbf{q} \tag{28.3}$$

where, $\mathbf{x}$ and $\mathbf{q}$ is the response and modal coordinate matrix. $\boldsymbol{\Theta}_{m \times n}$ is the modal transformation matrix, n and m is the number of modal response and measurements respectively. The measurement at the i-th DOF ($i = 1, 2, \ldots, m$) of Eq. (28.3) can be expressed as

$$x_i(t) = \sum_{j=1}^{n} \theta_{ij} q_j(t) \tag{28.4}$$

Performing MEMD of $\mathbf{x(t)}$, each signal of $\mathbf{x(t)}$ can be expressed in terms of its IMFs (i.e., I_{ij}):

$$x_i(t) = \sum_{j=1}^{n} I_{ij}(t) \tag{28.5}$$

where I_{ij} is the j-th IMF of $x_i(t)$.

Considering the similarity of Eqs. (28.4) and (28.5), we get:

$$I_{ij}(t) = \theta_{ij} q_j(t) \qquad i = 1, 2, \ldots, m \tag{28.6}$$

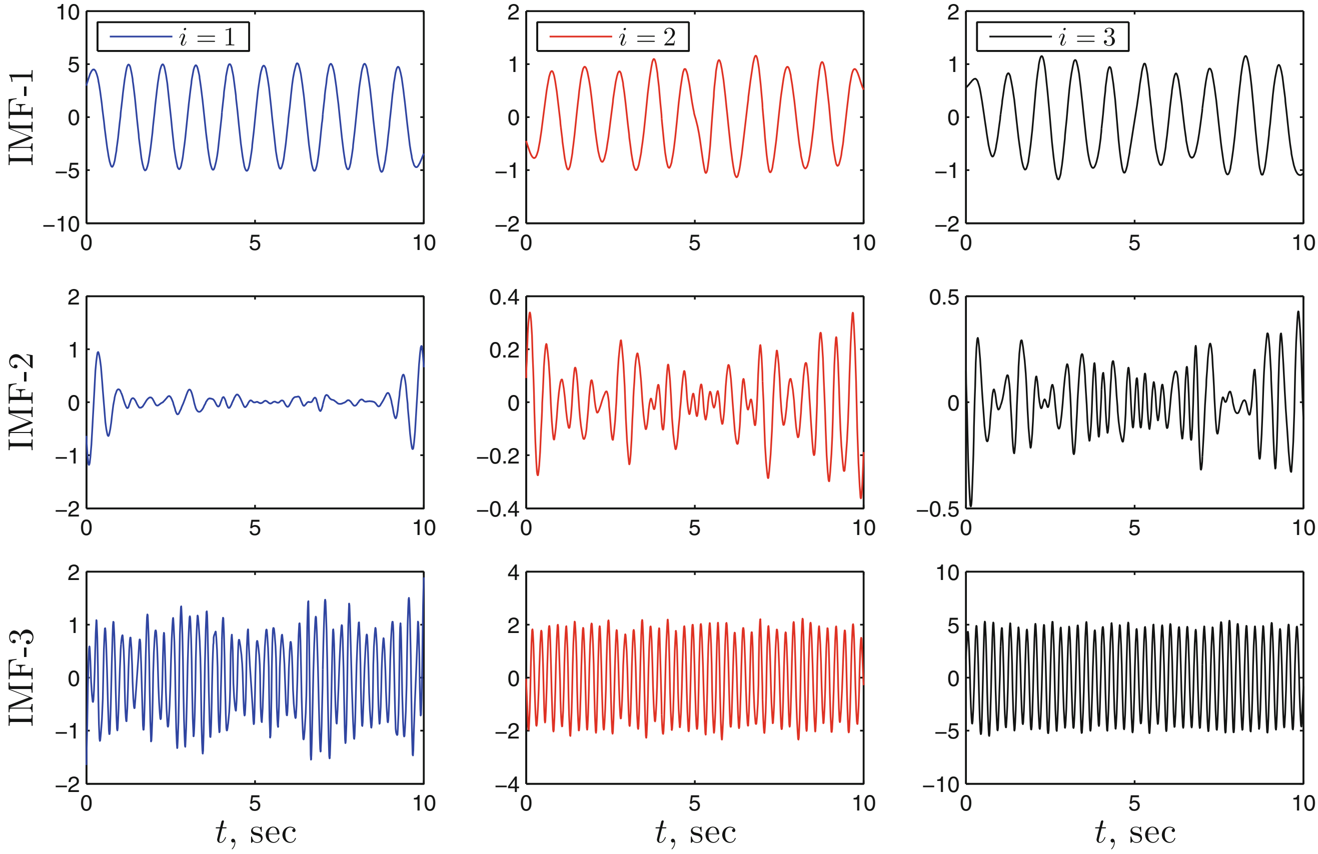

Fig. 28.2 Performance of the MEMD method under low energy signals

Equation (28.6) relates the IMFs of ith measurement with its modal responses. Therefore, following the same idea for $i = p$ and $i = r$ in Eq. (28.6), the partial mode shape coefficients of pth sensor measurement normalized with rth measurement can be expressed as:

$$\frac{I_{pj}}{I_{rj}} = \frac{\theta_{pj} q_j}{\theta_{rj} q_j} = \frac{\theta_{pj}}{\theta_{rj}} = \bar{\theta} pr; \qquad j = 1, 2, \ldots, n \tag{28.7}$$

Then, $\bar{\theta}_{pr} = \frac{\theta_{pj}}{\theta_{rj}}$ represents the estimated normalized mode shape coefficient of the jth mode at the pth DOF. Therefore, we get:

$$I_{pj} = \bar{\theta}_{pr} I_{rj} \tag{28.8}$$

If we pre-multiply both side with I_{pj}^T and take the expectation both sides, Eq. (28.8) can be simplified as:

$$\begin{aligned} \sigma_p &= |\bar{\theta}_{pr}| \sigma_r \\ |\bar{\theta}_{pr}| &= \frac{\sigma_p}{\sigma_r} \end{aligned} \tag{28.9}$$

where, σ_p is the standard deviation of I_{pj}. In order to estimate the sign of $\bar{\theta}_{pr}$, the cross-correlation coefficient (ρ) between I_{pj} and I_{rj} can be used. It may be noted that,

$$\rho_{I_{pj}, I_{rj}} = \rho_{pr} = \frac{E[I_{pj}.I_{rj}^T]}{\sigma_p \times \sigma_r} = \frac{\bar{\theta}_{pr}.\sigma_r^2}{|\bar{\theta}_{pr}| \sigma_r.\sigma_r} = \pm 1 \tag{28.10}$$

Thus the cross-correlation coefficient with a value of ±1.0 indicates the presence of a mono-component source. Following Eqs. (28.9) and (28.10), the true value of $\bar{\theta}_{pr}$ can be estimated:

$$\theta_{pr} = \frac{|\rho_{pr}|}{\rho_{pr}} \frac{\sigma_p}{\sigma_r} \tag{28.11}$$

Using this procedure, the normalized mode shape coefficients can be estimated using IMFs of sensor measurements. As discussed in the introduction section, the sifting operation in EMD sometimes leads to multi-component sources in the IMFs. However, Eqs. (28.7) and (28.11) are valid only when the IMFs are mono-component. In order to identify the mono-component sources in the IMFs, the cross-correlation between I_{pj} and I_{rj} can be used, and if more than one source is detected, then the source separation capability of EEMD is utilized to delineate the mono-component IMFs among these multi-component IMFs and then mode shape coefficients are estimated.

28.4 Numerical Illustration

The relative performance of MEMD method and the improved MEMD method is now compared using a 5-DOF building model comprising of low energy modes and measurement noise. The natural frequencies are 0.91, 3.37, 7.11, 10.66 and 12.73 Hz. White Gaussian noise is used to excite the building at all its floor locations. Fourier spectra of the floor measurements are shown in Fig. 28.3 that shows relatively low energy in 2nd and 5th mode as compared to other modes. The MEMD method is now performed using all vibration measurements and the resulting IMFs are shown in Fig. 28.4. It can be seen that, due to low energy content of the 2nd and 5th mode, the resulting modal responses are mixed with the other IMFs and have resulted in mode mixing. As given in Table 28.1, the correlation coefficients of the IMFs [using Eq. (28.10)] are successively used to detect the mode mixing. When ρ close to 1.0, the IMFs are considered mono-component and they are treated as modal responses. Then the mode shape coefficients are computed based on Eq. (28.11) and are tabulated for I_{i1} and I_{i2} in Table 28.1. For example, $\hat{\phi}_{31} = \frac{\sigma_3}{\sigma_1} = \frac{0.023}{0.039} = 0.59$. On the other hand, when $\rho \neq 1.0$, it indicates the mode mixing in the IMFs where EEMD is exploited to separate the modal responses from the IMFs. The details of the modal identification are finally tabulated in Table 28.2. The results show that the improved MEMD performs significantly well even under the presence of measurement noise which is attributed by the de-noising effect of EMD.

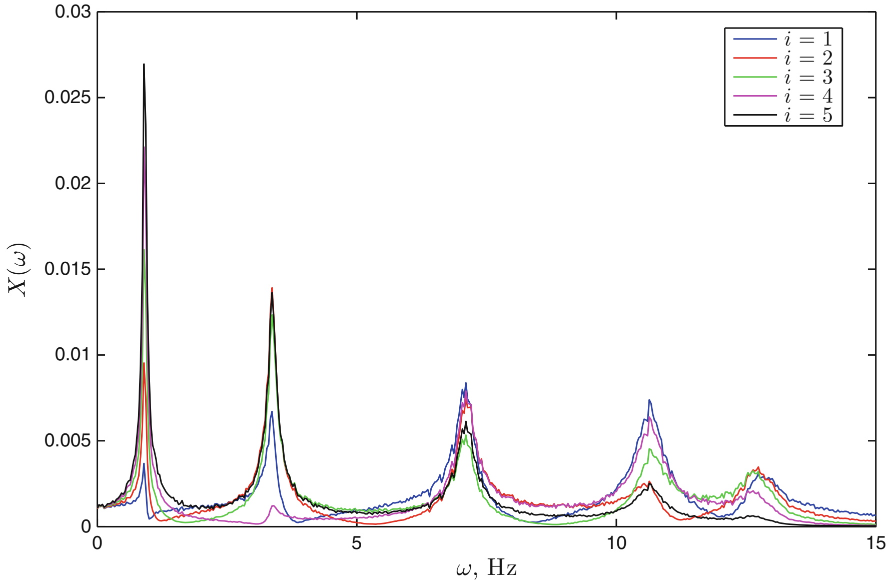

Fig. 28.3 Fourier spectra of floor vibration measurements of the 5-DOF building

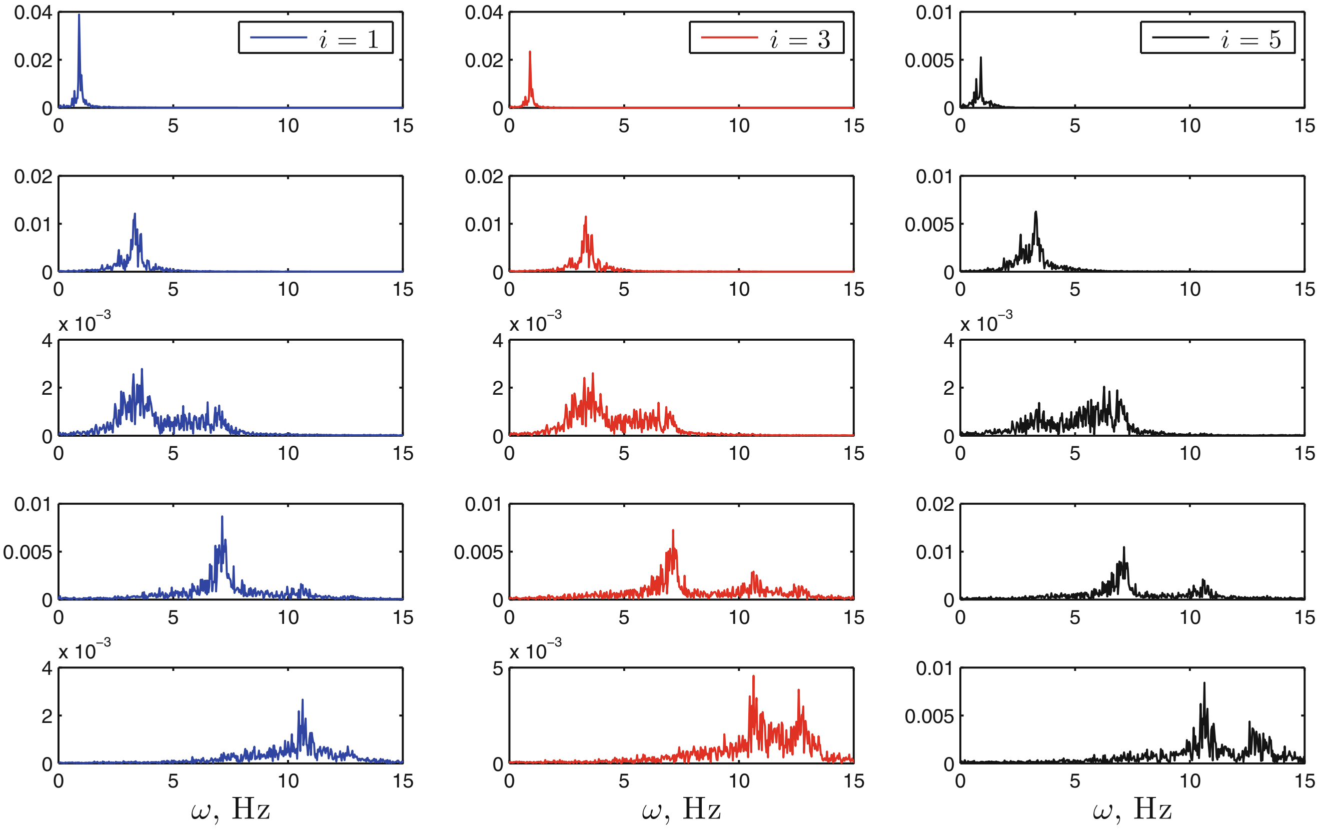

Fig. 28.4 MEMD method: presence of mode mixing

Table 28.1 Details of identification results of MEMD method

I_{ij}	σ_1	σ_3	σ_5	ρ_{13}	ρ_{15}	$\hat{\phi}_{3j}$ (ϕ_{3j})	$\hat{\phi}_{5j}$ (ϕ_{5j})
I_{i1}	0.039	0.023	0.0051	1.0	1.0	0.59 (0.59)	0.12 (0.11)
I_{i2}	0.012	0.011	0.006	−1.0	−0.99	−0.92 (−0.91)	−0.5 (−0.48)
I_{i3}	0.0028	0.0026	0.0021	−0.82	−0.79	EEMD	EEMD
I_{i4}	0.0087	0.0073	0.011	0.92	−0.9	EEMD	EEMD
I_{i5}	0.0027	0.0046	0.0084	0.85	0.87	EEMD	EEMD

Table 28.2 Identification results of the improved MEMD method

	IMF		MAC	
Mode	ω, Hz	ξ(%)	SNR=100	SNR=10
1	0.91	1.9	1.0	0.99
2	3.39	1.95	0.99	0.98
3	7.1	2.03	1.0	0.99
4	10.67	2.1	1.0	0.99
5	12.74	1.99	0.99	0.99

28.5 Conclusions

In this paper, the MEMD method is explored as a possible candidate of modal identification method using multiple vibration measurements. It is observed that the IMFs resulting from the MEMD method are prone to mode mixing which is then alleviated using the EEMD. While doing so, the proposed method is developed by combining the relative merits of MEMD (i.e., use of multiple sensors) and EEMD (i.e., eliminating mode mixing issues). The improved MEMD method is illustrated using a suite of numerical studies including the cases containing low energy and measurement noise. Future research is reserved to validate this method addressing the several other challenges of modal identification in a real-life structure.

Acknowledgements The author would like to thank Natural Science and Engineering Research Council (NSERC) of Canada to provide funding for this research.

References

1. Maia, N.M.M., Silva, J.M.M.: Modal analysis identification techniques. Philos. Trans. R. Soc. **359**(1778), 29–40 (2001)
2. Staszewski, W.J., Robertson, A.N.: Time-frequency and time-scale analyses for structural heal monitoring. Philos. Trans. R. Soc. **365**, 449–477 (2007)
3. Ghanem, R., Romeo, F.: A wavelet based approach for the identification of linear time-varying dynamical systems. J. Sound Vib. **234**(4), 555–576 (2000)
4. Yan, Y.J., Cheng, L., Wu, Z.Y., Yam, L.H.: Wavelet transform-based modal parameter identification considering uncertainty. J. Sound Vib. **291**, 285–301 (2006)
5. Antoni, J., Garibaldi, L., Marchesiello, S., Sidhamed, M.: New separation techniques for output-only modal analysis. Shock Vib. **11**, 227–242 (2004)
6. Sadhu, A.: Decentralized ambient modal identification of structures. Ph.D. thesis (2013)
7. Sadhu, A.: Blind source separation: a generalized modal identification tool for civil structures. In: Proceedings of the 33th International Modal Analysis Conference (IMAC), Orlando, FL (2015)
8. Yang, J.N., Lei, Y., Pan, S., Huang, N.: System identification of linear structures based on Hilbert Huang spectral analysis. Part 1: normal modes. Earthq. Eng. Struct. Dyn. **32**(9), 1443–1467 (2003)
9. Darryll, P., Liming, S.: Structural health monitoring using empirical mode decomposition and the Hilbert phase. J. Sound Vib. **294**(1–2), 97–124 (2006)
10. Huang N.E., et al.: The empirical mode decomposition for the Hilbert spectrum for nonlinear and non-stationary time series analysis. In: Proceedings of Royal Society of London Series, pp. 903–95 (1998)
11. Yang, J.N., Lei, Y., Lin, S., Huang, N.: Identification of natural frequencies and dampings of in-situ tall buildings using ambient wind vibration data. J. Eng. Mech. **130**(5), 570–577 (2004)
12. Rehman, N., Mandic, D.P.: Multivariate empirical mode decomposition. Proc. R. Soc. A **466**, 1291–1302 (2010)
13. Hazra, B., Sadhu, A., Roffel, A.J., Paquet, P. E., Narasimhan, S., Underdetermined Blind Identification of Structure by using the Modified Cross-Correlation method. J. Eng. Mech. **138**(4), 327–337 (2012)
14. Hazra, B., Sadhu, A., Roffel, A.J., Narasimhan, S.: Hybrid time-frequency blind source separation towards Ambient system identification of structures. Comput.-Aided Civ. Infrastruct. Eng. **27**(5), 314–332 (2012)
15. He, X., Hua, X., Chen, Z., Huang, F.: EMD-based random decrement technique for modal parameter identification of an existing railway bridge. Eng. Struct. **33**(4), 1348–1356 (2011)
16. Hazra, B., Sadhu, A., Lourenco, R., Narasimhan, S.: Re-tuning tuned mass dampers using ambient vibration response. Smart Mater. Struct. **19**(11), 115002 (2010)
17. Wu, Z., Huang, N.E.: Ensemble empirical mode decomposition: a noise assisted data analysis method. Technical Report 193, pp. 1898–1906 (2005)
18. Rehman, N., Mandic, D.P.: Filter bank property of multivariate empirical mode decomposition. IEEE Trans. Signal Process. **59**(5), 2421–2426 (2011)

Chapter 29
Dynamic Characterization of Milling Plant Columns

Filippo Cangioli, Steven Chatterton, Paolo Pennacchi, and Edoardo Sabbioni

Abstract Building structures the most rigid as possible is a common practice in order to guarantee extremely precise tool spindle positioning. However, very rigid structures are usually very lightly damped and this could lead to some dynamic problems in case of resonance conditions. In the case of milling machines, due to the variety of milling programs and of cutting tool types, the machine tool is often forced by a broad frequency spectrum excitation, quite impossible to be predicted at a design stage. Thus a near-resonance working condition could easily appear.

In recent years, to increase damping whilst maintaining very rigid structures, metal foam sandwiches have been used. However, it is quite rare to find comprehensive experimental studies demonstrating the effectiveness of this solution on a complete structure, such as a column of a milling machine.

In this paper, two columns of a milling machine built using different technologies, i.e. classic metalworking and metal foam sandwiches, are compared. On this purpose experimental modal analysis was applied.

Keywords Metal foams • Sandwiches structures • Damping estimation • Machine tool dynamic characterization • Experimental modal analysis

29.1 Introduction

Rigid structures are commonly the design solutions selected by machine tool manufacturers in order to obtain precise tool spindle positioning [1, 2]. However, as known, very rigid structures are often very lightly damped [3, 4] and this may lead to dynamic problems when working/passing through resonance conditions.

Considering milling plants, the variety of working conditions and tool types often produce a wide frequency spectrum excitation, which is difficult to predict at a design stage. As a consequence, near-resonance conditions can occur compromising good quality of machining or, in the worst case, leading to instabilities, causing the so-called "chatter" phenomenon [5–7].

A commonly adopted design solution to increase damping, whilst maintaining very rigid structures, is the use of metal foam sandwiches. Specifically, in tooling machines, stiff foamed parts or foam-filled columns are nowadays extensively used since they allow, not only to enhance damping, but also to reduce inertia.

However, evaluation of effectiveness of these design solutions from a damping enhancement point of view is still an open point. Due to unevenness of foamed parts, evaluation of mechanical properties of metallic foams is in fact quite challenging [8], and especially evaluation of damping properties (e.g. the loss factor) presents intrinsically even more difficulties. Some attempts to identify the loss factor and energy absorption capabilities of metallic foams are present in the technical literature [9–12]. An experimental approach is generally adopted and analyses are concerned with foam-filled specimen.

A comprehensive experimental study investigating the mechanical properties (especially damping) of a complete structure (such as a column of a milling machine) built using foam-filled parts is instead very rare to find. This kind of analysis is in fact generally believed as difficult, since foam-filled structures usually show a nonlinear behavior and so standard experimental modal procedures cannot be applied.

In this paper, a comparative study about the dynamic behavior of two columns of a milling machine is presented. One column is made according to traditional techniques (metal carpentry), while the other is built using panels of metal foam sandwiches shaped and welded together. To evaluate the dynamic behavior of the two columns, experimental modal analysis was applied.

F. Cangioli • S. Chatterton • P. Pennacchi • E. Sabbioni (✉)
Department of Mechanical Engineering, Politecnico di Milano, Via La Masa 1, 20156 Milan, Italy
e-mail: edoardo.sabbioni@polimi.it

© The Society for Experimental Mechanics, Inc. 2016

J. De Clerck, D.S. Epp (eds.), *Rotating Machinery, Hybrid Test Methods, Vibro-Acoustics & Laser Vibrometry, Volume 8*,
Conference Proceedings of the Society for Experimental Mechanics Series, DOI 10.1007/978-3-319-30084-9_29

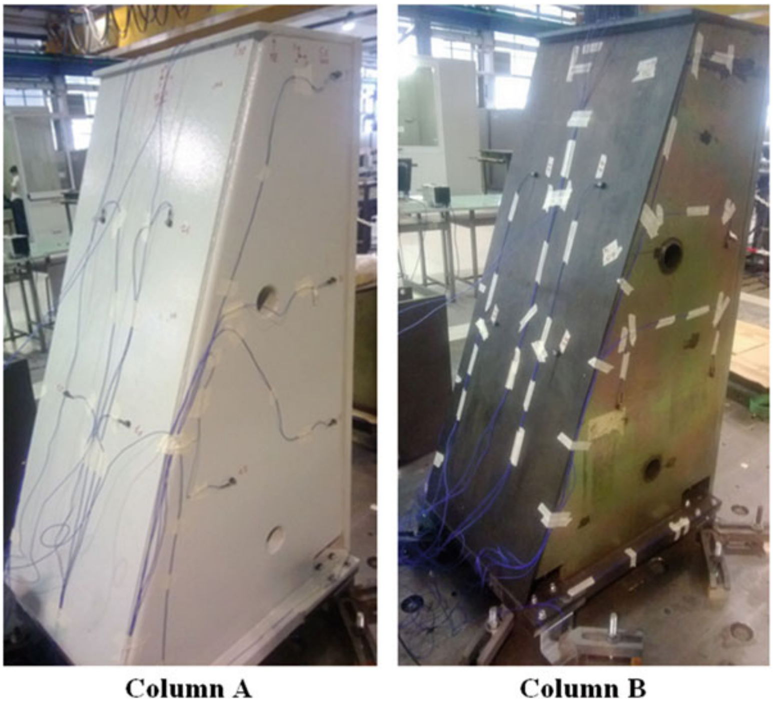

Fig. 29.1 Columns of a milling machine with table of fixed height and vertical spindle: conventional metal carpentry (*left*), panels of sandwich filled with metal foam (*right*). Note the position of the accelerometer on the column surfaces

As it will be shown in the details, despite the geometry of the two columns is essentially the same, from a dynamic point of view they present very different modes of vibration and damping properties.

29.2 Column Description and Setup of Experimental Tests

The two structures considered in the paper are the main columns of the milling machine, which support the vertical milling spindle. They are made by using two different technologies: the first one ("column A" in the following, which is painted white in Fig. 29.1) has a traditional "box" design and is manufactured by using classical metal carpentry, with welded steel plates of thickness up to 30 mm. The second column is a prototype ("column B" in the following, bare metal in Fig. 29.1) and is made of tiny sandwich panels filled with metal (aluminium based) foam, which resulted in a lighter structure. The macro-geometry is very similar, so that the columns are interchangeable: they can be connected to the same guides on the bed slideways and they have the vertical slideways for the same milling head; however, some inner parts and bracings are quite different in number and dimensions.

Column A has a mass of 958 kg, while that of column B is 805 kg, namely about 16 % less.

29.3 Experimental Set-Up

The experimental tests have been performed by following the same procedure for both the columns and aimed at evaluating the main dynamic differences between them, in order to assess the advantages of installing columns of type B in mass production machines.

The columns were fixed on a very massive suspended foundation by means of four special machined supports, which realized a very stiff connection. The stiffness of the connection was checked by installing one accelerometer on each support and another one close to it on the column side (see Fig. 29.2, left) and by comparing the results of the measured impulse response function during bump tests, as explained in the following.

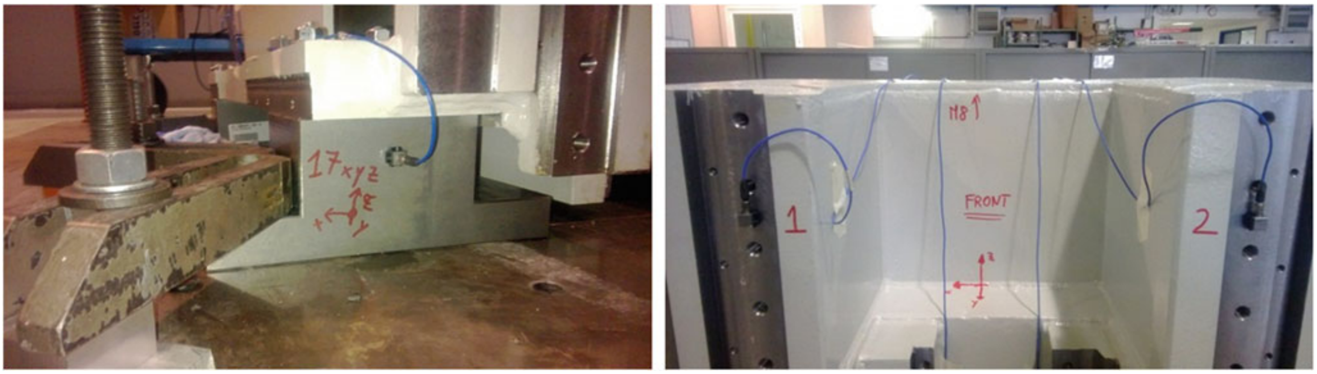

Fig. 29.2 Close up of accelerometers installed on the connections to the foundation (*left*) and on the top-front of the column (*right*)

Once the stiff connection has been verified, both columns have been instrumented with 18 piezoelectric accelerometers (see Figs. 29.1 and 29.2, right), four accelerometers for each lateral surface and two accelerometers on the bottom, in order to evaluate the stiffness of the ground constrain, as said before. Despite the columns were structurally different, the accelerometers have been installed in homologous positions, since the external geometry is quite similar.

The columns were excited by means of an impact hammer and several excitation points were considered (up to seven positions) to possibly avoid nodes of the modes of vibration of the surface. Several time histories of the vibration amplitude decays were recorded to calculate the average of the signal and to reduce noise. In addition, to evaluate possible non-linearities of column responses (especially for column B), several impulsive tests with different input force amplitudes were carried out. Tests were performed using a pendulum configuration with the impact hammer installed on it. No noticeable differences appeared in the impulse frequency response functions (FRFs) considering four different force amplitudes. This implies that the behavior of both the columns is linear. This is a first remarkable result of the test campaign and allows the application of standard modal analysis methods.

29.3.1 Sensors and Data Acquisition System

The system response to the input force has been measured by means of the following devices:

- Eighteen PCB Piezotronics 333B30 piezoelectric accelerometers (±50 g pk) conditioned with a PCB Piezotronics 483C50 conditioning unit;
- Five National Instruments NI9239 boards (4 channels each, resolution 24 bit, voltage ±10 V, maximum data sampling 50 kS/s per channel, antialiasing filter) installed on a National Instruments cDAQ 9172 chassis (8 slots).

The impulsive excitation was provided by using a PCB Piezotronics 086D05 dynamometric hammer, equipped with metal tip. The accelerometer positions on the column surfaces are shown in Fig. 29.3, with a red dot (•). These positions are also the nodes of the grid used for the identification of the mode shapes. Two additional accelerometers were installed close to the connection to the foundation (Fig. 29.2 right). The hammer impact points are also shown in Fig. 29.3, with a blue cross (×).

Each time history has been acquired for 5 s at the sampling frequency of 12500 Hz, then windowed around the decay. In order to reduce the uncorrelated measurement noise [13, 14], each test was repeated 15 times. The impulse FRFs has been calculated according to the H1 estimator:

$$H_1(f) = \frac{\overline{G}_{xy}(f)}{\overline{G}_{xx}(f)} \tag{29.1}$$

where $\overline{G}_{xy}$ and $\overline{G}_{xx}$ represent the averaged cross and auto spectra respectively, referred to the input $X(f)$ and of the outputs $Y(f)$ spectra. The top of Figs. 29.4 and 29.5 shows the magnitude of the calculated FRFs in accelerometer positions #2 and #9 respectively, for both kinds of columns.

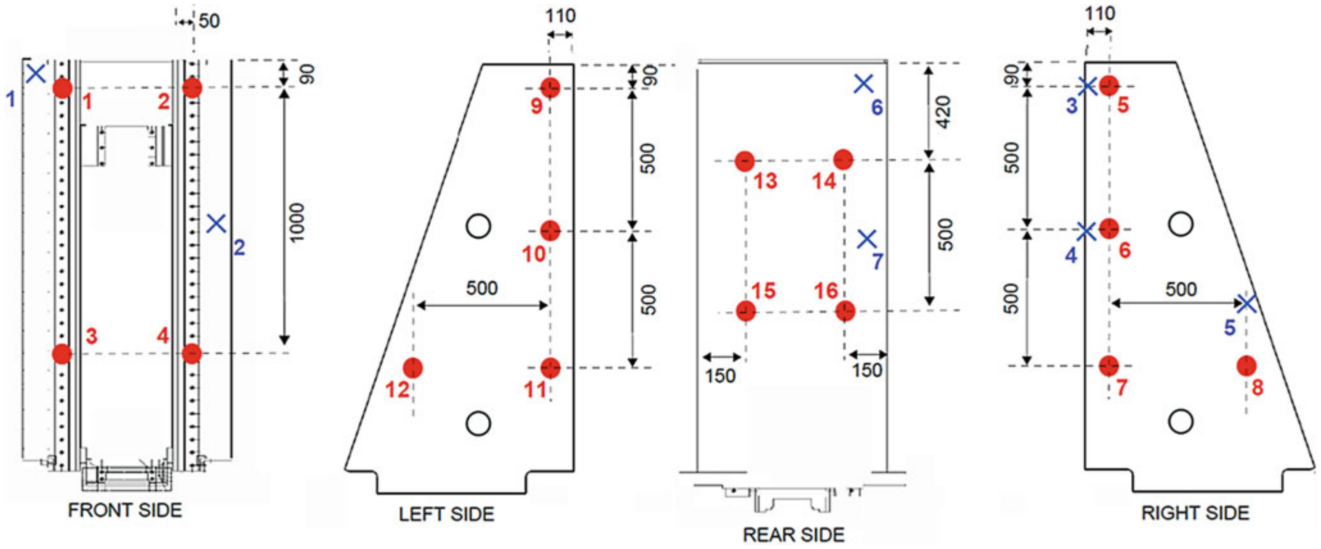
50
1
2
1
2
3
4
90
1000
FRONT SIDE
110
90
9
500
10
500
500
11
12
LEFT SIDE
6
420
13
14
7
500
15
16
150
150
REAR SIDE
110
90
3
5
500
4
6
500
500
5
7
8
RIGHT SIDE

Fig. 29.3 Position of the accelerometers (*red dot*) and of the hammer impact points (*cross*) on the columns

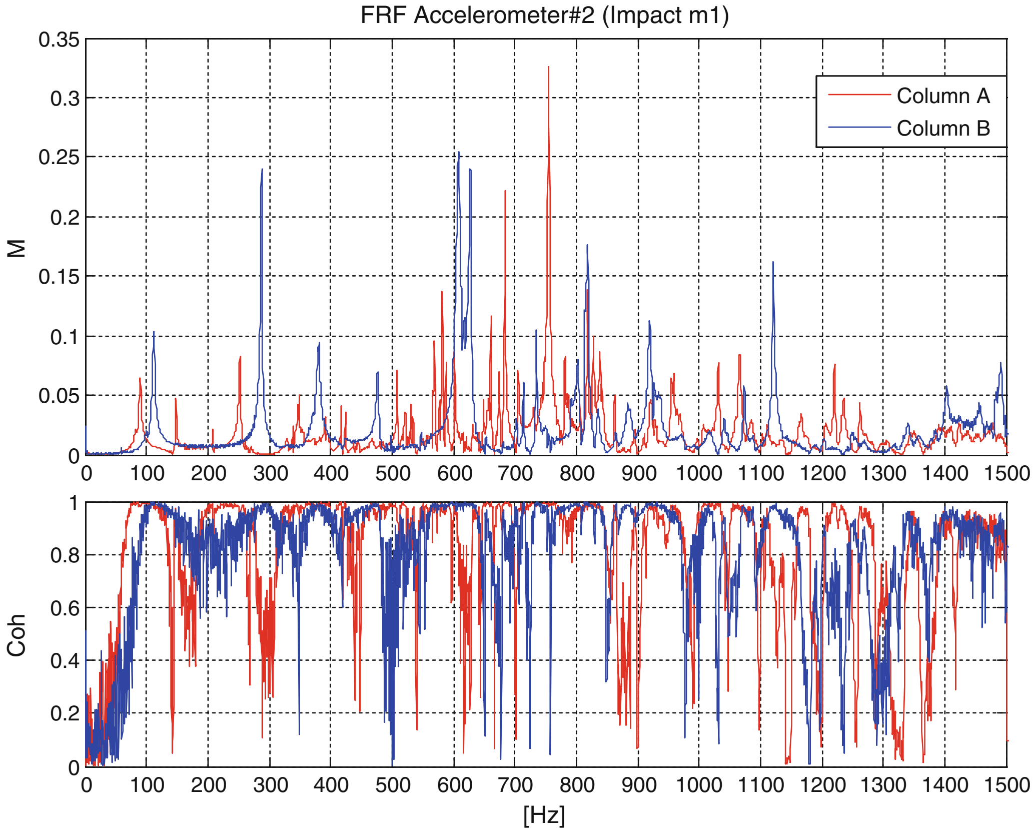

Fig. 29.4 Magnitude of FRF and coherence functions for the two columns: accelerometer #2—impact in m_1

In addition, the coherence functions were calculated as:

$$\gamma_{xy}^2 = \frac{\left|\overline{G}_{xy}(f)\right|^2}{\overline{G}_{xx}(f)\overline{G}_{yy}(f)} \tag{29.2}$$

Coherence values over 0.9 are commonly considered acceptable. The bottom of Figs. 29.4 and 29.5 shows the calculated coherences for accelerometer positions #2 and #9 respectively.

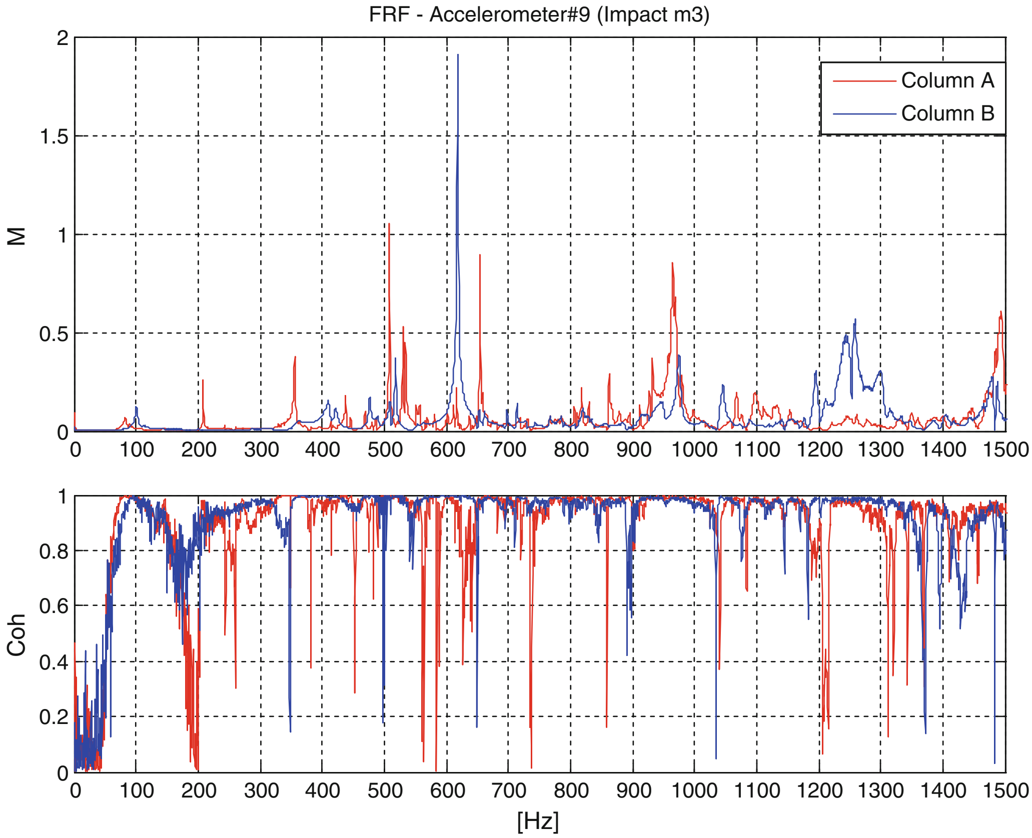

Fig. 29.5 Magnitude of FRF and coherence functions for the two columns: accelerometer #9—impact in m_3

29.3.2 Signal Processing

The modal identification of the mechanical parameters of the columns has been made by using the experimental FRFs of Eq. (29.1). The procedure has been divided in two steps:

1. In the first step, the LSCE—Least Squares Complex Exponentials algorithm [15] was used to identify the modal parameters. In this way, for each selected frequency range, the stability of each pole was evaluated with the increasing of the order of the system.
2. In the second step, a numerical optimization of the analytical FRF was carried out with respect to the experimental one. An analytical FRF is essentially defined as a limited sum of single degree of freedom systems of the second order, with upper n_2 and lower n_1 residual terms too:

$$\alpha_{jk}(\omega) = \frac{1}{\omega^2 M_{jk}^{(r)}} + \sum_{r=n_1}^{n_2} \frac{A_{jk}^{(r)}}{\omega_r^2 - \omega^2 + 2\,\mathrm{i}\,\xi\omega\omega_r} + \frac{1}{K_{jk}^{(r)}} \tag{29.3}$$

Actually, the modal identification relies on a multi-channel and multi-modal procedure, which allows performing simultaneous analysis of all the measurement channels for a quite wide frequency range (in this case up to 1500 Hz).

Finally, modal frequencies, modal masses and modal damping values are obtained. In order to compare the different identified modes between column A and B, MAC (Modal Assurance Criterion, [16]) indexes were calculated as:

$$MAC\left(\phi_{\varepsilon_A}, \phi_{\varsigma_B}\right) = \frac{\left|\sum_{i=1}^{n_{ch}} \left(\phi_{\varepsilon_A}\right)_i \left(\phi_{\varsigma_B}^*\right)_i\right|^2}{\sum_{i=1}^{n_{ch}} \left(\phi_{\varepsilon_A}\right)_i \left(\phi_{\varepsilon_A}^*\right)_i \sum_{i=1}^{n_{ch}} \left(\phi_{\varsigma_B}\right)_i \left(\phi_{\varsigma_B}^*\right)_i} \tag{29.4}$$

Table 29.1 Column A: natural frequencies and damping ratios

Mode	Frequency f (Hz)	Damping ratio ξ
1	84.0	0.4089
2	89.5	0.3104
3	148.5	0.0779
4	208.5	0.0484
5	253.0	0.1005
6	343.5	0.1301
7	346.5	0.2061
8	355.5	0.1005
9	343.5	0.0810
10	424.5	0.0319
11	469.0	0.0938
12	508.5	0.0288
13	530.5	0.0363
14	569.0	0.0299

Table 29.2 Column B: natural frequencies and damping ratios

Mode	Frequency f (Hz)	Damping ratio ξ
1	101.0	0.3410
2	112.0	0.2714
3	287.5	0.0678
4	381.0	0.1642
5	410.5	0.1484
6	476.0	0.0784
7	518.5	0.0385
8	608.0	0.0949
9	619.0	0.0296
10	698.0	0.0201
11	735.0	0.0265
12	756.5	0.0279
13	802.5	0.0466
14	934.0	0.0594
15	974.0	0.1283
16	1045.5	0.0590

where $\phi_{\varepsilon_{\mathrm{A}}}$ represents the ε-*th* modal shape of column A previously identified, compared with the ζ-*th* modal shape $\phi_{\varsigma_{\mathrm{B}}}$ of column B. Also AutoMAC indexes were calculated, in order to compare the modes of the same columns, by simply replacing index A with B, or vice versa, in Eq. (29.4). High MAC or AutoMAC values (that is, close to 1) reveal high similarity of the compared modes.

29.4 Results

As expected, the two columns show quite different dynamic behaviour, due to the different manufacturing method, and only few modes can be directly compared.

The identified modes for the two columns are reported in Tables 29.1 and 29.2, respectively. As a rule of thumb, the modes of the lighter column B have higher natural frequencies. The AutoMAC indexes are displayed in Figs. 29.6 and 29.7. While the diagonal terms are obviously equal to one, the off-diagonal terms are much smaller than one, thus indicating that enough sensors have been used to determine the modes and that they are well distinguished. The MAC values between the modes of columns A and B are shown in Fig. 29.8.

The values of $MAC\left(\Phi_{1_A}, \Phi_{1_B}\right)$ and $MAC\left(\Phi_{2_A}, \Phi_{2_B}\right)$ are very high (0.95 and 0.97 respectively) and this can be easily explained by considering the mode shapes in Figs. 29.9 and 29.10: the first and second modes, for both columns, are practically the “main” bending mode of the cantilever column, rigidly connected to the foundation. The two frequencies

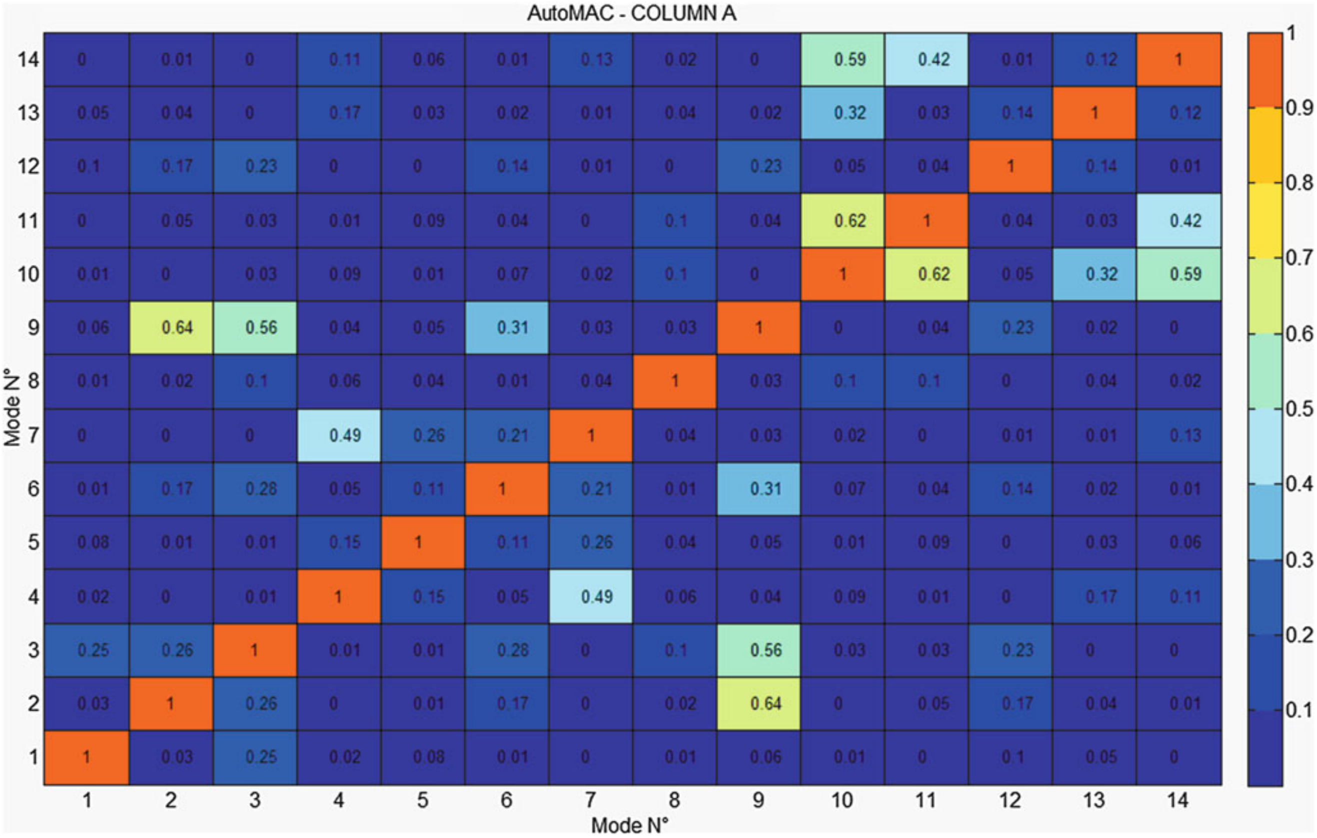

Mode N°	1	2	3	4	5	6	7	8	9	10	11	12	13	14
14	0	0.01	0	0.11	0.06	0.01	0.13	0.02	0	0.59	0.42	0.01	0.12	1
13	0.05	0.04	0	0.17	0.03	0.02	0.01	0.04	0.02	0.32	0.03	0.14	1	0.12
12	0.1	0.17	0.23	0	0	0.14	0.01	0	0.23	0.05	0.04	1	0.14	0.01
11	0	0.05	0.03	0.01	0.09	0.04	0	0.1	0.04	0.62	1	0.04	0.03	0.42
10	0.01	0	0.03	0.09	0.01	0.07	0.02	0.1	0	1	0.62	0.05	0.32	0.59
9	0.06	0.64	0.56	0.04	0.05	0.31	0.03	0.03	1	0	0.04	0.23	0.02	0
8	0.01	0.02	0.1	0.06	0.04	0.01	0.04	1	0.03	0.1	0.1	0	0.04	0.02
7	0	0	0	0.49	0.26	0.21	1	0.04	0.03	0.02	0	0.01	0.01	0.13
6	0.01	0.17	0.28	0.05	0.11	1	0.21	0.01	0.31	0.07	0.04	0.14	0.02	0.01
5	0.08	0.01	0.01	0.15	1	0.11	0.26	0.04	0.05	0.01	0.09	0	0.03	0.06
4	0.02	0	0.01	1	0.15	0.05	0.49	0.06	0.04	0.09	0.01	0	0.17	0.11
3	0.25	0.26	1	0.01	0.01	0.28	0	0.1	0.56	0.03	0.03	0.23	0	0
2	0.03	1	0.26	0	0.01	0.17	0	0.02	0.64	0	0.05	0.17	0.04	0.01
1	1	0.03	0.25	0.02	0.08	0.01	0	0.01	0.06	0.01	0	0.1	0.05	0

Fig. 29.6 *AutoMAC* values for the modes of columns A

Table 29.3 Comparison between modes with high MAC

	Frequency (Hz)			2πf ξ		
	Column A	Column B	$\Delta_{f\mathrm{BA}}$ (%)	Column A	Column B	$\Delta_{2\pi f\xi\mathrm{BA}}$ (%)
$\phi_{1_\mathrm{A}}, \phi_{1_\mathrm{B}}$	84.0	101.0	20.2	216	216	0
$\phi_{2_\mathrm{A}}, \phi_{2_\mathrm{B}}$	89.5	112.0	25.1	175	191	9
$\phi_{5_\mathrm{A}}, \phi_{3_\mathrm{B}}$	253.0	287.5	13.7	160	122	−24
$\phi_{12_\mathrm{A}}, \phi_{9_\mathrm{B}}$	508.5	619.0	21.7	92	115	25

associated to the modes are very close (see Tables 29.1 and 29.2, 84.0 and 89.5 Hz for column A and 101.0 and 112.0 Hz for column B) and the "first" bending mode is likely split owing to the unavoidable asymmetries of the manufactured columns. Also $MAC\,(\Phi_{5_A}, \Phi_{3_B})$ is quite high, i.e. 0.87. Figure 29.11 shows that mode 5 of column A and mode 3 of columns B are practically the first torsional mode of the cantilever columns. Finally $MAC\,(\Phi_{12_A}, \Phi_{9_B})$ is equal to 0.71. The corresponding mode shapes are shown in Fig. 29.12: the columns are "tapering" towards the top and bottom bases alternatively.

By considering only the mode pairs that show high MAC values (above 0.7 in Fig. 29.8), which are the only ones for which any comparison might have sense, a first possible result is reported in Table 29.3. For the considered mode pairs, frequencies exhibit a sensible increase, up to 25 %, in case of the structure made of metal foam sandwiches. However, the product $2\pi f \cdot \xi$, which is the actual system damping for the given frequency f, does not show any clear trend.

It must be pointed out that since columns are comparable only for geometric dimensions but differ in terms of construction, only few modes are directly comparable and however are characterized by very different frequencies. Thus comparing only damping of modes of vibration cannot provide any clear conclusion.

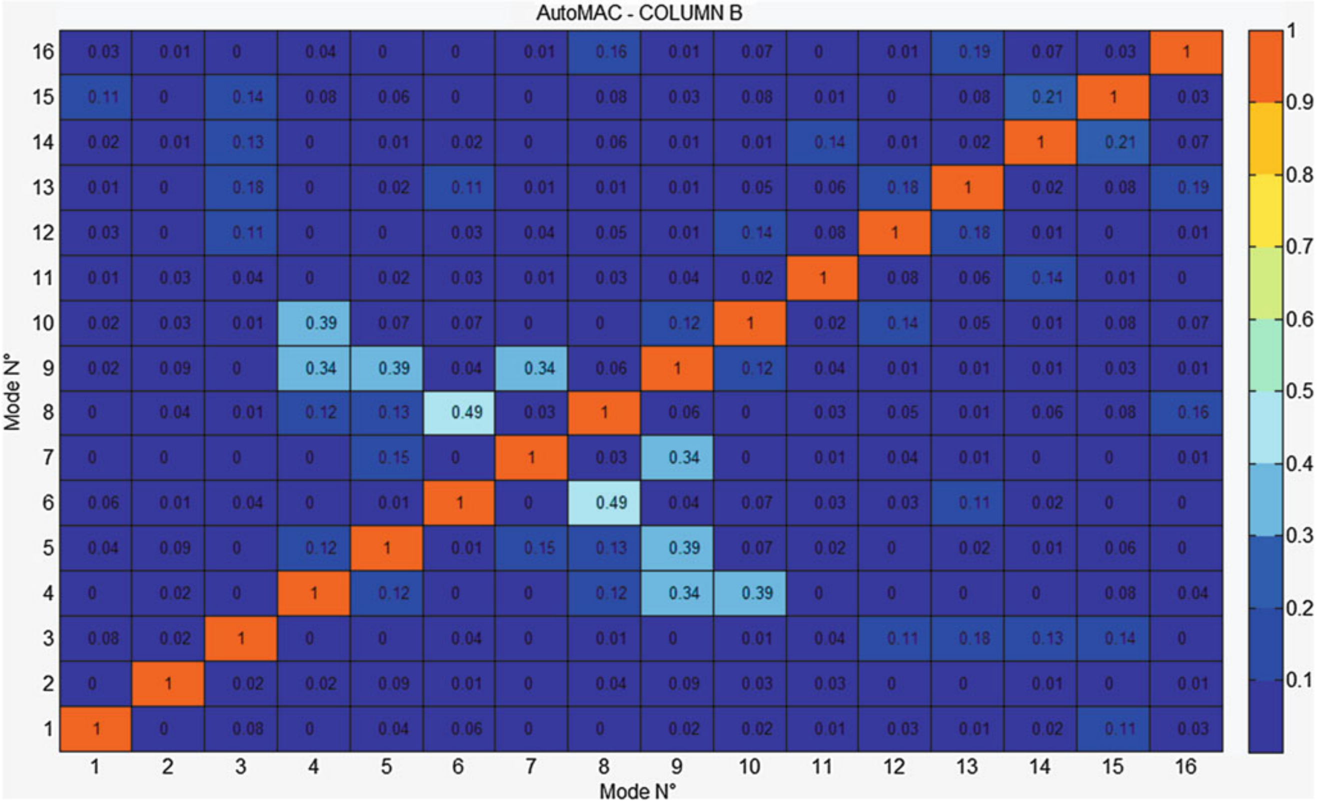

Mode N°	1	2	3	4	5	6	7	8	9	10	11	12	13	14	15	16
16	0.03	0.01	0	0.04	0	0	0.01	0.16	0.01	0.07	0	0.01	0.19	0.07	0.03	1
15	0.11	0	0.14	0.08	0.06	0	0	0.08	0.03	0.08	0.01	0	0.08	0.21	1	0.03
14	0.02	0.01	0.13	0	0.01	0.02	0	0.06	0.01	0.01	0.14	0.01	0.02	1	0.21	0.07
13	0.01	0	0.18	0	0.02	0.11	0.01	0.01	0.01	0.05	0.06	0.18	1	0.02	0.08	0.19
12	0.03	0	0.11	0	0	0.03	0.04	0.05	0.01	0.14	0.08	1	0.18	0.01	0	0.01
11	0.01	0.03	0.04	0	0.02	0.03	0.01	0.03	0.04	0.02	1	0.08	0.06	0.14	0.01	0
10	0.02	0.03	0.01	0.39	0.07	0.07	0	0	0.12	1	0.02	0.14	0.05	0.01	0.08	0.07
9	0.02	0.09	0	0.34	0.39	0.04	0.34	0.06	1	0.12	0.04	0.01	0.01	0.01	0.03	0.01
8	0	0.04	0.01	0.12	0.13	0.49	0.03	1	0.06	0	0.03	0.05	0.01	0.06	0.08	0.16
7	0	0	0	0	0.15	0	1	0.03	0.34	0	0.01	0.04	0.01	0	0	0.01
6	0.06	0.01	0.04	0	0.01	1	0	0.49	0.04	0.07	0.03	0.03	0.11	0.02	0	0
5	0.04	0.09	0	0.12	1	0.01	0.15	0.13	0.39	0.07	0.02	0	0.02	0.01	0.06	0
4	0	0.02	0	1	0.12	0	0	0.12	0.34	0.39	0	0	0	0	0.08	0.04
3	0.08	0.02	1	0	0	0.04	0	0.01	0	0.01	0.04	0.11	0.18	0.13	0.14	0
2	0	1	0.02	0.02	0.09	0.01	0	0.04	0.09	0.03	0.03	0	0	0.01	0	0.01
1	1	0	0.08	0	0.04	0.06	0	0	0.02	0.02	0.01	0.03	0.01	0.02	0.11	0.03

Fig. 29.7 *AutoMAC* values for the modes of columns B

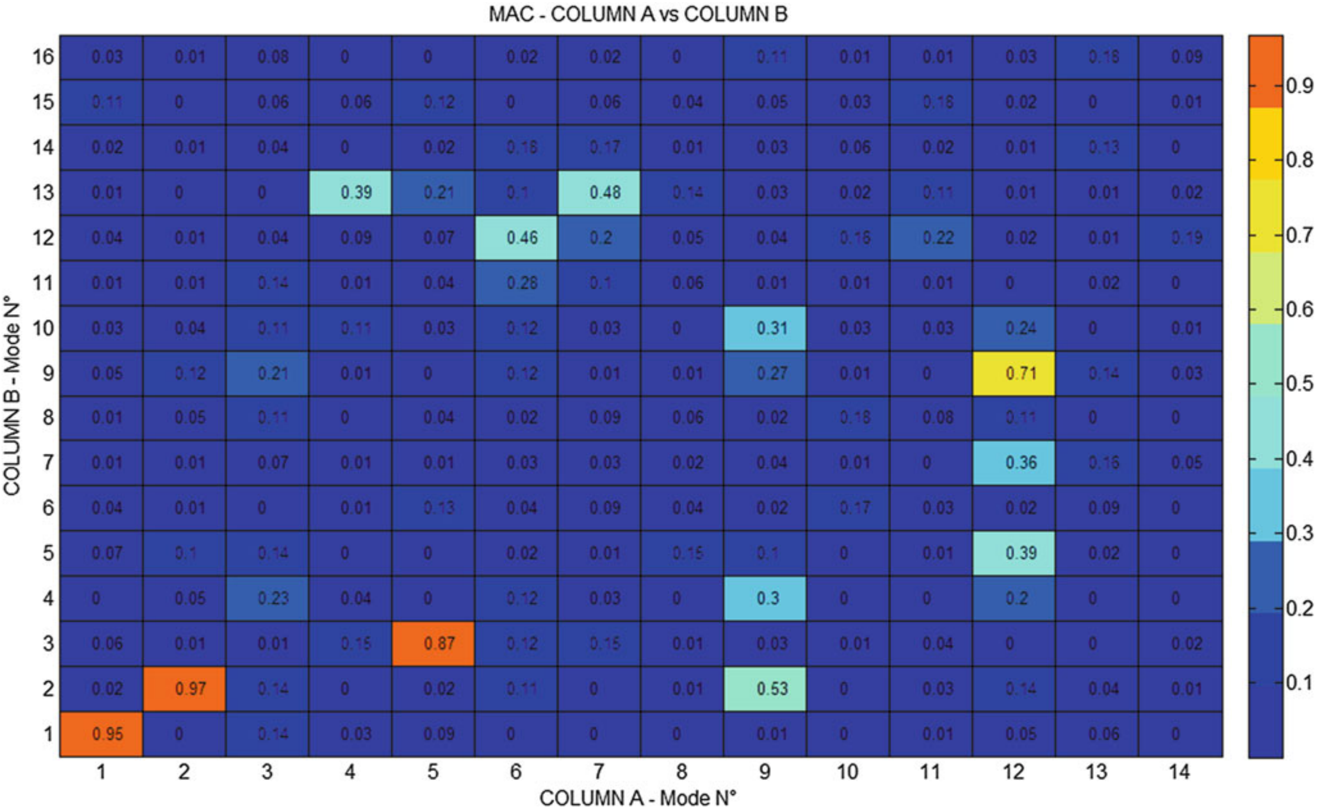

COLUMN B - Mode N°	1	2	3	4	5	6	7	8	9	10	11	12	13	14
16	0.03	0.01	0.08	0	0	0.02	0.02	0	0.11	0.01	0.01	0.03	0.16	0.09
15	0.11	0	0.06	0.06	0.12	0	0.06	0.04	0.05	0.03	0.16	0.02	0	0.01
14	0.02	0.01	0.04	0	0.02	0.18	0.17	0.01	0.03	0.06	0.02	0.01	0.13	0
13	0.01	0	0	0.39	0.21	0.1	0.48	0.14	0.03	0.02	0.11	0.01	0.01	0.02
12	0.04	0.01	0.04	0.09	0.07	0.46	0.2	0.05	0.04	0.16	0.22	0.02	0.01	0.19
11	0.01	0.01	0.14	0.01	0.04	0.28	0.1	0.06	0.01	0.01	0.01	0	0.02	0
10	0.03	0.04	0.11	0.11	0.03	0.12	0.03	0	0.31	0.03	0.03	0.24	0	0.01
9	0.05	0.12	0.21	0.01	0	0.12	0.01	0.01	0.27	0.01	0	0.71	0.14	0.03
8	0.01	0.05	0.11	0	0.04	0.02	0.09	0.06	0.02	0.18	0.08	0.11	0	0
7	0.01	0.01	0.07	0.01	0.01	0.03	0.03	0.02	0.04	0.01	0	0.36	0.16	0.05
6	0.04	0.01	0	0.01	0.13	0.04	0.09	0.04	0.02	0.17	0.03	0.02	0.09	0
5	0.07	0.1	0.14	0	0	0.02	0.01	0.15	0.1	0	0.01	0.39	0.02	0
4	0	0.05	0.23	0.04	0	0.12	0.03	0	0.3	0	0	0.2	0	0
3	0.06	0.01	0.01	0.15	0.87	0.12	0.15	0.01	0.03	0.01	0.04	0	0	0.02
2	0.02	0.97	0.14	0	0.02	0.11	0	0.01	0.53	0	0.03	0.14	0.04	0.01
1	0.95	0	0.14	0.03	0.09	0	0	0	0.01	0	0.01	0.05	0.06	0

Fig. 29.8 *MAC* values for column A and B modes

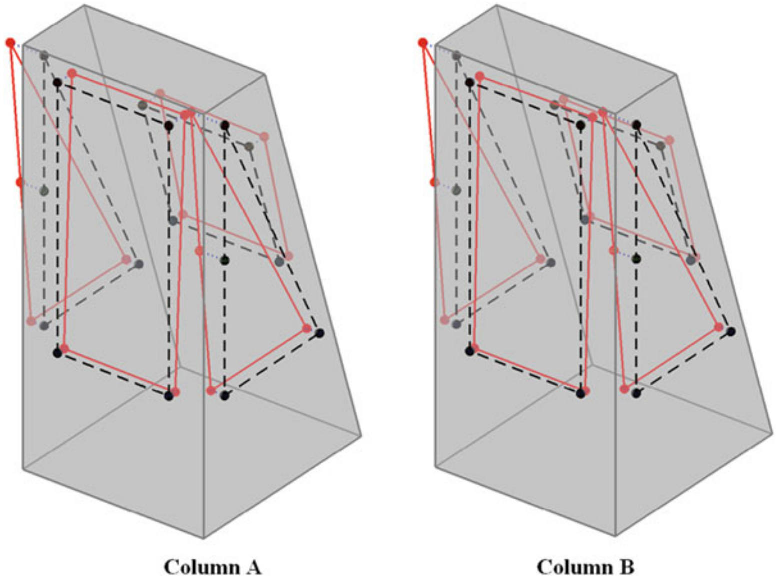
Column A Column B

Fig. 29.9 Mode 1 for column A and B

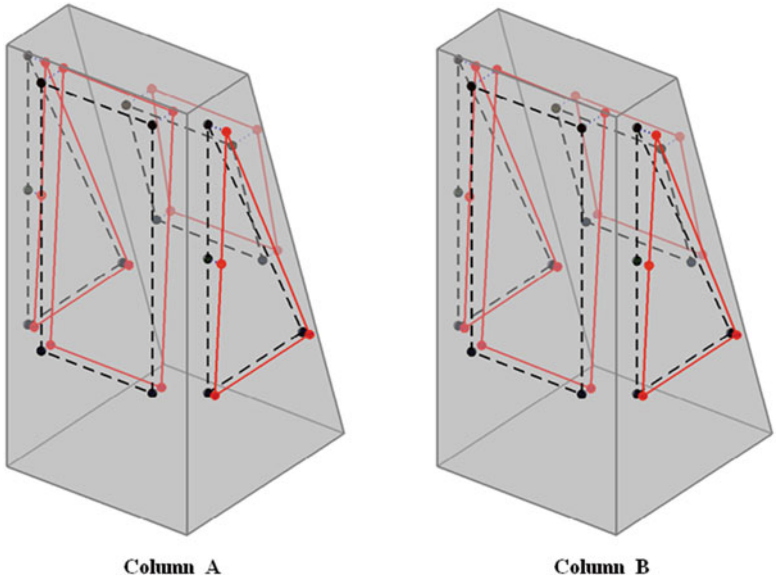
Column A Column B

Fig. 29.10 Mode 2 for column A and B

29.5 Concluding Remarks

Two columns of a milling machine were compared in this paper. One is made according to traditional techniques (classic metalworking), the other is built using metal foam sandwiches. Experimental modal analysis was applied to evaluate the mechanical parameters of the two columns and especially their damping capabilities.

A first interesting result of the performed analysis is the linearity of the response of the column made of metal foam sandwiches, which was not obvious a priori.

Since the two columns are comparable only for the geometric dimensions (they are interchangeable on the machine), but differ in terms of construction, a comparison based simply on modal damping is misleading. The modal analysis has shown that only few modes are directly comparable, but they have very different frequencies, so that the comparison of the damping is not significant and does not provide any clear conclusion.

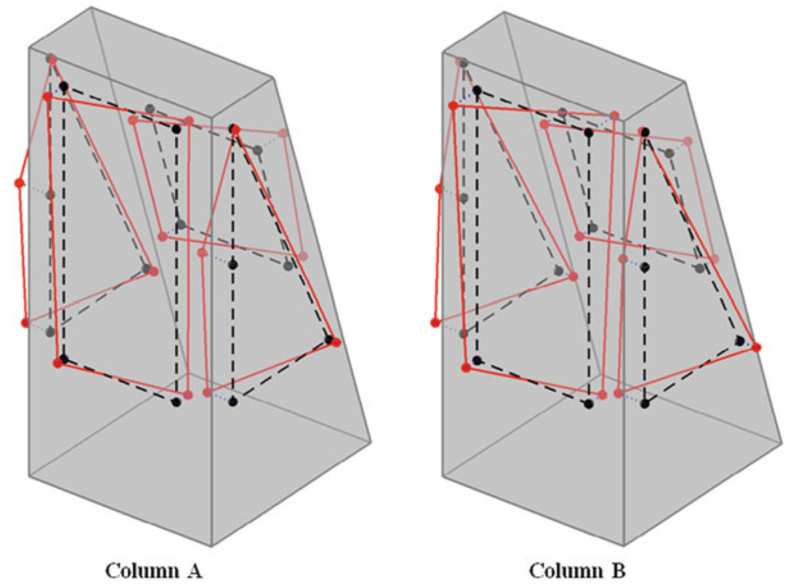

Fig. 29.11 Mode 5 for column A and mode 3 for column B

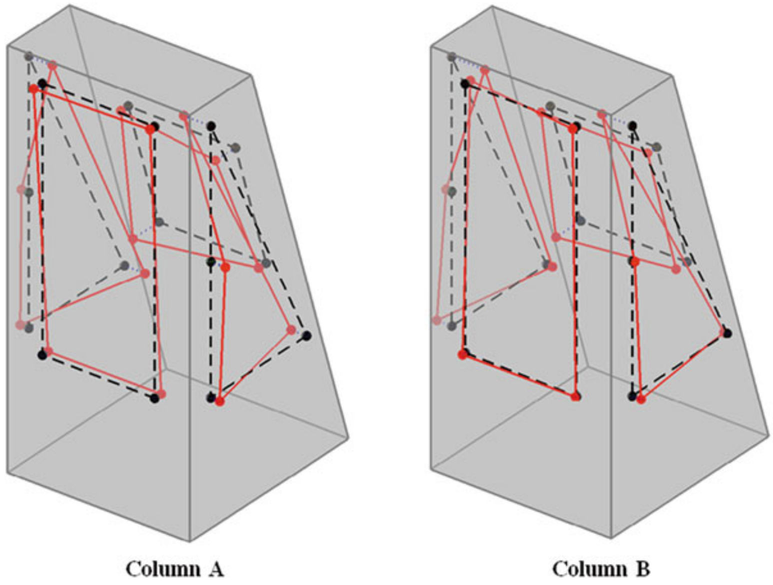

Fig. 29.12 Mode 12 for column A and mode 9 for column B

References

1. Knapp, W.: Measurement uncertanty and machine tool design. CIRP Ann. Manuf. Technol. **51**(1), 459–462 (2002)
2. Ahmadi, K., Ismail, F.: Machining chatter in flack milling. Int. J. Mach. Tools Manuf. **50**, 75–85 (2010)
3. Acherkan, N., Push, V., Ignatyev, N., Kudinov, V.: Machine Tool Design. University Press of the Pacific, Honolulu (2000)
4. Altintas, Y.: Manufacturing Automation: Metal Cutting Mechanics, Machine Tool Vibration, and CNC Design. Cambridge University Press, New York (2012)
5. Catania, G., Mancinelli, N.: Theoretical–experimental modeling of milling machines for the predicion of chatter vibration. I. J. Mach. Tools Manuf. **51**(4), 339–348 (2011)
6. Pratt, J., Nayfeh, A.: Design and modeling for chatter control. Nonlinear Dyn. **19**(1), 49–69 (1999)
7. Kim, J., Lee, J., Chang, S.: Robust design of microfactory elements with high stiffness and high damping characteristics using foam-composite sandwich structures. Compos. Struct. **86**(1–3), 220–226 (2008)
8. Ashby, M., Evans, A., Fleck, N., Gibson, L., Hutchinson, J., Wadley, H.: Chapter 4 - Properties of metal foams.In: Metal Foams, pp. 40–54. (2000)

9. Lee, G.: Rosonance apparatus for damping measurements. Metall. Mater. Trans. A **26**(11), 2819–2823 (1995)
10. Mu, Y., Yao, G., Luo, H.: Anisotropic damping behavior of closed-cell aluminium foam. Mater. Des. **31**(1), 610–612 (2010)
11. Basturk, S., Tanoglu, M.: Development and mechanical behaviour of FML/aluminium foam sandwiches. Appl. Compos. Mater. **20**(5), 789–802 (2013)
12. Vaidya, U., Pillay, S., Bartus, S., Ulven, C., Grow, D., Mathew, B.: Impact and post-impact vibration rsponse of protective metal foam composite sandwich plates. Mater. Sci. Eng. A **428**(1–2), 59–66 (2006)
13. Ewins, D.: Modal Testing: Theory, Practice and Application. John Wiley & Sons, Inc, Bognor Regis (2000)
14. Nilsson, A., Liu, B.: Vibro-Acoustics. Science Press, Beijing (2012)
15. Brown, D., Allemang, R., Zimmerman, R., Mergeay, M.: Parameter estimation techniques for modal analysis. In: SAE Technical Paper 790221, 1979
16. Friswell, M., Mottershead, J.: Finite Element Model Updating in Structural Dynamics. Kluweer Academic Publisher, Dordrecht (1995)

Chapter 30
Mixed Force and Displacement Control for Base-Isolation Bearings in RTHS

Richard Erb, Matthew Stehman, and Narutoshi Nakata

Abstract This study presents a real-time hybrid simulation of a base-isolated building. In this study, the base isolation layer is experimentally tested while the entire structure is computationally simulated. To impose the earthquake induced lateral displacement as well as the vertical gravitational force, a mixed force and displacement control strategy is developed and implemented in the experimental system. The mixed force and displacement control strategy in this study is a decentralized approach that consists of a loop shaping and the conventional PID controllers. Following a thorough experimental verification of the mixed control, hybrid simulation of a base isolated building was performed using a series of recorded earthquake ground motions. The experimental results showed that the mixed control provided accurate loading in both lateral and vertical directions. This study presents the implementation of the mixed force and displacement control as well as the results in real-time hybrid simulation.

Keywords Real-time hybrid simulation • Mixed force and displacement control • Base isolation • Seismic simulation • Actuator control

30.1 Introduction

Base isolation has become a favorable approach for the design of buildings and bridges in seismically active regions. The idea behind the base isolation is to make the fundamental frequencies of the structure lower than the predominant frequency of the ground motion so that not much vibration energy is transmitted to the structures from the ground [1]. In addition to the design of new structures, the base isolation technique has been adopted in the retrofit of existing structures in recent years, such as Salt Lake City and County Building and Los Angeles City Hall. The base isolation technique has been recognized as one of the most effective strategies to achieve performance goals in the performance-based earthquake engineering design framework.

Behavior of the base isolated structures is slightly different from structures with fixed base. Unlike the fixed-base structures where the earthquake loads are mostly resisted by the stiffness and energy dissipation of the entire structure, the base isolated structures have large deformation concentrated in the isolation layer and the structures behave more or less like a rigid body. While the structures remain/are designed to be linear elastic during ground motion, base isolation bearings and sliders typically exhibit complex nonlinear behaviors such as friction, slippage, and hysteresis in the displacement-force relation. Furthermore, base isolation bearings have dependence on the level of axial loads, temperature as well as aging deterioration. Therefore, in the seismic simulation of the base isolated structures it is critical to accurately account for the behavior of the base isolation layer.

One can apply shake table tests for the seismic simulation and assessment of the base isolated structures. Kelly and Hodder [2] conducted a series of shake table tests of base isolation systems with laminated neoprene bearings at the University of California, Berkeley. Sasaki et al. [3] utilized the Japan's E-defense shake table for assessment of Friction Pendulum and Lead-Rubber Bearings Systems. Other researchers also reported shake table tests of base isolation buildings. While shake table tests are ideal experimental approaches because the entire structure including the base isolation layer are modeled experimentally and the responses are directly obtained through the physical measurement, they may not be always the feasible options due to funding issues, limited access to facility, etc.

R. Erb • M. Stehman
Department of Civil Engineering, Johns Hopkins University, 3400 N. Charles Avenue, Baltimore, MD 21218, USA

N. Nakata (✉)
Department of Civil and Environmental Engineering, Clarkson University, 8 Clarkson Avenue, Potsdam, NY 13699, USA
e-mail: nnakata@clarkson.edu

© The Society for Experimental Mechanics, Inc. 2016

J. De Clerck, D.S. Epp (eds.), *Rotating Machinery, Hybrid Test Methods, Vibro-Acoustics & Laser Vibrometry, Volume 8*,
Conference Proceedings of the Society for Experimental Mechanics Series, DOI 10.1007/978-3-319-30084-9_30

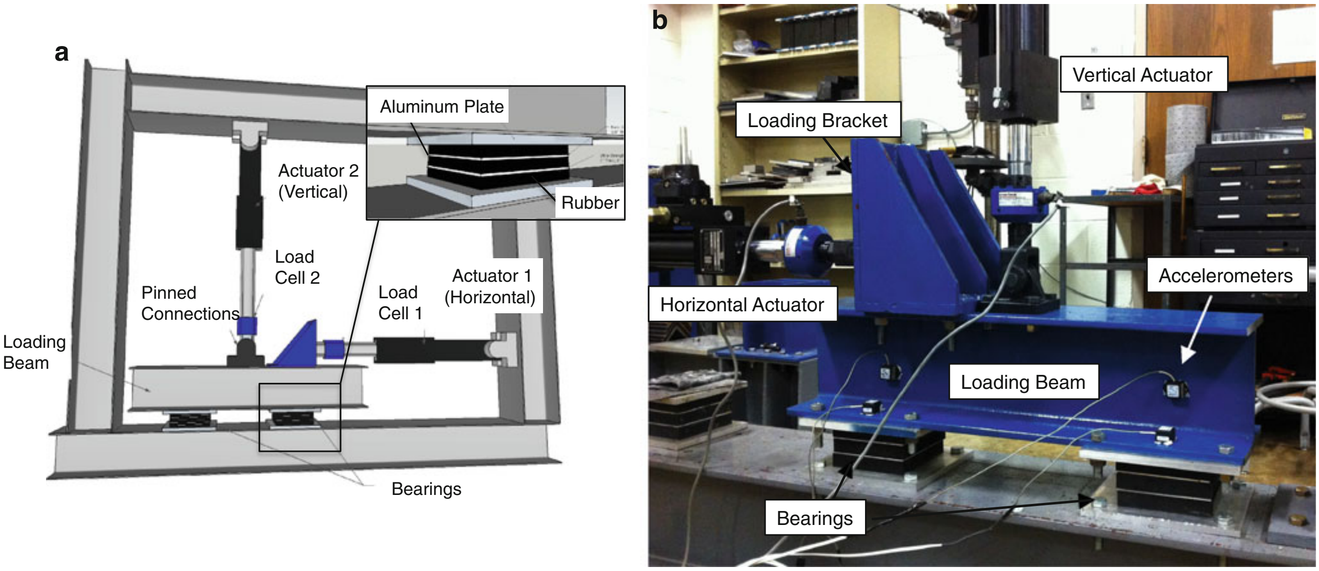

Fig. 30.1 Loading system and base-isolation bearings: (**a**) drawing and (**b**) photo

One of the cost-effective alternative approaches for investigation of the base isolated structures is real-time hybrid simulation (RTHS). Because of the high concentration of nonlinear behaviour in the base isolation layer, only the isolation layer needs to be physically tested while the rest of the structure (i.e., building) can be modelled numerically. This highly concentrated nonlinear behaviour makes the base isolated structures ideal applications of RTHS. However, there are technical challenges in the testing of base isolation bearings. Because behaviors of the base isolation bearings, including lateral stiffness, damping, hysteresis, stability, yield stress, and creep, are highly dependent on the axial load, the vertical force on the base isolation bearings has to be accurately imposed during hybrid simulation.

To address the need of such accurate vertical force control with lateral loading, this study proposes a mixed force and displacement control strategy. The proposed control strategy is a decentralized approach that consists of a loop-shaping controller for the force-controlled actuator and a PID controller for the displacement-controlled actuator. To verify the feasibility of the proposed mixed-mode control, a series of verification tests under various loading are performed. Furthermore, the mixed-mode control is also implemented in a RTHS framework for the simulation of a base isolated building. This paper presents experimental setup, verification tests, and RTHS of the base isolation building with the mixed force and displacement control.

30.2 Experimental Setup

This study utilizes an experimental setup for testing of base isolation bearings developed at the Johns Hopkins University. The experimental setup consists of a loading frame, base isolation bearings, and control, instrumentation and data acquisition systems that are described herein.

30.2.1 Loading Frame and Base Isolation Bearings

A schematic of the loading frame and base isolation bearings is shown in Fig. 30.1: (a) drawing and (b) photo. The loading frame is constructed with four steel W-Shapes: Three W8 × 40 sections make up both the vertical and top members, and a W12 × 58 section is used as the bottom support beam. The rubber bearings are bolted by end plates on the bottom of the frame, and they are spaced 22 in. from center to center. The rubber bearings are connected on top by a 34-inch long W8 × 40 section. The horizontal actuator is connected from one end of the loading frame to a bookend on top of the W8 × 40 section. The vertical actuator is bolted directly in the center of the two rubber bearings on the other end of the W8 × 40.

The bearings tested in this study are laminated elastomeric bearings (see Fig. 30.1). Each bearing is composed of three layers of square 152 × 152 mm ultra-strength neoprene rubber sheet and aluminum plates (Alloy 1100). The aluminum layers are 3.2 mm thick and the neoprene rubber layers are 25.4 mm thick. The aluminum and rubber are connected at each layer and to the end plates by epoxy. It should be noted that these bearings are specifically designed for proof-of-concept real-time hybrid simulation of base-isolated buildings using mixed force and displacement control that is developed and verified in this study.

30.2.2 Control, Instrumentation and Data Acquisition Systems

Two identical actuators, 911D series manufactured by Shore Western Inc., are utilized in the test setup: one is in the horizontal direction and the other is in the vertical direction. Those actuators are equipped with a G761 series servo valve by Moog, Inc., a 22.2 kN load cell by Interface, Inc., and a 152 mm DC operated linear variable differential transducer (LVDT). Maximum stroke and dynamic force capacity of the actuator are 152 mm and 24.5 kN, respectively. The hydraulic power is supplied by a 114 litter-per-second Whisper Pak Model 160 from Shore Western, Inc. The hydraulic pressure is rated at 3000 psi, and 3.8-litter accumulators are placed in both pressure and return lines to reduce the pressure drop. In addition to the LVDTs and load cells for the actuators, four accelerometers are attached to the loading beam to measure horizontal and vertical accelerations of the base isolation bearings.

For the control of the hydraulic actuators and data acquisition of the sensor signals, a National Instruments PXI Express system is employed in this study. An embedded real-time controller used in the setup, PXI-8031, allows analog-to-digital and digital-to-analog signal conversions at a sampling rate of 4 kHz. LabVIEW Real-Time is used as a software platform for the implementation of mixed force and displacement control strategies in this study. For more details of hardware and software systems at the Smart Structures and Hybrid Testing Laboratory, refer to Nakata [4].

30.3 Preliminary Investigation of the Bearing Behavior

Prior to the development of mixed force and displacement control strategies, fundamental behaviors of the base isolation bearings are investigated. The preliminary experimental investigations of the bearings are conducted under displacement control.

A series of harmonic displacement are imposed in the lateral direction of the base isolation bearings. In this series, the vertical displacement is kept constant to investigate the effect of the lateral displacement on the vertical force. Figure 30.2 shows results of a test case where the lateral displacement is 0.1 Hz sinusoidal input with the peak displacement of 2.54 mm. As can be seen in Fig. 30.2a, b, displacements in both lateral and vertical displacements are accurately controlled, showing good agreements between the reference and the measured. The time history of the lateral force shown in Fig. 30.2c is approximately a harmonic shape that is expected from the harmonic displacement input. On the other hand, the vertical force in Fig. 30.2d shows noticeable variation despite the constant vertical displacement. This variation has the same frequency as in the lateral displacement and is due to the influence of the lateral deformation that indications interaction between the lateral and vertical axes. Furthermore, it can be observed that the vertical force level decreases over time even after few cycles: 18.1 and 17.9 kN before and after the test, respectively. This reduction of the vertical force can be due to the wear of the bearing caused by the lateral deformation. Although not shown here due to the space limitation, the other test cases with different input frequency and amplitude show the similar trend in the vertical force of the base isolation bearings.

Next, the influence of the axial force on the lateral stiffness of the base-isolation bearings is examined. Fig. 30.3a shows displacement-force hysteresis of the base isolation bearings at two different levels of axial force: nominal forces at 0.5 and 19.2 kN. The nominal force is the initial force in the vertical direction at the zero lateral displacement. As shown in the previous Fig. 30.2, the vertical force fluctuates as the lateral displacement is increased despite the constant displacement in the vertical actuator. As can be seen in Fig. 30.3a, the stiffness, slope of the hysteresis, of the base-isolation bearings is higher at the nominal force level of 19.2 kN than that of 0.5 kN. Furthermore, judged from the fatness of the hysteresis, the base isolation bearings have higher energy dissipation capability at the higher axial force level. The stiffness evaluation test is performed at more nominal force levels and the lateral stiffness estimated from hysteresis using the least square method is plotted against the nominal vertical force in Fig. 30.3b. It can be clearly seen that the lateral stiffness of the base isolation bearings is highly influenced by the axial force.

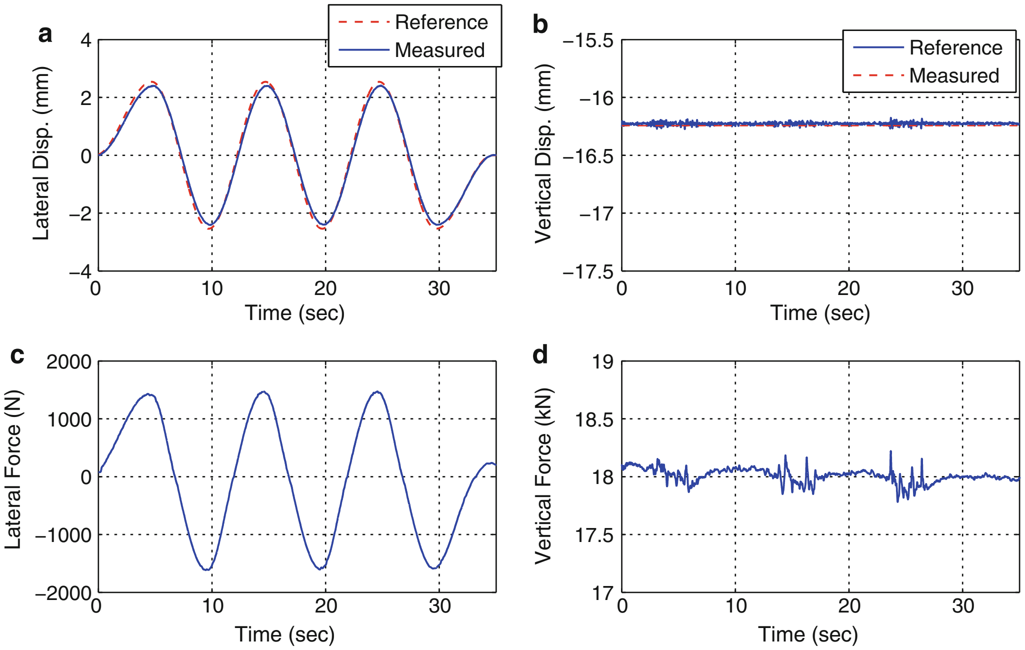

Fig. 30.2 Time histories under displacement control in both lateral and vertical directions: lateral input is a 0.1 Hz 2.54 mm harmonic signal whereas the vertical input is constant

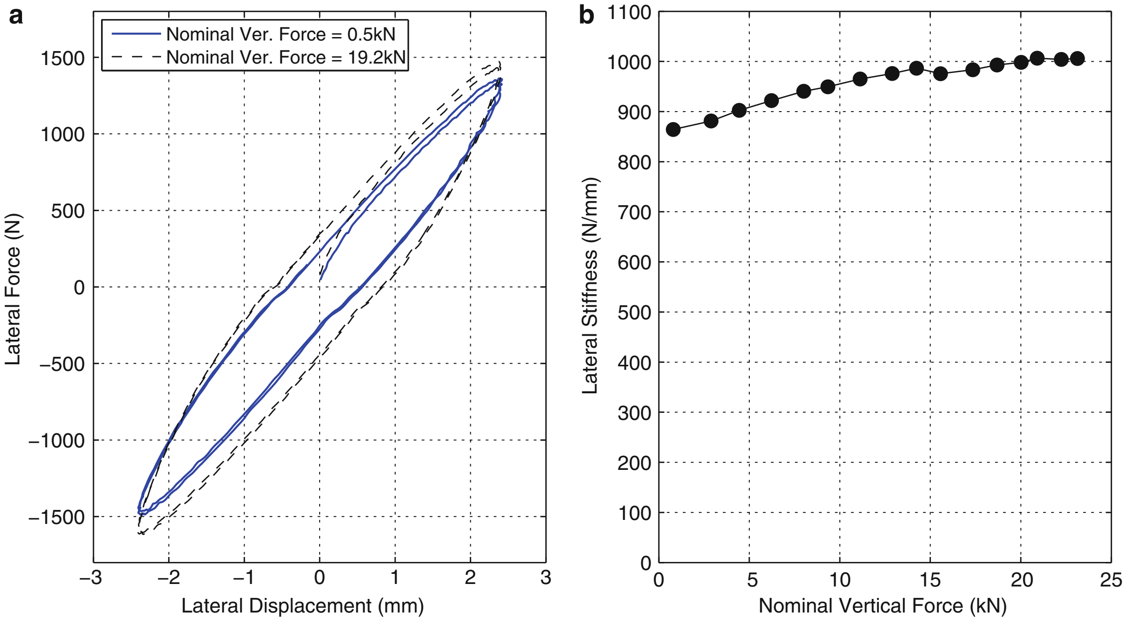

Fig. 30.3 Effect of the vertical force on the lateral behavior of the base isolation bearings: (**a**) displacement and force hystereses; and (**b**) lateral stiffness

The results in these preliminary experimental investigations demonstrate that the lateral behavior of the base isolation bearings is highly influenced by the axial force. Therefore, the axial force and its influence need to be carefully and accurately accounted in both numerical and experimental simulations of base isolated structures. Ignoring the effect of the axial force may cause non-negligible errors in the simulations.

30.4 Mixed Force and Displacement Control Design

Motivated by the need of the axial force control in the base isolation bearing tests, this study investigates actuator control strategies that enable challenging structural experiments. Specifically, mixed force and displacement control strategies are speculated. The mixed force and displacement control is often desired in testing of components that exhibit dependence of axial force on lateral and bending behaviors such as base isolation bearings and bridge piers. However, successful implementations of the mixed force and displacement control strategies are limited (Nakashima and Peng, Nakata et al.).

Figure 30.4 shows a general block diagram of the inner-loop servo controller for the actuators with mixed force and displacement control. In this diagram, two actuators are considered without loss of generality; in the mixed force and displacement control, at least one actuator has to be in displacement control and at least one actuator has to be in force control. If more than two actuators are used, they have to be added into the block diagram. In this diagram, actuator 1 is set in the displacement control while actuator 2 is in the force control.

The goal of the mixed force and displacement control is to produce accurate tracking in controlled displacement and force axes simultaneously. It should be noted that the mixed force and displacement controller is a multi-input and multi-output system. Therefore, if necessary, the controller has to take into account system dynamics and coupling between the two axes, dependent on the level of coupling and control demands. Design of the controller is essentially a development of algorithm that generates the actuator valve commands from the error signals to meet the control requirements.

30.4.1 Decentralized Control Approach with Loop Shaping in the Vertical Actuator

Multi-actuator experimental systems in structural testing are generally configured with individual serve control loops for actuators if all of the actuators are displacement controlled. However, previous studies (Nakata et al.) showed that a centralized control approach is necessary if one or more actuators are force controlled and significant coupling between actuators exists. For example, a decoupling centralized controller is essential in multi-degrees-of-freedom force control testing where multiple actuators are force controlled (Nakata et al.). In a substructure shake table testing, a centralized controller is crucial for force the controlled actuator while an independent controller is satisfactory for the displacement controlled actuator. Thus, if force control is included in the experimental system, careful control design is needed to successfully perform intended experiments.

In this study, a decentralized control approach is explored because of the orthogonal configuration of the actuators. Figure 30.5 shows the servo control loop design for the mixed force and displacement control in the base isolation bearing tests. In this configuration, a proportional-integral-differential (PID) control is adopted for the displacement control in the lateral actuator, and a loop-shaping control is employed for the force control in the vertical actuator.

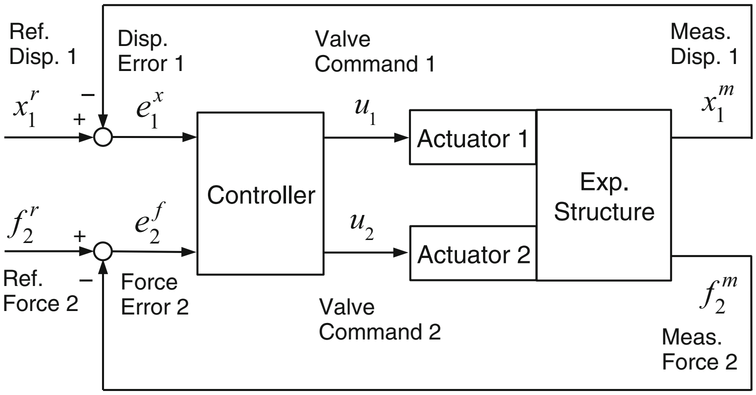

Fig. 30.4 A generalized block diagram for mixed force and displacement control inner servo loops

Fig. 30.5 Decentralized control approach with loop shaping for the force controlled actuator and PID for the displacement controlled actuator

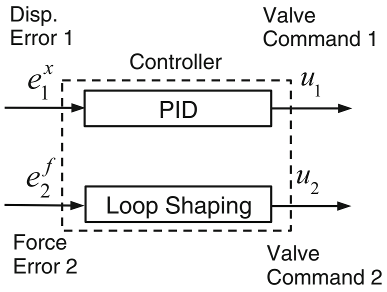

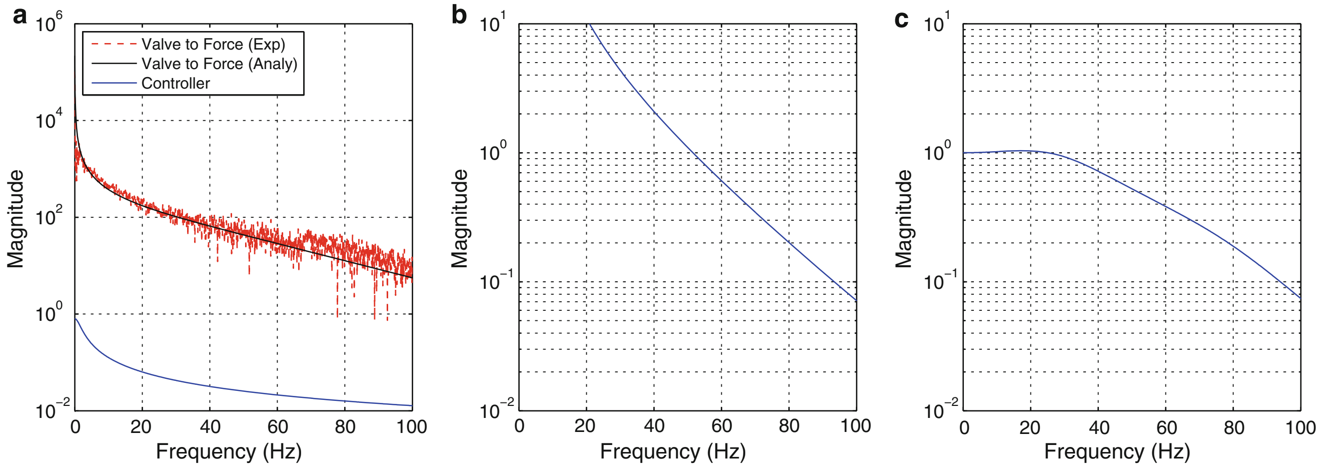

Fig. 30.6 Transfer functions for the loop shaping: (**a**) transfer function of the control plant and controller; (**b**) loop transfer function; and (**c**) the overall closed-loop transfer function of the force

30.4.2 Loop-Shaping Controller Design for the Force Controlled Actuator

The loop-shaping controller is a model-based control approach that can provide high performance and robustness. However, unlike the PID controller, it requires a dynamic model of the control plant, which in this case is the valve to force relation in the vertical actuator. To enable the loop-shaping control design for the force controlled actuator, a system identification test is conducted using a random excitation to the vertical actuator. During the system identification process, the horizontal actuator remains steady.

Figure 30.6a shows the frequency domain response of the valve to force relation in the vertical actuator. It can be seen that the magnitude of the force decays as the frequency increases. An analytical model shown in Fig. 30.6a is developed using a curve-fitting technique, and the loop-shaping controller is designed such that the loop transfer function, a product of the plant and controller, has following two desired frequency domain characteristics: (1) high gain in a low frequency range and (2) low gain in a high frequency range.

The frequency at which the magnitude passes 1.0 is called the crossover frequency and is designed to be around 30 Hz in this study. In general, the loop-shaping controller provides tracking performance at frequency less than the crossover frequency and robustness at frequency higher than the crossover frequency. The overall closed-loop transfer function in the force-controlled vertical actuator is shown in Fig. 30.6c. It can be seen that the designed loop-shaping force feedback controller provides tracking performance in a low frequency range and robustness in a high frequency range beyond 20 Hz.

30.5 Experimental Verification of Mixed-Mode Control

Prior to applications in real-time hybrid simulation, the mixed force and displacement control using the decentralized control approach is verified under various conditions and loadings. This section presents results of the verification tests and discusses capabilities and limitations of the mixed force and displacement control strategy.

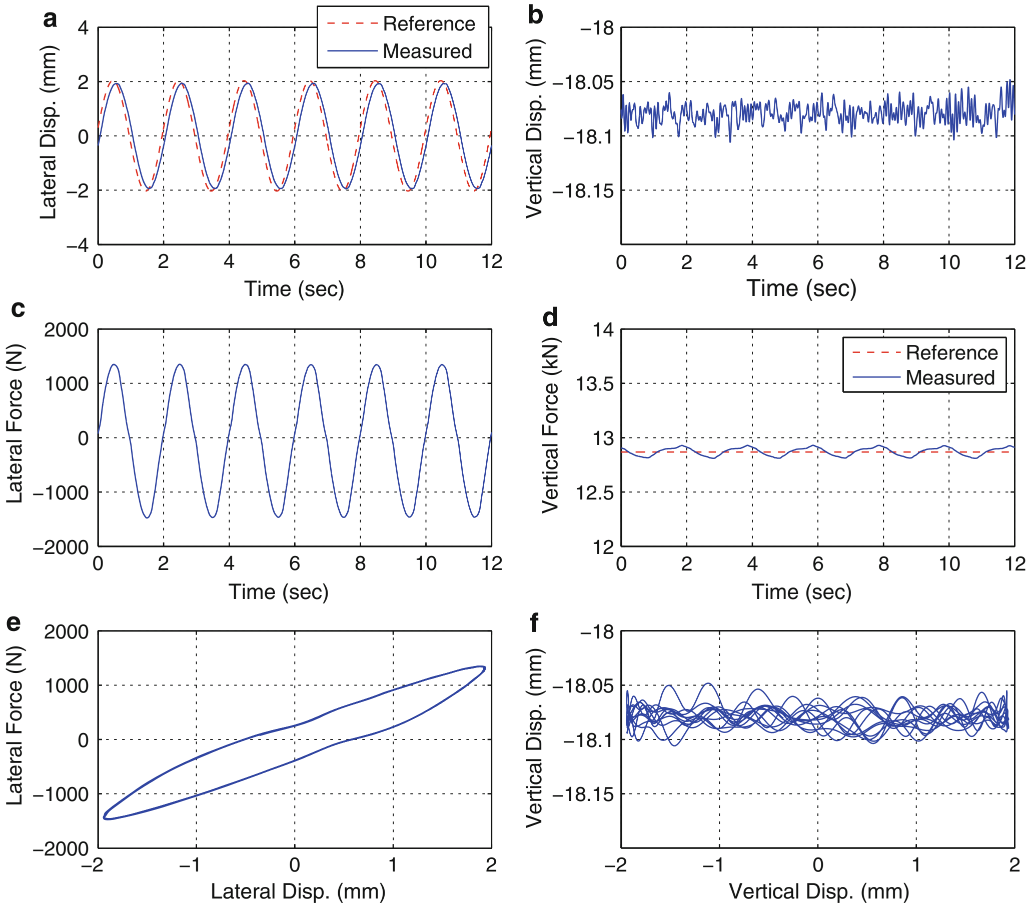

Fig. 30.7 Results of a constant vertical force control under harmonic lateral loading: (**a**) lateral displacement; (**b**) vertical displacement; (**c**) lateral force; (**d**) vertical force; (**e**) hysteresis; and (**f**) loading trajectory

30.5.1 Verification of Constant Vertical Force Control Under Harmonic Lateral Loading

The first verification presented here is a constant vertical force control test under harmonic lateral loading. Figure 30.7 shows time histories of the displacements and forces in both lateral and vertical axes as well as the hysteresis and the trajectory in the loading plane. As shown in the figure, the lateral loading is a 0.5 Hz continuous sinusoidal, and the bearings exhibit hysteresis showing energy dissipation. The vertical force time history in Fig. 30.7d shows that the force fluctuation is approximately within 1.5 % of the reference constant force of 13 kN. Although not clearly seen, the variations of the vertical displacement in Fig. 30.7b, d are the result of the vertical force control. More verification tests with different loading frequencies and amplitudes are also performed. Though not presented here, they show similar results with the same level of fluctuation in the vertical force.

30.5.2 Verification of Varying Vertical Force Control Under Earthquake Lateral Loading

The next verification presented here is a varying vertical force control test under earthquake lateral loading. Similar to Fig. 30.8, Fig. 30.9 shows time histories of the displacements and forces in both lateral and vertical axes as well as the hysteresis and the trajectory in the loading plane. The lateral loading is a simulated displacement using the 1995 Kobe earthquake KJM record. The force that is proportional to this lateral displacement is used as the reference force in the vertical direction. Although this lateral displacement and vertical force combination needs to be further investigated, it gives a little more realistic loading to the bearing such as rocking than the constant vertical force.

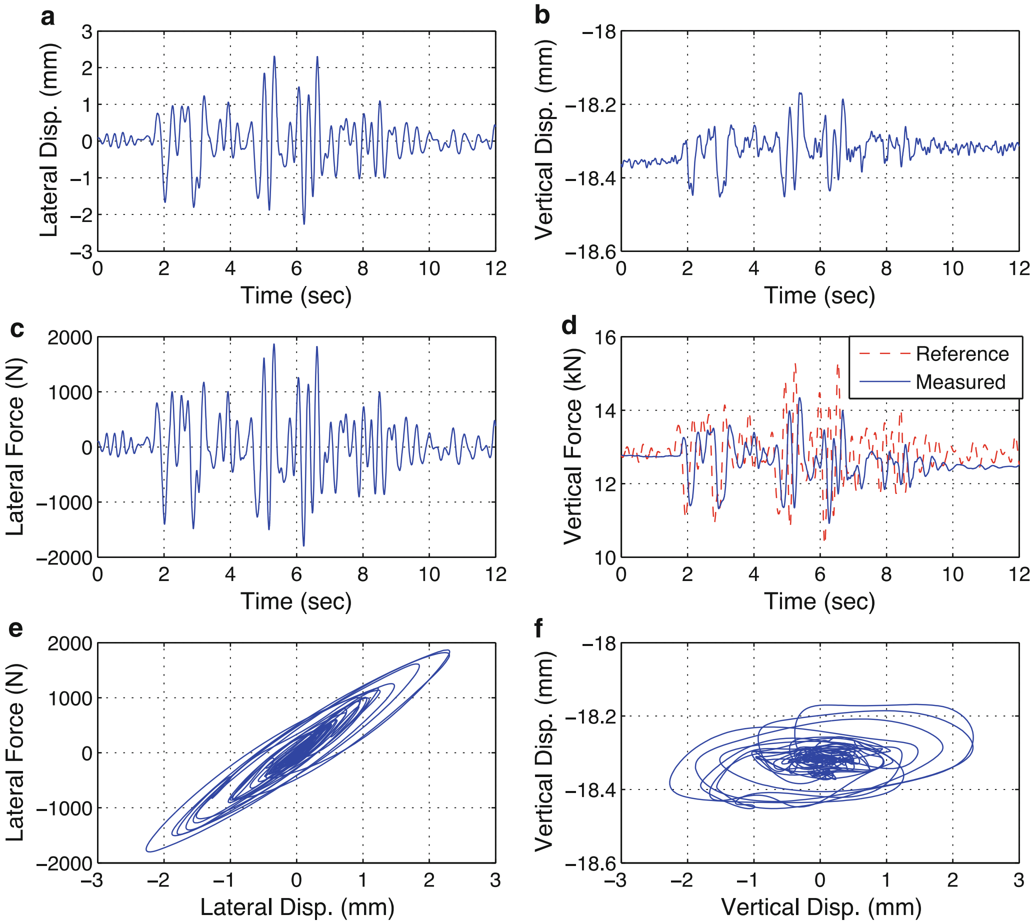

Fig. 30.8 Results of a varying vertical force control under earthquake lateral loading: (**a**) lateral displacement; (**b**) vertical displacement; (**c**) lateral force; (**d**) vertical force; (**e**) hysteresis; and (**f**) loading trajectory

As seen in the red dotted line in Fig. 30.9d, the reference vertical force is dynamically changing in this test. While there is a discrepancy between the reference and measured forces, the measured force shows a reasonable tracking to capture the variation in the vertical force. As the result of the vertical force control, the vertical displacement changes accordingly. It is interesting to note that while the vertical force levels before and after the loading are almost the same (12.5 kN), the vertical displacement drops after the loading. This change may imply a shrinkage of the rubber bearings due to thermal effect generated by the lateral loading.

The series of experimental verification tests show that the proposed mixed force and displacement control strategy provides accurate force tracking in vertical direction under lateral loading. With the accomplished level of accuracy, the proposed mixed-mode control algorithm is considered feasible for the implementation in real-time hybrid simulation.

30.6 Real-Time Hybrid Simulation of Base Isolation Bearings

Feasibility of the developed mixed force and displacement control strategy is evaluated in a real time hybrid simulation framework. The considered structural model is a base isolated building where the building is numerically modeled and the base isolation layer is experimental tested. The building model is a rigid block with 5306 kg mass and the experimental bearing component is assumed to be a ¼ of the entire base isolation layer. The estimated natural frequency of the structure is approximately 4.0 Hz.

Figure 30.9 shows results of a real-time hybrid simulation. In this simulation, the input lateral ground motion is the 1995 Kobe earthquake record and the reference vertical force is the constant gravitational force of 13 kN (=5306 × 9.8/4). As seen in the figure, despite a large variation in the lateral displacement and force (a) and (c), the vertical force is maintained at the

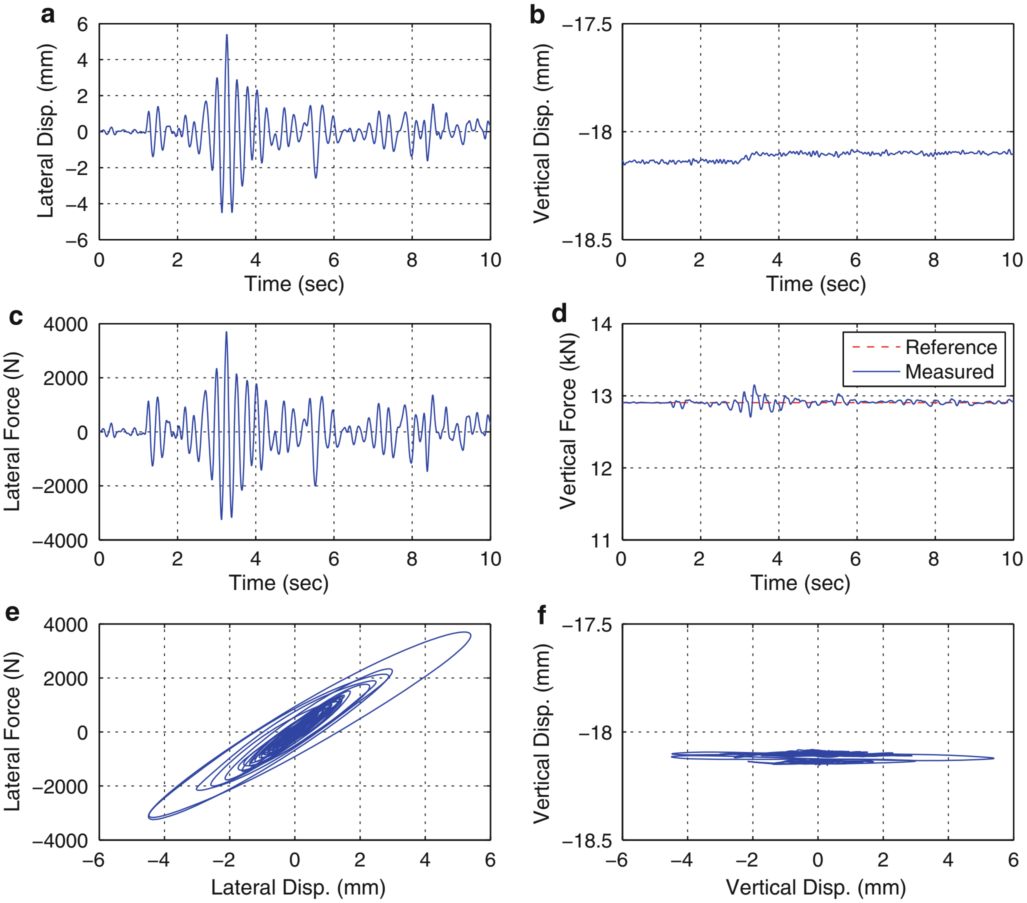

Fig. 30.9 Real-time hybrid simulation with the mixed force and displacement control: (**a**) lateral displacement; (**b**) vertical displacement; (**c**) lateral force; (**d**) vertical force; (**e**) hysteresis; and (**f**) loading trajectory

reference level almost all the time during the simulation. The peak force error to the reference force is about 1.53 %. As in the previous verification test, the change in the vertical displacement after the simulation is observed even for the constant force level. It should be noted that such observation cannot be made with the displacement control approach in the vertical direction.

30.7 Conclusions

This study presented a mixed force and displacement control strategy for testing of base isolation bearings in hybrid simulation. The controller strategy is a decentralized approach that consists of a loop-shaping controller for the force-controlled actuator and a PID controller for the displacement-controlled actuator. A series of experimental verifications were conducted and their results showed that the proposed mixed-mode control strategy provided acceptable tracking performance in the vertical force during lateral loading. Furthermore, the mixed-mode control was successfully verified in the real-time hybrid simulation of a base isolated building.

Acknowledgement This research is supported by the National Science Foundation under an award entitled ‘CAREER: Advanced Acceleration Control Methods and Substructure Techniques for Shaking Table Tests (grand number CMMI-1503579)’.

References

1. Kelly, J.M.: Aseismic base isolation: review and bibliography. Soil Dyn. Earthq. Eng. **5**(4), 202–216 (1986)
2. Kelly, J.M., Hodder, S.B.: Experimental study of lead and elastomeric dampers for base isolation systems in laminated neoprene bearings. Bull. Bull. N. Z. Soc. Earthq. Eng. **15**(2), 53–67 (1982)
3. Sasaki, T., Sato, E., Ryan, K., Okazaki, T., Mahin, S.A., Kajiwara, K.: NEES/E-defense base-isolation tests: effectiveness of friction pendulum and lead-rubber bearings systems. In: Proceedings of the 15th World Conference on Earthquake Engineering, Lisbon, 2012
4. Nakata, N.: A multi-purpose earthquake simulator and a flexible development platform for actuator controller design. J. Vib. Control **18**(10), 1552–1560 (2012)

Chapter 31
Leveraging Hybrid Simulation for Vibration-Based Damage Detection Studies

Timothy P. Kernicky, Michael Tedeschi, and Matthew J. Whelan

Abstract Approaches for structural health monitoring of civil infrastructure using vibration-based damage detection methods have progressed significantly over the past decade as a result of extensive experimentation on both full-scale and laboratory-scale structures. However, the field instrumentation of in-service structures involving well-characterized damage scenarios is a complex, costly, and high-risk investment. In contrast, the use of numerical simulations to generate synthetic data for structural health monitoring research is restricted by challenges associated with modeling experimental uncertainties associated with measurement devices and ambient disturbances. In both cases, the faithful representation of meaningful damage progression is often a technical limitation. Recently, hybrid simulation has been explored as a novel alternative for experimental structural health monitoring research that alleviates the expense and logistics associated with full structural testing, yet retains the empirical nature of experimentation by combining an experimental substructure with an analytical model. In this paper, the use of pseudo-dynamic hybrid simulation for exploration of vibration-based structural health monitoring techniques is demonstrated using a truss structure where a single member and bolted gusset plate connection are incorporated in the experimental model. Hybrid simulations are performed in the baseline state and following introduction of localized damage developed at a limit state of the bolted connection. The results correlate strongly with predictions obtained from a fully analytical model and support the further exploration of hybrid simulation as a tool for vibration-based structural health monitoring research.

Keywords Structural health monitoring • Hybrid simulation • Hybrid testing • Vibration-based damage detection

31.1 Introduction

Increasingly, structural health monitoring (SHM) systems have been developed and deployed on critical civil, mechanical, and energy infrastructure systems to assess and track the long-term performance of these structures and serve as a means of identifying the onset of adverse conditions resulting from natural deterioration or event-driven damage. Vibration-based monitoring (VBM) has emerged as a favored approach for civil infrastructure and has been facilitated by the development of numerous wireless sensor networks for low-cost distributed SHM. In addition to affording opportunities for performance assessment through simple serviceability-based monitoring, operational modal analysis, and finite element model updating, VBM has also extensively been explored as a tool for vibration-based damage detection (VBDD). However, despite numerous laboratory experiments and several controlled case studies, there remains reluctance from practitioners to pursue vibration-based SHM due to a lack of proven implementations that have correctly identified the onset of non-prescribed structural damage in real-world scenarios using VBDD techniques [1].

Research on vibration-based methods for damage detection for structural health monitoring of highway bridges has been facilitated largely by laboratory experimentation as well as several notable full-scale tests performed on highway bridges subjected to prescribed damage. However, one of the key challenges associated with full-scale experimental testing of highway bridges with controlled introduction of damage is the faithful generation of natural damage scenarios. Due to logistical constraints, damage has often been prescribed using torch cuts to simulate fatigue cracking [2, 3], forced settlement of bridge supports [4, 5], cutting of reinforcement [4], and removal of bolts from connections [5]. While such techniques introduce localized reductions in structural stiffness analogous to effects related to structural damage, they are surrogates to actual damage developed at controlling strength limit states. Furthermore, due to the cost and other logistical constraints,

---

T.P. Kernicky • M. Tedeschi • M.J. Whelan (✉)
Department of Civil and Environmental Engineering, University of North Carolina at Charlotte 9201,
University City Boulevard, Charlotte, NC 28223-0001, USA
e-mail: mwhelan3@uncc.edu

© The Society for Experimental Mechanics, Inc. 2016

J. De Clerck, D.S. Epp (eds.), *Rotating Machinery, Hybrid Test Methods, Vibro-Acoustics & Laser Vibrometry, Volume 8*,
Conference Proceedings of the Society for Experimental Mechanics Series, DOI 10.1007/978-3-319-30084-9_31

such full-scale damage studies have been relatively infrequent. In contrast, laboratory-scale models have been routinely used to assess proposed techniques for VBDD. However, such studies are often plagued by the same challenges related to faithfully modeling real-world structural damage and are further disadvantaged by scaling effects and by the introduction of detailing simplifications routinely adopted when developing laboratory structural models.

In this study, the increasingly popular hybrid simulation technique is explored as an intermediate solution between laboratory models and full-scale destructive testing for vibration-based monitoring and damage detection studies. In hybrid simulation, only a portion of the full structural system, referred to as the experimental substructure, is physically constructed and subjected to experimental testing. The remainder of the structural system is treated as a numerical model that interacts with the physical experimental substructure through a substructured form of the dynamic equation of motion. In this way, research investigating the performance of critical structural components or assemblages of components can be economically performed by only fabricating and testing the portion of the structure that experiences nonlinear, inelastic deformations that may be inadequately understood for a particular design or difficult to predict numerically [6]. Schematically, the interaction between the experimental and analytical substructure within hybrid simulation is illustrated in Fig. 31.1 using the structural model and bolted steel member used for the experimental substructure within the current study. Conventionally, hybrid simulation has largely been used to investigate the performance of members and connections providing lateral stability in buildings under seismic events, although additional applications have been demonstrated related to structural performance under fire [7] and in bridges under traffic loading [8]. The motivation for the current study is to explore whether hybrid simulation can be reliably used to first perform a simulation of a vibration test to obtain experimental modal analysis data for characterization of the dynamic properties of the hybrid structure, then generate realistic onset of damage in the experimental substructure through overloading, and subsequently perform a simulation of a vibration test in the damaged condition to facilitate VBDD research. Although the use of hybrid simulation to generate realistic structural damage has been proposed for evaluation of nondestructive evaluation (NDE) and other sensing technologies [9], the use of hybrid simulation for vibration-based methods of structural health monitoring has yet to be thoroughly explored. In this study, the damage was developed in the member by exceeding a bolted connection limit state through overloading independent of the hybrid framework, for simplicity. However, it is important to emphasize that the full benefit of the hybrid simulation technique could be achieved by introducing damage to the experimental substructure through hybrid simulation of an extreme loading, such as a seismic event. By leveraging the advantages of hybrid simulation, the general approach preliminarily explored in this study offers many of the advantages of full-scale structural experimentation without the costs and logistical challenges associated

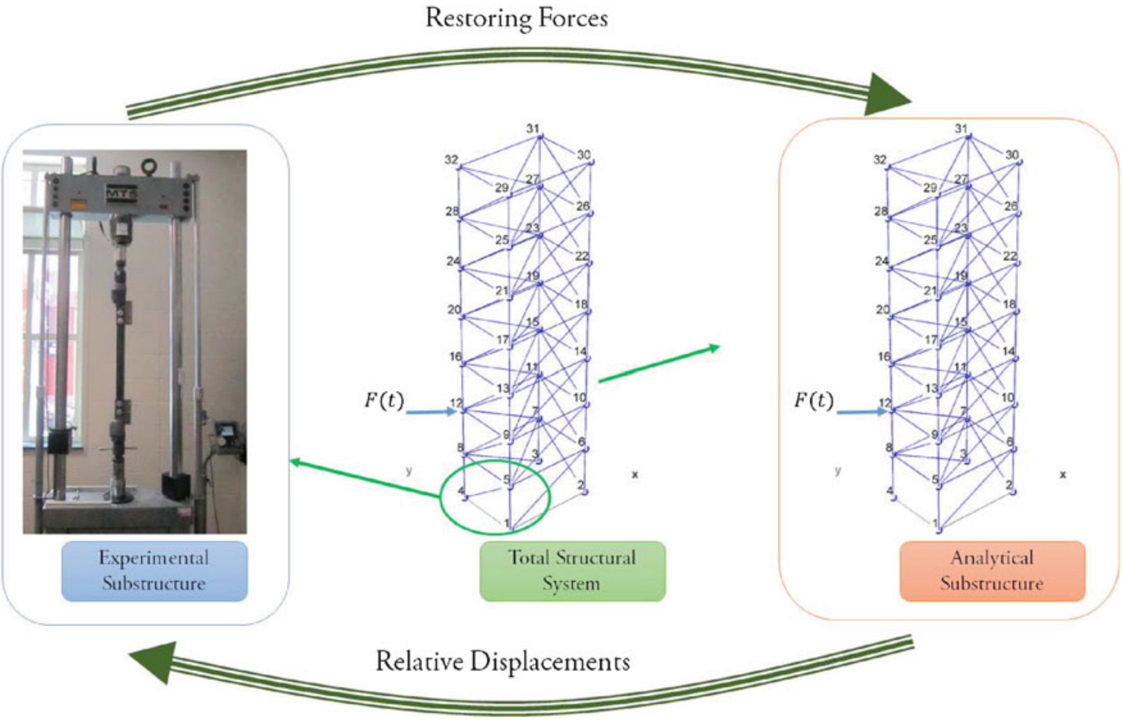

Fig. 31.1 Concept of hybrid simulation applied in the current study to vibration-based damage detection research on a three-dimensional lattice structure

with destructively testing field structures. Furthermore, in contrast to conventional experiments where damage is unnaturally prescribed using surrogate techniques to mimic structural damage mechanisms, damage can be naturally developed in the experimental substructure under specific prescribed loading scenarios, including historical records of extreme events.

31.2 Hybrid Simulation of Vibration Testing and Damage Progression

31.2.1 Description of Case Study Structure

The case study structure used in this paper is a seven story three-dimensional truss comprised of 32 nodes and 91 members (Fig. 31.2). Due to a limitation on the length of the experimental member introduced by the load frame used to prescribe displacements and record restoring forces in the hybrid simulation, the dimensions of the truss are relatively small producing an approximate 3.7 m total height of the structure. For simplicity, all members of the truss were modeled as nominally identical L51x51x4.8 (L2x2x$\frac{3}{16}$) A36 steel angles. Additionally, the experimental substructure was limited to a single diagonal strut at the first story of the structure (denoted in green in Fig. 31.2 between nodes 4 and 5). This 66 cm (26 in.) long member was bolted to a pair of 9.5 mm (0.375 in) thick steel gusset plates using 1.27 cm (0.5 in.) diameter grade 8 high strength bolts and flat washers. These gusset plates were then used to secure the experimental substructure to a MTS 810 load frame with 250 kN capacity using mechanical wedge grips. This experimental substructure within the load frame is visible in Fig. 31.1. Within the analytical substructure, all members were idealized with linear elastic material properties and pin-connections. However, nonlinear geometric effects were incorporated in the dynamic time history analysis performed within the hybrid simulation routine implemented and described in the following section. Lastly, joint masses were uniformly scaled to produce a fundamental period of approximately 2s for the structure, and Rayleigh damping was prescribed to produce a range of reasonable damping ratios across the first eight modes of the full structural model.

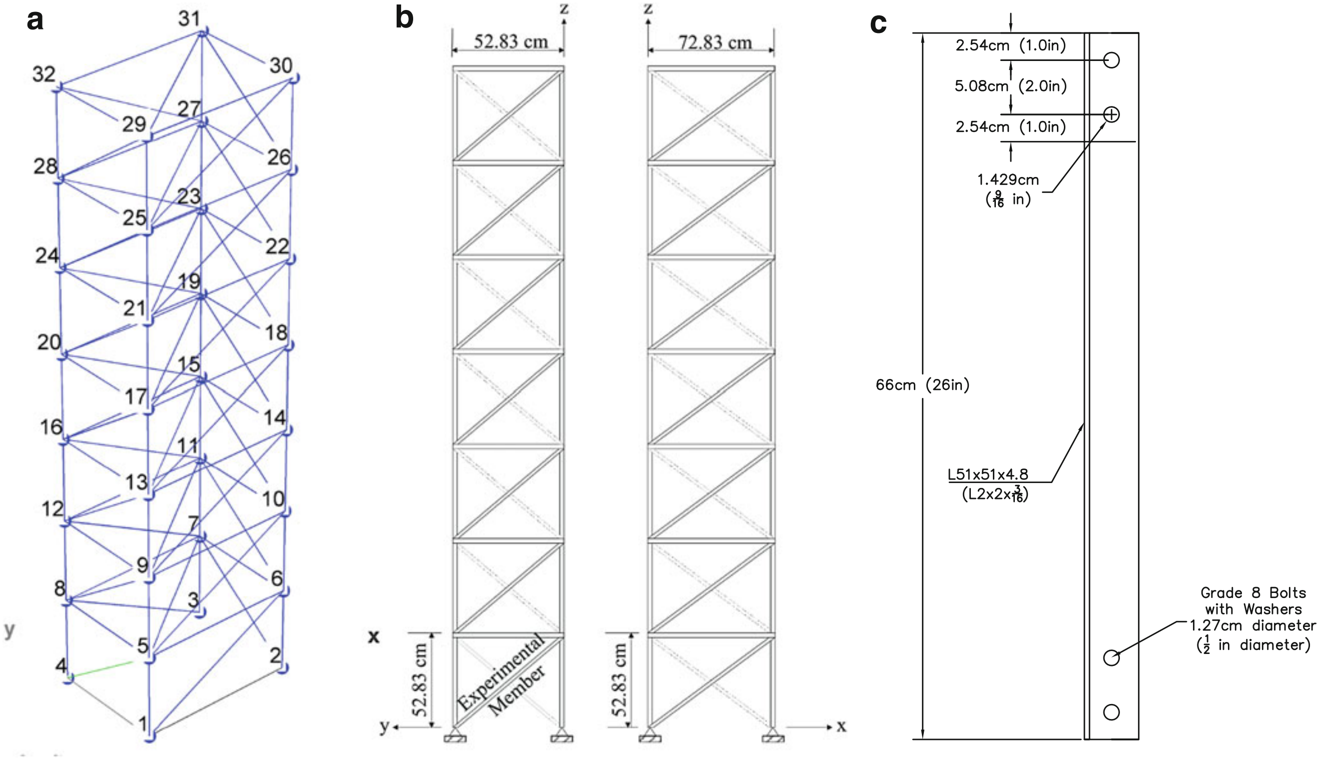
a
31
32
30
29
27
28
26
25
23
24
22
21
19
20
18
17
15
16
14
13
11
12
10
9
7
8
6
3
y
5
2
4
1
b
52.83 cm
z
72.83 cm
z
x
Experimental Member
52.83 cm
y
52.83 cm
x
c
2.54cm (1.0in)
5.08cm (2.0in)
2.54cm (1.0in)
1.429cm
($\frac{9}{16}$ in)
66cm (26in)
L51x51x4.8
(L2x2x$\frac{3}{16}$)
Grade 8 Bolts
with Washers
1.27cm diameter
($\frac{1}{2}$ in diameter)

Fig. 31.2 Seven story truss structure used for case study: (**a**) isometric view of truss geometry; (**b**) elevation views; (**c**) details of experimental substructure with bolted connection

31.2.2 Overview of Hybrid Simulation Methodology Employed

The hybrid simulation employed in this study was conducted using a MATLAB-based pseudo-dynamic implementation that was developed, verified, and experimentally validated in [10]. This hybrid simulation framework has been developed to incorporate nonlinear geometric effects in the numerical substructure and implements an incremental-iterative implicit integration scheme developed by Mosqueda and Ahmadizadeh [11]. In this scheme, the change in the acceleration vector over a time step is initially assumed to be zero but is then modified iteratively within the time step to remove the unbalanced force in the system, thereby converging on a state of dynamic equilibrium in the discrete-time equation of motion. The iterations in this scheme are used to account for nonlinearities in the system. In order to respect the path-dependent response of the experimental specimen and minimize the potential for unintended plastic deformations, iterations are performed virtually, rather than physically, using second-order polynomials fit to the most recent force-time and displacement-time measurements to model the virtual response of the experimental substructure during iterative adjustment of the displacements. This technique was originally developed and explained in greater detail by Mosqueda and Ahmadizadeh [11].

In the methodology used, a time step is initiated using a predicted displacement computed from the following equation, which is based on an initial assumption of zero change in acceleration ($\Delta \mathbf{a} = 0$):

$$\mathbf{d}_n = \mathbf{d}_{n-1} + \Delta t \mathbf{v}_{n-1} + \frac{\Delta t^2}{2} \mathbf{a}_{n-1} + \Delta t^2 \beta \Delta \mathbf{a} \tag{31.1}$$

where n is the index of the time step and β is the integration parameter computed as

$$\beta = \frac{(1-\alpha)^2}{4} \tag{31.2}$$

in the Hilber-Hughes-Taylor method, with $\alpha \in [-\frac{1}{3}, 0]$. Similarly, the predicted velocity is computed as

$$\mathbf{v}_n = \mathbf{v}_{n-1} + \Delta t \mathbf{a}_{n-1} + \Delta t \gamma \Delta \mathbf{a} \tag{31.3}$$

where γ is computed as

$$\gamma = \frac{1-2\alpha}{2} \tag{31.4}$$

The computed predictor displacements corresponding to the experimental substructure are then applied to the physical specimen, and the restoring force developed by the experimental substructure is measured. As suggested by Combescure and Pegon [12], the corresponding restoring force measurement is adjusted using the tangent stiffness of the specimen to account for small experimental errors that may be introduced during the application of the desired predictor displacement:

$$\tilde{\mathbf{r}} = \tilde{\mathbf{r}}^m + \mathbf{K}(\tilde{\mathbf{d}} - \tilde{\mathbf{d}}^m) \tag{31.5}$$

where the "∼" indicates that these forces and displacements are part of the predictor step, and the "m" superscript indicates measured displacement and restoring force [12]. The restoring force from the predictor step is then used along with the predicted inertial and damping terms to compute the imbalance in the following equation:

$$\mathbf{M}\mathbf{a}_n + \mathbf{C}\mathbf{v}_n + \mathbf{r}_n + \alpha[\mathbf{C}\Delta\mathbf{v} + \Delta\mathbf{r}] = \mathbf{f}_n + \alpha\Delta\mathbf{f} \tag{31.6}$$

The necessary corrected incremental acceleration vector to eliminate the imbalance for iteration j is computed as

$$\Delta\mathbf{a}_n^{j+1} = \Delta\mathbf{a}_n^j + \hat{\mathbf{M}}^{-1}\hat{\mathbf{f}} \tag{31.7}$$

where $\hat{\mathbf{f}}$ and $\hat{\mathbf{M}}$ are computed respectively as

$$\hat{\mathbf{f}} = \mathbf{f}_n + \alpha\Delta\mathbf{f} - \mathbf{M}\mathbf{a}_n - \mathbf{C}\mathbf{v}_n - \mathbf{r}_n - \alpha[\mathbf{C}\Delta\mathbf{v} + \Delta\mathbf{r}] \tag{31.8}$$

$$\hat{\mathbf{M}} = \mathbf{M} + \mathbf{C}\Delta t\gamma + \mathbf{K}\Delta t^2\beta + \alpha[\mathbf{C}\Delta t\gamma + \mathbf{K}\Delta t^2\beta] \tag{31.9}$$

The corrected incremental acceleration vector is then used as the new assumed or "predicted" change in acceleration for the time step, and the entire sequence of equations is repeated until the incremental acceleration vector converges, meaning the predicted and corrected state vectors are approximately equal. It should also be noted that the stiffness matrix is recomputed based on the updated displacements at the start of each iteration. In the implementation, nonlinear geometric effects within the full structural model are incorporated in the construction of the stiffness matrix. Following the computation of the stiffness matrix, the damping matrix is also recomputed as a linear combination of the mass and stiffness matrices, using the prescribed coefficients for mass-proportional and stiffness-proportional damping.

31.2.3 Details of Experimental Test Program

As previously detailed, the experimental substructure consisted of a single diagonal strut with bolted gusset plate connections that was subjected to prescribed displacement loading using a MTS 810 load frame. Since mechanical wedge grips displace during loading to increase the clamping force, the linear variable differential transformer (LVDT) integral to the actuator in the load frame could not be used to obtain a reliable measure of elongation in the experimental specimen. To address this technical challenge, a pair of unstressed steel bars were attached to the opposite side of the gusset plates and an Epsilon 3542 axial extensometer was used to measure the complete elongation of specimen including the bolted connection. A proportional-integral-derivative (PID) control loop was established using the extensometer signal as the feedback signal and this control loop was tuned using the actuator displacement as the control signal. Measurement of the restoring force from the experimental substructure was obtained using a MTS 661.23A-01 load cell. All measurements of force, displacement, and elongation were acquired with a MTS FlexTest GT controller with Series 493 electronics and were transferred to the computer running the developed hybrid simulation software over a RS485 digital communication bus. A programmable power supply interfaced to the host computer over a USB bus was used to prescribe target displacements during the hybrid simulations using an analog input channel from the MTS controller. All testing was performed at pseudo-dynamic rates under the necessary assumption that damage in the experimental substructure is reflected only in the structural stiffness. Real-time hybrid simulation techniques are ultimately necessary to include the effects of changes in mass and damping within the experimental substructure in the testing. This requirement is particularly important to consider when leveraging hybrid simulation to develop data for structural damage scenarios involving a loss of mass in the experimental substructure.

To establish a data set associated with the baseline condition of the structure, hybrid simulation of a vibration test with a single shaker excitation was initially performed using the as-built experimental substructure and analytical substructure. For this simulation, a swept-sine excitation with constant force amplitude over a frequency bandwidth from 0 to 10Hz was simultaneously applied in the "x" and "y" directions of the truss at node 12 to excite bending modes in each direction as well as torsional modes. The duration of the swept-sine excitation was 20 s and a simulation time step of 0.01 s was used in the hybrid simulation. The amplitude of the excitation was scaled to ensure linear elastic response of the experimental substructure and resulted in a peak amplitude of force in the experimental member of less than 8 kN (1.8 k). This simulation was performed with the specimen subject to an axial preload of 17.8 kN (4 k) to maintain tensile loading of the member during the simulation. This measure was taken to avoid nonlinear response in the transition between tension and compression that was found to result from the mechanical wedge grips used to attach the gusset plates to the load frame.

Following completion of this hybrid simulation of a vibration test, the specimen was subjected to tensile loading at a constant displacement rate until the limit state of bearing strength at the bolt holes was exceeded and ovalization of the bolt holes at both ends of the specimen was developed (Fig. 31.3). Again, it is emphasized that this realistic damage associated with the bolted connection limit state was realized not through hybrid simulation, but through quasi-static loading. However, an extended benefit of using hybrid simulation for vibration-based structural health monitoring and damage detection research is that damage in the experimental substructure could be developed under prescribed dynamic loading of the full structure. This would allow for investigation of the efficacy of VBDD methodologies when applied to structures following extreme loading events, such as recorded seismic ground motion time histories. Following the introduction of damage to the experimental substructure, a second hybrid simulation was performed by applying the same swept-sine force excitation to the structure at the same node and with the same simulation parameters. Again, the experimental member was subject to an axial preload of 17.8 kN (4 k) prior to simulating the vibration test to avoid nonlinear response associated with the transition from tension to compression. In this case, this measure that was taken to accommodate the employed experimental setup also precluded any significant sliding of the bolts within the ovalized holes. If no preload was applied to the experimental substructure, the response would be significantly different as there would be significant slip at the bolted connections during transitions between tension and compression. However, since structural members are normally subject to initial stresses due to dead load, the application of a preload can be justified. To improve the experiment, the level of axial prestress could

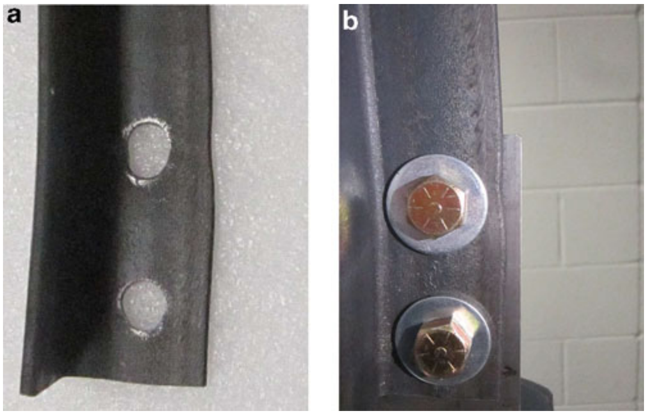

Fig. 31.3 Damage in bolted connections: (**a**) ovalization of bolt holes in member; (**b**) photograph of bolted connection after overload

be established through an initial static analysis of the structure under prescribed gravity loads, as well as resulting from any geometric imperfections, and then tracked through the progression of structural damage developed within a hybrid simulation to ensure an accurate estimate of the preload in the experimental substructure prior to the simulated vibration test in the damaged state.

31.3 Discussion of Results

31.3.1 Hybrid Simulation in the Healthy Condition

Following completion of the hybrid testing, the recorded stress-strain characteristics of the experimental substructure measured during the test program were used to update the initial analytical model of the full structure to facilitate comparisons between a calibrated fully analytical model and the hybrid simulation performed with one diagonal strut in the experimental substructure. Displacement and acceleration time histories resulting from the hybrid simulation of the vibration test in the healthy condition of the structure prior to introduction of damage both compared very well to those predicted by the fully analytical model. The displacement and acceleration time histories at the interface node between the analytical and experimental substructures (node 5) in the “y” direction are presented in Fig. 31.4. Since accelerations are typically measured in vibration-based structural health monitoring of civil structures, the Fast Fourier Transform of the predicted and generated accelerations for this location and direction over the bandwidth of the swept-sine excitation are also provided in Fig. 31.5. The frequency spectra correlate exceptionally well, which suggests that the hybrid simulation can be used to effectively generate vibration test data.

Combined deterministic-stochastic subspace state-space system identification, using the algorithm developed in [13], was applied to all 84 acceleration signals generated for the case study structure through the hybrid simulation. Stabilization plots were used to select stable estimates of structural poles over the 0–5Hz frequency bandwidth where resonance peaks were clearly present in the average normalized power spectral density. The modal parameter estimates obtained through this system identification routine are presented in Fig. 31.6 alongside the expected modal parameters generated through direct eigenvalue decomposition of the structural mass and stiffness matrices of the fully analytical model. The damping ratios provided for the fully analytical model are obtained using the proportional damping coefficients prescribed, whereas the damping ratios provided for the hybrid simulation results were obtained from the estimates of the poles obtained through the system identification. Statistical comparisons of the natural frequencies by percentage difference and mode shape estimates by use of the Modal Assurance Criterion (MAC) are presented in Table 31.1. The results express exceptionally strong correlation and suggest that hybrid simulation can reasonably be used to generate reliable synthetic test data for simulated vibration tests of civil structures. It is noted that the lower MAC correlation associated with the eighth mode can be attributed to a difficulty in achieving a reliable estimate of this mode through the system identification routine since this mode has a relatively high damping ratio and is closely spaced to another mode.

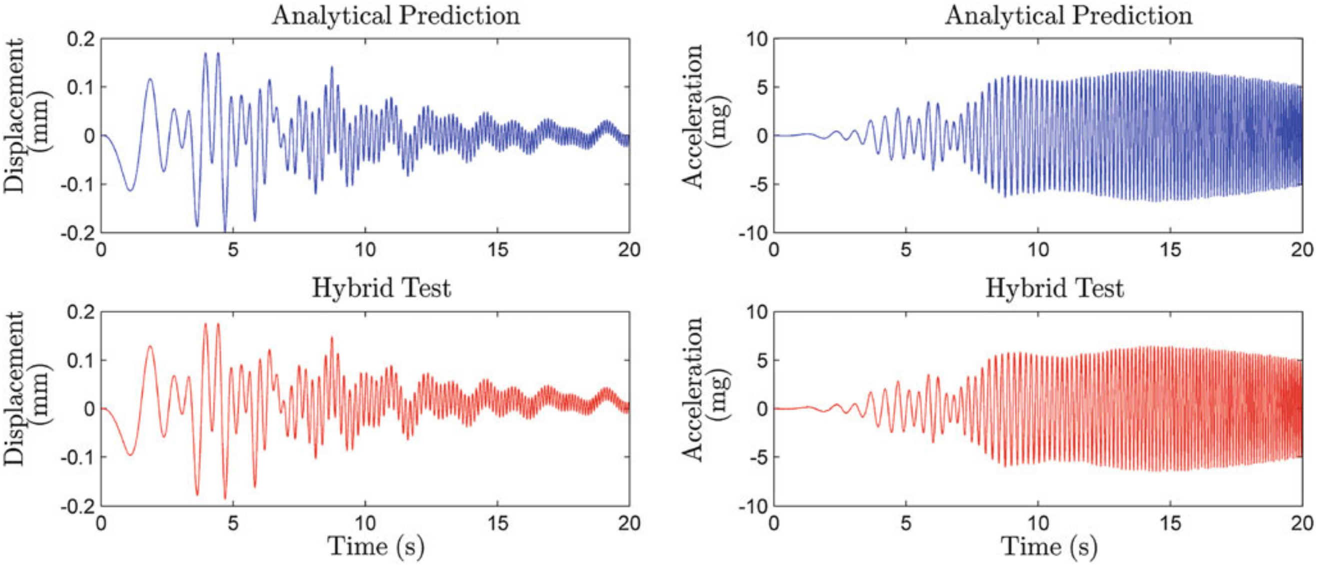

Fig. 31.4 Comparison of displacement time history and acceleration time history in the "y" direction at node 5 of the structure as predicted from the full analytical model and developed during the hybrid simulation

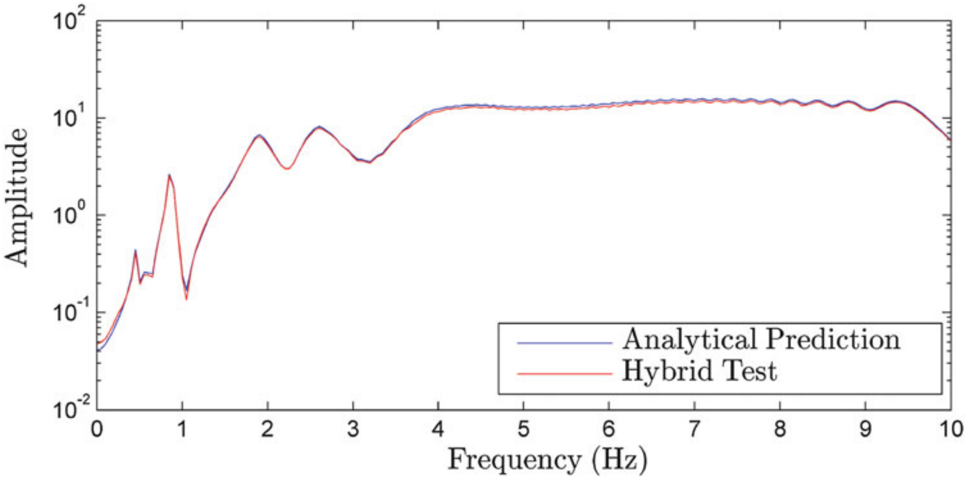

Fig. 31.5 Comparison of Fast Fourier Transform of acceleration at node 5 of the structure

31.3.2 Hybrid Simulation in the Damaged Condition

Combined deterministic-stochastic subspace state-space system identification was similarly applied to the test data obtained from the hybrid simulation of the vibration test performed after the introduction of damage at the bolted connection of the experimental member. In addition, stress-strain data recorded from the force-displacement response of the experimental substructure over the hybrid simulation was used to estimate an equivalent linear elastic stiffness of the experimental member to develop a fully analytical model of the damaged structure. The reduced stiffness of the experimental member was found to be approximately 63 % of the original stiffness of the member following the development of the damage evidenced by the ovalization of the bolt holes. Comparison between the modal parameter estimates obtained through eigenvalue decomposition of the full analytical model and those obtained through system identification of the test data recorded during the hybrid simulation is presented in Fig. 31.7. With the exception of the seventh mode, which was not well excited by the directional excitation applied in the hybrid simulation, the modal parameter estimates agree well.

The influence of the introduced damage on the modal parameter estimates is summarized in Table 31.2. This table provides the percent changes in natural frequencies and MAC correlations between the damaged and healthy data sets obtained through the hybrid simulation experiments as well as the expected changes predicted by the experimentally updated fully analytical

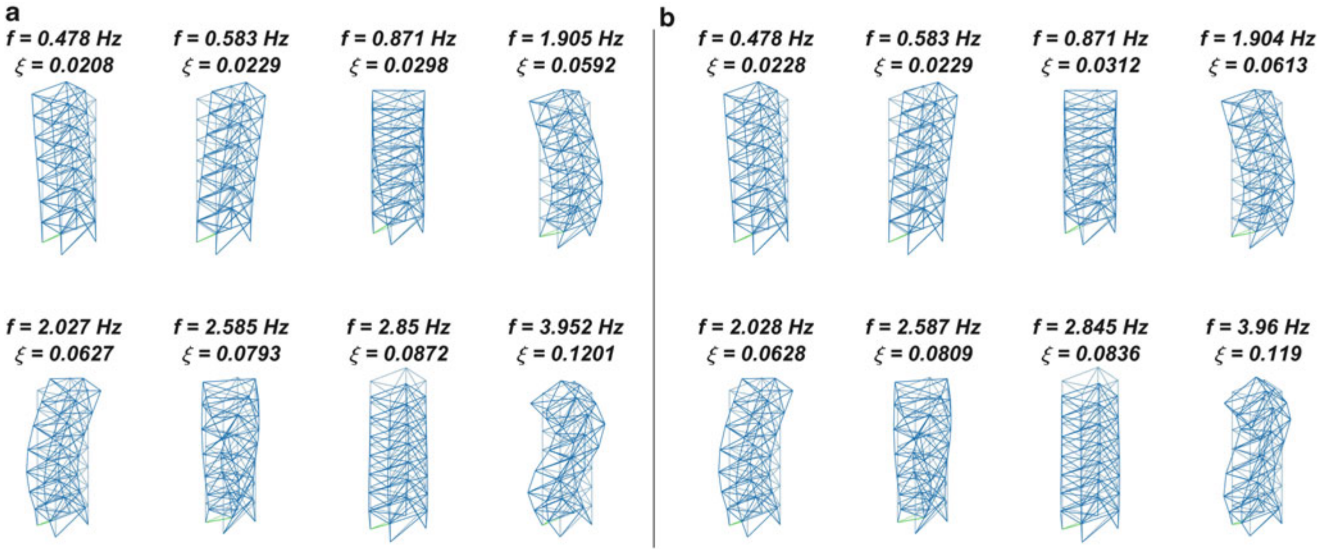
a
f = 0.478 Hz
ξ = 0.0208
f = 0.583 Hz
ξ = 0.0229
f = 0.871 Hz
ξ = 0.0298
f = 1.905 Hz
ξ = 0.0592
f = 2.027 Hz
ξ = 0.0627
f = 2.585 Hz
ξ = 0.0793
f = 2.85 Hz
ξ = 0.0872
f = 3.952 Hz
ξ = 0.1201
b
f = 0.478 Hz
ξ = 0.0228
f = 0.583 Hz
ξ = 0.0229
f = 0.871 Hz
ξ = 0.0312
f = 1.904 Hz
ξ = 0.0613
f = 2.028 Hz
ξ = 0.0628
f = 2.587 Hz
ξ = 0.0809
f = 2.845 Hz
ξ = 0.0836
f = 3.96 Hz
ξ = 0.119

Fig. 31.6 Comparison of modal parameter estimates for healthy structure: (**a**) obtained directly from fully analytical model, (**b**) obtained through application of system identification to hybrid simulation test data

Table 31.1 Comparison between modal parameter estimates of healthy structure obtained through hybrid simulation and through eigenvalue decomposition of a fully analytical model

Mode	1	2	3	4	5	6	7	8
$\Delta f(\%)$	−0.128	−0.017	−0.004	0.029	−0.075	−0.066	0.145	−0.196
MAC	0.9999	0.9999	1.0000	0.9999	0.9999	0.9999	0.9952	0.7135

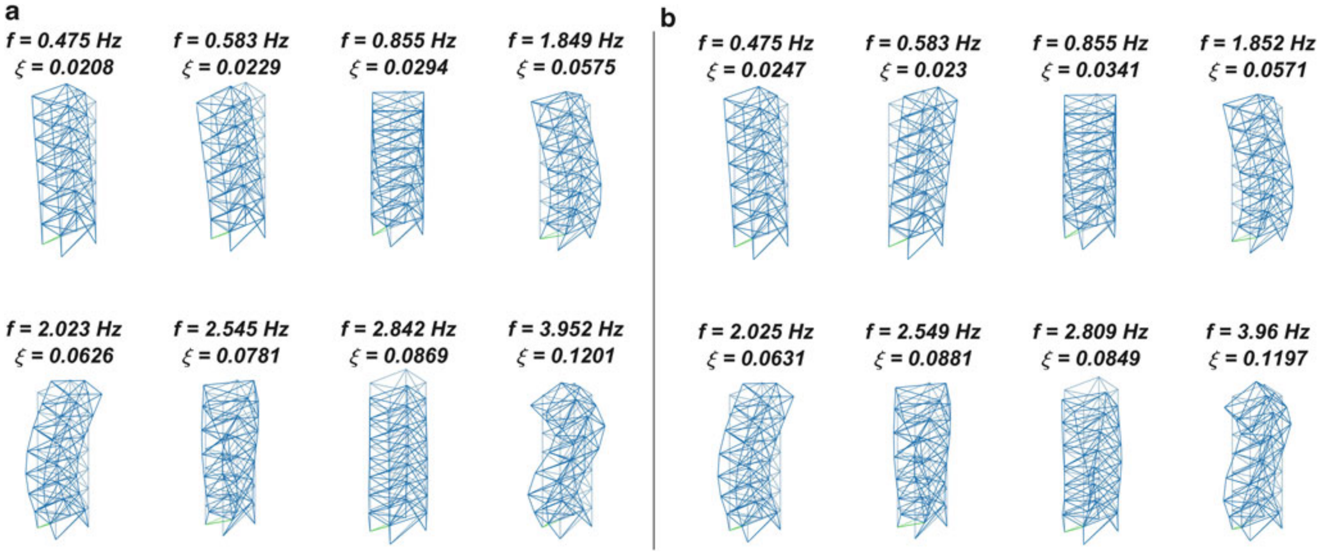
a
f = 0.475 Hz
ξ = 0.0208
f = 0.583 Hz
ξ = 0.0229
f = 0.855 Hz
ξ = 0.0294
f = 1.849 Hz
ξ = 0.0575
f = 2.023 Hz
ξ = 0.0626
f = 2.545 Hz
ξ = 0.0781
f = 2.842 Hz
ξ = 0.0869
f = 3.952 Hz
ξ = 0.1201
b
f = 0.475 Hz
ξ = 0.0247
f = 0.583 Hz
ξ = 0.023
f = 0.855 Hz
ξ = 0.0341
f = 1.852 Hz
ξ = 0.0571
f = 2.025 Hz
ξ = 0.0631
f = 2.549 Hz
ξ = 0.0881
f = 2.809 Hz
ξ = 0.0849
f = 3.96 Hz
ξ = 0.1197

Fig. 31.7 Comparison of modal parameter estimates for damaged structure: (**a**) obtained directly from fully analytical model, (**b**) obtained through application of system identification to hybrid simulation test data

models. The results obtained through the hybrid simulation correlate well with the expected changes while exhibiting generally small changes in natural frequencies and MAC values as a result of the introduced damage. Again, the discrepancy between the results obtained for the seventh mode merely reflect the difficulty in obtaining an experimental estimate of this mode since the shaker excitation was not applied in the vertical direction. Furthermore, note that experimental results correctly indicate that the second, fifth, and eighth modes are insensitive to the damage in the experimental substructure, which is expected since the experimental member contributes negligible stiffness to the direction of bending exhibited in those modes.

Table 31.2 Comparisons between modal parameter estimates of damaged and healthy structures

Mode	1	2	3	4	5	6	7	8
Comparison	$\Delta f(\%)$							
Fully Analytical Models	−0.625	−0.001	−1.769	−2.954	−0.170	−1.578	−0.276	0.000
Hybrid Simulations	−0.735	0.007	−1.795	−2.764	−0.150	−1.472	−1.294	0.021
Comparison	MAC							
Fully Analytical Models	0.9996	1.0000	0.9985	0.9828	0.9899	0.9865	0.9940	0.9999
Hybrid Simulations	0.9995	0.9999	0.9985	0.9838	0.9921	0.9884	0.8388	0.9994

31.4 Summary

Vibration-based methods for structural health monitoring have been supported extensively through acquisition of experimental data from laboratory models and full-scale destructive tests performed on field structures. However, such testing presents challenges in faithfully representing structural damage associated with controlling strength limit states and, when performed on field structures, presents significant cost, logistical, and time constraints. This paper suggests that the increasingly popular hybrid simulation methodology can be used to acquire laboratory vibration test data from both healthy and damaged structures, in addition to providing a means for developing realistic structural damage within the experimental substructure through simulation of extreme loading events. A case study application to a three-dimensional truss structure with a single bolted member serving as the experimental substructure was used to demonstrate the approach and explore the quality of the experimental data obtained through the hybrid simulation. The test data acquired from the hybrid simulations was found to correlate strongly with predictions obtained from a fully analytical model and the modal parameter estimates obtained through system identification of the test data reflected expected changes resulting from the introduced damage. The results of the study demonstrate the stated advantages of this proposed alternative to full-scale field testing and support further exploration of hybrid simulation as a tool for vibration-based structural health monitoring research.

Acknowledgements The authors acknowledge the financial support provided by the University of North Carolina at Charlotte Energy Production and Infrastructure Center (EPIC) through a graduate research fellowship award that provided support for the development, verification, and validation of the hybrid testing framework developed by the authors and used in this study.

References

1. Brownjohn, J., De Stefano, A., Xu, Y.-L., Wenzel, H., Aktan, A.: Vibration-based monitoring of civil infrastructure: challenges and successes. J. Civ. Struct. Heal. Monit. **1**(3–4), 79–95 (2011)
2. Farrar, C.R., Baker, W., Bell, T., Cone, K., Darling, T., Duffey, T., Eklund, A., Migliori, A.: Dynamic characterization and damage detection in the I-40 bridge over the Rio Grande. Technical Report, Los Alamos National Lab, NM (1994)
3. Alampalli, S., Fu, G., Dillon, E.W.: Signal versus noise in damage detection by experimental modal analysis. J. Struct. Eng. **123**(2), 237–245 (1997)
4. Peeters, B.: System identification and damage detection in civil engineering 2000
5. Whelan, M.J., Janoyan, K.D.: In-service diagnostics of a highway bridge from a progressive damage case study. J. Bridg. Eng. **15**(5), 597–607 (2009)
6. Saouma, V., Sivaselvan, M.: Hybrid simulation: theory, implementation and applications. CRC Press, London (2008)
7. Mostafaei, H.: Hybrid fire testing for performance evaluation of structures in fire-part 1 methodology. National Research Council Canada, p. 22 (2011)
8. Terzic, V., Stojadinovic, B.: Hybrid simulation of bridge response to three-dimensional earthquake excitation followed by truck load. J. Struct. Eng. **140**(8), A4014010 (2013)
9. Mercado, M.W., Zhang, Y.: Hybrid simulation testbed for experimental validation and characterization of NDE and sensor technology. J. Bridg. Eng. **17**(6), 907–920 (2012)
10. Tedeschi, M.: Development, verification, and validation of a hybrid testing framework for latticed structures with nonlinear geometric effects. M.S. thesis, University of North Carolina at Charlotte, Charlotte, N.C. (2015)
11. Mosqueda, G., Ahmadizadeh, M.: Iterative implicit integration procedure for hybrid simulation of large nonlinear structures. Earthq. Eng. Struct. Dyn. **40**(9), 945–960 (2011)
12. Combescure, D., Pegon, P.: α-operator splitting time integration technique for pseudodynamic testing error propagation analysis. Soil Dyn. Earthq. Eng. **16** (7), 427–443 (1997)
13. van Overschee, P., de Moor, B.: Subspace Identification for Linear Systems: Theory-Implementation-Applications. Kluwer Academic Publishers, Boston (1996)

Chapter 32
Real Time Hybrid Simulation with Online Model Updating on Highly Nonlinear Device

Ge Ou and Shirley J. Dyke

Abstract Hybrid Simulation (HS) and Real Time Hybrid Simulation (RTHS) are recognized as powerful techniques for civil infrastructure assessment. Typically in HS/RTHS, a critical component is isolated as the physical component in the simulation, while the remainder of the structure is modeled numerically. This approach enables response evaluation on both local and global level. Broadening the applications that would like to use HS and RTHS requires that we examine more complex structural systems. When multiple components in the structural system have the same design and contribute roughly equally to the response, it may be difficult to select the most appropriate physical component. However, modeling errors in those structural components that reside in the numerical component can influence the accuracy of the global responses. Model updating based on the responses of the physical component for determining the model parameters will reduce the influence of the modeling errors. Advances in online system identification techniques and their application to more complex structural models, enables the option of incorporating online model updating into HS/RTHS. Through a simplified case study, we explore the feasibility of HS/RTHS with model updating (HSMU/RTHSMU). A two story steel frame equipped with two identical magnetic-rheological (MR) dampers. In RTHS, the first story MR damper is loaded as the physical component and the remainder of the structure, including the frame and the second MR damper, is numerically modeled. Simulation and conventional RTHS response are considered. In each case the second story MR damper model uses one initial parameter set, which is then updated online using identified parameters based on the physical component (RTHSMU). Online model updating is then investigated using a validation signal, and the fidelity and advantages of RTHSMU are discussed.

Keywords Real time hybrid simulation • Online model updating • BoucWen model • MR damper model • Constrained unscented Kalman filter

32.1 Introduction

In contrast to conventional testing methods and pure numerical simulation, in hybrid simulation (also known as pseudo-dynamic testing or dynamic sub-structuring), the critical/hard to model component is isolated in the physical part while the rest is in the numerical part, with boundary condition secured by actuators linked between the two parts [1–3], both global performance of the infrastructure such as drift, failure mechanism, progressive collapse and local behavior includes hysteresis, local failure, and energy dissipation can be investigated [4–6]. When rate dependent component is involved, the test has to be done in real time scale. The applications of RTHS start with successfully examples in evaluating vibration control performance of damper devices and base isolators [7–9] and are further expanded to applications of evaluating structural components. However, difficulties on the selection of the physical component appear when multiple components with the same design contribute equally to the structural response.

With improvements on identification convergence rate and its robustness regards to noise, model uncertainties, and initial conditions, online system identification algorithms are made feasible to experimental applications. One popular class of system identification methods can be implemented in real time is the Kalman filter family. Initially started in linear system, the Extended Kalman Filter (EKF) and the Unscented Kalman Filter (UKF) were developed subsequently for nonlinear system, where EKF optimizes the linearization approximation of the system through Jacobian matrix while UKF uses the

G. Ou (✉)
Lyles School of Civil Engineering, Purdue University, West Lafayette, IN 47906, USA
e-mail: gou@purdue.edu

S.J. Dyke
School of Mechanical Engineering, Lyles School of Civil Engineering, Purdue University, West Lafayette, IN 47906, USA

© The Society for Experimental Mechanics, Inc. 2016

J. De Clerck, D.S. Epp (eds.), *Rotating Machinery, Hybrid Test Methods, Vibro-Acoustics & Laser Vibrometry, Volume 8*,
Conference Proceedings of the Society for Experimental Mechanics Series, DOI 10.1007/978-3-319-30084-9_32

Unscented Transformation (UT). UKF is first introduced to civil infrastructure application of updating steel hysteresis model in a simulation case study [10], with additional experimental validation implemented in both structural model [11] and highly nonlinear device model [12].

The opportunity of conceptually reforming HS/RTHS technique has been realized by researchers with advances in online model updating algorithms. Rather than only exchanging information at the interface (displacement, acceleration or restoring force level), model information can be extracted from the experimental substructure and feed into numerical substructure as well. Combining model updating in HS/RTHS, some numerical and experimental validation case studies are discussed in the literature [13–16], which demonstrated the need and benefits of the concept of HSMU/RTHSMU. This paper utilized a simple experimental case study of a two story frame with repeatable used nonlinear devices of two MR dampers one on each floor. In RTHS, the first story MR damper is loaded experimentally in the physical setup and the rest of the structure including the frame and the other MR damper is numerically modeled. In this paper, simulation response where both MR dampers are modelled with one initial parameter set and conventional RTHS response where the second story MR damper is modeled are compared with RTHSMU response where the second story MR damper model is updated in real time. Online model updating results are also investigated through validation signal, with RTHSMU advantage and current limitation discussed.

32.2 Real Time Hybrid Simulation with Model Updating

A nonlinear dynamic structure in conventional simulation can be written in the equation of motion:

$$\mathbf{M}\ddot{\mathbf{x}} + \mathbf{C}\dot{\mathbf{x}} + \mathbf{K}\mathbf{x} + \mathbf{R}\left(\mathbf{x}, \dot{\mathbf{x}}, \boldsymbol{\theta}_{\mathbf{R}}\right) = -\mathbf{M}\boldsymbol{\Gamma}\ddot{\mathbf{x}}_{\mathbf{g}} \tag{32.1}$$

where M, C, K are the linear mass, damping, stiffness matrices of the reference structure, **R** is the nonlinear restoring force, θ_R are the model parameters of the nonlinear behaviour, x, $\dot{x}$ and $\ddot{x}$ are structural responses (displacement, velocity, acceleration), and $\ddot{x}_g$ denotes earthquake excitation.

Considering HS/RTHS representation of the reference structure:

$$\mathbf{M}^{\mathbf{N}}\ddot{\mathbf{x}}^{\mathbf{N}} + \mathbf{C}^{\mathbf{N}}\dot{\mathbf{x}}^{\mathbf{N}} + \mathbf{K}^{\mathbf{N}}\mathbf{x}^{\mathbf{N}} + \mathbf{F}^{\mathbf{E}}\left(\mathbf{x}^{\mathbf{E}}, \dot{\mathbf{x}}^{\mathbf{E}}\right) + \mathbf{R}^{\mathbf{N}}\left(\mathbf{x}^{\mathbf{N}}, \dot{\mathbf{x}}^{\mathbf{N}}, \boldsymbol{\theta}_{\mathbf{R}}\right) = -\mathbf{M}\boldsymbol{\Gamma}\ddot{\mathbf{x}}_{\mathbf{g}} \tag{32.2}$$

$$\mathbf{M}^{\mathbf{E}}\ddot{\mathbf{x}}^{\mathbf{E}} + \mathbf{C}^{\mathbf{E}}\dot{\mathbf{x}}^{\mathbf{E}} + \mathbf{K}^{\mathbf{E}}\mathbf{x}^{\mathbf{E}} + \mathbf{R}^{\mathbf{E}}\left(\mathbf{x}^{\mathbf{E}}, \dot{\mathbf{x}}^{\mathbf{E}}\right) = \mathbf{F}^{\mathbf{E}}\left(\mathbf{x}^{\mathbf{E}}, \dot{\mathbf{x}}^{\mathbf{E}}\right) \tag{32.3}$$

where the superscript $()^N$ and $()^E$ denote the RTHS and Hybrid simulation numerical and experimental substructures respectively, $\mathbf{M} = \mathbf{M}^{\mathbf{E}} + \mathbf{M}^{\mathbf{N}}$, $\mathbf{C} = \mathbf{C}^{\mathbf{E}} + \mathbf{C}^{\mathbf{N}}$, $\mathbf{K} = \mathbf{K}^{\mathbf{E}} + \mathbf{K}^{\mathbf{N}}$. $\mathbf{F}^{\mathbf{E}}$ denotes the measured force in the experimental substructure. The fidelity of RTHS is based on how accurately Eqs. (32.2) and (32.3) represent the Eq. (32.1) when implemented.

However, when the physical specimen is selected to include structural components that are used in multiple instances within a structure, a significant portion of the nonlinear behavior resides in the numerical substructure ($\mathbf{R}^{\mathbf{N}} >> \mathbf{R}^{\mathbf{E}}$) and there maybe modelling errors present in $\mathbf{R}^{\mathbf{N}}$. Thus, the modified formulation of RTHS which includes model updating is:

$$\mathbf{M}^{\mathbf{N}}\ddot{\mathbf{x}}^{\mathbf{N}} + \mathbf{C}^{\mathbf{N}}\dot{\mathbf{x}}^{\mathbf{N}} + \mathbf{K}^{\mathbf{N}}\mathbf{x}^{\mathbf{N}} + \mathbf{F}^{\mathbf{E}}\left(\mathbf{x}^{\mathbf{E}}, \dot{\mathbf{x}}^{\mathbf{E}}\right) + \mathbf{R}^{\mathbf{N}}\left(\mathbf{x}^{\mathbf{N}}, \dot{\mathbf{x}}^{\mathbf{N}}, \tilde{\boldsymbol{\theta}}_{\mathbf{R}}\right) = -\mathbf{M}\boldsymbol{\Gamma}\ddot{\mathbf{x}}_{\mathbf{g}} \tag{32.4}$$

$$\mathbf{M}^{\mathbf{E}}\ddot{\mathbf{x}}^{\mathbf{E}} + \mathbf{C}^{\mathbf{E}}\dot{\mathbf{x}}^{\mathbf{E}} + \mathbf{K}^{\mathbf{E}}\mathbf{x}^{\mathbf{E}} + \mathbf{R}^{\mathbf{E}}\left(\mathbf{x}^{\mathbf{E}}, \dot{\mathbf{x}}^{\mathbf{E}}\right) = \mathbf{F}^{\mathbf{E}}\left(\mathbf{x}^{\mathbf{E}}, \dot{\mathbf{x}}^{\mathbf{E}}\right) \tag{32.5}$$

$$\tilde{\boldsymbol{\theta}}_{\mathbf{R}} = \boldsymbol{\Psi}\left(\mathbf{R}^{\mathbf{E}}, \mathbf{x}^{\mathbf{E}}, \dot{\mathbf{x}}^{\mathbf{E}}, \boldsymbol{\theta}_{\boldsymbol{\Psi}}\right) \tag{32.6}$$

where Ψ indicates the model updating is performed in real-time, θ_Ψ is the parameter being updated through the chosen model updating algorithm and $\tilde{\theta}_R$ is the recursively identified nonlinear model parameter that minimizes the associated cost function. Thus, in this implementation, the numerical restoring force $R^N\left(\mathbf{x}^{\mathbf{N}}, \dot{\mathbf{x}}^{\mathbf{N}}, \tilde{\boldsymbol{\theta}}_{\mathbf{R}}\right)$ adapts in real-time based on the physical responses.

32.2.1 Constrained Unscented Kalman Filter

Consider a stochastic nonlinear discrete-time dynamic system:

$$\boldsymbol{\theta}_{\mathbf{k}} = \mathbf{F}\left(\boldsymbol{\theta}_{\mathbf{k-1}}, \mathbf{u}_{\mathbf{k-1}}, \mathbf{k-1}\right) + \mathbf{w}_{\mathbf{k-1}} \tag{32.7}$$

$$\mathbf{y}_{\mathbf{k}} = \mathbf{H}\left(\boldsymbol{\theta}_{\mathbf{k}}, \mathbf{k}\right) + \mathbf{v}_{\mathbf{k}} \tag{32.8}$$

where F and H are process and observation models. For a parameter estimation problem, $\boldsymbol{\theta}_{\mathbf{k-1}}$ is the system parameter vector. Assume for all $k \geq 1$, input u_k, measurement y_k, and the PDFs of $\boldsymbol{\rho}(\boldsymbol{\theta}_{\mathbf{0}})$, $\boldsymbol{\rho}(\mathbf{w})$, $\boldsymbol{\rho}(\mathbf{v})$ are known. Also, $\mathbf{w}$ and $\mathbf{v}$ are the process noise and measurement noise, with zero mean and known variances, represented by $\mathbf{Q}$ and $\mathbf{R}$. $\boldsymbol{\theta}_{\mathbf{0}}$ is the initial condition (guess) of the parameter estimation vector.

Consider parameter set to be estimated θ_k has interval limit $d_k \leq \theta_k \leq e_k$, the interval constrained unscented transformation is defined as $[\boldsymbol{\gamma}_{\mathbf{k}}, \boldsymbol{\Theta}_{\mathbf{k}}] = \boldsymbol{\Phi}_{\mathbf{ICUT}}\left(\widehat{\boldsymbol{\theta}}_{\mathbf{k}}, \mathbf{P}_{\mathbf{k}}^{\boldsymbol{\theta\theta}}, \mathbf{d}_{\mathbf{k}}, \mathbf{e}_{\mathbf{k}}, L, \lambda_C\right)$ [5], where the current estimation parameter $\boldsymbol{\theta}_{\mathbf{k}}$ is projected to additional 2 L sigma points (L is the number of parameter to be identified) $\boldsymbol{\Theta}_{\mathbf{k}}$, the mean $\widehat{\boldsymbol{\Theta}}_{\mathbf{k}} = \sum_{0}^{j=2L} \gamma_{j,k} \boldsymbol{\Theta}_{\mathbf{j,k}}$ with weighting factors γ_j ($j = 1..2L$), and $\sum_{j=0}^{2L} \gamma_j = 1$.

Once we have defined the ICUT, the forecast step is given as:

$$\left[\boldsymbol{\gamma}_{\mathbf{k-1}}, \boldsymbol{\Theta}_{\mathbf{k-1}|\mathbf{k-1}}\right] = \boldsymbol{\Phi}_{\mathbf{ICUT}}\left(\widehat{\boldsymbol{\theta}}_{\mathbf{k}}, \mathbf{P}_{\mathbf{k}}^{\boldsymbol{\theta\theta}}, \mathbf{d}_{\mathbf{k}}, \mathbf{e}_{\mathbf{k}}, L, \lambda_C\right) \tag{32.9}$$

$$\boldsymbol{\Theta}_{\mathbf{j,k}|\mathbf{k-1}} = \mathbf{F}\left(\boldsymbol{\Theta}_{\mathbf{k-1}|\mathbf{k-1}}, \mathbf{u}_{\mathbf{k-1}}, k-1\right) + \mathbf{w}_{\mathbf{k-1}} \tag{32.10}$$

$$\widehat{\boldsymbol{\theta}}_{\mathbf{k}|\mathbf{k-1}} = \sum_{j=0}^{2L} \gamma_{j,k-1} \boldsymbol{\Theta}_{\mathbf{j,k}|\mathbf{k-1}} \tag{32.11}$$

$$\mathbf{P}_{\mathbf{k}|\mathbf{k-1}}^{\boldsymbol{\theta\theta}} = \sum_{j=0}^{2L} \gamma_{j,k-1} \left[\boldsymbol{\Theta}_{\mathbf{j,k}|\mathbf{k-1}} - \widehat{\boldsymbol{\theta}}_{\mathbf{k}|\mathbf{k-1}}\right] \left[\boldsymbol{\Theta}_{\mathbf{j,k}|\mathbf{k-1}} - \widehat{\boldsymbol{\theta}}_{\mathbf{k}|\mathbf{k-1}}\right]^{\mathbf{T}} + \mathbf{Q}_{\mathbf{k-1}} \tag{32.12}$$

$$\left[\boldsymbol{\gamma}_{\mathbf{k}}, \boldsymbol{\Theta}_{\mathbf{k}|\mathbf{k-1}}\right] = \boldsymbol{\Phi}_{\mathbf{ICUT}}\left(\widehat{\boldsymbol{\theta}}_{\mathbf{k}|\mathbf{k-1}}, \mathbf{P}_{\mathbf{k}|\mathbf{k-1}}^{\boldsymbol{\theta\theta}}, \mathbf{d}_{\mathbf{k}}, \mathbf{e}_{\mathbf{k}}, L, \lambda_C\right) \tag{32.13}$$

$$\mathbf{Y}_{\mathbf{j,k}|\mathbf{k-1}} = \mathbf{H}\left(\boldsymbol{\Theta}_{\mathbf{j,k}|\mathbf{k-1}}, k\right) \tag{32.14}$$

$$\widehat{\mathbf{y}}_{\mathbf{k}|\mathbf{k-1}} = \sum_{j=0}^{2L} \gamma_{j,k} \mathbf{Y}_{\mathbf{j,k}|\mathbf{k-1}} \tag{32.15}$$

$$\mathbf{P}_{\mathbf{k}|\mathbf{k-1}}^{\mathbf{yy}} = \sum_{j=0}^{2L} \gamma_{j,k} \left[\mathbf{Y}_{\mathbf{j,k}|\mathbf{k-1}} - \widehat{\mathbf{y}}_{\mathbf{k}|\mathbf{k-1}}\right] \left[\mathbf{Y}_{\mathbf{j,k}|\mathbf{k-1}} - \widehat{\mathbf{y}}_{\mathbf{k}|\mathbf{k-1}}\right]^{\mathbf{T}} + \mathbf{R}_{\mathbf{k}} \tag{32.16}$$

$$\mathbf{P}_{\mathbf{k}|\mathbf{k-1}}^{\boldsymbol{\theta}\mathbf{y}} = \sum_{j=0}^{2L} \gamma_{j,k} \left[\boldsymbol{\Theta}_{\mathbf{j,k}|\mathbf{k-1}} - \widehat{\boldsymbol{\theta}}_{\mathbf{k}|\mathbf{k-1}}\right] \left[\mathbf{Y}_{\mathbf{j,k}|\mathbf{k-1}} - \widehat{\mathbf{y}}_{\mathbf{k}|\mathbf{k-1}}\right]^{\mathbf{T}} \tag{32.17}$$

$\mathbf{P}^{\boldsymbol{\theta\theta}}_{\mathbf{k}|\mathbf{k-1}}$ is the forecast error covariance, $\mathbf{P}^{\mathbf{yy}}_{\mathbf{k}|\mathbf{k-1}}$ is the innovation covariance, $\mathbf{P}^{\boldsymbol{\theta}\mathbf{y}}_{\mathbf{k}|\mathbf{k-1}}$ is the cross covariance. Similar to classic KF update, the estimate step (also known as data assimilation step) is defined:

$$\mathbf{K_k} = \mathbf{P}^{\boldsymbol{\theta}\mathbf{y}}_{\mathbf{k}|\mathbf{k-1}} \left(\mathbf{P}^{\mathbf{yy}}_{\mathbf{k}|\mathbf{k-1}} \right)^{\mathbf{-1}} \tag{32.18}$$

$$\widehat{\boldsymbol{\theta}}_{\mathbf{k}|\mathbf{k}} = \mathbf{K_k} \left(\mathbf{y_k} - \widehat{\mathbf{y}}_{\mathbf{k}|\mathbf{k-1}} \right) \tag{32.19}$$

$$P^{\theta\theta}_{k|k} = P^{\theta\theta}_{k|k-1} - K_k P^{yy}_{k|k-1} K_k^T \tag{32.20}$$

where $\mathbf{K^k}$ is the Kalman gain matrix and $\mathbf{P}^{\boldsymbol{\theta\theta}}_{\mathbf{k}|\mathbf{k}}$ is the data-assimilation error-covariance.

32.3 Experimental Validation

The RTHSMU is investigated through an experimental example, where the behaviour of a two story frame with identical nonlinear MR dampers on each floor is studied, shown in Fig. 32.1. Three stages of simulation/test are conducted. In the simulation stage, both MR dampers are modelled in numerical with initial parameters; in the RTHS stage, MR damper on the first floor is tested experimentally and the frame and the MR damper on the second floor is modelled numerically with the same parameters as in the simulation stage, information exchange is implemented between boundary conditions (D_d denotes desired displacement, R_m is the measured force); in the RTHSMU stage, the same first floor MR is test experimentally and the rest are modelled in simulation. However, besides the interface information exchange, the numerical MR damper model parameters are updated in real time using the measured response from the experimental substructures (D_m denotes the measured displacement), the initial condition of the numerical MR damper is the same as in the simulation stage and the RTHS stage, shown in Fig. 32.1.

The two-story frame has natural frequency at 2.7 and 8.2 Hz, with mass m of 3.5×10^3 kg, stiffness k of 3.4×10^3 kN/m and 2 % damping at each floor. Three scaled earthquakes include El-Centro (E1), Gebeze (E2) and Mexico (E3), are used as ground motion excitation. The hysteretic behavior of the MR damper is modeled with phenomenon Bouc-Wen model [17], described as:

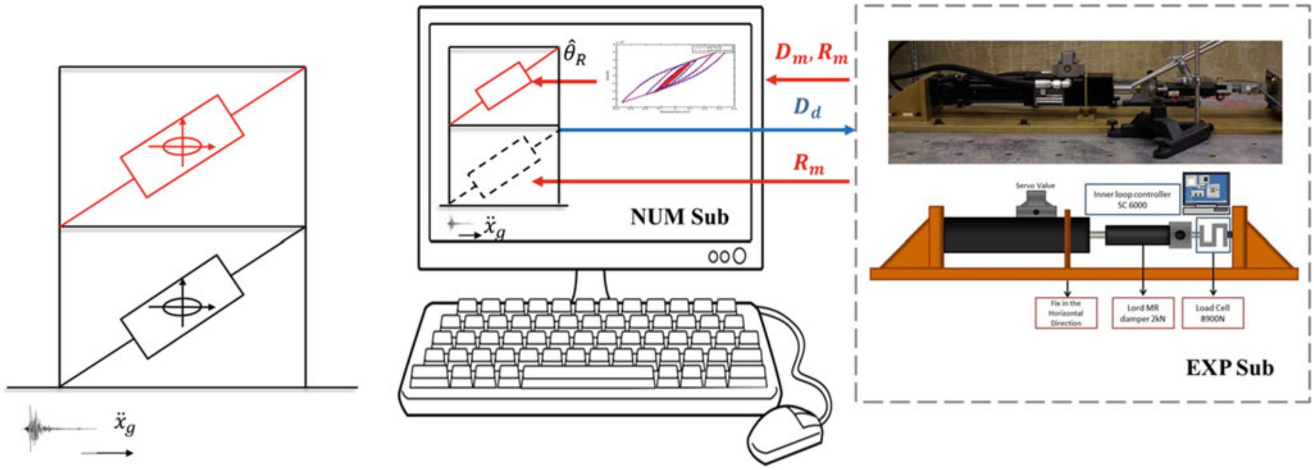

Fig. 32.1 Experimental case study and RTHSMU implementation

Table 32.1 Parameters in the MR damper phenomenon model

Case	β	γ	n	A	α	c_0
Initial	*300*	*300*	*1.21*	*300*	*150*	*50*
Final (E1)	388.9	417.1	1.00	195.46	121.69	46.29
Final (E2)	391.6	419.4	1.00	156.3	105.44	42.19
Final (E3)	358.8	465.8	1.00	175.64	124.22	42.18
Standard deviation	*18.1*	*27.5*	*0.0007*	*19.58*	*10.19*	*2.36*
Updating constraints	[0.1500]	[0.1500]	[1.4]	[0.1000]	[0.400]	[0.400]

$$f = \alpha z + c_0 \dot{x} \tag{32.21}$$

$$\dot{z} = -\gamma \left|\dot{x}\right| z \left|z\right|^{n-1} - \beta \dot{x} \left|z\right|^{n} + A\dot{x} \tag{32.22}$$

$$\alpha = \alpha_a + \alpha_b u \tag{32.23}$$

$$c_0 = c_{0a} + c_{0b} u \tag{32.24}$$

Where u is the command voltage to the MR damper, in this case study, to simplify the model complexity, the MR damper is assumed to be operated under a constant voltage. The power term n is set with narrower updating constraints ($4 > n > 1$) to avoid instability issue in model updating.

32.3.1 Model Updating Results

The model updating results are evaluated first through comparing the model estimation $\widehat{y}\big|_{k|k-1}$ result and the measured force response y_k. Convergence on data estimation is shown to be achieved at around 4 s after test started, where the estimated model output was following the initial model and then converged to the measured response. The estimation and convergence of each parameter is discussed with the final values listed in Table 32.1, it indicated the standard deviation of each parameter is within 10 % of the mean value. However, model parameters kept changing (does not converge) even the data between measured force and model estimation matches well, as in Fig. 32.2. In the previous numerical study [18], it has been demonstrated that more than one set of model parameters may meet the convergence criterion using CUKF, further validation means are needed to understand updating performance and its feasibility in RTHS application.

To evaluate the fidelity of model updating in RTHS, a validation test is performed in addition. In the validation test, 2nd story displacement time history after RTHSMU is extracted and sent to the experimental setup, meanwhile, the identified parameter sets $\tilde{\boldsymbol{\theta}}_{\mathbf{R}}(t)$ time history are also streamed to an MR damper numerical model. Comparison is made between the measured validation force f_v and the updated model output f_{mu} in order to understand if the updated parameter sets can represent the damper behavior on the 2nd floor loading condition, with results shown in Fig. 32.3. Results imply even the estimated force has some underestimation on MR damper force, overall the updated model with parameters $\tilde{\boldsymbol{\theta}}_{\mathbf{R}}(t)$ capture the behavior of the 2nd story MR damper.

32.3.2 RTHSMU Local and Global Results

After validating model updating fidelity using varies means, it is convinced that RTHSMU yields response more close to reality than RTHS and simulation with initial modeling error. Thus, the differences of the simulation, RTHS and RTHSMU are compared. For local level assessment, MR damper energy dissipation is investigated through the hysteresis behavior, as shown in Fig. 32.4. It demonstrates that, for the device on the first story, simulation response overestimates the energy dissipation of the MR damper, as MR damper was test in physical for RTHS and RTHSMU, both cases yield true behavior. For the second floor, as the MR damper is numerical modeled in simulation and RTHS with initial error, both cases

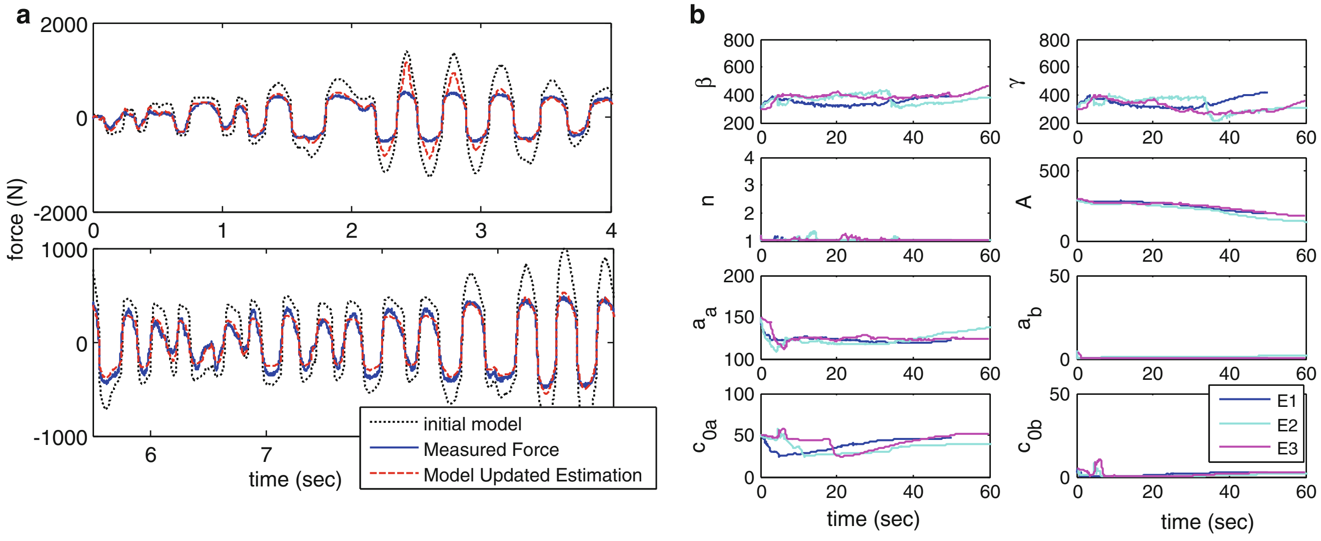

Time domain convergence

Parameter convergence

Fig. 32.2 RTHSMU convergence trend

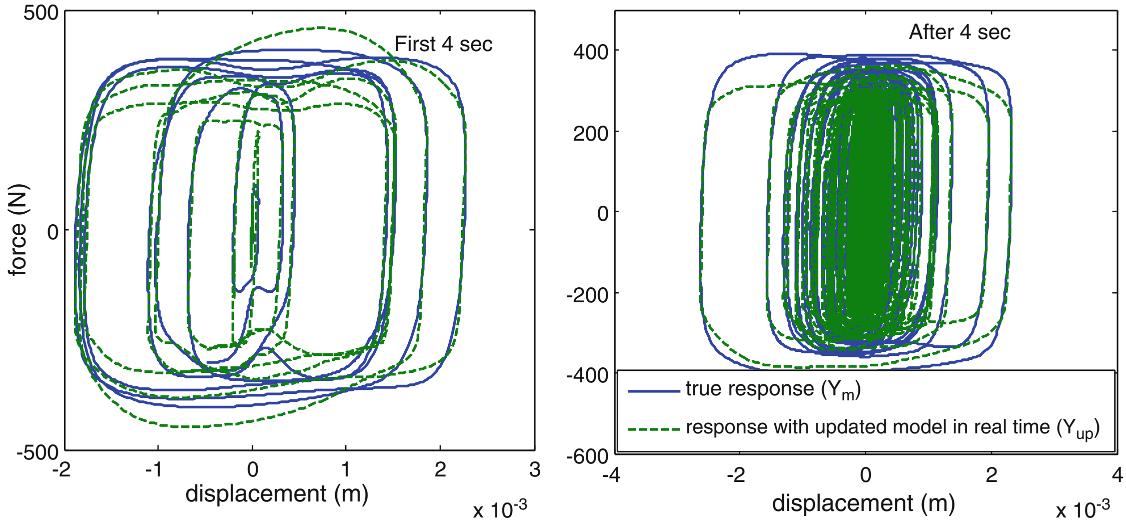

Fig. 32.3 Validation test results on 2nd story MR damper response, El-Centro earthquake

overestimate the energy dissipated by the damper, while with numerical model of MR damper accepting real time parameters in RTHSMU, hysteresis behavior is believed to be more accurately constructed.

The local performance of energy dissipation also transmitted to the global response, where the maximum story drift profile is formed for all earthquake cases as in Fig. 32.5 for elaborating the results. Significant differences are shown between RTHSMU and simulation case due to modeling error on both MR dampers in simulation, less differences are observed when compare RTHS to RTHSMU. This is because modeling error only exists in the second floor damper in RTHS which is contributing less to the global response. However, attention should be drawn, if nonlinear components are contributed equally to the global response and are with initial modeling error, the difference between RTHS and RTHSMU is expected to be more compelling. Therefore, the contribution of a single component in RTHS can be overcome by the modeling error of the rest. The tradeoff between tolerable modeling error in the numerical parts and the amount of effort required on implementing model updating to RTHS should be taken into account at the testing planning stage.

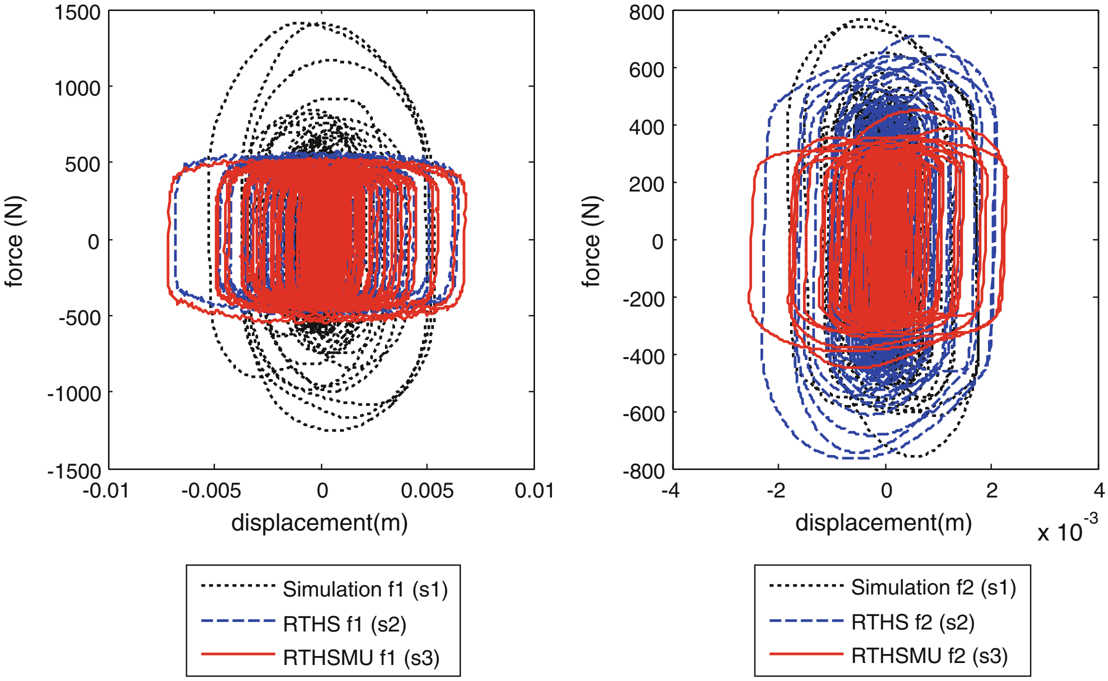

Fig. 32.4 Local behavior of first and second story MR damper under different stages, El-Centro earthquake

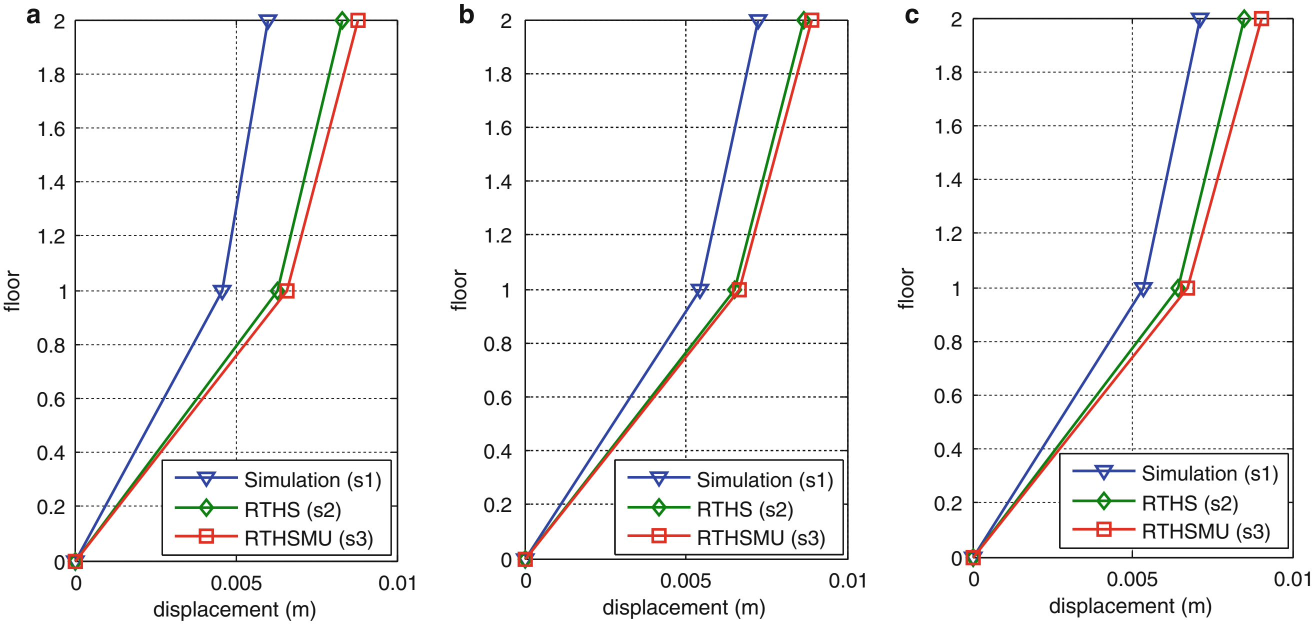

El-Centro case

Gebze case

Mexico case

Fig. 32.5 Maximum story drift profiles under different stages

32.4 Conclusion

In this paper, a highly nonlinear rate dependent device is used to experimentally validate the feasibility of RTHSMU with repeatability allows validation tests to be conducted. Results indicate the estimation error converges fast when applying CUKF. However, the parameter convergence is not simultaneously reached. The numerical model of the device accepts updated time varying parameter values can represent the real behavior of the device through a validation test using a different loading path. RTHSMU results are compared with RTHS and conventional simulation, both with modeling errors with different extents. The advantages of RTHSMU appear at both local and global level, it is believed with incorporating model updating the testing fidelity is improved. Due to the existing challenges in model updating implementation, there is a tradeoff between modeling error tolerance of the nonlinear components in the numerical parts and the efforts on applying the model updating algorithms to RTHS at the testing planning stage.

Acknowledgement This material is based upon work supported in the past by the National Science Foundation under Grant No. CMMI 0927178, CNS 1136075.

References

1. Chen, C., Ricles, J.M.: Analysis of actuator delay compensation method for realtime testing. Eng. Struct. **31**(11), 2643–2655 (2009)
2. Phillips, B., Spencer, B. Jr.: Model-based feedforward-feedback actuator control for real-time hybrid simulation. J. Struct. Eng. **139**, SPECIAL ISSUE: NEES 1: Advances in Earthquake Engineering, 1205–1214 (2013)
3. Ou, G., Ozdagli, A.I., Dyke, S.J., Wu, B.: Robust integrated actuator control: experimental verification and real time hybrid simulation implementation. Earthq. Eng. Struct. Dyn. **44**(3), 441–460 (2015)
4. Hashemi, M., Mosqueda, G.: Hybrid simulation of 4 story frame to collapse using 1.5 story substructure. Network for Earthquake Engineering Simulation (distributor), Dataset (2014). doi:10.4231/D3F18SG1T
5. Hashemi, M.J., Mosqueda, G.: Innovative substructuring technique for hybrid simulation of multistory buildings through collapse. Earthq. Eng. Struct. Dyn. **43**(14), 2059–2074 (2014)
6. Gomez, G., Dyke, S.J., Maghareh, A.: Enabling role of hybrid simulation across NEES in advancing earthquake engineering. Smart Struct. Syst. **15**(3), 913–929 (2014)
7. Christenson, R., Lin, Y., Emmons, A., Bass, B.: Large-scale experimental verification of semiactive control through real-time hybrid simulation. J. Struct. Eng. **134**(4), 522–534 (2008)
8. Zapateiro, M., Karimi, H.R., Luo, N., Spencer, B.F.: Real-time hybrid testing of semiactive control strategies for vibration reduction in a structure with MR damper. Struct. Control Health Monit. **17**, 427–451 (2010). doi:10.1002/stc.321
9. Friedman, A., Dyke, S., Phillips, B., Ahn, R., Dong, B., Chae, Y., Castaneda, N., Jiang, Z., Zhang, J., Cha, Y., Ozdagli, A., Spencer, B., Ricles, J., Christenson, R., Agrawal, A., Sause, R.: Large-scale real-time hybrid simulation for evaluation of advanced damping system performance. J. Struct. Eng. **141**(6), 04014150 (2015)
10. Wu, M., Smyth, A.: Real-time parameter estimation for degrading and pinching hysteretic models. Int. J. Non-Linear Mech. **43**(9), 822–833 (2008)
11. Song, W., Dyke, S.J.: Real-time dynamic model updating of a hysteretic structural system. J. Struct. Eng. **140**(3), 04013082 (2013)
12. Song, W.: Dynamic model updating with applications in structural and damping systems: from linear to nonlinear, from offline to real time. Doctorate Dissertation, Purdue University (2011)
13. Kwon, O.S., Kammula, V.: Model updating method for substructure pseudo-dynamic hybrid simulation. Earthq. Eng. Struct. Dyn. **134**(42), 1971–1984 (2013)
14. Shao, X., Mueller, A., Mohammed, B.: Real-time hybrid simulation with online model updating: methodology and implementation. J. Eng. Mech. 04015074 (2015). doi:10.1061/(ASCE)EM.1943-7889.0000987
15. Wu, B., Wang, T.: Model updating with constrained unscented Kalman filter for hybrid testing. Smart Struct. Syst. 1105–1129 (2014). doi:10.12989/sss.2014.14.6.1105
16. Ou, G. Ozdagli, A.I., Dyke, S. J., Prakash A.: RTHS with concurrent model updating on a distributed platform. In: Proceedings of the 6AESE/11ANCRiSST Conference, Urbana-Champaign, IL (2015)
17. Spencer Jr., B., Dyke, S., Sain, M., Carlson, J.: Phenomenological model for magnetorheological dampers. J. Eng. Mech. **123**(3), 230–238 (1997)
18. Ou, G. Ozdagli, S. J., Prakash A.: Real time hybrid simulation with online model updating: an accuracy analysis. Special Issue of Mechanical Systems and Signal Processing on Nonlinear System Identification (in review) (2015)

Chapter 33
Discrete-Time Compensation Technique for Real-Time Hybrid Simulation

Saeid Hayati and Wei Song

Abstract One of the challenges to perform Real-Time Hybrid Simulation (RTHS) test is to compensate time delay introduced by servo-hydraulic actuators. In the past decade, several compensators have been designed and successfully applied in RTHS to reduce actuators time delay. These compensators have shown great promises in tracking command signals with low frequency content. However, many dynamic testing applications require generating excitations with relatively high frequency contents. To address this need, the current study is to provide an optimal compensation technique which can allow hydraulic actuators to track inputs with higher frequency content. The feasibility of this method is proven both in numerical and experimental study.

Keywords Real-time hybrid simulation • Feedforward compensator • Time delay • Servo-hydraulic actuator

33.1 Introduction

Real-Time Hybrid Simulation (RTHS) is a powerful dynamic test method which is efficient and cost effective comparing to shake table test [1]. To have a successful RTHS test, the stability of the entire hybrid test system depends on time step (Δt) for the test, natural frequency (f) of both experimental and numerical substructures, ratio between the mass of substructures [2] and servo-hydraulic delay [3, 4]. In the past decades, several researches tackled this problem by proposing compensators to reduce the time delay in RTHS.

A model-based feedforward compensator based on a dynamic model of the actuator was proposed by Carrion and Spencer [5]. In their study, the transfer function of the actuator attached to a linear mass-spring system was written in the following form

$$TF(s) = \frac{\prod_{i=1}^{n} p_i}{\prod_{i=1}^{n} (s - p_i)} \tag{33.1}$$

where P_i are actuator poles. By inverting the transfer function of the actuator, a strictly improper compensator is expected. To overcome this problem, a unit gain low-pass filter is introduced to the inversion of the transfer function to provide a proper compensator shown as below:

$$G_{FF}(s) = \frac{\prod_{i=1}^{n} (s - p_i)}{\prod_{i=1}^{n} p_i} \times \frac{\alpha^n \prod_{i=1}^{n} p_i}{\prod_{i=1}^{n} (s - \alpha P_i)} = \alpha^n \frac{\prod_{i=1}^{n} (s - p_i)}{\prod_{i=1}^{n} (s - \alpha P_i)} \tag{33.2}$$

In Eq. (33.2), s is the Laplacian variable and α is a predetermined parameter that controls the performance of the compensator. In general, a larger α results in a compensator which can reduce the actuator delay more effectively [5]; however, an excessive α value may cause the poles of the overall RTHS system move beyond the Nyquist limit, and subsequently introduce inaccurate result or even lose stability. The performance of this model-based compensator in reducing the actuator time delay was investigated by using input signals with low frequency content ($\leq 15\,\text{Hz}$) [5, 6].

S. Hayati • W. Song (✉)
Department of Civil, Construction and Environmental Engineering, The University of Alabama, Tuscaloosa, AL 35487, USA
e-mail: wsong@eng.ua.edu

© The Society for Experimental Mechanics, Inc. 2016

J. De Clerck, D.S. Epp (eds.), *Rotating Machinery, Hybrid Test Methods, Vibro-Acoustics & Laser Vibrometry, Volume 8*,
Conference Proceedings of the Society for Experimental Mechanics Series, DOI 10.1007/978-3-319-30084-9_33

Chen [7], considered a different model for servo-hydraulic actuator dynamics, which is expressed in discrete-time domain as below

$$TF(z) = \frac{z}{\alpha_c.z - (\alpha_c - 1)} \tag{33.3}$$

where z is the z-transform variable and α_c is the ratio between the time that actuator needs to reach to command displacement and the controller time step. With the actuator dynamics given by Eq. (33.3), the corresponding compensator can be obtained by directly inverting it as [7].

$$G_{FF}(z) = \frac{1}{TF(z)} = \frac{\alpha_c.z - (\alpha_c - 1)}{z} \tag{33.4}$$

Chen et al. [8], implemented this inverse compensation method in RTHS. Obtained results have shown successful tracking performance with command signal, which was an earthquake record, in presence of accurate value of α_c.

33.2 Discrete-Time Compensator

The aforementioned feedforward compensators have been successfully applied in RTHS to reducing servo-hydraulic time delay for input signals with a relatively low frequency bandwidth. To advance the use of RTHS further to other dynamic testing applications, compensators that can provide effective reduction in time delay for command inputs with relatively high frequency contents are needed. For instance, certain equipment or mechanical devices are tested with relatively high frequency excitations. In this paper, a newly developed discrete-time based compensator is presented to reduce actuator time delay when the input has a broader frequency range (0 ~ 30 Hz). This compensator is designed based on an Auto-Regressive with Exogenous model (ARX model) which can be written as below

$$y(t) + a_1 y(t-1) + \cdots + a_{na} y(t - n_a) = b_1 u(t) + \cdots + b_{n_b} u(t - n_b + 1) + e(t) \tag{33.5}$$

In Eq. (33.5), y is the output of the dynamic system; in this study, it is the measured displacement of the actuator, u is the input of the dynamic system; in this study, it is the command displacement signal sent into the controller, e is the disturbance, n_a is the number of system poles, and n_b is the number of system zeros plus one. Transfer function of the servo-hydraulic actuator in z domain can be written using ARX model as

$$TF\left(z^{-1}\right) = \frac{b_1 + \cdots + b_{n_b} z^{-n_b+1}}{1 + a_1 z^{-1} + \cdots + a_{n_a} z^{-n_a}} \tag{33.6}$$

If the transfer function of the actuator is minimum phase, the corresponding compensator (G_{FF}) can be obtained directly by inverting Eq. (33.6) as

$$G_{FF}\left(z^{-1}\right) = \frac{1}{TF\left(z^{-1}\right)} = \frac{1 + a_1 z^{-1} + \cdots + a_{n_a} z^{-n_a}}{b_1 + \cdots + b_{n_b} z^{-n_b+1}} \tag{33.7}$$

However, most of the time, the transfer function of the actuator is nonminimum phase, which implies a direct stable inverse of the original servo-hydraulic actuator does not exist. To solve this problem, the unstable part of the compensator transfer function can be replaced by a Finite Impulse Filter (FIR). To demonstrate, Eq. (33.6) can be rewritten in the form of poles and zero as

$$TF\left(z^{-1}\right) = \frac{B^{+}\left(z^{-1}\right) \times B^{-}\left(z^{-1}\right)}{A\left(z^{-1}\right)} \tag{33.8}$$

In this equation, B^{+} and B^{-} are the terms in the numerator with stable and unstable zeros respectively and A contains system poles. After inverting Eq. (33.8), the inverse of B^{-} will be replaced by a FIR.

$$G_{FF}\left(z^{-1}\right)=\frac{A\left(z^{-1}\right)}{B^{+}\left(z^{-1}\right)}\times H\left(z^{-1}\right) \tag{33.9}$$

$H\left(z^{-1}\right)$ is the FIR and defined as below

$$H\left(z^{-1}\right)=h_1+h_2z^{-1}+\cdots+h_nz^{-n+1} \tag{33.10}$$

where h_1, h_2, … h_n are n unknown parameters that are determined by an optimization scheme. Different number of parameters (n) can be chosen to design this compensator. The delay compensation performance up to a desired frequency (cut-off frequency f_c) range will be guaranteed by the Optimization Schemes explained in the next section. Frequency range from 0 Hz to the cut-off frequency is called passband and the frequency range beyond the cut-off frequency is called stopband. Compensated system transfer function can be written as

$$TF_c\left(z^{-1}\right)=G_{FF}\left(z^{-1}\right)\times TF\left(z^{-1}\right)=B^{-1}\left(z^{-1}\right)\times H\left(z^{-1}\right) \tag{33.11}$$

33.3 Optimization Schemes

Three optimization schemes, namely least square (LS), weighted least square (WLS), and minimax (MM), are designed to find unknown parameters h_1, h_2, … h_n in the FIR. The objective functions of these three optimization schemes are to minimize the magnitude of the compensated system transfer function, $TF_c\left(z^{-1}\right)$, defined in Eq. (33.11). For WLS scheme, the objective function is defined as

$$\min\left\{\sum_i w_i.\|TF_c(i)-1\|^2\right\},\ \begin{cases} w_i \gg 1 & for\ i\in \text{passband}\\ w_i=1 & for\ i\in \text{stopband}\end{cases} \tag{33.12}$$

where i indicates discretized points in frequency domain (e.g., Fourier transform point); $TF_c(i)$ is the value of the compensated system transfer function (Eq. 33.11) at the ith point; w_i represents the weight assigned to the corresponding ith point. A w_i larger than 1 indicates higher importance is given to the corresponding error norm $TF_c(i)-1$; $||\cdot||$ represents modulus of complex number. In this study, $w_i=1000$ is chosen for the frequency points located in the passband, whereas $w_i=1$ for the points located in the stopband. The LS scheme has the same objective function as the WLS scheme does, except the weights (w_i) for all the frequency points are assigned as equal to 1. For MM scheme, the objective function is given as

$$\min\left\{\max_{i\,\in\,\text{stopband}}\|TF_c(i)\|\right\} \tag{33.13}$$

For all the above schemes, same constraints are applied during the optimization process:

1. Steady-state gain should equal one

$$TF_c\,(\mathrm{z}=1)=1 \tag{33.14}$$

2. Magnitude of the compensated system transfer function in passband range should be one

$$\sqrt{\sum_i (TF_c(i)-1)^2}=0 \tag{33.15}$$

3. Phase of compensated system transfer function in pass-band range should be zero

$$\sqrt{\sum_i \{\arg\left[TF_c(i)\right]\}^2}=0 \tag{33.16}$$

Where arg calculates the arguments of a complex number.

33.4 Implementation of the Compensator

To investigate the performance of the FIR feedforward compensator, an experimental study was performed in the Large Scale Structural Lab (LSSL) at The University of Alabama. Figure 33.1 shows the setup. The capacity of the actuator used in this setup is 110 kips. The steel mass box weighs 580 kg and the stiffness of the spring is 1403 kN/m. To identify the transfer function of the system (Eq. 33.8), three white noises with bandwidth = 128 Hz and amplitudes equal to 0.0127, 0.0254 and 0.0381 m were applied to the actuator. Sampling frequency of the controller was 1024 Hz. A total of 756 discrete-time models were fitted to the acquired data by considering different numbers of parameters used in ARX model. To determine the best model out of these 756 fitted models, four criteria were adopted.

1. Mean Square Error (MSE)

$$\mathrm{MSE} = \frac{\sum [e\left(t_i\right)]^2}{N} \tag{33.17}$$

where $e(t_i)$ is the error defined in ARX model at time step i and N is the total number of data samples.

2. Goodness of fit (FIT)

$$\mathrm{FIT} = \frac{\sum e\left(t_i\right)}{\mathrm{Var}\left[y\left(t_i\right)\right]} \tag{33.18}$$

where Var is the variance.

3. Akaike Information Criterion (AIC)

$$\mathrm{AIC} = \ln\left(\mathrm{MSE}\right) + 2 \times \frac{dim}{N} \tag{33.19}$$

where *dim* is number of parameters used in ARX model.

4. Bayesian Information Criterion (BIC)

$$\mathrm{BIC} = \ln\left(\mathrm{MSE}\right) + \ln(N) \times \frac{dim}{N} \tag{33.20}$$

All these criteria have indicated the same best choice as a model with $n_a = 21$, $n_b = 2$. This model is therefore used as the model for the actuator to design the discrete-time compensator. A total of 72 different compensators were obtained by using different number of parameters ($n = 25$, 50, 75, 100, 200 and 300) in Eq. (33.10), different cut-off frequencies ($f_c = 32$, 64, 96 and 128 Hz) and different optimization schemes to study the effects of these three variables on the performance of the resulting compensator. Figure 33.2 shows the numerical results for the transfer function of the compensated system after applying these compensators (WLS, LS, and MM) with 50 parameters and cut-off = 64 Hz. The results indicate the

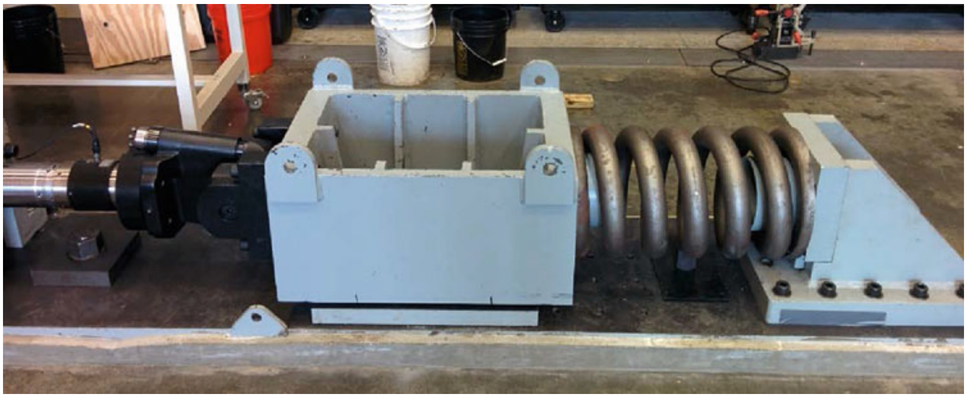

Fig. 33.1 Experimental setup

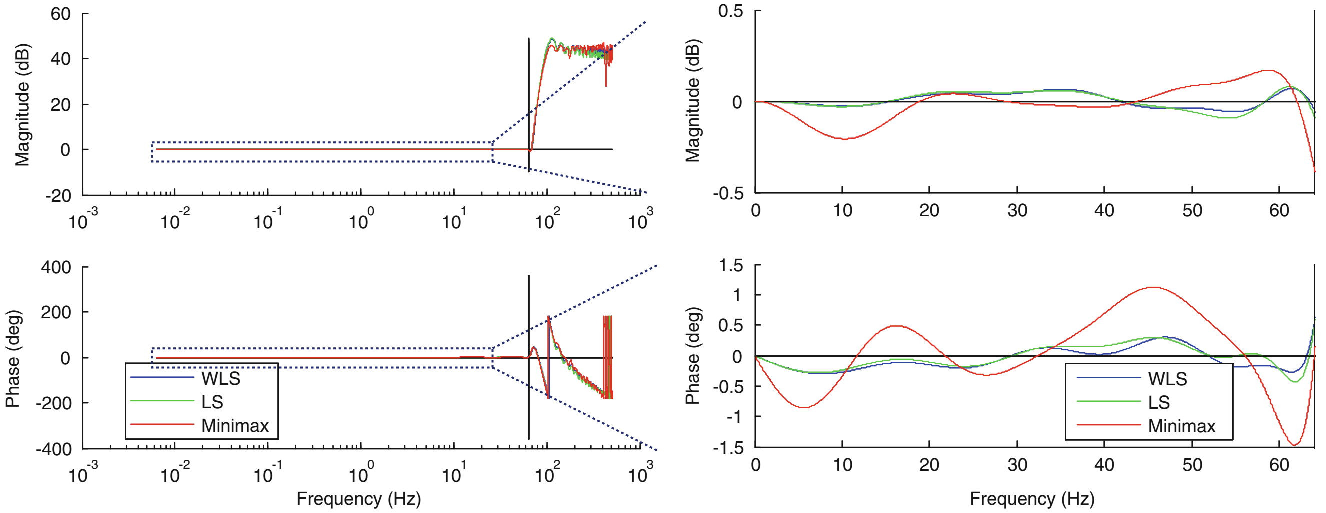

Fig. 33.2 Numerical study: *Left*: Transfer function of the compensated system (No. parameters = 50, cut-off = 64 Hz); *Right*: Zoom-in view

magnitudes of the compensated systems are all within 0.3 dB and the phase angles are also very close to 0° for all three compensators. Moreover, WLS and LS compensators have demonstrated slightly better performance in both magnitude and phase than MM compensators.

33.5 Experimental Study

Utilizing the experimental setup shown in Fig. 33.1, a series of actuator command tracking experiments were conducted using band-limited white noises with a maximum amplitude of 0.00508 m and 3 different frequency bandwidth—5, 10, 20 and 30 Hz. Time delay of the actuator at frequency ω is calculated as below

$$\text{Time delay} = -\frac{\arg\left[TF_c\left(\omega\right)\right]}{\omega} \tag{33.21}$$

where ω is the frequency at which time delay is required. In Fig. 33.3, the surface plot for delay contains the data obtained using 24 different WLS compensators. For these tests, input was a band-limited white noise with bandwidth = 20 Hz and maximum amplitude = 0.00508 m. Time delay obtained for frequency range 1–4 Hz were calculated by using Eq. (33.21) and then the average of the corresponding delays were reported as the time delay of the actuator. The surface plot indicates that the delay increases as the cut-off frequency (f_c) increases, and decreases as the number of parameter increases. In addition, the subplot on the bottom right of Fig. 33.3 shows the time history of the command reference signal and compensated actuator responses for four selected cases. The corresponding results are summarized in Table 33.1. In this table, the relative RMS error is defined as

$$\text{Relative RMS error} = \frac{\sqrt{\sum_j \left(d_j^m - d_j^c\right)^2}}{\sqrt{\sum_j \left(d_j^c\right)^2}} \tag{33.22}$$

Where j indicates discrete points in time domain; d_j^c and d_j^m are command displacement and measured displacement at jth time step, respectively. From Table 33.1, the results have shown that the RMS error also follows the same trend as the time delay, i.e. the RMS value increases as the cut-off frequency (f_c) increases, and decreases as the number of parameter increases.

To compare the performance of different optimization schemes, the delay obtained from a set of selected experimental cases and the corresponding numerical simulations are shown in Fig. 33.4. The associated command input for these selected experimental cases is a band-limited white noise with bandwidth = 10 Hz and maximum amplitude = 0.00508 m. This plots for both experimental and numerical cases show that the time delay increases by increasing the cut-off frequency and

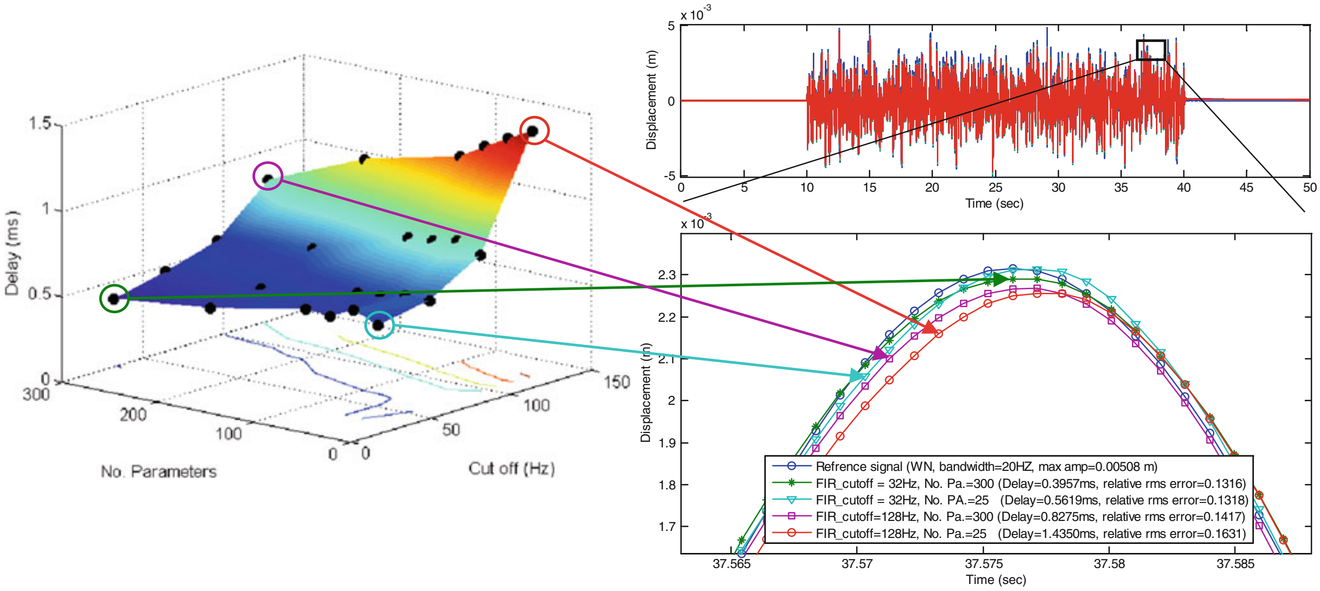

Fig. 33.3 Experimental data for WLS scheme. *Left*: delay plot for system with different compensator; *Top right*, system response to white noise with bandwidth = 20 Hz and maximum amplitude = 0.005 m; *Bottom right*: zoom-in view of the system response

Table 33.1 Time delay and RMS error for four different experimental cases using WLS compensator. Input: white noise with bandwidth = 20 Hz and maximum amplitude = 0.00508 m

Test	Number of parameters	Cut-off frequency (Hz)	Time delay (millisecond)	Relative RMS error
Case 1	300	32	0.3957	0.1316
Case 2	25	32	0.5619	0.1318
Case 3	300	128	0.8275	0.1417
Case 4	25	128	1.4350	0.1631

decreases by increasing the number of parameters used in compensator. This observation is consistent with the results shown in Fig. 33.3. Moreover, the numerical simulation results have shown similar delay compensation performance for all three optimization schemes, but the experimental results have clear indication that the delays for MM scheme are smaller than WLS and LS schemes, which implies a better compensation performance.

Figure 33.5 shows the experimental results obtained from four different compensators: Two model-based compensators (Eq. 33.2) with $\alpha = 7,\ 10$ and three actuator poles) and two discrete-time compensators developed in this study (Eq. 33.9) with $f_c = 64$ Hz and number of parameters = 50 and 200). The command signal in these tests were a band-limited white noise with bandwidth = 30 Hz and maximum amplitude = 0.00508 m. The results show that the discrete-time compensators successfully reduced the time delay to less than 1 millisecond and the delays for the model-based feedforward compensators are around 5 milliseconds. The relative RMS error between the command signal and the measured signal also indicates a better performance for the discrete-time compensators. This value for discrete-time compensators is around 0.25 and for model-based compensators is around 0.50.

33.6 Summary and Conclusion

A novel compensator in discrete-time domain is presented in this paper. Three different optimization schemes WLS, LS and MM have been adopted in acquiring the discrete-time compensator. The associated compensation performance has been demonstrated through both numerical simulations and experimental tests. Also by comparing the results obtained by the discrete-time compensator (Eq. 33.9) with the model-based feedforward compensator (Eq. 33.2), it is shown that the discrete-time compensator has superior performance in compensating for servo-hydraulic delays with relatively high frequency range (30 Hz). According to the results obtained in this study, three main conclusions can be stated:

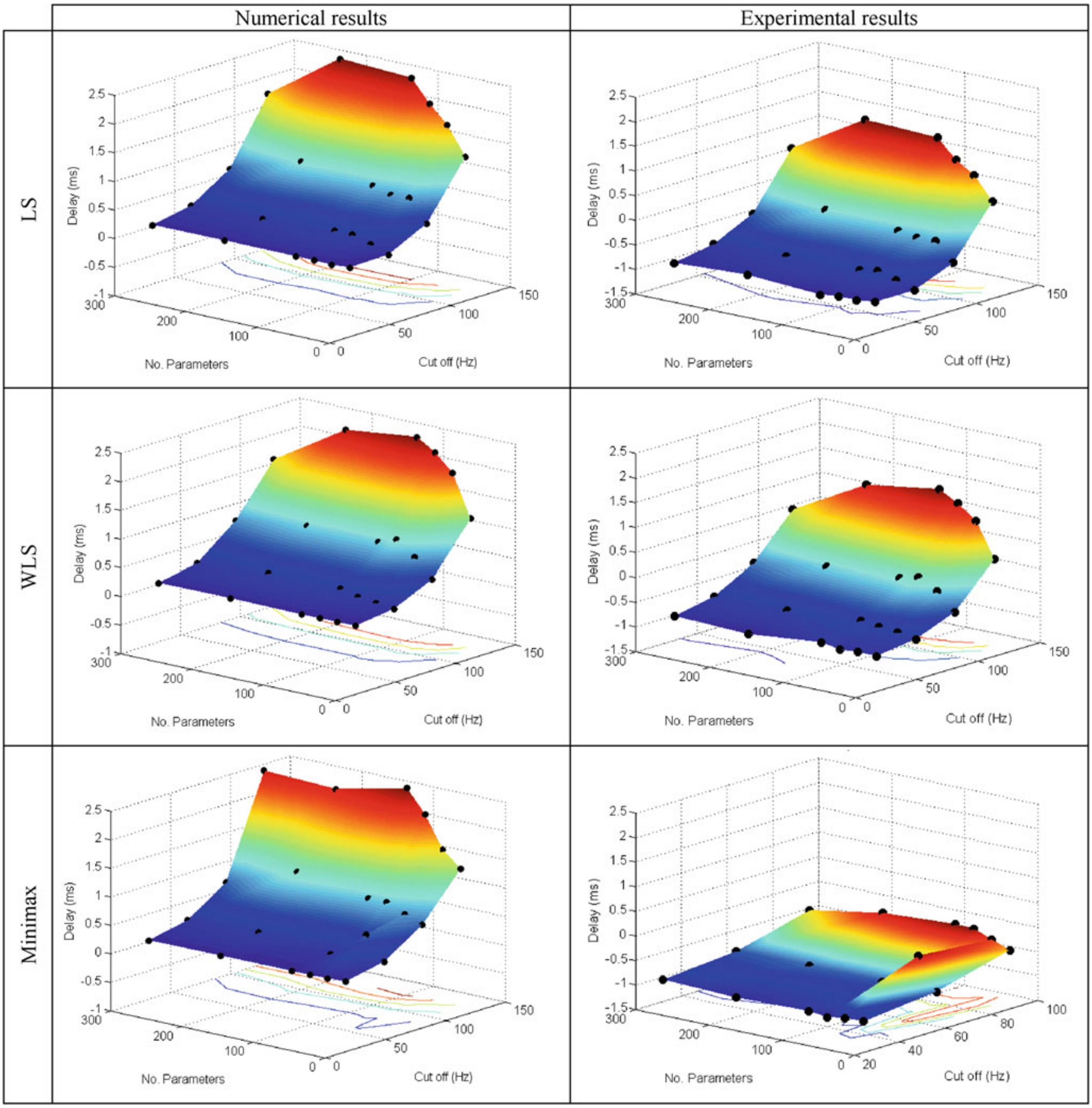

Fig. 33.4 Time delay based on the phase plot of the transfer function

1. All the obtained discrete-time compensators have effectively reduced the servo-hydraulic delay for inputs ranging from low, medium and high frequency bandwidth.
2. Increasing the number of parameters in the compensators will reduce the time delay.
3. Increasing the desired cut-off of the compensator will increase the time delay.

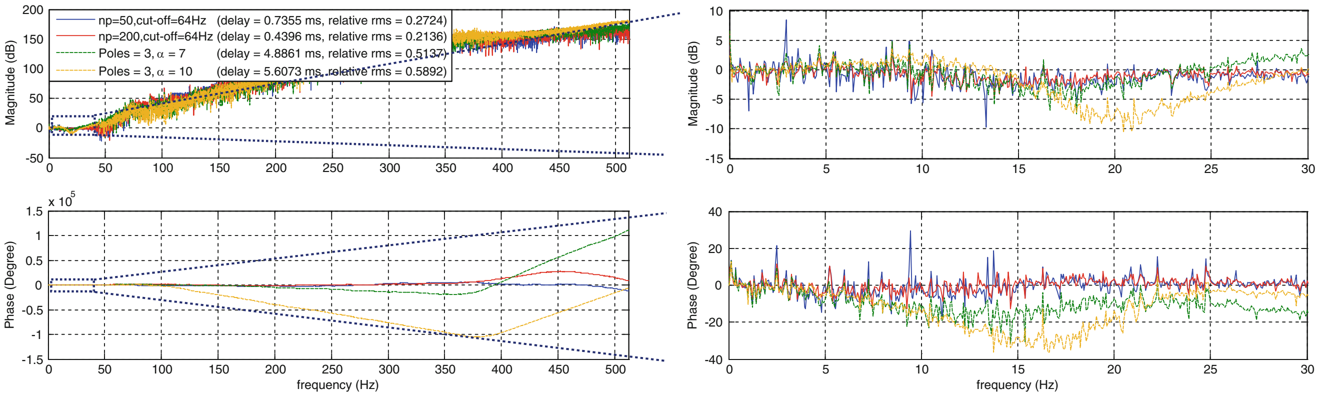

Fig. 33.5 Comparison between the experimental results obtained from discrete-time compensator (Eq. 33.9) and model-based feedforward compensator (Eq. 33.2). Input: band-limited white noise with bandwidth = 30 Hz and maximum amplitude = 0.00508 m. *Left*: Transfer function of compensated system; *Right*: Zoom-in view of the transfer function

References

1. Horiuchi, T., Inoue, M., Konno, T., Namita, Y.: Real-time hybrid experimental system with actuator delay compensation and its application to a piping system with energy absorber. Earthq. Eng. Struct. Dyn. **28**(10), 1121–1141 (1999)
2. Wu, B., Deng, L., Yang, X.: Stability of central difference method for dynamic real-time substructure testing. Earthq. Eng. Struct. Dyn. **38**(14), 1649–1663 (2009)
3. Chen, C., Ricles, J.: Stability analysis of SDOF real-time hybrid testing systems with explicit integration algorithms and actuator delay. Earthq. Eng. Struct. Dyn. **37**(4), 597–613 (2008)
4. Darby, A., Williams, M., Blakeborough, A.: Stability and delay compensation for real-time substructure testing. J. Eng. Mech. **128**(12), 1276–1284 (2002)
5. Carrion, J.E., Spencer, B.F. Jr.: Model-based strategies for real-time hybrid testing. NSEL report series (2007)
6. Phillips, B.M., Spencer, B.F. Jr.: Model-based framework for real-time dynamic structural performance evaluation. NSEL report series (2012)
7. Chen, C.: Development and numerical simulation of hybrid effective force testing method. Ph.D. dissertation, Department of Civil and Environmental Enginnering, Lehigh University, Bethlehem, PA (2007)
8. Chen, C., Ricles, J., Marullo, T., Mercan, O.: Real-time hybrid testing using the unconditionally stable explicit CR integration algorithm. Earthq. Eng. Struct. Dyn. **38**(1), 23–44 (2009)

Chapter 34
Evaluating the Effectiveness of a Lodengraf Damping Approach for String Trimmers

Nicholas Swanson and Jack Leifer

Abstract Reducing the magnitude of the vibrations transmitted to a user's hands through the loop handle and grip of a string trimmer is a priority for maintaining both health and comfort. Prior work on internal-combustion (IC) powered string trimmers has indicated that Lodengraf™ damping may be effective in reducing vibration amplitude at both the loop handle and grip. Lodengraf damping utilizes lightweight, low-density particles added to a vibrating device, either as a fill in existing cavities or as a wrap surrounding the device. The mechanism for the damping is that vibrations generated by the device are absorbed into the Lodengraf particles, where the energy of the vibrations is converted to heat and released before they can be transmitted to the user. In this set of experiments performed on battery-powered string trimmers, the effectiveness of applying Lodengraf particles using specially designed 3D printed loop handles as well as a clam-shell shaft enclosure, all comprised from ABS is explored. The 3D printed parts were designed to be hollow, forming cavities to accommodate the Lodengraf materials. The Lodengraf was found to be effective at frequencies above 200 Hz. Both trimmers have a first fundamental frequency that falls below the cutoff frequency for effective Lodengraf damping, but the approach effectively reduced the amplitude of higher frequency harmonics generated.

Keywords 3D printing • Rotating machinery • String trimmers • Lodengraf damping • Modal analysis

34.1 Introduction

Prolonged exposure to low frequency vibrations, such as those produced by a power tools or a string trimmer, has been shown to cause irreversible neurological, vascular, and muscle-skeletal damage [1]. This damage presents itself in a variety of symptoms collectively known as Hand-Arm Vibration Syndrome (HAVS). There is no known cure for HAVS, so efforts are focused on preventing the disease from developing by establishing guidelines for the maximum amount of time devices such as string trimmers are used, or reducing the magnitude of vibrations transmitted to a user. However, for a full time employee whose job is dependent on the use of string trimmers, limiting the amount of time these tools are used may be unfeasible, and developing approaches to reduce vibration amplitude may be the only viable option.

This set of experiments comprises a continuation of prior work done in pursuit of this overall goal [2], in which Lodengraf particles were packed around the shaft and within the loop handle of a Ryobi model RY28040SS26 IC-powered string trimmer. Fricke suggested the term Lodengraf for particles used to promote damping by filling voids already present in vibrating equipment with low-density granular materials. In his paper [3], he states:

> "Lodengraf™ is a trademark name and is used to describe technology associated with the use of low density granular materials for attenuating structural vibration. The technology is protected under U.S. Patent # 5,775,049, #5,820,348, and #5,924,261.... Edge Innovations & Technology, LLC controls all rights to the technology and trademark."

The new aspect of the approach presented in the prior work as well as herein is that already existing equipment is being redesigned to create voids that can then be filled to promote damping. Lodengraf materials are available in the form of Perlite, which is commercially used as filler in potting soils, and as such is inexpensive and readily available.

The initial set of experiments yielded the following results: (1) Surrounding the lower shaft of the string trimmer loaded with Perlite caused components of the RMS acceleration to decrease at both the loop handle and grip measurement locations. The most significant reductions were in the axial and radial components of acceleration measured at the loop handle. (2) Applying Perlite to the existing U-shaped channel in the loop handle caused a significant reduction in the radial and axial

N. Swanson • J. Leifer (✉)
Trinity University, One Trinity Place, San Antonio, TX 78212, USA
e-mail: jleifer@trinity.edu

© The Society for Experimental Mechanics, Inc. 2016

J. De Clerck, D.S. Epp (eds.), *Rotating Machinery, Hybrid Test Methods, Vibro-Acoustics & Laser Vibrometry, Volume 8*,
Conference Proceedings of the Society for Experimental Mechanics Series, DOI 10.1007/978-3-319-30084-9_34

components of acceleration measured at the loop handle. However, the Perlite applied to the loop handle caused an increase in measured circular components of RMS acceleration. (3) The frequency content of the measured vibrations was related primarily to the rotational speed of the string trimmer. (4) Despite the promising trends observed, there was substantial scatter in the experimental data.

Much of the scatter inherent in the data was attributed to the use of flexible materials in the form of wraps to maintain the Perlite around the string trimmers—Santoprene strips in the case of the Perlite packed into the loop handle, and a polyethylene tube used to encase the Perlite around the shaft. Using such flexible materials, the exact configuration of each wrap could not be maintained between successive experiments. Furthermore, while using flexible wraps to apply Perlite to an operating string trimmer could be justified in experiments designed to demonstrate the effectiveness of the approach, a simpler enclosure system more suitable for commercialization must be developed if this approach is to emerge from the lab and adapted widely for use by consumers. For these reasons, 3D printed components were designed that would easily attach as accessory items to existing string trimmers. The 3D-printed components, including a shell-like shaft enclosure, as well as a hollow loop handle, were designed to demonstrate that Perlite could be easily applied to the string trimmer in a way that provides predictable, repeatable results.

Finally, to serve as a basis for comparison, the performance of commercially-available Limbsaver® comfort-tech shaft dampener devices, designed to reduce vibrations in operating string trimmers, was evaluated.

34.2 Materials and Methods

34.2.1 Handles

String trimmers commonly employ a loop handle (Fig. 34.1) that an operator uses to control and maneuver the grass cutting tool over the landscape (Fig. 34.2). In order to better assess the ability of Perlite to diminish vibration amplitude, hollow handles emulating the geometry of the OEM parts were designed using PTC Creo 3.0 (Fig. 34.3), and printed (Fig. 34.4) using a Stratasys Fortus 20 mc 3D printer. Two handles were printed, each employing the different attachment geometries typically used. Each handle was evaluated both before and after adding the Perlite fill.

34.2.2 String Trimmers

Safety considerations required that the IC-powered string trimmers used in our prior studies be tested outside [2, 5]. We felt that some of the variability in our experimental results stemmed from the effect that different weather conditions (e.g.

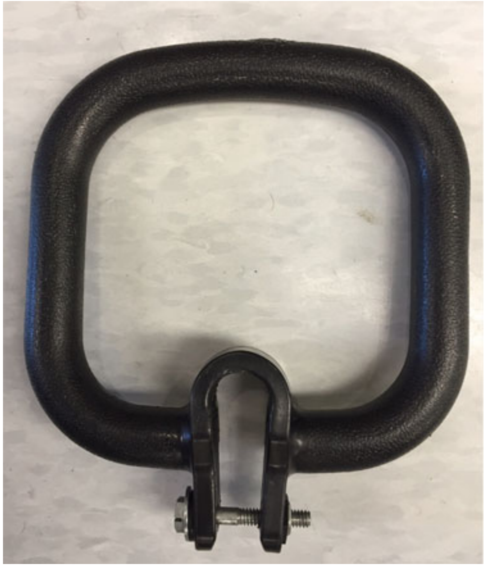

Fig. 34.1 A typical string trimmer loop handle is designed to clamp on its shaft

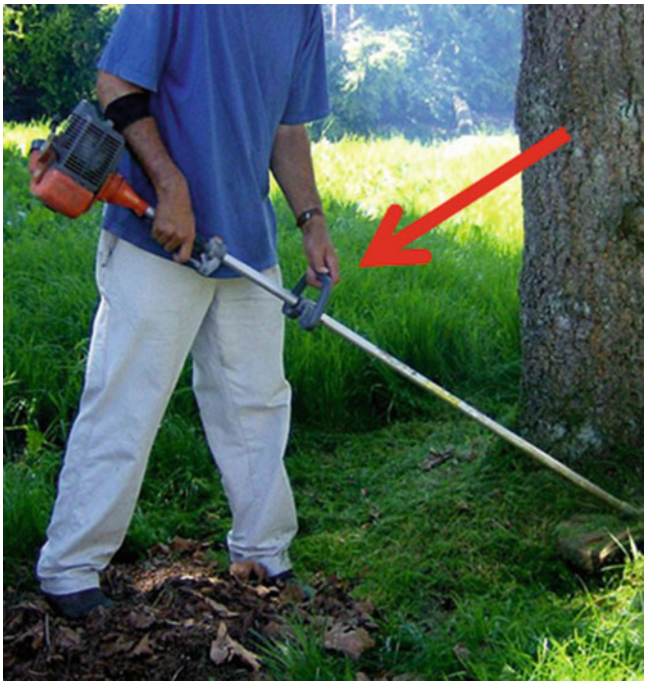

Fig. 34.2 The operator maneuvers the string trimmer over the landscape using the loop handle held in his *left hand* [4]

Fig. 34.3 PTC/Creo model of hollow the loop handle (configuration 1)

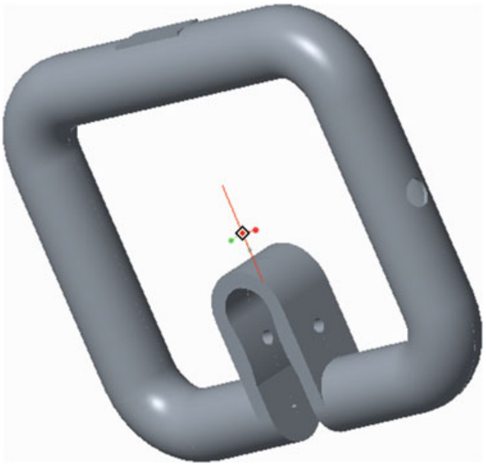

Fig. 34.4 Hollow 3D printed loop handle (1). Note the accelerometer mounting flat on the *top* section

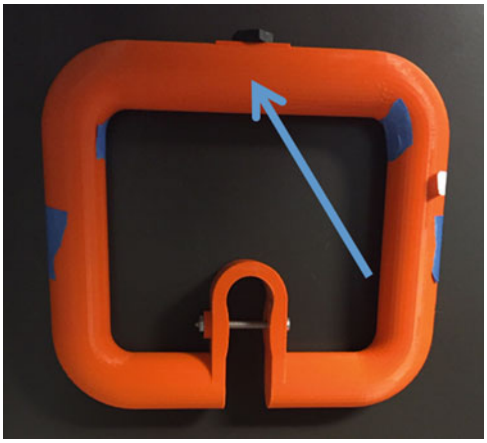

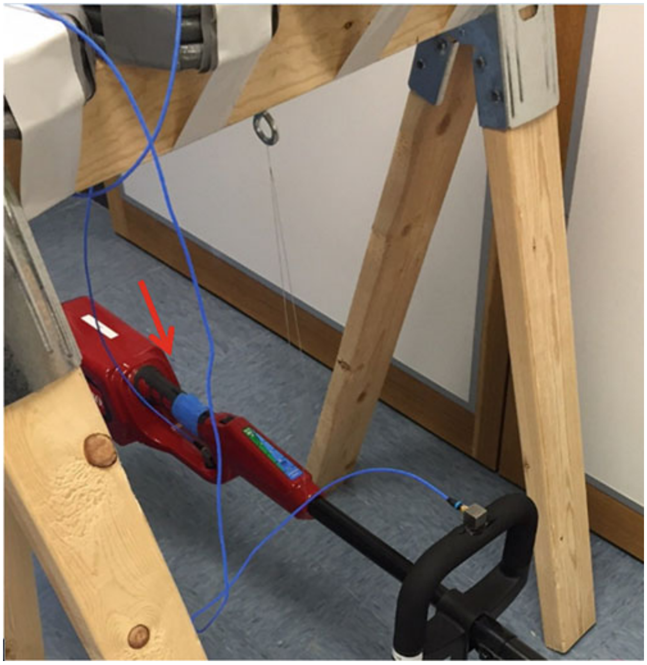

Fig. 34.5 To ensure a free-free support configuration, each string trimmer was suspended (at two points) by fishing line from a weighted test stand. During testing, power to the string trimmer was maintained by taping the trigger open, as indicated

humidity, temperature) had on engine performance. In contrast, battery operated string trimmers could be tested inside in a lab environment that was not subject to significant extremes in temperature and humidity. Two Lithium-ion powered units were selected for evaluation: the DeWalt DCST990 (40 V), and the Toro 51488 (48 V). For testing purposes, each string trimmer unit was hung (using fishing line) from a weighted set of stands to ensure a free-free support, and contact-free measurements were assured by taping down the trigger of each unit (Fig. 34.5). One issue encountered early in the experimental work related to the fact that the output voltage of the battery powering a string trimmer changes as it discharges. This affects the operating performance—specifically the measured vibration amplitude—of each string trimmer (Fig. 34.6). While it was not possible to find a period where the output vibration of the string trimmer remained flat, the vibration characteristics were fairly repeatable within a given time period of operation (i.e. number of minutes into run from full charge). To maintain consistency during testing, 12,500 readings (at a 10 kHz sampling rate) were taken by the Wavebook once every 30 s over a period of 5 min, starting with a fully charged battery each time. For each string trimmer vibration measurement reported, a total of three runs were performed. The RMS values were then averaged and plotted (with error bars), as a function of time, to allow the various conditions to be compared based on their performance over the first 5 min of their battery discharge cycle.

34.2.3 Accelerometers and Data Acquisition System

Two three-axis ICP accelerometers were used to allow multiple components of vibration to be simultaneously measured. The PCB U339B01 units had a measurement resolution of 0.002 g within the frequency range of interest, and produced 90.9, 89.1, and 90.9 mV/g (SN 2988) and 99.1, 93.9, and 71.6 mV/g (SN3198) of signal in the x, y and z directions, respectively. The accelerometers were attached to hexagonal bases (PCB 080A12) using threaded studs; each base was in turn attached to flat portions of the measurand using cyanoacrylate adhesive (i.e. superglue). Acquisition was accomplished using an Iotech Wavebook 16 DAQ board in conjunction with an eight-channel WBK14 expansion module designed to accommodate ICP accelerometers.

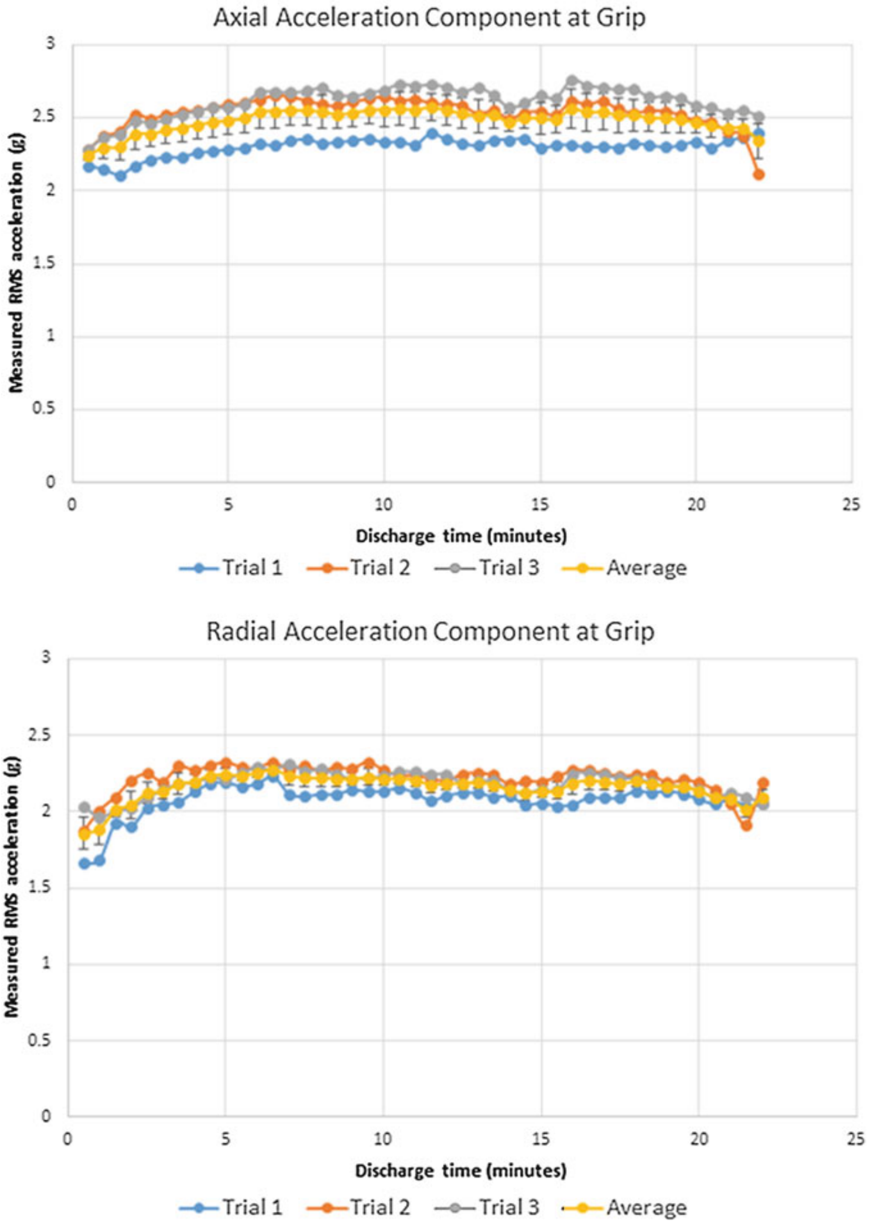

Fig. 34.6 Examples showing how the measured vibration components of the DeWalt string trimmer changed as the battery discharged from a fully-charged condition

34.2.4 Handle Shaker Tests and Modal Analysis

Each 3D-printed (hollow and filled condition) handle was individually tested on a single-axis modal shaker rig (Vibration Research Corporation modal shaker driven by a Wavetek FG3B signal generator and a Vibration Research Corporation CR565 driver). The handles were tested in three orientations (Fig. 34.7), to respectively simulate handle responses to radial, circumferential and axial excitations induced by the operating string trimmer (Fig. 34.8). Accelerometers were attached to the handle and to the vibrating shaker shaft so that the normalized frequency response of the handle could be obtained through a sine-dwell test. For each test, a constant torque was set for the bolt clamping the handle to the shaker apparatus. A modal analysis study was performed on the PTC/Creo models used to print the hollow ABS handles, and the results were compared with those obtained for the corresponding sine-dwell tests.

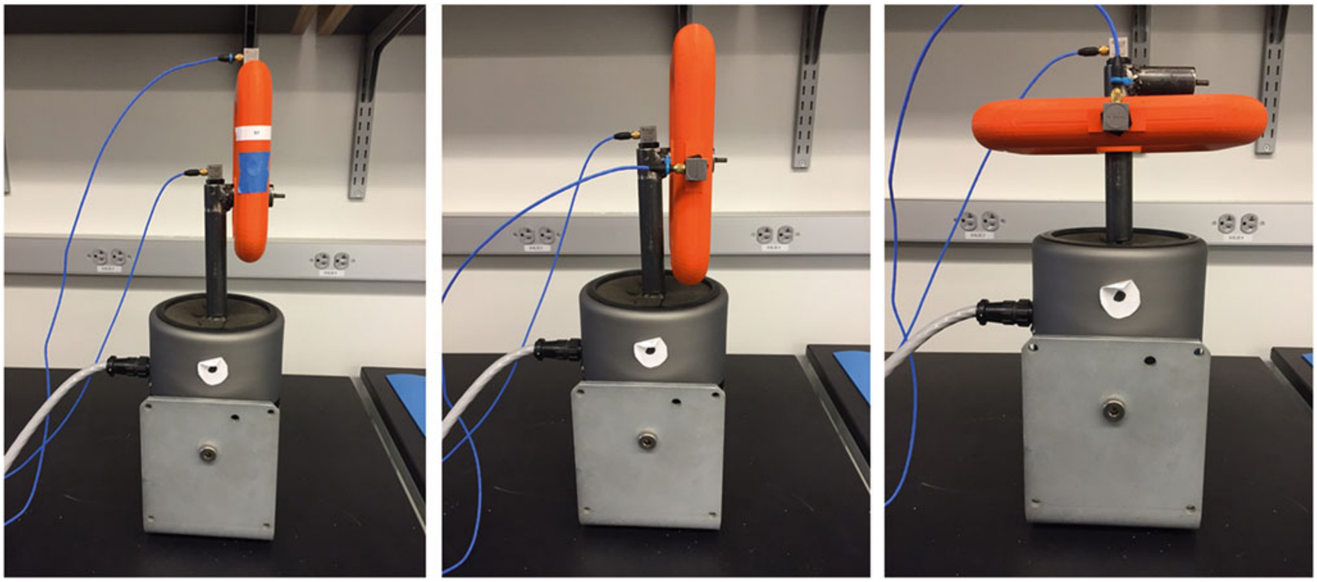

Fig. 34.7 A 3D-printed handle clamped in the shaker for the sine-dwell test showing the three different test orientations corresponding to radial-y (*left*), circumferential-z (*middle*), and axial-x (*right*) modes of excitation

Fig. 34.8 The axial (X), radial (Y) and circumferential directions (Z) relate directly to the geometry of the string trimmer

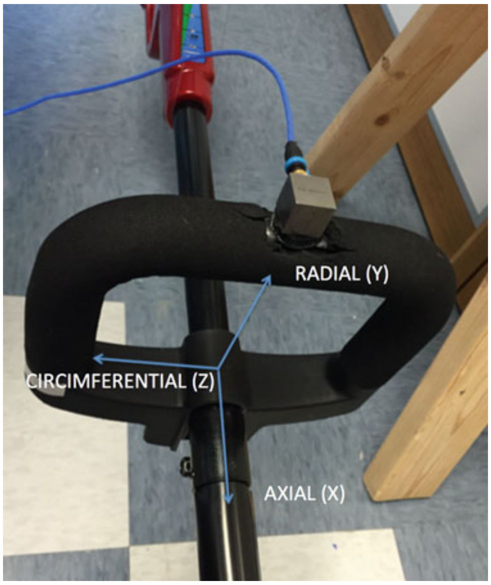

34.2.5 *Shafts*

To replace the polyethylene casing that was used to hold the Perlite against the shaft in the previous work [2], an ABS tube was designed to be 3D printed in two pieces to allow Perlite to be easily added and removed (Fig. 34.9). Because of its length, the tube was printed on a Makerbot Replicator 3D printer.

34.3 Experimental

The purpose of these experiments was to better characterize and quantify the amount of structural vibration attenuation at the grip and the loop handle that could be expected through the use of Perlite around the shaft and within the loop handles of the two battery-powered string trimmers described previously. The dynamic behavior of the loop handles were characterized by

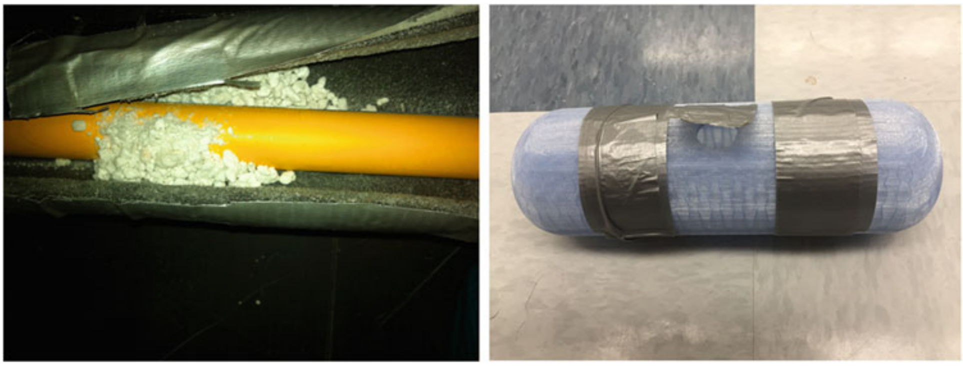

Fig. 34.9 The polyethylene tube used to encase the Perlite in the prior work (*left*, from Weisenburger [2]) was replaced with a 3D printed ABS tube (*right*). Created in two pieces and designed to fit around a shaft, the fill hole allowed the amount of Perlite added to be consistently regulated

performing sine-dwell tests on empty and Perlite-filled 3D printed handles between 5 and 1000 Hz. The results of the sine-dwell tests on the empty 3D printed handles were compared with numerical modal analysis performed using Creo/Simulate. The effects of the Perlite on the operating string trimmers were evaluated by comparing measured vibration at the grip and loop handle for the following: unmodified units; units incorporating a Perlite-filled shell around the shaft, units incorporating the empty shell only, and units fitted with a set of Limbsaver® dampeners. All of the filled and empty shell tests were conducted in conjunction with one of the OEM handles.

34.4 Results

34.4.1 Handle Shaker Tests

The results from the sine-dwell tests (Fig. 34.10) revealed resonance frequencies specific to each OEM and ABS handle. Peaks occur at 50–70, 210, 280, 400, 440, 800, 830, 850, and 870 Hz for handle 1. For most frequencies above 200 Hz, the perlite filled shells showed a reduction in the peak amplitude at the resonance frequencies. The lower frequencies did not show more variation than was typical during various repetitions of this test.

34.4.2 Modal Analysis

As shown in Fig. 34.11, the modal response of handle 1 generated using Creo/Simulate was closely correlated with the peaks obtained using the sine-dwell testing approach. In the Creo/Simulate model, excitation was provided through the inner loop, where the handle is attached to the string trimmer shaft. The first 11 modes were found, corresponding to excitation frequencies of 52, 75, 97, 134, 204, 259, 373, 540, 628, 871, and 944 Hz.

34.4.3 Suspended String Trimmer Trials

These trials were conducted using the previously described methods, and included a baseline test of an unmodified string trimmer, the trimmer with an empty ABS shell attached, the trimmer with a Perlite filled shell, and with the LimbSaver device. All of these measurements were performed using one of the OEM handles.

When placed on the Toro, the empty ABS shell consistently reduced the RMS value of the measured vibrations in the axial, circumferential, and radial directions at both the loop handle and the grip. Adding Perlite to the shell further decreased the measured RMS responses except for the radial component measured at the loop handle. When the LimbSaver devices were attached in place of the Perlite and shell, the measured RMS values were similar to those obtained from the Perlite and shell trials. The RMS acceleration components measured at the grip of the Toro for these experiments are shown in Figs. 34.12

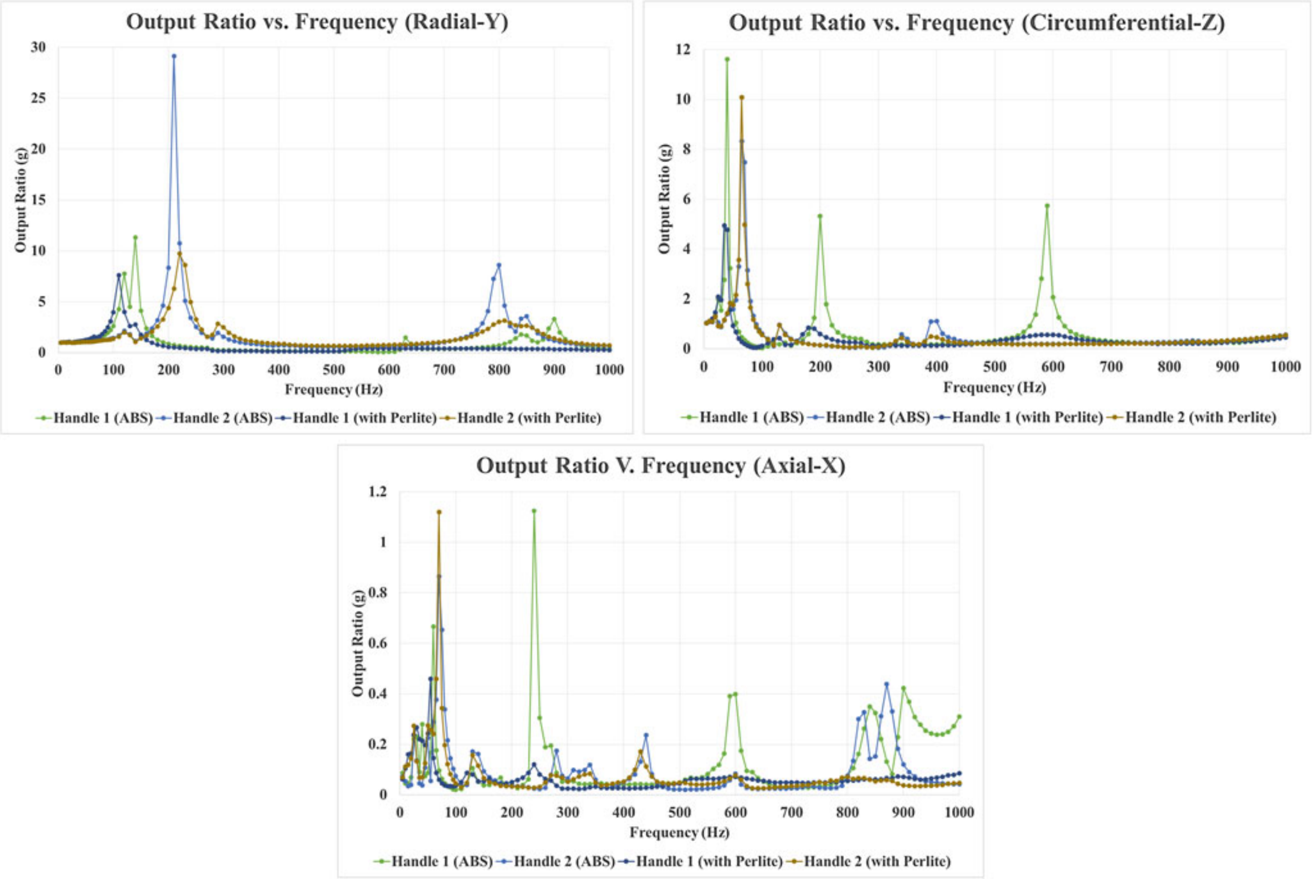

Fig. 34.10 Sine-dwell tests on ABS handles, both empty and filled with Perlite shown as a function of excitation direction, with radial (y—*top left*), circumferential (z—*top right*), and axial (x—*bottom*)

and 34.13. Figures 34.14 and 34.15 show the results of the Fast Fourier Transform performed on the measured outputs of the accelerometers from the unmodified and Perlite filled shell tests at the maximum battery charge using MATLAB.

The data collected from the DeWalt trimmer did not show all of the same trends. In the axial, radial, and circumferential directions at both the loop handle and the grip, the RMS values decreased from the baseline tests when the empty shell was attached, just as the Toro did. When the Perlite was added to the shell, however, the RMS values increased slightly in each direction at the loop handle and grip except for in the circumferential direction at the loop handle. When the LimbSavers were attached to the DeWalt, the measured RMS components all increased at the loop handle. At the grip, the measured RMS components were similar to the empty shell trials in the axial direction, higher than the Perlite trials in the circumferential direction, and lower than the empty shell trials in the radial direction. The collected data for the RMS values at the grip of the DeWalt are shown in Fig. 34.13. Figures 34.16 and 34.17 show the results of the Fast Fourier Transform performed on the measured outputs of the accelerometers from the unmodified and Perlite filled shell tests at the maximum battery charge using MATLAB.

34.5 Discussion, Conclusions and Future Work

34.5.1 Modal Response of 3D-Printed ABS Handles, and Effect of Perlite

The sine-dwell tests confirmed that Lodengraf particles are effective at damping structural vibrations in the top portion of the frequency range tested (Fig. 34.10). At input frequencies greater than 200 Hz, measured acceleration amplitudes were reduced between 25 and 90 % at resonant peaks, with smaller but still significant reductions occurring off-resonance. This is consistent with results reported by Fricke [3]. The modal analysis performed on the handle models yielded a

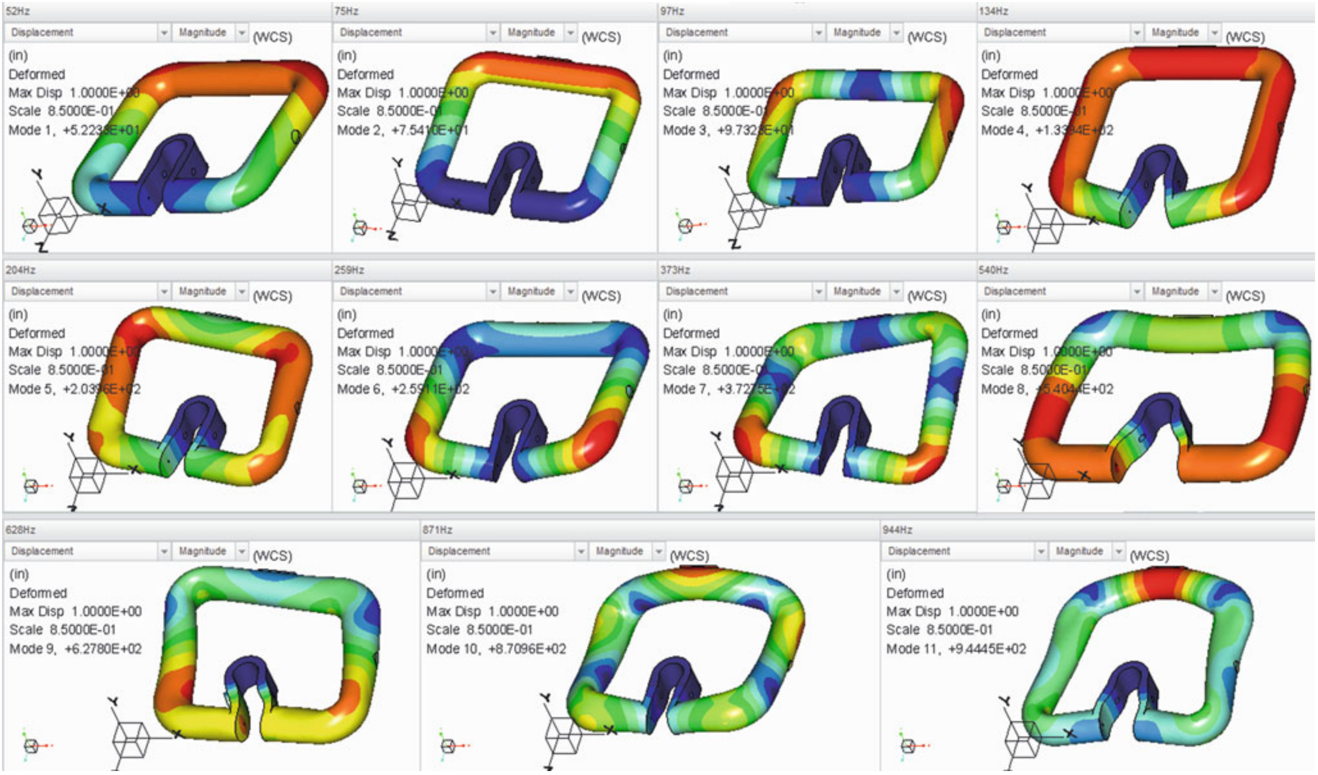

Fig. 34.11 Modes of Handle 1 calculated by Creo Simulate obtained by performing a modal analysis on the handle model. Material properties of ABS have been assigned and the handle has been constrained to simulate being attached to a shaft of a string trimmer. The modes are ordered from least to greatest (as noted), going from *left to right* and *top to bottom*

frequency response similar to that obtained experimentally via the sine-dwell tests performed on the 3D printed handles; some differences in peak location may stem from unmodeled compliance in the attachment between the modal shaker and the handles as well as small but visible imperfections that occurred during the printing process.

34.5.2 Effectiveness of Various Vibration Damping Approaches in Operating String Trimmers

The DeWalt and Toro string trimmers used in this set of experiments have a first fundamental frequency of 112 and 106 Hz, respectively. This frequency directly relates to the RPM of the string trimmer while it is in operation. These fall below the cutoff frequency for effective Lodengraf damping. Although the Lodengraf seems to be effective at damping high frequency vibrations (>200 Hz), it has significantly less impact at lower frequencies.

These initial tests showed that adding Perlite along the shaft of an operating string trimmer reduced the RMS acceleration components measured at the loop handle and grip of the Toro, but not on the DeWalt. At the grip of the DeWalt in the axial direction, the FFT shows that the higher range frequencies increased significantly when the Perlite was added, a response that is inconsistent with the expected and otherwise measured Lodengraf response. This uncharacteristic increase can also be seen in the measured RMS in the same location and direction in Fig. 34.13.

For effective vibration reduction at lower frequencies, it seems that the simple strategic addition of mass to the shaft—whether via the addition of an empty shell or a Limbsaver-type device—may be more generally effective than the addition of Perlite. This will be explored further in follow-up work. Finally, the effect of using the Perlite-filled handles on the string trimmers, both alone and in combination with the shaft treatments discussed herein, needs to be assessed for effectiveness.

Acknowledgements This project was funded in part by a grant from the U.S. Department of Education as well as local, non-institutional funds. The authors would further like to acknowledge machinist Manuel Garza who assisted with the sine-dwell test fixture, as well as undergraduate research assistant Bernardo Garza, who designed and fabricated the shells for containing the Perlite.

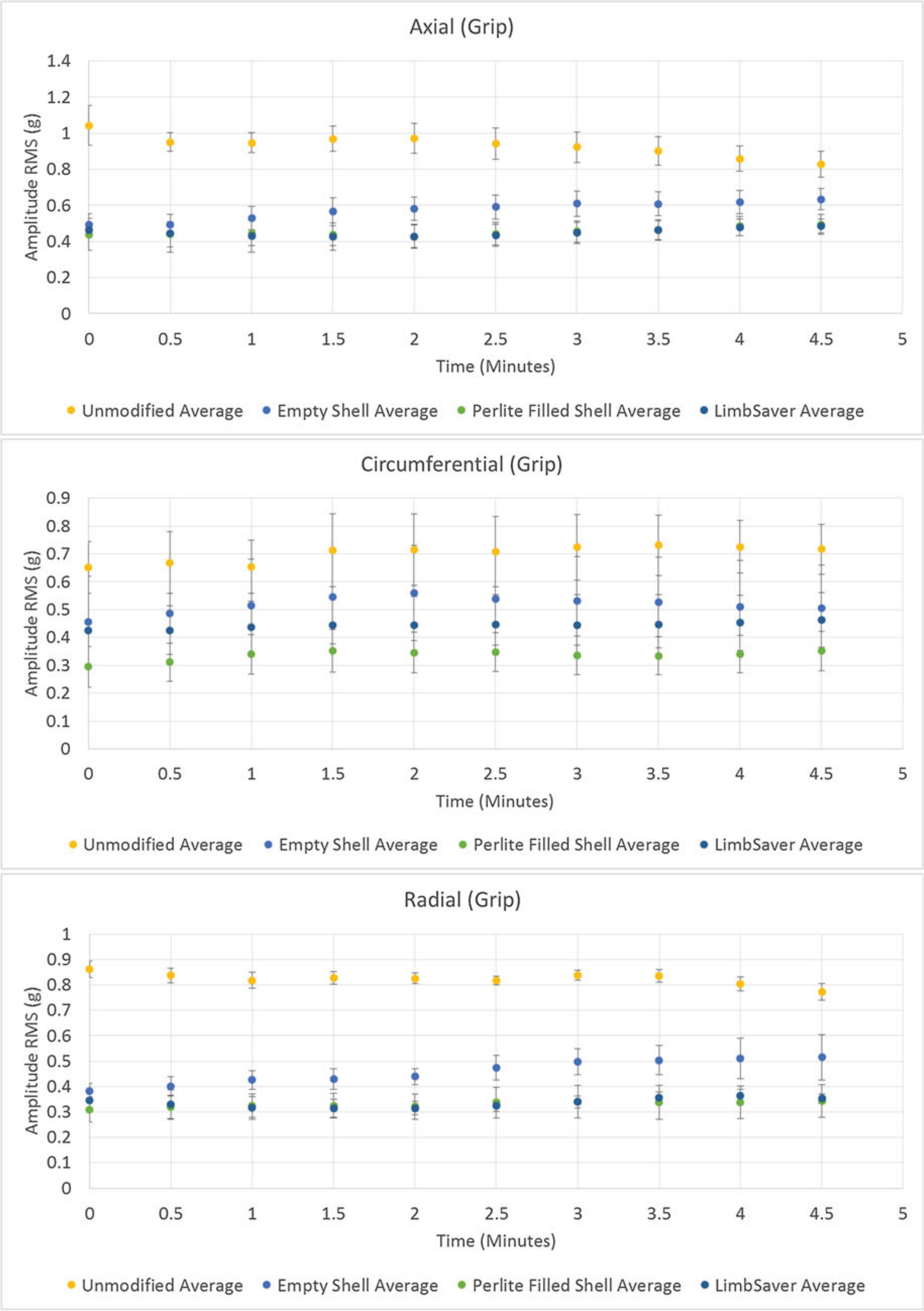

Fig. 34.12 Measured RMS components at the grip for the Toro in the axial, circumferential, and radial direction, for the unmodified device, the trimmer with an empty ABS shell attached, with the Perlite filled shell, and with the LimbSaver attachments

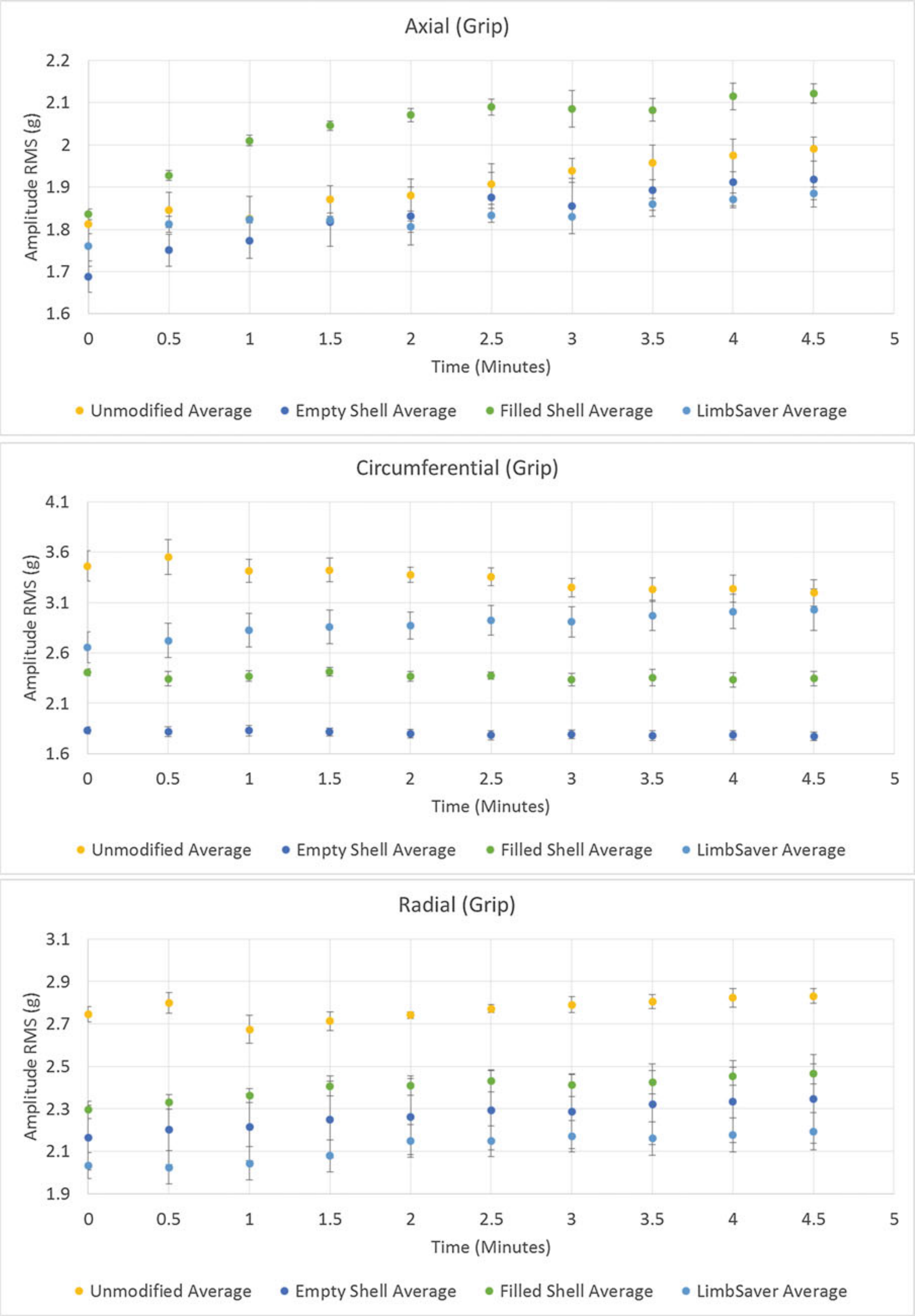

Fig. 34.13 Measured RMS components at the grip for the DeWalt in the axial, circumferential, and radial direction, for the unmodified device, the trimmer with an empty ABS shell attached, with the Perlite filled shell, and with the LimbSaver attachments

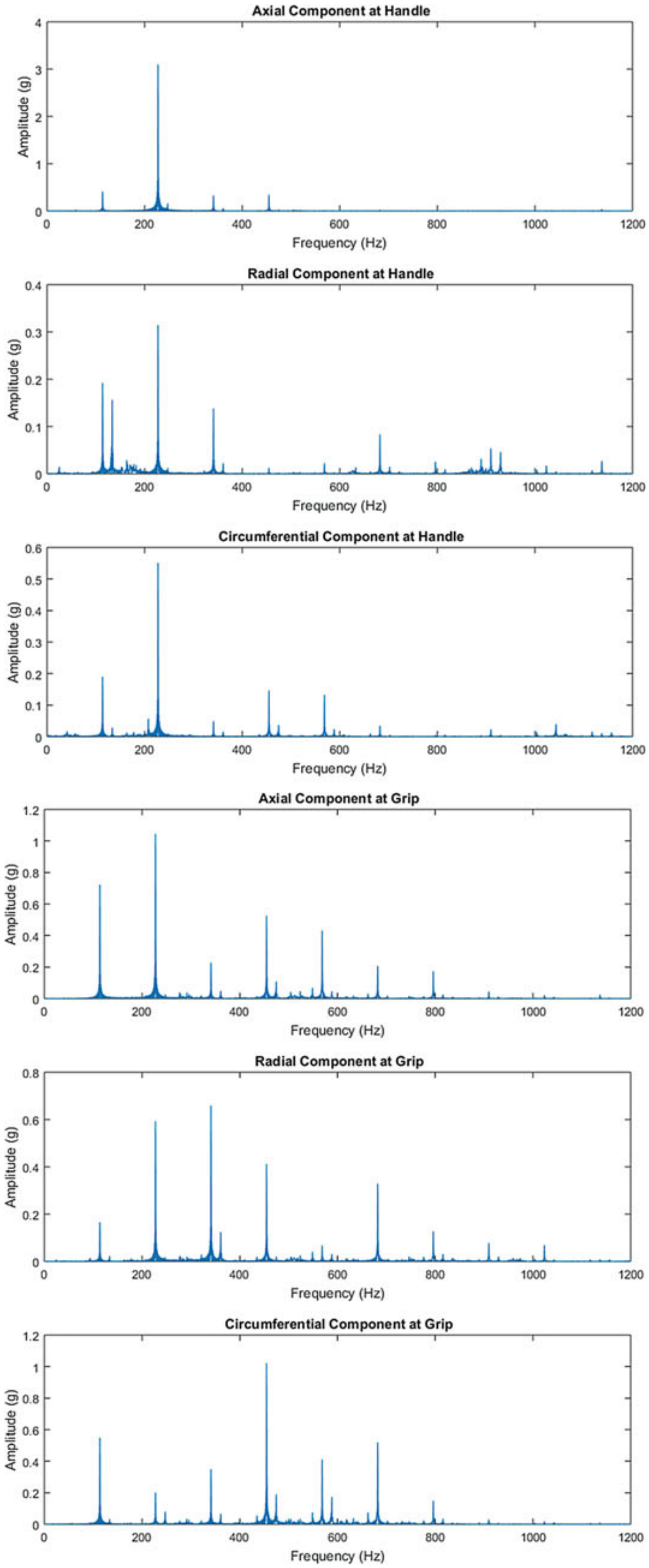

Fig. 34.14 Frequency content of the unmodified Toro trimmer at maximum battery charge in the radial, circumferential, and axial direction at the grip and loop handle, obtained by performing a fast Fourier Transform in MATLAB on the measured output

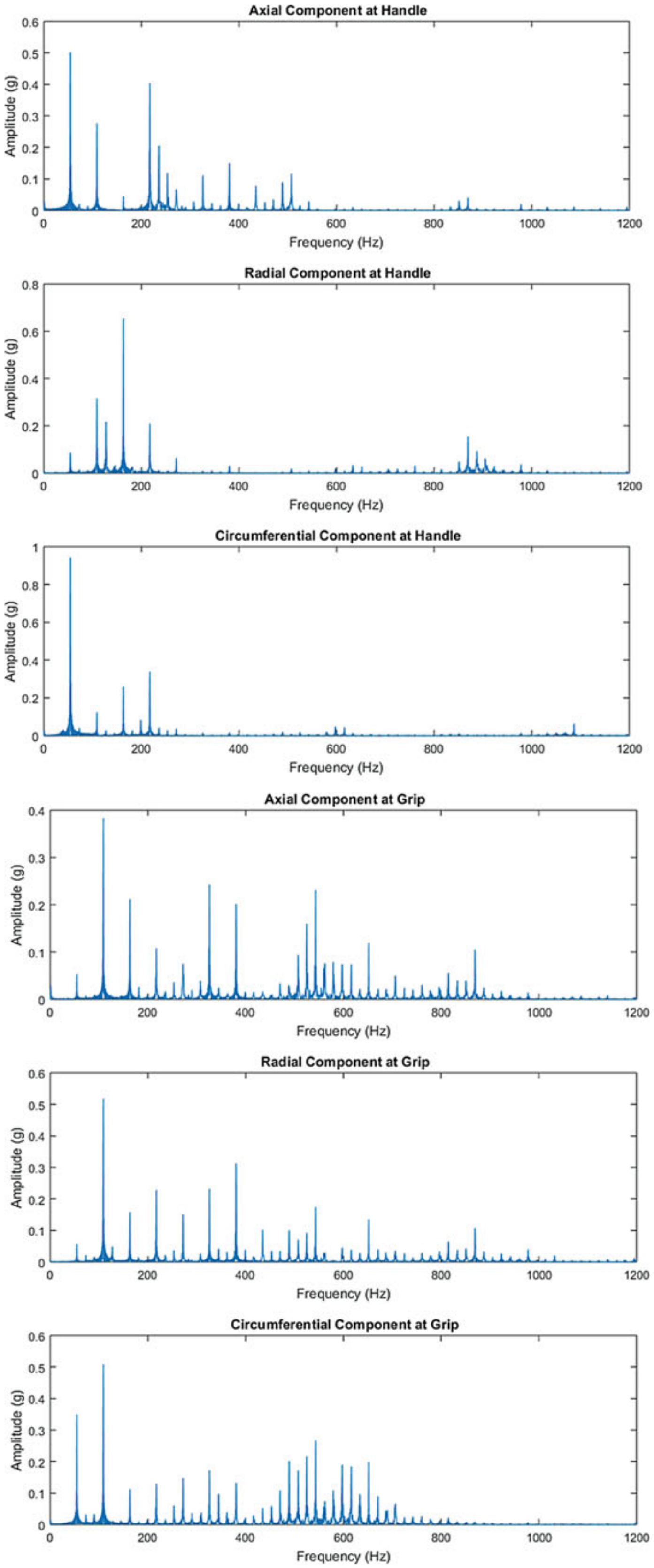

Fig. 34.15 Frequency content of the Toro trimmer with the Perlite filled shell attached at maximum battery charge in the radial, circumferential, and axial direction at the grip and loop handle, obtained by performing a fast Fourier Transform in MATLAB on the measured output

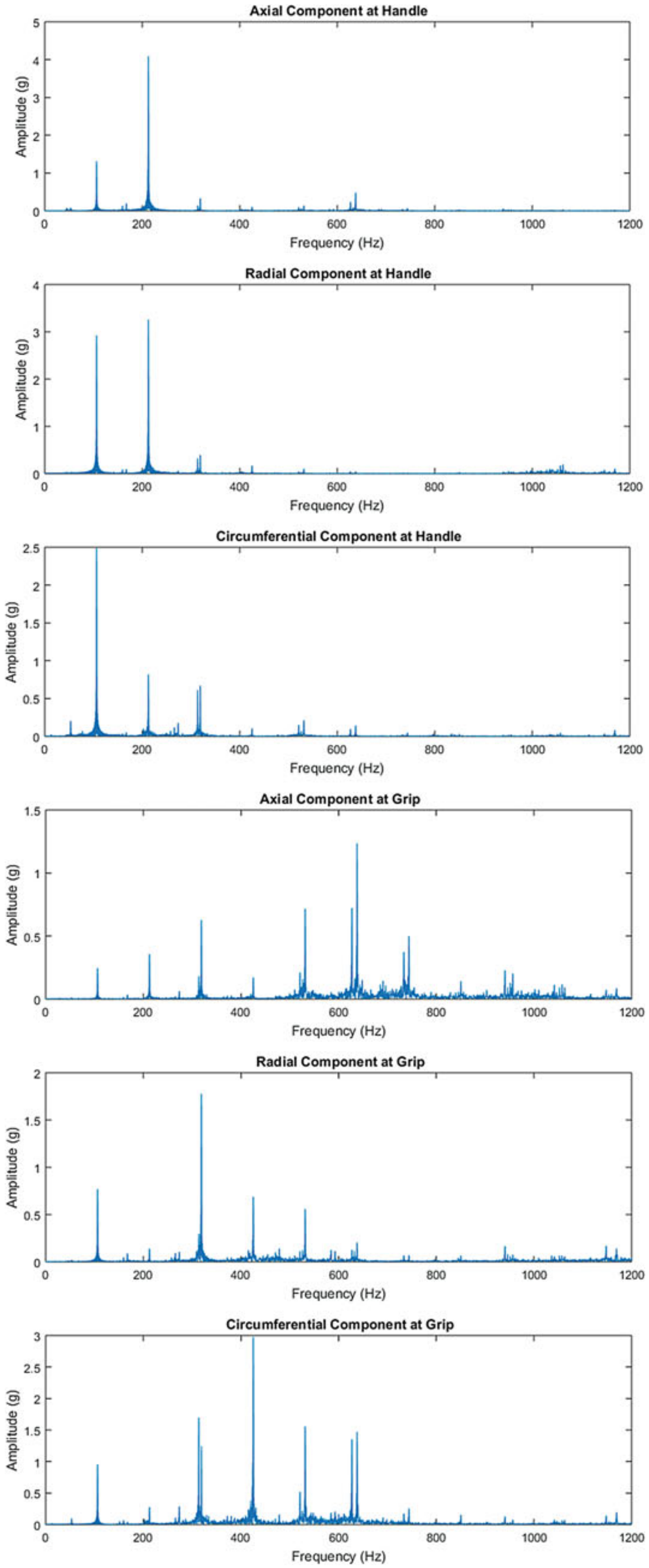

Fig. 34.16 Frequency content of the unmodified DeWalt trimmer at maximum battery charge in the radial, circumferential, and axial direction at the grip and loop handle, obtained by performing a fast Fourier Transform in MATLAB on the measured output

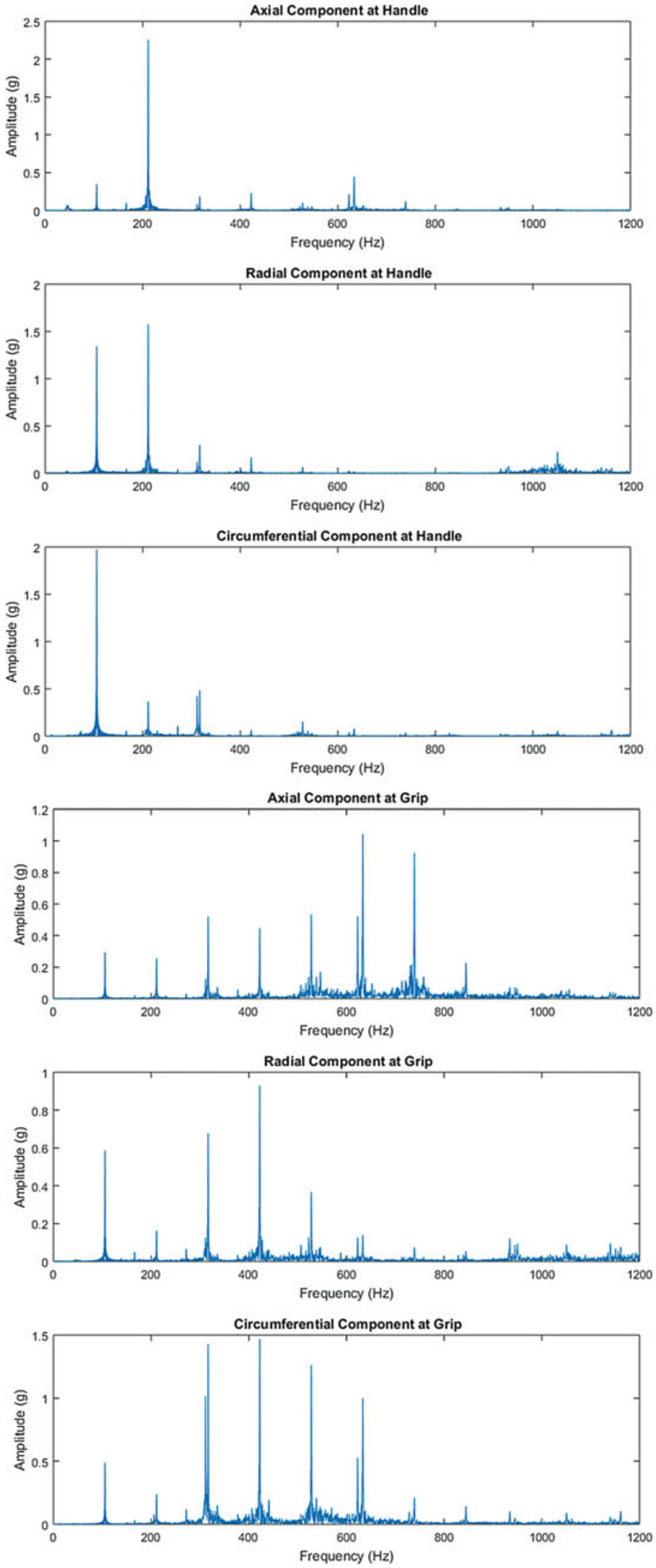

Fig. 34.17 Frequency content of the DeWalt trimmer with the Perlite filled shell attached at maximum battery charge in the radial, circumferential, and axial direction at the grip and loop handle, obtained by performing a fast Fourier Transform in MATLAB on the measured output

References

1. Pelmear, P.L., Wasserman, D.E.: Hand-Arm Vibration, 2nd edn. OEM, Beverly Farms (1998)
2. Leifer, J., Weisenburger, S. J.: Materials and techniques for reduction of vibration transmission in string trimmers, Paper 88064. In: Proceedings of the ASME 2012 International Mechanical Engineering Conference and Exposition IMECE 2012, Houston, November 2012
3. Fricke, J.R.: Lodengraf damping – an advanced vibration damping technology. Sound Vib. **34**(7), 22–27 (2000)
4. Yeo, D. R.: http://en.wikipedia.org/wiki/File:Man_weedeating.jpg. Accessed 18 Oct 2015
5. Rajbhandary, P., Leifer, J., Weems, B.J.: Reduction of vibration transmission in string trimmers, Paper 87. In: Proceedings of the 29th International Modal Analysis Conference, Jacksonville, FL

Chapter 35
Using Operating Data to Locate and Quantify Unbalance in Rotating Machinery

Shawn Richardson, Mark Richardson, Jason Tyler, and Patrick McHargue

Abstract In a previous paper entitled ***Using Operating Deflection Shapes to Detect Unbalance in Rotating Equipment*** [Ganeriwala, S.N., Schwarz, B., Richardson, M.: Using operating deflection shapes to detect unbalance in rotating equipment. In: IMAC XXVII, Orlando, February 2009], we introduced the idea of numerically comparing currently acquired operating data with archived data to identify unbalances in rotating machinery. In a follow-up paper [Richardson, S., Tyler, J., McHargue, P., Richardson, M.: A new measure of shape difference. In: IMAC XXXII, 3–6 February 2014], we introduced a new metric for comparing two deflection shapes called the ***Shape Difference Indicator*** or SDI. In this paper, we introduce a refined version of the SDI algorithm, and present new results to verify its utility for locating and quantifying unbalance in rotating machinery.

We make two underlying assumptions about rotating machines; (1) all rotating machines are excited by ***inherent unbalance forces*** which cannot be directly measured, and (2) order-related vibration levels acquired from multiple locations on a machine can be ***directly correlated*** with specific unbalance conditions. We show that by comparing current with archived ODS data, specific unbalance conditions can be pinpointed.

Keywords Fourier spectrum • Auto power spectrum • Cross power spectrum • ODSFRF • Operating deflection shape • Modal assurance criterion • Shape difference indicator

35.1 Introduction

Vibration measurements have been used for decades as a means of determining the health of rotating machinery. The use of vibration as a health metric is analogous to a medical doctor examining your electro-cardiogram in order to ascertain the health of your heart. Just as a doctor looks for small abnormalities in the time waveforms of the electronic signals from your chest, vibration signals also carry tell-tale signs that mechanical changes have taken place in a rotating machine.

Three of the most common health problems in rotating machine are ***unbalance*** of rotating parts, ***misalignment*** of rotating parts, and loose mountings or an overly compliant foundation, called ***soft foot***.

We believe that all three of these rotating machinery health problems can be detected using ODS data. Furthermore, we will show that by ***numerical correlation*** of current and archived ODS data, (i.e. a form of data mining), small unbalance conditions in a rotating machine can be detected and located.

In the previous paper [1], four tri-axial and two uni-axial accelerometers where attached to the rotating machine shown in Fig. 35.1. When the peak values at the running speed (or first order) of the machine were assembled together into a "deflection shape", it resulted in an ODS with 14 shape components (or DOFs) in it.

In this paper, only the operating data from the two tri-axial accelerometers on the bearing blocks is used, thus providing order-related ODS's with only 6 DOFs in them. This minimal amount of data was used not only to prove the viability of ODS comparison as a method for locating and quantifying unbalances, but also to show that a minimal amount of instrumentation is required to implement this method on rotating equipment in a process plant.

Both MAC and SDI will be applied to the same seven cases of machine unbalance that were used in [1], but instead of using all of the operating data, only a minimal set of data from the two bearing blocks will be used. In addition, an extension of the SDI method will be introduced which increases its sensitivity to small differences between two shapes.

S. Richardson • M. Richardson (✉) • J. Tyler • P. McHargue
Vibrant Technology, Inc., Scotts Valley, CA, USA
e-mail: mark.richardson@vibetech.com

© The Society for Experimental Mechanics, Inc. 2016

J. De Clerck, D.S. Epp (eds.), *Rotating Machinery, Hybrid Test Methods, Vibro-Acoustics & Laser Vibrometry, Volume 8*,
Conference Proceedings of the Society for Experimental Mechanics Series, DOI 10.1007/978-3-319-30084-9_35

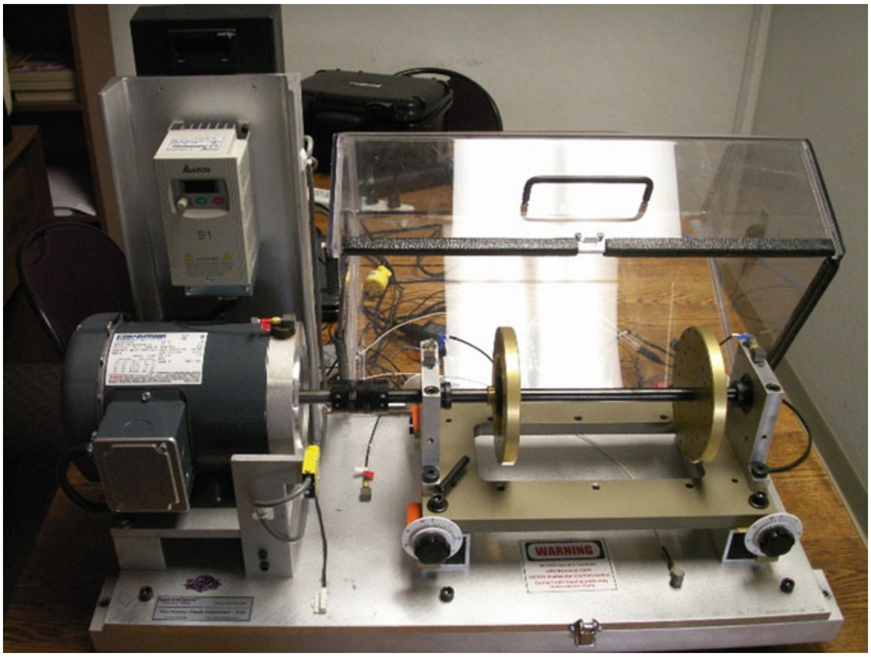

Fig. 35.1 Rotating machine with accelerometers attached

35.1.1 Output-Only Frequency Spectra

In operating machinery where the excitation forces cannot be measured, three types of ***output-only*** frequency spectra can be calculated from acquired time waveforms. The three types are Fourier spectra, Cross spectra, and ODSFRFs.

A **Fourier spectrum** is simply the Digital Fourier Spectrum (DFT) of a response digital time waveform. It is calculated with the FFT algorithm. A **Cross spectrum** is calculated between two simultaneously acquired responses. It is the DFT on one signal multiplied by the complex conjugate of the other. An **ODSFRF** is the Auto spectrum of a ***roving*** response combined with the phase of the Cross spectrum between the ***roving*** response and a (***fixed***) ***reference*** response.

35.1.2 Operating Deflection Shape

When a vibration response is measured at ***two or more points*** and ***directions*** on a machine, this data can be assembled into what is called an **Operating Deflection Shape** (or **ODS**) [5]. Three different types of ODS's are possible; ***time-based ODS*'*s***, ***frequency-based ODS*'*s***, and ***order-based ODS*'*s***.

35.1.3 Time-Based ODS

A time-based ODS is simply the values for the same time sample of two or more simultaneously acquired or calculated time waveforms. A time-based ODS contains the responses that were simultaneously acquired at a moment of time from the machine.

35.1.4 Frequency-Based ODS

A frequency-based ODS is the values for the same frequency sample of two or more frequency domain functions or spectra. A frequency-based ODS is the ***true overall response*** of the machine at a specific frequency sample for which the measurement functions were calculated.

All frequency domain functions (except an Auto spectrum) are complex valued (with magnitude and phase), and consequently all frequency-based ODS's are complex valued.

35.1.5 Order-Based ODS

In a rotating machine, the excitation forces are dominant at multiples of the machine running speed, called orders. An ***order-based ODS*** is assembled from the ***peak values*** at one of the order frequencies in a set of output-only frequency spectra. These spectra are calculated from response data that is acquired while the machine is running. When displayed in animation on a 3D model of the machine, an order-based ODS is a convenient way to visualize distributed relative vibration levels.

The components of an order-based ODS can also be used for monitoring the health of the machine by comparing their values with pre-defined warning levels. Three commonly used warning levels are termed ***alert***, ***alarm***, and ***abort*** levels.

35.2 Data Acquisition from a Rotating Machine

For our previous paper [1], operating data was acquired from the machinery fault simulator shown in Fig. 35.1. Tri-axial accelerometers were attached to the top of both bearing blocks and the motor. A tri-axial and 2 uni-axial accelerometers were also attached to the base plate. These accelerometers provided a total of 14 vibration signals, which were simultaneously acquired with a 16 channel data acquisition system.

A set of ODSFRFs was calculated between each of the channels of data and a ***single reference*** channel. An ODSFRF is a "***hybrid***" cross-channel measurement, derived from both an Auto and Cross spectrum. It is formed by combining the ***phase*** of the Cross spectrum between a roving and reference signal with the Auto spectrum (its ***magnitude***) of the roving response signal. The magnitude of an ODSFRF is the Auto spectrum of the response, which is a measure of the true magnitude of the machine response. The phase of an ODSFRF, which is its phase with the reference response, also provides a measure of the ***relative phase*** between its response and all other responses.

Data was acquired from the machine at an operating speed of 2000 RPM, under seven different unbalance conditions. A typical ODSFRF is shown in Fig. 35.2. It is clear that the dominant peaks in the ODSFRF are at the running speed and its higher orders (4000, 6000 RPM, etc.).

Order-based ODS's were created by saving the peak values in the ODSFRFs at each of the first three orders.

Note
An order-based ODS is the ***peak values*** from a set of ODSFRFs at ***one of the machine orders***.

35.3 Seven Unbalance Cases

Vibration data was acquired from the machine when it was considered to be in balance (the baseline condition), and under seven different unbalance conditions. Unbalance was created by adding weights to either or both of the rotors, as indicated in Fig. 35.3. Data was acquired for each of the following unbalance conditions;

1. Small unbalance (11.25 g)—Inboard rotor
2. Small unbalance—Outboard rotor
3. Large unbalance (22.5 g)—Inboard rotor
4. Large unbalance—Outboard rotor

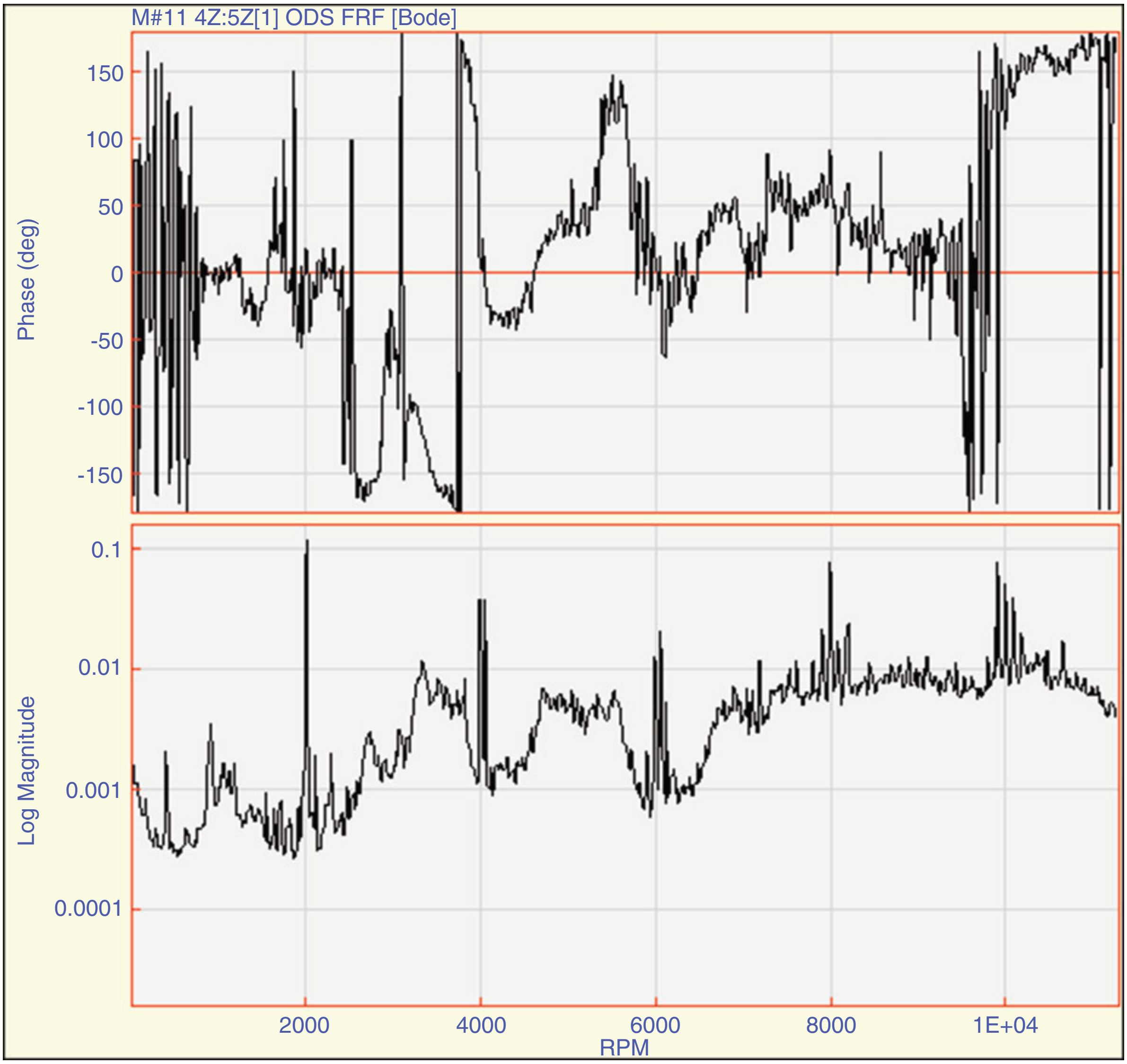

Fig. 35.2 ODSFRF showing peaks at machine orders

5. Two large unbalances—0° apart
6. Two large unbalances—90° apart
7. Two large unbalances—180° apart

For case 1, a small unbalance weight (11.25 g) was added only to the inboard rotor, closest to the motor. For case 2, the same small unbalance weight was added only to the outboard rotor, farthest from the motor. Cases 3 and 4 were the same as cases 1 and 2, but a larger unbalance weight (22.5 g) was used.

In cases 5, 6 and 7, the same large unbalance weight was added to both rotors, but the weights were added in different positions. In case 5, they were added at the same radial position on both rotors (with 0° difference between them). In case 6, they were added at 90° apart from one another, and in case 7 they were added at 180° apart.

ODS data for the unbalance cases previously used [1] was also used for this paper, but only data from the accelerometers ***on the two bearing blocks*** was used. This will illustrate the use of a ***minimal set of data*** for detecting and identifying each of the seven cases.

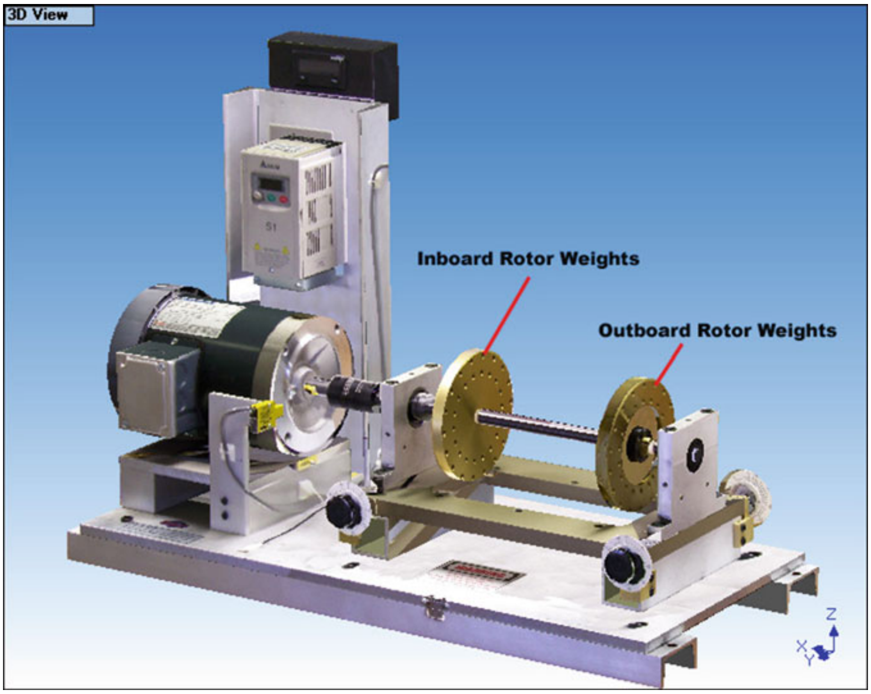

Fig. 35.3 Unbalance weights attached to rotors

35.4 Modal Assurance Criterion

One might ask, ***Isn't the Modal Assurance Criterion*** (***MAC***) ***used for numerically correlating two shapes***? ***Why introduce another correlation method***? MAC [3, 4] is useful for comparing two shapes but it has two limitations,

1. It only indicates the ***co-linearity*** of two shapes, not their difference.
2. It can only be applied to shapes with ***two or more*** shape components. Its value for two scalars is ***always* 1**.

MAC is calculated with the formula,

$$\mathrm{MAC} = \frac{\{\mathrm{u}\}^{\mathrm{h}}\{\mathrm{v}\}^{2}}{\{\mathrm{u}\}^{\mathrm{h}}\,\{\mathrm{u}\}\,\{\mathrm{v}\}^{\mathrm{h}}\,\{\mathrm{v}\}} \tag{35.1}$$

$\{\mathrm{u}\}$ = complex comparison shape (m-vector)
$\{\mathrm{v}\}$ = complex baseline shape (m-vector)
m = number of matching DOFs between the shapes
h–denotes the transposed conjugate vector

MAC measures the ***co-linearity*** of two shapes, so if they lie together on the same straight line, **MAC = 1**. Another way of understanding MAC is that it is the ***dot product*** of the two shapes squared, ***normalized*** by each of their magnitudes squared. MAC is not sensitive to the difference in the actual values of the shapes themselves, only to the difference in their "***shapes***". If two shapes do not lie on the same straight line, then **MAC < 1**.

MAC does not answer the question, "***How different are the shape component values of one shape from another***?" To answer that question, a new measure of the difference between two shapes was introduced in [2]. SDI has proven to be more useful than MAC for comparing ODS's to detect machine faults.

35.5 Shape Difference Indicator

The Shape Difference Indicator is defined with the formula,

$$\mathrm{SDI} = \left(1 - \frac{\{\mathrm{u}\} - \{\mathrm{v}\}^2}{\{\mathrm{u}\}^{\mathrm{h}}\{\mathrm{u}\} + \{\mathrm{v}\}^{\mathrm{h}}\{\mathrm{v}\}}\right)^2 \tag{35.2}$$

or

$$\mathrm{SDI} = \left(\frac{2\,\mathrm{real}\left(\{\mathrm{u}\}^{\mathrm{h}}\{\mathrm{v}\}\right)}{\{\mathrm{u}\}^{\mathrm{h}}\{\mathrm{u}\} + \{\mathrm{v}\}^{\mathrm{h}}\{\mathrm{v}\}}\right)^2 \tag{35.3}$$

$\mathrm{real}\left(\{\mathrm{u}\}^{\mathrm{h}}\{\mathrm{v}\}\right)$ = the real part of the vector dot product

$\{\mathrm{u}\}$ = complex comparison shape (m-vector)
$\{\mathrm{v}\}$ = complex baseline shape (m-vector)
m = number of matching DOFs between the shapes
h–denotes the transposed conjugate vector

SDI values also range between **0** and **1**. If two shapes have ***identical shape components***, **SDI = 1**. If two shapes have ***different shape components***, **SDI < 1**. Several examples illustrate typical SDI values.

- If $\{\mathrm{v}\} = \{\mathrm{u}\}$, SDI = 1
- If $\{\mathrm{v}\} = 0$ *or* $\{\mathrm{u}\} = 0$, SDI = 0
- If $\{\mathrm{v}\} = 2\{\mathrm{u}\}$, SDI = 0.64
- If $\{\mathrm{v}\} = 10\{\mathrm{u}\}$, SDI = 0.04

35.6 Applying MAC and SDI to Order-Based ODS'S

The following Figs. 35.4, 35.5, 35.6, 35.7, 35.8 and 35.9 are bar charts of the MAC and SDI values between order-based ODS pairs for the baseline and seven unbalance cases.

Each bar chart depicts an 8 by 8 matrix of MAC or SDI values. Each diagonal bar of value **1** is the MAC or SDI value of each ODS correlated with itself. Each bar chart also shows the ***worst case*** of a MAC or SDI value in the box at the top. Shape #1 is the baseline (balanced) case. Shapes #2 through #8 are the seven unbalance cases in order.

A MAC or SDI value ***less than* 1** indicates that a pair of ODS's are different from one another. A bar value ***close to zero*** is a clear indication that two ODS's are different.

Note
If all of the ***off-diagonal*** bars in these bar charts are ***close to zero***, the metric can be used to ***uniquely identify*** each unbalance condition.

Figure 35.4 shows the MAC values for the first order ODS data. Many of the MAC values for the off-diagonal pairs are ***close to* 1**. This bar chart shows that MAC values cannot be used on first order ODS data to uniquely identify each unbalance case.

Figure 35.5 shows the SDI values for the first-order ODS data. Overall, these values are closer to zero than the MAC values, but the ODS's for the worst case pair (cases 2 and 7) are still closely correlated (**SDI = 0.93**). Hence, SDI values cannot be used on first order ODS data to uniquely identify each unbalance case.

Figure 35.6 is the MAC values for the second order ODS's. This bar chart still shows that the MAC values cannot be used on second order ODS data to uniquely identify each unbalance case. Figure 35.7 is the SDI values for the second order

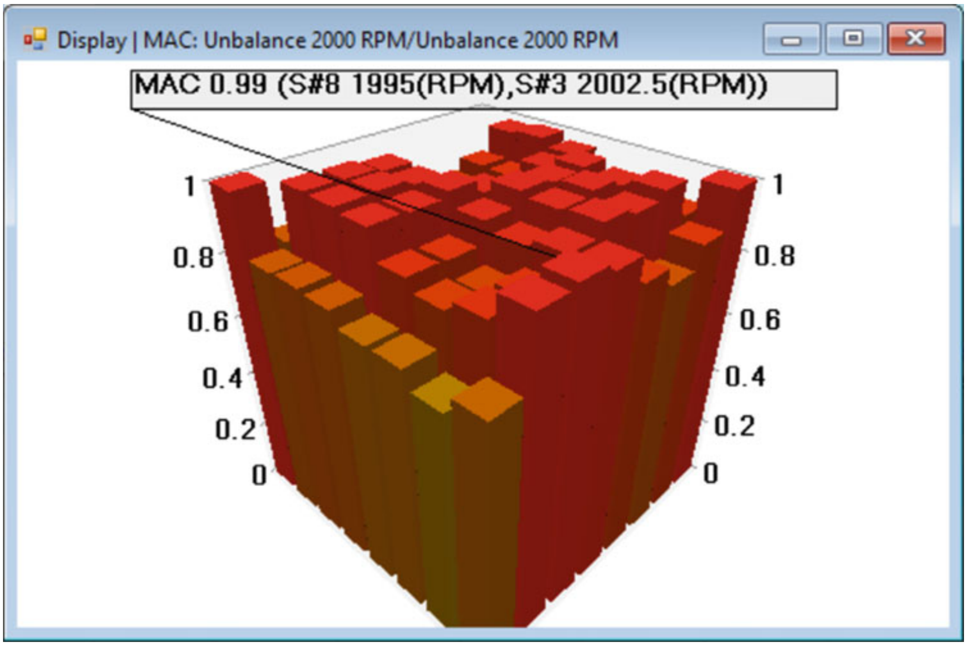

Fig. 35.4 MAC values (first order)

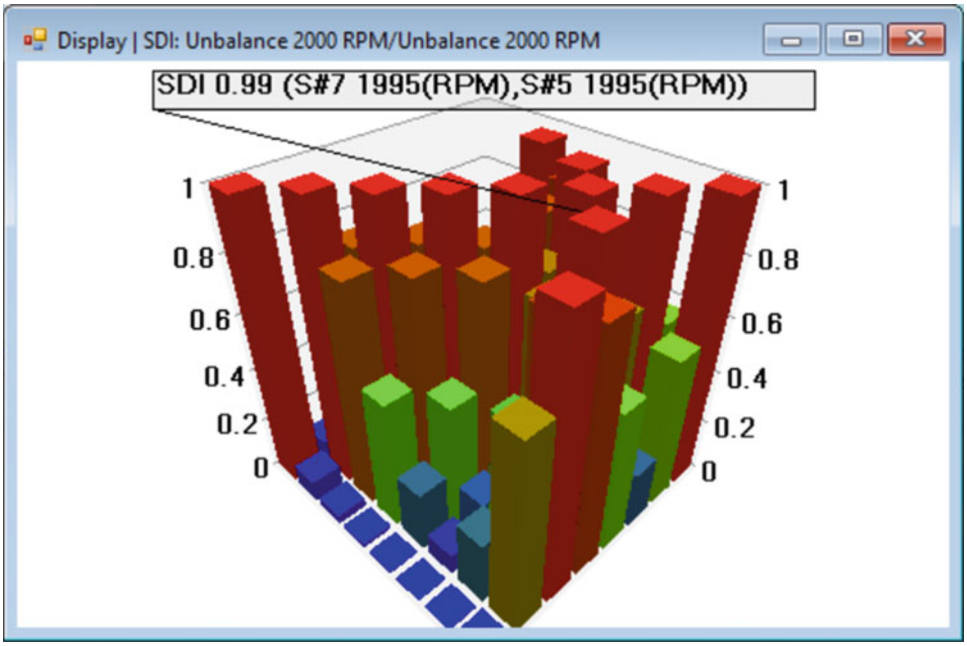

Fig. 35.5 SDI values (first order)

ODS's. It shows that the worst case pair (cases 4 and 6) has an **SDI = 0.88**. This bar chart also shows that SDI values cannot be used on second order ODS data to uniquely identify each unbalance case.

Figure 35.8 shows that the worst case pair (cases 3 and 6) has a **MAC = 0.93** for the third order ODS's. Even though overall these MAC values are closer to zero than for the first and second orders, these values still cannot be used to uniquely identify each unbalance case. Figure 35.9 shows that a worst case pair (cases 3 and 6) has an **SDI = 0.85**. Again SDI cannot be used on third order ODS data to uniquely identify each unbalance case.

Even though SDI is a stronger indicator of shape differences than MAC, it would still be an unreliable method for discriminating among the seven unbalance cases and the balanced case, regardless of which order of ODS data were used.

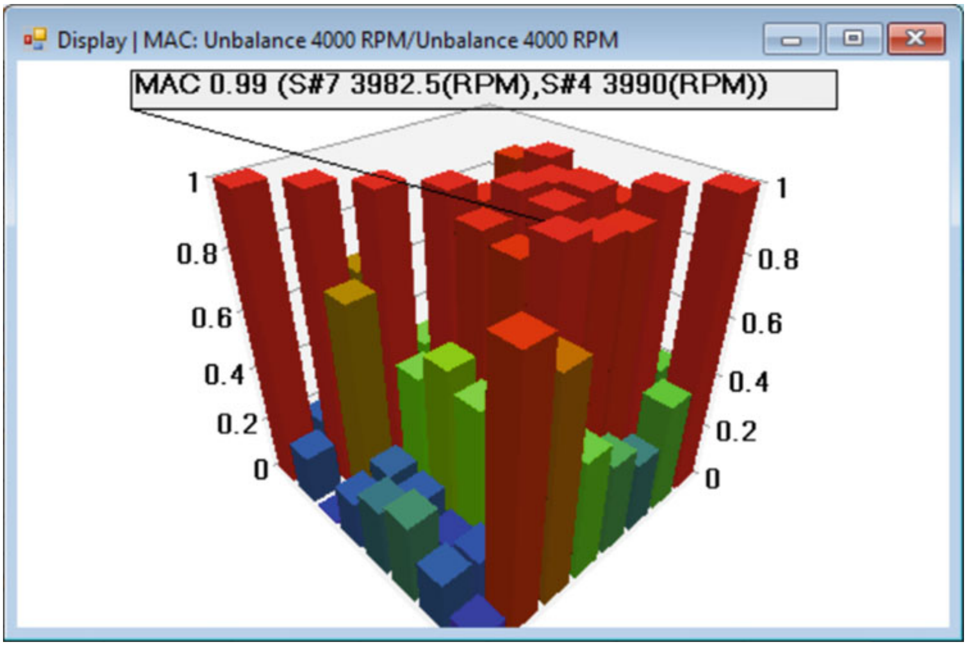

Fig. 35.6 MAC values (second order)

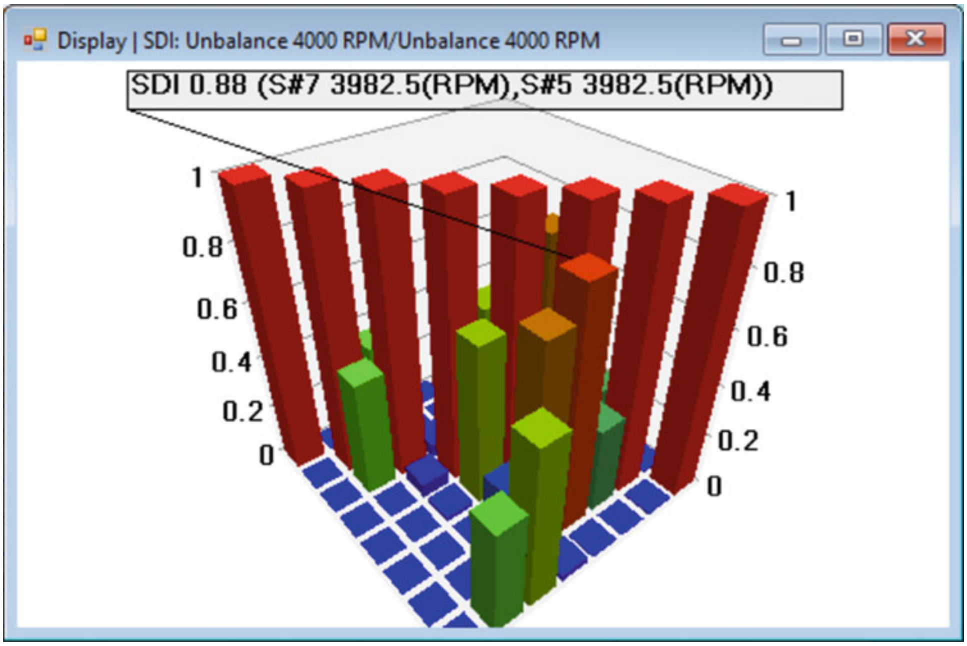

Fig. 35.7 SDI values (second order)

35.7 SDI Sensitivity

Figure 35.10 is a plot of three SDI curves for scalar values of {u} and {v}. In general, {u} and {v} are vectors, but in this case each vector only has one real component. Three curves are plotted for the baseline shape {v} = 1, 10, 100.

These SDI curves have two unique properties,

1. When {u} = 0, SDI = 0
2. Each SDI curve ***flattens out*** as it transitions from zero to its ***peak value*** (**SDI = 1**), which occurs when {u} = {v}

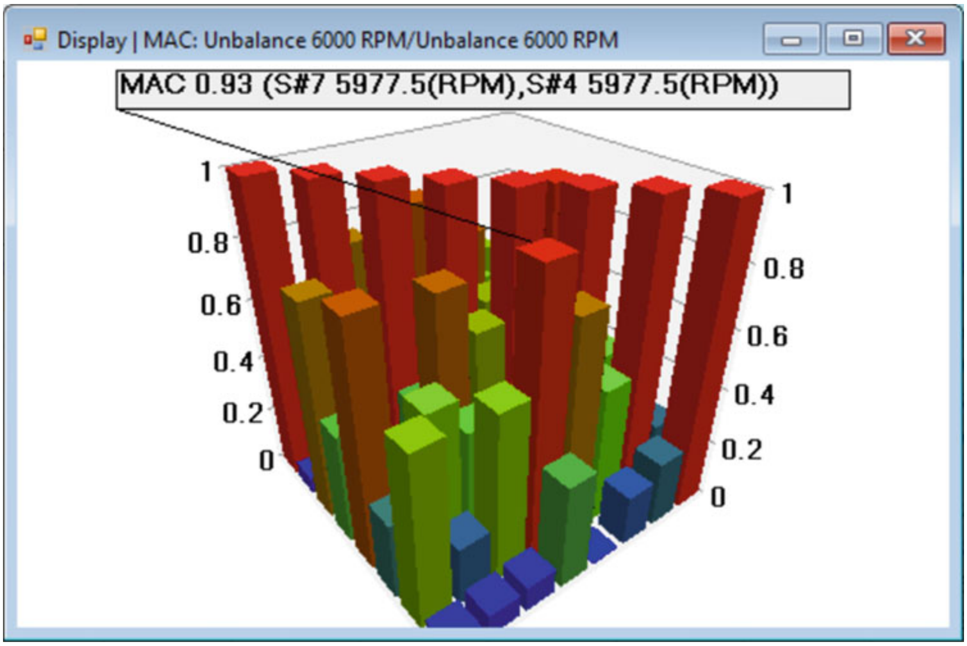

Fig. 35.8 MAC values (third order)

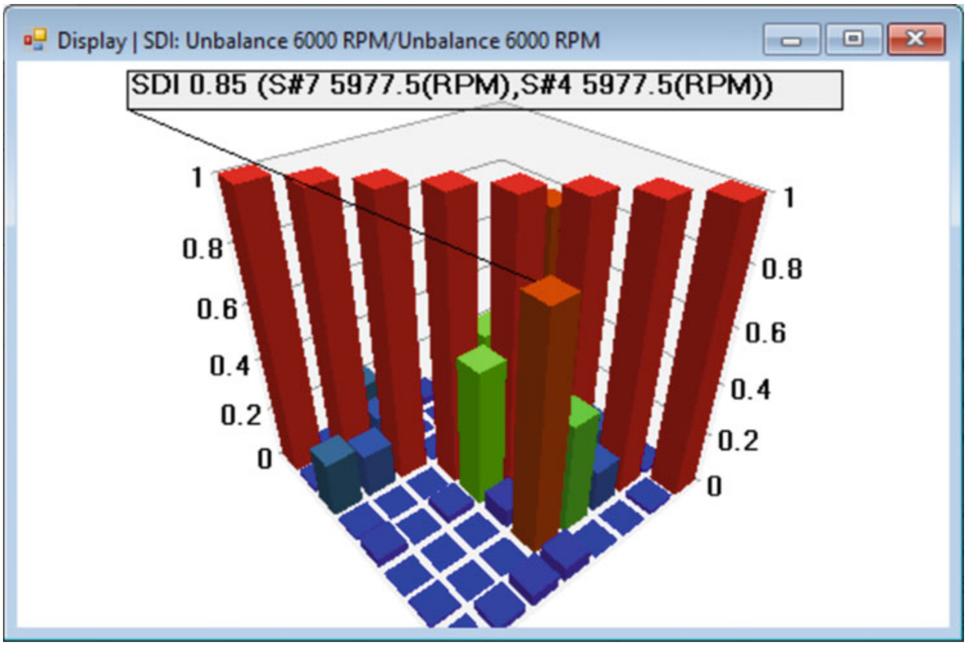

Fig. 35.9 SDI values (third order)

Another way of interpreting this is that the ***sensitivity*** of SDI becomes greater as {v} approaches zero. In order to increase the sensitivity of SDI, the vectors {u} and {v} can be replaced with the following vectors before calculating their SDI value.

$$\{\underline{v}\} = \{\text{sensitivity}\} \ \text{ where } \ (\text{sensitivity} > 0)$$

$$\{\underline{u}\} = \{u\} - \{v\} + \{\underline{v}\}$$

Replacing {u} and {v} with {u} and {v} makes the SDI calculation more sensitive to the difference between {u} and {v}.

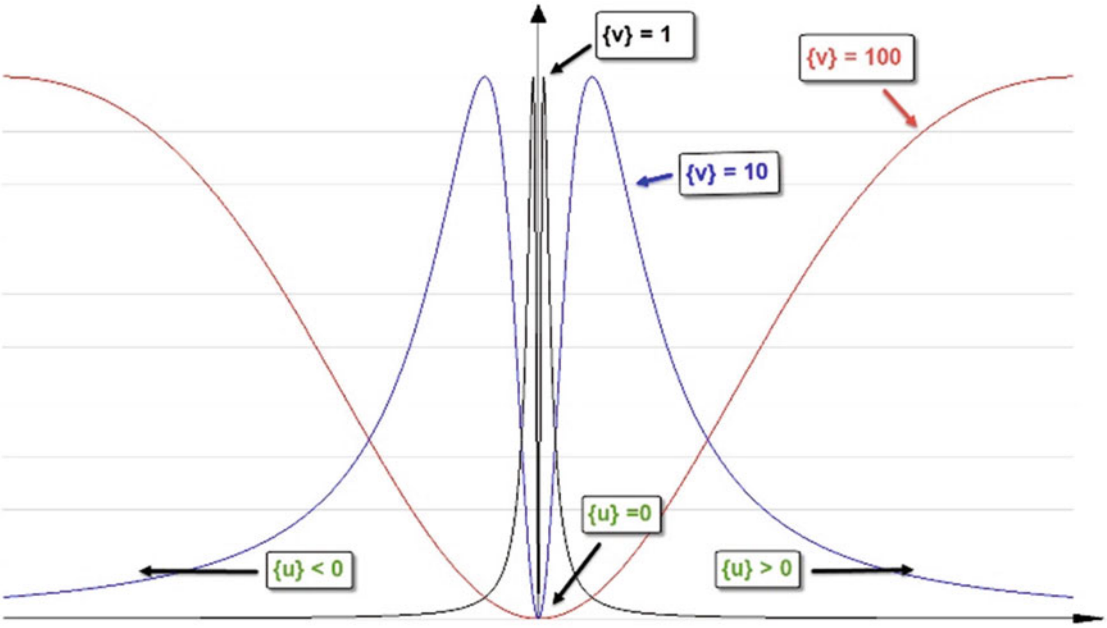

Fig. 35.10 SDI values for scalars {u} and {v}

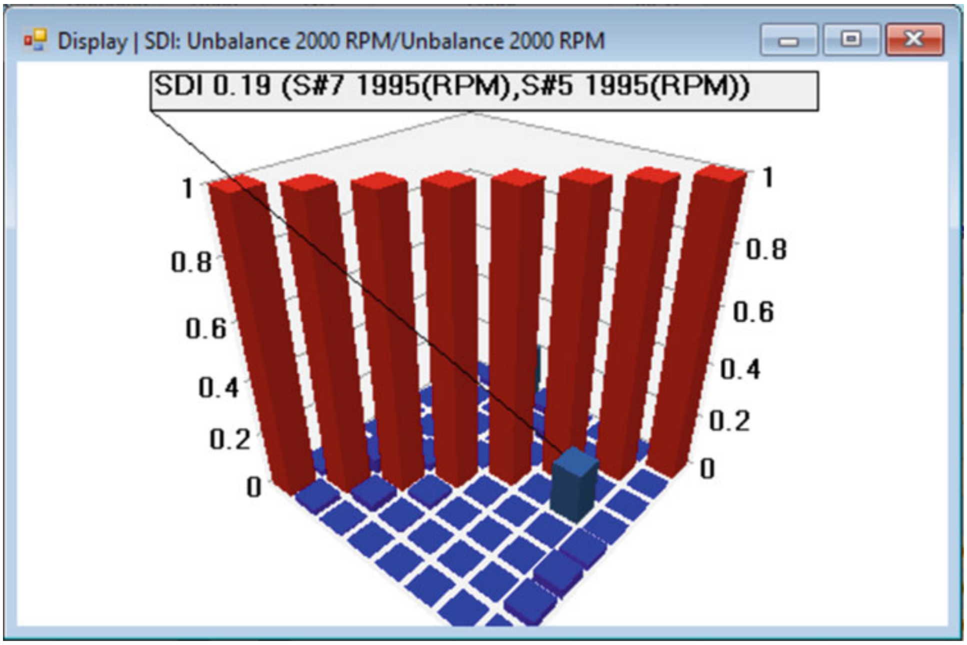

SDI 0.19 (S#7 1995(RPM),S#5 1995(RPM))

Fig. 35.11 SDI values (first order)

In order to distinguish the difference between a pair of vectors, a sensitivity should be chosen which drives their SDI value as close to zero as possible.

The following Figs. 35.11, 35.12, and 35.13 contain bar charts of the SDI values for the same order-based ODS data as Figs. 35.5, 35.7, and 35.9, but with ***sensitivity*** = **0.1**.

Figures 35.11, 35.12, and 35.13 are the graphic evidence that the SDI algorithm, with modifications to a pair of order-based ODS's to make it more sensitive to their difference, can be used as a discriminator between different unbalance conditions in a rotating machine. This algorithm has been implemented in the ME'scope software, a product of Vibrant Technology.

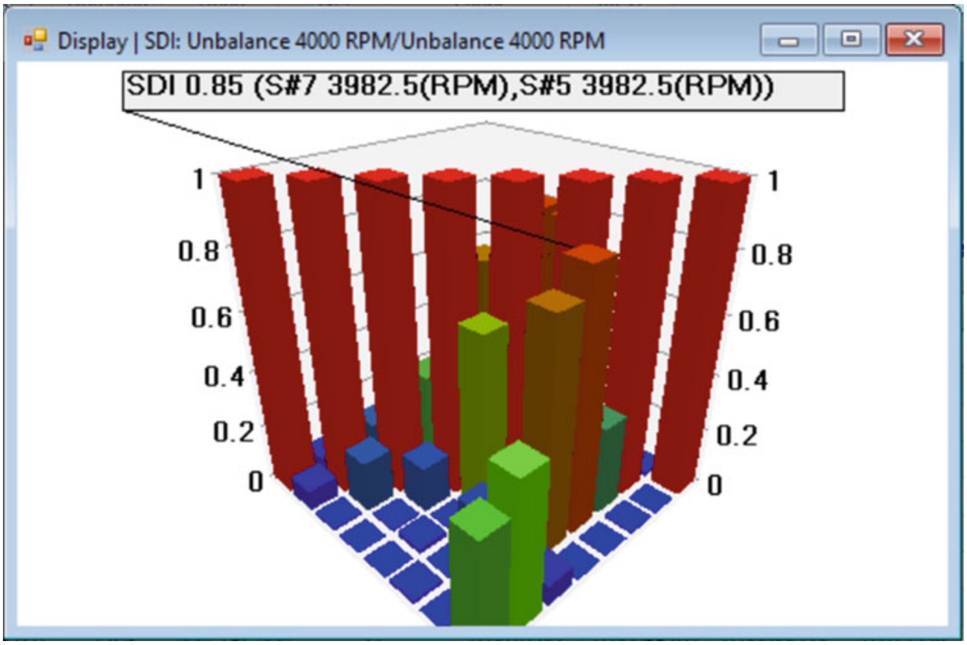

Fig. 35.12 SDI values (second order)

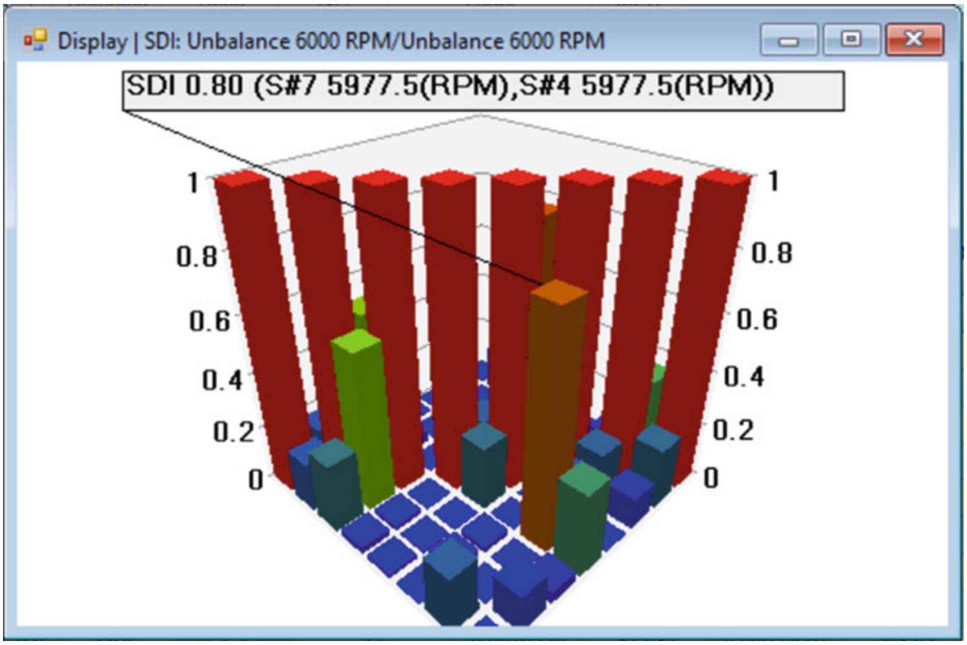

Fig. 35.13 SDI values (third order)

35.8 Fault Correlation Tools

When SDI is used together with an archival database, where archived ODS's have been associated beforehand with known unbalance conditions, SDI bars can be used to identify specific unbalance conditions. This capability has been branded as **FaCTs**™, an acronym for **Fault Correlation Tools**, in the ME'scope software.

FaCTs can be used in a number of ways as part of the post-processing software in an online machine health monitoring system. In addition to correlating current ODS data with archived data that has been associated with a known unbalance condition, FaCTs can also be used to graphically indicate any change in a machine operating condition by providing a real-time comparison of current versus baseline ODS data.

FaCTs can also be used as a pass/fail indicator as part of a qualification testing system where vibration data, or any other type of engineering data, is acquired from the machine or test article. Any type of engineering data can be added as components to a shape vector, and consequently can be used in an SDI calculation as part of FaCTs.

35.9 Conclusion

The purpose of this paper was to show that ODS data taken from the bearing blocks on a rotating machine can be post-processed to detect and identify various unbalance conditions of the machine. The idea behind this approach is to correlate currently acquired data with data that has been previously archived in a data base, and which has been associated with particular unbalance conditions.

We applied two different measures of shape correlation to the ODS data, MAC and SDI. Both measures indicate the likeness of a pair of shapes by giving values between 0 and 1. A value of 1 means that the shapes are the same, and a value less than 1 means that they are different. Both measures could be referred to as ***correlation coefficients***.

MAC indicates whether or not two shapes are ***co-linear***, lying together on the same straight line. SDI measures the ***true difference*** between two shapes. When both measures were applied to the bearing block ODS data, the SDI bar charts showed that the shape difference was stronger than shape co-linearity for discriminating between the unbalance cases. However, even SDI didn’t provide a clear distinction between all cases.

Therefore, it was also shown that the sensitivity of SDI can be increased by inputting two ***modified shapes*** to the SDI algorithm which are derived from the original shapes. By increasing its sensitivity, SDI was able to clearly discriminate between all of the unbalance conditions and the balanced condition of the rotating machine.

References

1. Ganeriwala, S.N., Schwarz, B., Richardson, M.: Using operating deflection shapes to detect unbalance in rotating equipment. In: IMAC XXVII, Orlando, February 2009
2. Richardson, S., Tyler, J., McHargue, P., Richardson, M.: A new measure of shape difference. In: IMAC XXXII, 3–6 February 2014
3. Allemang, R.J., Brown, D.L.: A correlation coefficient for modal vector analysis. In: Proceedings of the International Modal Analysis Conference, 1982
4. Allemang, R.J.: The modal assurance criterion (MAC): twenty years of use and abuse. In: Proceedings of the International Modal Analysis Conference, 2002
5. Richardson, M.: Is it a mode shape or an operating deflection shape? Sound Vibration magazine, March 1997

Chapter 36
Gear Dynamics Characterization by Using Order-Based Modal Analysis

Emilio Di Lorenzo, Antonio Palermo, Simone Manzato, Andrea Dabizzi, Bart Peeters, Wim Desmet, and Francesco Marulo

Abstract The aim of Operational Modal Analysis (OMA) is to estimate the modal parameters of a system in operating conditions. However, for the particular case of rotating machineries during run-up/run-down, it has been demonstrated that the method shows limitations because of the so-called "end-of-order effect". This is one of the main reasons why new techniques have been explored. The most promising one is Order-Based Modal Analysis (OBMA), which combines advanced Order Tracking techniques with Operational identification methods. To validate this technique, a measurement campaign has been performed on a gear test rig. The test rig has been heavily instrumented to perform the validation of the proposed methodology, combining several triaxial accelerometers on the support plates and gears with state-of-the-art angular position transducers. Firstly, Experimental Modal Analysis (EMA) has been performed to identify a reference dataset. Then, OBMA has been applied on several run-ups/run-downs. The results of modal analysis on orders from different Order Tracking techniques has been compared to those obtained by EMA, confirming that OBMA is capable of correctly evaluating mode shapes and natural frequencies of the gear test rig from operational data.

Keywords Order tracking • Operational modal analysis • Order-based modal analysis • Rotating machinery • Gears

36.1 Introduction

Rotating machinery exhibit a very complex dynamic behavior while they are operating. The main objective in a design phase is to identify the operating conditions which need to be avoided during the lifetime. On the other hand, during the normal operation, it is very important to assess the conditions of the machine in order to determine what repairs are needed without stopping or disassembly the structure. For this reason the investigation from a noise and vibration point of view must be performed even if it is a very challenging step. Several techniques have been introduced in the past years to identify with a good confidence the dynamic behavior of machines in operational conditions. The analysis could be performed in the time, frequency or order domain. Using time domain analysis allows to identify the overall vibration levels. The frequency content of the vibration signal can be determined by performing the analysis in the frequency domain so that the dominant natural frequencies can be identified. Operational Modal Analysis (OMA) is one of the most suitable techniques which allows to identify the modal parameters of a structure in a laboratory as well as in a real life environment and both for small and huge structures such as airplanes, bridges, buildings, stadiums and wind turbines. Previous studies [1, 2] have underlined the limitations of this technique in case of rotating machines. In order to overcome some of these limitations, a new technique has been proposed by combining together Order Tracking (OT) techniques and classical OMA algorithms. It allows identifying

---

E. Di Lorenzo (✉)
Siemens Industry Software, Interleuvenlaan 68, 3001 Leuven, Belgium

KU Leuven, Division PMA, Celestijnenlaan 300B, 3001 Heverlee, Belgium

Department of Industrial Engineering, University of Naples Federico II, Via Claudio 21, 80125 Naples, Italy
e-mail: emilio.dilorenzo@siemens.com

A. Palermo • S. Manzato • A. Dabizzi • B. Peeters
Siemens Industry Software, Interleuvenlaan 68, 3001 Leuven, Belgium

W. Desmet
KU Leuven, Division PMA, Celestijnenlaan 300B, 3001 Heverlee, Belgium

F. Marulo
Department of Industrial Engineering, University of Naples Federico II, Via Claudio 21, 80125 Naples, Italy

© The Society for Experimental Mechanics, Inc. 2016

J. De Clerck, D.S. Epp (eds.), *Rotating Machinery, Hybrid Test Methods, Vibro-Acoustics & Laser Vibrometry, Volume 8*,
Conference Proceedings of the Society for Experimental Mechanics Series, DOI 10.1007/978-3-319-30084-9_36

the experimental modal model of a structure with rotating parts by applying a two-steps procedure. First of all, the so-called orders are extracted and then the OMA procedure can be applied on the orders instead than on the spectra. Order domain analysis relates the vibration signal to the rotating speed of the system. In this way, vibration components that are proportional to multiples of this speed can be easily identified. The next sections will describe the implemented techniques and afterwards the gear test rig and its instrumentation will be introduced. Finally, the results will be discussed. This analysis will be mainly focusing on the test rig behavior and on how the whole structure is interacting with the gears. In the future, the rotating accelerometers mounted on the gears will be included in the analysis and their signals will be processed in order to have some more insights into gear dynamics.

36.2 Order Tracking Techniques

Order tracking is the estimation of the amplitude and phase of the response of a machine to a referenced rotating components that is allowed to vary in amplitude and frequency over the time. Regardless of the method used for performing the order tracking step, the most important channel is the tachometer signal which can be measured directly or generated virtually by using a response channel. Since the response amplitude and phase estimation of an order is referenced to a rotating component, it is obvious that the accuracy of the estimation is strictly dependent on the accuracy of the tachometer signal. Several techniques for extracting the orders can be found in the literature [3]. The Fourier transform methods are based on time domain data sampled with a constant time interval Δt. The two main assumptions of these methods are that the data has constant frequency across the length of the data block and that also amplitude and phase are constant across the same data block. The effect of variations will be reflected in the presence of leakage into the transform. The evolution of these methods into the first computed order tracking method was developed and patented by Potter at Hewlett Packard [4]. This method is based on the resampling of the data from the time domain to the angle domain which means from data with constant Δt to data with constant angular spacing $\Delta\theta$. The Fourier transform is applied to the angle domain data to transform it into the order domain data. Orders that sweep through several frequencies in the frequency domain will be constant in the order domain allowing a leakage free amplitude and phase estimation. This is true only if the estimation is performed over an integral number of revolutions.

Some more methods for extracting orders have been implemented. In this paper two methods have been used and a comparison with the classical techniques have been performed. The first method was proposed by Blough [5] and it has been named Time Variant Discrete Fourier Transform (TVDFT) method. It is defined as a discrete Fourier transform with a kernel that allows the frequency to vary in time, but amplitude of the data is assumed to remain constant across the data block. Also TVDFT allows a leakage free estimates of orders, but there is no need to resample the data from time to angle domain which allows the technique to be much less computational demanding and suitable for real-time processing. Borghesani [6] proposed the velocity synchronous discrete Fourier transform (VSDFT) for order tracking in the field of rotating machinery and compared its performances with the ones of TVDFT underlining advantages and drawbacks of the two methods. A method developed as a post-processing technique has been named Vold-Kalman filter since it was developed by Vold and Leuridan as an extension of the classical Kalman filter [7]. It requires information about "future" data points when estimating an order and it allows extracting close and crossing orders. Another method developed for post-processing purposes is the Gabor transform which has been compared to the Vold-Kalman filter and to other techniques as well [8].

36.2.1 Angle Domain Computed Order Tracking (AD)

A very well-known order tracking method which is widely used in commercial software is based on the angular resampling procedure. Data are acquired with a uniform Δt and then resampled to the angle domain through the use of an adaptive digital resampling algorithm. The final result of the technique is that uniform Δt data become uniformly spaced angle data. Estimates of amplitude and phase of the orders are obtained by processing these data by means of a Discrete Fourier Transform (DFT) instead of a FFT for computational flexibility in performing the transform without being restricted to a power of two samples. In order to perform the transformation from time domain data to angle domain data, a reference signal has to be identified to define the instant of time in which the uniform angular intervals have been spaced. Typically, this signal is considered to be the tachometer signal measured on a reference shaft of the operating machine. The kernels of the Fourier transform are reformulated as shown in Eq. (36.1) where o_m is the order which is being analyzed.

$$
\begin{aligned}
a_m &= \frac{1}{N}\sum_{n=1}^{N} x(n\Delta\theta)cos(2\pi o_m n\Delta\theta) \\
b_m &= \frac{1}{N}\sum_{n=1}^{N} x(n\Delta\theta)sin(2\pi o_m n\Delta\theta)
\end{aligned}
\tag{36.1}
$$

The advantages of the resampling based order tracking are leakage free estimates of orders which fall on spectral lines as well as an order resolution which is constant in terms of width. On the other hand this method has several restrictions. Orders may only be tracked with reference to one rotating shaft and it is very difficult to distinguish among orders which cross one another. Another limitation is due to the finite defined order resolution which makes very difficult the analysis of orders which do not fall on a spectral line.

36.2.2 *Time Variant Discrete Fourier Transform (TVDFT)*

The Time Variant Discrete Fourier Transform (TVDFT) method gives results very similar to the method presented in the previous section, but with less computational efforts. It is based on a Fourier transform kernel whose frequency can vary with time. The main advantage of this method is that it does not require the transformation from the time domain to the angle domain. The TVDFT is based on kernels in which the sine and cosine functions have unity amplitude and an instantaneous frequency matching that of the tracked order at each instant in time, as shown in Eq. (36.2).

$$
\begin{aligned}
a_m &= \frac{1}{N}\sum_{n=1}^{N} x(n\Delta t)cos\left(2\pi\int_0^{n\Delta t}(o_m * \Delta t * rpm/60)dt\right) \\
b_m &= \frac{1}{N}\sum_{n=1}^{N} x(n\Delta t)sin\left(2\pi\int_0^{n\Delta t}(o_m * \Delta t * rpm/60)dt\right)
\end{aligned}
\tag{36.2}
$$

The formulation can be extended for separating close and crossing orders through a secondary calculation. There can be a leakage error using the TVDFT with constant Δt sampled data because it is not guaranteed that the integer revolution values required for a constant order bandwidth analysis will fall on a Δt. If it is not the case, it will lead to a leakage error by performing the transformation over a non-integer number of revolutions. This error can be reduced by oversampling the data which means by providing a finer Δt. This method contains most of the advantages of the resampling based order tracking and it can be implemented in a very efficient manner without having the computational load and complexity of the transformation from the time domain to the angle domain.

36.2.3 *Vold-Kalman Filter Based Order Tracking (VK)*

Vold and Leuridan introduced an algorithm for high resolution, slew rate independent order tracking. The Vold-Kalman (VK) algorithm is based on the concepts of Kalman filter and it allows tracking multiple orders at the same time and it is able to decouple close and crossing orders. This method extracts the time history of the order as well as the estimate of the amplitude and the phase of the same order. Similarly as the Kalman filter is based on the process and measurement equations, the VK filter is based on the structural and data equations. The structural equation is an equation that describes the mathematical characteristics of the order to be extracted. It uses the information from the tachometer signal and it describes a sine wave whose frequency and amplitude is constant over three consecutive time points. In order to take into account the variations from a perfect sine wave over the time samples involved, the unknown non-homogeneity term $\varepsilon(n)$ is introduced on the right side of Eq. (36.3).

$$
x(n) - 2cos(\omega\Delta t)x(n-1) + x(n-2) = \varepsilon(n) \tag{36.3}
$$

where $x(n)$ represents the n-th discrete time sample and ω is the instantaneous frequency of the sine wave. The second equation on which the Vold-Kalman filter is based on is the so-called data equation and it is shown in Eq. (36.4). It describes the relationship between the order $x(n)$ and the measured data $y(n)$. Normally the measured data is a combination of all the orders generated from the machine and other random noise present in the data. The random noise and non-tracked orders are combined into the signal $\eta(n)$.

$$y(n) = x(n) + \eta(n) \tag{36.4}$$

A weighted solution can be obtained by introducing the Harmonic Confidence Factor (HCF) r. The value of this parameter is what determines the tracking characteristics of the filter. It is calculated, as shown in Eq. (36.5) as the ratio between the standard deviations of the structure and data equations.

$$r(n) = \frac{s_{\varepsilon}(n)}{s_{\eta}(n)} \tag{36.5}$$

The choice of a large value for the weighting factor r leads to a highly selective filtration in the frequency domain, while by choosing r small the resolution in frequency is very small, but a fast convergence in amplitude can be obtained. Applying the ratio as a weighting function and combining together the two equations, the set of linear equations shown in Eq. (36.6) is obtained.

$$\begin{bmatrix} 1 & -2cos(\omega\Delta t) & 1 \\ 0 & 0 & r(n) \end{bmatrix} \begin{bmatrix} x(n-2) \\ x(n-1) \\ x(n)) \end{bmatrix} = \begin{bmatrix} \varepsilon(n) \\ r(n)y(n) - \eta(n)) \end{bmatrix} \tag{36.6}$$

Applying Eq. (36.6) to all observed time points will give a global system of over determined equations for the desired waveform $x(n)$ which may be solved by using standard least squares techniques such as normal equations or the singular value decomposition. For the purpose of order tracking, the filtered waveform is most conveniently described in terms of amplitude and phase with respect to a reference channel such as the tachometer channel.

36.3 Order-Based Modal Analysis

Operational Modal Analysis (OMA) algorithms, such as Operational Polymax [9], allows the identification of the modal parameters of a structure by taking into account only operational measurements. Previous studies have demonstrated that the classical OMA has some drawbacks when it has to be applied in the rotating machinery field. Some of the peaks in the overall spectrum are originated from order components that suddenly stop at the maximum rpm. These components are identified as poles, while they are not physically present in the system. They have been named “end-of-order” related poles. Order-Based Modal Analysis (OBMA) estimates the modal parameters of a structure during a run-up or a run-down test by applying the curve fitting algorithms to the extracted orders instead than to the overall spectra. It can be assumed that the measured responses are mainly caused by the rotational excitation. Run-up and run-down can be assimilated to multi-sine sweep excitation in the frequency band of interest. Several observations need to be taken into account for applying the same OMA algorithms to the orders:

1. Displacement orders are proportional to the squared rotation speed and acceleration orders are proportional to the forth power of the same rotation speed. The main difference is that in the classical modal analysis the acceleration FRFs are proportional to the squared frequency axis.
2. Complex upper and lower residuals, while in classical modal analysis they are real.
3. Complex participation factor both in classical modal analysis and in order-based modal analysis.

Methods such as Operational Polymax are robust again these observations and they can be employed for estimating the modal parameters in case of rotating machineries by looking at the orders rather than at the spectra. Compared to other applications of order tracking, OBMA requires that the orders are calculated with respect to a reference signal $\Theta(t)$ which is synchronous with the excitation coming from the rotating source. This signal has been chosen as a sine sweep with frequency equal to the instantaneous rotational speed $\omega(t)$ of the machine multiplied by the order o_m which is being extracted, as shown in Eq. (36.7).

$$\Theta(t) = cos\left(\int_0^T o_m * \omega(t)dt\right) \tag{36.7}$$

36.4 Test Rig Description

The technique has been validated by considering a numerical example. In this paper a dedicated test rig has been used for performing an experimental validation and for evaluating the performances of the order tracking techniques available in commercial software and of the ones implemented in a Matlab environment. The test rig has been built for simulating different working conditions for the gears at a subsystem level without any other influence coming from the interaction with other systems [10]. A very precise and highly instrumented device is needed in order to get reliable results. Only a few precision gear test rig have been used for research so far. Figure 36.1 shows the CAD model of the test rig which has been used in our studies. It is composed by two main parts: the test side, which is dedicated to testing a cylindrical gear pair, and the reaction side, that is needed for retaining a torque preload in the system by means of a second gear pair. Its specification are reported in Table 36.1.

The test rig is mounted on a concrete base suspended on air springs which allows to isolate the overall system and separate the two sides for avoiding the propagation of stray vibrations between them. Such vibrations are damped through the concrete. A temperature-controlled pressurized lubrication system feeds oil to the test and the reaction side bearings and gears. High-precision spherical roller bearings are chosen to support test gears and maximize stiffness. Several different gears are used for the test side and they provide a very repeatable meshing excitation due to two main reasons: the gear ratio is equal to 1 and gears are precision ground to ISO 1328 Quality 3 standard. Furthermore, test gears and reaction gears are designed to have different tooth number to be able to distinguish the excitation belonging to each gear pair. Test gears have 57 teeth, while reaction gears have 64. Angular misalignment in an arbitrary plane and parallel misalignment in the transverse plane can be imposed thanks to the bearings: they are mounted in eccentric caps that can be turned to orient the eccentricity at a given angle. Same angles for the two caps on the same shaft result in imposing a parallel misalignment, while opposite angles result in imposing angular misalignment.

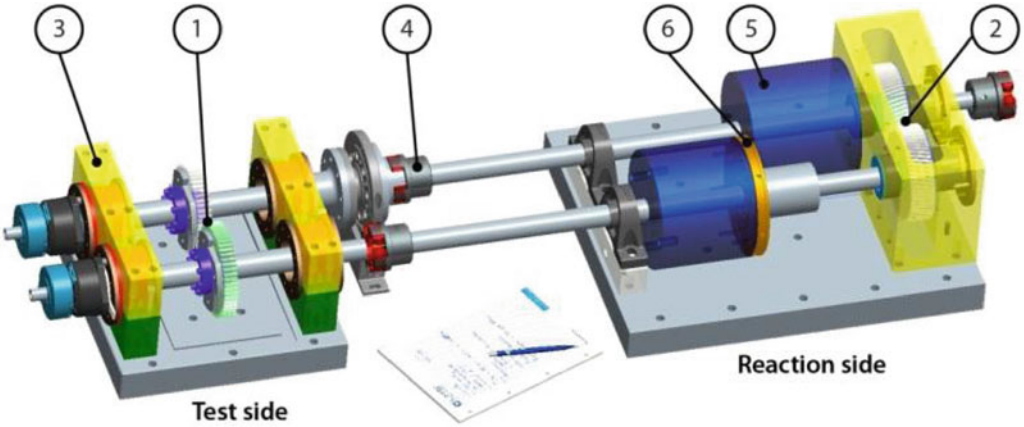

Fig. 36.1 Test rig three-dimensional representation. 1. Test gears; 2. Reaction gears; 3. Bearings support plates; 4. Flexible couplings; 5. Flywheel; 6. Clutch flange for preload

Table 36.1 Test rig specifications

Parameter	Range	Uncertainly
Speed	0–4500 rpm (0–75 Hz)	Measured
Torque	0–500 Nm	0.05 %
Angular misalignments	0–2 mrad	0.1 mrad
Parallel misalignments	0–0.3 mm	0.020 mm

36.5 Results

First of all, Experimental Modal Analysis (EMA) has been performed for characterizing the dynamic behaviour of the system in a considerably large frequency band [11]. Afterwards, the results of EMA has been used as baseline for comparing with the ones obtained by performing Order-Based Modal Analysis (OBMA).

36.5.1 Experimental Modal Analysis

The whole structure has been instrumented by means of several three-axial accelerometers placed along the test rig. The signals have been acquired by using the LMS SCADAS acquisition system in a master-slave configuration as shown in Fig. 36.2. An electro-dynamic shaker was used as source of excitation. The excitation has been applied on the clamping point of one of the gears, with the shaker acting in a direction parallel to the line of action as shown in Fig. 36.2. In this way the force has been applied exactly in the same direction of the gear contact force which is the main source of excitation in the structure.

To excite the structure, a chirp signal from 20 to 8 kHz with 5 N amplitude and a duration of 1 min was selected. The selection of the positions of the accelerometers is resulting from a trade-off between the necessity to have a high spatial resolution in order to get the mode shapes of the structure especially at high frequencies and the complexity of a measurement with a high number of sensors. In order to cover the complete measurement grid, several runs have been performed by shifting the location of most of the accelerometers and leaving the reference ones in the same place as phase references. Figure 36.3 shows the accelerometers locations along the test rig. In order to check the repeatability of the measurements among different runs, the Frequency Response Functions (FRFs) coming from the same accelerometer and the same measurement point, but from different runs, have been superimposed and shown in Fig. 36.4. The curves are almost perfectly overlapped showing that the system response was not affected by the fact that most of the accelerometers were moved from a location to another one. Afterwards, EMA has been performed considering all the measured channels together. Polymax algorithm has been used for estimating the modal model of the whole structure in stand-still conditions. The frequencies and damping ratios are shown in Table 36.2, while Fig. 36.5 shows the comparison between a measured FRF and the correspondent synthesized one. An example of a mode shape involving the whole structure is finally shown in Fig. 36.6.

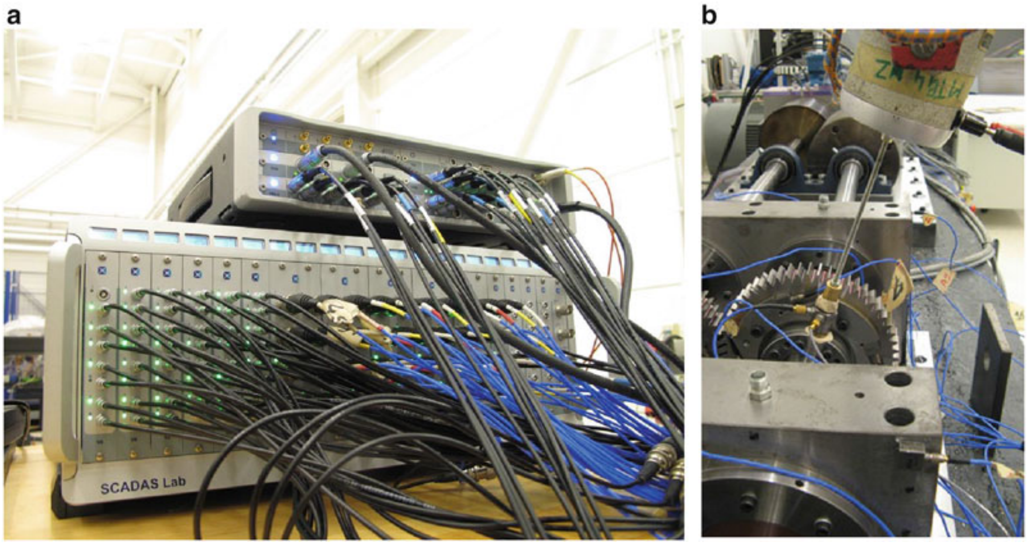

Fig. 36.2 Test rig instrumentation. (**a**) SCADAS acquisition system. (**b**) Shaker excitation

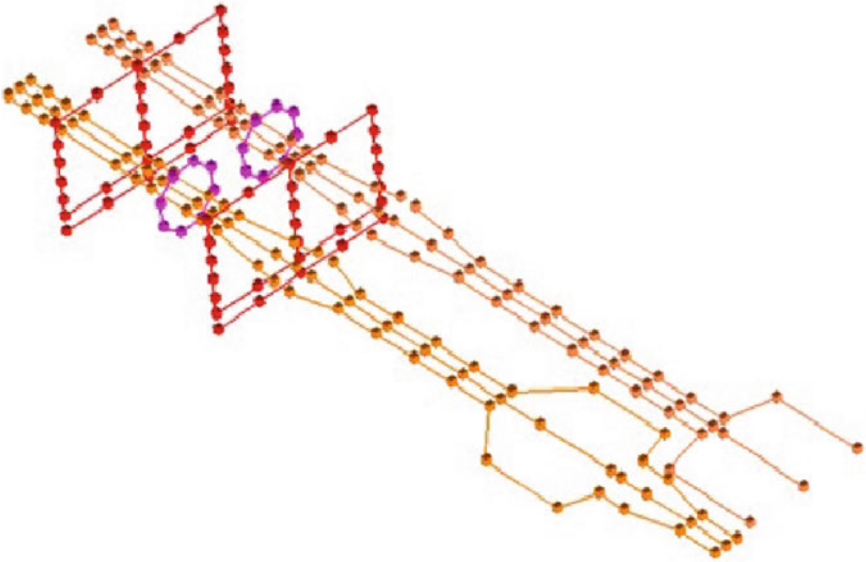

Fig. 36.3 Accelerometers locations along the test rig

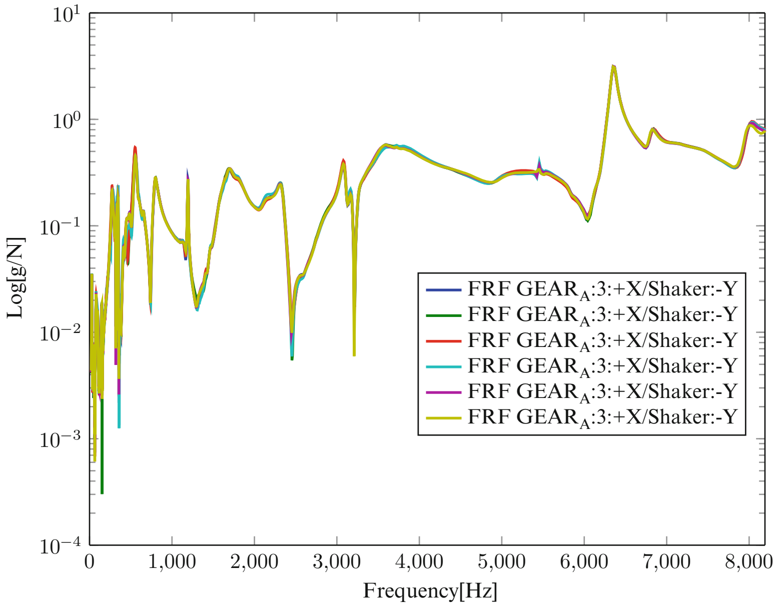

Fig. 36.4 Frequency response function (FRF) superposition for several runs

36.5.2 *Order-Based Modal Analysis: Order Tracking Step*

The identified EMA mode set has been chosen as reference data set to be compared with the results of the Order-Based Modal Analysis (OBMA) both using the classical Angle Domain Order Tracking (AD) as well as the Time Variant Discrete Fourier Transform (TVDFT) and Vold-Kalman filter Order Tracking (VK) described in Sects. 36.2.2 and 36.2.3. In this case 35 accelerometers have been used for instrumenting the test rig of which 22 were placed on the plates housing the bearings, 6 were placed on the gears and 7 on the reaction side. The accelerometer locations are shown in Fig. 36.7. As first step, in order to validate the procedure, the rotating accelerometers and the reaction side ones will not be considered in the following discussion. Several run-up and run-down experiments have been performed with varying speed rate and torque level.

Table 36.2 EMA—modal parameters identification

No.	Natural frequency [Hz]	Damping ratio [%]	No.	Natural frequency [Hz]	Damping ratio [%]
1	253.9	1.55	11	650.4	2.07
2	274.7	2.40	12	792.9	3.03
3	300.2	2.64	13	1191.8	0.17
4	329.2	2.11	14	1467.1	1.35
5	346.7	0.55	15	1637.7	1.22
6	409.1	2.39	16	1795.8	3.25
7	432.9	2.42	17	2135.5	2.25
8	449.1	2.47	18	2360.1	0.72
9	488.7	3.79	19	2746.7	0.26
10	557.8	2.86			

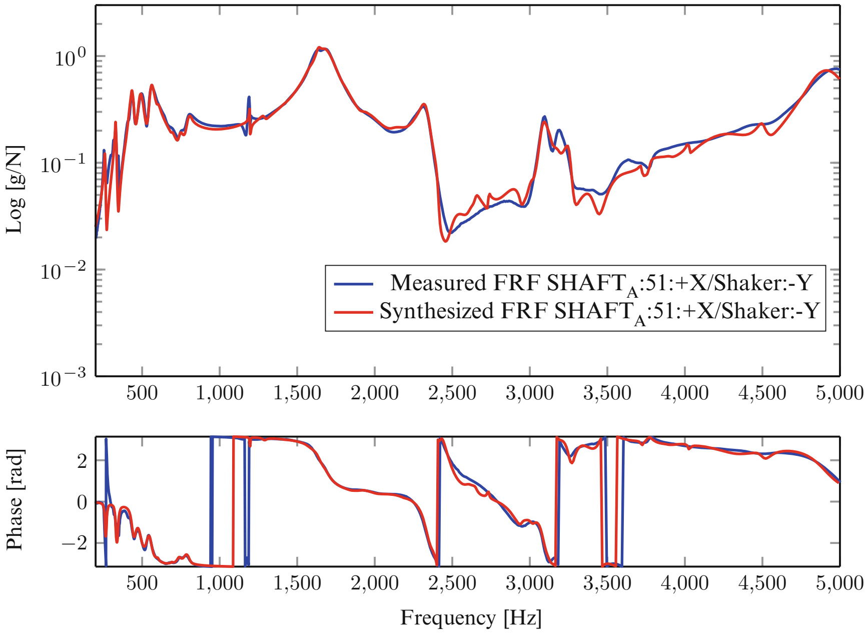

Fig. 36.5 Measured FRF vs. synthesized FRF

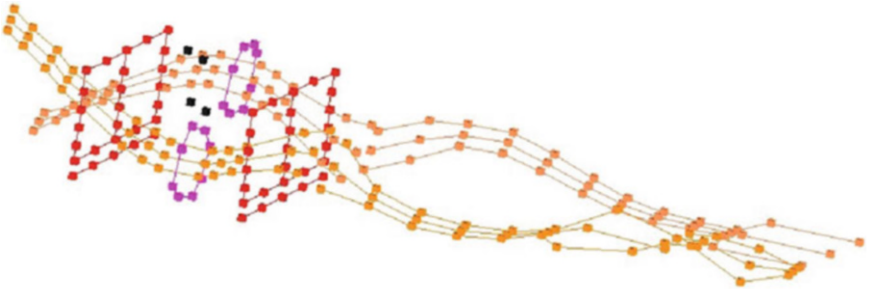

Fig. 36.6 Mode shape involving the whole structure

First of all, the standard technique (AD) has been used for extracting the orders. Some considerations can be done regarding the choice of the reference channel. Figure 36.8 shows that it is very important to choose a reference channel for applying a modal parameter estimation technique to the orders. If no reference channel is chosen when calculating the orders, their phase will look random (green curve), whereas of course the estimation of the amplitude is not affected at all. Figures 36.9 and 36.10 confirm that the reference channel must be chosen as shown in Eq. (36.7) by taking into account the order o_m that is being extracted from the data.

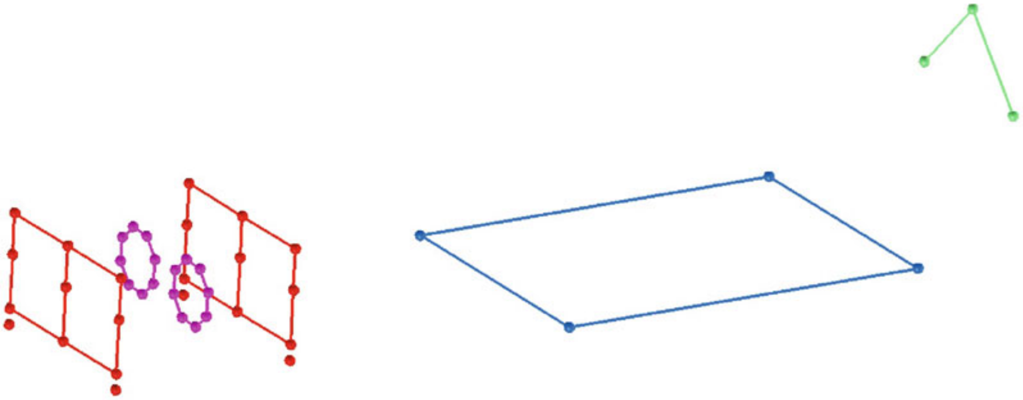

Fig. 36.7 Test rig OBMA

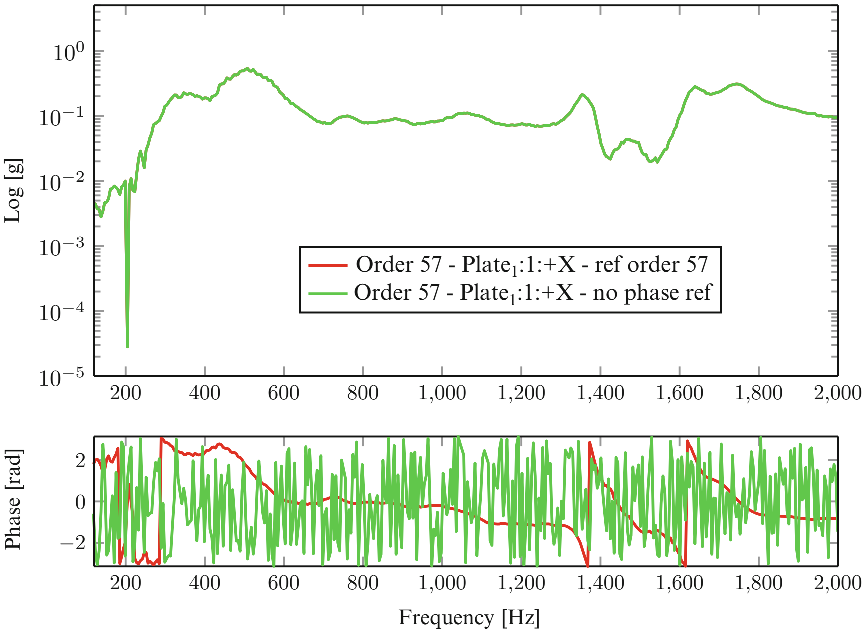

Fig. 36.8 Order 57 extracted with (*red*) and without (*green*) phase reference

Several parameters need to be set before extracting the orders. The two main parameters in this case are the rpm increment and the order resolution. As shown in Fig. 36.11, the order estimation is much more sensitive to the latter than to the former. In fact, Fig. 36.12 shows that, by varying the order resolution, the extracted order becomes very noisy. Finally, a rpm step equal to 5 and an order resolution equal to 0.2 have been chosen for comparing the orders with the other methods.

For what concern the Time Variant Discrete Fourier Transform (TVDFT) algorithm, only one parameter needs to be set and it is the number of revolutions n_{rev} to be taken into account in the data processing. Figure 36.13 compares three different values of this parameter (1, 2, 10). It can be noticed that by increasing the number of revolutions, the orders are estimated by taking into account less points. On the other hand, by decreasing the parameter value, the estimation becomes much coarser. For the following comparison with the other techniques a value equal to 2 has been chosen. Finally, the Vold-Kalman filter order tracking algorithm has been applied to the same data set. The results are shown in Fig. 36.14 for different values of the bandwidth of the filter which is the main parameter to be defined together with the number of filter poles. By increasing the bandwidth from 1 Hz to 5 Hz the orders improve their quality, but also the computational time increases significantly. A good compromise, in this case, is a bandwidth value equal to 3 Hz. Up to now only a fixed bandwidth for all the frequencies have been implemented, but in the future it will be possible to define several values for the bandwidth along the frequency axis. This should lead to further improvements of the results. Once the parameters have been set and the orders extracted by using the three different techniques, the results can be compared in Fig. 36.15. The first thing that can be noticed is that

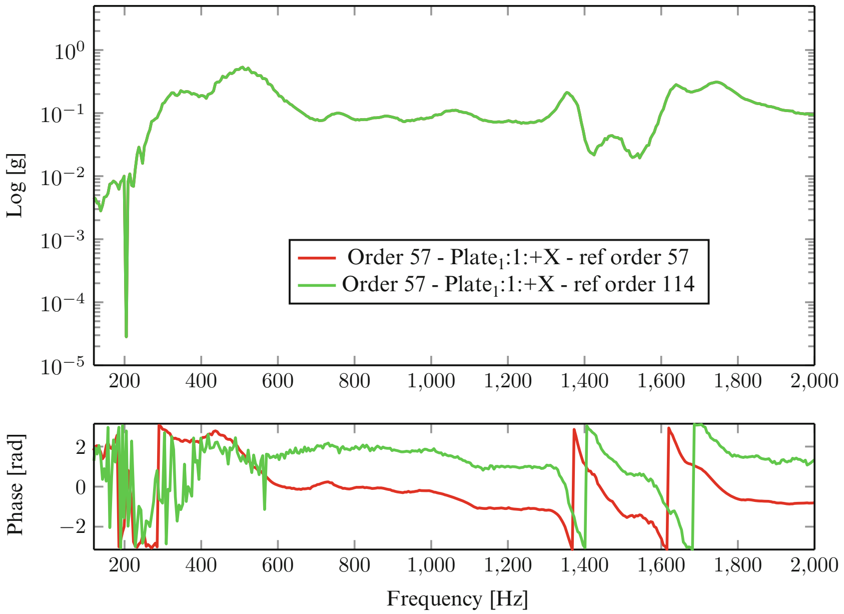

Fig. 36.9 Order 57 extracted considering Order 57 as phase reference (*red*) and Order 114 as phase reference (*green*)

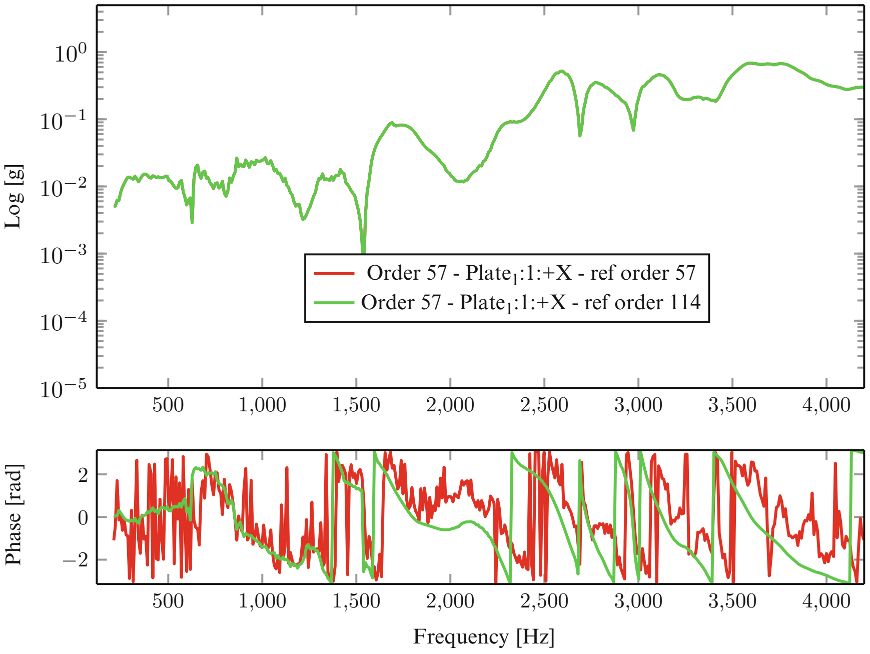

Fig. 36.10 Order 114 extracted considering Order 57 as phase reference (*red*) and Order 114 as phase reference (*green*)

in the amplitude estimation, the smoother curve is obtained by applying the VK algorithm. The number of lines are equal to the number of acquired samples because the time histories of the orders are being extracted. The phase behavior is very clear even at low frequencies, while the other methods have some difficulties in identifying both the amplitude and the phase at these frequencies. The AD method underestimates the amplitude with respect to the other methods, in particular at low frequencies. The TVDFT technique is able to identify quite well the behavior at high frequencies, but the resolution at low frequencies is quite low. The smoothness of the phase depends strongly on the number of rotation per order line. It causes some problems when a curve fitting algorithm is going to be applied for identifying a modal model on the orders.

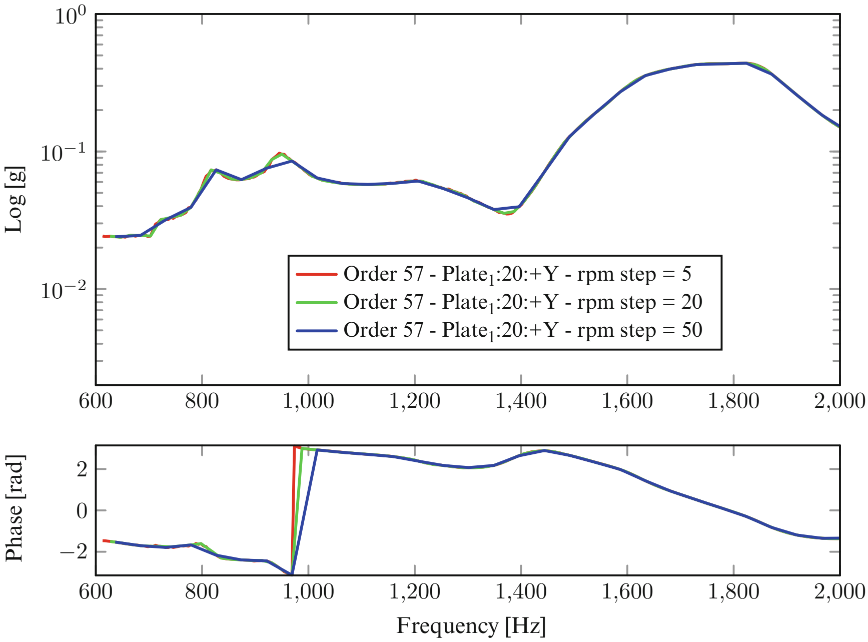

Fig. 36.11 Order 57 extracted by considering three different rpm steps

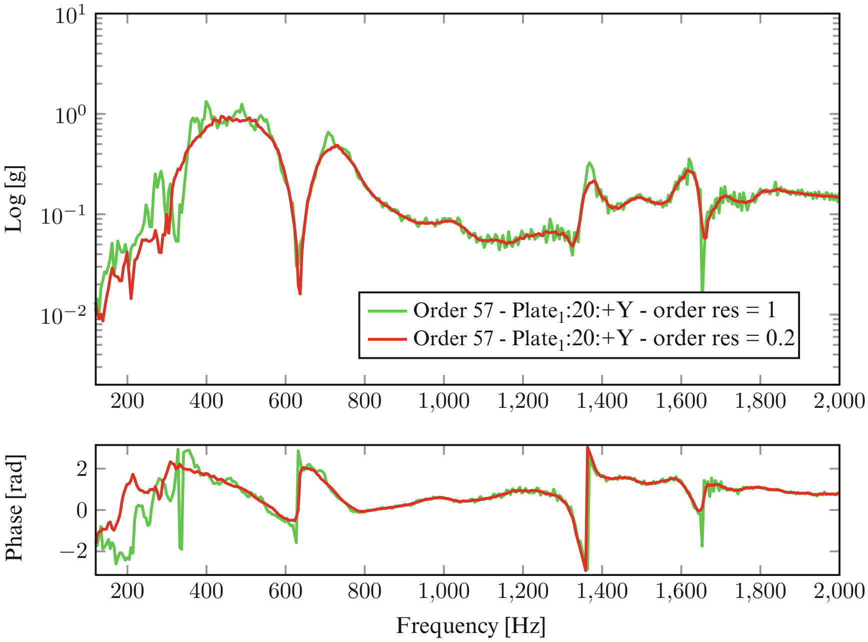

Fig. 36.12 Order 57 extracted by considering two different values for the order resolution

36.5.3 Order-Based Modal Analysis: Operational Modal Analysis Step

The final step of the OBMA procedure is the application of Operational Polymax to the extracted orders. Results in terms of modal parameters (natural frequencies, damping ratios and mode shapes) and modal synthesis can be compared for establishing which is the best order tracking technique for modal analysis purposes. Figure 36.16 shows the stabilization diagram obtained by taking as input the orders obtained by using the AD procedure. Figures 36.17 and 36.18 are obtained by taking into account the TVDFT and VK orders. By applying the VK algorithm, smoother curves could be obtained and some more stable column of poles could be identified.

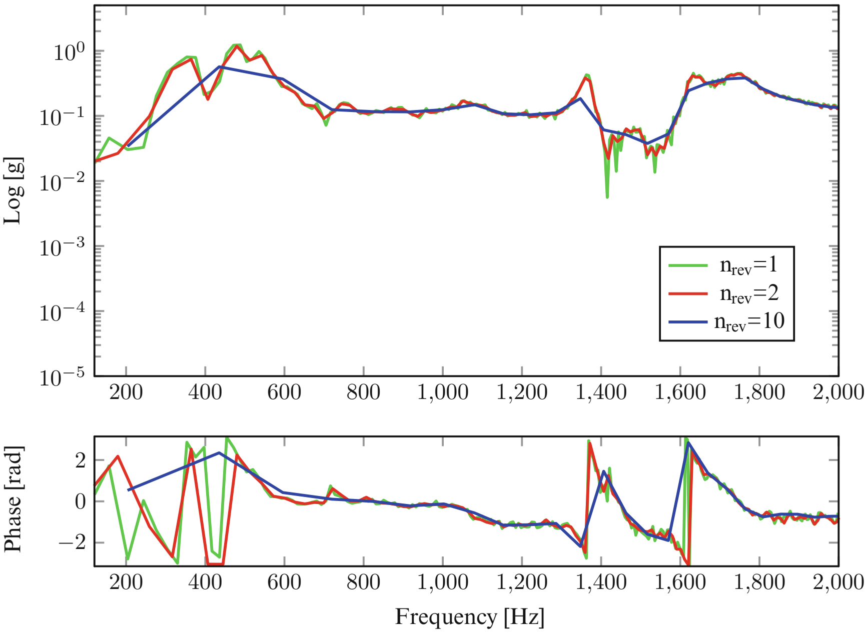

Fig. 36.13 Order 57 obtained by applying the TVDFT algorithm and choosing three values for the parameter n_{rev}

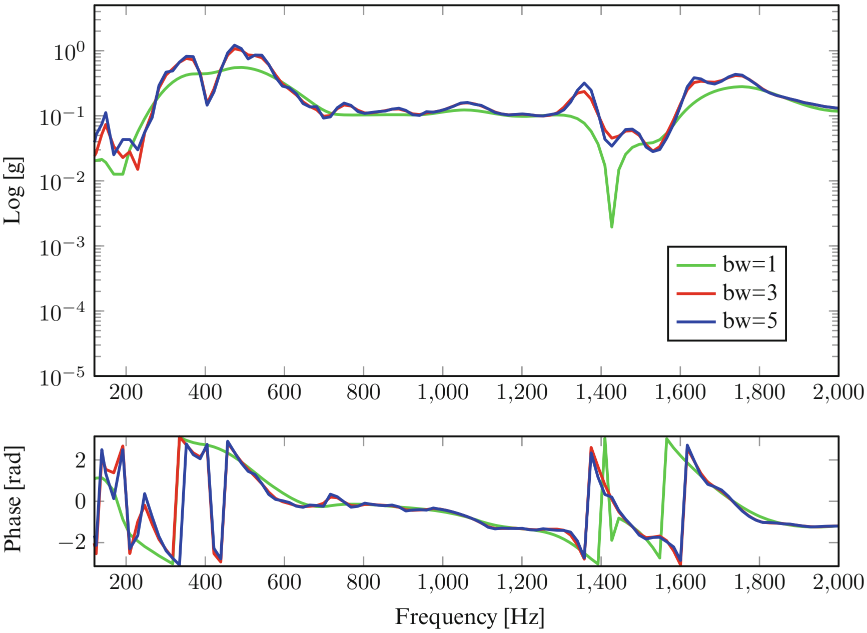

Fig. 36.14 Order 57 obtained by applying the Vold-Kalman algorithm and choosing three values for the bandwidth *bw*

Finally, the modal parameters are listed in Table 36.3 for the three cases and some examples showing how the synthesized models look like in the three different cases are illustrated in Fig. 36.19, 36.20 and 36.21. From Table 36.3, it can be noticed that when OBMA is applied to the Vold-Kalman orders, much more modes can be identified. The difference is mainly due to low frequency modes which are not identified by the other techniques. When a mode is identified from all of techniques, the values of natural frequencies and damping ratios are both quite consistent. The last two figures, Figs. 36.22 and 36.23 represent the Modal Assurance Criterion (MAC) for the three different mode sets. The consistency among the estimated modal models can be demonstrated by the high value of the MAC and by its almost perfect diagonal behavior.

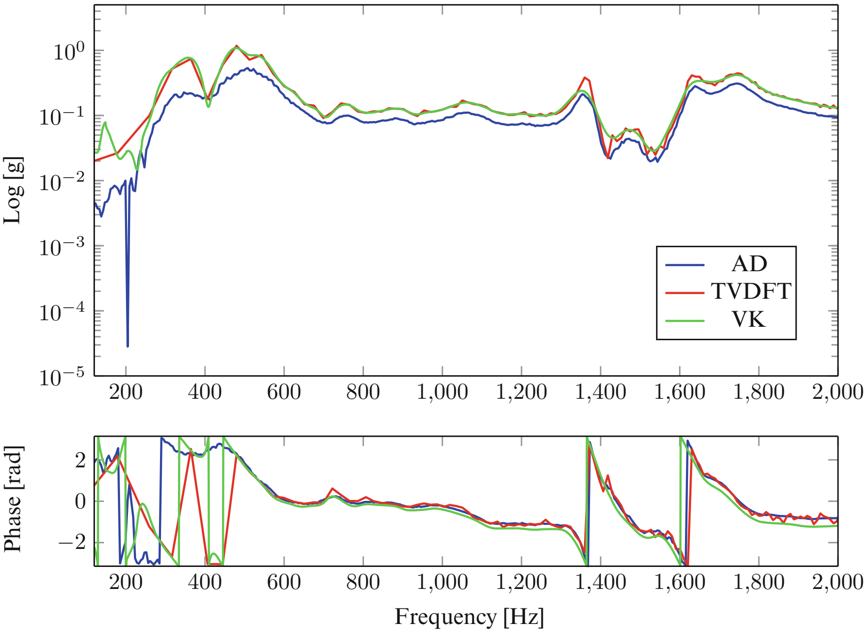

Fig. 36.15 Orders comparison among the three order tracking techniques

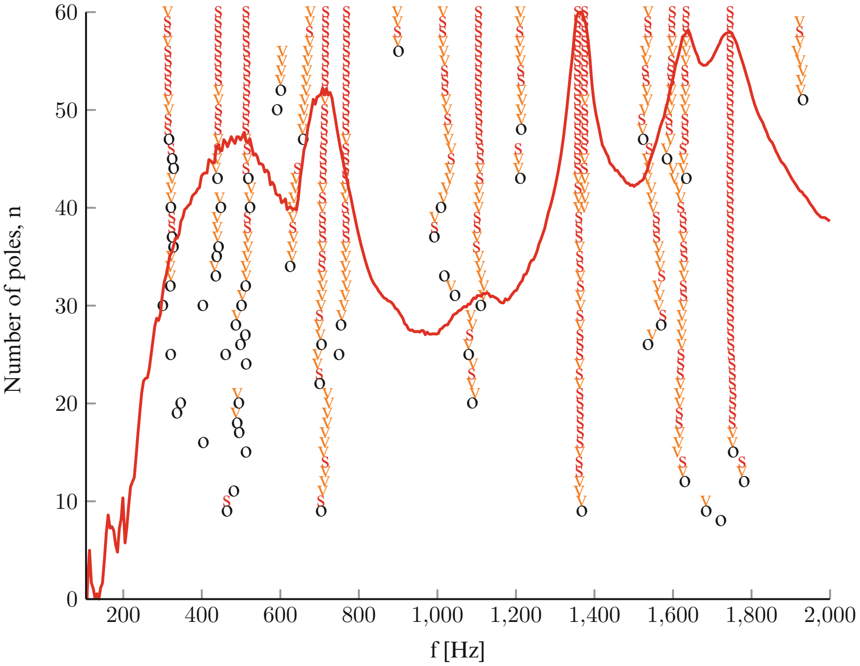

Fig. 36.16 Stabilization diagram obtained by applying Operational Polymax on the Angle Domain computed orders

36.6 Conclusions

The problem of estimating a modal model of a structure with many rotating parts has been assessed by using a dedicated gear test rig. The basic idea is to perform Operational Modal Analysis (OMA) on orders instead than on the spectra. The feasibility of this method has been explored by taking into account three different order tracking techniques. Orders were extracted from the time histories and Operational Polymax has been used to fit a modal model. The performances of the order tracking techniques have been deeply explored by analyzing advantages and drawbacks of all of them. Finally, by looking at the estimated modal models and at the quality of the fit as well as at the MAC values, it can be stated that the

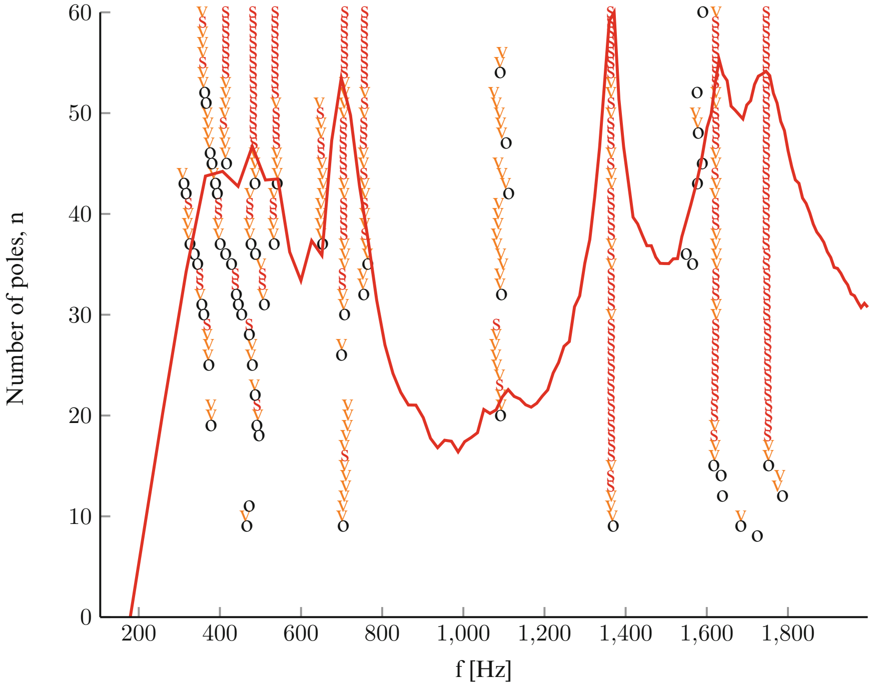

Fig. 36.17 Stabilization diagram obtained by applying Operational Polymax on the Time Variant Discrete Fourier Transform orders

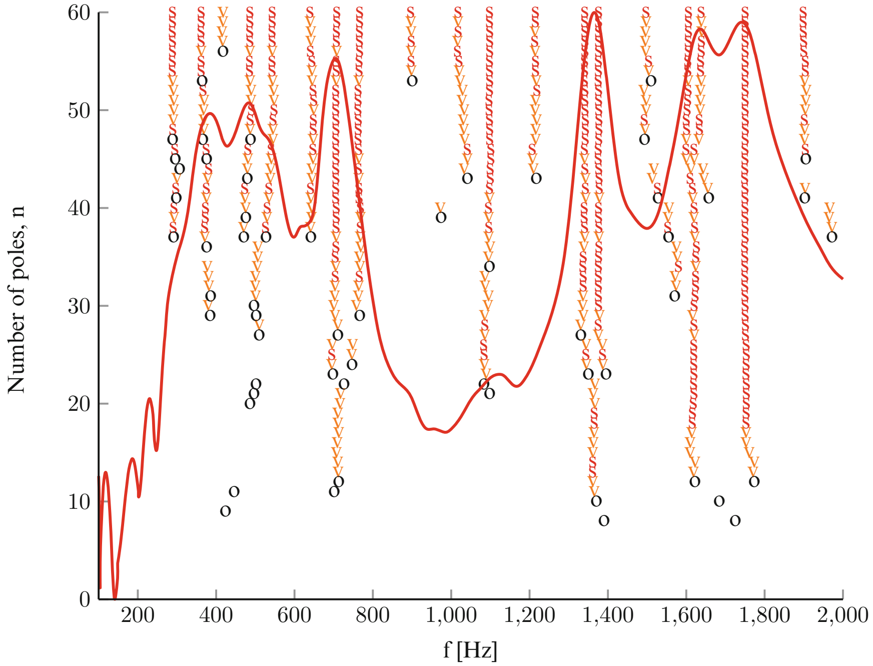

Fig. 36.18 Stabilization diagram obtained by applying Operational Polymax on the Vold-Kalman orders

best technique for performing Order-Based Modal Analysis is given by extracting the order by means of the Vold-Kalman filter order tracking. Further studies will be conducted by using the same test rig by considering both run up and run down cases with different speed rates and for several levels of applied torque. Another aspect which will be analyzed in the future is the integration of fixed accelerometers (on the plates) and rotating accelerometers (on the gears) in order to get some more insights into gear dynamics.

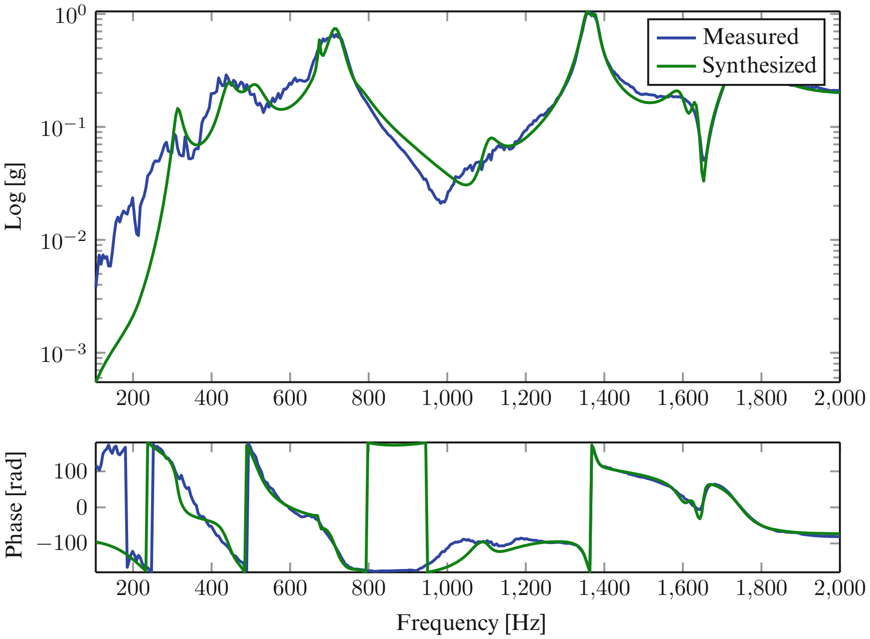

Fig. 36.19 Measured order vs. synthesized order (AD)

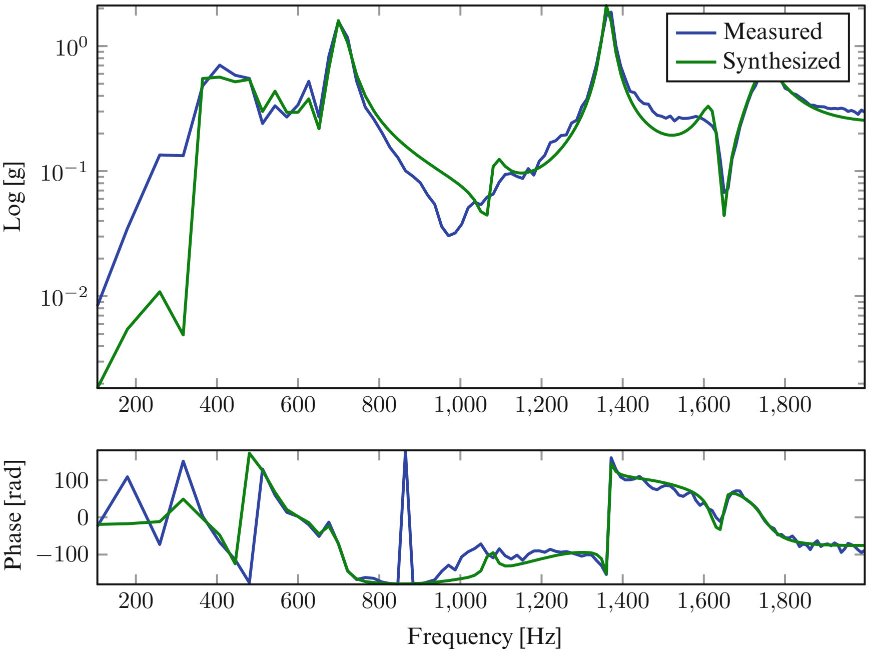

Fig. 36.20 Measured order vs. synthesized order (TVDFT)

Acknowledgements The authors acknowledge the European Commission (EC) for their research grant under the two European projects FP7-PEOPLE n. 309395 “MARE-WINT” (new MAterials and REliability in offshore WINd Turbines technology) and FP7-PEOPLE n. 324336 “DEMETRA” (Design of Mechanical Transmissions: Efficiency, Noise and Durability Optimization) (http://marewint.eu/, http://www.fp7demetra.eu).

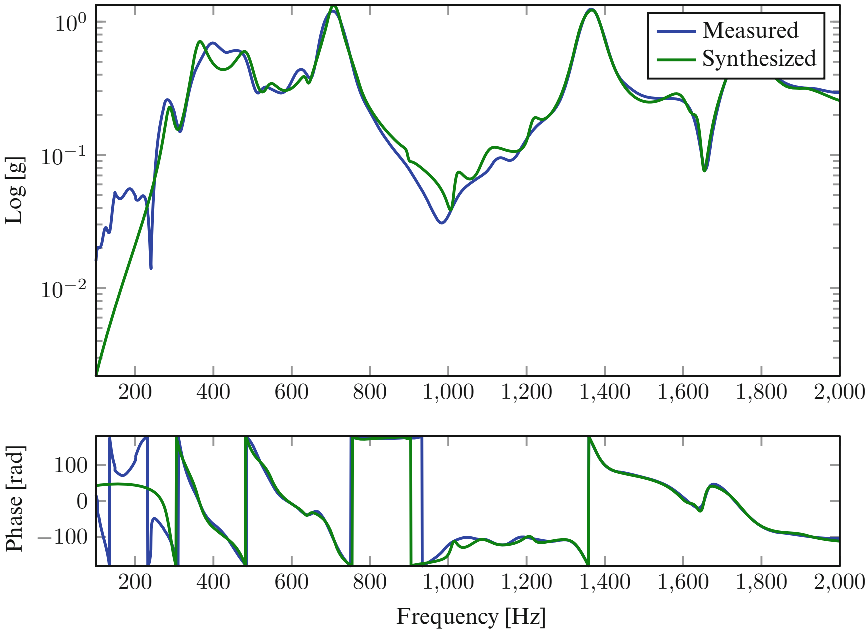

Fig. 36.21 Measured order vs. synthesized order (VK)

Table 36.3 OBMA—modal parameters identification

	Angle Domain computed order tracking		Time Variant Discrete Fourier Transform		Vold-Kalman filter based order tracking	
No.	Natural frequency [Hz]	Damping ratio [%]	Natural frequency [Hz]	Damping ratio [%]	Natural frequency [Hz]	Damping ratio [%]
1	312.7	3.10	357.5	0.42	288.7	4.09
2	441.7	4.33	414.3	4.92	361.8	5.17
3	513.0	5.35	481.3	4.54	486.1	4.99
4	674.5	0.44	536.3	2.90	543.0	4.04
5	715.2	2.77	647.5	1.04	639.1	1.63
6	768.6	3.08	706.9	1.75	707.9	2.68
7	1104.7	1.99	756.9	1.76	766.3	2.90
8	1357.1	0.98	1081.5	1.22	896.5	0.68
9	1375.3	0.58	1363.4	0.65	1097.9	3.17
10	1598.3	1.50	1621.7	1.19	1340.7	2.10
11	1633.6	0.68	1746.8	2.18	1376.0	1.89
12	1745.6	2.41			1605.7	2.31
13					1637.8	0.89
14					1750.2	2.70
15					1898.1	2.64

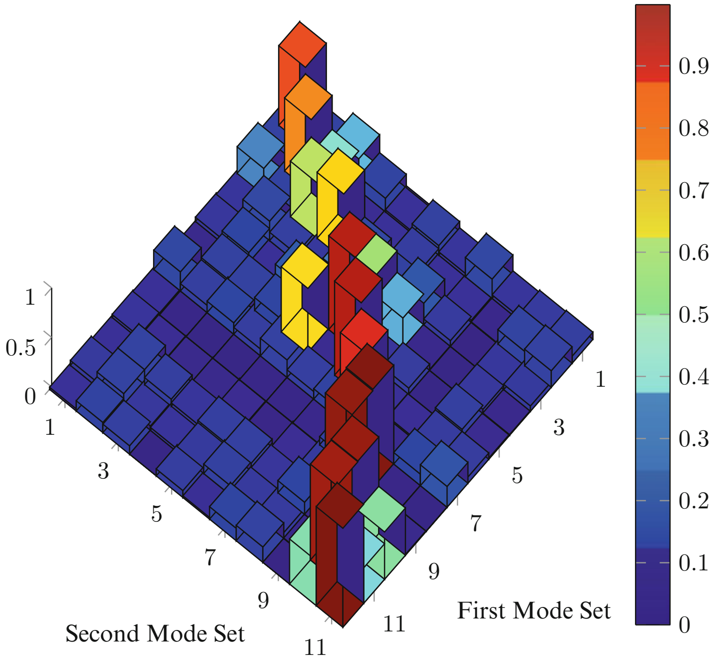

Fig. 36.22 Modal Assurance Criterion (AD vs. TVDFT)

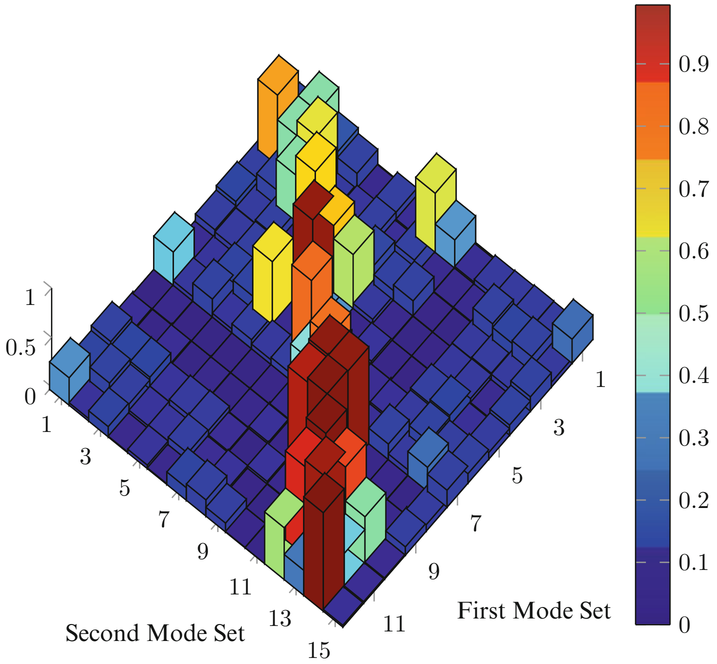

Fig. 36.23 Modal Assurance Criterion (AD vs. VK)

References

1. Janssens, K., Kollar, Z., Peeters, B., Pauwels, S., Van der Auweraer, H.: Order-based resonance identification using operational polymax. In: Proceedings of 24th International Modal Analysis Conference (IMAC), Saint Louis, MO (2006)
2. Di Lorenzo, E., Manzato, S., Vanhollebeke, F., Goris, S., Peeters, B., Desmet, W., Marulo, F.: Dynamic characterization of wind turbine gearboxes using order-based modal analysis. In: Proceedings of 26th International Conference on Noise and Vibration Engineering (ISMA), Leuven, Belgium (2014)
3. Blough, J.: Improving the analysis of operating data on rotating automotive components. Ph.D. thesis, University of Cincinnati (1998)
4. Potter, R.: A new order tracking method for rotating machinery. Sound Vib. **24**(9), 30–34 (1990)

5. Blough, J., Brown, D.L., Vold, H.: The time variant discrete fourier transform as an order tracking method. In: Proceedings of Society of Automotive Engineers Noise and Vibration Conference, SAE paper number 972006 (1997)
6. Borghesani, P., Pennacchi, P., Chatterton, S., Ricci, R.: The velocity synchronous discrete fourier transform for order tracking in the field of rotating machinery. Mech. Syst. Signal Process. (**44**), 118–133 (2014)
7. Vold, H., Leuridan, J.: High resolution order tracking at extreme slew rates, using kalman traking filters. In: Proceedings of Society of Automotive Engineers Noise and Vibration Conference, SAE paper number 931288 (1993)
8. Qian, S.: Application of Gabor expansion for order analysis. LabVIEW Application Notes, National Instruments, Austin, Texas (2003)
9. Peeters, B., Van der Auweraer, H., Vanhollebeke, F., Guillaume, P.: Operational modal analysis for estimating the dynamic properties of a stadium during a football game. Shock Vib. **11**, 395–409 (2004)
10. Palermo, A., Anthonis, J., Mundo, D., Desmet, W.: A novel gear test rig with adjustable shaft compliance and misalignments. part I: design. and part II: instrumentation. In: Proceedings of the 3rd International Conference on Condition Monitoring of Machinery in Non-Stationary Operations, Ferrara (2013)
11. Palermo, A., Toso, A., Heirman, G.H.K., Cerdá, R., Gulinelli, M., Mundo, D., Desmet, W.: Structural coupling and non-linear effects in the experimental modal analysis of a precision gear test rig. In: Proceedings of the International Gear Conference, Lyon (2014)

Chapter 37
A Design Framework to Improve the Dynamic Characteristics of Double Planet Planetary Gearsets

Dylan C. Fyler, Murat Inalpolat, Sang Hwa Lee, and Hyun Ku Lee

Abstract Double planet planetary gear sets have significantly more design options than their single planetary counterparts as the addition of the second planet set allows for greater flexibility in sizing and synthesizing transmission kinematic chains. Generally, the primary design constraints for these systems are based on transmitted load, speed ratio, and availability of space. However, once these specifications are met, few attempts are made to optimize the design any further as manual design techniques fail to assess all performance related aspects of the system. In this paper, a methodology to improve existing double planetary gear sets through adjustment of limited set of feasible design constraints is proposed. The improvement will be achieved through modifying the values of gear tooth profile shift, tooth thickness, and planet gear center distances. Design of experiments (DOE) approach is implemented to generate a finite set of models that accurately represent the entire design space. In order to investigate if the proposed alternative designs are an improvement from the baseline system, a finite element tool is used to model all of the potential configurations. The parameters that are used for the fundamental measurement of system performance in this study are bearing forces, gear mesh forces and transmission error spectra.

Keywords Contact • Dynamics • Design • Gears • Design of experiments

37.1 Introduction

Modern day transmission design processes predominantly focus on transmitting high mechanical power levels with carefully-selected multiple gear ratios while maintaining the overall volume and weight requirements. Planetary gear sets have become the sole source mechanical subsystems for automotive transmissions as they provide high power density output with a coaxial arrangement that saves space. Moreover, they exhibit the capability of achieving different gear ratios in a smooth way by fixing different members of these gearsets via clutches and/or bands. More specifically, double planet planetary gear sets, exhibited in Fig. 37.1, have the additional advantage of reversing the output rotation while with a minor increase in space and weight. One of the common applications for double planet planetary gear sets has been as a reversing gearset in passenger car automatic transmissions. The additional planet gear in each double planet planetary gear set planetary branch allows for significantly more design options than their single planetary counterparts. More recently they have also been employed in off-road as well as hybrid vehicle transmissions [1, 2].

In the current existing body of literature there are a number of studies which develop automated design processes either for simple planetary gear sets [3] or for parallel-axis gear pairs [4–9]. These studies rely on fast modeling and analysis of prospective gear designs using a mesh-by-mesh (i.e. based upon each individual gear mesh) approach which is not designed to account for system level phenomena. In order to observe the contribution of these system level design-oriented effects on the dynamic properties of gearsets, a generalized deformable body system level model is required. While a deformable body model would provide more information on system performance, it would require significantly more time to complete the analyses. However, the time taken to run the analysis could be reduced by using a statistical approach, also known as Design of Experiments (DOE), which in turn would enable the option to model only a limited number of designs and still get statistically and physically viable intermittent designs. Finally, the designer can select the design that balances each of the design requirements while not losing from the precision of the model as well as the data generated by these models.

D.C. Fyler • M. Inalpolat (✉)
University of Massachusetts Lowell, Lowell, MA 01854, USA
e-mail: Murat_Inalpolat@uml.edu

S.H. Lee • H.K. Lee
Hyundai Motor Company, Gyeonggi-Do 445-706, South Korea

© The Society for Experimental Mechanics, Inc. 2016

J. De Clerck, D.S. Epp (eds.), *Rotating Machinery, Hybrid Test Methods, Vibro-Acoustics & Laser Vibrometry, Volume 8*,
Conference Proceedings of the Society for Experimental Mechanics Series, DOI 10.1007/978-3-319-30084-9_37

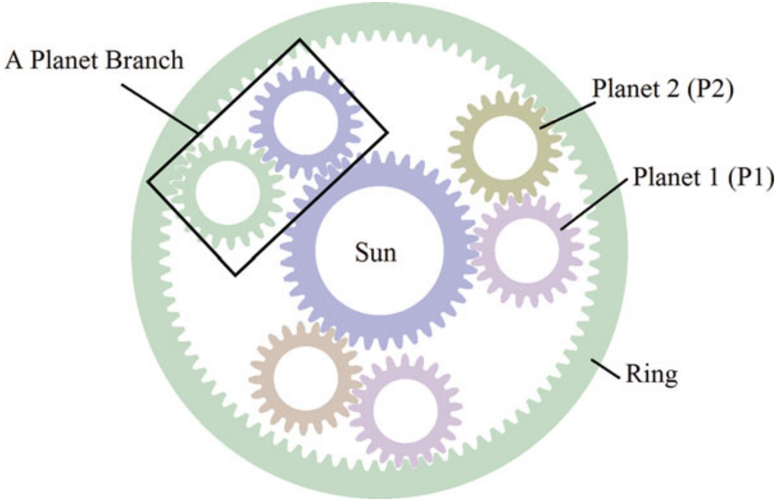

Fig. 37.1 A schematical representation of a double planet planetary gear set

Even though, there are a number of studies that develop design methodologies based upon a mesh-by-mesh approach, the literature on the design methodologies for double-planet gearsets based upon a system level approach is sparse. Kwon et al. developed an automated design search for single and double planet planetary gear sets utilizing a loaded tooth contact analysis tool and a mesh by mesh approach [3]. Harianto and Houser studied the effects of various micro-geometries on gear set performance [4]. Houser et al. also developed a method which was applied to optimize the design of helical gears [5]. Methods for using genetic algorithms and finite element analysis were used by Padmanabhan et al. to determine optimal spur gear pair designs [6]. Jeong developed an initial gear design tool using an artificial neural network [7].

In this study, the well-known statistical technique, *Design of Experiments* (*DOE*), is used in order to systematically select the right combination of computational experiments and later to create a *Response Surface* (*RS*) of all potential design configurations within a prescribed design space [10]. These limited numbers of designs are then modeled using Planetary2D, a deformable body contact model capable of analyzing planetary gear sets in two dimensions [11]. Outputs including root mean square (RMS) transmission error (TE), first harmonics of the transmission error, and gear tooth root maximum bending stresses (Von-Mises stresses used) from these models will be extracted to assess the strengths and weaknesses of potential design candidates in an automated and comparative fashion. Finally, equations are fit to the resulting data to predict the response of intermittent designs that were not modeled. An optimization method which balances the responses of the gearset is applied using a predicted relationship between design factors and system operating parameters.

37.2 Selection of the DOE Technique

Various Design of Experiment (DOE) techniques exist in order to develop a set of experiments that accurately explore a given design space and it is critical that the proper one is chosen for each distinctive application. Factorial designs are generally used as a screening DOE method used to determine which factors from a given set have a significant impact on outputs based upon their corresponding sensitivities with respect to the input variables [10]. Previous studies indicate that all the factors being adjusted in this study have a considerable impact on the performance of gear sets so screening with a factorial design is not necessary in this case. Response surface designs are used in succession to factorial designs in order to refine models and identify curvature in the response surface. Central Composite designs are a subset of response surface designs which are capable of fitting a full quadratic model. Figure 37.2 shows a visualization of a central composite design in three factors.

The cube in Fig. 37.2 represents a design space, where each black point represents a corner point and the corresponding green points and red points represent axial and center points respectively. It serves as a visual representation of a response surface design with three factors. By offsetting the axial points from the surface of the cube by some distance α, the design space is expanded to sphere. For this study a value of $\alpha = 2.8284$ is used. This increases the levels of each factor from three to five and allows for the model to capture cubic behavior in the responses [10]. The black points are referred to as corner points and observe the effects of combinations of different factor adjustments. Lastly the red points are the center points where all the factors are kept at their base levels. In this study a central composite full design (CCFD) is used to map the

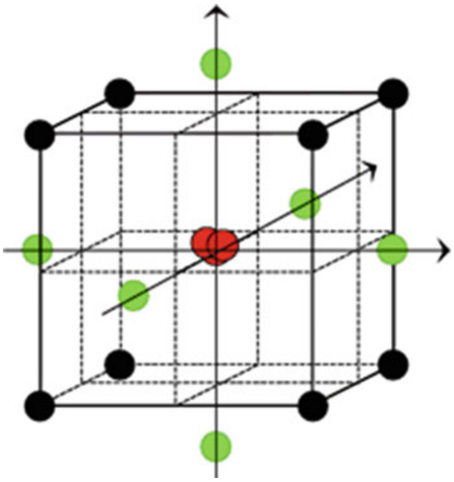

Fig. 37.2 Visual representation of the three factor central composite design

design space. The six design factors are Sun Tooth thickness, Ring tooth thickness , sun root diameter, ring root diameter, inner planet root diameter, and outer planet root diameter.

37.3 Layout of Design Space

The gear design parameters that are varied in order to create the response surface are the center distance, tooth thickness, and profile shift of the gears in the gearset. However, if all of these parameters were varied independent from each other, certain gear configurations will have interfering geometry. For example, if the tooth thicknesses of the sun and pinion gears are both increased, they will not mesh properly if there is not enough backlash. Likewise, if the root diameter of the sun gear and the outer diameter of the inner planet gear are both increased, there could be gear tooth root interference. To avoid these conditions, center distance, tooth thickness, and profile shift of the gears will be varied indirectly by exchanging tooth thickness in the sun-planet and ring-planet meshes. The changes in profile shift is controlled by increasing the addendum length of the ring gear and the sun gear, while increasing the dedendum length in the planet gears and vice versa. Center distance is then adjusted to keep backlash in the sun-planet, the planet-planet, and the ring-planet gear meshes at a constant value to ensure there is no interference in any candidate design using Eq. (37.1):

$$B = P_c - T_{op1} - T_{op2}. \tag{37.1}$$

In Eq. (37.1), B is the circular backlash, P_c is the circular pitch, and T_{opi} is the operating tooth thickness of the i^{th} gear in the mesh. Backlash is set to be 0.003 inches in each of the meshes in order to counter-balance the tooth thickness changes due to the center distance changes adjusts to keep the backlash constant. Root interference is checked by using Eq. (37.2).

$$CD > OD_1 - RD_2 \tag{37.2}$$

Here, OD_1 is the outer diameter of the first gear and RD_2 is the root diameter of the second gear in the corresponding mesh. If the root clearance (distance between the outer diameter and root diameter of mating gears) is kept constant in the ring planet and sun planet meshes but left as a variable for the planet-planet mesh. If a resulting design has root clearance less than 0.02 inches in the planet-planet mesh, then the center distance is increased to allow for space and the backlash is increased slightly for that specific case. Using these rules for constraining the design parameters, *the primary design parameters* are set as sun gear tooth thickness, ring gear tooth thickness, sun gear root diameter, P1 (inner planet) root diameter, ring root diameter, and P2 (outer planet) root diameter and represented as S_{tt}, R_{tt}, S_{rd}, $P1_{rd}$, R_{rd}, and $P2_{rd}$, respectively. The *secondary design parameters*, which are essentially controlled by the primary design parameters, are planet 1 tooth thickness, planet 2 tooth thickness, planet 1 outer diameter, sun outer diameter, planet 2 outer diameter, and ring inner diameter and are represented as $P1_{tt}$, $P2_{tt}$, $P1_{od}$, S_{od}, $P2_{od}$, R_{id}, respectively. A listing of the base design, primary design, secondary design, and response parameters are shown in Fig. 37.3.

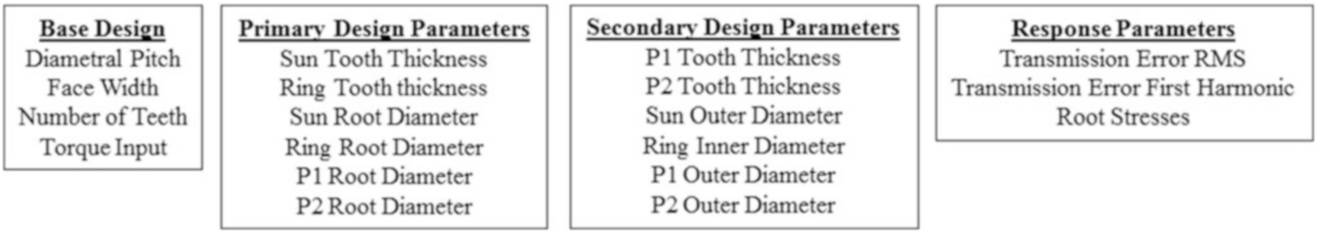
Base Design
Diametral Pitch
Face Width
Number of Teeth
Torque Input
Primary Design Parameters
Sun Tooth Thickness
Ring Tooth thickness
Sun Root Diameter
Ring Root Diameter
P1 Root Diameter
P2 Root Diameter
Secondary Design Parameters
P1 Tooth Thickness
P2 Tooth Thickness
Sun Outer Diameter
Ring Inner Diameter
P1 Outer Diameter
P2 Outer Diameter
Response Parameters
Transmission Error RMS
Transmission Error First Harmonic
Root Stresses

Fig. 37.3 Procedure to execute design of experiments and subsequent analyses

Table 37.1 Mapping of the gear design factors on to the design space

Design factor	Sun tooth thickness (inches)		Ring tooth thickness (inches)		Sun RD (inches)		P1 RD (inches)		Ring RD (inches)		P2 RD (inches)	
Effected factors	S_{tt}	$P1_{tt}$	R_{tt}	$P2_{tt}$	S_{rd}	$P1_{od}$	$P1_{rd}$	S_{od}	R_{rd}	$P2_{od}$	$P2_{rd}$	R_{id}
Base level	0.0901	0.0901	0.0901	0.0901	2.043	1.342	1.051	2.334	5.149	1.342	1.051	4.901
Corner point Variance	0.0961, 0.0841	0.0841, 0.0961	0.0961, 0.0841	0.0841, 0.0961	2.054, 2.031	1.329, 1.354	1.063, 1.038	2.322, 2.346	5.161, 5.136	1.329, 1.354	1.063, 1.038	4.914, 4.889
Axial point variance	0.1069, 0.0733	0.0733, 0.1069	0.1069, 0.0733	0.0733, 0.1069	2.077, 2.008	1.308, 1.376	1.085, 1.016	2.299, 2.368	5.183, 5.114	1.308, 1.376	1.085, 1.016	4.936, 4.867

Table 37.1 lists the total number of factors in the design of experiments and at what levels they're modeled, where subscript *rd* specifies root diameter, *od* specifies outer diameter, and *tt* specifies tooth thickness. The first value indicates the change is a positive shift (for example, sun tooth thickness increases and planet 1 tooth thickness decreases for a positive shift) and the second value after the comma indicates the change for a negative shift. Different variance amounts are assigned for the corner and axial points with the center points being described by the base level. Using the mapping layout in Table 37.1, a design space for candidate designs can be converted into a finite number of deformable body models.

37.4 A Computational Case Study

In this section, the design-based gear dynamics and noise improvement methodology proposed is demonstrated through the optimization of an example gear set. The gear set to be used is a generalized automotive example of a double planet planetary gear set. In the proposed systems the sun gear is the input, the carrier is the output, and the ring gear is fixed. To prevent the gears in any candidate design from seizing a minimum root clearance of 0.02 inches and a minimum backlash of 0.003 inches are used. Dynamic response of gearsets is generally associated with mesh excitations which are quantified as transmission error. Excitations in transmission error are magnified as the operating speed of the gearset is increased. These oscillations in transmission error can be modeled at low operating speeds to make dynamic response predictions in a more computationally efficient manner. In this investigation, a quasi-static analysis is used with an input torque of 1770 lb.in and an input speed of 10 RPM.

The planet, sun, and carrier are assumed to be supported by needle bearings which are modeled as support stiffnesses in the X and Y directions with stiffness values shown in Table 37.2. Additional geometry of the individual gears in the set are also shown in Table 37.2. The sun gear is assumed to be floating and accordingly has a significantly lower bearing stiffness. The ring gear is assumed to be splined into a relatively rigid housing and thus is treated as rigid in the X and Y directions by being assigned significantly larger support stiffness values. Bearings are assumed to be isotropic with equal stiffness in the X and Y directions.

The graphical representation of the deformable body model with the finite element mesh for the double planet planetary gear set is shown in Fig. 37.4. The mesh in the model is set up so more elements are allocated to the teeth and less toward the inner rim of the gears since the primary interest is the contact and deflection of the teeth.

Images with the sun-planet, planet-planet, and ring-planet are shown in Fig. 37.5 to illustrate the baseline tooth profiles.

Table 37.2 Baseline design parameters of individual gears in the example gearset

Member	Sun	Planets	Ring
Bearing stiffness (*lb*/*in*)	45.6e4	9.7e6	1e9
Number of teeth	38	21	86
Outer diameter (*inches*)	2.333	1.342	5.8
Root diameter (*inches*)	2.042	1.051	5.181
Inner diameter (*inches*)	1.5	.75	4.901
Pressure angle (*degrees*)	20	20	20
Diametral pitch (*1*/*inches*)	17.139	17.139	17.139
Circular tooth thickness (*inches*)	0.0916	0.0916	0.0916
Face width (*inches*)	1.181	1.181	1.181

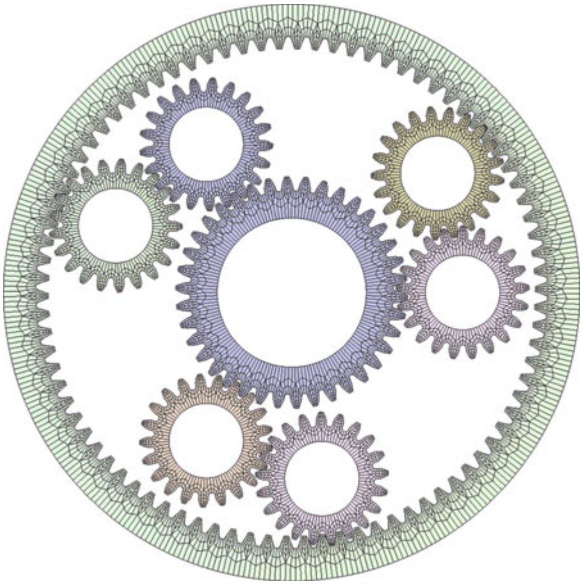

Fig. 37.4 FEM-based deformable body model for double planet planetary gear set

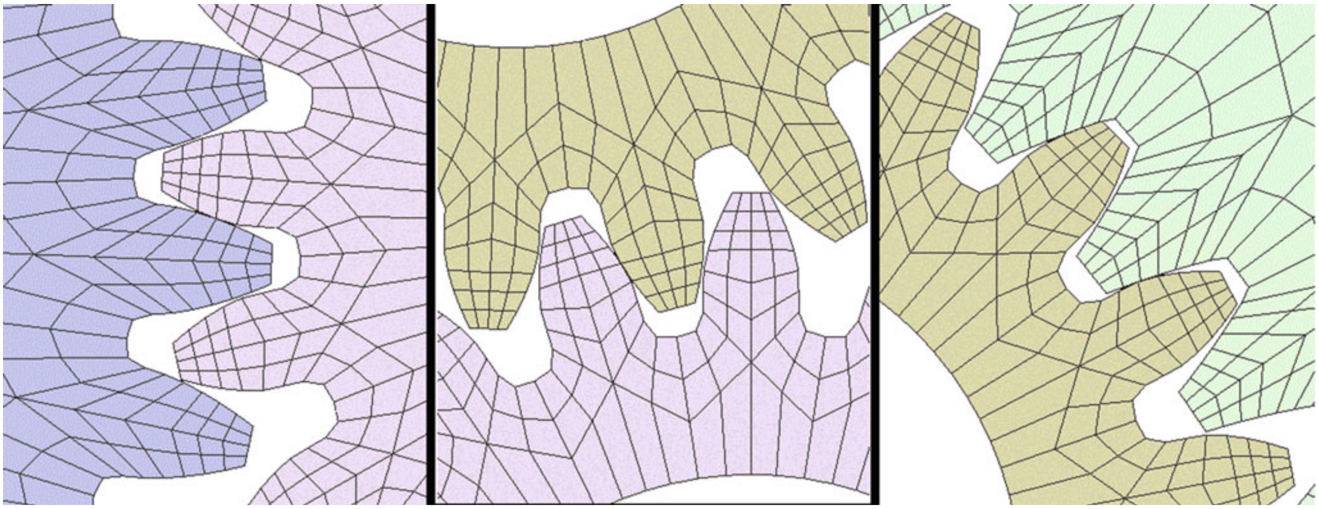

Fig. 37.5 From *left* to *right*, close up views of the sun/planet, planet/planet, and ring/planet meshes of the base design for planet branch 1

37.5 Results and Discussion

A response surface is used to map a total of 90 out of a potential 15625 computational tests with a combination of the input design parameters (stated in Table 37.1) utilizing a central composite full design scheme. Each design is then modeled in Planetary2D and solved by using a quasi-static solver for one mesh cycle. Over the course of the mesh cycle, 128 discrete time instances of the finite element models are solved to characterize each mesh position within the cycle. Considering that the system is a computational model with no manufacturing errors, it can be assumed that all planet branches will have identical system responses at slow speed. Using this assumption, all results are taken from the first planet branch for the sake of simplicity. Results from the finite element models are used to determine the root-mean-square (rms) of the transmission error of the sun-planet and ring-planet meshes, first harmonic of the quasi-static transmission error of the sun-planet and ring-planet meshes which are defined as sp_{rms}, rp_{rms}, sp_{h1}, rp_{h1} respectively. Gear tooth root stresses are also extracted from the deformable body model in the form of Von-Mises stresses. The maximum root stresses in P1 in the sun-planet and planet-planet meshes are defined as R_1 and R_2 respectively. The maximum root stresses in P2 in the ring-planet and planet-planet meshes are defined as R_3 and R_4 respectively. The location of these stresses in the gearset is shown in Fig. 37.6, which exhibits the stress contours for a loaded mesh analysis.

These output values (TE harmonics, TE_{rms}, root bending stresses) are used as the system performance criterion. A commercially available statistical software package is used to fit a response surface to the data mapping the relation between the design parameters and system performance parameters. Contour plots are generated from the response surface and can be used as a powerful design selection tool as they provide valuable information in regards to the sensitivities of each output parameter to the variations in the input parameters. They also provide insight into how the interactions of two design factors affect system operating parameters.

The two contour plots shown in Fig. 37.7 display how certain design parameters effect rp_{h1}. The X and Y axes are in coded units with 1 being corner point variance and 2.8284 being axial point variance and 0 representing the base design

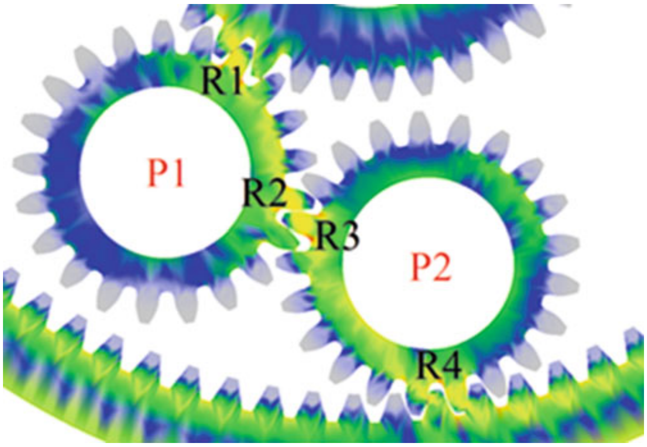

Fig. 37.6 Stress contours with locations of root stresses of interest

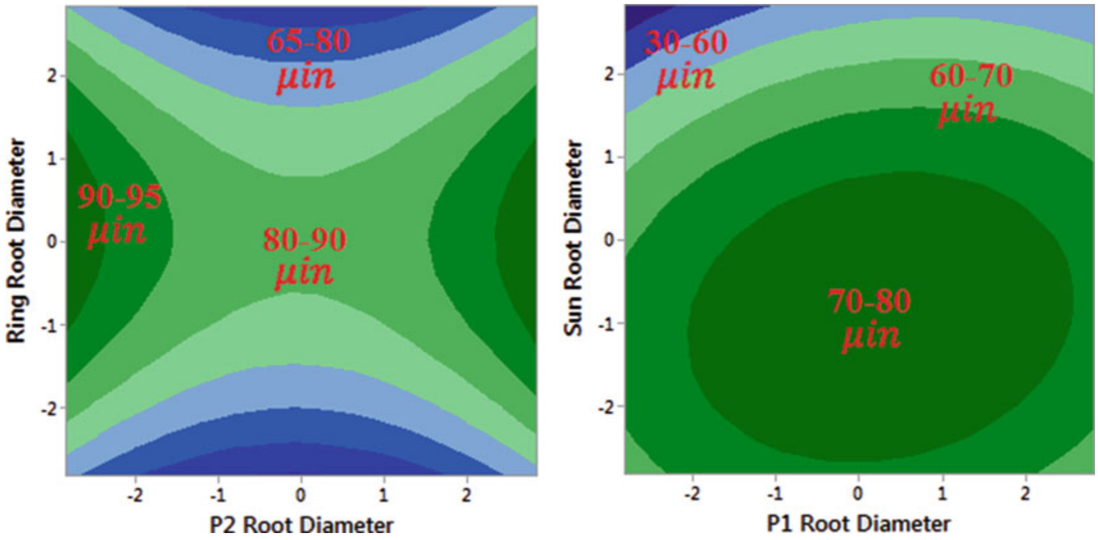

Fig. 37.7 Contour plots illustrating the effect of planet 2 and ring root diameter (*left*) planet 1 and sun root diameter (*right*) on rp_{h1}

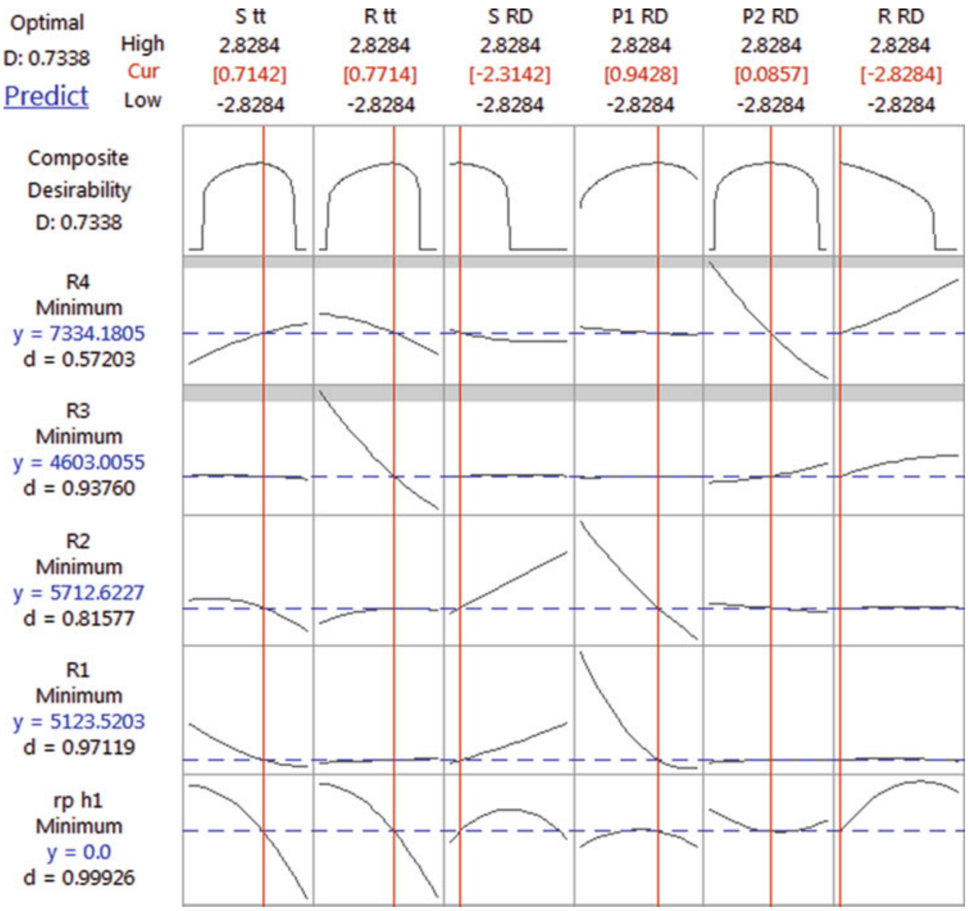

Fig. 37.8 Optimization plot for the response surface showing first five responses and composite desirability

value. The red numbers display the magnitude of rp_{h1} in micro inches for various color regions on the contour plots. While this plot only shows the effect of the gear root stresses on rp_{h1}, contour plots can be generated for any combination of two design parameters for any system response and essentially can be used for achieving a well-balanced design. While contour plots allow the designer to observe isolated effects of the design choices, they alone do not provide enough information for the designer to select a configuration that considers the simultaneous optimization of all system performance criteria. Response optimization techniques can be utilized to determine which design within the design space successfully minimizes stress and vibration/noise within the double planet planetary gear set. This is accomplished by using weighting coefficients for the response of the system performance criteria with respect to the design parameters and developing composite design desirability for each design parameter. Composite design desirability can then be maximized to select the most ideal combination of the design parameters.

The contribution of each of the design parameters (left to right) to several outputs (up and down) along with the composite desirability function is shown in Fig. 37.8. The change in all responses is mapped out for every variable and summed together to generate a composite desirability. The maximum value in composite desirability can then be selected as the predicted ideal setting for a given design parameter. The red values represent the design parameter value which yields a balanced minimized output between all of the system responses. They are in coded units where 2.8284 and -2.8284 are the boundaries for the design space set by the axial points and the α value. The blue values represent the system outputs predicted by the response surface.

Using these predicted optimal design parameter levels, a new finite element model is created to determine the accuracy of the predicted responses. The accuracy of the predictions from the response surface can be tested by creating a deformable body model with the predicted factor values. Aside from the first harmonic of the ring-planet mesh TE amplitude, the optimal design from the response surface is consistent with the results from the deformable body model as shown in Fig. 37.9. The geometry for the new balanced design is show in Table 37.3.

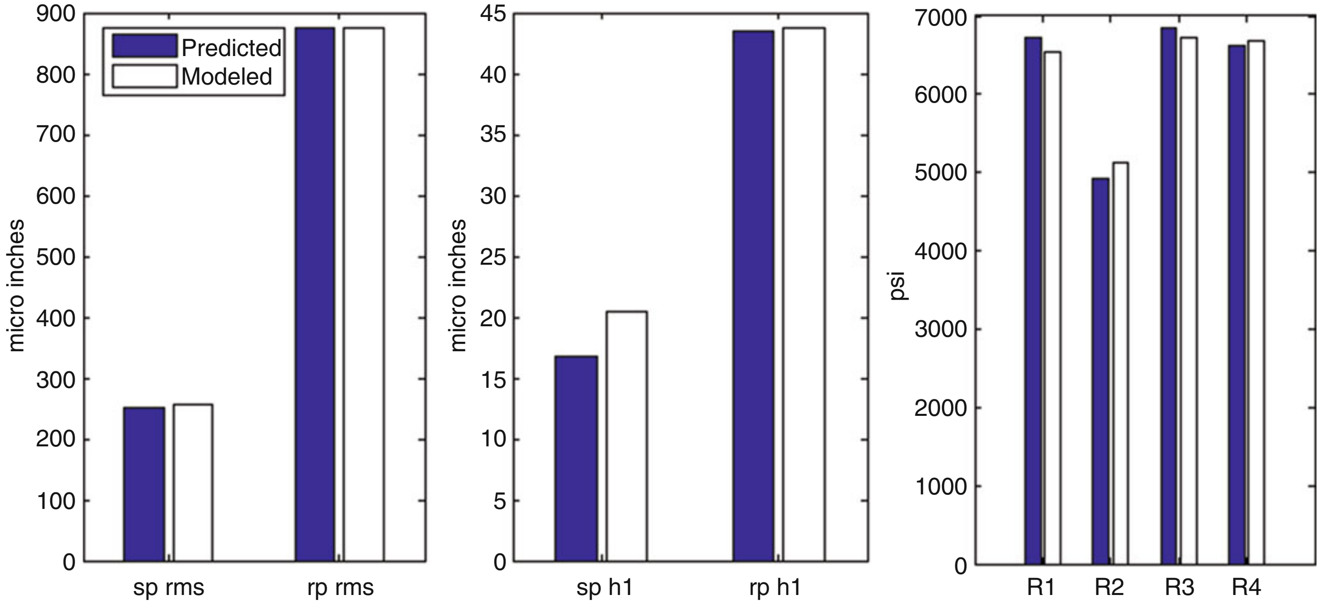

Fig. 37.9 Comparison between results predicted from the response surface (*solid bar*) and results from the deformable body model of the new design (*clear bar*)

Table 37.3 Design parameters for the balanced design

Member	Sun	Planet 1	Planet 2	Ring
Outer diameter (*inches*)	2.3209	1.3765	1.3612	5.8
Root diameter (*inches*)	2.0078	1.0634	1.062	5.168
Inner diameter (*inches*)	1.5	0.75	0.75	4.9127
Circular tooth thickness (*inches*)	0.0793	0.1009	0.08686	0.09334

The differences between the balanced design and the original are shown in Fig. 37.10. While most of the root stress values remain relatively unchanged, a large reduction in the first harmonic of the ring-planet transmission error is achieved at the expense of a small increase in the first harmonic of the sun-planet mesh transmission error. While the root stresses are moderately small in this case study, they are important to include as an optimization parameter as they constrain what the optimizer does with the tooth geometry. If only the magnitude of the first harmonic of transmission error is used in optimization the redesigned teeth will have very large working depths since the strength of the teeth is not being assessed.

The change in quasi-static transmission error between the original and redesign is demonstrated in Fig. 37.11. While there is a clear decrease in the quasi-static TE magnitudes in the ring-planet mesh, the sun-planet mesh is relatively similar in the amount of transmission error produced. Studies indicate that there is a relationship between noise generated and the magnitude of the first harmonic of transmission error [12]. From this design modification it can be inferred that the new design will have a reduced amount of noise radiating from the ring in comparison to the original due to the reduction of magnitude of the first harmonic of transmission error in the ring-planet mesh.

From Fig. 37.12, it is evident that a reduction in the magnitude of force in the inner and outer planet bearings has occurred. The bearing forces on the planet gears represent the net loads being applied to the carrier and indicate the magnitude of the loads on the carrier supports. Since the bearings couple the excitations from the gear meshes to the carrier which outputs torque from the system the loads on them serve as an indicator for noise produced by the system. While the bearing force is not one of the primary design parameters it provides insight into how the change in transmission error propagates into other aspects of the gear set.

Figure 37.13 shows the change in the root stress of the planet gears between the two designs. One and a half mesh cycles are used for this value to ensure that the maximum value of the root stress can be captured. Although there is not as significant decrease in comparison to the first harmonic of the ring planet transmission error it is important that the stress did not increase in the revised design. While these stress values are low, they increase proportionally with the input torque to the gear set and minimizing them can be very desirable when the gear set is operating under high load levels.

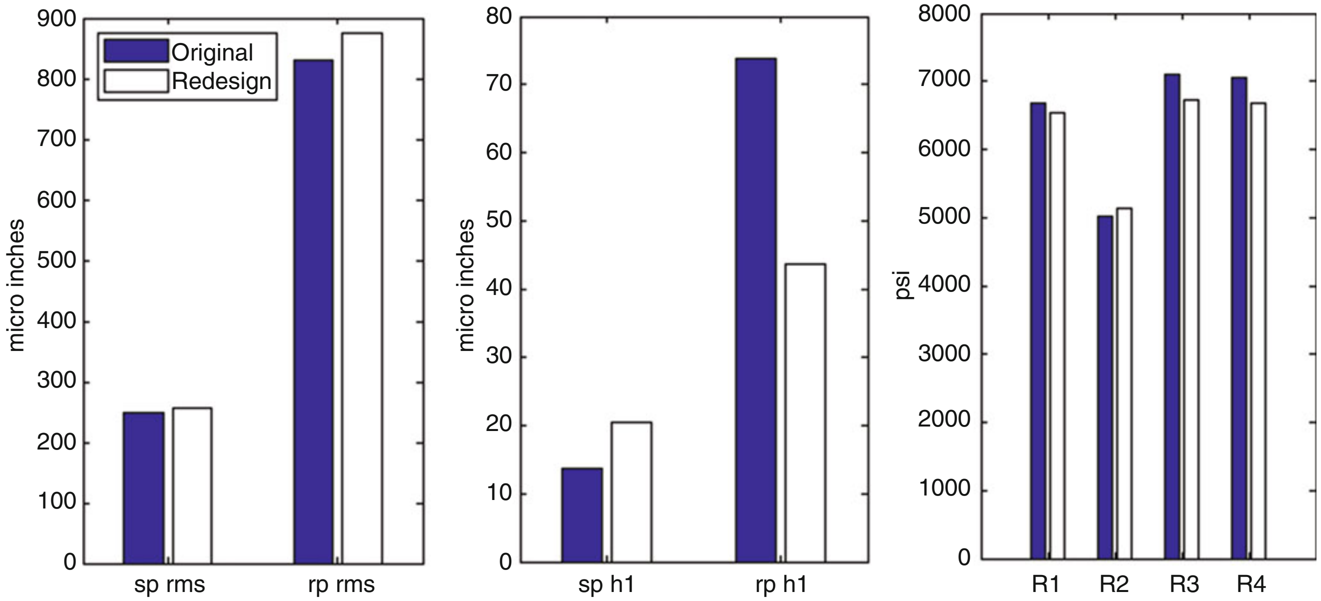

Fig. 37.10 Comparison of responses from original baseline design (*solid bar*) and the balanced design (*clear bar*)

Figure 37.14 shows the mesh force between the sun and the planet gear for the two designs. It is apparent that the amplitude of the mesh force has been slightly reduced in the second design. This reduction in magnitude is potentially due to the large reduction in rp_{h1} since mesh force and transmission error are proportionally related through the mesh stiffness. In comparison to the bearing force the mesh force in the gears has been affected less significantly.

Figure 37.15 shows the assessment of the outcomes of the equation which was used to model the effect of design parameters on sp_{rms}. From the normal probability plot it is evident that there are several outlying results from the analyses run. This is to be expected as certain nonlinear effects result from adjusting the geometry to the teeth profiles. The normal probability plot can be used to determine if the residuals are distributed normally. While there is some non-normality in the data evident by the uneven distribution about the centerline this is most likely due to some higher order polynomial effects that cannot be modeled using this response surface design. However, these inconsistencies in the fit are small enough that moderate accuracy will be maintained when fitting the response surface.

37.6 Conclusions

In this study, a procedural methodology to improve double planet planetary gearsets designs is proposed. This method searches through a range of key design dimensions to find a combination which yield a balanced set of selected performance aspects. An example double planet planetary gear set was optimized for noise reduction by using a deformable body model in combination with a response surface. The response surface helps identify key points within the design space such as center, corner, and axial points. The deformable body model is then used to calculate the response of certain performance aspects at the key points within the design space. Results are then used map a response surface to the data and predict the response for any configuration within the design space. Optimization techniques are then applied to predict the ideal combination of design parameters which minimize root stresses and transmission error. Quasi-static transmission error for the ring-planet and sun-planet mesh are compared between the original and optimized. By weighing all output parameters equally response optimization results in a new design which significantly decreases rp_{h1} while other system responses remain relatively unchanged.

Acknowledgements The authors would like to acknowledge Dr. S. Vijayakar and V. Ambarisha of Advanced Numerical Solutions for making the gear analysis package Planetary2D available and the financial support from the Hyundai Motor Company, which made this study possible.

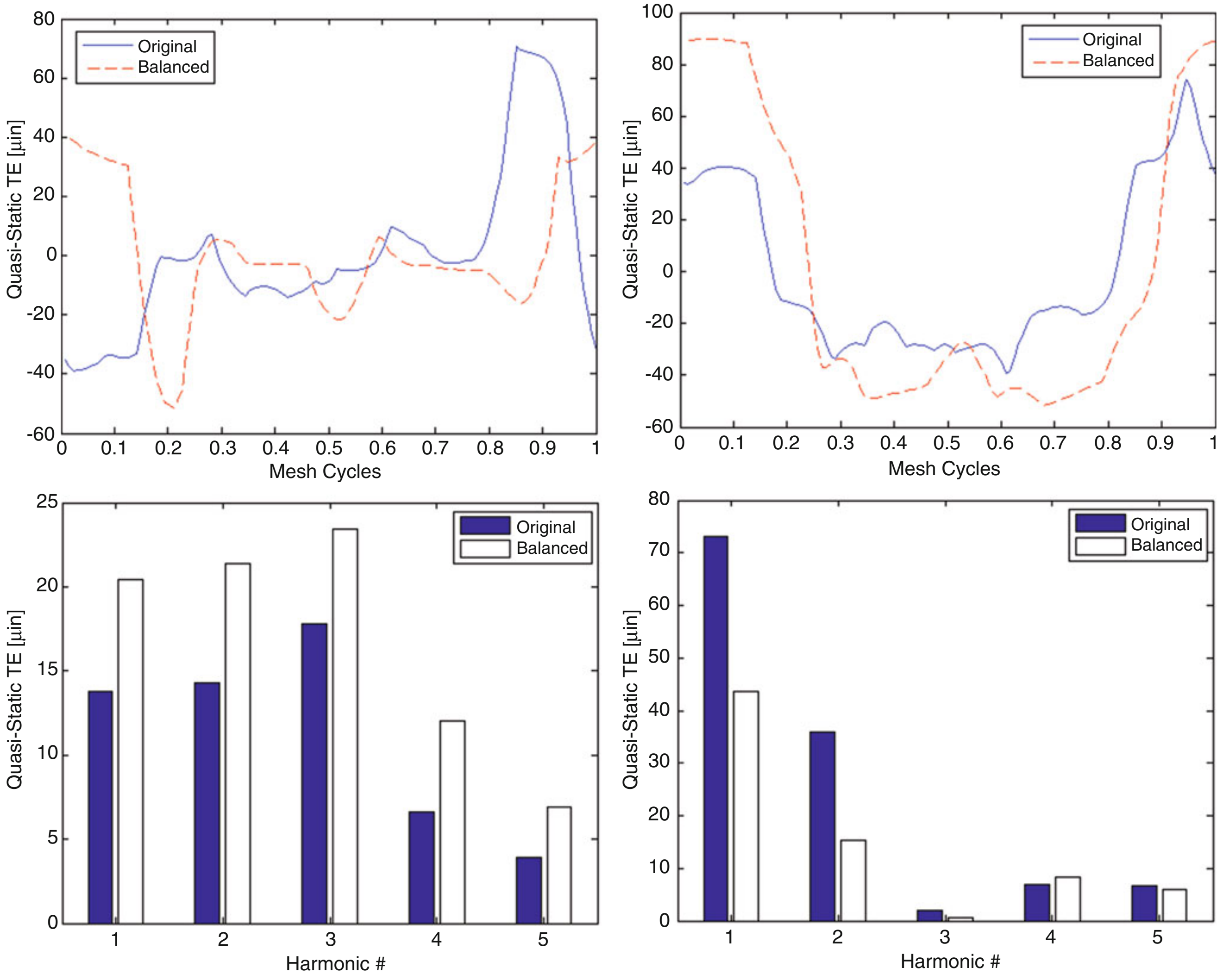

Fig. 37.11 Comparison of quasi-static TE for sun-planet (*left*) and ring planet (*right*) meshes

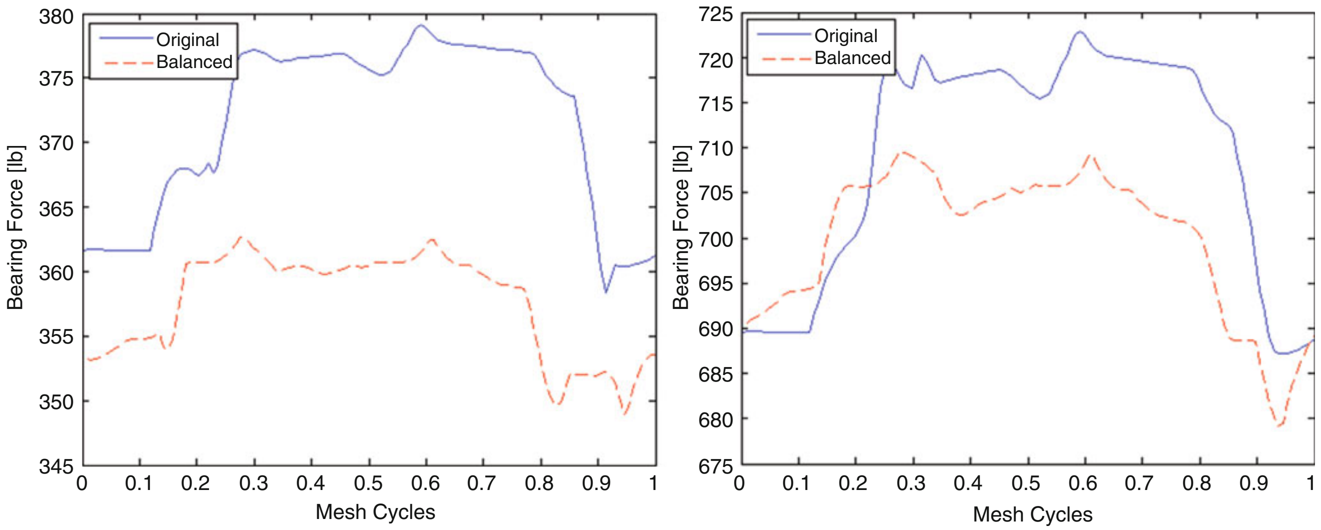

Fig. 37.12 Overlay of inner (*left*) and outer (*right*) planet bearing forces

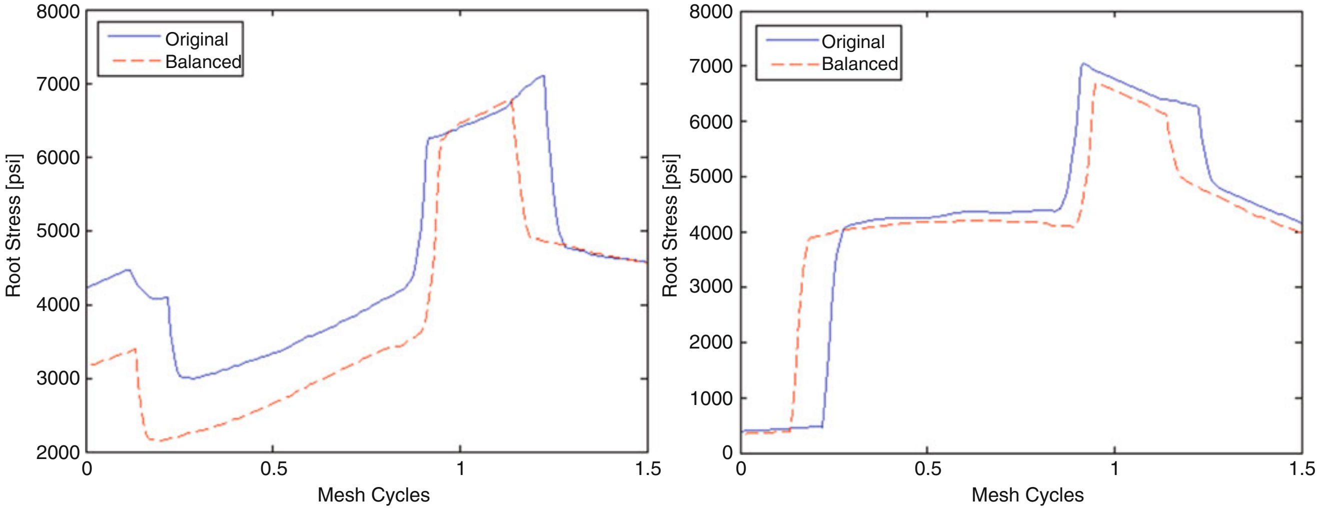

Fig. 37.13 Comparison of the inner (*left*) and the outer (*right*) planet tooth root stresses

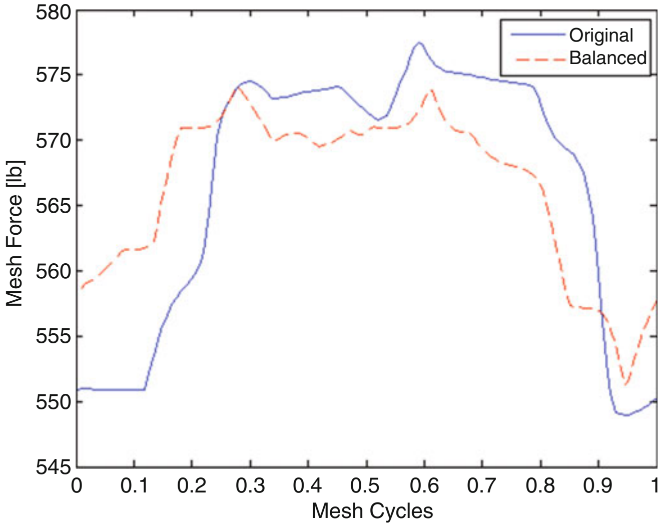

Fig. 37.14 Sun planet mesh force over one mesh cycle

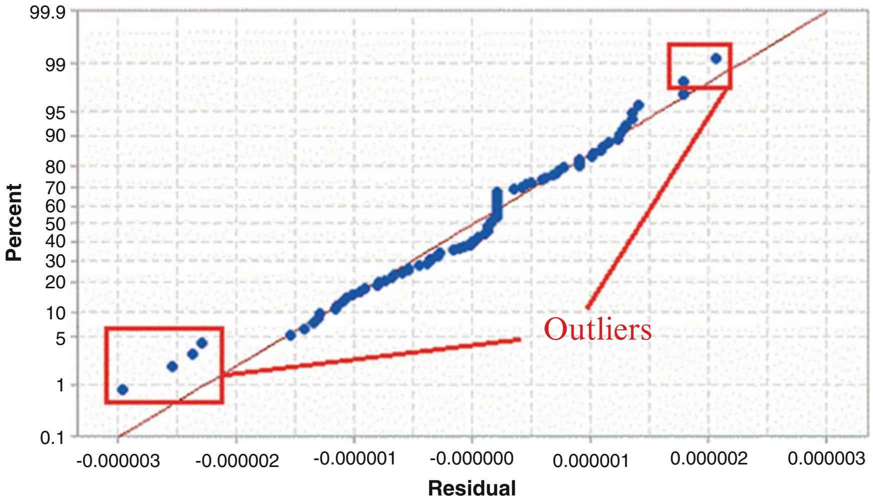

Fig. 37.15 Normal probability plot for sp_{rms}

References

1. Endo, H., Ito, M., Ozeki, T.: Development for Toyota's transaxle for minivan hybrid vehicles. JSAE Rev. **24**, 109–116 (2003)
2. Miyata, S., Liu, D.: Study of the control mechanism of a half-toroidal CVT during load transmission. J. Adv. Mech. Des. Syst. Manuf. **1**(3), 346–357 (2007)
3. Kwon, H.S., Kahraman, A., Lee, H.K., Suh, H.S.: An automated design search for single and double-planet planetary gear sets. ASME J. Mech. Des. **136**(1), 1–13 (2014)
4. Harianto, J., Houser, D.R.: A methodology for obtaining optimum gear tooth micro-topographies for noise and stress minimization over a broad operating torque range. In: ASME 2007 International Design Engineering Technical Conferences and Computers and Information in Engineering Conference, ASME 2007, Las Vegas, Nevada, USA
5. Houser, D.R., Harianto, J., Chandrasekaran, B., Josephson, J.R., Iyer, N.: A multi-variable approach to determine the "Best" gear design. In: ASME Power Transmission and Gearing Conference, Sept. 10–13, Baltimore, MD, Paper DETC2000/PTG-14362 (2000)
6. Padmanabhan, S., Ganesan, S., Chandrasekaran, M., Srinivasa, R.V.: Gear pair design optimization by genetic algorithm and FEA. In: IEEE Front. Automob. Mech. Eng., Nov. 25–27, 2010, Chennai, India, pp. 301–307 (2010)
7. Jeong, T., Kicher, T.P., Zab, R.J.: Initial design of gears using artificial neural net. In: AGMA Paper 91FTM11, AGMA Fall Technical Meeting, 1st Oct., Alexandria, VA (1991)
8. Reagor, C.P.: An optimal gear design method for minimization of transmission error and vibration excitation. Diss. The Pennsylvania State University (2010)
9. Golabi, S.'i., Fesharaki, J.J., Yazdipoor, M.: Gear train optimization based on minimum volume/weight design. Mech. Mach. Theory **73**, 197–217 (2014)
10. Eriksson, L., Johansson, E., Kettaneh-Wold, N., Wikström, C., Wold, S.: Design of Experiments: Principles and Applications, Third ed. MKS Umetrics AB (2008)
11. Vijayakar, S.M.: A combined surface integral and finite element solution for a three dimensional contact problem. Int. J. Numer. Methods Eng. **34**, 525–545 (1990)
12. Borner, J., Houser, D.R.: Friction and bending moments as gear noise excitations. No. 961816. SAE Technical Paper (1996)

Chapter 38
Dynamics and Pareto Optimization of a Generic Synchronizer Mechanism

Muhammad Irfan, Viktor Berbyuk, and Håkan Johansson

Abstract Transmission systems for passenger cars and trucks are equipped with synchronizer mechanism. It has a great impact on driving comfort and transmission efficiency. A synchronizer mechanism as a key component of a transmission system must be able to prevent gears from shocking and reduce the noise. Gear shifting improvement with respect to smooth, quick and energy efficient synchronizer's performance is still an important issue for automotive industry. This contribution studies the kinematics and dynamics of a generic synchronizer consisting of sleeve, blocker ring and gearwheel constituting a mechanical system with a set of time-varying constraints describing frictional contacts between system's components. The dynamic response is modelled using constrained Lagrangian formalism. Pareto optimization problem is stated and optimized the rate of the applied sleeve force, coefficient of friction and cone angle are found to attain a minimal synchronization time as well as speed difference between sleeve and gearwheel. One outcome of the study is that the obtained Pareto solution is characterized by the minimal admissible value of the cone angle of the synchronizer.

Keywords Transmission synchronizer • Synchronization time • Shift quality • Pareto optimization • Constrained Lagrangian formalism

38.1 Introduction

The synchronizer mechanism plays a key role in the functioning of the transmission systems for the vast majority of vehicles. The purpose of the synchronizer is to ensure smooth and quick gear shift in a wide range of operating conditions, and has been the study for a long time in automotive industry, see [1–9]. A concern for the designer of synchronizers is to determine the proper trade-off between several conflicting objectives such as reducing the forces involved the impulse during engagement, robustness to different operating conditions while the gear shift should be as quick as possible.

Due to the different contacts of the components of the mechanism, the synchronization process is usually described in terms of different phases, for which different models have been devised separately. Here, we shall adopt a model based on Constrained Lagrangian Formalism that gives a unified formulation for the whole event, as was reported in [10].

As representative for common synchronizer designs a generic synchronizer is studied in this paper. The considered synchronizer consists of an engaging sleeve, a synchronizer ring (sometimes called blocker ring) and gearwheel. A bi-objective optimization problem relevant to synchronizer design is formulated, and its Pareto solution is obtained and analyzed. The results show the trade-off between quickness of synchronization process and shift quality (risk for clashing) and the potential for improved synchronizer performance using cone angle, coefficient of friction and rate of shift force.

38.2 Generic Synchronizer

We shall in this paper consider a generic synchronizer as a representative for common synchronizer designs. The generic synchronizer consists of three bodies; engaging sleeve, the synchronizer ring and the gearwheel depicted in Fig. 38.1. The engaging sleeve is operated by the selector and is attached to the gearbox output shaft and the gearwheel is connected to the gearbox input shaft where clutch disengaged from motor. The kinematics and dynamics of synchronization process are explained schematically in Fig. 38.2. The shift force is applied on the sleeve and it moves axially. First the ring gets the axial

---

M. Irfan • V. Berbyuk (✉) • H. Johansson
Department of Applied Mechanics, Chalmers University of Technology, 412 96, Göteborg, Sweden
e-mail: irfan.muhammad@chalmers.se; viktor.berbyuk@chalmers.se; hakan.johansson@chalmers.se

© The Society for Experimental Mechanics, Inc. 2016

J. De Clerck, D.S. Epp (eds.), *Rotating Machinery, Hybrid Test Methods, Vibro-Acoustics & Laser Vibrometry, Volume 8*,
Conference Proceedings of the Society for Experimental Mechanics Series, DOI 10.1007/978-3-319-30084-9_38

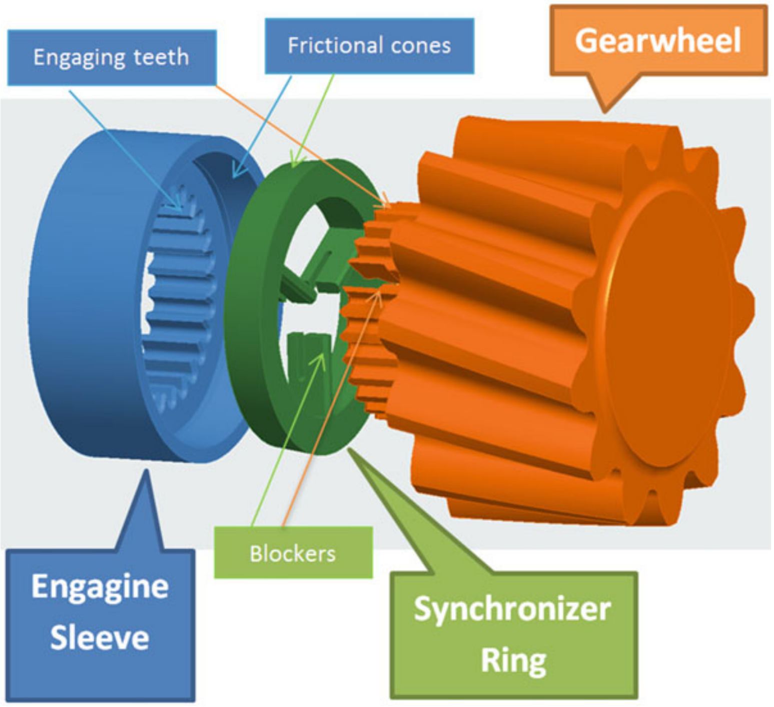

Fig. 38.1 A generic synchronizer

indexing during the phase 1a. In the phase 1b and the phase 1c the sleeve continues to move and the ring gets its angular indexing. Until now, the conditions between the cones are that of viscous friction. Phase 1d is characterized by mixed friction between cones and from 1e and onwards, dries friction. In the phase 1f the shift force exceeds the spring force and the purpose of the spring is to control the sleeve to go to the phase 2 before the ring gets the indexing position. Now the synchronizer is in the phase 2 which is the main phase. The sleeve translation is blocked due to the chamfer contact further and the speed difference decreases. The sleeve translates again when the blocker resistance is overcome and the phase 3 starts. Here is the risk that if engaging teeth come in contact with high speed difference, they will collide with each other and produce clashing. In the phase 4 the engagement teeth have full engaging position and the gear shift has done.

The generic synchronizer is considered as a multibody system consisting of three rigid bodies. The components are assembled on a shaft, on which the engaging sleeve and synchronizer ring may slide axially. The vector of generalized coordinates of the system in question is

$$\mathbf{q} = \left[x_s, \theta_s, x_r, \theta_r, \theta_g\right]^T \tag{38.1}$$

Here in θ_s, θ_r and θ_g are angular coordinates of the sleeve, ring and gearwheel, respectively; x_s and x_r are translational coordinates of the sleeve and ring, respectively. Due to the design of synchronizer, the motion of the system is restricted by a set of holonomic kinematic constraints $\boldsymbol{\Phi}(\mathbf{q}, t) = 0$. By introducing $\boldsymbol{\lambda}$ as the Lagrange multiplier vector, the motion of the system is described by a set of differential-algebraic equations (DAE), [11, 12]

$$\begin{cases} \frac{\mathrm{d}}{\mathrm{d}t}\left(\frac{\partial L}{\partial \dot{\mathbf{q}}}\right) - \frac{\partial L}{\partial \mathbf{q}} + \left[\frac{\partial \Phi}{\partial \mathbf{q}}\right]^T \boldsymbol{\lambda} = \mathbf{Q}^A \\ \Phi\left(\mathbf{q}, \mathrm{t}\right) = 0 \end{cases} \tag{38.2}$$

where $L\left(\mathbf{q}, \dot{\mathbf{q}}\right)$ is the Lagrangian of the system, $\boldsymbol{Q}^A$ is a vector of generalized forces due to non-conservative applied loads. The vector of non-conservative forces $\boldsymbol{Q}^A$ is further divided into $\boldsymbol{Q}^A = \boldsymbol{Q}^A_{app} + \boldsymbol{Q}^A_{fric}$, where $\boldsymbol{Q}^A_{fric}$ are generalized forces arising due to friction between bodies and other losses and $\boldsymbol{Q}^A_{app}$ are generalized forces due to applied forces arising from external stimuli. For the generic synchronizer under consideration, Eq. (38.2) is written as follows

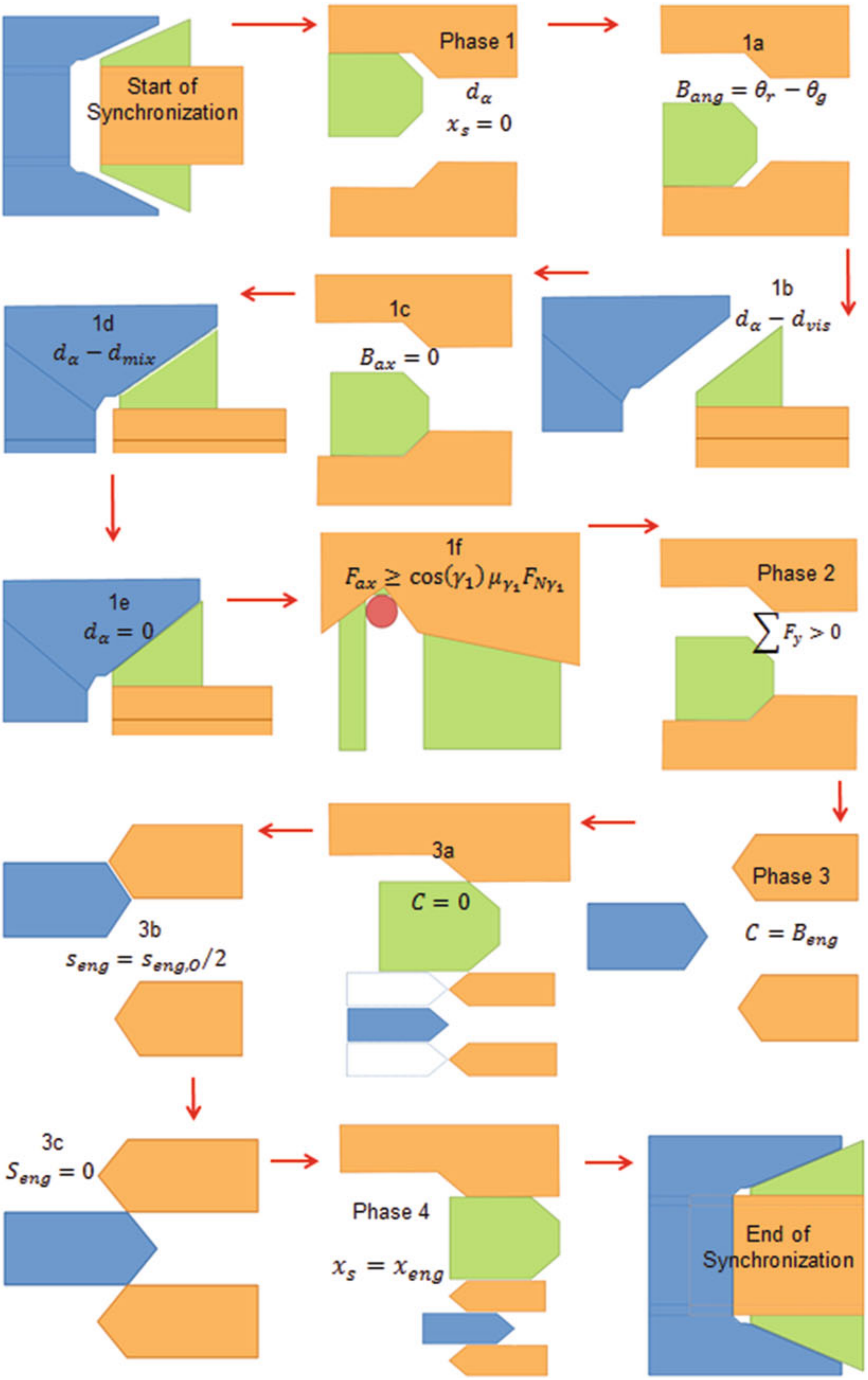
Start of Synchronization
Phase 1
d_α
$x_s = 0$
1a
$B_{ang} = \theta_r - \theta_g$
1b
$d_\alpha - d_{vis}$
1c
$B_{ax} = 0$
1d
$d_\alpha - d_{mix}$
1e
$d_\alpha = 0$
1f
$F_{ax} \geq \cos(\gamma_1)\,\mu_{\gamma_1} F_{N\gamma_1}$
Phase 2
$\sum F_y > 0$
Phase 3
$C = B_{eng}$
3a
$C = 0$
3b
$s_{eng} = s_{eng,0}/2$
3c
$S_{eng} = 0$
Phase 4
$x_s = x_{eng}$
End of Synchronization

Fig. 38.2 Division of synchronization process in different phase events

Table 38.1 Synchronization performance parameters

Variable	Name	Variable	Name
$m_s = 1.5$ kg	Sleeve mass	$I_r = 0.004$ kgm^2	Ring moment of inertia
$m_{spr} = 0.2$ kg	Spring ring mass	$I_s = 0.01$ kgm^2	Sleeve moment of inertia
$m_r = 0.5$ kg	Ring mass	$I_g = 0.2$ kgm^2	Gear moment of inertia
$r_\alpha = 0.1$ m	Cones mean radius	$r_\beta = 0.07$ m	Chamfers mean radius
$r_{spr} = 0.04$ m	Spring mean radius	$F_{spr} = 50$ N	Spring force
$b = 5$ mm	Cones contact length	$d_\alpha = 2$ mm	Cones Initial clearance
$d_{vis} = 1$ mm	Viscous friction clearance	$h_{\min} = 0.1$ mm	Mixed friction clearance
$T_{oil} = 90^o$ C	Temperature at start	$\Delta T_{oil} = 20^o$ C	Temperature change
$\alpha = 7°$	Cone angle	$B_{ang} = 5°$	Angular clearance
$\beta = 60^o$	Chamfer angle	$\gamma = 5^o$	Detent angle
$\rho = 15$ mm^2/s	Oil viscosity	$\mu_\alpha = 0.17$	Cones friction coefficient
$C_g = 5$	Gear oil splash losses	$C_s = 1$	Sleeve oil splash losses
$\boldsymbol{C_r} = 0.003$	Ring sliding friction	$C_{s\alpha} = 0.02$	Sleeve sliding friction
$\omega_{s_o} = 1000$ rpm	Sleeve rotational speed	$\omega_{g_o} = 700$ rpm	Initial gear rotational speed
$\mu_{spr} = 0.12$	Spring friction coefficient	$\mu_\beta = 0.09$	Chamfer friction coefficient
$C_{r\alpha} = 0.002$	Ring sliding friction	$T_c = \lambda_{cons}\ \mu_\alpha F_s$	Cone Torque
$F_{sf} = 16\pi\rho\dot{x}_s \sin(\alpha)\ r_c(b/h)^3$		Axial force transferred during viscous friction, [13	
$M_{sf} = 4\pi\rho\dot{x}_s r_c^3\ \omega_s b\left(1 - \omega_g/\omega_s\right)/h$		Torque transfer in viscous friction	

Table 38.2 Internal constraints during sub-phases of the synchronization

Phase	Constraint: $\Phi(q,t)^{internal} = 0$	Phase	Constraint: $\Phi(q,t)^{internal} = 0$
1a	$[x_r] = 0$	2	$\begin{bmatrix} x_r - d_\alpha \\ \theta_r - \theta_g - B_{ang} \end{bmatrix} = 0$
1b	$\begin{bmatrix} x_r \\ \theta_r - \theta_g - B_{ang} \end{bmatrix} = 0$	3a	$\begin{bmatrix} x_s - x_r - d_\alpha \\ \theta_r - \theta_g - B_{ang} - \frac{x_r - B_{ax}}{r_\beta} \tan\beta \end{bmatrix} = 0$
1c	$\begin{bmatrix} x_s - x_r - d_{vis} \\ \theta_r - \theta_g - B_{ang} \end{bmatrix} = 0$	3b	$\begin{bmatrix} x_s - x_r - d_\alpha \\ \theta_r - \theta_g - B_{ang} - \frac{x_r - B_{ax}}{r_\beta} \tan\beta \end{bmatrix} = 0$
1d	$\begin{bmatrix} x_s - x_r - d_{mix} \\ \theta_r - \theta_g - B_{ang} \end{bmatrix} = 0$	3c	$\begin{bmatrix} x_s - x_r - d_\alpha \\ \theta_r - \theta_g - B_{ang} - \frac{x_r - B_{ax}}{r_\beta} \tan\beta \end{bmatrix} = 0$
1e	$\begin{bmatrix} x_s - x_r - d_\alpha \\ \theta_r - \theta_g - B_{ang} \end{bmatrix} = 0$	4	$\begin{bmatrix} x_s - x_r - d_\alpha \\ \theta_r - \theta_s + \theta_{rs} \\ \theta_r - \theta_g - B_{ang} + \theta_{gs} \end{bmatrix} = 0$
1f	$\begin{bmatrix} x_s - x_r - d_\alpha \\ \theta_r - \theta_g - B_{ang} \end{bmatrix} = 0$		

$$\begin{cases} \begin{bmatrix} m_s & 0 & 0 & 0 & 0 \\ 0 & I_s & 0 & 0 & 0 \\ 0 & 0 & m_r & 0 & 0 \\ 0 & 0 & 0 & I_r & 0 \\ 0 & 0 & 0 & 0 & I_g \end{bmatrix} \begin{bmatrix} \ddot{x}_s \\ \ddot{\theta}_s \\ \ddot{x}_r \\ \ddot{\theta}_r \\ \ddot{\theta}_g \end{bmatrix} + \left[\frac{\partial \boldsymbol{\Phi}}{\partial \mathbf{q}}\right]^T \boldsymbol{\lambda} = \begin{bmatrix} F_s \\ 0 \\ 0 \\ 0 \\ 0 \end{bmatrix}^{app} - \begin{bmatrix} F_{sf} \\ M_{sf} \\ F_{rf} \\ M_{rf} \\ M_{gf} \end{bmatrix}^{fric} - \begin{bmatrix} C_{s\alpha} sign\left(\ddot{x}_s\right) \\ C_s \dot{\theta}_s \\ C_{r\beta} sign\left(\dot{x}_r\right) \\ C_r \dot{\theta}_r \\ C_g \dot{\theta}_g \end{bmatrix}^{fric} \\ \boldsymbol{\Phi} = \begin{bmatrix} \boldsymbol{\Phi}^{imposed} \\ \boldsymbol{\Phi}^{internal} \end{bmatrix} = 0 \end{cases} \tag{38.3}$$

where $\boldsymbol{\Phi}(\mathrm{q}, t)^{imposed} = \theta_s - \omega_s^{pres}\ t$. The system parameters and other notations are detailed in Table 38.1 and the set of internal constraints are presented in Table 38.2.

The applied shift force is modelled as follows

$$F_s(t) = \begin{cases} \dot{F}_s t & t \le t_{phase,2} \\ 300 + \dot{F}_{s,3} t & t_{phase,2} \le t_{phase,3a} \\ F_{bump} + \dot{F}_{s,3} t & t_{phase,3a} \le t_{synch} \end{cases} \tag{38.4}$$

where $\dot{F}_s$ is increasing force rate, $\dot{F}_{s,3}$ is decreasing force rate and F_{bump} is double bump force which is required to release the cones from sticking, to flush out the oil between teeth and to turn the gearwheel. To solve the dynamics problem for the synchronizer in question the initial conditions are chosen as follows

$$\begin{cases} x_s(0)=x_s^0 & \dot{x}_s(0)=0 \quad x_r(0)=x_r^0 \quad \dot{x}_r(0)=0 \\ \theta_s(0)=\theta_s^0 & \dot{\theta}_s(0)=\dot{\theta}_s^0 \quad \theta_r(0)=\theta_r^0 \quad \dot{\theta}_r(0)=\dot{\theta}_r^0 \end{cases} \theta_g(0)=\theta_g^0 \; \dot{\theta}_g(0)=\dot{\theta}_g^0 \tag{38.5}$$

38.3 Measures of Synchronizer Performance

From the design point of view, it is desired to shift the gear as quickly as possible while maintaining good quality of shift. A predominant case of bad quality is the clashing of the engaging teeth. Therefore, the two main objectives considered are total synchronization time $F_1 = t_{synch}$ and sleeve-gearwheel speed difference between $F_2 = \Delta\dot{\theta}_2 = \left|\dot{\theta}_s - \dot{\theta}_g\right|$ at end of Phase 2. These two objectives are expected to be contradictory, as a short synchronization time will not give time to reduce the speed difference between gearwheel and sleeve.

As subject for design parameters we here consider two structural parameters; cone angle α and coefficient of friction μ_α at cone contact in addition to a parameter defining the rate of applied shift force F_s(t). From sensitivity analysis reported in [10] showed that synchronization time is decreasing with increasing coefficient of friction and shift force but the synchronization time is increasing with increasing cone angle.

The dependency of the considered objective functions with respect to one parameter at the time is depicted in Fig. 38.3. It shows clearly the contradictory nature of the considered two objective functions with respect to the three design parameters in question. For instance with 2×10^4 N/ sec rate of applying shift force, the synchronization time is almost 0.12 s which can be the desired minimum time for design engineers but at the same shift force rate, the speed difference is almost 72 rpm which

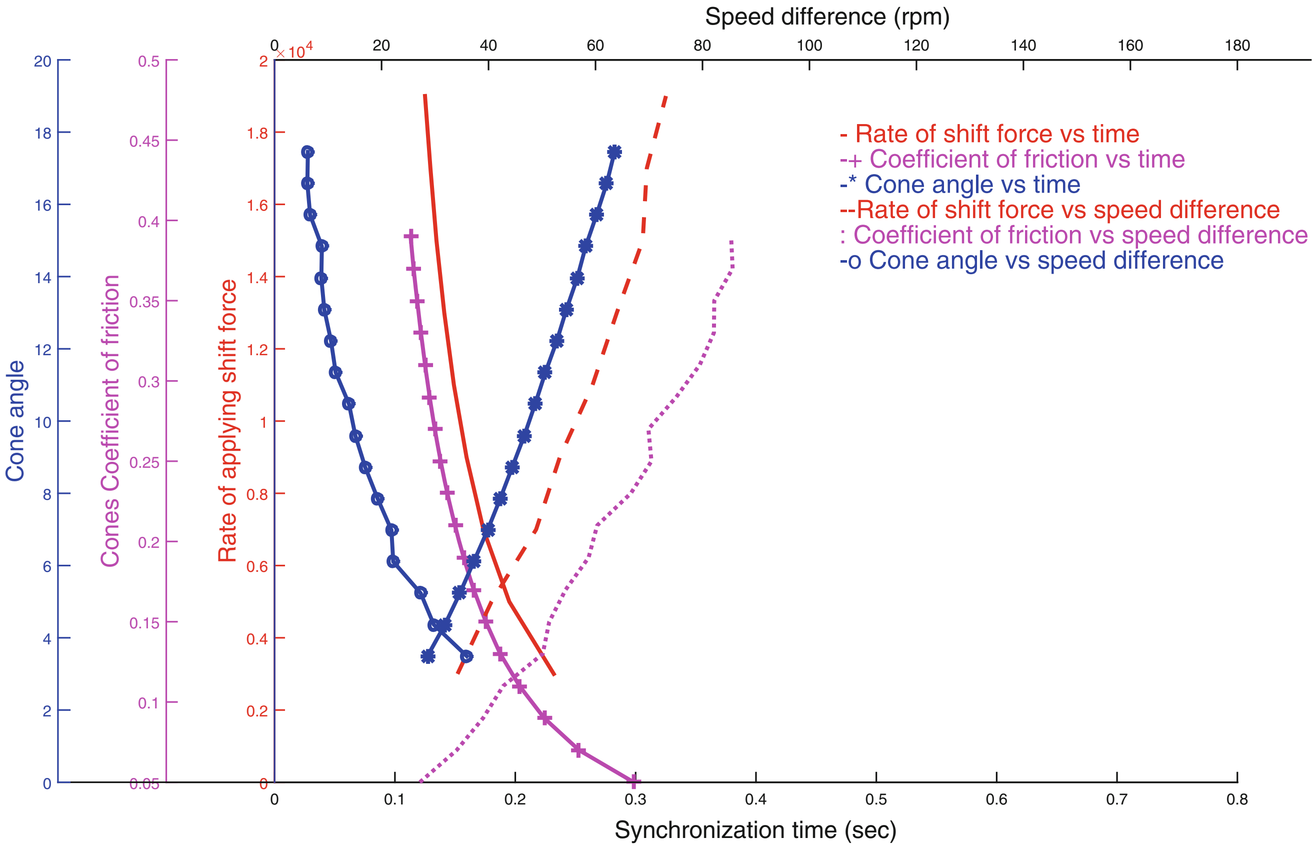

Fig. 38.3 Variations of two objective functions w.r.t three design variables

can be extremely undesired for the design engineers as shown in Fig. 38.3. Similarly at 3000 N/sec rate of applying shift force the speed difference is almost 35 rpm which can be the desired value but at the same shift force rate the synchronization time is almost 0.24 s which can be the extremely undesired. Next we seek to find the set of design parameters which can give compromise values (Pareto front) of the synchronization time and speed difference.

38.4 Optimization Problem Statement

We consider the following bi-objective optimization problem. Let the objective functions $F_1(\mathbf{q}, \mathbf{p}) = t_{synch}$, $F_2(\mathbf{q}, \mathbf{p}) = \left|\dot{\theta}_s\left(t_{phase2}\right) - \dot{\theta}_g\left(t_{phase2}\right)\right|$ are given and the vector of varying parameters $\mathbf{p} = \left[\dot{F}_s, \mu_s, \alpha\right]^T \in P_{adm}$ with the following set of parameter admissible values is chosen

$$P_{adm} = \left\{[3000, 50000], [0.1, 0.4], \left[4^0, 20^0\right]\right\}$$

It is required to determine all admissible values of the varying parameters, $\mathbf{p}^* \in P_{adm}$, that satisfy the following system of variational equations

$$\begin{cases} \min\limits_{\mathbf{p} \in P_{adm}} F_1(\mathbf{q}, \mathbf{p}) = F_1(\mathbf{q}, \mathbf{p}^*) = t^*_{synch}(\mathbf{p}^*) \\ \min\limits_{\mathbf{p} \in P_{adm}} F_2(\mathbf{q}, \mathbf{p}) = F_2(\mathbf{q}, \mathbf{p}^*) = \Delta\theta^*_2(\mathbf{p}^*) \end{cases}$$

subject to DAE of motion (38.3) and given initial conditions (38.5). The function $\Delta\theta^*_2(t^*_{\mathrm{synch}})$ is called the Pareto front and the set of values of varying parameters $\mathbf{p}^* \in P_{adm}$ is called the Pareto set.

The formulated problem was solved using genetic algorithm as defined in the function *gamultiobj* with default settings in Matlab version R2014b. The Pareto front obtained is depicted in Fig. 38.4, and the corresponding Pareto set is shown in Fig. 38.5. The synchronization performance diagrams for the quickest synchronization process (with smallest t_{synch}), for the

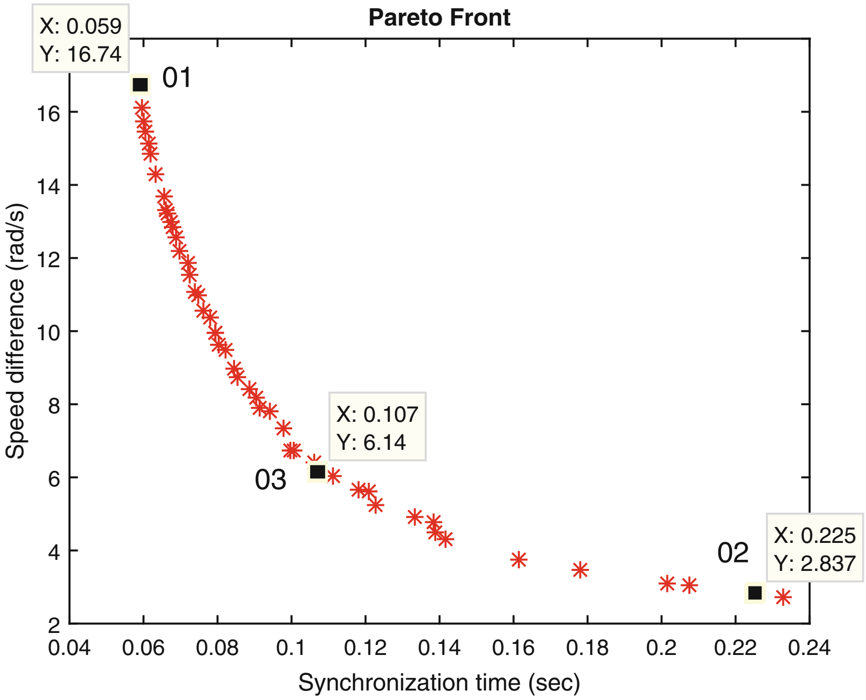

Fig. 38.4 Pareto front of the objective F_1 and objective F_2

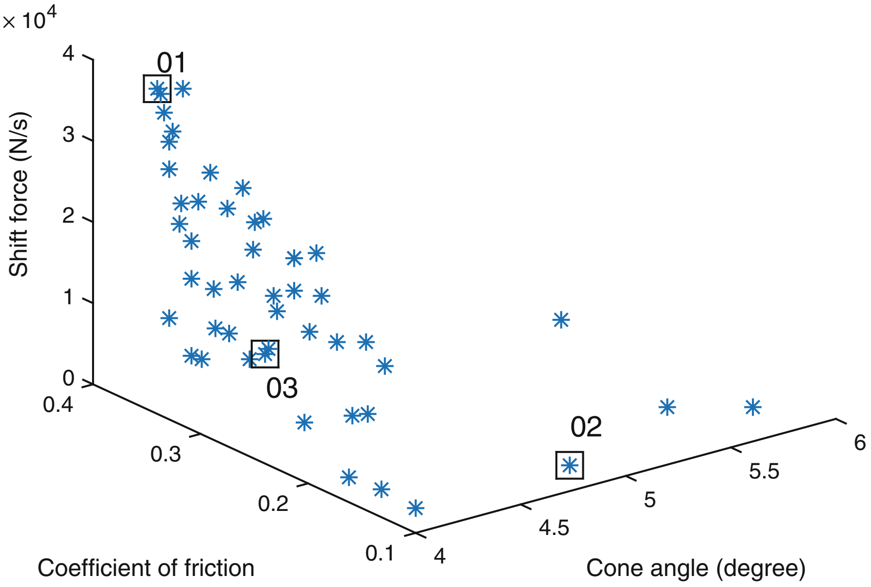

Fig. 38.5 Pareto set of μ_α, α and $\dot{F}_s$

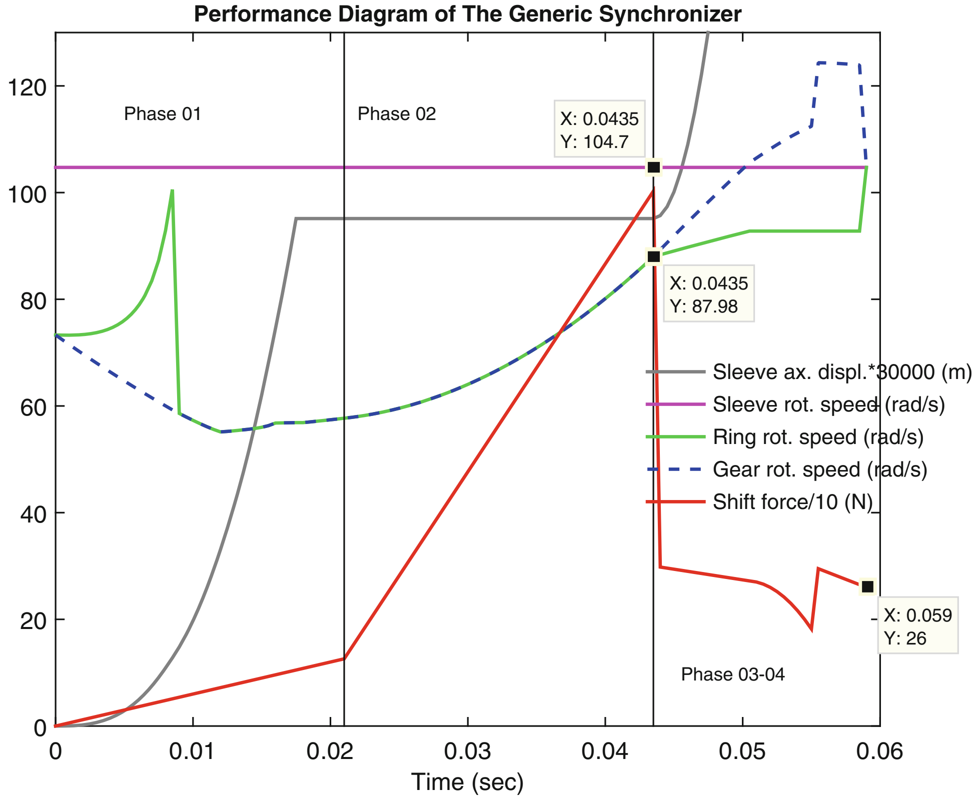

Fig. 38.6 Synchronization performance at smallest t_{synch}, (point 1), but highest $\Delta\dot{\theta}_2$

synchronizing process with the best shift quality (lowest $\Delta\dot{\theta}_2$), and for the synchronizing process with desirable trade-off between time and speed difference are presented in Figs. 38.6, 38.7, and 38.8, respectively. The values of the optimized varying parameters corresponding to underlying points of the Pareto front are presented in Table 38.3. The results show that a minimal cone angle is favored, and the trade-off is only between rate of shift force and coefficient of friction.

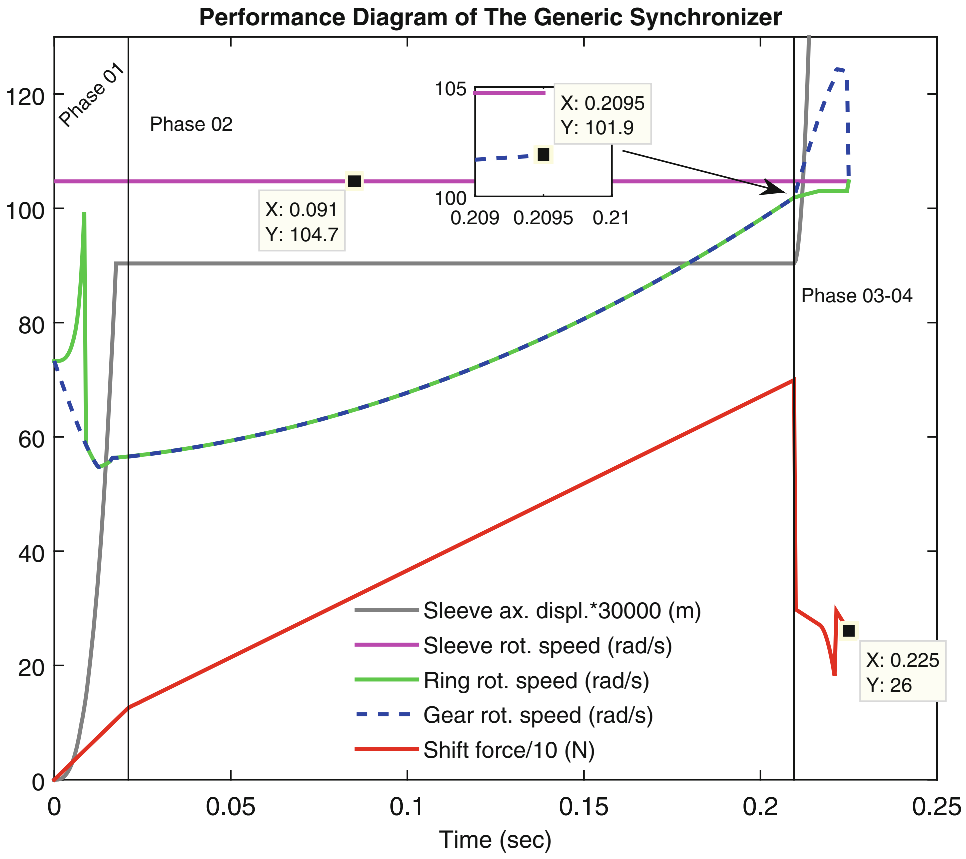

Fig. 38.7 Synchronization performance at smallest $\Delta\dot{\theta}_2$, (point 2), but highest t_{synch}

Table 38.3 Extremes and middle values from Pareto front for two objectives and three variables

S.No.	Synchronization time (sec)	Speed difference (rad/s)	Rate of shift force (N/s)	Coefficient of friction	Cone angle (degree)
2	0.225	27.0867	3041.7	0.1015	4.7433
3	0.1070	58.63	4530.4	0.3331	4.48
1	0.0590	159.82	38964.2	0.3519	4.06

38.5 Conclusion and Outlook

The sensitivity analysis of the sleeve-gearwheel speed difference and the synchronization time is studied with respect to the rate of the shift force, the cone angle and the coefficient of friction by using the CLF based computational model of generic synchronizer mechanism [10]. It is found that the speed difference has opposite trend than the synchronization time. The speed difference increases while the synchronization time decreases with increasing the rate of applying shift force and with increasing the cones coefficient of friction. But the speed difference decreases and the synchronization time increases with increasing the cone angle. Using the sleeve-gearwheel speed difference and synchronization time as objective functions the Pareto optimization problem has stated and solved by using genetic algorithm implemented in Matlab. Pareto front and Pareto set have been obtained. Several synchronizer performance diagrams have been plotted which give insight into synchronization process characteristics in case of the shortest possible synchronization time, the lowest possible difference between sleeve-gearwheel speeds, as well as in case of desirable trade-off between the synchronization time and sleeve-gearwheel speed difference.

For future studies different operating conditions will be taken into account to the generic synchronization process and optimal values of the input parameters will be found out from the Pareto front and the respective Pareto set.

Acknowledgments This paper was written in the context of the project "Robust and optimized synchronization of transmissions" funded by the Sweden's Innovation Agency, VINNOVA, Scania CV AB and Volvo GTT, (Project reference number: 2012-04619).

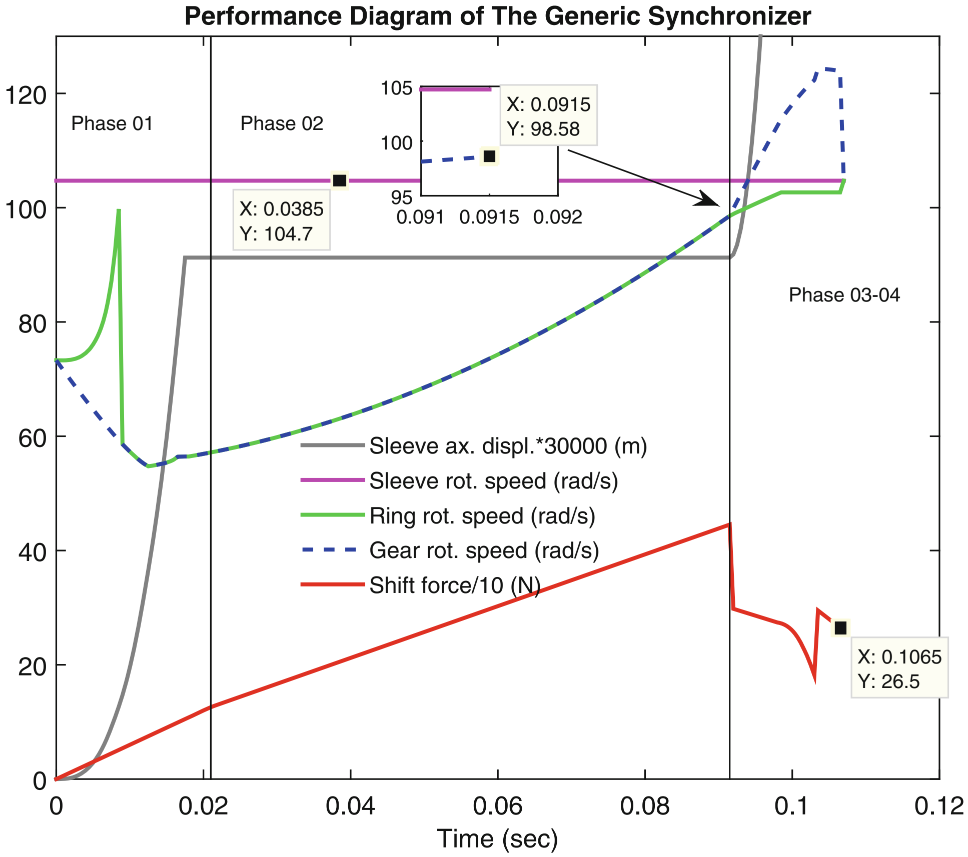

Fig. 38.8 Synchronization performance at the trade-off, (point 3), between $\Delta\dot{\theta}_2$ and t_{synch}

References

1. Neto, D.V., Fernandez, J., Rodrigues, P.: Manual transmission: synchronization main aspects. Soc. Automotive Eng. **1**(2519), 8 (2006)
2. Walker, P.D., Zhang, N.: Parameter study of synchronizer mechanisms applied to Dual Clutch transmissions. Int. J. Powertrains **1**(2), 198–220 (2011)
3. Häggström, D., Nordlander, M.: Development of a program for calculating gearbox synchronization. Master thesis, Department of Engineering Sciences and Mathematics, Luleå University of Technology, Södertälje, Luleå (2011)
4. Sharma, M.K., Salva, J.: Shift system inertia mass optimization techniques to minimize double bump for manual transmission. SAE technical paper series, 2012-01-1999 (2012)
5. Häggström, D., Sellgren, U., Björklund, S.: Robust pre-synchronization in heavy truck transmissions. In: Proceedings of the Int. gear conference, Lion (2014)
6. Lovas, L., Play, D., Marialigeti, J., Rigal, J.F.: Mechanical behaviour simulation for synchromesh mechanism improvements. J. Automob. Eng. **220**(7), 919–945 (2006)
7. Abel, A., Schreiber, U., Schindler, J.: Engine and gearbox modeling and simulation for improving the shifting behavior of powertrains with manual or automated transmission. SAE Technical Paper Series, 2006-01-1641 (2006)
8. Bedmar, A., *Synchronization processes and synchronizer mechanisms*, Diploma work no. 2013:20 Department of Applied Mechanics, Chalmers University of Technology., Göteborg, Sweden (2013)
9. Berbyuk, V.: Towards Pareto optimization of performance of a generic synchronizer of transmission systems. In: Proceedings of IDETC/CIE 2015 ASME Conference, Boston, USA, August 2-5, paper DETC 2015–46773 (2015)
10. Irfan, M., Berbyuk, V., Johansson, H.: Modelling of heavy vehicle transmission synchronizer using constrained Lagrangian formalism. In: Boltežar, M., Slavič, J., Wiercigroch, M. (eds.) Proceedings of the International Conference on Engineering Vibration, Ljubljana, 7–10 September. EBook. Ljubljana: Faculty for Mechanical Engineering, pp. 28–37 (2015)
11. Haug, E.J.: Intermediate Dynamics. Prentice Hall, Englewood Cliffs (1992)
12. Shabana, A.A.: Dynamics of Multibody System, 2nd edn. Cambridge University Press, Cambridge (1998)
13. Lovas, L.: Etude des relations entre le comportment et la fabrication des synchronisateurs des. PhD Thesis, National Institute of Applied Sciences Lyon (2004)

Chapter 39
Modeling and Characterization of a Flexible Rotor Supported by AMB

Marcus Vinicius Fernandes de Oliveira, Adriano Borges Silva, Adailton Borges Silva, Edson Hideki Koroish, and Valder Steffen Jr.

Abstract The present work is devoted to the conception of a representative numeric model of an experimental test rig, which consists of a flexible rotor supported by two Active Magnetic Bearings. Based on this model, the analysis and synthesis of new control strategies, as well as other relevant studies can be properly performed. For this purpose, the study was divided in two parts. The first is dedicated to the elaboration of individual numerical models in order to represent the dynamic behavior of each one of the sub systems that compose the entire system, as based on their design characteristics. Thereafter, the models of the sub systems are assembled together so that a representative model of the entire system is obtained. The following step is the model correlation with experimental results for validation purposes, which will be presented in a further contribution.

Keywords Rotor dynamics • Magnetic bearing • Modeling • Control • PID

39.1 Introduction

The first studies about magnetic levitation were presented by [1, 2] and a few years later [3] proposed the first industrial application of Active Magnetic Bearings (AMB) for aerospace momentum wheels [4]. In the last three decades, Active Magnetic Bearings (AMB) have been the subject of significant efforts in order disseminate their potentials and to make them more viable for industrial application [5, 6]. Nowadays, Active Magnetic Bearings (AMB) technology has achieved a considerable level of maturity and is regarded as one of the most promising solutions for several applications of rotating machinery [6, 7]. In such devices, the rotating shaft literally levitates suspended by magnetic forces, thus preventing any wear due to mechanical contact between the bearings and the bearings. In addition, this technology allows abolishing the need of lubricants, reaching very high rotation speeds without any relevant heating. According to [4], the AMB's can be classified as a mechatronic product, since they are composed by a combination of mechanic and electronic devices, controlled by a dedicated software. Besides, the inherent AMB's capabilities of sensing, data processing and actuation assure them a prominent position as a fundamental component for innovative designs of smart rotating machines, opening new possibilities for incorporating Active Vibration Control techniques as well as Structural Health Monitoring methodologies.

Active Vibration Control (AVC) is considered as the most sophisticated vibration attenuation strategy. This technique is based on the application of dynamic forces for the control the undesired system vibration [8]. In a simplified way, an AVC system is composed by sensors, actuators and a control unit. The sensors are responsible for providing information about the controlled variables. The control unit possesses the function of processing the information from the sensors and determining the command signals, calculated according to the control algorithms. Finally, the actuators convert the command signals, provided by the control unit, into effective actions upon the system. As an example of the application of AVC we can mention the work presented by [9], where a hybrid bearing, based on electromagnetic actuators, is employed to attenuate vibrations in rotating systems using different control strategies.

Due to its inherent instability, for any system supported by AMB's a mandatory requirement is to reach stable levitation along the operation range, which is only possible with the employment of a controller (such as a PID controller). Therefore, a very important step is the investigation of the main characteristics of the system in order to obtain representative computational models, which are necessary for the analysis and synthesis of the most advanced control design methods. In this context, several authors have addressed AMB's system identification. Among them, it is worth mentioning the work presented by [10], where the authors propose strategies for auditing systems with AMB's, discuss their main requirements

---

M.V.F. de Oliveira (✉) • A.B. Silva • A.B. Silva • E.H. Koroish • V. Steffen Jr.
LMEst–Laboratory of Mechanics and Structures, INCT (EIE)–National Institute of Science and Technology, School of Mechanical Engineering, Federal University of Uberlandia, Av. Joao Naves de Avila, 2121, Uberlandia, MG 38408-196, Brazil
e-mail: marcusfernandesss@doutorado.ufu.br

© The Society for Experimental Mechanics, Inc. 2016

J. De Clerck, D.S. Epp (eds.), *Rotating Machinery, Hybrid Test Methods, Vibro-Acoustics & Laser Vibrometry, Volume 8*,
Conference Proceedings of the Society for Experimental Mechanics Series, DOI 10.1007/978-3-319-30084-9_39

and also perform a brief review about the main architecture options and show guidelines for modeling the system components. Another important study was presented in [11] where the author performed the identification of a rotating system supported AMB’s and proposed an automated technique for robust controller design. In this context [12] modelled and characterized an AMB test rig for the design of robust controllers by using model based techniques with the objective of investigating rotordynamic instability in the presence of uncertainties.

The present work describes the first phase of a research project devoted to the investigation of robust control techniques applied to a rotating machinery supported by AMB’s. In this sense, the first problem that should be addressed is the development of a reliable computational model, based on the manufacturer specifications so that further analysis are supported for the consideration of several control strategies. Therefore, the process of modeling the various system components is presented in the following, as well as the assembling of the entire model.

39.2 Active Magnetic Bearings (AMB)

The operating principles of AMB’s are based on the concepts of electromagnetism. Therefore, their study is essential to the development of rotating machinery supported by AMB’s. The main purpose of analyzing the dynamic behavior of a magnetic actuator is to determine a relation between the forces resulting from the application of a voltage to its coils so that control action is provided. In [4], different aspects of AMB design are clearly presented.

A simplified analysis of the coils/geometry (forces and electrical properties) can be accomplished through a unidimensional representation of the magnetic structure of the actuator. Even though, this approach does not take into account some losses appearing in the AMB, such as eddy currents and fringing/leakage effects. It is assumed that that the flux density is uniformly distributed over the magnet core and airgap.

This simplified approach is based on the fact that the magnetic flux is generated at each pole due to an electrical current flowing through the coils, with N turns. Therefore, from the fundaments of electromagnetism, it is possible to obtain an expression for the force generated by the AMB, as described in Eq. (39.1) [6]:

$$F = \varepsilon \frac{\mu_0 N^2 i^2 A_g}{4g^2} \tag{39.1}$$

where μ_0 is the permeability of the air; g is the airgap; A_g is the cross sectional area of the magnetic actuator pole; ε is the geometric correction factor (0.9 for thrust bearings and 0.8 for radial bearings) and i is the current flowing in the system.

As the electromagnetic actuators can only generate attracting forces, it is usually necessary to employ configurations based on opposed pairs, as showed in Fig. 39.1a, in order to control the rotor and compensate for disturbance forces. A detailed representation of the forces on the rotor due to the action of two opposed actuators can be seen in Fig. 39.1b, where F_1 and F_2 are attracting forces acting to provide radial control of the rotor; F_{tot} is the resulting force acting on the rotor; g_1 and g_2 represent the airgap; i_1 and i_2 are the electric currents flowing through each one of the actuators.

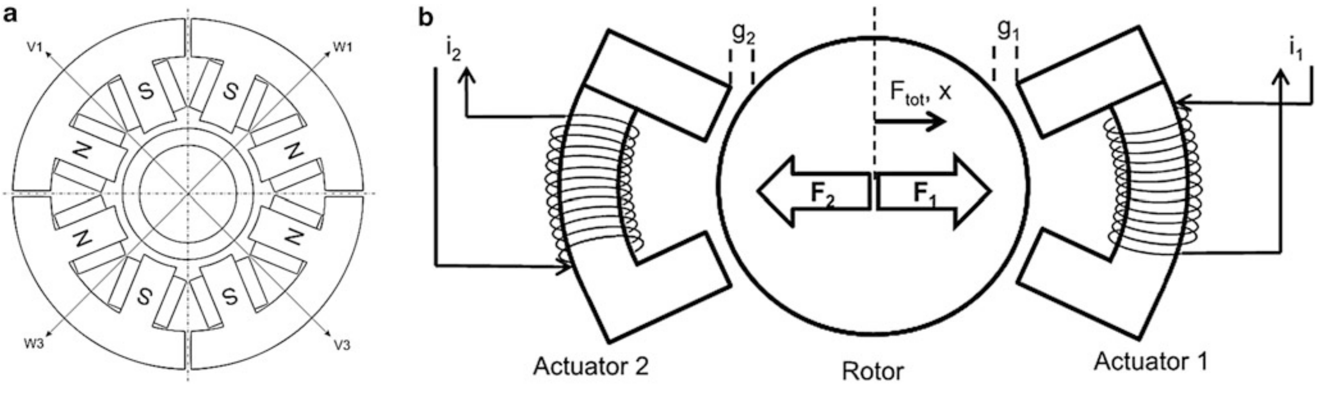

Fig. 39.1 AMB’s operation principle. (**a**) Eight pole configuration; (**b**) double sided configuration [6]

39.3 Model and Numerical Results

The test rig presented in Fig. 39.2 is composed by three main parts: the flexible rotor supported by radial AMB's, the controller and the external interface MBResearch™. It consists of a demonstration kit manufactured by SKF and is delivered with a control architecture based on a SISO PID controller, connected in series with a bank of filters. The shaft is supported by two identical radial AMB's to provide a maximum load capacity of 283 N. Such components are energized by a bias current of 1.0 A, and are capable of supporting a maximum current of 3.0 A. The shaft is driven by an electric motor of 500 W, operating in the range of 0–12,000 rpm. The kit is also equipped with two conventional backup ball bearings, located at both ends of the shaft, devoted to support the rotor in the case of any failure in the magnetic levitation. The nominal clearance between the surface of the shaft and the inner ring of the backup bearings is approximately 0.1 mm. Table 39.1 presents the main parameters of the system.

The first step was to develop individual computational models for each main component of the system (showed in Fig. 39.3) based on the design specification provided by the manufacturer. The following step was the assembling of those component models into a global one, as can be seen in Fig. 39.3.

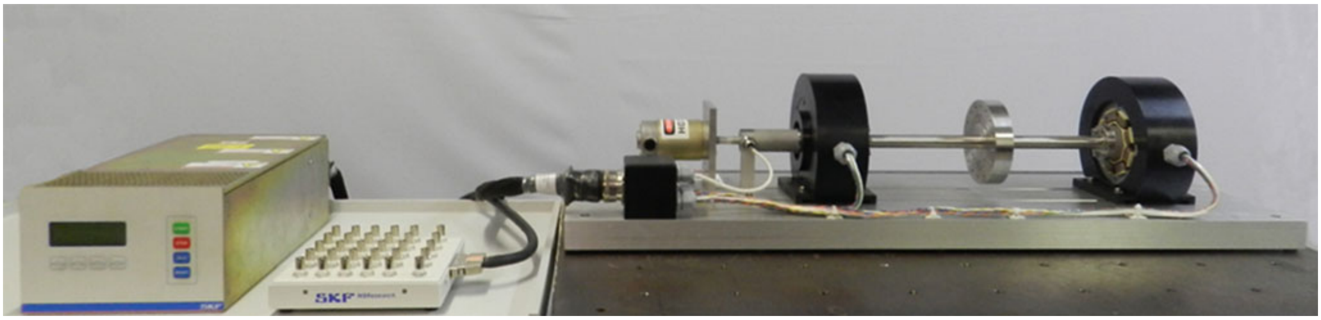

Fig. 39.2 Experimental Test Rig

Table 39.1 System parameters

Parameter description		Unit
Number of turns per coil, N	276	–
Air gap, g_0	0.364	mm
Pole cross sectional area, A_g	430.74	mm^2
Maximum voltage	10	V
Bias current, i_b	1	A
Current stiffness, k_i	143.76	N/A
Position stiffness, k_s	0.395	N/m
AMB load capacity	283	N
Shaft length	645	mm
Disc mass	5.89	kg
Motor power	500	W
Operation range	0–12,000	rpm

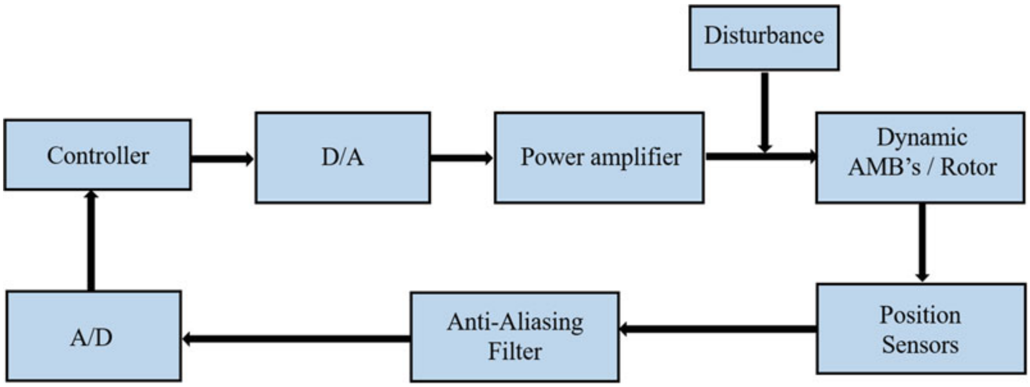

Fig. 39.3 Main components of an AMB system

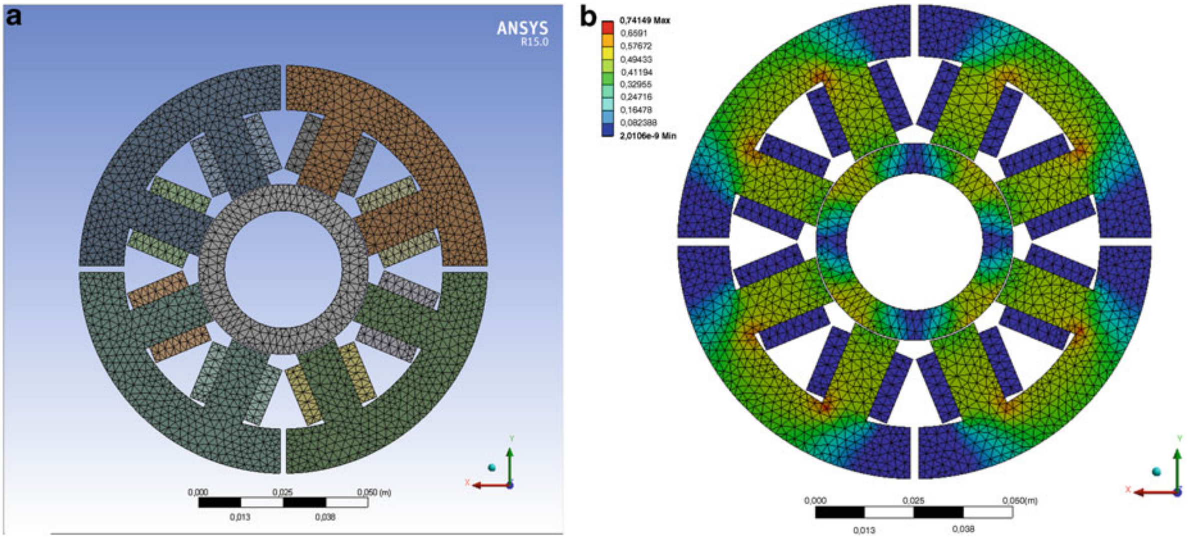

Fig. 39.4 AMB geometry: (**a**) meshed model, (**b**) flux density

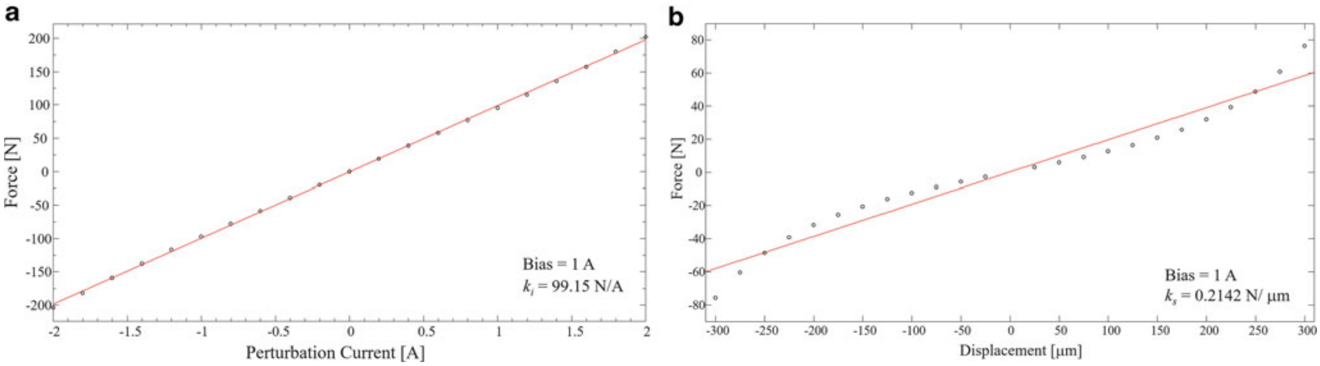

Fig. 39.5 Curve fitting to obtain the current stiffness k_i and position stiffness k_s

The first component addressed was the AMB subsystem, modeled by using the commercial Finite Element software ANSYS. The finite element model consisted of 209923 SOLID236 elements and was used to conduct simulations to obtain AMB parameters, such as the maximum static load capacity, current stiffness k_i and position stiffness k_s. Figure 39.4a presents the meshed finite element model and the Fig. 39.4b shows the flux density of the stator.

In the simulation test used to obtain the current stiffness [N/A], the rotor was kept fixed at the AMB center and the current through the axi-symmetric actuators was varied. The bias current was kept at 1.0 A during this simulation. The perturbation current, i_x, swept all the operating range, from -2.0A to 2.0A. The values of i_x and their corresponding electromagnetic forces were plotted to determine the current stiffness k_i, which is given by the tangent of the fitted curve presented in Fig. 39.5a, where one can observe that the curve describes a predominant linear behavior. The next simulated test was devoted to the determination of the position stiffness k_s. In this case, the perturbation current i_x was kept constant and the rotor was displaced in the range of $-300 \leq x \leq 300 \quad [\mu\text{m}]$. The results were plotted as illustrated in Fig. 39.5b. Similar to the determination of k_i, the position stiffness was given by the tangent of the fitted curve; however, only the points closer to the operating point $x = 0 \quad [\mu\text{m}]$ were considered. In the other hand, it is possible to observe that the curve obtained for this case presents a stronger nonlinear behavior, which is justified by the nonlinearity found in the electromagnetic force as a function of the airgap, as described in Eq. (39.1). It is worth mentioning that such nonlinearity does not compromise the determination of k_s since the system operates in the narrow range of $-100 \leq x \leq 100 \quad [\mu\text{m}]$, which is the clearance of the backup bearings. Therefore, only the values corresponding to this neighborhood were taken into account for the determination of k_s.

Once the AMB's stiffness parameters were determined, it was necessary to consider the subsystem rotor. In this case, the model was also based on the Finite Element method. For this aim, a proprietary software specially designed for handling rotordynamic problems was used, as developed in MATLAB environment. In order to properly represent this subsystem, the rotor was discretized into 51 Timoshenko beam elements, considering 4 dofs per node, two displacements and two rotations

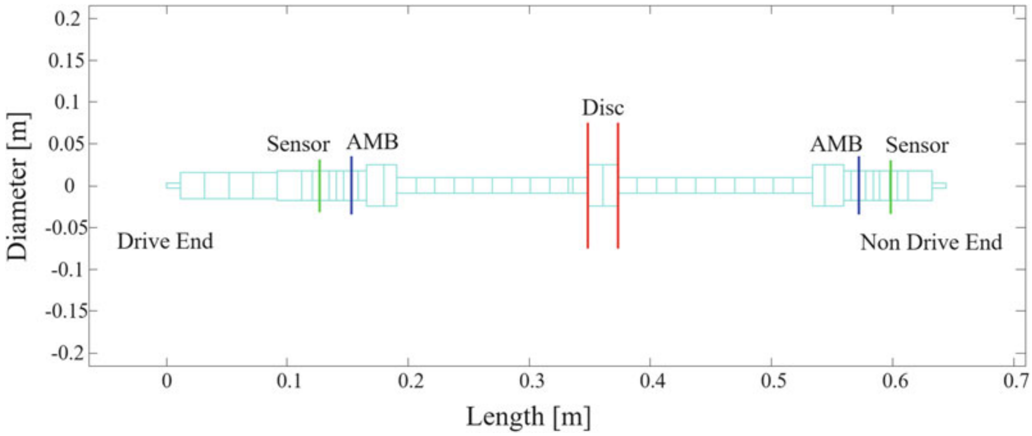

Fig. 39.6 Rotor Finite Element model

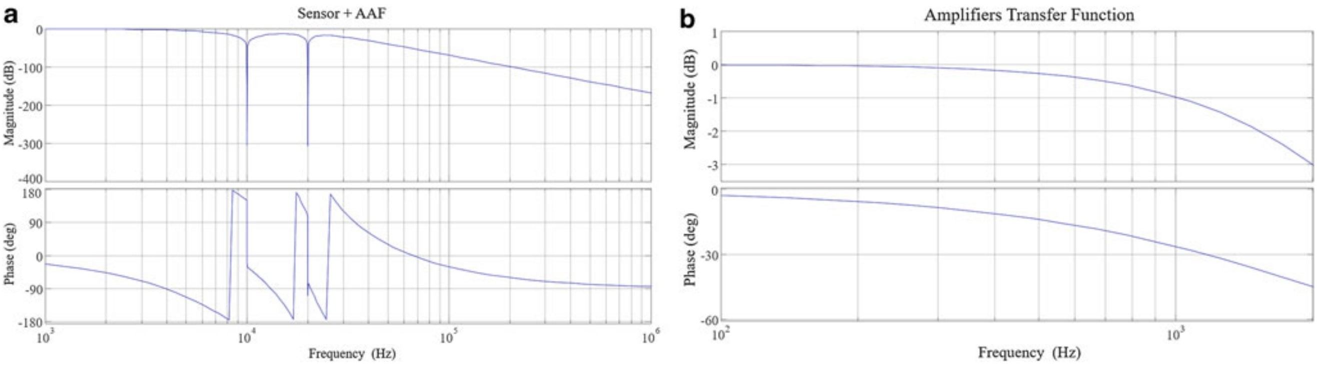

Fig. 39.7 Transfer functions: (**a**) position sensor, (**b**) amplifier

along the x and y directions. Figure 39.6 presents the rotor model, where the axial positions of the sensors and AMB's are also indicated. Due to the size of this model, the pseudo modal method [13] was used to reduce the system, thus keeping only the first ten rotor mode shapes, which were identified as relevant for the dynamic behavior of the system as pointed out by Hankel singular value analysis.

At this point, the efforts will be concentrated on the task of obtaining the transfer functions representing the electronic components. The first one addressed was the position sensor. According to the manufacturer, four position sensors were connected in series with anti-aliasing filters in order to remove high frequency disturbances. Figure 39.7a presents the transfer function of this subsystem, which consisted of four second order low pass filters in series with a first order system, respectively given by Eqs. (39.2) and (39.3):

$$LP_i = \frac{\omega_i^2}{s^2 + 2\xi_i\omega_i s + 1}, \quad i = 1, \ldots, 4 \tag{39.2}$$

$$LP_5 = \frac{\omega_5}{s + \omega_5} \tag{39.3}$$

where: $\omega_1 = \omega_2 = 1.289\text{e}5\ \text{rad/s}$; $\omega_3 = 6.28\text{e}4\ \text{rad/s}$; $\omega_4 = 1.256e5\ \text{rad/s}$; $\omega_5 = 1.24\text{e}5\ \text{rad/s}$; $\xi_1 = \xi_2 = 0.29$ and $\xi_3 = \xi_4 = 1.00$.

According to [14], the dynamic behavior of power amplifiers can be accurately modeled by a first order transfer function, as given by Eq. (39.4):

$$G_{amp} = K_{amp}\frac{1}{\frac{1}{\omega_{camp}}s + 1} \tag{39.4}$$

where G_{amp} is the power amplifier transfer function, K_{amp} is the system gain and ω_{camp} is the amplifier frequency bandwidth. According to the manufacturer: $K_{amp} \cong 1.0$ A/V; $\omega_{camp} \cong 2000$ Hz. We are interested on the frequency corresponding to an amplitude reduction of 3 dB (frequency bandwidth).

The time delay of the AMB system can be attributed mainly to the process of conversions A/D and D/A. In the literature [12, 14] this phenomena is usually modeled by a second order Padé approximation, as presented in Eq. (39.5). This approach considers that the time delay is given by $1.5T_s$, where T_s is the inverse of the acquisition rate. In this case, $T_s = 1/10,000$ s and $n = 2\ 0$.

$$e^{-T_s s} \approx \left(1 - \frac{T_s s}{2\,n}\right)^n / \left(1 + \frac{T_s s}{2\,n}\right)^n \tag{39.5}$$

After all individual models related to the main components of the system have been modeled, next step is to assemble them together in order to obtain the global open loop plant. This task was performed in MATLAB environment and the results for the rotor driven end (DE) and non-driven end (NDE) are presented in Fig. 39.8.

As the open loop rotor plants supported by AMB's are intrinsically unstable, the levitation is only possible if an initial control law is used to stabilize the closed loop system. In this sense, the rotor kit is equipped with an initial controller based on a SISO PI (Proportional-Integral) filter, associated to lead/lag and generic second order filters, as described in Eq. (39.6):

$$G_{ctrl} = (PI)\,(Lead/lag)\,(Gen) \tag{39.6}$$

where G_{ctrl} is the controller transfer function; *PI* is the Proportional-Integral control gain; *Lead/lag* and *Gen* represents the lead/lag and the generic second order filters transfer functions, respectively.

The PID controller is the most widely used in industry due to its simplicity and efficiency. Therefore, it is also commonly found in applications involving AMB's. However, this element alone is not capable of guaranteeing the required performance and stability. Equation (39.7) describes the standard transfer function for a PID controller.

$$PID = \frac{K_T\left(K_D s^2 + K_P s + K_I\right)}{s} \tag{39.7}$$

where K_T represents a total gain which multiplies all the other gains; and K_P, K_I and K_D are the proportional, integral and derivative gains, respectively. Table 39.2 presents the values employed for each bearing DE and NDE.

According to [15], a zero and a pole in the complex plane form lead phase compensators, where the pole frequency is higher than the zero frequency. Therefore, the addition of this element increases the phase and the gain in the frequency range located between the zero and the pole. In AMB's applications, this kind of element is indicated to deal with natural

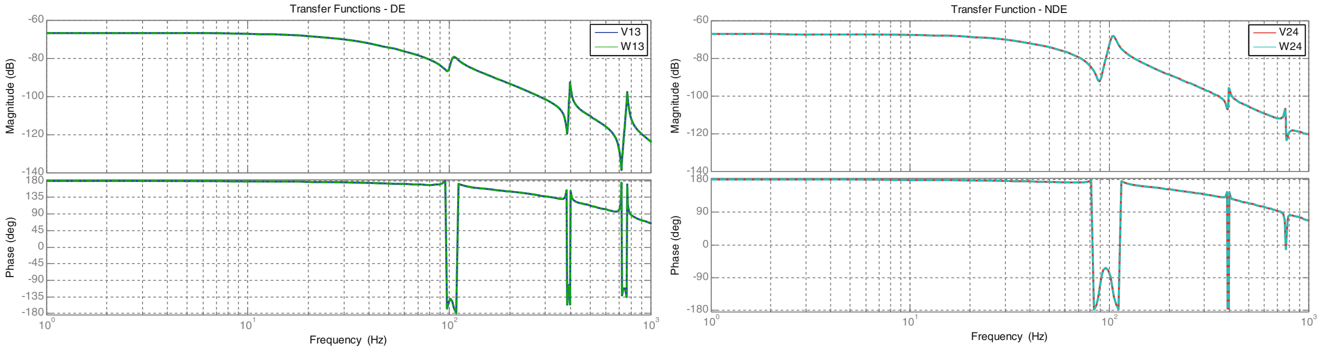

Fig. 39.8 Controller transfer functions

Table 39.2 Parameters of the PID controller

	AMB	
Parameter	DE	NDE
K_T	0.0062	0.0046
K_P	1.0	1.0
K_D	0.0	0.0
K_I	46.0	35.0

frequencies located inside the operation range. The effect of inserting a zero before a natural frequency and a pole after it yields a phase increment capable of providing a significant amount of damping to a given mode. This technique is called phase compensation. However, caution is recommended because, as a side effect, the amplitude is also increased in the same frequency range.

Similarly, the lag compensator also consists a zero and a pole. However, in this case, the zero is placed in a frequency higher than the one of the pole. This leads to an amplitude attenuation and a phase lag inside the region located between the pole and the zero. This technique is also employed to deal with models inside the operation range. Again, attention is required, since the side effect is a phase reduction. Equation (39.8) describes the transfer functions for both lead and lag compensators.

$$Lead/lag_i = K_c \alpha_i \frac{T_i s + 1}{\alpha_i T_i s + 1}, \qquad i = 1, 2 \tag{39.8}$$

where K_c is the gain, α_i is the attenuation factor (for $0 < \alpha_i < 1$ a lead compensator is obtained and for $1 < \alpha_i$ a lag compensator), $-1/\alpha_i T_i$ is the pole location, $-1/T_i$ is the location of the zero, and i indicates if it is the first or the second lead/lag filter. The parameters for the lead/lag compensator are listed in Table 39.3.

As a last resource for improving the system characteristics, there is a bank of second order generic filters, given by Eq. (39.9), which also permits to manipulate the amplitude and the phase.

$$Gen_i = \frac{s^2 + 2\xi_{Ni}\omega_{Ni}s + \omega_{Ni}^2}{s^2 + 2\xi_{Di}\omega_{Di}s + \omega_{Di}^2}, \qquad i = 1, \ldots 4 \tag{39.9}$$

The parameters used in these filters are shown in Table 39.4.

The controller transfer functions obtained for each AMB is presented in Fig. 39.9.

Table 39.3 Lead/lag parameters

Filter	Parameter	Value [rad/s]	
		DE	NDE
$Lead/lag_1$	$-1/T_1$	483	157
	$1/\alpha_1 T_1$	2513	471
$Lead/lag_2$	$-1/T_2$	779	1634
	$1/\alpha_2 T_2$	2569	10619

Table 39.4 Parameters for the generic filters

Filter	Parameter	AMB	
		DE	NDE
Gen_1	ω_{N1}, ξ_{N1}	2350 rad/s, 0.08	1791 rad/s, 0.41
	ω_{D1}, ξ_{D1}	1759 rad/s, 0.37	1791 rad/s, 0.26
Gen_2	ω_{N2}, ξ_{N2}	4712 rad/s, 0.03	2513 rad/s, 0.27
	ω_{D2}, ξ_{D2}	4178 rad/s, 0.16	2953 rad/s, 0.21
Gen_3	ω_{N3}, ξ_{N3}	9519 rad/s, 0.36	9739 rad/s, 0.14
	ω_{D3}, ξ_{D3}	7383 rad/s, 0.30	10,053 rad/s, 0.42

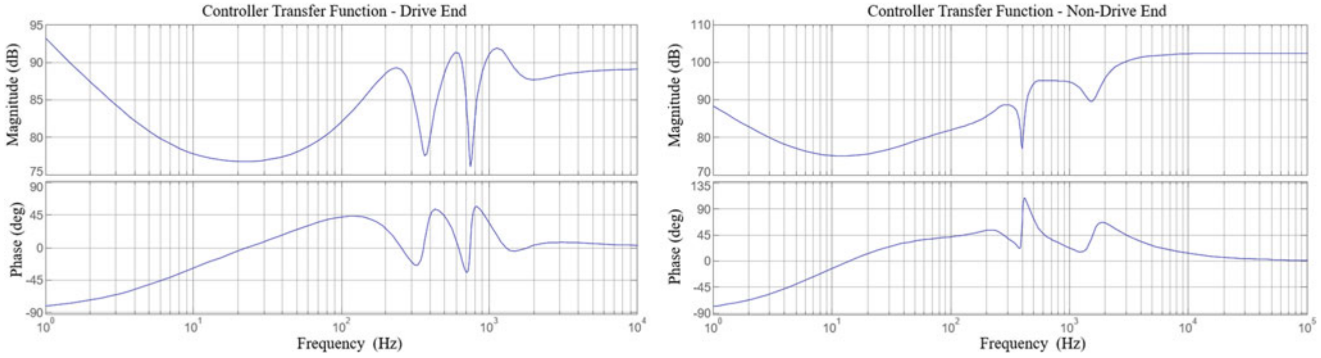

Fig. 39.9 Controller transfer functions

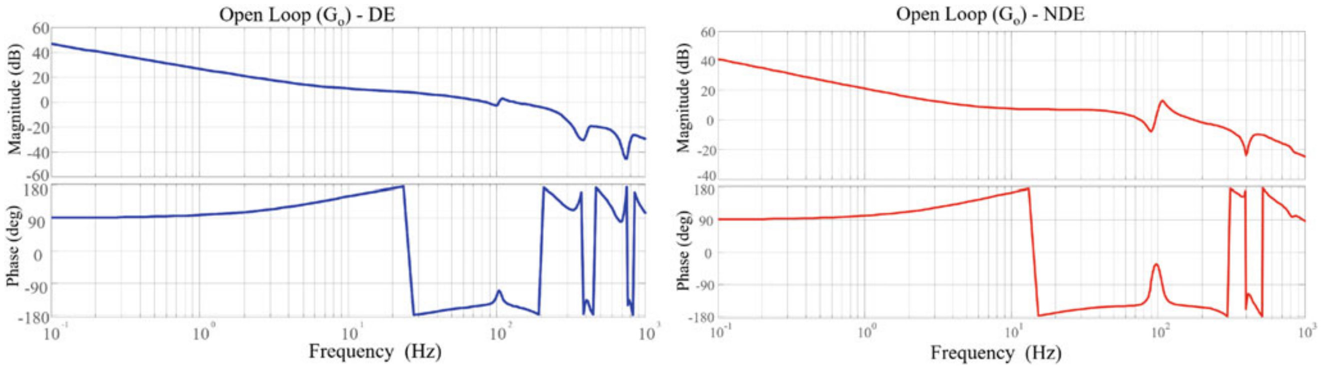

Fig. 39.10 Open Loop Transfer Functions—0 rpm, DE (*blue*) and NDE (*red*)

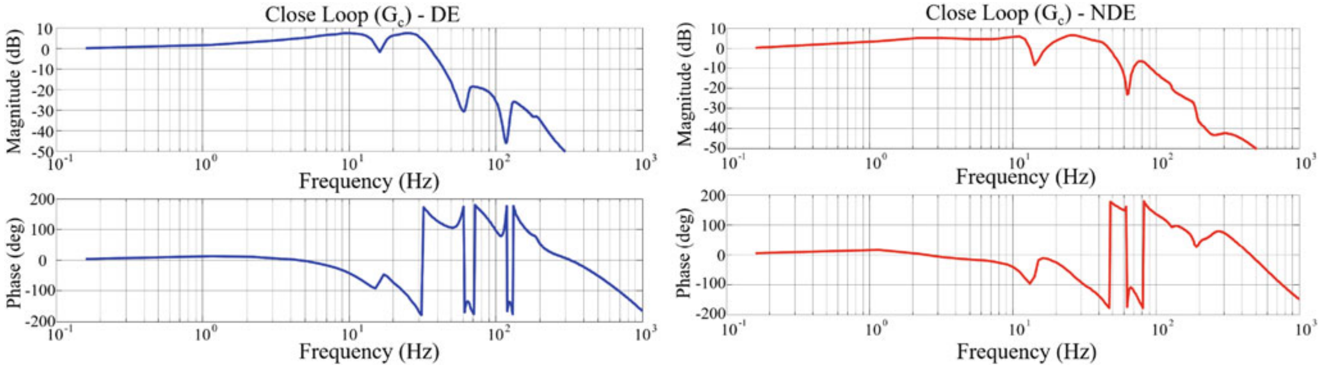

Fig. 39.11 Closed Loop Transfer Functions—0 rpm, DE (*blue*) and NDE (*red*)

According to ISO 14839 standard, the most important transfer functions for rotating systems with AMB's are the open loop G_o, the closed loop G_c, and the sensitivity function G_s. It is important to point out that, even though G_o is referred to as "open loop", this term is very specific since it is measured with all the loops closed. Otherwise, the system becomes unstable. Therefore, the transfer function $G_o(s)$ is different from de open loop transfer function obtained for all loops opened, as usually obtained for stable systems. The closed loop transfer function G_c is defined by Eq. (39.10):

$$G_c(s) = \frac{G_o(s)}{1 + G_o(s)} \tag{39.10}$$

Figures 39.9 and 39.10 present the open loop $G_o(s)$ and the closed loop G_c transfer functions for both sides: DE and NDE as based on the assembled model for the rotor a rest (0 rpm), in complete levitation. The sensitivity functions for the same situation are presented in Fig. 39.11.

The ISO 14839-3 standard classifies the stability margins of rotating systems suspended by AMB's in terms of the maximum peak of the sensitivity functions G_s, evaluated for a range where the superior limit is given by the higher of two options: three times the rated speed or until 2 kHz, but restricted to the half of the controller sampling rate. According to these recommendations, low values of the maximum peak of the sensitivity function implies a more robust system. In other hand, high values indicate that the system operates under a reduced stability margin. Therefore, the maximum peak of the sensitivity function $S_{\max}$, obtained by comparing the sensitivities along the four system axis in the range of frequency analyzed, must be used to classify the system stability margin.

Observing Fig. 39.12 it is possible to identify that the maximum peak of the sensitivity functions is obtained for the NDE side and occurs at approximately 170 Hz. As can be seen, at this point the maximum amplitude is close to 10 dB. According to the above-mentioned standard, this system is located close to the lower limit of Zone B, thus indicating that the machine is acceptable from the perspective of stability and can operate without restrictions.

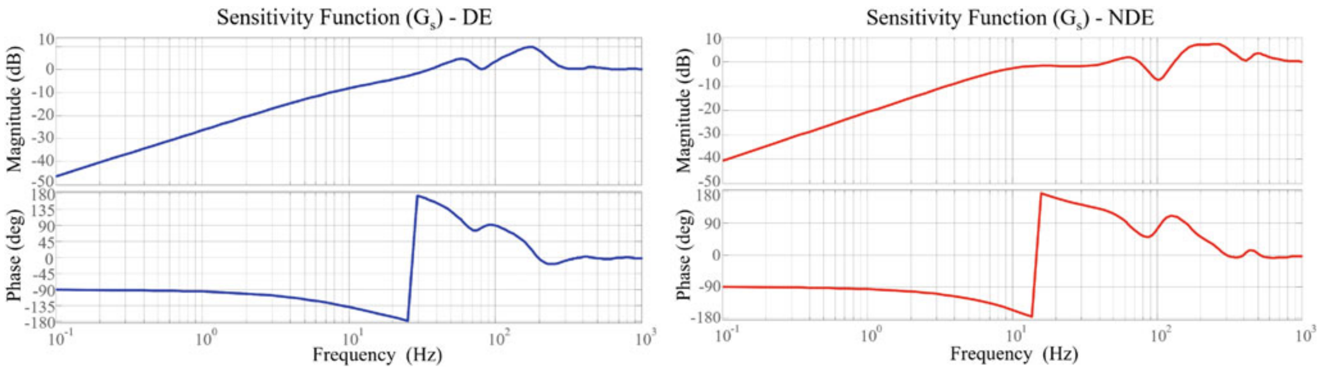

Fig. 39.12 Sensitivity Functions for Closed Loop—0 rpm, DE (*blue*) and NDE (*red*)

39.4 Conclusion

The present contribution presented the model and characterization of an experimental test rig encompassed by a flexible rotor supported by magnetic bearings at the ends. For this aim, existing techniques and technical standards have been taken into account. The goal of the presented procedure is to create a representative model of the system, so that other phenomena can be studied in further investigations. Particularly, the main interest is to consider and test various active control techniques for which reliable mathematical models are required. Further studies will focus on experimental investigations so that the PID controller can be replaced by more robust control strategies.

Acknowledgments The authors are thankful to the Brazilian Research Agencies FAPEMIG, CNPq, and CAPES for the financial support provided for this research effort through the INCT-EIE.

References

1. Earnshaw, S.: On the nature of the molecular forces which regulate the constitution of the luminiferous ether. Trans. Camb. Phil. Soc. **7**(Part I), 97–112 (1842)
2. Braunbek, W.: Frei schwebende Körper im elektrischen und magnetischen Feld. Z. Phys. **112**, 753–763 (1939)
3. Habermann, H., Liard, G.: Le palier magnetique active: un principe revolutionaire. SKF Rev. Roulements Nr. 192 (1977)
4. Schweitzer, G., Maslen, E.H.: Magnetic Bearings: Theory, Design, and Application to Rotating Machinery, 535 pp. Springer, Berlin (2009)
5. Steffen Jr., V., Lepore, N.F.P.: A control force to reduce magnetically excited rotor vibrations. Mécanique Matériaux Electricité **65**(404), 90–93 (1984)
6. Yoon, S.Y., Lin, Z., Allaire, P.E.: Control of Surge in Centrifugal Compressors by Active Magnetic Bearings: Theory and Implementation (Advances in Industrial Control), 275 pp. Springer, London (2013)
7. Chiba, A., Fukao, T., Ichikawa, O., Oshima, M., Takemoto, M., Dorrel, D.: Magnetic Bearings and Bearingless Drives, 400 pp. Newnes, Oxford (2005)
8. Tammi, K.: Active control of radial rotor vibrations: identification, feedback, feedforward, and repetitive control methods. PhD Thesis, Helsinki University of Technology, Espoo (2007)
9. Koroishi, E.H., Borges, A.S., Cavalini Jr., A.A., Steffen Jr., V.: Numerical and experimental modal control of flexible rotor using electromagnetic actuator. Math. Probl. Eng. **2014**, 14 pp (2014). ID 361418. http://dx.doi.org/10.1155/2014/361418
10. Swanson, E., Maslen, E.H., Li, G., Cloud, C.H.: Rotordynamic design audit of AMB supported machinery. In: Proceedings of the Thirty-Seventh Turbomachinery Symposium, pp. 133–158 (2008)
11. Lösch, F.: Identification and Automated Controller Design for Active Magnetic Bearing Systems, 239 pp. ETH Zürich, Zürich (2002)
12. Mushi, S.E.: Robust control of rotordynamic instability in rotating machinery supported by active magnetic bearings. PhD Thesis, University of Virginia (2012)
13. Lalanne, M., Ferraris, G.: Rotordynamics Prediction in Engineering, 266 pp. Wiley, New York (1998)
14. Sanadgol, D.: Active control of surge in centrifugal compressors using magnetic thrust bearing actuation. PhD Thesis, University of Virginia (2006)
15. Ogata, K.: Engenharia de controle moderno, 5th edn., 809 pp. Pearson Prentice Hall, Sao Paulo (2010)
16. ISO Standard 14839: Mechanical vibrations—vibrations of rotating machinery equipped with active magnetic bearings—Part 1: Vocabulary, Part 2: Evaluation of vibration, Part 3: valuation of stability margin, Part 4: Technical guidelines, system design (Draft), 2002/2006

Chapter 40
Nonlinear Reduced Order Modeling of a Curved Axi-Symmetric Perforated Plate: Comparison with Experiments

David A. Ehrhardt and Matthew S. Allen

Abstract Structures undergoing large amplitude deformations usually include nonlinear strain–displacement relationships defining a geometric nonlinearity. This type of nonlinearity can be observed in structures with fixed boundary conditions where mid-plane stretching occurs at large deflections. When considering the dynamic response of the structure under these circumstances, the once uncoupled linear normal modes become coupled at large response amplitudes changing the characteristic deformation shape as the fundamental frequency of vibration changes. Therefore, the development of nonlinear reduced order models to predict the dynamic response of such structures should account for any potential coupling between the linear normal modes. In this context, a structures' nonlinear normal modes provide a compact characterization of modal coupling in the structural response in nonlinear regimes. This work uses experimentally measured and numerically calculated nonlinear normal modes for a curved axi-symmetric perforated plate to build a nonlinear reduced order model and gain insight to the underlying modal coupling. A comparison is made between two models and corresponding experimental structures to assess the model's ability to describe the modal coupling.

Keywords Nonlinear normal modes • Circular plate

40.1 Introduction

Geometric nonlinearity manifests in structures experiencing large amplitude deformations where axial stretching causes coupling between in-plane and out-of-plane motion. The coupled in-plane and out-of-plane motion also leads to a coupling of the underlying linear normal modes of vibration. Since established structural design techniques rely on uncoupled linear modes of vibration, new methods are sought to address nonlinear behavior while preserving the simplicity of the traditional design and test paradigms. Geometric nonlinearity is of particular interest in thin, constrained structures since nonlinear deformations can occur in the elastic region of the material. Therefore, the design of such structures can be beneficial because the nonlinearity couples the linear modes, spreading energy into other modes that would otherwise not be excited. In other scenarios, the unexpected deformations in these modes may cause large stresses and unexpected failures. The examination and understanding of the structural response and modal coupling at large amplitudes of deformations provides insight to the structure's design.

This work uses the nonlinear normal mode (NNM) concept as a tool for testing and modeling of nonlinear structures. A structure's NNMs provide insight into the dynamic response and modal coupling at large amplitudes of deformation [1]. The presentation of NNMs in frequency-energy plots allow the entire structural deformation to be presented compactly. However, due to the spatial complexity of the expected deformations, an examination of the full field response is beneficial to understanding the underlying modal coupling.

Several advances in recent years have begun to make nonlinear modeling and testing for model updating a reality for practical structures. Peeters et al. [2] recently presented a technique to compute NNMs based on numerical integration and continuation which has proven effective for computing the NNMs of a structure with hundreds of degrees of freedom so long as the nonlinearities are localized. Allen et al. [3, 4] recently extended that approach to structures with geometric nonlinearities that are modeled within commercial finite element software. An alternative to the calculation of NNMs has also been established where NNMs are calculated using nonlinear reduced order models which are generated with commercial

---

D.A. Ehrhardt (✉)
Department of Mechanical Engineering, University of Bristol, Bristol, UK
e-mail: david.ehrhardt@bristol.ac.uk; de15845@bristol.ac.uk

M.S. Allen
Department of Engineering Physics, University of Wisconsin-Madison, Madison, WI, USA

© The Society for Experimental Mechanics, Inc. 2016

J. De Clerck, D.S. Epp (eds.), *Rotating Machinery, Hybrid Test Methods, Vibro-Acoustics & Laser Vibrometry, Volume 8*,
Conference Proceedings of the Society for Experimental Mechanics Series, DOI 10.1007/978-3-319-30084-9_40

finite element software [3, 5]. Although less computationally expensive than the full order model, the selection of the correct modal basis can be troublesome. The selection of the correct modal basis can be aided with the use of short time simulations of the full order model or an exploration of the experimental structure.

There are two approaches that have been successfully implemented in the experimental determination of NNMs. Both have relied on a stepped sine force appropriation technique to force a structure to vibrate in only one NNM [6]. The first method makes the assumption that the free decay of a structure that is initiated on a NNM should follow the NNM for lightly damped structures. Therefore, once an NNM is isolated, the excitation can then be removed and the response would then presumably decay along the NNM. Peeters et al. [7] applied this technique to a beam with a local nonlinearity at one end with good results. Additionally, Ehrhardt [8] also performed a free decay experiment on a clamped-clamped beam with geometric nonlinearity. It was found that for NNMs with a single dominant linear mode, the free decay traced the NNM well; however, for an NNM with coupled linear modes (i.e. the first and third mode) the free decay does not match the expected NNM. Kuether and Allen proposed a variant on this technique that was used to compute NNMs [9], but also has been extended to measure an NNM by progressively adjusting the excitation frequency and amplitude repeatedly using force appropriation to isolate NNMs. One additional benefit to this measurement of NNMs is the ease of implementation of full-field measurement techniques such as 3D digital image correlation (3D-DIC) or continuous-scan laser Doppler vibrometry (CSLDV) [10].

This work uses manually tuned stepped-sine testing to find the first nonlinear normal mode of the two curved axi-symmetric plates over a range of excitation amplitudes. The methods developed in [3, 4] are then used to compute the NNMs of the geometrically nonlinear structure using a detailed finite element model, and then the experimentally estimated nonlinear modes are compared with those computed from the model to determine how the model should be updated. This investigation focuses on the first symmetric mode of two different axi-symmetric plates.

40.2 Numerical Model and Experimental Structure

40.2.1 Finite Element Model

In this investigation, finite element models (FEMs) were built using the nominal measured geometries of the perforated plate described in the next section. It is assumed that the welded boundary between the plate and steel cylinder provide fixed boundary conditions in all models. The goal of modeling in this work is to determine an equivalent model that can capture the dynamic behavior of the structure. If a detailed representation of the stress distribution is needed, a very fine mesh would be required in order to model each of the perforations. However, Jhung and Jo [11] found that a perforated plate behaves dynamically identical to a non-perforated plate of the same dimensions, as long as the elastic properties are adjusted appropriately. Hence, the reduced elastic modulus and density were calculated based on the perforation geometry as detailed by Jhung and Jo [11], which for the triangular perforation pattern of this plate yields a new elastic modulus of 1.68 GPa and density of 5120 kg/m^3. The resulting meshed Abaqus model is shown in Fig. 40.1, and has 1440 S4R shell elements. The elastic modulus was later updated so numerically predicted and experimentally measured natural frequencies match. The

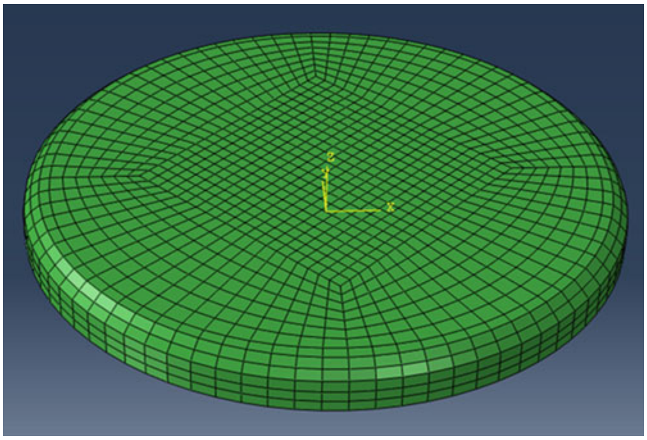

Fig. 40.1 Meshed dynamically equivalent plate model

reduced density was not updated because it can be computed from the geometric properties of the perforations (ex. size of hole and count) and hence should be quite accurate. On the other hand, the effective modulus is dependent on any residual stresses from the addition of perforations, or imperfections of the perforation location geometry.

The fundamental nonlinear normal mode of the plate was computed from this model using the procedure discussed in [3, 4]. Specifically, a reduced order model was created using the Implicit Condensation method [12–14] and the nonlinear reduced order model (NLROM) was integrated in the NNMCont Matlab routine provided by Peeters et al. [6] to compute the nonlinear modes. In [3, 4] this approach was found to provide an excellent approximation for the backbone of each NNM of a geometrically nonlinear beam. In the NLROMs presented here, only modes 1 and 6 are used as a modal basis since they are the first two symmetric modes with a nodal radius and hence both important to the response near the first natural frequency.

40.2.2 Experimental Structure

The article under investigation is a circular perforated plate with rolled ends which is shown in Fig. 40.2. A mechanical punch was used to create the circular perforations in a flat 16 gauge (1.52 mm thick) 409 stainless steel plate in an array of equilateral triangles with 10.16 mm long edges. Once this process was completed, the plate was formed around a 317.5 mm diameter mold with the excess trimmed so a lip of 24.5 mm remained. The plate was then welded to an 89 mm high cylinder made from a 14 gauge (1.9 mm thick) 409 stainless steel plate that was cold rolled to the 317.5 mm diameter as shown in Fig. 40.2b. The welded plate assembly was then bolted to a fixture with twelve 6.4 mm evenly spaced holes. An 8000 N shaker was used to provide base excitation at a single harmonic to trace the nonlinear normal modes of the fundamental frequency of vibration. It is important to note that all stated dimensions are nominal and subject to variation as is observed in the final geometry of the two plates investigated here.

The two plates considered for investigation are labeled perforated plate 1 (PP01) and perforated plate 2 (PP02). The initial geometry of both perforated plates were measured with 3D digital image correlation providing initial coordinates of the entire surface of the plates. The two plates presented here had an imperfect initial curvature induced by the method of formation as seen in Fig. 40.3. PP01 has an induced curvature with a peak deformation of 3.73 mm when compared with the nominal model. This is shown in Fig. 40.3a, b, where the colormap segments the coordinate location of the measured surface. PP02 has an induced curvature with a peak deformation of 4.84 mm when compared with the nominal model as seen in Fig. 40.3c, d.

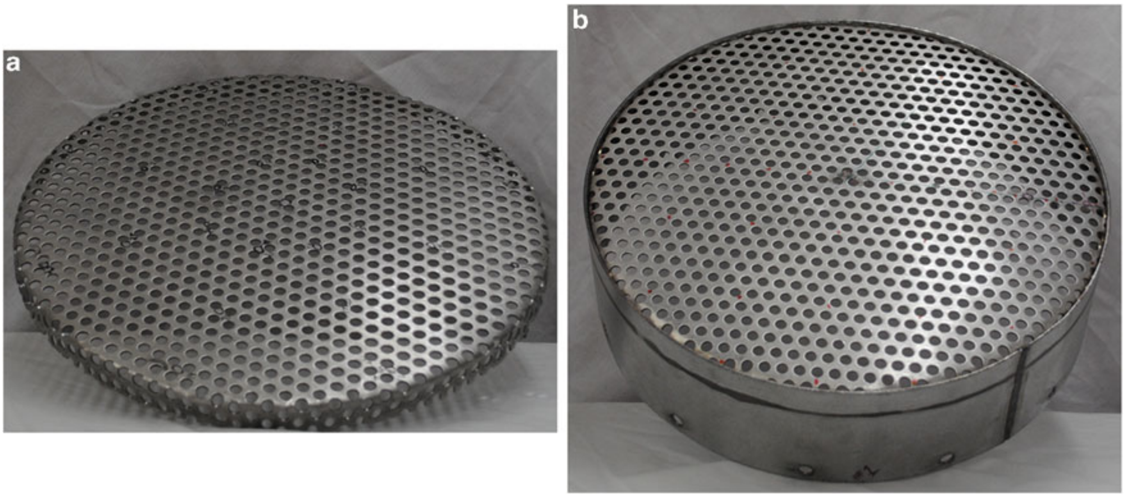

Fig. 40.2 Experimental setup of the perforated plates. (**a**) Perforated plate before welding into test configuration, (**b**) perforated plate welded into the supporting cylinder

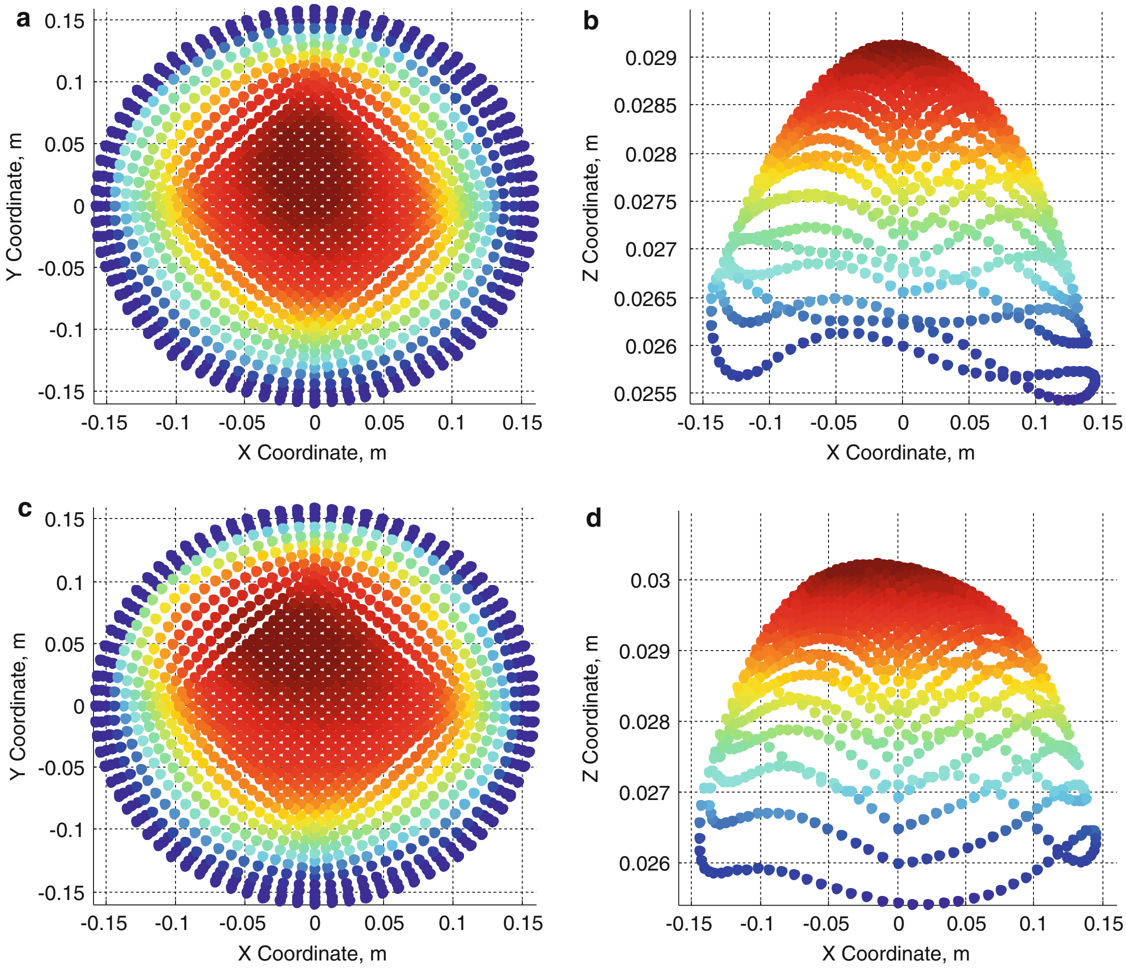

Fig. 40.3 Measured initial geometry of the perforated plates. (**a**) Front view of perforated plate 1 (PP01), (**b**) side view of perforated plate 1 (PP01), (**c**) front view of perforated plate 2 (PP02), (**d**) side view of perforated plate 2 (PP02)

40.3 Results

40.3.1 Model NNMs

Finite element models were created for each of these plates which are used to estimate the nonlinear normal mode (NNM) from a nonlinear reduced order model (NLROM) and are shown in Fig. 40.4 for the three models examined here. The frequency-energy plot (FEP), shown in Fig. 40.4a, highlights the difference in the energy dependence of the resonance frequency between the curved and flat models. The flat model (blue) exhibits only an increase in frequency as the amplitude of the response is increased, where PP01 (green) and PP02 (red) both show a decrease in frequency before an increase in frequency. The reason of this difference is further explained with the examination of the modal amplitudes shown in Fig. 40.4b. The flat model (blue) contains only the first mode of vibration in the dynamic response as the amplitude is increased. PP01 and PP02 both show a mode 1 dominance of the dynamic response as the frequency decreases; however, as the response reaches higher levels, the sixth mode begins to couple and takes a larger role in the dynamic response as the frequency increases. Although a different curvature is observed between PP01 and PP02, similar characteristics are observed in the dynamic response.

A further examination of the dynamic response also describes the harmonic coupling of the two mode NLROM. The response at the center of the plate at a change in frequency of $+1\,\%$ is shown in Fig. 40.5. As shown in the nominal model (blue) time domain, Fig. 40.5a, shows only a pure sinusoidal response while PP01 (green) and PP02 (red) shows a distortion in the time domain. Decomposing the signals into the frequency domain shows a single frequency in the nominal model response and multiple frequencies in PP01 and PP02. The higher frequency content points to a 1:3 harmonic coupling.

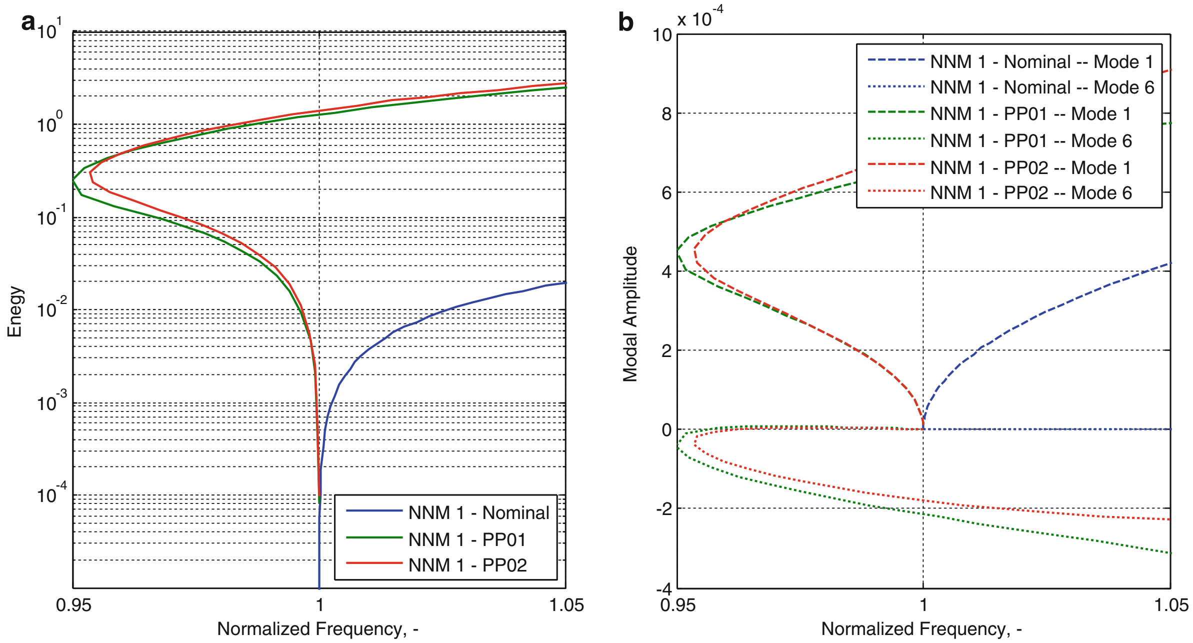

Fig. 40.4 Fundamental nonlinear normal mode of all models considered. (**a**) Frequency-energy plot of nonlinear reduced order model (NLROM), (**b**) modal amplitudes of two-mode NLROM

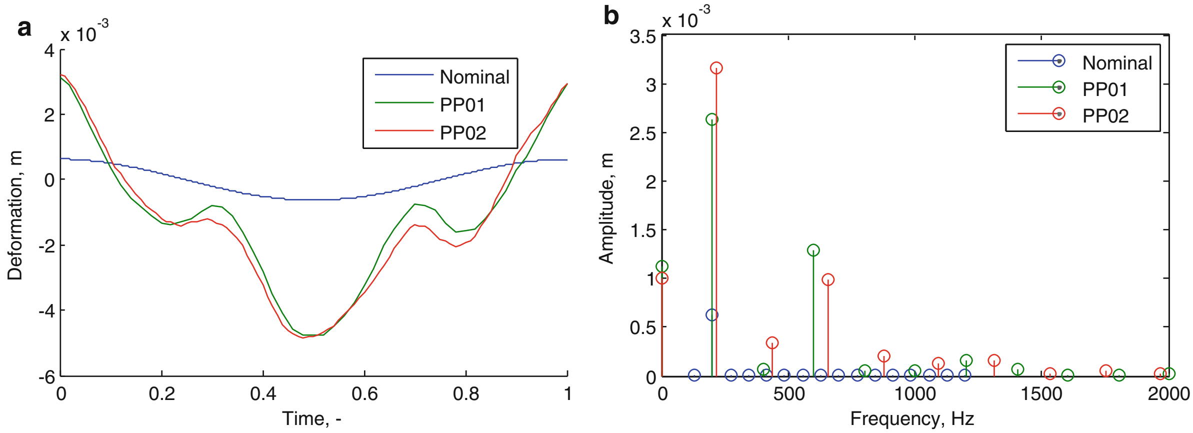

Fig. 40.5 NNM response at +1.0 % increase of frequency. (**a**) Time domain normalized to a period of the response, (**b**) frequency domain

Finally, an examination of the deformations observed at the peak harmonics in the response in the frequency domain provide a visualization of the modal coupling observed. Since the first harmonic is dominant in the nominal model and the first and third harmonic is dominant in PP01 and PP02 a comparison made between the full-field deformations of the plate at the same position on the FEP that was used in Fig. 40.5. The colorbars segment the out-of-paper deformations of the plate in meters. The first harmonic of the nominal model, shown in Fig. 40.6a, is purely a mode 1 deformation. Similarly, Fig. 40.6b, d, of the first harmonic of PP01 and PP02 which also resembles a mode 1 deformation. The third harmonic of PP01 and PP02 is also prominent in the response shown in Fig. 40.5. The deformation of the third harmonic of PP01 and PP02, shown in Fig. 40.6c, e, is a purely mode 6 deformation.

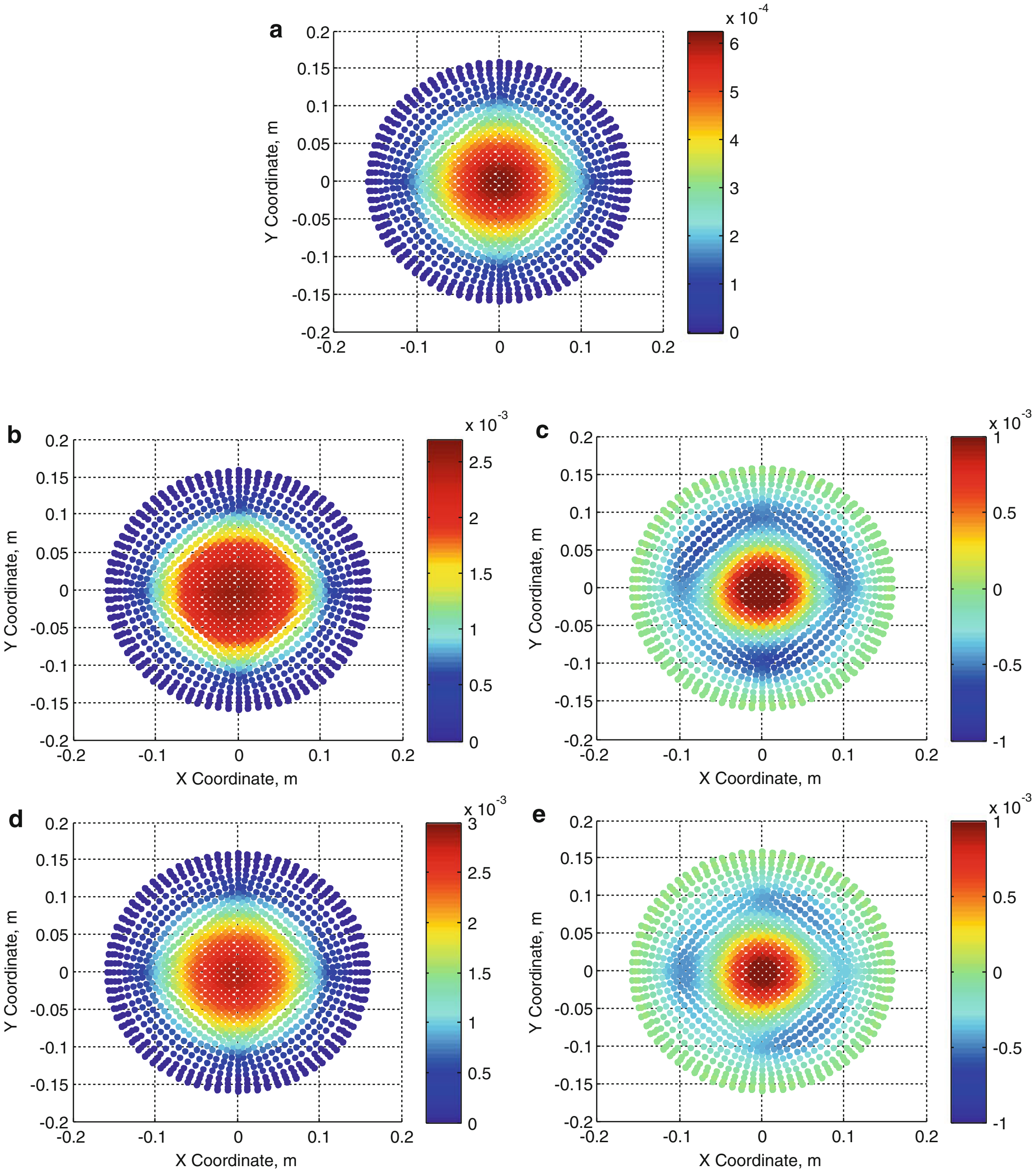

Fig. 40.6 Deformation shapes of the peak harmonics at +1 % of change in the fundamental frequency of vibration. (**a**) Deformation of the fundamental harmonic of the nominal model, (**b**) deformation of the fundamental and (**c**) third harmonic of PP01, (**d**) deformation of the fundamental and (**e**) third harmonic of PP02

40.3.2 Experimental NNMs

The experimentally measured NNMs are limited due to the experimental setup and the failure limit of the perforated plates tested. Therefore a complete examination of the NNM cannot be performed, as shown in Fig. 40.7, where the peak amplitude response of the center of the plate is plotted as a function of the resonance frequency. The decrease/increase of resonance frequency shown in Fig. 40.7 shows the ability of the NLROMs to capture the general trend of the nonlinear behavior of the perforated plates. The amplitude levels permitted by the experimental setup show an initial decrease in natural frequency larger than predicted by the numerical models for both plates. It is expected that as the response amplitude increases, the plate may pull on the external rim of the setup, requiring larger response amplitudes before the axial stretching reaches levels

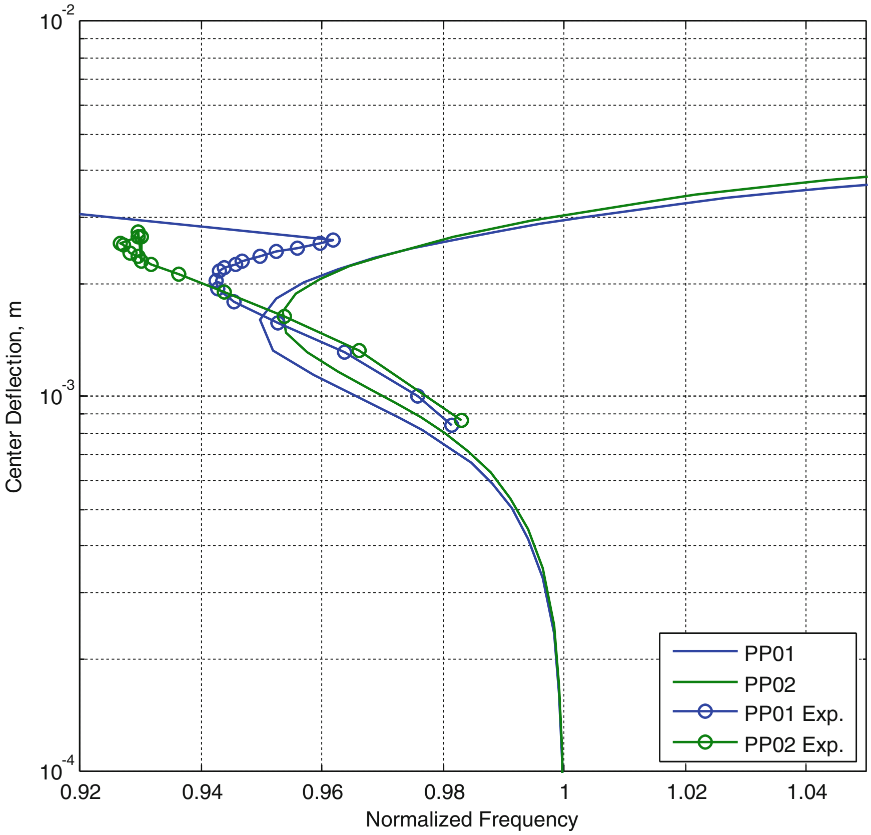

Fig. 40.7 Peak amplitude at center of plate

capable of changing the nonlinearity from a softening to hardening effect. The turning point can be captured experimentally; however the failure occurs as the change in frequency begins to increase limiting the full characterization of the increase in frequency.

The full field deformation at the point where the change in the fundamental frequency of vibration provides a good comparison of the dynamic response in nonlinear regimes as shown in Fig. 40.8. The colorbar accompanying each figure corresponds to the peak deformation observed in the full-field deformation. The full-field deformations observed for the modeled PP01, shown in Fig. 40.8a, b, has a peak deformation of 1.67 mm for the first harmonic and 0.29 mm for the third harmonic. The companion experimental deformations are shown in Fig. 40.8c, d, where a peak deformation of 1.94 mm is measured for the first harmonic and 0.41 mm for the third harmonic. The first harmonic for this structure is 16 % higher than predicted by the model, and the third harmonic is 40 % higher. The full-field deformations for PP02, shown in Fig. 40.8e, f, has a peak amplitude of 1.78 mm for the first harmonic and 0.27 mm for the third harmonic. The experimental deformations are shown in Fig. 40.8g, h, where a peak deformation of 2.43 mm is observed for the first harmonic and a peak deformation of 0.23 mm is observed for the third harmonic. The first harmonic for this structure is 36 % greater than that predicted by the model and the third harmonic is 17 % lower than predicted by the model. The difference between the harmonic amplitudes of the models suggest a modal coupling not accounted for in the NLROM. A further examination of the higher harmonics of the experimental setup is needed to characterize the modal coupling and will guide the next step in the creation of NLROMs. One interesting thing to note is the asymmetry in the third harmonic shown in Fig. 40.8h, which is not as pronounced in the experimental results, and could be a result of the base excitation loading which limits the ability to excite asymmetries in the structure fully.

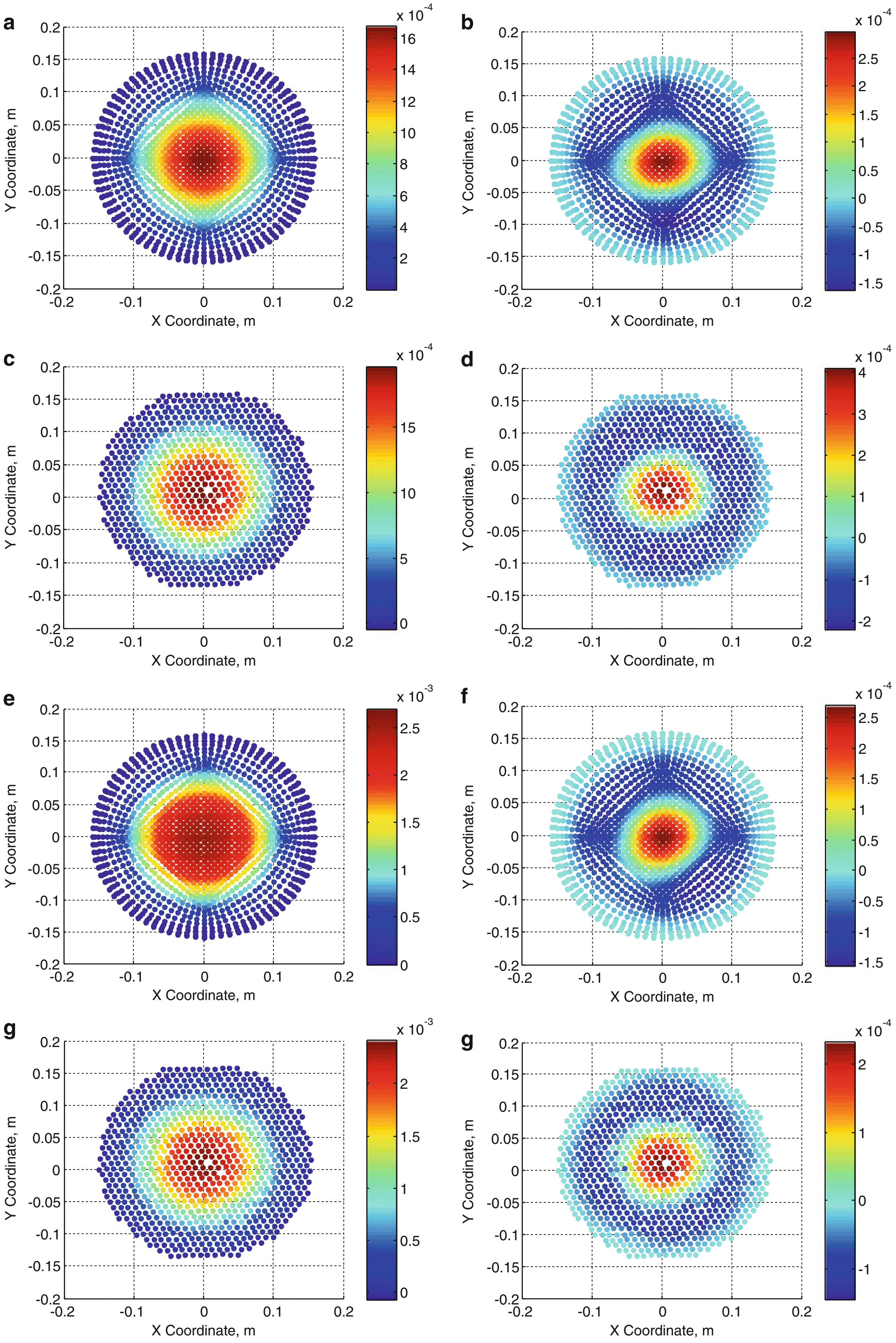

Fig. 40.8 Full field deformations of the perforated plates. PP01 first and third harmonic of the (**a**, **b**) numerically calculated and of the (**c**, **d**) experimentally measured point of maximum decrease in frequency. PP02 first and third harmonic of the (**e**, **f**) numerically calculated and of the (**g**, **h**) experimentally measured point of maximum decrease in frequency

40.4 Conclusion

The examination of the nonlinear normal modes (NNMs) has provided insight to the underlying modal and harmonic coupling observed in the perforated plates investigated. The nominal model, assuming a flat geometry, showed only an increase in the fundamental frequency of vibration as the response amplitude is increased. With the inclusion of the initial curvature of the perforated plates, a strong coupling is observed between mode 1 and mode 6 of the plate for the first NNM. Therefore, the inclusion of mode 1 and mode 6 into the nonlinear reduced order models is needed. As the structure is pushed at higher input forces the mode 6 deformation becomes more pronounced as shown experimentally and numerically. Although more tuning is needed to accurately account for the amount of coupling between mode 1 and mode 6.

Though the models have shown the ability to describe the trend of the dynamic behavior of the perforated plates, more work is needed to fully identify the modal coupling in the experimental results. Additionally, an examination of the stress distribution of the change in deformation observed in the plates is needed for accurate prediction of the failure of these plate.

References

1. Kerschen, G., et al.: Nonlinear normal modes, Part I: a useful framework for the structural dynamicist. Mech. Syst. Signal Process. **23**(1), 170–194 (2009)
2. Peeters, M., et al.: Nonlinear normal modes, Part II: toward a practical computation using numerical continuation techniques. Mech. Syst. Signal Process. **23**(1), 195–216 (2009)
3. Allen, M.S., et al.: A numerical continuation method to compute nonlinear normal modes using modal reduction. In: 53rd AIAA Structures, Structural Dynamics, and Materials Conference. Honolulu, Hawaii (2012)
4. Kuether, R.J., Allen, M.S.: A numerical approach to directly compute nonlinear normal modes of geometrically nonlinear finite element models. Mech. Syst. Signal Process. (2013)
5. Gordon, R.W., Hollkamp, J.J.: Reduced Order Models for Acoustic Response Prediction. Air Force Research Laboratory (2011)
6. Peeters, M., Kerschen, G., Golinval, J.C.: Dynamic testing of nonlinear vibrating structures using nonlinear normal modes. J. Sound Vib. **330**(3), 486–509 (2011)
7. Peeters, M., Kerschen, G., Golinval, J.C.: Modal testing of nonlinear vibrating structures based on nonlinear normal modes: experimental demonstration. Mech. Syst. Signal Process. **25**(4), 1227–1247 (2011)
8. Ehrhardt, D.A.: A full-field experimental and numerical investigation of nonlinear normal modes in geometrically nonlinear structures. In: Engineering Mechanics. University of Wisconsin-Madison (2015)
9. Kuether, R.J., Allen, M.S.: Computing nonlinear normal modes using numerical continuation and force appropriation. In: ASME 2012 International Design Engineering Technical Conferences IDETC/CIE 2012. Chicago, IL (2012)
10. Ehrhardt, D.A., Allen, M.S., Yang, S., Beberniss, T.J.: Full-field linear and nonlinear measurements using continuous-scan laser Doppler vibrometry and high speed three-dimensional digital image correlation. Mech. Syst. Signal Process. (2015). In Review
11. Jhung, M.J., Jo, J.C.: Equivalent material properties of perforated plate with triangular or square penetration pattern for dynamic analysis. Nucl. Eng. Technol. **38**(7) (2006)
12. Gordon, R.W., Hollkamp, J.J.: Reduced-order Models for Acoustic Response Prediction. Air Force Research Laboratory, Dayton, OH (2011)
13. Hollkamp, J.J., Gordon, R.W.: Reduced-order models for nonlinear response prediction: implicit condensation and expansion. J. Sound Vib. **318**(4–5), 1139–1153 (2008)
14. Hollkamp, J.J., Gordon, R.W., Spottswood, S.M.: Nonlinear modal models for sonic fatigue response prediction: a comparison of methods. J. Sound Vib. **284**(3–5), 1145–1163 (2005)

Chapter 41
Reduced Order Models for Systems with Disparate Spatial and Temporal Scales

Shahab Ilbeigi and David Chelidze

Abstract Simulations and parametric studies of large-scale models can be facilitated by high-fidelity *reduced order models* (ROMs). One of the methods to obtain these ROMs, which is of considerable current interest, is using linear subspaces obtained from spatiotemporal decompositions including *proper orthogonal decomposition* (POD) and *smooth orthogonal decomposition* (SOD). Previous studies showed that SOD has advantages over POD in obtaining a lower dimensional ROM. However, in many dynamical models, the data matrices used in multivariate analysis can be ill-conditioned. This leads to non-optimal results with POD, since it only aims to find the subspace on which the data projection has the maximal variance. Therefore, POD is likely to overlook small-variance state-variables.

A large-scale nonlinear system is used as the full-scale model of an ill-conditioned system, where some state variable have considerably smaller variations than others. Four different methods are applied to obtain ROMs. First, a conventional POD as well as SOD are applied to the whole state space data matrix of the model. Then, the position and velocity data of the full system are separated into two data matrices and POD and SOD are applied to them individually. Finally, the ROMs built based on these multivariate analysis are compared in terms of accuracy and stability. While separated POD-based ROM shows considerable improvement over the conventional POD ROM, SOD still provides lower-dimensional ROMs and it does not seem to benefit from the separated SOD reduction.

Keywords Proper orthogonal decomposition • Smooth orthogonal decomposition • Nonlinear model reduction • Ill-conditioned systems • Multivariate analysis

41.1 Introduction

Even with current advances in computing technologies, long-time simulations or parametric studies of complex systems are difficult or infeasible. High-fidelity reduced order models (ROMs) of large-scale dynamical systems can be used to avoid redundant computations and significantly speed up simulation times [1]. Examples of such complex systems that can benefit from ROM are large-scale finite difference/element models, multi-body dynamics or geometrically nonlinear models, and molecular dynamics simulations [2–7].

For linear systems, the methodologies for model order reduction (MOR) are well studied and established. The most popular ones of which include the Galerkin reduction using linear normal modes (LNMs) [8, 9], Krylov subspace projections [10], Hankel norm approximations [11–14], truncated balance realizations [15, 16], and POD (also known as singular value decomposition, principal component analysis, or Karhunen-Loeve expansion) [17–22].

Nonlinearity is the integral part of the observed complex dynamics of majority of the systems of interest. Commonly used methodologies for model reduction for nonlinear systems can be categorized into two groups. In the first, nonlinear normal modes (NNMs) [23–29] are used. In the second, combined with Galerkin projection, linear subspaces obtained from spatiotemporal decompositions such as proper orthogonal decomposition (POD) and smooth orthogonal decomposition (SOD) are utilized [19, 20, 30–32]. Linear subspaces are of considerable current interest because they are computationally tractable, and do not neglect the nonlinearity of the original vector field [18], while the calculation of NNMs is difficult [33–36]. An additional drawback of MOR based on NNMs is related to the changes in NNMs with change in system's level of energy [34, 37].

S. Ilbeigi • D. Chelidze (✉)
Department of Mechanical, Industrial, and Systems Engineering, University of Rhode Island, Kingston, RI 02881, USA
e-mail: chelidze@egr.uri.edu
http://egr.uri.edu/nld/

© The Society for Experimental Mechanics, Inc. 2016

J. De Clerck, D.S. Epp (eds.), *Rotating Machinery, Hybrid Test Methods, Vibro-Acoustics & Laser Vibrometry, Volume 8*,
Conference Proceedings of the Society for Experimental Mechanics Series, DOI 10.1007/978-3-319-30084-9_41

In our previous works [3, 38, 39], we showed that SOD outperformed POD in obtaining low-dimensional ROMs. However, the data matrices associated with many dynamical systems can be ill-conditioned. This may destabilize the low-dimensional ROMs or reduce their performance. For instance, we observed that some low-dimensional POD- and SOD- based ROMs were not stable for a particular system [3].

The data matrices from the full state-space models are composed of measured data corresponding to position and velocity state variables. Individually, the position and velocity data have a lower condition number, i.e., they can form better conditioned matrices separately. Therefore, we propose to perform the multivariate analysis separately to identify the so-called position and velocity modes. Following the identification of these modes, we can put them together to span the modal subspace for MOR.

In Sect. 41.2, after a brief review on POD- and SOD-based MOR methods, the mathematical formulation of the separated POD as well as the separated SOD-based MOR methods are provided. A nonlinear mass-spring-damper system is studied using these four different methods in Sect. 41.3. Finally, the results are compared, discussed, and concluded in Sects. 41.4 and 41.5.

41.2 Nonlinear Model Reduction

Full-scale model of a dynamical system can be written in the following form:

$$\dot{\mathbf{z}} = \mathbf{f}(\mathbf{z}, t) \tag{41.1}$$

where $\mathbf{z} \in \mathbb{R}^{2n}$ is a dynamic state variable, $\mathbf{f} : \mathbb{R}^{2n} \times \mathbb{R} \to \mathbb{R}$ is some nonlinear flow, and t is time. Given $n \in \mathbb{N}$ as the number of the system's degrees-of-freedom, $2n$ will be the number of state variables. The state variable time trajectories can be arranged in the matrix $\mathbf{Y} = [\mathbf{z}_1, \mathbf{z}_2, \ldots, \mathbf{z}_{2n}] \in \mathbb{R}^{r\times 2n}$, where $r \in \mathbb{N}$ is the number of time samples. A basis for $\mathbf{Y}$ can be calculated using either POD or SOD. These most dominant (according to appropriate metric) k basis vectors are arranged in the matrix $\mathbf{P}_k = [\mathbf{e}_1, \mathbf{e}_2, \ldots, \mathbf{e}_k] \in \mathbb{R}^{2n\times k}$. Now, we use a coordinate transformation $\mathbf{z} = \mathbf{P}_k\mathbf{q}$ to get the reduced k-dimensional state variable, $\mathbf{q}$, and the corresponding ROM:

$$\dot{\mathbf{q}} = \mathbf{P}_k^{\dagger}\mathbf{f}(\mathbf{P}_k\mathbf{q}, t) \tag{41.2}$$

where $(.)^{\dagger}$ indicates the pseudoinverse of (.).

41.2.1 *Proper and Smooth Orthogonal Decomposition*

To build ROMs using the extracted modes from the multivariate analysis, the state variable measurements of the full-scale system are recorded to form a position and velocity data matrices $\mathbf{X} \in \mathbb{R}^{r\times n}$ and $\mathbf{V} \in \mathbb{R}^{r\times n}$, respectively. $\mathbf{X}$ is composed of r snapshots of n position state variables. Similarly, $\mathbf{V}$ is composed of r snapshots of n velocity state variables. Thus, the data matrix $\mathbf{Y}$, which we call as full data matrix throughout this paper, is formed by combining $\mathbf{X}$ and $\mathbf{V}$ together, i.e., $\mathbf{Y} = [\mathbf{X}\ \mathbf{V}]$.

The time derivative of $\mathbf{X}$ is $\mathbf{V}$. To obtain a time derivative of V or an acceleration data matrix $\mathbf{A}$, we can use a numerical scheme for solving the dynamical system. Alternatively, it can be approximated by $\mathbf{A} \approx \mathbf{D}\mathbf{V}$, where $\mathbf{D}$ is the matrix form of some differential operator such as forward difference. Therefore, the ensemble of time derivative of $\mathbf{Y}$ will be $\dot{\mathbf{Y}} = [\mathbf{V}\ \mathbf{A}]$.

Provided that $\mathbf{Y}$ and $\dot{\mathbf{Y}}$ are zero mean, the auto-covariance matrices can be formed by

$$\mathbf{\Sigma}_{yy} = \frac{1}{r-1}\mathbf{Y}^{\mathrm{T}}\mathbf{Y}, \quad \mathbf{\Sigma}_{\dot{y}\dot{y}} = \frac{1}{r-1}\dot{\mathbf{Y}}^{\mathrm{T}}\dot{\mathbf{Y}} \tag{41.3}$$

In POD, we are looking for a basis vector $\boldsymbol{\phi}_k \in \mathbb{R}^n$ such that a projection of the data matrix onto this vector has maximal variance. The solution to the POD problem is achieved by solving the eigenvalue problem of auto-covariance matrix $\mathbf{\Sigma}_{yy}$ in Eq. (41.3):

$$\mathbf{\Sigma}_{yy}\boldsymbol{\phi}_k = \lambda_k\boldsymbol{\phi}_k \tag{41.4}$$

where λ_k are proper orthogonal values (POVs), $\boldsymbol{\phi}_k \in \mathbb{R}^n$ are proper orthogonal modes (POMs), and proper orthogonal coordinates (POCs) are columns of $\mathbf{Q} = \mathbf{Y}\mathbf{\Phi}$, in which $\mathbf{\Phi} = [\boldsymbol{\phi}_1, \boldsymbol{\phi}_2, \ldots, \boldsymbol{\phi}_n] \in \mathbb{R}^{2n\times 2n}$. POVs are ordered such that $\lambda_1 \geq \lambda_2 \geq \ldots \geq \lambda_n$.

In SOD, we are looking for a basis vector $\boldsymbol{\psi}_k \in \mathbb{R}^n$ such that a projection of the data matrix onto this vector has minimal roughness and maximal variance. The solution to the SOD problem, is achieved by solving the generalized eigenvalue problem of the matrix pair $\boldsymbol{\Sigma}_{yy}$ and $\boldsymbol{\Sigma}_{\dot{y}\dot{y}}$ in Eq. (41.3):

$$\boldsymbol{\Sigma}_{yy}\boldsymbol{\psi}_k = \lambda_k \boldsymbol{\Sigma}_{\dot{y}\dot{y}}\boldsymbol{\psi}_k \tag{41.5}$$

where λ_k are smooth orthogonal values (SOVs), $\boldsymbol{\psi}_k \in \mathbb{R}^n$ are smooth projection modes (SPMs), smooth orthogonal modes (SOMs) are $\boldsymbol{\Phi} = \boldsymbol{\Psi}^{-T}$, and smooth orthogonal coordinates (SOCs) are given by $\mathbf{Q} = \mathbf{Y}\boldsymbol{\Psi}$, where $\boldsymbol{\Psi} = [\boldsymbol{\psi}_1, \boldsymbol{\psi}_2, \ldots, \boldsymbol{\psi}_n] \in \mathbb{R}^{2n\times 2n}$. The degree of smoothness of the coordinates is described by the magnitude of the corresponding SOV. Thus, the greater in magnitude the SOV, the smoother in time is the corresponding coordinate. It should be noted that if we were to replace $\boldsymbol{\Sigma}_{\dot{y}\dot{y}}$ with the identity matrix, the formulation will yield the proper orthogonal decomposition.

41.2.2 Separated Multivariate Analysis for Reduced Order Models

The full data matrices in many dynamical systems are ill-conditioned. Therefore, the extracted modes using the aforementioned multivariate analysis methods may be noisy. These modes may have some unnecessary sign changes and they may not account for the true modal structure of the system. Here we propose to do multivariate analysis on position and velocity data matrices separately, since they usually have a lower condition number.

The separated multivariate analysis as its name suggests will be done on $\mathbf{X}$ and $\mathbf{V}$ separately. The solution of separated POD analysis on position data matrix is given by:

$$\boldsymbol{\Sigma}_{xx}\boldsymbol{\phi}_k^x = \lambda_k^x \boldsymbol{\phi}_k^x \tag{41.6}$$

Likewise, the solution of separated POD analysis on velocity data matrix is given by:

$$\boldsymbol{\Sigma}_{vv}\boldsymbol{\phi}_k^v = \lambda_k^v \boldsymbol{\phi}_k^v \tag{41.7}$$

In the above equations, $\boldsymbol{\Sigma}_{xx}$ and $\boldsymbol{\Sigma}_{vv}$ are auto-covariance matrices of position and velocity data. Also, the superscript x and v denote that the corresponding scalar or vector is related to the position and velocity data matrices, respectively. The obtained $\boldsymbol{\phi}_k^x$'s and $\boldsymbol{\phi}_k^v$'s are arranged in a position modal matrix $\boldsymbol{\Phi}^x = \left[\boldsymbol{\phi}_1^x, \boldsymbol{\phi}_2^x, \ldots, \boldsymbol{\phi}_n^x\right] \in \mathbb{R}^{n\times n}$ and a velocity modal matrix $\boldsymbol{\Phi}^v = \left[\boldsymbol{\phi}_1^v, \boldsymbol{\phi}_2^v, \ldots, \boldsymbol{\phi}_n^v\right] \in \mathbb{R}^{n\times n}$. After choosing l dominant position modes given in the matrix form $\boldsymbol{\Phi}_l^x$ as well as p dominant velocity modes given in the matrix form $\boldsymbol{\Phi}_p^v$, they can be put together to, at last, yield the modal matrix:

$$\boldsymbol{\Phi}_k = \begin{bmatrix} \boldsymbol{\Phi}_l^x & \mathbf{0}_{n\times p} \\ \mathbf{0}_{n\times l} & \boldsymbol{\Phi}_p^v \end{bmatrix}_{2n\times k} \tag{41.8}$$

where $k = l + p$ is the dimension of the modal matrix.

For separated SOD analysis, we need to solve the following generalized eigenvalue problems on position and velocity data and their time derivatives. For position data, one has:

$$\boldsymbol{\Sigma}_{xx}\boldsymbol{\psi}_k^x = \lambda_k^x \boldsymbol{\Sigma}_{vv}\boldsymbol{\psi}_k^x \tag{41.9}$$

similarly for velocity data, one obtain:

$$\boldsymbol{\Sigma}_{vv}\boldsymbol{\psi}_k^v = \lambda_k^v \boldsymbol{\Sigma}_{aa}\boldsymbol{\psi}_k^v \tag{41.10}$$

in which $\boldsymbol{\Sigma}_{vv}$ and $\boldsymbol{\Sigma}_{aa}$ are autocovariance matrices of velocity and acceleration data, respectively. Similar to POD, the modal matrix $\boldsymbol{\Psi}$ will be composed of l-dimensional $\boldsymbol{\Psi}_l^x$ and p-dimensional $\boldsymbol{\Psi}_p^v$. Thus, one gets:

$$\boldsymbol{\Psi}_k = \begin{bmatrix} \boldsymbol{\Psi}_l^x & \mathbf{0}_{n\times p} \\ \mathbf{0}_{n\times l} & \boldsymbol{\Psi}_p^v \end{bmatrix}_{2n\times k} . \tag{41.11}$$

41.3 Nonlinear Mass-Spring-Damper System

The nonlinear system under investigation can be obtained by adding a nonlinear spring to a simple linear mass-spring-damper system. As shown in Fig. 41.1, n blocks of masses are connected in series to each other as well as both sides of the support by linear dampers and springs. The masses can vibrate in x-direction with no friction. The system can be described by its governing differential equations:

$$\begin{cases} m_i\ddot{x}_i + (c_i + c_{i+1})\dot{x}_i - c_{i+1}\dot{x}_{i+1} + & \\ (k_i + k_{i+1})x_i - k_{i+1}x_{i+1} = f_i(t) & \text{for } i = 1 \\ & \\ m_i\ddot{x}_i - c_{i-1}\dot{x}_{i-1} + (c_i + c_{i+1})\dot{x}_i - c_{i+1}\dot{x}_{i+1} & \\ -k_{i-1}x_{i-1} + (k_i + k_{i+1})x_i - k_{i+1}x_{i+1} = f_i(t) & \text{for } 2 \le i \le n-1 \\ & \\ m_i\ddot{x}_i - c_i\dot{x}_{i-1} + (c_i + c_{i+1})\dot{x}_i - k_i x_{i-1} + & \\ (k_i + k_{i+1})x_i + \alpha x_i^3 = f_i(t) & \text{for } i = n \end{cases} \tag{41.12}$$

where $n \in \mathbb{N}$ is the number of the system's degrees of freedom and $f_i(t)$ is the external forcing applied to the ith mass. Defining $\mathbf{z} = [x_1, x_2, \ldots, x_n, \dot{x}_1, \dot{x}_2, \ldots, \dot{x}_n]^T$ as the vector of $2n$ state variables, the full state-space model of the system can be obtained as follow:

$$\dot{\mathbf{z}} = \begin{bmatrix} \mathbf{0} & \mathbf{I} \\ -\mathbf{M}^{-1}\mathbf{K} & -\mathbf{M}^{-1}\mathbf{C} \end{bmatrix} \mathbf{z} + \mathbf{f}_\mathrm{e} + \mathbf{f}_\mathrm{n}(\mathbf{z}) \tag{41.13}$$

where $\mathbf{0} \in \mathbb{R}^{n\times n}$ is a zero matrix, $\mathbf{f}_\mathrm{n}(\mathbf{z}) \in \mathbb{R}^{2n}$ has only one nonzero element: $[\mathbf{f}_\mathrm{n}(\mathbf{z})]_{2n} = -\alpha z_n^3$, $\mathbf{f}_\mathrm{e}(t) = [[0, \ldots, 0]_{1\times n}, [1, \ldots, 1]_{1\times n}]^T f_\mathrm{e}(t)$, $\mathbf{I} \in \mathbb{R}^{n\times n}$ is an identity matrix, and $\mathbf{K}$ and $\mathbf{C}$ are stiffness and damping matrices, respectively.

As an numerical example, the number of DOFs is 60 and other parameters of the system are set as follows:

$$m = 1\,\mathrm{kg}, k = 3600\,\mathrm{N/M}, c = 720\,\mathrm{N\,M/s}, \alpha = 2 \tag{41.14}$$

This will result in a rich dynamic response with two stable, static equilibrium points. Subjected to harmonic forcing with $\Omega = 7.97\,\mathrm{Hz}$, which is close to the frequency of the first LNM, the bifurcation diagram is plotted using the full scale model of the system as shown in Fig. 41.2. We aim to reproduce these results using ROMs.

While any type of data obtained from the system oscillations could be used for multivariate analysis, the data from random excitation would be the best choice for MOR subspace identification. With random forcing, we are more likely to explore nearly all phase space of the system and activate most of its dominant modes.

Therefore, to get the data matrices, the white noise is applied to the system for a total time of 272 s. The response of the system is obtained using Runge-Kutta method with the sampling time of 2.178×10^{-3} s. Thus, a total of $1, 25, 000$ data will be recorded to form position, velocity, and acceleration data matrices. These data will be processed using the four methods explained in Sects. 41.2.1 and 41.2.2.

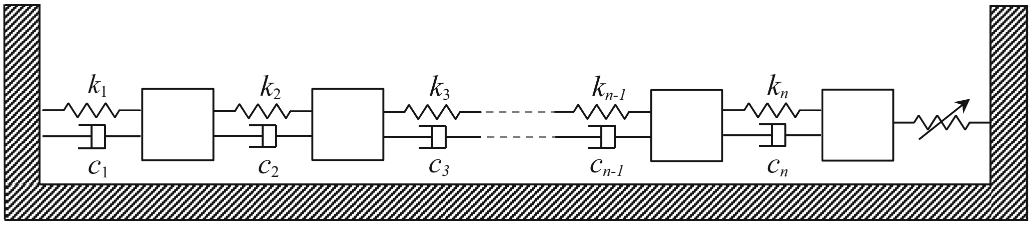

Fig. 41.1 Schematic of the system with nonlinear spring coupling

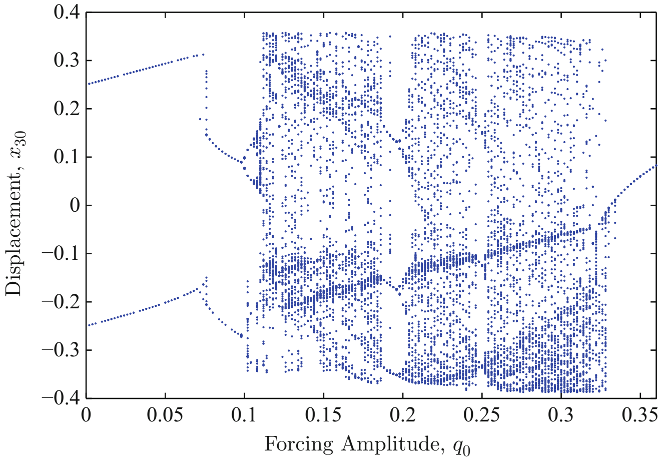

Fig. 41.2 Bifurcation diagram for full scale nonlinear system for harmonic forcing with $\omega = 7.97$ Hz

41.4 Results

The aim is to reproduce the results of the full-scale model using the ROMs. It is needed to have a ROM that can account for a relatively wide range of amplitudes; otherwise MOR would be pointless. Therefore, we excited the system by the white noise with 12 different amplitudes to get 12 independent cases. For each case, the data matrices were recorded as explained in the previous section. Following the data analysis using the four methods in Sects. 41.2.1 and 41.2.2, the resultant modes were mixed using the method in [3, 39]. The obtained modes are then used for ROMs.

The 120-dimensional full-scale model of the system can be reduced down to a five-dimensional full POD-based ROM. The full POD-based ROMs were not stable for the dimensions lower than five. Yet, the full-scale model of the system is reduced down to a six-dimensional full POD-based ROM, since five-dimensional models did not correlate well with the full-scale model. For full SOD, four and higher dimensional models were stable and had a good correlation with the full-scale model.

The results from the full POD- and SOD-based ROM simulations are depicted in the left columns in Figs. 41.3 and 41.4. These results correspond to the harmonic excitation amplitudes of $[0.05, 0.12, 0.22, 0.35]$. While both POD and SOD have a reasonable accuracy, the four-dimensional full SOD-based model has a slightly better performance than the six-dimensional full POD-based model. This is in consistent with the previous works that were done on SOD-based MOR [3, 39], where SOD-based ROMs were shown to capture the dynamics of the nonlinear systems using lower dimensional models.

An interesting result is the effect of separating the data matrices on stabilizing the low-dimensional POD-based ROMs. Now not only the separated POD-based ROMs are stable for all dimensions, but also the performance of the models is improved. This is illustrated in Fig. 41.3, where six-dimensional POD-based and six-dimensional separated POD-based ROMS are compared. The figure shows that the ROM simulation results are slightly improved.

The performance of separated SOD-based ROMs is also investigated and reported via Fig. 41.4. The figure shows that separated SOD-based ROM does not improve the results. In some cases the results do not change much and in some cases, e.g. $q_0 = 0.12$, the performance of ROM reduces.

With a more than 50 times faster ROM, we are able to reproduce the bifurcation diagrams in more details. Figure 41.5 shows the bifurcation diagrams obtained for the four methods. It can be observed that there is a slight improvement in the diagram of the separated POD-based ROM compared to that of the full POD-based ROM. For instance, there is better match for the forcing amplitude in the range of 0.2 to 0.25 for the separated POD diagram with that of the full-scale model in Fig. 41.2. Although this improvement is not significant, it shows the improving nature of the separated POD-based reduced order modeling.

The bifurcation diagram of four-dimensional full SOD-based ROM is consistent with that of the full scale model. However, it is little shrunk around the forcing amplitude of 0.31. Also, the diagram of four-dimensional separated SOD-based ROM is slightly corrupted for higher amplitudes.

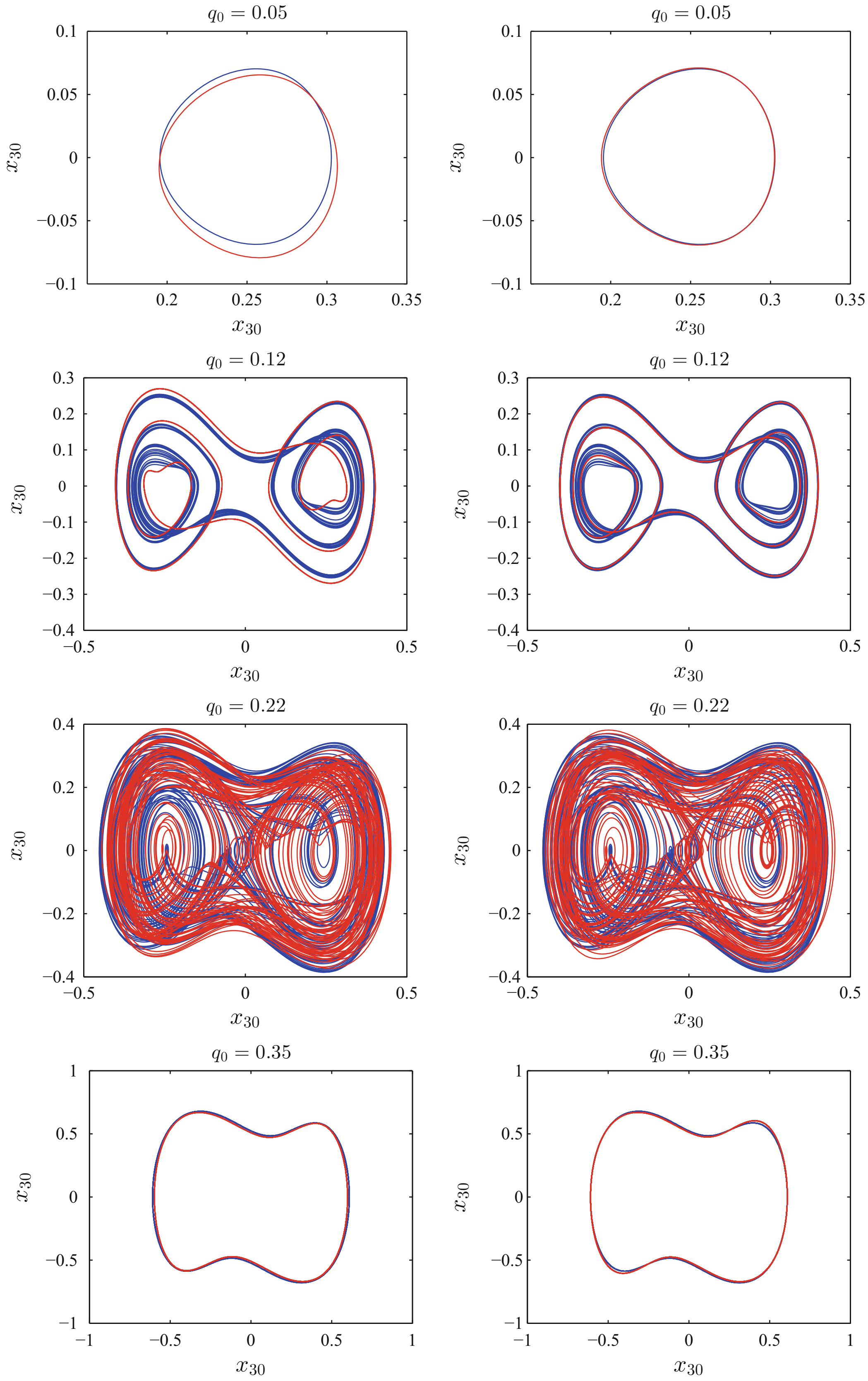

Fig. 41.3 Phase portraits of the 30th mass of the nonlinear system obtained from full scale (*blue*) and reduced order models (*red*): six-dimensional POD-based ROMs (*left*); six-dimensional separated POD-based ROMs (*right*)

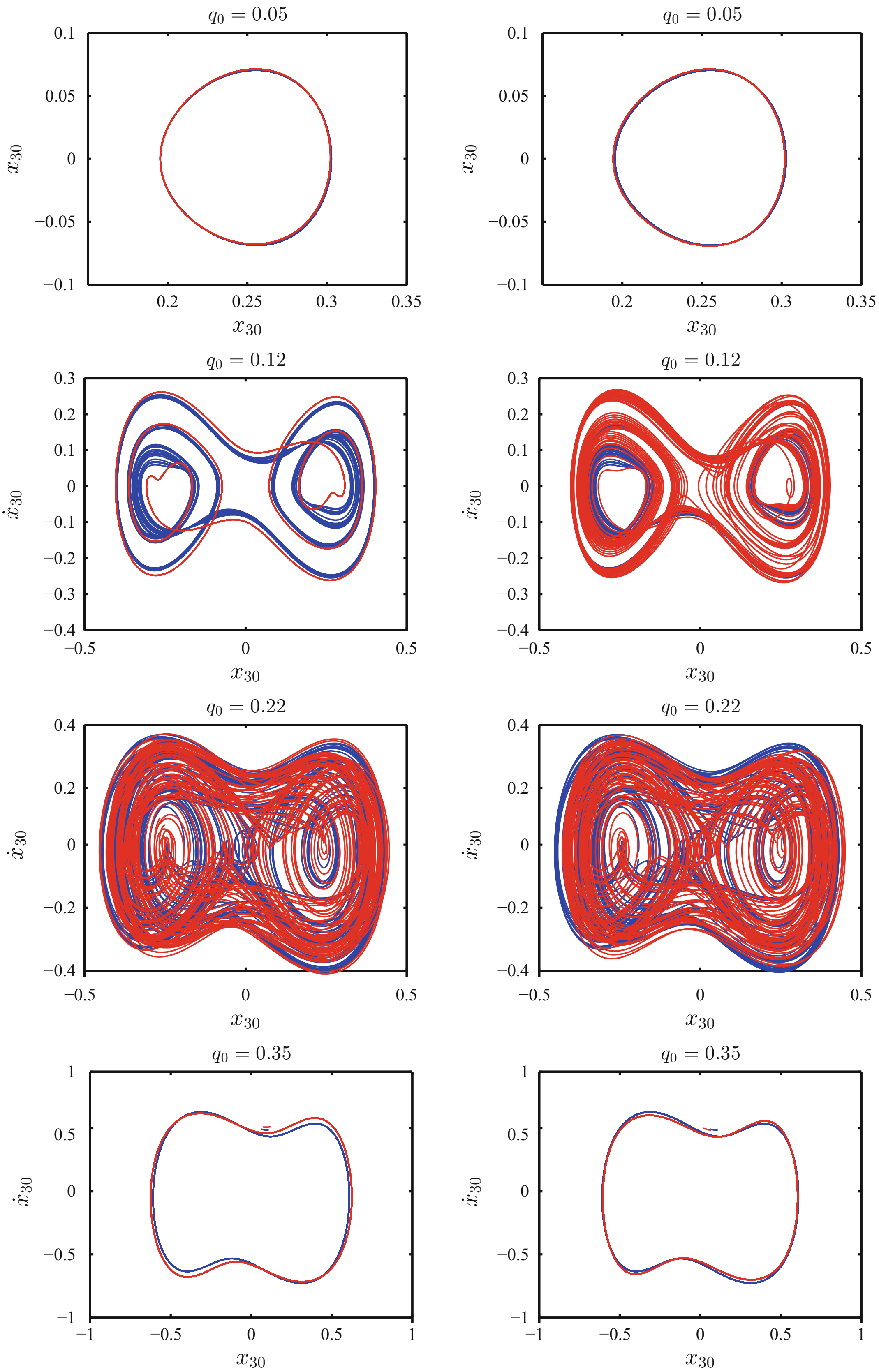

Fig. 41.4 Phase portraits of the 30th mass of the nonlinear system obtained from full scale (*blue*) and reduced order models (*red*): four-dimensional SOD-based ROMs (*left*); four-dimensional separated SOD-based ROMs (*right*)

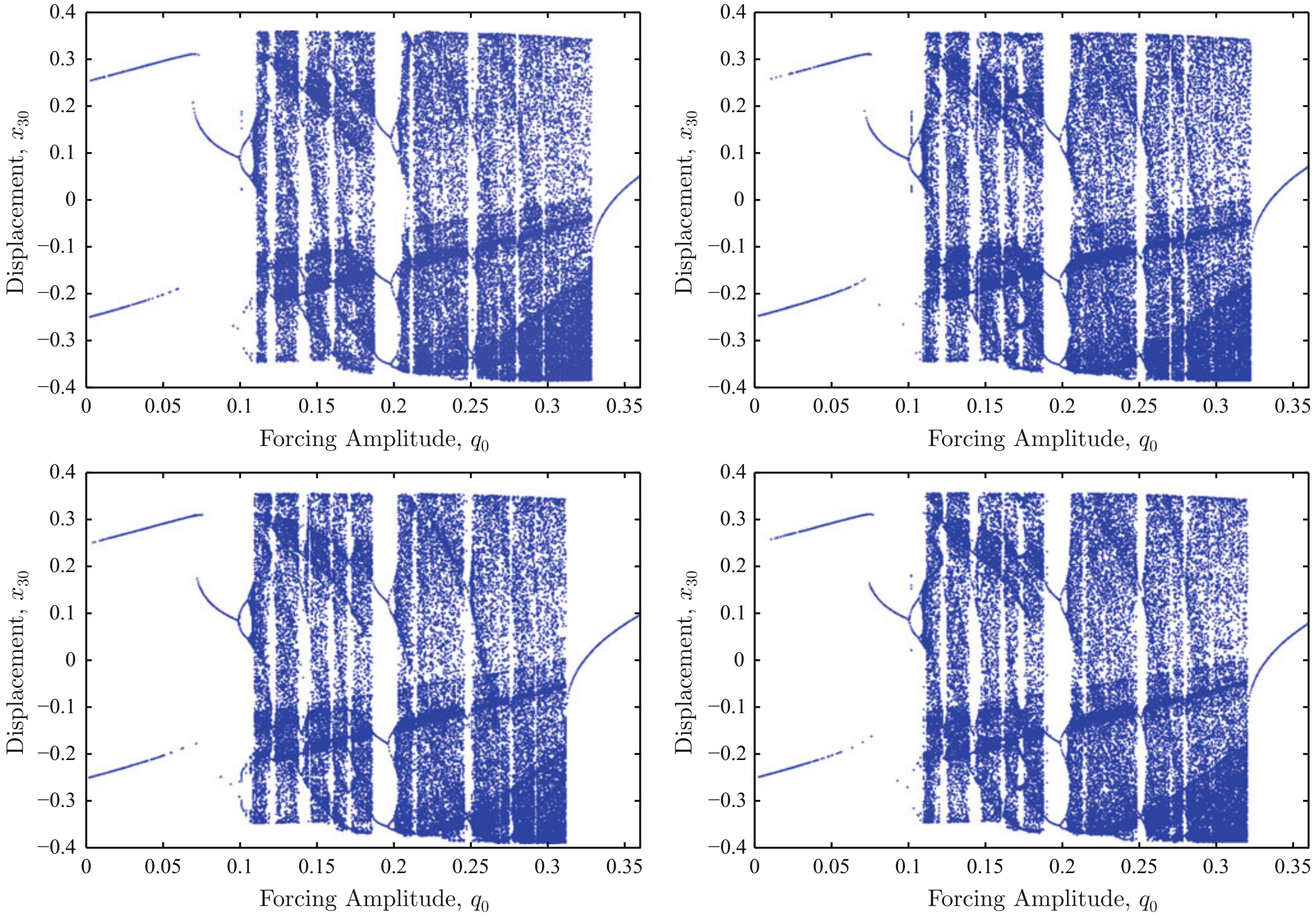

Fig. 41.5 Bifurcation diagram for ROMs: of the nonlinear system; for harmonic forcing with $\omega = 7.97$ Hz: six-dimensional POD (*top left*); six-dimensional separated POD (*top right*); four-dimensional SOD (*bottom left*); four-dimensional separated SOD (*bottom right*)

41.5 Conclusions

The separated multivariate analysis using POD and SOD was proposed to deal with the rank-deficiency of nonlinear dynamical systems. Following the mathematical formulation of the separated POD- and SOD-based MOR, a nonlinear mass-spring-damper was studied. The full-scale state-space model of the system was obtained and the data matrices were extracted. The performance of four methods for MOR including POD, SOD, separated POD and separated SOD was investigated in terms of stability and accuracy. The results confirmed that SOD was able to capture the dynamics of the system in a lower dimensional space. Separated multivariate analysis was shown to improve the accuracy and stability of the POD-based MOR. However, it had a worsening effect on the SOD-based MOR.

Acknowledgements The authors would like to thank National Science Foundation under Grant No. 1100031.

References

1. Balajewicz, M., Amsallem, D., and Farhat, C.: Projection-based model reduction for contact problems. Int. J. Numer Meth Eng (2015).
2. Benner, P., Mehrmann, V., Sorensen, D.C.: Dimension Reduction of Large-Scale Systems, vol. 45. Springer, Berlin (2005)
3. Ilbeigi, S., Chelidze, D.: Model order reduction of nonlinear euler-bernoulli beam. In: Nonlinear Dynamics, vol. 1, pp. 377–385. Springer, Berlin (2016)
4. Antoulas, A.C., et al.: Model order reduction: Methods, concepts and properties. In: Coupled multiscale simulation and optimization in nanoelectronics, pp. 159–265. Springer, Berlin (2015)

5. Maier, D., Hager, C., Hetzler, H., Fillot, N., Vergne, P., Dureisseix, D., Seemann, W.: A nonlinear model order reduction approach to the elastohydrodynamic problem. Tribol. Int. **82**, 484–492 (2015)
6. Kudryavtsev, M., Rudnyi, E., Korvink, J., Hohlfeld, D., Bechtold, T.: Computationally efficient and stable order reduction methods for a large-scale model of mems piezoelectric energy harvester. Microelectron. Reliab. **55**(5), 747–757 (2015)
7. Benner, P., Feng, L.: Model order reduction for coupled problems. Appl. Comput. Math. Int. J. **14**(1), 3–22 (2015)
8. Foias, C., Jolly, M., Kevrekidis, I., Sell, G., Titi, E.: On the computation of inertial manifolds. Phys. Lett. A **131**(7), 433–436 (1988)
9. Pesheck, E., Pierre, C., Shaw, S.: A new galerkin-based approach for accurate non-linear normal modes through invariant manifolds. J. Sound Vib. **249**(5), 971–993 (2002)
10. Feldmann, P., Freund, R.W.: Efficient linear circuit analysis by padé approximation via the lanczos process. IEEE Trans. Comput. Aided Des. Integr. Circuits Syst. **14**(5), 639–649 (1995)
11. Rahrovani, S., Vakilzadeh, M.K., Abrahamsson, T.: Modal dominancy analysis based on modal contribution to frequency response function $\mathcal{H}2$-norm. Mech. Syst. Signal Process. **48**(1), 218–231 (2014)
12. Vakilzadeh, M.K., Rahrovani, S., Abrahamsson, T.: Modal reduction based on accurate input-output relation preservation. In: Topics in Modal Analysis, vol. 7, pp. 333–342. Springer, New York (2014)
13. Glover, K.: All optimal hankel-norm approximations of linear multivariable systems and their L, ∞-error bounds†. Int. J. Control. **39**(6), 1115–1193 (1984)
14. Zhou, H., Su, X., Song, Y.-D., Yan, Q.: Hankel-norm model reduction for delayed fuzzy systems. In: IEEE 2015 27th Chinese Control and Decision Conference (CCDC), pp. 964–968 (2015)
15. Phillips, J.R., Daniel, L., Silveira, L.M.: Guaranteed passive balancing transformations for model order reduction. IEEE Trans. Comput. Aided Des. Integr. Circuits Syst. **22**(8), 1027–1041 (2003)
16. Baur, U., Benner, P., Feng, L.: Model order reduction for linear and nonlinear systems: a system-theoretic perspective. Arch. Comput. Meth. Eng. **21**(4), 331–358 (2014)
17. Kerschen, G., Golinval, J.-C., Vakakis, A.F., Bergman, L.A.: The method of proper orthogonal decomposition for dynamical characterization and order reduction of mechanical systems: an overview. Nonlinear Dyn. **41**(1–3), 147–169 (2005)
18. Rathinam, M., Petzold, L.R.: A new look at proper orthogonal decomposition. SIAM J. Numer. Anal. **41**(5), 1893–1925 (2003)
19. Willcox, K., Peraire, J.: Balanced model reduction via the proper orthogonal decomposition. AIAA J. **40**(11), 2323–2330 (2002)
20. Benner, P., Breiten, T.: Two-sided projection methods for nonlinear model order reduction. SIAM J. Sci. Comput. **37**(2), B239–B260 (2015)
21. Georgiou, I.: Advanced proper orthogonal decomposition tools: using reduced order models to identify normal modes of vibration and slow invariant manifolds in the dynamics of planar nonlinear rods. Nonlinear Dyn. **41**(1–3), 69–110 (2005)
22. Ghasemi, M., Yang, Y., Gildin, E., Efendiev, Y., Calo, V., et al.: Fast multiscale reservoir simulations using pod-deim model reduction. In: SPE Reservoir Simulation Symposium. Society of Petroleum Engineers, Richardson, TX (2015)
23. Shaw, S., Pierre, C.: Non-linear normal modes and invariant manifolds. J. Sound Vib. **150**(1), 170–173 (1991)
24. Pesheck, E., Pierre, C., Shaw, S.W.: Modal reduction of a nonlinear rotating beam through nonlinear normal modes*. J. Vib. Acoust. **124**(2), 229–236 (2002)
25. Kerschen, G., Peeters, M., Golinval, J.-C., Vakakis, A.F.: Nonlinear normal modes, part i: a useful framework for the structural dynamicist. Mech. Syst. Signal Process. **23**(1), 170–194 (2009)
26. Grolet, A., Thouverez, F.: Computing multiple periodic solutions of nonlinear vibration problems using the harmonic balance method and groebner bases. Mech. Syst. Signal Process. **52**, 529–547 (2015)
27. Mohammadali, M., Ahmadian, H.: Efficient model order reduction of structural dynamic systems with local nonlinearities under periodic motion. Shock. Vib. **2014** (2014)
28. Blanc, F., Touzé, C., Mercier, J.-F., Ege, K., Ben-Dhia, A.-S.B.: On the numerical computation of nonlinear normal modes for reduced-order modelling of conservative vibratory systems. Mech. Syst. Signal Process. **36**(2), 520–539 (2013)
29. Wang, Y., Palacios, R., Wynn, A.: A method for normal-mode-based model reduction in nonlinear dynamics of slender structures. Comput. Struct. **159**, 26–40 (2015)
30. Amabili, M., Sarkar, A., Paıdoussis, M.: Reduced-order models for nonlinear vibrations of cylindrical shells via the proper orthogonal decomposition method. J. Fluids Struct. **18**(2), 227–250 (2003)
31. Smith, T.R., Moehlis, J., Holmes, P.: Low-dimensional modelling of turbulence using the proper orthogonal decomposition: a tutorial. Nonlinear Dyn. **41**(1–3), 275–307 (2005)
32. Kerschen, G., Feeny, B., Golinval, J.-C.: On the exploitation of chaos to build reduced-order models. Comput. Methods Appl. Mech. Eng. **192**(13), 1785–1795 (2003)
33. Vakakis, A.F., Gendelman, O.V., Bergman, L.A., McFarland, D.M., Kerschen, G., Lee, Y.S.: Nonlinear Targeted Energy Transfer in Mechanical and Structural Systems, vol. 156. Springer Science & Business Media, Berlin (2008)
34. Kuether, R.J., Deaner, B.J., Hollkamp, J.J., Allen, M.S.: Evaluation of geometrically nonlinear reduced-order models with nonlinear normal modes. AIAA J. **53**(11), 3273–3285 (2015)
35. Wang X, Construction of frequency-energy plots for nonlinear dynamical systems from time-series data, Thesis, partial fulfillment of the requirements for the degree of Master of Science in Mechanical Engineering, Graduate College of the University of Illinois, Urbana-Champaign (2010).
36. Peter, S., Grundler, A., Reuss, P., Gaul, L., Leine, R.I.: Towards finite element model updating based on nonlinear normal modes. In: Nonlinear Dynamics, vol. 1, pp. 209–217. Springer, Berlin (2016)
37. Vakakis, A.F., Manevitch, L.I., Mikhlin, Y.V., Pilipchuk, V.N., Zevin, A.A.: Normal Modes and Localization in Nonlinear Systems. Springer, Berlin (1996)
38. Segala, D.B., and Chelidze, D. Robust and dynamically consistent model order reduction for nonlinear dynamic systems. J. Dyn. Syst. Meas. Control. **137**(2), 021011 (2015)
39. Chelidze, D.: Identifying robust subspaces for dynamically consistent reduced-order models. In: Nonlinear Dynamics, vol. 2, pp. 123–130. Springer, Berlin (2014)

Chapter 42
Using NNMs to Evaluate Reduced Order Models of Curved Beam

Christopher I. VanDamme and Matthew S. Allen

Abstract Reduced order modeling of geometrically nonlinear structures has gained significant attention over the recent years due to its ability to reduce detailed finite element models into computationally efficient yet accurate models. The reduced order models (ROMs) generated can be used to compute the nonlinear normal modes (NNMs) of a structure which serve as a metric to determine the accuracy of the reduced order models; if the NNMs are reproduced accurately then the response to various inputs can also be shown to be accurate. A majority of work has been focused on flat structures while relatively few works have focused on curved structures, those that have, suggested that these structures may introduce complexities to the system. This paper will provide a criteria for selecting basis vectors and load amplitudes for generating accurate ROMs for a curved beam, where softening nonlinearity and snap through are significant. Two methods will be considered: implicit condensation and expansion (ICE) and enforced displacements (ED). A framework for mode selection, load scaling factors and model sensitivity testing will be presented in order to accurately compute the NNMs.

Keywords Reduced order modeling • Geometric nonlinearities • Nonlinear normal modes • Finite element analysis • Structural dynamics

42.1 Introduction

Future hypersonic vehicles may experience high thermal and acoustic loading due to extreme flow fields and engine noise [1]. These extreme loading conditions cause thin walled skin panels to vibrate nonlinearly, sometimes even about a buckled equilibrium point [2]. Linear approximations are insufficiently accurate in being able to predict the geometrically nonlinear response of the panels which leads to an over conservative design of the system [2]. Modeling is performed using the finite element method because the discretization capabilities allows for complicated geometries to be accurately modeled. The finite element models of these structures, in order to account for the complex geometries, may contain millions of degrees-of-freedom (DOF) resulting in millions of equations of motion of the system that need to be solved to find the dynamic response of the system. Computational methods are available to calculate the nonlinear response of the system to such loads using either implicit or explicit time integration of the equations of motion. The problem with explicit time integration schemes is that in order to achieve a geometrically accurate model some elements of the system must be significantly small resulting in small time step requirements. To accurately predict the response of the structure, the equations must be integrated over many cycles of the lowest frequency mode for a large set of loading conditions to account for the random loading environment the vehicles experience. This, coupled with the small time steps, cause the analysis to be prohibitively expensive. For example, a 96,000 DOF finite element model of a multi-bay aircraft panel required 6 days of computation on a quad-core computer for 100,000 time steps [3]. Analysis cycles of this length are prohibitive to the design of structures experiencing geometric nonlinearities.

Nonlinear Reduced Order Models (NLROMs) provide a method to decrease the number of DOF by approximating the full finite element model resulting in fewer equations of motion to solve. The ability to create accurate NLROMs of the discretized finite element model decreases the computational cost of the analysis resulting in decreased design cycle time. However, it is not necessarily straightforward to create an accurate ROM. An analyst must determine how many modes to include, and since each mode comes with substantial cost, the analyst should include as few as possible. The analyst must also determine how large of loads to apply to estimate the ROM. Furthermore, once the ROM is created, it comprises thousands of coefficients so it is difficult to tell what has been captured in the ROM. In the past, the static or time response of the

---

C.I. VanDamme (✉) • M.S. Allen
Department of Engineering Physics, University of Wisconsin-Madison, 1500 Engineering Drive Madison, WI 53706, USA
e-mail: matt.allen@wisc.edu; cvandamme@wisc.edu

© The Society for Experimental Mechanics, Inc. 2016

J. De Clerck, D.S. Epp (eds.), *Rotating Machinery, Hybrid Test Methods, Vibro-Acoustics & Laser Vibrometry, Volume 8*,
Conference Proceedings of the Society for Experimental Mechanics Series, DOI 10.1007/978-3-319-30084-9_42

ROMs have typically been compared with simulations from the full order model which are very expensive to obtain. Kuether and Allen recently proposed an alternative, in which the NNMs of the ROMs are compared to understand what dynamics the ROM has captured and to assess its quality. This paper tests the methodology developed by Kuether and Allen [4]. The validation of the ROMs are measured by evaluating the convergence of computed NNMs, which provide great insight into the free, forced and random response of structures [5].

In the linear domain a ROM must account for the range of loading frequencies the structure will encounter. In essence, the ROM only needs to be validated in terms of frequency; if the frequency range of the ROM encompasses the loading frequencies, then one can expect accurate predictions of the response. When geometric nonlinearities are encountered the response becomes amplitude dependent, adding a second dimension that must be considered. The ROM must now account for both the frequency and amplitude range of the loadings the structure may encounter. NNMs account for both frequency and loading amplitude, represented as energy of the system, typically plotted as a Frequency Energy Plot (FEP). A FEP represents the NNM with the structure's computed periods on the vertical scale and energy (potential + kinetic) on a logarithmic horizontal scale.

In previous works, Kuether and Allen compared the NNMs of the ROMs with NNMs computed directly from the full FEM. The latter are quite expensive to compute, so this work will instead follow the suggestion in [4]. This work will not compute the full finite element model NNM because in order for time efficient design and analysis cycles, the full model NNM would not be computed. The analyst will need to validate the accuracy of the ROM without a truth solution. This work will apply these tools to a structure with curvature, whose nonlinear dynamics are far more complicated.

Two methods of creating ROMs, Enforced Displacements (ED) and Implicit Condensation and Expansion (ICE), will be evaluated with NNMs. The two methods presented have been given large attention over the past few years for flat structures, this paper will study the two methods of model reduction on a curved structure, which is more prevalent in real designs. The curvature of the structure provides increased complexity of the problem due to strong modal coupling, presence of snap through and less deterministic load case factors.

42.2 Theory

The linear elastic finite element model equation of motion for N degree-of-freedom (DOF) system with no damping can be written as

$$\mathbf{M}\,\ddot{\mathbf{x}} + \mathbf{K}\mathbf{x} = \mathbf{f}(t) \tag{42.1}$$

where $\mathbf{M}$ is the $N \times N$ mass matrix, $\mathbf{K}$ is the $N \times N$ linear stiffness matrix and $\mathbf{f}(t)$ is the $N \times 1$ external force vector. The displacement and acceleration vectors $\mathbf{x}$ and $\ddot{\mathbf{x}}$ are both $N \times 1$ vectors. This equation is valid for small displacement approximations and assumes no nonlinearities within the model. In order to account for geometric nonlinearities within the finite element model equation (42.1) must be altered to include the nonlinear restoring force vector, $\mathbf{f}_{NL}$, to form the nonlinear equation of motion of the form

$$\mathbf{M}\,\ddot{\mathbf{x}} + \mathbf{K}\mathbf{x} + \mathbf{f}_{NL}(\mathbf{x}) = \mathbf{f}(t) \tag{42.2}$$

where $\mathbf{f}_{NL}$ is a $N \times 1$ vector. The creation of the ROM follows similarly from that of the linear modal ROM where the reduction basis is a set of linear modes of the system The linear modes of the system are found by solving the eigenvalue problem of the linear system shown in Eq. (42.1)

$$\left(\mathbf{K} - \omega^2\mathbf{M}\right)\boldsymbol{\phi}_{\mathbf{r}} = \mathbf{0} \tag{42.3}$$

which can be solved to find the coordinate reduction equation represented as

$$\mathbf{x}(t) = \boldsymbol{\Phi}_m\mathbf{q}(t) \tag{42.4}$$

where $\boldsymbol{\Phi}_m$ is the $N \times m$ the mass normalized mode matrix comprised of the mode vectors, $\boldsymbol{\phi}_r$, and $\mathbf{q}$ is the $m \times 1$ vector of time-dependent modal displacements. The motivation for representing the linear equation of motion in this fashion is that the modal coordinates and mode shape matrix are able to accurately predict the response of the system while reducing the number of degrees of the freedom since $m \ll N$.

When the linear equation of motion in Eq. (42.1) is premultiplied by $\boldsymbol{\Phi}^T$, where ^{T} is the transpose operator, the rth modal equation becomes uncoupled and is represented as

$$\ddot{q}_r + \boldsymbol{\omega}_r^{\mathbf{2}} q = \boldsymbol{\phi}_r^{\mathbf{T}} \mathbf{f}(t) \tag{42.5}$$

When the same coordinate transformation is applied to the nonlinear equations of motion, Eq. (42.2), for the rth modal equation becomes

$$\ddot{q}_r + \boldsymbol{\omega}_r^{\mathbf{2}} q + \boldsymbol{\theta}_r(q_1, q_2, \ldots, \mathbf{q}_m) = \boldsymbol{\phi}_r^{\mathbf{T}} \mathbf{f}(\mathbf{t}) \tag{42.6}$$

where the nonlinear restoring force, $\boldsymbol{\theta}_r$, is represented as a function of modal displacements by

$$\boldsymbol{\theta}_r(\mathbf{q}) = \boldsymbol{\phi}_r^{\mathbf{T}} \mathbf{f}_{NL} \left(\boldsymbol{\Phi}_m \mathbf{q}\right) \tag{42.7}$$

In [6, 7] it was shown that the restoring forces for a linear elastic system with geometric nonlinearities can be well approximated as

$$\boldsymbol{\theta}_r(\mathbf{q}_1, \mathbf{q}_2, \ldots, \mathbf{q}_m) = \sum_{i=1}^{m} \sum_{j=1}^{m} \mathbf{B}_r(i,j) \mathbf{q}_i \mathbf{q}_j + \sum_{i=1}^{m} \sum_{j=1}^{m} \sum_{k=1}^{m} \mathbf{A}_r(i,j,k) \mathbf{q}_i \mathbf{q}_j \mathbf{q}_k \tag{42.8}$$

where the nonlinear restoring force is a function of quadratic and cubic polynomials with coefficients B_r and A_r respectively for the rth nonlinear modal equation. These coefficients are computed differently depending on whether using Enforced Displacements or Implicit Condensation and Expansion as described below.

42.2.1 *Enforced Displacement (ED)*

The enforced displacements procedure applies a set of known displacements in the shape(s) of the linear modes. The general form of the applied displacements for a basis set with multiple modes is described as

$$\mathbf{X}_i = \boldsymbol{\phi}_1 \hat{\mathbf{q}}_1 + \boldsymbol{\phi}_2 \hat{\mathbf{q}}_2 + \ldots + \boldsymbol{\phi}_m \hat{\mathbf{q}}_m \tag{42.9}$$

where $\mathbf{q}_r$ is the scaling factor for the rth mode in the basis set and $\mathbf{X}_i$ is the $N \times 1$ applied displacement vector. The reactions forces, $\mathbf{F}_l$ are then extracted from the finite element model for the applied displacement field. The calculated reaction forces are then used as a static load terms in the NLROM equation of motion of the system as

$$\boldsymbol{\omega}_r^2 \mathbf{q}_r + \sum_{i=1}^{m} \sum_{j=1}^{m} \mathbf{B}_r(i,j) \mathbf{q}_i \mathbf{q}_j + \sum_{i=1}^{m} \sum_{j=1}^{m} \sum_{k=1}^{m} \mathbf{A}_r(i,j,k) \mathbf{q}_i \mathbf{q}_j \mathbf{q}_k = \boldsymbol{\phi}_r^{\mathbf{T}} \mathbf{F}_l \tag{42.10}$$

where the nonlinear stiffness coefficients, A_r and B_r are solved using the method described in [8]. It is important to note that for the ED method the number of nonlinear static solutions required to find the stiffness coefficients for $m > 3$ [7] is

$$2\mathrm{m} + \frac{3\mathrm{m}!}{2(\mathrm{m}-2)!} + \frac{\mathrm{m}!}{6(\mathrm{m}-3)!} \tag{42.11}$$

42.2.2 *Implicit Condensation and Expansion (ICE)*

The implicit condensation and expansion method is similar to the enforced displacement method but instead of applying a set of displacements in the linear mode shapes of the system, a set of forces are applied that would each excite only one linear mode if the structure were linear. The general equation for a forcing with multiple modes can be given as

$$\mathbf{F}_l = \mathbf{M}(\boldsymbol{\phi}_1 \hat{\mathbf{f}}_1 + \boldsymbol{\phi}_2 \hat{\mathbf{f}}_2 + \ldots + \boldsymbol{\phi}_m \hat{\mathbf{f}}_m) \tag{42.12}$$

where $\mathbf{F}_l$ is the vector of applied forces, $\mathbf{M}$ is the mass matrix and $\mathbf{f}_r$ is the scaling factor for the rth modal force. The mass matrix is included above to exploit orthogonality, so that the shapes $\boldsymbol{\phi}_r\hat{\mathbf{f}}_r$ each only excite one mode of the linear system [9]. For the ICE method the number of required load permutations required to generate the static response data [1] (for m >3) is

$$2\mathrm{m}+2\frac{\mathrm{m}!}{(\mathrm{m}-2)!}+\frac{4\mathrm{m}!}{3(\mathrm{m}-3!)} \tag{42.13}$$

42.2.3 Nonlinear Normal Modes

Nonlinear Normal Modes are the foundation of evaluating the accuracy of the computed ROMs in this work. NNMs defined by Vakakis, Kerschen and others [5] as "a not necessarily synchronous periodic solution of the conservative, nonlinear equations of motion." NNMs provide the backbone of the nonlinear dynamics of the system and provide strong quantitative metrics for which to evaluate the ROM [9]. Typically NNMs are plotted on a frequency versus energy plot, or FEP, which shows how the resonance frequency changes with energy of the system. The NNMs of the undamped ROMs as represented in Eq. (42.6) are computed in this work using a pseudo-arclength continuation method developed in [9]. The continuation algorithm uses the linear mode shape to initiate the branch for each NNM of the system. From there the algorithm finds a branch of solutions that satisfy the following shooting function.

$$\mathbf{H}(\mathrm{T},\mathbf{q}_0,\mathbf{q}_0)=\begin{Bmatrix}\mathbf{q}(\mathrm{T},\mathbf{q}_0,\ \dot{\mathbf{q}}_0)\\ \mathbf{q}(\mathrm{T},\mathbf{q}_0,\ \dot{\mathbf{q}}_0)\end{Bmatrix}-\begin{Bmatrix}\mathbf{q}_0\\ \dot{\mathbf{q}}_0\end{Bmatrix}=\{\mathbf{0}\} \tag{42.14}$$

where T, $\mathbf{q}_0$, and $\dot{\mathbf{q}}_0$ are the period of integration, initial modal displacements, and initial modal velocities respectively.

42.2.4 Proposed Methodology for Creating a Valid ROM

Previous work [4] established a methodology for generating valid ROMs of a finite element model using the convergence of NNMs as an accuracy metric; this study follows the general procedure with some additions. Before generating the ROM the analyst must analyze the loading environment the structure will experience to determine the range for which the ROM must maintain accuracy. This includes both the frequency and amplitude of the loadings. Prior work [4] focused on finding a ROM that would accurately reproduce each NNM individually. This work seeks to generate a ROM that will accurately reproduce a set of NNMs to assure that the model is accurate over a range of frequency and energy.

In prior works, it has proven helpful to consider static load cases in terms of how much the nonlinear deformation deviates from a linear response. This is done by defining

$$\mathbf{x}_{rat}=\frac{max\left(\mathbf{w}_{\mathrm{NL}}\right)}{max\left(\mathbf{w}_{linear}\right)} \tag{42.15}$$

where x_{rat} is the ratio of the calculated displacement of the nonlinear system to the displacement that would be computed using a linear model. This ratio is less than one for hardening nonlinearities, and can also be greater than one for structures that exhibit snap-through or other softening nonlinearities.

The general procedure for creation of valid ROM is:

1. Conduct a pre-processing step to determine the dominant modes and initial load scaling factors for each NNM branch
   (a) Define static loads that will generate $\mathbf{x}_{rat}$ values between 0.80–0.9 for hardening nonlinearity or $\mathbf{x}_{rat}$ values between 1.05–1.20 for softening nonlinearity for each linear mode based on [10]. This provides a baseline for load scaling factors for each linear mode in the basis set.
   (b) Use $\mathbf{q}=\mathbf{\Phi}^{\mathbf{T}}\mathbf{M}\mathbf{x}$ to compute the modal displacement of the each mode in response to the applied load in order to find the strongest modal coupling to mode of interest. This determines which modes should be included in the basis set of the ROM by selecting the modes in the order of dominance in the static response.
2. Generate a 1-mode ROM and compute the corresponding NNM

3. Add additional modes as found to be strongly coupled to the desired NNM branch in step (1b)
4. Recompute the NNM for the multi-mode ROM and compare the results with the previously computed NNM by checking:
   (a) Convergence of NNMs energy at a specific frequency.
   (b) Check the periodicity, ε, of the undamped free response of the full finite element model using the NNM solution transferred back to the real domain as initial condition. The periodicity of the response is evaluated using

$$\frac{\|\mathbf{X}_T - \mathbf{X}_0\|}{\|\mathbf{X}_0\|} = \varepsilon \tag{42.16}$$

   where X_0 and X_T are the displacement vectors of system for the initial conditions and at the end of one period respectively, and $\| \; \|$ is the norm operator on a vector. The lower the ε value the more accurate representation the ROM is of the full FEM. A value of ε below 10^{-1} is desirable. This step should be used sparingly and as a final check due to the computational cost associated with integrating the full FEM over one period.

5. After evaluation of the above parameters if convergence has not been achieved, the analyst can either:
   (a) Add additional modes to the basis set in the order of their dominance by using one of the following methods:
      (i) Refer to the statically coupled modes found in the pre-processing presented in step (1b).
      (ii) Computing the modal amplitudes found in the free response of the full FEM model in step (4b). This is accomplished by transferring the real domain response to modal amplitudes as a function of time $\mathbf{q}(t) = \mathbf{\Phi}^{\mathbf{T}}\mathbf{M}\mathbf{x}(t)$. This transformation gives insight into which modes are contributing to the dynamic response but may not be included in the ROM.
   (b) Change load scaling factors of the basis vectors.
6. Repeat steps (4–5) until convergence is achieved for the current NNM.
7. Expand ROM to next NNM using steps (2–6) until the ROM is accurate over the desired range of frequency and energy encompassed by the NNMs.

42.3 Numerical Results of an Asymmetric Curved Beam

The methodology described above was tested on a curved beam using both the ED and ICE methods of generating ROMs. The beam was modeled using 80 3-D beam finite elements generated in Abaqus®with a total of 480 DOF constrained to in-plane motion and rotation. The curved beam has a rectangular cross section with clamped-clamped end conditions as shown in Fig. 42.1. The properties of the beam can be found in Table 42.1.

The curved beam has an 81.5 in radius of curvature with a slight asymmetry imposed on it. Note that the figure of the beam is not to scale, this is in order to show the curvature of beam and the slight asymmetry present.

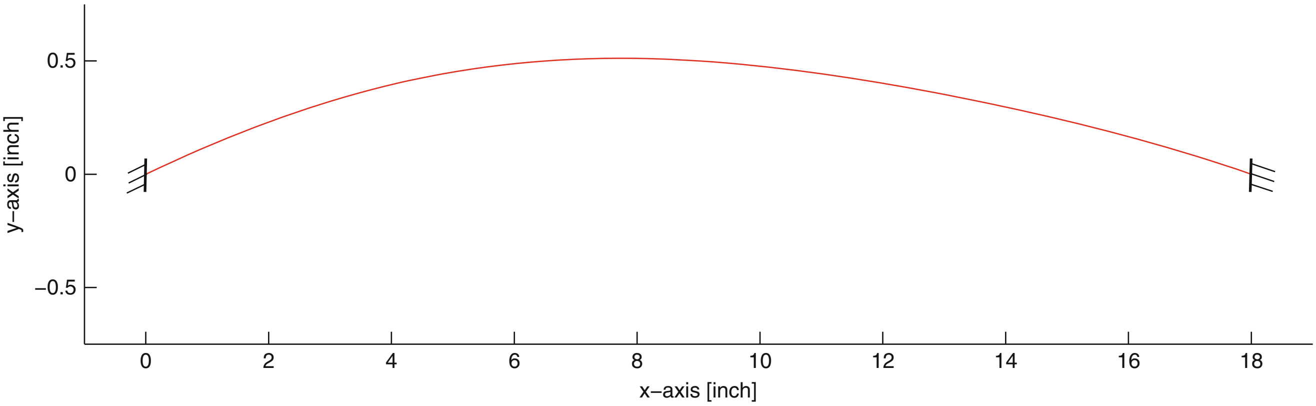

Fig. 42.1 Curved beam diagram showing the curvature and asymmetry with clamped clamped boundary conditions

Table 42.1 Properties of asymmetric curved beam

Young's modulus $\left(\frac{\text{lb}}{\text{in}^2}\right)$	Poison's ratio (ν)	Density $\left(\frac{\text{lb}}{\text{in}^3}\right)$	Thickness (in)	Width (in)	Length (in)
10,600,000	0.325	0.000259	0.09	1	18

Table 42.2 Static modal coupling rankings for first four linear modes used to create ROMs basis set

Linear mode	Frequency (Hz)	Contribution (highest → lowest)
1	145	[1, 3, 2, 4, 5, 7, 15, 22, 6, 38]
2	270	[2, 3, 1, 4, 5, 7, 22, 15, 9, 42]
3	415	[3, 1, 2, 4, 5, 7, 15, 6, 9, 22]
4	514	[4, 3, 1, 2, 5, 7, 22, 50, 9, 57]

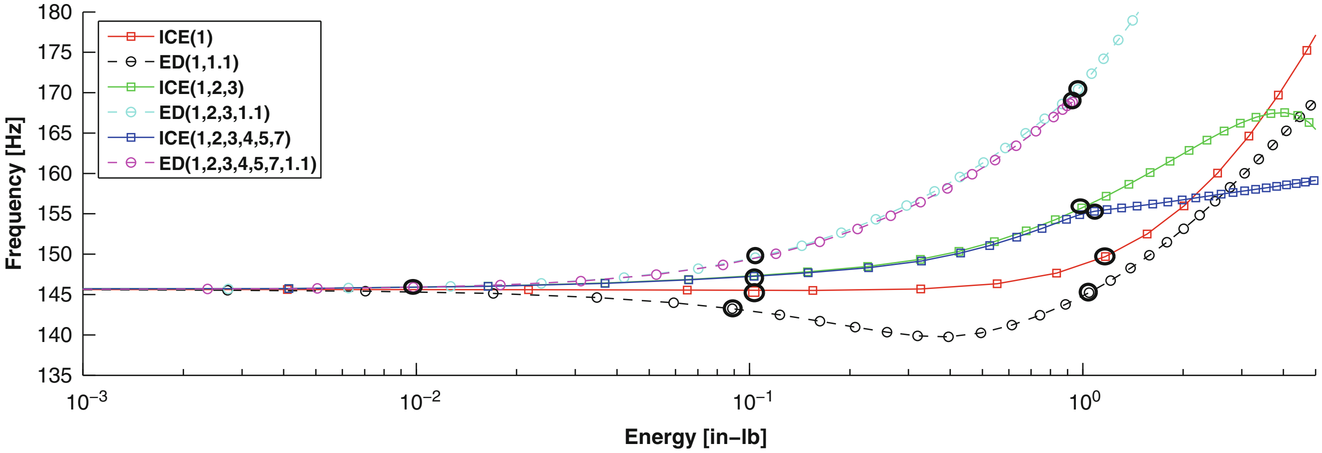

Fig. 42.2 First NNM computed from ROMs using similar basis sets for both ED and ICE methods. The *black circles* represent NNM solution points used to test the periodicity of the full FEM model in Table 42.3

42.3.1 Pre-Processing

The first step in creating the ROMs is to apply static loads as described in step 1(a). The static coupling results from the pre-processing are found in Table 42.2. Notice that for the first four linear modes that the six most strongly coupled modes are all the same, this is helpful since, we seek to create one ROM that accurately reproduces the first four NNMs. The scaling factors are chosen such that they properly excite the nonlinearities of the structure. The original load factors were calculated so that the x_{rat} value was between 0.8 and 0.9 for hardening nonlinearities and 1.05–1.2 for softening nonlinearities as recommended by Mignolet et al. [7] and Gordon and Hollkamp [11]. Load scaling factors were also perturb outside the recommended range to test the sensitivity of their values on generating ROMs for curved beams.

42.3.2 Computed NNMs

Once the pre-processing is complete the analyst is now able to compute the NNMs and validate the ROM. The results for the first NNM using both the ED and ICE method with similar basis sets are shown in Fig. 42.2. The legend shows the method of ROM generation and the modes included within the basis set. The designation "1.1" represents a dual mode included within the basis set for the ED method corresponding to the 1st bending mode. The ROMs presented in Fig. 42.2 contained scaling factors that created x_{rat} values of approximately 0.85 based on the pre-processing.

In Fig. 42.2 it is shown that for both the ED and ICE method that the one-mode ROMs varies significantly from the multi-mode ROMs. As additional modes are included within the basis set the NNMs show less change in energy of the system for a specific period. Each method of model reduction shows to trend towards a different solution of the NNM. In order to validate which method is approaching the true solution the periodicity of the full order finite element model to initial conditions of

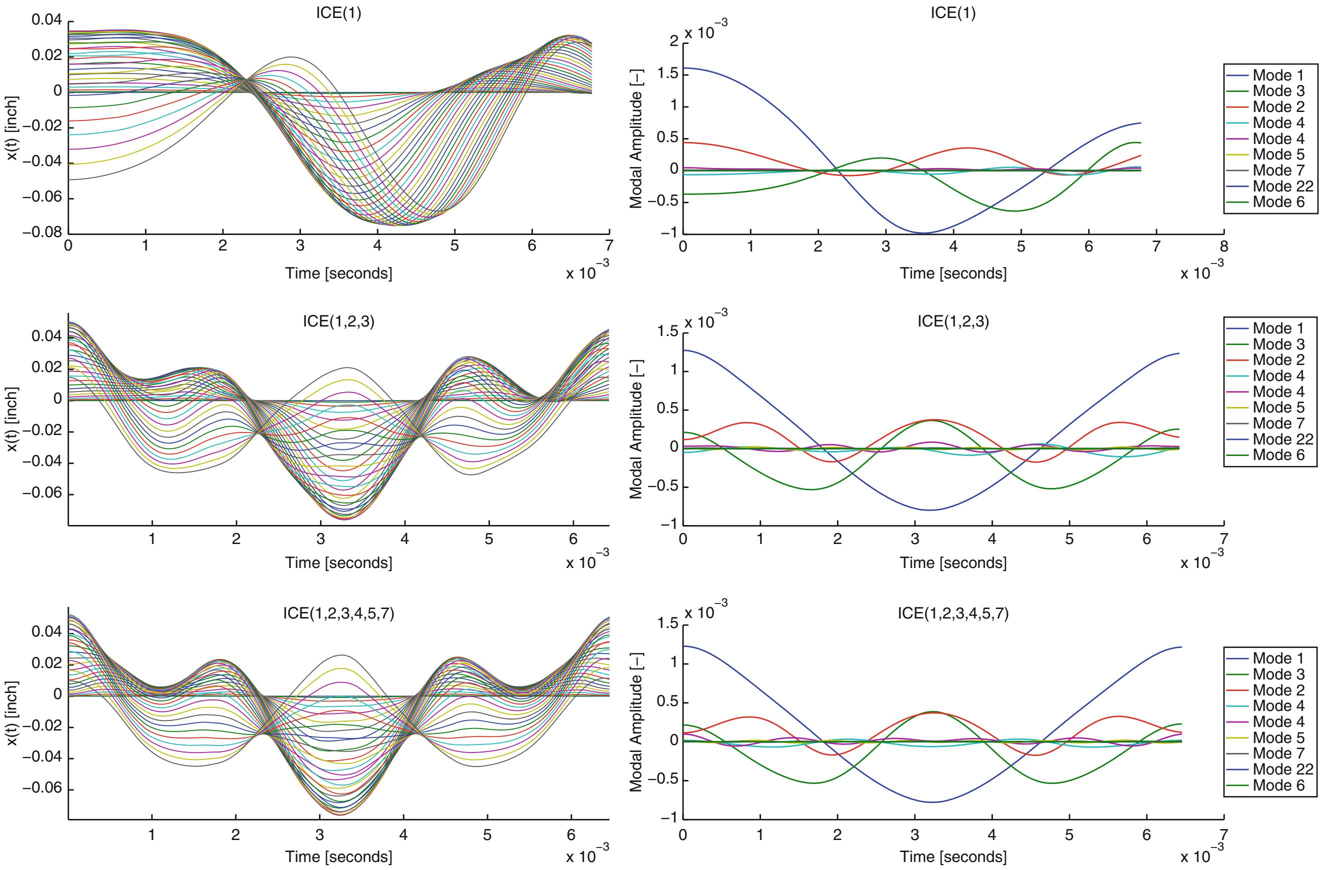

Fig. 42.3 *Left*: Time histories found from integrating the initial conditions from NNM computed using ICE ROMs at points (3) near Energy = 1 [in-lb] in Fig. 42.2; *Right*: Time histories of modal amplitudes of the linear modes found in the dynamic response of the system shown on the *left*

the computed NNMs is evaluated. The initial modal conditions computed from the NNMs are transferred from the modal domain to the real and used as initial conditions in the free response of the system as described is step (4a). If the response shows to be periodic over one period of the solution then the computed NNM is a solution to the FEM. Figure 42.3 shows the free response due to initial conditions taken from point 3 on the NNM plot near an Energy of 1 [in-lb] for ICE ROMs for a set of nodes of the beam over time. The modal amplitudes of the linear modes within the dynamic response are plotted on the right side.

The free response due to initial conditions taken from points on the NNM plot for ED ROMs for a set of nodes of the beam over time and the modal amplitudes of the linear modes within the response are presented in Fig. 42.4 on the left and right side respectively. These figures contain the results from several ROMs that were computed following the procedure explained earlier. Initially, a one-mode ICE ROM was computed and the periodicity was checked at a few points. When this revealed that the ROM was inadequate, additional modes were added according to the ordering in Table 42.2. While the resulting ROM was greatly improved, an additional ROM was created with the next most dominant modes to check convergence. The same approach was applied to ED method. These figures provide a strong qualitative metric to evaluate ROMs, Table 42.3 presents the periodicity, ε, of the free response solution, which provides a quantitative metric.

The results of Table 42.3 show that for each energy point the ICE ROM provided a more periodic solution of the FEM when compared to the ED results. It is also noted that there is significant increase in periodicity of the solution as more modes are added to the basis set as seen in Figs. 42.3 and 42.4. As energy of the system increases the periodicity of the ROMs decreases but the 3-mode and 6-mode ICE ROMs still maintain an ε value of less than 10^{-1} for all three energy points.

In both Figs. 42.3 and 42.4 the one mode ROMs for ED and ICE have a dominant first mode that is included in the basis as shown in the plot but modes 3 and 2 are on the same order within the response so they should be included as well. The legend ranks the modal amplitude of the nine most strongly coupled modes in the dynamic response. The modes that show to have the strongest influence on the response correspond to those presented in Table 42.2. This shows that the pre-processing was effective at predicting the statically coupled modes that will show up in the dynamic response of the curved beam.

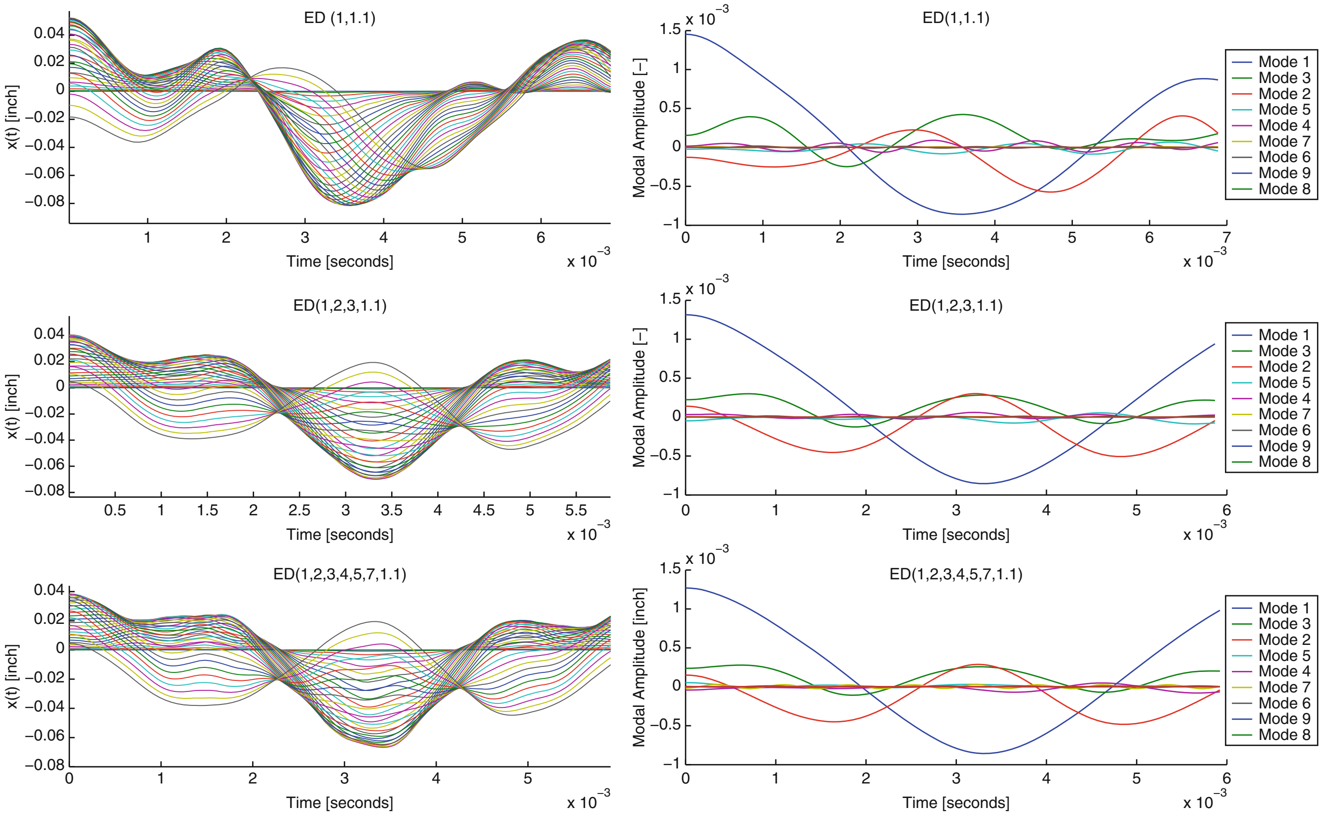

Fig. 42.4 *Left*: Time histories found from integrating the initial conditions from NNM computed using ED ROMs at points (3) near Energy = 1 [in-lb] in Fig. 42.2; *Right*: Time histories of modal amplitudes of the linear modes found in the dynamic response of the system shown on the *left*

Table 42.3 Periodicity (ε) from Eq. (42.16) for the points shown with *black circles* in Fig. 42.2

Point	Energy [in-lb]	ED(1)	ED(1, 2, 3)	ED(1, 2, 3, 4, 5, 7)	ICE(1)	ICE(1, 2, 3)	ICE(1, 2, 3, 4, 5, 7)
1	≈0.01	0.0303	0.00269	0.00193	0.023	0.00082	0.00020
2	≈0.10	0.132	0.0303	0.0235	0.129	0.012	0.00082
3	≈1.00	0.460	0.316	0.278	0.714	0.085	0.01967

The ED method was tested with additional dual modes within the basis set but the results were still less accurate than the ICE method ROMs containing a lower number of modes. Since the ICE method showed a more accurate computation of the 1st NNM than the ED method for a smaller set of modes, this work focused on expanding the ROM of just the ICE method to higher NNMs. An important aspect to note between the two methods is that as more modes were included to the basis set the ICE method encountered an internal resonance branch at 157 Hz as seen in Fig. 42.2. The continuation algorithm was diverted down this branch and then encountered a region where the step size became very small and hence never returned to the main branch. In contrast, the ED ROMs didn't include this internal resonance so the algorithm readily computed the branch up to a frequency shift of 250 Hz. Hence, if the backbones are of primary interest then the ED ROM might be preferred for this system.

Once it was discovered which ROMs accurately capture the 1st NNM, it was sought to test the ROM for the 2nd NNM. Since the 2nd NNM was found to be coupled to the same modes that were important for NNM1, it was not necessary to create any new ROMs to investigate the convergence of NNM2. The plot of the second NNM is shown in Fig. 42.5 where the converged ROMs for the ICE method are shown as well as low order ROMs to show that they lead to the converged solutions of each.

Figure 42.5 shows that the one-mode ROM of the 2nd NNM varies significantly from the multi-mode ROMs. There is a change between the four-mode and five-mode ROMs solution of the NNM but between the 5-mode and 6-mode ROMs the solution remains consistent. The 6-mode ICE ROM showed convergence for the 2nd NNM and was used to calculate the 3rd and 4th NNMs. The NNMs calculated from a one-mode ROM, the original 6-mode ROM and higher order ROMs are presented in Fig. 42.6 for the 3rd NNM. The addition of the 7-, 8-, and 9-mode ROMs shown in Fig. 42.6 were added to

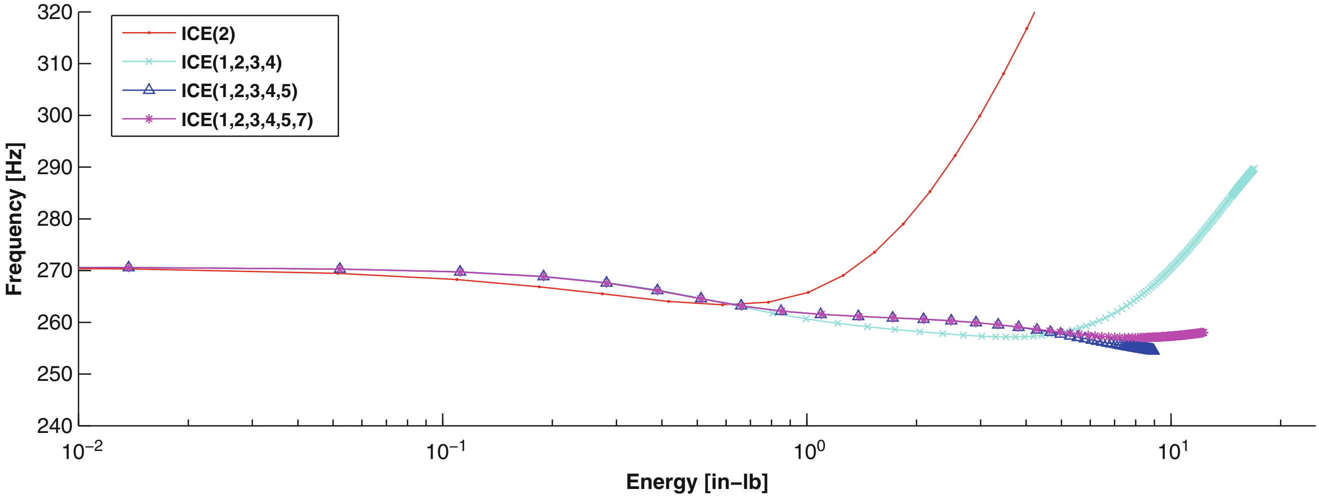

Fig. 42.5 Second NNM computed from the ROMs using: 1-mode ROM at the 2nd NNM linear mode branch; 4-, 5-, 6-mode ICE ROM from the 1st NNM computed

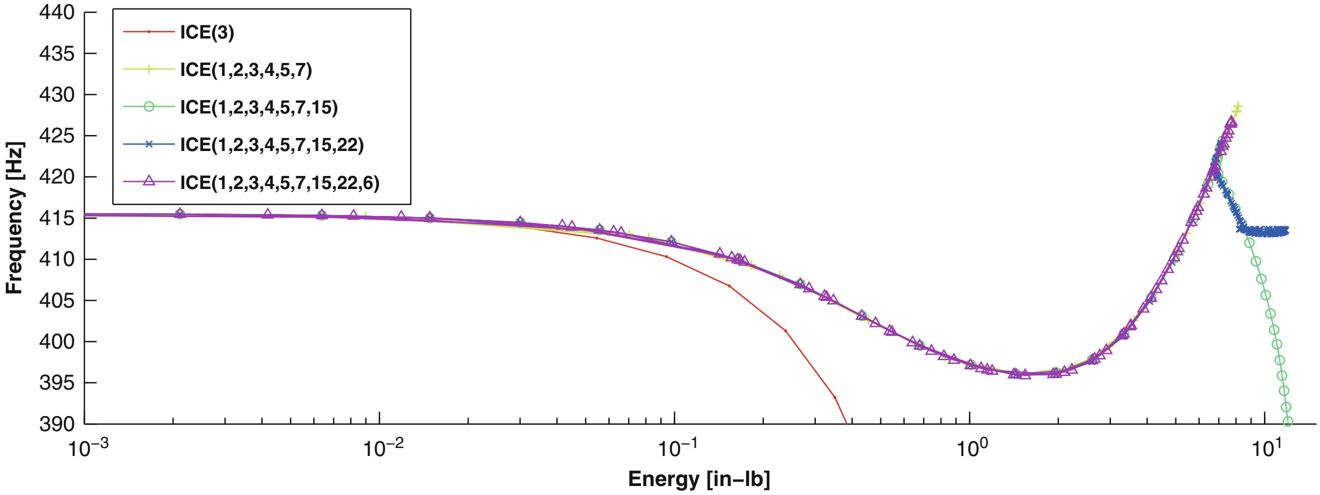

Fig. 42.6 Third NNM computed from the ROMs using: 1-mode ICE ROM at the 3rd NNM linear mode branch; 6-mode ICE ROM from the 1st NNM computed; 7-, 8-, 9-mode ICE ROMs

determine if the solution of the NNM for the 6-mode ROM would remain in the same region. It is shown that the solution did remain converged when adding the higher mode ROMs.

The 4th NNM computed is shown in Fig. 42.7 with a 1-mode ROM, the original 6-mode ROM and additional higher order ROMs. As with the 3rd NNM, additional higher order ROMs are included in order to test if the NNM solution remains in the same region. The solution of the NNMs remained converged until the ROMs encountered internal resonances as more modes were added to the basis set. The 4th NNM presented in Fig. 42.7 shows the effect on the computed NNM of the ICE method when adding linear modes to the basis set. As more modes are added to the basis set the NNM computed encounters internal resonances at lower frequencies.

Table 42.4 shows the periodicity values, ε, for the 6-mode ROM for each computed NNM. The table shows that the original 6-mode ROM stays consistently accurate up to that energy level of loading based on the periodicity of the full FEM model from computed NNM solutions. Since the ROM is accurate up to an energy level of 1 [in-lb] and for the first four NNMs ranging from 147 to 750 Hz then if the loading environment is within those bounds the ROM can be considered an acceptable approximation of the full FEM model.

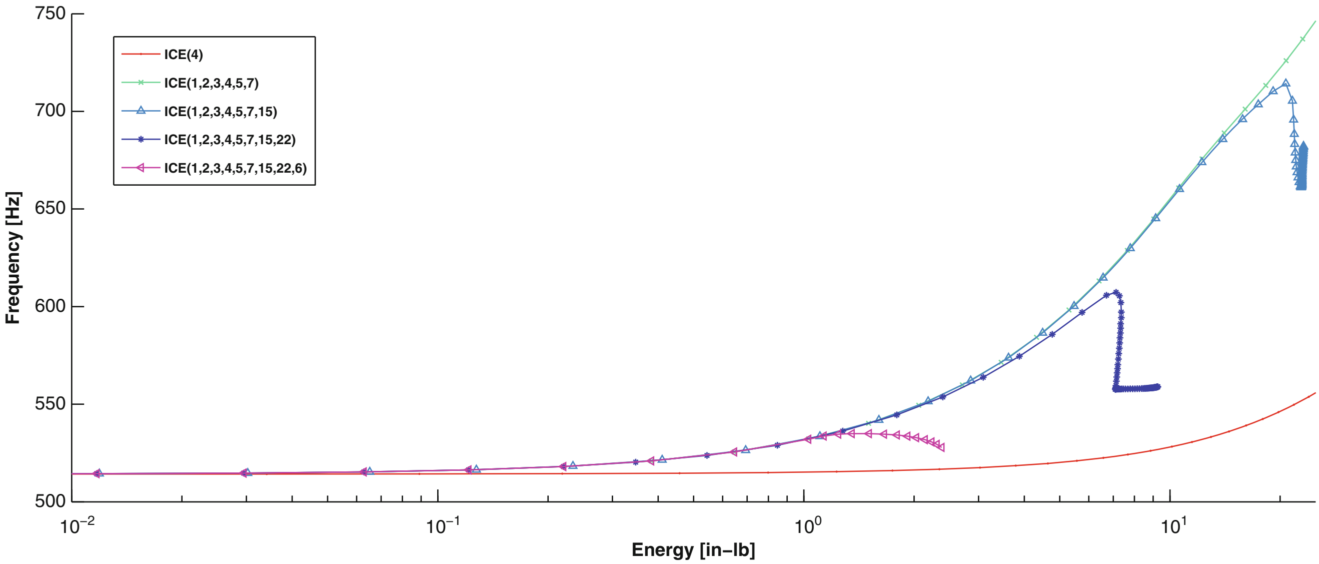

Fig. 42.7 Fourth NNM computed from the ROMs using: 1-mode ICE ROM at the 4th NNM linear mode branch; 6-mode ICE ROM from the 1st NNM computed; 7-, 8-, 9-mode ICE ROMs

Table 42.4 Periodicity (ε) from Eq. (42.16) for each NNM taken at solutions near an Energy = 1 [in-lb] for: 1-mode ICE ROM at the NNM linear mode branch; 6-mode ICE ROM with scale factors of (0.45, 0.21, 0.22, 0.31, 0.21, 0.20)

NNM	1-mode ICE ROM (ε)	ICE(1, 2, 3, 4, 5, 7) (ε)
NNM1	0.714	0.0197
NNM2	0.402	0.0122
NNM3	1.850	0.0051
NNM4	0.335	0.0153

Table 42.5 Table of load scaling factors for one-mode ROM using ICE method with associated $\mathbf{x}_{rat}$ values

ROM	Load scaling value	$\mathbf{x}_{rat}$
1	0.28	0.89
2	0.45	0.85
3	0.62	0.80
4	0.78	0.76
5	0.93	0.72
6	1.86	0.56

Note that this study used energy of the computed NNM as one of the metrics to evaluate the range that the ROM must maintain accuracy. Other metrics could be used including maximum displacement at a specific point along the beam or force values required to hold a steady state response at a NNM solution. This paper focused on energy due to the common representation of NNMs on a FEP plot.

42.3.3 Load Scaling Sensitivity Analysis

The second aspect of this work was to test the sensitivity of the ROMs to the load case factors used to extract the non-linear stiffness term. In previous work [7, 10] it was found that an $\mathbf{x}_{rat}$ value of 0.8 and 0.9 was desired to properly excite the nonlinearity of a structure showing hardening while an $\mathbf{x}_{rat}$ value of 1.05 and 1.2 was desired for structures with softening nonlinearities. The load scaling factors were altered outside the bounds of those that generated $\mathbf{x}_{rat}$ values between 0.8 and 0.9 in order to test how they affect the computed NNMs. Table 42.5 shows the load scaling factors used that are associated

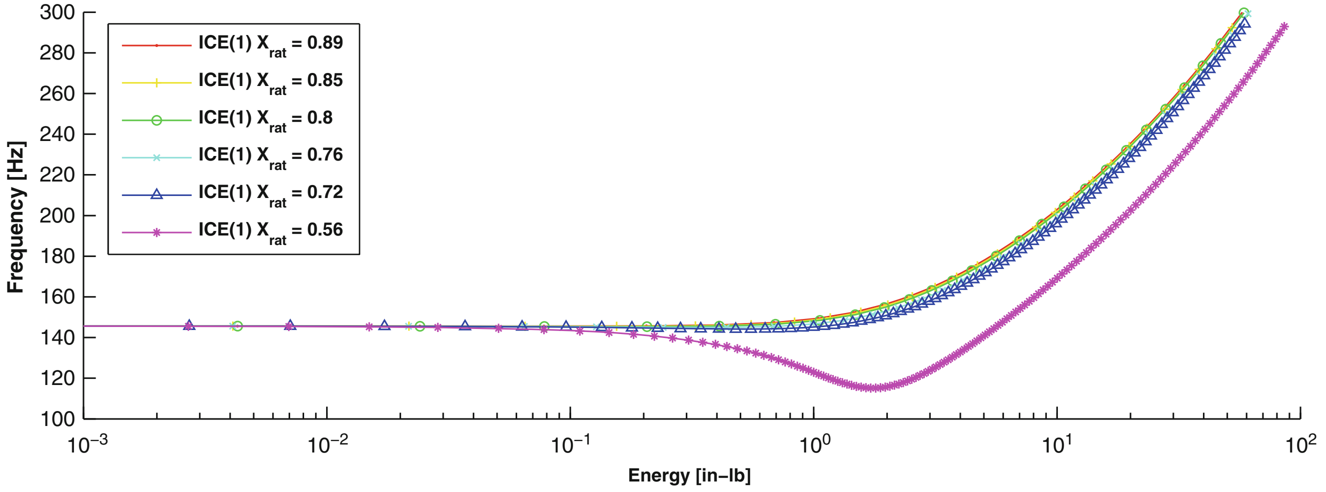

Fig. 42.8 NNM1 computed from ICE(1) ROM using x_{rat} values from 0.89 to 0.55

Table 42.6 Table of load scaling factors for 6-mode ROM using ICE method with associated $\mathbf{x}_{rat}$ and ε values

ROM	Load scaling values	$\mathbf{x}_{rat}$ values	Periodicity (ε) at E = 1 [in-lb]
1	[0.28 0.12 0.13 0.21 0.13 0.10]	0.90	0.0305
2	[0.45 0.21 0.22 0.31 0.21 0.20]	0.85	0.0197
3	[0.62 0.30 0.30 0.41 0.28 0.17]	0.80	0.0113
4	[1.86 0.90 0.90 1.23 0.84 0.41]	0.60	0.0097
5	[6.82 3.30 3.30 4.51 3.08 2.97]	0.34	0.0117
6	[13.02 6.30 6.30 8.61 5.88 5.67]	0.25	0.0681
7	[25.42 12.30 12.30 16.81 11.48 11.07]	0.18	0.823

with each $\mathbf{x}_{rat}$ value for the 1-mode ROMs that are presented in Fig. 42.8. The increase in the load scaling factor results in a lower $\mathbf{x}_{rat}$ value. The system energy changes slightly as the load scaling factor is increased until it is increased to a value of 1.86 causing an $\mathbf{x}_{rat}$ of 0.56 where the energy and period of the NNM solution significantly changes.

A 6-mode ROM using the ICE method was also analyzed to evaluate the sensitivity of the ROMs with a larger basis set to load case factors. The method for determining load scaling factors for a multiple mode ROM is less straightforward than a single mode ROM. The original scaling values were determined for each linear mode individually to determine which values would generate $\mathbf{x}_{rat}$ values at 0.9, 0.85 and 0.8. These values were then perturbed similar to the single-mode ROMs, the load scaling values and calculated $\mathbf{x}_{rat}$ values for the 6-mode ROM are presented in Table 42.6. The x_{rat} values presented in Table 42.6 are the average of the three most dominant modes x_{rat} values.

The load scaling values were extended to values 90 times the scaling that would provide and $\mathbf{x}_{rat}$ value of 0.8 for each individual mode. The NNMs of the ROMs computed using the load scaling factors presented in Table 42.5 are shown in Fig. 42.9. In Table 42.5 the periodicity of the 6-mode ROM remains consistent up to an x_{rat} value of 0.25 then greatly changes at a x_{rat} value of 0.18. This corresponds to the results seen in Fig. 42.9 where the NNMs of the computed ROMs show to remain in the same region from $\mathbf{x}_{rat}$ values of 0.9–0.34 corresponding to a 23 amplification in load scaling factors. Once the scaling factor was amplified to 45 times the base value a noticeable amount of change of the energy of the NNM solution can be seen. When approaching an increase of 90 times a significant amount of change of energy of the system can be noticed as the NNM starts to diverge from the other NNMs. Note that the ε value reached an optimum value of 0.0097 at an x_{rat} value of 0.60 for the curved been using the same basis vector shown in Table 42.6.

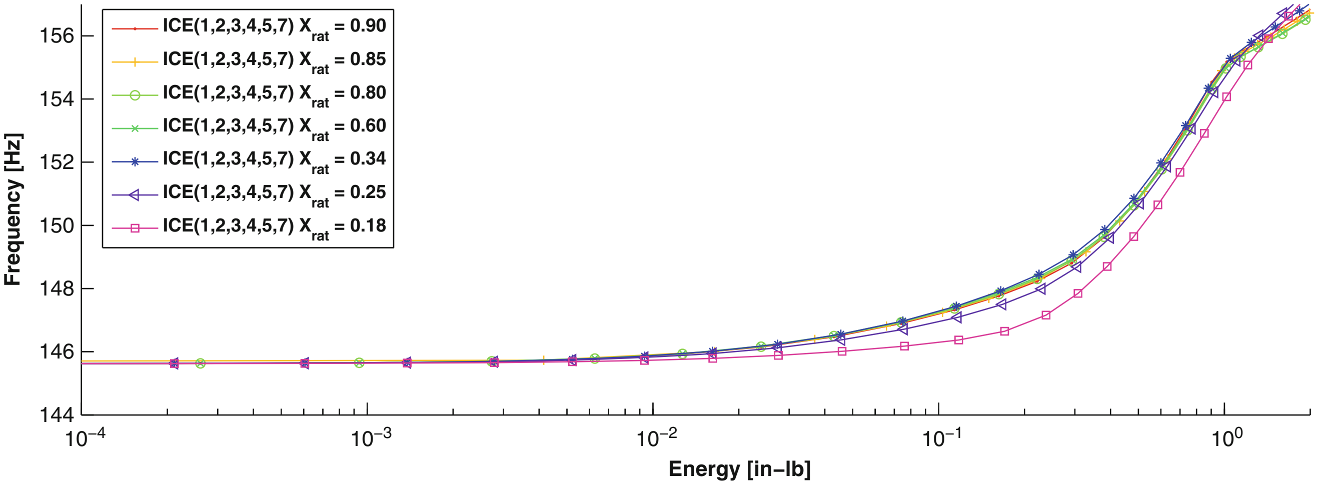

Fig. 42.9 First NNM Computed from ICE(1,2,3,4,5,7) ROM various x_{rat} values from 0.90 to 0.18

42.4 Conclusion

This work implemented the procedure put forth in [4] on a structure with curvature whose nonlinear dynamics are highly complex. In addition this work expanded on [4] by validating the ROM for multiple NNMs as required by the loading amplitude and frequency range of the structure. This addition provides an approach useful to an analyst who will need to ensure that only one ROM is accurate for the model. A study was conducted on the sensitivity of load scaling values for the ICE method when generating a ROM. This is helpful for an analyst in order to determine whether to add another mode to the ROM, which comes with a substantial cost, or alter load scaling factors for the modes within the basis set.

The ROM creation procedure was applied to a curved beam with geometric nonlinearity and fixed boundary conditions at both ends. It is shown that the methodology proposed by Kuether and Allen [4] provides a strong foundation for generating and evaluating ROMs for the curved beam. The accuracy of the ROM for both methods was significantly increased as additional modes were included in the basis set. The ED and ICE methods converged towards their own set of approximation of the NNM. In order to evaluate which method was approaching the correct solution of the NNM, the periodicity of the full FEM to initial conditions of the NNM solution was compared. The ICE method of generating a ROM provided a more accurate representation of the full FEM than the ED method for the first NNM using a smaller basis set of modes. Further investigation needs to be done on determining why the ED method approached a significantly different approximation of the NNM.

The work then expanded the 6-mode ICE method ROM computed for the 1st NNM to higher NNMs. Due to the strong modal coupling of the curved beam the procedure of expanding ROMs to higher NNMs as needed by the loading environment scaled well. No additional modes were required to be added to basis set of the original 6-mode ICE ROM in order to remain accurate, up to the specified energy level, for the first four NNMs. This was evaluated by testing the periodicity of the system at similar energy points of the NNM. This ensures that the ROM is accurate for the amplitude and frequency of the loading environment represented in this work as energy and frequencies of the computed NNMs.

The ICE method for curved structures showed to be less sensitive to the scaling factors for ROMs that have larger basis sets. This was shown by the difference in the computed NNMs of the 1-mode and 6-mode ROMs for a range of load scaling factors. The 1-mode ROM showed a consistent change in NNM solution as the load scaling factors were perturbed. The 6-mode ROM remained consistent for a large window of deviation of load scaling factors. The periodicity of the full FEM to the NNM solution of the 6-mode ROM corresponded with the NNMs on the FEP plot for the range of load scaling factors applied.

Overall the procedure established in [4] provided a straightforward method for generating an accurate ROM of a curved beam for a single NNM. The procedure then scaled well to higher NNMs as required due to the strong modal coupling of the beam. The effect of a structure's curvature on computed NNMs and ROM generation needs to be evaluated in further detail in order to provide a stronger metric off determining load scaling values. It is also recommended that this methodology be tested on a more complicated structure in order to further validate the process.

Acknowledgements The authors also acknowledge Joseph Hollkamp from the Air Force Research Laboratory's Structural Sciences Center, for providing the Abaqus interface that was used in this work.

References

1. Gordon, R.W., Hollkamp, J.J.: Reduced-order models for acoustic response prediction. Air Force Research Laboratory (AFRL), Wright-Patterson Air Force Base, OH AFRL-RB-WP-TR-2011-3040 (2011)
2. Tzong, G., Liguore, S.L.: Verification studies on hypersonic structure thermal/acoustic response and life prediction methods. Presented at the 54th AIAA/ASME/ASCE/AHS/ASC Structures, Structural Dynamics, and Materials Conference (2013)
3. Perez, R., Wang, X.Q., Mignolet, M.P.: Nonintrusive structural dynamic reduced order modeling for large deformations: enhancements for complex structures. J. Comput. Nonlinear Dyn. **9**, 031008-031008-12 (2014)
4. Kuether, R., Allen, M.: Validation of nonlinear reduced order models with time integration targeted at nonlinear normal modes. In: Nonlinear Dynamics, vol. 1. Conference Proceedings of the Society for Experimental Mechanics Series, pp. 363–375 (2016)
5. Vakakis, A.F.: Non-linear normal modes (NNMs) and their applications in vibration theory: an overview. Mech. Syst. Signal Process. **11**, 3–22 (1997)
6. Hollkamp, J.J., Gordon, R.W., Spottswood, S.M.: Nonlinear modal models for sonic fatigue response prediction: a comparison of methods. J. Sound Vib. **284**, 1145–63 (2005)
7. Mignolet, M.P., Przekop, A., Rizzi, S.A., Spottswood, S.M.: A review of indirect/non-intrusive reduced order modeling of nonlinear geometric structures. J. Sound Vib. **332**, 2437–2460 (2013)
8. Muravyov, A.A., Rizzi, S.A.: Determination of nonlinear stiffness with application to random vibration of geometrically nonlinear structures. Comput. Struct. **81**, 1513–1523 (2003)
9. Kuether, R., Deaner, B., Hollkamp, J., Allen, M.: Evaluation of geometrically nonlinear reduced-order models with nonlinear normal modes. AIAA J. **53**, 1–13 (2015)
10. Hollkamp, J.J., Gordon, R.W., Spottswood, S.M.: Nonlinear sonic fatigue response prediction from finite element modal models: a comparison with experiments. In: Proceedings of the 44th AIAA/ASME/ASCE/AHS/ASC Structures, Structural Dynamics, and Materials Conference (2003)
11. Gordon, R.W., Hollkamp, J.J.: Reduced-order modeling of the random response of curved beams using implicit condensation. In: 47th AIAA/ASME/ASCE/AHS/ASC Structures, Structural Dynamics, and Materials Conference, Newport, RI (2006)

Chapter 43
Simulation of Rotor Damping Assembled by Disc Shrink Fits

Lothar Gaul and André Schmidt

Abstract The paper at hand shows how structural damping and stiffness parameters in shrunk joints can be determined by a generic joint experiment. With thin layer elements these parameters from the joint experiment are coupled to the structures Finite Element Model. Equivalent modal damping factors can be determined by performing a complex numerical modal analysis, by which the stability of the rotor can be tested. The two disc rotor is examined as an application sample. This rotor consists of a shaft with two shrunk-on discs. With the above mentioned approach, and by considering structural damping added to material damping, the modal damping of the first torsional eigenfrequency is calculated and then compared to the results of an experimental modal analysis. The paper shows that the presented approach leads to a reliable approximation of the examined structure's dissipation properties. It serves as a prediction tool for the response behavior of a turbo-generator.

Keywords Finite element method • Damping • Modal analysis • Generic joint experiment • Model of constant hysteresis

43.1 Introduction

For many applications damping is the major factor when stable operating states of a rotating machine are to be identified. In order to reliably predict if the operation state of a system is stable, dissipation properties have to be considered [1]. Predictive conclusions regarding stability therefore are only possible if the damping properties of a structure under consideration can be determined and then included into a numerical model as e.g. the FEM. Besides material damping, which can easily be determined from experiments or from literature, dissipation of a standardized joint is of particular importance. In metallic structures damping of joints usually outweighs material damping by one to two decades depending on the torsional modes.

In order to quantitatively determine damping of joints, experimental testing needs to be developed by which properties of joints can be identified. Besides its dissipation properties also the tangential stiffness of the joint is relevant, since the structure is weakened by the joint which reduces eigenfrequencies compared to a solid connection. However, normal stiffness of joints only has minor influence on eigenfrequencies and -modes. Therefore it can simply be estimated or taken from experience. Alternatively the normal stiffness can also be determined by numerical contact analysis.

43.2 The Two Disc Rotor as a Test Structure

The examined structure consists of a shaft with two shrunk discs (see Fig. 43.1) which will perform torsional vibrations. All pieces are made of steel. Measures such as material allowance in the contact area, surface roughness and press fit are common parameters used for turbine construction.

A FE-analysis of the contact pressure with a press fit of 0.05 % contact overlap is shown in Fig. 43.2. This results in an average contact pressure of 100 MPa; locally the pressure is as high as 150 MPa. This contact pressure corresponds to common values for rotating turbines. However, the two-disc rotor structure is examined without rotation and therefore shows the above mentioned contact pressure in a stationary state. A numerical modal analysis of the FE-model of the test structure shows that the torsional eigenfrequency is approximately 165 Hz.

L. Gaul (✉) • A. Schmidt
Institute of Nonlinear Mechanics, University of Stuttgart, Pfaffenwaldring 9, 70550 Stuttgart, Germany
e-mail: gaul@inm.uni-stuttgart.de; andre.schmidt@inm.uni-stuttgart.de

© The Society for Experimental Mechanics, Inc. 2016

J. De Clerck, D.S. Epp (eds.), *Rotating Machinery, Hybrid Test Methods, Vibro-Acoustics & Laser Vibrometry, Volume 8*,
Conference Proceedings of the Society for Experimental Mechanics Series, DOI 10.1007/978-3-319-30084-9_43

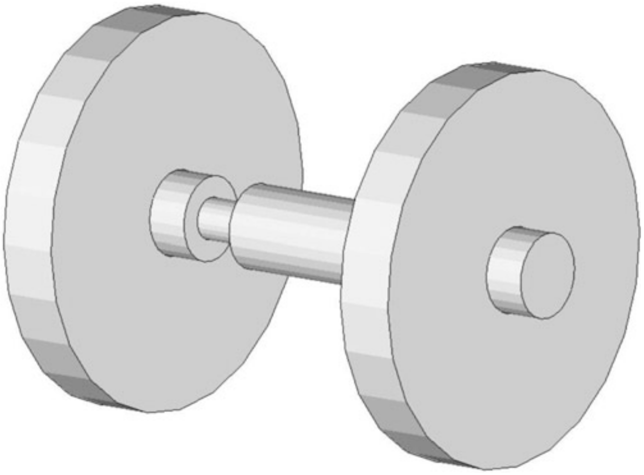

Fig. 43.1 3-D view of the two-disc rotor

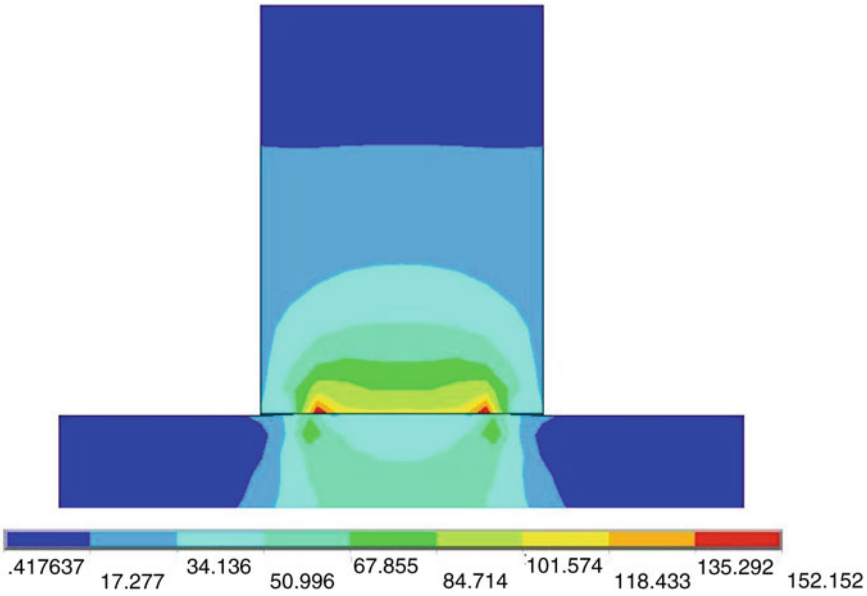

Fig. 43.2 Calculated contact pressure distribution between rotor and shrunk-on disc

43.3 Layout of the Generic Joint Experiment

Since the contact parameters between rotor and discs are known in terms of surface roughness, contact pressure and frequency, a generic experiment can be conducted in order to determine the corresponding isolated joint's parameters. Figure 43.3 shows the measurement set-up. It consists of two small contact interfaces which are pressed against each other. The normal force in the joint is controlled by a bolt and measured by a force measurement ring. An excitation of the joint in the axial direction is realized by two masses on both sides of the joint where one mass is attached to a shaker. The mass shown on the right is connected to a leaf spring, such that the set-up is a two-mass resonator. When the resonance frequency is transmitted the axial force is increased considerably. On both sides of the joint two 3-dimensional accelerometers are placed. Their signals are used for the calculation of the relative displacement and therefore also for the stiffness of the joint and its dissipation behavior (see Sect. 43.4).

The boundary conditions for this generic experiment are known from the examination of the two-disc rotor: an experiment should be conducted with normal pressure of about 100 MPa and an excitation frequency nearby 165 Hz. The surface roughness also corresponds to the two-disc rotor.

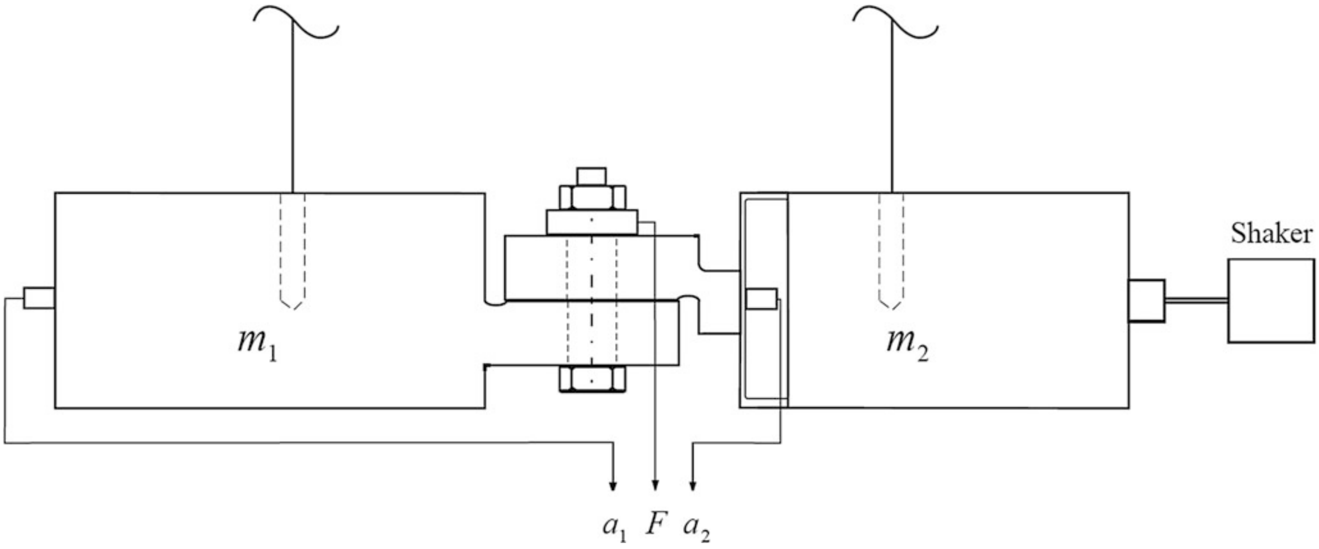

Fig. 43.3 Layout of the measurement set-up for determination of isolated joint's parameters

The size of the contact interfaces measures 30 × 40 mm with a 14 mm diameter drilled hole in the middle. This results in a contact area of A = 1046 mm^2, for which a bolt force of 104.6 kN is needed. The amplitude of the axial force is defined by the input signal of the shaker.

43.4 Determination of Isolated Joint's Parameters

In order to determine stiffness and damping of the joint, the resonator is suspended by two thin wires attached to the masses at their centers of gravity. The excitation frequency shaker is at 165 Hz. The relative displacement Δx is calculated by integrating the acceleration signals twice with respect to time.

$$\Delta x(t) = \iint a_1(t)\ dt\ dt - \iint a_2(t)\ dt\ dt \tag{43.1}$$

The tangential force F_T transmitted by the joint is obtained from the product of the free suspended mass m_1 and its acceleration a_1

$$F_T(t) = m_1 a_1(t) \tag{43.2}$$

Using the results from these two time-dependent parameters, a hysteresis curve is determined (see Fig. 43.4). The area of the hysteresis curve equals the energy W_d dissipated in one period. The ratio of the energy dissipated W_d divided by 2π times the maximum potential energy $U_{\max}$ gives the loss factor

$$\chi = \frac{W_d}{2\pi\ U_{\max}} \tag{43.3}$$

representing the damping in the examined joint. The slope of the hysteresis curve represents the tangential stiffness of the joint.

$$c = \frac{F_T}{\Delta x} \tag{43.4}$$

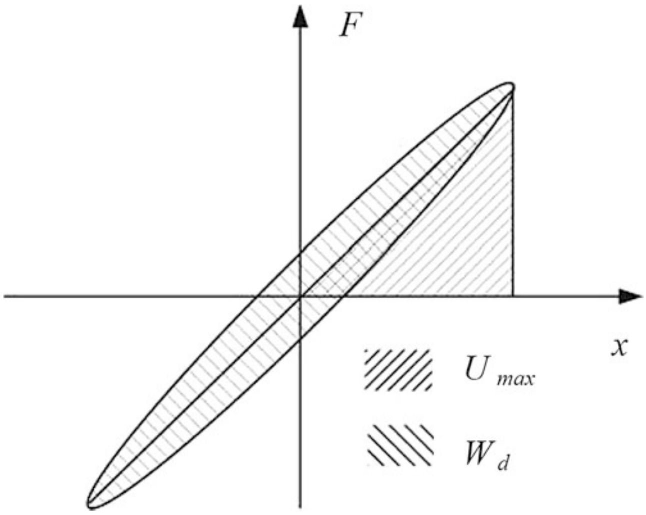

Fig. 43.4 Example of a hysteresis curve

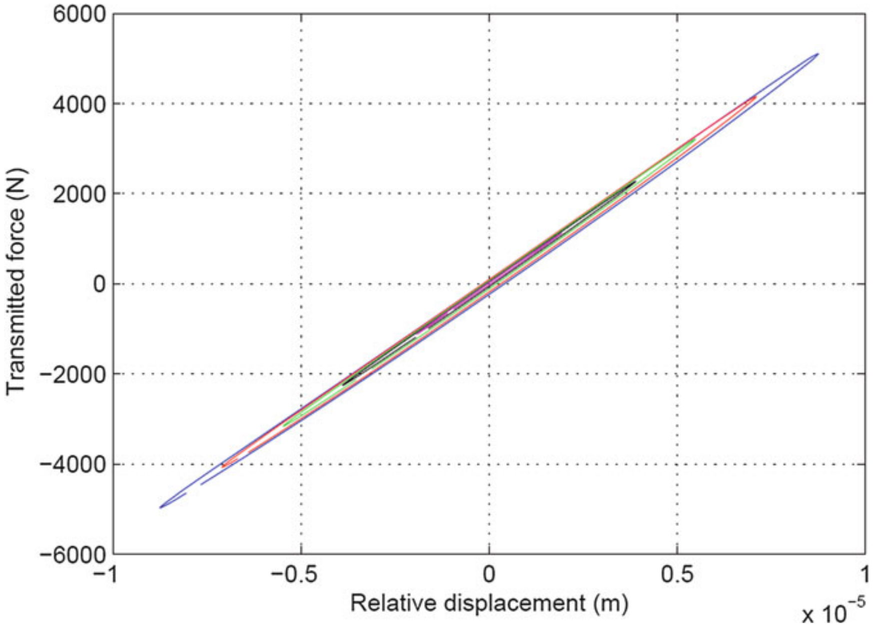

Fig. 43.5 Measured hysteresis curves

Figure 43.5 shows several measured hysteresis curves recorded at different excitation amplitudes. The received signals are filtered in order to smoothen the curves. It can be seen that the joint's stiffness is nearly constant and the energy dissipation is small. This is due to the fact that with the chosen contact pressure and the excitation amplitudes only microslip occurs.

The experiment is carried out with different parameters in order to determine their influence on the parameters of the joint. In Fig. 43.6 the influence of the contact pressure on the loss factor and the tangential stiffness are shown. The excited tangential force is between 2 kN and 6 kN. It can be seen that above the contact pressure of 20 MPa the parameters of the joint nearly stay the same. If the contact pressure is small only macro slip occurs and the measured loss factor increases significantly, while the contact stiffness collapses.

As shown in Fig. 43.7 an increase of the excitation force results in a moderate change of the loss factor. However, it has to be taken into account that identifying the loss factor is related to some uncertainty. An influence of the excitation force on the tangential stiffness cannot be found (see Fig. 43.5).

The influence of the surface finish is studied by changing its roughness R_z 16 to R_z 2. However, a change of the joint parameters cannot be found.

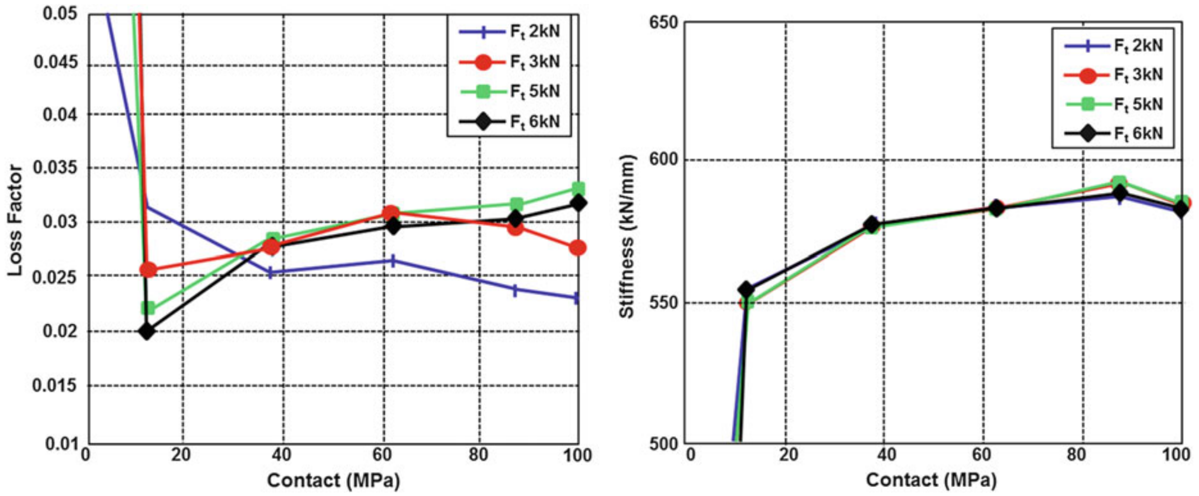

Fig. 43.6 Influence of contact pressure on loss factor and tangential stiffness

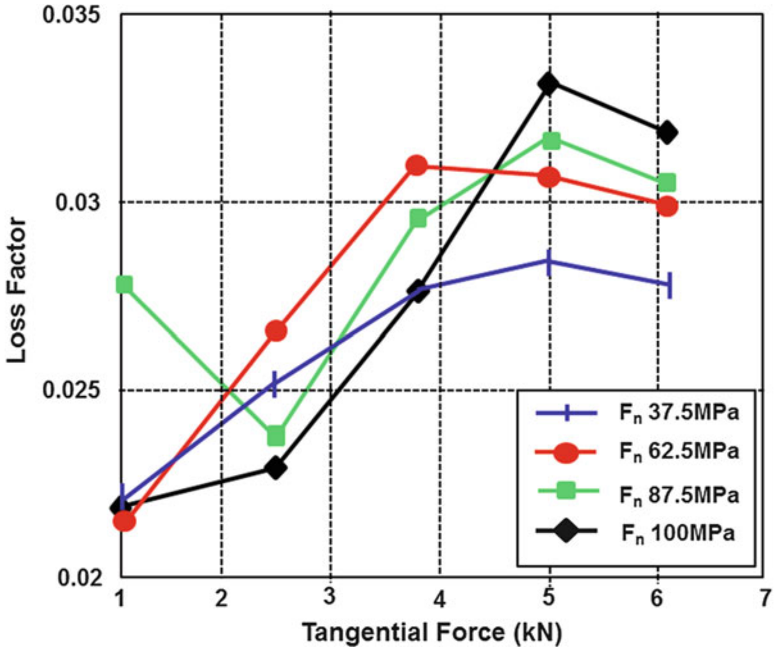

Fig. 43.7 Influence of tangential force on loss factor

In order to quantify the uncertainties of the measurements, the experiments are repeated a number of times with multiple reassemblies of the joint. Figure 43.8 shows an example of all measured results with variation of the excitation force. The result shows that the stiffness of the joint can be measured with high accuracy while the damping measurements contain a relatively high degree of uncertainty ($\pm 30\,\%$). The problem of precisely determining the energy dissipation in joints is also known in literature [2, 3].

The average data determined by the joint measurements are:

$$\chi \approx 0.028 \quad c \approx 580\ \mathrm{kN/mm} \tag{43.5}$$

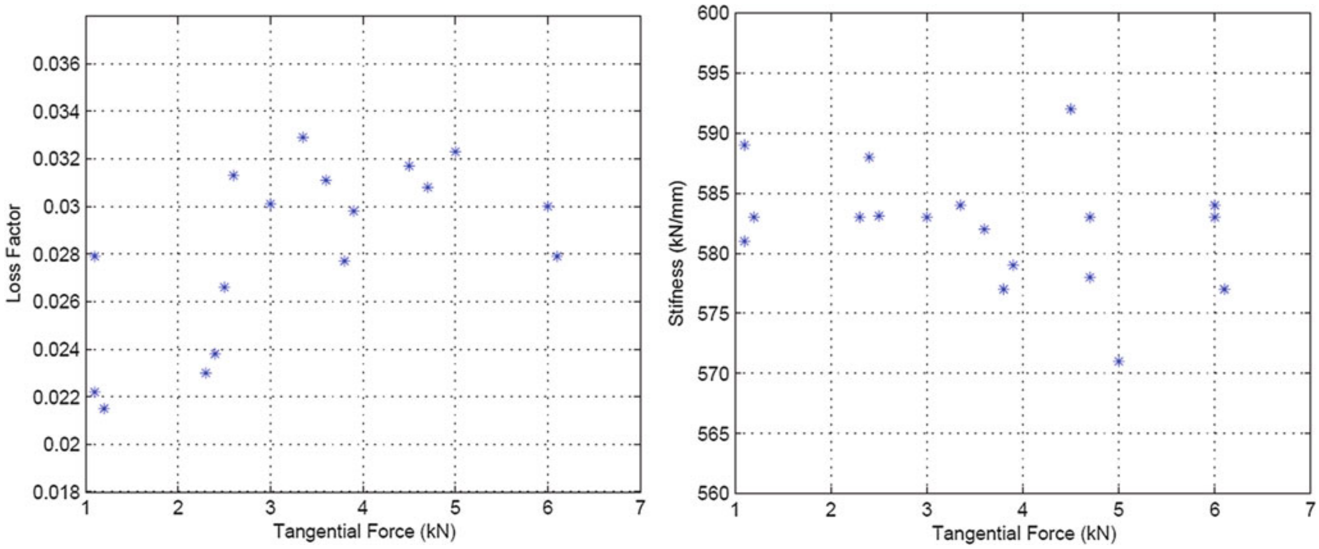

Fig. 43.8 Variation of loss factor (*left*) and tangential stiffness (*right*) measurements plotted versus different excitation levels

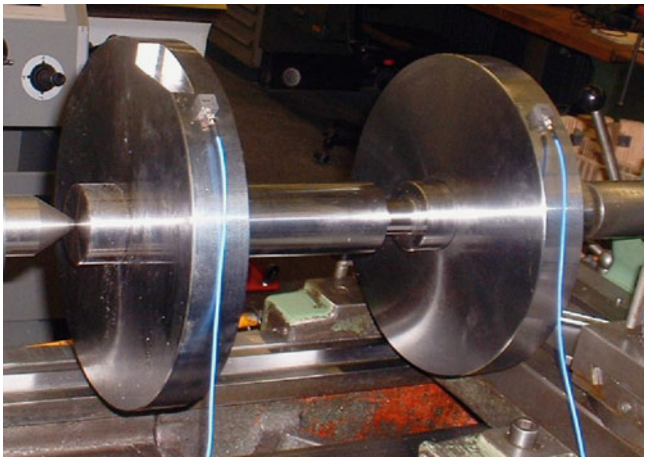

Fig. 43.9 Examined two-disc rotor with bearings and accelerometers

43.5 Two-Disc Rotor Measurements

The experimental test set-up for measurements on the two-disc rotor is shown in Fig. 43.9. The rotor is held by two cone-shaped supports in a lathe. This set-up minimizes the losses on the boundaries at the same time allowing torsional vibration of the rotor. A small cut-out at one disc allows for torsional excitation. Modal analysis with two accelerometers and impact excitation is performed. Later, additional measurements at the driving point are made.

The FRF is shown in Fig. 43.10. It can be seen that the torsional mode at 162 Hz is excited. The measurements are done with a block size of 28.800 points and a limit frequency of $f_{\max} = 1125$ Hz. The measurement time per sample is 26 s. During the measurement time the acceleration signal decayed to noise level.

The amplitude decay measurement is shown in Fig. 43.11. Three parameter identification methods are used to obtain damping and frequency of the first mode. At first, Me'Scope software is used to extract the damping from all measured data. Then, the measurements are transferred to MatLab and the damping is estimated by half-power method. Finally, an exponential function is curve-fitted to the amplitude decay measurements (Fig. 43.11). The extracted modal damping factors ξ range from 0.024 % to 0.029 % of critical damping, with amplitude decay measurements showing a better consistency and a value of $\xi = 0.025$ % [4].

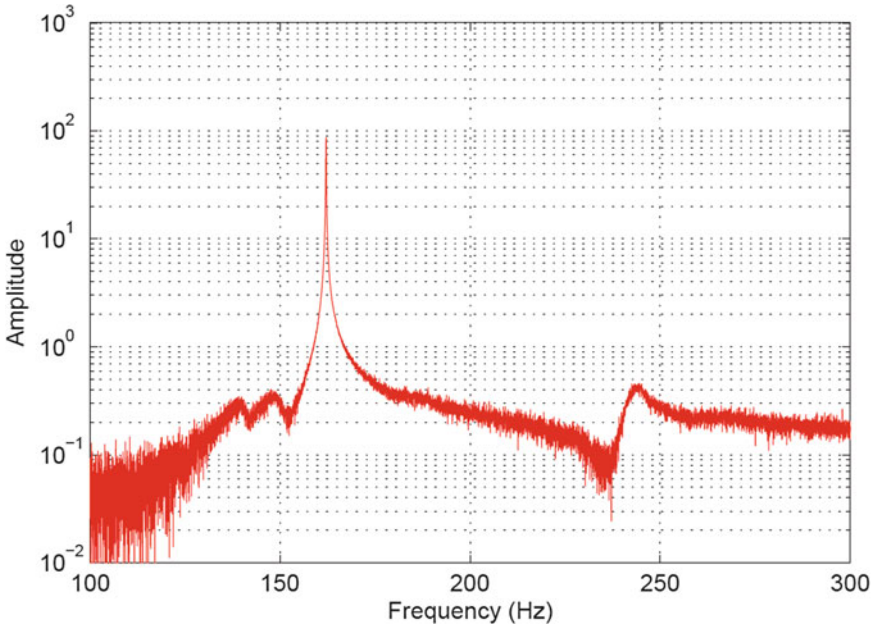

Fig. 43.10 Frequency Response Function (FRF) of the Laval rotor

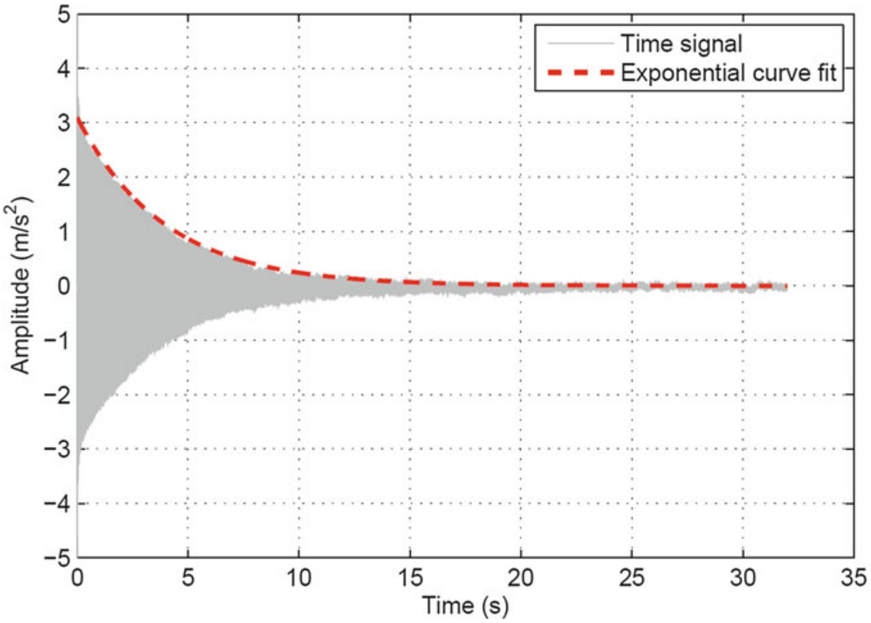

Fig. 43.11 Determining the damping factor by amplitude decay measurement

43.6 FE-Modeling

It has been shown by experimental investigations that joint damping in metal structures is nearly frequency independent. Similar results have been shown for material damping in metals. Thus, for FE modeling the principle of constant hysteresis will be used. Such model makes sense only in frequency domain, while in time domain it might lead to non-casual material behavior [5]. The principle of constant hysteresis of structural damping implies that damping is frequency independent.

Derivation of the FE equation begins with an undamped system

$$\underline{M}\,\underline{\ddot{x}} + \underline{K}\,\underline{x} = \underline{0} \tag{43.6}$$

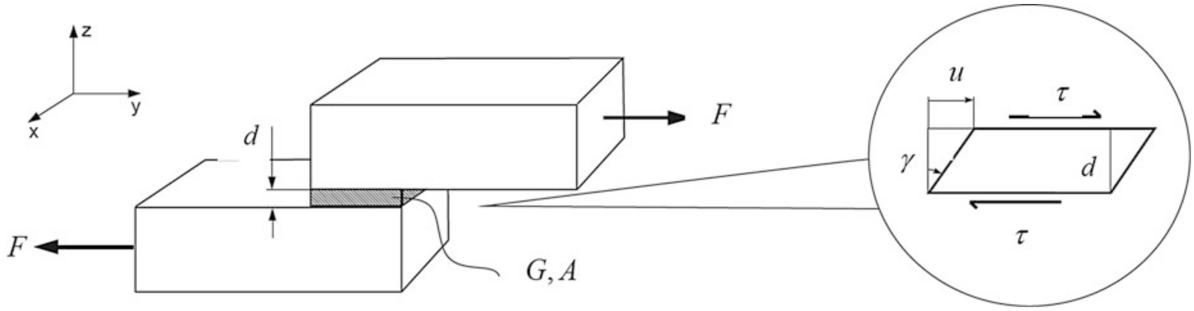

Fig. 43.12 Schematic of a joint with a thin-layer element

where $\underline{M}$ is a mass matrix, $\underline{K}$ is a real valued stiffness matrix, and $\underline{x}$ is the displacement vector. Eigenvalues and eigenmodes can be determined from a numerical modal analysis. Using the model of constant hysteresis, the damping in frequency domains will be incorporated by complex stiffness matrix $\underline{K}^*$ [1, 4–8] domain with experimentally determined dissipation multipliers α_i and β_i for the material and the joint damping [9–11], respectively, and the associated elements stiffness matrices

$$\underline{K}^* = \underline{K} + j\sum_{i=1}^{n} \alpha_i \underline{K}_i^{(\text{material})} + j\sum_{i=1}^{m} \beta_i \underline{K}_i^{(\text{joint})}, \tag{43.7}$$

where n, m are the number of different materials and joints with different properties used in the model, respectively. The damping is low, implying $\alpha_i, \beta_i << 1$. The modified equation of motion (43.6), (43.7) can be solved for complex eigenvalues and eigenmodes with some commercial FE packages offering a complex solver, and in this case was performed with MSC.Nastran. The modal damping factors of the structure are read out from the solution file.

Thin layer elements are used for the simulation of joints in the FE model [12]. The experimentally determined contact stiffness and dissipation parameters are used for constructing the stiffness matrices.

Thin layer elements are normal hexahedral or pentahedral elements in which length or width to thickness ratio can be up to 1000:1 without causing numerical problems during the calculation.

The stiffness of the generic joint (43.5) must be transferred into the FE model as a parameter of the thin-layer elements. A schematic of an arbitrary joint modeled by a thin layer is depicted in Fig. 43.12. The force F, acting on both sides of the joint produces a shear stress τ in the layer. This stress can be expressed as

$$\tau = G\gamma \approx G\frac{u}{d}, \tag{43.8}$$

where G is the shear modulus and γ is the shear angle. The shear stress can also be calculated from the ratio of the applied tangential force F and the area of contact A

$$\tau = \frac{F}{A}. \tag{43.9}$$

By combining both equations the force can be calculated as

$$F \approx \frac{GA}{d}u = cu. \tag{43.10}$$

The stiffness c in the equation is obtained from the generic joint experiment.

A basis for further examinations is that the joint shows orthotropic behavior, thus the thin layer elements are modeled with respective material characteristics. Consequently the contact stiffness in normal and tangented direction may differ significantly. From Eq. (43.10) the shear modulus can be approximated as

$$G = \frac{cd}{A}, \tag{43.11}$$

which depends linearly on the thickness d of the thin-layer elements.

Normal stiffness is not determined experimentally, but can be estimated from contact analysis. Limiting values for the selection of the normal stiffness Youngs modulus of the surrounding material for the upper limit; for the lower limit isotropic joint behavior with disappearing transversal contraction $E = 2G$ can be used. The orthotropic matrix is defined as follows

$$\begin{bmatrix} \sigma_{xx} \\ \sigma_{yy} \\ \sigma_{zz} \\ \sigma_{xy} \\ \sigma_{yz} \\ \sigma_{zx} \end{bmatrix} = \begin{bmatrix} E_{11} & E_{12} & E_{13} & 0 & 0 & 0 \\ & E_{22} & E_{23} & 0 & 0 & 0 \\ & & E_{33} & 0 & 0 & 0 \\ & & & E_{44} & 0 & 0 \\ & & & & E_{55} & 0 \\ & & & & & E_{66} \end{bmatrix} \begin{bmatrix} \varepsilon_{xx} \\ \varepsilon_{yy} \\ \varepsilon_{zz} \\ \varepsilon_{xy} \\ \varepsilon_{yz} \\ \varepsilon_{zx} \end{bmatrix}. \tag{43.12}$$

The off-diagonal terms are zero for physical reasons (there is no transversal contraction generated by the contact interface). Also, since the interface has no stiffness in x and y direction (parallel to the joints surface), the terms E_{11} and E_{22} disappear. E_{33} represents the normal stiffness, whereas $E_{55} = E_{66} = G$ define the tangential stiffness of the joint. Since the joint exhibits no stiffness for in-plane shearing, E_{44} is also zero.

43.7 FE Simulation

The FE-model of the simulated two-disc rotor can be seen in Fig. 43.13. It is modeled exclusively with isotropic hexahedral elements where the thin-layer elements have $d = 0.1$ mm thickness. In MSC.Nastran hysteretic damping can be defined by a material property card. In the FE calculation material damping is applied to all elements belonging to one of the three components of the structure, and joint damping is realized by application of damping to thin layer elements. The parameters for the thin-layer elements are acquired from the generic joint experiment, while material damping was found in literature with a value of $\chi = 0.0001$ [2]. For normal stiffness a value of $E_{33} = 80$ GPa is assumed, the result for the tangential direction is $E_{55} = E_{66} = 52$ MPa. The Youngs modulus of steel is presumed with $E = 212$ GPa and Poisson's ratio $\nu = 0.3$.

With these values the torsional eigenfrequency is 160 Hz and the corresponding damping coefficient is $\chi = 0.00038$, converted to a modal damping factor $\xi = 0.019\,\%$.

A comparison of these values with the measured data (see Chap. 5) shows very good agreement. The difference in the eigenfrequency is only about 1 %, the modal damping factor can be very well estimated under the given uncertainties. The deviation is less than 25 %.

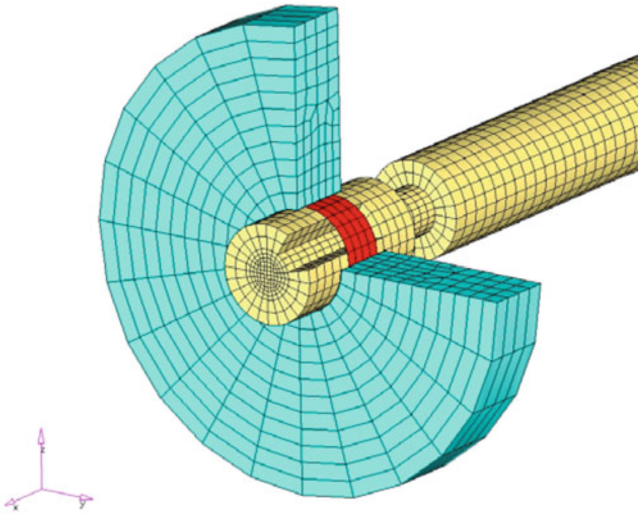

Fig. 43.13 FE-model of the examined two-disc rotor

43.8 Summary

In this article a generic joint experiment is presented which enables an engineer to extract both, the tangential stiffness and the damping properties of a bolted joint connection. It turns out that the determination of damping properties of weakly damped structures, such as joints which only show microslip, goes along with substantial uncertainties. However, it succeeds to properly determine the dimension of damping. With this procedure at hand, a design engineer is enabled to make general statements about a structure's dynamic behavior before a prototype is being built and investigated.

As an example a two-disc rotor was investigated. The above mentioned approach was used to model the dynamic behavior of the structure with the FEM. The results of a numerical modal analysis were compared with the outcome of an experimental investigation by means of the first torsional eigenmode. It shows that the eigenfrequency can be calculated accurately, while the deviation of damping properties is in the range of 25 %. Due to the difficulties of measuring small damping values the results are quite satisfactory.

References

1. Crandall, S.: The role of damping in vibration theory. J. Sound Vib. **11**(1), 3–18 (1970)
2. Nashif, A.D., Jones, D.I.G., Henderson, J.P.: Vibration Damping. Wiley, New York (1985)
3. Ottl, D.: Schwingungen mechanischer Systeme mit Strukturdämpfung. VDI Verlag, Düsseldorf, (VDI-Forschungsheft Nr. 603) (1981)
4. Ewins, D.: Modal Testing: Theory Practice and Application, 2nd edn. Research Studies Press, Baldock (2000)
5. Gaul, L., Bohlen, S., Kempfle, S.: Transient and forced oscillations of systems with constant hysteretic damping. Mech. Res. Commun. **12**(4), 187–201 (1985)
6. Gaul, L., Nitsche, R.: The role of friction in mechanical joints. Appl. Mech. Rev. **54**(2), 93–106 (2001)
7. Inaudi, J.A., Makris, N.: Time-domain analysis of linear hysteretic damping. Earthq. Eng. Struct. Dyn. **25**, 529–545 (1996)
8. Schmidt, A., Gaul, L.: On the numerical evaluation of fractional derivates in multi-degree-of-freedom systems. Signal Process. **86**(10), 2592–2601 (2006)
9. Garibaldi, L., Onah, H.N.: Viscoelastic Material Damping Technology. BeccisOsiride, Torino (1996)
10. Henwood, D.J.: Approximating the hysteretic damping matrix by a viscous matrix for modeling in the time domain. J. Sound Vib. **254**(3), 575–593 (2002)
11. Lakes, R.S.: Viscoelastic Solids. CRC Press, Boca Raton (1999)
12. Desai, C.S., Zaman, N.M., Lightner, J.G., Siriwardane, H.J.: Thin-layer element for interfaces and joints. Int. J. Numer. Anal. Meth. Geomech. **8**, 19–43 (1984)
13. Gasch, R., Nordmann, R., Pfützner, H.: Rotordynamik, 2.Aufl. Springer-Verlag, Berlin, Heidelberg (2002)
14. Gaul, L., Schmidt, A., Bograd, S.: Experimentelle Ermittlung von Kennwerten zur Werkstoff- und Fügestellendämpfung sowie deren Berücksichtigung in Finite-Elemente-Berechnungen, *Abschlussbericht des gleichnamigen Forschungsvorhabens*. Forschungsvereinigung Verbrennungskraftmaschinen (FVV), Heft 859, Frankfurt (2008)

Chapter 44
Developments in the Prediction of Full Field Dynamics in the Nonlinear Forced Response of Reduced Order System Models

Sergio E. Obando and Peter Avitabile

Abstract Recent developments in the efficient modeling and reduction of finite element models (FEM) have been shown to provide a viable alternative to current approaches in the nonlinear simulation of computationally expensive detailed models of structural systems. This paper presents a summary of results in the prediction of nonlinear response from highly reduced order models interconnected with discrete nonlinear connections. The nonlinear response is approximated by piecewise linear solutions with reduction methodologies employed for the efficient computation; expansion is performed to retain system level response at a full set of FEM degrees of freedom and allows the calculation of stress and strain to ensure the practical usefulness of the techniques. Several cases will be shown here to illustrate the accuracy and efficiency of these methodologies in models with multiple components/cascaded configurations.

Keywords Forced nonlinear response • Reduced order modeling

44.1 Introduction

With the advent of the supercomputer and the wide availability of modern computing, finite element models for typical engineering applications have reached orders beyond millions of degrees of freedom (DOF). Such complex models carry a large cost and lead to a significant amount of time and computational resources. Moreover, better approximations of the physical phenomena present in the behavior of the structure require the modeling of nonlinear effects which in turns precipitates the need for nonlinear solvers. However, these complex systems are often times made up of multiple components whose overall behavior is linear and that only induce nonlinear response due to interactions of contact regions or connecting elements. A nonlinear solution scheme for these types of models is inefficient considering that the effect of the nonlinearity is limited to a small set of discrete point contact locations in the structure and its influence on the response is limited to a few lapses in time in comparison to the full time block of the system response.

With such large complex models, reduction methodologies are currently employed to efficiently decrease the set of active degrees of freedom (ADOF) down to a more manageable size and allow the accurate computation of response at the smaller set of FEM points. In particular, reduction and expansion techniques have been shown to produce comparable results to the full scale model for a family of nonlinear problems consisting of linear components interconnected with nonlinear elements. In this setting, the model and solution rely on the approximation of the nonlinear system response as the piecewise linear combination of all possible configurations in the structure.

The work presented here is a summary of recent developments and applications of efficient reduced order modeling and expansion techniques. The work by Thibault [1–3] and Marinone [4–6] showed that system level response can be accurately and efficiently calculated for highly reduced system models. Moreover, Pingle [7–10] and Carr [11–14] demonstrated that the expansion of such systems can be used for the prediction of full field results as well as stress and strain from limited sets of data. Harvie [15–17] extended this work to include the application of expansion to nonlinear systems made out of linear components but subjected to nonlinear interactions. In that work, the expansion was greatly simplified by using the unconnected component modes to expand the response of the reduced system model as developed by Nonis [18–20]. In addition, Obando [21–24] showed that these techniques can not only be used for the prediction of the dynamics of the full system but also the characterization of complicated subcomponent configurations (such as appended/ancillary subsystem components). The approach was shown to accurately predict the response at all DOF using embedded subcomponent information even in cases where no DOF were placed on the appended subcomponent and/or the connecting locations.

S.E. Obando (✉) • P. Avitabile
Structural Dynamics and Acoustic Systems Laboratory, University of Massachusetts Lowell, One University Avenue, Lowell, MA 01854, USA
e-mail: sergio.e.obando@gmail.com

© The Society for Experimental Mechanics, Inc. 2016

J. De Clerck, D.S. Epp (eds.), *Rotating Machinery, Hybrid Test Methods, Vibro-Acoustics & Laser Vibrometry, Volume 8*,
Conference Proceedings of the Society for Experimental Mechanics Series, DOI 10.1007/978-3-319-30084-9_44

The novel part of the expansion and prediction at all DOF is that the response is essentially being extrapolated from the embedded information in the reduction process by using a linear combination of the mode shapes of the structure as building blocks to all possible configurations in the system.

A summary of the salient results of these efficient reduced order modeling techniques is presented here. The methodology is applied to cantilever and multiple beam assemblies.

44.2 Theoretical Background

The techniques summarized here rely on the use of the mode shapes (eigenvectors) of the system as building blocks of all possible dynamic behavior of the structure and utilize well-established modal modeling (SDM [25]) and reduction techniques (Guyan Condensation [26] and SEREP [27]). An overview of the relevant theory of reduced order modeling and forced response is presented with references for more in depth treatment of each topic.

44.2.1 Equations of Motion for Multiple DOF System

The general equation of motion for a multiple degree of freedom system written in matrix form is

$$[M_1]\{\ddot{x}\} + [C_1]\left\{\dot{x}\right\} + [K_1]\{x\} = \{F(t)\} \tag{44.1}$$

Assuming proportional damping, the eigensolution is obtained from

$$[[K_1] - \lambda\,[M_1]]\,\{x\} = \{0\} \tag{44.2}$$

The eigensolution yields the eigenvalues (natural frequencies) and eigenvectors (mode shapes) of the system. The eigenvectors are arranged in column fashion to form the modal matrix [U_1]. Often times, only a subset of modes is included in the modal matrix to save on computation time and due to the fact that only certain modes actually contribute to the response. Exclusion of modes results in truncation error which can be serious if key modes are excluded. Truncation error will be discussed in further detail in the structural dynamic modification section.

The physical system can be transformed to modal space using the modal matrix as

$$[U_1]^T[M_1][U_1]\{\ddot{p}_1\} + [U_1]^T[C_1][U_1]\left\{\dot{p}_1\right\} + [U_1]^T[K_1][U_1]\{p_1\} = [U_1]^T\{F(t)\} \tag{44.3}$$

Scaling to unit modal mass yields

$$\begin{bmatrix} \ddots & & \\ & I_1 & \\ & & \ddots \end{bmatrix}\{\ddot{p}_1\} + \begin{bmatrix} \ddots & & \\ & 2\zeta\omega_n & \\ & & \ddots \end{bmatrix}\left\{\dot{p}_1\right\} + \begin{bmatrix} \ddots & & \\ & \Omega_1^2 & \\ & & \ddots \end{bmatrix}\{p_1\} = \left[U_1^n\right]^T\{F(t)\} \tag{44.4}$$

where [I_1] is the diagonal identity matrix, [${\Omega_1}^2$] is the diagonal natural frequency matrix and [$2\zeta\omega_n$] is the diagonal damping matrix (assuming proportional damping). More detailed information on the equation development is contained in [25].

44.2.2 System Modeling and Mode Contribution

The approach used for the prediction of the nonlinear system response uses concepts from system modeling. In order to create multi-component models, various techniques are available for the coupling of several component models into a single system model. These system modeling techniques are used to define the various states that the system will undergo when the different nonlinear contact connections occur. The system modeling can be performed in physical space, modal space, or a combination of both physical and modal space. Consider two beams that are completely independent of one another, as illustrated in Fig. 44.1.

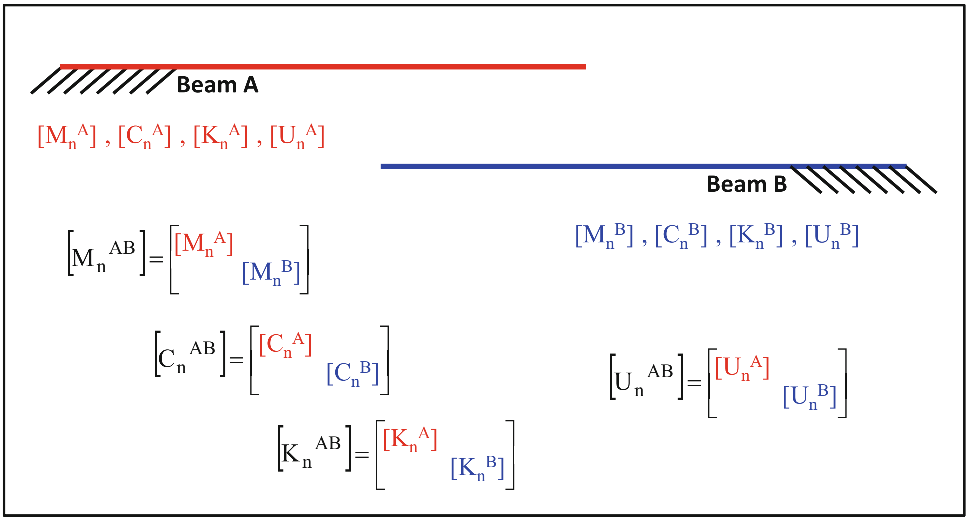
Beam A
$[M_n^A]$, $[C_n^A]$, $[K_n^A]$, $[U_n^A]$
Beam B
$[M_n^B]$, $[C_n^B]$, $[K_n^B]$, $[U_n^B]$
$[M_n^{AB}] = \begin{bmatrix}[M_n^A] & \\ & [M_n^B]\end{bmatrix}$
$[C_n^{AB}] = \begin{bmatrix}[C_n^A] & \\ & [C_n^B]\end{bmatrix}$
$[U_n^{AB}] = \begin{bmatrix}[U_n^A] & \\ & [U_n^B]\end{bmatrix}$
$[K_n^{AB}] = \begin{bmatrix}[K_n^A] & \\ & [K_n^B]\end{bmatrix}$

Fig. 44.1 Sample components arranged into common matrix space. The mass, stiffness, and damping matrices of each component are assembled for the combined system as well as the resulting mode shapes (U_n) of the two beam structure

The two beams shown in Fig. 44.1 are completely uncoupled and will respond independent of one another when excited. A system model of the uncoupled components is generated by simply writing the variables in common matrix space, as shown in the diagram. To generate a coupled system model, specific coupling terms must be introduced at the desired locations. To include the spring(s) in the system modeling, either a modal or physical approach can be employed. The modal approach involves using Structural Dynamic Modification (SDM) and Component Mode Synthesis (CMS). The physical approach involves using a physical tie matrix to couple the beams. Both approaches involve the use of a mode contribution matrix to determine the appropriate number of component modes that contribute to the system modes. For the results presented here, physical system modeling techniques were used to generate databases for the various configurations.

44.2.2.1 Physical Space System Modeling

To form a physical system model, the mass and stiffness matrices of each component (A and B) are assembled in stacked form into the system mass and stiffness matrices. In physical space, these are coupled with a stiffness tie matrix; a mass tie can also be included if desired but not included in this work.

$$\begin{bmatrix}[M^A] & \\ & [M^B]\end{bmatrix}\{\ddot{x}\} + \left[\begin{bmatrix}[K^A] & \\ & [K^B]\end{bmatrix} + K_{TIE}\right]\{x\} = \{F\} \tag{44.5}$$

This can be cast in a modal space representation as

$$\begin{aligned}\left[\left[\begin{bmatrix}[\overline{M}^A] & \\ & [\overline{M}^B]\end{bmatrix}\right]\right]\left\{\begin{matrix}\{\ddot{p}^A\}\\ \{\ddot{p}^B\}\end{matrix}\right\} + \begin{bmatrix}[\overline{K}^A] & \\ & [\overline{K}^B]\end{bmatrix}\left\{\begin{matrix}\{p^A\}\\ \{p^B\}\end{matrix}\right\}\\ + \left[[U]^T[\Delta K][U]\right]\left\{\begin{matrix}\{p^A\}\\ \{p^B\}\end{matrix}\right\} = \{0\}\end{aligned} \tag{44.6}$$

where $[\,\overline{M}\,]$ and $[\,\overline{K}\,]$ are diagonal matrices and with the mode shapes of each component stacked as

$$[\mathrm{U}] = \begin{bmatrix}[\mathrm{U}^A] & \\ & [\mathrm{U}^B]\end{bmatrix} \tag{44.7}$$

Equation (44.5) is a general equation of motion in physical space; Eq. (44.6) is the modal space equation used for the eigensolution.

44.2.2.2 Structural Dynamic Modification

Structural Dynamic Modification (SDM) is a technique that uses the original mode shapes and natural frequencies of a system to estimate the dynamic characteristics due to changes in the mass and/or stiffness of the system. First, the change of mass and stiffness are transformed to modal space as shown

$$\left[\Delta\overline{M}_{12}\right] = [U_1]^T\,[\Delta M_{12}]\,[U_1] \tag{44.8}$$

$$\left[\ \Delta\overline{K}_{12}\right]\ = [U_1]^T\ [\ \Delta K_{12}]\ [U_1] \tag{44.9}$$

The modal space mass and stiffness changes are added to the original modal space equations as seem in Eq. (44.6) to obtain

$$\left[\begin{bmatrix}\ddots & & \\ & \overline{M}_1 & \\ & & \ddots\end{bmatrix} + \left[\Delta\overline{M}_{12}\right]\right]\{\ddot{p}_1\} \ + \left[\begin{bmatrix}\ddots & & \\ & \overline{K}_1 & \\ & & \ddots\end{bmatrix} + \left[\Delta\overline{K}_{12}\right]\right]\{p_1\} = [0] \tag{44.10}$$

The eigensolution of the modified modal space model is computed and the resulting eigenvalues are the new frequencies of the system. The resulting eigenvector matrix is the $[U_{12}]$ matrix, which is used to transform the original modes to the new modes as indicated by

$$[U_2] = [U_1]\,[U_{12}] \tag{44.11}$$

The new mode shapes are $[U_2]$. The new mode shapes are formed from linear combinations of the original mode shapes. The $[U_{12}]$ matrix shows how much each of the $[U_1]$ modes contributes to forming the new modes. Figure 44.2 shows the formation of the new mode shapes as seen on Eq. (44.11). Harvie [15] and Avitabile [25] has additional information on SDM, mode superposition and participation.

The mode contribution matrix is used to determine which original mode shapes are necessary for the accurate reconstruction of each of the desired final mode shapes. If a dynamic response involves multiple system states, then the $[U_{12}]$ matrix must be computed for each configuration to determine the number of original system modes to appropriately span the space of the solution and avoid truncation.

44.2.3 *General Reduction and Expansion Methodology*

Model reduction is a tool used to reduce the number of degrees of freedom (DOF) in order to minimize the required computation time of an analytical model, while attempting to preserve the full DOF dynamic characteristics. The relationship between the full space and reduced space model can be written as

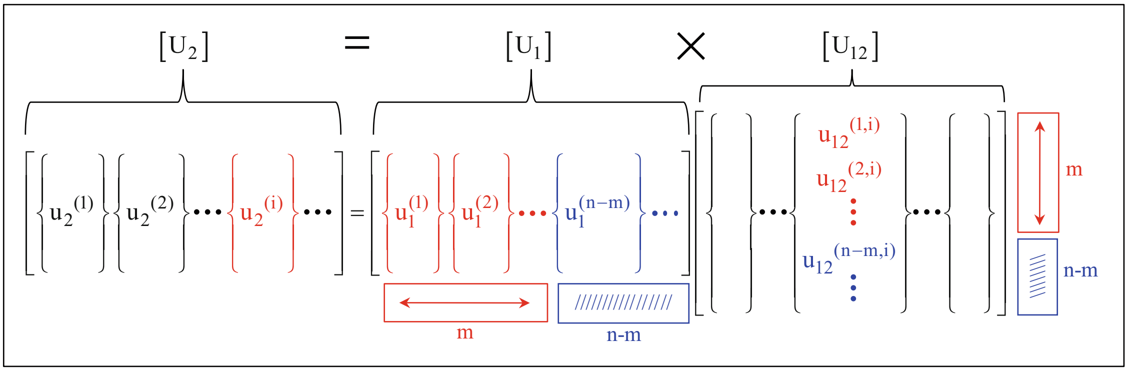

Fig. 44.2 Structural Dynamic Modification, mode contribution identified using $[U_{12}]$

$$\{X_n\} = \begin{Bmatrix} X_a \\ X_d \end{Bmatrix} = [T]\{X_a\} \tag{44.12}$$

where subscript ‘n’ signifies the full set of DOF (NDOF), ‘a’ signifies the reduced set of DOF (ADOF) and ‘d’ is the deleted DOF (those DOF not used during the reduced computation process). The transformation matrix [T] relates the full set of NDOF to the reduced set of ADOF. The transformation matrix is used to reduce the mass and stiffness matrices as

$$[M_a] = [T]^T [M_n] [T] \quad \text{and} \quad [K_a] = [T]^T [K_n] [T] \tag{44.13}$$

The eigensolution of these ‘a’ set mass and stiffness matrices are the modes of the reduced model. These modes can be expanded back to full space using the transformation matrix

$$[U_n] = [T][U_a] \tag{44.14}$$

If an optimal ‘a’ set is not selected when using methods such as Guyan Condensation [26] or Improved Reduced System Technique [28], the reduced model may not perfectly preserve the dynamics of the full space model. If System Equivalent Reduction Expansion Process (SEREP) [27] is used, the dynamics of selected modes will be perfectly preserved regardless of the ‘a’ set selected as long as the matrix is formed from a linearly independent set of vectors.

44.2.3.1 Guyan Reduction

Guyan Condensation is a stiffness based approach with long tradition of use in modal analysis [26]. The Guyan transformation matrix is calculated as

$$[T_S] = \begin{bmatrix} [I] \\ [t_s] \end{bmatrix} = \begin{bmatrix} [I] \\ -[K_{dd}]^{-1}[K_{da}] \end{bmatrix} \tag{44.15}$$

where a represents the active DOF and d represents the embedded or deleted DOF. Due to the formulation of the Guyan reduction process, the reduced model error increases for the higher preserved modes and the selection of DOF location has a large influence on the accuracy of the preserved eigenvalues.

44.2.3.2 SEREP

The SEREP modal transformation relies on the partitioning of the modal equations representing the system using selected DOFs and modes to obtain a reduced model that perfectly preserves the eigenvalues and eigenvectors of interest [27]. The SEREP technique utilizes the mode shapes from a full finite element solution to map to the limited set of active DOF. SEREP is not performed to achieve efficiency in the solution but rather is intended to perform an accurate mapping matrix for the transformation. The SEREP transformation matrix is formed using a subset of modes at full space and reduced space as

$$[T_U] = [U_n][U_a]^g \tag{44.16}$$

where $[U_a]^g$ is the generalized inverse and $[T_U]$ is the SEREP transformation matrix. When the SEREP transformation matrix is used for model reduction/expansion as outlined in the previous section, the reduced model perfectly preserves the full space dynamics of the modes in $[\mathrm{U_n}]$ [27].

44.2.3.3 KM_AMI

A more recent technique has been developed that utilizes Guyan Reduction (or any reduced matrix for that matter) along with direct updating of the reduced system matrices with the full space modal vectors as targets for the updating process [29, 30]. This reduction technique also overcomes some of the rank problems associated with SEREP and provides a reduced set of ADOF that retain all the eigenvalues and eigenvectors of the full system matrices. The Guyan reduced mass and stiffness matrices are updated using

$$[M_I] = [M_S] + [V]^T \left[[\,I\,] - \left[\overline{M}_S\right] \right] [V] \tag{44.17}$$

and

$$[\,K_I] = [K_S] + [V\,]^T \left[\left[\Omega^2_{REF}\right] + \left[\overline{K}_S\right] \right] [V] - [[\,K_S\,]\ [\,U_{REF}]\ [\,V]] - [[\,K_S]\ [\,U_{REF}]\ [V]]^T \tag{44.18}$$

with

$$[V] = \left[\overline{M}_S\right]^{-1} [U_{REF}]^T\, [M_S] \tag{44.19}$$

44.2.4 Expansion of System Modes from Uncoupled Component Modes

Expansion is generally used for providing full N-space mode shape information extracted from limited a-space information. The expansion to full space in this work is based on recent work by Nonis [18–20] showing that full N-space mode shape information for an assembled system model can be obtained using the expansion matrices from the uncoupled, unconnected, original component modes of each component. Figure 44.3 shows the entire expansion process schematically to further describe the overall procedure. The uncoupled components (red and blue beams where each circle identifies a DOF in the model) are reduced and assembled into a coupled system model. The mode shapes of the coupled two beam system are obtained from the eigensolution but only for the limited set of DOF available in the model. In order to obtain mode shapes with the full resolution of the full space model, expansion is performed using the transformation matrices (T_u^A and T_u^B) of the original uncoupled components that are available from the reduction process. Nonis and Avitabile [20] further details the expansion process and considerations for modes included.

While the systems studied here undergo several configurations, the expansion can be performed with a single transformation matrix obtained from the original unconnected unmodified systems. As long as the modes retained during the reduction process span the space of the full space solution of the system, the transformation matrix will produce accurate expanded predictions of the multi-configuration response.

Using a single transformation matrix of the unconnected individual components/systems is much more efficient since the full space modes of the connected system are not computed.

44.2.5 Expansion of Reduced Order Real Time Response

Chipman [31, 32] and others [9, 12–14] showed that a transformation matrix can be used to expand not only mode shapes, but dynamic time response data. Therefore the same principles presented above can be extended to the expansion of coupled response using uncoupled component information. The response of the coupled system at reduced space can be expanded to full space using the transformation matrices of the individual, unconnected beams systems because the dynamic characteristics of the system are directly related to the dynamic characteristics of the uncoupled components. If the $[U_{12}]$ matrix is evaluated to include enough modal information in the reduced model to accurately represent the system with the coupling elements present, then the time response of the coupled system is accurately expanded to full space using information from the uncoupled components.

In this paper, nonlinear systems are analyzed where several possible configurations can exist during response. If all possible configurations are made up of linear combinations of the component mode shapes, then the expansion of nonlinear response of a reduced model can be expanded using the original transformation matrix regardless of the configurations encountered. Figures 44.4, 44.5, and 44.6 show the process for determining full space dynamic response of a nonlinear system using the original transformation matrices. The full space linear subcomponents are assembled into System 1 and System 2 and reduced to a smaller set of ADOF (red and blue points in Fig. 44.4a). Nonlinear contacts in green (Fig. 44.4b) indicate when the spring comes in contact with the structure and thus changes from one configuration to another. Mode contribution is an essential part of this step as the necessary number of modes must be determined from all possible configurations of the system.

Although several configurations exist within the time block shown, all modified states can be generated based on the mode shapes of the original system. Therefore only the transformation matrices of the original, uncoupled components are necessary to expand the nonlinear dynamic response of the system regardless of the configurations encountered. In Fig. 44.5,

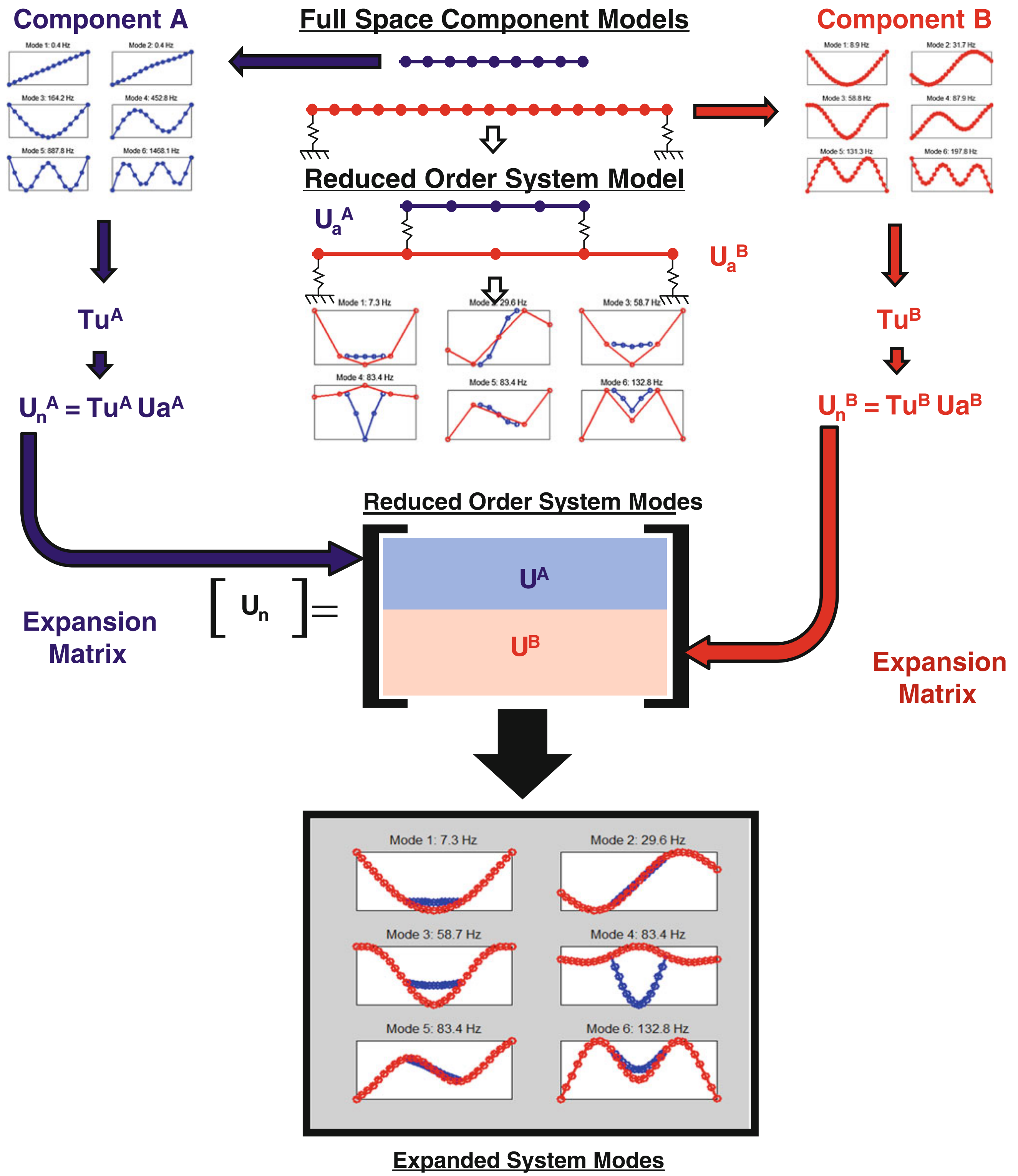
Component A
Full Space Component Models
Component B
Mode 1: 0.4 Hz
Mode 2: 0.4 Hz
Mode 3: 164.2 Hz
Mode 4: 452.8 Hz
Mode 5: 887.8 Hz
Mode 6: 1468.1 Hz
Mode 1: 8.9 Hz
Mode 2: 31.7 Hz
Mode 3: 58.8 Hz
Mode 4: 87.9 Hz
Mode 5: 131.3 Hz
Mode 6: 197.8 Hz
Reduced Order System Model
U_a^A
U_a^B
Tu^A
Tu^B
$U_n^A = Tu^A\,Ua^A$
$U_n^B = Tu^B\,Ua^B$
Mode 1: 7.3 Hz
Mode 2: 29.6 Hz
Mode 3: 58.7 Hz
Mode 4: 83.4 Hz
Mode 5: 83.4 Hz
Mode 6: 132.8 Hz
Reduced Order System Modes
Expansion Matrix
$[U_n] =$
U^A
U^B
Expansion Matrix
Mode 1: 7.3 Hz
Mode 2: 29.6 Hz
Mode 3: 58.7 Hz
Mode 4: 83.4 Hz
Mode 5: 83.4 Hz
Mode 6: 132.8 Hz
Expanded System Modes

Fig. 44.3 Overall expansion process schematic using the transformation matrices (T_u^A and T_u^B) from unconnected system components. The reduced order model mode shapes are expanded to obtain full resolution mode shapes of the two beam system, where the *red* and *blue circles* indicates DOF available in each of the models

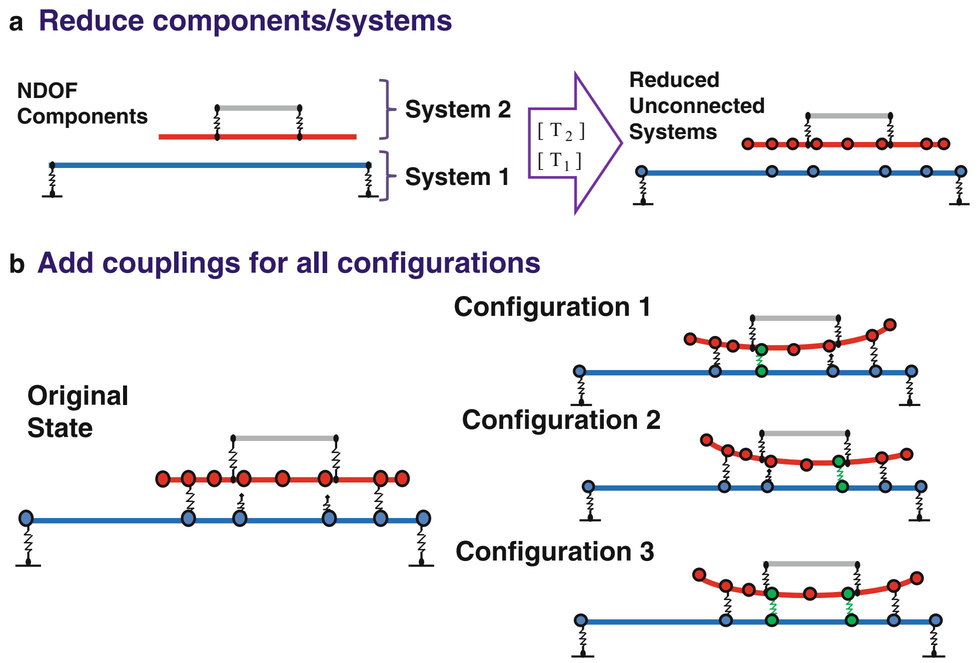
a Reduce components/systems
NDOF Components
System 2
System 1
[T2]
[T1]
Reduced Unconnected Systems
b Add couplings for all configurations
Original State
Configuration 1
Configuration 2
Configuration 3

Fig. 44.4 (**a**) Assembly of reduced order model from uncoupled full space subcomponents and (**b**) computation of relevant system configurations due to nonlinear interactions of the gap-springs (in *green*)

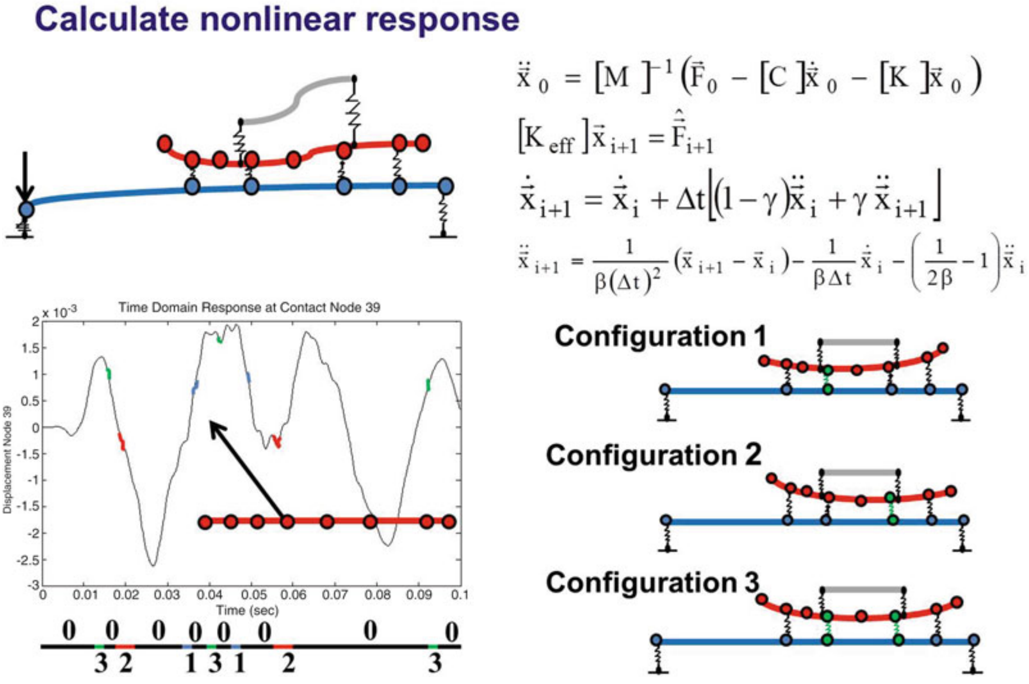
Calculate nonlinear response
$\ddot{x}_0 = [M]^{-1}(\vec{F}_0 - [C]\dot{x}_0 - [K]\vec{x}_0)$
$[K_{eff}]\vec{x}_{i+1} = \hat{\vec{F}}_{i+1}$
$\dot{\vec{x}}_{i+1} = \dot{\vec{x}}_i + \Delta t[(1-\gamma)\ddot{\vec{x}}_i + \gamma\ddot{\vec{x}}_{i+1}]$
$\ddot{x}_{i+1} = \frac{1}{\beta(\Delta t)^2}(\vec{x}_{i+1} - \vec{x}_i) - \frac{1}{\beta\Delta t}\dot{\vec{x}}_i - \left(\frac{1}{2\beta} - 1\right)\ddot{\vec{x}}_i$
Time Domain Response at Contact Node 39
x 10-3
Displacement Node 39
Time (sec)
2
1.5
1
0.5
0
-1.5
-1
-1.5
-2
-2.5
-3
0
0.01
0.02
0.03
0.04
0.05
0.06
0.07
0.08
0.09
0.1
0 0 0 0 0 0 0 0
3 2 1 3 1 2 3
Configuration 1
Configuration 2
Configuration 3

Fig. 44.5 Calculation of nonlinear response of three beam system from the linear combination of all configurations of the structure (indicated from the contact interactions of the *green* gap-spring as seen on the time response) and obtained using Newmark direct integration of the equations of motion

the response of the nonlinear reduced order model is obtained as the piecewise combination of all linear states (configurations 0–3) and calculated from the direct integration of the equations of motion of the system.

The response is obtained for the selected ADOF present in the reduced model (blue and red dots in Figs. 44.4, 44.5, and 44.6). Expansion is performed using the same projection mode shape vectors obtained from the reduction process of the unassembled unreduced subcomponents as seen in Fig. 44.6a.

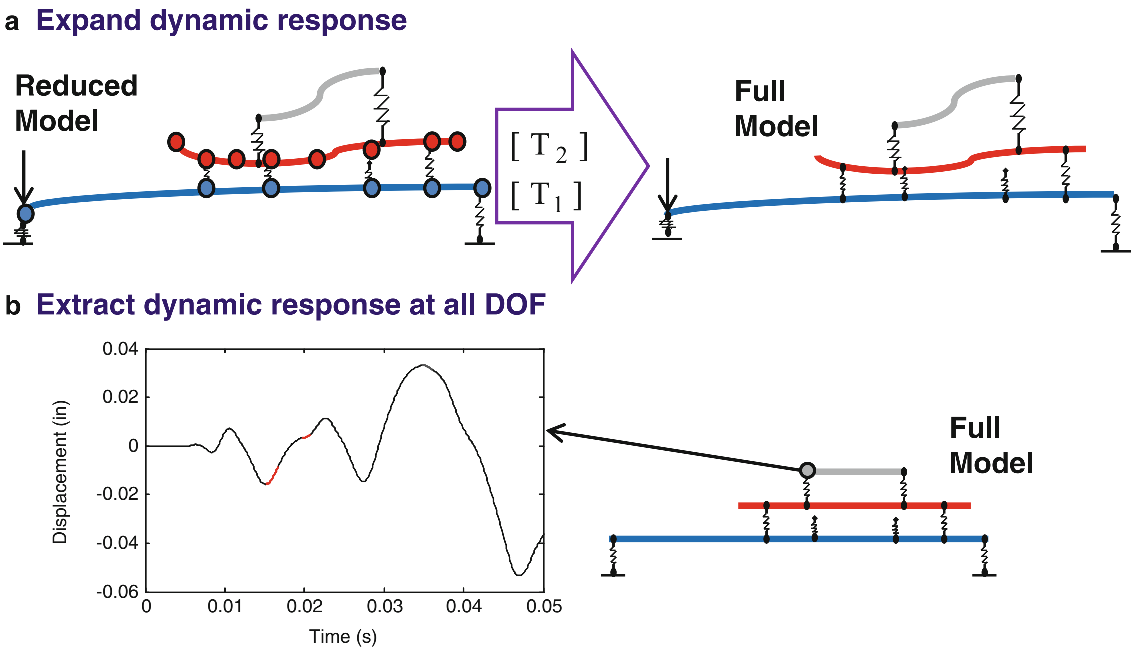
a Expand dynamic response
Reduced Model
[T₂]
[T₁]
Full Model
b Extract dynamic response at all DOF
Displacement (in)
0.04
0.02
0
-0.02
-0.04
-0.06
0
0.01
0.02
0.03
0.04
0.05
Time (s)
Full Model

Fig. 44.6 Prediction of subcomponent dynamics from expansion of reduced order model time response using uncoupled subsystem component transformation matrices

The full field dynamics at all DOF in the model are obtained from the expansion process and the response at the subcomponent level obtained (as in Fig. 44.6b) despite the fact that no ADOF where placed there during the reduction process.

44.2.6 *Timer Response Correlation Tools*

In order to quantitatively compare two different time solutions, two correlation tools were employed: The Modal Assurance Criterion (MAC) and the Time Response Assurance Criterion (TRAC).

44.2.6.1 Modal Assurance Criteria (MAC)

The Modal Assurance Criterion (MAC) [33] is widely used as a vector correlation tool. In this work, the MAC was used to correlate all DOF at a single instance in time. The MAC is written as

$$MAC_{ij} = \frac{\left[\{X1_i\}^T \ \{X2_j\}\right]^2}{\left[\{X1_i\}^T \ \{X1_i\}\right] \ \left[\{X2_j\}^T \ \{X2_j\}\right]} \tag{44.20}$$

where X1 and X2 are displacement vectors. MAC values close to 1.0 indicate strong similarity between vectors, whereas values close to 0.0 indicate minimal or no similarity.

44.2.6.2 Time Response Assurance Criteria (TRAC)

The Time Response Assurance Criterion (TRAC) [34] quantifies the similarity between a single DOF across all instances in time. The TRAC is written as

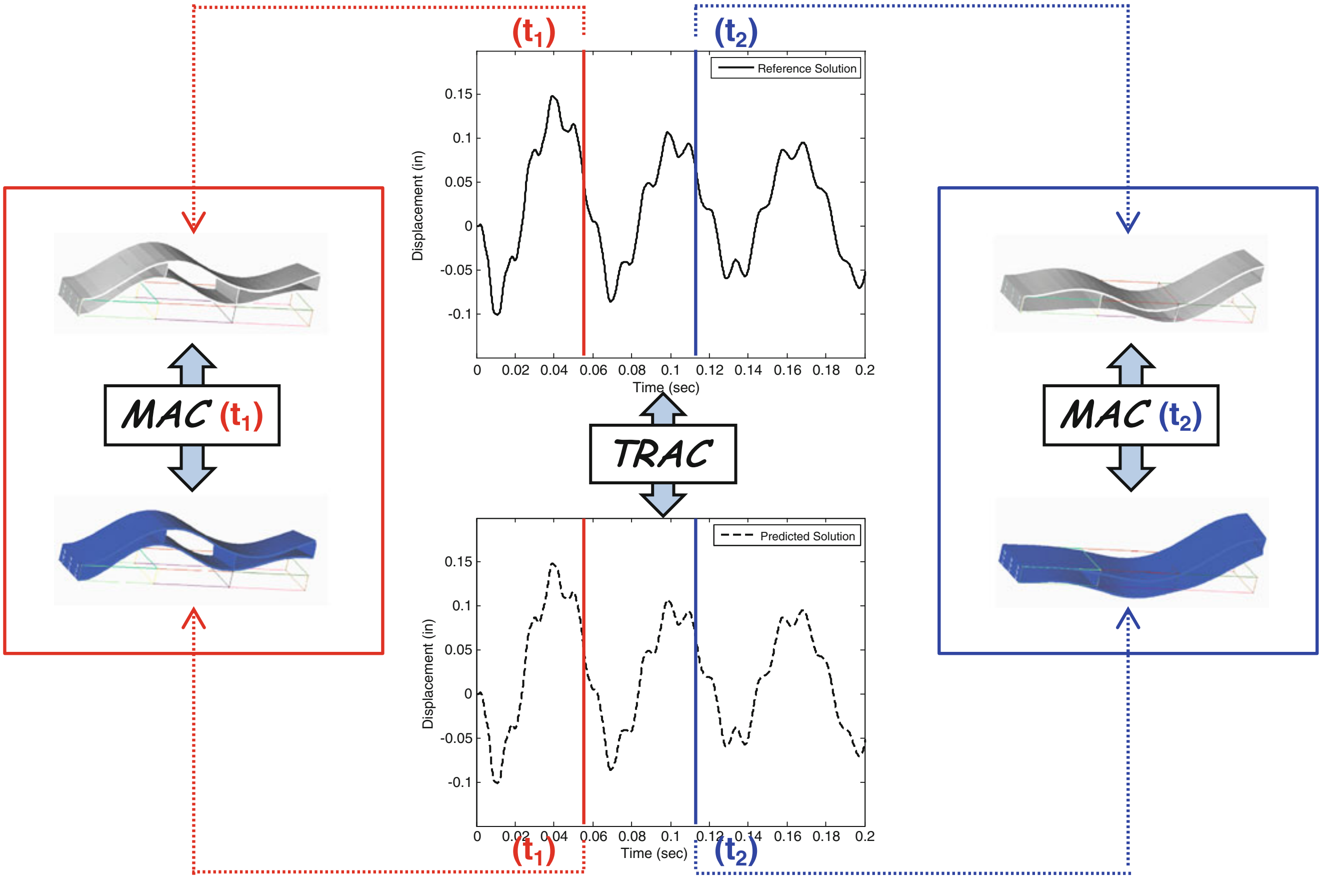

Fig. 44.7 Physical interpretation of MAC and TRAC. MAC is a vector to vector correlation taken at an instance in time t_i, while TRAC compares the response for its full duration at each DOF in the model. In the figure, the shape of two models (*blue* and *grey*) are correlated at a particular time step and the TRAC is computed for the displacement vector at one DOF

$$TRAC_{ji} = \frac{\left[\left\{X1_j(t)\right\}^T \ \left\{X2_i(t)\right\}\right]^2}{\left[\left\{X1_j(t)\right\}^T \ \left\{X1_j(t)\right\}\right] \left[\left\{X2_i(t)\right\}^T \ \left\{X2_i(t)\right\}\right]} \tag{44.21}$$

where X1 and X2 are time response vectors for a particular DOF. TRAC values close to 1.0 indicate strong similarity between vectors, while values close to 0.0 indicate minimal or no similarity.

The MAC is calculated between the shapes of the full space reference solution and estimated solution obtained from the reduced order model at each time step. Similarly, the TRAC is used to compare the time response from the reduced order model to the time response from the full space finite element solution at each degree of freedom. A diagram detailing the two correlation techniques is shown in Fig. 44.7.

44.2.7 *Numerical Computations*

The computation of the time response developed in this work is based on the Equivalent Reduced Model Technique (ERMT), a technique developed by Avitabile and Thibault [1, 35]. This technique uses an exact reduced model representation for the calculation of the system response. Newmark integration technique [36–39] is used to perform the direct integration of the equations of motion for the ERMT solution process due to similarity with the HHT (Hilber–Hughes–Taylor [38, 39]) method commonly used in FEA software. From the known initial conditions for displacement and velocity, the initial acceleration vector is computed using the equation of motion and the applied forces as

$$\ddot{\vec{x}}_0 = [M]^{-1}\left(\vec{F}_0 - [C]\,\dot{\vec{x}}_0 - [K]\,\vec{x}_0\right) \tag{44.22}$$

Choosing an appropriate Δt, α, and β, the displacement vector is

$$\begin{aligned}\vec{x}_{i+1} = {} & \left[\tfrac{1}{\alpha(\Delta t)^2}[M] + \tfrac{\beta}{\alpha(\Delta t)}[C] + [K]\right]^{-1} \\ & \Big\{\vec{F}_{i+1} + [M]\left(\left(\tfrac{1}{\alpha(\Delta t)^2}\right)\vec{x}_i + \left(\tfrac{1}{\alpha(\Delta t)}\right)\dot{\vec{x}}_i + \left(\tfrac{1}{2\alpha} - 1\right)\ddot{\vec{x}}_i\right) \\ & + [C]\left(\left(\tfrac{\beta}{\alpha(\Delta t)}\right)\vec{x}_i + \left(\tfrac{\beta}{\alpha} - 1\right)\dot{\vec{x}}_i + \left(\tfrac{\beta}{\alpha} - 2\right)\tfrac{\Delta t}{2}\ddot{\vec{x}}_i\right)\Big\}\end{aligned} \tag{44.23}$$

The values chosen for α and β were ¼ and ½, respectively. This assumes constant acceleration and the integration process is unconditionally stable, where a reasonable solution will always be reached regardless of the time step used. However, the time step should be chosen such that the highest frequency involved in the system response can be characterized properly to avoid numerical damping in the solution. Following the displacement vector calculation, the acceleration and velocity vectors are computed for the next time step using

$$\dot{\vec{x}}_{i+1} = \dot{\vec{x}}_i + (1-\beta)\,\Delta t\,\ddot{\vec{x}}_i + \beta\Delta t\,\ddot{\vec{x}}_{i+1} \tag{44.24}$$

$$\ddot{\vec{x}}_{i+1} = \frac{1}{\alpha(\Delta t)^2}\left(\vec{x}_{i+1} - \vec{x}_i\right) - \frac{1}{\alpha\Delta t}\,\dot{\vec{x}}_i - \left(\frac{1}{2\alpha} - 1\right)\ddot{\vec{x}}_i \tag{44.25}$$

This process is repeated at each time step for the duration of the time response solution desired. Additional information on the Newmark formulation can be found in [37, 39].

44.3 Analytical Case Studies

The approach taken in this work utilizes detailed linear finite element models, transformed to a smaller reduced order model, and addresses nonlinear phenomena such as contact with discrete elemental connections for these reduced order models. Figure 44.8 shows a summary of the efficient modeling approaches implemented in this work. The left side of the figure shows the traditional modeling approach using a costly nonlinear solution scheme for the full size model. The efficient modeling approaches are shown on the right side of Fig. 44.8, where the reduced system is modeled through linear approximations in physical space (Equivalent Reduced Model Technique [1]) or modal space (Modal Modification Response Technique [4]) and then solved by direct integration of the equations of motion. Expansion is then performed to return to the full field solution and compute displacement/strain at all DOF. On the other hand, the traditional approach (on the left side of Fig. 44.8) requires the discretization of the structure, calculation of all relevant loads and boundary conditions as well as the appropriate modeling of the nonlinear behavior of the structure before a costly nonlinear numerical methodology can be implemented to solve the full space problem usually stated through a set of partial differential equations. The end result of the traditional approaches is the same type of full field displacement/strain calculated in the reduced methodology but computed through a much more lengthy and costly process. The approximation of loads as well as the simplified modeling of the nonlinear behavior involved in the traditional modeling approach can lead to significant errors without any gains through the use of large computationally costly models. In contrast, an efficient reduced order modeling approach bypasses these typical limitations and allows for modification/tuning and quick testing of many configurations due to the fast solution times in the techniques.

The reduced order modeling techniques are identified as:

Equivalent Reduced Model Technique (ERMT) utilizes highly accurate model reduction schemes (SEREP, HYBRID and KM_AMI) to formulate extremely reduced models to form dynamic descriptions of linear components which are then interconnected with highly nonlinear connection elements for the dynamic response evaluation using direct integration techniques.

Modal Modification Response Technique (MMRT) utilizes the Structural Dynamic Modification process and mode superposition method to develop modal representations that are interconnected with highly nonlinear connection elements and solve using direct integration of modal based equations.

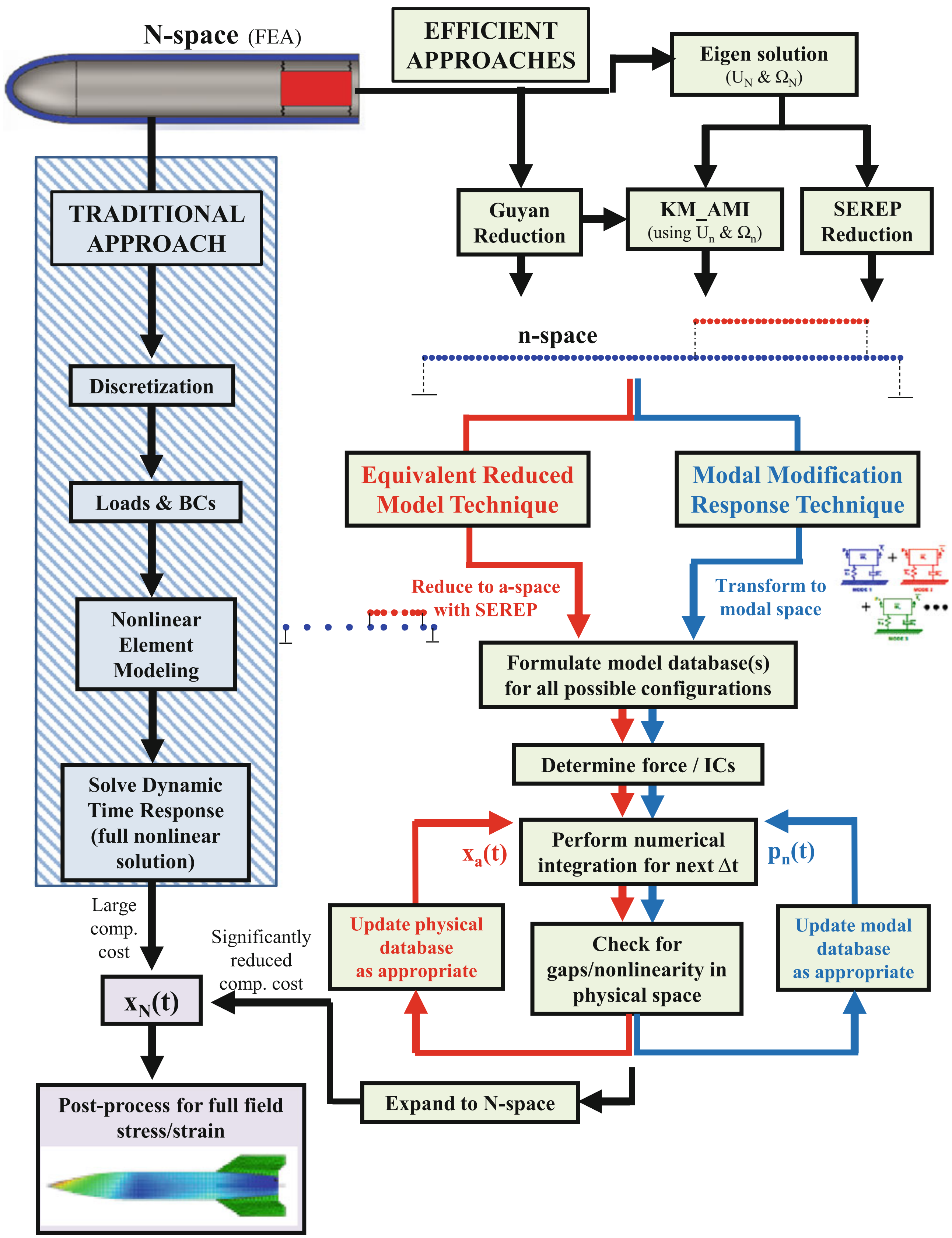
N-space (FEA)
EFFICIENT APPROACHES
Eigen solution
$(U_N \& \Omega_N)$
TRADITIONAL APPROACH
Guyan Reduction
KM_AMI
(using $U_n \& \Omega_n$)
SEREP Reduction
n-space
Discretization
Equivalent Reduced Model Technique
Modal Modification Response Technique
Loads & BCs
Reduce to a-space with SEREP
Transform to modal space
Nonlinear Element Modeling
Formulate model database(s) for all possible configurations
Determine force / ICs
Solve Dynamic Time Response (full nonlinear solution)
$x_a(t)$
Perform numerical integration for next Δt
$p_n(t)$
Large comp. cost
Significantly reduced comp. cost
Update physical database as appropriate
Check for gaps/nonlinearity in physical space
Update modal database as appropriate
$x_N(t)$
Expand to N-space
Post-process for full field stress/strain

Fig. 44.8 Traditional modeling of structural systems compared to efficient modelling approaches. *Left side* shows traditional approach of full space model using a nonlinear solver, while the efficient approaches (on the *right side*) use a piecewise linear formulation at reduced space and performs expansion to obtain full field results [15]

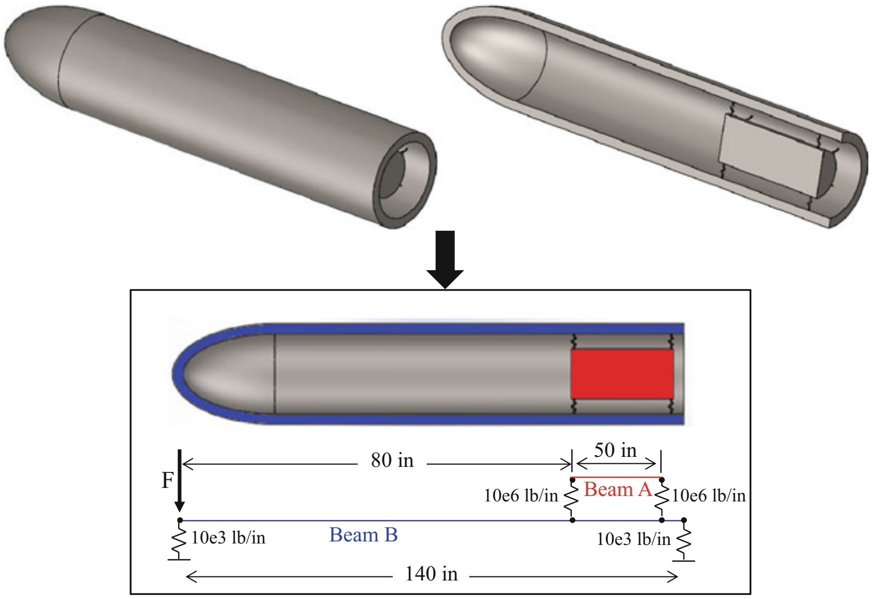

Fig. 44.9 Physical representation of two-beam system

Table 44.1 Overall comparison of results for all cases studied [15]

Case	Model	# of DOF	Solution time (s)	Average MAC	Average TRAC
Linear	Full space	1904	740.83	1.0000	
	Reduced	13	0.23	0.9960	0.9997
		24	0.29	0.9998	1.0000
Soft contacts	Full space	1904	741.95	1.0000	
	Reduced	13	0.23	0.9960	0.9997
Hard contacts	Full space	1904	740.18	1.0000	
	Reduced	13	0.23	0.9892	0.9918
		24	0.28	0.9998	0.9999

A variety of analytical cases were studied using both ERMT and MMRT to show the use of these efficient reduced modeling techniques for the prediction of full field dynamics. Only the case analyzed using a physical space formulation (ERMT) will be discussed. The model consists of a simple two-beam system as illustrated in Fig. 44.9. This case was used to demonstrate the proposed approach for calculating full field dynamics at a fraction of the full space computational cost; additionally one of the beam components has an ancillary subcomponent/appendage that is dynamically active during the response of the structure. Many other models have been studied with results in the references to fully demonstrate the approach.

The analytical cases were studied first in order to validate the methodology for the proposed techniques [2, 3, 5, 16, 17, 30]. For all of the cases shown, the efficient models were found to be accurate in comparison to the full space solution, while drastically reducing the computation time required. Table 44.1 summarizes the results obtained for both techniques in comparison to the full space solution [15]. The average modal assurance criterion (MAC) and time response assurance criterion (TRAC) are two time correlation tools used in this work and are included; values approaching 1 indicate a high level of similarity, while values close to 0 indicate a minimal level of correlation.

The full space beam model contains nodes with 0.2 inch spacing on each beam. Each node contains a shear DOF and a rotational DOF to capture planar beam bending only. Discrete nonlinearities are introduced to the system as a gap-spring contact. The stiffness of the spring contact is set to a predefined stiffness value when the specified gap distance is closed or set to zero when the gap distance is open and the beams are not in contact. The nonlinear cases have two contact locations between the beams, as shown in Fig. 44.10 [15]. The contact locations were chosen so that both gap-springs could engage during the response. The three possible configurations that the beams can encounter with the springs engaged are also shown in Fig. 44.10. For the cases shown in the table, a frequency band-limited analytical force pulse was used to excite a frequency range of roughly 400 Hz; the frequency range excited by the force pulse includes roughly 13 modes in all configurations. The use of such a force pulse allows for minimal excitation of higher modes and controls the number of modes that substantially participate in the system response due to the impulse.

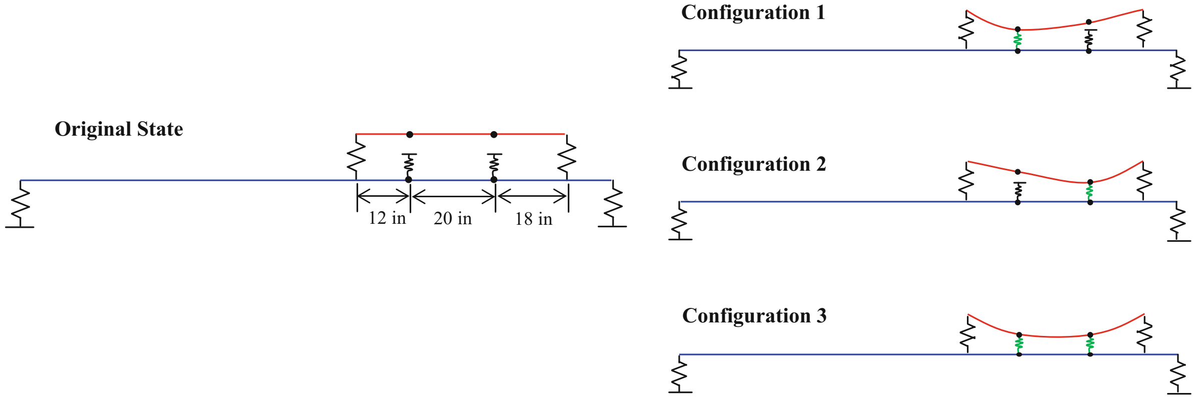

Fig. 44.10 Contact locations and configurations for nonlinear cases [15]

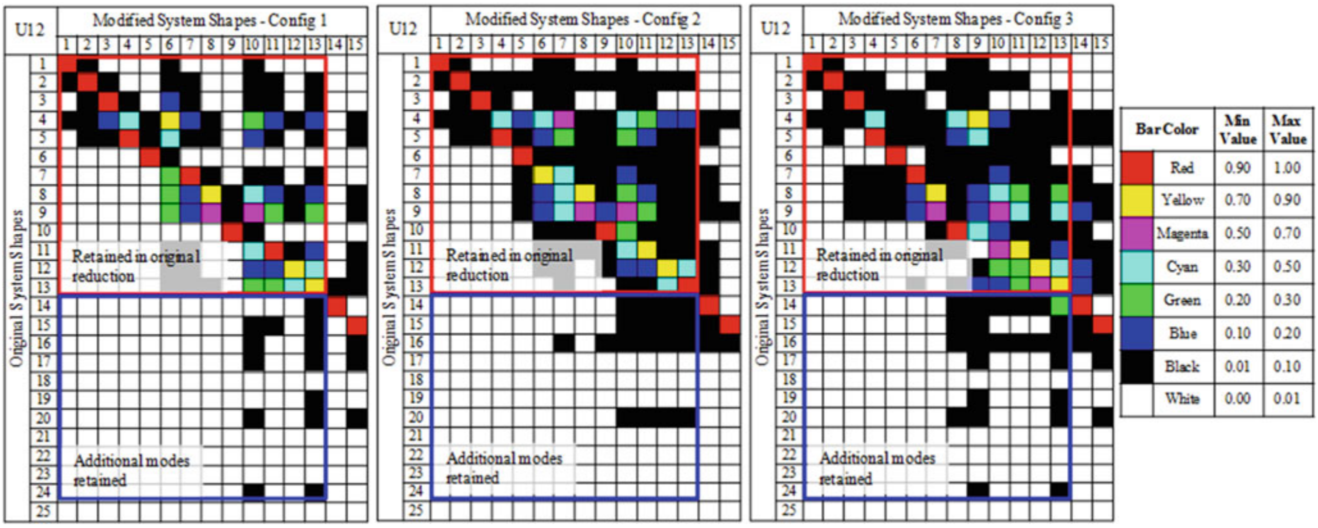

Bar Color		Min Value	Max Value
🟥	Red	0.90	1.00
🟨	Yellow	0.70	0.90
🟪	Magenta	0.50	0.70
🟦	Cyan	0.30	0.50
🟩	Green	0.20	0.30
🟦	Blue	0.10	0.20
⬛	Black	0.01	0.10
⬜	White	0.00	0.01

Fig. 44.11 Mode contribution matrix [U12] for all configurations [15]

For this study, there were a couple of considerations needed to obtain the accurate response. The first consideration involves the number of modes or degrees of freedom needed in the efficient model. Both techniques can suffer from the effect of truncation, which refers to the error caused by reducing the number of modes or degrees of freedom. Truncation error can be mitigated by including a sufficient number of modes or degrees of freedom such that all of the modes with significant energy are included in the response.

The second consideration involved forming the modified system database of mode shapes from the original mode shapes of the uncoupled components. Truncation error is again significant when assembling reduced order components or component mode shapes together. In order to reduce truncation error, the mode contribution matrix or [U_{12}] matrix is used to determine the necessary modes required to form the final system assembly. This matrix contains the scaling coefficients necessary to form the final modal vectors from the linear combination of the starting modal vectors and is more easily visualized as plotted using a color bar chart as in Fig. 44.11.

44.3.1 Nonlinear Solution with Reduced Model from Beam/Line Elements

Using 24 modes and ADOF produces a proper representation for this system. The use of fewer modes leads to inaccuracies as the results of this case show; more detailed discussion on these cases is presented in [15]. The full space displacements were determined using both a full space solution and the proposed efficient technique. Comparisons of the computation time and accuracy for this case are shown in Table 44.1 (Hard Contact Case). The solution time was reduced significantly by utilizing

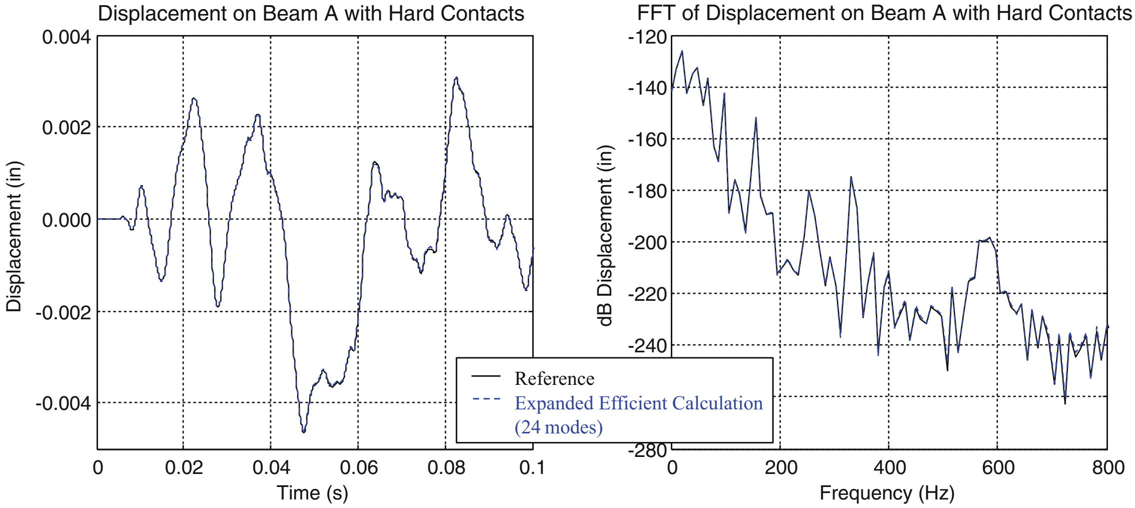

Fig. 44.12 Time response and corresponding FFT on Beam A (*top beam*) for hard contact case with 24 modes [15, 16]

such a smaller model to solve for the response. For this case, very high accuracy was obtained using an extremely reduced model. The displacement results for the full and predicted displacement are shown in the time and frequency domains in Fig. 44.12. The comparison of displacement overlays nearly perfectly in both domains between the two response calculations. The frequency range of the original system modes included in the reduction extends over 1300 Hz, so the energy distribution of the response is accurately captured in the frequency domain.

The displacement is also shown in Fig. 44.13 with the corresponding dynamic strain at the location of interest [16]. Both the displacement and strain are predicted accurately using the reduced order model implemented in this case. The model used in the efficient technique is able to better predict the higher order curvature in the dynamic displacement and strain response because more modes were included in the reduction. While the efficient calculation of the dynamic displacement matches nearly perfectly to the reference solution, some high frequency content is present in the reference strain solution that is not captured using the efficient calculation. The slight differences in the strain calculations can be further reduced by including even more modes in the reduced order model. The strain and displacement results calculated matched well those of the full space model for this case, yet the solution time for the reduced order model is substantially lower than the time required for a full space calculation.

The full solution took over 12 minutes to compute using the large beam/line element model, but accurate strain and displacement data could be obtained in less than a second without compromising accuracy. While the hard contact springs in the system causes the necessity for additional modes to be retained in a reduced order model, the full space model can still be substantially reduced to retain only the dynamic characteristics that are necessary to the response.

44.3.2 Expansion of Beam/Line Elements to a Full 3D Finite Element Model

The results obtained above clearly show the efficiency of the proposed technique. The computational savings are significant without any appreciable loss in accuracy. However, the expansion process can also be used to further expand the results from the beam/line element model to a full 3D model. Using an alternate model reduction expansion process proposed by Truong [40], these beam element results can be expanded to a much larger space/size model without any loss in accuracy. To illustrate this, a 3D model of the beam line element was created along with an appropriate mapping to the neutral axis of the beam where no geometry exists [17, 40]. Special constraint elements are utilized to form an additional transformation matrix to map from the beam neutral axis to the surface of the 3D model; the details of this work can be found in [40]. Figure 44.14 shows the model reduction from a 3D finite element model to a line element model.

For the full 3D model, the N-space was set at 7616 nodes with six DOF per node for a total of 45,696 DOF. The results obtained from the expansion process have been shown to be well correlated to the expected results as seen in Fig. 44.15, which shows the results for just one time step.

Figure 44.16 shows the time response and predicted strain for multiple steps of the system response obtained from the expansion of the reduced line model.

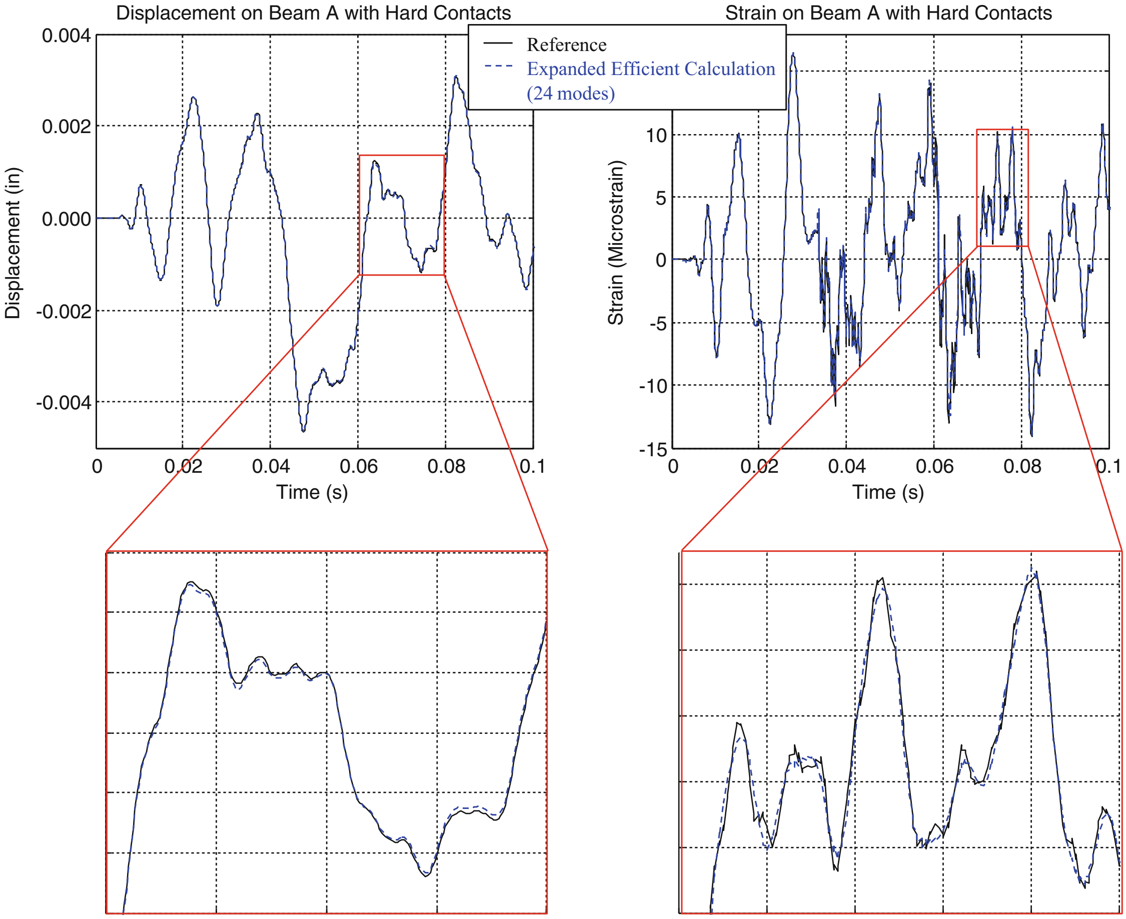

Fig. 44.13 Displacement and corresponding strain on Beam A (*top beam*) for hard contact case with 24 modes [16]

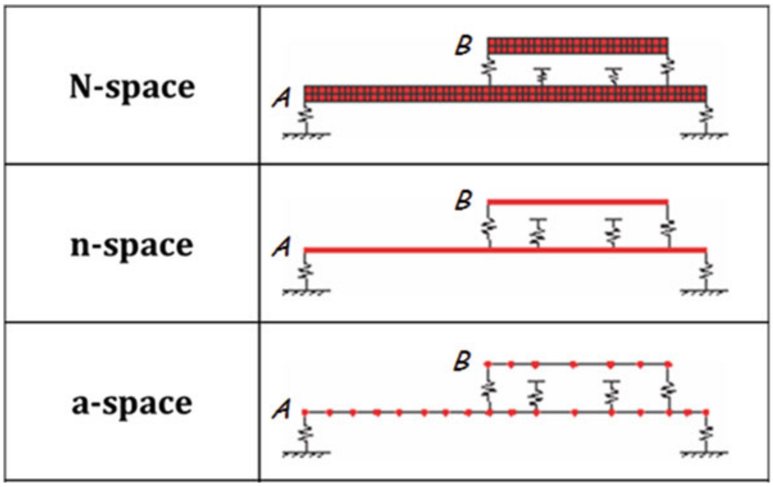

Fig. 44.14 Model reduction of full 3D FEM of two-beam system with nonlinear contacts

44.3.3 *Ancillary Subcomponent Response from Embedded Reduced Order Model*

Multi-component structural systems were addressed in the context of retaining embedded structural information of ancillary subcomponents for the calculation of nonlinear reduced order model time response. For linear forced response, expansion was shown to return a precise approximation of the ancillary subcomponent even in cases where the reduction does not

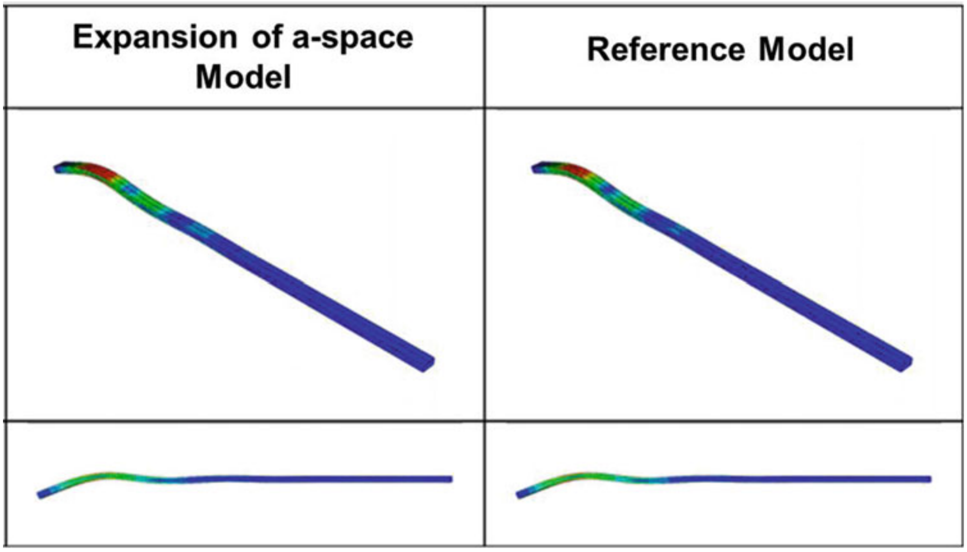

Fig. 44.15 Dynamic strain on Beam B for one time step of hard contact case from 3D model reduction

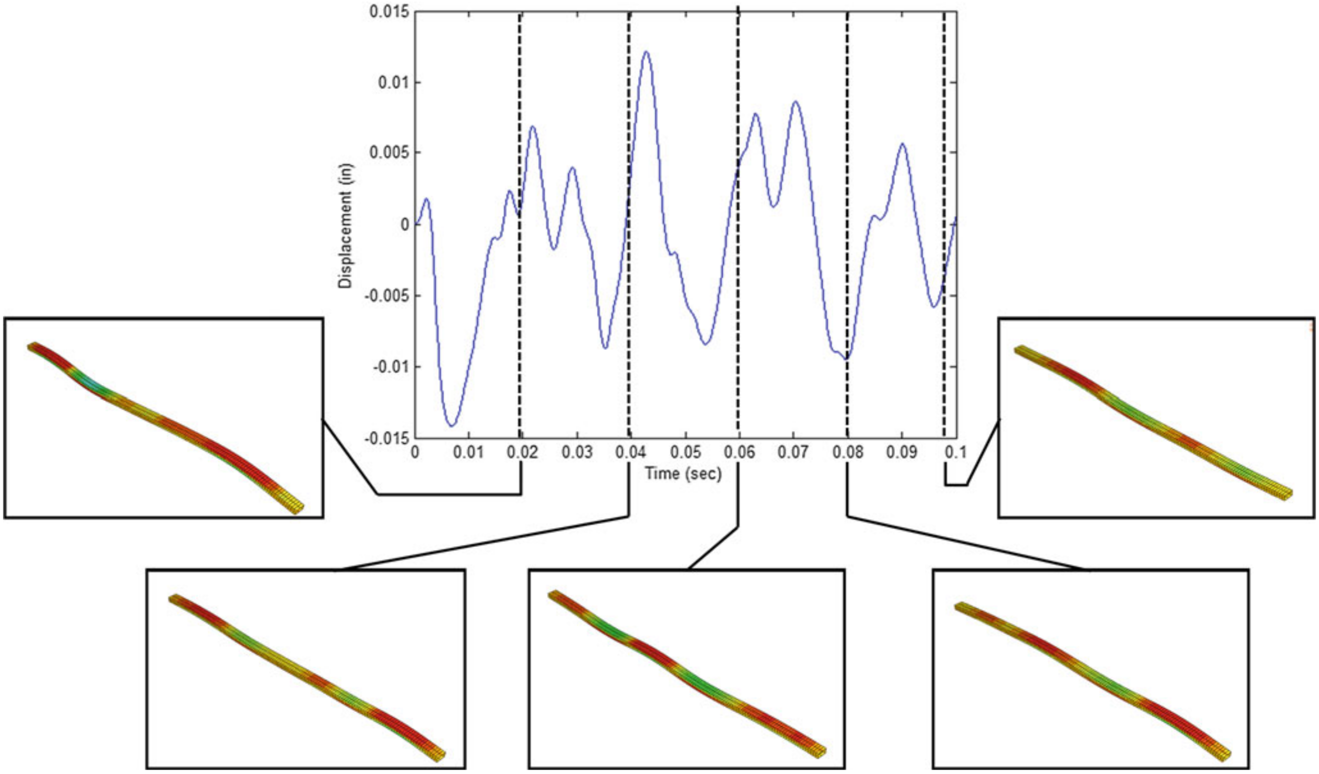

Fig. 44.16 Predicted dynamic strain on Beam B from expansion of reduced line model to full 3D FEM at multiple time steps

include active DOF at that subcomponent level [21]. The model was developed as a natural extension of the nonlinear worked discussed in the last cases. A full space finite element model consisting of two systems, one of which contains a dynamically active ancillary subcomponent, were reduced to a smaller set of degrees freedom and used for the prediction of the forced time response of the system as seen in Fig. 44.17. Gap-spring contact elements were introduced to generate nonlinear response between the two systems. The reduced order model (with embedded ancillary subcomponent information)

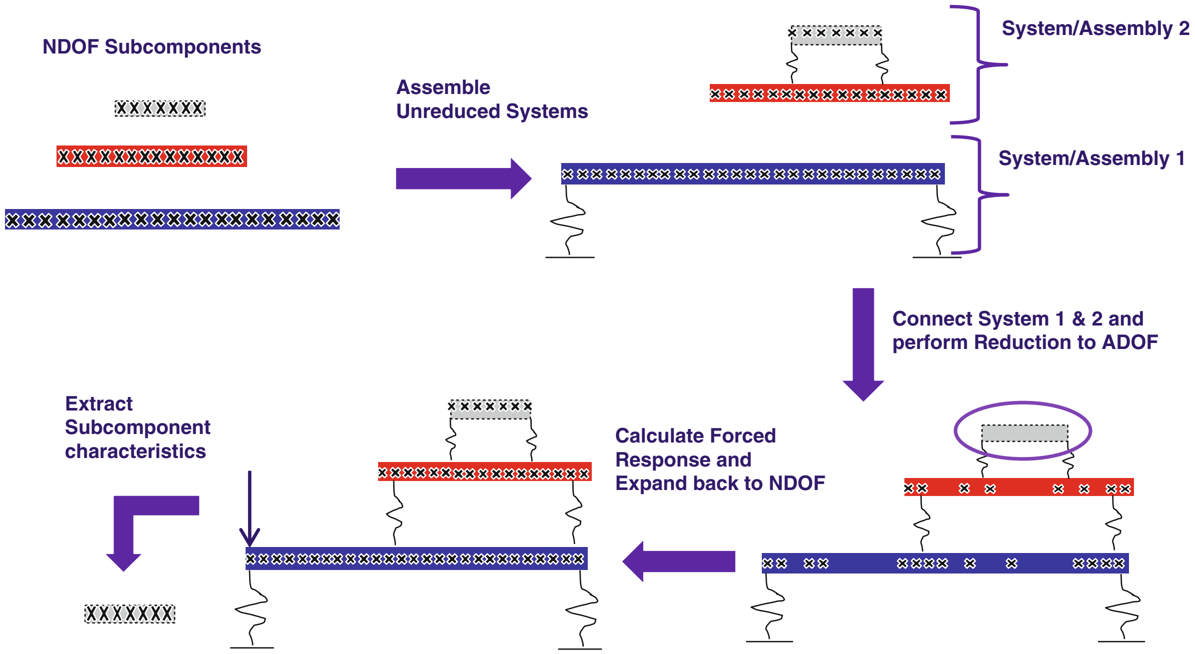
NDOF Subcomponents
Assemble
Unreduced Systems
System/Assembly 2
System/Assembly 1
Connect System 1 & 2 and
perform Reduction to ADOF
Extract
Subcomponent
characteristics
Calculate Forced
Response and
Expand back to NDOF

Fig. 44.17 Sequence for the development of reduced system response models

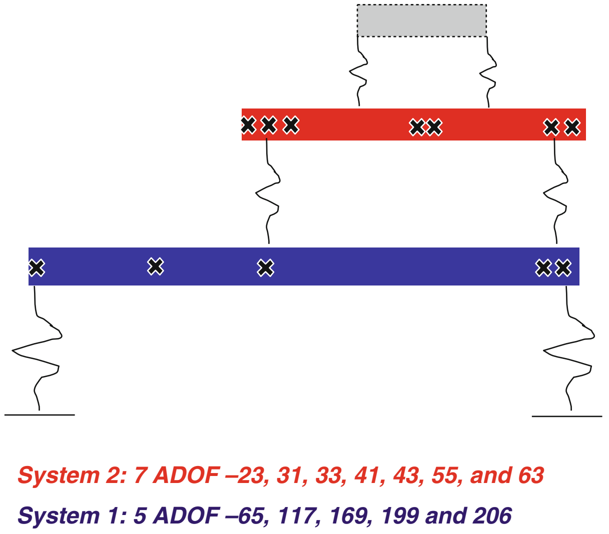
System 2: 7 ADOF –23, 31, 33, 41, 43, 55, and 63
System 1: 5 ADOF –65, 117, 169, 199 and 206

	Reference System Freq. (Hz)	SEREP Reduced System Freq. (Hz)	% Difference
Mode 1	16.8	16.8	0%
Mode 2	37.5	37.5	0%
Mode 3	68.1	68.2	0%
Mode 4	84.6	84.6	0%
Mode 5	102.1	102.1	0%
Mode 6	129.1	130.2	1%
Mode 7	210.0	211.5	1%
Mode 8	282.0	283.2	0%
Mode 9	343.0	351.2	2%
Mode 10	396.2	396.6	0%
Mode 11	477.3	2611.8	447%
Mode 12	645.3	3023.1	369%

Fig. 44.18 Comparison of SEREP reduced order model (12 DOF) frequencies with respect to (206 DOF) reference solution. "x" indicates relative location of nodes in FEM

was then used to calculate the response at ADOF and then to expand back to the full space finite element model and extract the predicted forced response of the ancillary subcomponent. The models studied were similar to those of Figs. 44.9 and 44.10 except that now the top beam has an appendage/ancillary beam attached and active during the response of the system. The results for the linear and the nonlinear hard and soft contact cases will be discussed here but further information can be found in [21, 23, 24].

In the linear case, SEREP model will be discussed. A reduced model was computed such that no DOF from the ancillary subcomponent (grey beam at the top of the red beam) was preserved in the reduction process. The model is shown in Fig. 44.18 and a comparison of the response as well as correlation results of the expansion process in Fig. 44.19.

The SEREP reduction and expansion process resulted in high correlation with full space model using only a very small fraction of the DOFs. Furthermore, the omission of the connecting DOF for the ancillary subcomponent did not yield any

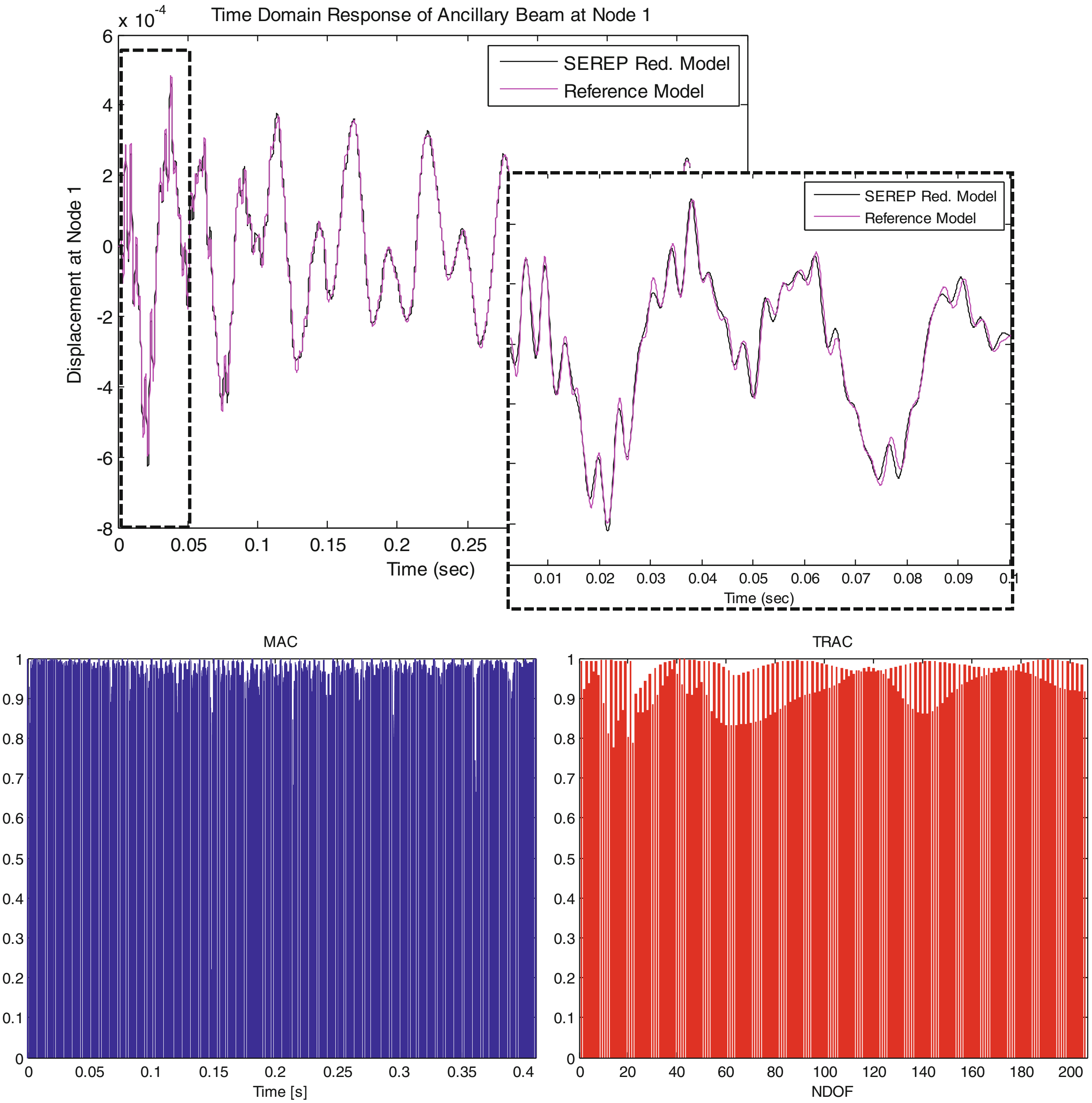

Fig. 44.19 *Top*: Comparison of time response at node 1 of the ancillary subcomponent from the expansion of a 12DOF SEREP reduced model versus the 206 DOF full space reference solution (in *magenta*). Zoomed in region shows the response for the first 0.1 s. *Bottom*: MAC and TRAC bar plots showing the correlation of the expanded SEREP reduced model to the reference model

additional error. Addition of modes beyond the 12 modes indicated in the $[U_{12}]$ matrix in the SEREP reduced model showed large improvement from the resulting expanded model response as illustrated in Fig. 44.20 where expansion is used on a 17 mode and DOF reduced model. When the reduction process is successful (as it was with the SEREP and KM_AMI models), the modes selected span the space of the system response. Modes beyond the 12 indicated by the $[U_{12}]$ smooth the approximation of the system response and further addition of modes results in better results until the reduced ‘a’ space model approaches the full ‘N’ space solution and hence spans the whole space of the full assembled system response.

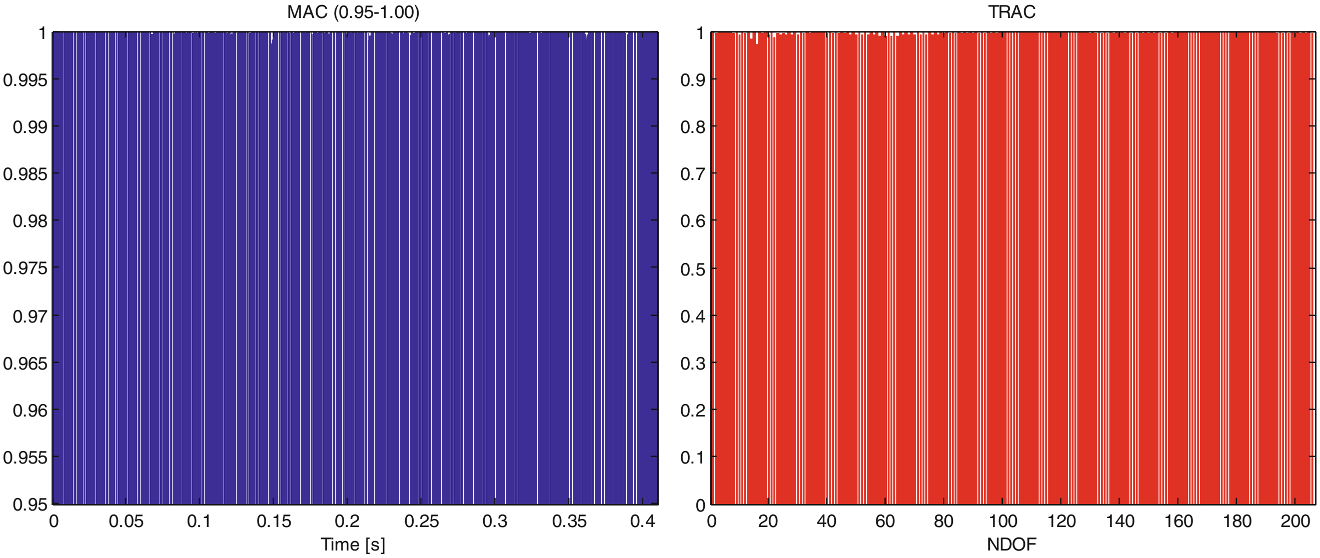

Fig. 44.20 MAC and TRAC plots showing correlation of the expanded 17 DOF SEREP reduced model to reference model. MAC y-axis is showing values from 0.95 to 1.0

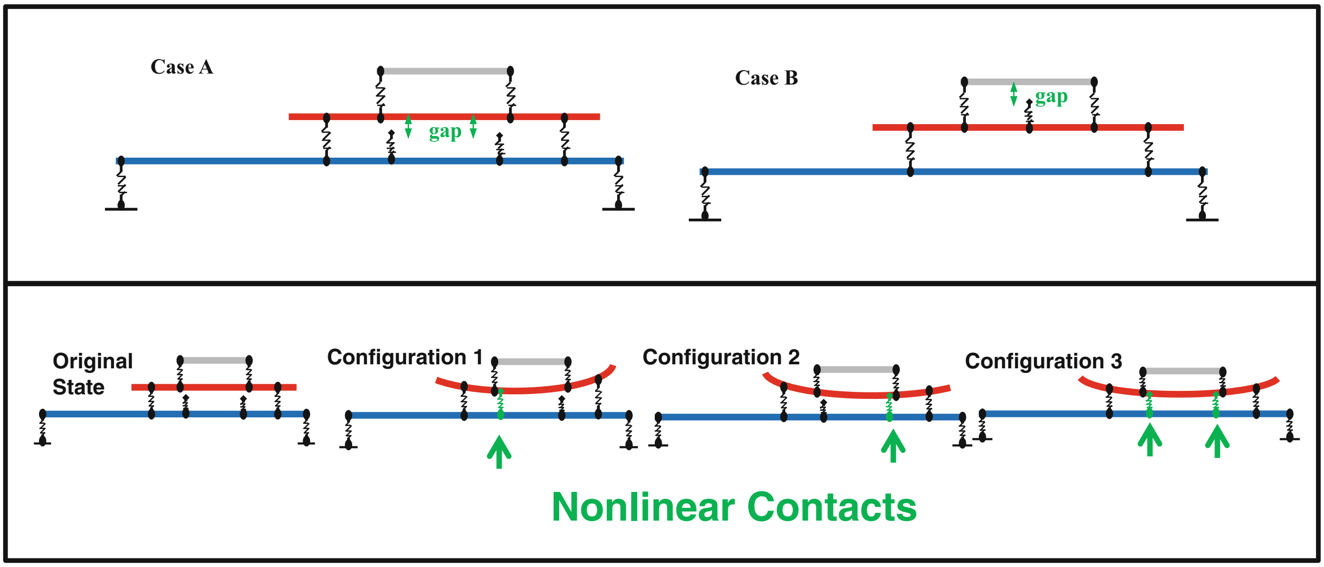

Fig. 44.21 Nonlinear gap-spring contact cases analyzed. The nonlinear configurations for Case A are shown. Each case indicates the closing or opening of the gap springs (in *green* when closed)

The following models expand the reduced order modeling of the three beam system to include nonlinear response. Gap-spring contact elements are introduced to generate nonlinear response between the two systems as done in the first example shown here. However, the possibility of nonlinear contacts is introduced at the subcomponent level as shown in Fig. 44.21. For the first nonlinear case, four different configurations are possible (initial configuration, one configuration for each spring coming in contact, and one for both springs in contact) as seen in Fig. 44.21. Using the calculated [U_{12}] for all configurations, the necessary number of component modes were determined in order to properly characterize the system; using the force described above, the system modes must be able to characterize the response over a 250 Hz frequency span. While this is the initial frequency range of interest for any structural dynamic study, there also needs to be consideration for the nonlinear contacts which occur that may require a frequency range beyond that initially determined from the applied forcing function.

In these nonlinear cases, the location of the nonlinearity can have a significant effect on the accuracy of the prediction and on the number of modes (and DOF) required in the reduction/expansion process. SEREP reduction was used to reduce the active DOF of the system to an ‘a’ set not including DOFs on the ancillary beam. The forced responses of the reduced ADOF

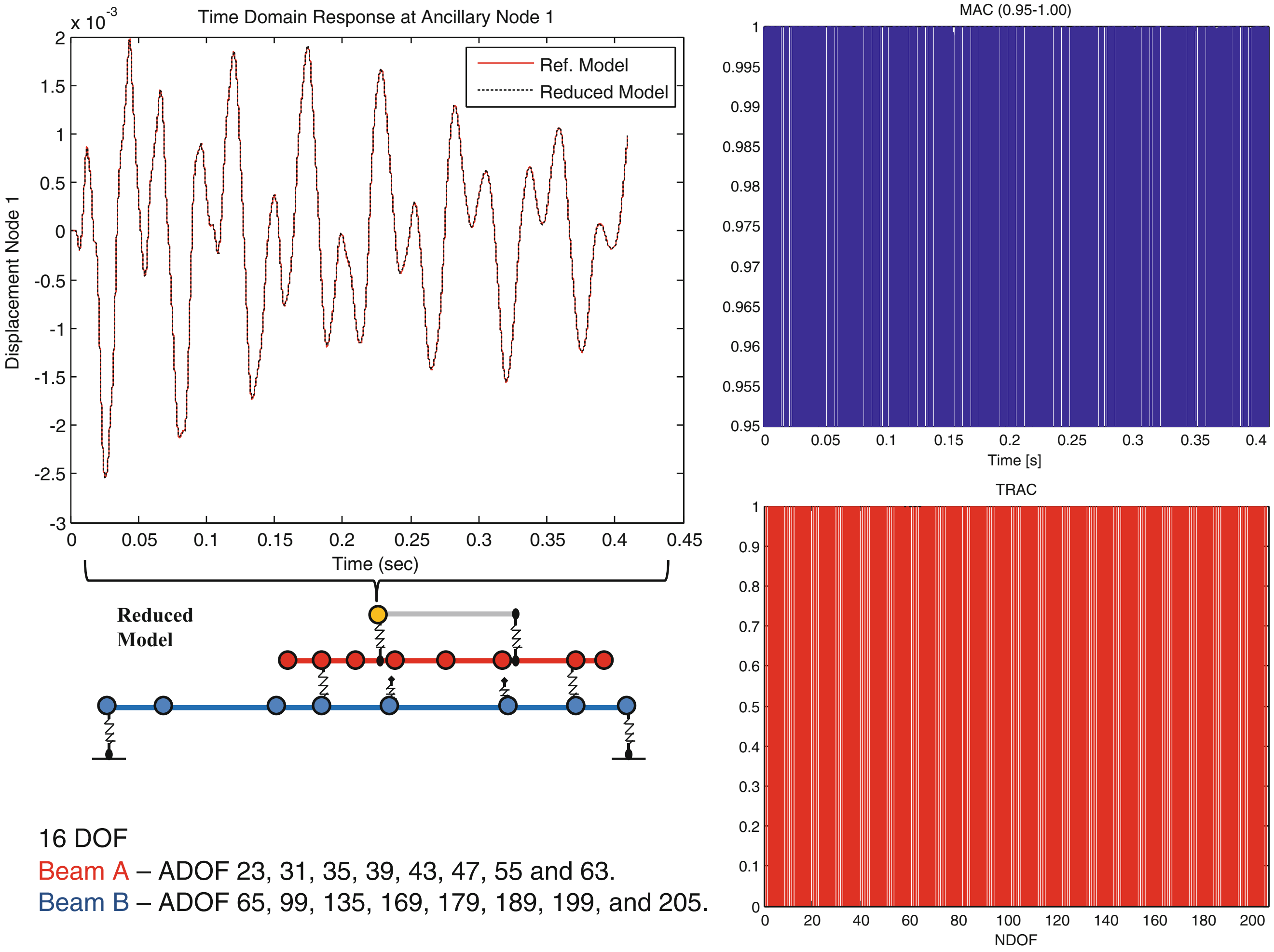

Fig. 44.22 Predicted response at ancillary node 1 (in *yellow*) from 16 DOF reduced model. MAC from 0.95 to 1.0 (*top right*) and TRAC (*bottom right*) correlation of models

systems were computed. The dynamic characteristics of the ancillary subcomponent were then extracted using the system information available from the reduction process. A SEREP reduced model using 16 modes was created. Figure 44.22 shows the comparison of the predicted response of the expanded model and the reference model.

Using 16 modes allows for the accurate prediction of up to 8 modes (which spans approximately 300 Hz) of the three-beam assembled system. Figure 44.23 shows the comparison of the FFT of the displacement at the left spring contact location.

The FFT of the displacement at the left contact location in Fig. 44.23 shows no significant effect of mode truncation of the higher order modes and the response is accurate approximation of the full NDOF solution. Note that no ADOF has been placed at the ancillary subcomponent or at the DOFs that connect the ancillary beam to the top beam. Nevertheless, the embedded information in the reduction process has successfully allowed the prediction of the time response at all NDOF.

The effect of higher order modes can be exacerbated if the type of contact is a hard impact, thus producing a narrow time pulse that translates into a high order pulse in the frequency domain. The next case will explore a hard contact spring acting at two locations of the structure. A comparison of the two types of contacts, soft and hard, can be seen in Fig. 44.24.

Nonlinear contacts of 10,000 lb/in were implemented instead of the soft contacts of 100 lb/in previously used. Because the hard contact excites frequencies in the range of 700 Hz, the 16 mode model previously used cannot give the best approximation of the response of the system. The selection of modes preserved in the reduction must form a linearly independent set of vectors spanning the space of the full response of the system. In other words, the selected projection vectors in the transformation matrix must be able to approximate any other vector in the space as linear combinations of the mode shape vectors preserved in the reduced space. A 21 modes and DOF model was created to better approximate the hard contact nonlinear response of the system. Figure 44.25 shows the correlation and response for the 21 DOF model and the reference model.

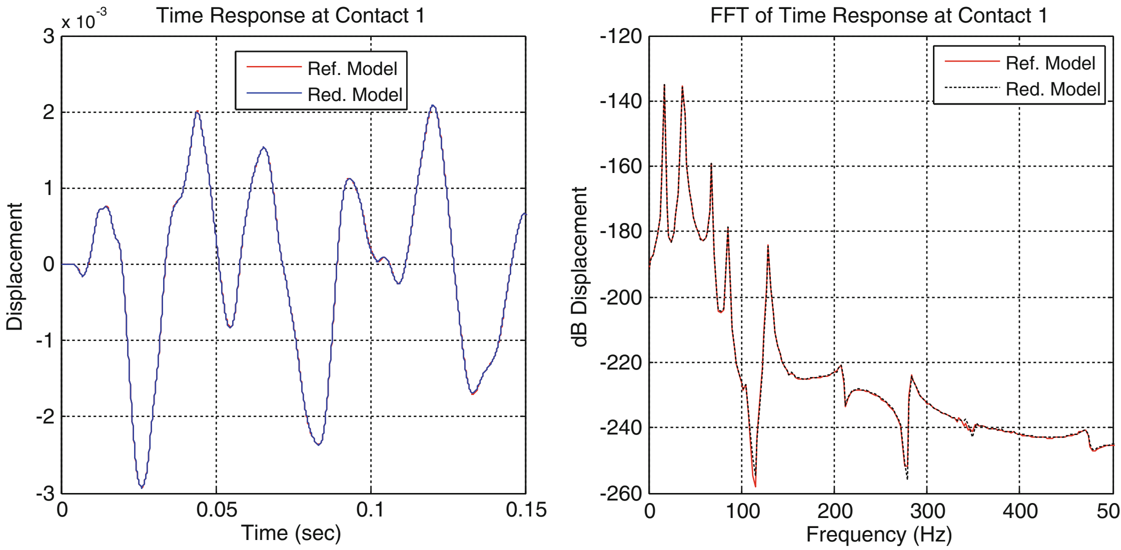

Fig. 44.23 Comparison of response (*left*) and FFT (*right*) of reference model and 16 mode reduced order model at spring contact location 1

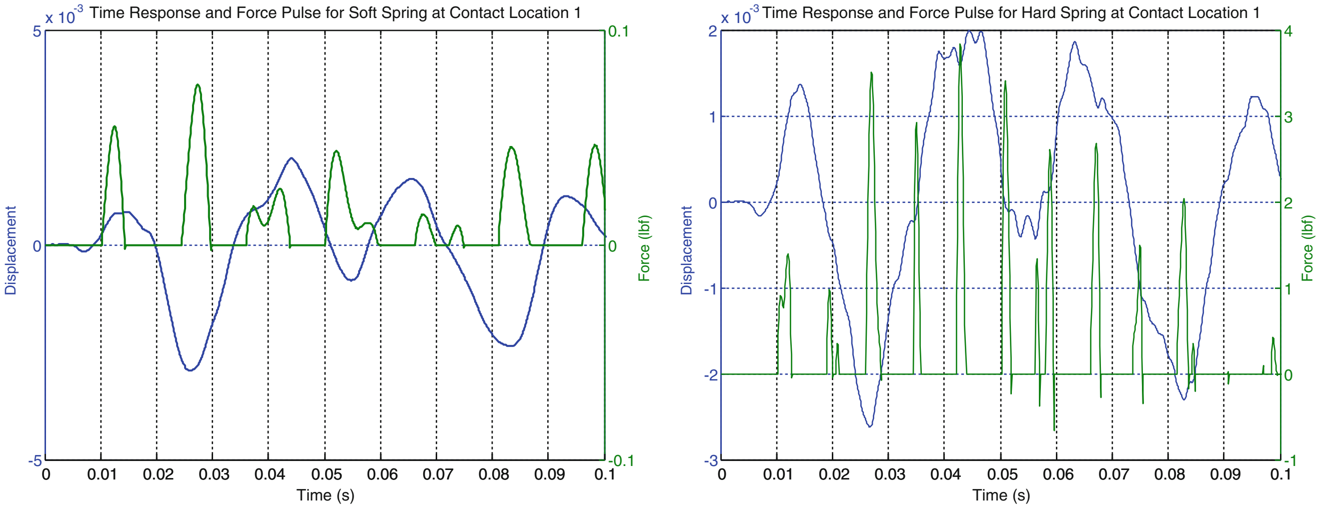

Fig. 44.24 Comparison of displacement and force magnitude for soft (*left*) and hard (*right*) type of nonlinear contacts at DOF 37 of the three beam system at contact location 1 (*left gap spring*)

The modes used in the reduced model resulted in an accurate approximation of the response of the NDOF system. However, the effects of mode truncation could not be completely mitigated. Caution must be exercised when simply adding modes to the reduced order model since linear independence of the vectors formed in the expansion process is very important. The reduced space matrices can become ill-conditioned for certain choice and number of DOF and the predicted response is then subjected to high levels of numerical error. Figure 44.26 shows that the FFT and response at the contact location 1 is reasonably approximated by the reduced model of 21 modes.

The cases considered thus far have shown that full field results can be obtained from reduced order models with subcomponent interactions from the embedded information preserved in the reduction process. Using the necessary number of modes in the reduced model to span the space of all modes of interest allows the response at the ancillary and any other DOF to be predicted accurately. The $[U_{12}]$ contribution matrix and the effect of the higher order modes from nonlinear interactions must be taken into account as well as the linear independence and well-determined behavior of the reduced matrices in order to obtain a good approximation of the dynamic characteristics of the system. Moreover, when proper precautions are taken to reduce the N space system to ‘a’ space, no ADOF are needed in the dynamically active ancillary subcomponent.

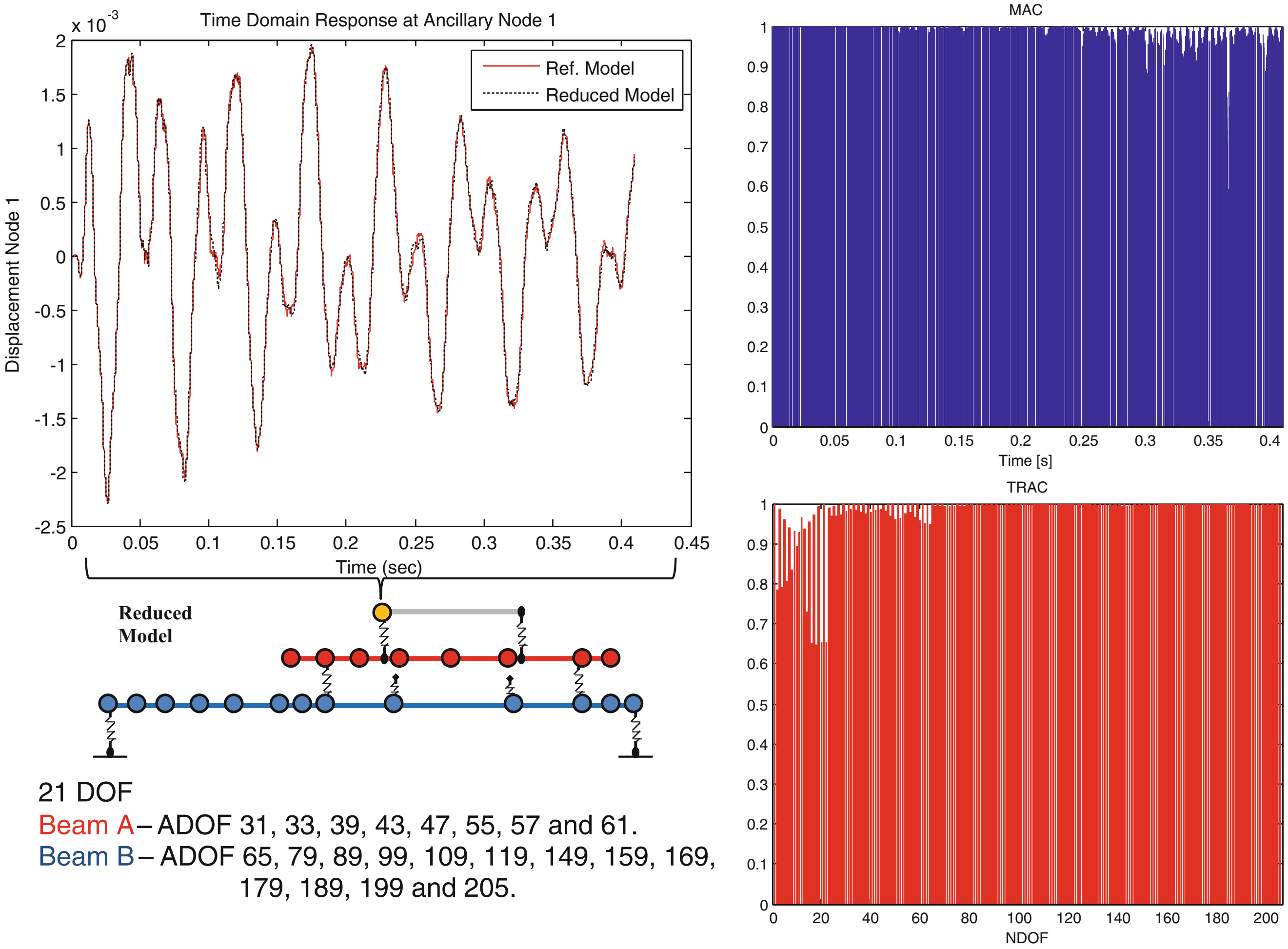

Fig. 44.25 Predicted response at ancillary node 1 from expansion of 21 DOF reduced order model with hard contacts. MAC (*top right*) and TRAC (*bottom right*) correlation of models

The next case explores the natural extension of this work to include a nonlinear contact occurring at the ancillary subcomponent. The nonlinear contact of 100 lb/in was placed at Ancillary but no ADOF were selected on the ancillary subcomponent or the connecting DOF between the red beam and the ancillary. In order to check for a change of configuration during the time response of the reduced model, the algorithm used the expansion of the displacement at time t_i for the contact DOF and then continued to the next time step t_{i+1} making the necessary adjustments if the spring came in contact with the ancillary subcomponent. Only the response at the contact DOF was expanded throughout the response since no other DOF are needed during the computation of the reduced model response. The response at ‘a’ space was expanded to NDOF using the transformation matrices (mode shape projection vectors) from the reduction process. Figure 44.27 shows a comparison of the response at DOF 1 of the ancillary as well as the correlation with the reference model.

Figure 44.28 shows a comparison of the response and its FFT at the contact location. In the previous case, the contact point was included in the active set of DOF. In this case, the contact point was not included. The results obtained were not as accurate and well behaved as in the previous case. This may be due to many different factors such as numerical issues, rank problems, need for more modes, and many other factors which need to be addressed in future work.

Additional models of the SEREP reduced case where more modes were included in the reduction process (beyond 18 modes) lead to issues with the condition number of the reduced matrices. Furthermore, as the goal is to avoid placing ADOF at the ancillary subcomponent in order to gage the accuracy of the technique in reconstructing the subcomponent response from embedded information, there was limited number of choices for DOF locations in the new reduced models.

Guyan reduced models with KM_AMI improvement provided a way to create larger reduced models without the possible rank deficiencies of the SEREP reduced models. A 25 mode KM_AMI model is discussed next.

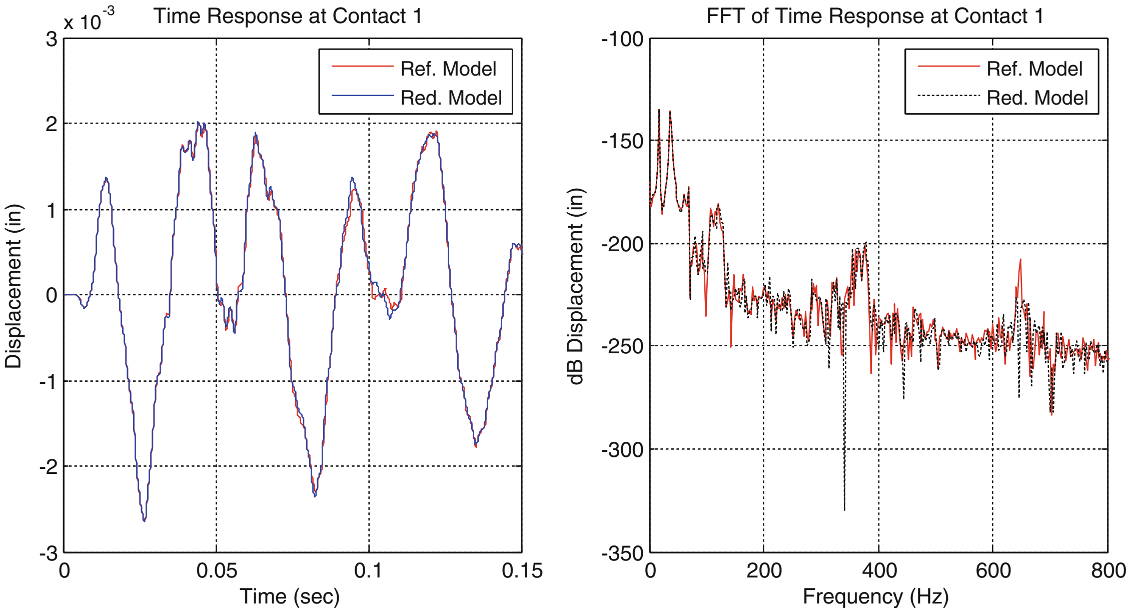

Fig. 44.26 Comparison of response (*left*) and FFT (*right*) of reference (in *red*) and expansion of 21 DOF reduced order model at contact location 1 (*left gap spring*)

Figure 44.29 shows a comparison of the predicted response at the ancillary DOF 1 from this model and the correlation plots with the full space reference model. The addition of modes resulted in a noticeable improvement in the quality of the predicted response. Note that the locations of low correlation for TRAC occur at the rotary DOF and not at the translational DOF.

Figure 44.30 shows a comparison of the FFT and response at the contact location. The addition of modes is shown to better characterize the influence of the higher order modes present due to the nonlinear contacts but the effects of mode truncation cannot be completely eliminated.

Additional cases were studied involving hard and soft. When enough modes of the unconnected components are preserved such that they form a linearly independent set of vectors spanning the space of the full response, the response was accurately predicted at all DOF of the system. The prediction at the ancillary subcomponent was successfully performed even when no active DOF were preserved in the reduced model. These studies are further explained in [21, 23, 24].

44.4 Conclusion

Understanding of the linear reduction/expansion methodology showed the advantage of using reduced models for full field prediction of systems that may undergo localized nonlinear response due to component contact or coupling interactions. For these types of problems, the presence of highly nonlinear coupling elements such as hard contacts, isolation mounts, gap springs, bilinear springs, etc. is predicted with a piecewise linear approximation providing the dynamic response of the structure as a superposition of all possible configurations of the system.

For all cases considered, linear and nonlinear, high correlation values were obtained between the reference model and the predicted expanded model response. For such models, the computation time was greatly reduced as well as the number of DOF in the model. The scalability of the expansion process was previously demonstrated by other researchers as well as the application of these methodologies for the prediction of strain.

Acknowledgements Some of the work presented herein was partially funded by Air Force Research Laboratory Award No. FA8651-10-1-0009 “Development of Dynamic Response Modeling Techniques for Linear Modal Components”. Any opinions, findings, and conclusions or recommendations expressed in this material are those of the authors and do not necessarily reflect the views of the particular funding agency. The authors are grateful for the support obtained.

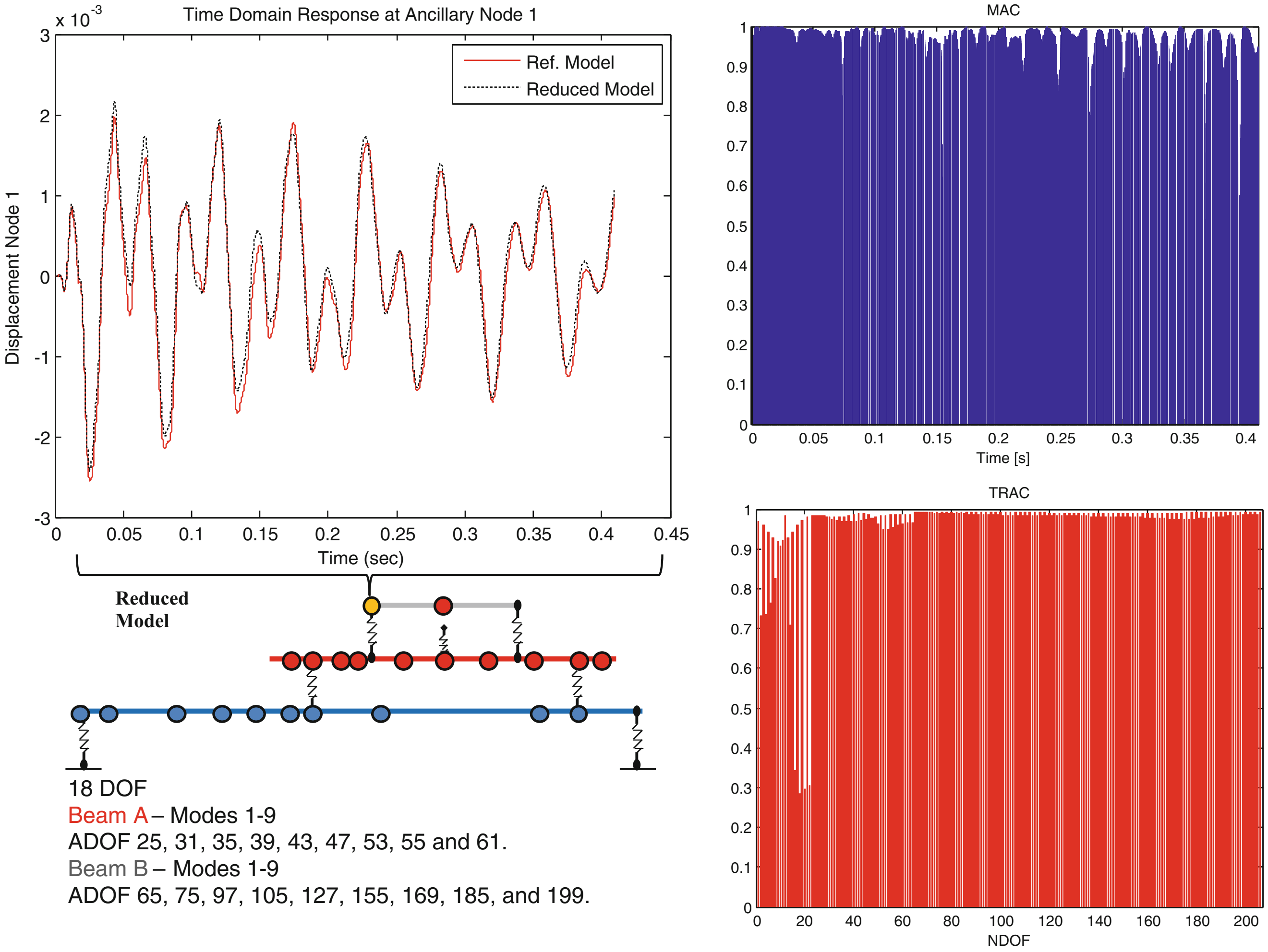

Fig. 44.27 Predicted response at ancillary node 1 from 18 DOF reduced model with soft contact. MAC (*top right*) and TRAC (*bottom right*) correlation of models

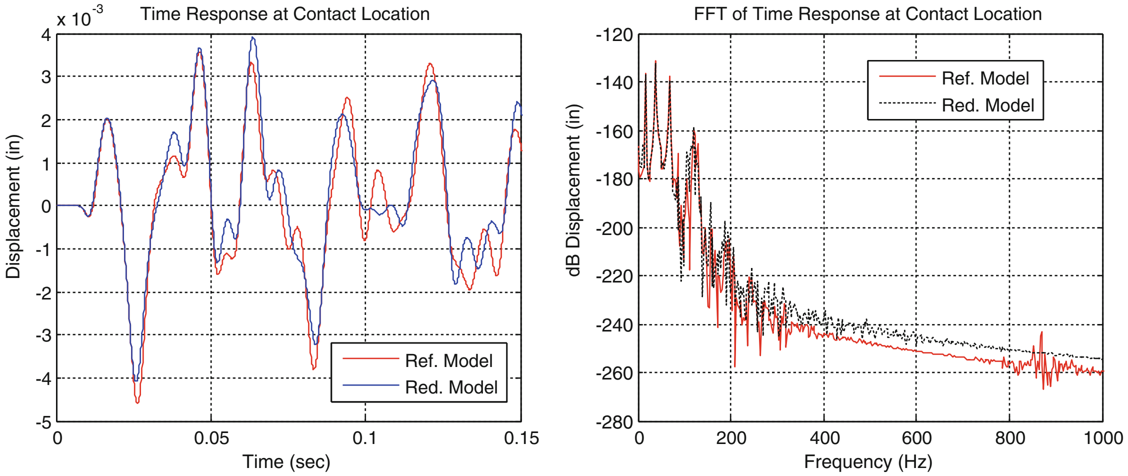

Fig. 44.28 Comparison of time response (*left*) and FFT (*right*) of reference model and expansion of 18 DOF reduced order model at contact location. Reference model is shown in *red*

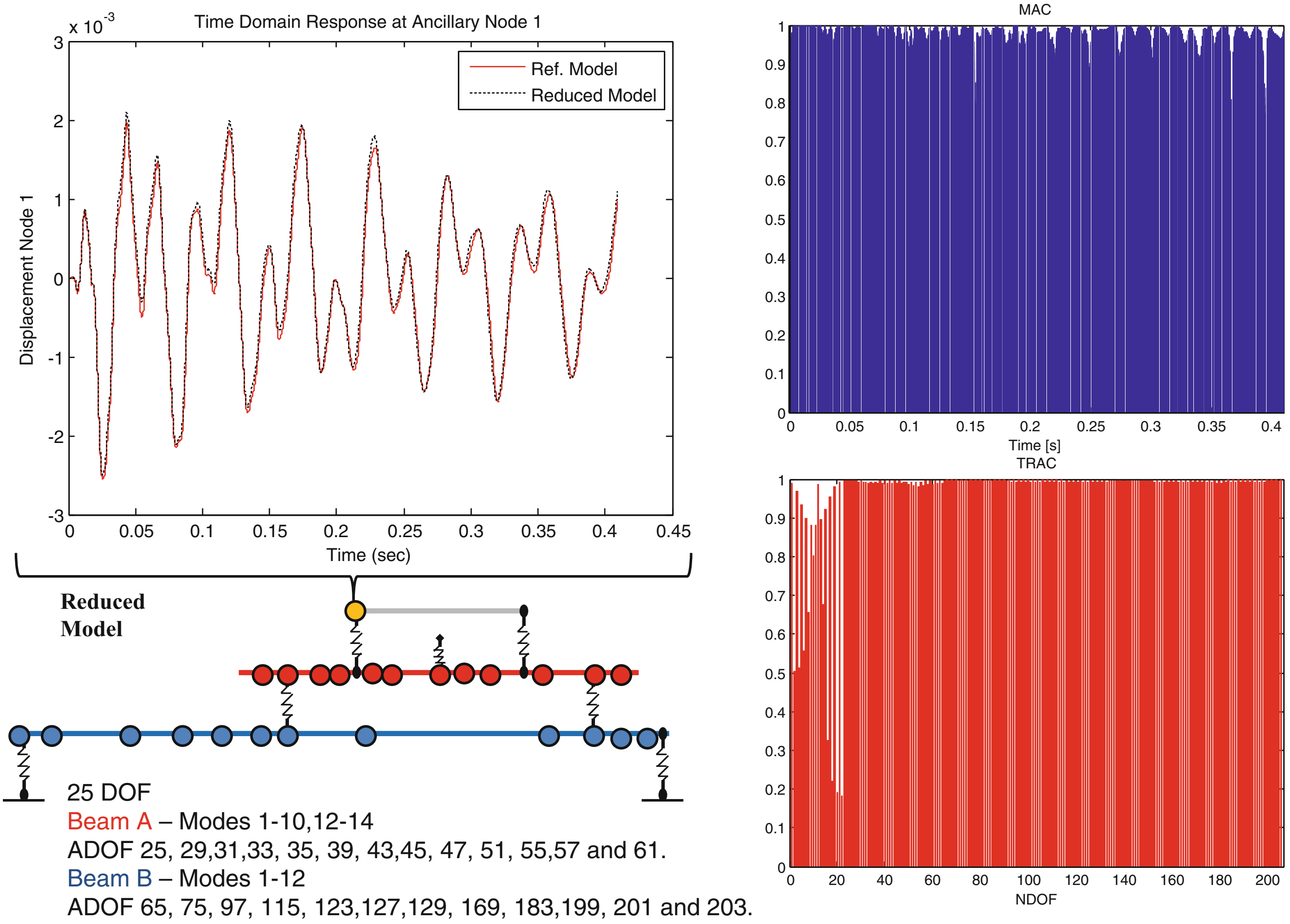

Fig. 44.29 Predicted response at ancillary DOF 1 from expansion of 25 DOF KM_AMI improved Guyan reduced model with soft contact. MAC (*top right*) and TRAC (*bottom right*) correlation of models

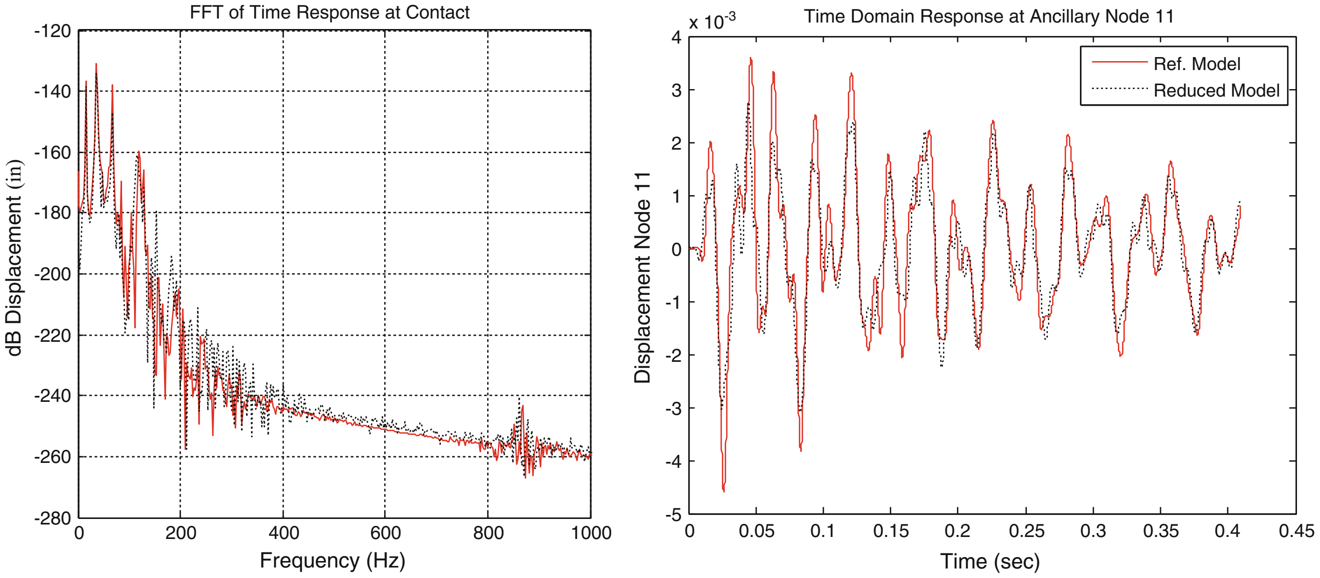

Fig. 44.30 Comparison of FFT (*left*) and time response (*right*) of reference model and expansion of 25 DOF reduced order model at contact location. Reference model is shown in *red*

References

1. Thibault, L.: Development of Equivalent Reduced Model Technique for Linear Modal Components Interconnected with Nonlinear Connection Elements. University of Massachusetts Lowell (2012)
2. Thibault, L., et al.: Equivalent reduced model technique development for nonlinear system dynamic response. Mech. Syst. Signal Process. **36**(2), 422–455 (2013)
3. Thibault, L., et al.: Equivalent reduced model technique development for nonlinear system dynamic response. Top. Nonlinear Dyn. **3**, 95–127 (2012)
4. Marinone, T.: Efficient Computational Nonlinear Dynamic Analysis Using Modal Modification Response Technique. University of Massachusetts Lowell (2012)
5. Marinone, T., et al.: Efficient computational nonlinear dynamic analysis using modal modification response technique. Mech. Syst. Signal Process. **31**, 67–93 (2012)
6. Marinone, T., Thibault, L., Avitabile, P.: Expansion of nonlinear system response using linear transformation matrices from reduced component model representations. In: Topics in Modal Analysis, vol. 7, pp. 743–769. Springer (2014)
7. Pingle, P., Niezrecki, C., Avitabile, P.: Full field numerical stress–strain from dynamic experimental measured data. In: Eighth International Conference on Structural Dynamics EURODYN, Leuven (2011)
8. Pingle, P., Avitabile, P.: Limited experimental displacement data used for obtaining full-field dynamic stress strain information. In: Linking Models and Experiments, vol. 2, pp. 201–217. Springer, New York (2011)
9. Pingle, P., Avitabile, P.: Prediction of full field dynamic stress/strain from limited sets of measured data. In: Structural Dynamics, vol. 3, pp. 883–895. Springer, New York (2011)
10. Pingle, P.: Prediction of full-field dynamic stress/strain from limited sets of measured data. In: Mechanical Engineering. University of Massachusetts Lowell (2010)
11. Carr, J.: Application of Dynamic Expansion from Limited Measurements for Full-Field Stress/Strain on Wind Turbine Blades. University of Massachusetts Lowell (2013)
12. Carr, J., et al.: Dynamic stress–strain on turbine blade using digital image correlation techniques part 1: static load and calibration. In: Topics in Experimental Dynamics Substructuring and Wind Turbine Dynamics, vol. 2, pp. 215–220. Springer (2012)
13. Carr, J., et al.: Dynamic stress–strain on turbine blades using digital image correlation techniques part 2: dynamic measurements. In: Topics in Experimental Dynamics Substructuring and Wind Turbine Dynamics, vol. 2, pp. 221–226. Springer (2012)
14. Carr, J., et al.: Predicting dynamic strain on wind turbine blade using digital image correlation techniques in conjunction with analytical expansion methodologies. In: Special Topics in Structural Dynamics, vol. 6, pp. 295–302. Springer (2013)
15. Harvie, J.: Computationally Efficient Reduced Order Models for Full Field Nonlinear Dynamic Strain Predictions, in Mechanical Engineering. University of Massachusetts Lowell (2013)
16. Harvie, J., Avitabile, P.: Computationally efficient nonlinear dynamic analysis for stress/strain applications. In: Special Topics in Structural Dynamics, vol. 6, pp. 89–108. Springer (2014)
17. Harvie, J., Avitabile, P.: Reduced order system model nonlinear response and expansion for full field results. In: RASD 2013 11th International Conference on Recent Advances in Structural Dynamics 1st–3rd July 2013 (2013)
18. Nonis, C., et al.: Development of full space system model modes from expansion of reduced order component modal information. In: Topics in Modal Analysis, vol. 7, pp. 353–367. Springer (2014)
19. Avitabile, P., Nonis, C., Obando, S.E.: System model modes developed from expansion of uncoupled component dynamic data. Strojniški vestnik-J. Mech. Eng. **60**(5), 287–297 (2014)
20. Nonis, C., Avitabile, P.: System model modes developed from expansion of uncoupled component dynamic data. In: Eleventh International Conference on Recent Advances in Structural Dynamics, Pisa, Italy (2013)
21. Obando, S.E., Avitabile, P.: Prediction of forced response on ancillary subsystem components attached to reduced linear systems. In: Dynamics of Coupled Structures, vol. 1, pp. 51–72. Springer (2014)
22. Obando, S.E., Avitabile, P., Foley, J.: Prediction of forced response using expansion of perturbed reduced order models with inexact representation of system modes. In: Special Topics in Structural Dynamics, vol. 6, pp. 13–34. Springer (2015)
23. Obando, S.E.: Use of expansion of highly reduced order models for the accurate prediction of full field dynamic characteristics in the forced response of linear and nonlinear systems and components. In: Mechanical Engineering. University of Massachusetts Lowell, Lowell, MA (2015)
24. Obando, S.E., Avitabile, P., Foley, J.: Prediction of nonlinear forced response on ancillary subsystem components attached to reduced linear systems. In: Nonlinear Dynamics, vol. 1, pp. 23–51. Springer International Publishing (2016)
25. Avitabile, P.: Twenty years of structural dynamic modification-a review. Sound Vib. **37**(1), 14–27 (2003)
26. Guyan, R.J.: Reduction of stiffness and mass matrices. AIAA J. **3**(2), 380–381 (1965)
27. O'Callahan, J., Avitabile, P., Riemer, R.: System equivalent reduction expansion process (SEREP). In: Proceedings of the 7th International Modal Analysis Conference. Union College Schenectady, NY (1989)
28. O'Callahan, J.C.: A procedure for an improved reduced system (IRS) model. In: Proceedings of the 7th International Modal Analysis Conference. Union College Press, Schenectady, NY (1989)
29. Butland, A., Avitabile, P.: A reduced order, test verified component mode synthesis approach for system modeling applications. Mech. Syst. Signal Process. **24**(4), 904–921 (2010)
30. Marinone, T., Butland, A., Avitabile, P.: A reduced model approximation approach using model updating methodologies. In: Topics in Modal Analysis II, vol. 6, pp. 625–636. Springer (2012)
31. Chipman, C., Avitabile, P.: Expansion of transient operating data. Mech. Syst. Signal Process. **31**, 1–12 (2012)
32. Chipman, C.C.: Expansion of Real Time Operating Deformations for Improved Visualization. University of Massachusetts Lowell (2009)
33. Allemang, R.J., Brown, D.L.: A correlation coefficient for modal vector analysis. In: Proceedings of the 1st International Modal Analysis Conference. SEM, Orlando (1982)

34. VanZandt, T.: Development of Efficient Reduced Models for Multi-Body Dynamics Simulations of Helicopter Wing Missile Configurations. University of Massachusetts Lowell (2006)
35. Avitabile, P., Callahan, J.O.: Techniques for forced response involving discrete nonlinearities. I-Theory. II-Applications. In: 10th International Modal Analysis Conference (1992)
36. Bathe, K., Wilson, E.: Stability and accuracy analysis of direct integration methods. Earthq. Eng. Struct. Dyn. **1**(3), 283–291 (1973)
37. Newmark, N.M.: A method of computation for structural dynamics. J. Eng. Mech. Div. **85**(3), 67–94 (1959)
38. Chung, J., Hulbert, G.: A time integration algorithm for structural dynamics with improved numerical dissipation: the generalized-α method. J. Appl. Mech. **60**(2), 371–375 (1993)
39. Hilber, H.M., Hughes, T.J., Taylor, R.L.: Improved numerical dissipation for time integration algorithms in structural dynamics. Earthq. Eng. Struct. Dyn. **5**(3), 283–292 (1977)
40. Truong, K., Avitabile, P.: Development of reduced order models to non-modeled regions. In: Special Topics in Structural Dynamics, vol. 6, pp. 1–11. Springer (2015)

Chapter 45
On the Behaviour of Structures with Many Nonlinear Elements

T. Rogers, G. Manson, and K. Worden

Abstract One of the most powerful methods currently available for the analysis of structural dynamics at high frequencies is Statistical Energy Analysis (SEA). The fundamental idea behind the method is that, at higher frequencies, so many modes are present in the response of the structure that individual modes cease to be resolvable and a simplified statistical order emerges in the response. Although the details of the context are very different to SEA, the current paper is motivated by it and provides a preliminary investigation into what happens when very many nonlinear elements are present in a structure under random vibration; the question being, does a simplified statistical order emerge as the influence of the nonlinearities increases? A number of case studies are provided based on computer simulation, arguing the case that order does indeed appear to emerge and a parallel with the SEA case is thus drawn.

Keywords Nonlinear structural dynamics • Random vibration • Emergent properties • Effective models

45.1 Introduction

As the use of numerical modelling techniques, such as Finite Element Analysis (FEA), becomes more commonplace as a key part of the design process, as opposed to physical testing, the requirement for reliability of the results produced increases. This is especially the case for high-value structures such as aircraft, bridges and offshore structures. This is not simply a matter of going to ever-increasingly complex models in the hope of modelling ever more detailed behaviour; it is also a matter of understanding the uncertainties inherent in the modelling process and quantifying the resulting uncertainty in predictions. These issues are particularly felt in the case of nonlinear structures and systems because of the very different types of behaviour they can exhibit. The understanding of nonlinear dynamic behaviour, therefore, is vital for producing reliable model predictions, from detailed time series behaviour to fatigue life estimates. Because even systems with very small numbers of degrees of freedom (DoFs) can exhibit complex behaviour, the focus of much academic research up to this point has been in understanding the behaviour of simple nonlinear systems with few nonlinearities present in low DoF cases [1].

In contrast to analytical work, the typical FEA model may have a very high number of degrees of freedom present, around which a great number of nonlinear elements could be located. (However, the models used in FEA will typically be used to identify only the lower frequency modes of a structure and, therefore it is usually considered a low frequency method.) For nonlinear systems there is a clear disconnect between what is possible with theoretical methods and what is possible with numerical methods. Another issue in modelling nonlinear systems is associated with the computational cost of calculating natural frequencies for very large system matrices. Even for linear systems, the cost of solving the eigenvalue problems may be high, even with modern approaches [2]; in order to compute nonlinear responses using FEA, explicit time step solvers are used for which the computational cost is extremely high. For linear FEA, one option is to compute reduced order models, and there are many techniques which can be considered reliable [3]; the situation is not so well-developed in the case of nonlinear models. There remains a great deal of work to be done on the general problem of understanding and modelling nonlinear systems with many DoFs and there remains a gulf between what can be modelled and what can be analysed mathematically.

One possibility that may allow analytical progress is that nonlinear systems with many DoFs and nonlinear elements may allow the use of *effective models* with low numbers of DoFs which are obtained by system identification or learning from data. The term ‘effective model’ is borrowed from theoretical particle physics where it is used to denote a model which does not encompass all of the detailed physics, but can nonetheless make predictions in certain regimes of energy.

T. Rogers • G. Manson • K. Worden (✉)
Dynamics Research Group, Department of Mechanical Engineering, University of Sheffield, Mappin Street, Sheffield S1 3JD, UK
e-mail: k.worden@sheffield.ac.uk

© The Society for Experimental Mechanics, Inc. 2016

J. De Clerck, D.S. Epp (eds.), *Rotating Machinery, Hybrid Test Methods, Vibro-Acoustics & Laser Vibrometry, Volume 8*,
Conference Proceedings of the Society for Experimental Mechanics Series, DOI 10.1007/978-3-319-30084-9_45

The analogy explored in this paper is a simplified effective model for nonlinear systems which might make predictions at certain levels of excitation. This analogy was motivated by test results communicated to the authors based on a modal test of a helicopter structure. When the structure was tested on the ground, the low-frequency response was dominated by clear modes as expected; however, the structure was revealed to be nonlinear because the resonance frequencies shifted when the level of excitation was increased. Somewhat surprisingly, when the structure was tested in flight at much higher levels of excitation, the modal structure disappeared and an almost flat power spectrum was obtained. Although the context is very different, the authors were reminded of the situation where Statistical Energy Analysis (SEA) applies. SEA can be used at high frequencies where the high modal densities render individual modes indistinguishable and a statistical order emerges which allows a much simplified analysis based on power flow between substructures [4, 5]. This observation led to the hypothesis considered in this paper, that a system with many nonlinearities may have a simplified response at levels of forcing where the nonlinearities are all fully excited. To stretch the analogy with SEA somewhat, the idea was to investigate if a sort of statistical order can emerge. To be perfectly clear, there is no intention here to propose a nonlinear theory of SEA; that is an entirely different problem which is being pursued effectively elsewhere [6].

The layout of the paper is as follows: in Sect. 45.2, the methods of numerical simulation used in the paper are discussed and benchmarked. In Sect. 45.3, the developed solver is used to simulate the behaviour of multi-DoF systems with many nonlinear elements. The paper is finalised with a short conclusions section.

45.2 Framework for Simulation

Although the methods used could apply to many different types of nonlinearity it was chosen that this investigation would focus on systems whose equations of motion take the form,

$$[m]\{\ddot{y}\} + [c]\{\dot{y}\} + [k]\{y\} + \{f(\{y\})\} = \{x(t)\} \tag{45.1}$$

i.e. the standard linear second order system with stiffness nonlinearities. To further simplify matters, only hardening cubic stiffness nonlinearities were included between DoFs via the vector $\{f(\{y\})\}$. In order to allow the inclusion of many nonlinear springs, a solver was constructed in Matlab [7] which could integrate systems of equations with moderate numbers of DoFs i.e. up to a few hundred. A number of different methods were assessed for solving the initial value problem, these included both fixed step and adaptive methods. Since the system response was to be measured against a simulated Gaussian white noise input, a fixed step method was adopted; This was due to the adaptive methods sometimes becoming ‘stuck’ when trying to take account of the large gradients in the random forcing. The integration method used was a 5th order Runge-Kutta method-Butcher’s Method [8]. Because the algorithm is not so common, the update equations are given here,

$$\begin{aligned}
y_{i+1} &= \frac{1}{90}\left(7k_1 + 32k_3 + 12k_4 + 32k_5 + 7k_6\right)h \\
k_1 &= f\left(t_i, y_i\right) \\
k_2 &= f\left(t_i + \frac{1}{4}h, y_i + \frac{1}{4}k_1 h\right) \\
k_3 &= f\left(t_i + \frac{1}{4}h, y_i + \frac{1}{8}k_1 h + \frac{1}{8}k_2 h\right) \\
k_4 &= f\left(t_i + \frac{1}{2}h, y_i - \frac{1}{2}k_2 h + k_3 h\right) \\
k_5 &= f\left(t_i + \frac{3}{4}h, y_i + \frac{3}{16}k_1 h + \frac{9}{16}k_4 h\right) \\
k_6 &= f\left(t_i + h, y_i - \frac{3}{7}k_1 h + \frac{2}{7}k_2 h + \frac{12}{7}k_3 h - \frac{12}{7}k_4 h + \frac{8}{7}k_5 h\right)
\end{aligned} \tag{45.2}$$

where the vector braces for the iterates y_i have been suppressed and it should be understood that the equations have motion have been cast in first-order form; the timestep is denoted h. For all the simulations run here, the initial conditions adopted were $\{y\} = \{\dot{y}\} = \{0\}$. A sampling frequency of 10 kHz was adopted throughout, yielding a timestep of 0.1 ms. All Frequency

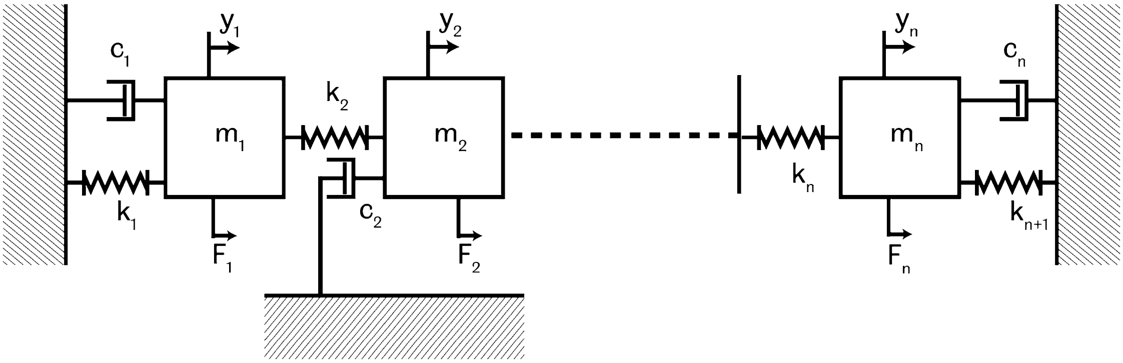

Fig. 45.1 *n*-DoF linear chain system which forms the basis for the analysis

Response Function (FRF) plots were generated by running 200 parallel simulations each for 100 s at 10 kHz with a different realisation of the random forcing. The FRF of each of the 200 time domain signals was computed after discarding the first 10 s of time domain data to remove transient behaviour. The FRF values were then averaged across the 200 realisations.

As a basis for investigating the effect of nonlinearities on high DoF systems, first a linear chain system (Fig. 45.1) was generated with a unit mass matrix, tri-diagonal stiffness matrix and damping matrix proportional to the mass matrix. All springs were set to have stiffness coefficient $k_i = k = 10^4\,\mathrm{N\,m^{-1}}$, damping coefficients were all set to $c_i = c = 5\,\mathrm{N\,s\,m^{-1}}$ and masses $m_i = m = 1\,\mathrm{kg}$. This prescription gives a damping ratio $\zeta = 0.025$ for an SDoF system which is 2.5 % of critical damping. The system matrices are thus $[m] = [I]$, $[c] = 5 \times [I]$ (where $[I]$ is the identity matrix) and $[k]$ is a tridiagonal matrix with the diagonal values equal to $2k$ and the off diagonal non-zero elements equal to $-k$. The linear system is well understood and its natural frequencies, mode shapes and frequency response can be computed straightforwardly.

The integration method was checked, initially, by numerically generating FRFs for known linear systems and comparing them with analytical predictions. First, a low DoF system was considered. For a three DoF system, generated with the parameters described previously, the numerical and theoretical results can be seen to be in excellent agreement for both the magnitude and phase components of the FRF (Fig. 45.2). When the number of simulated DoFs was increased to 30, the same agreement could be seen (Fig. 45.3).

The next benchmark assessed the ability of the modeller to handle nonlinear equations of motion. For this exercise, the chain system with three degrees of freedom was considered. A single cubic spring was added as discussed in [9]; for this system, the effect of the position of the cubic spring can be classified in three ways. System Type A is an asymmetric system, obtained when the nonlinearity is placed between mass one and ground, mass three and ground, mass one and two or mass two and three. In this case all modes will exhibit nonlinear behaviour. System Type B occurs when the nonlinear spring is between mass two and ground; in this case mode two is linear since mass two remains stationary in that mode. Type C is obtained if the nonlinear spring connects masses one and three; in this case modes one and three remain linear since masses one and three move in phase in these modes. The simulation results for these systems can be seen in Fig. 45.4. A further set of simulations considered the effects of harmonic forcing at 4 Hz on the systems with a single DoF or 30 DoF; the linear systems and those with a single cubic spring connecting mass one to ground were considered. When spectra were computed for the responses (Figs. 45.5–45.8), the expected variation in harmonic content with level of excitation was observed. This exercise concluded the benchmarking of the numerical solver.

45.3 Effect of Nonlinear Elements

With the conviction that the numerical modeller accurately represents the motion of the systems of interest, a routine was developed to investigate the effect of cubic nonlinearities being introduced into the system in multiple random locations. This allowed the number of nonlinearities in the system to be controlled by automatically generating a matrix with a given number of nonlinear springs equal in size to the linear stiffness matrix. The first set of investigations considered the effect of inserting a single cubic spring into the linear chain system.

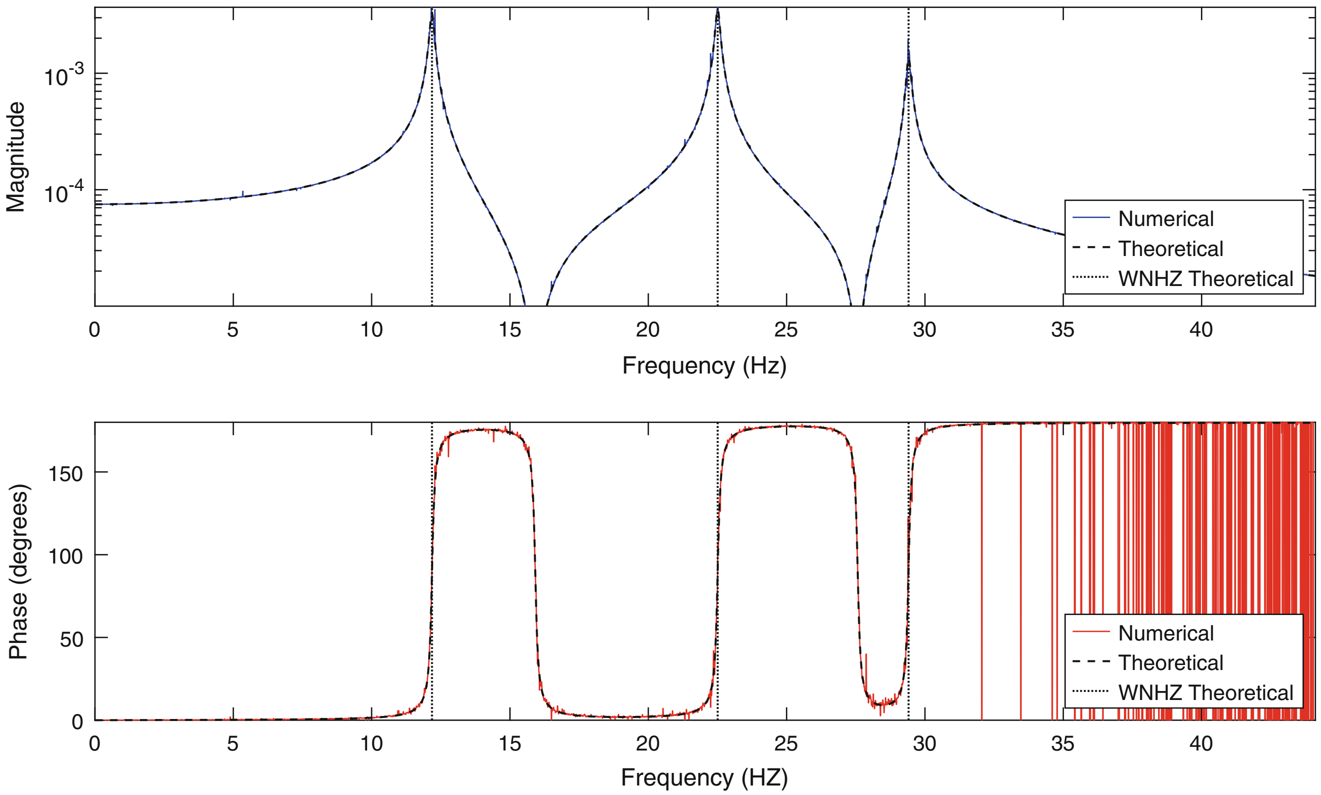

Fig. 45.2 Theoretical and numerical FRFs for 3DoF benchmark system. *Vertical lines* indicate the natural frequencies (WNHZ Theoretical)

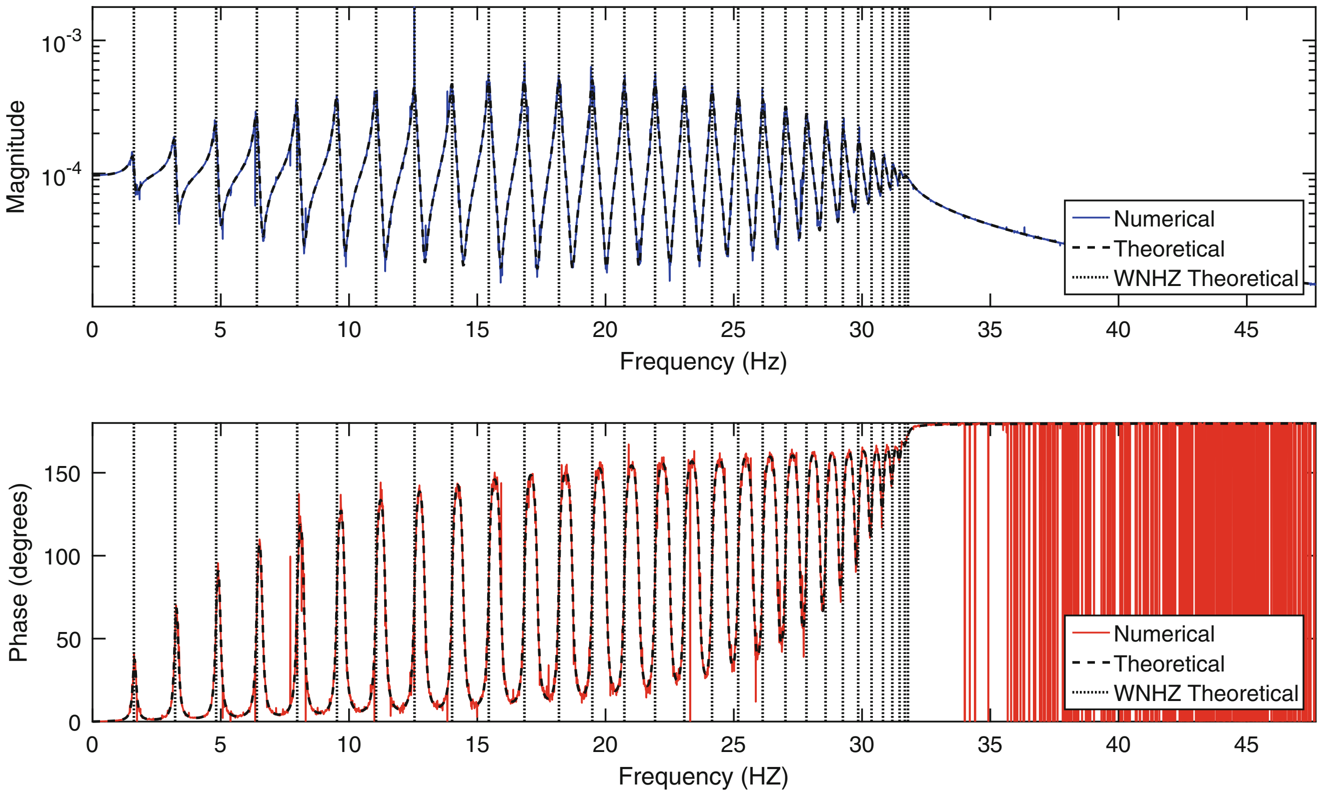

Fig. 45.3 Theoretical and numerical FRFs for 30DoF benchmark system. *Vertical lines* indicate the natural frequencies (WNHZ Theoretical)

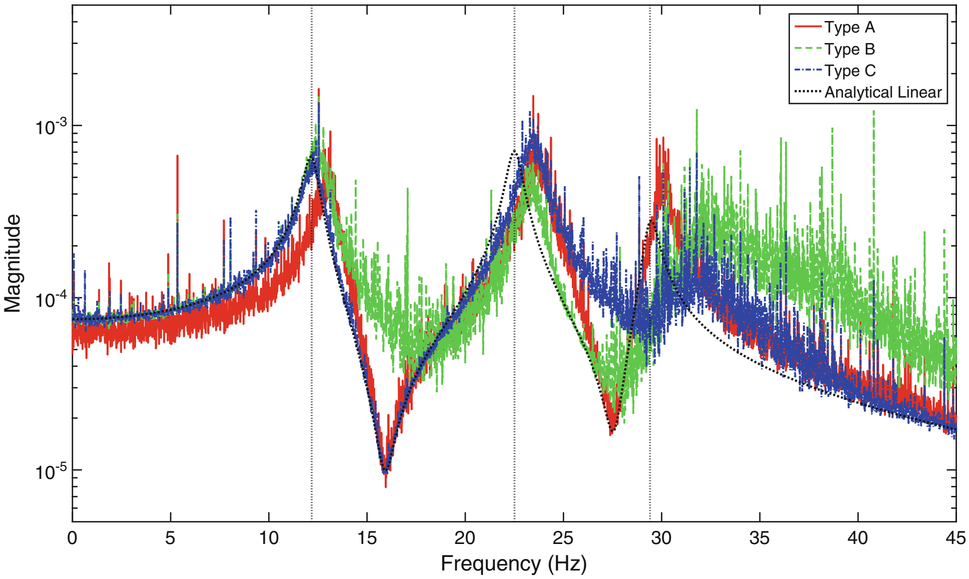

Fig. 45.4 Figure showing comparison of FRFs produced for three characteristic types of nonlinear 3DOF system

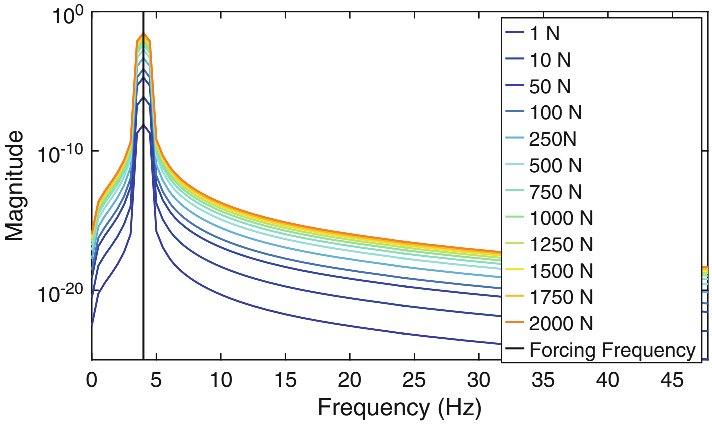

Fig. 45.5 Response of a SDOF linear system to varying magnitude 4 Hz sine wave input

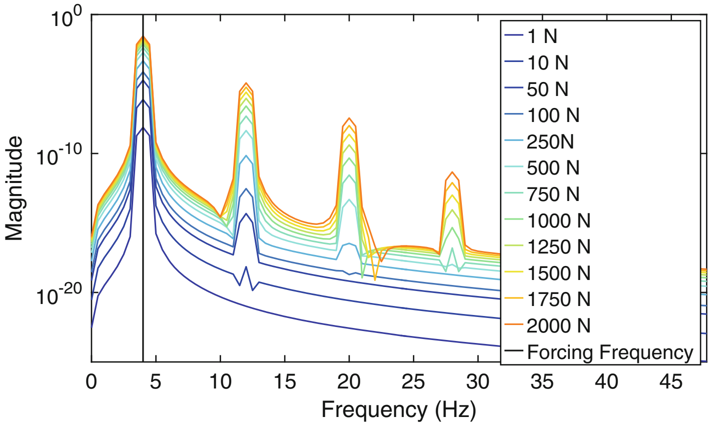

Fig. 45.6 Response of a SDOF system with a cubic nonlinearity at mass 1 to varying magnitude 4 Hz sine wave input

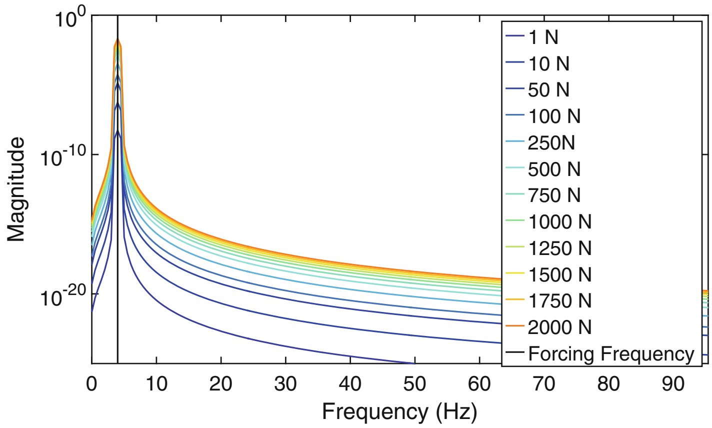

Fig. 45.7 Response of a 30DOF linear system to varying magnitude 4 Hz sine wave input

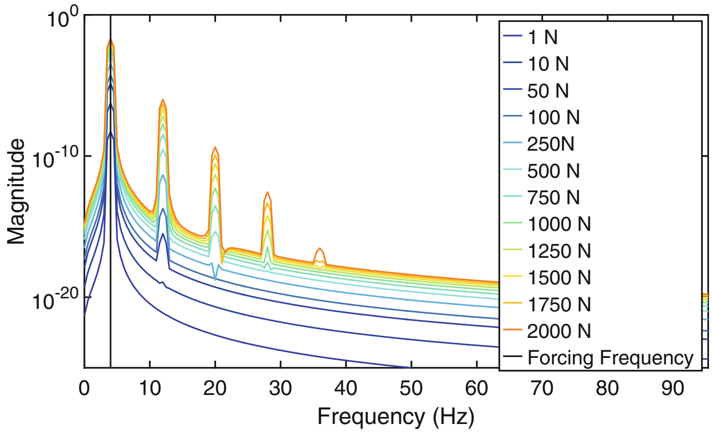

Fig. 45.8 Response of a 30DOF system with a cubic nonlinearity at mass 1 to varying magnitude 4 Hz sine wave input

45.3.1 Single Element Location

Three tests were run with a single nonlinearity randomly placed in the system. The nonlinear springs respectively connected masses 7 and 26, 1 and 6 and 22 and 26 in each of the three tests. The nonlinear coefficient k_3 of these springs was initially set to a constant value at $10^4\,\mathrm{N\,m^{-3}}$. First of all, the responses were obtained with an increasing magnitude of Gaussian white noise forcing. For the first position, the effect of the nonlinearity can be seen as the forcing is increased (Fig. 45.9); the linear modal structure seen at low forcing is clearly disrupted by the presence of the nonlinear spring between masses seven and 26. Even at very high magnitude there is still a clear modal structure; many distinct peaks can be clearly seen.

The results for the other two positions are shown in Figs. 45.10 and 45.11. It is clear that even when there is only a single nonlinearity in the system, the location of that nonlinearity has a large effect on the system response. This makes sense; if a nonlinear spring connects two masses that move in phase for many of the modes, there will be less overall distortion, even with very high forcing. If the nonlinear spring connects two masses that have low relative displacement in many of the modes there will be minimal distortion at lower excitations, but with increased excitation the nonlinear behaviour will become evident.

It is also clear that the presence of a single nonlinear element in a system with many DoFs is inadequate to mask or ‘wash out’ the modal structure as was observed in the helicopter test mentioned in the introduction. It was next investigated whether the introduction of many more nonlinear elements to the system would lead to masking of the modal structure; a form of statistical order emerging where the effects of the nonlinearities at many points in the structure would interact leading a simpler FRF.

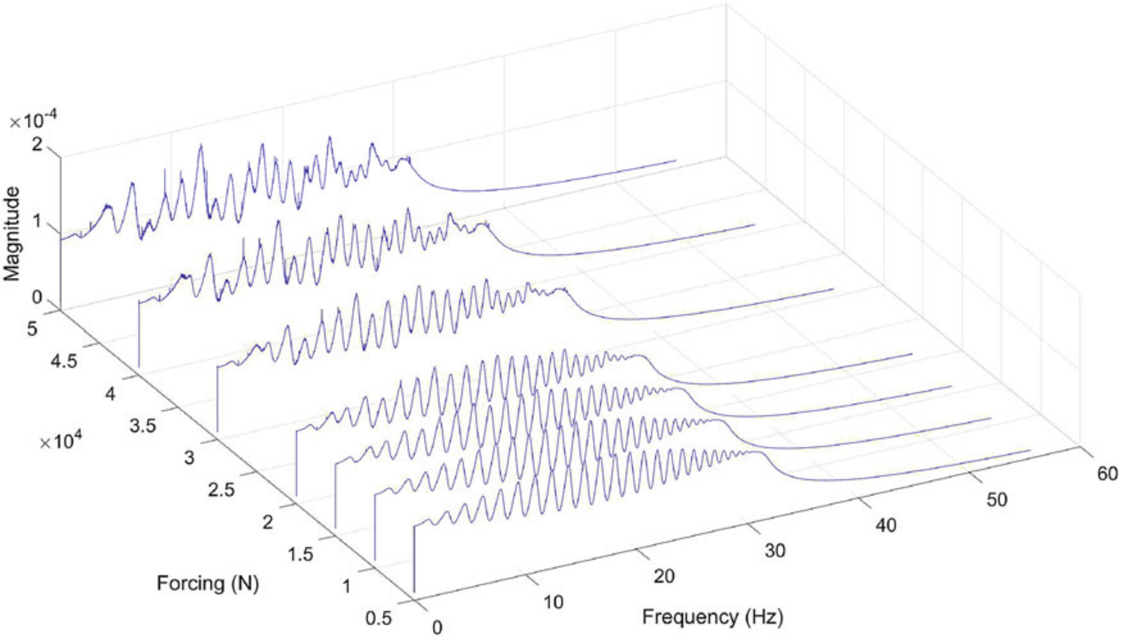

Fig. 45.9 Effect on the FRF of a single cubic spring with coefficient $k_3 = 10^4$ N m^{-3}, positioned between masses 7 and 6, for varying magnitude of Gaussian white noise forcing

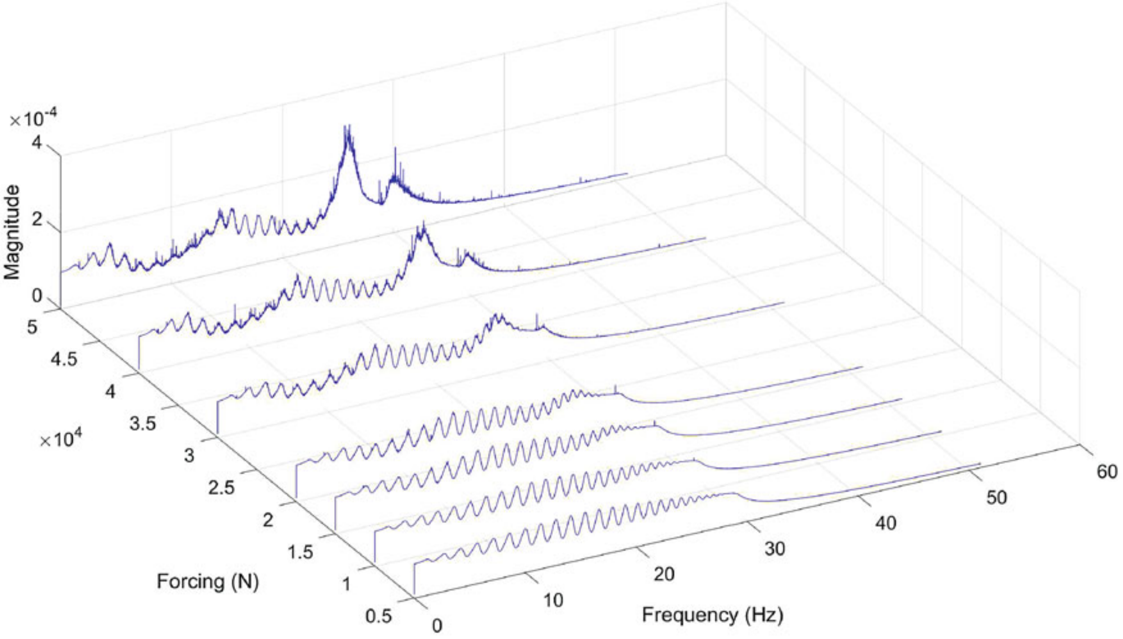

Fig. 45.10 Effect on the FRF of a single cubic spring with coefficient $k_3 = 10^4$ N m^{-3}, positioned between masses 1 and 6, for varying magnitude of Gaussian white noise forcing

45.3.2 Multiple Nonlinearites

Simulations were next run by adding randomly distributed nonlinear cubic springs to the underlying linear chain system. Systems containing 30, 50 and 100 nonlinear springs were investigated initially with a variable magnitude forcing and fixed k_3 values; then with fixed forcing and variable k_3. The results presented here will be for the simulations with increasing k_3 (Figs. 45.12, 45.13, and 45.14).

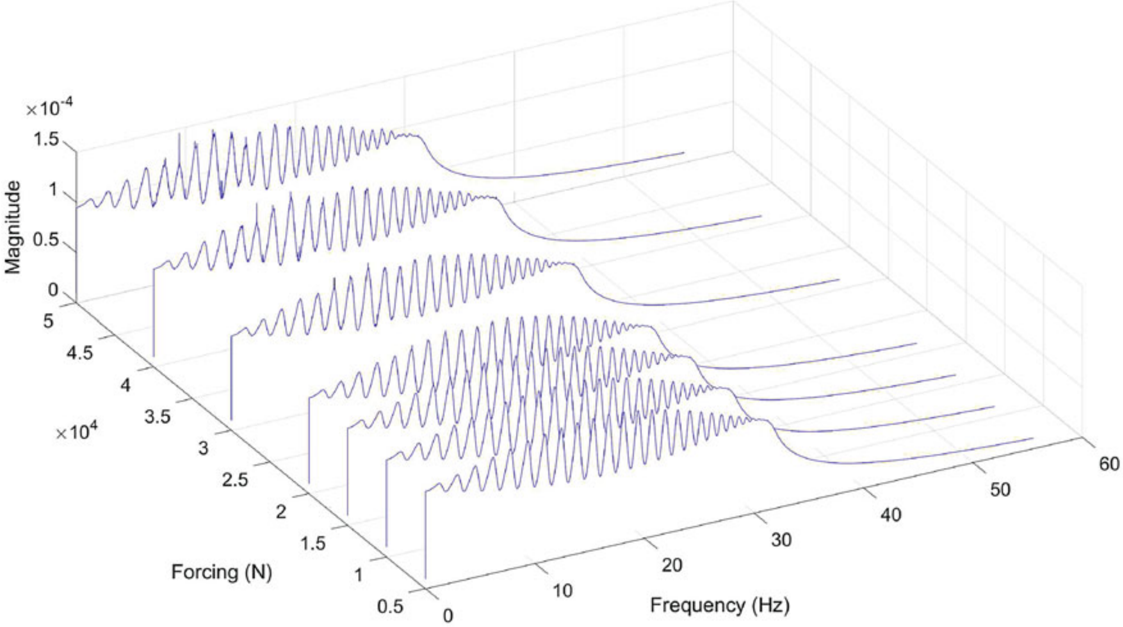

Fig. 45.11 Effect on the FRF of a single cubic spring with coefficient $k_3 = 10^4\,\mathrm{N\,m^{-3}}$, positioned between masses 22 and 26, for varying magnitude of Gaussian white noise forcing

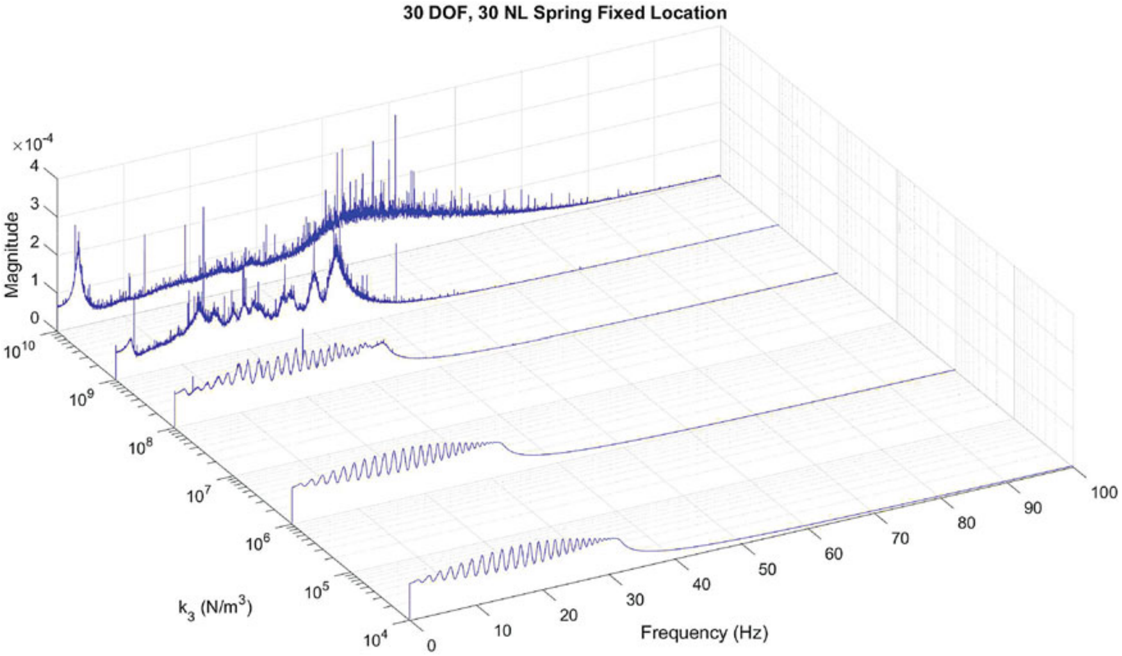

Fig. 45.12 FRF of response at mass 1 for Gaussian random forcing of 100 N on a 30 DoF linear chain system with 30 cubic nonlinearities randomly located in the system. The value of k_3 is increased and the modal structure of the system is clearly removed as the effect of the nonlinearity increases

Considering Fig. 45.12, there is a clear modal structure at low values of k_3. This structure closely resembles that of the underlying linear system seen in Fig. 45.3; it may be inferred that the presence of the nonlinearities in the system are having little effect on the modal behaviour. With increasing coefficient size, distortion to the linear modal structure becomes apparent by $k_3 = 10^8\,\mathrm{N\,m^{-3}}$; the effect is a complete disruption of the linear modal structure by $k_3 = 10^9\,\mathrm{N\,m^{-3}}$ and by $k_3 = 10^{10}\,\mathrm{N\,m^{-3}}$ it has become almost impossible to distinguish more than two ‘resonance’ peaks: one at low frequency and one at high.

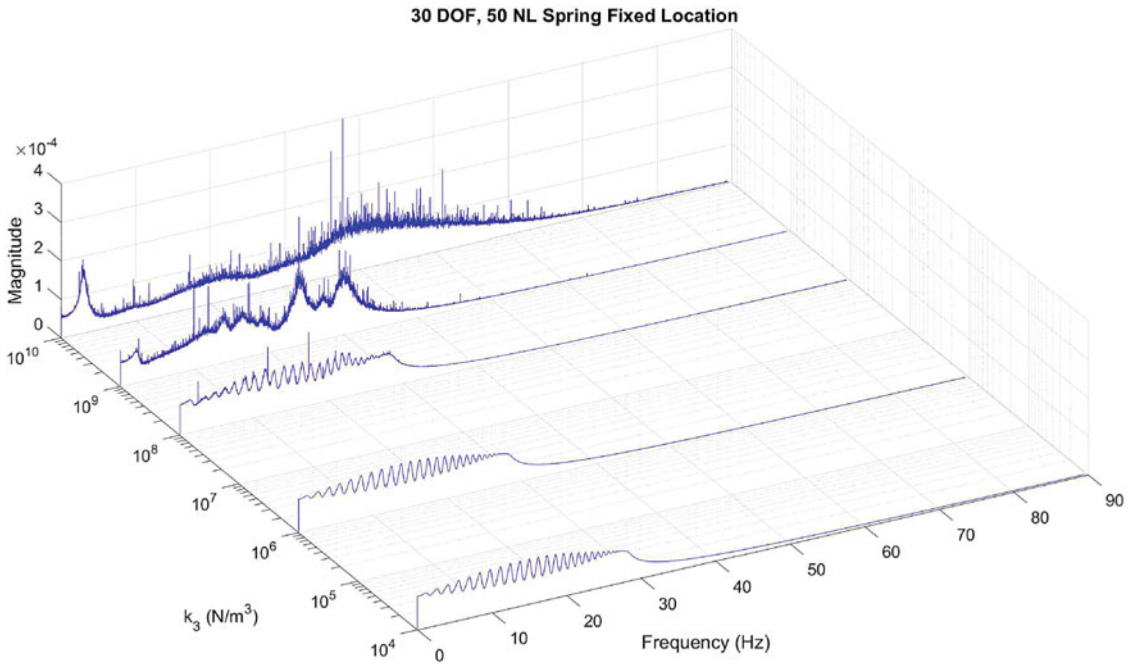

Fig. 45.13 FRF of response at mass 1 for a Gaussian random forcing of 100 N on a 30 DoF linear chain system with 50 cubic nonlinearities randomly located in the system. The value of k_3 is steadily increased as before

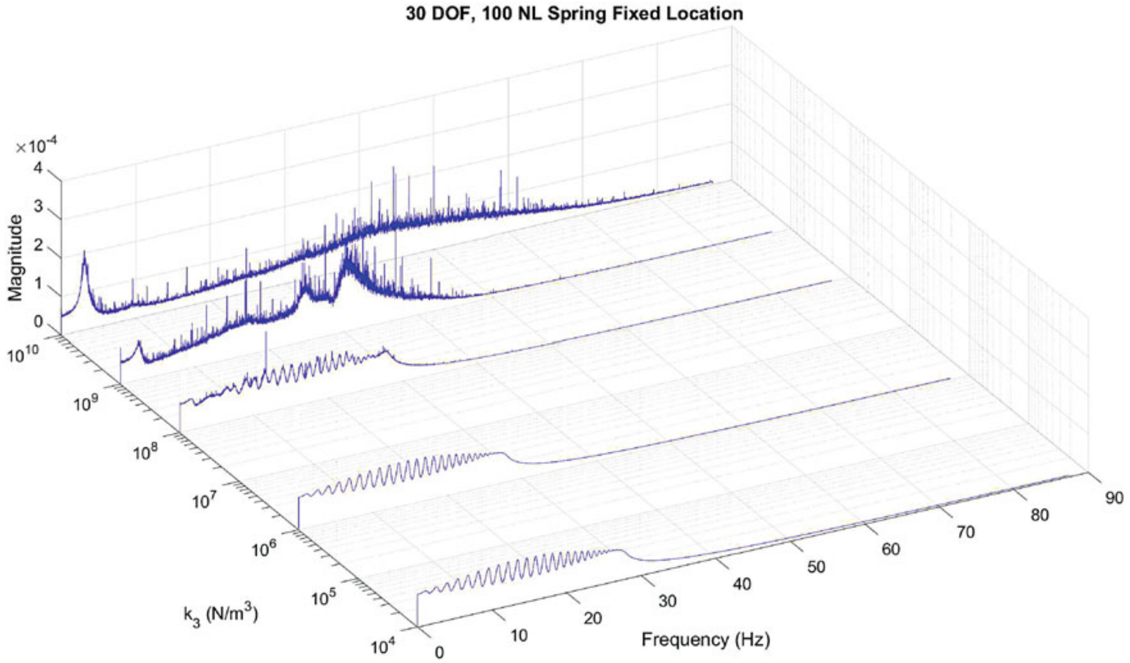

Fig. 45.14 FRF of response at mass 1 for a Gaussian random forcing of 100 N on a 30 DoF linear chain system with 100 cubic nonlinearities randomly located in the system. The value of k_3 is steadily increased as before

It is therefore seen that, as the nonlinear effects in the system increase, the linear modal structure is washed out, with the FRF tending towards only two identifiable peaks. A significant low frequency peak is seen close to the first natural frequency of the linear system and another peak is seen at frequencies significantly above the highest natural frequency of the underlying linear system. It appears that the action of the nonlinearities is to channel energy up and down the spectrum, washing out the linear modal structure, it is this washing out that may allow parallels to be drawn with SEA and opens up the possibility of using average energies to understand response across all frequency ranges.

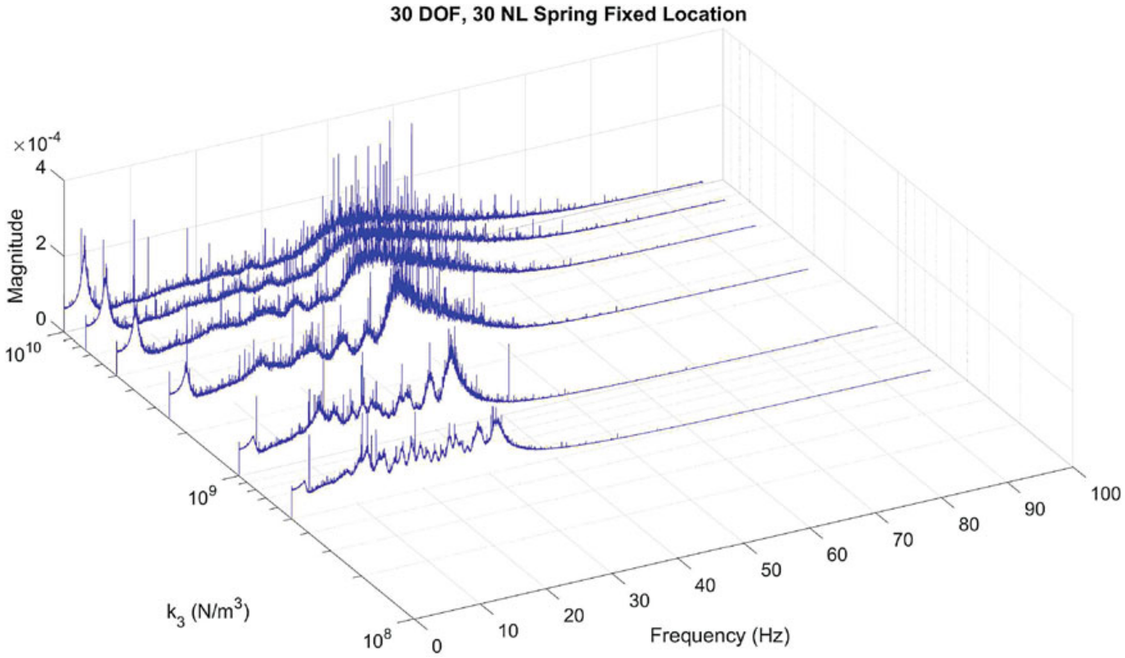

Fig. 45.15 FRF generated in the same manner as Fig. 45.12 investigating $5 \times 10^8 < k_3 < 1 \times 10^{10}\,\mathrm{N\,m^{-3}}$

The hypothesis that increasing the number of nonlinearities in the system would amplify this effect can be supported by the results shown in Figs. 45.13 and 45.14. With increasing numbers of nonlinearities in the system, the degradation of linear modal structure happens to a greater extent and at a lower value of k_3. There is potentially a simple physical interpretation of the low frequency behaviour seen in the FRF plots; the build up of energy around the first natural frequency of the system is representative of the system stiffening to the point of 'locking up' with all the masses moving in phase.

In all three cases the transition, from structure with many clearly visible peaks to a situation where the structure is washed out, occurs in the range $10^8 < k_3 < 10^{10}\,\mathrm{N\,m^{-3}}$. In order to observe the change in a little more detail, simulations were run with a number of k_3 values in this range. The results of these additional runs are shown in Figs. 45.15, 45.16, and 45.17. The closer inspection of the transition away from distinct modal structure shows more clearly the movement of energy towards the ends of the spectrum. The lower frequency modes, except the first, appear to be the first to be washed out by the increasing effect of the nonlinearities.

These plots show more clearly the effect of the increased number of nonlinearities in the system. For the cases with 30 or 50 nonlinearities (Figs. 45.15 and 45.16) more remnants of the linear modal structure can be seen even at very high values for k_3. In addition to this, the higher frequency peak becomes flatter in the presence of an increased number of nonlinearities. Interestingly, on close inspection, the two surviving peaks at high levels of nonlinearity both show the behaviour of an SdoF Duffing oscillator system using statistical linearisation i.e. with increasing nonlinearity, the peaks shift upward in frequency and down in magnitude.

A number of further simulations were run to confirm that the effects here were genuinely an effect of the increased nonlinearity in the system and not artefacts of the solver or the specific realisations of the nonlinear spring positions. These runs considered different realisations of the random spring positions and showed that the results were insensitive to the realisations as long as many springs were added.

45.4 Conclusions

The results shown in this paper demonstrate that for a system under random excitation with many nonlinear components, when those components are sufficiently excited, the underlying linear modal structure of the system is largely 'washed out' by nonlinear effects. Given a sufficient number of nonlinearities this appears to lead to a simplified statistical order in the

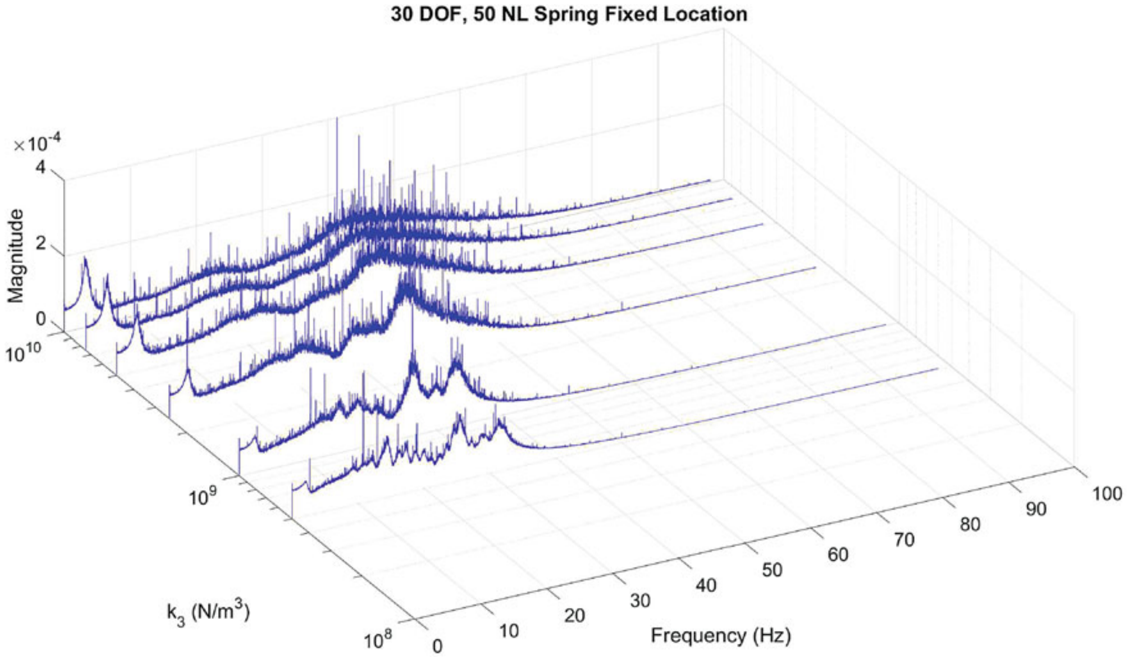

Fig. 45.16 FRF generated in the same manner as Fig. 45.13 investigating $5 \times 10^8 < k_3 < 1 \times 10^{10}\,\mathrm{N\,m^{-3}}$

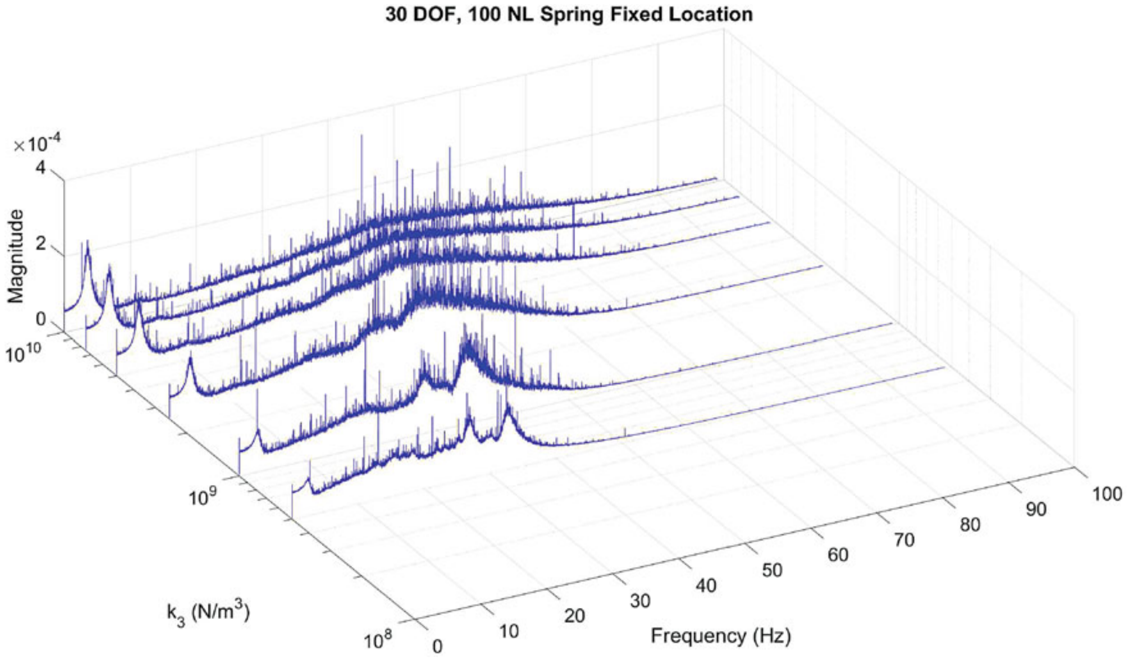

Fig. 45.17 FRF generated in the same manner as Fig. 45.14 investigating $5 \times 10^8 < k_3 < 1 \times 10^{10}\,\mathrm{N\,m^{-3}}$

system from which analogies may potentially be drawn with methods such as SEA. This order emerges more readily with increasing numbers of nonlinearities in the system and the positions of those nonlinearities become less significant as the number increases. It is very clear that this paper has only scratched the surface of this issue and a great deal of further work remains to be done to confirm the results presented here and to begin the process of theoretical explanation.

References

1. Worden, K., Tomlinson, G.R.: Nonlinearity in Structural Dynamics: Detection, Modelling and Identification. Institute of Physics Publishing, London (2001)
2. Lanczos, C.: An Iteration Method for the Solution of the Eigenvalue Problem of Linear Differential and Integral Operators. United States Government Press Office, Washington, DC (1950)
3. Guyan, R.J.: Reduction of stiffness and mass matrices. AIAA J. **3**, 380–380 (1965)
4. Lyon, R.H.: Statistical Energy Analysis of Dynamical Systems: Theory and Applications. MIT, Cambridge (1975)
5. Lyon, R.H.: Theory and Application of Statistical Energy Analysis. Elsevier, Amsterdam (2014)
6. Spelman, G.M., Langley, R.S.: Statistical energy analysis of nonlinear vibrating systems. Phil. Trans. R. Soc. A 2015 373 20140400; DOI: 10.1098/rsta.2014.0400, **373** (2015)
7. The Matlab Primer. The Mathworks (2015)
8. Chapra, S.C., Canale, R.P.: Numerical Methods for Engineers, 5th edn. McGraw-Hill, New York (2010)
9. Hickey, D., Worden, K., Platten, M.F., Wright, J.R., Cooper, J.E.: Higher-order spectra for identification of nonlinear modal coupling. Mech. Syst. Signal Process. **23**, 1037–1061 (2009)

Chapter 46
Estimation of Instantaneous Speed for Rotating Systems: New Processing Techniques

Achyut Vemuri, Randall J. Allemang, and Allyn W. Phillips

Abstract One of the most important parameters in the analysis of rotating systems is the instantaneous speed or RPM. The estimates from a tachometer data generally contain rapid unacceptable fluctuations. A new technique called the **Adaptive n^{th} Pulse Algorithm** is presented in this paper which addresses the fluctuations in values from the conventional RPM estimation procedure through a root cause analysis. In addition to significantly improving the signal to noise ratio of the curve, this method has the advantage of transforming the rotation speed from being a function of angle of rotation to a function of time. An alternative approach has been developed by B&K called the **Autotracker Algorithm** where instantaneous speed is estimated using Bayesian statistics from measured accelerometer or microphone data thereby avoiding the need for tachometers. In the current paper, a smart algorithm built upon this Autotracker Algorithm has been developed which is more robust and as much as 100 times faster. Analysis of data with crossovers between orders and dominant natural frequencies is possible using a reprocessing step in this algorithm. Data with very high slew rate and speeds reaching 25,000 RPM has been shown to be processed in under 5 sec. Comparison is made between the Bayesian and n^{th} pulse estimates for several data sets to show that the results are consistent with each other. Examples include data from a rotor rig, a 6 – cylinder engine powertrain and a vacuum cleaner.

Keywords Tachometer • Instantaneous RPM • Bayesian • n^{th} Pulse • Harmonics

Nomenclature

$\{\theta\}$	Set of parameters to be estimated
ω	Frequency in rad/s
D	Acquired data
σ	Noise variance
M_i, I	Model chosen
e_n	Error in the estimation of the n^{th} data point
t	Time recording or sample
$B_{2n-1},\ B_{2n}$	Coefficients corresponding to frequency ω_n
d_i	The i^{th} data point
N, BS	Data block size
ω^l	Frequency estimate of the l^{th} data block
T	Total time sampled
Δf	Frequency resolution
Δt	Discrete sampling time
n	Number of pulses skipped
F_{samp}	Sampling frequency
F_{nyq}	Nyquist frequency
FFT	Fast Fourier Transform
RPM	Rotations per minute

A. Vemuri (✉) • R.J. Allemang • A.W. Phillips
Structural Dynamics Research Lab, University of Cincinnati, Cincinnati, OH 45221, USA
e-mail: vemuriat@mail.uc.edu; vemuri.achyut@gmail.com; Randy.Allemang@uc.edu; Allyn.Phillips@uc.edu

© The Society for Experimental Mechanics, Inc. 2016

J. De Clerck, D.S. Epp (eds.), *Rotating Machinery, Hybrid Test Methods, Vibro-Acoustics & Laser Vibrometry, Volume 8*,
Conference Proceedings of the Society for Experimental Mechanics Series, DOI 10.1007/978-3-319-30084-9_46

46.1 Introduction

Dedicated tachometers like photo probes, magnetoresistive, magnetic and Hall effect sensors are typically used along with post processing for RPM estimation at any arbitrary time. The signal obtained from tachometers is a waveform of varying frequency depending on the rotating speed. Post processing involves fitting a spline to the initial speed estimate to eliminate any rapid fluctuations that are not physically possible due to the inertia of the system. The instantaneous speed estimation and the following curve fit process is described in detail in [1]. Curve fitting might generate a speed profile consistent with the inertia of the system but it is a mathematical approximation relying heavily on the control parameters used and not governed by the physics of the system. The inertia control is applied through brute force by shaving the data to remove any outlier data points. Depending on the data set, it might be very difficult to attain a curve fit which stays within bounds of the fluctuating initial estimate.

The **Adaptive *n*th Pulse Algorithm** was developed as an attempt to minimize the fluctuations in the estimate while using the same formulation as in the conventional estimate. On revisiting the formulation, it can be concluded that the fluctuations in speed come from small but significant errors in recording the zero crossings during interpolation. In order to minimize the effect of these errors on the formulation, several pulses can be skipped so as to maintain a larger time interval between samples. The underlying assumption is that there is very little variation in the true speed over the duration of the pulses skipped. A process by which the signal to noise ratio of the curve can be improved is described. This results in a data that is more conducive to curve fitting than the traditional raw estimation method (conventional). An averaging technique for a smooth instantaneous speed profile without the need for a curve fit is also proposed.

The hardware (tachometer) based approach to instantaneous speed estimation presents disadvantages like cost, space constraints and unsuitable operating conditions in addition to the curve fitting required. It is well known that the orders or harmonics of a rotating system, which are caused due to geometry and/or imperfections in the system, are responses related to the rotating speed which is the forcing function. By observing a time spectral map, it can be clearly seen that the path traced by the dominant harmonics through the data blocks is similar to the RPM profile. Hence, with some prior knowledge of dominant orders in the system and operating speed conditions, the instantaneous speed can be extracted from measured vibration/acoustic data by tracking these orders [2]. Bayesian statistics provides an intuitive way of estimating parameters from spectral data based on the laws of probability. In the present context, the dominant frequencies in a given time series can be estimated using Bayesian inference. The tool has come back into prominence as the computational power increased over recent decades.

46.2 Smart Bayesian Algorithm

The Baye's rule as applied to data blocks and parameter estimation is given by,

$$P\left(\theta \middle| D,\ M_i\right) = \frac{P\left(D \middle| \theta,\ M_i\right) * P\left(\theta \middle| M_i\right)}{P\left(D \middle| M_i\right)} \tag{46.1}$$

Any prior knowledge about the system can be included in the model as appropriate [2] (e.g. dominant harmonics, rate of change of speed, etc.).

For a single dominant frequency model [3], 'M_i' or 'I' is defined by,

$$I \Rightarrow f(t) = B_1 \cos(\omega t) + B_2 \sin(\omega t) \tag{46.2}$$

Then, with a uniform prior [4], the posterior probability can be given as [5],

$$P\left(\omega \middle| D, I\right) \propto \left[1 - \left(\frac{2C(\omega)}{N\overline{d^2}}\right)\right]^{\frac{2-N}{2}} \tag{46.3}$$

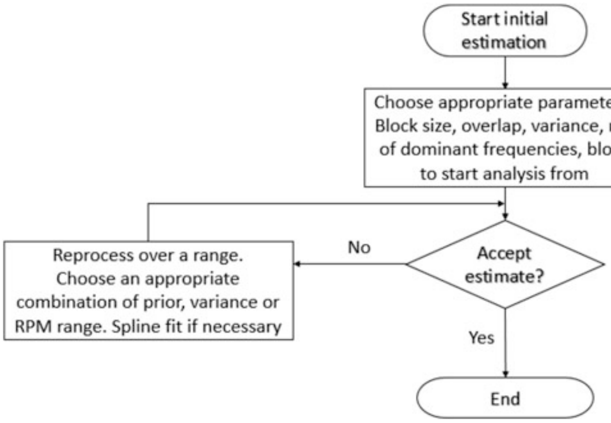
Start initial estimation
Choose appropriate parameters: Block size, overlap, variance, no. of dominant frequencies, block to start analysis from
Accept estimate?
No
Reprocess over a range. Choose an appropriate combination of prior, variance or RPM range. Spline fit if necessary
Yes
End

Fig. 46.1 Flow chart illustrating the Bayesian RPM estimation algorithm

where $C(\omega)$ is the Schuster Periodogram [6] and,

$$\overline{d^2} = \frac{1}{N}\sum_{i=1}^{N} d_i^2 \tag{46.4}$$

$$C(\omega) = \frac{1}{N} * \left[R(\omega)^2 + I(\omega)^2\right] \tag{46.5}$$

$$R(\omega) = \sum_{i=1}^{N} d_i \cos(\omega t_i)\,;\; I(\omega) = \sum_{i=1}^{N} d_i \sin(\omega t_i) \tag{46.6}$$

$$P\left(\omega_0^l \left|\omega_0^{l-1}, \omega_0^{l-2}\right.\right) = \frac{1}{\sqrt{2\pi\sigma^2}} \exp - \frac{\left(\omega_0^l - 2\omega_0^{l-1} + \omega_0^{l-2}\right)^2}{2\sigma^2} \tag{46.7}$$

Equation (46.7) represents a prior function which is a modification of the one described in [2]. It can be multiplied by the likelihood function to weigh the frequencies surrounding the estimates of the two previous data blocks more than the others. To initiate the algorithm, a uniform prior can be used for the first two blocks. The speed of rotation is estimated as the frequency from the set $\{\omega\} = 0 : resolution : F_{nyq}$ which maximizes the posterior probability. Straight forward application of this formulation might not yield satisfactory results. An algorithm which overcomes the problems associated is given in Fig. 46.1.

To initiate the process, a data block in which the order to be tracked is dominant is to be chosen. The estimation procedure then starts from this data block with a uniform prior and proceeds from there to the beginning and to the end data blocks with the prior (Eq. 46.7) applied. An important feature of the algorithm is the ability to reprocess over a subset of the data with different control parameters. Also, to reduce contamination from frequencies that are far away from the order of interest, the user can choose to limit the estimation to a subset of the frequency range $\{\omega\}$. If some regions of the curve cannot be improved further, a spline interpolation can be used. The instantaneous speed curve is overlaid on the time spectral map at every step to give the user a feedback as to which regions require further processing. The following is an illustration of the process for a vacuum cleaner data.

Figure 46.2 shows the initial tachometer estimate and the time spectral map. The results obtained by applying the Bayesian algorithm discussed previously are shown in Figs. 46.3, 46.4, 46.5, and 46.6.

The variance chosen was 0.15 and the initiation block was chosen as the middle block.

While a smooth curve with satisfactory results is obtained from this algorithm, the total processing time is too high to justify the elimination of tachometers. The inertia of the system can be used to advantage in order to reduce the processing time. As the speed can only change by a small value from one block to the next (when taken with high overlap), the estimation procedure can be limited to frequency range $\{\omega\} = \omega^{previous\ block} - x\ :\ \omega^{previous\ block} + x$. Here, '$x$' is the number of frequency lines chosen by the user. This facilitates quick processing while making the algorithm more robust as there will be minimal contamination from frequencies that are not close to the order of interest. The computation time for the vacuum cleaner data with the single dominant frequency model was brought down from 104 s to about 1.1 s using the same processing parameters by applying the smart algorithm. The results are identical to those from analysing the entire frequency range.

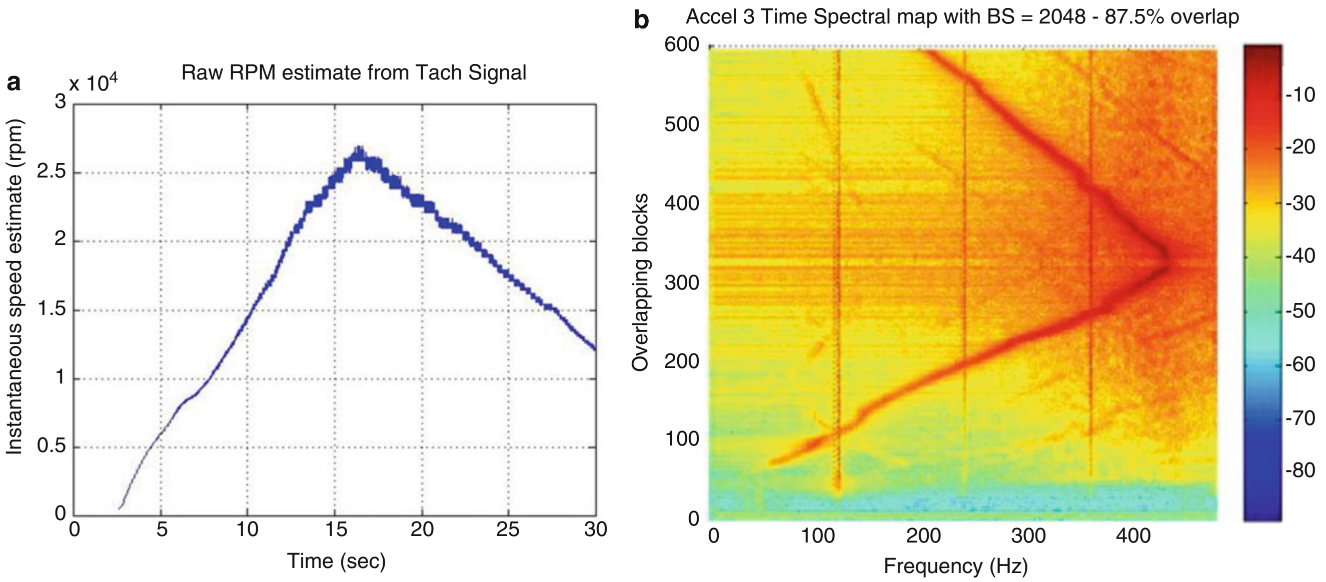

Fig. 46.2 Vacuum cleaner data—(**a**) initial tachometer estimate and (**b**) time spectral map

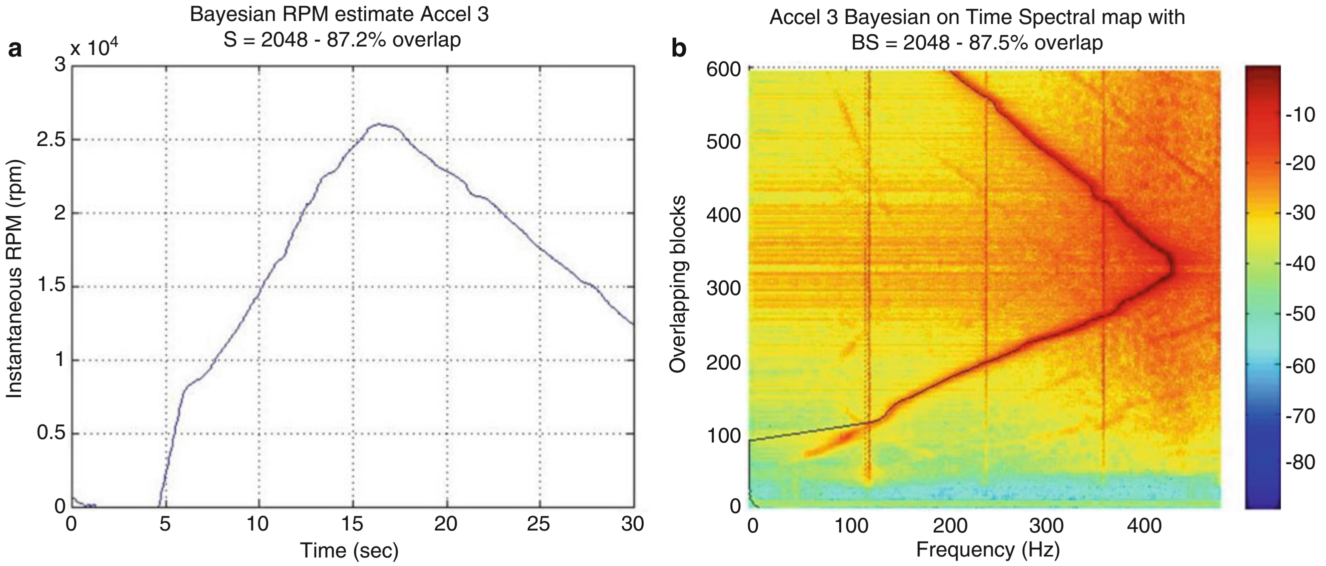

Fig. 46.3 (**a**) Bayesian estimate set off-track and (**b**) Bayesian estimate over the time spectral map

46.3 New Technique: Adaptive n^{th} Pulse Algorithm

Though the Bayesian estimation provides many benefits, there are several shortcomings due to which tachometers are required. For real time analysis (for example in a vehicle), a sophisticated computer is needed to analyse the data which might not be viable financially. Tachometers have become an integral part of the industry and do not require a skilled operator. As such, the Bayesian estimate would find more applications in the laboratory and academics for fault diagnosis or other similar applications. It would be beneficial to develop better estimation procedures from tachometers for the sake of practical applications in industry.

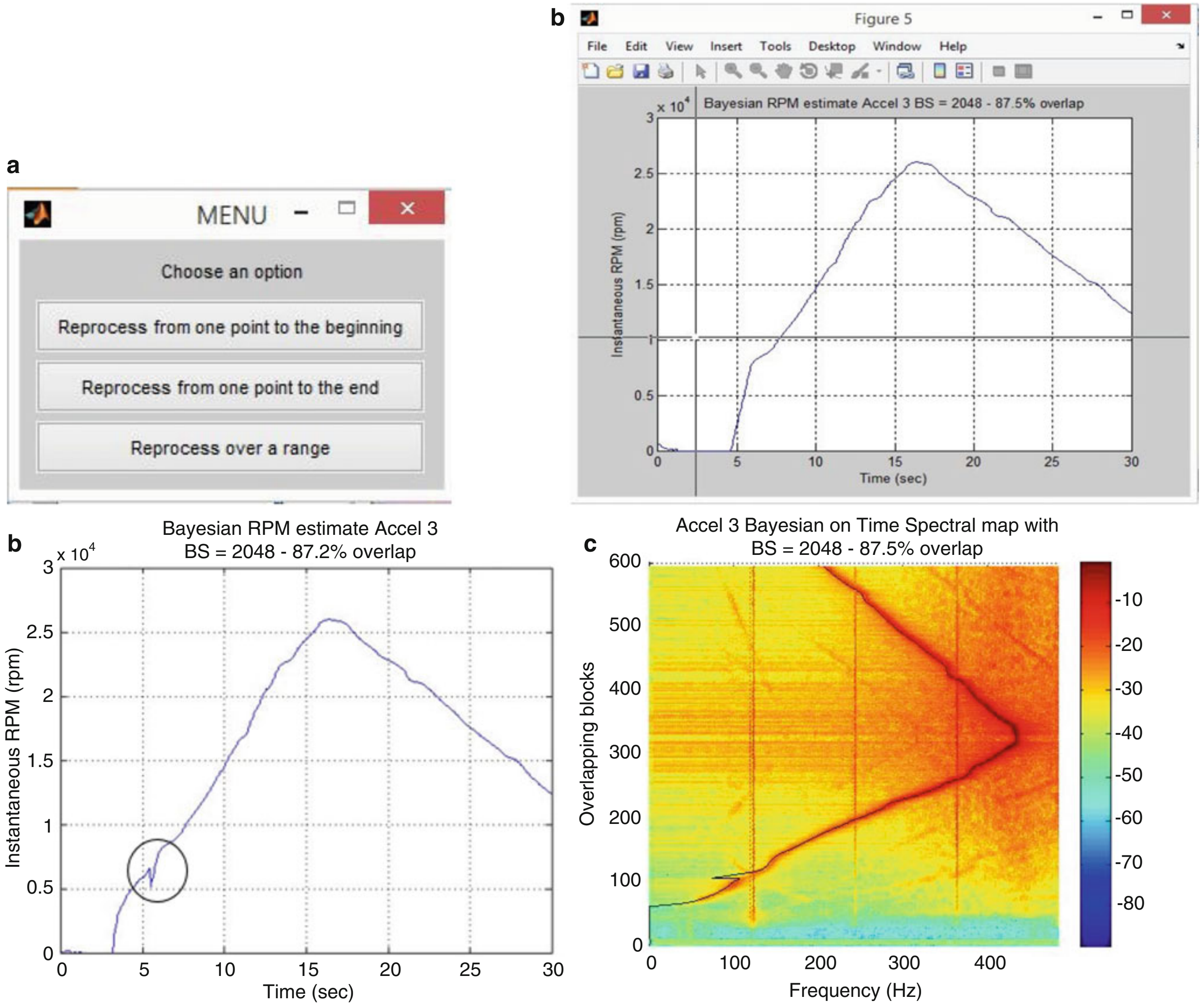
a
MENU
Choose an option
Reprocess from one point to the beginning
Reprocess from one point to the end
Reprocess over a range
b
Figure 5
File Edit View Insert Tools Desktop Window Help
Bayesian RPM estimate Accel 3 BS = 2048 - 87.5% overlap
x 10^4
Instantaneous RPM (rpm)
Time (sec)
b
Bayesian RPM estimate Accel 3
BS = 2048 - 87.2% overlap
x 10^4
Instantaneous RPM (rpm)
Time (sec)
0 0.5 1 1.5 2 2.5 3
0 5 10 15 20 25 30
c
Accel 3 Bayesian on Time Spectral map with
BS = 2048 - 87.5% overlap
Overlapping blocks
0 100 200 300 400 500 600
Frequency (Hz)
0 100 200 300 400
-10 -20 -30 -40 -50 -60 -70 -80

Fig. 46.4 (**a**) User input, (**b**) choosing a range to reprocess, (**c**) reprocessed estimate and (**d**) reprocessed estimate over the time spectral map

To understand the problem, it is necessary to revisit the formula used for Instantaneous RPM estimation [1].

$$\text{Instantaneous RPM} = \frac{60}{t2 - t1} \times (n + 1) \tag{46.8}$$

Here ‘n’ denotes the number of pulses between zero crossings considered. The values $t2$ and $t1$ are the zero crossings of two consecutive pulses that are approximated by a linear interpolation between two points which are ‘Δt’ apart in time. Hence the error that can occur in the estimation of a zero crossing ranges across $\pm\Delta t/2$. When this error is a significant percentage of the absolute value of time difference, the corresponding speed values can fluctuate across an unacceptable range. This is basically a sampling problem and the RPM curve when observed closely shows similar characteristics to bit noise. Figure 46.7 shows a zoomed in version of the data from the vacuum cleaner and the corresponding fluctuations.

Consider a set of consecutive time instances recorded at zero crossings at around 24,500 RPM. $t(2725) - t(2724) = 0.00244\ s$, $t(2726) - t(2725) = 0.00238\ s$ and so on. Corresponding RPM estimates are 24,599 RPM and 25,249 RPM assigned at 15.2629 s and 15.2653 s respectively. Hence, in 0.002408 s, there has been a change of about 650 RPM which corresponds to a rate of change of 269,933 RPM/s. This is impossible considering the inertia of the system.

While increasing the sampling rate is the best solution to reducing the error, increasing the absolute time difference between the recordings of zero crossings is less complicated and does not require sophisticated equipment. When the time

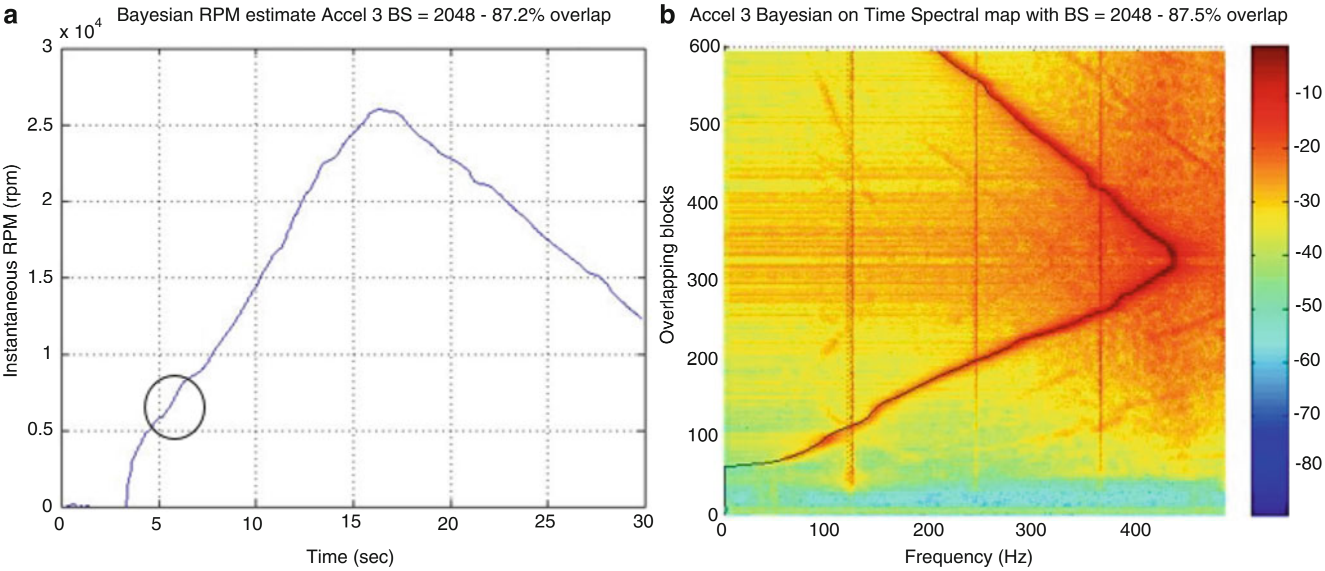

Fig. 46.5 (**a**) Spline fit to correct a small region and (**b**) final estimate over the time spectral map

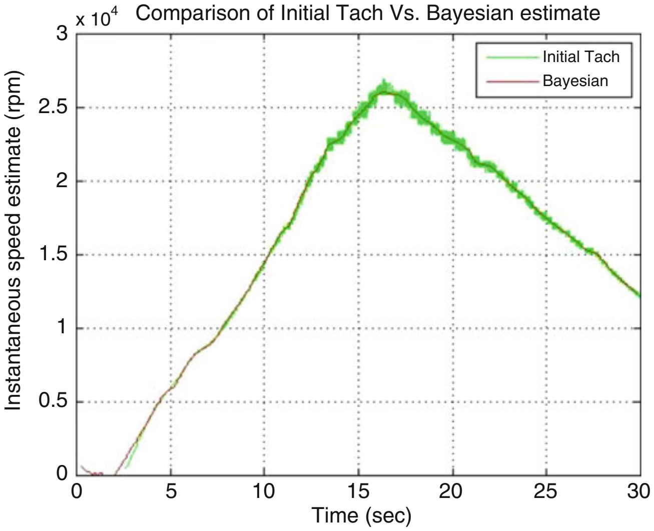

Fig. 46.6 Final Bayesian estimate over the raw tachometer estimate

interval between successive pulses is too small to be affected by the error (at high speeds or very low rate of change of speed or a combination of these), it would make sense to skip '*n*' number of pulses to achieve a sufficiently large spacing. To demonstrate the reduction in error by the use of this method, the following error analysis is presented.

$$t(2725) - t(2724) = 0.00244\ s \tag{46.A}$$

$$t(2726) - t(2725) = 0.00238\ s \tag{46.B}$$

Since the error in each time estimate can be $\pm\Delta t/2$, the overall error in $t(k) - t\,(k-1)$ for any 'k' can be $\pm\Delta t$. Now, the true value of instantaneous RPM must satisfy the following,

$$\frac{60}{t(k) - t\,(k-1) + \Delta t} \times (n+1) \leq \mathit{True\ value\ of\ RPM} \leq \frac{60}{t(k) - t\,(k-1) - \Delta t} \times (n+1) \tag{46.9}$$

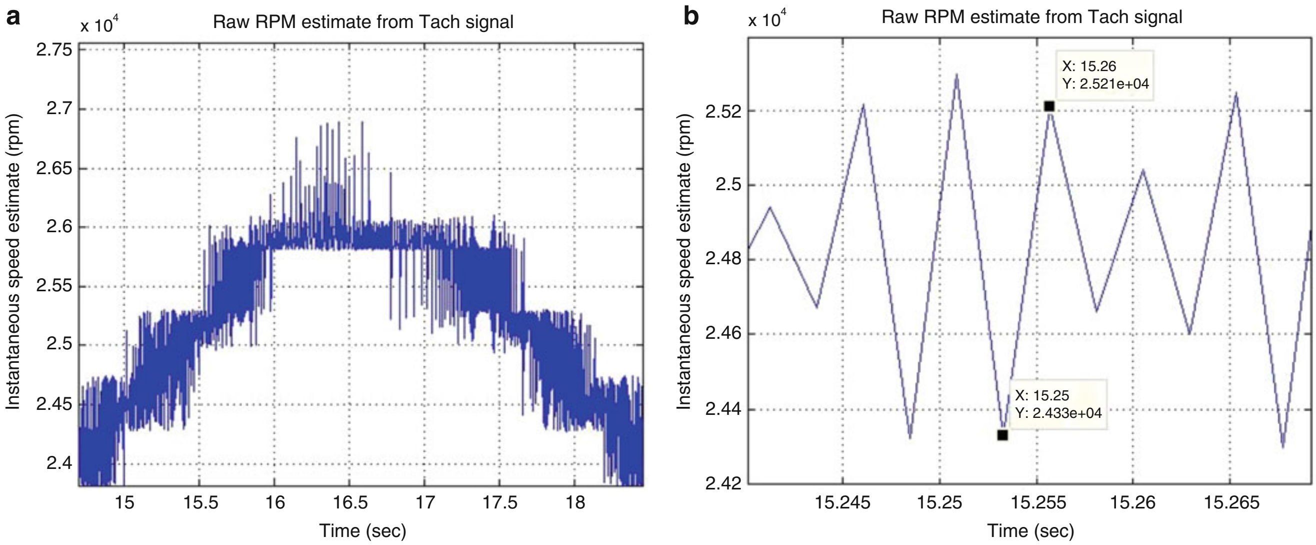

Fig. 46.7 (**a**) Fluctuations in the raw estimate at ∼25,000 RPM and (**b**) range of fluctuations in the raw estimate at 25,000 RPM

Plugging in the values of time differences given in 46.A and 46.B into Eq. (46.9) gives,

$$22775.91 \leq True\ A \leq 26741.11$$

$$23331.37 \leq True\ B \leq 27510.06$$

The values might fluctuate anywhere within the specified range (almost 4000 RPM here). The time interval between these estimates is 0.002408 s. The fluctuation would not usually lie to the extremities of the error range but is around 650 RPM which is about 6.5 times lower than the maximum error possible. However, these are still unacceptable fluctuations which need to be minimized.

Now, consider 18 pulses skipped during the above given time period:

$$t(2745) - t(2725) = 0.048061\ s \tag{46.C}$$

$$t(2746) - t(2726) = 0.048263\ s \tag{46.D}$$

The corresponding speed ranges for 46.C and 46.D as estimated by Eq. (46.9) are,

$$24766.77 \leq True\ C \leq 24968.06$$

$$24763.54 \leq True\ D \leq 24964.78$$

Here, the values can fluctuate by a maximum of about 200 RPM. Again, the fluctuation usually does not lie in the extremities of this range and so, the change from one estimate to the next might be well under this maximum value. In fact, the corresponding RPM values are 24,867 RPM and 24,863 RPM assigned at 15.2883 s and 15.2907 s respectively. Hence within a time interval of 0.00238 s, the RPM changed by about 4 RPM which is a rate of change of about 1680 RPM/s which is much more believable given that the system goes from 0 to 25,000 RPM in 15 s. The resulting instantaneous speed curve for 18 pulses skipped is shown in Fig. 46.8.

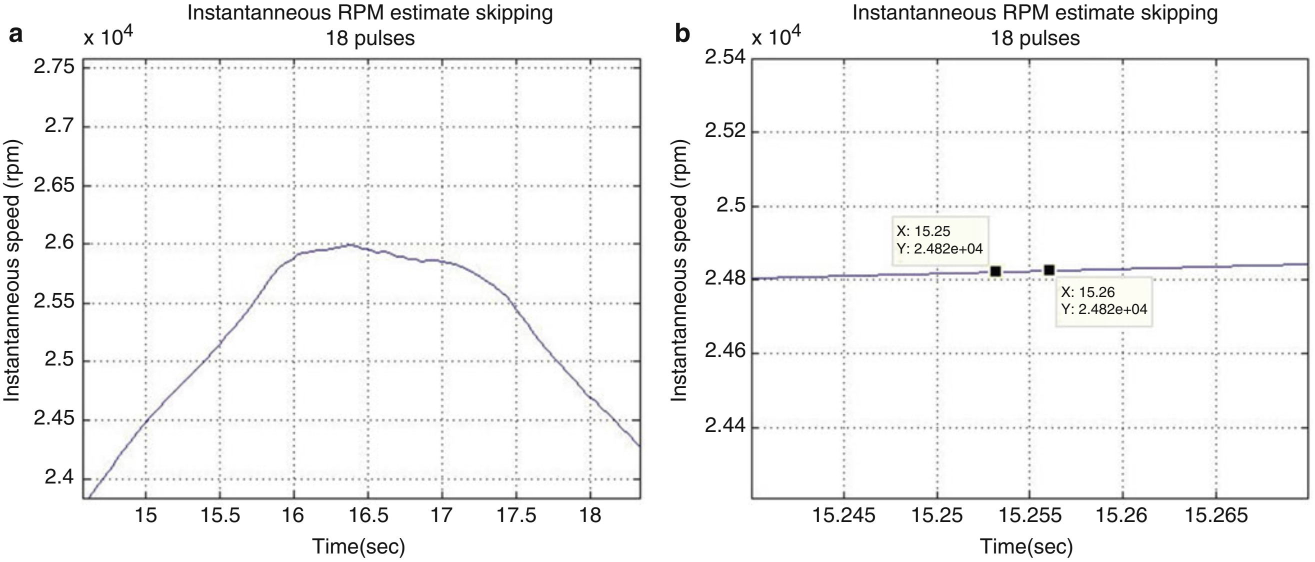

Fig. 46.8 (**a**) Instantaneous RPM estimate with 18 pulses skipped and (**b**) reduction in fluctuations with 18 pulses skipped

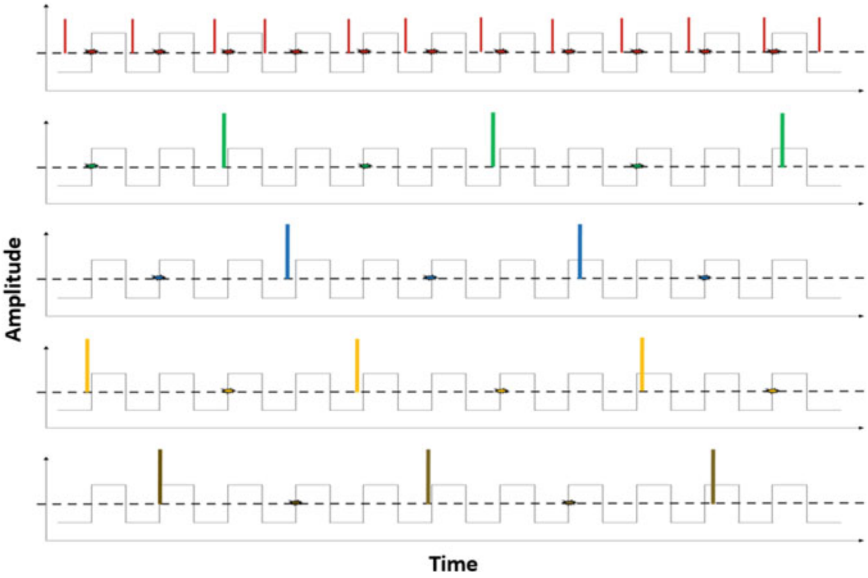

Fig. 46.9 From *Top* to *Bottom*: RPM estimation procedure with no pulses skipped; RPM estimation with 3 pulse skipped starting with the first, second, third and fourth pulses. Vertical bars denote the time instances to which the RPM has been assigned and the small explosions denote the time instances of zero crossings; Different colors represent different initiating pulses

Skipping 'n' pulses provides a smooth instantaneous speed curve that can be seen to have lesser fluctuations. However, a lot of data is being discarded in the process which can be used for a statistical advantage. There is no reason to believe that it is beneficial to start with one particular pulse and skip 'n' pulses rather than to start with the next pulse and skip 'n' pulses and so on to starting with the $(n-1)^{th}$ pulse and skip 'n' pulses. Thus, there are $n+1$ estimates of speed over the same data set when skipping the same 'n' number of pulses. This is represented pictorially in Fig. 46.9. There is very little difference in the speed profile generated from these cases.

One use that immediately comes to mind is to average the estimates for a smooth RPM curve. However, this cannot be done straight away as the time instances associated with the estimated speeds are not the same for all the curves. Different estimates of speed are assigned to different time instances and a logical way to use all of this information is to combine them as shown in Fig. 46.10. This also provides the benefit of obtaining an instantaneous speed estimate at intervals consistent with the case where every pulse is used without skipping. This is very convenient as the instantaneous velocity will now be estimated at the same sampling times as any other response data that is recorded. Clearly, the corresponding curve from

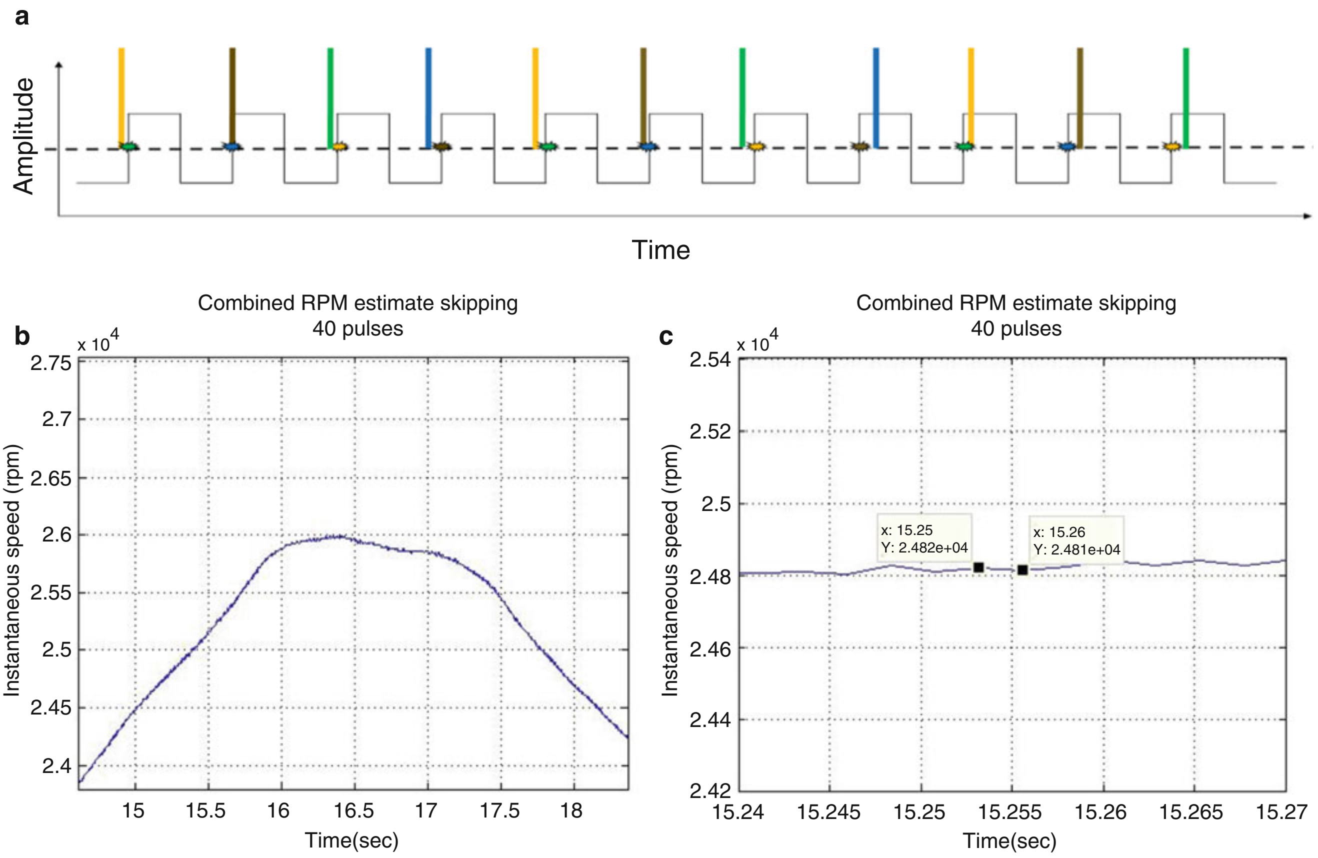

Fig. 46.10 (**a**) Combination technique for the n^{th} pulse estimates, (**b**) combined instantaneous RPM curve and (**c**) reduction in fluctuations with combination curve. Vertical bars denote the time instances to which the RPM has been assigned and the small explosions denote the time instances of zero crossings; Different colors represent different initiating pulses

Fig. 46.10 has a superior signal to noise ratio as compared to the raw estimate as shown in Fig. 46.7. Fitting a spline through this curve would be numerically much easier and physically more compatible than through the raw estimate.

For averaging the different estimates, the RPM values have to correspond to the same time instances. This can be achieved by simply taking the time points associated with one estimate as a reference (for convenience the estimate starting from the 1st pulse) and then interpolating all other curves to the RPM values at the time instances corresponding to this reference vector. This is shown in Fig. 46.11. The function ‘spline’ can be used to do this in MATLAB. Once this is done, all the curves can be averaged. The obtained curve did not require curve fitting to eliminate noise.

Though the n^{th} pulse approach gives superior signal to noise characteristics to that of the spline fit, there is an underlying assumption that during the period of every ‘n’ pulses throughout the span of the data, the speed remains fairly constant. This might not be the case throughout the data and for all data sets. For example, at low speeds and high slew rates, though the conventional estimate generates a smooth enough curve, a number of pulses would be skipped unnecessarily. This causes varying time resolution throughout the curve. Any smooth inflections might be missed as a result of the skipping.

Figure 46.12 demonstrates the effect of varying time resolution. Almost 1 s worth of data is skipped in a total data record of 30 s with 40 pulses skipped when the speed is below 5000 RPM. At about 26,000 RPM, this time interval is 0.1 s. Thus, there is a need for an adaptive algorithm which takes this time resolution issue into account while skipping pulses.

If the time resolution of the curve is maintained fairly constant throughout, the instantaneous RPM curve can be transformed from a function of angle of rotation of the shaft (pulses and corresponding times) into a function of absolute time with a defined resolution. This would also provide an optimization for the number of pulses to be skipped.

Consider a system rotating at ‘R’ RPM.
Number of pulses recorded by tachometer per second $= R/60$
Therefore, time period for each pulse $= 60/R$
Time interval between ‘n’ pulses $= 60 \times n/R$

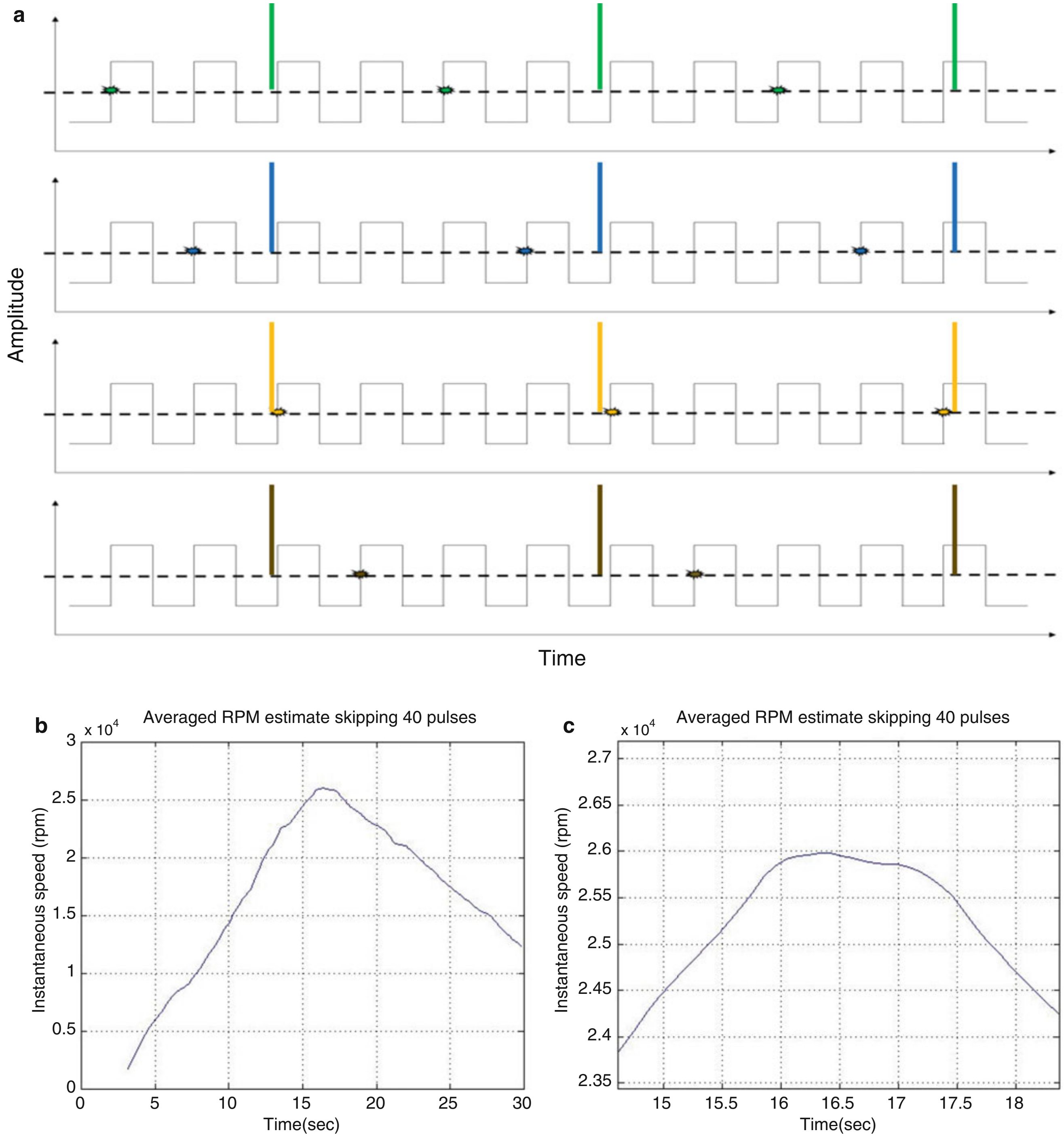

Fig. 46.11 (**a**) Reassigning RPM estimates to a reference time vector, (**b**) averaged RPM estimate—40 pulses skipped throughout and (**c**) zoomed image showing smooth averaged curve. Vertical bars denote the time instances to which the RPM has been assigned and the small explosions denote the time instances of zero crossings; Different colors represent different initiating pulses

Now, the entire time data can be divided into a number of time blocks and the number of pulses 'n' to be skipped in each block can be identified as the integer which provides the time interval between estimates ($60 \times n/R$) that is closest to the desired resolution. The smaller the block, the better will be the estimate. However, if the block size becomes too small, it might not even be possible to skip a certain number of pulses as suggested by the above method. Hence, the user must be careful in choosing the number of blocks to divide the data into.

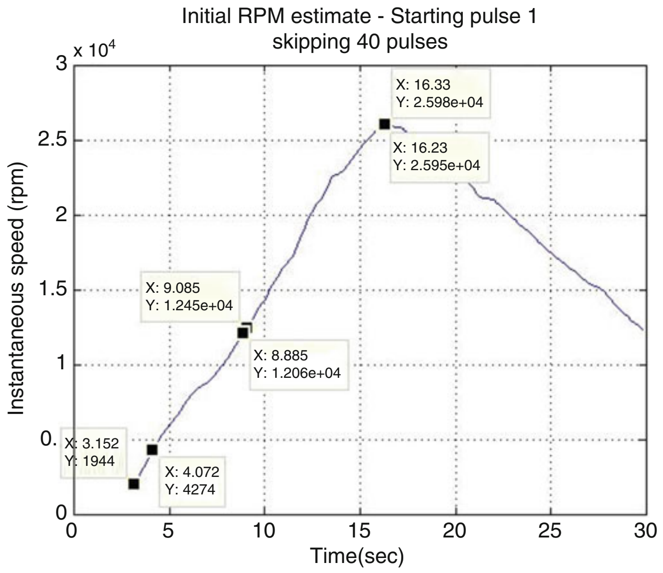

Fig. 46.12 Instantaneous RPM estimate with constant no. of pulses skipped throughout

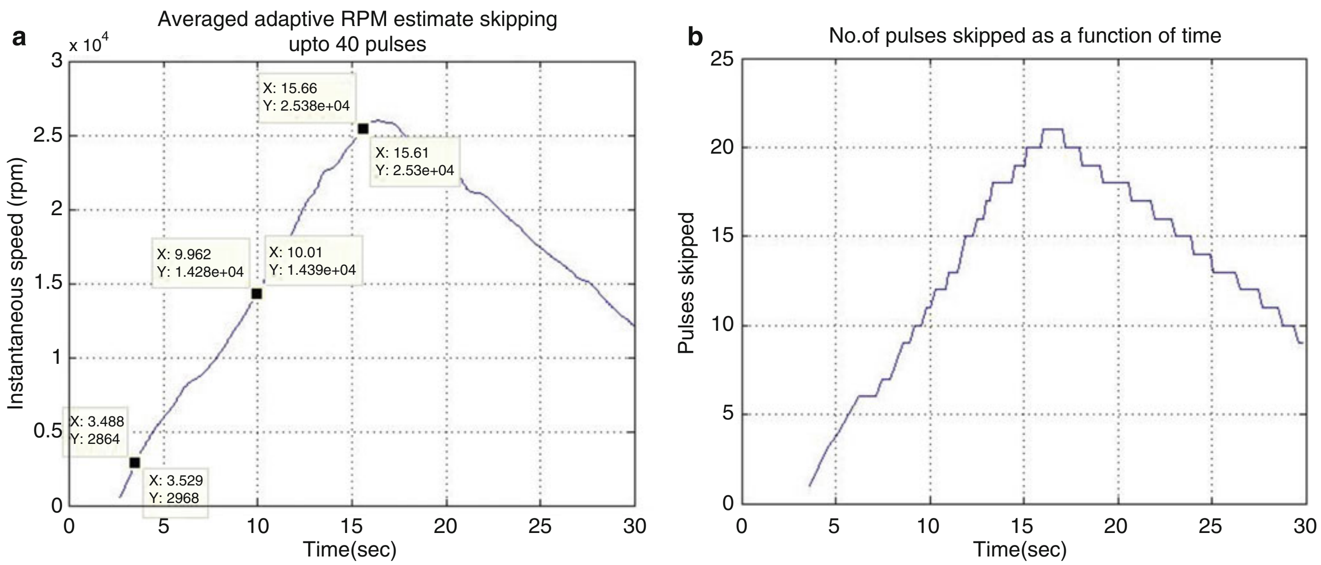

Fig. 46.13 (**a**) Instantaneous RPM estimate from the Adaptive n^{th} Pulse Algorithm and (**b**) no. of pulses skipped vs time

The result from this approach is shown in Fig. 46.13 with consecutive points that are consistently 0.05 s apart throughout the curve which was the user input. The corresponding number of pulses skipped as a function of time is also shown.

A whole revolution of the system need not be counted for the instantaneous speed formulation. For a square wave output, a half revolution can also be considered by taking two consecutive zero crossings and not two zero crossings from consecutive pulses. Thus, ‘n’ need not necessarily be a whole number (2.5 pulses or 8.5 pulses can also be skipped). To check whether the estimate is accurate, it is plotted against the raw estimate in Fig. 46.14. It can be seen that the curve is always within bounds of the fluctuating raw estimate.

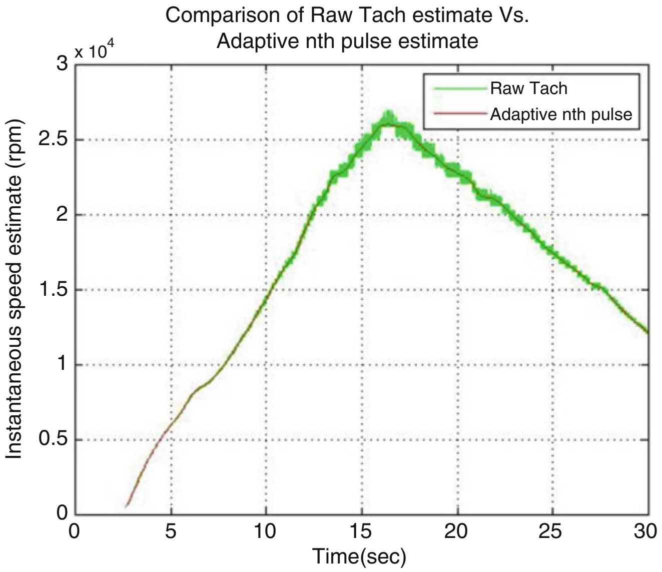

Fig. 46.14 Averaged n^{th} pulse estimate vs raw tachometer estimate

46.4 Comparison and Other Examples

There is no way to assert any degree of confidence in these algorithms as the true value of the instantaneous speed is not known. However, the two algorithms operate on independent philosophies. If they generate curves that are within bounds of the raw curve and are in close agreement with each other, it can be safe to proceed with one of them for further analysis. This section contains comparisons between the results from Bayesian and n^{th} pulse algorithms for various systems.

Figure 46.15 shows the comparison for the vacuum cleaner data. The overall error stays within 2 % throughout the data and is mostly within 0.2 %. The error is large initially when the order is not dominant enough to be estimated accurately by the Bayesian algorithm. This happens because the algorithm works on the criterion of amplitude of vibration.

Figure 46.16 shows the results and comparison for data from a 6 cylinder engine powertrain. In contrast to the vacuum cleaner data, this system operates at very low speeds and has a low slew rate. The error mostly stays within 0.1 % and 1.5 RPM.

Figure 46.17 shows the results and comparison for data from a rotor rig. The overall error stays within 0.2 % and within 15 RPM for most of the data. As all the methods involve assumptions, comparison to the true value of instantaneous speed cannot be made. It can be seen that the estimates from the Bayesian and Adaptive n^{th} Pulse Algorithms agree to within satisfactory limits. Moreover, they provide a smooth and precise estimate which stays within bounds of the raw estimate.

46.5 Conclusion

The conventional way of estimating instantaneous speed involves fitting a curve (spline) to an initial estimate for which each consecutive pulse is considered in the formulation. The sampling process and error in interpolation give rise to unacceptable fluctuations in the instantaneous speed profile. The Adaptive n^{th} Pulse Algorithm is an effective new technique which can address this issue. The main idea behind the algorithm is to increase the absolute time interval over which a single speed estimate is being calculated so that it is not affected by the errors (zero crossing uncertainty). The number of pulses to be skipped for different parts of the data has to be regulated according to the speed and rate of change of speed. This optimization is achieved by matching the time interval between estimates to a desired time resolution. The averaging technique presented generates a smooth curve which does not require a spline fit. The combination technique generates a curve with high signal to noise ratio to which a spline can be fit easily. It is a fairly simple procedure to apply and the operator/user does not have to be skilled in rotating systems analysis to understand it.

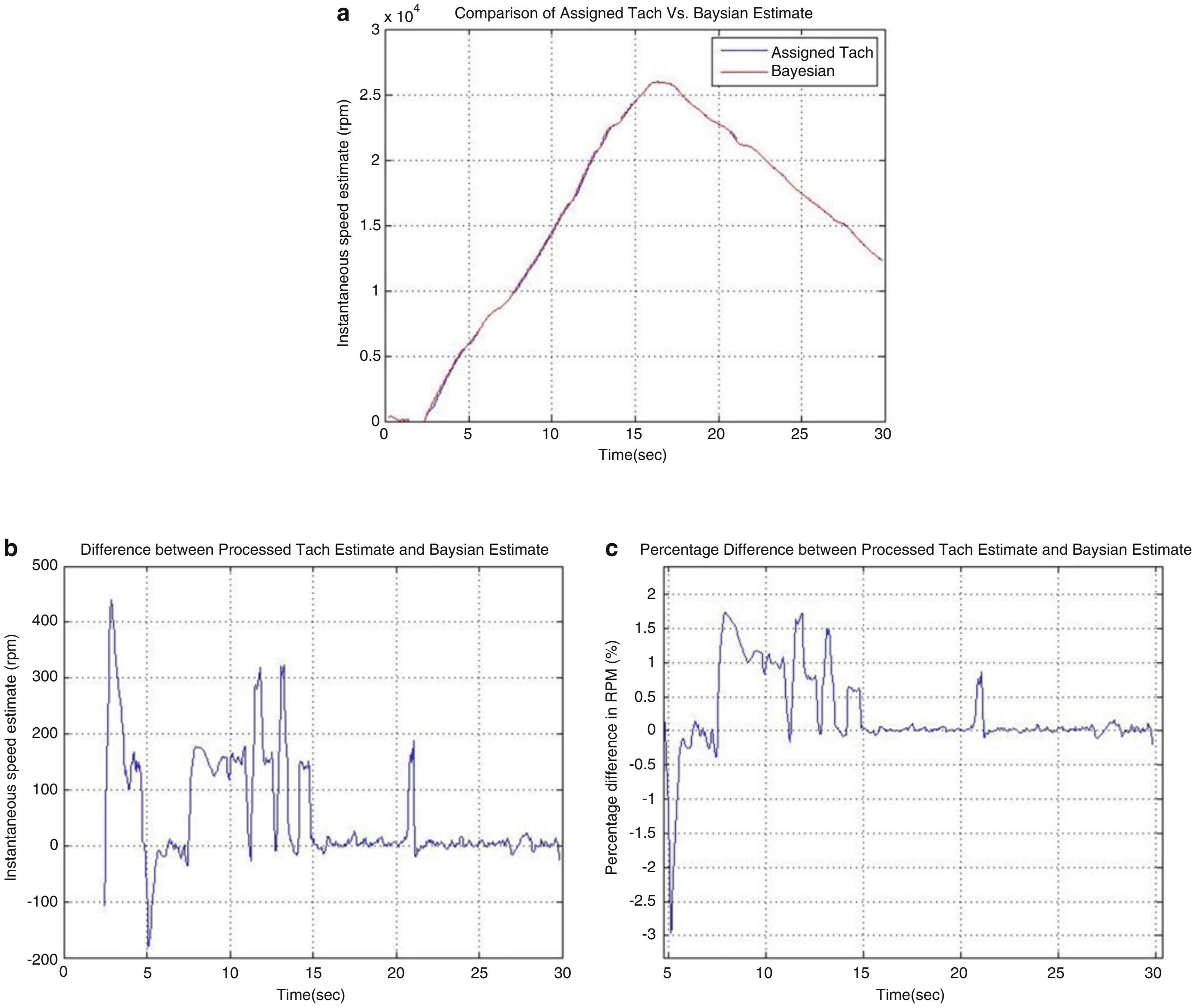

Fig. 46.15 (**a**) Bayesian estimate vs n^{th} pulse estimate, (**b**) absolute difference and (**c**) % difference

The Bayesian algorithm provides a way of estimating the speed from vibration data without the need for a tachometer. This can prove highly advantageous for applications with constraints like space, cost or unfavourable operating conditions. The smart algorithm developed in this work greatly reduces the analysis required and thus brings down the processing time by as much as 100 times. The most important contribution of this algorithm is the ability to reprocess with different parameters over different parts of the data. The results have a high signal to noise ratio and can directly be used for generation of RPM spectral maps. There is no need for approximations and assumptions in the assignment of a particular speed to a given data block [7]. Though the benefits from this method are attractive, there are several shortcomings like the requirement of a high speed computer and a skilled operator due to which it might not be viable for all practical real time applications.

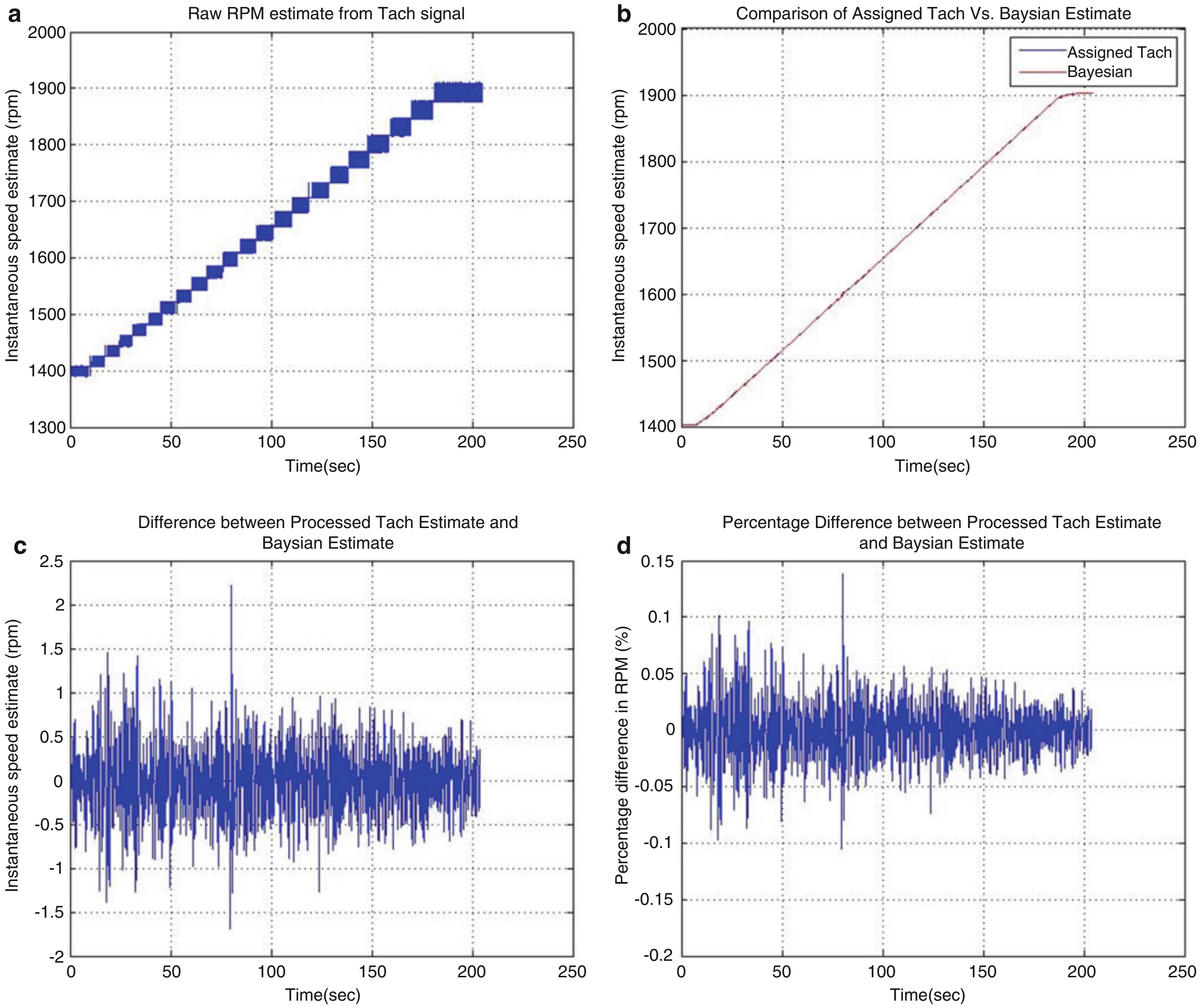

Fig. 46.16 6 cylinder engine powertrain—(**a**) raw estimate, (**b**) Bayesian estimate vs $\boldsymbol{n^{th}}$ pulse estimate, (**c**) absolute difference and (**d**) % difference

The comparisons presented show that both the Adaptive n^{th} Pulse and the Bayesian algorithms arrive at similar speed profiles although the processes are independent of each other. Also, the curves always lie within bounds of the raw tachometer estimate and seem to be a better fit to the data than the mathematical spline fit. It should be noted however that there is no way to know the true value of instantaneous speed. As such, no error analysis can be done with respect to the true value. These two methods support each other and provide results that are more physically reasonable than the spline fit approach.

For a detailed description of the work presented in this paper, refer to the Master's thesis from which this paper was extracted [8].

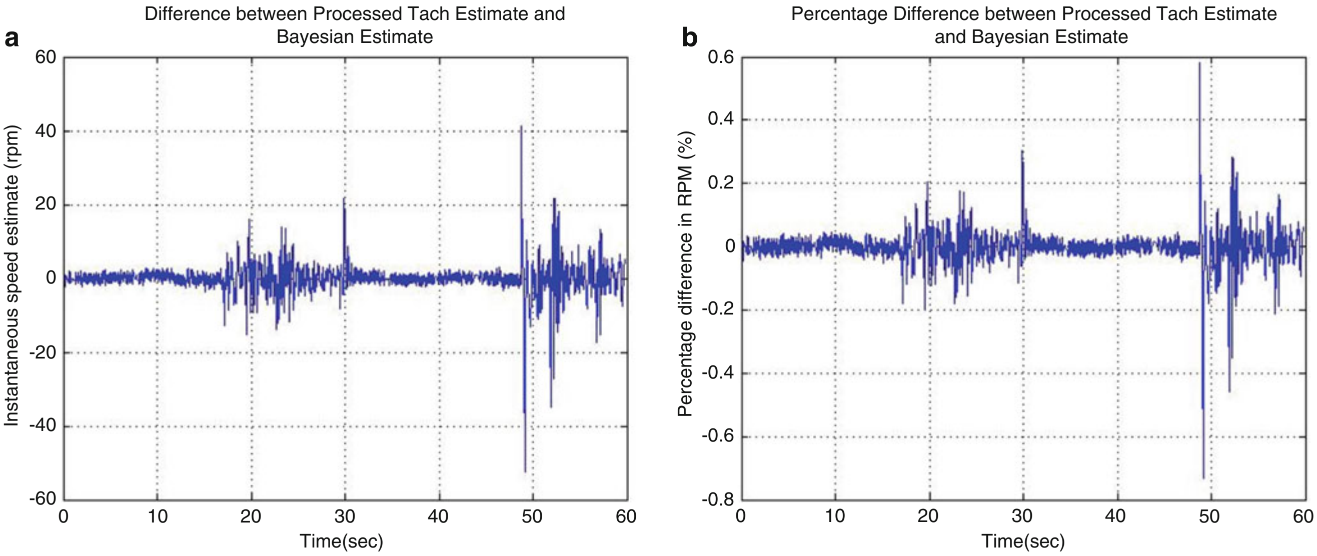

Fig. 46.17 Structural mechanics lab rotor rig—(**a**) raw estimate, (**b**) Bayesian estimate vs n^{th} pulse estimate, (**c**) absolute difference and (**d**) % difference

References

1. Blough, J.R.: Improving the Analysis of Operating Data on Rotating Automotive Components. PhD Dissertation, University of Cincinnati (1998)
2. Pedersen, T.F., Herlufsen, H., Konstantin-Hansen, H.: Order Tracking in Vibro-acoustic Measurements: A Novel Approach Eliminating the Tacho Probe. SAE paper 01-2266 (2005)
3. Bretthorst, G.L.: Bayesian Spectrum Analysis and Parameter Estimation, vol. 48 of Lecture Notes in Statistics. Springer-Verlag (1988)
4. Jaynes, E.T.: In: Zellner, A. (ed.) Marginalization and Prior Probabilities in Bayesian Analysis in Econometrics and Statistics. North-Holland Publishing Company, Amsterdam (1980)
5. Ruanaidh, J.J.K., Fitzgerald, W.J.: Numerical Bayesian Methods Applied to Signal Processing, Statistics and Computing. Springer (1998)
6. Schuster, A.: The periodogram and its optical analogy. Proc. R. Soc. Lond. **77**, 136 (1905)
7. Deshpande, S.: Improving Observability in Experimental Analysis of Rotating Systems. Master's Thesis, University of Cincinnati (2014)
8. Vemuri, A.: Estimation of Instantaneous Speed for Rotating Systems: New Processing Techniques. Master's Thesis, University of Cincinnati (2016)

Chapter 47
Identification of Breathing Cracked Shaft Models from Measurements

Michael I. Friswell, Ralston Fernandes, Nidhal Jamia, and Sami El-Borgi

Abstract Cracks in the shafts of rotating machinery are a serious problem that can lead to significant costs. Condition monitoring is required to identify the presence of cracks before the machine fails. However, methods based on linear models and low frequency dynamics are very insensitive because the local stiffness reduction leads to only small changes in critical speeds. Cracks in a shaft are often breathing; they open and close depending on the local curvature of the shaft. In the general case this makes the crack nonlinear, and leads to the presence of harmonics. In larger rotating machines the cracks will open and close because the self weight of the rotor; for a constant rotor spin speed this leads to a parametric variation in stiffness. There are various breathing crack models, many of which model the stiffness as a truncated Fourier series. However the parameters of this series are estimated based on an idealized model of the crack front. This paper suggests a method to directly estimate the breathing crack stiffness using the measured synchronous response and its harmonics. The approach is demonstrated on a simple laboratory test rig. These improved models are vital to enable accurate model based condition monitoring of rotating machines.

Keywords Rotating machine • Breathing crack • Condition monitoring

47.1 Introduction

The idea that changes in a rotor's dynamic behavior could be used for general fault detection and monitoring was first proposed in the 1970s. Of all machine faults, probably cracks in the rotor pose the greatest danger and research in crack detection has been ongoing for the past 40 years. Current methods examine the response of the machine to unbalance excitation during run-up, run down or during normal operation. In principle, a crack in the rotor will change the dynamic behaviour of the system but in practice it has been found that small or medium size cracks make such a small change to the dynamics of machine system that they are virtually undetectable by this means. Only if the crack grows to a potentially dangerous size can they be readily detected.

Detecting faults in rotating machines presents certain problems that do not occur in fixed structures. First of all, in addition to cracks there are several other types of faults that can be present in a machine, such as a seal rub or a misaligned bearing. Ideally we wish to detect a crack in a machine rotor at an early stage in its development and estimate its size and location. However, compared to static structures, access to a rotor can be limited either in order to contain the working fluid or for safety reasons. On the other hand, compared to a large static structure, the rotor of a machine is easily excited by the residual out-of-balance that always exists.

Crack detection methods fall into two groups, model updating and pattern recognition (see, for example, [1, 2]). In the former method, the dynamic behavior of the rotor is used to update a model of the rotor and in the process determine both the severity and location of any crack. Clearly the crack model used must be adequate for the task. If the pattern recognition approach is used, then whilst a crack model is not directly required, it is desirable to have some idea of the dynamic behavior that will result from a cracked rotor in order that it can be recognized in the pattern of behavior. There are a number of

---

M.I. Friswell (✉) • N. Jamia
College of Engineering, Swansea University, Bay Campus, Fabian Way, Crymlyn Burrows, Swansea SA1 8EN, UK
e-mail: m.i.friswell@swansea.ac.uk

R. Fernandes • S. El-Borgi
Department of Mechanical Engineering, Texas A&M University at Qatar, PO Box 23874, Education City, Doha, Qatar

© The Society for Experimental Mechanics, Inc. 2016

J. De Clerck, D.S. Epp (eds.), *Rotating Machinery, Hybrid Test Methods, Vibro-Acoustics & Laser Vibrometry, Volume 8*,
Conference Proceedings of the Society for Experimental Mechanics Series, DOI 10.1007/978-3-319-30084-9_47

approaches to the modeling of cracks in beam structures reported in the literature, that fall into three main categories; local stiffness reduction, discrete spring models, and complex models in two or three dimensions. A number of authors have given comprehensive surveys of crack modeling and detection approaches [3–7]. Friswell and Penny [8] considered the performance of various crack models in structural health monitoring.

If the vibration due to any out-of-balance forces acting on a rotor is greater than the static deflection of the rotor due to gravity, then the crack will remain either opened or closed depending on the size and location of the unbalance masses. In the case of the permanently opened crack, the rotor is then asymmetric and this condition can lead to stability problems. If the vibration due to any out-of-balance forces acting on a rotor is less than the static deflection of the rotor due to gravity the crack will open and close (or breathe) as the rotor turns. This is the situation that exists in the case of large horizontal machines and this paper will concentrate on this condition.

This paper considers the effect of the breathing crack mechanism on the dynamics of the machine. In particular, the breathing function, which is a function between 0 and 1 that determines the extent of the crack opening, can be expressed as a Taylor series for weight dominated machines. The common breathing crack models will be expressed in terms of the Taylor series, and the effect on the rotor response will be given for a simple model. These effects are then demonstrated on a finite element model of a machine, and compared to experimental data. The possibility of identifying the breathing crack model from experimental data is then discussed.

47.2 Equations of Motion and Breathing Crack Models

The analysis of a rotor-bearing system may be performed in fixed or rotating co-ordinates. If neither the bearings and foundations nor the rotor is axi-symmetric then the resulting differential equations, whether described in fixed or rotating coordinates, will be linear equations with harmonic coefficients. Typically foundations of a large machine will be stiffer vertically than horizontally and the cracked rotor will not be axi-symmetric when the crack is open. Thus there is no compelling reason to used fixed or rotating coordinates for the analysis. To determine the stiffness of the rotor as the crack opens and closes it is easier to work in co-ordinates that fixed to the rotor and rotate with it. The reduction in stiffness due to a crack is then calculated in directions perpendicular to and parallel to the crack face, and these directions will rotate with the rotor. Having determined the rotor stiffness in rotating coordinates we transform the stiffness matrix to fixed coordinates and join the stiffness to the system inertia to obtain the equation of motion in fixed coordinates.

The equations of motion are developed by assuming that the foundation has no internal degrees of freedom and that the rotor is represented by a shaft-line model. Thus all of the degrees of freedom are located on the rotor. The extension to general systems is straight-forward and requires the transformation from rotating to stationary co-ordinates is only applied to those degrees of freedom located on the rotor. The full equations of motion of a rotor with a breathing crack, excited by unbalance and additional excitation, are non-linear. However, the assumption of weight dominance, where the static displacement is significantly greater than the dynamic displacement, turns the non-linear equations into linear equations with a stiffness matrix that varies periodically based on the rotational spin speed of the rotor [9]. Thus the equations of motion in stationary co-ordinates are

$$\mathbf{M}\ddot{\mathbf{q}} + [\mathbf{D} + \Omega\mathbf{G}]\,\dot{\mathbf{q}} + [\mathbf{K}_0 - \mathbf{K}_c(t)]\,\mathbf{q} = \mathbf{Q}_u(t) \tag{47.1}$$

where $\mathbf{Q}_u$ is the unbalance force and Ω is the rotor spin speed (assumed constant). Damping and gyroscopic effects have been included as a symmetric positive semi-definite matrix, $\mathbf{D}$, and a skew-symmetric matrix, $\mathbf{G}$, although they have little direct bearing on the analysis. If there is axi-symmetric damping in the rotor then there will also be a skew-symmetric contribution to the undamaged stiffness matrix, $\mathbf{K}_0$. $\mathbf{M}$ is the mass matrix of the system, and $\mathbf{q}$ is the generalized dynamic displacement relative to the static deflection. The stiffness reduction to the crack is modeled by $\mathbf{K}_c(t)$, which with the assumption of weight dominance is a periodic function with time period $2\pi/\Omega$.

The breathing crack was initially studied by Gasch [10] who modeled the crack as a *hinge*. In this model the crack is open for one half and closed for the other half a revolution of the rotor, and the transition from open to closed (and vice-versa) occurs abruptly as the rotor turns. Mayes and Davies [11] developed a similar model except that the transition from fully open to fully closed is described by a cosine function. Penny and Friswell [12, 13] compared the response due to different crack models and considered the effect on the dynamic response of the rotor.

In this paper the fully open crack is modeled by reducing the element stiffness in orthogonal directions (parallel and perpendicular to the crack face). The stiffness matrix of the machine when the crack is open, in rotating co-ordinates, is then $\tilde{\mathbf{K}}_1$ (the tilde will denote quantities in the rotating frame), and the change in stiffness due to the crack is $\mathrm{d}\tilde{\mathbf{K}} = \mathbf{K}_0 - \tilde{\mathbf{K}}_1$. If weight dominance is assumed, then the opening and closing of the crack is periodic at the rotor spin speed. This periodic opening and closing may be represented by a general Fourier series, although three specific possibilities will be considered here. The first is that the crack remains open, and hence $\tilde{\mathbf{K}}_c(t) = \tilde{\mathbf{K}}_1$ is constant. In the Mayes model the time dependent stiffness matrix in rotating coordinates (where the choice of time origin is based on the crack orientation) is

$$\tilde{\mathbf{K}}_c(t) = \mathbf{K}_0 - 0.5\,(1 - \cos\Omega t)\,\mathrm{d}\tilde{\mathbf{K}} \tag{47.2}$$

When $\cos\Omega t = 1$ the crack is fully closed, the stiffness is the un-cracked rotor stiffness and thus the rotor is axi-symmetric. When $\cos\Omega t = -1$ the crack is fully open, and the rotor is asymmetric. The hinge or Gasch model has an abrupt change in stiffness and is given by

$$\tilde{\mathbf{K}}_c(t) = \mathbf{K}_0 - 0.5\,(1 - \mathrm{sgn}\,(\cos\Omega t))\,\mathrm{d}\tilde{\mathbf{K}} \tag{47.3}$$

where sgn is the signum function that returns the sign of a number. The signum function can be written in terms of a Taylor series so that Eq. (47.3) becomes

$$\tilde{\mathbf{K}}_c(t) = \mathbf{K}_0 - \left\{0.5 - \sum\nolimits_{n=1}^{\infty}\frac{2}{n\pi}\sin\left(\frac{n\pi}{2}\right)\cos\left(n\Omega t\right)\right\}\mathrm{d}\tilde{\mathbf{K}} \tag{47.4}$$

Note that the $\cos\Omega t$ term of the hinge model is $2/\pi = 0.6366$, compared to 0.5 for the Mayes model. The coefficients of a general Fourier series may be used to give a general breathing model of the form

$$\tilde{\mathbf{K}}_c(t) = \mathbf{K}_0 - \left\{a_0 - \sum\nolimits_{n=1}^{\infty} a_n\cos\left(n\Omega t\right)\right\}\mathrm{d}\tilde{\mathbf{K}} \tag{47.5}$$

Converting from rotating to fixed co-ordinates gives the stiffness matrix in stationary co-ordinates, $\mathbf{K}_c(t)$, which is a periodic function of time only, showing that Eq. (47.1) is a linear parametrically excited equation. Penny and Friswell [12] showed that the Mayes model generates a constant term plus 1X, 2X and 3X rotor angular velocity components in the stiffness matrix. An open crack will generate a constant term plus 1X and 2X components in the stiffness matrix. The hinge model will generate all harmonics.

47.3 Rotor Response to Breathing Crack Models

In order to check the frequency content of the machine response a time simulation will be performed on a detailed model of the machine. This will allow realistic features of the real machine to be easily incorporated. To ensure the transient response decays within a reasonable time, damping is added to the bearings and/or disks. The equations of motion are integrated using ode45 in MATLAB. However the number of degrees of freedom of a detailed finite model is likely to be large, requiring a long computational time to simulate the response. Thus the equations of motion in the rotating frame are reduced using the lower mode shapes of the undamped and undamaged machine, neglecting gyroscopic effects. A sufficient number of modes should be included to simulate the range of excitation frequencies, and also any significant combinational frequencies. This reduction has two beneficial effects; not only are the number of degrees of freedom reduced, leading to a lower computational cost per time step, but also the higher frequencies are removed, thus allowing a larger time step.

The equations are integrated until a steady state has been established and then the FFT is calculated. The steady state response should only contain the rotor spin frequencies and its harmonics, and therefore the spectrum of the response should only contain discrete frequencies. However, leakage is likely to occur because of the difficulties in choosing a sample period so that every sinusoidal component in the response has an integer number of cycles in the sample. The effect of leakage may be reduced by using time window functions. Furthermore the sample period must be sufficiently long to ensure that the frequency increment is small enough to distinguish the individual frequency components. Friswell et al. [9] gave more detail.

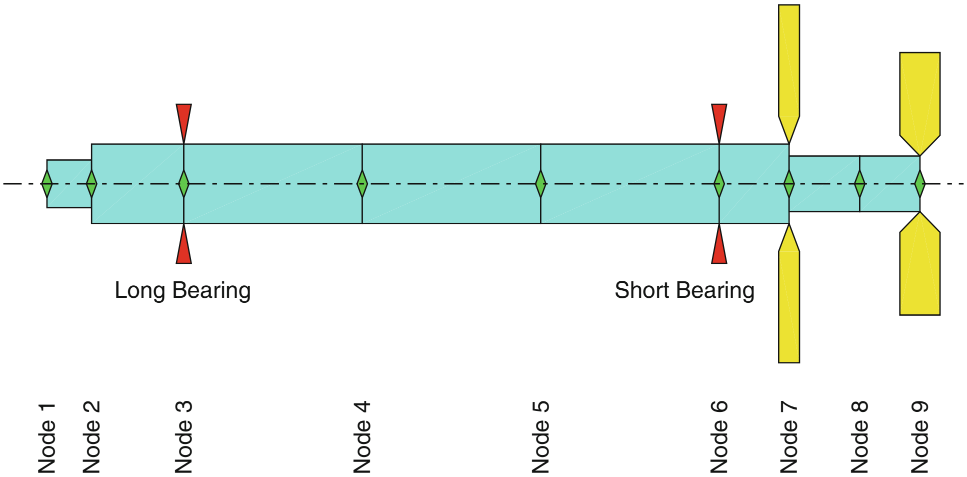

Fig. 47.1 The simulated rotor

Figure 47.1 shows the model used for the simulations, which approximates an experimental test rig at Texas A&M at Qatar. The rotor is modeled by nine shaft finite elements in MATLAB [14]. The system comprised of a long shaft with diameter 20 mm and length 502 mm, coupled to a short flange of 14 mm diameter and 85 mm of length. The assembly of the disk and the flange have been modeled as one disc at node 7, with 14 mm thickness and 90 mm diameter. The small pulley has been modeled as a disk at node 9 with 27 mm thickness and 66 mm diameter. The left bearing at node 3 is modeled as a long rigid bearing (i.e. displacements and rotations fixed) and the right bearing at node 6 is modeled as a short rigid bearing (i.e. only displacements fixed). To reduce the time needed to simulate the transient response, damping in both lateral directions with value 100 Ns/m has been added at disk 1 (node 7). The rotor is made of steel with modulus of elasticity $E = 200$ GPa, Poisson's ratio $\nu = 0.24$ and mass density $\rho = 7840$ kg/m^3. The shaft crack is modeled as a stiffness reduction in element 7. An unbalance of magnitude 10^{-3} Nm was added at disk 2 (small pulley, node 9). The flange on the overhung part of the rotor has six bolts which may be loosened to simulate a crack.

The first critical speed of the undamaged machine is 7700 rev/min. The rotor is simulated at 1500 rev/min; this is well below the critical speed but does allow the parametric excitation to be demonstrated without the risk of exciting any resonances. Figure 47.2 shows the spectra of the response at the flange when a crack is modeled as a fully open crack and also a breathing crack using the Mayes model and the hinge model. The open crack is modeled by a 20 % reduction in the lateral stiffness of element 7 in one plane in the rotating frame. The spectrum for the uncracked rotor is also shown, and highlights that the harmonics of the rotor spin speed are not excited in this case. The harmonics are excited in the cracked cases, and the amplitude of the harmonics increases from the fully open crack to the Mayes model to the hinge model. For the open crack the rotor is asymmetric, although no harmonics in the response will be excited because the bearing and support model is isotropic. The hinge model also gives responses at other frequencies because resonances of the machine have been excited which give combination frequency responses at many different frequencies.

47.4 Experimental Test Rig and Results

The experimental test rig is manufactured by GUNT and incorporates a flange with bolts that may be loosened to simulate a crack. Since the size and weight of the rotor is too small to give weight dominance to the breathing crack behavior, a belt is used to provide a lateral (horizontal) load that is approximately constant in amplitude and direction in the stationary frame. If this force is sufficiently large then the crack will exhibit breathing behavior. Figure 47.3 shows the test rig and Fig. 47.4 shows the belt system used to apply the lateral load. The response is measured by accelerometers in the vertical and horizontal directions at the outer bearing support.

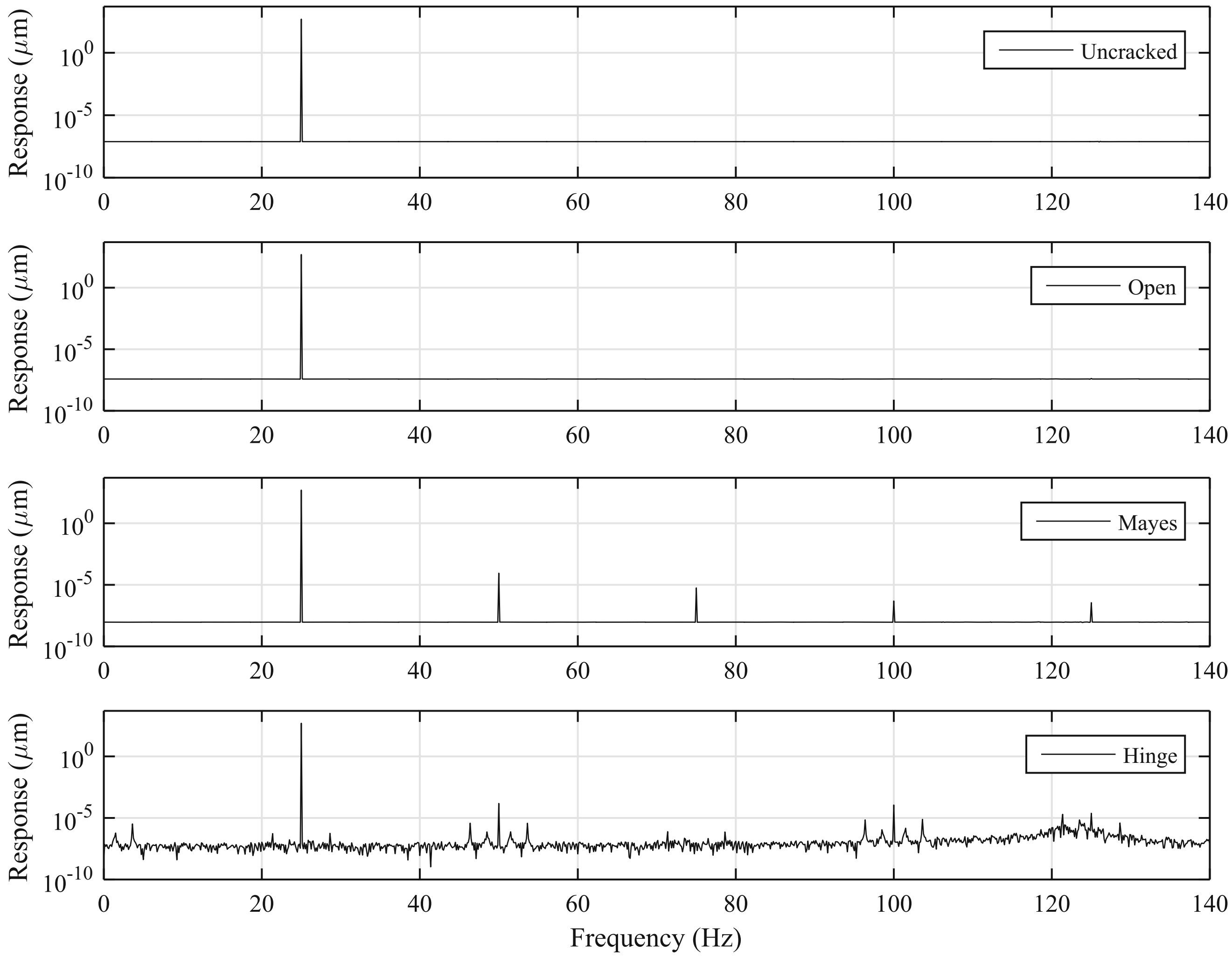

Fig. 47.2 Spectra of the vertical displacement at node 7 for the simulated rotor

Figure 47.5 shows the spectra when the machine is run at a constant speed of approximately 1500 rev/min (25 Hz) for four different cases. This speed is well below the critical speed for this system. The crack is simulated by loosening three bolts. The test runs involve both cracked and uncracked rotors, and both with and without the belt to introduce the lateral load. Without the belt the spectra are similar, with some response at the second and third harmonic, although the amplitude is relatively low. The harmonics indicate the presence of nonlinearities other than the breathing crack and some asymmetry in the rotor. The cracked shaft without any side load from the belt does not breathe because the curvature of the operational deflection shape on the overhung part of the shaft is very low. Adding the belt to the uncracked shaft produces extra frequencies due to the belt resonances but does not significantly affect the response at the fundamental and harmonics of the rotor spin speed. Note that the diameters of the belt pulleys mean that the system is also excited at half the rotor spin speed. When the belt is used for the cracked rotor the response at the second harmonic is increased, and the response at the fundamental is reduced. The third harmonic changes very little. This significant change in the ratio of the response at the second harmonic to the fundamental is vital to identify the presence of a crack.

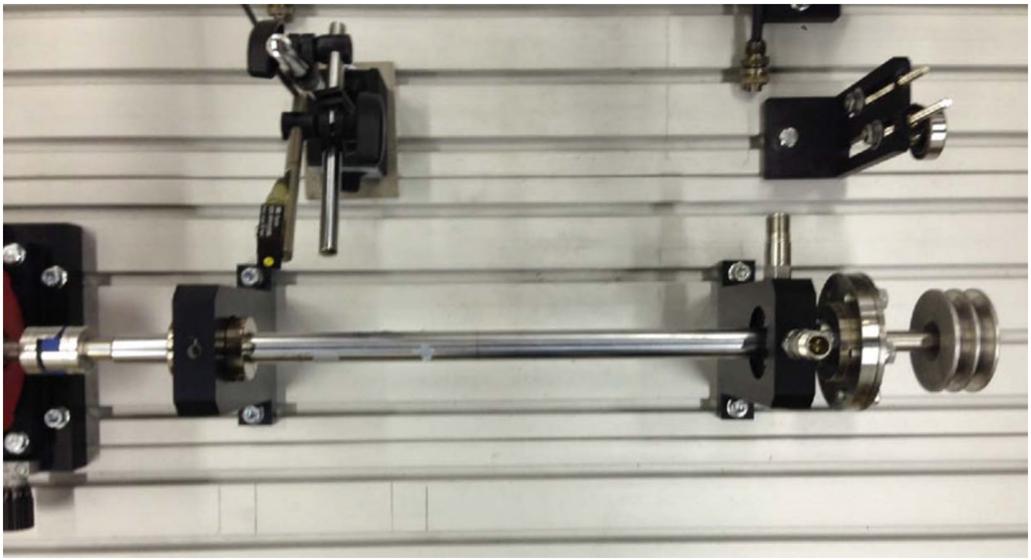

Fig. 47.3 The experimental test rig

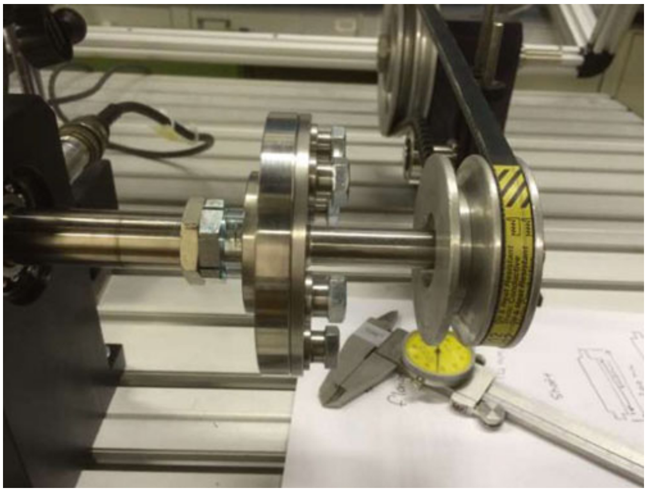

Fig. 47.4 The belt system to apply the lateral load

47.5 Conclusions

This paper has considered the breathing function for an opening and closing crack in the shaft of a rotating machine. The breathing behavior generates harmonics in the system response, and the amplitude of these harmonics depends on the form of the breathing function used in the crack model. This breathing function may be modeled as a Fourier series, if weight dominance is assumed for the machine. This has been demonstrated in both simulation and experiment. Since the response harmonics depend on the breathing crack function, the inverse problem should be feasible, where the coefficients of the Fourier series of the breathing function are estimated from the amplitude of the harmonics in the response.

Acknowledgements The authors gratefully acknowledge the support of the Qatar National Research Fund through grant number NPRP 7-1153-2-432.

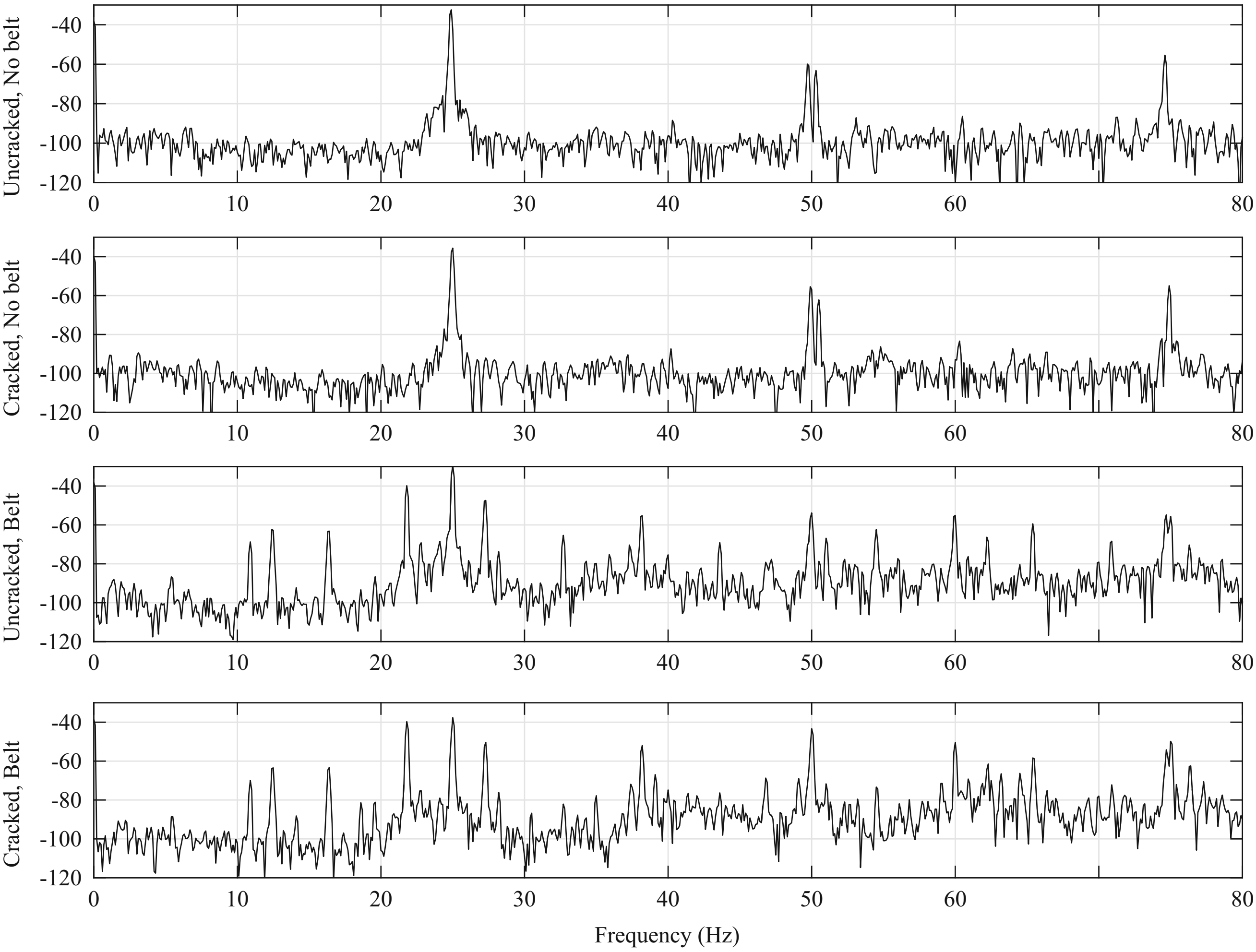

Fig. 47.5 Spectra of the vertical acceleration (in dB) of the experimental test rig

References

1. Bachschmid, N., Pennacchi, P., Tanzi, E., Vania, A.: Identification of transverse crack position and depth in rotor systems. Meccanica **35**, 563–582 (2000)
2. Markert, R., Platz, R., Seidler, M.: Model based fault identification in rotor systems by least squares fitting. Int. J. Rotating Mach. **7**(5), 311–321 (2001)
3. Dimarogonas, A.D.: Vibration of cracked structures: a state of the art review. Eng. Fract. Mech. **55**, 831–857 (1996)
4. Bovsunovsky, A., Surace, C.: Non-linearities in the vibrations of elastic structures with a closing crack: a state of the art review. Mech. Syst. Signal Process. **62–63**, 129–148 (2015)
5. Kumar, C., Rastogi, V.: A brief review on dynamics of a cracked rotor. Int. J. Rotating Mach. **2009**, Article ID 758108 (2009)
6. Sekhar, A.S.: Some recent studies on cracked rotors. In: Proceedings of IUTAM Symposium on Emerging Trends in Rotor Dynamics, pp. 491–503 (2011)
7. Ostachowicz, W., Krawczuk, M.: On modeling of structural stiffness loss due to damage. In: Proceedings of the DAMAS, Cardiff, UK, pp. 185–199 (2001)
8. Friswell, M.I., Penny, J.E.T.: Crack modelling for structural health monitoring. Struct. Health Monit.: Int. J. **1**(2), 139–148 (2002)
9. Sawicki, J.T., Friswell, M.I., Kulesza, Z., Wroblewski, A., Lekki, J.D.: Detecting cracked rotors using auxiliary harmonic excitation. J. Sound Vib. **330**(7), 1365–1381 (2011)
10. Gasch, R.A.: A survey of the dynamic behaviour of a simple rotating shaft with a transverse crack. J. Sound Vib. **160**(2), 313–332 (1993)
11. Mayes, I.W., Davies, W.G.R.: Analysis of the response of a multi-rotor-bearing system containing a transverse crack in a rotor. ASME J. Vib. Acoust. Stress Reliab. Des. **106**(1), 139–145 (1984)
12. Penny, J.E.T., Friswell, M.I.: Simplified modelling of rotor cracks. In: Proceedings of the ISMA 27, Leuven, Belgium, pp. 607–615 (2002)
13. Penny, J.E.T., Friswell, M.I.: The dynamics of cracked rotors. In: Proceedings of the IMAC XXV, Orlando, Florida, paper 198 (2007)
14. Friswell, M.I., Penny, J.E.T., Garvey, S.D., Lees, A.W.: Dynamics of Rotating Machines, 512 pp. Cambridge University Press (2010)